

**INSTABILITY OF HARD ROCKMASSES:
THE ROLE OF
TENSILE DAMAGE AND RELAXATION**

by

Mark Stephen Diederichs

A thesis
presented to the University of Waterloo
in fulfillment of the
thesis requirement for the degree of
Doctor of Philosophy
in
Civil Engineering

**Waterloo, Ontario, Canada, 1999
© Mark S. Diederichs 1999**



National Library
of Canada

Acquisitions and
Bibliographic Services

395 Wellington Street
Ottawa ON K1A 0N4
Canada

Bibliothèque nationale
du Canada

Acquisitions et
services bibliographiques

395, rue Wellington
Ottawa ON K1A 0N4
Canada

Your file *Votre référence*

Our file *Notre référence*

The author has granted a non-exclusive licence allowing the National Library of Canada to reproduce, loan, distribute or sell copies of this thesis in microform, paper or electronic formats.

The author retains ownership of the copyright in this thesis. Neither the thesis nor substantial extracts from it may be printed or otherwise reproduced without the author's permission.

L'auteur a accordé une licence non exclusive permettant à la Bibliothèque nationale du Canada de reproduire, prêter, distribuer ou vendre des copies de cette thèse sous la forme de microfiche/film, de reproduction sur papier ou sur format électronique.

L'auteur conserve la propriété du droit d'auteur qui protège cette thèse. Ni la thèse ni des extraits substantiels de celle-ci ne doivent être imprimés ou autrement reproduits sans son autorisation.

0-612-51189-8

Canada

BORROWER'S PAGE

The University of Waterloo requires the signatures of all persons using or photocopying this thesis. Please sign below, and give address and date.

Signature	Address	Date

ABSTRACT

In low stress environments, stability of rockmasses around underground excavations is typically controlled by rockmass structure. At depth and in highly stressed areas the rockmass strength controls stability. Tensile strength and tensile damage processes as well as abutment relaxation or reduced confinement often play dominant roles as agents of rockmass conditioning and failure control. This study focuses primarily on stability issues related to underground excavations in “hard” rockmasses, rockmasses that are sparsely to moderately jointed with rock of high strength, high stiffness, and brittle response.

This thesis is divided into two parts. In Part I, the author examines structurally dominated failure modes, investigating the role of residual tensile rockmass strength and relaxation on the stability of tunnels and mining stopes. Because of the demonstrated significance of these mechanisms, the results of this study are used to modify empirical design tools for stability assessment.

In Part II, the author investigates the importance of microscopic and mesoscopic tensile crack growth on compression-induced damage and near-excavation fracturing of heterogeneous rockmasses at depth. The sensitivity of insitu rockmass compressive strength to low near-excavation confining stress is examined. It is demonstrated that tensile failure processes, even under moderately compressive stress fields, control rockmass failure and fracture development near excavations in hard rock. The findings of this work explain the success of empirical strength criteria and damage prediction tools, improving confidence for future design applications.

Two simple numerical analogues for rock and rockmass behaviour are used in this study. The voussoir beam model is applied to the study of structurally controlled instability while an elastic-brittle bonded-contact discrete element model is used to study damage processes of stressed rock.

For excavations in sparsely to moderately jointed hard rockmasses, the extent of gravity driven failures can be prevented or limited if the joints, which bound the potentially unstable blocks, are even slightly discontinuous. That is, even a small proportion of intact area (rock bridge) over the plane of a joint can generate significant self-supporting, load bearing capacity. The support pressure achieved for most practical support systems can be matched by a very small proportion of rock bridges as demonstrated using example analyses of wedge and jointed beam (voussoir) stability. This observation has implications for short-term or first-pass support design as well as for accurate back analysis of failures and stability assessment of areas that are affected by mining.

Limit equilibrium analyses of rock blocks and wedges are highly conservative if the effects of clamping (compressive stresses) are ignored. Conversely, abutment relaxation or unclamping of excavation backs and walls may also be a significant factor controlling rockmass stability and failure. This relaxation can be the result of geometry change, mining induced local stress change, e.g., undercutting or inappropriate wall design, or abutment deterioration. Empirical stope and tunnel design guidelines are modified in this work to account for the effects of relaxation.

An empirical insitu damage criteria for use with elastic models, based on a reduced uniaxial compressive strength intercept ($\sigma_1 = 30$ to 50% of laboratory *UCS*) and a limited dependency on confining stress, σ_3 ($\Delta\sigma_1 = 1$ to 1.5 times $\Delta\sigma_3$), has proven useful and dependable for the prediction of rockmass damage around excavations. This criterion closely resembles the experimentally determined threshold for crack initiation in laboratory and field scale tests. The success of this approach is related to the nature of the damage process in hard rock.

Two important aspects of this process, investigated in this thesis, are the tensile nature of damage mechanisms and the consequent sensitivity to low confinement conditions. Mechanisms of extension crack initiation, accumulation and interaction and the impact of low effective confining stress are explored through a review of the nature of solid bonding and damage, a study of granite behaviour in laboratory strength tests, and through the use of a bonded contact analogue. In particular, the numerical model, Particle Flow Code (discrete element) is used to examine, as a baseline case, a damage accumulation process in which individual crack extension is restricted.

While such accumulation in a heterogeneous solid shows a first order sensitivity to confinement, it is then demonstrated that increased sensitivity, to low confinement, of actual rockmass yield strength is related to the mechanics of crack extension. Rock yield strength is shown to be coincident with the onset of crack interaction. Mechanisms which cause individual nucleating cracks to extend further, do significantly increase the interaction potential and reduce the yield strength. A number of mechanisms affecting this process are addressed in this work.

Finally, it is shown that many of these mechanisms act together insitu, reducing the yield strength of rockmasses to the crack initiation threshold. These findings improve our understanding of the rockmass failure process and explain the success, in near-excavation conditions, of the empirical damage threshold described above. Now, verified mechanistically, this threshold, used with robust three dimensional elastic boundary element analyses, can be applied with confidence to determine the potential extent of excavation-induced rockmass damage and associated support requirements for complex mine openings or underground civil works.

ACKNOWLEDGEMENTS

This research was funded by the Natural Sciences and Engineering Research Council of Canada and by the Geomechanics Research Centre, Sudbury, Canada.

Many individuals have contributed to this research:

Dr. Peter Kaiser provided support, inspiration and motivation to complete this work.

A special thanks to Dr. Derek Martin for being an indispensable resource and a valued friend, and to Drs. Evert Hoek, Bruce Hutchinson, Dougal McCreath, Dwayne Tannant and Maurice Dusseault for the emails and discussions which gave wind to my sails in times of need.

Dr. Dave Potyondi and Dr. Peter Cundall provided valuable assistance in the early stages of the numerical experimentation while Dr. Leo Rothenburg first opened my eyes, elegantly and enthusiastically to the hidden wonders of discrete simulation and micromechanics.

In addition to creating an atmosphere of collaborative discovery and symbiotic inspiration, my fellow graduate students and good friends, Veronique Falmagne, Jay Aglawe, Jane Alcott, Fidelius Suorineni, Samantha Espley, Chris Langille, Luis Castro and Chris Lee have collectively been an invaluable support system.

For putting up with my ups and downs, for lending an ear here and for offering sage advice there, eternal thanks are due to my mother Pamela and my sisters Rebecca and Sara.

This work would never have been completed without the unwavering strength and support provided by my incredible wife, Dr. Douglas Jean Hutchinson, and the joyful inspiration and perspective provided by our little treasures Kaitlyn Douglas and Elizabeth Valentine.

DEDICATION

To

KARL "VON" DIEDERICHS

1932-1983



IN MEMORIUM

TABLE OF CONTENTS

Abstract	iv
Acknowledgements	vi
Dedication.....	vii
Table of Contents	viii
List of Tables	xvi
List of Illustrations	xviii
Nomenclature.....	xi
1. Introduction	1
1.1. Rockmass instability	1
1.2. Research focus.....	2
1.2.1. Terminology.....	4
1.2.2. Tensile strength and relaxation in structural instability.....	6
1.2.3. Tensile strength and relaxation in stress driven instability	7
1.3. Approach.....	8
1.4. Objectives.....	9
1.4.1. Part I.....	9
1.4.2. Part II.....	9
1.5. Synopsis of findings.....	11
1.5.1. Part I: Structurally controlled instability	11
1.5.2. Part II: Stress driven instability.....	12
1.6. Practical implications.....	14
1.7. Thesis structure.....	15
PART I:	
Structural or gravity driven instability.....	17
2. Tensile strength and relaxation: Control mechanisms for structural failure.....	19
2.1. Introduction	19
2.1.1. Stability assessment.....	20
2.1.2. Short term strength and delayed failure.....	21
2.2. Structural stability.....	22
2.2.1. Structural failures at Canadian mines	22
2.2.2. Evidence of clamping as a failure control.....	27

2.3. Boundary-normal tensile strength.....	29
2.3.1. Tensile fracture strength models	30
2.3.2. Support equivalency of rock bridges	37
2.3.3. Strength corrosion and time dependency.....	39
2.4. Relaxation as a destabilizing mechanism.....	40
2.4.1. Clamping, joint friction and wedge stability.....	40
2.4.2. Induced relaxation and ground failure.....	44
2.4.3. Relaxation and failure of laminated ground.....	48
2.5. Summary	52
3. The voussoir analogue for laminated rock masses	53
3.1. Introduction	53
3.1.1. General voussoir-type conditions	54
3.1.2. Development of the voussoir analogue	55
3.1.3. Voussoir failure modes	56
3.2. The voussoir model	58
3.2.1. The simple elastic beam	58
3.2.2. The fractured or jointed beam	59
3.2.3. A rational “buckling limit” for forward design	67
3.2.4. Significance of the compression arch assumption	72
3.3. Field evidence of snap-through limit	73
3.3.1. Mount Isa Mine	73
3.3.2. Winston Lake Mine	75
3.4. Numerical verification (snap-through)	79
3.5. Stability guidelines	86
3.6. Discussion	93
4. Tensile Strength, Relaxation and the Voussoir Beam	95
4.1. Introduction	95
4.1.1. Review of the voussoir solution	95
4.1.2. Incorporation of relaxation and interlaminar bridging	99
4.2. Boundary normal tensile strength	100
4.3. Abutment relaxation and the voussoir beam	105
4.3.1. Relaxation and equivalent elastic tensile stress	105
4.3.2. Relaxation and beam response	107
4.3.3. Critical span reduction by relaxation	110

4.4. Relaxation and empirical design	111
4.4.1. Elements of rockmass classification - the Q system	113
4.4.2. The Modified Stability Graph technique	116
4.4.3. Calibration of the voussoir model to the Stability Graph	118
4.4.4. Application of relaxation adjustment to no-support limit	123
4.5. Application to empirical support design	127
4.5.1. Cablebolt support database	127
4.5.2. Cablebolt support function	128
4.5.3. Cablebolt design recommendations	130
4.5.4. Relaxation and cablebolt support	132
4.6. Summary	133
PART II:	
Stress Driven Instability	135
5. Strength of hard rockmasses near excavations: Review and background	137
5.1. Introduction	137
5.2. Rock strength and failure - a review	143
5.2.1. Strength of geomaterials	143
5.2.2. Non-linear techniques and fracture theory.....	146
5.3. Insitu strength of competent rockmasses	155
5.3.1. Empirical strength of non-massive rockmasses	155
5.3.2. Damage observations in hard rocks	157
5.3.3. Insitu crack initiation	161
5.3.4. Crack initiation thresholds	167
5.4. Empirical evidence of insitu damage threshold	171
5.4.1. Damage around square openings ($\sigma_3/\sigma_1 = 0.5$)	171
5.4.2. Other excavation shapes	176
5.5. Case examples of insitu damage threshold	178
5.5.1. Mine-by test tunnel - URL	178
5.5.2. Victor Mine shaft	185
5.5.3. Creighton Mine: Deep levels and SNO excavation	189
5.5.4. Sudbury Neutrino Observatory	195
5.5.5. Damage accumulation levels - discussion	198
5.6. Summary	199

6. Tensile Strength and Compressive Damage	201
6.1. Introduction	201
6.1.1. Extension cracking and rock failure	201
6.1.2. Structure of the chapter.....	205
6.2. Rock as a bonded solid	207
6.3. Damage initiation and Accumulation.....	221
6.3.1. Damage initiation criterion	221
6.3.2. Crack accumulation and interaction	223
6.3.3. Rock testing and stress paths	226
6.3.4. Damage measurement.....	227
6.3.5. Comparison of tensile strength and <i>UCS</i>	230
6.3.6. Tensile and compressive damage: a case for distinct thresholds	230
6.4. Test configurations	233
6.4.1. Direct tensile testing of rock samples	233
6.4.2. Fracture toughness - Mode I and II	234
6.4.3. Brazilian test - indirect tensile strength	236
6.4.4. Uniaxial and confined compression	241
6.5. Properties of Lac du Bonnet granite	243
6.6. Tensile testing of Lac du Bonnet granite	245
6.7. Brazilian testing of Lac du Bonnet granite	251
6.8. Compressive tests on Lac du Bonnet granite	258
6.8.1. Damage initiation	258
6.8.1.1. Confinement dependency of crack initiation	258
6.8.1.2. Unconfined crack initiation	261
6.8.2. Effect of unloading or sample damage	263
6.8.3. Sliding crack model vs. Griffith tensile crack	267
6.8.4. Damage initiation and accumulation	271
6.8.5. Confinement dependency of damage interaction	277
6.9. Discussion	283
7. A Bonded contact analogue for damage accumulation	287
7.1. Introduction	287
7.1.1. Stress flow and bond rupture - a schematic model	290
7.1.2. Numerical model selection	294
7.2. Discrete element basics	298

7.2.1.	Computation cycle and contact stiffness	298
7.2.2.	Contact models	301
7.2.3.	Stresses and strains	303
7.2.4.	Fabric and damage	306
7.2.4.1.	Fabric and crack tensors	306
7.2.4.2.	Crack intensity	308
7.2.4.3.	Crack anisotropy	308
7.2.4.4.	Crack interaction	310
7.2.4.5.	Energy measurements and damage	310
7.2.5.	Stress and strain relationships	311
7.2.5.1.	Elastic strain - Young's modulus and Poisson's ratio	311
7.2.5.2.	Strain measurement	313
7.2.5.3.	Linear and non-linear strain	314
7.2.5.4.	Inelastic strain and dilation	315
7.2.6.	Other internal descriptors	317
7.2.6.1.	Coordination number, porosity, sliding fraction	317
7.2.6.2.	Cumulative rotation	317
7.2.6.3.	Crack number and crack rate	317
7.3.	Creation and calibration of model	318
7.3.1.	Unconfined compression of Lac du Bonnet granite	318
7.3.2.	Sample creation	319
7.3.3.	Boundary conditions	323
7.3.3.1.	Lateral stress/strain control and confining stress	323
7.3.3.2.	Deviatoric stress/strain application	324
7.3.4.	Bond stiffness calibration	325
7.3.5.	Bond strength calibration	328
7.3.6.	Loading rate	333
7.3.7.	Shape effects	334
7.3.8.	Locked in stresses	335
7.4.	Compressive sample behaviour	337
7.4.1.	Typical test results	337
7.4.2.	Damage thresholds	339
7.4.2.1.	Sampling or unloading damage	341
7.4.2.2.	First crack (loading)	341
7.4.2.3.	Systematic crack growth and crack density	341

7.4.2.4. Primary (first) interaction	344
7.4.2.5. Damage and strain localization	345
7.4.2.6. Peak and ultimate damage	345
7.4.3. Dilation phases	346
7.4.4. Tensile versus shear bond strength	348
7.4.5. The importance of crack interaction	352
7.5. Uniaxial compression test summary	353
7.6. Compression at low to moderate confinement	356
7.6.1. Damage thresholds	357
7.6.2. Damage and lateral strain	359
7.6.3. Peak and post peak strain	362
7.6.4. Compression test simulation summary	364
7.7. Tensile test simulations	365
7.7.1. Tensile test samples	366
7.7.2. Typical results	368
7.8. Tensile strength and confinement	373
7.8.1. Confined direct tensile tests	373
7.8.2. Brazilian test simulation	377
7.8.3. Critical crack intensity in tension and compression	385
7.9. Discussion and summary	386
7.9.1. The bonded disc analogue for rock failure	386
7.9.2. Lessons regarding rock damage and yield	388
8. Insitu strength reduction: Heterogeneity, scale, stress path and confinement	391
8.1. Introduction	391
8.1.1. Strength reduction mechanisms	393
8.2. Elemental variation and damage initiation	398
8.2.1. Elemental strength variation and weak link theory	398
8.2.2. Elemental stiffness variation	403
8.2.3. Contact property variation - compression simulations	407
8.3. Scale Effect	411
8.3.1. Effect of internal flaw size	411
8.3.2. Fracture initiation, propagation and yield	414
8.3.3. Scale effects in compressive test simulations	417
8.4. Statistical weak link theory	428

8.4.1.	A serial model for crack initiation and accumulation	428
8.4.2.	A new statistical model for interaction	434
8.5.	The effect of pre-existing damage	439
8.5.1.	A statistical model for pre-existing damage	440
8.5.2.	UCS simulations with pre-existing damage	443
8.5.3.	Comparison of UCS simulations to statistical model	451
8.5.4.	Stress path and damage initiation	452
8.5.5.	Effect of confinement and pre-existing damage (no crack extension)	454
8.5.6.	Effective gap	457
8.6.	The effect of crack length and confinement	460
8.6.1.	Statistical consideration of crack length	460
8.6.2.	Effect of confinement on isolated crack propagation	463
8.6.3.	Effect of propagation on critical crack density	467
8.6.4.	Crack interaction with a free surface	470
8.6.5.	Stress gradients and crack extension	476
8.7.	Variable confinement and local tension	478
8.7.1.	Heterogeneity and local tension	478
8.7.2.	Geometric sources of local tension	489
8.8.	Primary shear failure and local tension	492
8.8.1.	The effect of notch propagation - circular tunnel	492
8.8.2.	Corner crushing and wall tension - rectangular tunnel	499
8.8.3.	Geometric correction around mine pillars	501
8.9.	Discussion	504
9.	Summary, conclusions and recommendations	505
9.1.	Summary	505
9.1.1.	Tensile strength and relaxation in structural domains	505
9.1.2.	Tensile strength and relaxation in stressed rockmasses	507
9.2.	Conclusions	508
9.2.1.	Wedge stability in underground excavations	508
9.2.2.	The voussoir analogue	508
9.2.3.	Stability of laminated or blocky rockmasses	509
9.2.4.	Empirical insitu strength	510
9.2.5.	Rock as a bonded solid	510
9.2.6.	A bonded disc analogue for rock	512

9.2.7. Insitu strength reduction	514
9.3. Recommendations	515
9.3.1. Structural failure and the voussoir model	515
9.3.2. The bonded disc analogue	516
9.3.3. Rock strength and damage assessment	516
REFERENCES	517
Software Summary	548
APPENDIX A: Effect of confining stress on a symmetric roof prism.....	549
A.1. Horizontal force and pullout force.....	549
A.2. Factor of safety, stress and span.....	551
APPENDIX B: NTBEAM: Routines for parametric voussoir solution	553
APPENDIX C: Catalogue of FISH routines for PFC simulations	555
C.1. FISH routines created by Itasca Ltd.	555
C.2. FISH routines modified by the author	556
C.3. FISH routines created by the author	556
APPENDIX D: Stress intensity factors for a sliding crack.....	559
D.1. Wing crack initiation	559
D.2. Wing crack growth for an isolated crack	560
D.3. Interaction with a free surface.....	564

LIST OF TABLES

Table 2.1:	Support patterns (from Stillborg 1994) and equivalent rock bridge area (N = 125)	38
Table 3.1:	Minimum predicted thickness, t (m) from this analysis (ubiquitous joint assumption), and UDEC results from Sofianos (1998) for the 3-Hinge Beam. UDEC results presented as a range of Stable - Failed.	85
Table 3.2:	Maximum predicted span (m) and UDEC results (this study) for the ubiquitously jointed beam ($t=1m$).	85
Table 4.1:	RQD and J_n for the Q System.....	113
Table 4.2:	J_r values for the Q system - roughness of the dominant joint set.....	113
Table 4.3:	J_a values for the Q system - condition of the dominant joint set	114
Table 4.4:	J_w values for the Q system - water inflow and pressure.....	114
Table 4.5:	Excavation Support Ratio (modified after Barton 1988).....	115
Table 5.1:	Typical damage initiation and yield criteria used for rock materials.	145
Table 5.2:	Adjusted Hoek-Brown strength parameters for rockmasses (modified after Hoek et al. 1995).	156
Table 5.3:	Analysis and conversion of Wiseman's (1978; 1979) damage database, with stresses normalized with respect to <i>UCS</i>	175
Table 5.4:	Far field stresses at depth of URL Mine-By Tunnel (Martin, 1997).	181
Table 6.1:	Examples of uniaxial compression thresholds for various rock types.	229
Table 6.2:	Properties of Lac du Bonnet granite.	243
Table 6.3:	Direct tensile test summary data for Lac du Bonnet granite.	245
Table 6.4:	Summary of crack accumulation thresholds for Brazilian tests on Lac du Bonnet granite.	254
Table 6.5:	Examples of uniaxial compression thresholds for various rock types.	262
Table 6.6:	Damage initiation stress for Lac du Bonnet granite.	262
Table 6.7:	Summary of damage thresholds for cycle tests in terms of axial stress and lateral strain.	275
Table 6.8:	Critical damage thresholds for confined compression tests at URL 420m level.	279
Table 7.1:	Target parameters for Granite simulation.	318
Table 7.2:	Parameters (calibrated for this work) used in "granite" simulations.	319
Table 7.3:	Primary mechanical properties (14 samples).	353
Table 7.4:	Detailed damage threshold data.	354
Table 7.5:	Uniaxial compressive stress in MPa and lateral strain ($\times 10^{-3}$) damage thresholds in PFC simulations and Lac du Bonnet granite for 240 Level to surface quarry.	354

Instability of Hard Rockmasses: The Role of Tensile Damage and Relaxation

Table 7.6:	Damage threshold data for direct tension.	372
Table 7.7:	Detailed damage threshold data.	384
Table 8.1:	Key minerals affecting the strength of Lac du Bonnet Granite.	400
Table 8.2:	Parameters used in PFC simulations shown in Figures 8.19 through 8.21.	408
Table 8.3:	Scale effect simulation samples.	417

LIST OF ILLUSTRATIONS

Figure 1.1:	Influence of stress and structure on rockmass failure modes (modified after Hoek et al 1995).....	2
Figure 1.2:	Issues for structural instability examined in this thesis: a) Residual tensile strength due to rock bridges and incomplete jointing; b) Excavation parallel confinement (top) and abutment relaxation (bottom)	3
Figure 1.3:	Issues for stress driven instability examined in this thesis: a) Compression induced extension crack growth; b) boundary parallel spalling; c) Crack propagation, yield strength and low confinement sensitivity.....	4
Figure 1.4:	Explanation of confinement dependency (and independency) in deviatoric-hydrostatic stress space (left) and principal stress space (right).....	5
Figure 1.5:	a) Increased confinement around well designed civil excavation b) relaxation due to complex mining geometries	6
Figure 1.6:	Empirical threshold for insitu damage in moderately jointed hard rockmasses.....	7
Figure 1.7:	Numerical analogues: a) Voussoir beam; b) bonded contact discrete elements.....	8
Figure 1.8:	Yield thresholds (crack initiation) for a) bonded contact analogues and b) laboratory test samples of real rock. Crack propagation dominates at low σ_3 in b).....	13
Figure 1.9:	Insitu strength reduction, near excavations, to crack initiation threshold.....	13
Figure 2.1:	Gravity collapse of moderately jointed to massive ground after stress induced fracturing (Brunswick Mine, N.B.).....	21
Figure 2.2:	Relative percentages of failure mechanisms identified in major groundfalls at mines in the Sudbury Region.....	23
Figure 2.3:	Kinematically feasible (present but not necessarily failed) wedges formed from intersecting joints in Figure 2.4. (Main accessway at North Mine 175 Ore Body).....	23
Figure 2.4:	Joints mapped in the back of the main access at INCO's North Mine 175 Orebody	24
Figure 2.5:	Wedge failure in the back of a stope. Material in foreground is backfill.	24
Figure 2.6:	Boundary parallel laminations in underground excavation back (a) and stope walls (b and c).	25
Figure 2.7:	Failure of a voussoir arch in a laminated stope back. Tendons visible are failed cablebolt supports.....	26
Figure 2.8:	Stress induced boundary parallel spalling resulting in laminations that failed under gravity loading due to stress change and relaxation. Horizontal field of view is (left) 4m and (right) 5m. Direction of original compression shown by arrows.	26

Figure 2.9: Examples of dominant joint sets from two INCO mines. Most prominent roof wedges shown in dark shading. Light shading at right indicates a 2-D roof prism.....27

Figure 2.10 Examples of typical (theoretical) full span wedges at INCO's Sudbury mines. these wedges are formed from the most probable joint intersections in Figure 2.9.....28

Figure 2.11: Actual wedge aspect ratios (for groundfalls at INCO mines) with respect to excavation span and to actual wedge base width (Hutchinson 1998).....28

Figure 2.12: Crack geometries: a) 2D non-interacting crack; b) 2D rock bridge; c) 3D assembly of cracks; d) 3D isolated non-interacting crack; e) 3D isolated rock bridge.....30

Figure 2.13: Tensile strength vs. normalized cracked cross-sectional area.....32

Figure 2.14: Example of Griffith Locus and vertical stiffness relationships for a rock sample containing isolated horizontal cracks.....35

Figure 2.15: Example of Griffith Locus and vertical stiffness relationships for rock sample containing isolated horizontal rock bridges.36

Figure 2.16: Example of residual tensile strength of rock bridges ($N=125m^3$) acting as effective wedge support (gravity loaded 45 degree prismatic wedge).39

Figure 2.17: Example of clamped wedge stability (for geometry and joint friction as shown).41

Figure 2.18: Example of clamped wedge stability (for steeper wedge than Figure 2.17).42

Figure 2.19: Equivalent support pressure required to maintain F.S.=1 at varying confinements. The capacity of a typical cablebolt support system is shown for comparison.43

Figure 2.20: Stereonet representation of wedges which are a) unstable; b) stable with confinement but unstable if clamping stresses are relaxed; b) highly stable except under extreme (tensile) relaxation. (total joint friction angle = 45 degrees).....43

Figure 2.21: Liberation and failure of steep wedges due to a) low stress near surface; b) localized deflection-induced tangential relaxation.....44

Figure 2.22: a) High induced compressive (horizontal) stresses aligned parallel to back of isolated mining drift ($\sigma_H / \sigma_V = 2$); b) Induced tension or relaxation parallel to drift back adjacent to large subvertical stope; c) Induced hangingwall relaxation (expressed as equivalent elastic tension parallel to face) due to long stope axis perpendicular to major principle stress. Stresses are in MPa.45

Figure 2.23: A portion of model geometry (using Map3D) for Stobie Mine. Bounded area in central pillar indicates a large cave which was observed above the 1600 topsill.46

Figure 2.24: Section (Grid 3 in figure 2.23) showing calculated elastic tensile stresses corresponding to observed caving zone above stope back (1600 level).....46

Figure 2.25	735 stopes at Kidd #3 Mine (Falconbridge Ltd.) showing drill layout, cavity surveys (with observed hangingwall caving) and cablebolt support.	47
Figure 2.26	Major and minor principal stresses (red indicates tension) after successive mining steps (note that field of view shifts upwards in views above as mining progresses).	48
Figure 2.27:	Failure of jointed hangingwall due relaxation of lower abutment above crosscut (modified after Hutchinson and Diederichs 1996)	49
Figure 2.28:	Stress changes monitored in the hangingwall during the excavation in Figure 2.27. (modified after Kaiser and Maloney 1992).	49
Figure 2.29:	UDEC simulation of failure in Figure 2.27; Significant inelastic softening of lower abutment in model was required to induce failure (modified after Kaiser and Maloney 1992;1993).....	50
Figure 2.30:	Relaxation due to a) & b) unfavourable stress ratio; c)&d) changes in mining geometry (excavation step 2 creates stress shadow around excavation 1); e) abutment yield; f) intersection (roof relaxes in the direction of tunnel branches); g) undercut; h) concave geometries.....	51
Figure 3.1:	a) Jointed rock beams; b) Voussoir beam analogue.	54
Figure 3.2:	Voussoir beams encountered at a) Winston Lake Mine, Ontario, and b) North Mine, Sudbury.....	55
Figure 3.3:	Failure modes of the voussoir beam: a) snap-through; b) crushing; c) sliding; d) diagonal cracking.....	57
Figure 3.4:	Elastic Beam with a) fixed ends and b) simple (pin) supports.....	59
Figure 3.5:	Voussoir beam (half-span shown) and nomenclature.....	60
Figure 3.6:	External beam loading due to : a) uniformly distributed support pressure; b) linearly varying support pressure; c) parabolically varying support pressure and d) parabolically varying surcharge loading.	62
Figure 3.7:	Conventional assumptions for compressive stress variation inside the beam compared with the parabolic variation proposed in this paper.	64
Figure 3.8:	Flow chart for the determination of stability and deflection of a voussoir beam.	66
Figure 3.9:	Variation of N and Buckling Limit with span to thickness ratio.....	68
Figure 3.10:	Example determination of beam “yield” limit (example span = 20m).....	69
Figure 3.11:	Effect of Buckling Limit on critical beam geometry for snap-through failure of a horizontal beam ($E_{rm}=10$ GPa, $\gamma=0.03$ MN/m ³).	70
Figure 3.12:	Typical critical limits for the stability of slender beams (Axis scales are identical for both plots).....	71
Figure 3.13:	Influence of surcharge loading on beam stability and failure mode.....	72
Figure 3.14:	Laminated Hangingwalls at Mount Isa Mine (Photo courtesy MIM. Pty).	73
Figure 3.15:	Hangingwall response to mining compared with voussoir limits. Based on extensometer data from Milne (1996).	75

Figure 3.16:	Potential parting planes in foliated chert hangingwalls at Winston Lake Mine (hangingwall boundary to the left)	76
Figure 3.17:	Plan layout and typical cross sections through study area - Winston Lake Mine.....	77
Figure 3.18:	Measured displacements and observed lamination thicknesses (data points), compared with voussoir predictions - Winston Lake Mine.....	78
Figure 3.19:	Rockmass stiffness for a uniformly jointed rockmass.....	80
Figure 3.20:	Exaggerated displacement profile (top) for a typical UDEC voussoir beam simulation and contours of internal horizontal compressive stress (bottom).	81
Figure 3.21:	Predicted variation of horizontal stress along arch axis (ABC) compared with UDEC results (top) and predicted and simulated stress distributions at abutment and at midspan (bottom).	82
Figure 3.22:	Midspan displacements (data points) from UDEC beam simulations compared with voussoir predictions (T = 1m).....	83
Figure 3.23:	Maximum compressive stress in UDEC beams compared with voussoir predictions (T=1m).....	84
Figure 3.24:	Empirical relationships between rockmass modulus and rockmass classification.	87
Figure 3.25:	Non-linear joint stiffness response under low confinements.	87
Figure 3.26:	Simplified relationships for rockmass modulus as a function of rock quality and confinement.	88
Figure 3.27:	Stability guidelines for jointed rock beams (tunnel spans). Effective Specific Gravity, $S.G.*=S.G.\cos\alpha$	89
Figure 3.28:	Stability guidelines for jointed rock plates (square spans). Effective Specific Gravity, $S.G.*=S.G.\cos\alpha$	90
Figure 3.29:	Examples of parallel weight correction to critical span for inclined beams.....	93
Figure 3.30:	Corrected equilibrium midspan deflections for stable steeply dipping beams (dip=80 degrees), accounting for parallel weight component.	94
Figure 4.1:	Voussoir design charts for horizontal tunnel and square span ($\gamma=30\text{kN/m}^3$); Maximum stable span for a given thickness is the minimum value determined from Erm or UCS limit.....	98
Figure 4.2:	Definition of a) abutment relaxation and b) interbed tensile strength due to interlaminar rock bridges.....	99
Figure 4.3:	Composite ground reaction curve for laminated rockmass based on voussoir calculations: (Span=20m; $E=10\text{GPa}$; $\gamma=30\text{kN/m}^3$; UCS = 25MPa); Response curves for typical support patterns are shown for comparison; Internal tensile strength refers to boundary normal strength.....	101
Figure 4.4	Ground reaction curve: Relationship between rockmass modulus and tensile support demand (Span = 20m; Buckling Limit, B.L. =100%).....	102

Figure 4.5	Limiting demand for boundary normal tensile strength in laminated ground (Modulus = 10 GPa; Collapse B.L. = 100%; Yield B.L. = 35%).....	104
Figure 4.6	Effect of modulus on minimum tensile strength demand (B.L.=100%).....	105
Figure 4.7:	a) Calculated tension across an drift back and b) equivalent abutment relaxation	106
Figure 4.8:	Calculated tension across a hangingwall and equivalent abutment relaxation, δ	106
Figure 4.9	Equivalent elastic tension corresponding to abutment displacement.	107
Figure 4.10	Ground reaction curves for laminated ground illustrating the impact of abutment relaxation (Modulus=10GPa, B.L. =100%, Span=20m)	108
Figure 4.11	Impact of abutment relaxation on the minimum demand for boundary normal tensile strength (B.L. =100%)	109
Figure 4.12:	Same simulation as in Figure 4.11 showing limits for yield (B.L. =35%) and collapse (B.L. =100%)	109
Figure 4.13	Critical relaxation limits for unsupported voussoir beam: $E_{rm}=10GPa$	110
Figure 4.14:	a) Effect of modulus on critical relaxation or critical span.....	110
Figure 4.15	Elements of rockmass classification - properties controlling rockmass behaviour	111
Figure 4.16:	Relationship between engineering behaviour and rockmass classification	112
Figure 4.17:	Support recommendations for underground tunnels based on the Q system (modified after Grimstad et al. 1993 and Hutchinson and Diederichs 1996).....	112
Figure 4.18:	Evaluation of Stress Reduction factor, SRF of non-faulted and non-swelling rockmasses (Hutchinson and Diederichs 1996). Adjustments for discrete weakness zones given by Barton et al. 1974.....	114
Figure 4.19:	Case history database for the Q system (modified after Barton 1988).....	115
Figure 4.20:	No-support limits for underground mining applications (modified after Hutchinson and Diederichs 1996).....	115
Figure 4.21:	Stability parameters for the Modified Stability Graph (modified after Hutchinson and Diederichs 1996).....	116
Figure 4.22:	Calculation of "Hydraulic Radius", HR for use in the Stability Chart.	117
Figure 4.23:	Unsupported stope data from Potvin (1988) and Nickson (1992) and No-Support Limits for Modified Stability Graph (Hutchinson and Diederichs 1996).....	117
Figure 4.24:	Variation with respect to N' of voussoir parameters used in this simulation (for model calibration purposes only)	119
Figure 4.25:	Voussoir calibration for square span. Linear tunnel spans require geometric correction.....	120
Figure 4.26:	Revised no-support limits for N' resulting from abutment relaxation (negative relaxation values in mm correspond to stope wall compression).....	121

Figure 4.27:	No-Support Limits resulting from abutment relaxation plotted with respect to LogHR: Function shown is for Potvin's (1988) upper No-Support Limit.	122
Figure 4.28:	Equivalent elastic tensile stresses corresponding to the relaxation displacements in Fig. 4.27	123
Figure 4.29	Correlation of relaxation adjustment for upper no-support limit; Slope backs were under moderate to high compression while elastic models predicted tension in hangingwalls	124
Figure 4.30:	Revised definition of Stress Factor, A, used to determine the Modified Stability Number, N'. For consistency with compressive function, relaxation is reflected as the normalized maximum tension parallel to the face near midspan.	125
Figure 4.31:	Tangential elastic tensile stresses corresponding to abutment relaxation and the shift in the Q no-support limit; Q limits are calculated from N' limits in Figure 33; ESR limits (Barton 1988) are plotted for comparison.....	126
Figure 4.32:	Cablebolted stope data (Potvin, 1988; Nickson, 1992) and cablebolting limits.....	127
Figure 4.33:	Primary cablebolt functions in open stopes.	128
Figure 4.34:	Maximum cablebolt spacing to control unravelling (after Hutchinson and Diederichs 1996).....	129
Figure 4.35:	Zones of critical support function (i.e. the support function which dictates the maximum recommended cablebolt spacing)	130
Figure 4.36:	Pattern spacing recommendations for single strand cablebolts.....	131
Figure 4.37:	Pattern spacing recommendations for double strand cablebolts.	131
Figure 4.38:	Adjusted spacing requirements for hangingwalls with moderate tangential relaxation (tension = 10 to 20 MPa in elastic models).	132
Figure 4.39:	Reduction in frictional bond strength of plain strand grouted cablebolts due to rockmass stress change after installation (Hutchinson and Diederichs 1996).....	133
Figure 5.1	Stages of yield in hard rocks.....	138
Figure 5.2:	Schematic failure modes for: a) continuum plastic shear, and b) brittle spalling.	138
Figure 5.3:	Examples of compression-induced grain-scale spall damage around a 3.5m diameter tunnel in massive granite (original courtesy of AECL Ltd.).....	139
Figure 5.4:	Examples of spall damage around deep openings at (top) Brunswick Mine, (bottom left) Bousquet Mine and (bottom right) Makassa Mine.	140
Figure 5.5:	Decay of uniaxial compressive strength with sample size for cylindrical specimens, after a) Hoek and Brown (1980), and b) Martin (1994), and c) with long-term static loading (after Schmidtke and Lajtai 1988).....	141
Figure 5.6:	Hoek-Brown yield envelopes in a) 3-dimensional (modified after Shah 1992) and b) 2-dimensional stress spaces.....	144

Figure 5.7:	Typical yield criterion (modified after Cividini 1993) a) Drucker-Prager (outer) and Von Mises; b) Mohr-Coulomb (outer) and Tresca.	146
Figure 5.8:	a) Associative and b) non-associative flow rules (Cividini 1993).	146
Figure 5.9:	Post yield response as a function of confinement in rock (after Fairhurst 1990).....	147
Figure 5.10:	Crack modes considered in fracture mechanics.	148
Figure 5.11:	Multi-mode crack interaction (after Bobet and Einstein 1996).....	149
Figure 5.12:	Scalar and tensor damage variables and examples of damage mechanics equations (after Cheng 1994; Kachanov 1980 and Sellers 1994).	150
Figure 5.13:	Discontinuum simulation of brittle rock failure (Handley 1995).	151
Figure 5.14:	Displacement discontinuity simulation of rock fracture (Napier and Hildyard 1992).	151
Figure 5.15:	Numerical simulations incorporating material heterogeneity and a simplified two stage (intact - yielded) elastic element (Tang and Kaiser 1996).....	152
Figure 5.16:	Example micromechanical assemblage with bonded contacts between discs.	153
Figure 5.17:	Contact and particle map from particle model (Potyondi et al. 1995) showing compressive forces (thick lines) flowing around circular opening (stress field sub-vertical with respect to page - tunnel rotated 90 degrees ccw.). Force -shadowed zones on roof and floor (left and right of opening in image above) sidewalls indicate areas of contact rupture and macro-failure.	154
Figure 5.18	Hoek-Brown envelope for blocky, undisturbed rock (e.g. granite).	156
Figure 5.19:	Progressive axial crack damage in laboratory samples (Martin 1994).	158
Figure 5.20:	Measurement of crack initiation and crack damage thresholds for hard rock.	158
Figure 5.21:	Typical (Hoek-Brown) envelopes for peak, critical damage σ_{cd} , and crack initiation σ_{ci} , for granite, after Read et al. (1998).	159
Figure 5.22:	Peak strengths and detectable damage initiation thresholds (onset of dilation) for slow and fast loading of Westerly Granite.	160
Figure 5.23:	a) Cylindrical slabs from uniaxial test specimen (Ormonde and Szwedzicki 1993); b) planar slabs through pillar (Brunswick Mine - courtesy P. K. Kaiser).....	163
Figure 5.24:	Notch development as a process of crack damage, localized shear (at reduced strength) and exploitation of damage through dilation and slab formation (Martin et al. 1997).....	164
Figure 5.25:	Effect of confinement on crack propagation length, c , with respect to initial flaw half length, c_0 , based on (A) experimental data for an open crack (Hoek 1965), and (B) a sliding crack relationship calculated by Martin (1997).	165
Figure 5.26:	Effect of stress gradient on damage zone (schematic).....	165

Figure 5.27:	Schematic of effective confinement (or effective gap) concept.....	166
Figure 5.28:	Reduction of strength due to humidity (from Priest and Selvakumar, 1982).....	167
Figure 5.29:	Summary of potential damage initiation criteria for Lac du Bonnet granite.....	170
Figure 5.30:	Stability classifications according to Hoek and Brown (1980).....	171
Figure 5.31:	Principal (elastic) stress distribution around a square opening with $k=0.5$	172
Figure 5.32:	Boundary stress distribution around a square opening with varying corner radii.....	173
Figure 5.33:	Conversion of Hoek and Brown stability classifications (Figure 5.30) to normalized boundary stresses.....	174
Figure 5.34:	Sidewall spalling induced by mechanical action of localized shearing (modified after Vasak and Kaiser 1995).....	176
Figure 5.35:	Excavation shapes and typical failures used in Figure 5.36.....	177
Figure 5.36:	Depth of failure around equivalent circular openings (circumscribed around actual opening) in hard rock (after Martin et al. 1996).....	177
Figure 5.37:	Location and underground layout of the Underground Research laboratory, URL (modified after Read and Martin 1991).....	179
Figure 5.38:	420 level at the URL showing the location of the test tunnel or mine-by experiment (after Martin 1996).....	179
Figure 5.39:	Non-explosive excavation procedure employed in Mine-by tunnel (after Onagi et al. 1992).....	180
Figure 5.40:	Notch formation due to spalling in roof and floor of URL "Mine-by" test tunnel (photo courtesy AECL).....	180
Figure 5.41:	Calculated elastic stresses on tunnel surface at location of notch apex (notch not simulated - cylindrical tunnel geometry only).....	181
Figure 5.42:	Microseismic event data ahead of the face plotted according to elastic stress calculations at event locations.....	182
Figure 5.43:	Notch profile, microseismic event locations, constant deviatoric stress threshold and tensile crack threshold for typical tunnel round (after Martin, 1996).....	183
Figure 5.44:	Major principal stress contours (3D stress field) and notch geometry.....	184
Figure 5.45:	Modified insitu stress relationships (based on data from Herget 1998).....	186
Figure 5.46:	Shaft spalling observations and predictions for Victor Shaft.....	187
Figure 5.47:	Typical spall and breakout in vertical bored raise (Hoek and Brown 1980).....	188
Figure 5.48:	Perspective view of Creighton Mine Deep Levels. The upper horizon shown is 6400 level. The Upper most VRM as labeled is the study area. The SNO cavern is in the foreground on 6800 level.....	189

Figure 5.49:	Longitudinal section showing the mechanical cut and fill blocks, the sills created by this method and the vertical retreat method test block beneath the 6600 topsill.....	190
Figure 5.50:	Major and Minor (top and middle) principal stresses in the center of the sill beneath 6600 topsill (top of images). The section runs north-south. The lower image is of contours of maximum shear stress (half of deviatoric stress). Stresses analyzed using a 3D boundary element elastic solution (Map3D).....	191
Figure 5.51:	Map3D model geometry for completed MCF and VRM stopes for Creighton deep (to 7200 ft level). Arrow shows the 6600-6700 VRM block.....	192
Figure 5.52:	Major principal stress around the completed 66-6700 VRM (West). Right figure shows extraction sequence for study block (plan view).	192
Figure 5.53	Observations of yielding and damage for six excavation stages (modified after Landriault and Oliver 1992).....	194
Figure 5.54:	Analysis results for grid points through the 6700 level showing damaged and undamaged zones and several likely damage initiation envelopes. The intact envelope and first two (most competent) Hoek and Brown rockmass envelopes (Table 5.1) are shown for comparison.	195
Figure 5.55:	Sudbury Neutrino Observatory: a) plan view showing instrument stations; b) numerical model geometry for cavern; c) composite section through instrument stations - numbers indicate excavation stages (modified after Castro 1996).....	196
Figure 5.56:	Summary of "yield" observations at instrument locations (based on modelling data from Castro 1996).	197
Figure 5.61:	Summary of observed damage thresholds (constant deviator shown for example) determined using observational methods of varying sensitivity.	198
Figure 5.62:	Examples of complex mine model geometries: a) Little Stobie Mine, b) McCreedy East Mine; c) Lac Short Mine; d) North Mine.(a,b,d courtesy GRC; c courtesy V. Falmagne).....	200
Figure 6.1:	a) Axial microcracks in Westerly Granite (after Wong 1982); b) cracks (dyed white) in compressive test sample of Lac du Bonnet Granite and c) excavation spall damage (AECL-URL) In all cases maximum compression is vertical.	202
Figure 6.2:	Macro-scopic shear propagation, sloping up to the right, under high confinement with secondary extension and rotational or kink cracks, sloping down to right. shear extension induced by deep South African gold stopes. (Ortlepp 1997).	202
Figure 6.3:	Microscopic section through shear fault in granite formed at very high confinement with high intensity primary extension cracking around shear surfaces. Maximum compression horizontal (modified after Wong 1982).	203
Figure 6.4:	a) Modes of solid fracture; b) Mode I crack generation in compression; c) coalescence of axial cracks to form macroscopic rupture	204

Figure 6.5:	Compression sample (compression horizontal) showing shear surface formed by coalescence of axial (sub-horizontal in picture) extension cracks, forming jagged surface of shear zone. (Courtesy AECL).....	204
Figure 6.6:	a) Macroscopic extension crack forming from interacting microcracks; b) en echelon (shear) array of interacting axial Mode I extension cracks around hole in uniaxial compression. Arrows show stress flow. (modified after Lajtai et al. 1994).	205
Figure 6.7:	Strength testing configurations used in this chapter: a) direct tension; b) Brazilian tension; c) uniaxial compression and d) triaxial compression	206
Figure 6.8:	Typical yield thresholds for a) purely frictional materials (sand); b) purely cohesive materials (metals) and c) geomechanics models (cohesion + friction).	207
Figure 6.9:	Post-yield behaviour: a) elasto-plastic; b) strain hardening/softening; c) brittle.	208
Figure 6.10:	Solid bonding types and associated damage mechanisms and dominant macroscopic strength components.....	209
Figure 6.11:	a) Potential energies due to atomic repulsion and attraction. b) Bond strength and stiffness	210
Figure 6.12:	Lattice slip: a) continuous slip and b) corresponding stress strain relationship. c) Progressive dislocation slip.....	211
Figure 6.13:	Metal bars under direct tension resulting in dislocation slip (plastic shear deformation) a) along a single set of crystal planes; b) opposing slip planes (photos after Illston et al. 1979).	212
Figure 6.14:	Strength vs. Confinement relationships (data from Lundborg 1968). Compare the purely cohesive nature of metals with the confinement dependency of other materials.	213
Figure 6.15:	Schematic comparison between plastic (continuum) shear (A) and extension crack damage mechanisms (B). B1 illustrates localization and discontinuum transition while B2 indicates full shear development through kink band rotation.....	215
Figure 6.16:	Mechanisms of extension crack generation under compressive stress: a) pore; b) Griffith crack; c) sliding crack; d) indentation; e) boundary compliance.	215
Figure 6.17:	Effect of confinement on ultimate rupture mode: a) unstable Mode I crack extension in direct tension; b) quasi-stable Mode I spalling; c) dilational shear by coalescence of axial Mode I micro-cracks; d) non-dilational shear by coalescence of Mode II lattice slip planes (very high confinement).	216
Figure 6.18:	Change in minimum potential energy state during bond rupture and resultant irreversible crack dilation (increase in separation d_2-d_1).....	216
Figure 6.19:	Cohesion loss and friction mobilization in two saturated clays. (modified after Schmertman and Osterberg (1968)).....	218
Figure 6.20:	Cohesion loss and friction mobilization deduced from cycled loading tests on granite (after Martin 1994).....	219

Figure 6.21: Uniaxial compression test simulation performed as part of this work showing final (a) ball, (b) bond rupture and (c) "meso-crack" geometry. No inter-particle shear rupture is allowed - only tensile bond rupture (damage) permitted in these tests. (d) Cross section through actual test (after Li et al. 1998) on Gneiss..... 223

Figure 6.22: Crack iso-density contours for a) non-extending cracks - accumulation only b) cracks allowed to extend under appropriate conditions (low confinement) 225

Figure 6.23: Elastic stress paths for different laboratory test configurations. 227

Figure 6.24: Strain thresholds incurred during uniaxial compression loading: a) damage initiation; b) axial non-linearity; c) volumetric strain reversal d) peak strength..... 228

Figure 6.25: Compressive/tensile strength comparison. LdB = Lac du Bonnet Granite data from this study. (Other data from Okubo and Fukui 1996 and from Lama and Vutukuri 1978)..... 230

Figure 6.26: Lac du Bonnet Granite (modified/annotated after original micrograph courtesy AECL): large filled, high friction microcrack (middle) in Quartz which could be critical in normal (vertical) applied tension; small, inclined, low friction flaws (lower left) which have generated extension wing cracks under (vertical) compression. Horizontal field width = 2.5mm..... 231

Figure 6.27: a) Direct tensile test configuration; b) Modified test geometry (after Gorski 1991); c) Confined tensile test (after Hoek and Brown 1980)..... 233

Figure 6.28: a) Mode I and II critical stress intensity factors or fracture toughness; b) Example configuration for KI determination (3 Point Bending Test) 234

Figure 6.29: Variation of KI and KII with crack length based on data from a) Okubo and Fukui (1996) and b) Laqueche et al. (1986)..... 235

Figure 6.30: Brazilian test geometry a) actual configuration; b) ideal line load; b) analytical arc load c) elastic boundary element model geometry (Fig. 6.31). 236

Figure 6.31: Comparison between ideal solution, finite contact width solution (Hondros 1959) and Examine2D results for the specimen centerline. (3 is centre-line lateral strain. 238

Figure 6.32: Normalized tensile (top-left), deviatoric (bottom left) stresses and minor principal strain (bottom right). Stress trajectories are shown in top right. Note that nominal calculated tensile stress is valid over central 20% of sample. Also note high but spatially constrained deviatoric stress levels near platens. 239

Figure 6.33: Mohr construction of Brazilian test showing range of open (Griffith) flaws available for crack initiation. 240

Figure 6.34: a) Uniaxial compression test configuration. b) Triaxial compression test sample (Hoek and Brown 1988). 242

Figure 6.35:	Axi-symmetric elastic finite element calculation (Phase2) of stress perturbation due to non-compliant end caps. Left image is for "stiff" end platens. Right image is for "soft" platens. Note confining effect of stiff platens and tensile stresses due to soft platens.....	242
Figure 6.36:	Site plan and general section through Lac du Bonnet Batholith (after Martin 1994)	244
Figure 6.37:	Stress / strain results for direct tension samples of Lac du Bonnet Granite. Data acquisition was very noisy and results have been smoothed (moving average). Bottom plot presents the same data in log-log space for comparison to other tests in this section.....	246
Figure 6.38:	Rock bridges disrupting the continuity of microcracks in Westerly Granite (image modified and inverted from Sprunt and Brace 1974).....	247
Figure 6.39	Rock bridges and en echelon microcracks in Lac du Bonnet Granite Granite (modified/annotated after original micrograph courtesy AECL).....	247
Figure 6.40:	Relationship of critical stresses (top) and strains (bottom) to elastic modulus for direct tension tests on Lac du Bonnet Granite.....	249
Figure 6.41	Microcracks in LdB granite Granite (modified/annotated after original micrograph courtesy AECL): quartz and feldspar (horizontal field scale =7mm).	250
Figure 6.42:	Brazilian tensile tests on Lac du Bonnet Granite.	252
Figure 6.43	Comparison of threshold definition using lateral stress - lateral strain response, axial strain - lateral strain response, and volumetric strain reversal: a) Crack initiation; b) systematic crack accumulation; c) volumetric strain reversal; d) primary crack development and yield; e) rupture.	253
Figure 6.44	Comparison of damage and yield thresholds in the Brazilian Test and in the direct tension test. Identical sample ID numbers indicate samples from the same core stock.	254
Figure 6.45:	Correction of Brazilian test results for non-equal tensile and compression moduli.....	255
Figure 6.46:	Comparison of damage thresholds for the Brazilian test and direct tension.....	256
Figure 6.47	Acoustic emissions (left) and tensile axes (right) within Brazilian Test sample at 64-78% (top), 78-93% (middle) and 93-100% (bottom) of failure load (modified after Falls 1993).....	257
Figure 6.48	Correlation between non-linear lateral strain and microcrack accumulation as indicated by acoustic emissions (modified after Eberhart et al 1998).	259
Figure 6.49:	Comparison of Lac du Bonnet damage initiation threshold with other criterion.....	260
Figure 6.50:	Reduction in secant modulus, in damaged granite samples, at low confinements due to open cracks (Martin 1997).....	265

Figure 6.51:	Schematic illustration of core axis-normal crack damage due to drilling in high stress environments. PHASE2 finite element simulation: axis-symmetrical section about core axis; a) Minor principal elastic stresses and b) yield points showing tensile rupture planes (discing) at core stub.	266
Figure 6.52:	Scanning electron micrograph of intermittent cracks along grain boundary between two feldspar grains in Westerly granite. Image inverted. After Hobbs et al (1976) and Brace et al. (1972).....	270
Figure 6.53	Compressive load cycle tests on unconfined (top) and 10MPa confinement (bottom) samples showing axial, lateral and volumetric strain response.....	272
Figure 6.54:	Definition of damage thresholds under axial compression. (unconfined sample).	273
Figure 6.55:	Summary of damage thresholds for cycle compression tests and Brazilian tests. (top = axial compressive stress; bottom = lateral extension strain).....	274
Figure 6.56:	Summary of cycled load tests on granite samples at various confinements. The locus formed by the dots indicates the volumetric strain reversal point in each cycle. (based on data from Martin 1994).....	278
Figure 6.57:	Critical damage threshold data from Figure 6.54 and Table 6.8. Best-fit Hoek-Brown envelopes shown for comparison ($s=1$).	279
Figure 6.58:	Critical damage threshold from axial stress-strain non-linearity. Bilinear envelope generated from best-fit lines through 1st five and 2nd five data points from Table 6.8.	280
Figure 6.59:	Calculated stress state at locations of recorded AE events in front of mine-by tunnel face at URL. Line indicates lower bound threshold.	281
Figure 7.1:	a) Schematic illustration of mechanisms which generate a crack extension force under deviatoric loading. b) Trellis, bonded disc or lattice analogue.....	288
Figure 7.2:	An a) homogenous and b) stochastic lattice with resultant contact forces for uniaxial loading.	292
Figure 7.3:	Tensile force generation within trellis cells under confined loading (PFC simulation)	292
Figure 7.4:	Crack accumulation (normal to ruptured contacts) in PFC sample under compressive load.....	294
Figure 7.5:	PFC simulation of confined loading test illustrating micro-crack accumulation, localization and macroscopic behaviour.	295
Figure 7.6:	Typical results from simulation in Figure 7.5, showing relative accumulation of tensile (extension) cracks and shear (cohesive) cracks. Model parameters are discussed in detail later in this chapter.....	297
Figure 7.7:	Basic calculation cycle in PFC simulations.	298
Figure 7.8:	a) ball -ball contact b) ball-wall contact	299

Figure 7.9:	a) Initial contact geometry; b) normal contact compression and elongation (tension); c) contact shear without rotation; d) contact shear due to rotation; e) complementary rotation without shear (no resistance); f) lattice trapping in disc assembly – rotation creates shear resistance in at least one contact (which thereby resists rotation).....	299
Figure 7.10:	a) Behaviour of normal component of contact bond model; b) behaviour of shear component of contact bond model and frictional slip model (bonding and slip are mutually exclusive); c) General bond and frictional slip envelopes for PFC bonds.....	302
Figure 7.11:	Contact normal (n), contact vector (l) and force vector (f) definitions.....	303
Figure 7.12:	a) Crack definition; b) distribution of crack normals with respect to direction.....	307
Figure 7.13:	Tensor approximations for an isotropic and anisotropic assembly of cracks.....	309
Figure 7.14:	Comparison (left) of stresses “measured” within the sample (Mid) and calculated from the boundary platens or sidewall discs (Applied). Measured strains (right) within the top middle and bottom portions of the sample.....	313
Figure 7.15:	Experimental determination of instantaneous modulus and strain ratio.	314
Figure 7.16:	Typical variation, during an unconfined compression test simulation, of effective tangent modulus, ET^* , secant modulus, ES^* , tangent strain ratio, νT^* , and secant strain ratio, νS^*	315
Figure 7.17:	Post peak velocities (showing failure surfaces) and axial stress-strain response measured in three sample areas (constant lateral stress = 2.5 MPa). Crack intensity development is also shown.....	316
Figure 7.18:	Sample tested at 20 MPa of lateral stress. Comparison of lateral strain measurements. Volumetric strain response is calculated as the average from the three areas.....	316
Figure 7.19:	Sample assembly: a) generation of platen disc layers (top and bottom) and distributed internal discs with varying (under-sized) radii; b) radius expansion under specified lithification pressure and bond formation; c) sidewall control discs (constant horizontal force) replace lateral walls while top and bottom walls converge to axially load sample; d) final ruptured sample.....	320
Figure 7.20:	Typical Variation, in PFC samples, of contact bond strength, stiffness and length.....	322
Figure 7.21:	a) Internal stresses (cutaway view) in unloaded sample due to contact heterogeneity; b) unloading damage under low lithification pressure and c) under high lithification pressure.....	322
Figure 7.22:	Experimentally determined values of Poisson’s ratio for PFC simulations	326
Figure 7.23:	Comparison of model results with simulations by Bathurst and Rothenburg (1988) and ideal results for dense assemblies ($\gamma=6$).....	326

Figure 7.24:	Measured variation of Young's modulus and invariance of bulk modulus with respect to $\lambda=ks/kn$	327
Figure 7.25:	Measured shear modulus from PFC simulation compared with predicted relationship (to $\lambda=ks/kn$).....	327
Figure 7.26:	Uniaxial compression simulations with normal bond strength held constant ($N=0.3$ MN) as shear bond strength varied as shown (80x200mm samples with 3.1mm mean disc diameter).	329
Figure 7.27	Uniaxial compression simulation with bond shear strength held constant ($S=1.2$ MN) as normal bond strength varied.....	329
Figure 7.28 :	Results of simulations as in Figures 7.26 and 7.27. Damage thresholds are determined as described later in this chapter.....	330
Figure 7.29:	Total and component crack densities for strength calibration tests (crack intensities at residual strength).....	330
Figure 7.30:	Peak strength data for confined tests with different S/N ratios.....	331
Figure 7.31	Peak and residual sample strength envelopes for different contact friction coefficients.....	332
Figure 7.32	Effect of numerical loading rate on post peak behaviour	333
Figure 7.33:	Uniaxial compression tests with varying sample aspect ratio.....	334
Figure 7.34:	Residual forces in contacts after unloading from lithification pressure. Force distribution is isotropic.	336
Figure 7.35:	Samples lithified at different pressures and unloaded. Coordination numbers are measured prior to unloading. Damage accumulates during the unloading process.	336
Figure 7.36:	Sample performance at 0, 20 and 60 MPa of confining pressure. In these tests, $S/N = 100$. Samples with $S/N = 4$ performed comparably.	338
Figure 7.37:	Stages of damage accumulation (schematic).	339
Figure 7.38:	Example of damage accumulation in confined compression test.....	340
Figure 7.39:	Accumulated damage at first interaction (critical crack intensity) and after failure. (2.5MPa lateral confinement).....	342
Figure 7.40:	Identification of damage thresholds from crack intensity and tangent strain increase.....	342
Figure 7.41:	Damage threshold identification from record of interacting crack pairs (top), crack anisotropy and tangent modulus (middle) and from volumetric strain (bottom).	343
Figure 7.42:	Damage threshold identification from kinetic energy and frictional loss.	344
Figure 7.43:	Top: Inelastic strain calculated from total strains shown at two different resolutions ("x100 magnification" gives detail at yield). Bottom: Relative lateral strains expressed as dilation angle (wrt. axial strain).....	347
Figure 7.44:	Meso-crack geometry for samples in Figure 7.36. Mesocrack definition is based on geometric crack connectivity logic as shown in left-hand inset (relative inset magnification=6x with respect to right hand images)	348

Figure 7.45:	Detail of macroscopic shear surfaces from a compression test on granite showing en echelon sub-axial tension gashes (modified after Martin 1994).....	349
Figure 7.46:	Sample failure for shear/normal strength ratios: $S/N=4$ (left) and $S/N=0.5$ (right). Ratio of shear to normal cracks at end of test: 2 % (left) and 700 % (right). Inter-disc friction angle (after bond rupture) in both cases = 45 degrees.....	351
Figure 7.47	Comparison of PFC damage (at peak strength and at residual strength or ultimate damage) with marble test data from Wong et al. (1996).....	355
Figure 7.48:	Stress – strain response for typical confined compression test simulations ($S/N = 4$; sample size 400 x 150mm).....	356
Figure 7.49:	Damage thresholds for confined compression test simulations.....	357
Figure 7.50:	Crack intensities measured at interaction peak and residual strength.	359
Figure 7.51:	Relative proportions of shear cracks with respect to normal cracks for samples with $S/N=4$	360
Figure 7.52:	Crack density intensity contours for stress path shown.....	361
Figure 7.53:	Contours of total lateral strain for the same stress path as Figure 7.52.	361
Figure 7.54:	Total and elastic lateral strains at crack interaction.....	362
Figure 7.55:	Total and inelastic axial strain for confined compression.....	363
Figure 7.56:	Comparison of inelastic deviatoric and volumetric strain.	363
Figure 7.57:	Comparison of spontaneous crack propagation (upon initiation) as a function of confinement, for (A) homogenous solids and (B) lattice or bonded contact model.....	365
Figure 7.58:	Two sample configurations (rectangular and “dumbbell”) for tensile test simulations.....	367
Figure 7.59:	Damage threshold detection in tensile test simulations (rectangular samples).....	369
Figure 7.60:	Damage threshold detection in tensile test simulations (dumbbell samples).....	370
Figure 7.61:	Contact force and crack distribution in typical tensile sample at approximately 75% of interactions stress (A); Disc, intact bond and crack distribution after failure (B).	371
Figure 7.62:	Discrepancy between relative rock tensile strength and PFC results (schematic).....	373
Figure 7.63	Sample preparation and stress path for confined tension tests.....	374
Figure 7.64:	Tensile stress – lateral strain and crack accumulation for three examples of confined compression simulations.	375
Figure 7.65:	Total lateral strain measured for confined tensile tests.....	375
Figure 7.66:	Crack damage thresholds determined from confined compression simulations.....	376

Figure 7.67:	Stress strain response and cumulative damage at increasing vertical strain	378
Figure 7.68:	Test configuration showing stress sampling grid, contact forces and calculated equivalent stress distribution. Sample at approximately 60% peak load.....	379
Figure 7.69:	Stresses and strains (averaged over circles shown) for Brazilian test.	380
Figure 7.70:	Comparison of measured and theoretical stresses at sample centre (top plot) and comparison of measured strains in regions as shown.	381
Figure 7.71:	Damage thresholds in the Brazilian test	382
Figure 7.72:	Sample damage and internal forces at stages marked in Figure 7.71.....	383
Figure 7.73:	Comparison of Brazilian Tests damage thresholds with confined tension simulations.....	385
Figure 7.74:	Contrast between PFC damage thresholds and granite strength.	387
Figure 8.1	Strength of rock samples versus a) grain size (marble after Wong et al. 1996) and b)sample size (after Hoek and Brown 1980)	392
Figure 8.2:	Effect of sample size on compressive strength (after Bienawski 1968)	392
Figure 8.3:	Variation in a) strength, b) stiffness and c) length of contacts within PFC lattice model (standard assumed means and variabilities used throughout this thesis).	394
Figure 8.4:	Local variation in stress field due to material or structural heterogeneity (based on Cook 1998 and on Gramberg 1989)	395
Figure 8.5:	Effect of confinement on crack propagation length, c , with respect to initial flaw half length, c_0 , based on experimental data (A) for an open crack (Hoek 1965) and a sliding crack (B) relationship calculated by Martin (1997).....	396
Figure 8.6:	Schematic of effective confinement (or effective gap) concept.....	397
Figure 8.7:	Laminae slip in critically oriented calcite grains inducing compression parallel cracking in surrounding grains. (after Ollson and Peng 1976).....	398
Figure 8.8:	Cleavage [001] separation and kinking in biotite grains (Westerly Granite) close to peak stress (after Tapponier and Brace 1976).	399
Figure 8.9:	Crushed magnetite grain creating subsequent soft inclusion or focused dilation source, inducing cracks in surrounding grains. Stress direction same as Fig. 8.7. (after Tapponier and Brace 1976).....	400
Figure 8.10:	Grain size of mineral components for Lac du Bonnet granite and granodiorite.....	401
Figure 8.11:	Grain Size and uniformity contrast between URL granite (left and granodiorite (right). The granodiorite is also more equi-granular (Photo courtesy AECL)	401
Figure 8.12:	Crack initiation stress for Lac du Bonnet granite and granodiorite (Read 1994).....	401
Figure 8.13:	Strength data for a homogenous sandstone (Kostak and Bielenstein 1971)	402

Figure 8.14:	Force pathways through a uniform lattice under uniaxial compressive stress.....	403
Figure 8.15:	Compressive (a) and tensile (b) contact forces in heterogeneous assembly (disc radius and contact stiffness). Cutaway insets in (a) show disc assembly and stress measurement circles for creation of stress contours (c&d - tension +ve)	404
Figure 8.16:	Uniform melt (a) compressed to form crystal network (b&c). Internal tensile (d) shear (e) and compressive (f) forces generated by confined compression	405
Figure 8.17:	Internal stress distribution (tension +ve) within the crystal lattice. Sample dimensions and measurement circle size and distribution are the same as shown in Figure 8.15a.	406
Figure 8.18:	Spatial distribution and sample probability density distributions for elemental strength (tensile bond strength - force) for 3 PFC samples in Table 8.2.	407
Figure 8.19:	Axial response and crack accumulation for heterogeneous samples in Table 8.2.	408
Figure 8.20:	a) Crack accumulation and elemental strength distribution in heterogeneous samples; b) crack damage thresholds (schematic).....	410
Figure 8.21	Tensile strength reduction with increasing rod diameter from experimental data reported by Griffith (1921) Strength for 1mm corresponds to nominal tensile strength for larger samples.	412
Figure 8.22:	Flaws and crack nucleation: a) elliptical crack; b) sliding crack with nascent wing cracks; c) sliding crack with developed wing cracks; d) circular pore.	412
Figure 8.23:	Effect of sample scale on direct tensile strength (data from Wijk et al 1977).....	416
Figure 8.24:	Crack length and grain size relationship in marble (after Wong et al 1996).....	416
Figure 8.25:	Samples (after failure) used in PFC scale effect study (BSA series had different random seeds and therefore different particle arrangements).....	417
Figure 8.26:	Stress-Strain responses (top) and crack accumulation (bottom) for PFC scale effect samples.	418
Figure 8.27:	Cumulative contact strength distribution for PFC scale effect samples	419
Figure 8.28.	Crack initiation thresholds for PFC samples. Best fit linear and power functions are shown.....	419
Figure 8.29	Effect of Sample Diameter on Strength Thresholds for Lac du Bonnet Granite (data from Martin and Chandler (1994).	420
Figure 8.30	Effect of scale on sample strength for various rock types. Note truncation of strength increase for very small samples ($D < 50$ mm).....	420
Figure 8.31:	Localization indicators for PFC simulations: a) accelerated crack growth; b) kinetic energy increase; c) interacting crack pairs.	423

Figure 8.32:	Estimation of fractal dimension for crack arrays at key thresholds.....	424
Figure 8.33:	Localization stress threshold for samples of varying scale.....	424
Figure 8.34:	Scale effect for peak strength. best fit for larger samples normalized with respect to strength at 120mm.	425
Figure 8.35:	Scale independence (with respect to sample size) of shear zone development.....	425
Figure 8.36:	Examples of density distributions for different heterogeneity indices (m). Normal function shown for comparison.	428
Figure 8.37	Weibull weak link model: a) schematic representation of global dependency on elemental rupture probabilities; b) Composite failure probability (cumulative distribution). Modified after Illston et al 1979.....	429
Figure 8.31.	Example relationship between Weibull heterogeneity and strength - scale relationship. a) $\sigma_0=200\text{MPa}$, $\sigma_i=0\text{MPa}$, $V_0=50\text{mm}$; b) $\sigma_0=150\text{MPa}$, $\sigma_i=50\text{MPa}$, $V_0=50\text{mm}$	432
Figure 8.39:	“Strongest Link” parallel system.	434
Figure 8.40:	Series-parallel system. Both (parallel) elements within a single (serial) tier are required for sample failure.	435
Figure 8.41:	Relative crack initiation (from Equation 8.20) and crack interaction (Equation 8.28) thresholds predicted by statistical model.	437
Figure 8.42:	Comparison of series-parallel predictions with PFC (calibrated for "first crack")	438
Figure 8.43:	Comparison of series-parallel predictions (calibrated for "systematic damage").....	438
Figure 8.44:	A schematic illustration of stress path related damage in the absence of stress rotation (based on the experimental findings of Pestman and Munster (1996)).....	439
Figure 8.45:	Isotropic damage (crack intensity) incurred in heterogeneous PFC samples from Chapter 7, during virgin unload from hydrostatic lithification pressure.	440
Figure 8.46:	Statistical model incorporating pre-existing cracks.....	440
Figure 8.47:	Crack interaction threshold as a function of initial damage (statistical model predictions based on parameters from Figures 8.42 and 8.43).	442
Figure 8.48:	Observed crack damage and compressive strengths for samples of marble (based on data from Wong et al. 1996)	443
Figure 8.49:	Typical Crack arrays generated after unloading from lithification pressure (and before compression testing) Crack orientations referred to in subsequent discussions refer to orientation of principal anisotropy for crack normals (0 degrees = horizontal - right).	445
Figure 8.50:	Influence of pre-existing isotropic cracks on new damage thresholds	446
Figure 8.51:	Reduction of critical damage threshold with initial damage in Lac du Bonnet granite. Crack closure strain used as an index for crack intensity (Martin 1994).	446

Figure 8.52:	Influence of intensity and orientation of pre-existing damage on new damage and strength thresholds.	448
Figure 8.53:	Influence of intensity and orientation of pre-existing damage on stiffness parameters (measured prior to systematic damage).....	449
Figure 8.54:	Exponential functions to moduli from simulations (Figure 8.53-mid). Theoretical relationship for isotropic damage in direct tension is shown for comparison.	450
Figure 8.55:	Lateral strain at crack interaction for previously damaged samples.....	450
Figure 8.56:	Comparison of PFC simulation results to statistical interaction model (with pre-existing damage).	451
Figure 8.57:	Stress paths for two locations in the roof of an advancing tunnel and comparison between failure geometry and damage initiation limits from 2D elastic models.	453
Figure 8.58:	Effect of isotropic damage on confined peak strength ($\chi_d=0.2$).....	454
Figure 8.59:	Effect of confinement and isotropic damage on new damage thresholds ($\chi_d=0.2$).....	455
Figure 8.60:	Damage thresholds for damaged Lac du Bonnet granite (URL 420 level). Damage initiation and crack interaction thresholds from data in Section 6.7. Peak Strength from Martin and Stimpson (1994).....	455
Figure 8.61:	Elastic model schematically illustrating the effect of boundary parallel damage.....	456
Figure 8.62:	Effective gap concept. A stressed medium: a) deviatoric applied compression; b) uniaxial applied compression; c) confined compression (oedometer stress path); d) effective uniaxial state due to "gap".	457
Figure 8.63:	Elastic boundary element model with open cracks. Hydrostatic applied stress state ($\sigma=20\text{MPa}$), $\chi_d=0.4$. Note confinement shadows around and between cracks.	458
Figure 8.64:	Estimation of crack closure stress from hydrostatic loading data (Lac du Bonnet granite (URL - 420 level).....	458
Figure 8.65:	Effective confinement adjustment for insitu strength and damage prediction.	459
Figure 8.66:	Effect of assumed crack extension length on crack interaction stress (statistical model using calibration parameters from Section 8.4).	461
Figure 8.67:	Composite effect of crack propagation length and pre-existing damage on yield strength (crack interaction). Two assumptions for extension of pre-existing cracks are used in Equation 8.XX and shown here.	463
Figure 8.68:	Confining stress and crack propagation for sliding crack analogue.....	464
Figure 8.69:	Alternative example relationship between confining stress and crack propagation for sliding crack analogue (friction angle = 0).....	465
Figure 8.70:	Crack extension (top) and crack accumulation (bottom).....	468
Figure 8.71:	Correction of critical crack intensity (interaction) threshold, accounting for crack extension. Granite data shown for comparison.	469

Figure 8.72:	Effect of crack-surface separation on equilibrium crack length thresholds.....	471
Figure 8.73:	Effect of crack length on fracture equilibrium in the presence of a free surface.	472
Figure 8.74:	Limits of stable propagation for a single crack near a free surface.	474
Figure 8.71:	Grain scale spall damage from tunnel boundary (courtesy of AECL)	474
Figure 8.76:	Comparison of boundary conditions for dilating cracks insitu and in lab samples.	475
Figure 8.77:	Effect of borehole diameter on sidewall failure stress (Martin 1994).	476
Figure 8.78:	Effect of excavation stress gradients on spalling extent (crack propagation).	477
Figure 8.79:	PFC test sample (left) for this study (0.15mx0.4m, 7200 discs); crack array after sample failure (middle) and sampling array (right) for local stress contouring (Inset: spatial coverage of stress sampling circle).	479
Figure 8.80:	Internal distribution of minor principal stress for uniaxial compression sample (Contour interval = 5MPa, thick lines indicate tension, internal contour label are tension positive convention) Stress levels under each sample are the applied axial stress (bracketed values are ratio of peak strength = 180MPa).	480
Figure 8.81:	Distribution of minor principal stress for compression at 2.5 MPa of applied lateral confinement (Interval = 5MPa, thick lines = tension, internal contour label are tension positive convention) Stress levels under each sample are the applied axial stress (bracketed values are ratio of peak strength = 189 MPa).	481
Figure 8.82:	Samples tested at increasing confinements using contour properties from Figure 8.80 and 8.81.	482
Figure 8.83:	Distribution of sampled local stress states in a) uniaxial compression and b) compression at 20MPa confinement. Ellipses represent 1,2,and 3 standard deviations for a bivariate normal distribution.	484
Figure 8.84:	a) Connected variability limit traces for low confinement in a uniaxial compression test; b) limits from population of measurement circles containing cracks.	485
Figure 8.85:	Confinement variability limit traces for different applied (average) confining stresses and different limit assumptions. Plots from left to right correspond to nominal limits of spatial distribution of 0.1%,1% and 10% (relative area covered by limit condition). Solid and dashed thresholds are unstable propagation limits for an isolated crack and a near surface crack respectively.	486
Figure 8.86:	Strength reduction due to local tensile zones and isolated crack propagation.	487
Figure 8.87:	Strength reduction due to local tensile zones and near surface crack propagation.	488

Figure 8.88:	Locii of required applied stress to minimize local tension within the sample (i.e. restrict the spatial coverage (2D) to the limits (0.1%,1% and 10%) shown.	489
Figure 8.89:	Stress flow around an excavation with re-entrant roof geometry.....	490
Figure 8.90:	Effect of a notch on boundary stresses around a circular opening.	491
Figure 8.91:	Finite Element Mesh and Yield Criterion for URL simulation.....	492
Figure 8.92:	Post-failure stresses and yield zones above circular opening	493
Figure 8.93:	Yield zones and vertical displacement distribution above circular opening	494
Figure 8.94:	Yield zones and vertical displacement for dilatant flow rule.....	495
Figure 8.95:	Boundary conditions, random mesh and post failure results for URL simulation.	495
Figure 8.96:	a) Yield zones from random mesh model of URL "mine-by" tunnel. Interconnected yield zones bounded by "notch" profile; b) Actual observed notch development (after Martin 1994); Microseismic events recorded during period of notch development (data reanalyzed and presented by Cai et al 1999).	497
Figure 8.97:	Excavated cross-section (Top photo) through the floor notch at the URL "mine-by" tunnel showing the smooth sides generated by tensile slabbing; Bottom photo show a close-up of the highly fractured notch-tip process zone. (Photos and annotation from Martin 1994).....	498
Figure 8.98:	a) Elastic finite element results for stresses around a rectangular opening in a deviatoric initial stress field; b) Total displacement and yield zone for plasticity simulation (same material parameters as in Section 8.8.1).	500
Figure 8.99	a) Undamaged and b) significantly spalled but internally competent (core intact) pillars at the Black Angel Mine, Greenland (photos courtesy E. Hoek).....	501
Figure 8.100:	Pillar simulation: Discs (a) cracks (b) and forces (c&d) immediately prior to core yield (Figure 8.101). Note spall damage in pillar sidewalls	502
Figure 8.101:	Average core stress path and crack accumulation for pillar in Figure.100.....	503
Figure A.1:	Confined roof wedge.....	549
Figure B.1:	Solution options for NTBEAM (voussoir)	553
Figure B.2:	Example solution for critical thickness.....	553
Figure D.1:	Geometry for wing crack initiation	559
Figure D.2:	Nomenclature for a sliding crack with idealized wing cracks	560
Figure D.3:	Effective beam created by crack-surface interaction.....	564

NOMENCLATURE

α	Wedge apex angle
α	Dip of lamination plane
α	Crack normal anisotropy
$\dot{\alpha}_{ij}$	Velocity gradient tensor
A	Cross sectional area
A	Rock stress factor
A_a^*, A_c^*	Ratio of rock bridge (a) and crack (b) to total area
a	Wing crack segment length
a	Rock bridge radius
B	Joint orientation factor
β	Angle from crack plane
$B.L.$	Buckling limit for voussoir calculations
b	Sample depth (normal to section)
χ	Crack intensity
χ'	Crack intensity associated with rock bridges
C	Gravity adjustment factor
c	Crack radius
c	Cohesion
c'	Width of cracked annulus around idealized rock bridges
δ	Displacement, deflection
δ_a	Abutment relaxation displacement
D	Depth from ground surface
D	Fractal dimension
d, \bar{d}_0	Contact length, average initial contact length
$\varepsilon_1, \varepsilon_3$	Major, minor principal strain (compression positive)
ε^p	Plastic strain
$\varepsilon_{lateral}, \varepsilon_{axial}$	Lateral and axial strain

Instability of Hard Rockmasses: The Role of Tensile Damage and Relaxation

ε_v	Volumetric strain
ε_{cr}	Critical (extension) strain
$\dot{\varepsilon}_{ij}$	Strain rate tensor
E	Young's modulus
ESR	Excavation support ratio
F	Support load
F	Contact compression force magnitude
F^n, F^s	Contact normal and shear force
$F.S.$	Factor of safety
F_{ij}	Normalized fabric tensor
\mathbf{f}	Assembly contact force vector
f_{max}, f_{av}	Maximum, average fibre stress in voussoir beam arch
ϕ	Friction angle
γ	Unit weight
γ	Angle of crack normal to direction of tensile loading
γ	Coordination number
G	Shear modulus
G	Crack driving force
HR	Excavation "hydraulic radius" (area/perimeter)
I	Moment of inertia
I_1	First stress invariant
J_n	Joint set number
J_r	Joint roughness number
J_a	Joint alteration number
J_w	Joint water number
J_2, J_3	Second and third invariant of the deviatoric stress tensor
K	Bulk modulus
K_I, K_{II}, K_{III}	Mode i, ii and iii stress intensity factors
K_{IC}, K_{IIC}	Critical stress intensity factors (mode i and ii)

K_s, K_n	Joint shear and normal stiffness
k	Insitu stress ratio (horizontal/vertical)
k	Number of elements in a tier (series-parallel failure model)
k_n, k_s	Contact normal and shear stiffness (force per strain)
k_n^*	Contact normal stiffness (force per unit displacement)
λ	Stiffness ratio
L	Generic linear dimension
L	Length of voussoir compression arch
L	Ratio of wing crack length to initial flaw length (a/c)
l	Assembly contact (half contact) vector
μ	Friction coefficient
μ	Mean strength
M_w, M_R	Moment (in voussoir beam) due to weight and resistance
m	Ratio of rock bridge radius to cracked annulus width (a/c')
m	Number of series terms
m	Weibull constant
m	Moment
m, m_i	Hoek-brown slope constant (i indicates intact rock)
m_v	Number of assembly contacts per volume
N	Normal bond strength (force)
N	Normalized voussoir arch thickness
ν	Poisson's ratio
N	Number of cracks
N'	Modified stability number
\mathbf{n}	Contact normal unit vector
n	Porosity
P	Relative joint trace persistence
P	Applied load
P	Total potential energy

$P(\sigma)$	Probability of failure for a given stress
p	Support pressure
p_z	Vertical insitu pressure
Q	Tunneling quality index
R	Radius of Brazilian sample
R_f	Radius of failure zone
RQD	Rock quality designation
RMR	Rock mass rating
$R.H.$	Relative humidity
R_{ij}	Crack tensor
r_0, r	Tunnel radius, radial distance
$\sigma_1, \sigma_2, \sigma_3$	Major intermediate, minor principal stresses (compression +ve)
σ_t	Tensile strength (expressed as a magnitude)
σ_{ci}	Crack initiation stress
σ_{cd}	Critical crack damage stress
σ_c	Peak uniaxial compressive strength
σ_h	Horizontal stress
σ_{ij}	Stress tensor
σ_o	Initial pressure
σ_2, σ_1	Weibull constants
S	Excavation span
S	Shear bond strength (force)
SRF	Stress reduction factor
SCF	Stress concentration factor
$S.G.$	Specific gravity
s	Hoek-brown intercept
s	Variance of strength
τ	Shear stress
τ'	Net or effective shear stress

T	Tensile strength (alternative to σ_t - expressed as a magnitude)
T	Beam thickness (parallel to section)
T	Contact tensile force
T	Surface traction force
$t, \Delta t$	Time, time step
\mathbf{t}	Contact tangent unit vector
θ	Lode angle
θ	Crack orientation
U_n, U_s	Contact normal overlap, contact shear displacement
U	Strain energy
UCS	Unconfined compressive strength
u	Relative surface displacement
V	Volume
V_0	Elemental volume
ω_{ij}	Rotational tensor
W	Applied line load
W	Work
w	Sample width
ξ	Dimensionless constant
x_i^P, x_i^C	Particle and contact location coordinate
x	Number of potential interactions per element in statistical model
ψ	Dimensionless geometric constant
ψ	Dilation angle
ζ	Dimensionless constant
Z	Voussoir moment arm
Z_0	Initial voussoir moment arm

CHAPTER 1

Introduction and Executive Summary

1.1 ROCKMASS INSTABILITY

Rockmass instability in underground excavations, from an engineering point of view can be classified in two broad categories:

- structurally controlled or gravity driven fallout
- strength controlled or stress driven rockmass yield.

This thesis is presented in two parts. Structurally controlled and strength controlled modes of instability are considered in Part I and Part II, respectively. The role of damage induced by tensile stress conditions at a local level and the impact of relaxation or confinement reduction, near excavation boundaries, are examined with respect to both failure domains.

The dominant behaviour is a function of the relative insitu stress and degree of jointing and fracturing in the rockmass. This is schematically represented in Figure 1.1. Massive rock under low stress (Figure 1.1a) should be free of instability issues unless damaging excavation practices disrupt the integrity of the rockmass. Under high stress (Figure 1.1b) the rock responds to excavation by spalling or crushing. At the other extreme, heavily jointed rock (Figure 1.1e and f) takes on soil-like engineering properties, unravelling in the absence of stress and flowing under high stress.

The structures represented in Figure 1.1 are ubiquitous in nature, consisting primarily of jointing, bedding and other distributed discontinuities. Instability caused by the presence of continuous faults and discrete shear features is not considered here.

This work is concerned with massive (Figure 1.1b) and moderately jointed rockmasses only, as shown in Figure 1.1c (low stress) and Figure 1.1d (high stress). In particular, only "hard" rockmasses are considered in this thesis (e.g. unweathered granite, norite, metasediments, etc.).

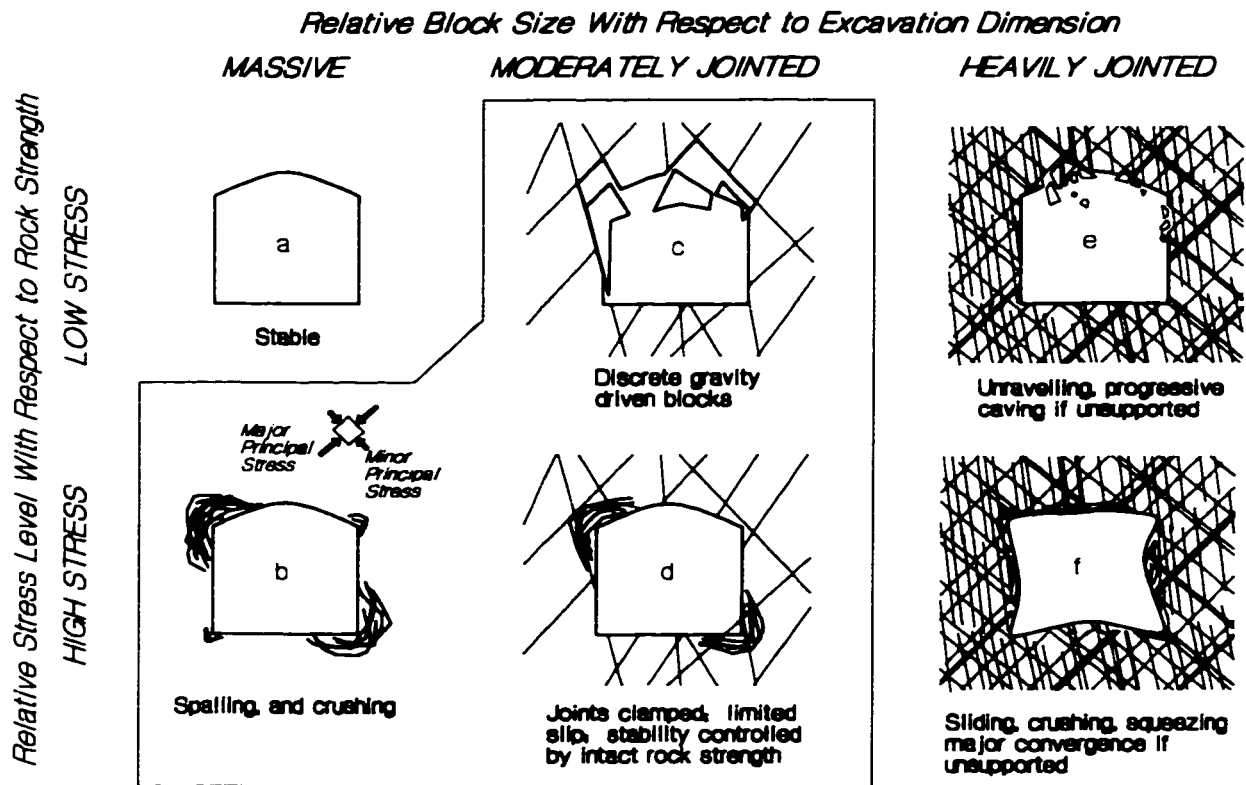


Figure 1.1: Influence of stress and structure on rockmass failure modes (modified after Hoek et al 1995). Cases inside of border are the focus of this thesis.

1.2 RESEARCH FOCUS

The important role of the following factors controlling rockmass damage, instability and failure:

- inherent tensile strength and tensile damage, and
- relaxation or confinement reduction

are examined in this thesis.

In conventional analysis of both structurally controlled and stress driven failure, the effects of tensile strength and the elevated sensitivity to low confinement are typically neglected, leading to erroneous predictions of groundfall potential or rock yield. The important role of these two elements in underground excavation stability in hard rock environments is examined in detail.

In Part I, the role of the residual tensile strength or the tensile self-supporting capacity of a discontinuously jointed or fractured rockmass (afforded by incomplete separation of joint planes) and of relaxation (confinement loss) on the structural stability of shallow or unstressed underground openings (Figure 1.2) is investigated. In Figure 1.2(a), the joint-normal tensile strength allows load transfer normal to a wedge-bounding surface or to laminations. This affords direct gravity support in the first case and effectively thickens the active beam in the second, laminated, case - increasing stability in both situations.

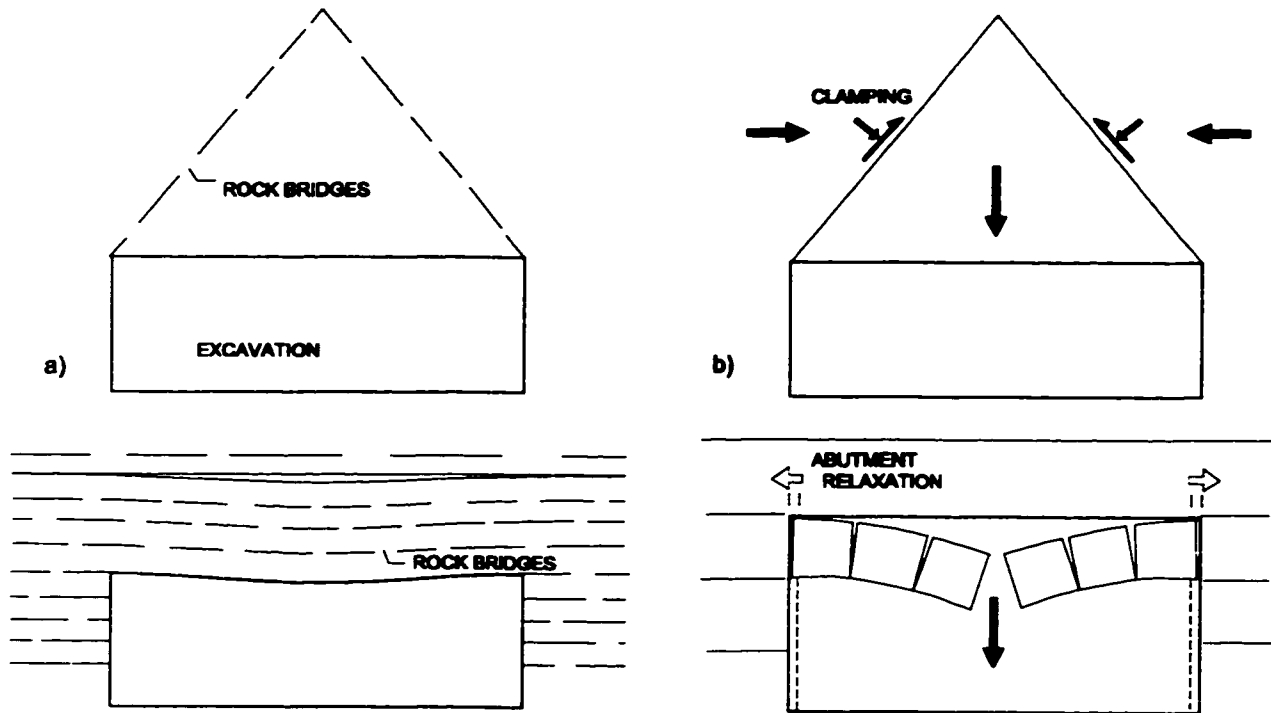


Figure 1.2: Issues for structural instability examined in this thesis:
a) Residual tensile strength due to rock bridges;
b) Excavation-parallel confinement (top) and abutment relaxation (bottom).

In Part II, the role of internal tensile fracture and extension cracking (Figure 1.3a) on rock damage and yield under high, compressive stress is explored. The dominant role, at low to moderate confinements, of this form of damage initiation and propagation in hard rock yield processes is investigated and verified.

Of particular interest is the process of spalling around deep excavations in hard rock (Figure 1.3b). It is shown that while the initiation of crack damage is relatively insensitive to confinement, crack propagation, a requisite process for macroscopic spalling, is highly sensitive to the low confinement conditions near an excavation boundary (Figure 1.3c).

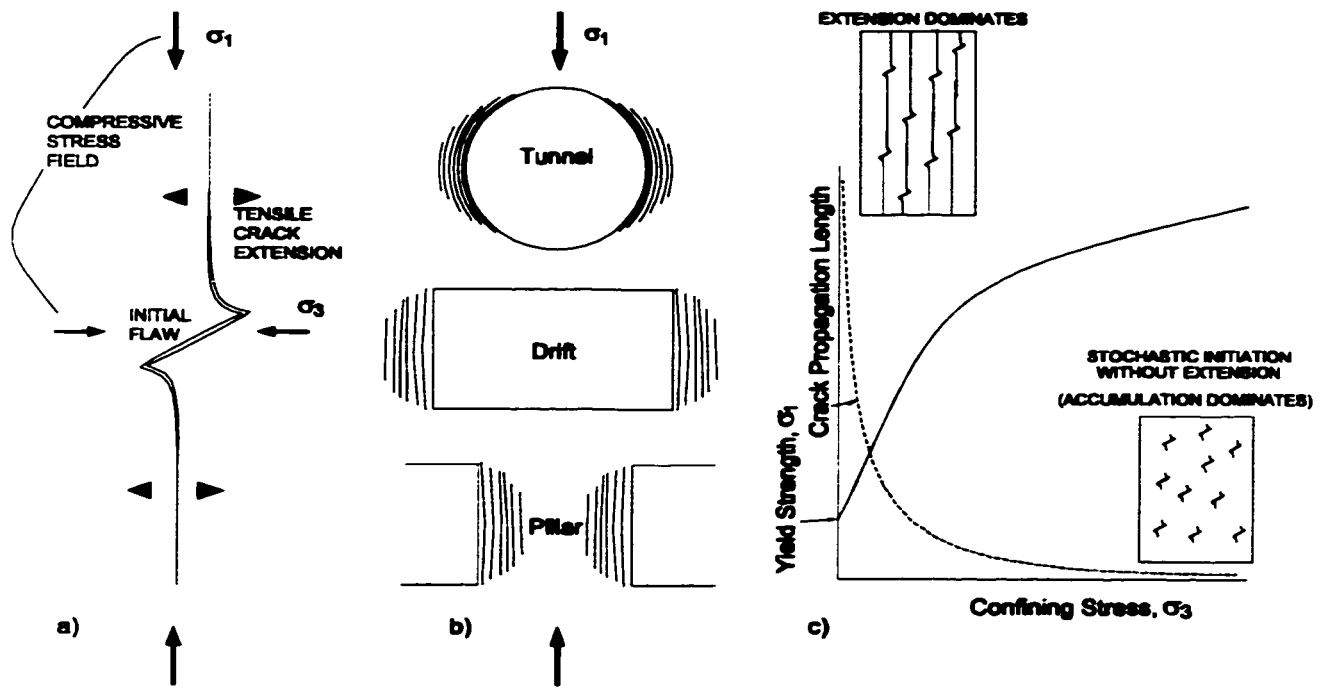


Figure 1.3: Issues for stress driven instability examined in this thesis:
 a) Compression-induced tension cracking;
 b) Field-scale boundary-parallel spalling;
 c) Crack accumulation vs. propagation:
 yield strength and confinement sensitivity.

1.2.1 Terminology

Before proceeding it is necessary to clarify the specific application of a number of terms in this thesis, specifically those referring to tensile capacity and confinement.

In Part I the *residual load bearing tensile capacity* of the rockmass refers to the resistance to direct loading by gravity. In the case of a laminated beam, this term and its variants applies to the interlaminar resistance to loading perpendicular to the beam structure afforded by incomplete bed separation.

On the other hand, the Voussoir analogue, updated and used extensively in Part I, is a *no-tension beam* model. This refers to the assumption that deflection induced tensile stresses, parallel to the beam, cannot be sustained (in contrast to the conventional closed form elastic approach for a continuous beam).

In Part II, the equivalent terms *tensile damage*, and *extension cracking* refer to the creation of cracks through separation normal to the crack axis. This is the result of highly local tensile forces

or stresses. These may be generated by externally applied global tension but are also present as the result of compressive stress flow (globally applied compressive conditions) through a heterogeneous medium.

In Part I, the term *confinement* is used to describe the boundary-parallel compressive stress acting across the wall or back of an excavation. *Confinement reduction* and *relaxation* refer, respectively, to the partial or full elimination of this confinement. Relaxation typically leads to the opening of boundary normal joints and is equivalent to local boundary parallel tensile stress calculated by a numerical elastic continuum model.

In Part II, the term *confining stress* and *confinement* are used differently and may lead to confusion if understood in the same sense as used in Part I. *Confining stress* is used in Part II in reference to the minor principal stress component, σ_3 .

Confinement, on the other hand is used, for distinction, to describe the composite volumetric or hydrostatic stress component, I_1 ($=\sigma_1+\sigma_2+\sigma_3$) or simply $\sigma_1+\sigma_3$ in two dimensions or in axisymmetric conditions. *Confinement insensitivity*, therefore, refers to the insensitivity of the deviatoric stress ($\sigma_1-\sigma_3$) to the confinement ($\sigma_1+\sigma_3$). A two-dimensional *confinement independent* criterion, for example, results in a 1:1 dependency between σ_1 and σ_3 as shown in Figure 1.4.

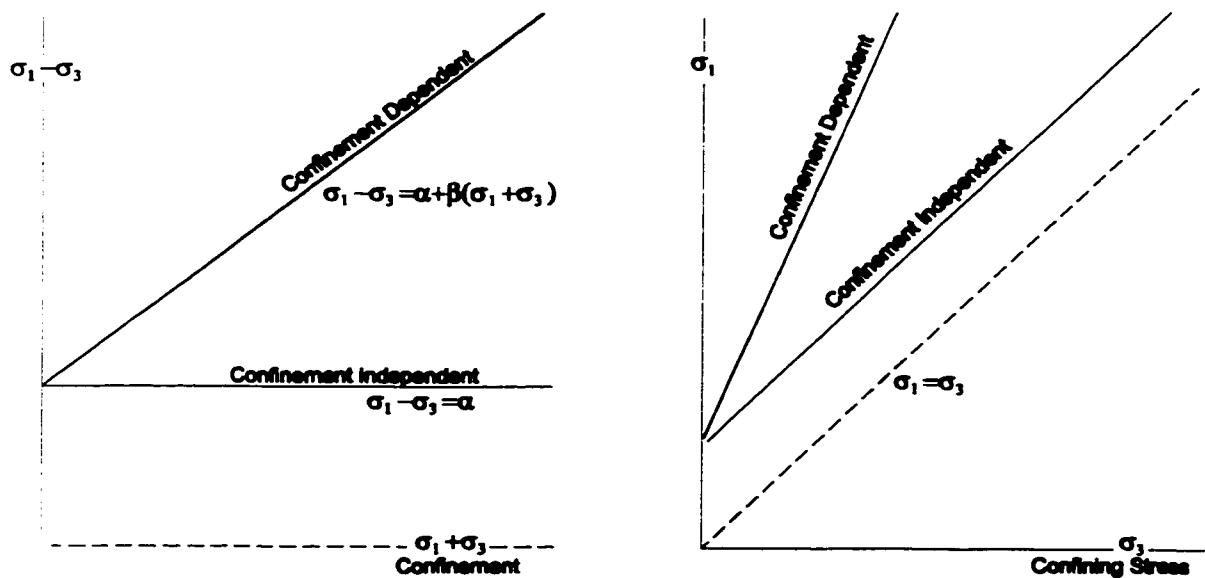


Figure 1.4: Explanation of confinement dependency (and independency) in deviatoric-hydrostatic stress space (left) and principal stress space (right).

1.2.2 Tensile Strength and Relaxation in Structural Instability

While structural analyses normally consider full persistence of bounding discontinuities, non-persistent jointing is more common at depth in hard rocks, away from major fault or folding zones. It will be shown that intact rock bridges, in hard rock formations, need only occupy a very small percentage of the joint-coplanar area in order to provide internal or self-supporting load carrying capacity equivalent to conventional underground support systems. Consideration of this internal support mechanism, at least for short-term or "first-pass" applications, could lead to reduced primary support requirements and more efficient tunnel development.

Delayed failure in mining environments is often the result of induced abutment relaxation. Changes in rock quality, excavation geometry, mining induced stress changes or surface deflection can lead to relaxation induced collapse of otherwise stable rockmasses. It is necessary to recognize the potential for this mechanism in order to improve mine sequencing and support design to minimize these types of failures.

This is an issue of particular importance to mining. In civil engineering applications at low or moderate depth (tunnels, caverns, etc), roof geometries are typically arched to attract compression or clamping in the roof, thereby increasing stability (Figure 1.5a). In contrast, complex mining geometries, driven by operational constraints and orebody geometries actually reduce confinement and induce structural instability (Figure 1.5b).

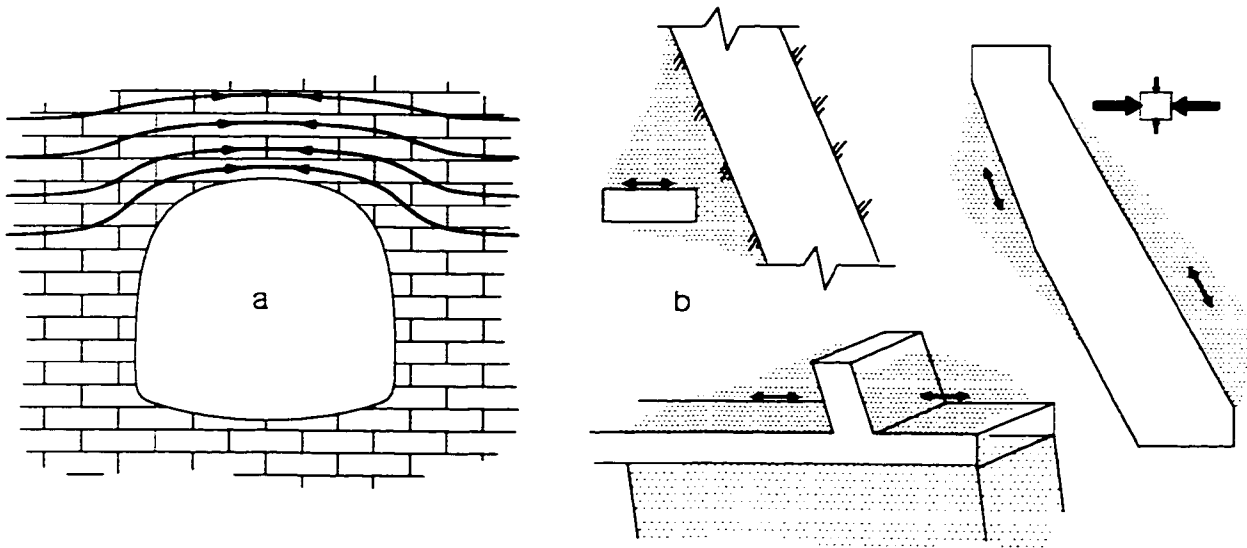


Figure 1.5: a) Increased confinement around well designed civil excavation;
b) relaxation due to complex mining geometries.

1.2.3 Tensile Strength and Confinement Reduction in Stress Driven Instability

Commonly applied geomechanical constitutive models are based on the assumption of shear failure and continuum shear strain, and have proven to be limited in their ability to accurately represent insitu failure of massive or moderately jointed rockmasses at depth around excavations.

Past research has suggested that the origins of compressive damage and yield in hard rocks such as granite are, in fact, tensile in nature, induced by extension strain normal to the direction of maximum compression, σ_1 . Microcracks, once initiated, tend to propagate parallel to σ_1 . An understanding of this damage process is essential in order to explain the observed insitu strength of hard rockmasses.

Experience has shown that the insitu strength of the rockmass near excavations in massive to moderately jointed rock consistently falls to a lower bound ($\sigma_1 - \sigma_3 = 0.4 UCS_{lab}$) coincident with the damage initiation threshold for intact rock samples (Figure 1.6). A primary goal of this work is to explain this observation through a detailed examination of the damage process.

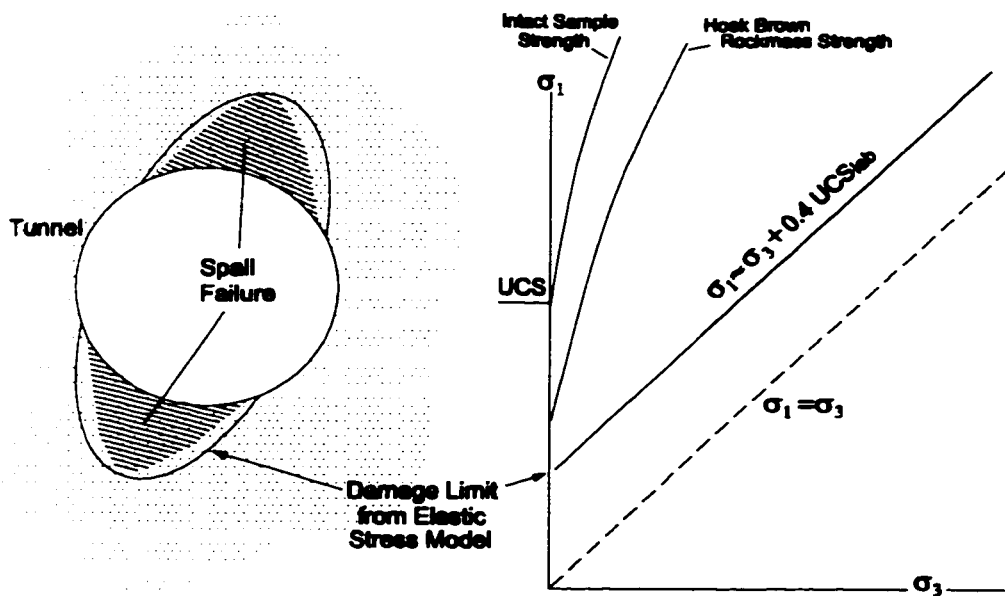


Figure 1.6: Empirical threshold for insitu damage in moderately jointed hard rockmasses.

Due to the associated tensile mechanisms, damage propagation in hard rockmasses is highly sensitive to the effects of excavation induced confinement reduction, free-boundary interaction, and localized tensile stress caused by material and geometric heterogeneity. This thesis demonstrates that these factors contribute to the observed reduction of insitu rockmass strength near underground excavations at depth.

1.3 APPROACH

Observational and empirical evidence is presented to demonstrate the importance of the above listed factors and mechanisms. In addition, numerical experimentation based on simple behavioural analogues is employed to illuminate key aspects of tensile strength and relaxation. Two numerical analogues are adopted in this study.

In Part I, the voussoir model (Figure 1.7a) for a jointed beam is modified to account for interlaminar tensile strength and for abutment relaxation. It is then applied to the study of structurally controlled instability around tunnels and underground mining stopes. In Part II, a bonded disc contact model (Figure 1.7b) is used to explore aspects of grain-scale tensile damage accumulation under both macroscopically tensile and compressive conditions.

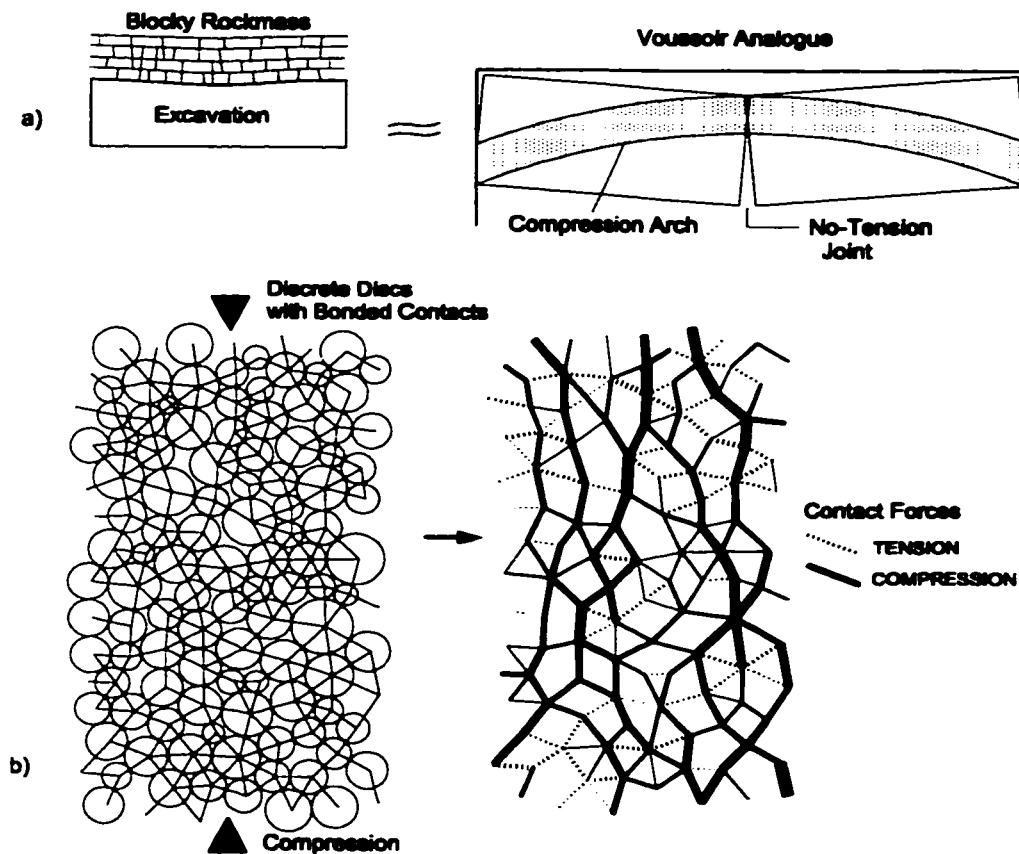


Figure 1.7: Numerical analogues: a) voussoir beam; b) bonded contact discrete elements.

Other investigative tools are used in this thesis to compliment these analogues including:

- Case study and laboratory test evidence,
- analytical relationships based on fracture mechanics, and
- a new statistical model developed herein for damage accumulation.

1.4 OBJECTIVES

The implications of this work on empirical and mechanistic approaches, for excavation dimensioning and support design, are demonstrated in this thesis. The influence of tensile damage and relaxation are quantified and used to explain observed behaviour and validate empirically based design guidelines for structurally controlled and for stress driven failure modes.

1.4.1 Part I

The objectives of Part I of this study are:

- Present observational and case history evidence to demonstrate the limitations of limit equilibrium analysis of gravity driven (structurally controlled) failure modes, based on the assumption of full joint persistence, and also to demonstrate the antithetic impacts of clamping and relaxation on rockmass stability in low stress environments.
- Update and verify a simple voussoir model for stability of jointed beams using case histories and discrete element numerical simulation.
- Apply the voussoir analogue to the study of interlaminar tensile strength (rock bridges) and abutment relaxation as failure control mechanisms.
- Using a voussoir model calibrated to empirical design curves, update these empirical techniques to account for abutment relaxation in underground drifts and stopes for the purpose of modifying limiting excavation dimensions and support design where necessary.

1.4.2 Part II

The objectives of Part II of this study are:

- Through a review of previous observational research and through new case history evidence, demonstrate the validity of an insitu rockmass yield threshold which correlates with damage initiation limits observed in laboratory testing and in field studies. This compressive or deviatoric stress threshold for delineating depth of damage and ultimate failure, is empirically validated for massive rock insitu and for moderately jointed rockmasses.
- Mechanistically validate this otherwise anecdotal threshold to allow confidence in its use with elastic models to predict yield and damage extent. Due to the relative ease of use, linear

elastic (boundary element) models are currently in routine use at Canadian mine sites for evaluation of complex three dimensional mining geometries.

- In order to better understand the mechanics defining this threshold, investigate the nature of strength, in bonded solids such as polycrystalline rock, through a review of bonding mechanisms, theoretical damage processes, fracture mechanics, conventional strength criteria and a study of experimental results from conventional laboratory testing on granite.
- Investigate the relationship between damage initiation, crack or fracture interaction and failure in granite samples under direct tension, combined tension and compression, uniaxial compression and confined compression.
- Investigate the hypothesis that a lower and upper bound for long-term composite rock strength is related to stress thresholds for (crack) damage initiation and crack interaction respectively. Demonstrate that damage initiation is a stress-sensitive phenomenon while crack interaction is a strain-dependent process.
- Present a bonded-contact analogue (discrete element model) for damage accumulation. Demonstrate the relationship between "microscopic" or element scale tensile cracking and sample scale "shear band" formation and the compressive failure of unconfined and confined assemblies of bonded particles. Investigate the validity and limitations of such a model for explicit modelling of hard (polycrystalline) rock behaviour.
- After calibrating the model to emulate the uniaxial compressive behaviour of granite, apply the discrete element model to the study of damage accumulation and interaction. In particular, investigate the relationship between damage initiation and crack interaction within a heterogeneous solid.
- Through the application of the bonded contact model, as well as through the application of fracture mechanics and statistical tools, investigate the effect of low confinement and boundary-normal tensile conditions, crack-surface interaction, local effective confinement loss, and pre-existing extensile damage on compressive rock yield.
- Investigate these and other mechanisms by which the strength of massive undisturbed rock is reduced, adjacent to an underground excavation at depth, to a lower limit coincident with crack initiation, in order to provide a mechanistic basis for and improve understanding of the associated empirically successful criterion.

1.5 SYNOPSIS OF FINDINGS

A brief summary of key findings of this thesis is presented here. A detailed discussion of conclusions is found in Chapter 9.

1.5.1 PART I: Structurally Controlled Instability

In moderately jointed rockmasses at depth, joints are rarely continuous or fully persistent as assumed in the use of limit equilibrium stability calculations. Bridges of intact rock are likely to be present across joint surfaces. The significant impact of these remnant rock bridges is demonstrated in this thesis:

- As shown using a fracture mechanics approach, even a relatively small percentage of intact area in the plane of a joint (e.g. less than 1%) can provide a distributed load capacity equal to heavy support systems used in hard rock mining today. This impact is quantified using wedge stability calculations and using the modified Voussoir beam approach.
- This internal or natural gravity support may be sensitive to long term weakening effects (stress corrosion, dynamic disturbance) but can be relied upon to provide adequate short term support for efficient excavation cycling, development and stope extraction.

While civil excavations (tunnels, caverns) are designed to maintain compressive stress flow parallel to the surfaces of the openings (thereby increasing structural stability), mining openings are constructed in accordance with operational requirements and ore geometries. As such confinement loss and complete relaxation are common around geometrically complex mining excavations. The associated impact on stability is demonstrated and quantified:

- Small amounts of confinement are required to mobilize frictional resistance on joint surfaces such that wedges or blocks become stable under gravity loading. Loss of this confinement is responsible for delayed failure of structurally defined rockmasses.
- Loss of confinement in laminated ground leads to increased gravity induced displacements and failure as demonstrated by an updated voussoir beam analogue.
- A calibrated voussoir model is used to compute the impact of relaxation on empirical stability limits which do not explicitly consider this effect. Comparison to field data in which relaxation is identified as a major influence show that the adjusted stability limit, determined with consideration of relaxation, accurately quantifies and predicts relaxation induced instability in mining openings.

1.5.2 PART II: Stress Driven Instability

The minerals which make up hard rocks such as granite are dominated by covalently bonded complexes. Unlike the microscopic slip processes which are permitted by ionic and secondary bonding (e.g. salt and clay respectively), the compressive damage initiation and accumulation process in hard rocks at low to moderately confinement is primarily tensile in nature. As verified in this thesis, extension crack accumulation and propagation dominate the inelastic behaviour at increasing loads until crack interaction occurs, such that:

- Both spalling and macroscopic shear rupture are shown to be the result of tensile damage initiation and accumulation. Microscopic shear initiation mechanisms only become dominant at very high confinements or at ultra slow loading rates. At lower confinements, shear zone formation is the result of extension crack interaction.
- Macroscopic or intergranular friction is not a factor in the damage process until well after the peak strength has been exceeded and fully localized failure has developed.
- Crack initiation (crack nucleation at the weakest elements) is dependent on deviatoric stress and is relatively insensitive to confinement. Crack accumulation is a stochastic process and in a heterogeneous solid occurs as stress levels increase and stronger elements are exploited.
- Yield is related to a critical probability of crack interaction which in turn is associated with a critical amount of accumulated lateral extension strain (normal to major compression).
- Crack interaction marks the onset of true yield, and determines the upper bound for long term, sample and geometry independent strength in laboratory tests. If crack extension length is increased, crack interaction and yield occur with less crack accumulation (fewer individual crack nucleations) and therefore at a lower compressive stress level.
- The bonded disc model does not simulate the effects of crack extension and spalling. It does permit a study of crack accumulation in the absence of these effects. It also demonstrates that macroscopic shear failure can result from purely tensile damage (Figure 1.8a).
- In reality, crack extension length increases dramatically under low or macroscopically tensile confining stress. Sample yield strength is therefore highly sensitive to these conditions, resulting in a non-linear yield envelope in standard cylindrical laboratory tests (Figure 1.8).
- A number of mechanisms, all investigated in this thesis, reduce the crack interaction threshold near excavations insitu including:
 - ▷ Scale effects
 - ▷ Unloading damage and oblique damage to stress rotation

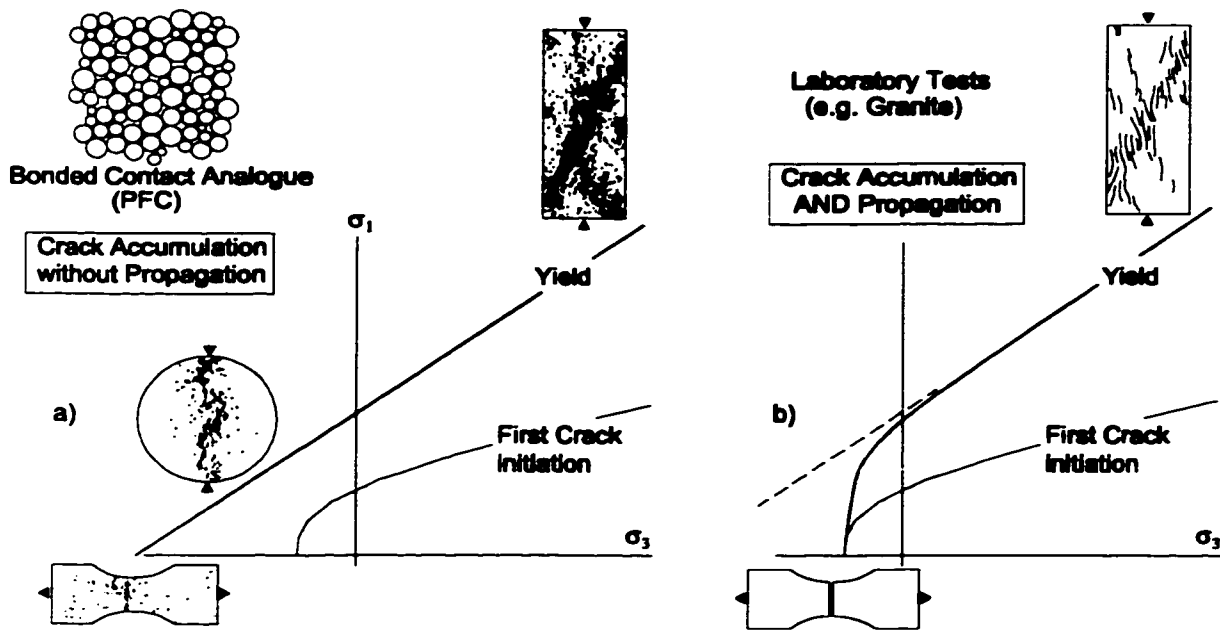


Figure 1.8: Yield thresholds (= crack interaction) for a) bonded contact analogues and b) laboratory test samples of real rock. Crack propagation dominates at low σ_3 in b).

- ▷ Effective gap or local confinement loss due to open cracks
- ▷ Crack - surface interaction (and enhanced crack propagation)
- ▷ Heterogeneity and induced local tension

The stress threshold for crack initiation is unaffected by these factors. The cumulative impact of these mechanisms, however, is to reduce the insitu yield strength, near excavation boundaries, to a lower bound defined by the threshold for crack initiation ("spall failure" shown in Figure 1.9).

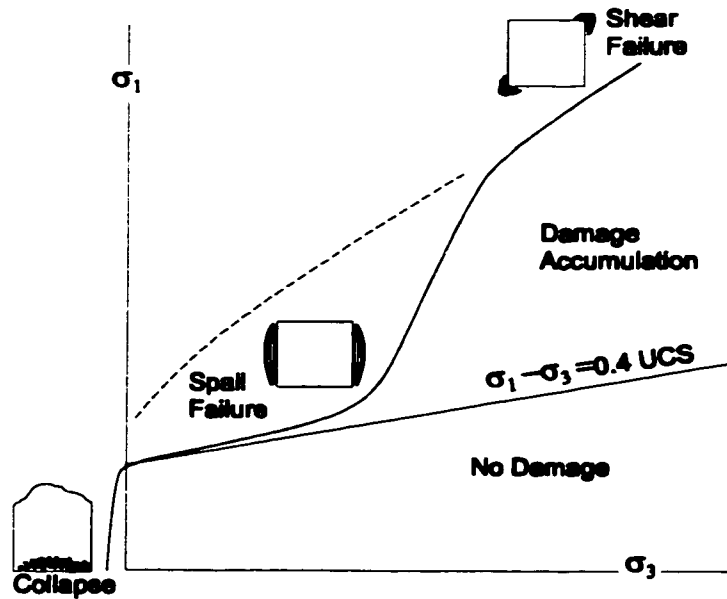


Figure 1.9: Insitu strength reduction, near excavations, to crack initiation threshold.

1.6 PRACTICAL IMPLICATIONS

Residual tensile load capacity within a rockmass results from incomplete joint formation. Rupture of remnant rock bridges occurs with very small strains. It is therefore critical to use measures to retain rock bridges, for example by:

- improved blast practices, and
- the use of stiff reinforcement such as grouted rebar.

If rock bridges can be preserved through improved blasting procedures or mechanical excavation, then primary heading support can be reduced in competent areas. This has major economic implications through:

- increased development cycle rates via delayed installation of primary support (bolts) and the ability to muck immediately after blasting (support installation can occur later in parallel with a subsequent drilling cycle rather than as a separate activity).

Relaxation causes structural instability. Relaxation can be minimized through:

- optimized stope sequencing, and
- improved drift geometries, positioning and orientation.

Generally applied support standards, typically based on worst-case conditions, can be significantly reduced in remote drifts with simple geometries due to the presence of stabilizing confinement.

Conventional rockmass strength criteria do not work near excavations. Numerous mechanisms reduce insitu yield strength of moderately jointed rock to a lower bound defined by crack initiation. In particular, spalling is highly sensitive to low confinement near openings so that:

- Crack initiation is a practical measure to determine rockmass strength and depth of failure near excavation walls (but not for yield of confined rock).
- Crack propagation and yield sensitivity to local induced tension explains the success of a confinement independent strength to damage prediction approach ("friction" component of yield function set to nil) using continuum modelling.
- Initial spall damage, while visually alarming does not indicate engineering failure (loss of support capacity) of the underground opening or pillar core. Acceptable long term service can be achieved from significantly spalled excavations.
- Near excavation micro-seismicity is more successfully analysed using tensile crack models rather than conventional slip source models.

1.7 THESIS STRUCTURE

Part I of this thesis including Chapters 2, 3 and 4 is focussed on the effects of residual tensile strength and relaxation on structurally controlled instability.

The role of rock bridge tensile strength and boundary-parallel confinement on the stability of blocky structurally controlled rockmasses are demonstrated in Chapter 2 and applied to rock wedge support demand assessment. Sources and impacts of confinement reduction and abutment relaxation in complex mining environments are discussed.

In Chapter 3, the classic voussoir beam model is revisited and updated as an analogue for studying the stabilizing mechanism of compressive arch formation in laminated or blocky rockmasses. The model is verified using field evidence and numerical simulation (discrete element model with deformable blocks and joint interfaces). Building on previous solutions, an iterative scheme is developed (solving the indeterminate beam problem) to produce design charts for critical beam dimensions and material properties. While previous applications of the voussoir analogue for excavation dimensioning have been based on the absolute limit of stability, a more rationale engineering design limit (e.g. for critical span) is presented which is based displacement bounds and parametric sensitivity limits.

In Chapter 4, the voussoir model is further enhanced to include abutment relaxation and internal support pressure (internal rock bridge strength). The model is applied to investigate the impacts of these mechanisms on the stability of laminated rockmasses. The voussoir beam is then calibrated to empirical stability limits and used to update these limits to account for relaxation effects in underground stopes as well as to modify cablebolt support recommendations.

Part II of this thesis explores stress driven instability and examines the tensile nature of rock damage and the effects of confinement reduction on near-excavation rock strength at depth.

Chapter 5 provides an introduction to the nature of extensile spall damage and failure around excavations in hard rock at depth. Conventional approaches to rock strength and non-linear analyses of rock behaviour are reviewed. Evidence from previous empirical research and recent case histories demonstrates a linkage between lower bound rock strength insitu and thresholds for crack initiation in laboratory experiments. In order to apply this empirically viable insitu damage criterion, with confidence, it is necessary to further examine the mechanics of rock strength (notably, the mechanics of extensile crack damage) which lead to its apparent predictive success.

The nature of damage in bonded solids such as polycrystalline hard rock is the subject of investigation in Chapter 6. A review of material science reveals the fundamentally tensile nature of rock damage. Rock friction due to particle sliding, cited to explain confinement dependency in laboratory tests, is shown to be inactive until the post peak region is reached in rock tests.

A series of conventional tests on Lac du Bonnet granite are used to illustrate the relationships between damage initiation, accumulation and sample yield in conditions of direct tension, mixed compression and tension and pure compression. The nature of crack initiation in each case is discussed from a microscopic perspective, considering the characteristics of pre-existing intragranular and intergranular microcracks. These flaws serve as primary nucleation sites for new cracks under compressive and tensile applied load respectively.

As an analogue for bonded solids, a discrete element disc model with bonded contacts is verified and applied to the study of damage accumulation in Chapter 7. The model is calibrated based on the uniaxial compressive behaviour of granite samples. The model is used to simulate standard tensile, Brazilian and compressive tests. The inability of the model to simulate unstable crack propagation is discussed, both as a limitation to explicit modelling, but also as an opportunity to investigate damage accumulation without extension. Both mechanisms are coincidentally active in real rock yield, simultaneously contributing to the overall crack intensity (a function of crack accumulation and individual crack length). This limitation of the model provides the opportunity to isolate and examine damage accumulation (without propagation) in a heterogeneous solid.

The bonded contact model is applied in conjunction with fracture mechanics and statistical models, in Chapter 8, to explore the mechanisms of insitu strength reduction, including, scale effect, crack length and surface interaction, pre-existing damage and the effects of stress path (and stress rotation during excavation). The impact of dilating cracks as well as material heterogeneity on effective local confinement reduction (and effective strength) is examined.

A discussion and summary of the thesis including major conclusions and recommendations for future research is provided in Chapter 9.

PART I
STRUCTURAL OR GRAVITY DRIVEN
INSTABILITY

CHAPTER 2

Tensile Strength and Relaxation: Control Mechanisms for Structural Failure

2.1 INTRODUCTION

Classical assessment of instability potential in underground excavations is normally based on yield and rupture criteria for stress driven failure and on limit equilibrium analysis of structurally controlled failure. While it is true that ultimate failure and falls of ground can be an eventual consequence of stress fracturing and unfavourable structure within the rockmass, the timing of such failure is often controlled by the presence and subsequent destruction of residual rockmass tensile capacity. This self-supporting capacity can often be attributed to the distributed load bearing capacity of "rock bridges" separating joint segments and fractures. Structurally bounded rock blocks can also be supported by the effects of clamping and allowed to fail, due to gravity, by the relaxation of the surrounding rock or abutments.

Using crack and rock bridge analogues in conjunction with field evidence and an updated voussoir beam model, Part I of this thesis (including Chapters 2, 3 and 4) explores the influence of residual tensile strength and boundary-parallel relaxation on the failure process in structurally controlled, low-stress environments. The impact on support design is also examined.

In underground hard rock mines with complex geometries and interacting openings, relaxation is identified as a key controlling factor in groundfall occurrence. Empirical stability assessment techniques for underground tunnels and for mining stopes are updated later in Part I to account for relaxation. In this chapter, the importance of residual rock bridge tensile strength and boundary-parallel clamping and relaxation is introduced, focussing on the stability of blocks and wedges. As part of the thesis requirements, much of what is presented in Part I has been published in the form of journal articles by the author (Diederichs and Kaiser 1999a; 1999b and Diederichs et al 1999).

2.1.1 Stability Assessment

Stability assessment of underground excavations is classically divided into two procedural domains. These two domains are based on a distinction between structurally controlled and stress driven modes of instability. It is the premise of this thesis, however, that in non-squeezing and non-bursting ground, structure and stress serve merely as ground conditioning mechanisms. Gravity loading is ultimately responsible for large-scale groundfalls or for significant loading of support.

When the rockmass jointing is non-persistent or if the near surface crack damage is not yet fully continuous, the intervening rock bridges contribute to the stability of an excavation through the rockmass residual tensile strength or load bearing capacity. Failure to consider the rockmass self-supporting capacity and the effects of abutment confinement or abutment relaxation can lead to erroneous predictions of failure or of support load.

Gravity induced groundfalls are common occurrences in underground excavations of all depths. Numerous techniques can be applied to assess the potential for such groundfalls provided that an appropriate failure mode is assumed. Typical failure modes which can be analyzed include wedge fallout, slab or plug failure, gravity driven caving and beam failure. Models taking these failure modes into account are generally utilized for stability assessments in low-stress or near-surface excavations. The underlying assumptions of most of these models are that through-going joints or discontinuities are fully persistent and that stability is controlled by structural geometry and by friction (with or without dilation). The inherent tensile or cohesive strength of moderately jointed rockmasses is often assumed to be negligible in these models.

Alternatively, for excavations at depth or for shallower excavations in weaker rockmasses, linear elastic stress analysis can be used to determine the location and extent of problematic stress concentrations around the openings using an empirical damage threshold (Kaiser et al 1996). Initial cracking or fracturing is generally parallel to the excavation surface and therefore parallel to the major compressive stress. This crack damage is strain dependent and may be exacerbated by preferential deflection and dilation into an opening and by existing planes of weakness such as foliation or meta-bedding resulting eventually in moderately persistent planar laminations in otherwise massive or moderately jointed rock (Figure 2.1).



Figure 2.1: Gravity collapse of moderately jointed to massive ground after stress induced fracturing (Brunswick Mine, N.B., courtesy P.K. Kaiser)

2.1.2 Short-term Strength and Delayed Failure

A prediction of rockmass stress in excess of yield limits, based on elastic models, or the delineation of a kinematically feasible and apparently unstable wedge, does not inevitably correspond to actual catastrophic failure of the underground opening. This is fortunate given the depths encountered in modern mining, where much of the ground above mining openings has reached a damage or yield stress threshold at some point in the mining sequence and yet, with the exception of highly stressed ground experiencing rockbursting, shearing or stress buckling, generally remains in place in the short-term. This is due to the rockmass residual tensile strength normal to the excavation boundary and transfer of load to the abutments (arching).

Paradoxically, ultimate failure of this damaged ground is often induced by changes in mine geometry which reduce (Maloney and Kaiser 1992; Kaiser et al. 1992; Milne 1996; Suorineni 1998; Falmagne 1999) rather than increase the stresses across the back or walls. This seems to have been the case in Figure 2.1. It is the premise of this thesis that the key to this discrepancy between modeled or predicted failure and the actual observed occurrence of failure in underground excavations in hard rock is due to the dominance of the rockmass's tensile load bearing capacity.

However, if combined with abutment relaxation, the influence of gravity can exceed the tensile load bearing capacity of naturally jointed or stress fractured rockmasses leading to the type of failure illustrated in Figure 2.1.

Part II of this thesis explores the mechanics of formation for boundary-parallel stress cracks. The following discussions, on the other hand, assume that such induced fracture damage or naturally occurring jointing is omnipresent in underground excavations.

The nature of residual tensile capacity in jointed or fractured rockmasses will be discussed, comparing its capacity to that of economical engineered support systems. The effect of abutment relaxation on rock wedge and blocky slab stability is demonstrated. Different mining scenarios are described which may lead to destabilizing relaxation. The voussoir arch analogue, described in Chapter 3 is used in Chapter 4 to further demonstrate the importance of boundary-normal tensile capacity and abutment relaxation. The voussoir analogue is then calibrated to correspond with empirical stability guidelines for rockmass stability. The effect of relaxation is further demonstrated in this context.

2.2 STRUCTURAL STABILITY

2.2.1 Structural Failures at Canadian Mines

Structurally controlled failure of backs and walls in underground excavations poses a severe hazard to mine personnel. A survey analyzed by Hutchinson (1998), of 194 reported groundfalls between 1985 and 1996 at 12 mines owned by International Nickel Corporation (INCO) in the Sudbury Region, reveals the importance of such instability (Figure 2.2).

Even though this database covers depths ranging from 150m to 2300m in the Canadian Shield, structural failure makes up approximately 68% of cases in which the failure mode was determined. Cases involving stress-induced shear on structural planes (faults) involves 15% of explained cases. This database includes officially reported (i.e. to Ontario Ministry of Labour) cases of falls of ground greater than 5 tonnes. Blasting (42%), drilling (13%) and mucking (10%) are identified as major catalysts for the "structural" failures shown in Figure 2.2. Observed relaxation (e.g. open joints, etc) without blasting is identifies as the cause of failure in 13% of the cases. In addition, the category of "blasting" includes local geometry changes causing relaxation of roof blocks, and can also be responsible for the destruction of rock bridges and internal support loss.

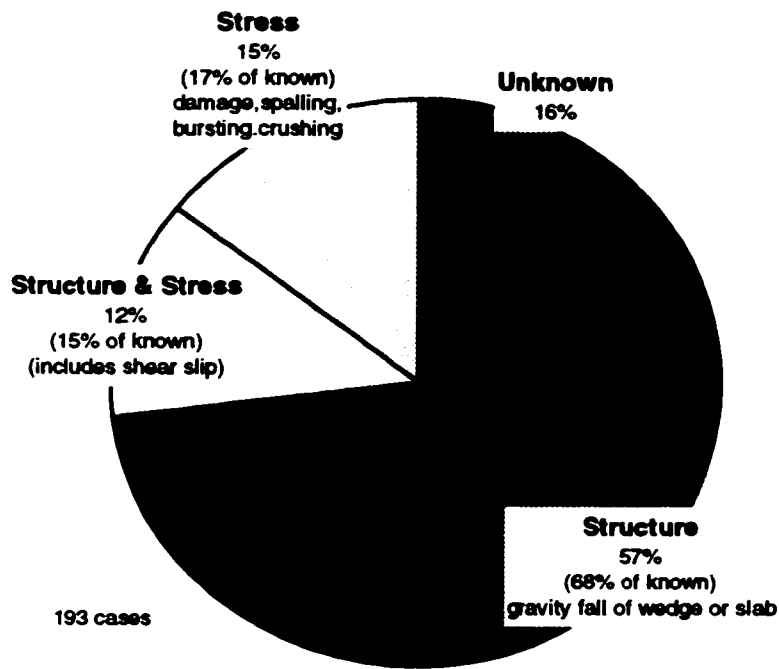


Figure 2.2: Relative percentages of failure mechanisms identified in major groundfalls at INCO Ltd. mines in the Sudbury Region.

Typical wedge formation (the most common form of structural instability in drifts and accessways) is illustrated in Figure 2.3. Persistent jointing as mapped in the back of the same excavation is shown for comparison in Figure 2.4.

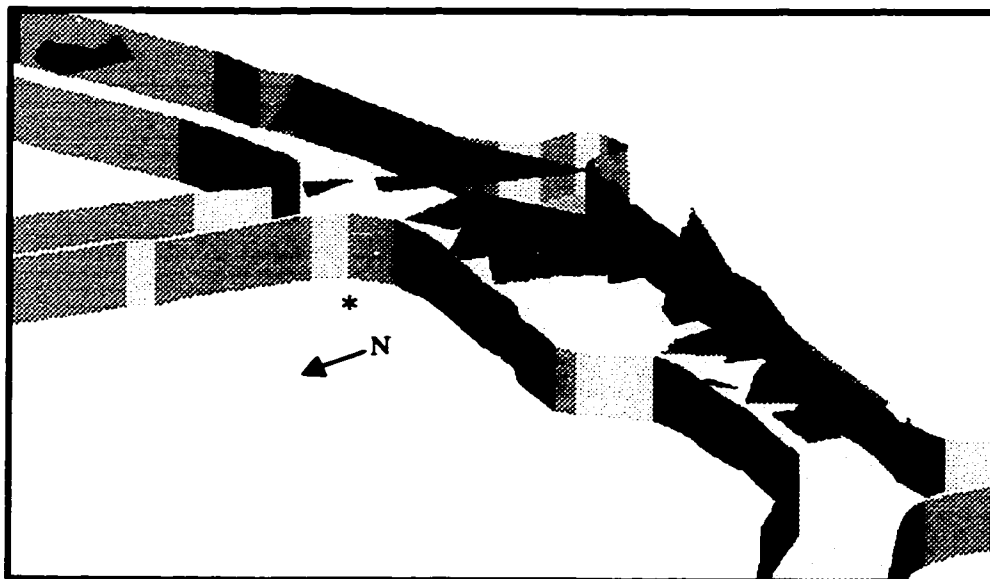


Figure 2.3: Kinematically feasible (present but not necessarily failed) wedges formed from intersecting joints in Figure 2.4. (Main accessway at North Mine 175 Ore Body).

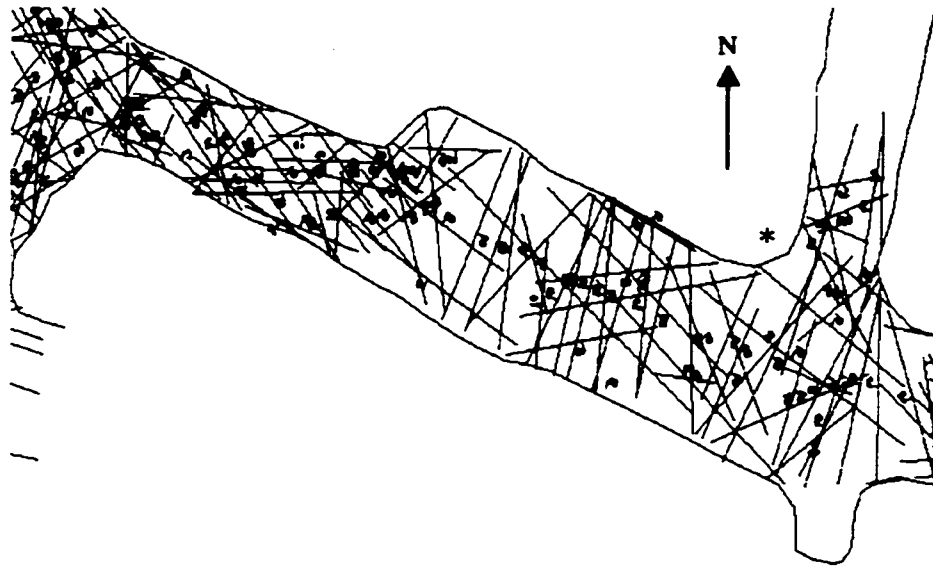


Figure 2.4: Joints mapped in the back of the main access at INCO's North Mine 175 Orebody.

Wedges form when these joints mutually intersect to form a free block which can move into the opening. Such a block is termed kinematically feasible. A large wedge failure in a stope topsill is shown in Figure 2.5.

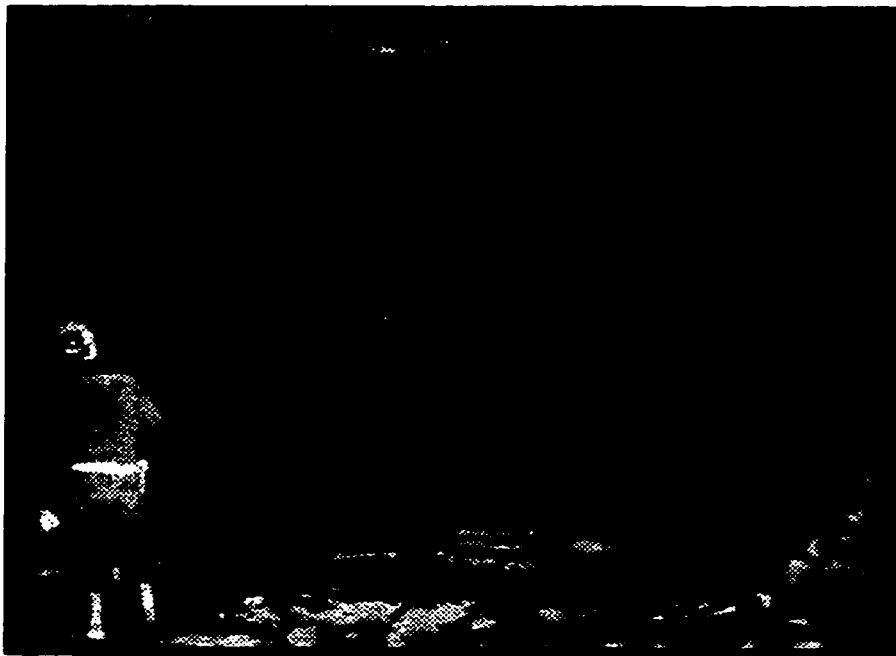


Figure 2.5: Wedge failure in the back of a stope. Material in foreground is backfill.

Another common structural control is boundary-parallel lamination. Examples of walls and backs with natural laminations are shown in Figure 2.6. Lamination parallel tensile stress resistance, necessary for the stability of an elastic beam (Hoek and Brown 1980) is often negated by cross-jointing normal to the excavation boundary (visible in Figure 2.6b). This creates a so-called "voussoir" beam which can be stabilized by a compression arch if the beam is thick enough. If not failure such as that illustrated in Figure 2.7 results.

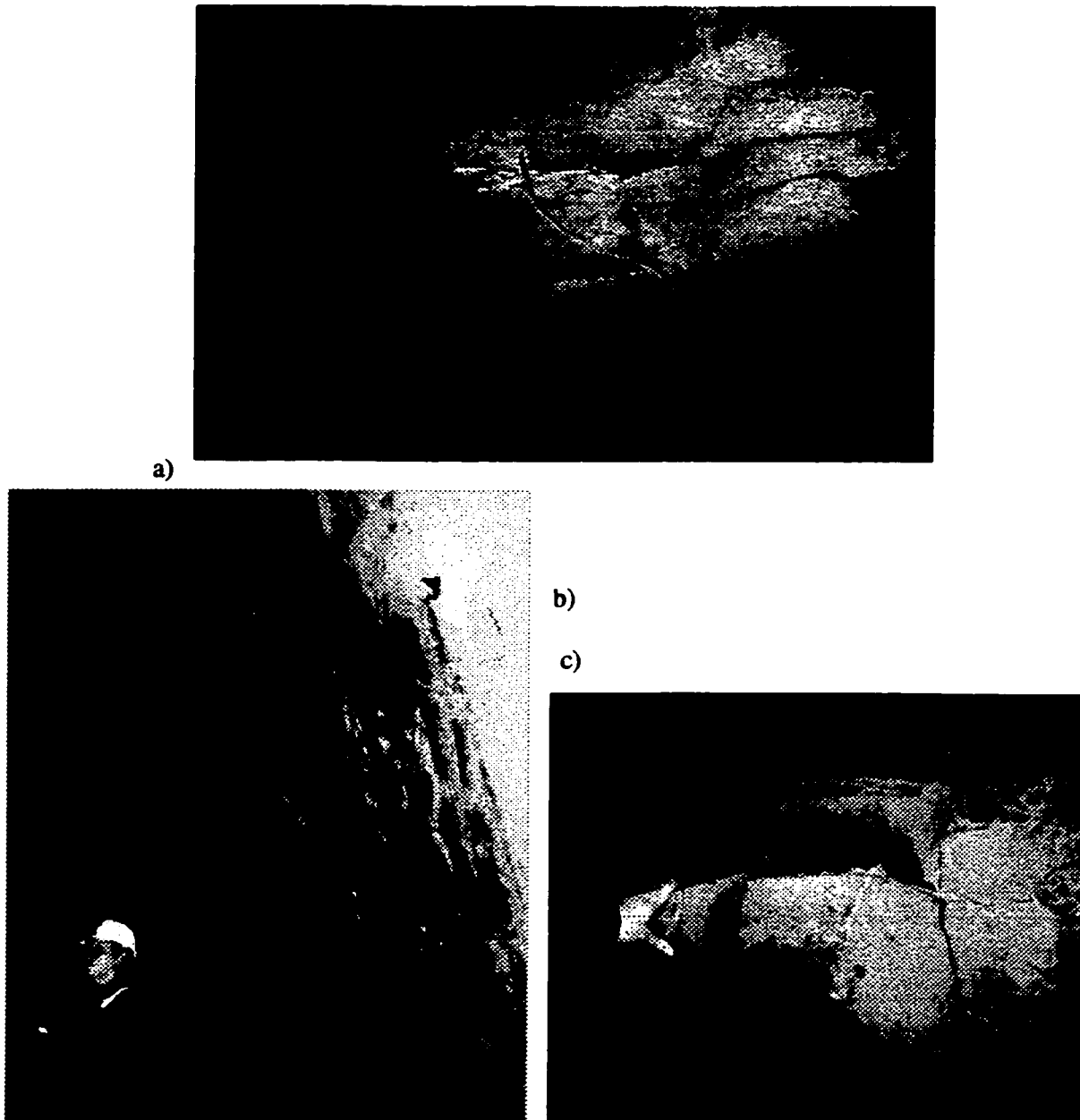


Figure 2.6: Boundary-parallel laminations in underground excavation back (a) and stope walls (b and c).

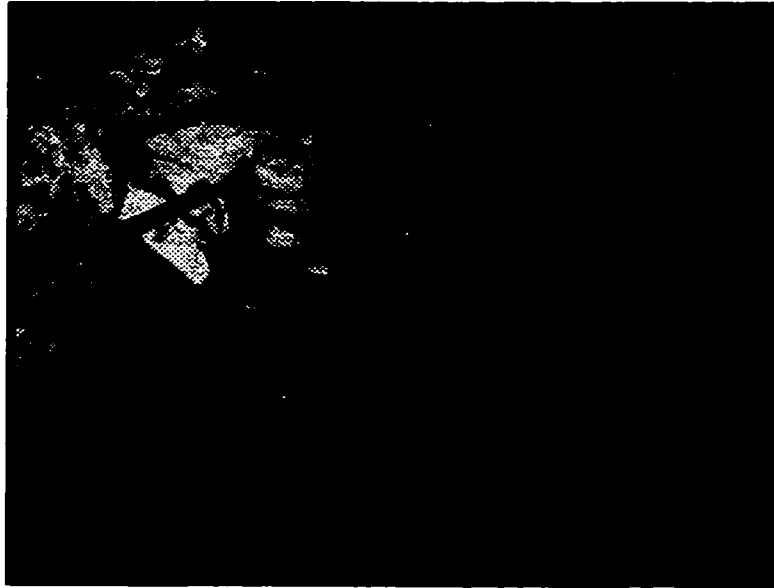


Figure 2.7: Failure of a voussoir arch in a laminated stope back. Tendons visible are failed cablebolt supports.

A similar mechanical character can also be induced by boundary-parallel crack extension (spall damage) due to high compressive stresses across the back (Figure 2.8). This stress damaged rock may remain stable due stress arching and the stability of the surface-parallel "beams". Stress relaxation at a later date, however, may cause this damaged rockmass to fall in a manner similar to joint controlled unravelling. This is common above large open stopes (Falmagne 1999).



Figure 2.8: Stress induced boundary-parallel spalling resulting in laminations that failed under gravity loading due to stress change and relaxation. Horizontal field of view is (left) 4m and (right) 5m. Direction of original compression shown by arrows.

2.2.2 Evidence of clamping as a failure control

The rockmass structure in INCO's Sudbury mines is dominated by steeply dipping joint sets (dip > 60°) as illustrated in Figure 2.9. Moderately inclined structure is present but sparsely distributed. Intersections of major joints sets are analyzed to produce the typical wedge geometries in Figure 2.10. The wedges shown are assumed to occupy the full span of the excavation (worst-case analysis). If only the joint orientations are considered (i.e. theoretical kinematic feasibility) typical wedges are predicted to occur (frequently) which have heights in excess of the span.

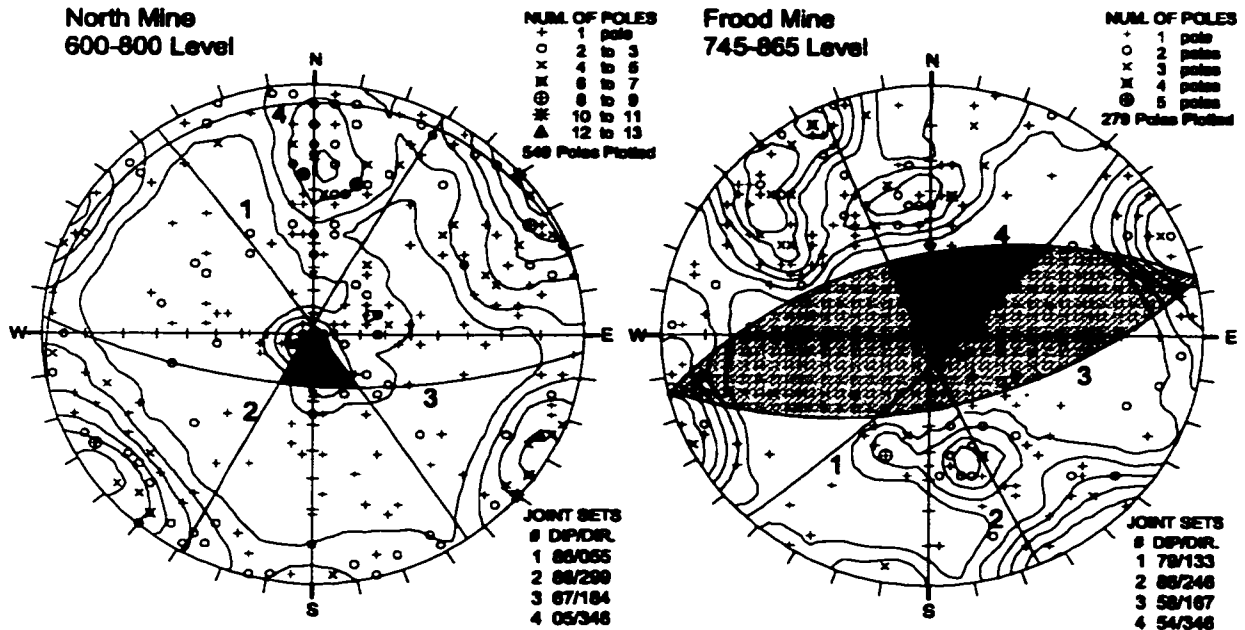


Figure 2.9: Examples of dominant joint sets from two INCO mines. Most prominent roof wedges shown in dark shading. Light shading at right indicates a 2D roof prism

Figure 2.11, however, shows the actual aspect ratios for wedges in drifts and intersections (no stope sills included). The height-span ratios are considerably less than would be expected from Figures 2.9 and 2.10. Of course, most wedges do not traverse the entire span. If the actual wedge geometry is considered, the "Failure Height / Failure Width" ratios are still lower than predicted.

Mining drifts, in the Canadian Shield, isolated from stopes or faults, will normally have significant clamping stress acting across the back (due to the horizontal orientation of the major insitu stress). This clamping stress does not allow steeper joint-bounded wedges to be released, although small wedges with a higher aspect ratio may fall from the centre of a drift as deflection reduces the local clamping at midspan. In addition, limited joint persistence results in the presence of internal rock bridges which provide internal (tensile) support for the wedge or block below.

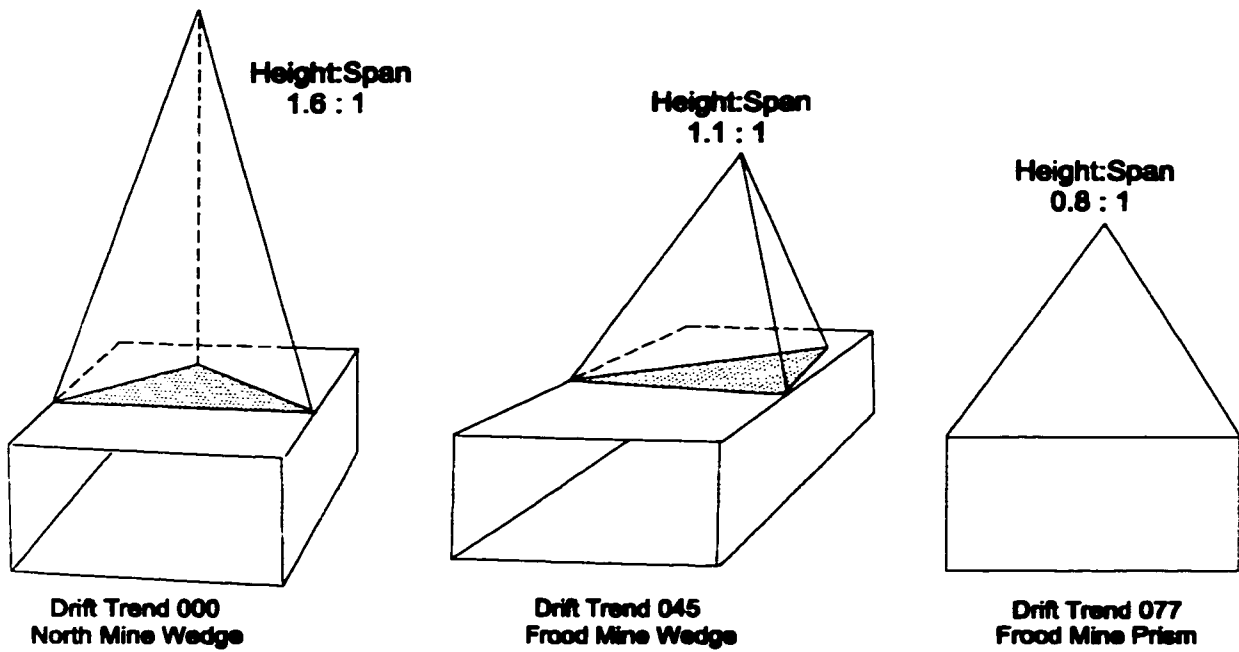


Figure 2.10: Examples of typical (theoretical) full span wedges at INCO's Sudbury mines. These wedges are formed from the most probable joint intersections in Figure 2.9.

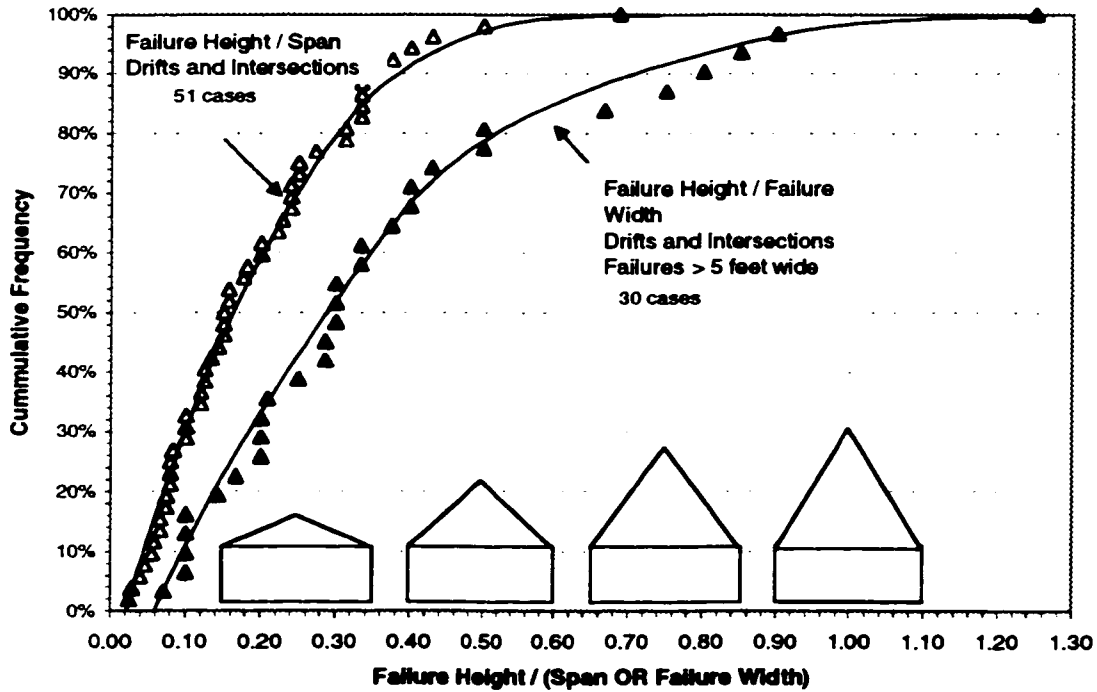


Figure 2.11: Actual wedge aspect ratios (for groundfalls at INCO mines) with respect to excavation span and to actual wedge base width (Hutchinson 1998).

2.3 BOUNDARY-NORMAL TENSILE STRENGTH

While tensile strength can often be justifiably neglected in cases of weak and highly fractured rock, the residual strength of rock bridges in moderately jointed and bedded hard rockmasses contributes significantly to self supporting capacity and must be considered. Extension joints are rarely fully persistent at depth (Priest and Hudson 1981; Kulatilake and Wu 1984; Villaescusa and Brown 1992). Hence, it would be realistic to expect the initial presence of intact rock bridges.

Foliation planes and bedding planes are weaker than the surrounding rock but still possess some limited tensile strength in many cases until full parting occurs due to excessive deformations. This can be seen in the case of progressive hangingwall delamination reported by Maloney and Kaiser (1993), for example, and partially explains why ground can remain unsupported in spite of contrary limit equilibrium calculations based on the stability of a fully bounded wedge, block or slab.

In spite of this initial and static stability, however, support may still be required to protect against groundfalls induced by dynamic disturbance, time and stress dependent tensile strength corrosion (Lajtai and Bielus 1986), and mining induced deformations. Support in such conditions can also prevent or inhibit the propagation of fractures and the degradation of rockmass tensile capacity.

In jointed or in massive rockmasses at depth, under the low normal confinement conditions encountered adjacent to an excavation, surface-parallel cracks can develop as a result of compressive stress. This micro-cracking parallel to the maximum principal stress direction has limited effect on the ultimate compressive strength since it is an inherently stable fracture process (Fairhurst 1971). The same cracks, however, subjected to tensile loading, normal to the plane of the crack (as occurs above a horizontal excavation roof), propagate easily when a critical tensile strain is exceeded and have a profound impact on the strength, particularly if the compressive stress parallel to the boundary is maintained.

Under such compressive stress, boundary interaction also plays a role in the enhanced propagation of near-excavation cracks (Dykin and Germanovich 1993; Ashby and Hallam 1986). It can be assumed however, that in many cases the initial jointing or parallel fracturing is not complete and that intermittent rock bridges remain to be exploited by gravity.

2.3.1 Tensile Fracture Strength Models

The ratio of tensile (σ_T) to uniaxial strength (UCS) of intact rock is significantly lower than for other materials such as steel. Typical tensile values range from one tenth to one twentieth of the UCS for hard rocks (Stacey and Page 1986). These relatively low values, combined with the conservative assumption of fully persistent jointing, lead to the common neglect of the rockmass tensile strength as a practically significant factor in excavation stability.

Griffith theory (1924) has become a classic means of explaining the relatively low tensile strength of heterogeneous and imperfect solids such as rock, describing how small imperfections such as cracks serve to concentrate tensile stresses locally, resulting in a reduction in macroscopic sample strength. The associated stress intensity relationships for internal and external cracks in plates (Irwin 1957; Sih 1973; Kemeny and Cook 1986) can be extended for isolated cracks and rock bridges in three dimensions (Figure 2.12).

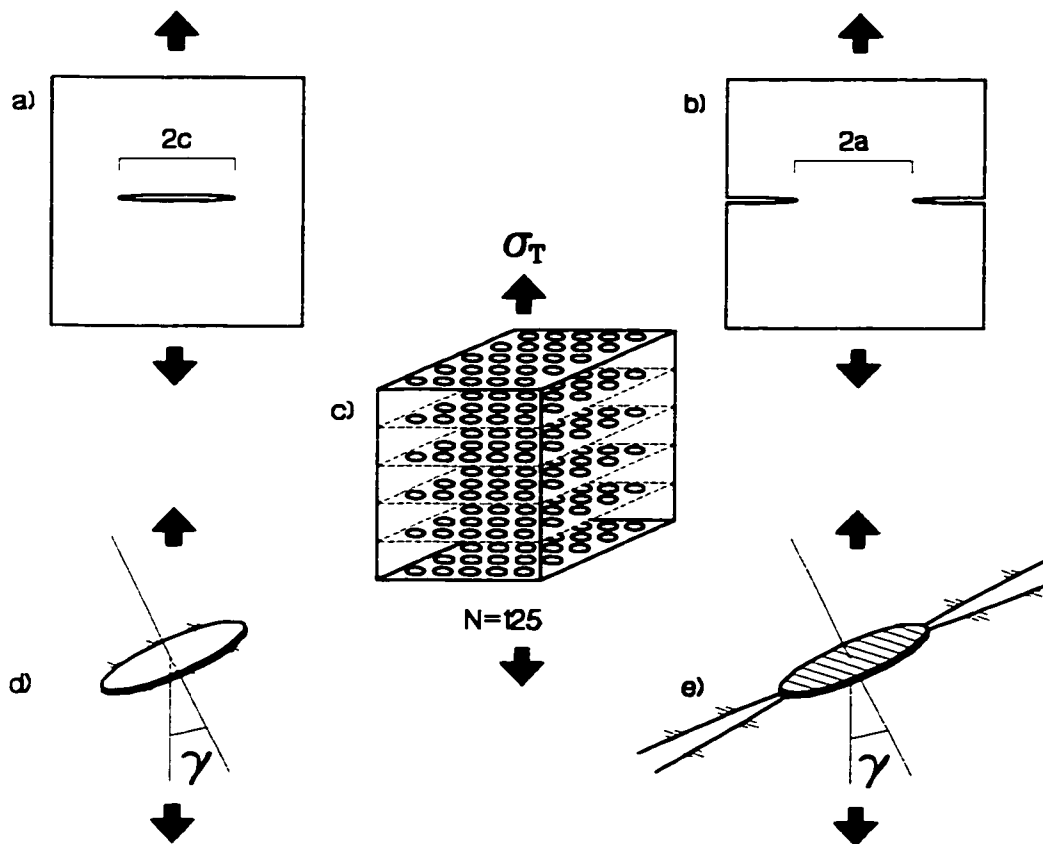


Figure 2.12: Crack geometries: a) 2D non-interacting crack; b) 2D rock bridge; c) 3D assembly of cracks; d) 3D isolated non-interacting crack; and e) 3D isolated rock bridge.

For a given Mode I stress intensity factor at crack extension K_{IC} , the tensile strength for a partially cracked solid can be computed for circular non-interacting cracks (Figure 2.12:a & d) of radius c , with crack normals oriented at angle γ to the direction of tensile loading:

$$\sigma_T = K_{IC} \left(\frac{\pi}{2\sqrt{\pi c}} \right) \frac{1}{\cos^2 \gamma} \quad [2.1]$$

Using Kemeny and Cook's (1986) solution for the so-called external crack, the tensile strength of a cylinder of rock with a total cross sectional area, A , containing a circular rock bridge of radius a (surrounded by a planar, annular crack) is given by:

$$\sigma_T = K_{IC} \left(\frac{2a\sqrt{\pi a}}{A} \right) \frac{1}{\cos^2 \gamma} \quad [2.2]$$

If N/V is the number of regularly distributed cracks or rock bridges in a unit cubic volume ($V = 1\text{m}^3$), then the total coplanar cross sectional area (cracked and uncracked) associated with the crack or rock bridge, A is:

$$A = \frac{1}{N^{2/3}} \quad [2.3]$$

If $(A_c^*)A$ is the area of the crack and $(A_a^*)A$ is the area of the rock bridge (where A_c^* and A_a^* are the ratios of cracked and intact area, respectively, to the total cross sectional area):

$$c \approx \sqrt{\frac{A_c^*}{\pi N^{2/3}}} \quad [2.4]$$

$$a \approx \sqrt{\frac{A_a^*}{\pi N^{2/3}}} \quad [2.5]$$

where $A_a^* = 1 - A_c^*$.

It is possible now to express the tensile strength with respect to the percentage of cracked cross sectional area for cracks perpendicular to loading ($\cos^2 \gamma = 1$):

$$\sigma_T = \frac{\pi}{2} K_{IC} \sqrt{\frac{N^{1/3}}{\sqrt{\pi(A_c^*)}}} \text{ for } A_c^* \ll 1 \quad [2.6]$$

or inversely, with respect to percentage of intact rock bridges :

$$\sigma_T = 2K_{IC} \sqrt{\frac{(A_c^*)^{3/2} N^{1/3}}{\sqrt{\pi}}} \text{ for } A_c^* \ll 1 \quad [2.7]$$

These equations for isolated cracks and isolated rock bridges, analyzed as “external cracks” by Kemeny and Cook (1986), serve as limiting cases for progressive crack damage as illustrated in Figure 2.13 using a unit stress intensity factor. The actual tensile strength varies linearly with K_{IC} as per Equations 2.6 and 2.7. Figure 2.13 clearly illustrates the significant reduction in theoretical tensile strength with small amounts of distributed micro-cracking ($A_c = 0$ to 0.1). It is acceptable to presume that even intact rock samples normally contain a significant amount of internal damage and therefore exhibit tensile strengths which are lower than those for a perfect solid.

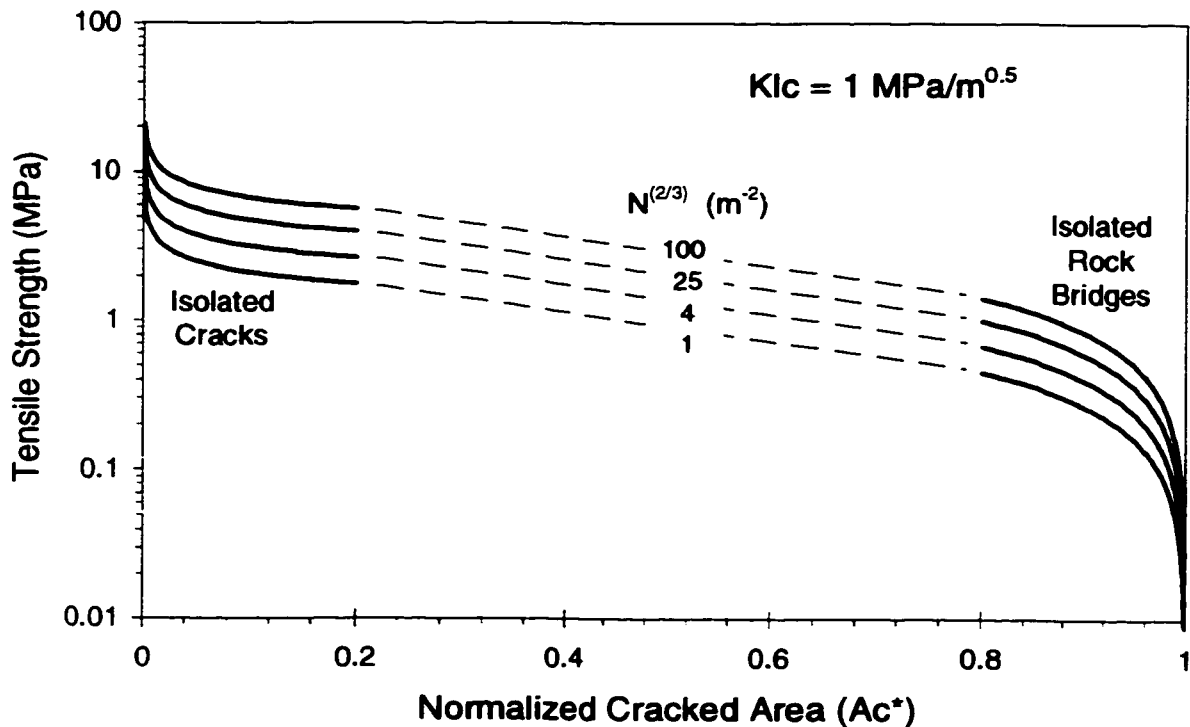


Figure 2.13: Tensile strength vs normalized cracked cross-sectional area.

Figure 2.13 also illustrates that the theoretical tensile strength is apparently insensitive to the areal extent of cracking for the intermediate range, $A_c = 0.1$ to 0.9 . For values of $A_c > 0.9$ or $A_c < 0.1$, however, the tensile strength decays rapidly until complete (fully persistent) cracking is achieved. Figure 2.13 also shows that a few large cracks (low N) within the rock degrade the strength more than numerous smaller cracks (high N) with the same total crack area. For comparison with measurements of relative linear joint trace persistence, P , the regular array of cracks in Figure 2.?? yields the approximate relationship for average linear persistence, P :

$$P = \psi \frac{c}{c+a} = \psi \frac{A_c^*}{1 + 2\sqrt{A_c^*(1-A_c^*)}} \quad [2.8]$$

where ψ is a factor which ranges from $1/\sqrt{2}$ to 1 for small (isolated) cracks and from 1 to $\sqrt{2}$ for rock bridges (extensive cracking), depending on the linear persistence measurement direction in the plane of the circular crack or rock bridge. This factor appears due to the superposition of a circular crack or bridge within a square associated area.

In order to fully examine the role of tensile strength as a support mechanism it is also necessary to examine the impact of crack damage on rock stiffness. This is achieved using the Griffith locus for tension (Berry 1960). By assigning spherical averages to the orientation terms in an expression for the strain energy due to an individual crack, and incorporating the result into a variation of Betti's reciprocal theorem, Kemeny and Cook (1986) calculate the ratio of Young's modulus for a solid with randomly distributed non-interacting cracks:

$$\frac{E_c}{E_o} = \frac{1}{1 + \frac{16}{45} \chi (1-\nu)^2 \frac{10-3\nu}{2-\nu}} \quad [2.9]$$

and for rock bridges in a randomly cracked solid:

$$\frac{E_c}{E_o} = \frac{1}{1 + \frac{\pi^2}{15} \chi (1+\nu) \frac{5-4\nu}{m(m+1)}} \quad [2.10]$$

Equation 2.9 can be simplified for the case of mono-directional cracks perpendicular to the direction of tensile loading:

$$\frac{E_c}{E_o} = \frac{1}{1 + \frac{16}{3} \chi (1 - \nu^2)} \quad [2.11]$$

while Equation 2.10 can be simplified for regularly spaced parallel rock bridges within an axisymmetric (cylindrical) volume:

$$\frac{E_c}{E_o} = \frac{1}{1 + \frac{\pi^2 \chi' (1 - \nu)^2}{m(m+1)}} \quad [2.12]$$

where $\chi = N(c)^3/V$ is the crack density for isolated cracks, $\chi' = N(c')^3/V$ is the crack density associated with isolated rock bridges, N is the number of cracks or rock bridges, $V=1$ is the unit volume in the study and a is the average radius of rock bridges surrounded by a cracked annulus of width c' such that:

$$c' = \frac{1 - \sqrt{A_a^*}}{\sqrt{\pi N^{2/3}}} \quad [2.13]$$

$$m = a/c' = \frac{\sqrt{A_a^*}}{1 - \sqrt{A_a^*}} \quad [2.14]$$

The value of c' represents the average edge separation for an array of equivalent cylindrical (and not cubic) rock bridge volumes. The definition is different than that obtained for $c=f(a)$ from Equations 2.4 and 2.5 and differs from the three dimensional formulation of Kemeny and Cook (1986). These modified terms are necessary to obtain a three dimensional solution for rock bridges which is behaviourally compatible with the original two dimensional formulation.

Equations 2.11 and 2.12 combined with Equations 2.6 and 2.7, define the Griffith Locus and the stress/strain relationships for isolated cracks (Figure 2.14) and isolated rock bridges (Figure 2.15). In Figure 2.14, the cracks nucleate at points arranged in a regular cubic array with the initial separation defined by Equation 2.3. These cracks then propagate in a plane perpendicular to loading.

In Figure 2.15 the cracks have coalesced leaving a regular array of intact and progressively shrinking rock bridges with the same separation as the original cracks. The total number of cracks, N , remains constant.

The genesis of natural and induced joints or fractures is undoubtedly sensitive to initial boundary condition and response and may not necessarily progress to full rupture in a single stage, terminating at some point in this sequence. At issue here is the renewed response of non-persistent cracks and rock bridges upon exposure to excavation induced gravity loading.

In Figure 2.14, it is interesting to note that while a drastic loss in crack propagation stress does occur in the presence of very small cracks, practically detectable reduction of the reloading modulus does not occur until the cracks occupy more than 10% of the cracked area. Even at 20%, the modulus is still 95% of the initial value.

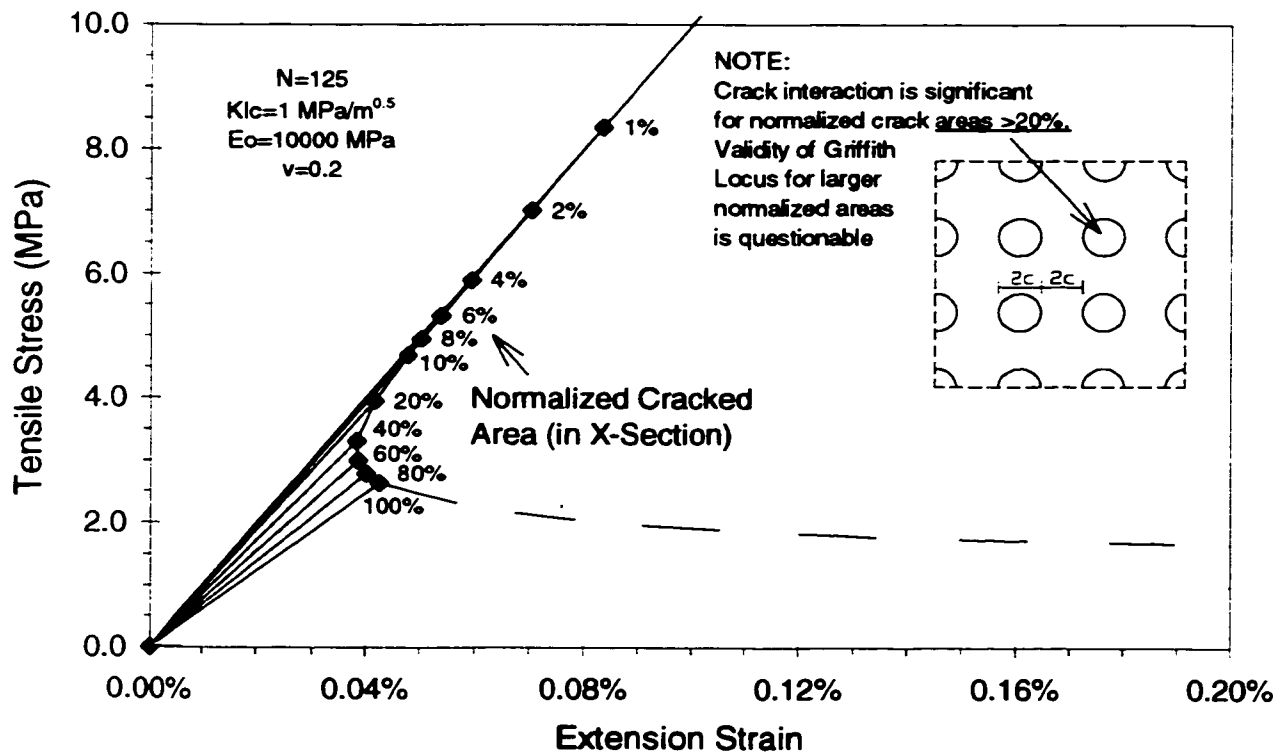


Figure 2.14: Example of Griffith Locus and vertical stiffness relationships for a rock sample containing isolated horizontal cracks.

The effect on stiffness is limited but at 20% relative area, the crack diameter exceeds the separation between the edges of neighbouring cracks ($a:c = 1:1$ and in inset in Figure 2.14). At this point crack coalescence becomes critical according to the theoretical work of Pollard and Segall (1987) who show that the strain perturbation due to a crack decays considerably at an inter-crack edge separation of one crack length and becomes insignificant for an edge separation of 2 crack lengths.

At a level of crack density beyond the limit of 10 to 20% cracked area, it is also difficult to reconcile the Griffith locus for isolated cracks with the locus for isolated rock bridges (Figure 2.15) as end members of a transitional cracking process (requiring the dashed lines in Figure 2.13). Figure 2.15 shows the response after coalescence and rock bridge development is well established.

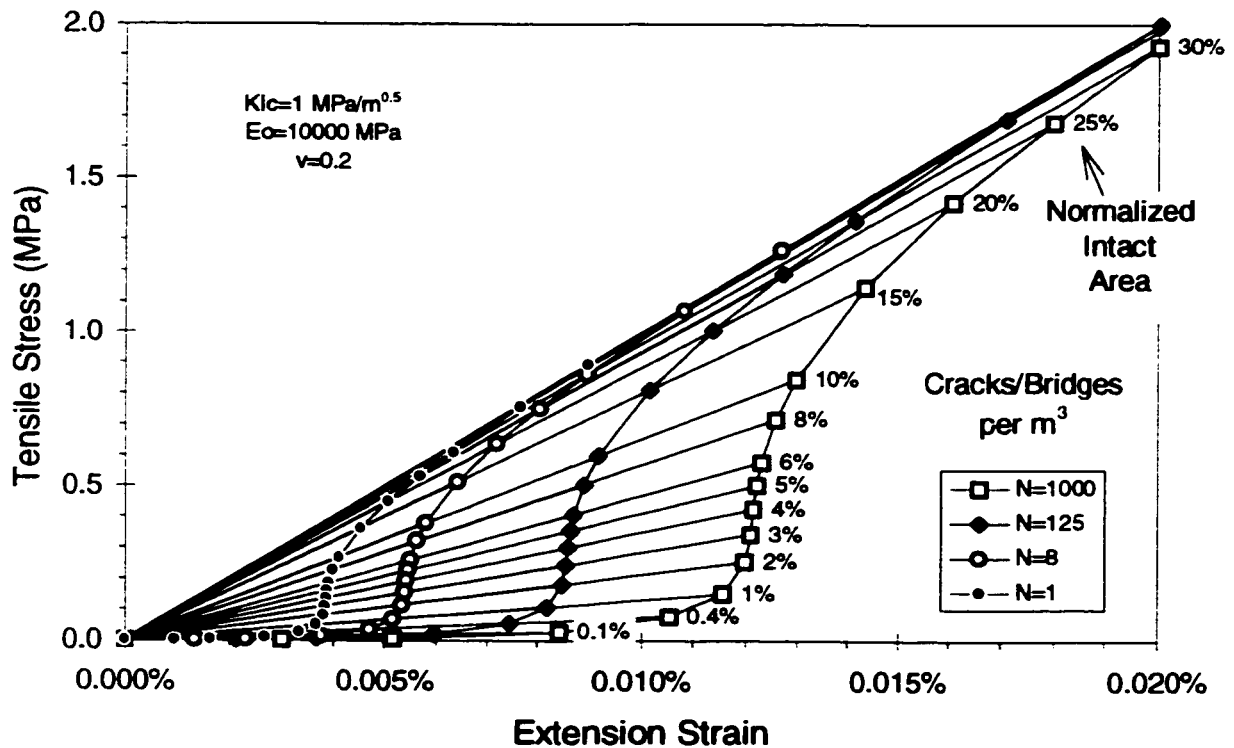


Figure 2.15: Example of Griffith Locus and vertical stiffness relationships for rock sample containing isolated horizontal rock bridges.

Figure 2.15 illustrates the theoretical stress-strain relationships and crack propagation strengths for a highly cracked solid. In this plot, the cracks have coalesced and are converging on remnant (circular) rock bridges, a more realistic end process for insitu fracturing. There is a stage between

approximately 15% intact area and 1% intact area (corresponding to 85% and 99% cracked area respectively) through which the rupture occurs at a near-constant level of overall extension strain.

For a single crack ($N=1$), a unit fracture toughness and with $E=10\text{GPa}$ and $\nu=0.2$ for the intact rock, this corresponds to a range of residual tensile strength between 0.3MPa and 0.03MPa at a strain limit of approximately 0.004%. For $N=1000$ (indicating a highly distributed cracking process), this threshold strain is approximately 0.012%, spanning residual strengths of 1 to 0.1MPa for the same range of cracked areas. Okubi and Fukui (1996) performed direct tensile tests on numerous rock types using an extremely high resolution servo-control and reported residual tensile strengths within these ranges of magnitude.

2.3.2 Support Equivalency of Rock Bridges

Of particular interest for support design, given an assumption for crack or rock bridge distribution (N), is the constant nominal strain limit which can be expected of residual rock bridges. The threshold is small, indicating that if failure is to occur due to gravity loading, only relatively stiff or pre-stressed support systems such as resin grouted rebar or tensioned bolts on a tight pattern can prevent the loss of rock bridges and residual strength.

Pattern support in the form of regularly spaced mechanical rockbolts, grouted rebar, split sets or cablebolts serve primarily to resist gravity and to “hold” the rockmass adjacent to an excavation. These support configurations also contribute to the inherent integrity of the rockmass, resisting dilation and increasing frictional resistance of rough fractures and discontinuities. In stress damaged rock, stiff or actively pre-loaded reinforcement can also serve to prevent the failure of rock bridges and thus the complete loss of rockmass tensile strength.

In their primary role, however, these support systems can provide distributed tensile load capacities ranging from 20kPa to 300kPa, respectively, for sparse and for economically limiting support patterns as shown in Table 2.1. The demand equivalence in terms of vertical height of supported rock (assuming no other stabilizing mechanism) is given for comparison. Table 2.1 also illustrates the very small relative cross sectional areas of intact rock (rock bridges) required to achieve the same tensile load capacity using the example values from Figures 2.13 and 2.15.

Table 2.1: Support patterns (from Stillborg 1994) and equivalent rock bridge area ($N=125$).

Support Type	Support Pattern m x m	Equivalent Pressure	Maximum Supported Thickness	Capacity Equivalent Rock Bridge Area (% cross section)
Rockbolts	2 x 2	20kPa	0.7 m	0.1%
Rebar	1.3 x 1.3	60kPa	2.0 m	0.4%
Single Strand Cablebolts	2 x 2	65kPa	2.2 m	0.4%
Double Strand Cablebolts	2 x 2	130kPa	4.3 m	1.2%
Double Strand Cablebolts	1.3 x 1.3	300kPa	10 m	4.0%

Note: 1% rockbridge area is equivalent to a 10cm x 10cm rockbridge per 1m² total area

The main difference between the supporting mechanisms of artificial tendons and internal rock bridges is the magnitude of the rupture strains in the direction of tensile loading. While steel tendons such as rockbolts and cables typically yield at strains of approximately 1% to 2% for average grades of steel (Illston et al 1979), reasonably intact rock specimens (Figure 2.14) begin to rupture at tensile strains of less than 0.1% and small rock bridges ($A_c^* < 10\%$) such as those modeled in Figure 2.15 rupture at strain levels below 0.01%. The convex shape of the locus in Figure 2.15 also indicates that any tensile rupture involving rock bridges will be sudden, unstable or catastrophic and can be considered brittle constitutive behaviour for the purpose of comparison to most artificial support systems. Only extremely stiff or pre-stressed reinforcement can be considered effective in the preservation of the rockmass tensile strength.

If tensile rupture of rock bridges is considered a small-strain brittle phenomenon, then it is appropriate to consider residual tensile strength as a supporting mechanism for gravity loaded blocks as illustrated in Figure 2.16. Consider, for example, a design factor of safety of 2 against gravity loading for the 45 degree wedge. This dictates a maximum span of 4m if full persistence (intact area = 0%) is assumed and a 2m x 2m pattern of single strand cablebolts is installed.

If it could be determined that rock bridges exist across the bounding planes of the wedge and that the relative intact area across these planes is merely 1%, then a maximum span of 11m would be acceptable without the need for support. This result demonstrates that the stability of an excavation or the factor of safety can be profoundly influenced by the presence of small rock bridges within the jointed rockmass and thus draws into question the conventional assumption of full joint persistence in limit equilibrium analyses. It also points to the importance of blasting control for the preservation of such rock bridges in moderately jointed rockmasses. Most importantly, it illustrates the potential economic benefits of practical strain control measures.

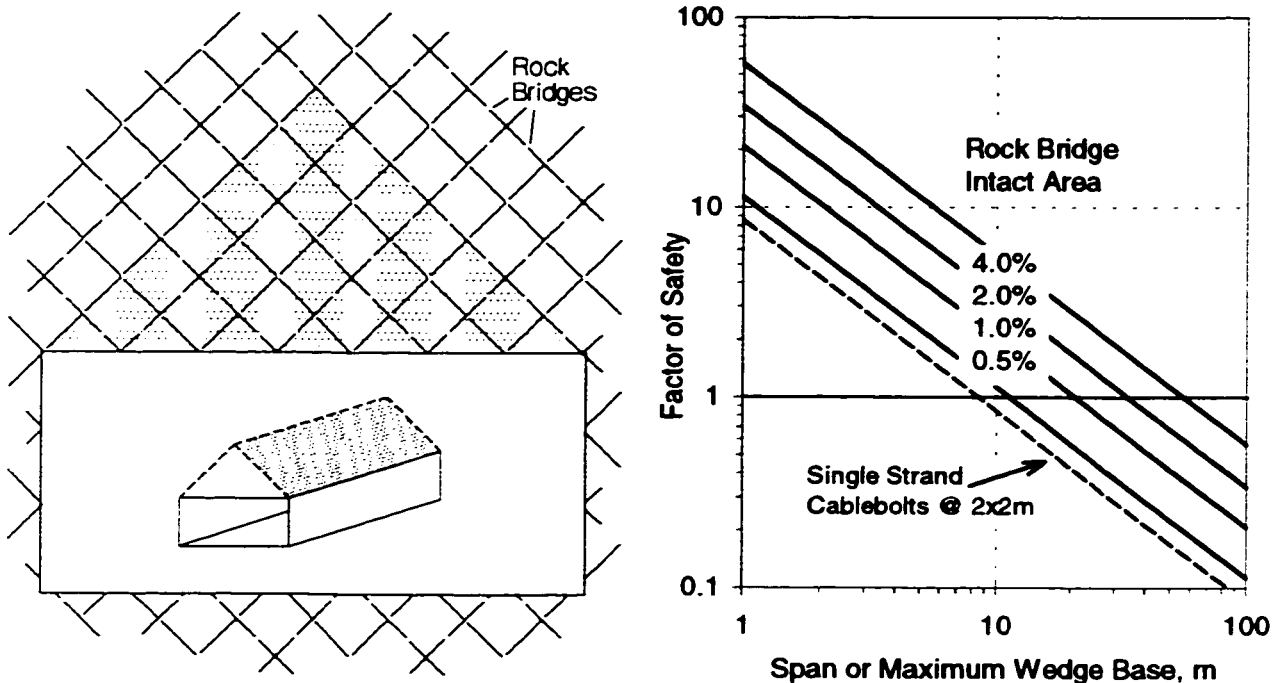


Figure 2.16: Example of residual tensile strength of rock bridges ($N=125\text{m}^{-3}$) acting as effective wedge support (gravity loaded 45 degree prismatic wedge).

2.3.3 Strength Corrosion and Time Dependency

A caution is warranted with respect to long-term rock bridge strength. Delayed failure of excavations is an issue of major concern in mining and in particular, with respect to support costs for temporary openings. Spans, which can remain safely unsupported upon excavation, can fail suddenly and catastrophically after a long period of stability with little displacement warning.

Subcritical crack growth (Atkinson and Meredith 1987) and mechanisms of humidity (crack surface energy reduction by physical or chemical adsorption) and chemically assisted stress corrosion (Dunn 1966; Wiid 1970; Lajtai and Bielus 1986; Diederichs 1987) are recognized as controlling factors for the time-dependent rupture of cracked solids.

Such crack growth under constant strain can lead, over time, to a critical cracked area (Figure 2.15) resulting in unstable propagation and ultimate rupture. In particular, the humidity fluctuations or chemically laden air in underground mines exacerbate crack instability. Rock bridges, in loose and permeable ground, which are acting as a significant supporting component and are strained, are particularly susceptible.

2.4 RELAXATION AS A DESTABILIZING MECHANISM

In order for a fractured or jointed rockmass to support itself against gravity driven failure, it must have the ability to transfer load to the abutments through a frictional or arching mechanism. Both mechanisms rely on the existence of stable abutments and on boundary-parallel confinement which can result from the insitu stresses or from deflection-induced compression. Abutment deformation or displacement leading to tangential stress relaxation in the adjoining roof or hangingwall can be an important catalyst for failure in jointed or fractured ground (Kaiser et al. 1997).

In the context of this discussion “relative relaxation” is synonymous with confinement reduction, while “absolute relaxation” or simply “relaxation” is used to describe a state of complete confinement loss, parallel to the excavation boundary. Relaxation displacement results in the opening of joints and fractures and is equivalent in elastic models to the generation of boundary-parallel tensile stresses. Of particular interest are situations in which an entire wall is engulfed in such a “tensile” or relaxed zone. This scenario is common in mining where high insitu stress ratios and complex and extreme excavation geometries are present.

It is important to note first, however, that while the analyses here are based on simple analogues for relaxation insitu, the processes leading to abutment and boundary-parallel relaxation are complex and depend on rock properties and geological setting, mining method and sequence, backfill procedures, etc. The objective of this discussion is to convince the reader of the importance and ubiquity of relaxation in complex mining environments and to qualitatively and semi-empirically accommodate the concept into design.

2.4.1 Clamping, Joint Friction and Wedge Stability

For purposes of illustration, reconsider the simple example of a gravity driven (non-sliding) wedge above a horizontal excavation with lateral clamping stress, σ_k , acting across the back. A number of researchers have presented solutions for this problem, taking into account joint shear and normal stiffnesses, wedge symmetry (Suorineni 1998; Brady and Brown 1993; Sofianos 1986; Elsworth 1986; Crawford and Bray 1983) and three dimensional geometries (Hart 1993).

Consolidating the relationships presented by Brady and Brown (1993), for a two dimensional unsupported wedge which is symmetrical about the vertical axis, the Factor of Safety ($F.S.$ = ratio of the resisting force to the wedge weight) is given by:

$$F.S. = \frac{\frac{\sigma_h S}{\tan \alpha} \left(\frac{K_s \cos^2 \alpha + K_n \sin^2 \alpha}{K_s \cos \alpha \cos \phi + K_n \sin \alpha \sin \phi} \right) \sin(\phi - \alpha)}{\gamma \frac{S^2}{4 \tan \alpha}} \quad [2.15]$$

where S is the excavation span, α is the half-apex angle of the wedge (angle of side joint from vertical), ϕ is the friction angle on the joint surface, K_n and K_s are the joint normal and shear stiffness and γ is the unit weight of the rock. Stress gradient above the back is not considered (σ_h represents the average horizontal stress). The Factor of Safety for a supported wedge is obtained by adding the support load (capacity), F , to the numerator in Equation 2.15.

For a moderate span and a two dimensional symmetrical wedge with an semi-apex angle less than the inherent friction angle (including dilation) and with $K_n \gg K_s$ (a reasonable assumption for hard rock environments):

$$F.S. = \frac{4\sigma_h \sin \alpha \sin(\phi - \alpha)}{\gamma S \sin \phi} \quad [2.16]$$

Crawford and Bray (1983) and Elsworth (1986) found Equation 2.16 to represents a lower bound for $F.S.$ Results for a minimum friction angle for granite joint surfaces (Martin 1994) and two wedge geometries are shown in Figures 2.17 and 2.18. In the case of a 0.9:1 (wedge) height:span ratio, a confining stress of only 0.5 MPa is required to stabilize a typical excavation span of 10m.

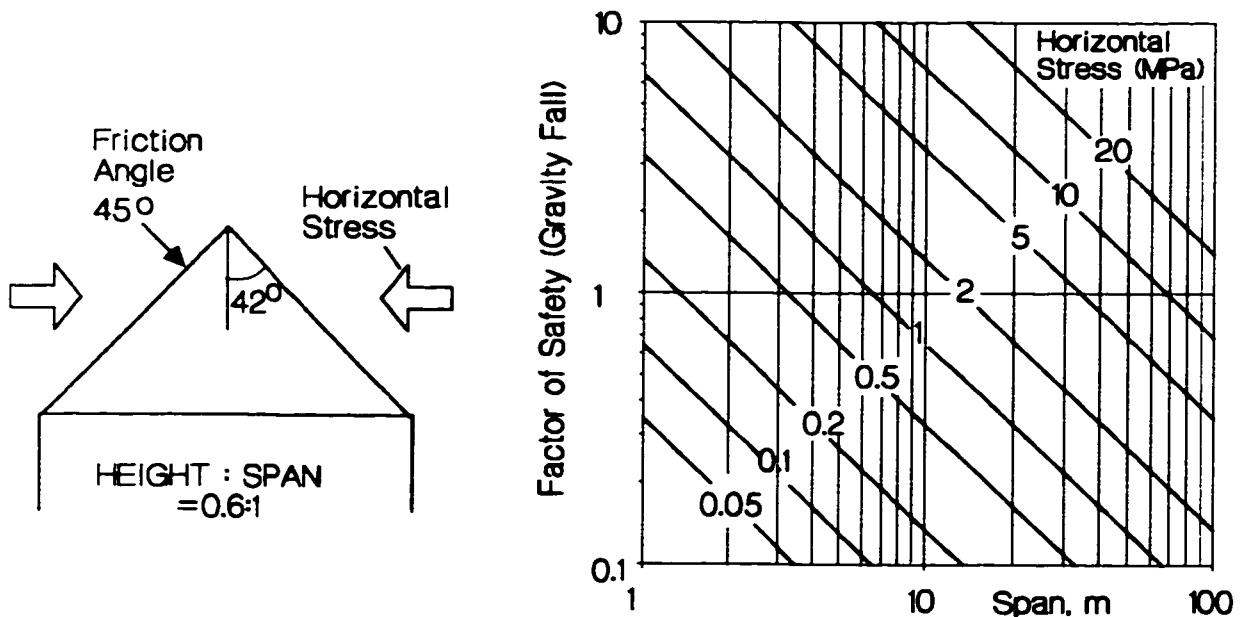


Figure 2.17: Example of clamped wedge stability (for geometry and joint friction as shown).

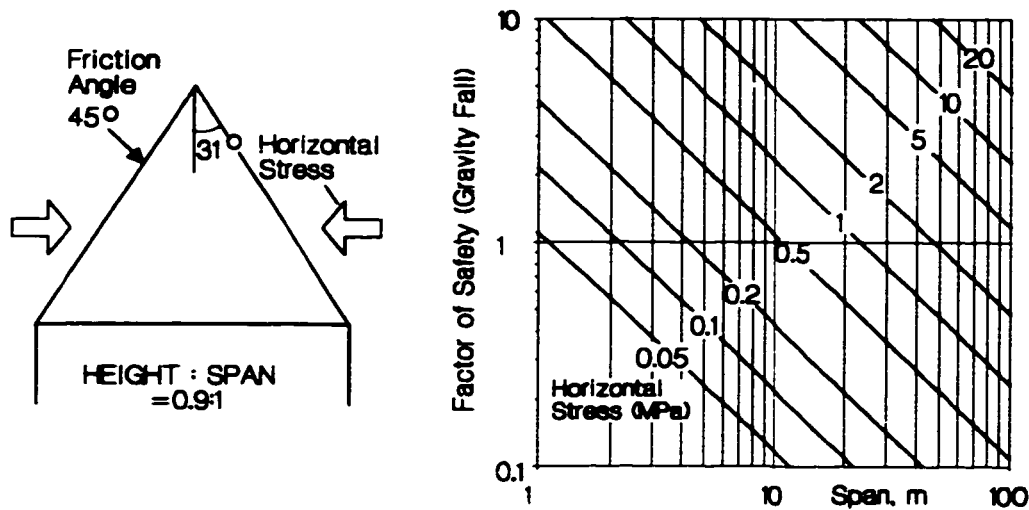


Figure 2.18: Example of clamped wedge stability (for steeper wedge than Figure 2.17).

The solution for three dimensional wedges is more complex and requires a numerical solution such as that described by Brady and Brown (1993) and by Hart (1993). Alternatively, a crude approximation is derived here using Equation 2.15 and integrating the horizontal stress and wedge weight for an axisymmetric wedge (cone with internal half-apex angle α):

$$F.S. = \frac{\frac{\pi \sigma_h S^2}{4 \tan \alpha} \left(\frac{K_s \cos^2 \alpha + K_n \sin^2 \alpha}{K_s \cos \alpha \cos \phi + K_n \sin \alpha \sin \phi} \right) \sin(\phi - \alpha) + F}{\gamma \frac{\pi S^3}{24 \tan \alpha}} \quad [2.17]$$

where F is the rockbolt (or rock bridge) support load (assumed to act vertically upwards in a passive manner with no effect on joint surface friction). For an unsupported wedge:

$$F.S. = \frac{6 \sigma_h \sin \alpha \sin(\phi - \alpha)}{\gamma S \sin \phi} \quad \text{for } K_s \ll K_n \quad [2.18]$$

An example result based on Equation 2.17 (with $K_s \ll K_n$) is shown in Figure 2.19. This Figure illustrates the support pressure (capacity of bolts or internal rock bridges divided by the base area of the cone) required to maintain a factor of safety of unity.

In the Canadian Shield, below a depth of several hundred metres, isolated drifts (away from faults, stopes and other anomalies) invariably have compressive stresses in excess of the lateral insitu stress. It is unlikely that a wedge steeper than the friction angle ($\alpha < \phi$) will be liberated. On the other hand when ($\alpha > \phi$), the wedge must be assumed to be unstable and to constitute dead weight (no internal resistance) for the purposes of support design unless incomplete jointing has left residual rock bridges to carry the weight as discussed previously.

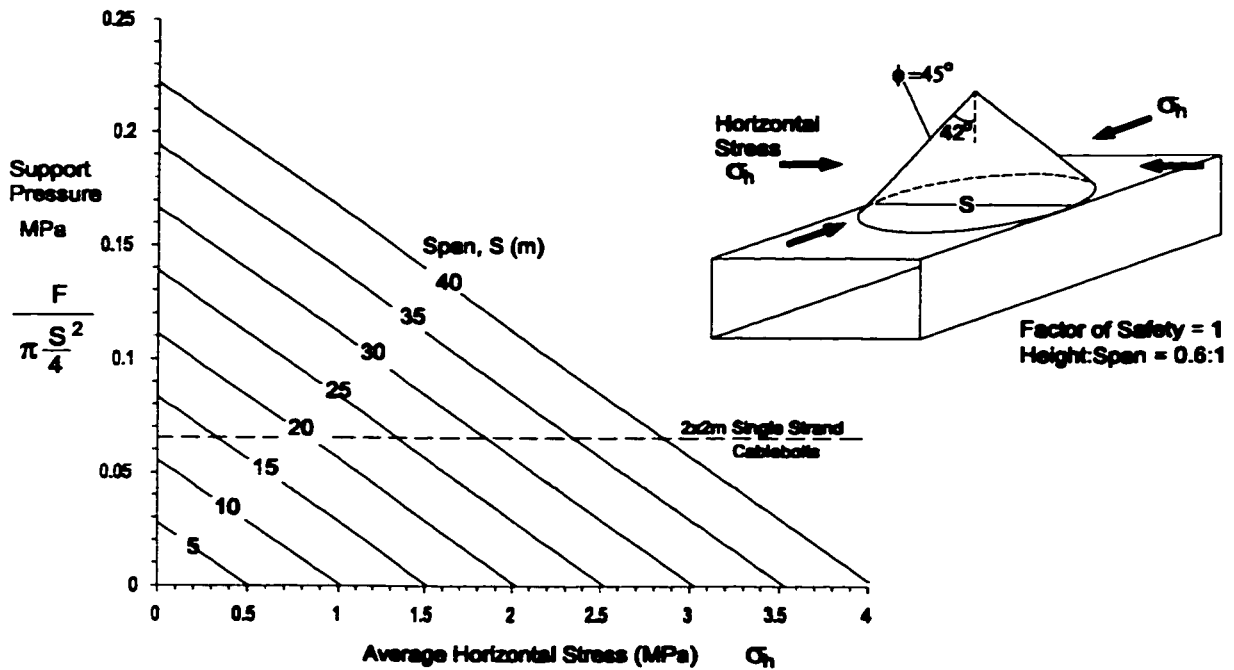


Figure 2.19: Equivalent support pressure required to maintain F.S.=1 at varying confinements. The maximum capacity of a typical cablebolt support system is shown for comparison.

As a simplification based on these two dimensional and axisymmetric solutions, it is valid to presume that a kinematically feasible (three dimensional) pyramid shaped wedge is inherently stable, for a practical excavation span and under modest confinement, if its sides and edges fall entirely within an inverted vertical cone with an angular radius equal to the friction angle of the joints (Figure 2.20).

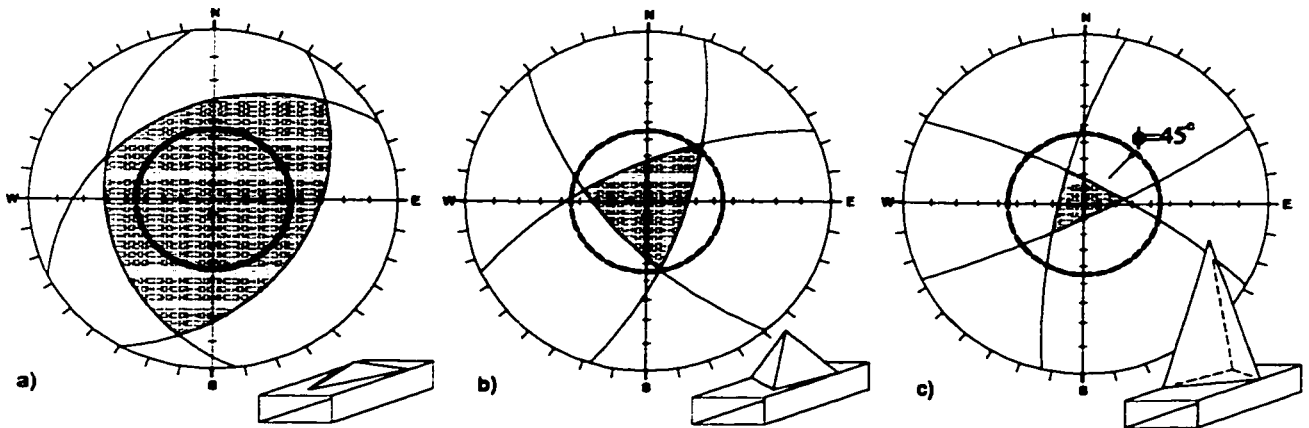


Figure 2.20: Stereonet representation of wedges which are a) unstable; b) stable with confinement, but unstable if clamping stresses are relaxed; and c) highly stable except under extreme (tensile) relaxation. Total joint friction angle = 45 degrees.

This explains why, in confined hard rock environments, full span failures of wedges steeper than 45 degrees, equivalent to a minimum value for the friction angle of tight, non-sheared granite joint surfaces, are rare (Figure 2.11). On the other hand, Figures 2.17 through 2.19 show that if subsequent and surrounding mining activities contribute to a significant reduction in confinement, (i.e. below several MPa), the factor of safety drops rapidly.

In low stress situations near surface (Figure 2.21a) or where significant relaxation has occurred due to back deflection (Figure 2.21b) or changes in mine geometry (Figure 2.22), steep wedges (and of course shallow wedges as well) which would normally have been clamped in place can be liberated and destabilized causing serious and often catastrophic failures.

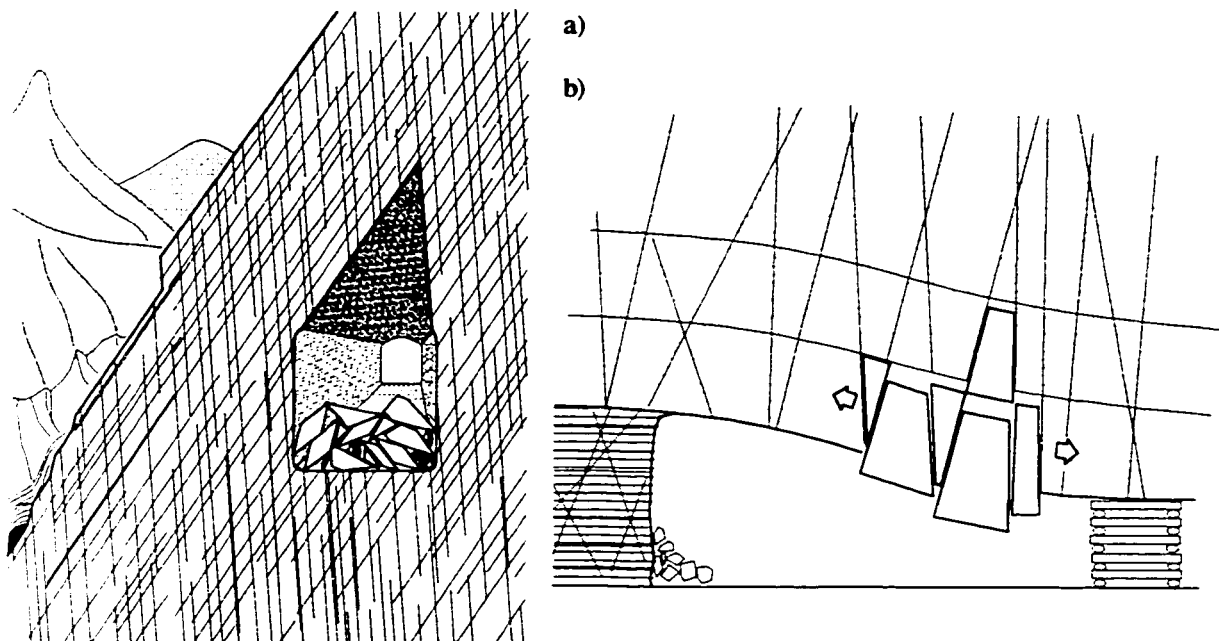


Figure 2.21: Liberation and failure of steep wedges due to a) low stress near surface; and b) localized deflection-induced tangential relaxation.

2.4.2 Induced Relaxation and Ground Failure

At depth in the Canadian Shield, for example, where the far field horizontal stress is 1.5 to 2 times the vertical stress, isolated mining drifts will have high confining stresses across the back as shown by the example boundary element analysis in Figure 2.22a. Such a drift will tend to exhibit fewer groundfalls than excavations adjacent to mining blocks (even after discounting those failures directly induced by stope blasting).

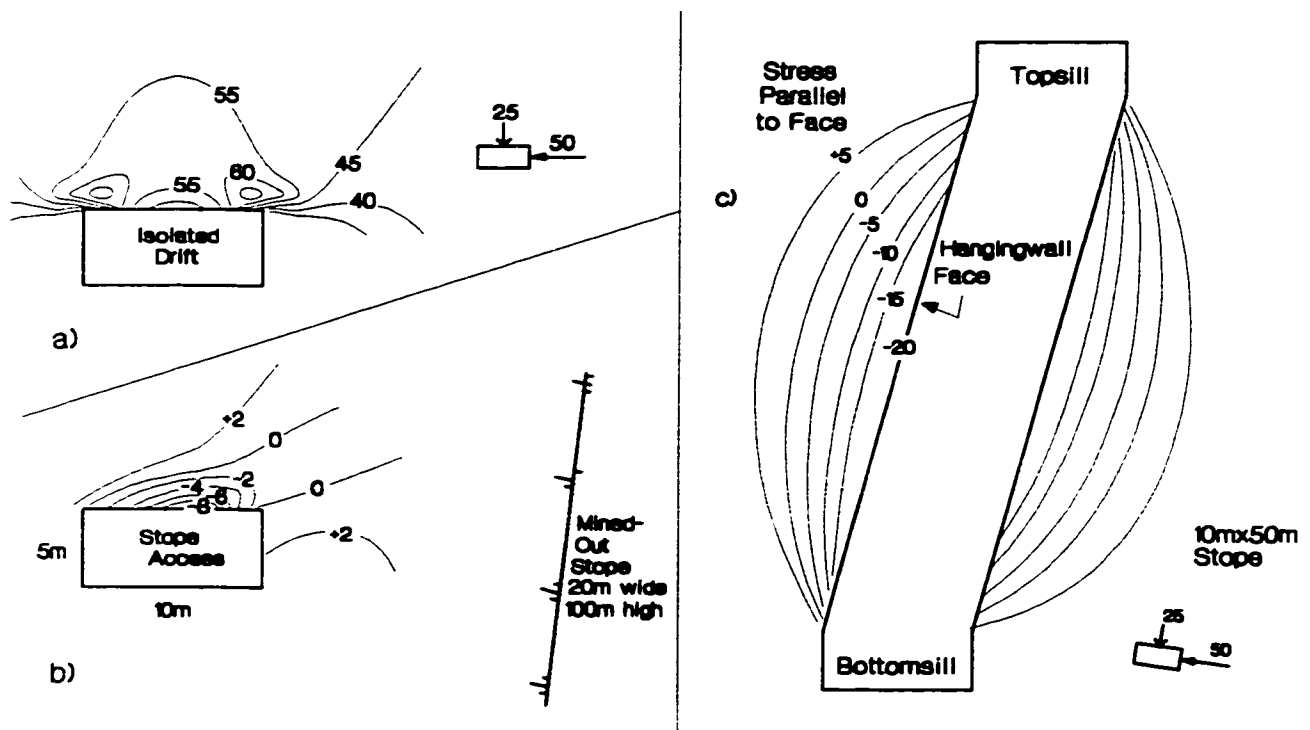


Figure 2.22: a) High induced compressive (horizontal) stresses aligned parallel to back of isolated mining drift ($\sigma_H / \sigma_V = 2$); b) Induced tension or relaxation parallel to drift back adjacent to large subvertical stope; c) Induced hangingwall relaxation (expressed as equivalent elastic tension parallel to face) due to long stope axis perpendicular to major principal stress. Stresses are in MPa.

For near-stope drifts, the stress flow can be disrupted by large sub-vertical stopes creating back relaxation (indicated by horizontal elastic tension parallel to the back) and groundfall potential in the access drifts (Figure 2.22b). Stopes which are aligned normal to the major principal compressive stress can, in extreme cases, generate extensive tensile stresses in elastic models which reflect, in reality, tangential hangingwall relaxation (Figure 2.22c).

Complex geometries (e.g. multiple stopes and pillars) common in modern mining can result in local zones of zero confinement or even extension (corresponding to tension in elastic models). Figure 2.23 illustrates a portion of a three dimensional boundary element model of Stobie Mine in Sudbury (depths shown are in feet below surface). The failed area indicated corresponds to a zone of calculated elastic tension in the model as shown in a vertical section through the area (Figure 2.24) which ultimately collapsed. Such elastic models do not explicitly simulate the failure process but can provide a convenient tool for assessing caving potential due to low confinement.

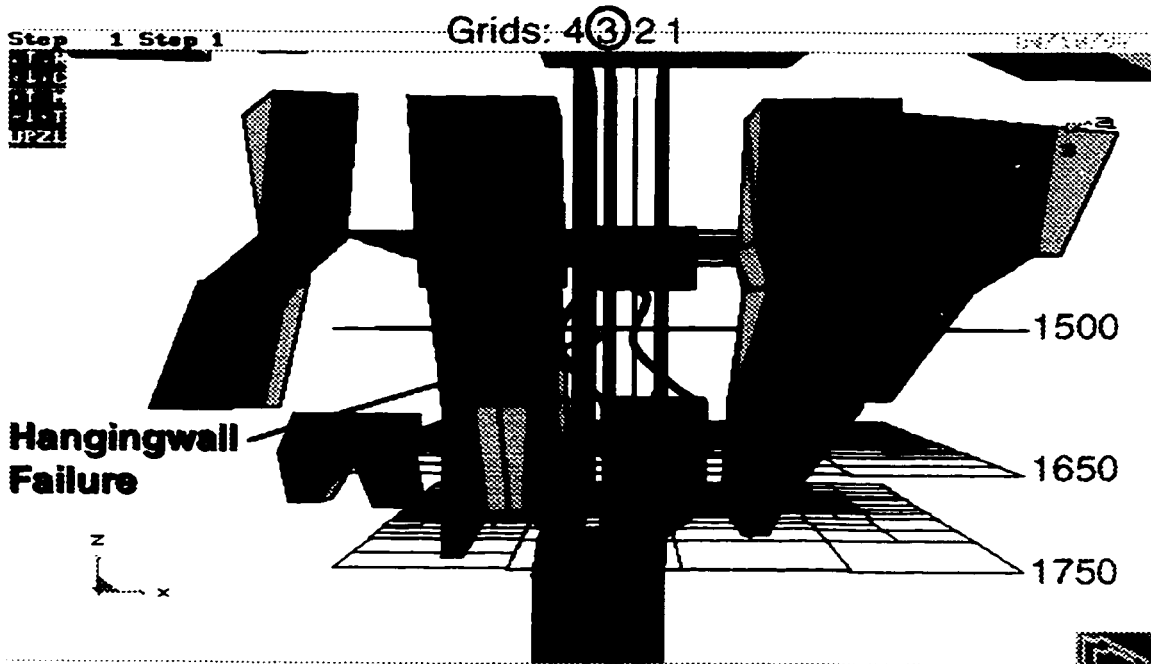


Figure 2.23: A portion of model geometry (using Map3D) for Stobie Mine. Bounded area in central pillar indicates a large cave which was observed above the 1600 topsill.



Figure 2.24: Section (Grid 3 in Figure 2.23) showing calculated elastic tensile stresses corresponding to observed caving zone above stope back (1600 level).

Another example (Tannant and Diederichs 1997) of the use of elastic models to identify relaxation, and of the importance of such relaxation to hangingwall stability, is the Kidd #3 Mine near Timmins Ontario. The series of stopes shown in section in Figure 2.25 were mined from the bottom up in three stages (56, 54 and 53 blocks). At each stage the rhyolite hangingwall (and any associated caving beyond the planned drill layouts) was surveyed with laser instruments. The extent of the caving zones correlated with the zone of tensile stresses calculated using a simple 2D elastic boundary element model (Examine2D) as shown in Figure 2.26.

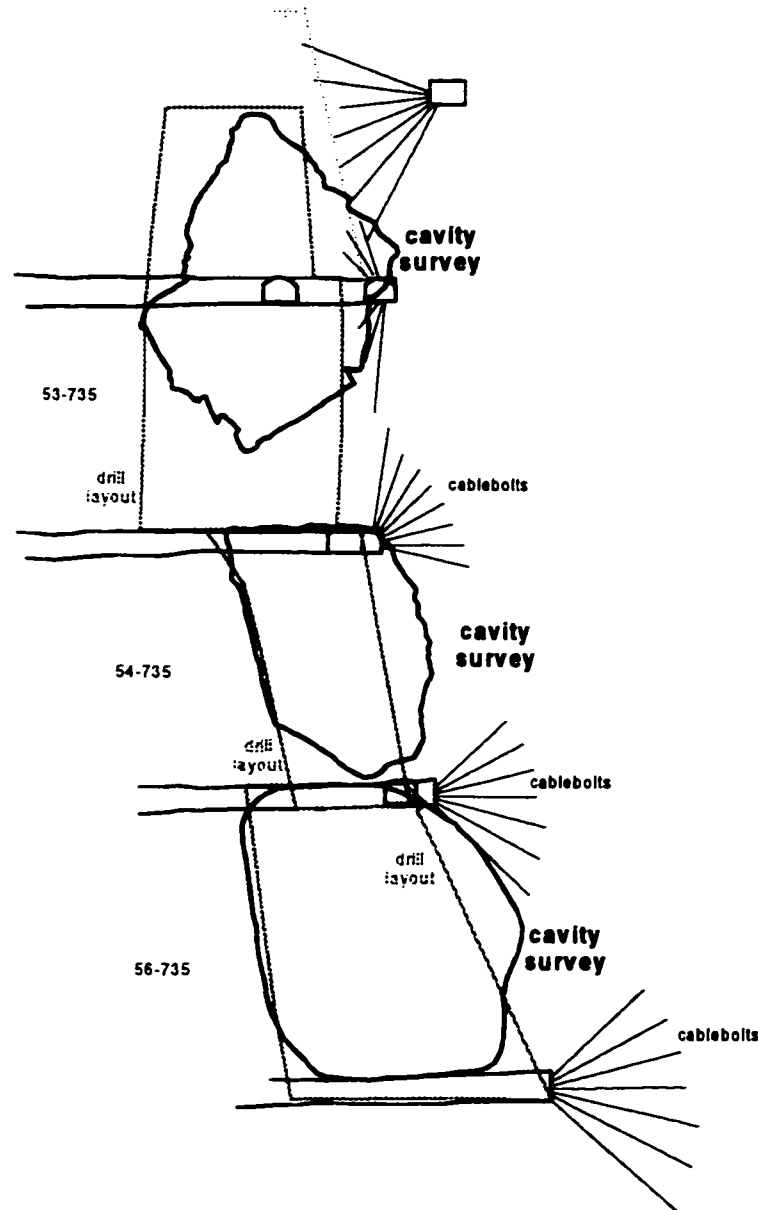
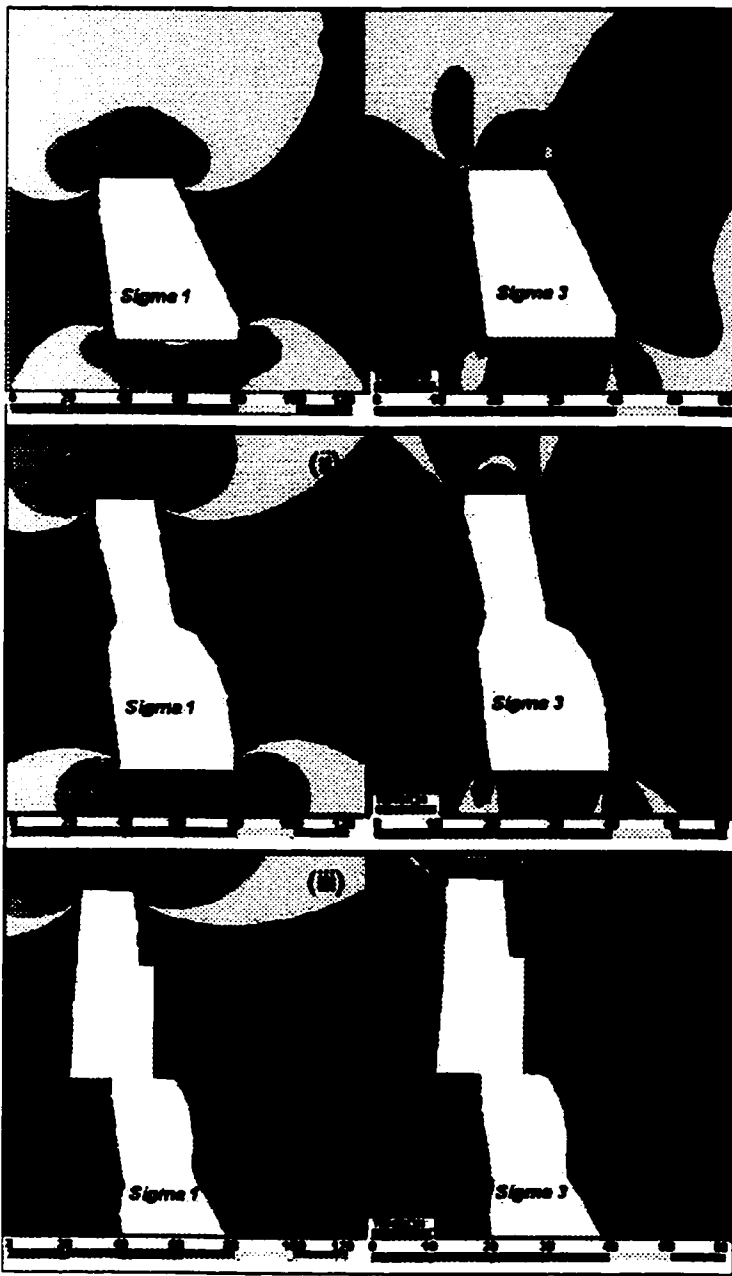


Figure 2.25 735 stopes at Kidd #3 Mine (Falconbridge Ltd.) showing drill layout, cavity surveys (with observed hangingwall caving) and cablebolt support.



Calculated stresses around 56-735 stope after mining

Model geometry with caved 56-735 stope (lower region) and the newly mined 54-735 stope (upper rectilinear portion)

Model geometry with caved 56-735 stope (below bottom of image, caved 54-735 (lower to middle visible region) and the newly mined 53-735 stope (upper rectilinear portion)

Figure 2.26 Major and minor principal stresses (red indicates tension) after successive mining steps (note that field of view shifts upwards in views above as mining progresses).

2.4.3 Relaxation and Failure of Laminated Ground

In tabular stopes in hard rock mines, inclined hangingwalls, composed of blocky or laminated ground, which are inherently stable under design conditions, can be brought to the point of failure both in reality (Figures 2.27 and 2.28) and in simulation (Figure 2.29) by abutment softening or inelastic displacement resulting in stress relaxation within the hangingwall.

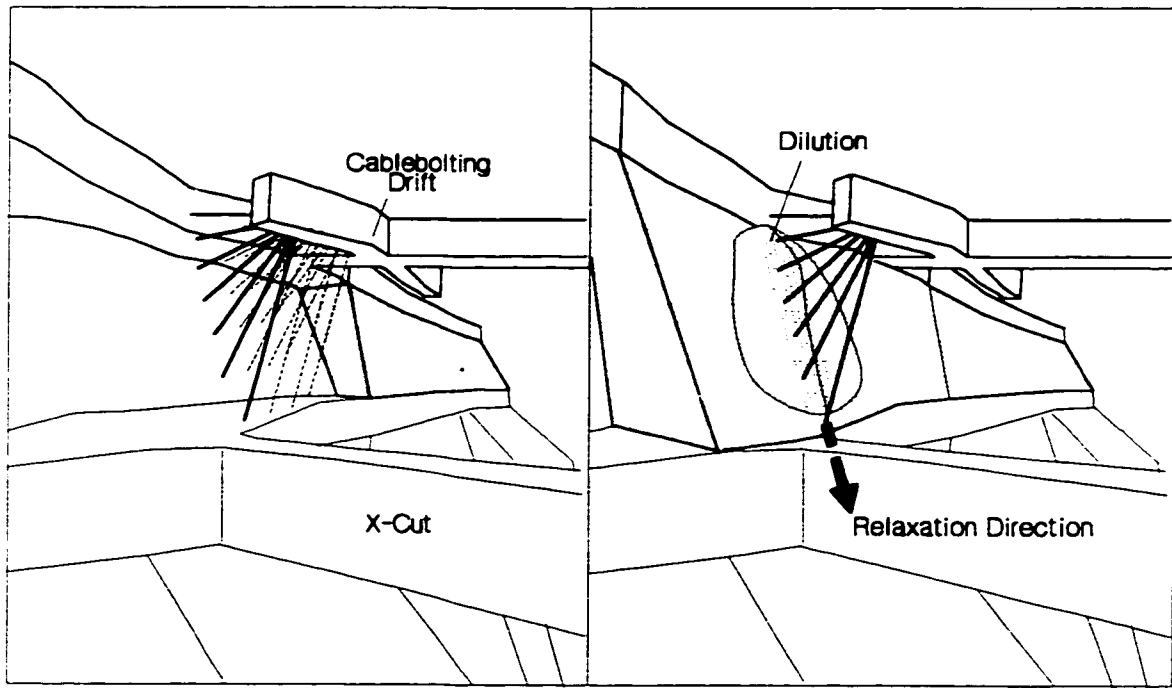


Figure 2.27: Failure of jointed hangingwall due relaxation of lower abutment above crosscut (modified after Hutchinson and Diederichs 1996).

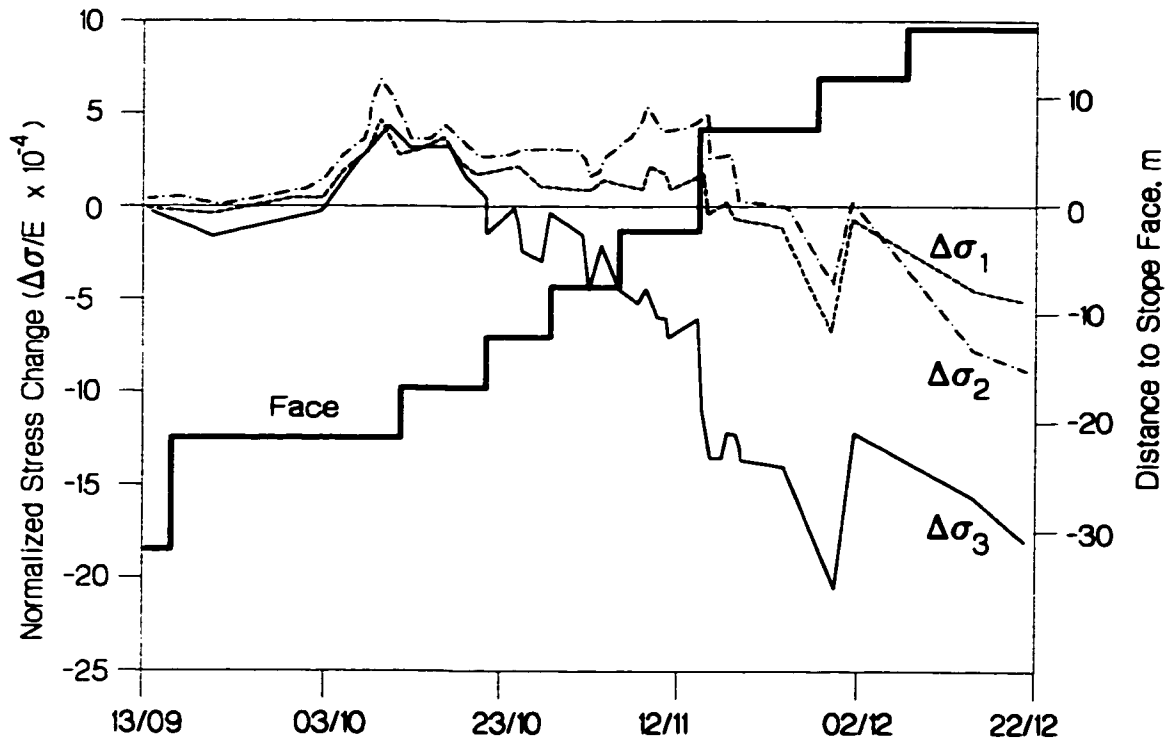


Figure 2.28: Stress changes monitored in the hangingwall during the excavation in Figure 2.27 (modified after Kaiser and Maloney 1992).

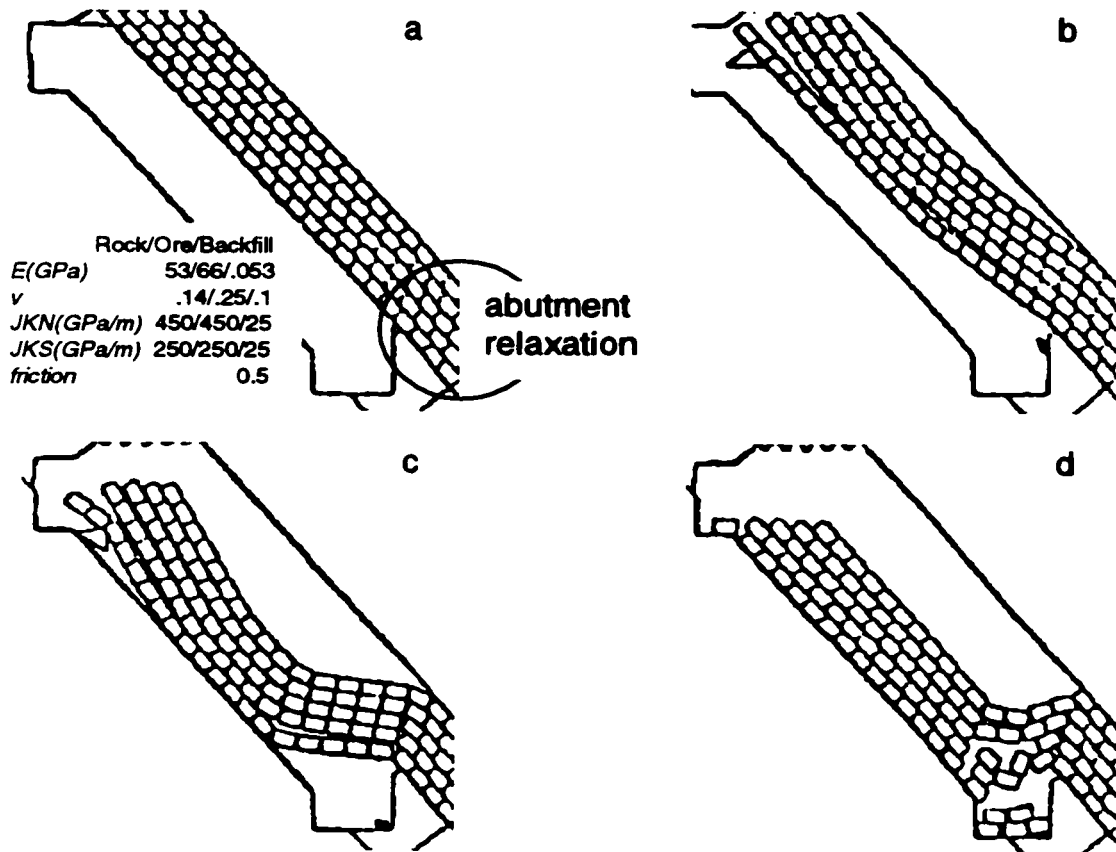


Figure 2.29: UDEC simulation of failure in Figure 2.27. Significant inelastic softening of lower abutment in model was required to induce failure (modified after Kaiser and Maloney 1992; 1993).

Figure 2.28 shows the results of stress change monitoring in the hangingwall, in the vicinity of the cablebolt array shown in Figure 2.27, as the stope was mined past the array. All directions show a significant measured reduction in stress in the hangingwall due to stress shadowing and also due to relative abutment relaxation. The model in Figure 2.29 is a discrete element model with elastic deformable blocks representing the hangingwall and surrounding rockmass.

The stope in Figure 2.29 was highly stable until the lower hangingwall abutment was softened using viscous constitutive behaviour (Kaiser and Maloney 1992) to account for the undercutting due to the crosscut shown in Figure 2.27. This undercut and the induced relaxation in the hangingwall resulted in failure both in the model and in reality (Kaiser et al. 1999).

Gravity driven failure of stress fractured ground can also be triggered by relaxation caused by mining of adjacent panels. Stress driven or structurally controlled failures can induce unraveling and caving of adjacent fractured ground (Kaiser et al. 1992). Creation of intersections in jointed or fractured rockmasses reduces the arching ability of the rockmass in the back by extending the zone of deformation outward. This is equivalent to relaxing the abutments of a tunnel span. Barton et al. (1974) suggest that the destabilizing impact of intersection creation is equivalent to a minimum 50% reduction in effective rockmass quality, a factor confirmed by Diederichs and Hutchinson (1996). A number of examples of relaxation mechanisms are illustrated in Figure 2.30.

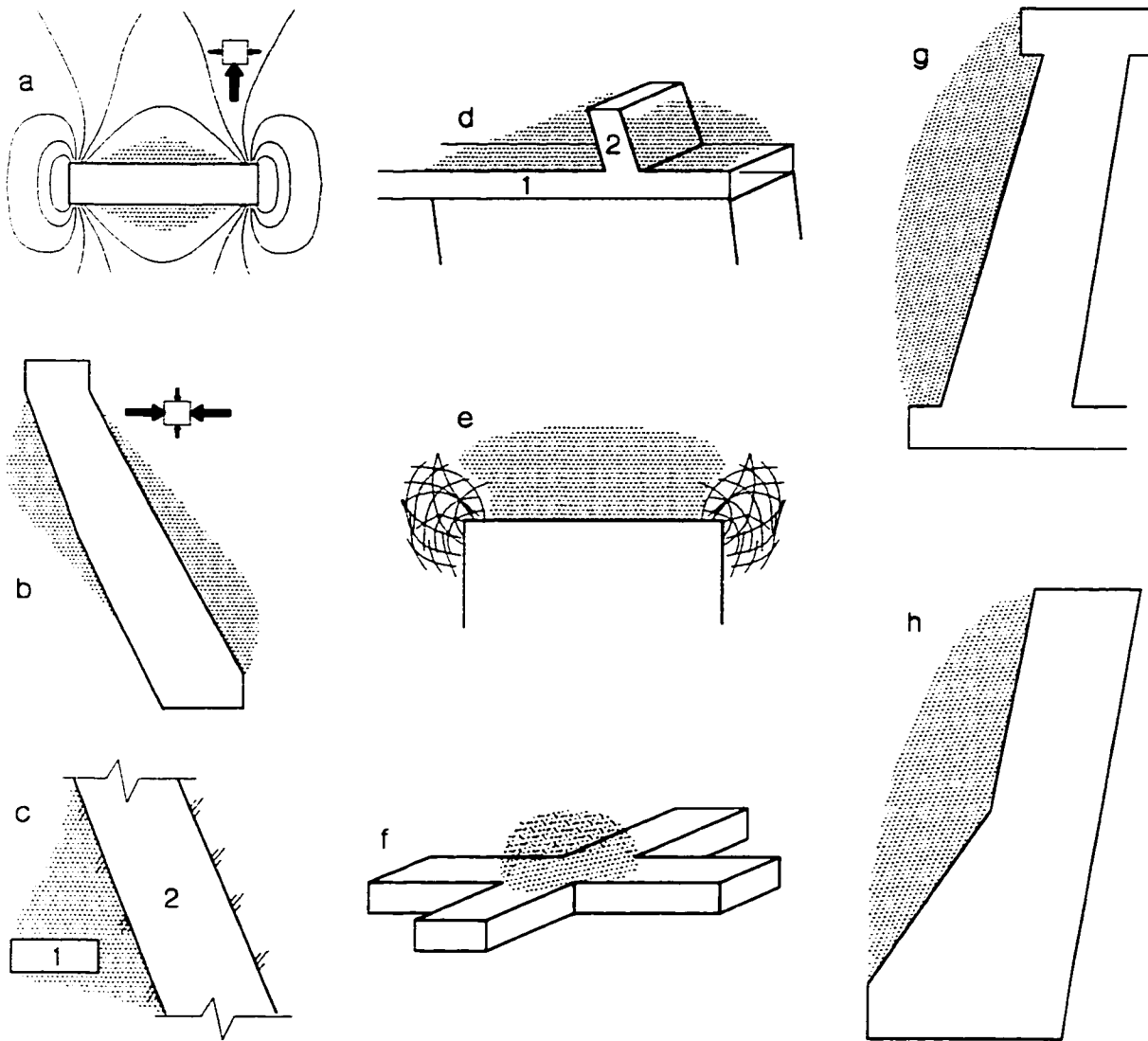


Figure 2.30: Relaxation due to a) & b) unfavourable stress ratio; c) & d) changes in mining geometry (excavation step 2 creates stress shadows around excavation 1); e) abutment yield; f) intersection (roof relaxes in the direction of tunnel branches); g) undercut; and h) concave geometries

2.5 SUMMARY

Conventional limit equilibrium or gravity load analyses for stability of rock wedges in underground excavations is based on the assumption of full joint persistence. Transmission of gravity load and wedge support can, however, be accommodated by rock bridges resulting from incomplete separation of joint or fracture planes. The small amount of tensile strength afforded by such rock bridges can be sufficient to temporarily replace most typical mining support systems.

Stress corrosion and sub-critical crack growth can ultimately cause these rock bridges to rupture. This explains the delayed nature of ground failure often observed in underground mining. The ability of the engineer to rely on short-term rock bridge strength, however, could significantly increase development economy by reducing first pass support and decreasing development cycle time (drill, blast, primary or first pass support, muck, secondary support). Careful blasting and stiff primary support such as grouted rebar can help to preserve the residual tensile strength of the rockmass and improve overall stability.

Compressive stress, normally acting across the back of isolated underground drifts and caverns can effectively clamp wedges with half-apex angles less than the friction angle of the joint surfaces. This clamping provides sufficient frictional resistance to prevent gravity induced groundfall. In hard rockmasses, several MPa of back compression is sufficient to prevent wedge failures, higher than 0.5 times the span, for spans in excess of 20m.

Loss of confinement can occur through changes in mining geometry (e.g. creation of an adjacent stope), through undercutting of stope walls, through abutment disintegration, and through unfavourable excavation shapes. Loss of clamping can result in catastrophic failure of joint bounded kinematically feasible rock wedges or failure of ground which has been previously fractured by high stress. Elastic models can be used to identify areas of geometrically induced relaxation or tension within a complex mining environment. These areas indicate loss of clamping stress and the ability for gravity to exploit structure or previous damage, causing a groundfall.

A useful analogue for the stability of laminated or blocky rockmasses is the jointed voussoir. This model is based on the assumption that in the presence of cross jointing, beam deflection results in compression that transfers load to the abutments. The model will be developed further in Chapter 3. In Chapter 4, the voussoir analogue will be used to further explore the importance, for rockmass stability, of residual tensile strength between beam laminations and abutment relaxation.

CHAPTER 3

The Voussoir Analogue for Laminated Rockmasses

3.1 INTRODUCTION

In order to study the effect of residual tensile stress and relaxation on laminated rockmasses, such as those commonly forming the walls and backs of stopes in hard rock mining stopes, a model based on the voussoir analogue is developed here and verified for application in this study.

The voussoir beam analogue has provided a useful stability assessment tool for more than 55 years and has seen numerous improvements and revisions over the years. In this chapter, a simplified and robust iterative algorithm is presented for this model. This approach includes an improved assumption for internal compression arch geometry, simplified displacement determination, support pressure and surcharge analysis and a corrected stabilizing moment in the two dimensional case. A discrete element simulation is used to verify these enhancements and to confirm traditional assumptions inherent in the model. In the case of beam snap-through failure, dominant in hard rock excavations of moderately large span, design criteria are traditionally based on a stability limit which represents an upper bound for stable span estimates. A deflection threshold has been identified in this study, and verified through field evidence and numerical modelling, which corresponds to the onset of non-linear deformation behaviour and therefore, of initial instability. This threshold is proposed as a more reasonable stability limit for this failure mode in rockmasses and particularly for data limited cases. Design charts, based on this linearity limit for unsupported stability of jointed rock beams, are presented here summarizing critical span-thickness-modulus relationships.

3.1.1 General Voussoir-Type Conditions

Rockmass behaviour dominated by parallel laminations is often encountered in underground excavations in numerous geological environments. These laminations can be the result of sedimentary layering, extensile jointing, fabric created through metamorphic or igneous flow processes, or through excavation-parallel stress fracturing of massive ground. This structure can be the dominant factor controlling the stability of roofs in large civil excavations, in coal or other horizontal mining stopes [Snyder 1983; Betournay 1987], and can also dominate the stability of inclined open stope hangingwalls such as those encountered in hard rock mining in Canada (Miller and Choquet 1988; Milne et al. 1995), in Australia (Villaescusa 1996; Beer et al. 1981) and elsewhere.

In rare circumstances, the lamination partings represent the only joint set present in the rockmass. Roof stability and deflection in this instance can be assessed using conventional elastic beam deflection and lateral stress calculations (Obert and Duvall 1966; Hoek and Brown 1980). It is more common, however, to encounter joint sets cutting through the laminations (Figure 3.1).

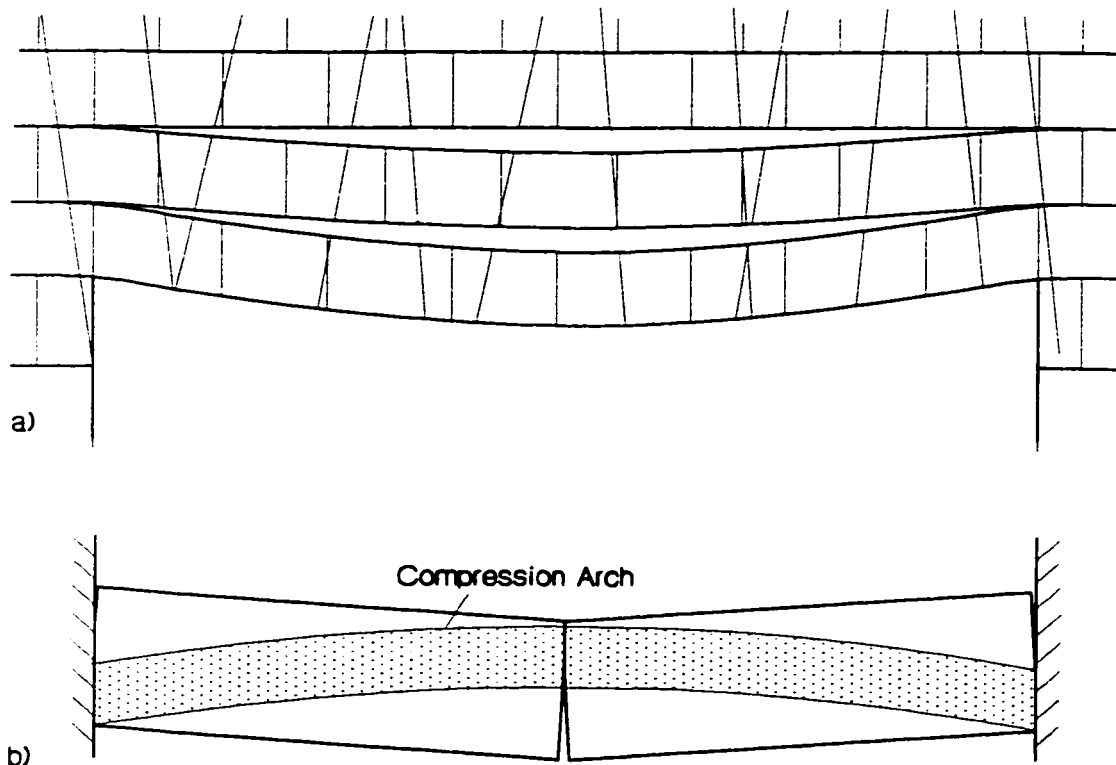


Figure 3.1: a) Jointed rock beams; b) Voussoir beam analogue.

These joints reduce and, in the extreme, eliminate the ability of the rockmass to sustain boundary-parallel tensile stresses such as those assumed in conventional beam analysis. However, where these joints cut across the laminations at steep angles, or where reinforcement has been installed, it is possible to assume that a compression arch can be generated within the beam which will transmit the beam loads to the abutments.

3.1.2 Development of the Voussoir Analogue

It was noted by Fayol (1885) that underground strata seemed to separate upon deflection such that each laminated beam transferred its own weight to the abutments rather than loading the beam beneath. Stability of an excavation in this situation, it was concluded, could be determined by analyzing the stability of a single beam deflecting under its own weight. Conventional beam analysis, however, significantly underestimated the inherent stability of such beams. Even intact laminations would crack at midspan as predicted, but would, after additional deformation, become stable again. The notion of the voussoir, while traceable back to the architecture of ancient Rome (Corlett 1956), was first proposed by Evans (1941) specifically to explain the stability of a jointed or cracked beam. After generating a great deal of controversy when first published, the voussoir beam analogue has been generally accepted and has since been reworked and presented as a simplified tool for stability analysis of excavations in civil construction and in mining (Corlett 1956, Beer and Meek 1982; Brady and Brown 1993; Hutchinson and Diederichs 1996). Figure 3.2

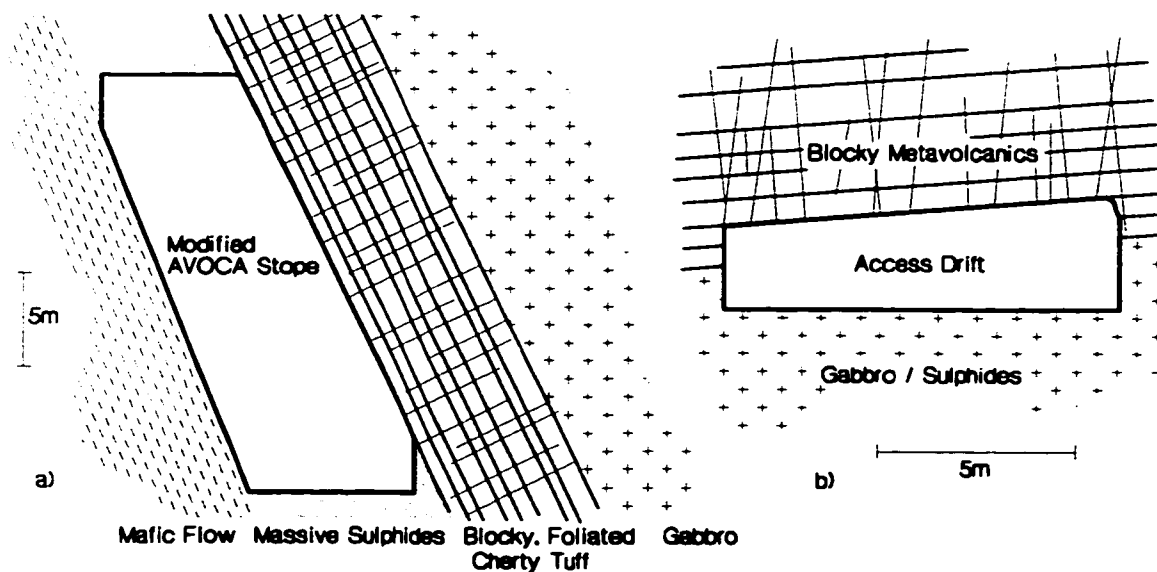


Figure 3.2: Voussoir beams encountered at a) Winston Lake Mine, Ontario, and b) North Mine, Sudbury.

illustrates two example cases where the voussoir analogue can be invoked to explain the inherent stability of a laminated hangingwall (3.2a) and cross jointed back (3.2b) in hard rock environments.

3.1.3 Voussoir Failure Modes

The primary modes of failure assumed in the model and verified in laboratory tests by Sterling (1980) are buckling or snap-through failure, lateral compressive failure (crushing) at the midspan and abutments, abutment slip, and diagonal fracturing (Figure 3.3). Shear failure (Figure 3.3c) is observed at low span-to-thickness ratios (thick beams), while crushing (Figure 3.3b) and snap-through failure (Figure 3.3a) are observed at higher span-to-thickness ratios (thin beams). An examination of the model data presented by Ran et al. (1994), shows that if the angle between the plane of the cross-cutting joints and the normal to the lamination plane (and the normal to the excavation surface) is less than one third to one half of the effective friction angle of these joints, then it is valid to apply the voussoir beam solution. For shallower cross-jointing, slip along these joints and premature shear failure of the beam is likely (Ran et al. 1994).

Stimpson and Ahmed (1992) also showed by physical modelling that for thick beams, external loading (surcharge) can produce diagonal tensile ruptures (Figure 3.3d) extending from the upper midspan to the lower abutments (parallel to the compression arch). While this failure mode is partially the result of the loading configuration, it may also be an important mechanism where weak or broken material exists above the beam or where internal rockmass damage and bulking due to stress overloads the surface beam. This study deals with thin laminations (span-to-thickness ratio greater than 10) under the influence of self-weight or moderate surcharge loading. Therefore, only crushing and snap-through failure are hereafter considered. Sliding stability is included in the analyses but does not control limiting dimensions for thin beams.

The following is a summary of the voussoir analysis procedure based on the iterative scheme proposed by Brady and Brown (1993), including a number of improvements and corrections by this author. Most importantly, a more realistic yield threshold is introduced for snap-through failure, to replace the ultimate rupture limit originally proposed (Evans 1941; Beer and Meek 1982). This procedure is summarized in several design charts and has been verified using a discrete element simulation.

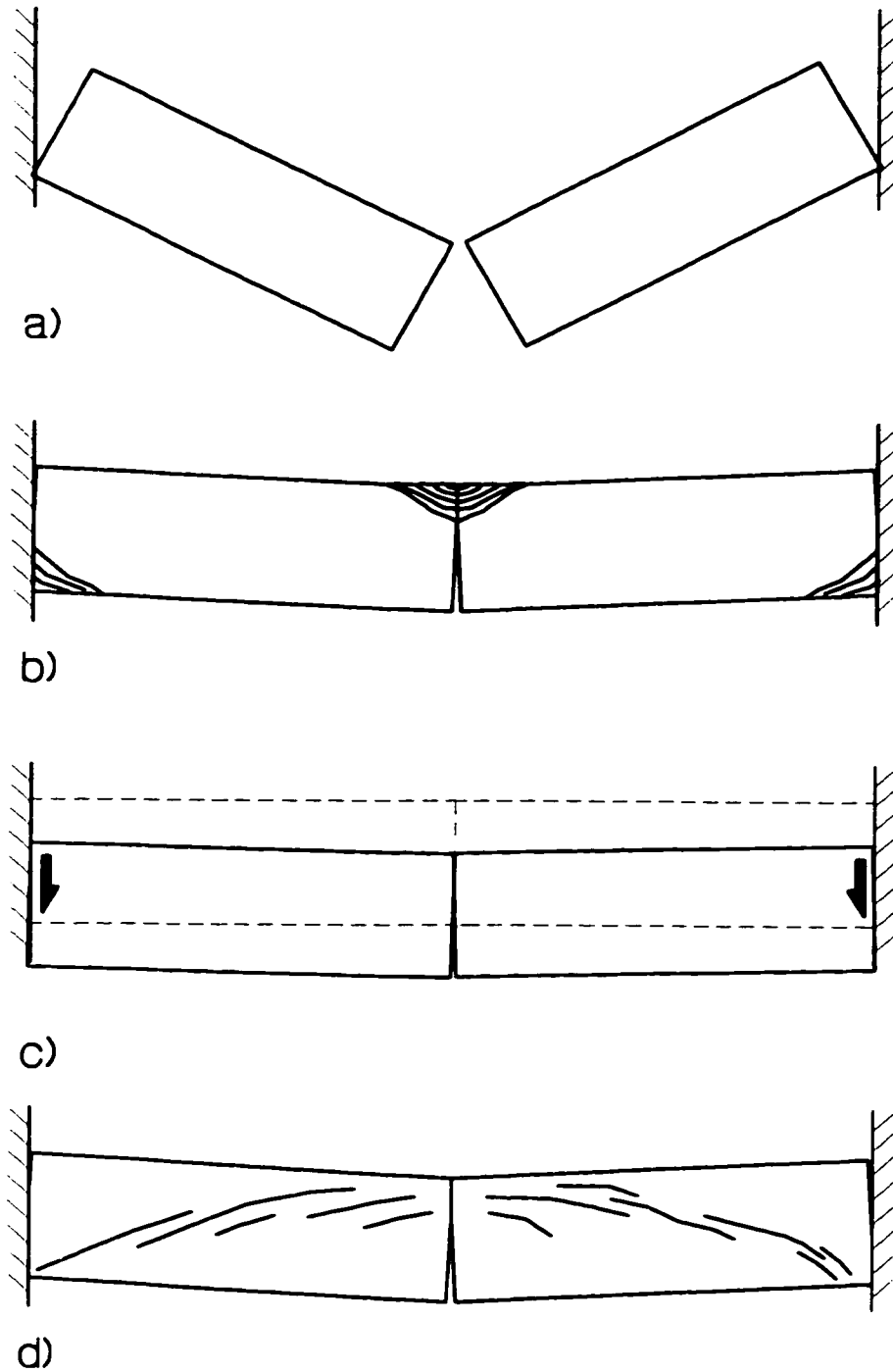


Figure 3.3: Failure modes of the voussoir beam:
a) snap-through;
b) crushing;
c) sliding;
d) diagonal cracking.

3.2 THE VOUSOIR MODEL

3.2.1 The Simple Elastic Beam

Consider a laminated rock beam above an excavation with a horizontal span given by S . The normal thickness of the single layer under analysis is T . For an elastic beam, with no joints and with constant cross section, a distribution of compression and tension, symmetrical about the horizontal centreline of the beam, is found across all plane sections within the beam (Figure 3.4a). The solution (Equations 3.1 and 3.2) for the maximum values at the abutments, for compression (beam bottom) or tension (beam top), σ_{\max} , and the maximum beam deflection, δ , can be easily calculated using closed form beam equations (Obert and Duvall 1966).

$$\sigma_{\max} = \frac{\gamma S^2}{2T} \quad [3.1]$$

$$\delta = \frac{\gamma S^4}{32ET^2} \quad [3.2]$$

E is the Young's modulus of the rock and γ is the specific weight. The maximum stress at the midspan is one half of the maximum stress at the abutments. Therefore, for such a beam with fixed ends and distributed loading, yield is assumed when the maximum tensile stress, in the upper part of the beam at the abutments, exceeds the tensile strength of the rock. Vertical tensile fractures form at the abutments and the beam becomes simply supported (assuming no slip at the abutments), as shown in Figure 3.4b), with a maximum tensile stress at the midspan given by Equation 3.3.

$$\sigma_{\max} = \frac{2\gamma S^2}{3T} \quad [3.3]$$

This stress is now higher than the previous abutment stress, and therefore higher than the rock tensile strength. This leads to subsequent fracturing centred about the midspan as shown by Stimpson and Ahmed (1992). This process of progressive cracking at the abutments, followed by cracking at the midspan and other parts of the beam can be responsible for a flurry of low-level seismic emissions (rock noise), often encountered in newly developed underground spans at low to moderate depth. This initial elastic phase followed by progressive fracture and deformation of laminated hangingwalls has been observed and is described in detail by Milne (1996).

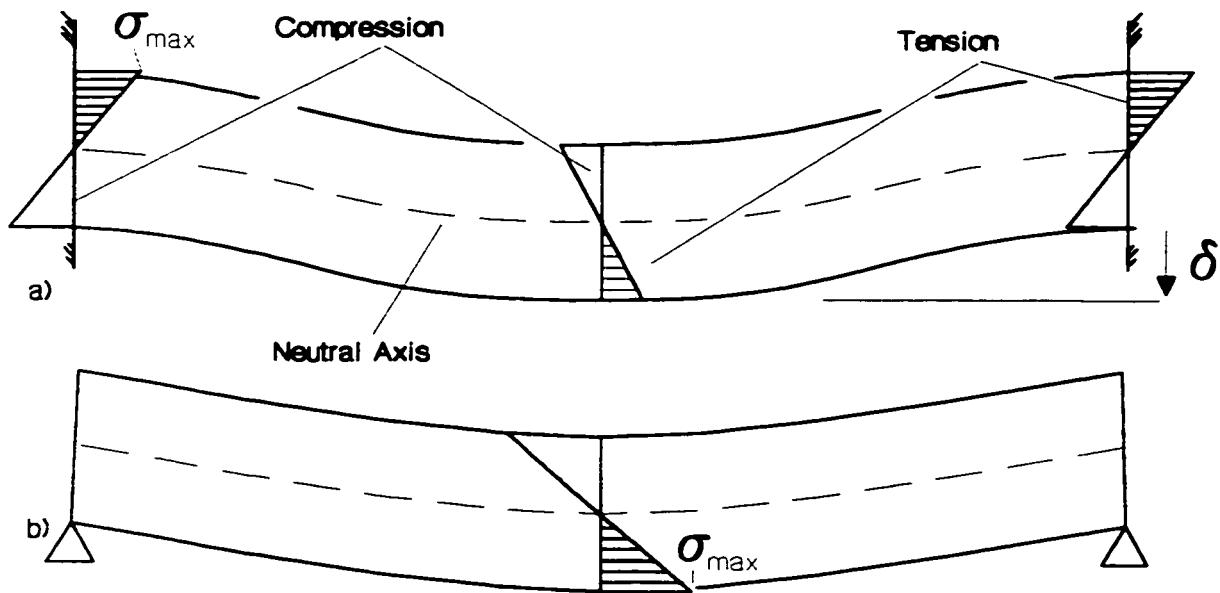


Figure 3.4: Elastic Beam with a) fixed ends and b) simple (pin) supports.

3.2.2 The Fractured or Jointed Beam

It is highly unlikely that any thinly laminated roof structure will remain in a completely continuous and elastic state after excavation. The transition from continuous elastic beam to voussoir beam is normally assured and assumed in most cases. Failure is not inevitable in this situation, however. When the tensile cracking, described above, or lamination-normal joints crosscut the beam and render it incapable of sustaining tensile stresses, a compression arch develops within the beam, rising from the abutments to a high point at midspan. For a half-span, this arch generates a moment between the reaction force at midspan and at the abutments (Figure 3.5) which acts to resist the moment imposed by self-weight. Horizontal stress symmetry within the beam is lost, making a closed form solution impossible without assuming an average thickness NT for this arch. This is the case for the solution introduced by Evans (1941) and later by Beer and Meek (1982). In both cases N is assumed to be 0.5. Numerical experimentation by Evans showed that this was an incorrect assumption, and that the equilibrium value was closer to 0.7. Nevertheless, Evans chose the value, $N = 0.5$, to simplify the practical solution which he was presenting. Investigations by the author of this thesis have shown that N is variable. While N is closer to 0.75 for stable beams at equilibrium, N drops to below 0.5 as the critical (unstable) beam geometry is approached.

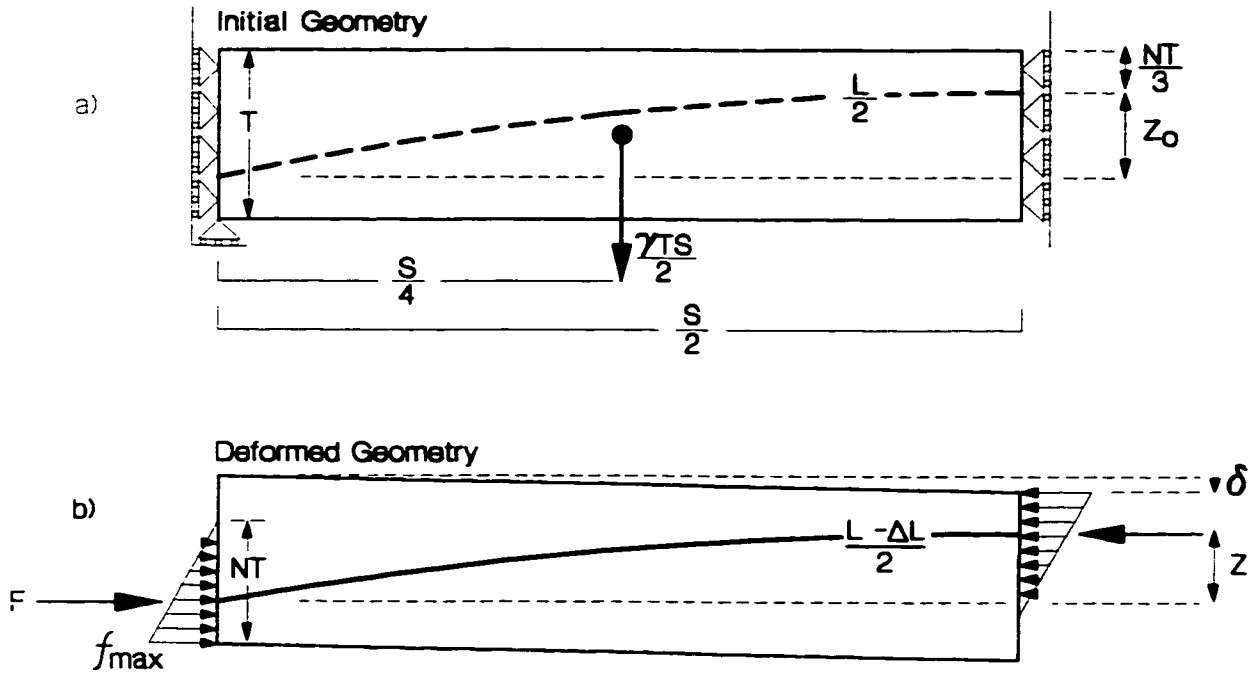


Figure 3.5: Voussoir beam (half-span shown) and nomenclature.

In this formulation, the average thickness, NT , of the compression arch within the beam is initially unknown, as is the ultimate moment arm, Z_0 , between the horizontal reaction forces, F , at the midspan and at the abutments. Considering the half beam (Figure 3.5), and building on the algorithm introduced by Brady and Brown (1993), the solution procedure begins with an assumption of the initial moment arm prior to deflection, Z_0 :

$$Z_0 = T \left(1 - \frac{2}{3} N \right) \quad [3.4]$$

The length of the reaction arch (horizontal reaction force locus) is given by:

$$L = S + \frac{8}{3S} Z_0^2 \quad [3.5]$$

This equation is based on the assumption of a parabolic compression arch. Numerical (Ran et al. 1994) and physical (Stimpson and Ahmed 1992) experiments confirm this assumption. Note that this equation is correctly reported by Beer and Meek (1982) but is in error in the summary of Brady and Brown (1993).

The solution proceeds on the assumption that for stability to be obtained, the moment generated at the abutment due to self-weight of the beam, given by:

$$M_w = \frac{\gamma T S^2}{8} \quad [3.6]$$

must be exactly compensated, as the beam deflects a distance δ at the midspan, by an opposite or resisting moment, M_R . This moment is generated by the opposing horizontal reaction forces in the beam centre and at the abutments separated by a distance $Z = Z_0 - \delta$:

$$M_R = FZ = \frac{f_{\max} NTZ}{2} \quad [3.7]$$

where f_{\max} is the maximum stress acting in the beam (at the bottom edge of the abutment and at the top edge of the midspan section).

In Equation 3.6, the specific weight, γ , of the rockmass can be replaced with an effective specific weight, γ_e , given by:

$$\gamma_e = \gamma \cos \alpha \quad [3.8]$$

where α is the dip (angle from the horizontal) of the lamination plane. This analogue considers only the component, of the driving weight, oriented normal to the beam. For inclined beams, therefore, the effect of beam-parallel loads due to settling is not considered. In this model, as in reality, an inclined roof is more stable under gravity loading than a horizontal roof.

In addition, active support pressure can be considered in the equation by further adjustment of the effective specific weight:

$$\gamma_{ep} = \gamma_e - \frac{p}{T} \quad [3.9]$$

for the case of a uniformly applied support pressure, p , illustrated in Figure 3.6a.

If the support pressure is applied in a triangular distribution varying from zero at the abutments to p at the midspan (Figure 3.6b) as in the case of passive rockbolts, then use:

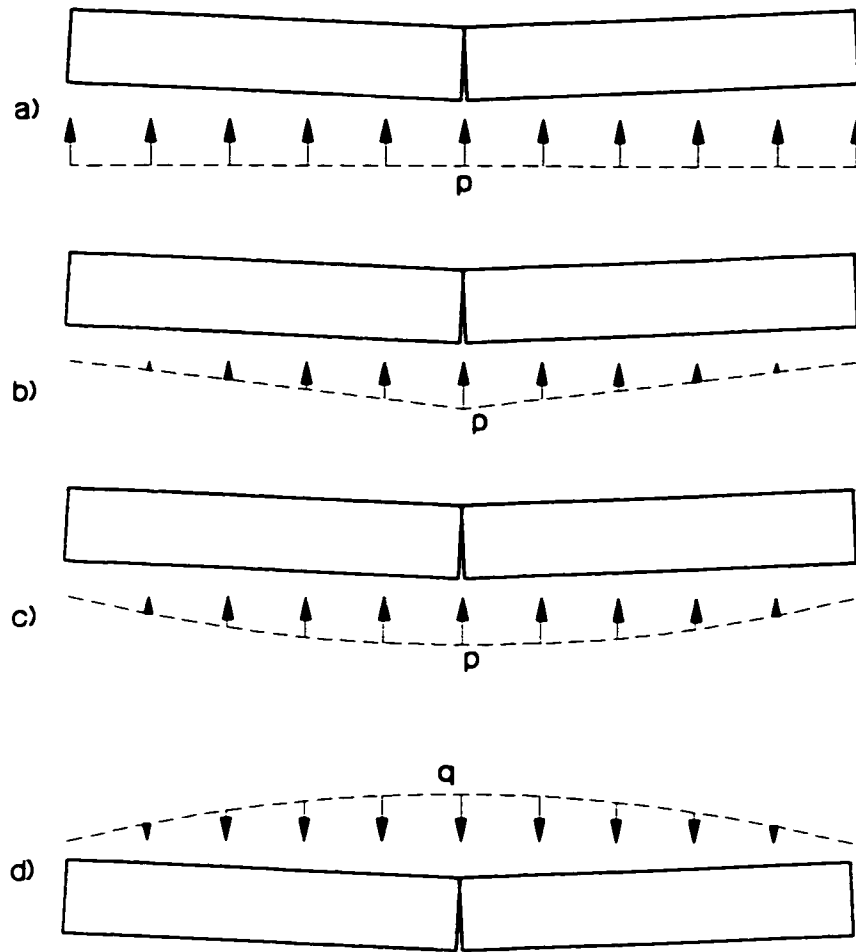


Figure 3.6: External beam loading due to:
 a) uniformly distributed support pressure;
 b) linearly varying support pressure;
 c) parabolically varying support pressure; and
 d) parabolically varying surcharge loading..

$$\gamma_e^* = \gamma_e - \frac{2p}{3T} \quad [3.10]$$

This relationship is obtained by solving for moment equilibrium (equations 3.6 and 3.7) with the actual surcharge distribution and computing an equivalent change in uniform specific weight to simulate the effects of this surcharge.

Similarly, a parabolic distribution of support pressure (Figure 3.6c) can be applied as:

$$\gamma_e^* = \gamma_e - \frac{7p}{9T} \quad [3.11]$$

To introduce a distributed surcharge, q , replace $(+ p)$ with $(- q)$ in Equations 3.9, 3.10 or 3.11 as appropriate. For example, in the case of a distributed surcharge loading ranging parabolically, as in Figure 3.6d, from 0 to q (due to broken rock above the beam for example) the modified effective specific weight becomes:

$$\gamma_c^* = \gamma_c + \frac{7q}{9T} \quad [3.12]$$

Assuming a triangular horizontal stress distribution within the compression arch (of thickness NT) at the abutments and at the midspan as illustrated in Figure 3.5, the following equilibrium equation is obtained for f_{max} :

$$f_{max} = \frac{(\gamma_c^*) S^2}{4NZ} \quad [3.13]$$

In order to calculate the elastic shortening of the arch (and thereby calculate the central deflection) an assumption must be made about the internal distribution of compressive stress within the beam. Previous authors (Evans 1941; Beer and Meek 1982; Brady and Brown 1993) have based their calculations on the assumption of a quasi-linear variation of stress (Figure 3.7) along a constant arch section NT , yielding an average stress along the reaction line, f_{av} , given by:

$$f_{av} = \frac{f_{max}}{2} \left(\frac{2}{3} + \frac{N}{2} \right) \quad [3.14]$$

Careful examination of this assumption shows it to be in error. It is reasonable to expect that at some point the entire beam section must be under compression and that at the point where the reaction line crosses the centreline of the beam, this stress is constant across the entire beam section T . It is also reasonable to assume that the variation of stress along the reaction line is not linear. Numerical experimentation by the author of this work and examination of numerical results obtained by others (Ran et al. 1994; Mottahed and Ran 1995) confirm that the distribution of stress along the centreline of the arch is in fact parabolic (Figure 3.7). This yields the following corrected equation for average stress in the beam:

$$f_{av} = \frac{f_{max}}{3} \left(\frac{2}{3} + N \right) \quad [3.15]$$

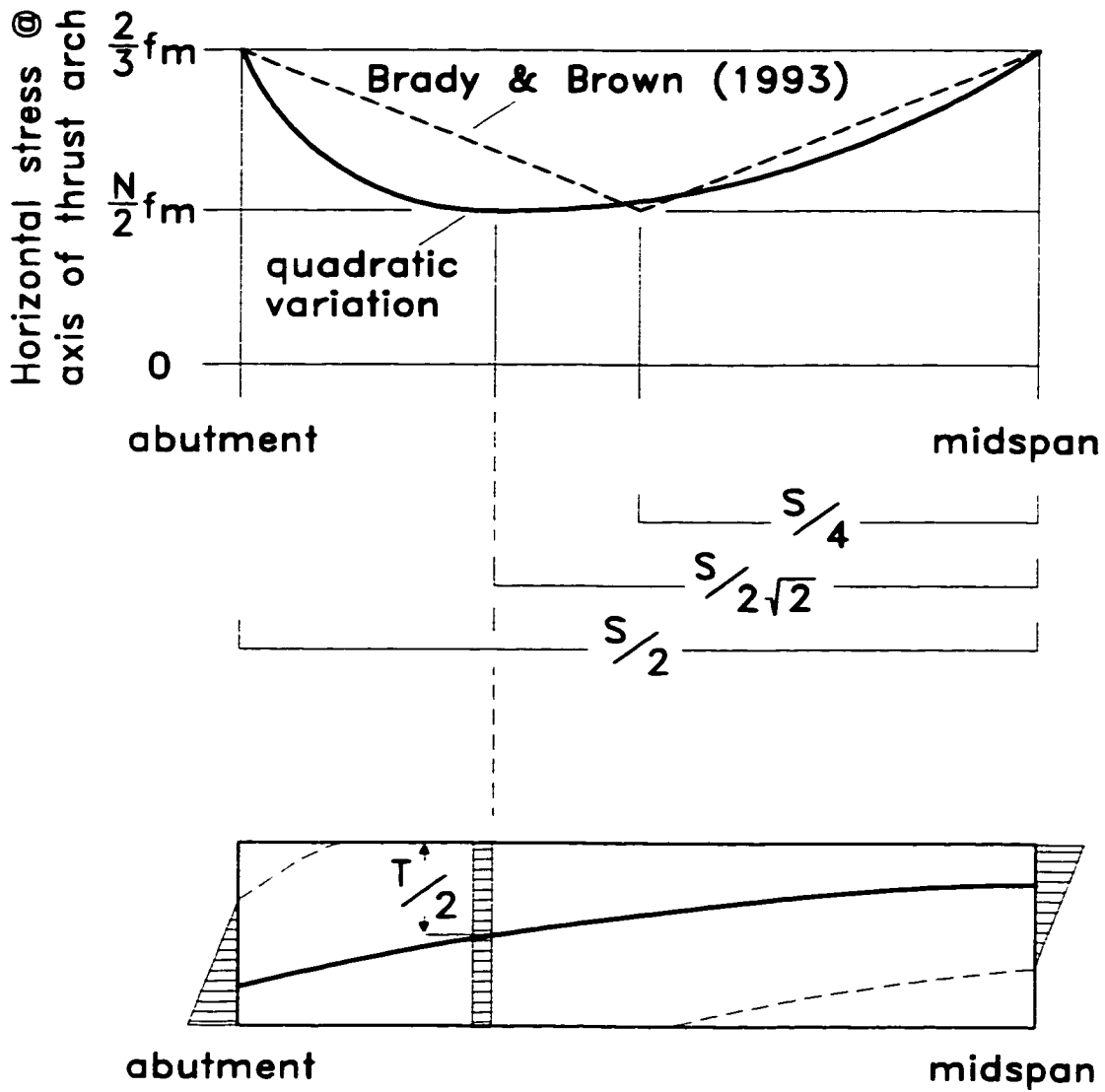


Figure 3.7: Conventional assumptions for compressive stress variation inside the beam compared with the parabolic variation proposed in this thesis.

Elastic shortening of the arch can then be obtained from:

$$\Delta L = L \frac{f_{av}}{E} = \frac{L}{E} f_{max} \left(\frac{2}{9} + \frac{N}{3} \right) \quad [3.16]$$

where E is the rockmass modulus in the direction parallel to the beam.

This shortening leads to a downward displacement of the arch midspan and a new reaction moment arm given by:

$$Z = \sqrt{\frac{3S}{8} \left(\frac{8}{3S} Z_0^2 - \Delta L \right)} \quad [3.17]$$

The deflection, δ , at midspan is given by $(Z - Z_0)$ and a negative value for the term under the square root sign in Equation 3.17 indicates that the critical beam deflection has been exceeded. In other words, as deflection increases, the resisting moment, M_R , a product of increasing reaction force, F , and decreasing moment arm, Z , passes through its maximum without achieving equilibrium with the weight moment M_W . In this case, snap-through failure would occur for the specified value of compression arch thickness, NT . If there are no values for N (between 0 and 1) for which a stable solution can be obtained, ultimate collapse of the beam is assumed to occur.

In order to find a solution for the equilibrium position of the beam, Evans (1941) chose to maximize the product of the resisting moment and the moment arm, Z , although by his own admission, this choice was somewhat arbitrary. In the procedure of Brady and Brown (1993) a two-variable relaxation technique is employed to solve for N , the arch thickness and Z , the final moment arm. The equilibrium solution corresponds to the unique pair (N, Z) which results in analytical equality through the sequence of equations summarized in the forgoing discussion. This approach was found by this author to be highly unstable and convergence was often difficult. Fortunately it can be seen through examining the results of this process that equilibrium solution also corresponds with the minimization of f_{max} , the maximum stress at the abutments and midspan.

In the approach presented here, N is varied in increments (e.g. 0.01) over its finite range (0 to 1). Z is modified in an iterative fashion and a convergent solution is thereby obtained with only a few steps for each value of N . For a stable beam with a span well below the critical limit for the given geometry and rockmass properties, a solution for Z is possible for all values of N . Equilibrium corresponds to the minimum value of f_{max} . As the critical span is approached, the percentage of N values which yield rational results for Z decrease, converging to a single rational solution pair (N, Z) at the absolute critical limit.

Finally, taking Z and Z_0 (as determined using the equilibrium value of N), the deflection, δ at the midspan is simply $Z - Z_0$. The complete procedure for the determination of stability and equilibrium deflection is summarized in Figure 3.8.

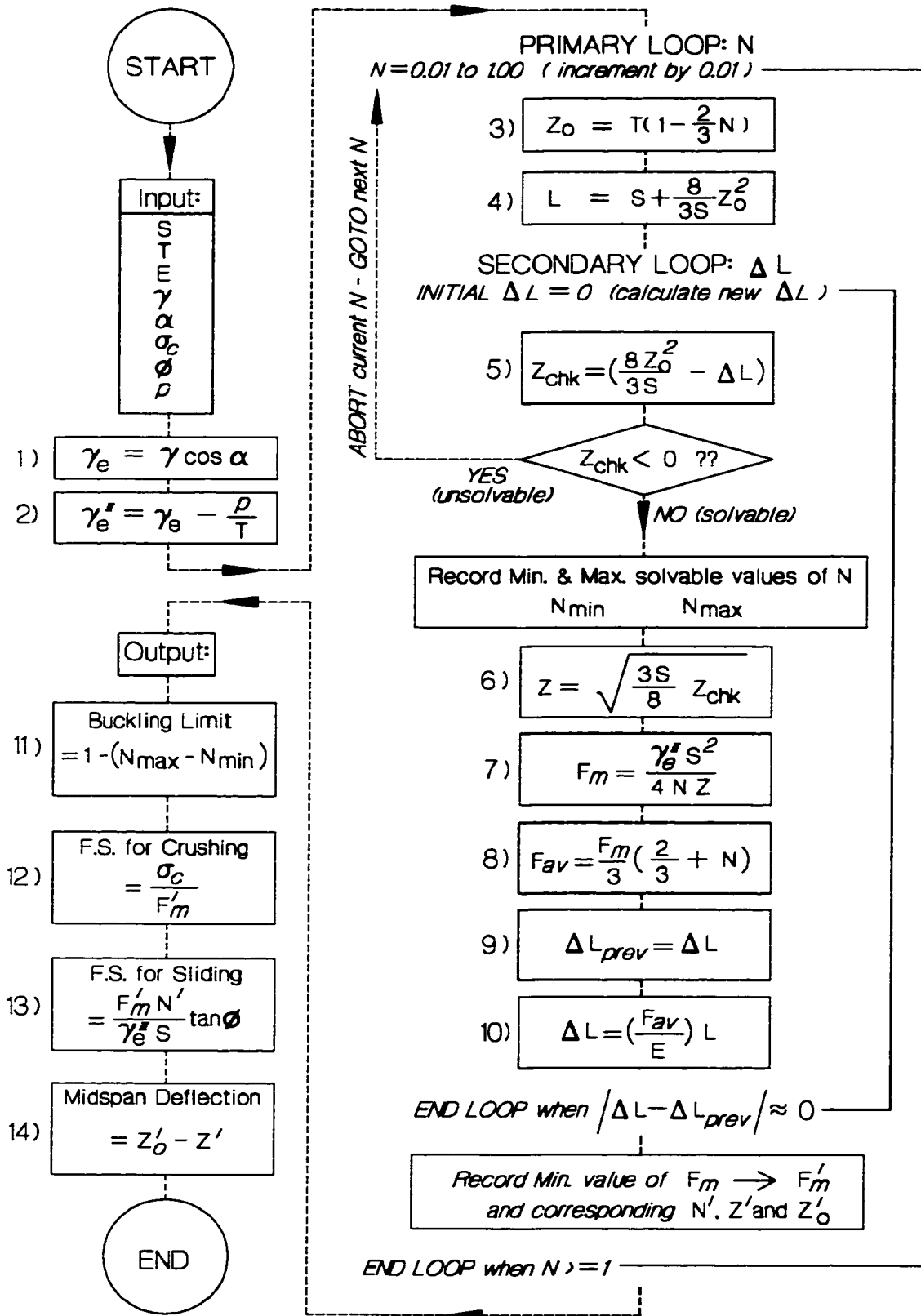


Figure 3.8: Flow chart for the determination of stability and deflection of a voussoir beam.

The factor of safety with respect to crushing (compressive failure) at the abutments and at midspan is given by the ratio of unconfined compressive strength of the rock with respect to the maximum compressive stress calculated in the model:

$$F.S._{crush} = \frac{UCS}{f_{max}} \quad [3.18]$$

The factor of safety with respect to vertical sliding, of an unsupported beam under self-weight, along joints at the abutments is given by:

$$F.S._{side} = \frac{f_{max} N}{\gamma_c S} \tan \phi \quad [3.19]$$

3.2.3 A Rational "Buckling Limit" for Forward Design

A numerical Buckling Limit, *B.L.*, is introduced here which is the percentage of values of *N* within the range of 0 to 1 for which a solution (i.e. a real value of *Z*) cannot be obtained. Figure 3.9 illustrates the decrease in normalized equilibrium arch thickness, *N*, and the increase in Buckling Limit, *B.L.*, with increasing span/thickness ratio. *N* consistently drops below 0.5 as the critical span/thickness ratio is approached and reaches a limit of 0.35 immediately prior to failure (snap-through). Ultimate collapse, and the critical span vs. thickness relationships proposed by Evans (1941) and by Beer and Meek (1982) correspond to a Buckling Limit of 100%. In other words, stability is impossible if there is no arch thickness which yields an equilibrium solution. For a more conservative approach, however, a threshold can be specified for the Buckling Limit in order to obtain design dimensions for the beam.

In order to obtain a reasonable yield threshold for the Buckling Limit, the relationship between midspan displacement, δ , and thickness, *T*, was considered. Figure 3.10 illustrates summary results for several beam stiffnesses. The deflection/thickness relationships are log-linear for beam geometries with ample thickness. As the thickness is reduced (or the span is increased) the relationship becomes non-linear and eventually becomes undefined at ultimate failure. Ultimate failure occurs at a Buckling Limit of 100%, corresponding to a displacement equivalent to approximately $0.25 \times T$. The onset of non-linearity consistently occurs at a displacement equivalent to approximately $0.1 \times T$. This "yield" point also consistently corresponds to a Buckling Limit, *B.L.*, of 35%.

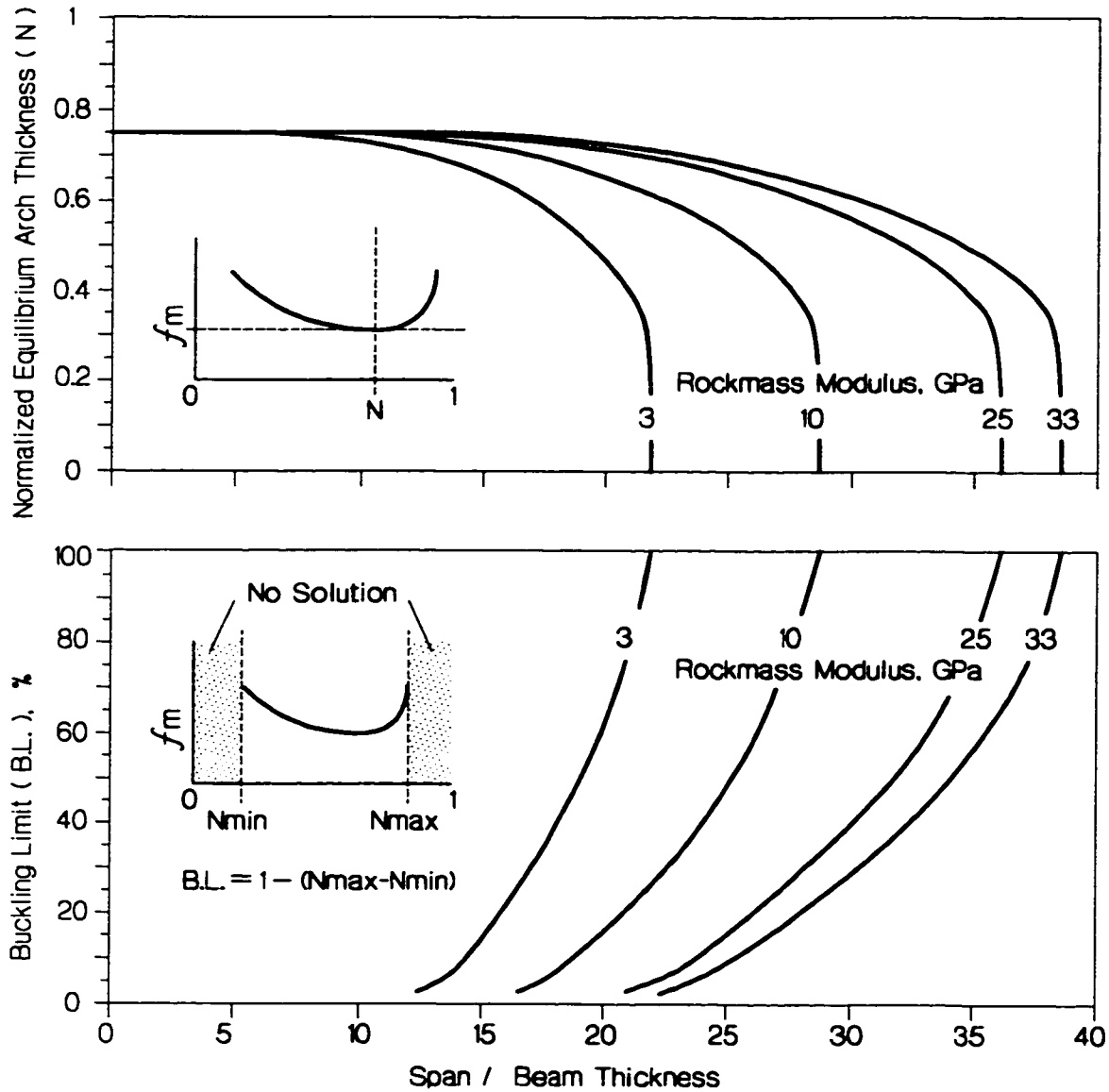


Figure 3.9: Variation of N and Buckling Limit with span to thickness ratio.

The yield threshold determined in Figure 3.10 more closely corresponds to the critical displacement limit of approximately $0.15T$ obtained by Mottahed and Ran (1995) through numerical modelling. Beyond this displacement the jointed beam model used in their experimentation began to exhibit unstable behaviour and failure became imminent. This limit was independent of span and the modulus.

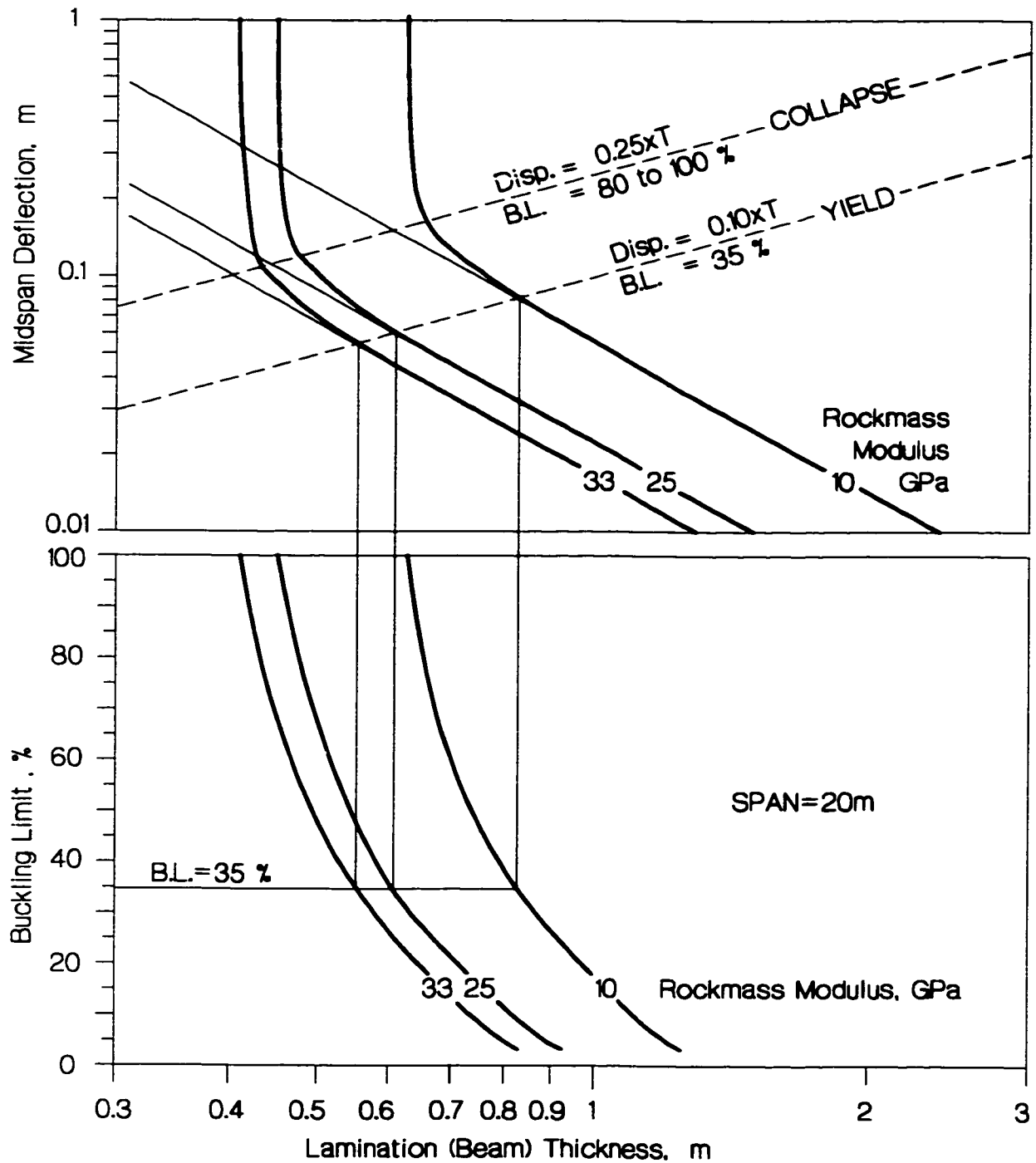


Figure 3.10: Example determination of beam “yield” limit (example span = 20m).

The choice of Buckling Limit affects the calculated critical span or the critical thickness (limiting case for beam stability) as illustrated by the example in Figure 3.11. These limits are obtained by including the analysis outlined in Figure 3.8 inside a simple iterative bisection algorithm to find the

critical value of a specified input parameter (in this case, thickness) which gives a value (span) straddling the interface between stability and failure.

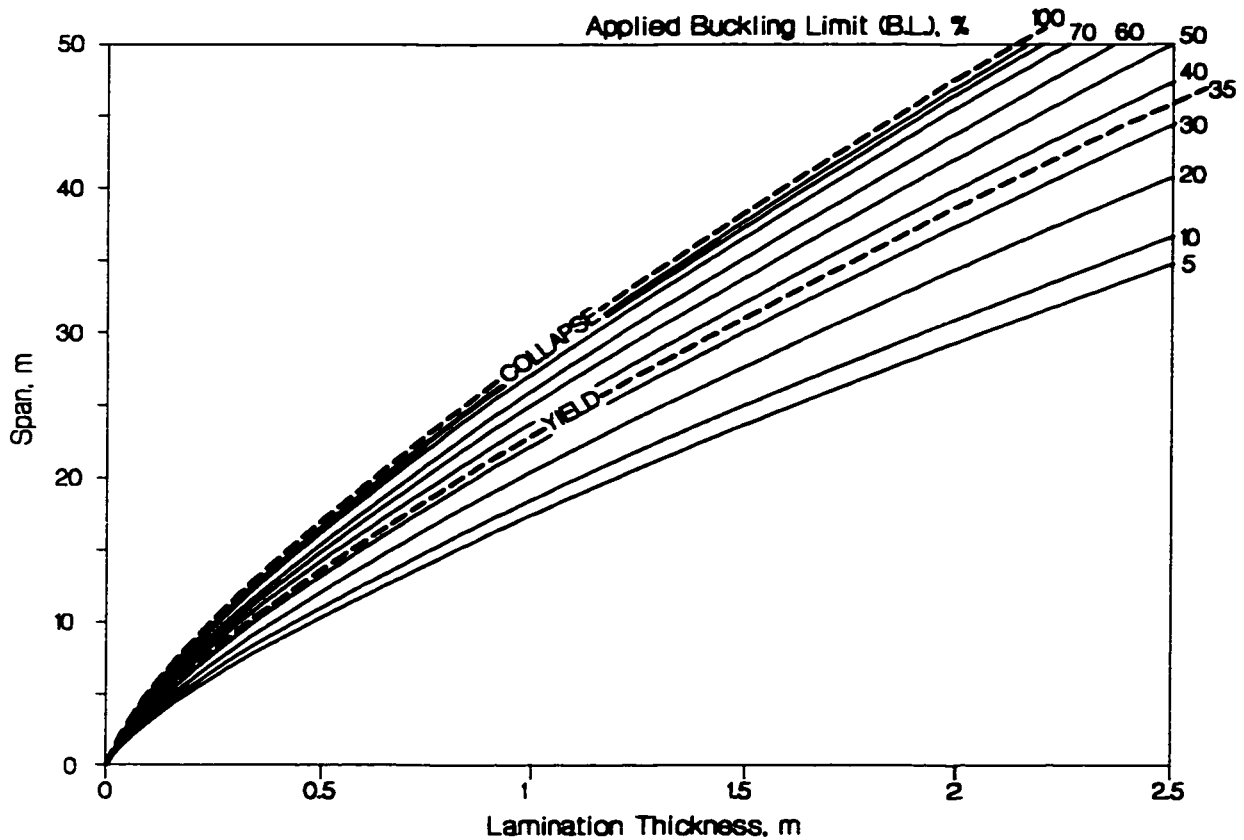


Figure 3.11: Effect of Buckling Limit on critical beam geometry for snap-through failure of a horizontal beam ($E_m=10$ GPa, $\gamma=0.03$ MN/m³).

The displacement limit of $0.1 \times T$ ($B.L. = 35\%$) is used forthwith, as a yield limit, due to its convenience and to account conservatively for uncertainties in the approach. This limit is important for monitoring applications since it is independent of the span and represents a universal rule of thumb for determining the significance of measured displacements. Displacements of less than 10% of the effective lamination thickness (determined using a borehole camera or from mapping data) can be confidently assessed as being within the elastic limit of the voussoir beam, independent of rock modulus or effective span.

Figure 3.11 indicates critical limits for snap-through failure of the beam. Crushing failure is also considered in the discussion which follows. Typically thin hard rock beams (significant compressive strength) under their own self-weight will tend to snap-through before they crush

(Figure 3.12). If an otherwise stable beam is subjected to surcharge loading, however, as is the case in many of the laboratory experiments described in the literature, then crushing failure will result (as may abutment sliding or diagonal cracking). The influence of surcharge loading on the stability of the beam as well as on the failure mode is demonstrated in Figure 3.13. The transition line (snap-thru / crushing) indicates which failure mode controls the critical limits as shown.

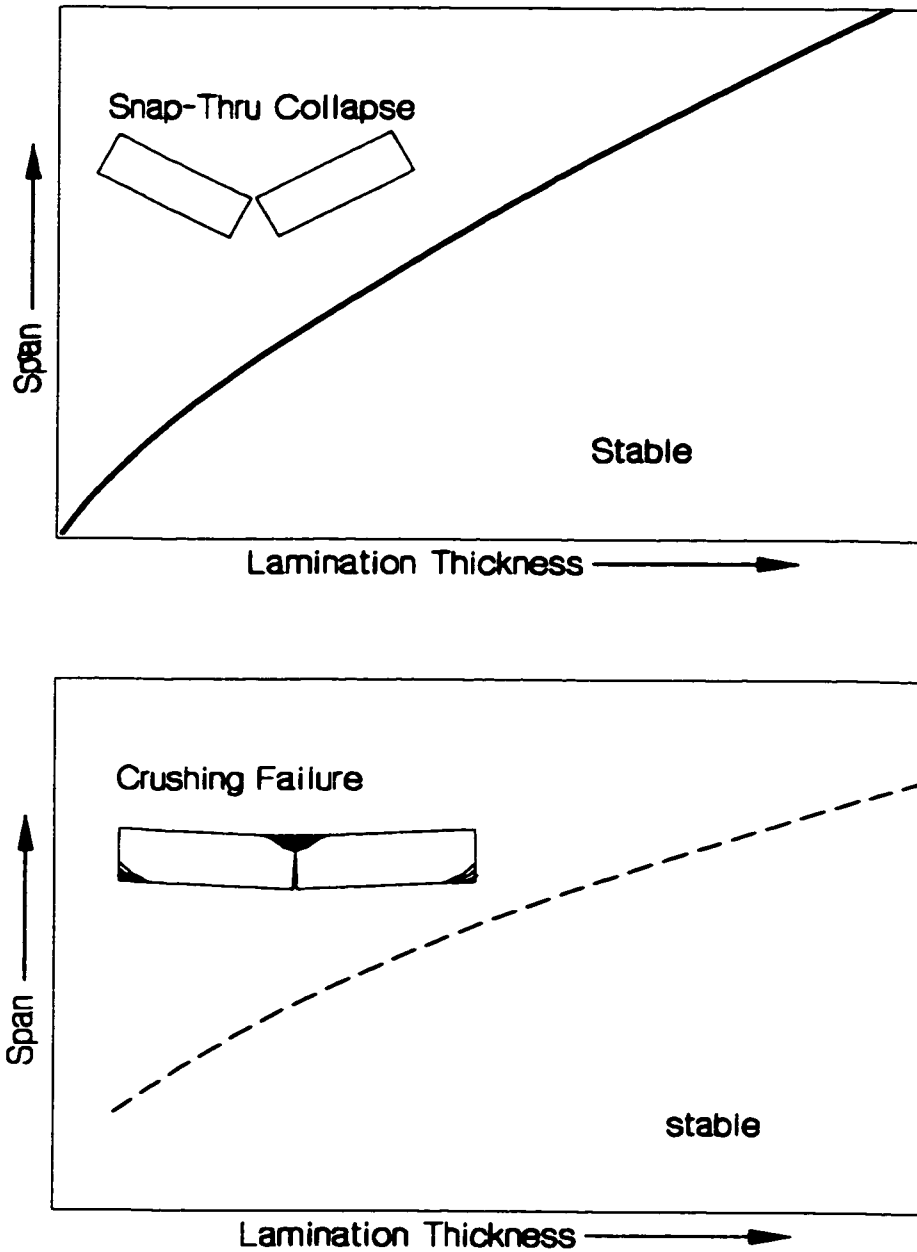


Figure 3.12: Typical critical limits for the stability of slender beams. (Axis scales are identical for both plots).

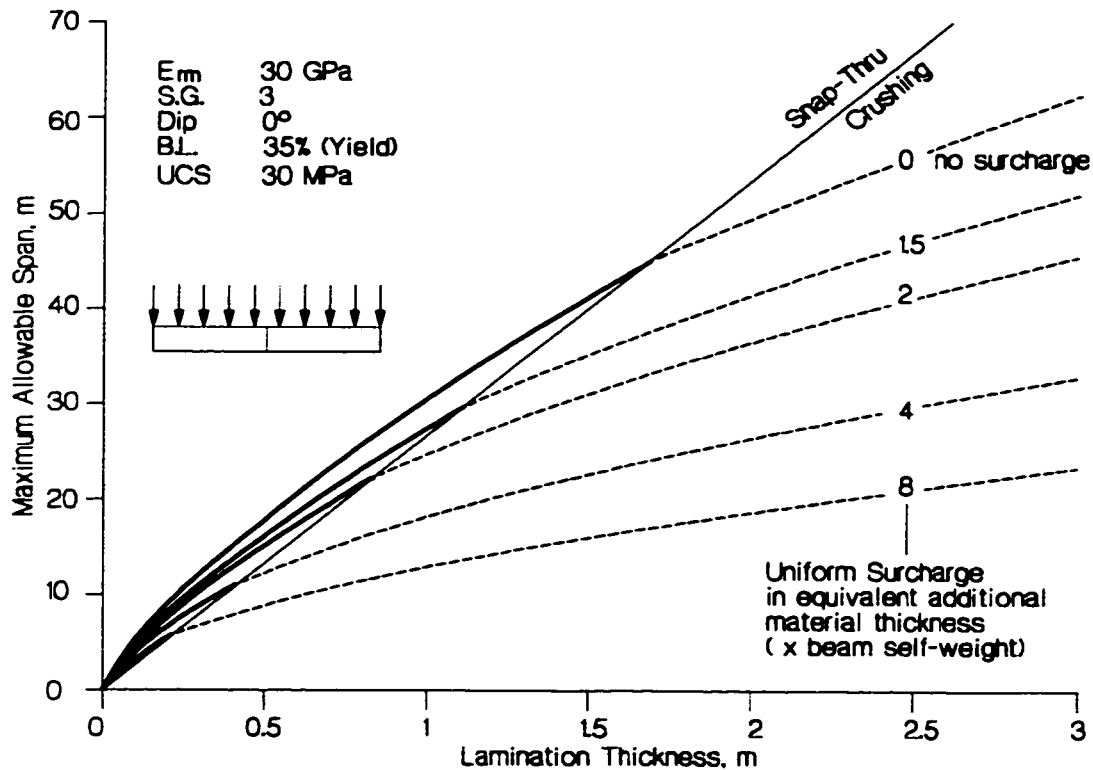


Figure 3.13: Influence of surcharge loading on beam stability and failure mode.

3.2.4 Significance of the Compression Arch Assumption

Sofianos and Kapenis (1998) discuss the mechanical differences between a three hinged Voussoir model (central crack) and a ubiquitous joint model (many vertical joints across beam). The assumption of the triangular wedge of abutment and midspan stress is valid for the ubiquitous beam (Figure 3.1a) as demonstrated in Section 3.4. The ubiquitous model is perhaps more appropriate for hard rock environments where natural cross jointing is present. In a competent sedimentary laminate, the voussoir may develop as the result of a single central crack induced by deflection. In this case the three hinged model may be more appropriate.

Sofianos and Kapenis (1998) performed numerical models using geometries similar to Figure 3.1b). In these analyses, the value of n (normalized compression arch thickness) was very low (approximately 0.1). The consequence of this reduced arch thickness is a higher maximum compressive stress resulting in compression damage at smaller spans than predicted by the ubiquitous model. As discussed in Section 3.4, the predictions for snap-through stability obtained using the ubiquitous model presented here, result in a 5 to 10% over-prediction in critical thickness, a conservative result.

3.3 FIELD EVIDENCE OF SNAP-THROUGH LIMIT

3.3.1 Mount Isa Mine

A limiting displacement (for linear voussoir behaviour) of 0.1 to 0.15 times the mapped bedding thickness is observed in the data, presented by Milne (1996), from numerous extensometers installed in the stope hangingwalls at Mount Isa Mine in Australia (Figure 3.14).



Figure 3.14: Laminated Hangingwalls at Mount Isa Mine (Photo courtesy M.I.M. Pty).

The displacement data from one of the extensometers is summarized in Figure 3.15. In this case, the extensometer was installed in the hangingwall, slightly above the stope midspan and prior to mining of a 50m high stope at a depth of 870m. The hangingwall consists of laminated shale with bedding plane partings observed every 20 to 25cm. The stope was mined via full face longitudinal retreat. Measurements were recorded as the stope was progressively mined past and beyond the location of the extensometer.

The Radius Factor shown on the horizontal axis of Figure 3.15 is a scale and shape index developed by Milne (1996). The details of this index are summarized elsewhere (Milne et al. 1996). For illustrative purposes, the Radius Factor describes the harmonic average of distance, from a point on an excavation surface or face, to all abutments. The Radius Factor, *R.F.*, of the hangingwall at the extensometer location increases as the stope is widened along strike (constant height and thickness). The maximum *R.F.* prior to backfilling was approximately 14.

Milne (1996) identifies four displacement zones with respect to increasing span including:

- 1) elastic rock behaviour,
- 2) stable voussoir beam behaviour,
- 3) unstable voussoir beam behaviour and
- 4) ultimate failure.

Stage 1) is not presented in Figure 3.15 due to the scale. Stages 2 through 4 are clearly apparent in this figure. The lamination thickness, *T*, is determined to be relatively consistent and equal to 0.2 to 0.25m (Milne 1996). The onset of non-linear or unstable voussoir displacement (interface between stages 2 and 3) occurs at a surface displacement of approximately 20 to 30mm ($0.08 \times T$ to $0.15 \times T$), reflecting the proposed yield limit for deflection of 10% of the beam thickness. A further transition to rapidly increasing displacement occurs at around 55 to 60mm. This is consistent with the ultimate collapse limit of $0.25T$. No extensometer anchor displacements are recorded beyond 80mm although it is assumed that had mining and recording continued beyond a *R.F.* of 14, without backfilling, this stope wall would have experienced significant surface failure. This corresponds (given uncertainties regarding the local parting thickness) with the predictions from the voussoir analogue.

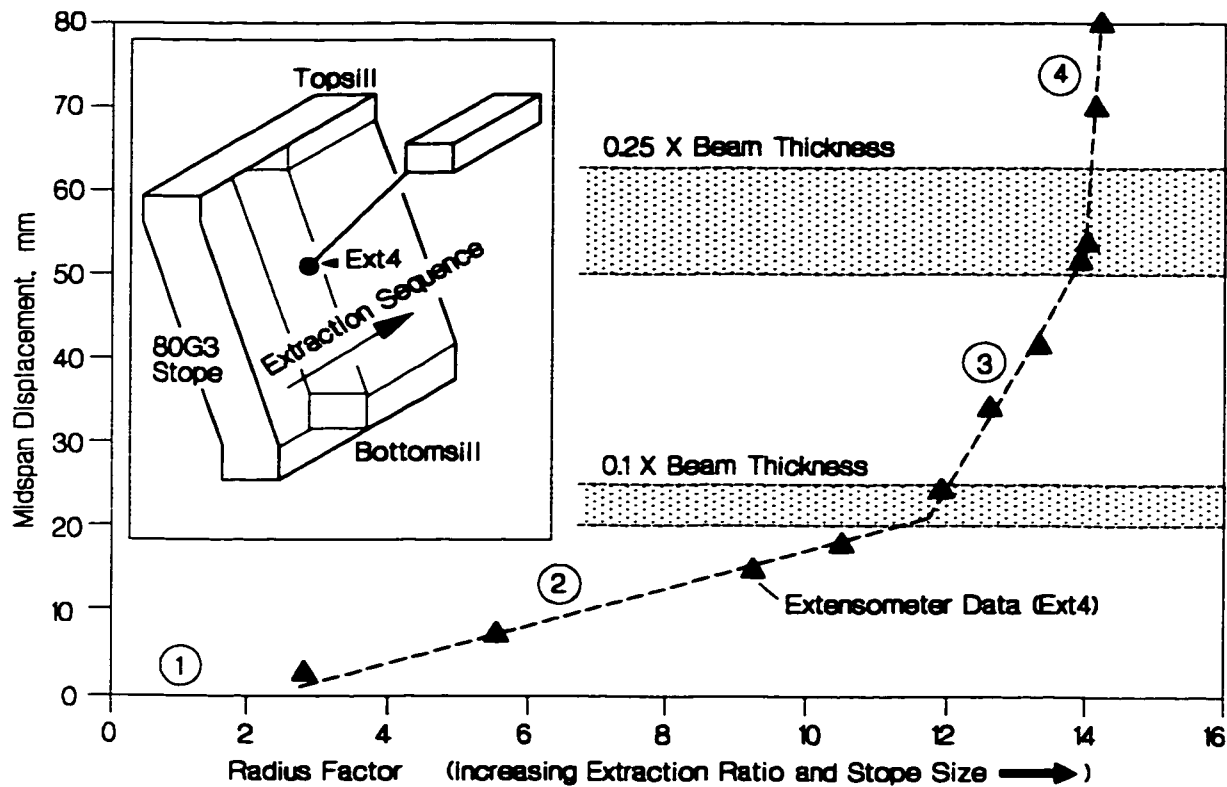


Figure 3.15: Hangingwall response to mining compared with voussoir limits. Based on extensometer data from Milne (1996).

3.3.2 Winston Lake Mine

A second case study from Winston Lake Mine in Ontario, Canada is used here to demonstrate the utility and validity of the voussoir analogue. The typical stope geometry is similar to that in the previous example except that the stopes are smaller (20m high) and less steeply dipping (45 to 60 degrees) and in this case, shallower (550m). Winston Lake Mine uses a modified version of the longitudinal retreat technique called modified AVOCA, in which the stope is blasted in full height slices perpendicular to the strike of the ore body. Rock fill is introduced by end dumping some distance back from the active face, creating an open stope of variable open strike length. The fill is compressible rockfill and cannot be considered tight fill until significant closure has occurred. As a stability analogue, therefore, the two dimensional beam is valid in this case.

As previously illustrated in Figure 3.2a, the hangingwall is composed of blocky chert with surface parallel jointing along foliation planes and two orthogonal sets of cross-joints.



Figure 3.16: Potential parting planes in foliated chert hangingwalls at Winston Lake Mine (hangingwall boundary to the left)

Cablebolt support (Hutchinson and Diederichs 1996) is installed from a remote drift to supply full coverage at the hangingwall. Figure 3.17 shows the layout of drifts, stopes, cablebolts and instrumentation for an experiment investigating cablebolt performance in hangingwalls and the impact of stress change (Maloney et al. 1992; Kaiser et al. 1992). Extensometer data (Maloney and Kaiser 1991) from this study is used here to illustrate the voussoir beam behaviour of the chert hangingwall. Borehole camera data (Maloney and Kaiser 1993) is also used to estimate the effective thickness of continuous partings parallel to the hangingwall as the wall deflects.

The rockmass quality as indicated by the index Q (Barton et al. 1974) is approximately 7 to 28 which, using the relationship (Barton et al. 1980):

$$E_m = 25 \log_{10} Q \quad [3.19]$$

indicates a rockmass modulus in the range of 20GPa to 35GPa. The data set, collected from numerous sources contains a large scatter and according to variability limits proposed by Barton (1983) this rockmass quality could have a modulus as low as 10 GPa and as high as 50GPa. The lower modulus could apply if the rockmass was relaxed due to undercutting, as was the case in some of the stopes (Kaiser and Maloney 1992).

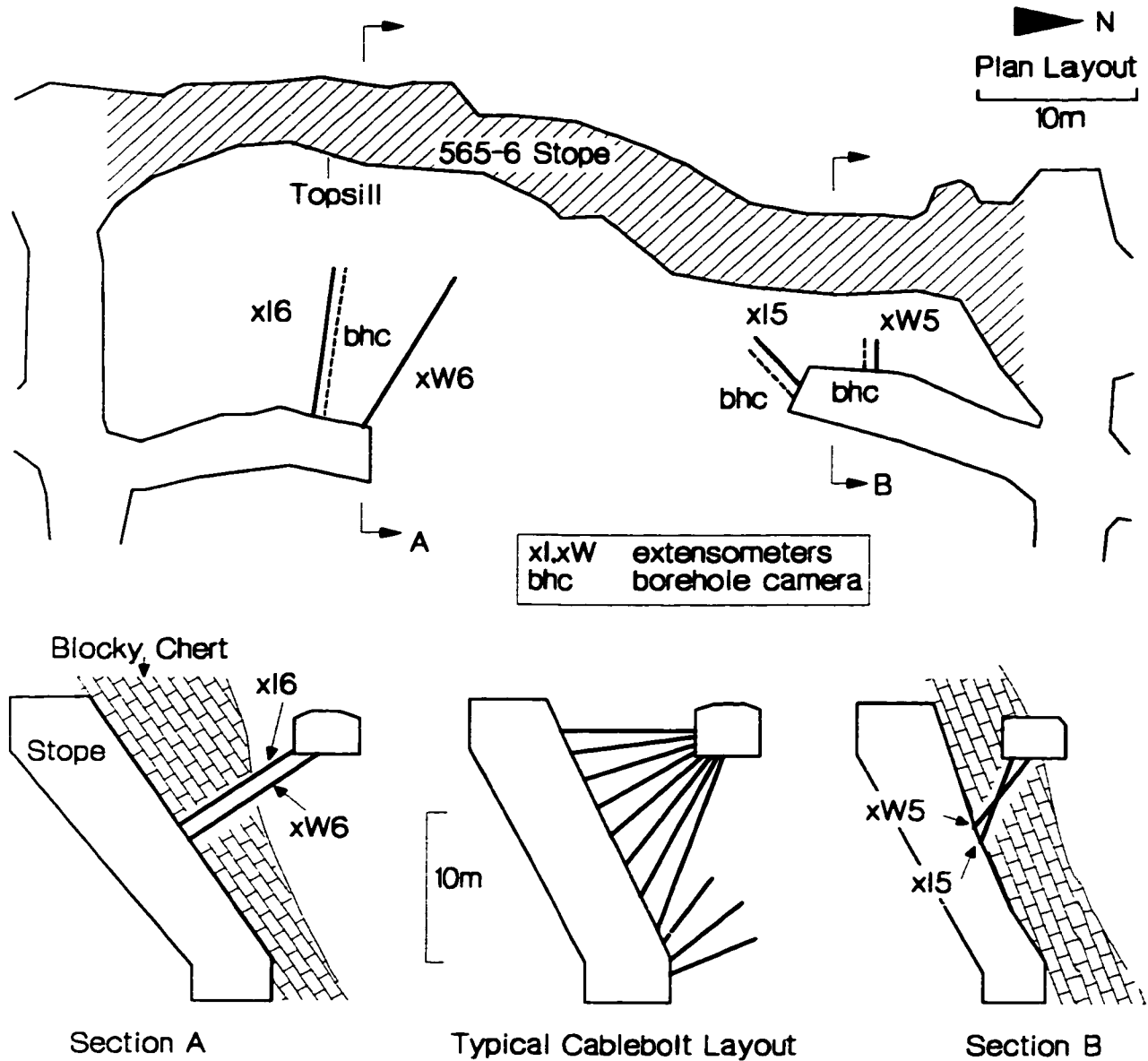


Figure 3.17: Plan layout and typical cross sections through study area - Winston Lake Mine.

The displacement of the hangingwall can be predicted by the voussoir analogue. The results for this case are shown in Figure 3.18. The equilibrium displacements are plotted (thick curves) as a function of lamination thickness and rockmass modulus. The critical displacement limits for yield (10% of the thickness) and for collapse (25% of the thickness) are overlain on the plot.

The joints at Winston Lake were not fully continuous and the effective lamination thickness, therefore, evolved as the hangingwall deflected and as joints propagated along the foliation planes or connected with other joints. The change in lamination thickness was determined using borehole

camera surveys. Estimates of the effective beam thickness can be made at any point in space and time. The measured displacements at these points, measured by an adjacent extensometers, are plotted against the estimated lamination thickness in Figure 3.18 for specific points along different extensometer-borehole camera clusters (Figure 3.17). In Figure 3.18, data points with identical labels (e.g. I5) indicate the same spatial location at different times.

The results show that the rockmass behaviour correlates well with the predicted displacements. The data with higher beam thicknesses are from earlier in the mining. As more partings form, the effective thickness decreases and the points move to the left on Figure 3.18. It interesting that while the earlier points correlate with a rockmass with low modulus, the later data beyond 40mm of deflection seems to deviate (lower than expected displacements).

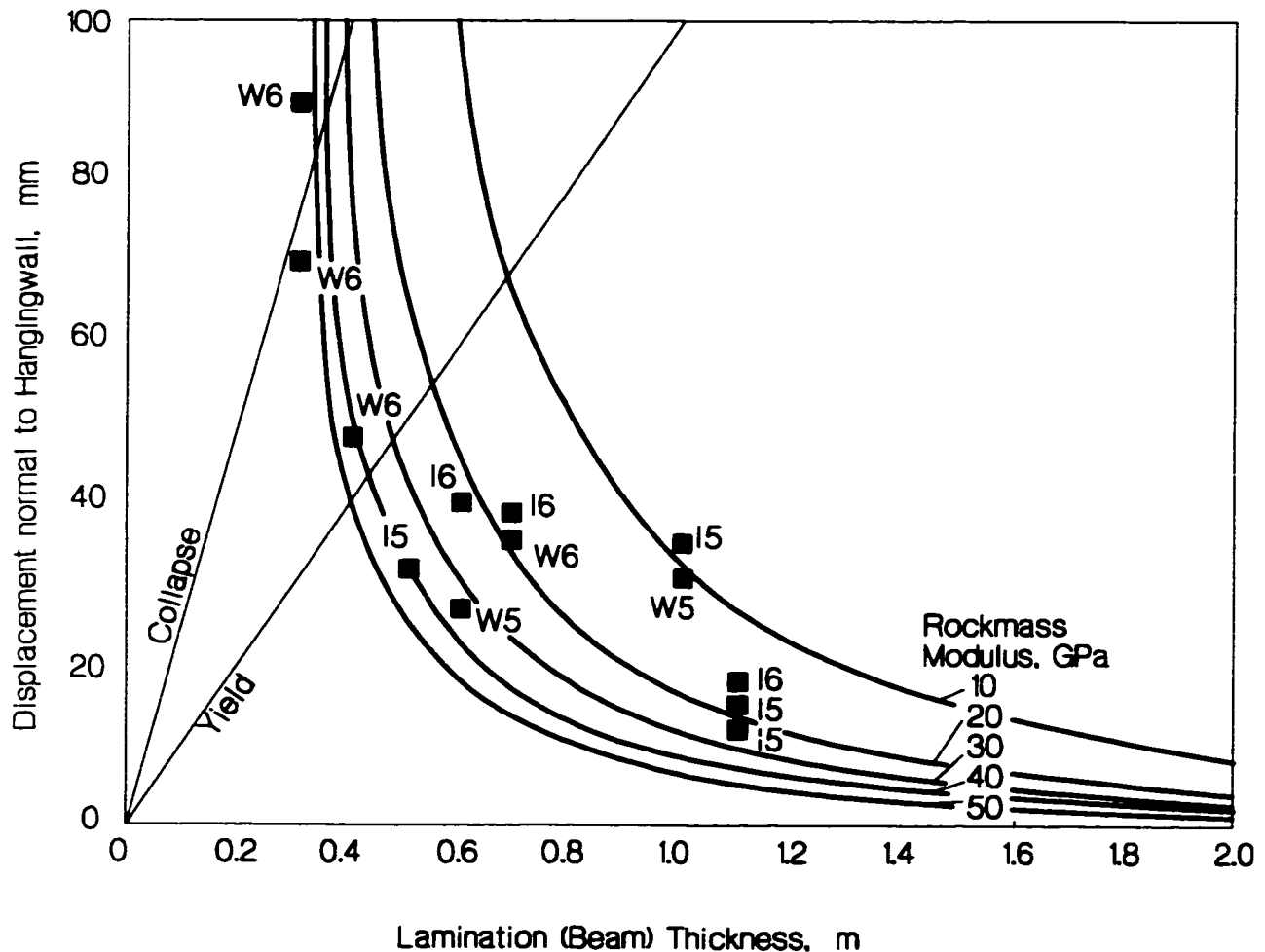


Figure 3.18: Measured displacements and observed lamination thicknesses (data points), compared with voussoir predictions - Winston Lake Mine.

This stope is supported with remotely installed cablebolts. Plain strand, cement grouted cablebolts tend to require up to between 30 and 40mm of slip to develop their peak frictional capacity (Hutchinson and Diederichs 1996). If the effective embedment length of the strand, equal to the lamination thickness, is less than the critical length required to break the steel, the cablebolt can provide this capacity over relatively large rockmass displacements. It can be seen that late in the experiment, as mining progresses farther past the instrumentation sites, deflection beyond 40mm follows a more stable trend than that predicted by the model. Cablebolts must be contributing to the stability of the hangingwall by applying an effective support pressure.

3.4 NUMERICAL VERIFICATION (SNAP-THROUGH)

Discrete element modelling (Itasca 1996) was employed to further verify the analogue. Others have performed similar analyses with mixed results. Sofianos (1996) describes a simulation using finite elements which appears to show that the voussoir model presented by Brady and Brown (1993), which is similar to the model described here, poorly predicts the simulated displacements and beam stresses, primarily due to an over-prediction of the effective thickness of the compression arch at the midspan and at the abutments. The numerical simulations of Sofianos (1996) predict a normalized arch thickness of less than 0.3 at equilibrium and less than 0.1 near failure. These are low compared to the values 0.75 for equilibrium and 0.3 to 0.4 at failure, predicted by the iterative approach in this study. Numerical simulations by Ran et al. (1994) indicate an arch thickness more consistent with the predictions in this study.

Clearly, something is amiss. The answer appears to be the numerical boundary conditions and discretization used in the model. It was found during the course of this research that a UDEC model (Itasca 1996) composed of rigid blocks and elastic joints (no tension) and a model composed of deformable blocks and elastic joints (no tension) both seemed to exhibit similar behaviour to the model of Sofianos (1996) if the beam had fixed supports or was bounded by rigid blocks as abutments. This creates problems with discretization which do not seem to permit the formation of a stress triangle ($0 < N < 1$) at the abutments. Instead, reaction forces are concentrated at the bottom corner of the abutments leading to over-prediction of the moment arm and inaccurate deflection predictions. Further work by Sofianos and Kapenis (1998) indicates this problem may reflect a fundamental difference between a 3-hinged beam and a ubiquitously jointed beam (Section 3.2.4).

The model ultimately used for this study utilized deformable elastic blocks (discrete blocks with internal finite difference zones), elastic joints (no tension) and flexible (elastic and internally discretized) but very stiff abutment blocks. This provided better displacement compatibility at the abutments. The results of this model correlate very well with the voussoir analogue as will be discussed presently. Simulations included single beams only since the purpose of the model was a comparison with the analogue. Hatzor and Benary (1998) have recently examined the influence of multiple layers with interbed friction. The single beam prediction represents the worst-case failure initiation potential in cases where lamination thickness and modulus is uniform.

The beam was first allowed to deflect elastically while maintaining a non-zero tensile strength within the joints. If this initial elastic deflection is not permitted, sliding will occur before arch stresses are generated. It is assumed that excavation is a gradual process such that beam deformations occur before the abutments are fully liberated. After elastic equilibrium was achieved, the joint tensile strength was set to zero and the beam was allowed to continue deforming until either equilibrium or failure occurred. The joints had no cohesion but had a frictional strength. The initial elastic deformation stage allowed lateral stress and frictional strength to accumulate in the joints, particularly at the abutments. Without this stage the beam would simply slip past the abutments under its own weight.

Several configurations were tested, using different rock stiffnesses, E_i , different joint normal stiffness, K_n and joint spacings, s_j . The rockmass modulus, E_m for comparison with voussoir predictions, was calculating according to the analogue in Figure 3.19 using the relationship:

$$\frac{1}{E_m} = \frac{1}{E_i} + \frac{1}{(K_n)s_j} \quad [3.20]$$

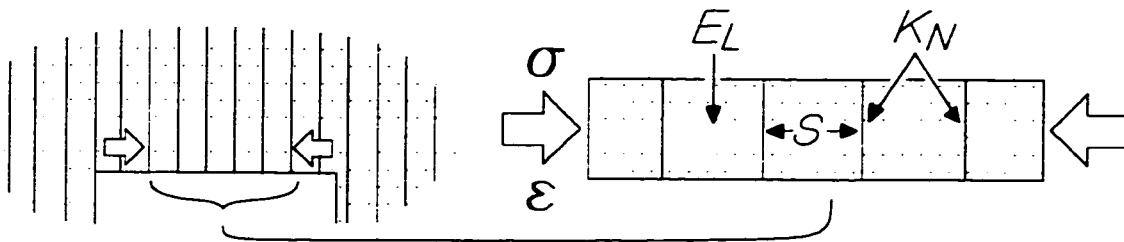


Figure 3.19: Rockmass stiffness for a uniformly jointed rockmass.

The deflection profile and the internal stress distribution are shown in Figure 3.20 for one example simulation. The parabolic nature of the compression arch is immediately apparent.

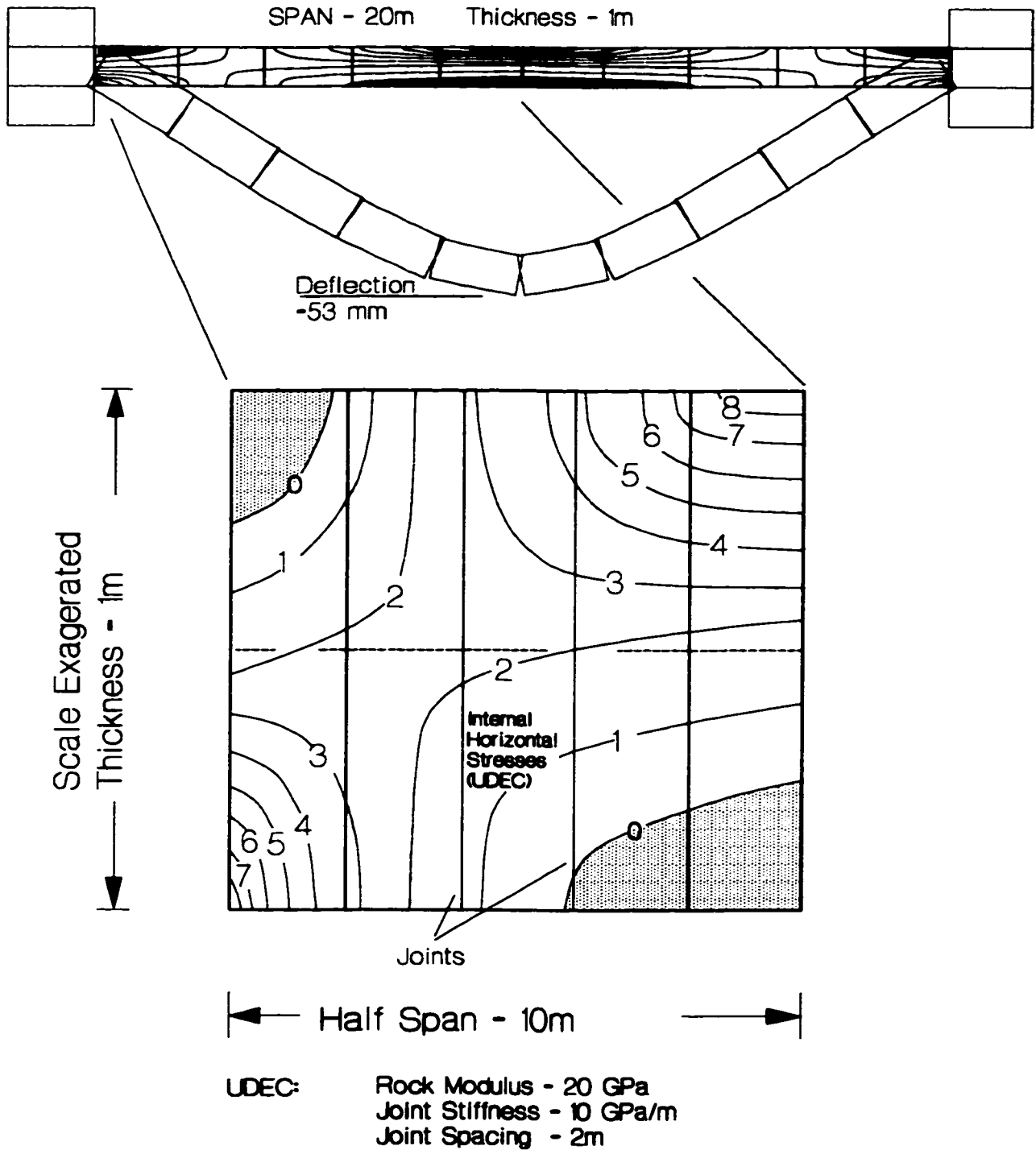


Figure 3.20: Exaggerated displacement profile (top) for a typical UDEC voussoir beam simulation and contours of internal horizontal compressive stress (bottom).

Figure 3.21 compares the lateral stress distribution at the abutment and at the midspan with the assumed triangular distribution and the predicted voussoir arch thickness ($0.65T$).

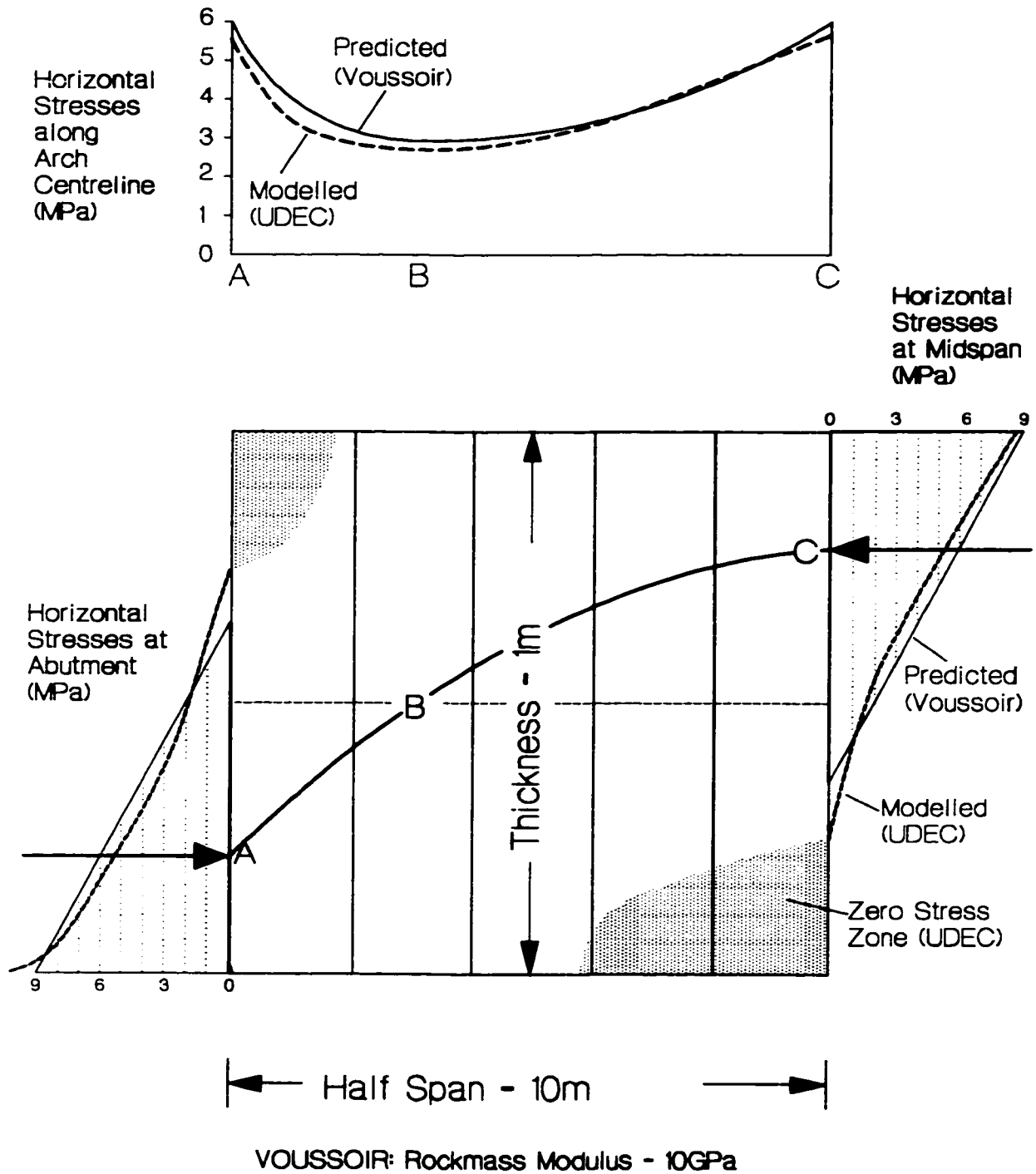


Figure 3.21: Predicted variation of horizontal stress along arch axis (ABC) compared with UDEC results (top) and predicted and simulated stress distributions at abutment and at midspan (bottom).

The distribution at midspan correlates very well, while the numerically simulated abutment stress distribution is more non-linear, resulting in a higher maximum stress near the bottom edge of the beam. In addition, the lateral stress variation along a parabolic path, ABC, in the UDEC model is compared with the assumed parabolic variation introduced in this thesis. Again the match is acceptable for engineering application of the method.

Models of unit thickness ($T=1$) with several different rockmass moduli were analyzed with increasing span, in increments of 5m, up to snap-through failure (blocks fall and beam disintegrates). Crushing failure was not investigated in this analysis. Figure 3.22 illustrates the calculated equilibrium displacements in the UDEC models and the associated voussoir predictions.

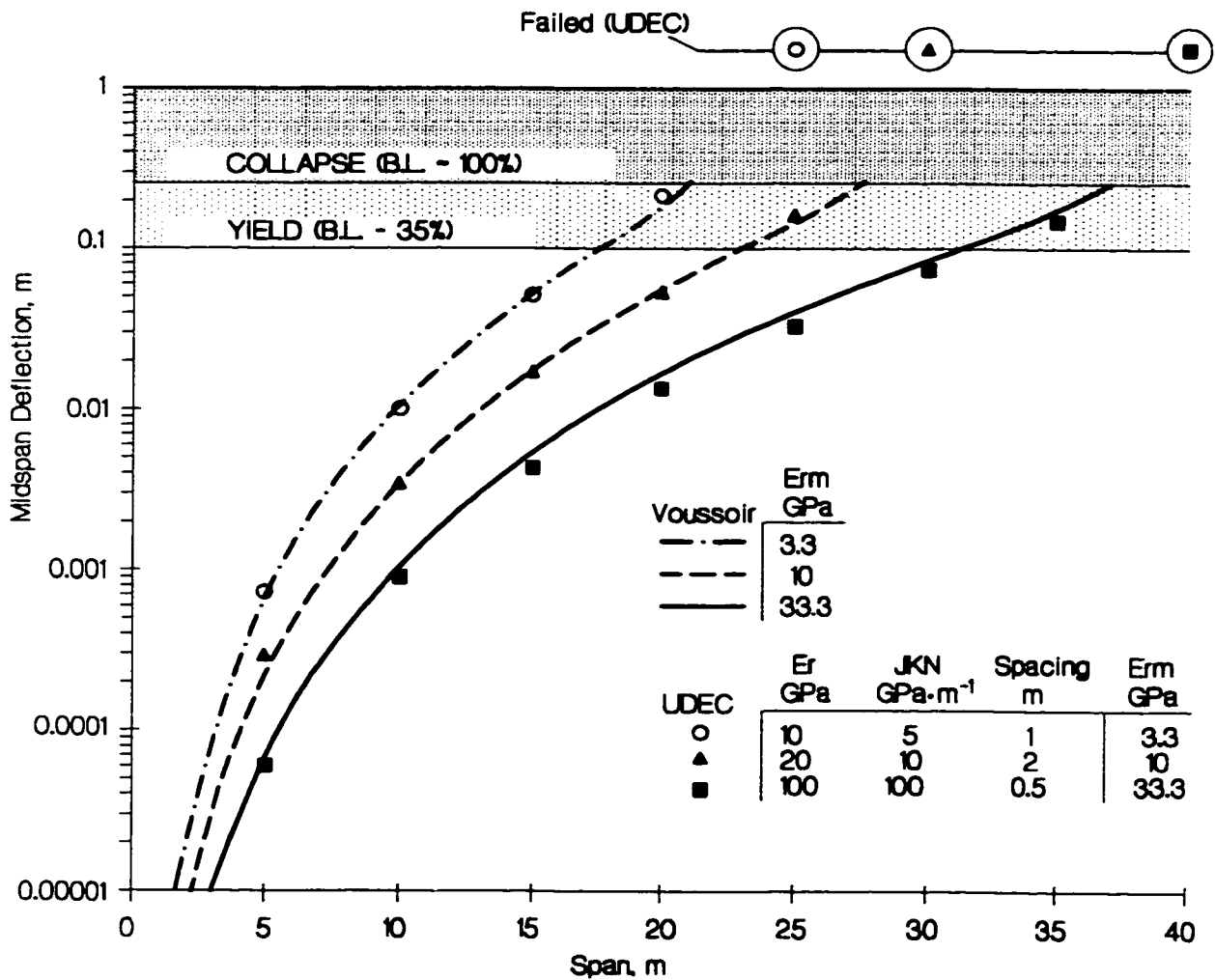


Figure 3.22: Midspan displacements (data points) from UDEC beam simulations compared with voussoir predictions ($T = 1m$). Note that $JKN=k_n$

The modeled deflections match the predicted relationships well, with the exception of a slight over-prediction by the voussoir model at higher stiffnesses. In addition the UDEC model failed in each case immediately beyond the critical span predicted by the voussoir analogue.

The maximum stress occurred inevitably at the bottom edge of the beam at the abutment. The midspan maximum stress correlated fairly well with predictions (Figure 3.23) while the abutment stress was consistently higher. If this is real and not an artifact of the modelling, it is unlikely to devalue the predicted crushing limit for the voussoir analogue, since the area over which the increased stresses occur in the UDEC model is quite limited and any resulting initial crushing would be highly localized. These numerical results, therefore, give us confidence that the voussoir model can be used to predict the deflection and stability of rock beams which form in laminated ground.

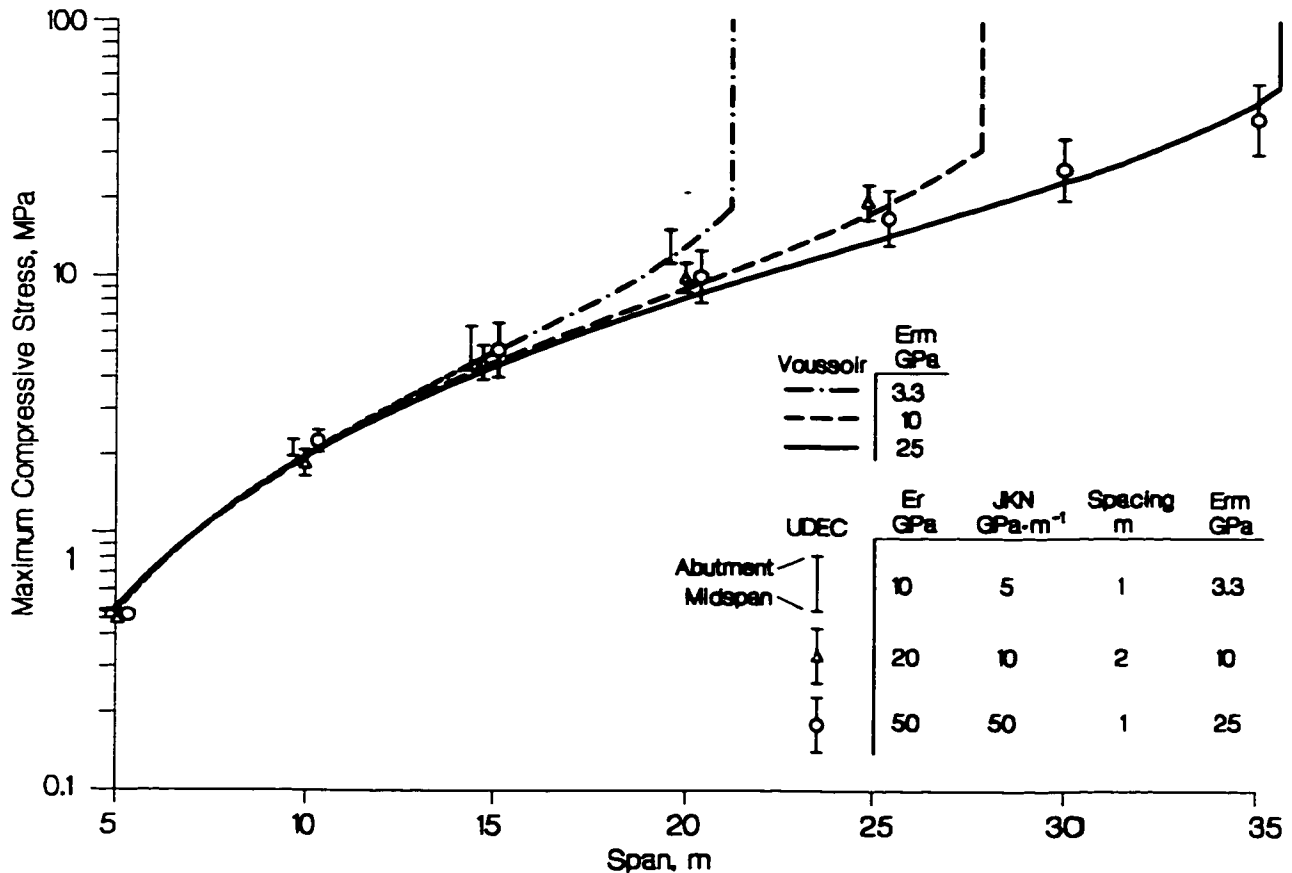


Figure 3.23: Maximum compressive stress in UDEC beams compared with voussoir predictions ($T=1$ m).

A large-deflection comparison is in order between the iterative solution presented here and the analytical solution and numerical results presented by Sofianos et al. (1996 and 1998). Table 3.1 presents a comparison of predicted critical thickness for the ubiquitously jointed beam and numerical results using a 3-hinge model. Collapse occurs for thicknesses less than these values. The analytical values are extreme limits based on a *B.L.* of 1 (only one allowable value of *N*).

Table 3.1: Minimum predicted thickness, *t* (m) from this analysis (ubiquitous joint assumption), and UDEC results from Sofianos and Kapenis (1998) for the 3-Hinge Beam. UDEC results presented as a range of [Stable –Failed].

Modulus	10m Span		20m Span		50m Span	
	Analytical [1]	UDEC [3]	Analytical [1]	UDEC [3]	Analytical [1]	UDEC [3]
0.24-0.25	0.268	0.24-0.25	0.674	0.62-0.64	2.29	2.1-2.2
16 GPa	0.212	0.20-0.22	0.535	0.47-0.49	1.82	1.67-1.7
32 GPa	0.169	0.15-0.17	0.425	0.38-0.4	1.44	1.35-1.37

In general the solution presented here over predicts the minimum critical thickness (for the 3-hinged model) by only 5 to 10%. For the ubiquitously jointed beam Table 3.2 gives a favourable comparison of predicted critical spans (*B.L.* = 1) with the range predicted by UDEC simulations.

Table 3.2: Maximum predicted span (m) and UDEC results (this study) for the ubiquitously jointed beam (*t*=1m).

E_{rm}	Critical Span (analytical [1])	UDEC [1] (<i>stable-failed</i>)
3.3 GPa	21.5m	20m - 25m
10 GPa	28.4m	25m - 30m
33 GPa	38.3m	35m - 40m

Midspan displacement (prior to rupture) for the extreme case is 34% of the critical thickness according to the solution in this work, for a *B.L.* of 1. This compares (as an upper bound) to an average maximum normalized displacement in the UDEC simulations by Sofianos and Kapenis (1998) of 32%. Their analytical solution, with internal variables calibrated using UDEC data predicts a value of 35 to 38%. Either solution (3-hinged or ubiquitously jointed) seems to provide a reasonable upper bound. Note, however, that these displacements are extreme values in the context of design. The maximum prudent allowable normalized displacements for design (not back analysis) according to this work correspond to a lower “safe” limit of 10% (of beam thickness) and

a practical upper bound of 25%. The corresponding “buckling limits”, *B.L.*, are 0.35 and 0.80 respectively. In addition, crushing failure may reduce these displacement limits.

The ubiquitous model is felt to be a valid analogue for design and for the main focus of this work - the study of abutment relaxation and residual tensile strength (Chapter 4) in the context of underground excavation stability in hard moderately jointed rockmasses.

3.5 STABILITY GUIDELINES

The results of this work can be summarized into normalized stability charts for use in design of underground openings. The material properties required are the rockmass modulus and an estimate of the compressive yield strength.

Crushing failure is local in nature and therefore relates to the strength of the intact rock. However, in accordance with recommendations by Martin (1994) regarding the strength of intact rock insitu, one third to one half of the laboratory *UCS* is used for this analysis.

Rockmass modulus is used (instead of the intact modulus) since, by definition there are joints normal to the direction of compression, and these must influence the stiffness of the beam. Modulus is the critical parameter in determining snap-thru stability (or failure). In order to simplify the estimation of rockmass modulus based on rockmass classification, the test data for field modulus presented by Barton et al. (1980), Bieniawski (1989) and Serafim and Pereira (1983), collectively illustrated in Figure 3.24, were reexamined by Hutchinson and Diederichs (1996) to account for the effect of confinement and sample disturbance.

Joint stiffness is in reality dependent on the normal stress resulting in a non-linear closure response at low confinements as illustrated in Figure 3.25. Much of the data for lower range stiffness data in Figure 3.25 comes from near-surface insitu testing. In these tests, joints are initially unconfined and have a more significant impact on the measured rockmass modulus.

The results have been further modified here to provide convenient functions for modulus based on rock quality and confinement (Figure 3.26). These functions can be used to estimate rockmass modulus for the voussoir beam. For most excavations where the voussoir analogue is valid, the lower bound moduli should be used.

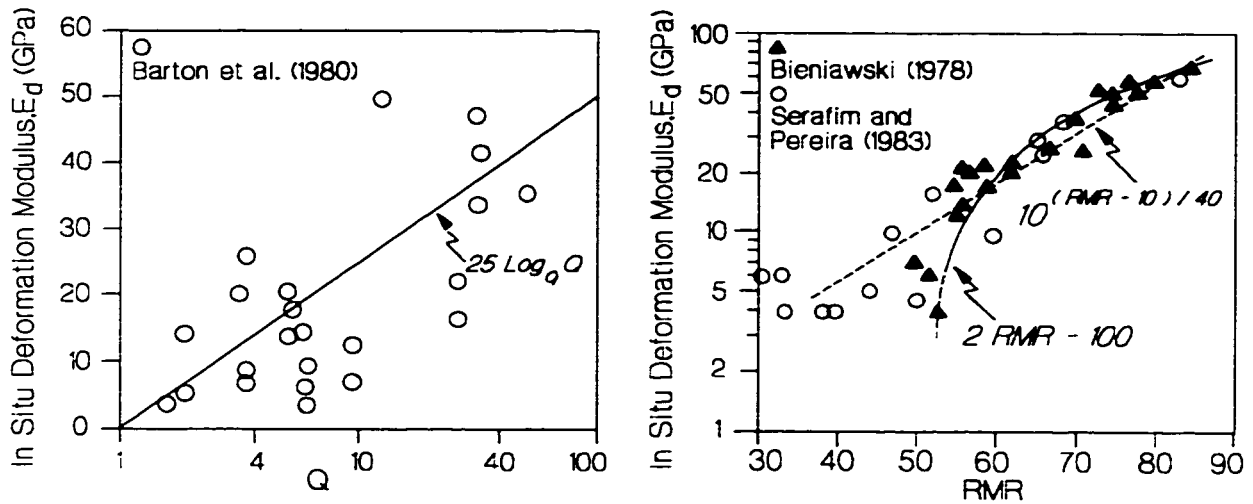


Figure 3.24: Empirical relationships between rockmass modulus and rockmass classification.

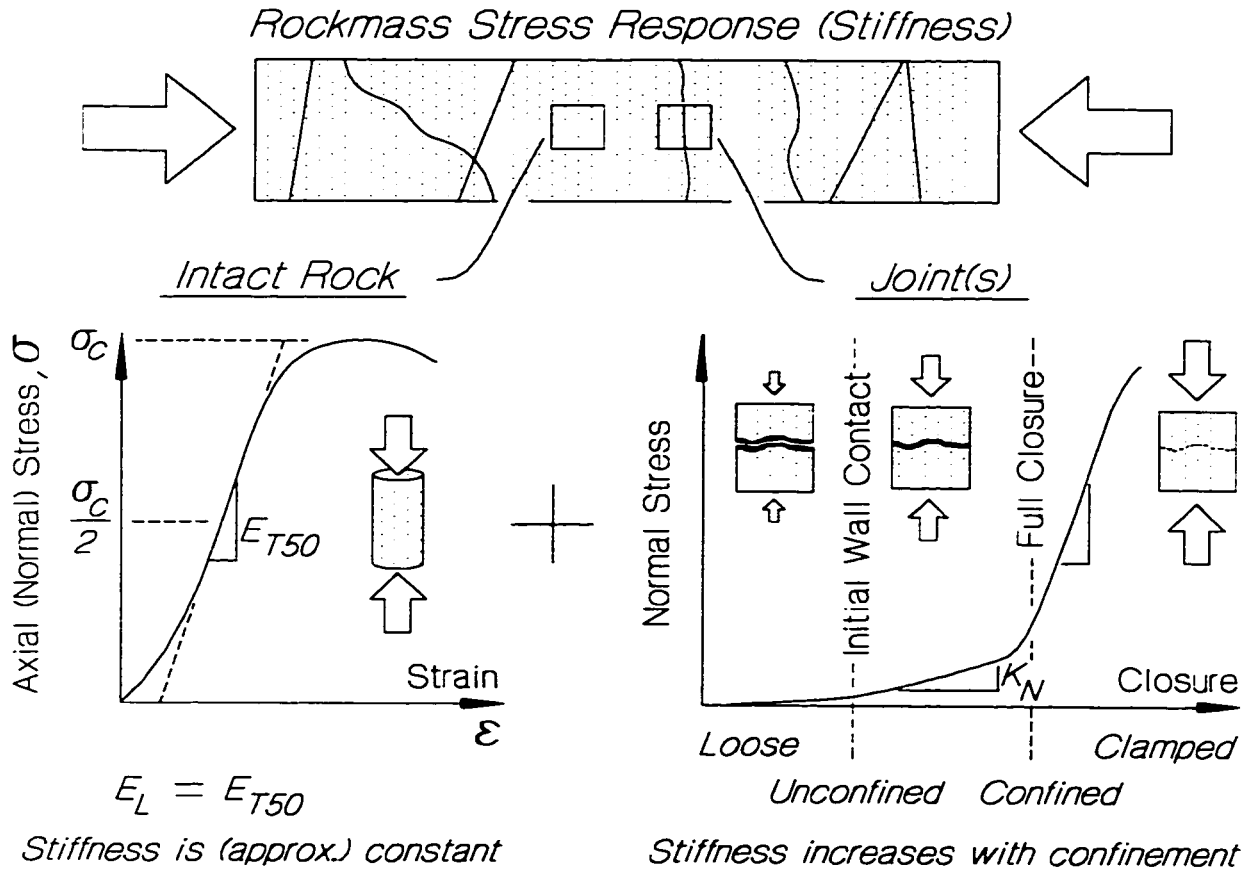


Figure 3.25: Non-linear joint stiffness response under low confinements.

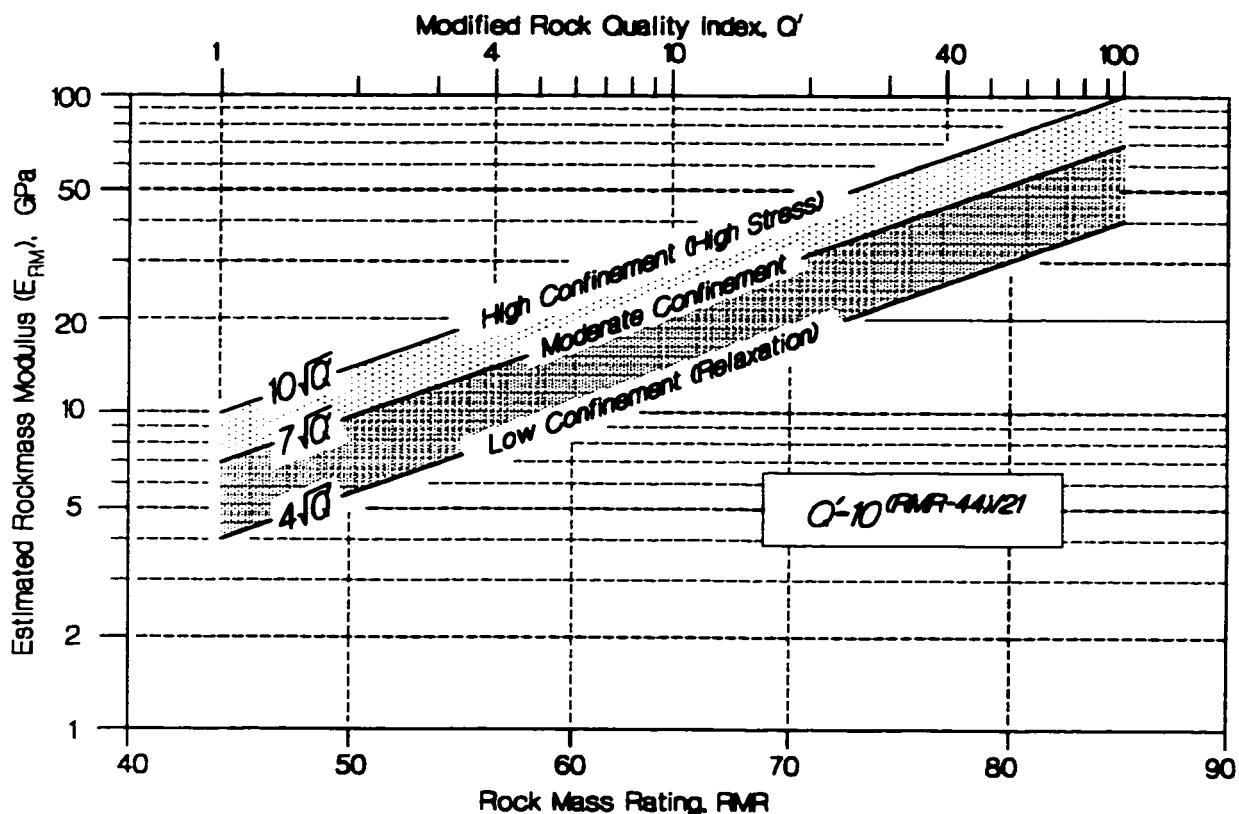


Figure 3.26: Simplified relationships for rockmass modulus as a function of rock quality and confinement.

Parametric modelling has shown that the snap-through stability limits for critical span and thickness can be related to the normalized rockmass modulus, E^* , which is equal to the modulus divided by the effective specific gravity, $S.G.^*$ ($E^* = E / S.G.^*$). Similarly, the limits for crushing failure can be related to the normalized compressive strength ($UCS^* = UCS / S.G.^*$).

The effective specific gravity, $S.G.^*$, for a beam with a dip of α can be obtained from:

$$S.G.^* = S.G.(\cos \alpha) \quad [3.21]$$

The summary design limits based on yield (Buckling Limit = 35%) are presented in Figure 3.27. If a beam thickness is specified, then a critical span is obtained for snap-through failure and for crushing failure. The design span is the lesser of the two values. Likewise, if a span is specified, the critical thickness is the greater of the two.

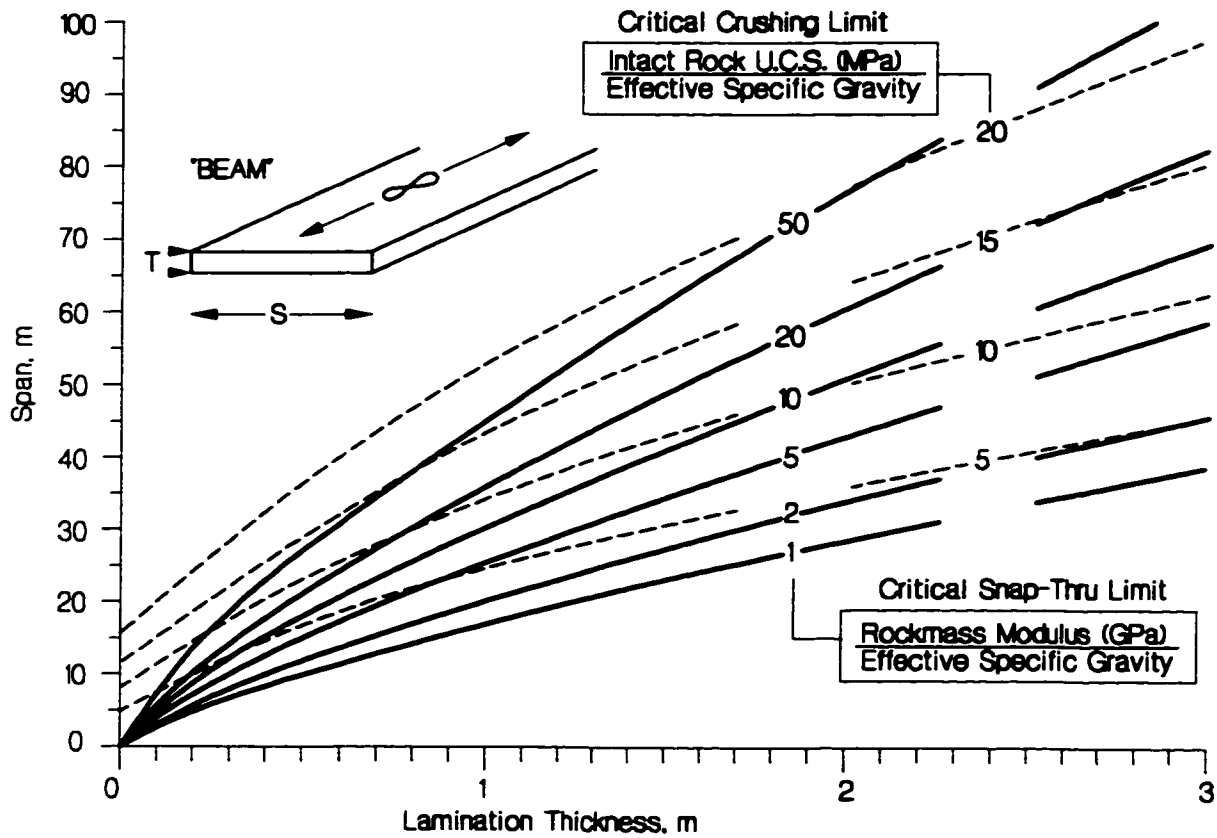


Figure 3.27: Stability guidelines for jointed rock beams (tunnel spans). Effective Specific Gravity, $S.G.*=S.G.\cos\alpha$.

Actual spans are rarely fully two dimensional in nature. In fact the two dimensional beam represents a lower bound model for determining critical span. An upper bound is obtained from the model for a square span. Again, Brady and Brown (1993) derive a relationship for a square span by assuming that the span fails as four triangular panels.

The weight of each panel creates a moment about the abutment edge:

$$M_w = \frac{\gamma T S^3}{24} \tag{3.22}$$

which is resisted by a reaction moment

$$M_R = \frac{f_{max} N T S Z}{2} \tag{3.23}$$

This equation, however, is in error due to the assumption of a constant moment arm, Z , through all sections of the triangular panel. The deflection at the hinge point is zero and therefore, the moment

arm must vary from $Z = Z_0 - \delta$ at the midspan, to Z_0 at the corners. Equation 3.23 must therefore be revised to:

$$M_R = \frac{f_{\max} N T S (Z + Z_0)}{4} \quad [3.24]$$

Combining Equations 3.22 and 3.24 yields a modified relationship for f_{\max} :

$$f_{\max} = \frac{\gamma_e S^2}{6N(Z + Z_0)} \quad [3.25]$$

Equation 3.25 is then substituted for Equation 3.13 in the original analysis. One final adjustment is necessary, however. For the square span, incorporating the rockmass Poisson's Ratio, ν , Equation 3.16, for the shortening of the beam must be replaced by:

$$\Delta L = \frac{(1-\nu)L}{E} f_{\max} \left(\frac{2}{9} + \frac{N}{3} \right) \quad [3.26]$$

Results for the square span are summarized in Figure 3.28.

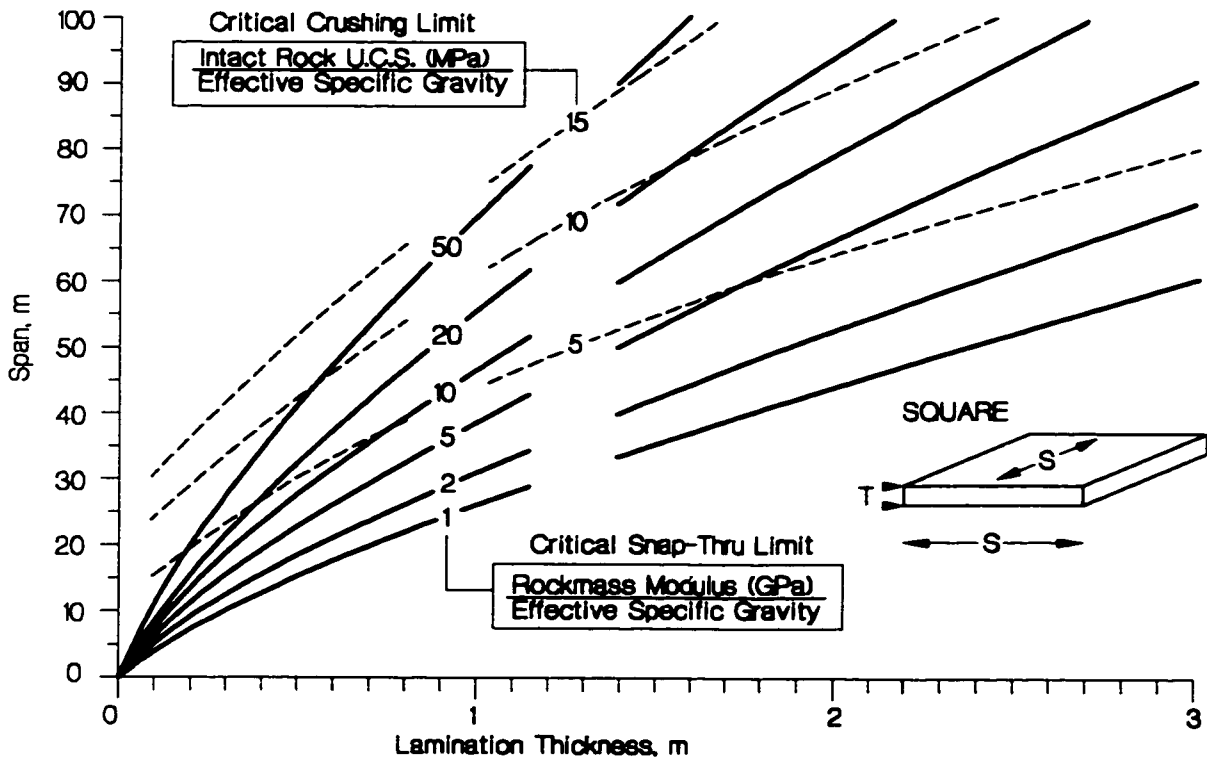


Figure 3.28: Stability guidelines for jointed rock plates (square spans). Effective Specific Gravity, $S.G.* = S.G.\cos\alpha$.

A few limitations with respect to these charts should be noted:

- These charts can be used with confidence in laminated ground where the lamination thickness is known and where the modulus can be estimated with some degree of reliability.
- It is imprudent to rely on such an assumptive method for very large spans (> 100m for steeply inclined spans and > 60m for horizontal spans) where other influences, not considered here, may govern stability. Consistent excavation quality is also assumed. Over-blasting, or uneven excavation surface geometry will negatively impact roof stability.
- The assumption in these charts is that the joints are rough enough to provide frictional resistance under low to moderate confinement (ie. no slickensides or low friction coating) and that the span to thickness ratios are greater than 10. Sliding failure along joints at the abutments or within the beam is not considered.
- It is assumed that there is no frictional or cohesive resistance along the interfaces between the laminations. This represents a worst-case assumption since such resistance increases the stability of the beams. Snyder (1983) showed that limited friction (generated by the active pressure created by mechanical rockbolts) resulted in a small increase in stability, while cohesive resistance (no slip) generated by fully grouted bolts (or rock bridges) had a significant stabilizing effect.
- These charts are only valid if no low to mid angle jointing is present. In this case or in the case of thinly laminated ground, support is necessary in order to create a reinforced beam. Rockbolts or grouted rebar should be approximately equivalent in length to the desired beam thickness. Assuming a lower-bound rockmass modulus, a reinforced thickness can be estimated from the Figures 3.27 and 3.28 which will ensure adequate stability.
- This method is not suitable for poor rockmasses with a low RQD rating (< 50) and more than three joints sets.
- This technique is designed to predict the onset of roof instability. Thus only the first (lowermost) lamination is considered and not a composite beam structure. This is based on the assumption that, provided the beam thickness is adequate, stability of the whole roof is controlled by the stability of this first beam.

- The influence of the gravity load component parallel to inclined laminations is ignored in order to achieve a tractable solution.

This last assumption leads to the apparently reasonable conclusion that inclined layers (dip = α) are significantly more stable than horizontal layers. The deflecting beam must still achieve the same moment equilibrium (between the perpendicular weight component and the compression arch reaction force) regardless of initial (gravitational) compression within the beam.

The beam does, however, settle under this imposed loading. The effect of this additional compression can be considered implicitly by imposing an initial shortening of the beam, $\Delta\delta_c$, equivalent to the compression due to gravity (parallel to the beam) given by Equation 3.25. The beam must first close this gap before additional compression can be created during beam deflection. This gap is used to calculate a new initial moment arm in Equation 26. This value is substituted for Z_0 in equation 17.

$$\Delta\delta_c = \frac{S^2\gamma \sin \alpha}{E} \quad [3.25]$$

$$Z_0^* = \sqrt{\frac{3S}{8} \left(\frac{8}{3S} Z_0^2 - \Delta\delta_c \right)} \quad [3.26]$$

Examples of the influence of this correction on critical span are shown in Figure 3.29. Given the bevy of simplifying assumptions already inherent in the model, the impact of this correction is of limited practical significance for rockmass moduli greater than one GPa and can be neglected in the interest of producing the simplified and unified charts in Figures 3.27 and 3.28. On the other hand, according to this simplified correction, non-critical equilibrium deflections are significantly affected as in the examples shown in Figure 3.30, with increases, at one half of the critical span, exceeding 100% for near-vertical beam (dip = 80 degrees).

Undoubtedly, the influence of the parallel weight component is more complex than described here, leading to asymmetrical beam deflection and other complications. It is likely, however, that the impact of this skewed gravity loading is small compared to the end stresses generated by deflection. A program of numerical experimentation is warranted to investigate this influence and provide more accurate stability predictions for inclined beams. Such a program is beyond the scope of this thesis.

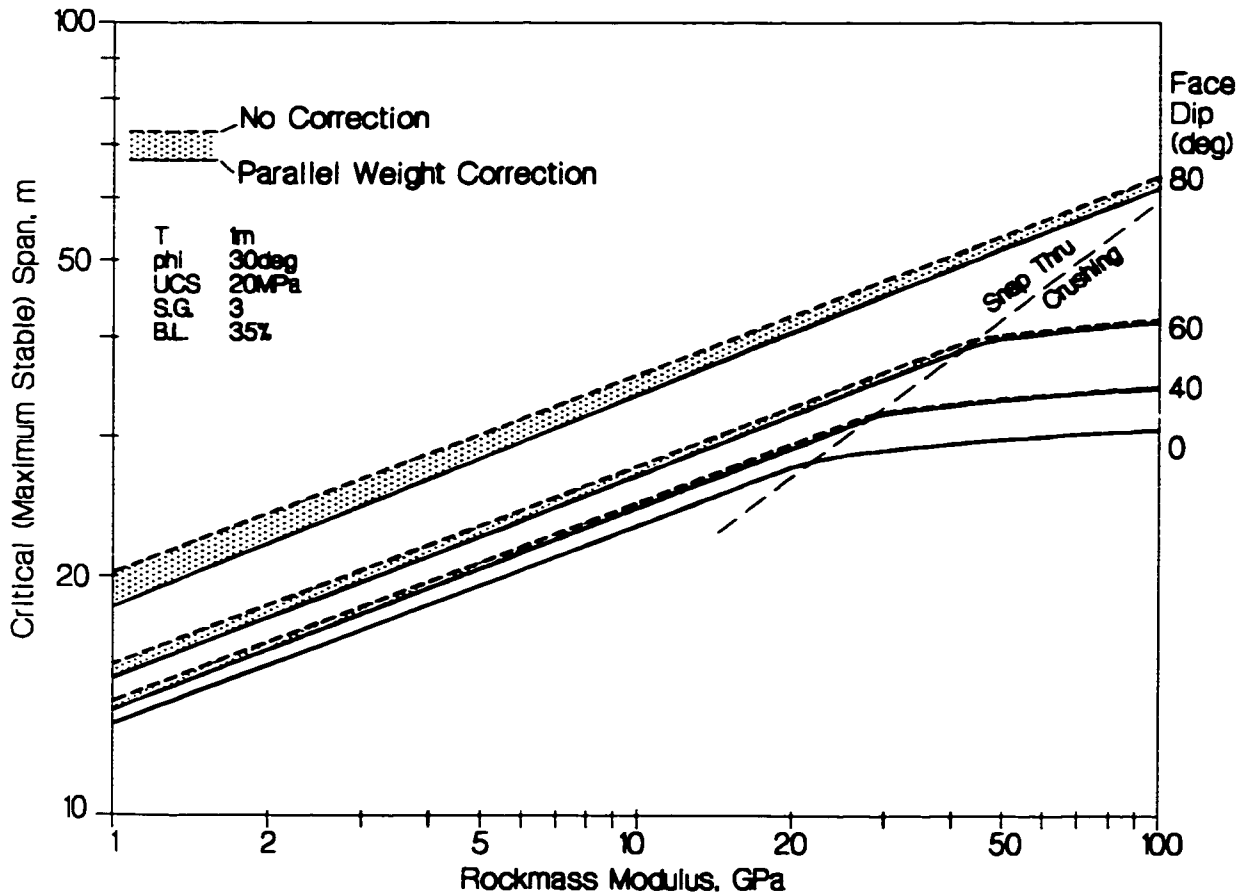


Figure 3.29: Examples of parallel weight correction to critical span for inclined beams.

3.6 DISCUSSION

An improved iterative approach to a classic analogue for stability assessment of laminated ground has been presented with several improvements and corrections, including an improved assumption for lateral stress distribution and arch compression, the application of support pressure and surcharge loading, simplified displacement determination and a robust iteration scheme.

A linearity limit or yield limit has been identified, corresponding to a midspan displacement of approximately 10% of the lamination thickness. This displacement limit appears to be independent of rockmass modulus and is a useful guideline for performance monitoring and observational design. Beyond this displacement, stability cannot be assured. The yield limit and the methodology in general has been verified using field evidence and numerical simulations.

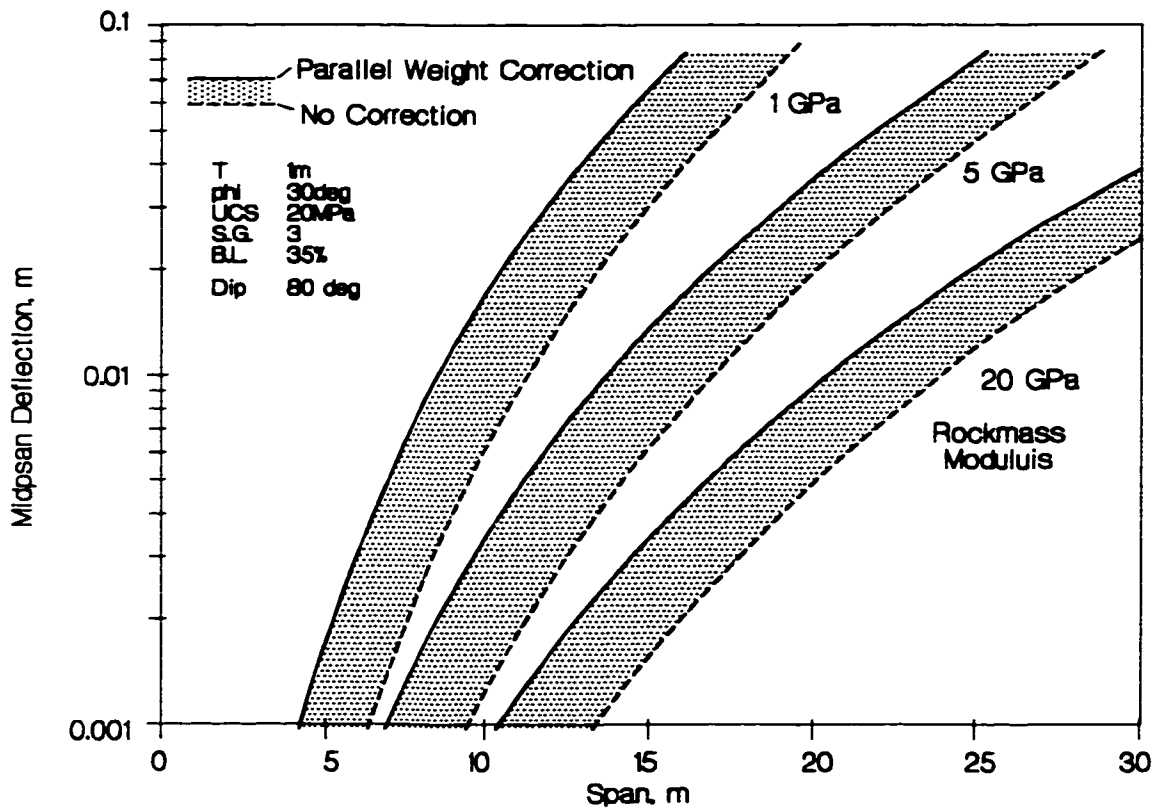


Figure 3.30: Corrected equilibrium midspan deflections for stable steeply dipping beams (dip=80 degrees), accounting for parallel weight component.

This limit is used to present stability charts for design. These design charts have been normalized with respect to effective specific gravity which is a function of rock density, excavation dip angle and surcharge loading or support pressure. Two failure modes are presented for thin laminations. These are snap-through and crushing. Other failure modes apply to thick beams and are not considered. Critical span of the beam is determined by the critical failure mode (mode which gives the lowest critical span).

More work is needed to account for the boundary-parallel component of weight in steeply dipping voussoir beams. While geometrical limits for stability are marginally affected by the neglect of this component, equilibrium displacement predictions may be significantly in error for steeply dipping beams.

This model has been sufficiently verified to serve as intended in this thesis - as a tool for investigating the influence of residual tensile strength and abutment relaxation (low confinement) on excavation stability and support requirements in Chapter 4.

CHAPTER 4

Tensile Strength, Relaxation and the Voussoir Beam

4.1 INTRODUCTION

The voussoir beam analogue was reviewed, updated and verified in the previous Chapter for laminated ground. The model is also a general analogue for the mechanisms of arching and self-support in moderately blocky rockmasses. It is applied in this chapter to investigate and quantify the impact of interlaminar tensile strength and abutment relaxation on roof and wall stability in underground openings.

Again it should be noted that the simplicity of the following analogue is not intended to explicitly represent the normally complex mechanisms of relaxation nor is it intended as a rigorous treatment of deflection dependent (frictional and tensile) interaction between laminations. Rather, it is a tool to obtain an understanding of the impact of tensile strength and relaxation and to modify empirical recommendations accordingly.

4.1.1 Review of the Voussoir Solution

As discussed in Chapter 3, the voussoir beam forms in laminated or blocky ground when the resistance to tensile stress parallel to the laminations is reduced to zero by through-going fractures perpendicular to the beam. The symmetrical distribution of compression and tension through a cross-section of the elastic beam of thickness, T , is replaced by a compressive arch which varies in thickness but is typically between 0.5 and 0.75 times the beam thickness for a highly stable beam.

Failure of slender beams is by snap-through or by crushing at the upper side of the beam at midspan where the compressive stress is the highest. Thicker beams can also fail through slip along the lamination normal joint set.

The problem is statically indeterminate but can be solved in an approximate fashion as described in Chapter 3. A quick review is given here before introducing terms accounting for boundary normal tensile strength and abutment relaxation.

The moment generated at the abutment by the self weight of the half-span must be balanced with the opposing moment generated by the offset reaction force, F , at the midspan. Two key independent unknowns are the thickness of the compressive arch, NT , and the moment arm between the reaction resultants at the abutment and at midspan, Z .

The reaction stresses at the abutment and at the midspan section are assumed to be triangular such that the reaction force, F , acts at the one-third point of the distribution. The reaction distributions at the midspan and at the abutments are assumed to be identical such that the initial moment arm is given by:

$$Z_0 = T \left(1 - \frac{2}{3} N \right) \quad [4.1]$$

Elastic shortening of the internal arch ΔL , due to compression leads to a downward deflection at midspan and a new, reduced moment arm Z :

$$Z = \sqrt{\frac{3S}{8} \left(\frac{8}{3S} Z_0^2 - \Delta L \right)} \quad [4.2]$$

The deflection, D , at midspan is given by $(Z-Z_0)$ and a negative value for the term under the square root sign in Equation 4.2 indicates that the critical beam deflection for the assumed thickness, NT , has been exceeded.

The shortening of the arch, ΔL in Equation 4.3, is calculated for iterative substitution by assuming a parabolic distribution of stress along the length of the (parabolically shaped) reaction arch:

$$\Delta L = \frac{f_{\max}}{E} \left(\frac{2}{9} + \frac{N}{3} \right) \left(S + \frac{8}{3S} Z_0^2 \right) (1 - \xi) \quad [4.3]$$

where ξ is zero for a tunnel (2D span) and equal to Poisson's Ratio, ν , for a square span. The peak compressive stress at the half-span for a horizontal beam is given by:

$$f_{\max} = \frac{\gamma S^2}{4NZ} \quad [4.4]$$

for a tunnel and:

$$f_{\max} = \frac{\gamma S^2}{6N(Z_0 + Z)} \quad [4.5]$$

for a square span.

An iterative solution as described in Chapter 3 is used to find the parametric pair $(N, Z(N))$ which minimizes f_{\max} , giving the equilibrium solution for the stable beam. The limit of stability is determined when no solution is possible for Equation 4.2 for any possible value of N and the beam fails by "snap-through". For the two dimensional case this point corresponds to a deflection at the midspan equivalent to approximately 25% of the thickness.

Chapter 3 introduced a more conservative stability threshold based on the onset of snap-through instability (deviation from a linear deflection-thickness relationship). This limit corresponds to a deflection of 10% of the thickness and is defined by the parametric set which yields a minimum of 35% invalid values of N in the range 0 to 1. This lower bound stability threshold (i.e. for critical span) also corresponds to a critical displacement of 10% of the beam thickness. In this work, the 10% displacement threshold is termed "yield" while the ultimate critical dimensions and the 25% displacement limit define certain "collapse".

The peak stress in the beam, f_{\max} , is also compared with the unconfined compressive strength, UCS to determine crushing potential. In addition the frictional stability of the abutments and midspan joint are assessed.

In order to provide baselines for the investigations in this chapter, summary design charts for a rock with a unit weight of 30kN/m^3 , based on the first two failure modes for horizontal beams and square slabs are given in Figure 4.1. The slightly elevated value for unit weight accommodates the potential for sulphide inclusion in the rockmass for mining applications.

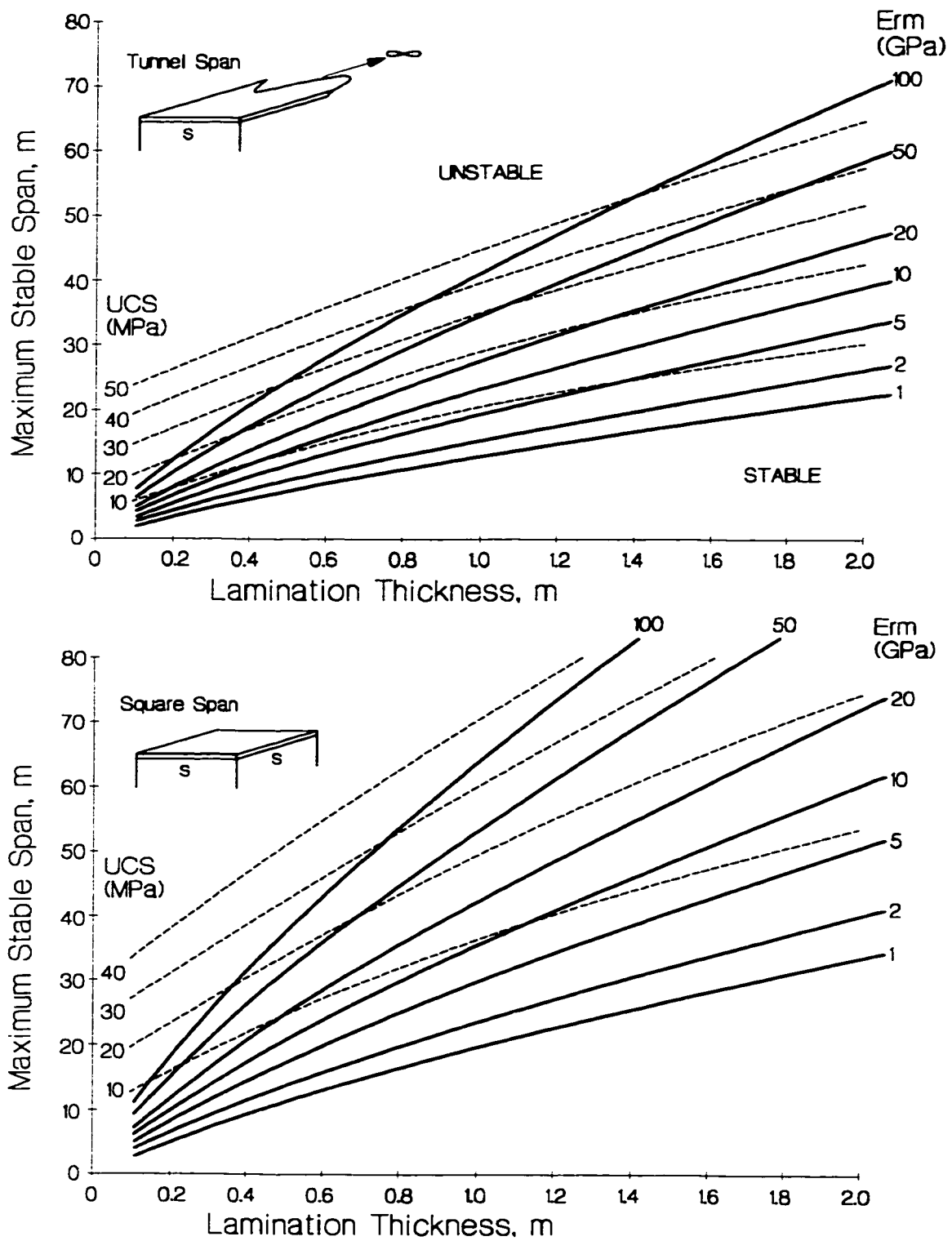


Figure 4.1: Voussoir design charts for horizontal tunnel and square span ($\gamma=30\text{kN/m}^3$); Maximum stable span for a given thickness is the minimum value determined from E_{rm} or UCS limit.

4.1.2 Incorporation of Relaxation and Interlaminar Bridging

Prior to calculating the shortening of the arch due to deflection and compression, it is possible to introduce an symmetrical displacement δ_A , acting in opposite directions at each abutment. This displacement yields a reduced initial moment arm, Z_0^* :

$$Z_0^* = \sqrt{\frac{3S}{8} \left(\frac{8}{3S} Z_0^2 - 2\delta_A \right)} \quad [4.6]$$

for substitution into Equation 4.2.

For support pressure p distributed evenly over the length of the beam, a solution can be obtained by substituting an equivalent unit weight, γ^* :

$$\gamma^* = \gamma - \frac{p}{T} \quad [4.7]$$

into Equation 4.4 or 4.5. If $\gamma^* \leq 0$, then the beam is fully supported and no voussoir deflection can occur. For triangular distributions of support pressure varying from 0 at the abutment to p at the midspan, use $p^* = \frac{2}{3} p$ in Equation 4.7. Equation 4.7 also provides a simplified means of including the effect of residual interlaminar tensile strength (due to rock bridges).

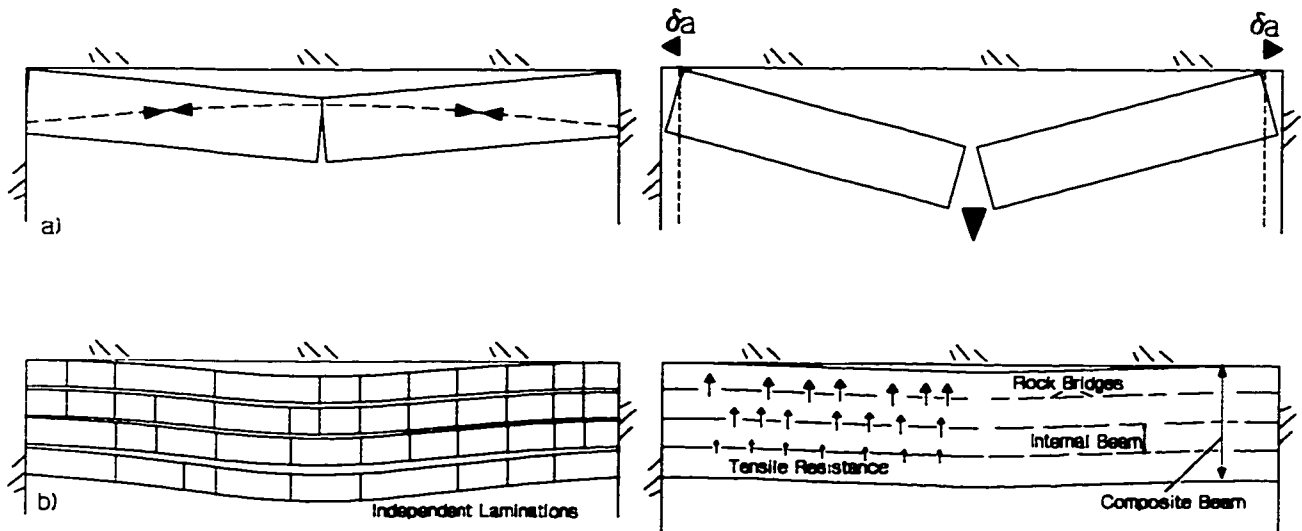


Figure 4.2: Definition of a) abutment relaxation and b) interbed tensile strength due to interlaminar rock bridges.

4.2 BOUNDARY NORMAL TENSILE STRENGTH

From Figure 4.1 it is immediately apparent that thicker laminations are more stable than thinner laminations. This is because the compression arch is able to rise higher within a thicker beam increasing the resisting moment and reducing the necessary deflections required to reach equilibrium. The theoretical solution applies to completely independent surface beams fully separated from the rockmass above. A condition for the transmission of compressive stresses within the arch is that there is continuity through the nominal beam thickness.

Within a fully separated and independent beam there may, however, be partially separated laminations (internal beams) with small and sparse rock bridges (Figure 4.2b). A proportion of the weight of the lowermost internal beam can be transferred to the next internal beam above through tensile stress in the rock bridges. This is analogous to a "tensile" support pressure acting from above the beam. If the distributed capacity of the rock bridges is equal to the self weight of the underlying internal rock beam it can be considered fully supported and fully connected to the beam above forming a composite independent beam of twice the thickness.

This is, of course, a major simplification of the internal mechanisms within the beam structure. It does not consider the important (and complimentary) effects of interlaminar shear strength. Nevertheless, this analogue can be used to generate a valid ground reaction curve as shown in Figure 4.3. In this figure, the array of linear curves represent the elastic response for varying lamination thicknesses as indicated on the left-hand axis. The required support pressure or boundary normal resisting stress is indicated on the right-hand axis.

Figure 4.3 illustrates the minimum support requirements or alternatively the minimum internal boundary normal tensile strength required to limit the beam deflections and to achieve stability. The minimum lamination thickness is assumed, in this example, to be 0.1m and the composite curve represents the results of stacking or of partial delamination (rock bridges). In this case both the support pressure and the tensile resistance are assumed to be constantly distributed across the span. For tensile strength this is likely to be a valid assumption due to the small strain nature of rock bridge rupture. This Figure could also be generated using a parabolic or triangular distribution due to greater interbed separation likely towards the midspan of the beam. This simplification will suffice for illustrative purposes.

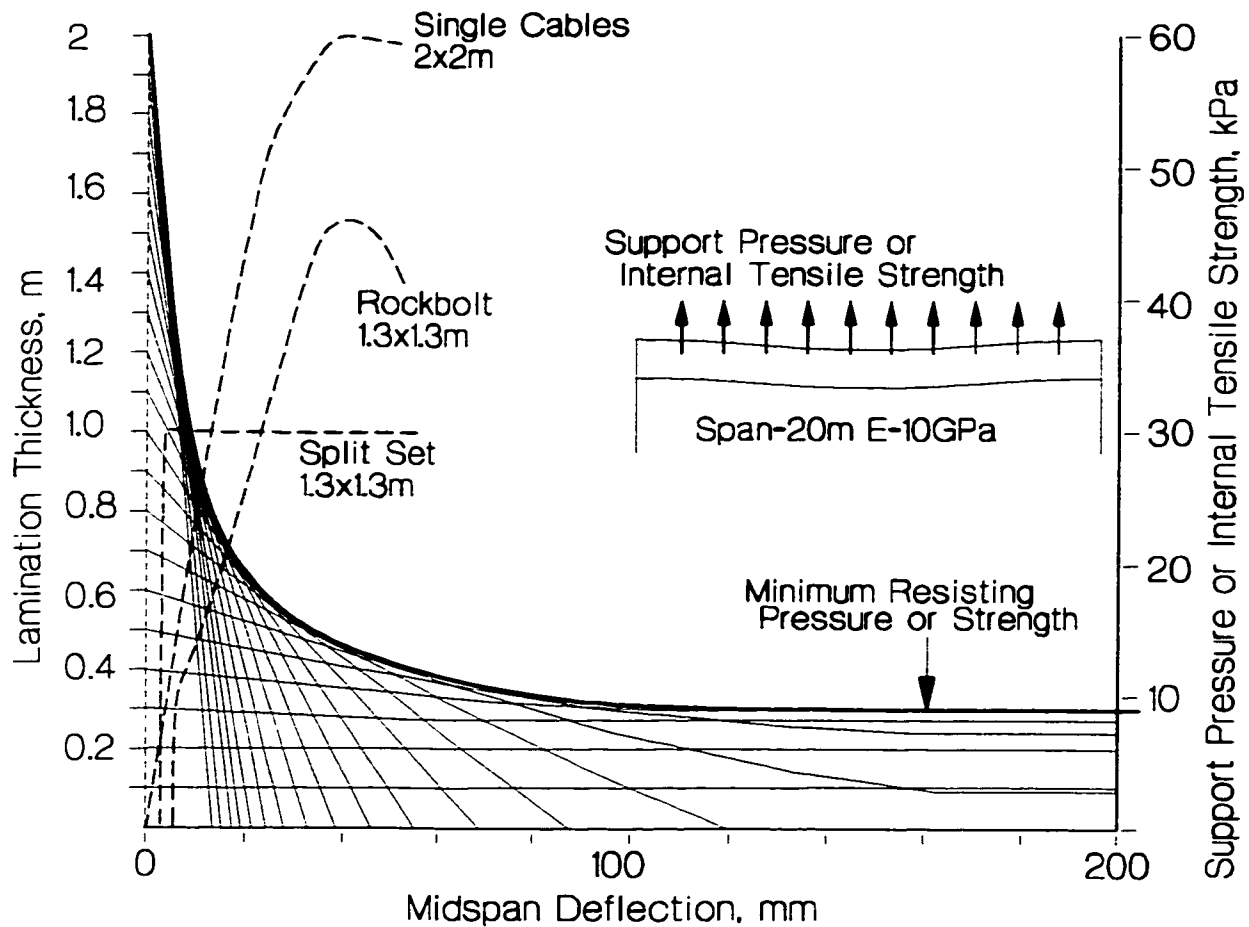


Figure 4.3: Composite ground reaction curve for laminated rockmass based on voussoir calculations: (Span=20m; E=10GPa; $\gamma=30\text{kN/m}^3$; UCS = 25MPa); Response curves for typical support patterns are shown for comparison; Internal tensile strength refers to boundary normal strength.

For this configuration, an independent beam with a thickness of less than 0.75m will not be able to develop enough moment resistance to be self-supporting and will fail (snap-through). Laminations above this thickness will stabilize at a deflection which decreases with increasing thickness, as shown (reaction lines intersecting horizontal axis). Thinner laminations must transfer their weight to laminations above, through internal boundary normal tensile resistance, creating a thicker and more stable composite beam.

Halting the deflection of composite beams at lower displacement limits requires progressively thicker composite beams and therefore increased tensile strength (or internal support pressure). This relationship produces the composite and familiar ground reaction curve for a laminated

rockmass shown as the dark upper curve, tangent to the linear responses of progressively thickening (stacking) beams.

This limit represents the minimum support pressure or internal tensile strength required to create a stable voussoir beam at this span. It is independent of the thicknesses of the internal stacking laminations (assumed here to be very small for support demand assessment purposes). The response curves for typical support patterns are shown for comparison.

The capacity requirements (support or tensile demand) increases with reduced rockmass modulus as shown in Figure 4.4. These demand values are very low for the span in question, falling in the range of residual tensile strength presented in Chapter 2 for small rock bridges.

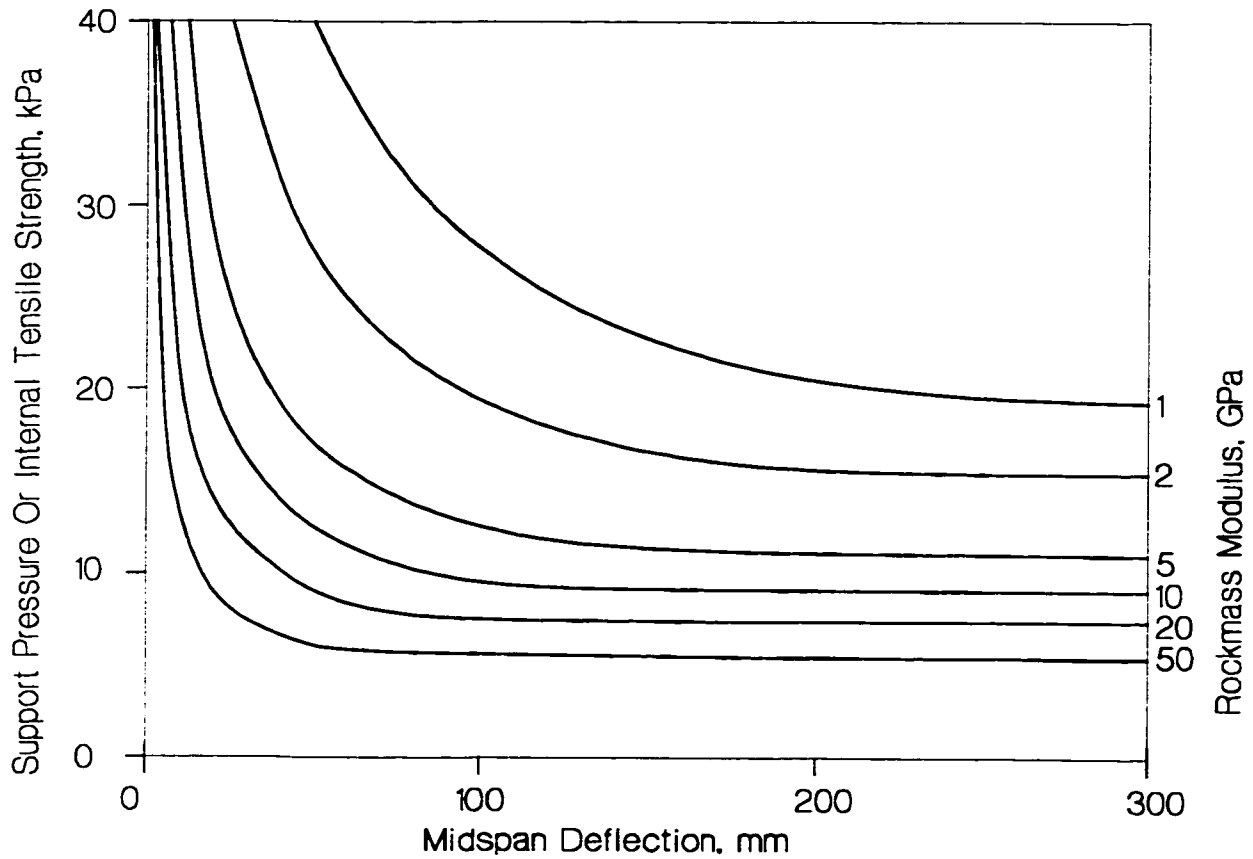


Figure 4.4 Ground reaction curve: Relationship between rockmass modulus and tensile support demand (Span = 20m; Buckling Limit, B.L. =100%).

Recalling the values in Table 2.1, it can be seen that for the 20m span illustrated, a sparse 2mx2m array of split-sets (frictional tendon stabilizer with large deflection capacity and 100kN capacity) is capable of providing enough reinforcement to stabilize a laminated rockmass of 1MPa stiffness (a soft shale, for example). The deflections (> 200mm) may be too severe, however, for certain applications. A moderately dense array of rockbolts or rebar (100kN at 1.5mx1.5m spacing) would stabilize a 5GPa rockmass (competent shale or schist) at very low displacements (<20mm).

Alternatively, interlamine rock bridges comprising approximately 0.1% or 0.25% of the lamination surface would provide, respectively, internal tensile support pressure equivalent to the sparse and moderately dense bolt arrays. For higher rockmass stiffnesses, typical of hard sandstones, limestones or jointed igneous rockmasses, the support or internal tensile strength requirements are even less.

The effectiveness of interbed tensile strength, however, is limited to small strains and therefore to small beam deflections. As deflections increase, interbed shear becomes dominant (not considered here). This shear stress may rupture rock bridges directly or will induce oblique tensile increments which will in turn create bridge failure. For a given midspan deflection, the effect of interbed shear is less for thinner component laminations as the internal shear strain within the composite beam is distributed over a greater number of interbed surfaces.

The limiting tensile strength (required for stability) as a function of span is summarized in Figure 4.5. In this figure, the upper and lower bounds for tensile strength are defined by initial yield (Buckling Limit=35%, deflection=10% of thickness) and absolute collapse (Buckling Limit=100%). The thinner lines below the composite collapse threshold represent the collapse limits for incremental beam thicknesses. Figure 4.6 illustrates the impact of modulus on the composite collapse limit.

It is important to note the extremely small values of tensile strength required for stability of large spans. This is not surprising in light of the large number of large spans found in natural caverns, overhangs and arches. The strength required to resist gravity loading of rock blocks and wedges is commonly found even in jointed rock due to the lack of complete persistence and the presence of rock bridges (Chapter 2). If the self supporting and arching ability of moderate quality rockmasses is considered, as in the voussoir analogue, the tensile strength requirements for stability are further reduced.

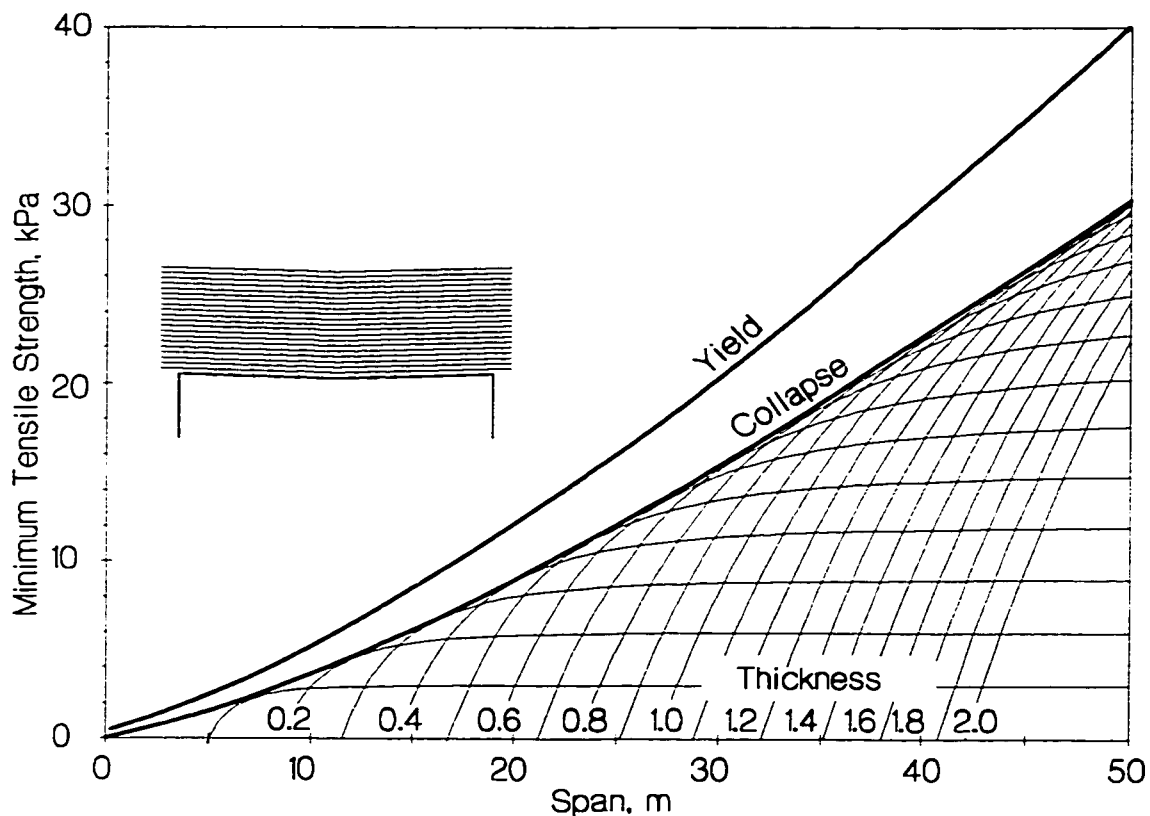


Figure 4.5 Limiting demand for boundary normal tensile strength in laminated ground (Modulus = 10GPa; Collapse *B.L.* = 100%; Yield *B.L.* = 35%).

Support is still required, however, in many applications in moderately jointed rock, particularly those with longer stand-up time requirements. In mining it is commonly and correctly held as imprudent to leave fractured ground unsupported (if human traffic is a concern) in spite of the fact that residual tensile strength may create a self-supporting opening over the short-term.

The dynamic nature of mining combined with the effects of moisture on long-term tensile strength can lead to delayed failure of unsupported ground. The presence of rock bridges, however, provides significant capacity reserve at small deformations, before tensile strength degradation is allowed, thus reducing first pass or short-term support requirements in some cases. Very stiff support such as grouted rebar can serve to reduce this degradation, leading to economic benefits through the use of shorter tendon support elements designed to preserve tensile strength and allowing voussoir-like arching, carrying load to the abutments. For modern development methods, process cycle time (drilling, blasting, primary support, mucking, secondary support, etc) at the heading is critical. The ability to confidently rely on short-term internal support through incomplete fracturing (careful excavation) can have significant benefits by reducing primary support requirements.

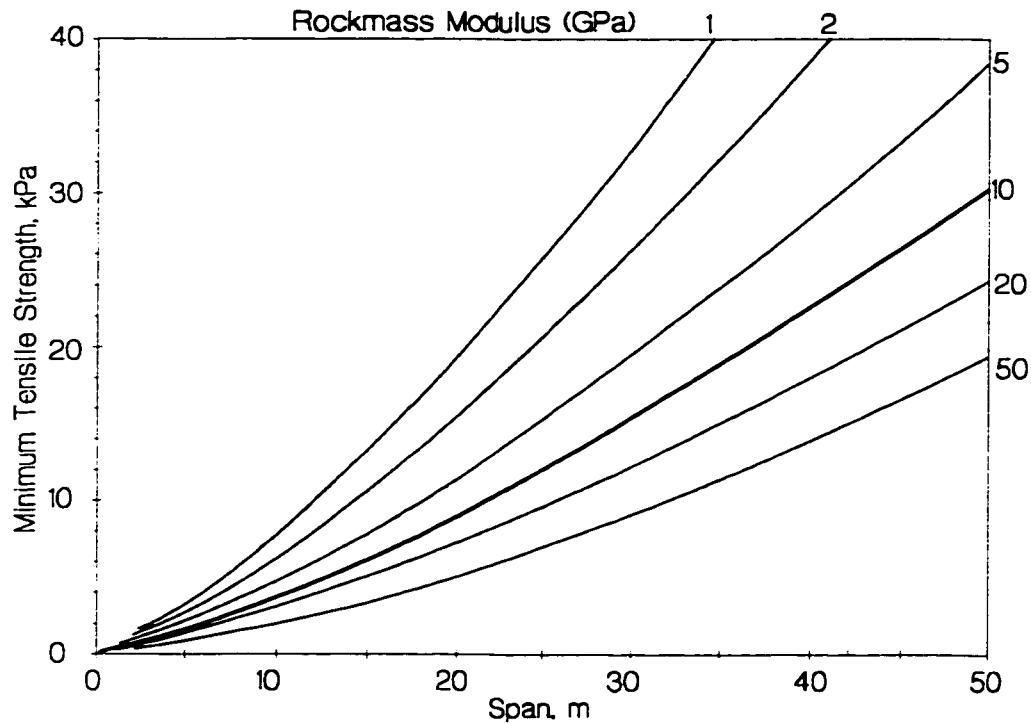


Figure 4.6 Effect of modulus on minimum tensile strength demand ($B.L.=100\%$).

4.3 ABUTMENT RELAXATION AND THE VOUSSOIR BEAM

Another dominant factor in the reduction of stand-up time for unsupported (and inadequately supported) excavations is relaxation, parallel to the excavation face, which is influentially, if not mechanistically, equivalent to an outward displacement of the abutments. Figure 4.2a illustrated the physical implementation of relaxation for the voussoir beam analogue. The quoted displacements in the following figures apply to a single abutment. An equal and opposite displacement is assumed at the other abutment.

4.3.1 Relaxation and Equivalent Elastic Tensile Stress

Before beam deflection occurs in this schematic and in the classic voussoir analogue, the beam is assumed to be stress free, corresponding to a zero local insitu stress. The relaxation displacement shown is based on this datum and does not include additional displacement incurred as initial compressive insitu stress and strain reduce to zero. In other words, the displacement pictured here is equivalent to the presence of tangential tension in the back of an excavation in an elastic continuum such as that simulated in Figure 4.7.

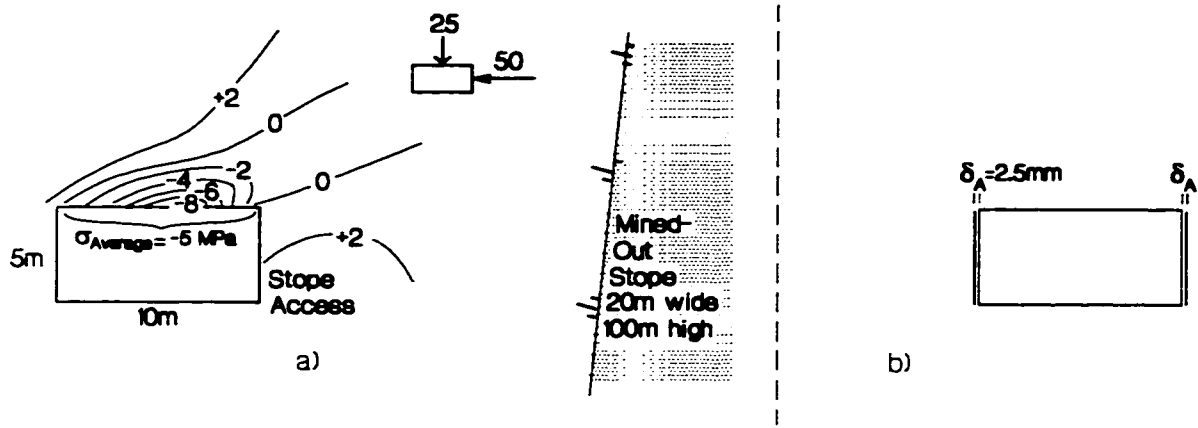


Figure 4.7: a) Calculated tension across a drift back, and b) equivalent abutment relaxation.

In Figure 4.7, the average tension adjacent and parallel to the back of the 10m wide access drift was approximately 5MPa. Using an assumed rockmass modulus of 10GPa, for example, the equivalent symmetrical abutment displacement, δ_A , is 2.5mm. Calculated peak magnitudes of tensile stresses parallel to hangingwalls (and footwalls) in the horizontally dominant stress fields of the Canadian Shield can easily exceed (-)20MPa as shown by Maloney et al. (1992). Taking an average tangential tension of (-)10MPa across a 50m hangingwall yields an equivalent δ_A , at both the topsill and the bottomsill, of approximately 25mm (Figure 4.8).

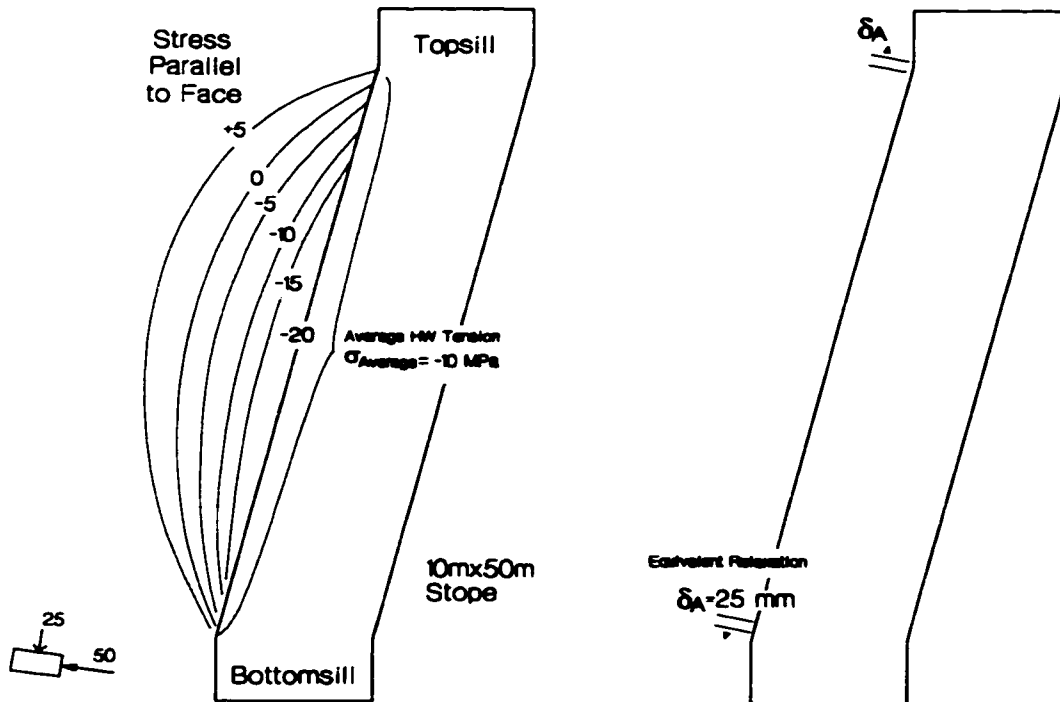


Figure 4.8: Calculated tension across a hangingwall and equivalent abutment relaxation, δ .

These examples represent only a first approximation and will likely underestimate the true analogous relaxation displacement since stress shedding is not taken into account in the elastic model. In addition, the calculated tension may not actually exist, but rather is reflected in the opening of boundary normal joints. Admittedly it is very difficult to accurately estimate δ_A for many situations. This should not, however, be a deterrent to the consideration of relaxation in design. Three dimensional elastic modelling is now routine in Canadian mining operations. This simplified treatment of relaxation permits such consideration.

In order to compare the absolute relaxation displacements in these figures to modeled strains and equivalent tensile stresses in elastic stress analysis models, Figure 4.9 provides a conversion chart. Remember that the displacements indicated are “measured” from the state of zero stress and do not include recovery of the initial compressive strain present insitu.

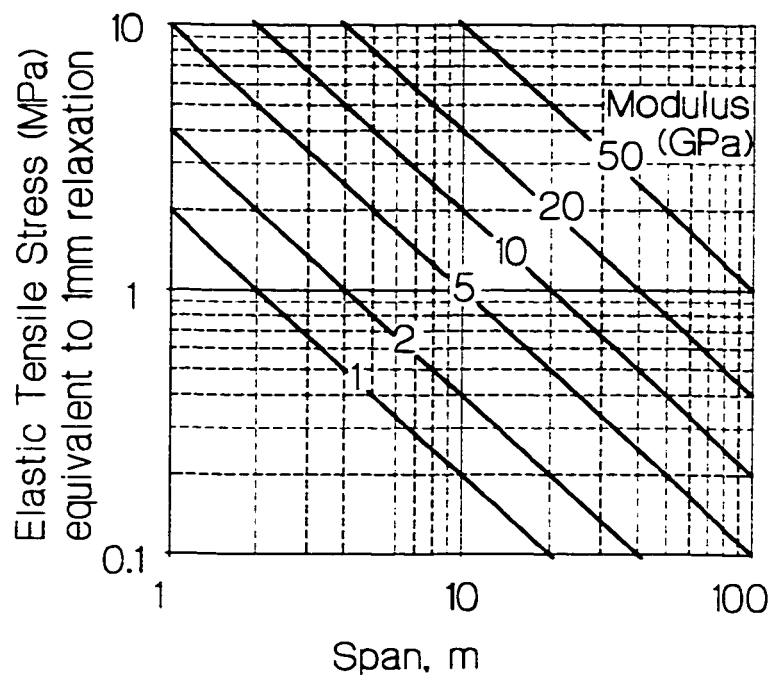


Figure 4.9: Equivalent elastic tension corresponding to abutment displacement.

4.3.2 Relaxation and Beam Response

The impact of abutment deformation or relaxation is to increase the beam deflection required to generate sufficient compressive stress and resisting moment for equilibrium. This additional deflection brings the beam closer to failure. This effect is illustrated in the ground reaction diagram in Figure 4.10. The individual curves are generated in a similar fashion to the composite curve in

Figure 4.3, assuming that thin laminations would stack and create a composite beam with a thickness determined by the available tensile strength (rock bridges) or artificial support. For comparison, an abutment relaxation of 10mm over a half-span of 10m is equivalent to a tensile strain (parallel to the excavation face) of 0.1% or 10MPa of analogous tensile stress using a modulus of 10GPa. This is realistic for deep mining excavations.

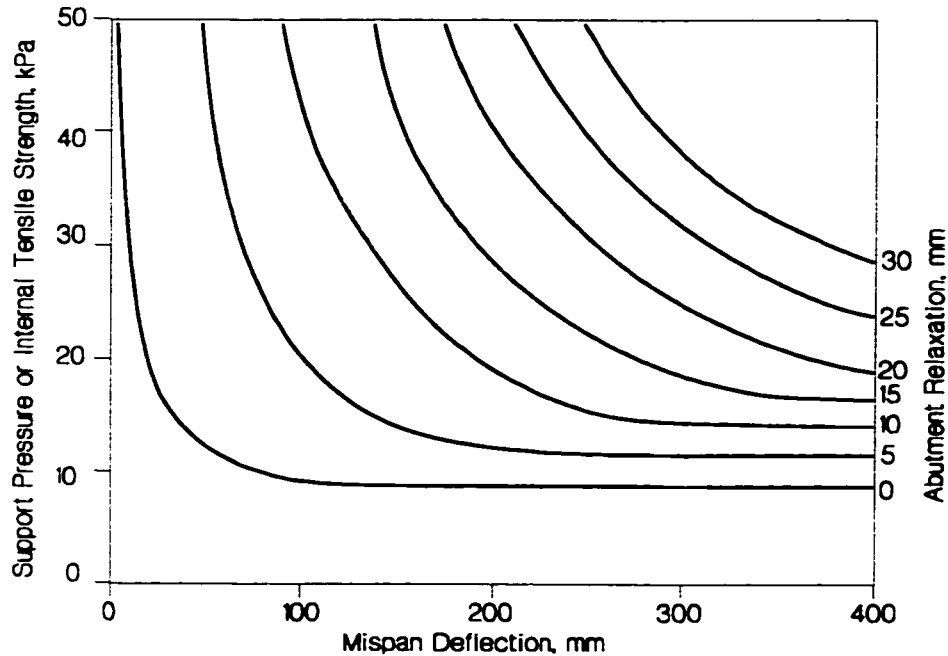


Figure 4.10: Ground reaction curves for laminated ground illustrating the impact of abutment relaxation (Modulus=10GPa, *B.L.* =100%, Span=20m).

Effective abutment relaxation can occur as a result of changing geometry around an excavation, by unfavourable stress ratios or by increased deflections due to the creation of intersections or undercuts. (e.g. Kaiser and Maloney 1992).

Figures 4.11 and 4.12 show the corresponding increase in support or tensile strength demand due to abutment relaxation. The term "yield" in these figures corresponds to midspan deflections equivalent to 10% and a Buckling Limit, *B.L.*, of 35% as discussed earlier. The term collapse (*B.L.* = 100%) describes the least conservative solution.

These figures show that very little tensile strength (normal to laminations) can compensate for abutment deformation, but that the maximum span to ensure the marginal stability of unsupported openings (stopes) decreases significantly in the presence of relaxation if additional strength or support is not available.

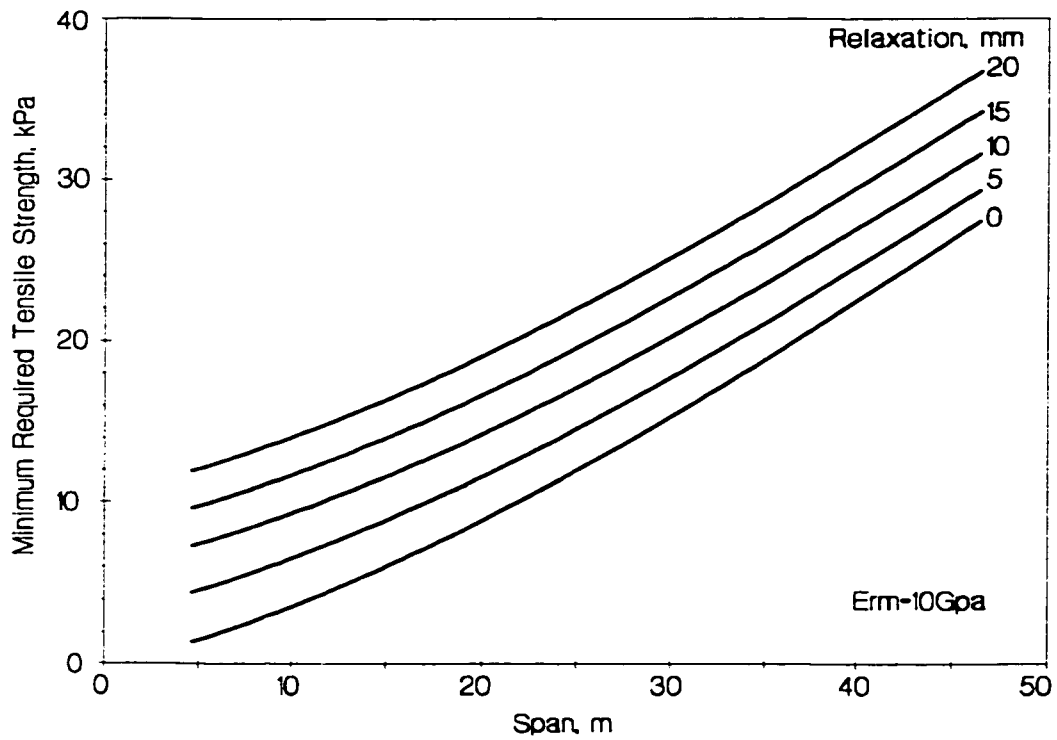


Figure 4.11: Impact of abutment relaxation on the minimum demand for boundary normal tensile strength (B.L. =100%).

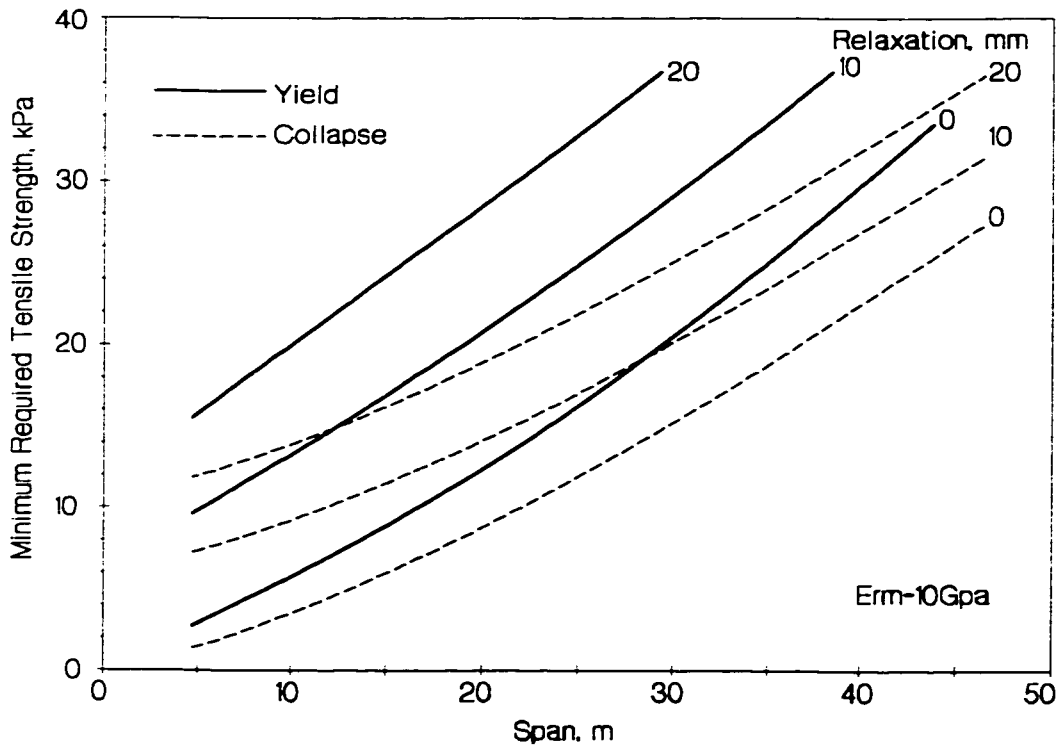


Figure 4.12: Same simulation as in Figure 4.11 showing limits for yield (B.L. =35%) and collapse (B.L. =100%).

4.3.3 Critical Span Reduction by Relaxation

For unsupported beams, there exists a critical relaxation at which failure (snap-through) occurs. For a rockmass with a modulus of 10GPa, Figure 4.13 shows the critical relaxation (as a function of span and thickness) for yield and collapse of a horizontally laminated roof (without rock bridges). Critical relaxation varies, of course, with rockmass modulus as illustrated in Figure 4.14. Remember that the displacements indicated are “measured” from the state of zero stress and do not include recovery of the initial compressive strain present insitu.

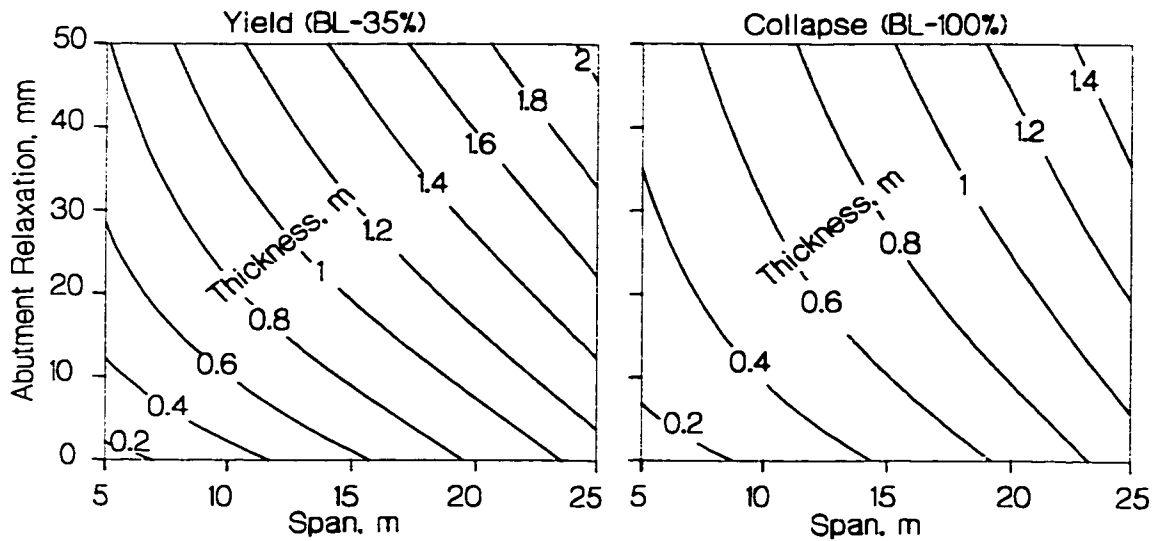


Figure 4.13 Critical relaxation limits for unsupported voussoir beam: $E_{rm}=10\text{GPa}$.

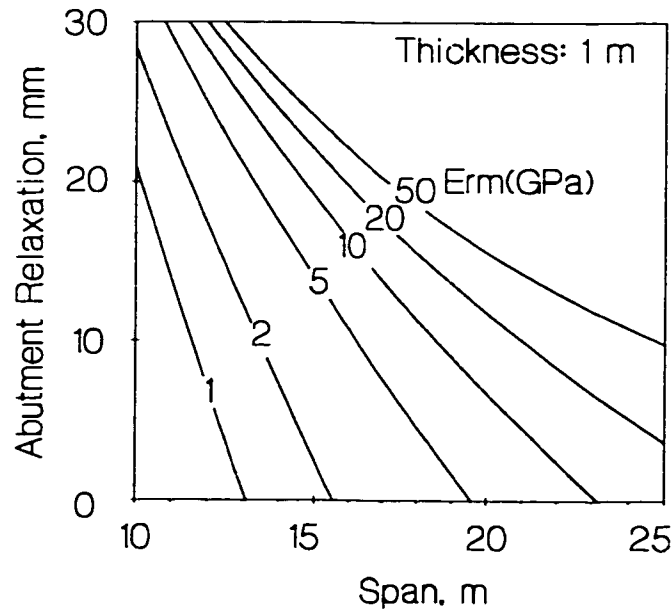


Figure 4.14: Effect of modulus on critical relaxation or critical span.

4.4 RELAXATION AND EMPIRICAL DESIGN

Major components of the modern underground engineer's toolbox include rockmass classification and empirical design. Rockmass classification methods began with early work by Terzaghi (1946), Lauffer (1958), Deere 1968, Wickam et al. (1972), Laubscher (1977) and many others. The two most common empirical methods for tunnelling are *RQD* (Deere 1968), the *RMR* system (Bieniawski 1989) and the *Q* system (Barton et al. 1974, 1992). The Modified Stability Number *N'* (Potvin 1988) and the accompanying design system is used routinely in Canadian Mining.

These techniques all involve the quantitative and qualitative assessment of key rockmass properties and characteristics (Figure 4.15), the assignment of an index value to each and an arithmetic relationship resulting in a rockmass quality value within a numerical range representative of the best to the worst rockmass quality. This rockmass classification result is representative of engineering quality (Figure 4.16). Rockmass classification values can be subsequently used in calibrated (empirical) design charts to establish critical spans for excavations, stand-up times for unsupported openings, support requirements (e.g. Figure 4.17).

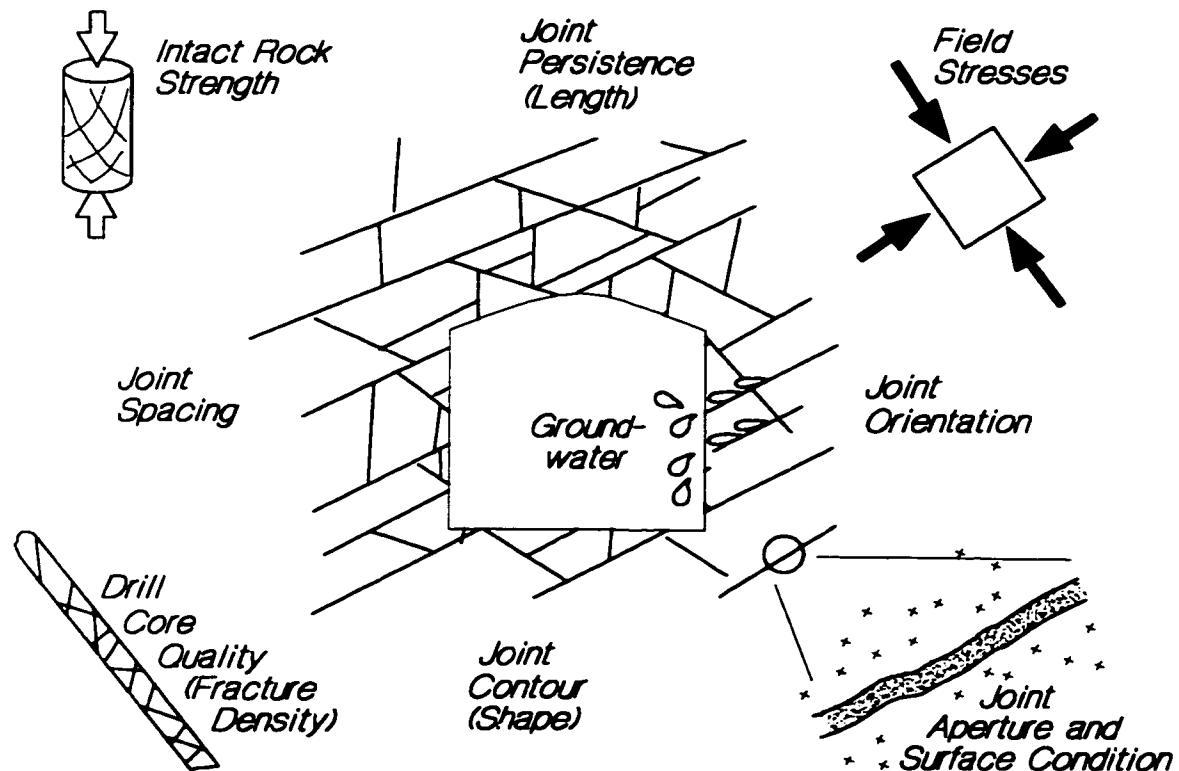


Figure 4.15: Elements of rockmass classification - properties controlling rockmass behaviour.

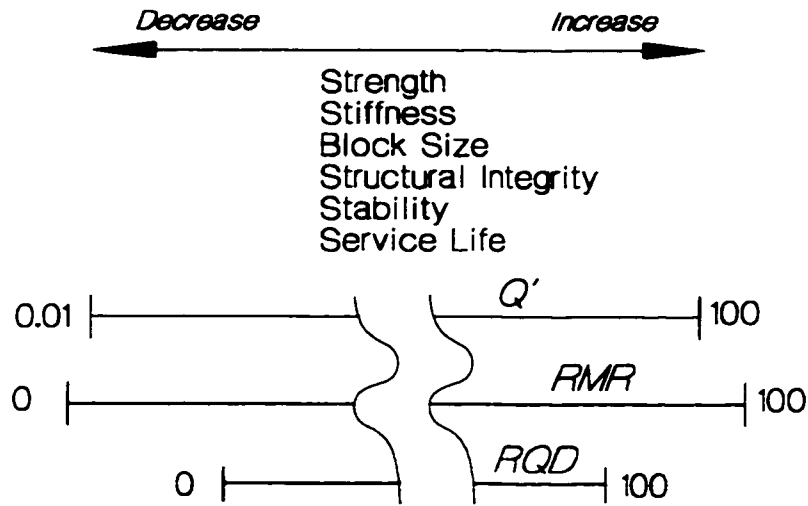


Figure 4.16: Relationship between engineering behaviour and rockmass classification.

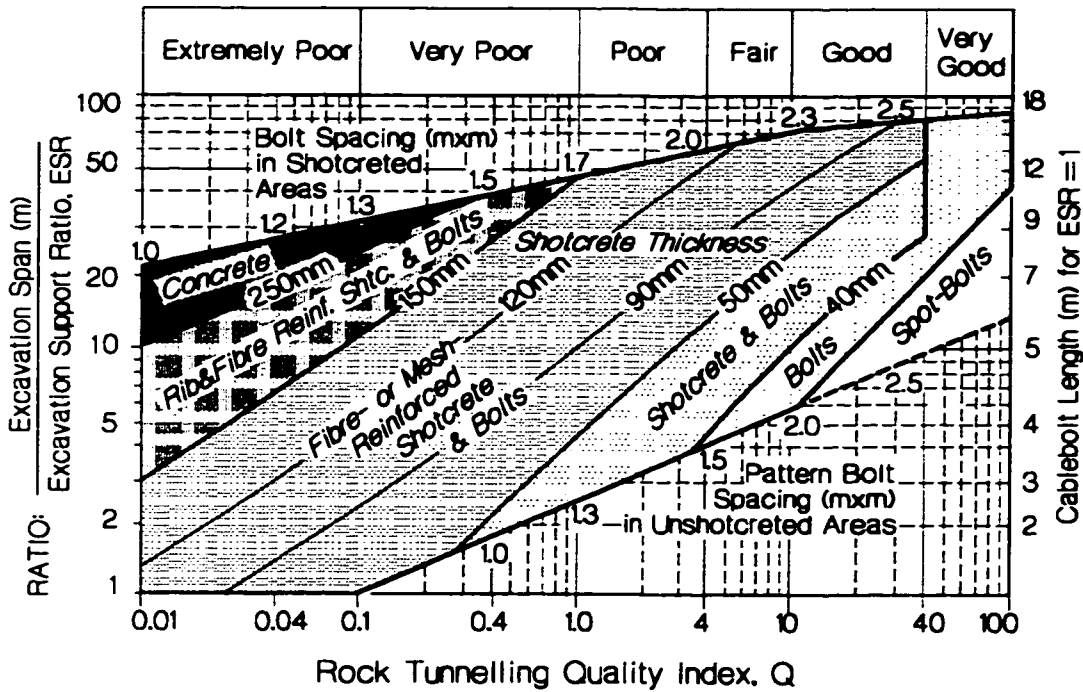


Figure 4.17: Support recommendations for underground tunnels based on the Q system (modified after Grimstad et al. 1993 and Hutchinson and Diederichs 1996).

To explore the effect of relaxation on empirical slope design methods, it is desirable to apply the voussoir analogue for relaxation to more general excavation design. This can be achieved by calibrating voussoir analysis to an existing empirical design limit such as the Modified Stability Graph Method (Potvin 1988). This method is based, in part on a more widely used empirical system known as the Q -System, developed for tunnel design.

4.4.1 Elements of rockmass classification - the Q System

The Q system was first developed and applied to engineering problems by Barton et al. (1974). The quality terms associated with each range interval are illustrated in Figure 4.17 (top and bottom axes). The Q value itself is calculated as:

$$Q = \frac{RQD}{J_n} \times \frac{J_r}{J_a} \times \frac{J_w}{SRF} \quad [4.8]$$

- RQD* = Rock Quality Designation - rock core index (Deere 1968)
- J_n* = Joint Set Number (number of unique joint sets)
- J_r* = Joint Roughness Number (based on large and small scale roughness)
- J_a* = Joint Alteration Number (joint surface condition)
- J_w* = Joint Water Reduction Number (effect of water and water pressure)
- SRF* = Stress Reduction Factor (accounts for high stress and low confinement)

Detailed descriptions and descriptive scales are given for each of these parameters in Barton et al (1974) and also in Hoek and Brown (1980). The following represents a brief summary provided by Hutchinson and Diederichs (1996) for hard rock environments.

Table 4.1: *RQD* and *J_n* for the Q System

<i>RQD</i>	= $\frac{\text{Sum of lengths of core sticks greater than 10cm long}}{\text{Total length of core run}} \times 100$
<i>J_n</i>	Number of joint sets (families or statistically similar joints)
0.5 - 1	<i>Intact rock (no joints) - Few random joints only</i>
2 - 3 - 4	<i>1 joint set - 1 set + random - 2 joint sets</i>
4 - 6 - 9	<i>2 joint sets - 2 sets + random - 3 joint sets</i>
9 - 12 - 15	<i>3 joint sets - 3 sets + random - 4 joint sets</i>
15-20	<i>greater than 4 sets - crushed rock</i>

Table 4.2: *J_r* values for the Q System - Roughness of the dominant or critical joint set

Large Scale	<i>Planar</i>	<i>Undulating</i>	<i>Stepped</i>	<i>Discontinuous</i>
Small Scale				
<i>Slickensided</i>	0.1	1.5	1.5	2
<i>Smooth</i>	1.0	2.0	2.5	3.0
<i>Rough</i>	1.5	3.0	3.5	4.0
<i>Gouge-Filled</i>	1.0	1.0	1.0	1.5

Table 4.3: *Ja* values for the *Q* system - condition of dominant or most critical joint set

<i>Ja</i>	<i>Joint surface description</i>
0.75 - 1	Tightly healed, clean or surface staining only
2-3	Slightly altered joint walls, sparse mineral coating
3-6	Low friction coating (chlorite, mica, talc, clay) < 1mm thick
6-10	Thin gouge, low friction coating or swelling clay 1 - 5mm thick
10-20	Thick gouge, low friction coating or swelling clay > 5mm thick

Table 4.4: *Jw* values for the *Q* system - water inflow and pressure

<i>Jw</i>	<i>Description</i>
1.0	Dry excavation (< 5 litres / min ; < 100kPa)
0.66	Medium inflow or pressure (100 - 250kPa)
0.5	Large inflow or pressure (250 - 1000kPa) with no joint infilling
0.33	Large inflow or pressure with outwash of joint infilling
0.2 - 0.1	Exceptionally large inflow or pressure (decay after excavation)
0.1 - 0.05	Exceptionally large inflow or pressure (no decay)

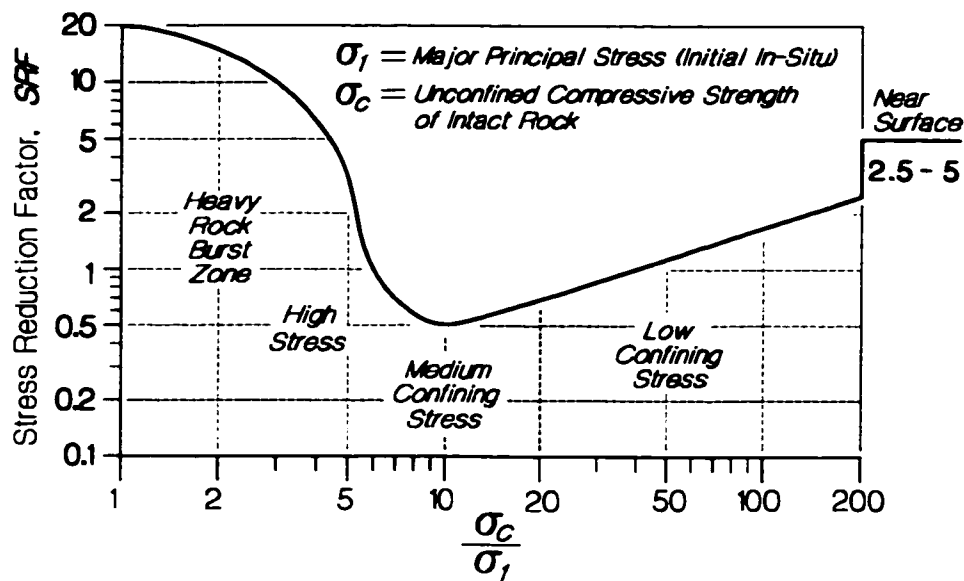


Figure 4.18: Evaluation of Stress Reduction factor, *SRF* of non-faulted and non-swelling rockmasses (Hutchinson and Diederichs 1996). Adjustments for discrete weakness zones given by Barton et al. (1974).

Using a factor called the Excavation Support Ratio (*ESR*) summarized in Table 4.5, Barton (1988) calibrated the *Q* system to allow the determination of allowable unsupported excavation span as shown in Figure 4.19. Hutchinson and Diederichs adapted *ESR* for mining excavations (Figure 4.20) while Grimstad et al. (1993) updated the system for support selection (Figure 4.17).

Table 4.5: Excavation Support Ratio (modified after Barton 1988)

Type and importance of excavation	ESR
Temporary mine openings	3-5
Permanent mine openings, low pressure water tunnels, pilot tunnels	1.6
Storage caverns, minor road/rail tunnels, surge chambers, pressure tunnels	1.3
Power stations, major road/rail tunnels, portals, intersections, public facilities	1 - 0.8

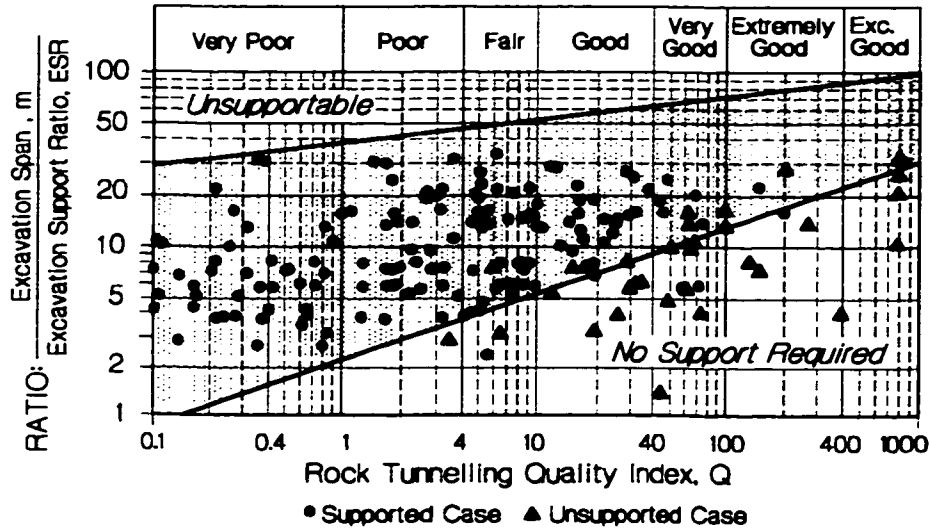


Figure 4.19: Case history database for the Q system (modified after Barton 1988).

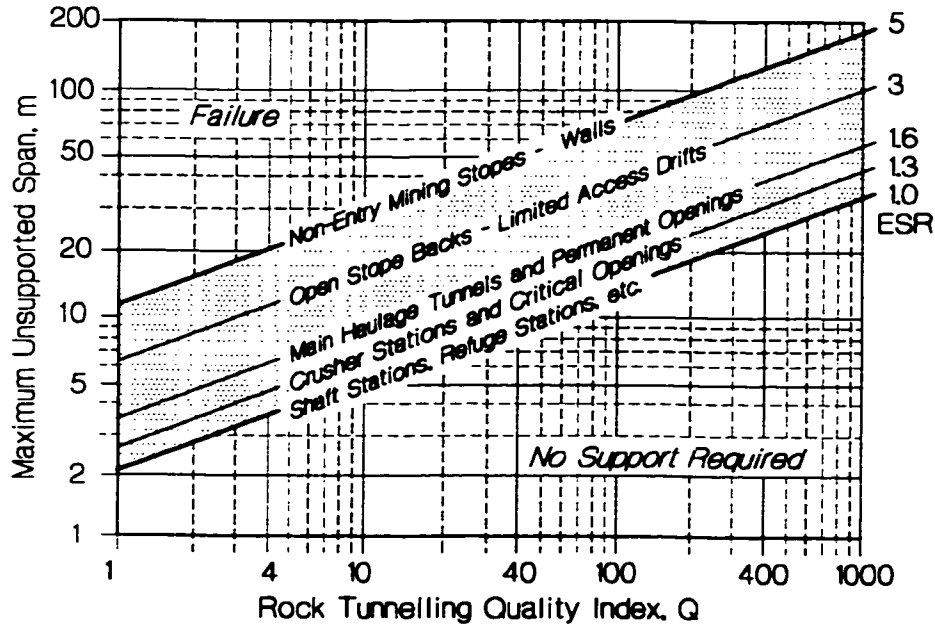


Figure 4.20: No-support limits for underground mining applications (modified after Hutchinson and Diederichs 1996).

4.4.2 The Modified Stability Graph Technique

The Stability Graph technique dates back to work by Mathews et al. (1981). Potvin (1988) and Nickson (1992) updated the methodology and together collected numerous case studies of unsupported stopes from Canadian Mines, calibrating the stability graph for hangingwall and back stability.

The characterization of the rockmass by means of a stability number N' is based initially on the Q' (prime) system. The stress reduction factor is dropped (set to 1) as is the Joint Water Factor (since deep mines are typically dry). Three new factors A , B and C are defined to account for induced stress, relative joint orientation and gravity loading respectively such that:

$$N' = \frac{RQD}{J_n} \times \frac{J_r}{J_a} \times A \times B \times C = Q \times A \times B \times C \quad [4.9]$$

where A , B and C are defined in Figure 4.21.

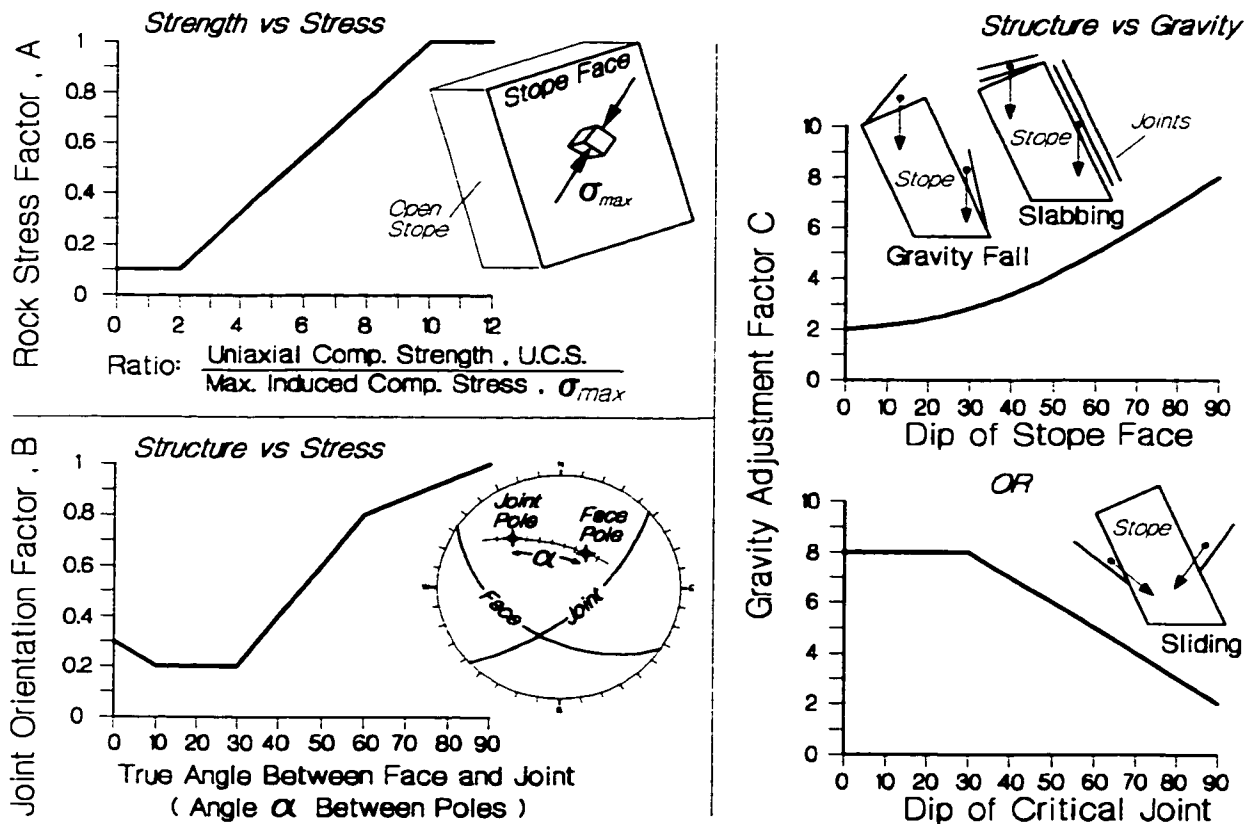
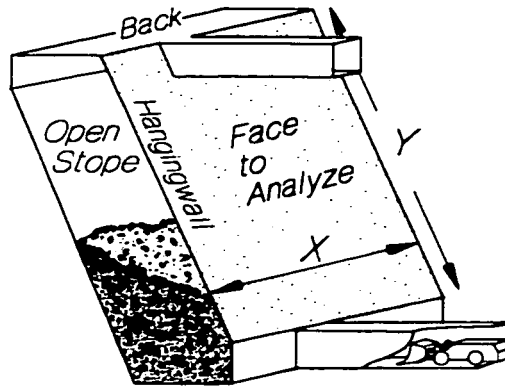


Figure 4.21: Stability parameters for the Modified Stability Graph (modified after Hutchinson and Diederichs 1996).

Excavations of different geometries are equated through the use of a shape factor or hydraulic radius, HR , which describes the geometry and size of the stope face in question (Figure 4.22). The database for unsupported stopes and the resulting no-support limits is shown in Figure 4.23.



$$HR = \frac{\text{Area}}{\text{Perimeter}} = \frac{X \times Y}{2X + 2Y}$$

Figure 4.22: Calculation of "Hydraulic Radius", HR for use in the Stability Chart.

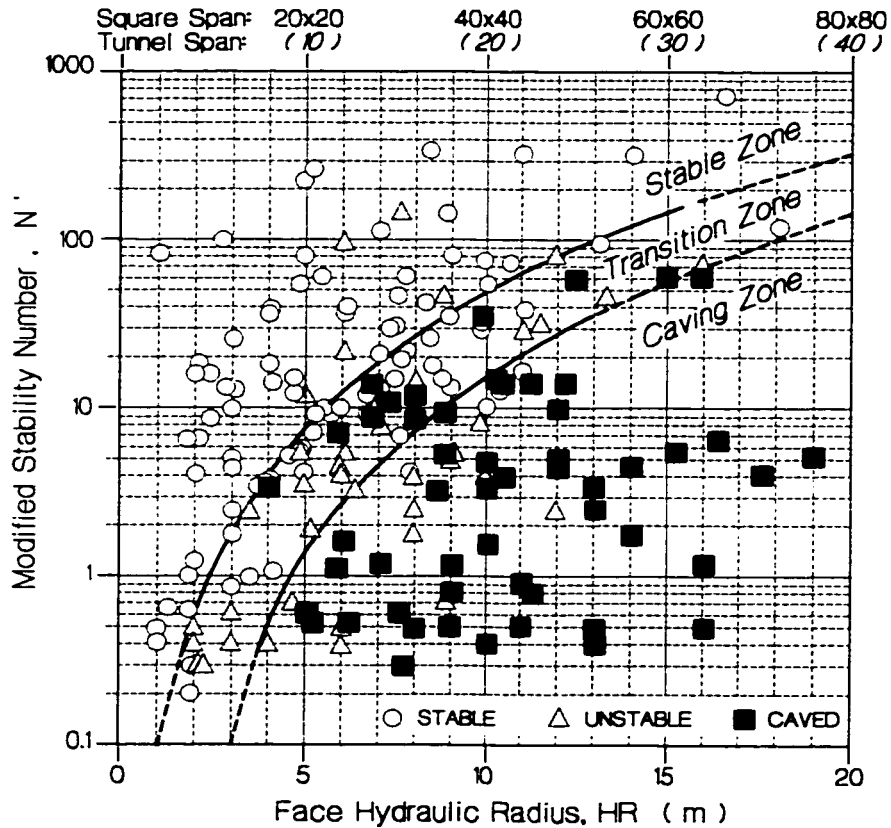


Figure 4.23: Unsupported stope data from Potvin (1988) and Nickson (1992) and No-Support Limits for Modified Stability Graph (Hutchinson and Diederichs 1996).

Using Figure 4.22 the hydraulic radius, HR , of a tunnel roof (with length much longer than the span) is given as one half of the span. For a square excavation, the hydraulic radius is equivalent to one quarter of the span. The hydraulic radius expression, therefore, defines that a horizontal tunnel is equally as stable as a square excavation surface of twice the linear span (measured orthogonal to the face edge). This assumption creates some difficulties which will be discussed.

4.4.3 Calibration of the Voussoir model to the Stability Graph

In order to link the voussoir analogue to the modified stability graph, it is necessary to relate the voussoir parameters to rockmass quality and the modified stability number N' . In the absence of comprehensive case data, an iterative procedure was used, bounded by logical upper and lower parametric limits. The values of A, B and C are taken to correspond to the voussoir assumptions such that $A=1$ (low stress), $B=0.3$ (surface parallel jointing) and $C=2$ (horizontal roof). This yields a relationship between N and Q' :

$$Q' = N/0.6 \quad [4.10]$$

Next a simplified relationship between rockmass modulus and Q' in a moderately relaxed setting (as provided in Chapter 3) and a similar (arbitrary but reasonable) relationship for unconfined compressive strength (UCS) are assumed:

$$E_{rockmass} \text{ (GPa)} = 5\sqrt{Q'} \approx 6.5\sqrt{N} \quad [4.11]$$

$$UCS \text{ (MPa)} = 20\sqrt{Q'} \approx 25.8\sqrt{N} \quad [4.12]$$

These relationships are used here, not as engineering recommendations, but rather as reasonable baseline assumptions in order to create a generalized model to assess the effects of relaxation. In addition, while intact UCS is independent of Q' , it is related to A . Equation 4.12 is included in this calibration since in hard rock masses, increased RQD and lower Q' is in general associated with weaker rock such as schists, rhyolites, talcs and meta-shales, for example. The effective UCS values resulting from this relationship represent approximately one half of the nominal lab strength (as discussed and justified in Part II of this thesis). Using these relationships, for E and UCS , in analyses of voussoir stability for different hydraulic radii and lamination thicknesses, it is possible

to derive the following relationship for N' as a function of critical lamination thickness for unsupported openings (in metres):

$$N' = 150 \times (\text{Thickness})^3 \quad [4.13]$$

While this calibration procedure is somewhat subjective and is confined in its application to the assumptions described, it yields reasonable parametric ranges for thicknesses between 0.1m to 1m. “Yield” calculations were used for the voussoir simulation (Buckling Limit =35%), corresponding to a long-term no-support limit for span. The calibration resulting in the parametric set in Figure 4.24 is based on the upper no-support limit in Potvin’s (1988) stability graph. This limit corresponds to the onset of instability or yield. Figure 4.24 is not for general application and is intended for model calibration purposes only.

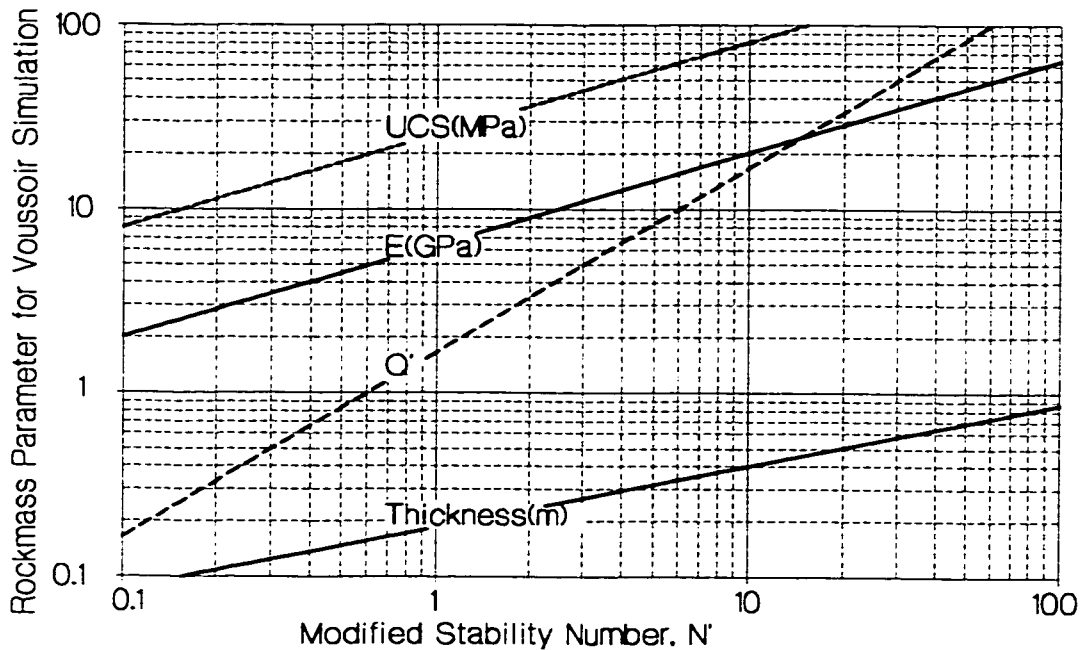


Figure 4.24: Variation with respect to N' of voussoir parameters used in this simulation (for model calibration purposes only).

The resultant calibration is shown in Figure 4.25 for both the square and the long (tunnel) span. The hydraulic radii for critical square openings are uniformly 0.77 times that of critical tunnel spans for equivalent N values. This results from a relative over-prediction of square span stability inherent in the definition of Hydraulic Radius. The definition of HR infers that a square span is as stable as a long tunnel of half (0.5 times) the linear span. Voussoir predicts that a square opening

of span, S , is as stable as a long tunnel of span $0.65S$. The hydraulic radii, therefore, of critical square spans (as predicted by voussoir simulation) are 0.77 times the HR of critical tunnel spans (for a uniform set of voussoir parameters).

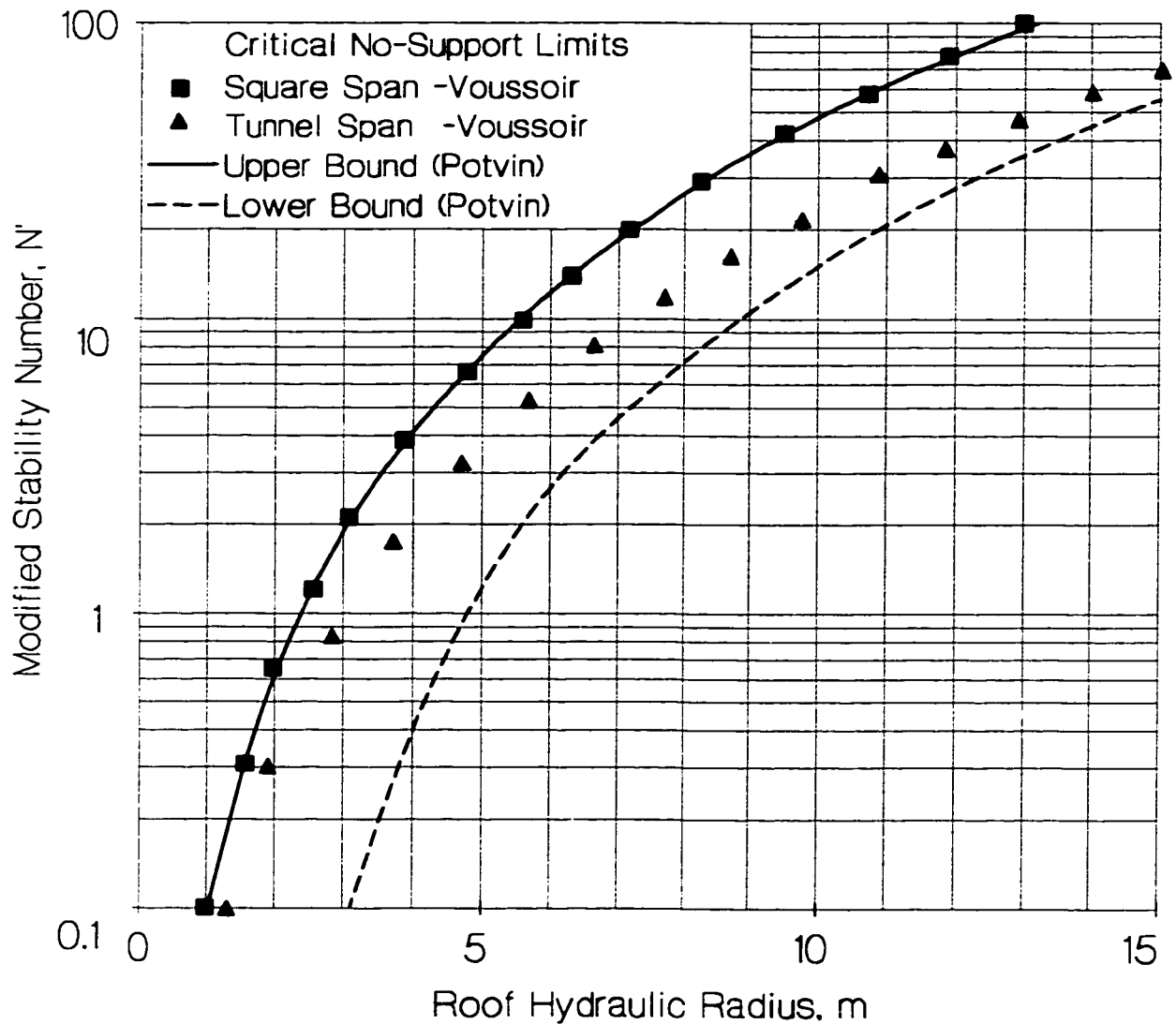


Figure 4.25: Voussoir calibration for square span. Linear tunnel spans require geometric correction.

This discrepancy corresponds closely to a correction (approximately 0.72) proposed by Milne (1996) using a radius factor based on a harmonic average distance from the centre of the span to the perimeter. It can be shown that the hydraulic radius for a circular face is equal to that for the corresponding circumscribed square. Failure to account for the additional mass and deformation due to the corners of the square is partly responsible for this error. For the purposes of this

calibration, the square span is used to determine HR . HR 's derived from tunnel spans (2D voussoir calculations) should be multiplied by 0.77.

Now that the voussoir simulation is calibrated to the Stability Graph it is possible to simulate the impact of abutment relaxation on the no-support limit. The stress parameter A does not consider relaxation, unlike the stress reduction factor, SRF , which it replaced. This factor monotonically increases from a low of 0.1 at high stress to a maximum of 1 at low or zero induced stress. A is set to one in this simulation (no stress) so that the impact of relaxation can be examined explicitly.

In the calibrated voussoir calculations, outward abutment deflection corresponds to relaxation. Figure 4.26 shows the new no-support limits for varying degrees of abutment relaxation. It is apparent that very little relaxation displacement is required to significantly increase the potential for instability.

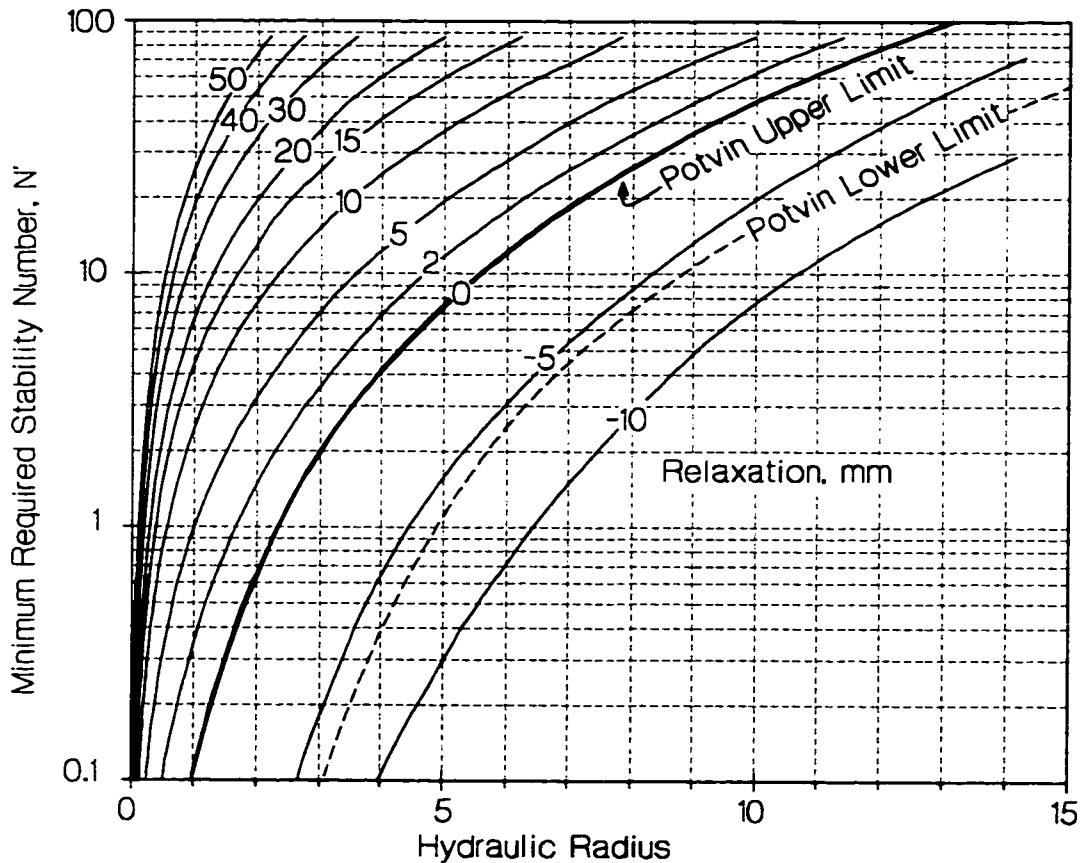


Figure 4.26: Revised no-support limits for N' resulting from abutment relaxation (negative relaxation values in mm correspond to stope wall compression).

Figure 4.27 shows the same results plotted against the log of the hydraulic radius. Using the modulus relationship in Figure 4.24 and the relaxation-stress equivalence calculated in Figure 4.9, it is possible to express the no-support limit alternatively as a function of induced average tensile stress tangential to the span (as derived from elastic models). For the voussoir analogue, relaxation is defined with respect to the position of the abutments under zero lateral stress (or strain). Therefore the relaxation displacement used in the voussoir analysis corresponds directly to equivalent tensile stress (parallel to the span) in an elastic model. The effect of relaxation in terms of the equivalent tensile stress is shown in Figure 4.28. For competent rockmasses, modeled elastic tensile stress magnitudes, of appreciable spatial extent, in excess of 30MPa are rare. If inelastic compressive strain has occurred adjacent to the excavation, as in the case of joint slip or abutment crushing, full relaxation (tension) may not be necessary to cause failure. In previously stressed ground around excavations, any significant reduction in lateral compression in the surrounding regional rockmass may result in relaxation induced groundfall.

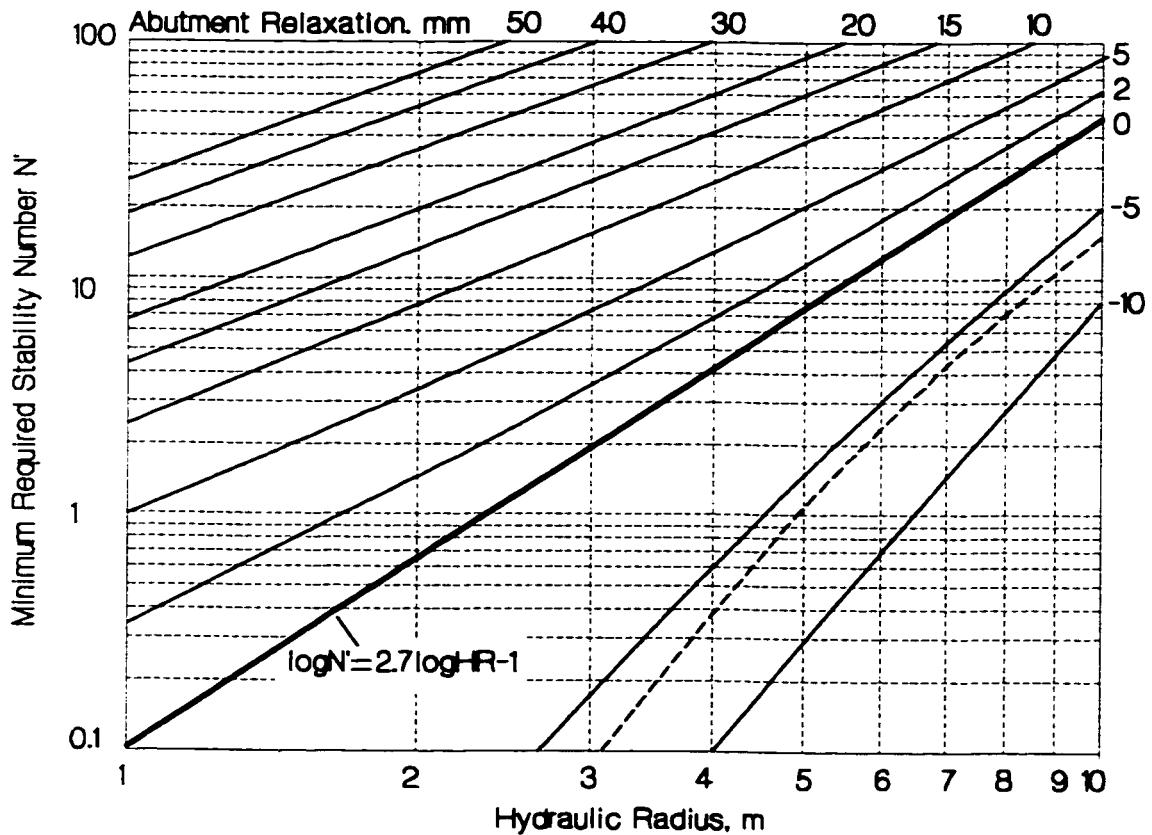


Figure 4.27: No-Support Limits resulting from abutment relaxation plotted with respect to $\log HR$: Function shown is for Potvin's (1988) upper No-Support Limit.

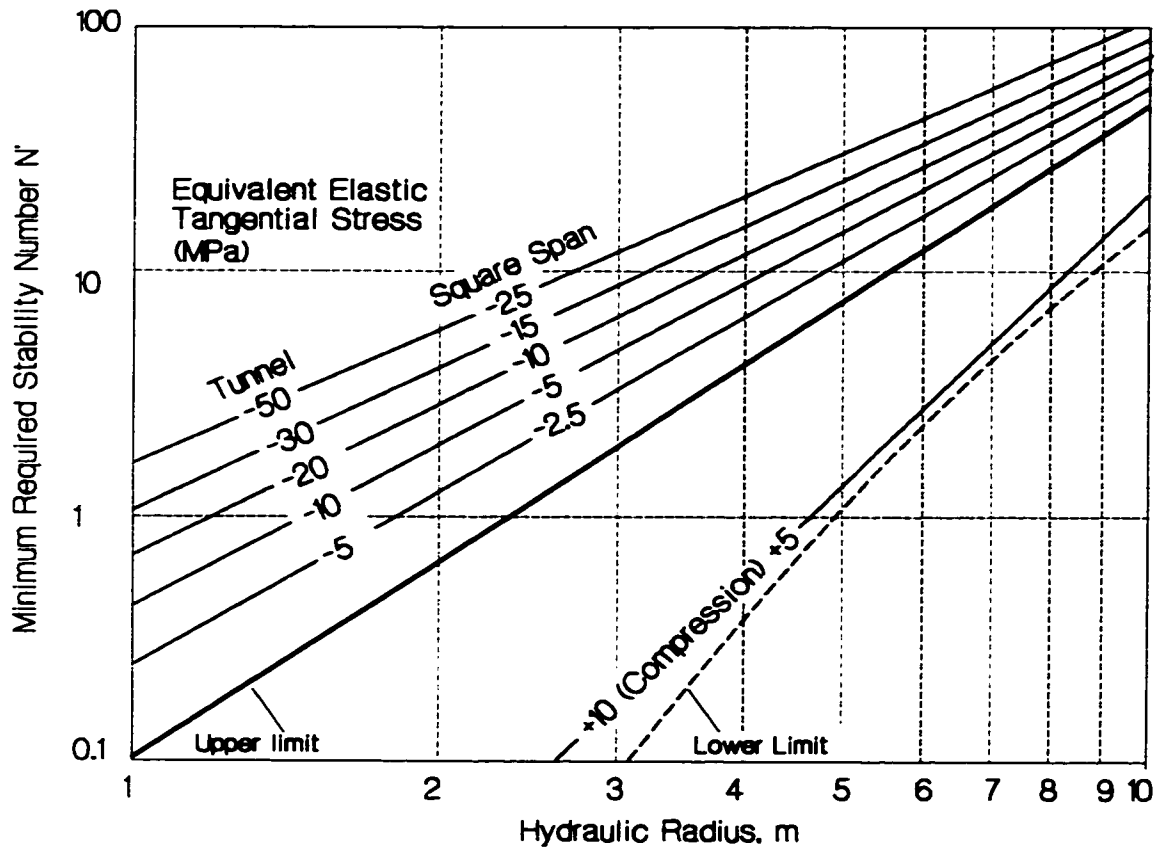


Figure 4.28: Equivalent elastic tensile stresses corresponding to the relaxation displacements in Figure 4.27.

4.4.4 Application of Relaxation Adjustment to No-Support Limit

Field evidence confirms the impact of relaxation as illustrated in Figure 4.29. A subset of the data from Greer (1989) and reanalyzed by Bawden (1993) is plotted in the lower half of Figure 4.29, corresponding to horizontal stope backs. Bawden (1993) reports that these backs are under high compression (Factor $A = 0.1$ to 0.4). The data seems to correspond well to the original stability limits proposed by Potvin (1988). Data for the inclined hangingwalls are plotted in the upper portion of Figure 4.29. Bawden (1993) reports that many of these faces have tangential tensile stresses according to elastic models. In spite of this relaxation effect, the stress factor A must be set to its maximum ($=1$) in accordance with the stability graph procedure. Note that Mathews et al. (1981) in their original discussion of this method state that it is not valid for cases of tangential relaxation. In the data of Figure 4.29, the method overpredicts the stability of these hangingwalls. Adjusted stability limits corresponding to average elastic tangential tension values of 4, 8, and

16MPa are superimposed on the data. While the magnitude of tension in these cases is not documented, the value shown is not unreasonable for typical hangingwall geometries in elastic analyses as indicated in Figure 4.8. If the stability limit is shifted up as indicated by these stress-defined curves, the unstable stopes can be appropriately captured. This is equivalent to a corresponding reduction in N' for the affected data points.

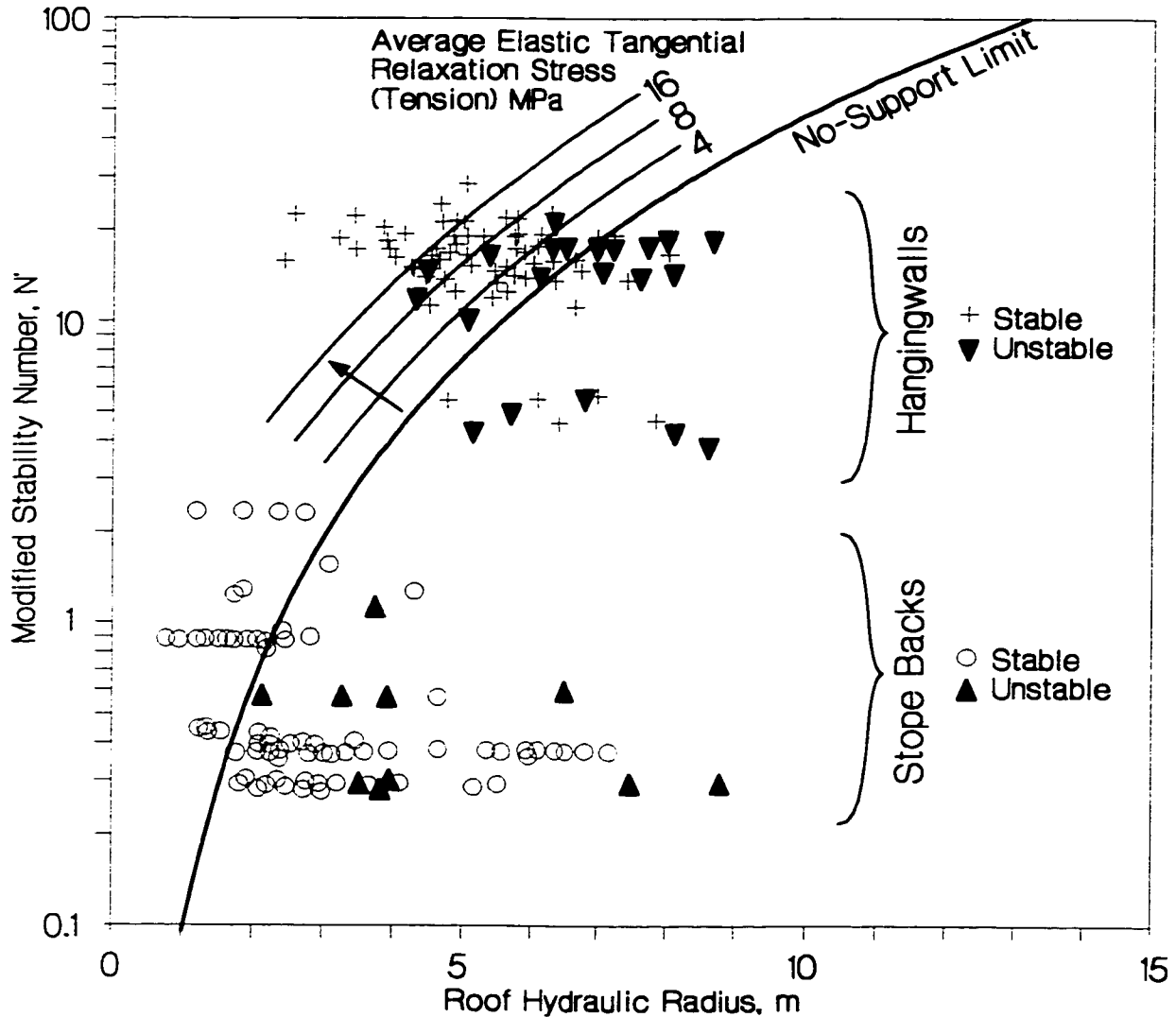


Figure 4.29: Correlation of relaxation adjustment for upper no-support limit; Stope backs were under moderate to high compression while elastic models predicted tension in hangingwalls.

Using the apparent shift in N' , illustrated in Figures 4.28 and 4.29, as a result of tangential tensile stress or relaxation, it is possible to derive an approximate function for a revised Stress Factor A which reflects the influence of relaxation. The modeled tensile stresses are first normalized with

respect to a range for nominal UCS of intact lab samples which is typical of hard rock (eg. 200MPa at $N' = 10$). The relationship illustrated in Figure 4.30 can be obtained from an examination of Figures 4.28 and 4.29. An average shift of N' (applied through the A factor), for a practical range of HR, is determined for different values of tension in order to provide for a simple and general correction to A. The general equation for Factor A adjustment:

$$A = 0.9e^{11\left(\frac{\sigma_T}{UCS}\right)} \quad \text{for } \sigma_T < 0 \quad [4.14]$$

for tangential boundary stress values (σ_T) in tension, is obtained as an exponential best-fit. For practical purposes a linear fit with extrapolation limits may also be adequate given the uncertainties in relating equivalent relaxation displacement with elastic tensile stress.

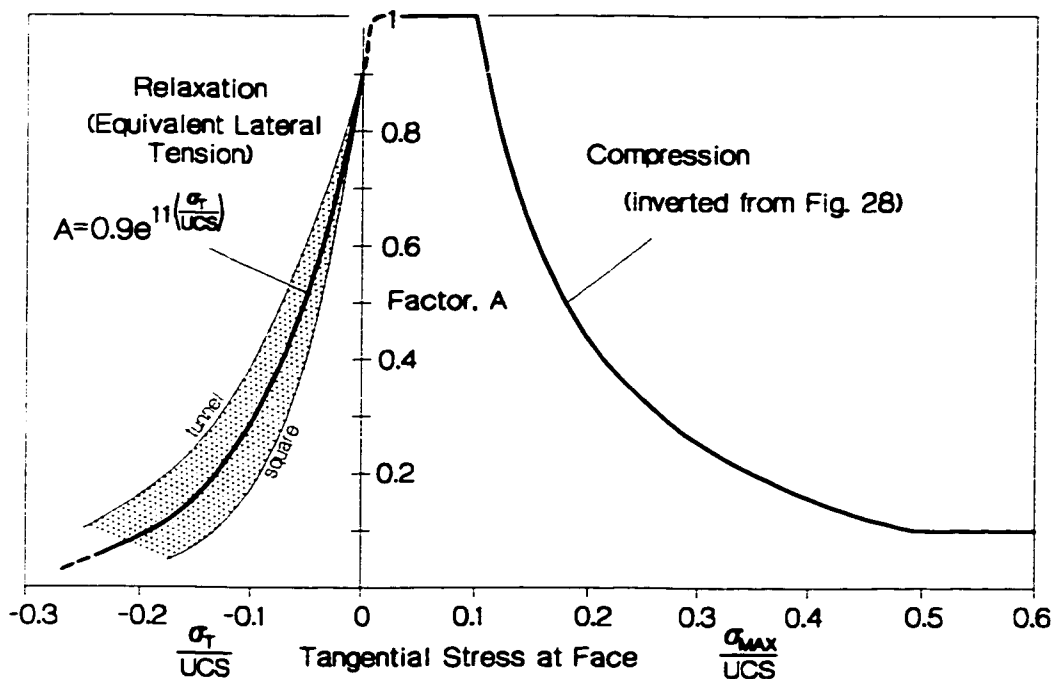


Figure 4.30: Revised definition of Stress Factor, A, used to determine the Modified Stability Number, N' . For consistency with compressive function, relaxation is reflected as the normalized maximum tension parallel to the face near midspan.

It is important to realize that other failure modes such as wedge fallout are likely to be even more sensitive to relaxation than the voussoir beam. The destabilizing effect of relaxation, therefore, may be significantly greater than that illustrated in Figure 4.30 and Equation 4.14. It is important to note that this relationship, derived through the voussoir analogue is valid only for low to moderate relaxation or tension. For higher values of tension, it has been suggested that A drops to zero and that the method, as a whole, becomes invalid (Mathews et al. 1981).

The best-fit coefficient 0.9 in Equation 4.14 creates an intercept which indicates an initially vertical slope to the relationship. In fact it is likely that the left-hand decline (Figure 4.30) in the A factor begins at compressive stresses below several MPa (Sourineni 1998) particularly if wedges are present. It be emphasized, again, that Equation 4.14 represents an upper bound for the A factor and that the impact of relaxation can be much greater than that indicated.

The results presented here can also be applied to the No-Support Limit of the Q-system (Barton et al 1974) as initially discussed in Kaiser et al. (1997). Using the calibration presented here and plotting against span and Q , instead of HR and N' , and assuming dry conditions and an initial SRF of 2, Figure 4.28 can be replotted with respect to the Q -system as shown in Figure 4.31. The equivalent tunnel spans are calculated by dividing the stable HR values from the square (voussoir) spans by 0.77 (long span correction according to voussoir analysis). Note that the base-line No-Support Limit for tunnels (long spans) corresponds to the limit for $ESR=3$, while that for the square span corresponds to $ESR = 5$. Barton (1988) defined this range of stability suitable for temporary mine openings.

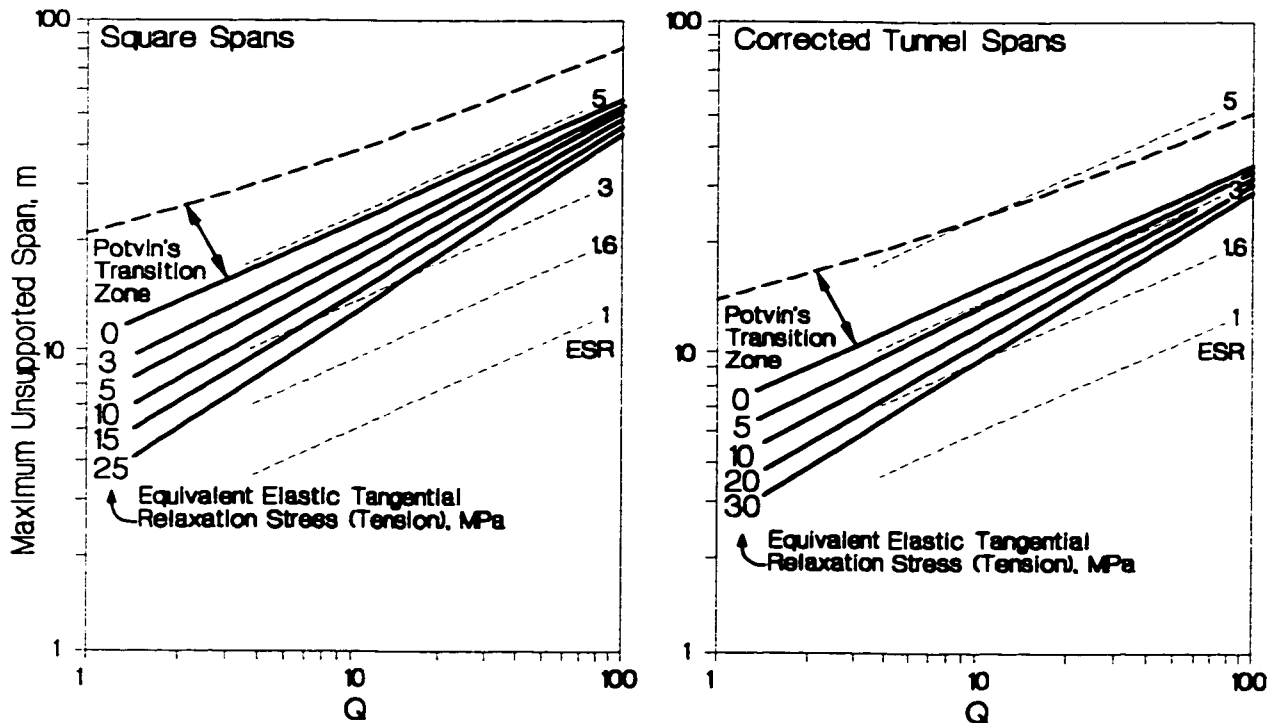


Figure 4.31: Tangential elastic tensile stresses corresponding to abutment relaxation and the shift in the Q no-support limit; Q limits are calculated from N' limits in Figure 4.28; ESR limits (Barton 1988) are plotted for comparison.

4.5 Application to Empirical Support Design

For stopes which can be supported, abutment relaxation can also impact the intensity of support required (the support demand). This impact will be examined with respect to cablebolt support. Cablebolts are essentially tendons placed into long boreholes, normally at a high angle with respect to the supported surface (e.g. back or hangingwall). The tendons, composed of seven-wire helically wound high strength steel strand, are grouted in the hole with cement or resin grout to affect load transfer between the rock and the strand. Cablebolts are discussed in detail by Hutchinson and Diederichs (1996).

4.5.1 Cablebolt Support Database

Potvin (1988), Potvin and Milne (1992) and Nickson (1992) collected 112 cases of cablebolted stopes and determined the limits of effective cablebolt support within the Modified Stability Graph. These are presented in Figure 4.32 with cablebolting limits by Nickson.

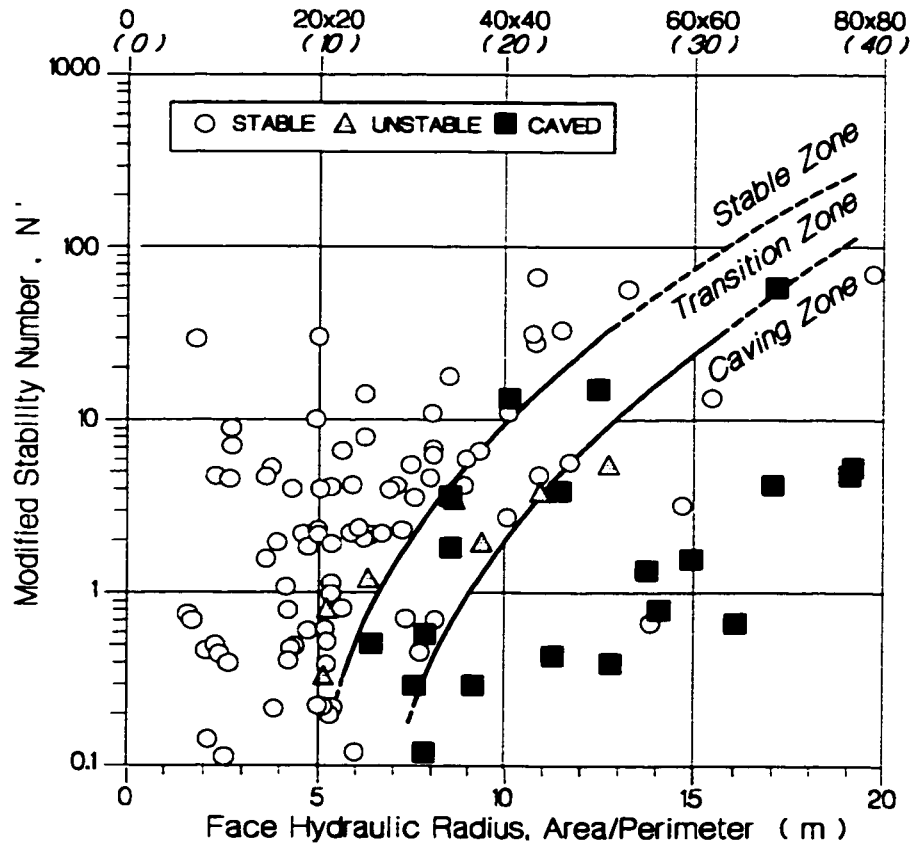


Figure 4.32: Cablebolted stope data (Potvin, 1988; Nickson, 1992) and cablebolting limits.

These cablebolting limits represent the average performance of all of the cablebolted stopes. It is also necessary to consider array density (cablebolt spacing). The approach which follows is described in detail in Hutchinson and Diederichs (1996) and will be summarized here briefly.

4.5.2 Cablebolt Support Function

Three primary cablebolt system functions are considered; retention, reinforcement and holding. These are illustrated in Figure 4.33.

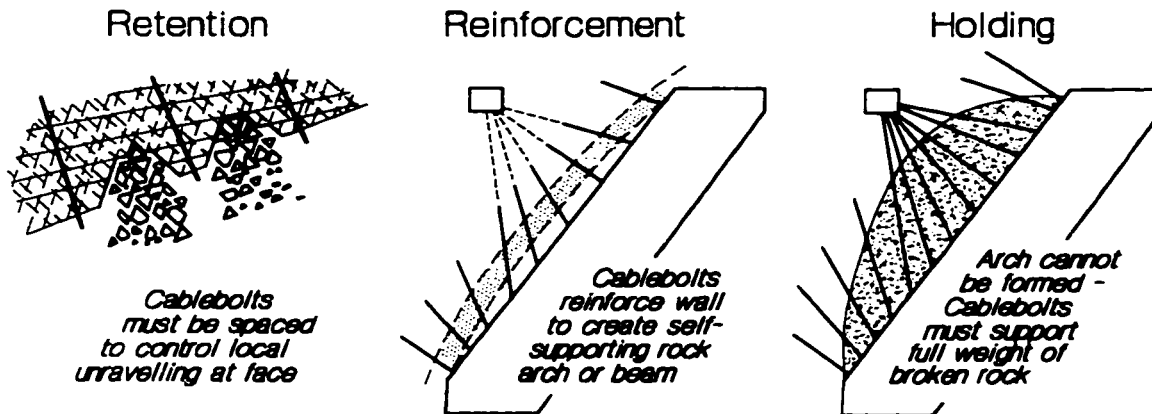


Figure 4.33: Primary cablebolt functions in open stopes.

A tendon support system such as cablebolts must be spaced closely enough so that ravelling of small blocks is restricted. Pre-installed cablebolts act as reinforcement, preventing joint dilation and internal separation within the rockmass, thereby preserving the inherent self-supporting capacity of the rockmass. Ultimately, however, if the span is large enough or the rockmass poor enough, or in the case of contiguous gravity wedges, the cablebolts perform a simple deadload support or holding function.

Retention involves maintaining the integrity of the excavation face, preventing the local fallout of small blocks which can lead to a progressive unravelling and a larger scale failure. This is a scale dependent phenomena involving the block size, represented empirically by RQD/J_n , as well as the influence of confinement, structural orientation and the dip of the excavation face. These are all summarized within N' . Nickson (1992) proposed normalizing N' with respect to HR to account for scale. A modified approach (Hutchinson and Diederichs 1996) is shown in Figure 4.34.

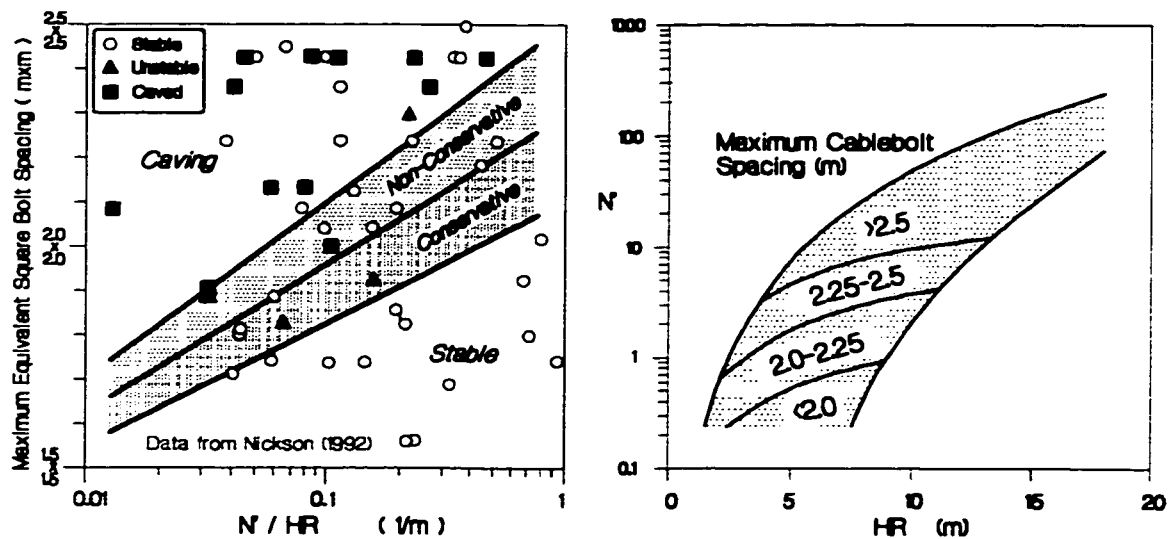


Figure 4.34: Maximum cablebolt spacing to control unravelling (after Hutchinson and Diederichs 1996).

The next step is to quantify the cablebolt spacing requirements for reinforcement. The upper boundary of Potvin's unsupported transition zone (Figure 4.23) is, by definition, a no-support limit. The rock is just beginning to lose its ability to support itself. In a jointed rockmass this support comes from compressive arching, as the face deflects, which transfers loads to the abutments. An adequate support system should be designed to hold together the minimum self-supporting beam (voussoir beam) across the slope face.

For engineering design purposes, a range of conservative rockmass moduli are obtained from Q based on the recommended relationships in Chapter 3 (setting A , B and C to the upper limits to give the lowest value of Q and therefore the lowest modulus result). Using the moduli so obtained for the voussoir model, cablebolt spacing based on a 20 tonne per strand capacity (yield) can be determined to support the minimum stable beam thickness obtained from Figure 4.1 for a given span (calculated from HR).

This procedure is similar to that used in the calibration exercise in Section 4.4 although a degree of subjective conservatism has been used throughout this development to provide built-in safety margin for design (Hutchinson and Diederichs, 1996) and to correlate with accepted practice for "average" conditions. The purpose of presenting this design procedure in this current work is to provide a basis to demonstrate the impact of relaxation in Section 4.5.4.

At the limit of supportability, the lower boundary of Nickson's cablebolting transition zone in Figure 4.32, the ultimate holding function of cablebolts must prevail. Stopes below and to the right of this limit are deemed unsupported. Therefore, "conservative" civil engineering practice is adopted for effective cablebolt systems (Lang and Bischoff, 1984) along this line. Cablebolts are spaced to support a deadload thickness equivalent to one quarter of the equivalent square span. The three design zones are superimposed as shown in Figure 4.35.

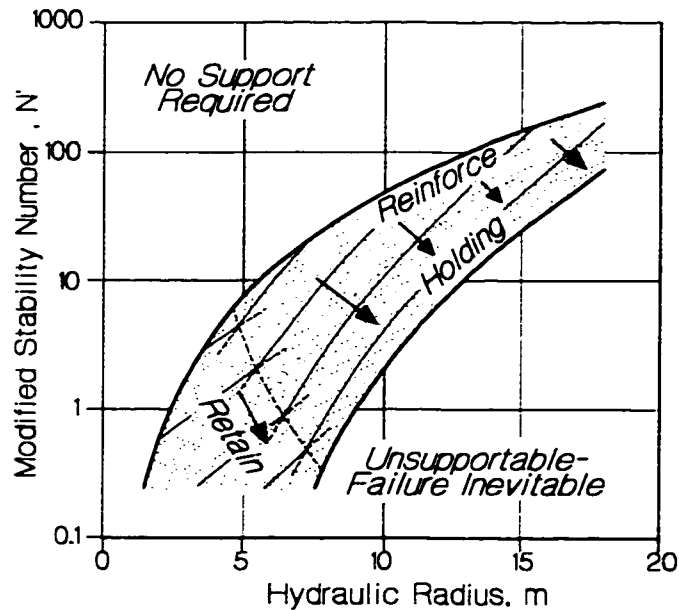


Figure 4.35: Zones of critical support function (i.e. the support function which dictates the maximum recommended cablebolt spacing).

The support function which requires the smallest cablebolt spacing dominates and determines the design at any given point on the graph. Note that the "retain" function, while not necessarily critical in terms of required cablebolt spacing, is active over the entire graph as is a combination of reinforcement and holding. The design zones indicated in Figure 4.35 only indicate the most critical function. In an area where retention is critical, grouted rebar or shotcrete added to the face to retain the surface allows the cablebolt pattern to be widened out to the maximum limit for reinforcement.

4.5.3 Cablebolt Design Recommendations

Figures 4.36 and 4.37 represent the composite recommendations for cablebolt spacing for single strand (20 tonnes at yield) and double strand (40 tonnes at yield) cablebolts. The design resolution is deliberately coarse to reflect the uncertainty in predicting rockmass behaviour across a wide

range of stope configurations. Nevertheless, these overlays provide a useful tool for more rational semi-empirical cablebolt design. Note, however, that good quality control and adequate bond strength is assumed in all cases. If bond strength is inadequate, modified geometry strand (such as birdcaged or bulbed cablebolts) may be required (Hutchinson and Diederichs, 1996).

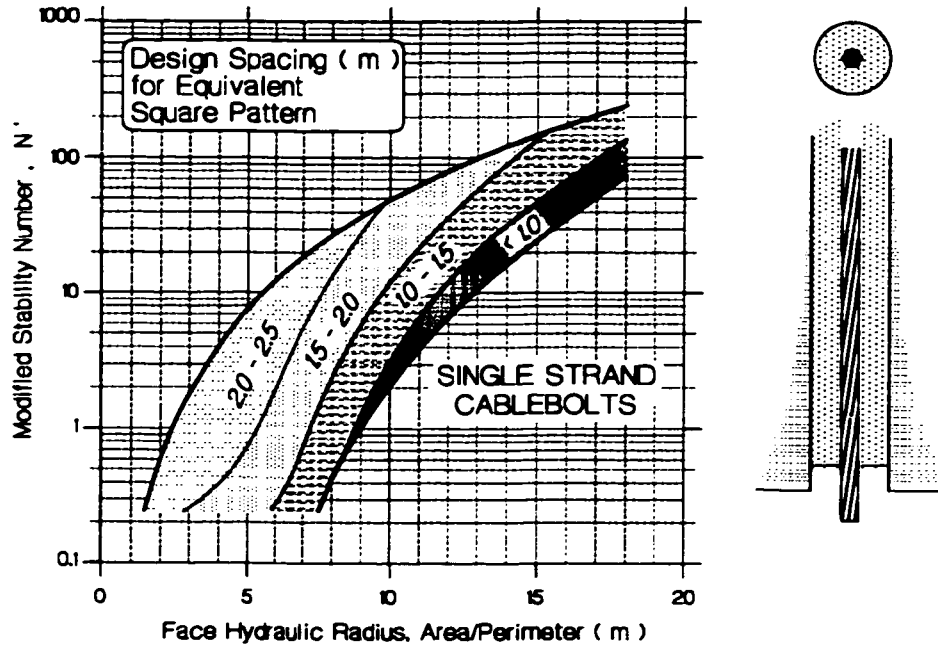


Figure 4.36: Pattern spacing recommendations for single strand cablebolts (Hutchinson and Diederichs 1996).

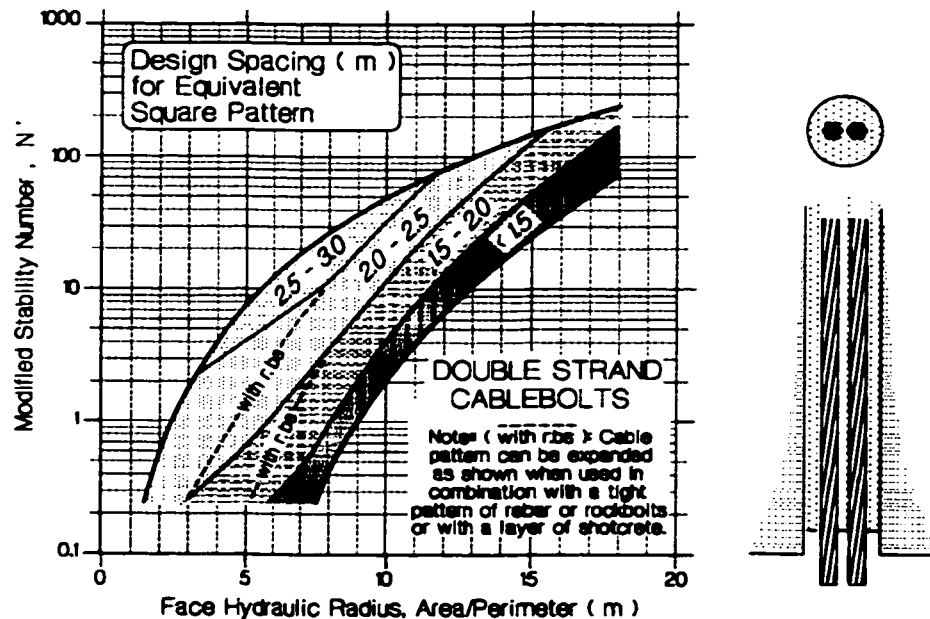


Figure 4.37: Recommendations for double strand cablebolts (Hutchinson and Diederichs 1996).

4.5.4 Relaxation and Cablebolt Support

The Stress Factor A does not allow for relaxation effects ($A=1$ at low stress). The no-support limit must move up (into the previously “stable” zone) as support is required in otherwise stable rockmasses. The calculated values of N' for the upper bound are adjusted accordingly. The lower bound represents worst-case already and is not affected. The recommendations between these bounds are transitional. Figure 4.38 shows the adjusted recommended cablebolt spacings for a pattern of double strand cablebolts for a slope hangingwall subjected to moderate relaxation (equivalent to a tensile stress of 10 to 20MPa in an elastic model).

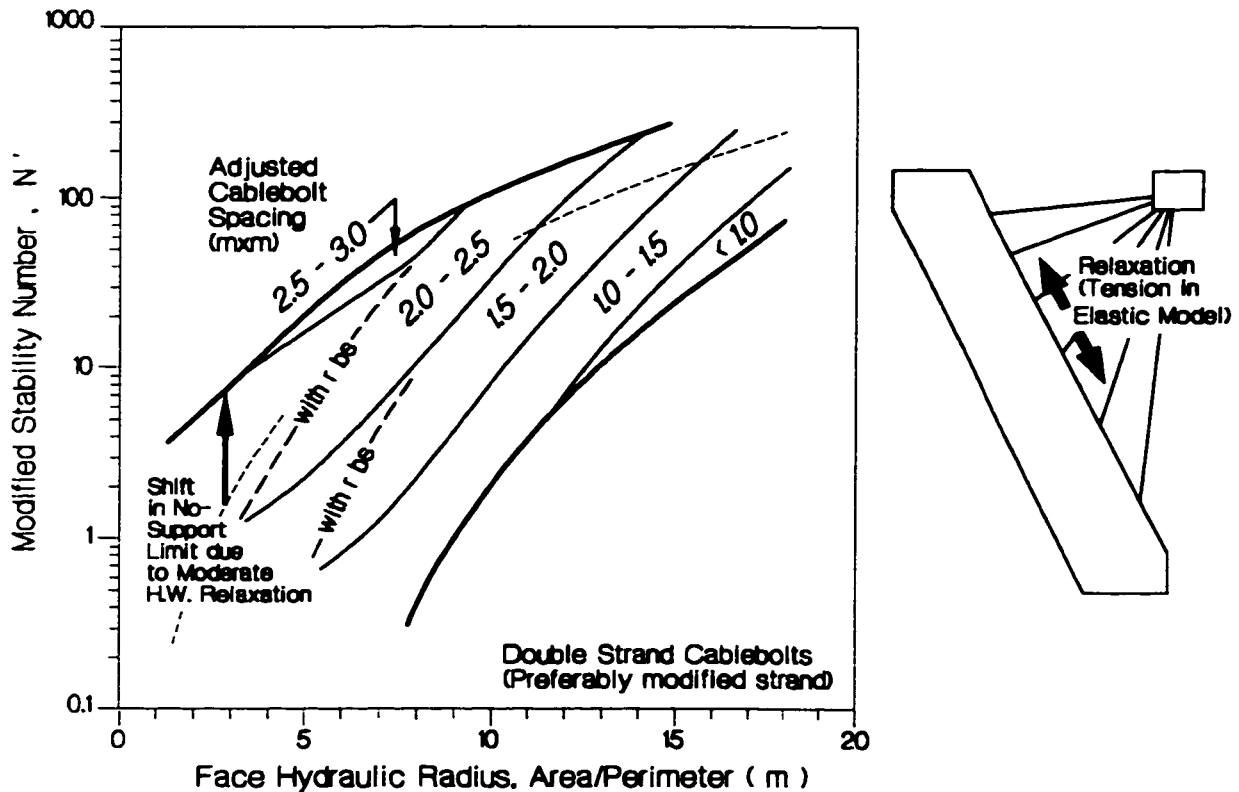


Figure 4.38: Adjusted spacing requirements for hangingwalls with moderate tangential relaxation (tension = 10 to 20MPa in elastic models).

Finally, it has been conclusively proven that stress reduction in the surrounding rockmass, after cablebolt installation, has a profound negative impact on the bond strength (load transfer from rock to grout to cable) of plain strand cablebolts (Hutchinson and Diederichs 1996, Kaiser et al. 1992a). The normalized frictional strength of the cablebolt-grout interface (the most critical in hard rock applications) defines the bond strength. The reduction in this bond strength due to stress change

(average net change normal to the cablebolt axis after installation) is shown in Figure 4.39. In typical installations, stress drop can cause plain strand cables to lose virtually all of their effectiveness just when they are needed the most. In a rockmass which experiences any significant relaxation or drop in compressive stress, it is highly recommended that modified strand cablebolts such as bulged or caged strand be used, since they are much less sensitive to stress change.

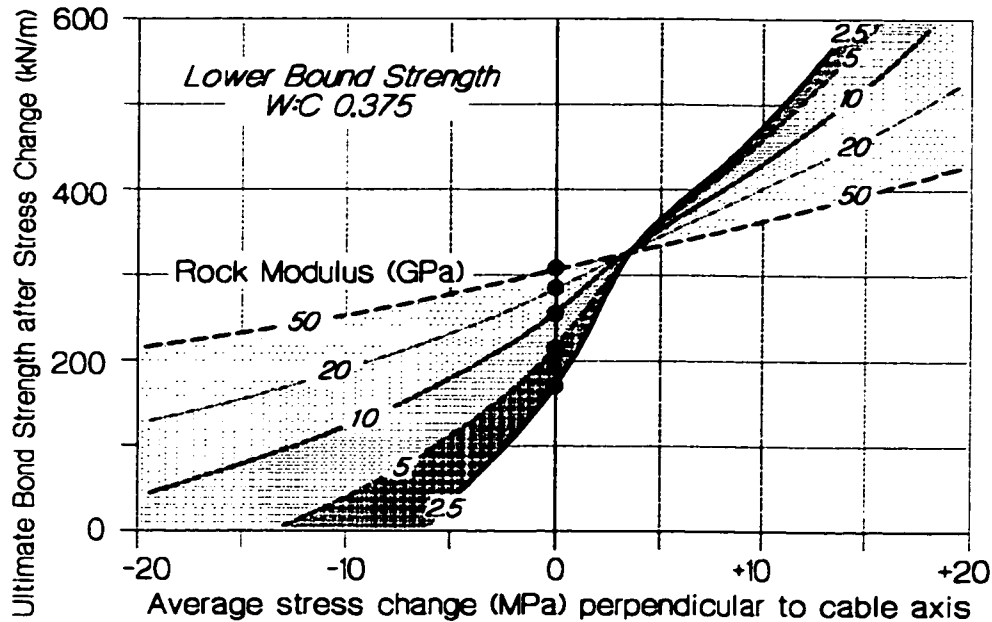


Figure 4.39: Reduction in frictional bond strength of plain strand grouted cablebolts due to rockmass stress change after installation (Hutchinson and Diederichs 1996).

4.5 SUMMARY

In massive to moderately jointed rock, residual tensile load bearing strength arising from incomplete fracturing or from rock bridges separating non-persistent jointing is a key factor in the control of ultimate gravity driven failure of jointed or stress damaged ground. Very little rock bridge cross-sectional area (less than 1% in most cases) is required in hard rocks to replace most artificial support systems for short-term applications. The time dependency of this residual tensile strength due to stress corrosion and atmospherically induced crack growth controls stand-up time and mandates the use of support systems in most underground excavations.

Boundary parallel relaxation is another dominant factor in delayed mining induced failure of spans in underground excavations, significantly shifting conventional no-support limits so that smaller spans are designed or additional support is required. Dangerous abutment relaxation can occur

even at depth, driven by unfavourable stress ratios, complex mine geometries, abutment damage, intersection development and undercutting.

Abutment relaxation increases support demands by reducing the natural ability of the rockmass to transfer loads to the abutments through arching. In addition, boundary normal stress relaxation has been shown to reduce the capacity of frictional support systems, exacerbating ground control problems.

A voussoir beam analogue was used to illustrate the importance of internal boundary normal tensile strength and of abutment relaxation in controlling the stability of spans in laminated rockmasses. The results of the voussoir simulation were used to modify empirical stope design limits, accounting for abutment relaxation.

A few millimetres of hangingwall or back abutment relaxation can significantly shift the no-support limit, inducing failure in previously stable spans. It is therefore important to sequence development and stope extraction properly to minimize this relaxation and to minimize the size of secondary stopes. The creation of high relaxation geometries, such as hangingwall undercutting, must be avoided.

Empirical support design has been combined with a more rational approach involving an examination of multiple failure modes and the support demand imposed by each. The composite result is an improved semi-empirical design tool for open stope cablebolt support. Within this context, relaxation can have a two-fold detrimental impact on stope stability by robbing the rockmass of its arching capacity and by reducing the bond strength of plain strand cablebolts.

These support recommendations are based on open stope, non-entry (or limited access) mining environments where dilution is the primary concern. These guidelines should not be used to design support for high traffic excavations where safety concerns dominate the support demand.

The importance of tensile strength and relaxation (low and negative confinement) on the structural integrity of excavations in shallow or locally unstressed environments has been explored in Part I of this thesis, through the use of simple analogues.

In Part II, including Chapters 5 to 8, the author will investigate the impact of tensile damage and low boundary normal confining stresses on the yield behaviour of hard rockmasses in high stress (deep) environments.

PART II
STRESS DRIVEN
INSTABILITY

CHAPTER 5

Strength of Hard Rockmasses near Excavations: Review and Background

5.1 INTRODUCTION

Part I of this thesis examined the influence of residual tensile strength and boundary parallel relaxation on structural integrity and stability in low to moderate stress conditions. Part II examines the role of tensile strength at the micro- and macro-scale on rock damage and yield under high deviatoric stress in low confinement conditions. Such conditions exist adjacent to underground excavations and as such are of prime concern to the engineer. Conventional rock strength criteria such as Hoek-Brown (1980;1988), Mohr-Coulomb and numerous three dimensional derivatives (summarized by Shah 1992 and by Cividini 1993, for example), are based on curve fits to data obtained at low and at high confining stresses. In the process of such a generalized fit of finite order, the high sensitivity of hard rock strength to near-zero and negative confining stress is often inadequately captured.

As discussed in more detail in Chapters 6 and 7, yield and fracture of intact or massive hard rock is typified by four general categories of behaviour (Figure 5.1), dependent on the confining stress. In direct tension, the rock splits in a catastrophic fashion along a discrete planar or curvilinear surface. At near-zero confining stress (σ_3 , or lateral stress, for a two dimensional simplification) compressive failure occurs in the form of axial (parallel to σ_1) splitting and high angle shear fractures formed from coalescing extension cracks. As confining stress increases, the axial splitting or spalling soon subsides, giving way to moderate angle shear zone development. This shear zone or kink band is composed of short and closely spaced axial extension cracks. Only at ultra-high confining pressures (e.g. $\sigma_3 \gg$ Unconfined Compressive Strength, *UCS*) does pure shear fracture initiation and development dominate yield behaviour.

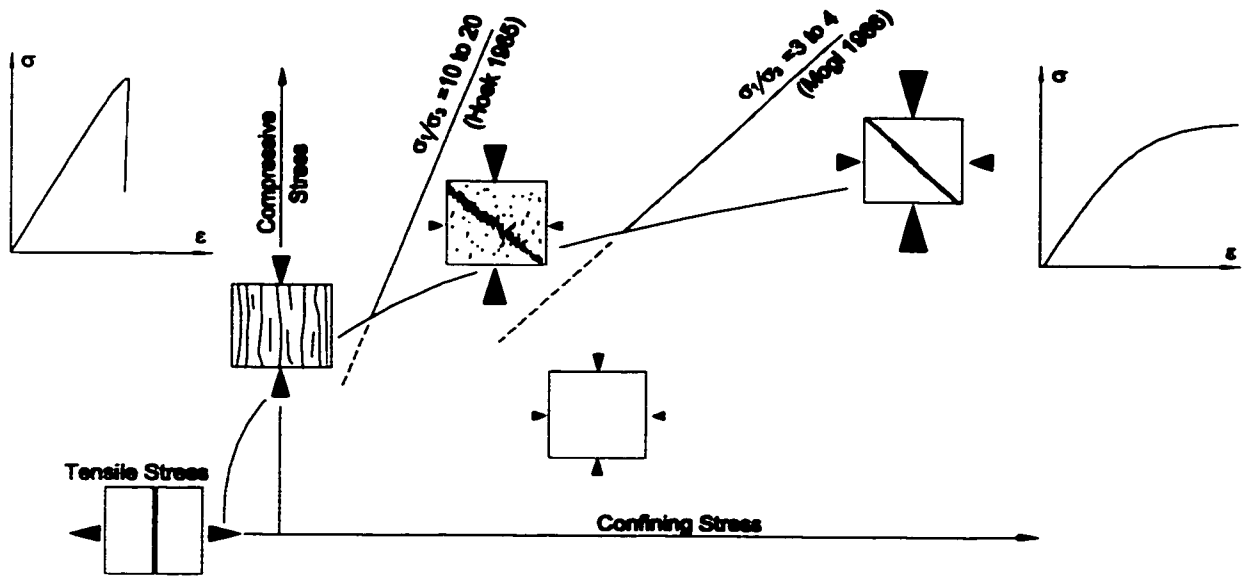


Figure 5.1: Schematic stages of yield in hard rocks.

These four mechanisms are introduced here in order of decreasing confinement dependency. This change in behaviour with confinement is reflected in the curved strength envelopes such as Hoek-Brown. The dominance of extensile cracking at low confinement contrasts with the behaviour of materials in which frictional slip is dominant at all confining pressures. Frictional shear with or without an accompanying cohesive component (zero-confinement intercept for shear strength) is the physical assumption behind the Mohr-Coulomb criterion and the accompanying plasticity formulation and flow rule. However, the yield function itself may also reflect confinement dependency due to non-frictional mechanisms such as axial crack extension. This contrast in behaviour is illustrated by comparing the assumed and observed slip surfaces in yielding frictional materials, with the near-boundary spalling behaviour found in hard rock (Figure 5.2.)

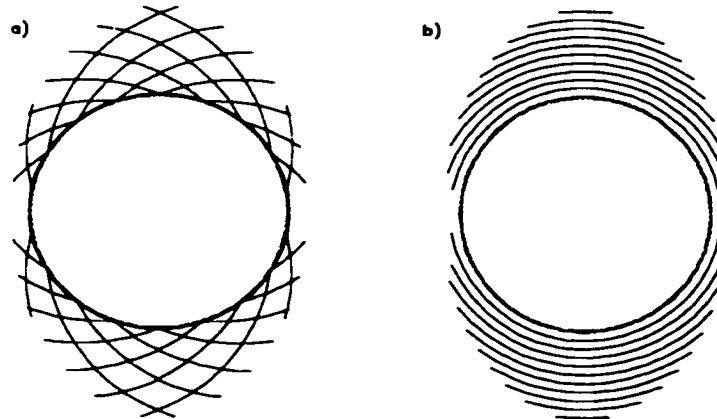


Figure 5.2: Schematic failure modes for: a) continuum plastic shear, and b) brittle spalling.

Examples of near-excavation spalling, due to extensile propagation of compression parallel cracks, are illustrated in Figure 5.3, around a carefully excavated 3.5m diameter tunnel in massive granite and in moderately jointed rock in mining environments in Figure 5.4 (fractures shown are stress induced and are not associated with joint sets). This spalling is often driven by localized, dilatant shearing (left of centre in Figure 5.3a), or corner crushing (Vasak and Kaiser 1995, Martin et al. 1997), or develops spontaneously from induced microscopic cracks or pre-existing flaws in the wall rock (Myer et al. 1992).

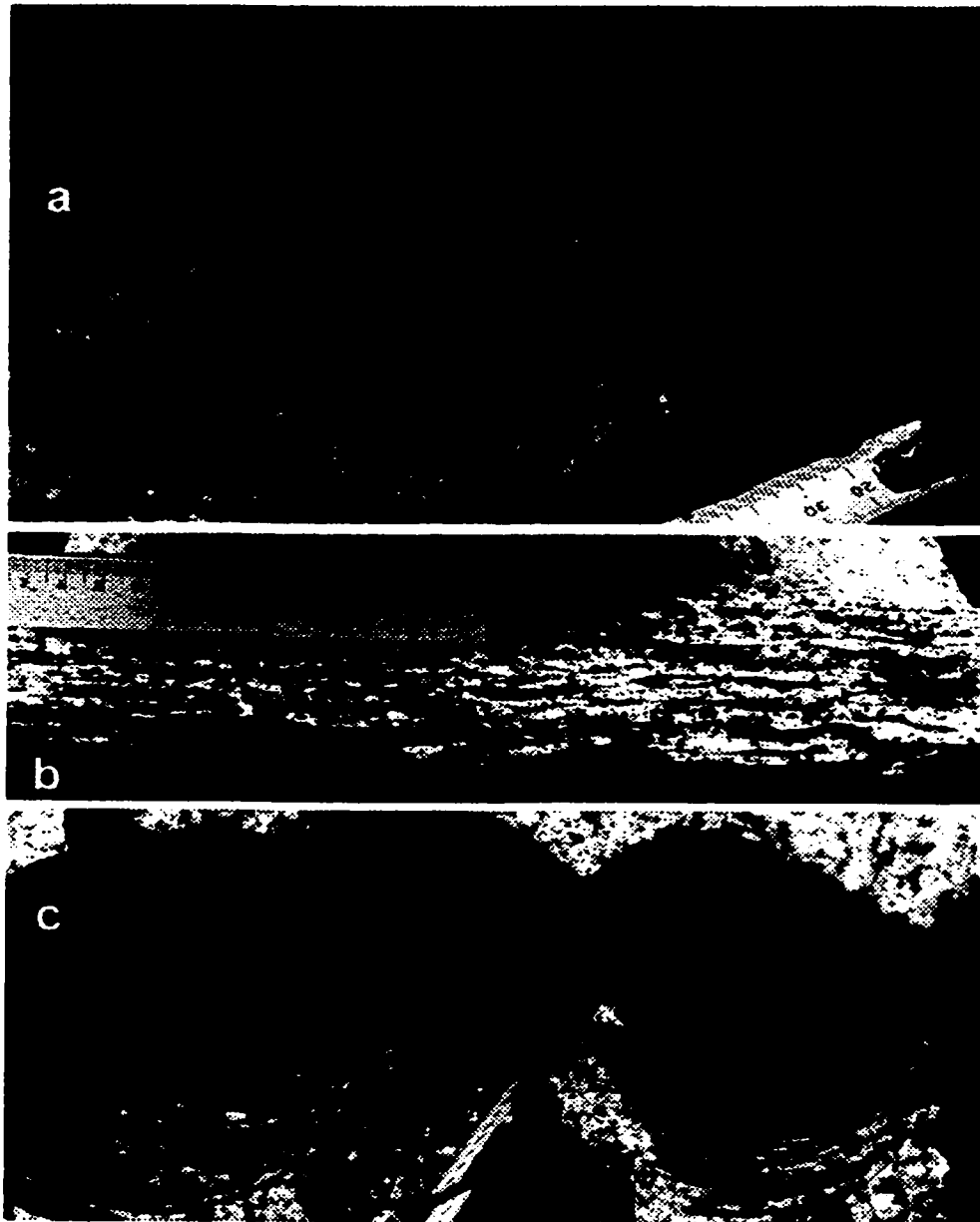


Figure 5.3: Compression-induced grain-scale spall damage around a 3.5m diameter tunnel in massive granite (assembled from original photos courtesy of AECL Ltd.).

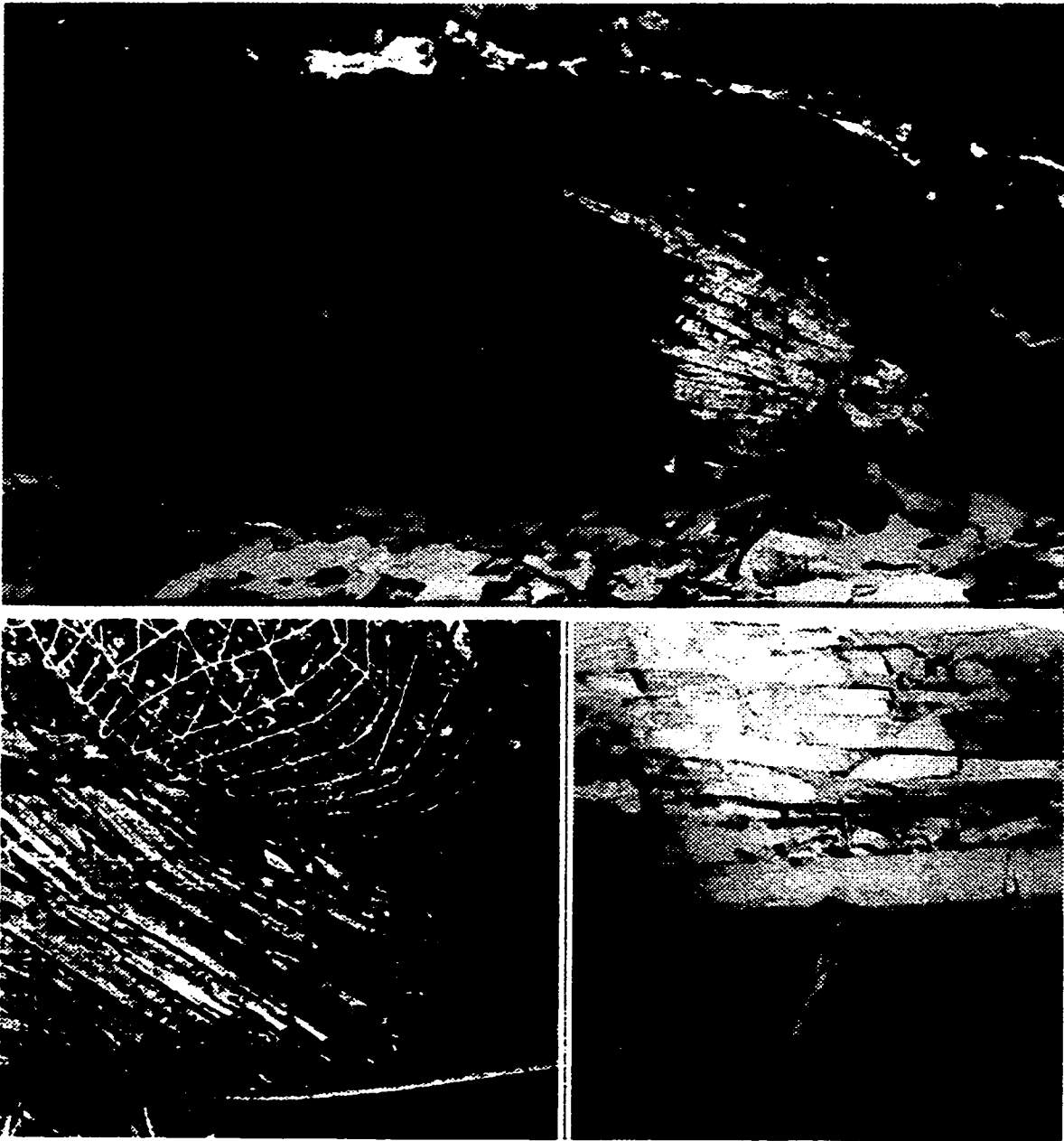


Figure 5.4: Examples of spall damage around deep openings at (top and bottom left) Brunswick Mine and Bousquet Mine (courtesy P.K. Kaiser), and (bottom right) Makassa Mine.

The formation of through-going shear rupture zones is promoted in laboratory testing through the use of height to width ratios in excess of 2.5 (I.S.R.M. 1979), and by the lateral confining (and crack suppression) action of the end platens (Peng 1971). While such shear zones have been observed in conditions of extreme stress (and confining pressure), and in cases of tabular excavation geometry (Brummer 1987; Ortlepp 1997), the dominant sidewall failure mode observed in deep underground excavations in hard rock is generally described as spalling

(Fairhurst and Cook 1966; Hoek and Brown 1980). Pelli et al. (1991) discuss the limitations of the plasticity approach to failure prediction and simulation in these conditions.

Much of the compressive strength contribution beyond initial yield in lab-scale cylindrical samples of hard rock is likely due to the effects of friction mobilization and dilation. This component, however, is absent in large sample strength and in long-term strength (Martin 1994; Lajtai 1988). The strength threshold obtained by these two test extremes are similar (Figure 5.5) and can be considered coincident with the true upper bound yield strength of hard rock. This threshold occurs, for hard rocks such as granite, at approximately 65% to 80% of the standard laboratory UCS.

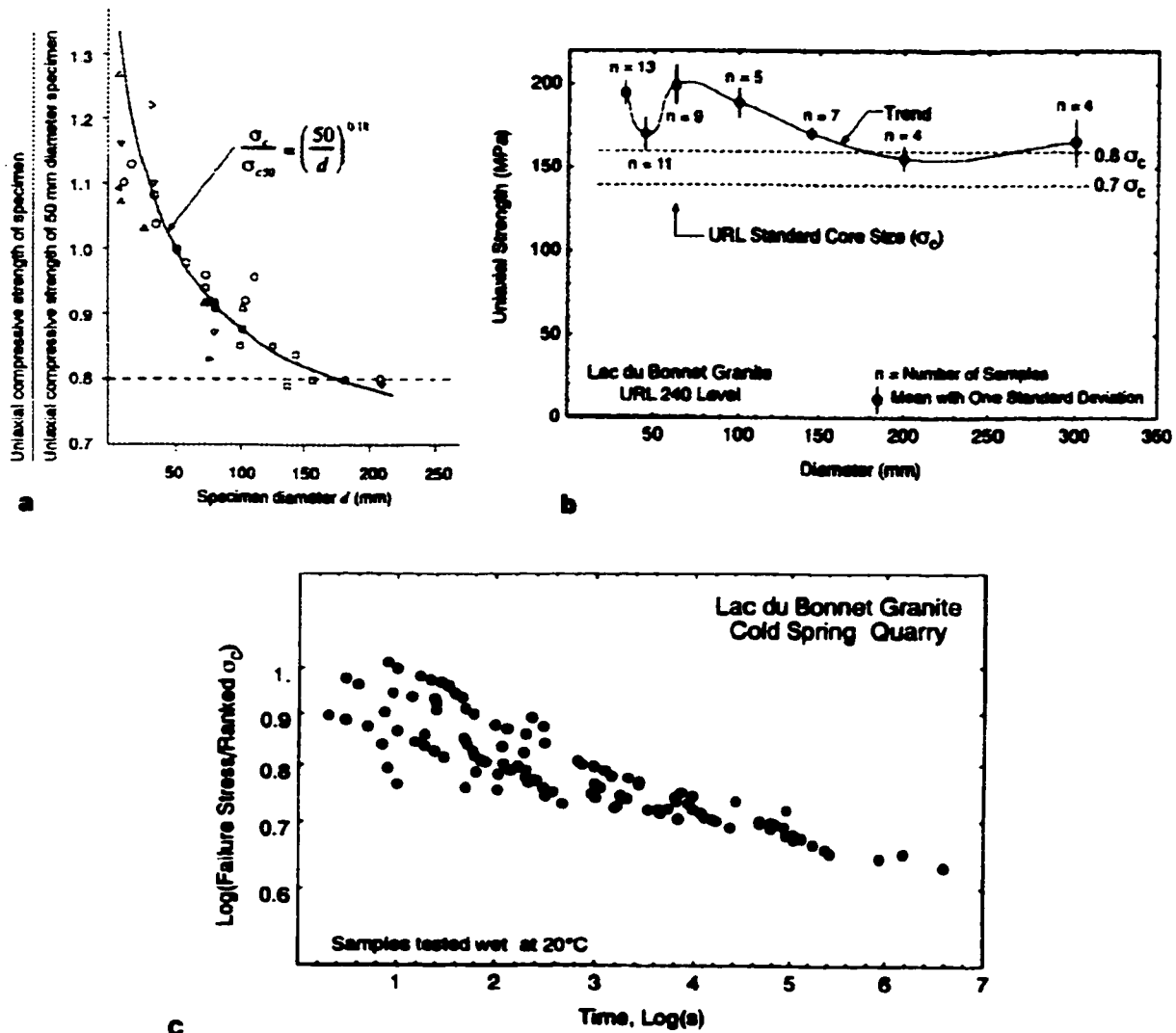


Figure 5.5: Decay of uniaxial compressive strength with sample size for cylindrical specimens, after a) Hoek and Brown (1980), and b) Martin (1994), and c) with long-term static loading (after Schmidtke and Lajtai 1985).

Chapter 6 will demonstrate that this uniaxial yield strength also corresponds to the unconfined intercept of a σ_3 dependent threshold (of σ_1) which represents the onset of non-linear and inelastic axial stress/strain behaviour. One of the key conclusions of this thesis is that this threshold represents the first mechanical interaction within an array of accumulating, extending and otherwise isolated axial microcracks.

This yield threshold occurs at a critical crack intensity (a function of the number and length of the cracks) and is a true material property. Behaviour beyond this threshold, including peak strength, is heavily influenced by loading system properties, loading rates, sample geometry and other external factors. As such, this critical damage stress, yield stress or linear limit, represents an upper bound for insitu strength in massive undisturbed rockmasses.

Empirical evidence discussed later in this chapter suggests that a lower bound for rockmass strength is defined by a crack initiation limit. Due to internal heterogeneity, an elemental strength distribution exists within the material. Random crack initiation occurs at a deviatoric stress level typically 0.3 to 0.4 times the uniaxial compressive strength, while systematic and rate-accelerating crack initiation occurs between 0.4 and 0.5 times the UCS. Observations suggest that this initiation threshold is relatively insensitive to confinement following a relationship similar to:

$$\sigma_{1critical} \approx 0.4(\pm 0.1)UCS + 1.5(\pm 0.5)\sigma_3 \quad [5.1]$$

A biaxial form is used here for simplicity, for comparison to two dimensional simulations and to be consistent with the assumption that crack initiation is influenced by extreme stresses only. The relationship between this compressive damage initiation threshold and internal tensile strength is examined in this thesis using granite as a test material and using a bonded contact analogue for damage accumulation. Another primary subject of investigation here is the suite of mechanisms leading to the reduction in crack interaction stress or material yield strength. This upper limit for insitu strength typically falls to a level coincident with the crack initiation threshold in the vicinity of underground excavations.

This explains the success of the empirical strength relationship in Equation 5.1 for delineating damaged zones and failure extent around tunnels and caverns, and boreholes. Without contesting the empirical validity of such a criterion, used with success by Kaiser et al. (1995), Castro (1996) and Martin et al. (1996;1997;1998) this thesis will illustrate and investigate the mechanisms which lead to this behaviour and apparent insitu strength relationship, highlighting the impact of tensile strength and low confinement.

5.2 ROCK STRENGTH AND FAILURE - A REVIEW

Before examining the relationship between extensile crack initiation, damage accumulation, crack interaction and insitu strength, a review of conventional strength criteria and non-linear techniques for modelling rock failure is in order. This discussion is by no means comprehensive and is intended only as a brief review.

5.2.1. Strength of Geomaterials

In a general sense, peak strength for isotropic rock or rockmasses can be expressed as:

$$f(\sigma_1, \sigma_2, \sigma_3) = 0 \quad [5.2]$$

where the principal stresses indicated (σ_i =most positive or most compressive in this convention) are those at a stress state lying on the failure envelope in three dimensional stress space (Figure 5.6a). This general three dimensional form can also be derived as a function of stress invariants:

$$f(I_1, J_2, \theta) = 0 \quad [5.3a]$$

$$I_1 = \sigma_{kk} \quad [5.3b]$$

$$J_2 = 0.5s_{ij}s_{ij} \quad \text{where} \quad s_{ij} = \sigma_{ij} - \frac{1}{3}I_1\delta_{ij} \quad [5.3c]$$

$$\theta = \frac{1}{3} \cos^{-1} \frac{3\sqrt{3}J_3}{2J_2^{3/2}} \quad \text{where} \quad J_3 = \frac{1}{3}s_{ij}s_{jk}s_{ki} \quad \text{and} \quad 0 \leq \theta \leq \frac{\pi}{3} \quad [5.3d]$$

where σ_{ij} is the stress tensor, s_{ij} is the deviatoric stress tensor and δ_{ij} is the Kroneker delta. I_1 represents the state of hydrostatic confinement while J_2 is a measure of the deviatoric stress components. A two dimensional equivalent expression directly analogous to Equation 5.3a is as follows:

$$(\sigma_1 - \sigma_3) = f(\sigma_1 + \sigma_3) \quad [5.4]$$

The expression above is common to soil mechanics and is normally associated with a shear-type failure mechanism. The term on the right defines the normal stress acting on a defined or assumed failure surface while the term on the left contributes to the driving shear stress on that plane.

A simplifying assumption employed in many practical applications is that rock damage, yield and ultimate strength are independent of the intermediate principal stress. This clearly mandates the

assumption of initial isotropy (no fabric or jointing) and a predisposition for damage to occur in a direction controlled by σ_1 and σ_3 . In addition, fracture modelling and experimental work (summarized in Chapters 6 and 8) clearly show that damage initiation and propagation is highly sensitive to σ_3 (acting normal to a propagating extension crack) rather than to the full hydrostatic component ($\sigma_1 + \sigma_3$) or I_1 .

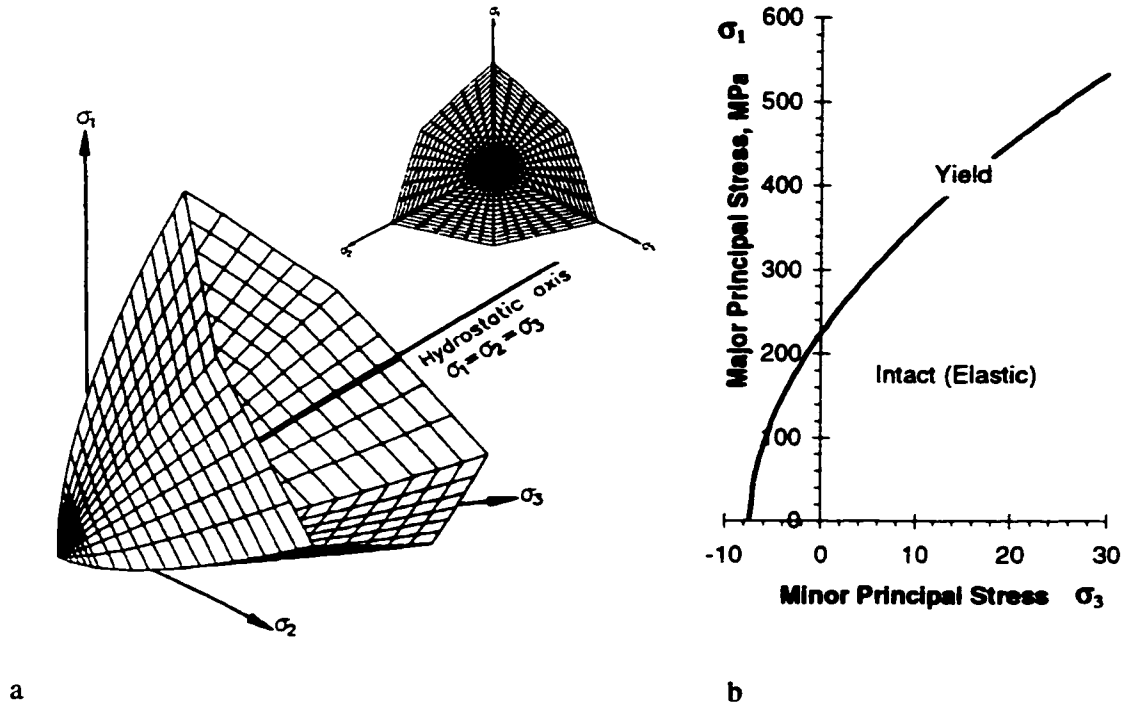


Figure 5.6: Hoek-Brown yield envelopes in a) three dimensional (modified after Shah 1992) and b) two dimensional stress spaces.

While numerous researchers (e.g. Aubertin and Simon 1997) have developed general three dimensional criterion for damage initiation and many more have developed such criterion for yield and failure (Table 5.1), it is unclear whether such complexity is warranted for practical application. In order to provide transferability between case study work, laboratory studies and numerical modelling, the traditional and simple expression:

$$\sigma_1 = f(\sigma_3) \quad [5.5]$$

and the stress space shown in Figure 5.6b) will be used in this work for damage initiation, yield and peak strength. Clearly, in this simplification, no distinction is made between the typical axisymmetric confining stress found in laboratory tests on cylindrical samples and the three component stress field insitu. In the latter case, the intermediate stress is simply disregarded.

Table 5.1: Typical Damage Initiation and Yield Criteria Used for Rock Materials.

(no damage or yield if left side < right side)		
<i>A = cohesion / tension constant (intercept); B = 1st order slope constant; C = non-linearity constant</i>		
Griffith (1924)	$(\sigma_1 - \sigma_3)^2 = 8A(\sigma_1 + \sigma_3)$	$A = \sigma_t$ (tensile strength)
Murrell (1963)	$J_2 = 4A I_1$	$A = \sigma_t$
Tresca	$\sigma_1 - \sigma_3 = A$;	$A =$ critical deviatoric stress
Von-Mises	$\sqrt{J_2} = A$	$A =$ yield constant
Stacey (1981)	for $\sigma_2 = \sigma_3$: $A + B\sigma_1 = \sigma_3$ general: $A + B(\sigma_1 + \sigma_2) = \sigma_3$	$A = \frac{E\epsilon_{cr}}{1-\nu}$; $B = \left(\frac{\nu}{1-\nu}\right)$ $A = E\epsilon_{cr}$; $B = \nu$
Aubertin and Simon (1997)	$\sqrt{J_2} = \frac{1}{\sqrt{3}}[(A_1 - A_2)f_d I_1 + A_1 A_2]^{1/2} F_\pi$ $f_d = 1 + \frac{3B^2 \left\langle I_1 - \left(\frac{A_1 - A_2}{12B^2} - \frac{A_1 A_2}{A_1 - A_2} \right) \right\rangle}{A_1 - A_2}$ $F_\pi = C \left[C^2 + (1 - C^2) \sin^2 \left(\frac{\pi}{4} - 1.5\theta \right) \right]^{-1/2}$	$A_1 =$ UCS; $A_2 =$ Tensile Strength, T For this formulation: $\theta = \frac{1}{3} \sin^{-1} \left(\frac{3\sqrt{3}}{2} \left(\frac{J_3}{J_2^{3/2}} \right) \right)$ $-\pi/6 \leq \theta \leq \pi/6$
Mohr Coulomb (Coulomb 1773; Paul 1961; Jaeger & Cook 1971; Desai & Siriwardane 1984)	$\sigma_1 - \sigma_3 = (\sigma_1 + \sigma_3) \sin B + 2A \cos B$ or $\sqrt{J_2} \sin \left(\theta + \frac{\pi}{3} \right) =$ $A \cos B - \left(\frac{1}{3} I_1 + \sqrt{\frac{J_2}{3}} \cos \left(\theta + \frac{\pi}{3} \right) \right) \sin B$	$A = c$ (cohesion); $B = \phi$ (friction angle);
Drucker-Prager (1952)	$\sqrt{J_2} = A + B I_1$	Using Mohr-Coulomb parameters for axisymmetric confinement ($\sigma_2 = \sigma_3$): $A = \frac{6c \cos \phi}{\sqrt{3}(3 - \sin \phi)}$; $B = \frac{2 \sin \phi}{\sqrt{3}(3 - \sin \phi)}$
Hoek Brown (1980, 1988)	$\frac{\sigma_1 - \sigma_3}{A_1} = \left(B \frac{\sigma_3}{A_1} + A_2 \right)^C$	$A_1 =$ UCS; $A_2 = s$; $B = m$; $C = 0.5$
3D Hoek Brown (Shah 1992)	$\frac{\sqrt{J_2}}{A_1} (\sqrt{3} \cos \theta + \sin \theta) = \left(B \frac{I_1}{3A_1} - B \frac{\sqrt{J_2}}{\sqrt{3}A_1} (\cos \theta + \sqrt{3} \sin \theta) + A_2 \right)^C$	
Pan & Hudson (1988): Simplified Hoek-Brown Criterion.	$\frac{\sqrt{3}}{A_1} \sqrt{J_2} = \left(\frac{B}{3} \frac{I_1}{A_1} + \frac{\sqrt{3}}{2} m \frac{\sqrt{J_2}}{A_1} + A_2 \right)^C$	
Modified Hoek Brown ($s = 0$) (Shah 1992)	$\sqrt{J_2} (\sqrt{3} \cos \theta + \sin \theta) =$ $B^C A_1^{1-C} \left(\frac{I_1}{3} - \frac{\sqrt{J_2}}{\sqrt{3}} (\cos \theta + \sqrt{3} \sin \theta) \right)^C$	$A =$ UCS; $B = m$; $C = a$

5.2.2 Non-Linear Techniques and Fracture Theory

Continuum models, which use conventional plastic constitutive laws, meet with limited success at best in adequately simulating the post-yield behaviour of brittle rock masses. Numerous variations of this approach are reviewed by Desai and Siriwardne (1984) and by Cividini (1993). Typically a yield surface in stress space (Figure 5.7), based on a combination of cohesive and frictional parameters and defining the limit of elastic behaviour, is combined with an associative or non-associative flow rule (Jain 1980) as shown in Figure 5.8. This surface, as a function of some dilation expression, defines the incremental plastic strain vector. Total accumulated strains are the sum of the accumulated plastic strains and the elastic strains. Stresses are linked to the elastic strain components through a compliance relationship.

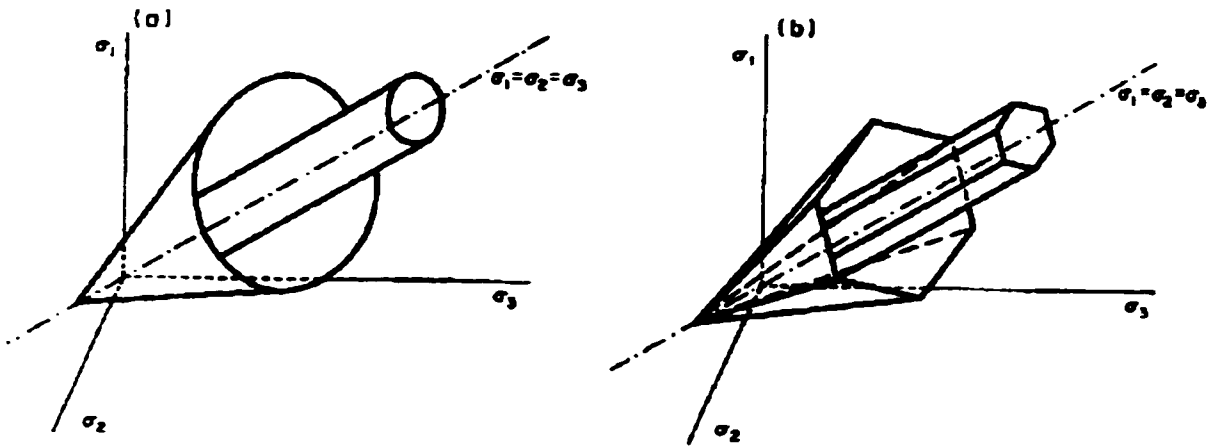


Figure 5.7: Typical yield criterion (modified after Cividini 1993) a) Drucker-Prager (outer) and Von Mises; b) Mohr-Coulomb (outer) and Tresca.

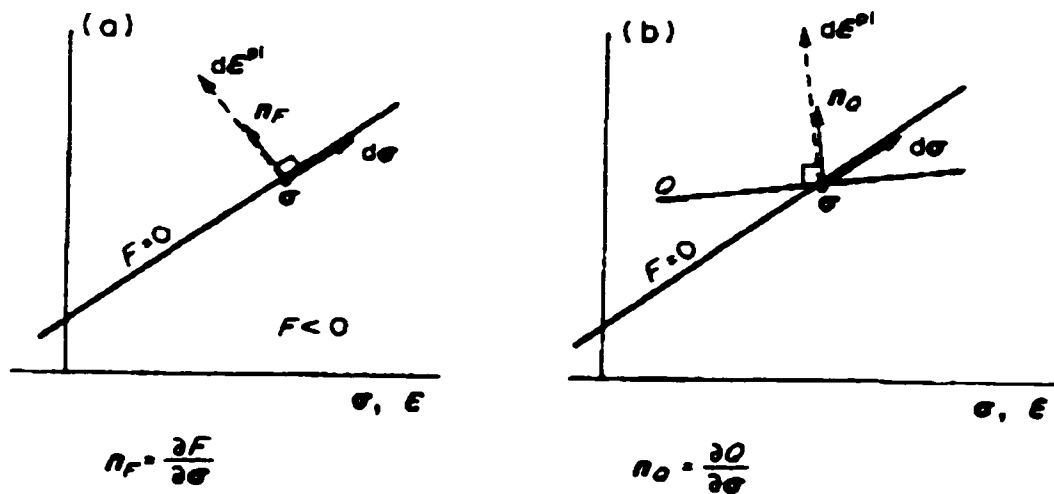


Figure 5.8: a) Associative and b) non-associative flow rules (Cividini 1993).

These constitutive formulations can, in their simplest form, be elastic-perfectly plastic. In the case of a Mohr-Coulomb criterion, this means that the residual values for cohesion and friction angle are constantly equal to the "peak" or initial yield values. This is clearly not the case in hard (brittle) rock environments which exhibit strain softening (Figure 5.9) at low confinements. Associated Mohr-Coulomb plasticity infers that dilation is the direct result of post peak shear through frictional sliding. Martin (1994) indicates that volumetric expansion (dilation) takes place before any appreciable internal shearing has occurred within the sample and that internal dilation in the initial stages of loading can be attributed to axial (aligned with the major compressive stress direction) extension cracking. This is consistent with the findings of Brace et al. (1966), Wawersik et al. (1970; 1971), Hallbauer et al. (1973), and Tapponier and Brace (1976).

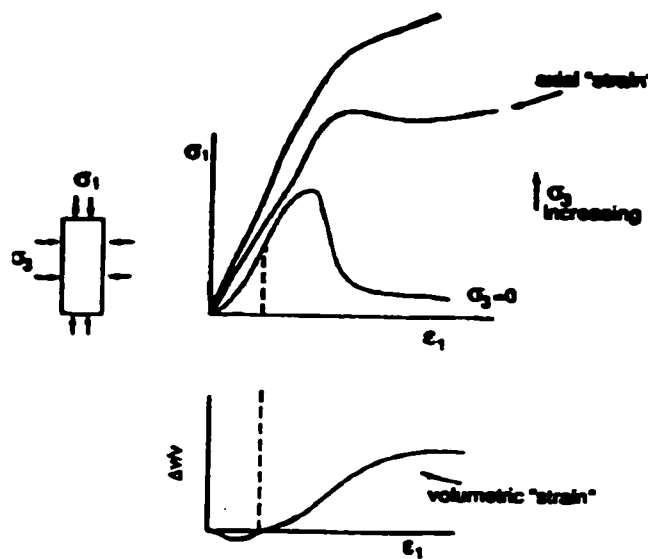


Figure 5.9: Post yield response as a function of confinement in rock (after Fairhurst 1990).

Strain softening models, which can in the extreme simulate complete (brittle) loss of cohesion, friction angle or tensile strength within an element, have been used with some success to model excavation response (Vasak and Kaiser 1995; Cundall 1994b). These "brittle continuum" models do not create for themselves the many new degrees of freedom of movement which arise as a result of fracture generation (Handley 1995). This shortcoming is the subject of a branch of bifurcation research (Vardoulakis and Sulem 1993) utilizing a Cosserat continuum model (Mulhaus 1993) to represent internal rotation within a model continuum. It is interesting to note that the philosophical basis of the Cosserat continuum (that strain localization is the result of internal rotational freedom) is similar to that realized in the micromechanical modelling in this thesis (although post yield response is not the focus of this work).

An interesting situation arises when dealing with strain softening models within discretized continuum domains. While the experimental evidence, detailed in the literature (Scholz 1968; Hallbauer et al. 1973; Lockner et al. 1992), and in micromechanical experiments contained in this thesis, indicates that strain softening is the result of strain localization, it can be shown that localization or shear banding in numerical models is a consequence (rather than a cause) of strain softening (Rudnicki and Rice 1975; Vermeer and de Borst 1984; Tang and Kaiser 1996). Because of this artifact, the nature and width of the localized regions of strain in discretized models become heavily mesh-scale dependent (Kuijpers and Napier 1996).

Fracture mechanics research based on the original work by Griffith on tensile (1921) and compressive fracture (1924) has, over the last few decades, yielded some glimpses of the essence of brittle rock damage and rupture. The basic premise is that small defects and heterogeneities within a macroscopic continuum such as rock (such as those revealed by Sprunt and Brace 1974; Fonseka et al. 1985), serve to concentrate stresses, inducing crack propagation (Figure 5.10), thereby inducing damage and rupture at stress levels well below the theoretical molecular strength of the material. A brief and by no means comprehensive overview is given here: a detailed history and state of the art review is contained in Atkinson (1987).

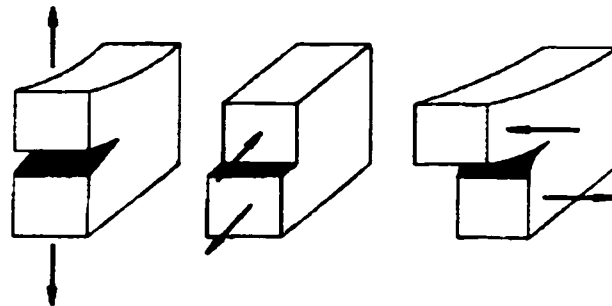


Figure 5.10: Crack modes considered in fracture mechanics (left to right: Mode I , II and III).

McClintock and Walsh (1963) modified the Griffith theory to account for compressive stress conditions in rock and the effect of friction on a closed crack. Brace (1960) showed that this derivation gave a yield criterion similar (in terms of the value of the frictional coefficient) to the empirically derived Mohr-Coulomb criterion for the rocks under investigation. While numerous experimental workers failed to observe sliding microcracks in rock specimens under varying degrees of loading (Brace et al. 1966; Wawersik and Brace, 1971; Hallbauer et al. 1973; Tapponier and Brace, 1976; Fonseka et al. 1985; Reyes 1991), and while experimental work (Brace et al. 1966) has attributed inelastic pre-rupture dilation phenomena to axial (extension) microcracking, the sliding crack model remains a popular tool for explaining rock behaviour.

In addition to damage and rupture studies, numerous researchers (Koiter 1961; Walsh 1965; Budiansky and O'Connell 1976; Kemeny and Cook 1986, 1987; Hudson et al. 1996) have related micro-deformability within distributed arrays of cracks to macro-elastic properties of the damaged material.

In spite of some significant success in explaining rock strength and deformation behaviour in the laboratory, fracture mechanics has not, however, resulted in a practically useable technique for failure prediction and behavioral modelling of field scale problems (Kuijpers and Napier 1996). The techniques arising from fracture mechanics research are primarily analytical and consider isolated or regularly distributed cracks of known geometry and scale. Within these constraints, fracture propagation and material response can be analyzed with limited success.

One shortcoming of linear elastic fracture prediction techniques is the assumption of material homogeneity within the sample (Kuijpers and Napier 1996). This is not only a limitation, but may be the key missing link in understanding the behaviour of polycrystalline rock. For example, while it is generally accepted that extension cracking under compression is a key component of material damage, fractures can neither nucleate, nor extend beyond several initial crack lengths without significant local inhomogeneity. In addition while fracture mechanics often considers the different crack modes separately, the actual fracturing can be extremely complex, even in controlled experiments (Figure 5.11).

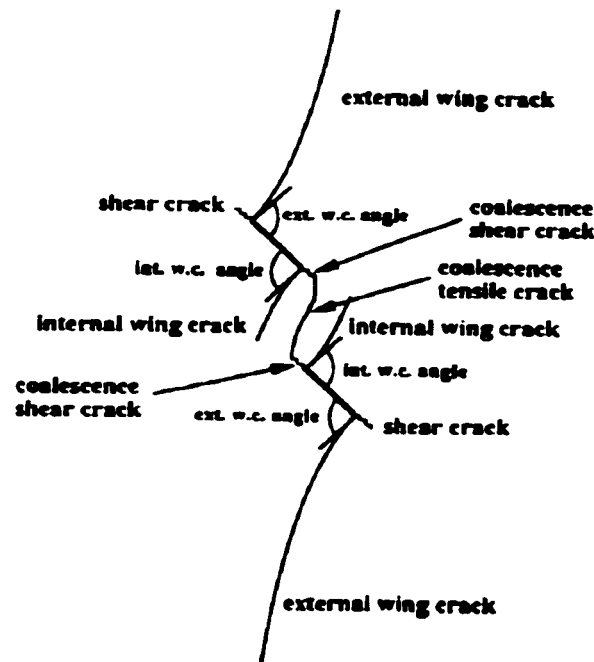
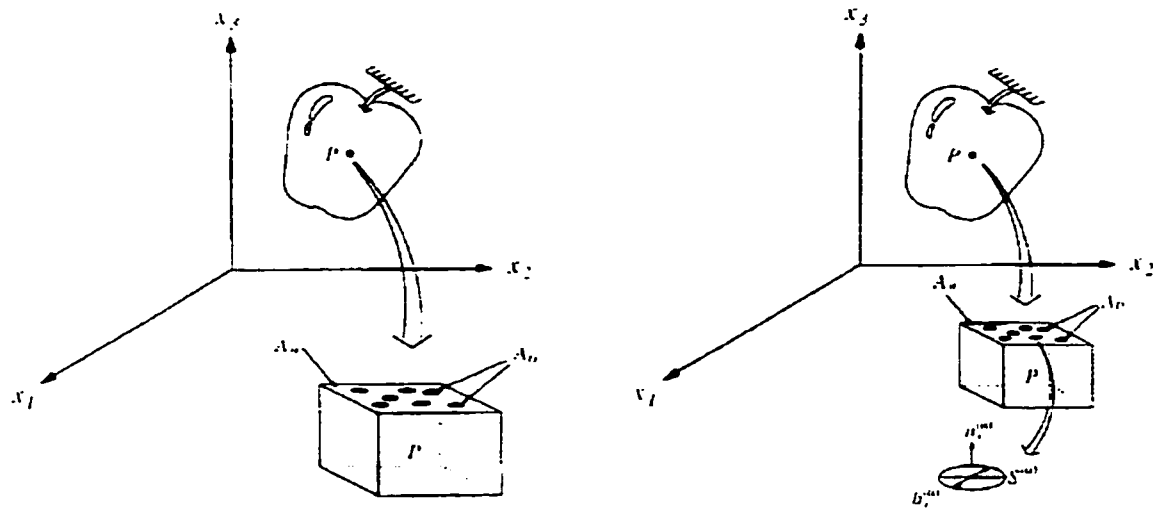


Figure 5.11: Multi-mode crack interaction (after Bobet and Einstein 1996).

Continuum damage mechanics is a field that takes aim at the larger scale problem of rockmass behaviour using the notion of distributed microscopic damage. These phenomenological models modify the mechanical properties of the material as functions of a damage variable (Figure 5.12). The evolution of damage can be based on thermodynamics principles or on mechanistic or physical models. The damage variable can be scalar and therefore limited to simulation of isotropic damage, or it can be a vector (Cheng 1994) or tensor quantity (Sellers 1994), capable of capturing the anisotropic nature of brittle rock damage (micro-cracking) under directed (deviatoric) loading.



$$D = \frac{A_D}{A} \quad \bar{\sigma}_{ij} = \frac{\sigma_{ij}}{1-D} \quad D_{ij} = \frac{1}{V} \sum_{k=1}^m S^{(k)0.3} \int_{S^k} n_i^k n_j^k dS^k \quad \sigma_{ij} = (I - D_{kl}) C_o \epsilon_{ij}$$

Figure 5.12: Scalar and tensor damage variables and examples of damage mechanics equations (after Cheng 1994; Kachanov 1980 and Sellers 1994).

The influence equations relating the degree of damage to mechanical properties are normally based on an equivalent damaged area and the consequential effective or net stress, or the effective stiffness of the non-damaged solid. This technique has been used to describe the influence on material behaviour of existing damage in the form of discontinuities and jointing (Oda 1982; 1983; Beichuan 1991; Kulatilake et al. 1996). The evolution of induced damage is a significant complication and one that often has arbitrary and controversial solutions. The evolution of damage can be defined as a function of stress and strain history using thermodynamic principles (Krajcinovic and Fonseka 1981; Cheng 1994) or through the incorporation of fracture mechanics logic (Costin 1983; 1985; Costin and Holcomb 1983).

Discontinuum modelling techniques developed for the analysis of jointed blocky ground (Cundall and Hart 1993) are of little use here, since joints of arbitrary orientation are normally clamped under high stresses minimizing their influence on excavation response.

Nevertheless, Handley (1995) adapted one such model to simulate the interaction of grains within a crystalline material (Figure 5.13). While the results were promising, his success was limited by the size of the problem and resultant boundary influences.

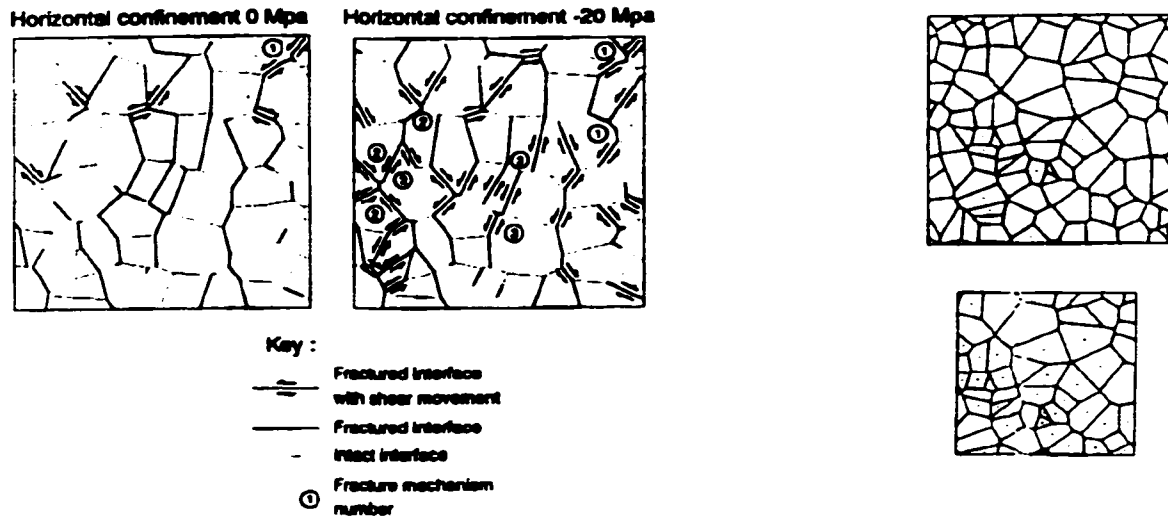


Figure 5.13: Discontinuum simulation of brittle rock failure (Handley 1995).

There is some promise in an approach by Napier and Hildyard (1992) using "self-fracturing" discontinuum models to simulate rock disintegration (Figure 5.14).

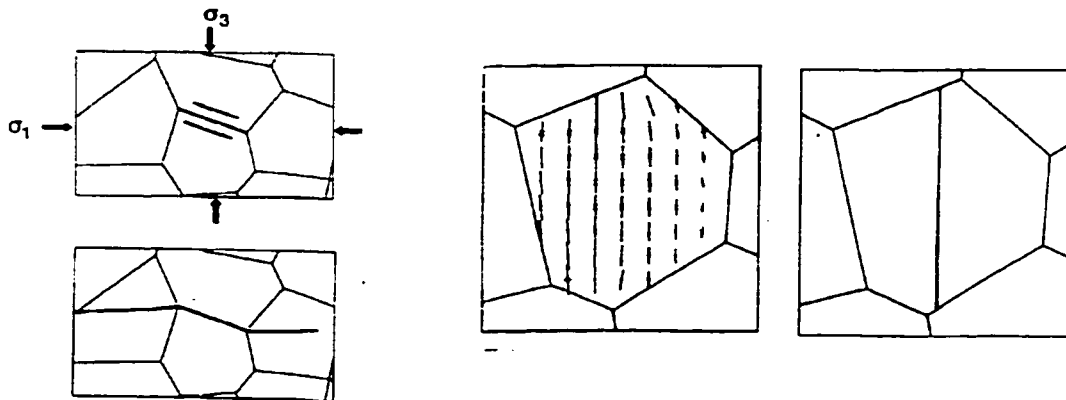


Figure 5.14: Displacement discontinuity simulation of rock fracture (Napier and Hildyard 1992).

A novel approach presented by Kaiser and Tang (1996) and Tang and Kaiser (1996) involves the construction of a matrix of micro-elements which are linear elastic in nature. These elements have non-uniform stiffness and yield strength. When the yield strength within an element is exceeded, the stiffness is dropped to some residual value (or to zero). The constitutive properties of each element are extremely simple and yet the macro behaviour simulated can be extremely complex. In addition the results match assumptions from fracture mechanics and exhibit realistic bifurcation behaviour (Figure 5.15).

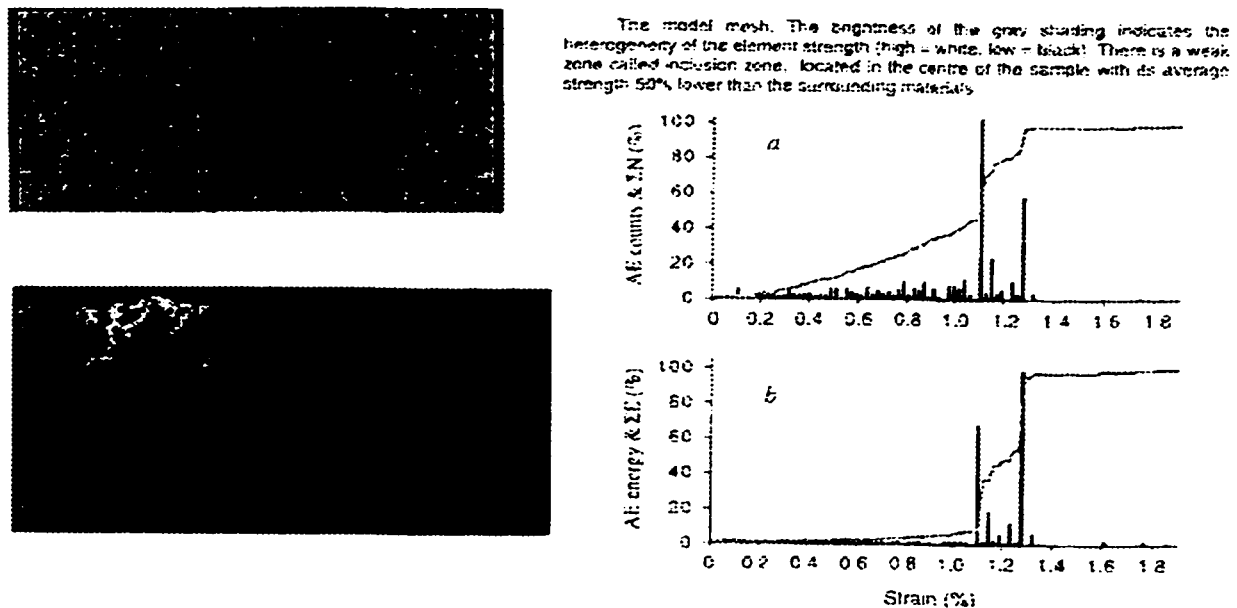


Figure 5.15: Numerical simulations incorporating material heterogeneity and a simplified two stage (intact - yielded) elastic element (Tang and Kaiser 1996).

The interesting point about this modelling work is that much of the complex behaviour observed in laboratory testing and in excavation response can be simulated with extremely simple micro-element behaviour, provided that heterogeneity is included in the model (Liu et al. 1994; Kuijpers and Napier 1996; Tang and Kaiser 1996).

Numerical experimentation in this thesis is based on the discrete element model. This technique dating back to work by Cundall (1978), and Cundall and Strack (1979), was originally developed for unbonded granular materials. Through the use of bonded contact logic, it can also simulate many of the micro-processes assumed to act in brittle rock under load. Internal contact structure leads to the generation of non-uniform extensile forces in an externally applied compressive stress field. Bonds can rupture in shear or in tension creating "cracks" within the bonded solid.

The evolution of micro-damage (crack tensor) can be tracked through the course of the simulation, and real average internal stresses and strains can be directly measured (not calculated from continuum assumptions). Heterogeneity can be introduced through particle size, contact strength, contact stiffness and internal particle rotation control.

The model chosen for this thesis work is a disc model, created using PFC-2D (Itasca 1995a). The model is composed of rigid discs with linear elastic contacts. An example assemblage is shown in Figure 5.16.

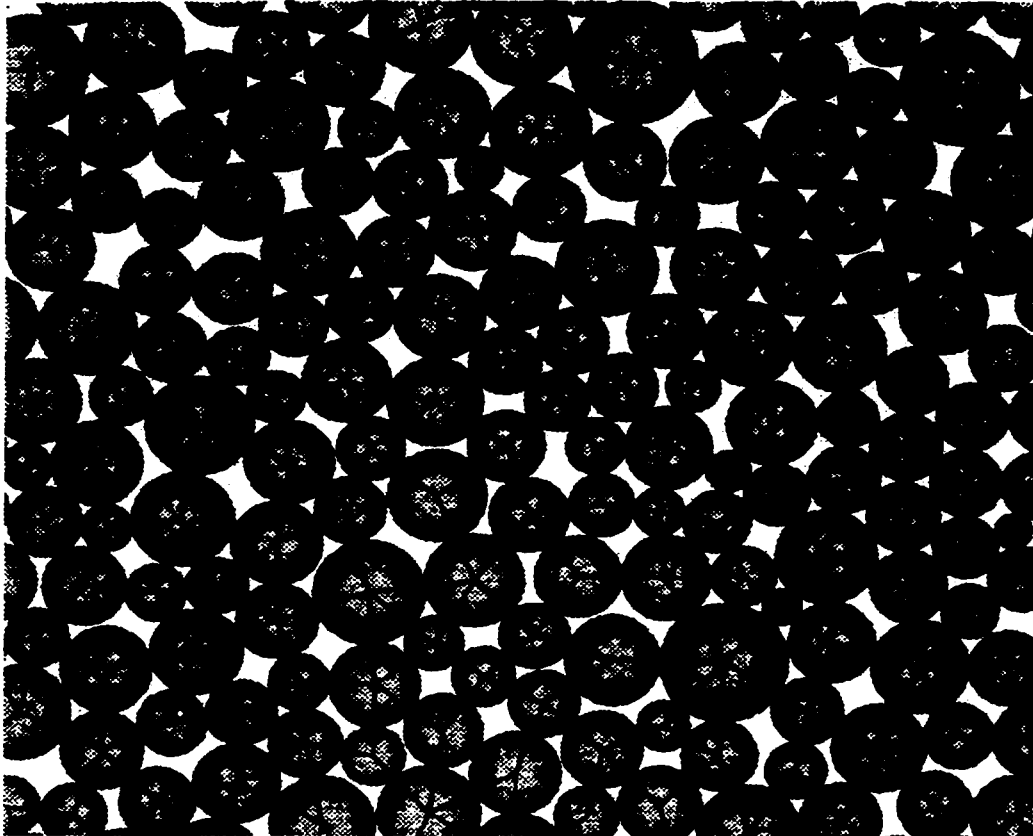


Figure 5.16: Example micromechanical assemblage with bonded contacts between discs.

Figure 5.17 shows the contact force map of a full-scale model of an experimental tunnel at the Underground Research Laboratory (Atomic Energy of Canada Ltd., AECL). The bonded disc model will be described in detail in Chapter 7. While such excavation scale models are possible, simulations in this thesis are restricted to simple laboratory test configurations in order to focus the study on the internal mechanics of damage accumulation, and on material heterogeneity effects.

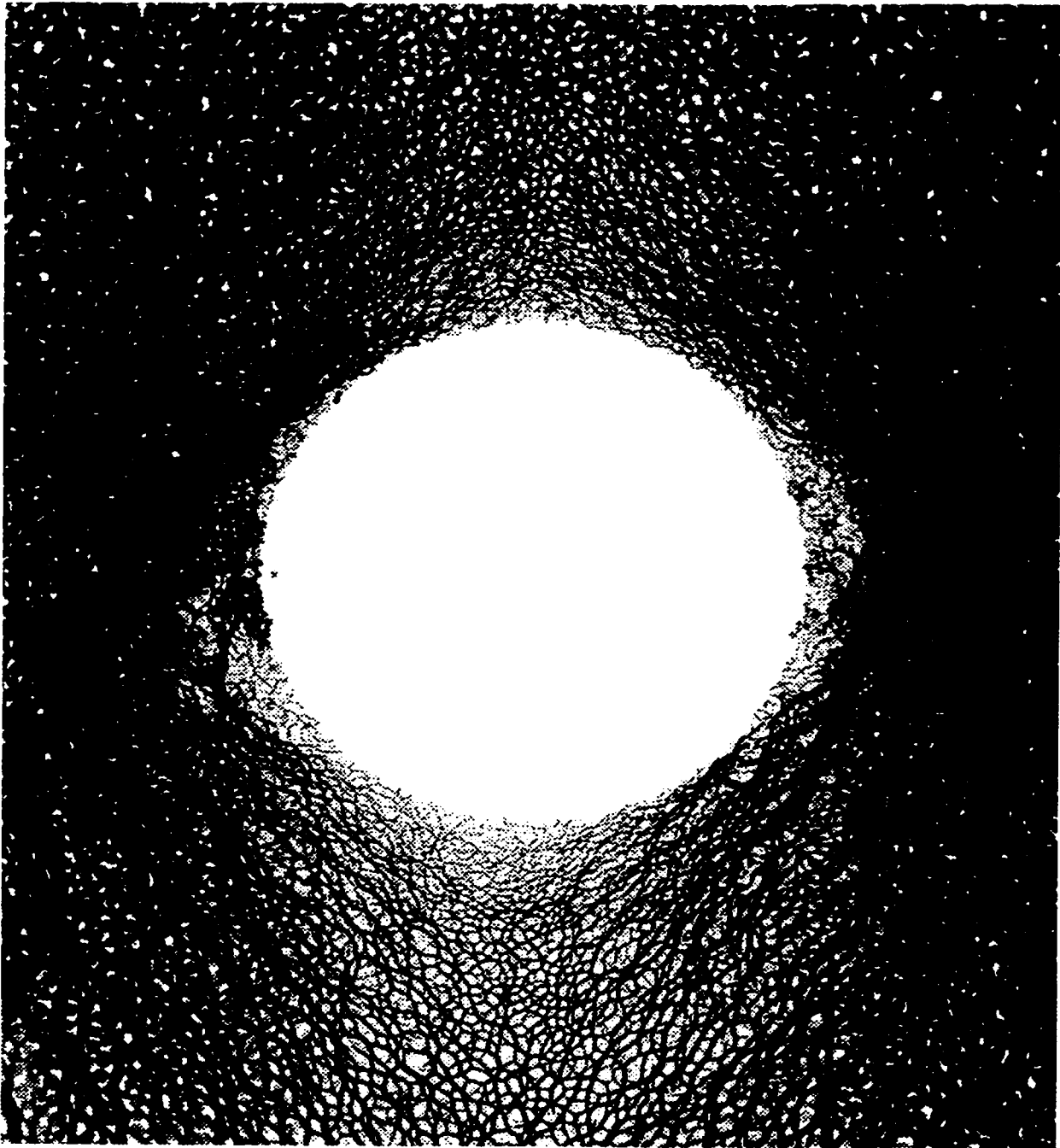


Figure 5.17: Contact and particle map from particle model (Potyondi et al. 1995) showing compressive forces (thick lines) flowing around circular opening (stress field sub-vertical with respect to page - tunnel rotated 90 degrees counterclockwise). Force -shadowed zones in roof and floor (left and right of opening in image above) sidewalls indicate areas of contact rupture and macro-failure.

5.3 INSITU STRENGTH OF COMPETENT ROCKMASSES

The uniaxial strength of rock and the strength-confinement (or σ_{1max} , σ_3) envelope obtained from the testing of laboratory samples are rarely representative of the rockmass strength around boreholes, tunnels and larger excavations. The strength of rockmasses insitu is almost always considerably less than the laboratory results would indicate. While this is not surprising for highly fractured, disturbed or heavily jointed or sheared rockmasses, it is also the case for apparently intact or massive to moderately jointed rock insitu. This latter class of rockmasses is the subject of this work.

5.3.1 Empirical Strength of Non-Massive Rockmasses

Insitu strength reduction has traditionally been explained as a scale effect. Larger samples contain more flaws while larger representative volumes of rock insitu contain macro-fractures, joints or inclusions which contribute to the reduction in strength (Hoek and Brown 1980).

In order to address this problem for a wide range of rock types and excavation conditions, Hoek and Brown (1980; 1988) and Hoek et al. (1995) developed a scaleable rockmass strength criterion, in which the base parameters of uniaxial compressive strength, UCS , m_i and s in the following equation for intact laboratory samples ($s_i=1$):

$$\frac{\sigma_1}{UCS} = \frac{\sigma_3}{UCS} + \sqrt{m_i \frac{\sigma_3}{UCS} + s_i} \quad [5.6]$$

are reduced to account for the presence of field scale joints and fractures and to account for insitu weathering and weakening of these structural components. The scheme also accounts for the softening effect of open and weathered joints. The recommendations for strength adjustment are summarized in Table 5.2.

A large percentage of the rockmasses currently hosting development for base metal mining at depth in the Canadian Shield fall into the top left category in Table 5.2. The value of the cohesion parameter, s , specified for this type of moderately jointed and undisturbed rockmass is 0.19, such that the insitu unconfined compressive strength is given by \sqrt{s} or 0.435 times the laboratory UCS . The frictional parameter m reduces to 0.6 times the intact value m_i . The strength envelope for such a rockmass, using values obtained for intact granite samples (Martin 1994), is shown in Figure 5.18.

Table 5.2 Adjusted Hoek-Brown strength parameters for rockmasses (modified after Hoek et al. 1995).

Joint Surface Condition		Very Good	Good	Fair	Poor	Very Poor
Barton's J_r/J_a		3 to 5	1 to 3	0.3 to 1	0.05 to 0.3	< 0.05
Rockmass Structure		rough clean tight	rough stained	smooth altered	slick weathered filled	very slick weathered gouge
Blocky $RQD/J_n > 7.5$	m / m; s	0.60	0.40	0.26	0.16	0.08
Very well interlocked, undisturbed rockmass consisting of cubical blocks: 3 orthogonal joint sets	E(GPa) v	75 0.20	40 0.20	20 0.25	9 0.25	3 0.25
Very Blocky $RQD/J_n = 0.25-7.5$	m / m; s	0.40	0.29	0.16	0.11	0.07
Interlocked, partially disturbed with polyhedral angular blocks formed from 4 or more joint sets	E(GPa) v	40 0.2	24 0.25	9 0.25	5 0.25	2.5 0.3
Extremely Blocky/Seamy $RQD/J_n < 0.25$	m / m; s	0.24	0.17	0.12	0.08	0.06
Folded and faulted with many intersecting discontinuities forming angular blocks	E(GPa) v	18 0.25	10 0.25	6 0.25	3 0.3	2 0.3

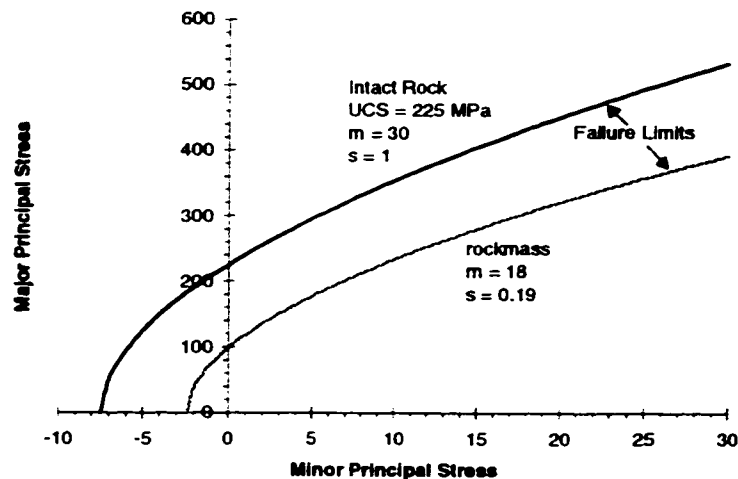


Figure 5.18: Hoek-Brown envelope for blocky, undisturbed rock (e.g. granite).

While this reduction in strength is explained by the presence and influence of joints, an extensively monitored and meticulously controlled excavation experiment at the Underground

Research Laboratory in Pinawa, Manitoba, has shown that the presence of joints or blast damage are not required for the insitu strength to fall well below the intact values (Martin 1994; Martin et al. 1997; Read et al. 1998). Observed damage was in the form of highly localized shearing and spatially dominant sidewall spalling. Insitu failure strength of massive non-jointed granite dropped to less than half of the intact rock strength around a test tunnel excavated using a non-explosive excavation technique. In addition, microseismic monitoring indicated a damage initiation threshold of less than a third of the *UCS*.

Similar observations can be made in rotary-bored ore passes and vent raises at depth in hard rock mines (Kaiser and McCreath 1993). There is also evidence that damage initiation in rockmasses at depth is not influenced by the presence of moderately spaced non-continuous and non-displaced jointing (Castro 1996; Castro et al. 1996).

Typically, the zone of spall failure is larger than and is not coincident with the failure predicted by the Hoek-Brown criterion (Martin et al. 1998). While this failure mode is expected in a massive rockmass with no significant jointing, it also dominates at depth in rockmasses with moderately dense and persistent jointing (Castro 1996). The value of $0.44UCS_{lab}$, predicted by Hoek et al. (1995) for field compressive strength, has been shown to be practically accurate for predicting the onset of boundary spalling, although the significant frictional component represented by $m=0.6m_i$ (Table 5.2 and Figure 5.18) is inconsistent with this mode of spalling damage (extensile compression parallel cracking) which would not appear to involve the frictional slip surfaces assumed in conventional plasticity.

5.3.2 Damage Observations in Hard Rocks

Numerous researchers (Fairhurst and Cook 1966; Hallbauer et al. 1973; Tapponier and Brace 1976; Fonseka et al. 1985; Martin 1994; and many others) have described the formation, in uniaxial and confined tests on hard rock, of parallel microcracks aligned with σ_1 . These cracks initiate at a level of deviatoric stress 1/4 to 1/2 of the rock rupture strength. At low stress levels, the cracks initiate within or at the boundary of the grains and propagate parallel to σ_1 to the next nearest grain boundary (Figure 5.19). At higher stress levels exceeding, for example, at about 0.7 *UCS* in the uniaxial case, these cracks extend beyond the grain boundaries and coalesce to form long axial cracks (only at low confinements) or a through-going shear rupture.

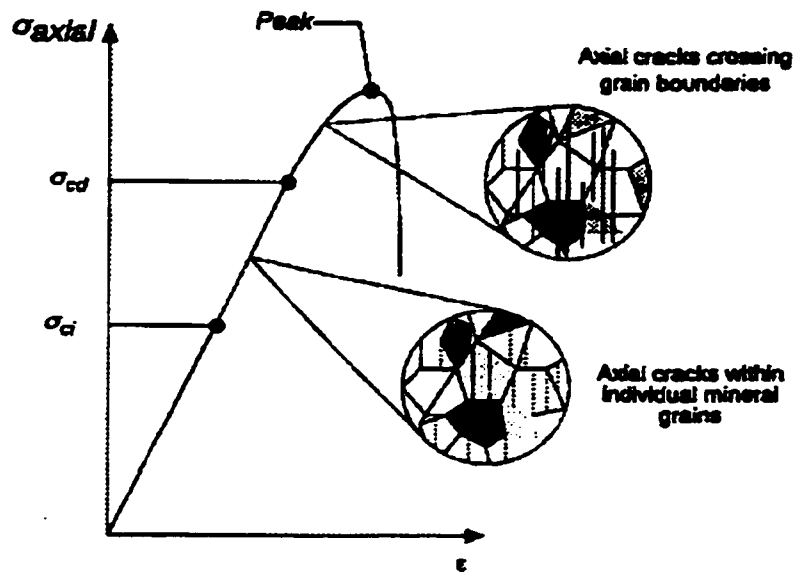


Figure 5.19: Progressive axial crack damage in laboratory samples (Martin 1994).

The non-linear portion of the stress-strain curve (Figure 5.19) above the critical crack damage stress, σ_{cd} (>0.65 to 0.8 UCS), has been shown (Lockner et al. 1992) to involve crack interaction and eventually mesofracture localization. The crack damage threshold, σ_{cd} , is associated by Bieniawski (1967) and by Martin (1994) with the point of volumetric strain reversal in axisymmetric testing (Figure 5.20) and to the long-term strength of the material.

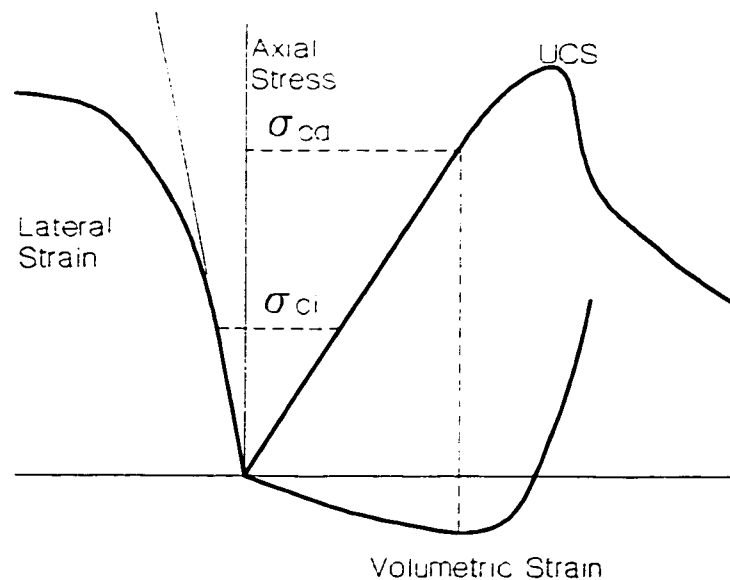


Figure 5.20: Measurement of crack initiation and crack damage thresholds for hard rock.

Martin (1994) and Brace et al. (1966) show that for slow loading rates, failure of uniaxial samples occurs at 70 to 80% of the normal loading strength. The 80% UCS threshold also corresponds to the lower bound of peak strength which is approached as the cylindrical sample size is increased, while the long-term strength of granite decays to 65% of the standard UCS for static loading in wet conditions (as in Figure 5.4).

The σ_{cd} threshold, shown as a function of confinement by Read et al. (1998) in Figure 5.21, could be called the yield strength of rock. Strain hardening beyond this point is a result of friction mobilization and dilational resistance and is therefore only present if fracture contact is maintained (by crack normal stress sufficient to ensure microcrack closure throughout the yield process). It will be shown in this thesis that the true yield strength, defined by non-linear axial stress-strain response and indicative of crack interaction and a critical crack accumulation intensity, is coincident with σ_{cd} (volumetric strain reversal), but possesses a much shallower slope with respect to confinement (i.e. $m= 10$ to 15 for Hoek-Brown).

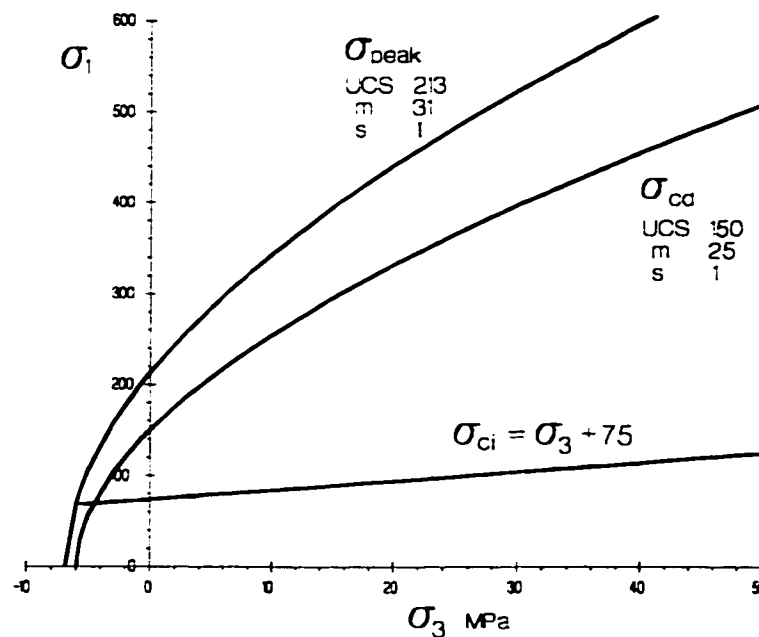


Figure 5.21: Typical (Hoek-Brown) envelopes for peak, critical damage σ_{cd} , and crack initiation σ_{ci} , for granite, after Read et al. (1998).

σ_{ci} in Figure 5.21 is the threshold range identified by Martin (1994) for crack initiation and is identified from acoustic emissions (Holcomb and Costin 1986; Pestman and van Munster 1996) or from the point of non-linearity of lateral strain readings as suggested by Brace et al. (1966) and illustrated in Figure 5.22.

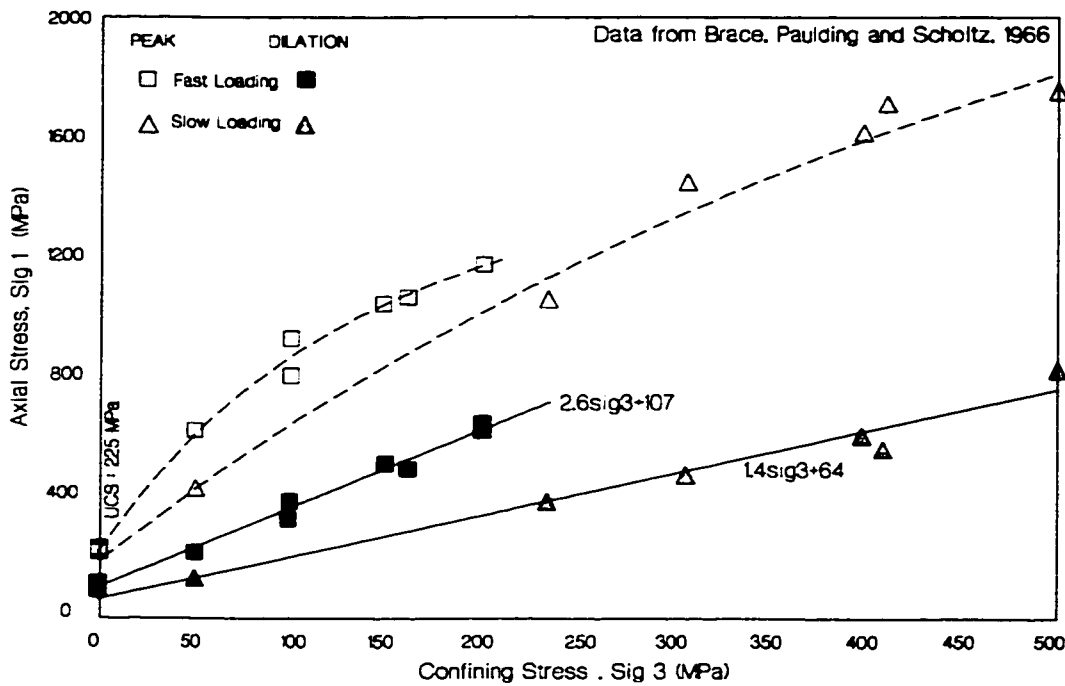


Figure 5.22: Peak strengths and *detectable* damage initiation thresholds (onset of dilation) for slow and fast loading of Westerly Granite.

In the laboratory, it is apparent that σ_{cd} , the long-term strength or the strength of the rock at slow loading rates, is probably a more accurate indicator of rock strength for engineering applications. The ratio of σ_{cd} to UCS in the case of granite, however, is not low enough to explain the much reduced insitu strength of reasonably intact or massive hard rockmasses (Martin 1994). The insitu strength is often closer to the threshold for crack initiation and accumulation which is observed to be around 0.4 times the laboratory UCS in unconfined conditions. The observed confinement dependency is given by Equation 5.1 with the lower bound slope (onset of low level acoustic emissions in laboratory tests) shown in Figure 5.21.

As illustrated in Figure 5.19, the initial damage accumulation parallel to σ_1 , at axial stress levels below 0.7 UCS , has little effect on the stress-strain characteristics (the stiffness) in the axial direction. In the field, this allows damage to accumulate in what are essentially elastic conditions parallel to the excavation boundary. The rockmass may, however, suffer a directional degradation in compressive and tensile strength or stiffness in directions other than that of the initial damaging load. Subsequent relaxation (Chapters 2 and 4), changes in loading direction, or localized shear nucleation (e.g. at corners) can lead to catastrophic collapse or buckling of the slabs defined by this damage (Aglawe 1999).

There is empirical evidence (Castro 1996; Martin et al. 1998) which strongly suggests that in deep underground excavations, induced damage leading to back failure and in massive and moderately jointed rock, can be directly linked to a crack initiation threshold (deviatoric stress limit from elastic analysis) for the wall rock. Hence, this apparent strength threshold seems to be associated with a property of the intact rock rather than a composite property for the rockmass.

In other words, for near-excavation conditions, crack initiation (measured from intact rock samples) represents a reliable lower bound for insitu rockmass yield strength. The ultimate extent of damage around underground openings can be predicted by comparing elastic stress contours to a deviatoric stress limit, corresponding to a crack initiation (or systematic accumulation) threshold. This is further demonstrated in Section 5.4.

If this empirical criterion, and the elastic analysis approach that accompanies it, can be mechanistically verified, it could be used with confidence for future analyses. This would be a valuable addition to the mining engineer's toolkit, since the complex geometries involved are often an impediment to economical non-linear analysis. Elastic boundary element techniques are popular due to the ease of geometric modelling, discretization and updating as well as the low solution times (as compared to domain discretization methods and non-linear solutions).

A simple and effective predictive tool for damage extent is an excellent compliment to these models, provided that such an approach is supported by a verified mechanical rationale (as opposed to pure empiricism). Through a study of damage initiation, accumulation and interaction, such a verification is a focus of Part II of this thesis.

5.3.3 Insitu Crack Initiation

In the case of monotonic loading in the lab, axial cracks initiated at low stress levels do not appear to influence the ultimate strength of the rockmass and are indeed a fundamental component of the behavioural sequence which defines the laboratory strength. The critical crack intensity that results in crack interaction and yield (a threshold measurable in the lab), is the result of these very axial microcracks. Why then, should insitu rock strength be coincident with, or only slightly higher than, the threshold of crack initiation in the field (i.e. at less than one half of the laboratory strength even in the absence of joints)? A number of contributing factors can be at work here, including:

1. Well-formed parallel slabs may fail through buckling at compressive stresses much lower than those required for shear (curvilinear slabs in cylindrical laboratory samples have less buckling potential). This phenomenon was investigated by Aglawe (1999).
2. Initial extension cracks (precursors to slabbing) may be exploited by small, localized regions of high shear stress and rupture such as at corners, creating a region of observed failure which extends far beyond the predicted shear rupture.
3. It is easier for a nucleated shear rupture to propagate through a systematic network of parallel microcracks adjacent to the surface of a tunnel, than through an equally dense biaxially isotropic or circumferential network of σ_1 -parallel cracks in a cylindrical sample.
4. Significant microcracking results in a reduction in tensile strength perpendicular to the excavation, creating conditions that can be exploited by gravity in larger spans.
5. In situ stress paths for typical excavations include significant stress rotation and promote the creation of microcracks oblique to the direction of ultimate compressive loading, thereby weakening the rock.
6. Small fractures and non-persistent joints, while not affecting crack initiation, serve to promote larger scale propagation of newly induced cracks, by creating a larger scale of heterogeneity than that created by the grains of the polycrystalline rock.
7. Boundary parallel cracks and joints dilate, reducing the effective confinement in the surrounding rock. Crack damage can move the effective $\sigma_3=0$ boundary away from the boundary, extending the conditions of unconfined loading and reducing the apparent strength below that predicted using continuum confinement calculations.
8. Small cracks increase the porosity of the rockmass and allow moisture and airborne chemical agents to penetrate, resulting in stress corrosion and strength reduction.

The first four points address the geometry of cracks formed at low to moderate stress levels. Figure 5.23 illustrates typical fracture patterns generated within a cylindrical uniaxial test sample and at the surface of an underground rock pillar. These examples have been selected because the stress paths are reasonably similar since the mine pillar typically experiences a monotonic load increase after formation due to progressive mining away from the pillar. It is suggested here

(Point 3 above) that the slabs shown in Figure 5.23b are more kinematically unstable and less affected by geometric constraints than the curvilinear husks in Figure 5.23a.



Figure 5.23: a) Cylindrical slabs from uniaxial test specimen (Ormonde and Szwedzicki 1993); b) planar slabs through pillar (Brunswick Mine - courtesy P. K. Kaiser).

Even in cases of shear propagation, such geometrical factors affect both the stress level required for cracks to interact (σ_{cd}) and the strength generated by dilation as the shear surface forms through the sample (σ_{peak}).

In addition parallel slab propagation in the flat and subhorizontal back of an excavation creates a rockmass susceptible to gravitational forces, abutment relaxation and tensile rupture as discussed in Chapters 2 and 4. Ultimate failure of the wall rock insitu (through sloughage, buckling, beam collapse or shear) may therefore be more closely associated with damage initiation stress levels than in the laboratory sample.

Point 6 addresses the observation that, in tunnels excavated in highly deviatoric insitu stress fields, the damage may not be parallel to the ultimate excavation profile due to rotation, during tunnel advance, of stresses close to the damage initiation threshold. This will result in a higher density of cracks as well as cracks that are obliquely aligned to the direction of ultimate loading. This type of oblique damage has been observed to significantly reduce the peak shear strength of the rock (Read et al. 1998). Stress rotations of 20 degrees or more are not uncommon in

tunnelling (Abel and Lee 1973; Martin 1994) and have been observed in excess of 45 degrees in mining excavations (Kaiser 1994; Kaiser et al. 1999).

The damage incurred during these stress rotations can effectively reduce the peak long-term strength to a lower bound defined by the crack initiation threshold. Localized shearing can create a catalyst for larger scale slabbing in the surrounding damaged rock, propagating failure beyond the limits predicted by a purely shear-based criterion. This process is described by Martin et al. (1997) and is illustrated in Figure 5.24 (and also in Figure 5.3a).

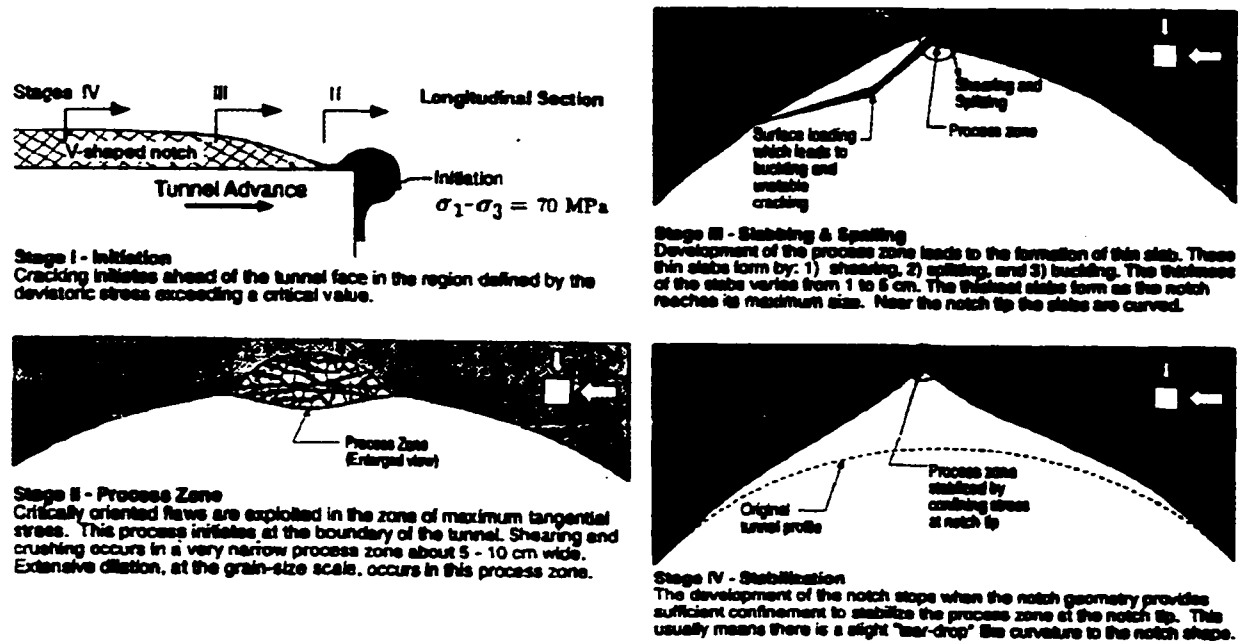


Figure 5.24: Notch development as a process of crack damage, localized shear (at reduced strength) and exploitation of damage through dilation and slab formation (Martin et al. 1997).

Points 7 and 8 are illustrated in the experimental findings of Hoek (1968), and in the calculations of Martin (1997) shown in Figure 5.24, which show that the extension of cracks are proportional to the size of the initial nucleating flaw and inversely proportional to the confining pressure perpendicular to the propagating crack. While crack initiation can theoretically occur at any level of confinement, given sufficient deviatoric stress. Figure 5.25 shows that the significance of extensile cracking becomes highly magnified near an excavation boundary where the ratio of σ_3/σ_1 drops below 0.05.

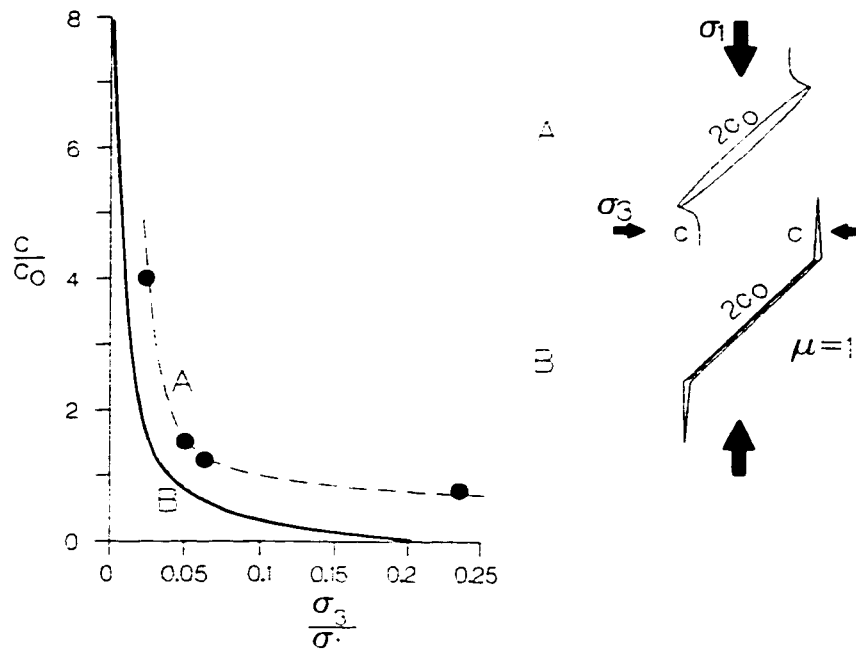


Figure 5.25: Effect of confinement on crack propagation length, c , with respect to initial flaw half length, c_0 , based on (A) experimental data for an open crack (Hoek 1968), and (B) a sliding crack relationship calculated by Martin (1997).

This confinement dependence of crack propagation length is key to an understanding of field observations of damage in underground excavations. Damage which may appear severe at the exposed tunnel wall (Figure 5.26) may quickly dissipate into the rock (away from the opening) due to the crack extension constraints illustrated in Figure 5.25. This stress gradient effect is investigated in Chapter 8.

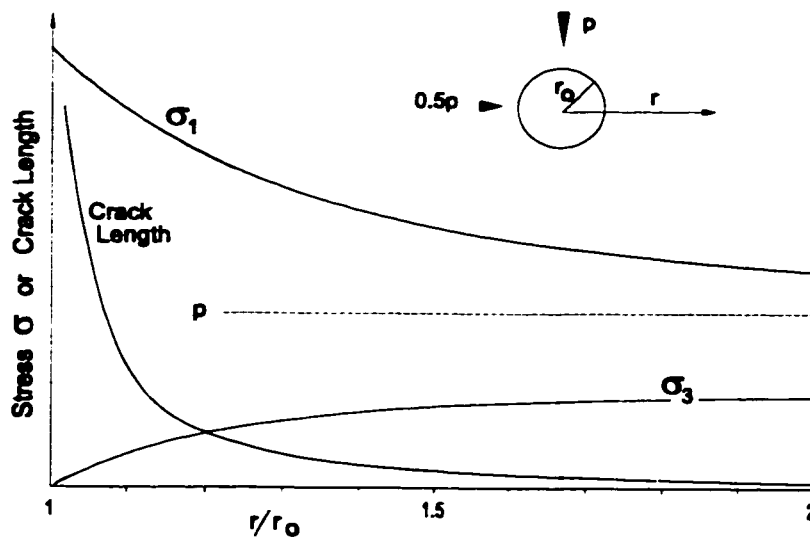


Figure 5.26: Effect of stress gradient on damage zone (schematic)

Cracks which initiate at low stress levels tend to dilate, in effect creating reduced confinement in the immediate region around the crack, exacerbating the impact of low confinement on further crack initiation and propagation (i.e. by reducing the effective σ_3 within a damaged rockmass below that predicted by continuum analysis). This concept (P.K. Kaiser, pers. comm.) is illustrated in Figure 5.27 and is discussed further in Chapter 8.

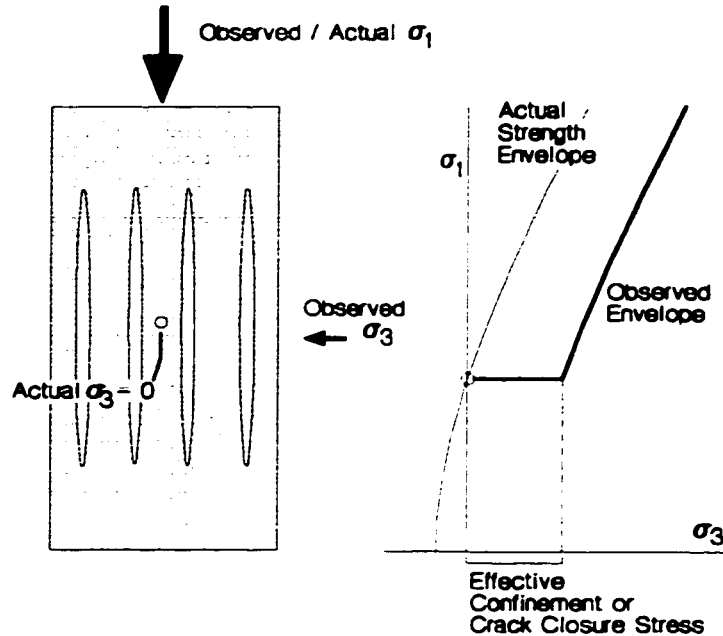


Figure 5.27: Schematic of effective confinement (or effective gap) concept. ("Crack closure stress" = σ_{30})

Finally, as noted in point 9 and illustrated in Figure 5.28, it is widely recognized that humidity plays a significant role in reducing the Mode I surface energy (Simpson and Fergus 1968; Parker 1970; Wiid 1970; Weiderhorn et al. 1982; Diederichs 1987) and therefore the extension crack propagation resistance. In underground hard rock environments, the micro- and meso-crack damage initiated at low deviatoric stress levels increases the penetration of moisture and chemically laden air into the rockmass. This allows moisture penetration to most critical areas (i.e. the crack tips) resulting in stress corrosion, a time and stress dependent reduction in rock strength, and ultimately, delayed failure. In Figure 5.28, it is interesting to note that the sample strength has dropped within range of the expected crack initiation threshold (50% of UCS). This suggests that cracks, once initiated, undergo crack propagation in the presence of humidity and without additional applied stress, resulting in premature failure nearly coincident with the initiation threshold.

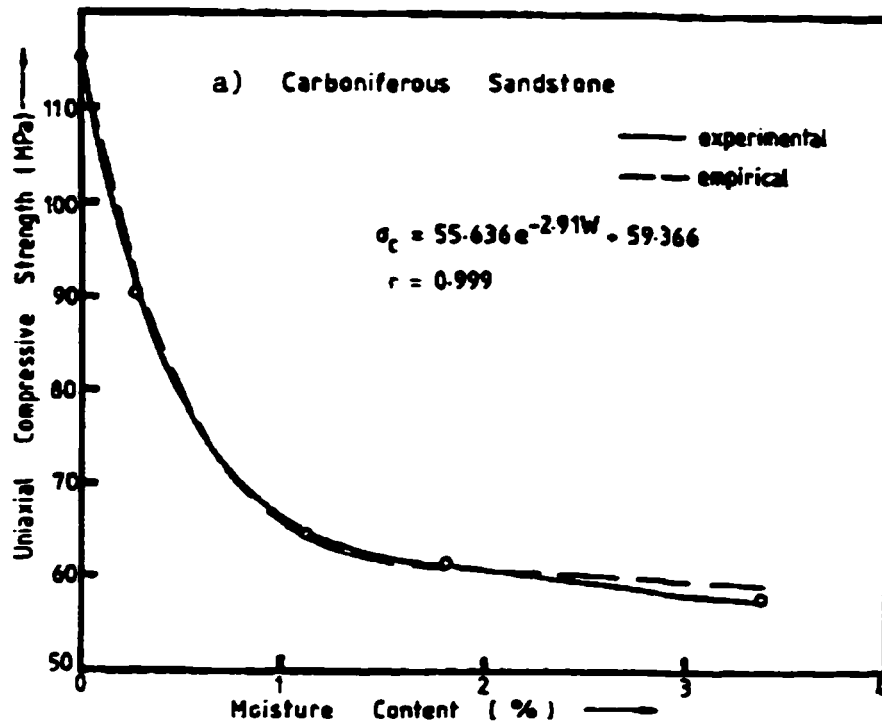


Figure 5.28: Reduction of strength due to humidity (from Priest and Selvakumar, 1982).

In massive to moderately jointed rockmasses, these mechanisms work in combination to reduce the insitu failure strength of the rockmass towards the lower bound predicted by the damage initiation threshold for the intact rock. These mechanisms will be examined in detail in Chapter 8 of this thesis.

It is important to first identify the damage initiation threshold. At stress levels below this threshold, only elastic-stress related behaviour will be of practical significance. Above this limit, however, new cracks begin to form and existing cracks may propagate. Yield occurs when single cracks propagate in an unstable fashion or extending cracks interact with one another. Crack initiation and crack interaction are the focus of Chapters 6 and 7.

5.3.4 Crack Initiation Thresholds

In uniaxial conditions, it has already been stated that crack initiation occurs at a compressive stress level equivalent to 1/4 to 1/2 of the uniaxial strength, depending on the rock type, of the intact specimen. It has also been suggested through field observation and laboratory

experimentation that this damage threshold, formulated as a deviatoric stress limit, is insensitive to confining stress (Martin 1994):

$$\sigma_1 - \sigma_3 = 0.4(\pm 0.1)UCS_L \quad [5.7]$$

This empirical finding, corresponding to the Tresca Criterion developed for (ionic) metals and to the undrained failure envelope of a clay, has practical significance for rock engineering, although it is not mechanistically sound for covalent solids such as hard rock as discussed in Chapter 6. In poly-mineralic rock and similar materials, it is difficult to imagine that pure dislocation shear (a dominant mechanism in yield of metals and creep of ionic solids such as salt) is the dominant mechanism of damage.

The observational evidence (Griffith 1921; Tapponier and Brace 1976; Stacey 1981; Myer et al. 1992; Lee and Haimson 1993) suggests that the initial damage process is one of extension crack initiation and propagation, a predominantly tensile and confinement dependent (although non-frictional) phenomenon. While extensile cracking is recognized as the sole process of tensile failure in most non-metallic solids (metal crystals can fail under tension purely via dislocation slip (Illston et al. 1979)), the process is also a necessary precursor to compression induced shear rupture in polycrystalline covalent solids, such as hard rock, where slip dislocation is not prevalent (Lockner et al. 1992). This is discussed further in Chapter 6.

In uniaxial conditions, a crack initiation threshold stress equivalent to $1/3UCS$ for igneous rocks (Lajtai and Dzik 1996) and up to $1/2 UCS$ for clastics has been identified (Pestman and van Munster 1996). If damage begets damage, it is possible that each progressive front of crack damage is initiating in a uniaxial stress field, caused by crack dilation in the previous and immediately adjacent damage zone, or by the opening of boundary parallel joints. This would result in a damage threshold:

$$\sigma_1 = A \cdot UCS \quad [5.8]$$

with A being a constant (0.3-0.5). This criterion would be horizontal in $\sigma_1:\sigma_3$ space. It is likely that such a criterion would be valid only in the immediate vicinity of an excavation, as a finite external confinement would result in closed cracks. Alternatively, taking into account the confinement, σ_{3o} , required to close all cracks (Figure 5.27), Equation 5.4 represents the initiation threshold for $\sigma_3 < \sigma_{3o}$, and the strength for $\sigma_3 \geq \sigma_{3o}$ can be approximated by (P.K.Kaiser, pers. comm. 1993):

$$\sigma_1 = A \cdot UCS + B(\sigma_3 - \sigma_{3o}) \quad [5.9]$$

where B is a constant >1 .

Numerous researchers have identified damage initiation surfaces in $\sigma_1:\sigma_3$ space which have slopes ranging from 0 to 2 (Brace et al. 1966; Pestman and van Munster 1996) indicating a more significant confinement dependence than that suggested by Martin (1994).

Concrete design guidelines developed by Hobbs et al. (1977) suggest a serviceability limit for concrete that takes the form:

$$\sigma_1 = 0.3UCS + 2\sigma_3 \quad [5.10]$$

and an ultimate stress limit (installed concrete) of:

$$\sigma_1 = 0.45UCS + 3\sigma_3 \quad [5.11]$$

According to (Illston et al. 1979) stress can be cycled ad nauseum below the threshold in Equation 5.6 with no detrimental effects on the concrete performance. Of significance in this limiting stress surface corresponding to the onset of damage, is the intercept of $0.3UCS$ and the slope of 2 with respect to confining pressure; both values reflective of hard rock. Similarly, the ultimate insitu stress limit (Equation 5.7) is similar to that which is found to be applicable for crack interaction and yield in hard rock environments as illustrated in Chapters 6 and 7.

Based on the concept that material flaws, in particular existing open microcracks, can lead to direct failure in tension, and to extensile crack propagation and presumably failure in compression, in both cases parallel to the direction of maximum compression, Griffith (1921) proposed the Griffith criterion for compressive strength which is more appropriately used as a extension crack initiation criterion for compressive loading:

$$(\sigma_1 - \sigma_3)^2 = 8\sigma_t(\sigma_1 + \sigma_3) \quad [5.12]$$

The criterion expresses the rock crack initiation strength as a function of the tensile strength, σ_t .

Stacey (1981) stated that insitu strength around excavations was, as a lower bound, determined by the extension strain capacity of the intact rock (e.g. $\epsilon_{critical}=0.0025$ for granite (Stacey and Page 1986)). As such, the compressive strength can be related to the strain limit, Poisson's ratio and the confining stresses:

$$\varepsilon_{cr} = \frac{1}{E} [\sigma_3 - \nu(\sigma_1 + \sigma_2)] \quad [5.13]$$

which converts, for axisymmetric confinement to:

$$\sigma_1 = -\frac{E\varepsilon_{cr}}{\nu} + \left(\frac{1-\nu}{\nu}\right)\sigma_3 \quad [5.14]$$

where ε_{cr} is the extension strain and is of negative sign. Discussions in Chapters 6 and 7 suggest that this criterion is better suited to crack interaction and yield in laboratory samples, rather than to crack initiation as normally assumed.

While not all are necessarily appropriate, these various initiation criteria are illustrated in Figure 5.29 for Lac du Bonnet granite. Axisymmetric confinement and axial loading is assumed. The peak strength envelope, determined from laboratory studies, is shown for comparison.

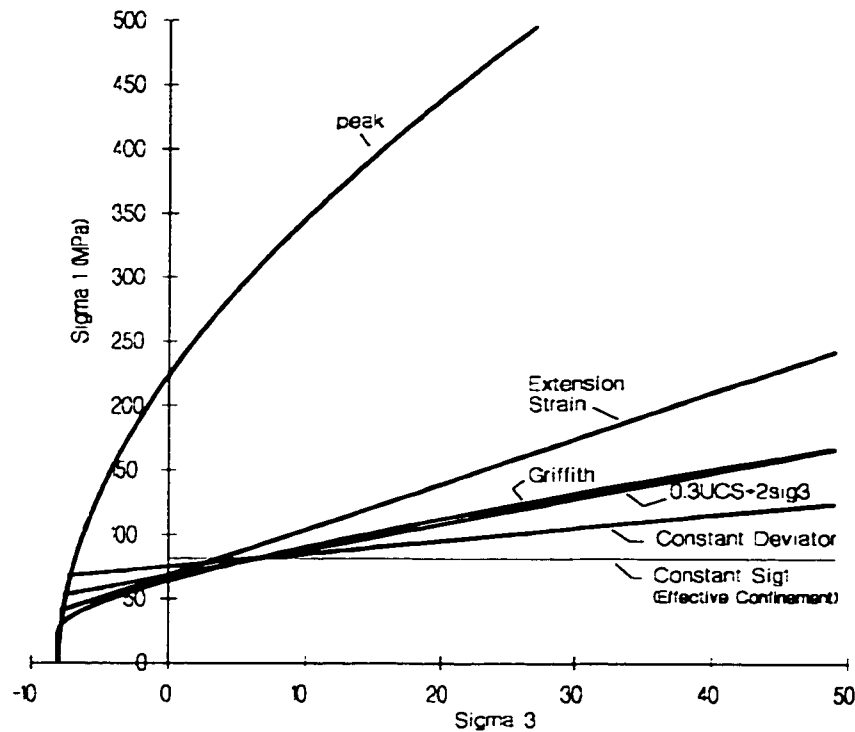


Figure 5.29: Summary of potential damage initiation criteria for Lac du Bonnet granite.

Field evidence, from established empirical relationships and specific case studies, supporting the use of a lower bound strength criterion related to stages of crack initiation and accumulation, will be presented in the next section.

5.4 EMPIRICAL EVIDENCE OF INSITU DAMAGE THRESHOLD

This section includes numerous examples, from the literature and from the author's experience, which demonstrate the applicability of an insitu strength criterion corresponding to a lower bound yield strength limited by crack initiation requirements.

5.4.1 Damage Around Square Openings ($\sigma_3/\sigma_1 = 0.5$)

Ortlepp et al. (1972) examined square tunnels of varying depth in the gold mines of South Africa. They noted that when the far field major principal stress (in this case approximately equal to $\gamma \times h$) was greater than 0.2 times the uniaxial compressive stress of intact rock, sidewall spalling would begin to occur. Cook (1972) also showed that for South African conditions, the value of the vertical field stress (σ_1 in this case) is sufficient to predict the extent of damage, and failure around typical mine openings becomes significant at around $\sigma_1 = 0.25 UCS$, and becomes unduly costly and practically unsupportable when $\sigma_1 > 0.5 UCS$.

Hoek and Brown (1980) examined additional cases of observed damage and failure in similar environments. In addition they added other stability classifications based on the ratio of far field stress to uniaxial compressive stress. These stability predictions are illustrated in Figure 5.30. Castro (1996) compiled other cases to illustrate the continued usefulness of this index chart.

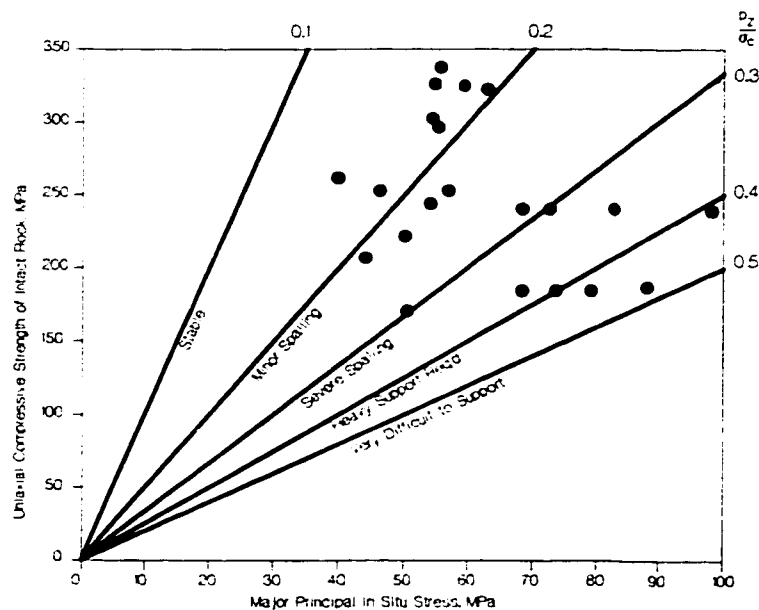


Figure 5.30: Stability classifications according to Hoek and Brown (1980).

In most of these cases, the excavations were approximately square and were between 3m and 4m wide. In addition the major compressive stress was vertical and the horizontal stress ratio ($k = \sigma_{horizontal} / \sigma_{vertical} = \sigma_h / \sigma_v$) was approximately 0.5. These stability predictions are also valid for square openings in the conditions of the Canadian Shield, although in these environments, far field σ_1 is horizontal and, below 100m, $\sigma_3 = \sigma_v = 0.3$ to $0.7 \times \sigma_1$, the ratio approaching unity at great depth (Arjang and Herget 1997). The chart in Figure 5.30 is not, however, directly applicable to openings of arbitrary shape.

As suggested by Wiseman (1978; 1979) and then adopted by Kaiser et al. (1996) and later by Martin et al. (1997), it may be more appropriate to equate these classifications to an equivalent maximum (compressive) boundary stress. For circular openings the normalized boundary stress (σ_1/UCS) is given by:

$$\frac{\sigma_1}{UCS} = \frac{(3-k)\sigma_{1ff}}{UCS} \quad \text{where } ff \text{ indicates far field} \quad [5.15]$$

The stresses around a square opening are more complex to evaluate, since a perfect square opening will have a compressive stress singularity at each corner. The principal stress distribution around a square opening in the conditions assumed in Figure 5.30 are shown in Figure 5.31.

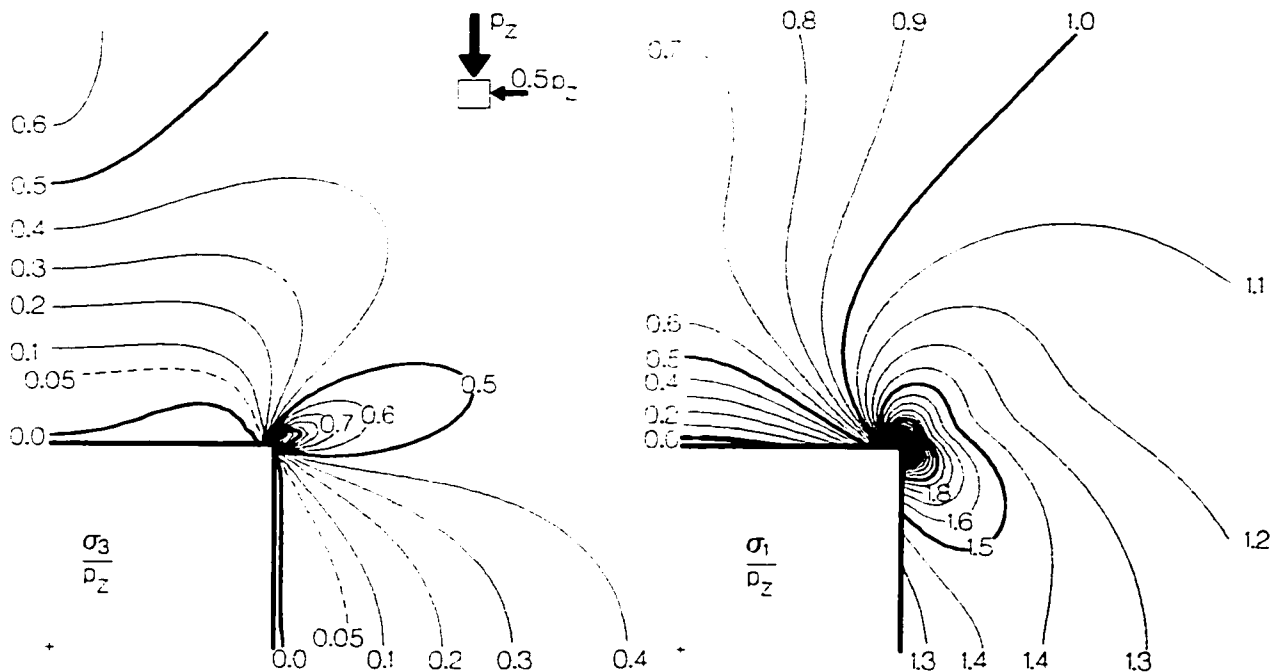


Figure 5.31: Principal (elastic) stress distribution around a square opening with $k = 0.5$.

Figure 5.31 is based on the results of an elastic boundary element program Examine^{2D}. Using this approach, the stresses around the boundary can be accurately determined for squares with different corner radii. As shown in Figure 5.32, the maximum tangential stress for very sharp corners approaches infinity. Very little rounding is necessary to reduce this value to a rational level. It would not be unreasonable to expect even carefully excavated openings to have corners with radii of 0.2 to 0.3 times the half-span of the opening. This would yield a boundary stress of 3 to 4 times the insitu far field stress at the corners and a sidewall stress distribution at mid height similar to that shown in Figure 5.31.

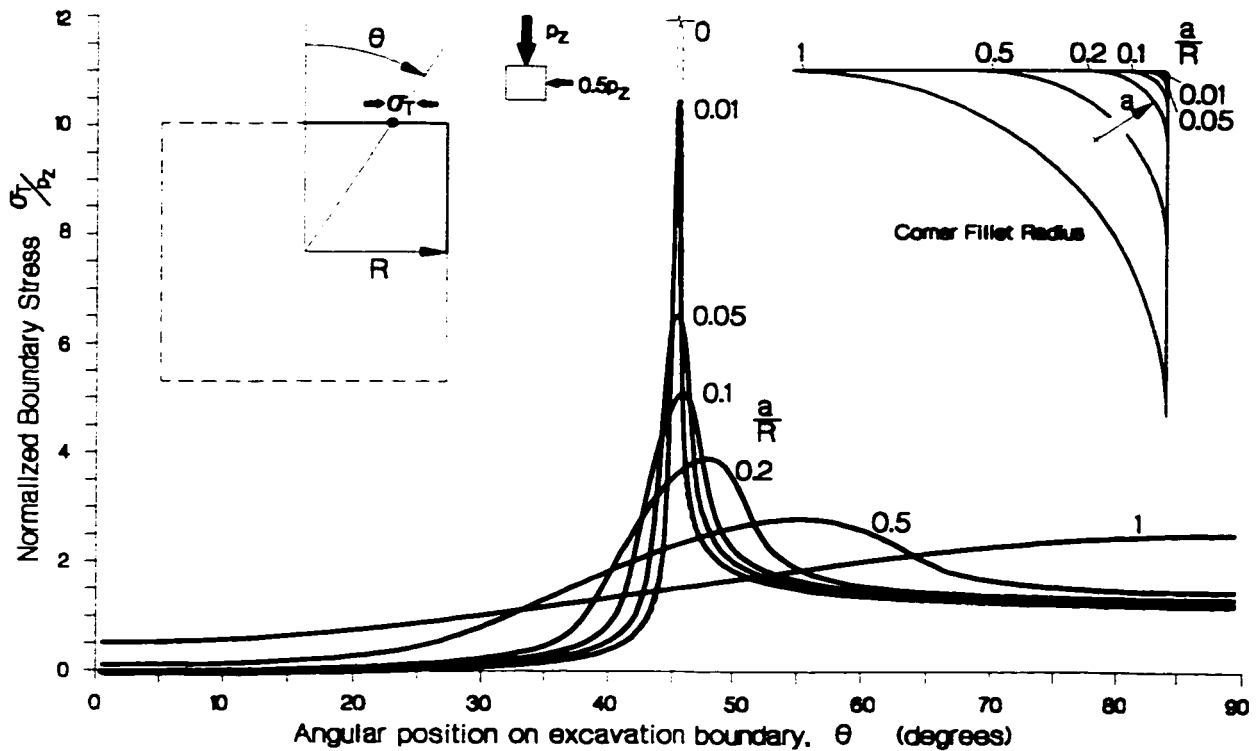


Figure 5.32: Boundary stress distribution around a square opening with varying corner radii (calculated using elastic boundary element analysis - Examine^{2D})

Alternatively, Martin et al. (1998) use a parametric formulation by Greenspan (1944) based on geometric mapping equations to equate the maximum corner stress around a pseudo-square. A selection of parameters which yield realistic corner geometries (corner radii approximately 1/8 of tunnel span are typical in mining) results in a practically relevant corner stress of approximately 3.3 times the far field maximum stress. The maximum stress in the sidewall of a square opening (from Figure 5.31) away from the corners is approximately 1.4. Combining the sidewall stress concentration with that assumed for the corners, a maximum stress equivalency for Hoek and Brown's stability classifications can be obtained as shown in Figure 5.33.

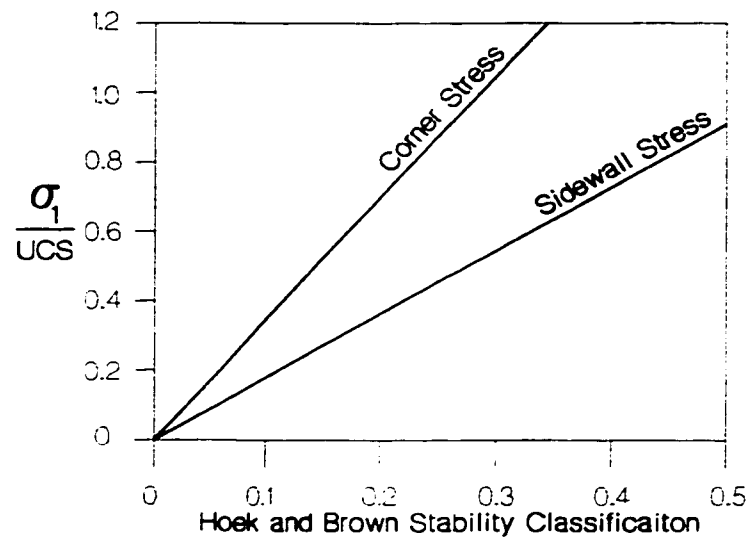


Figure 5.33: Conversion of Hoek and Brown stability classifications (Figure 5.30) to normalized boundary stresses.

In this Figure it can be seen that the first observed damage in Hoek and Brown's database occurs when the corner stresses exceed $0.5 UCS$. ($\sigma_{1ff}/UCS = 0.15$) and the sidewall stresses exceed $0.25 UCS$. The damage becomes significant (requiring support at $\sigma_1/UCS > 0.3$) when the corner stresses exceed the UCS and the normalized sidewall stress exceeds 0.5 (a level in the upper range of values for damage initiation obtained in the lab for hard rocks such as granite). According to this interpretation, crushing and shearing in the corners coincides with damage initiation in the sidewalls. In a manner similar to the mechanical action of the notch process zone described by Martin (1994) and illustrated in Figure 5.24, the dilational shear failure in the corners can exploit newly initiating damage (boundary-parallel cracks) to generate continuous slabs which spall off or buckle. The risk of severe failure requiring heavy support (from Figure 5.30) becomes critical when the sidewall stresses exceed $0.7 UCS$, a level equivalent to the long-term laboratory strength (compressional shear failure) of many hard rocks.

Wiseman (1978; 1979), also working with predominantly square openings in a $k=0.5$ stress field, analyzed deep tunnels in a South African mine and quantified the stress state using the stress concentration factor:

$$SCF = \frac{3\sigma_{1ff} - \sigma_{3ff}}{UCS} \quad [5.16]$$

where σ_{1ff} and σ_{3ff} are the far field principal stresses. This factor is based on the tangential stresses around a circular opening, although all of the tunnel sections in his database are approximately square or rectangular. Wiseman subjectively quantified the fracture damage and the ground movement in the walls roof and floor and gave an assessment of excavation performance for each tunnel segment.

Here, Wiseman's stress factor is converted into corner and sidewall stresses. An examination of the converted data for unsupported and lightly supported openings indicates fracture thresholds as summarized in Table 5.3.

Table 5.3 Analysis and conversion of Wiseman's (1978; 1979) damage database, with stresses normalized with respect to *UCS*.

	Wiseman's stress intensity factor	Square excavation corner stress	Square excavation max. sidewall stress
Onset of visible damage (spalling)	0.25 - 0.4	0.33 - 0.56	0.14 - 0.22
Significant spall and fracture damage	0.6 - 0.75	0.8 - 1.0	0.34 - 0.42
Serious degradation of tunnel integrity	> 0.9	> 1.2	> 0.5

These findings for unsupported and lightly rockbolted excavations are similar to the interpretation of Hoek and Brown's data summarized in Figures 5.30 and 5.33. Spall damage initiates at tangential (boundary) stresses in excess of 1/3 intact *UCS* and become significant from an engineering point of view (corner crushing/shearing sidewall spalling) when the boundary stresses exceed 1/2 *UCS*.

As previously noted, highly localized stresses leading to rock crushing and shear rupture in the corners have the effect of generating, through mechanical action (jacking and tearing), severe spall damage in the sidewalls, exploiting the damage created at lower stress levels in the walls. This is a phenomenon which appears in simulations by Vasak and Kaiser (1995) of actual dynamic failures at the El Teniente mine in Chile (Figure 5.34), and in pillars observed by Pritchard and Hedley (1993), creating what Kaiser et al. (1995) call the *baggage zone* commonly found around non circular excavations at depth.

The generation of this baggage zone is an important support consideration and according to Kaiser et al. (1995) is an inevitable issue for rectangular excavations subject to high stress.

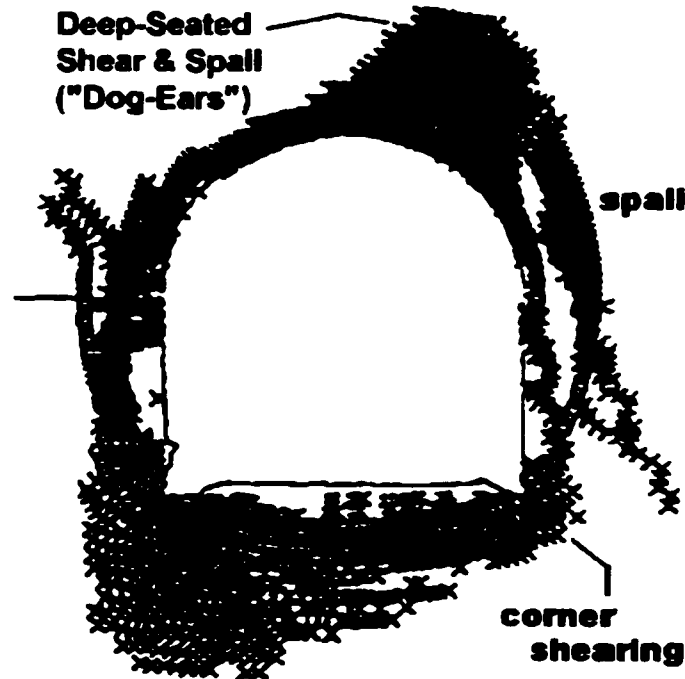


Figure 5.34: Sidewall spalling induced by mechanical action of localized shearing (modified after Vasak and Kaiser 1995).

5.4.2 Other Excavation Shapes

Kaiser et al. (1995) compiled a number of case histories in which sidewall stress was calculated and depth of damage measured. Since then, Martin et al. (1996) collected further cases of varying shapes including horseshoe and circular openings (Figure 5.35). The best-fit relationship, relating normalized stress and depth of failure, is shown in Figure 5.36. The equation of the best-fit line in Figure 5.36 can also be expressed in the following form yielding the depth of failure, d , directly:

$$d = 1.25a\left(\frac{\sigma_1}{UCS} - 0.41\right) \quad [5.17]$$

indicating a typical damage initiation threshold when the maximum normalized boundary stress at the walls of an equivalent circular opening exceeds 0.41. The "model" line in Figure 5.36 was obtained by Martin et al. (1998) by calculating the depth of the iso-deviatoric contour ($\sigma_1 - \sigma_3 = 1/3 UCS_{lab}$) around an equivalent circumscribed circular opening in an elastic analysis.

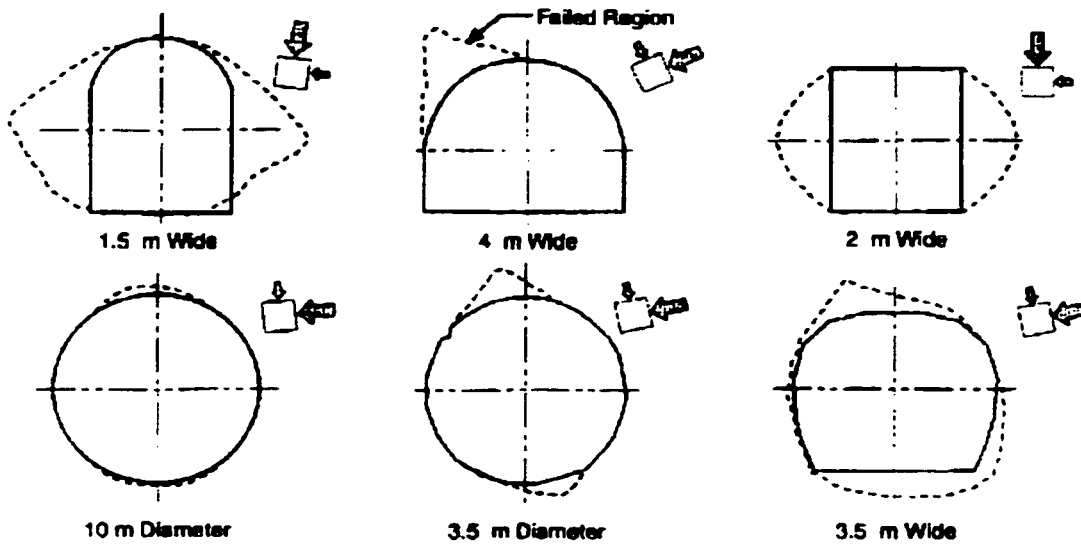


Figure 5.35: Excavation shapes and typical failures used in Figure 5.36.

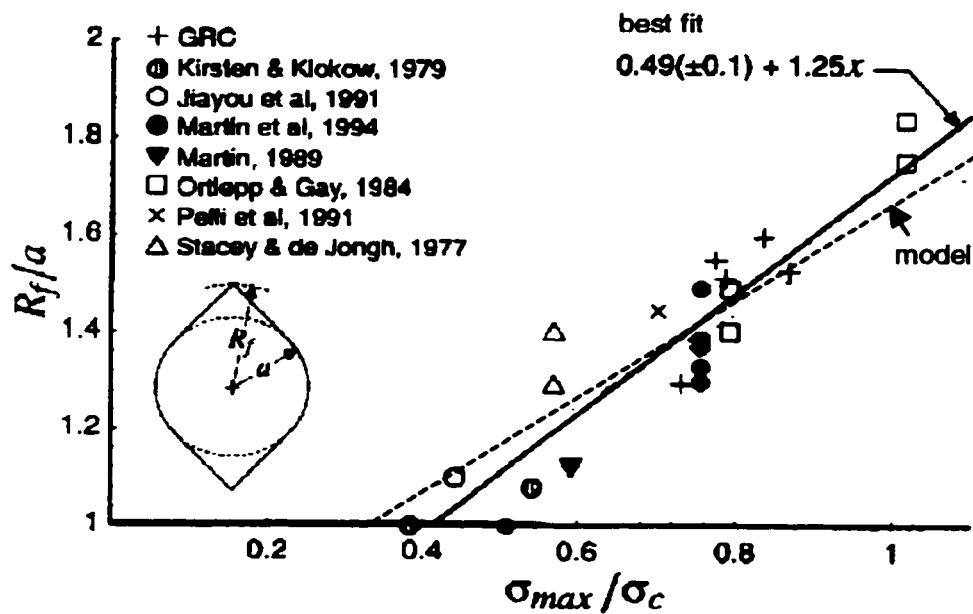


Figure 5.36: Depth of failure around equivalent circular openings (circumscribed around actual opening) in hard rock (after Martin et al. 1996).

Again this value is consistent with the earlier observations based on square geometries showing that an excavation damage threshold exists which corresponds to one quarter to one half of the laboratory *UCS* of the intact (and undamaged) rock. Specific case studies are presented in the next section to further illustrate this point.

5.5 CASE EXAMPLES OF INSITU DAMAGE THRESHOLD

Several case histories are examined in this Section. The first is a circular test tunnel driven in unjointed massive (plutonic) granite using a non-explosive “non-damaging” excavation procedure (Onagi et al. 1992; Martin and Read 1996) developed at the Underground Research Laboratory (URL) operated by Atomic Energy of Canada Ltd. (AECL). It has been analyzed by numerous researchers (Martin 1994; Read 1994; Castro 1996; Read et al. 1998; Potyondi and Cundall 1998) and by this author.

The other examples analyzed as part of this thesis are from the Sudbury Basin (Ontario), and include, a new shaft development at INCO’s Victor Site; a damage assessment and back analysis at North America’s largest and currently deepest nickel mine, Creighton Mine; as well a review of analysis involving a large cavern (Sudbury Neutrino Observatory) at great depth. These case studies are not intended as rigorous analyses but rather as illustrative examples of the usefulness and effectiveness of a lower bound insitu yield threshold associated with damage initiation.

5.5.1 Mine-By Test Tunnel - URL

The previously discussed observations and failure databases illustrated that the compressive stress required to initiate damage and ultimately failure of rock in the field is considerably less than the laboratory failure strength of the same material, with a trend which seems consistent for massive, sparsely and moderately jointed hard rockmasses. While numerous authors have attributed this reduction in strength to the presence of joints insitu and therefore to the so-called effects of scale, an extensive experiment documented by Martin (1994; 1997), demonstrated that this reduction occurs even in the complete absence of jointing and with the most meticulous and non-damaging excavation procedures.

A circular test tunnel was excavated at 420m below surface in massive unjointed plutonic granite (Figure 5.37 and Figure 5.38). Each round consisted of a dense and interconnecting circular pattern of perimeter drill holes to delineate a disk 1m thick (Figure 5.39). This disk was then separated from the face using hand held splitters. This process was intended to eliminate any excavation-induced damage.

While the maximum boundary stress levels were significantly less than the strength of undamaged granite samples, however, crushing and spalling resulted in a large notch formed in the floor and roof of the test tunnel exposed after tunnel completion as shown in Figure 5.40.

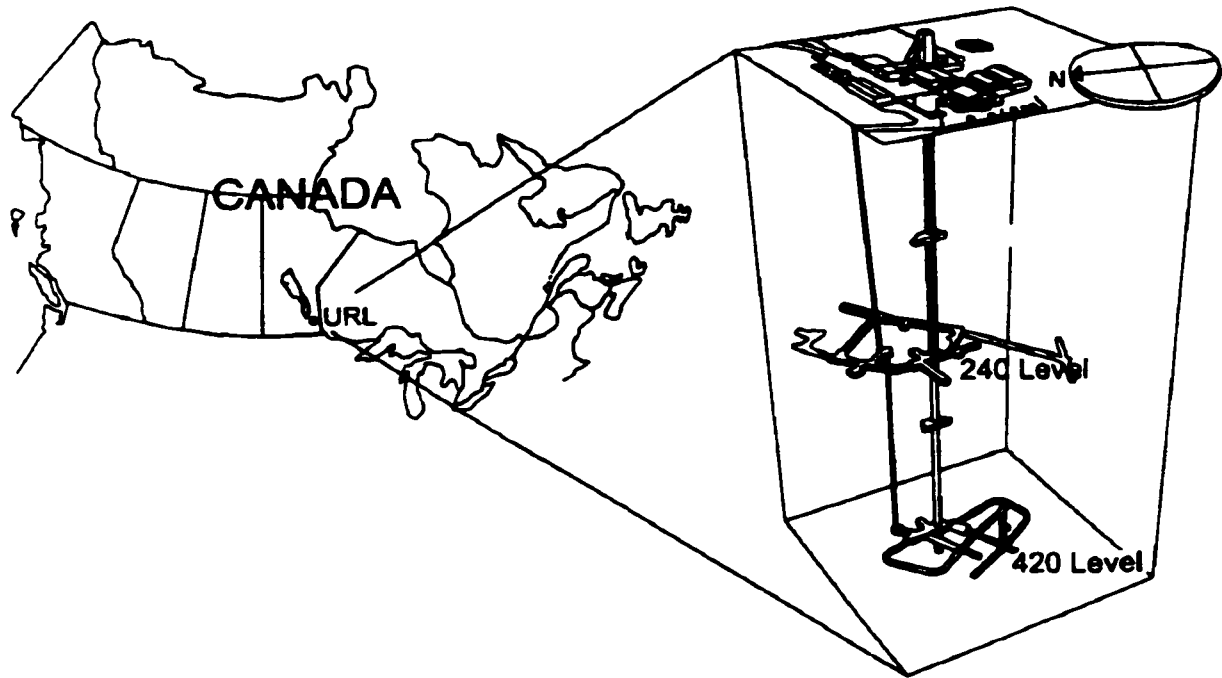


Figure 5.37: Location and underground layout of the Underground Research laboratory, URL (modified after Read and Martin 1991).

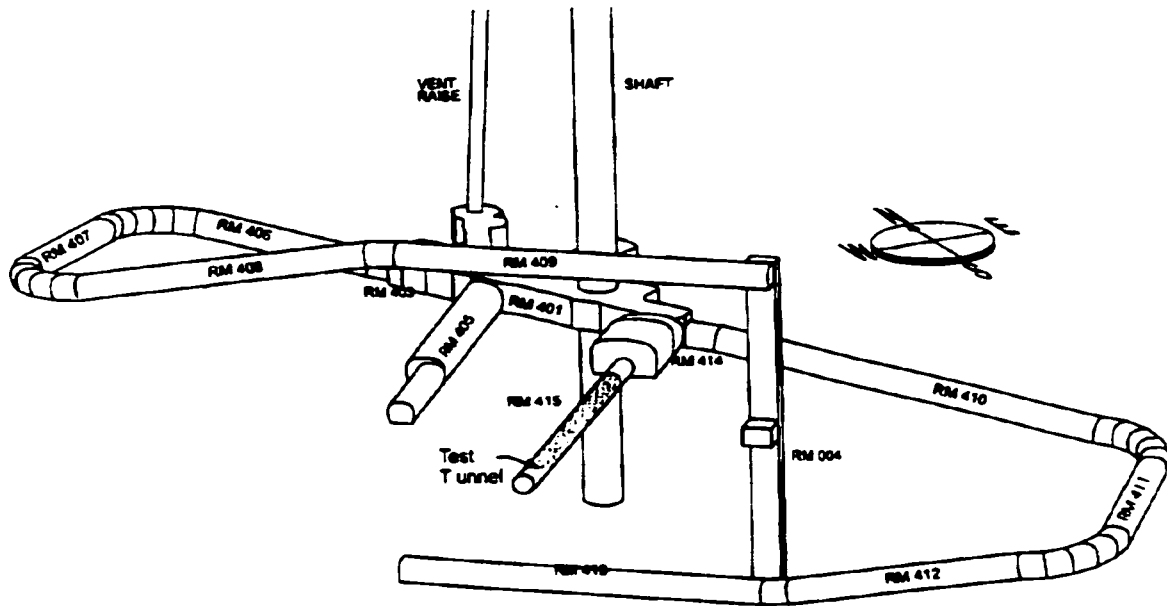


Figure 5.38: 420 level at the URL showing the location of the test tunnel or mine-by experiment (after Martin 1997).

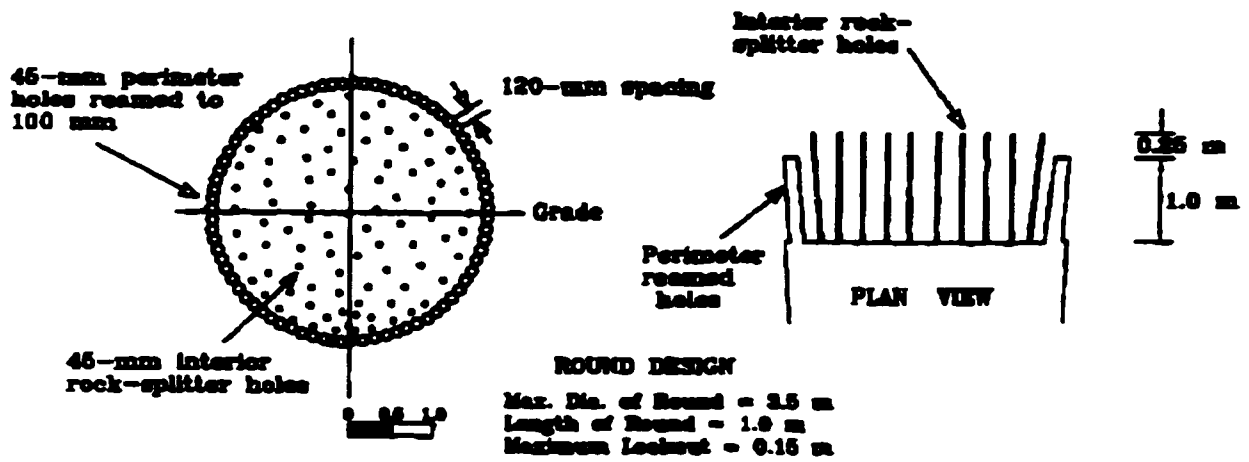


Figure 5.39: Non-explosive excavation procedure employed in Mine-by tunnel (after Onagi et al. 1992).



Figure 5.40 Notch formation due to spalling in roof and floor of URL "Mine-by" test tunnel (photo courtesy AECL).

The visible initiation of the notch was compared with the tangential stresses on the boundary, based on three dimensional (elastic & homogenous material) boundary element analysis (Examine^{3D}) of a cylindrical tunnel geometry, as the face advanced beyond a reference point (Figure 5.41). The stress state is summarized in Table 5.4.

Table 5.4: Far field stresses at depth of URL Mine-By Tunnel (Martin, 1997).

Principal Stress	Magnitude, MPa (st.dev.)	trend/plunge (deg.) (tunnel axis trend = 045)
Major, σ_1	60 (3)	145 / 11
Intermediate, σ_2	45 (4)	054 / 08
Minor, σ_3	11 (2)	290 / 77

The representative *UCS* of this rock, based on laboratory testing of undamaged samples from near-surface drill holes and outcrops, is 225MPa (Martin 1997). The notch began to form at a point 0.2 to 0.5m from the face (Martin 1994) where the boundary stress was calculated by this author to be to be approximately 100 to 115MPa or 0.44 to 0.52 times the *UCS*, a value consistent with the findings of Hoek and Brown (1980) and of Wiseman (1978;1979).

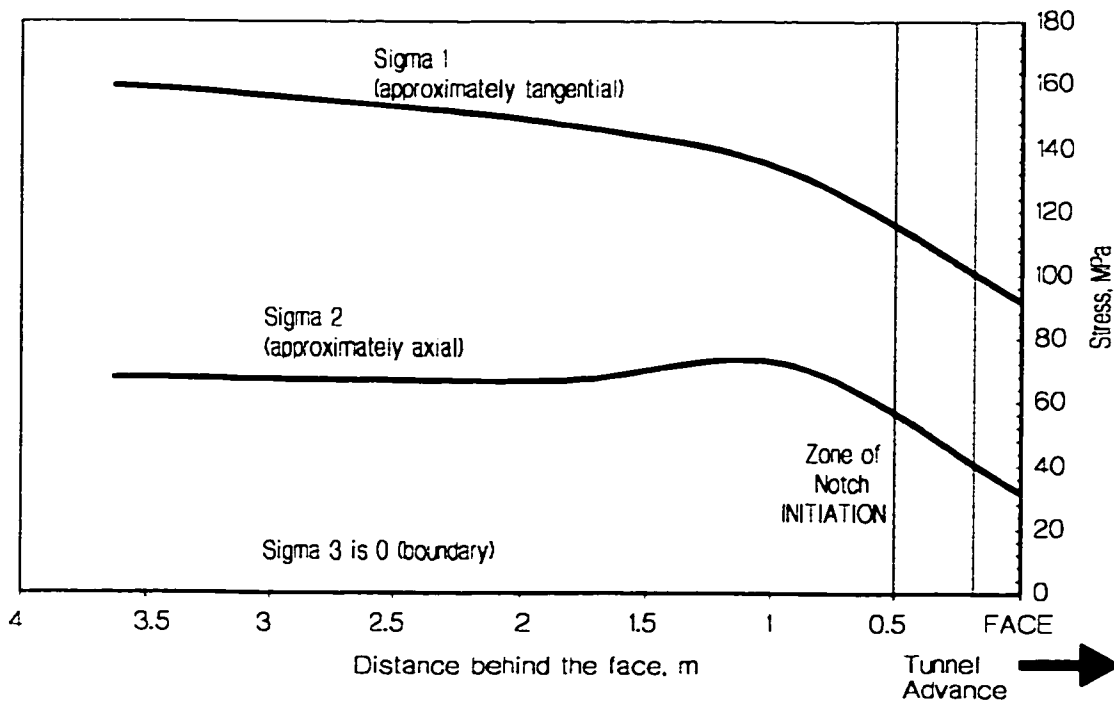


Figure 5.41: Calculated elastic stresses on tunnel surface at location of notch apex (notch not simulated - cylindrical tunnel geometry only).

Away from the face, when the boundary stresses reach a maximum (and can be approximated by a 2D analysis), the stress state for the URL test tunnel and the total notch depth is plotted as solid circles in Figure 5.36, consistent with the observational trend plotted by Martin et al. (1996) for other case studies.

While the notch denotes the ultimate exploitation of micro- and meso-damage within the granite around the URL test tunnel, microseismic monitoring within several meters ahead of the face indicated that damage began to occur at stress levels (σ_1) above a limit defined by Martin (1997) as:

$$\sigma_1 - (1.0)\sigma_3 = 70 \text{ to } 75 \text{ MPa} \quad [5.18]$$

The modelled stress state at the location of these pre-excitation seismic events is shown in Figure 5.42. The damage initiation threshold ("lab σ_{ci} ") obtained in the lab (Hommand-Etienne et al. 1995) from acoustic emissions and lateral strain measurements is shown for comparison. Martin selects the uniaxial intercept of 70MPa for damage initiation, which corresponds to approximately one third of the UCS of laboratory samples. In addition, Martin proposes the constant deviator criterion (Equation 5.14) for this damage threshold.

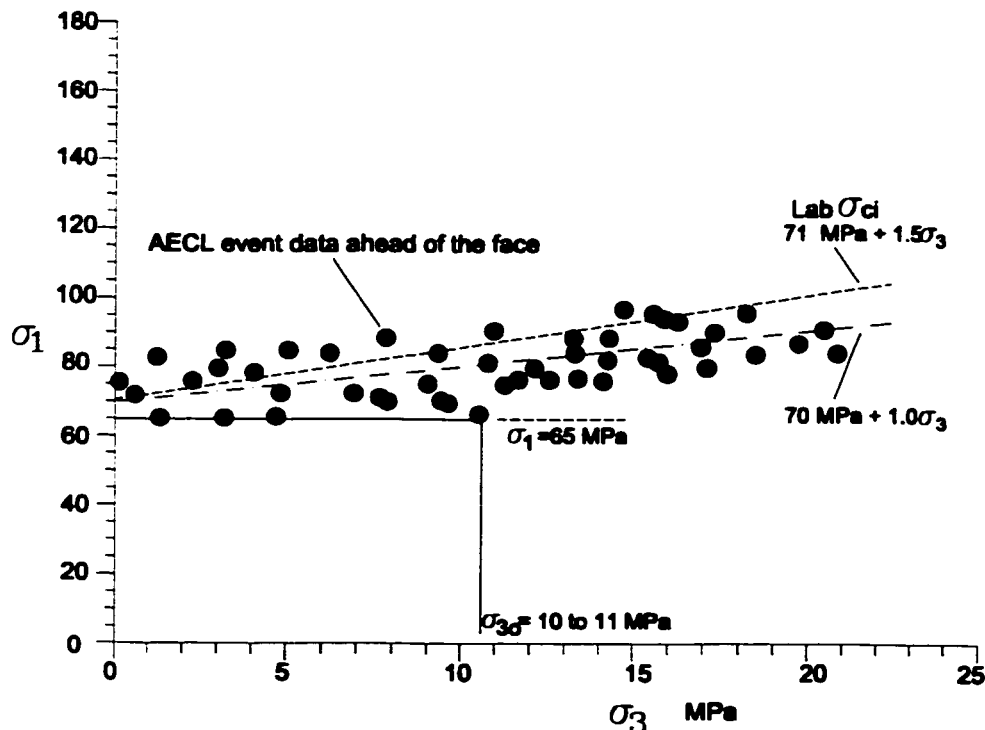


Figure 5.42: Microseismic event data ahead of the face plotted according to elastic stress calculations at event locations.

Martin et al. (1998) suggest that the constant deviator criterion, applied to the stresses after the face has advanced far beyond the section in question, provides an adequate approximation for the distribution of microseismic events and predicts the depth, not the shape, of ultimate failure (notch formation). This is illustrated in Figure 5.43.

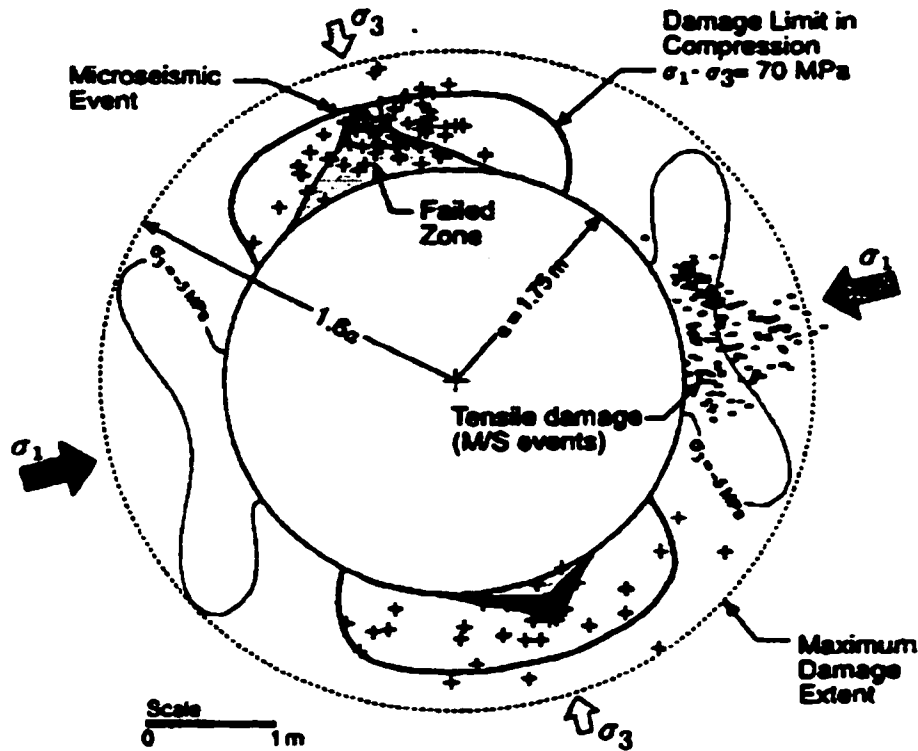


Figure 5.43: Notch profile, microseismic event locations, constant deviatoric stress threshold and tensile crack threshold for typical tunnel round (after Martin, 1997).

According to Castro (1996), the constant deviator contour encloses the limit of ultimate notch formation while the angular extent of the notch around the tunnel boundary is limited by the same strength threshold which determined the initial notch generation; $\sigma_1 = 0.5UCS$ or 110MPa. It is also apparent however, that a simple threshold of $\sigma_1 = 0.5UCS$ performs equally as well at predicting the notch depth but also more accurately predicts the lateral (angular) extent of the notch (Figure 5.44). This could be the result of effective confinement approaching zero due to progressive crack dilation within the eventual notch region (“effective gap” concept illustrated in Figure 5.26 and discussed further in Chapter 8). Similarly a threshold equivalent to $\sigma_1 = 65\text{MPa}$ provides a lower bound for the microseismic event data in Figure 5.42 at confining stresses below 11 MPa (equivalent to the insitu σ_3). The difference between this threshold and that in Figure

5.44 is the result of the difference in observational resolution required to detect "first crack" microseismic events and the visible crack accumulation and spall generation in Figure 5.44.

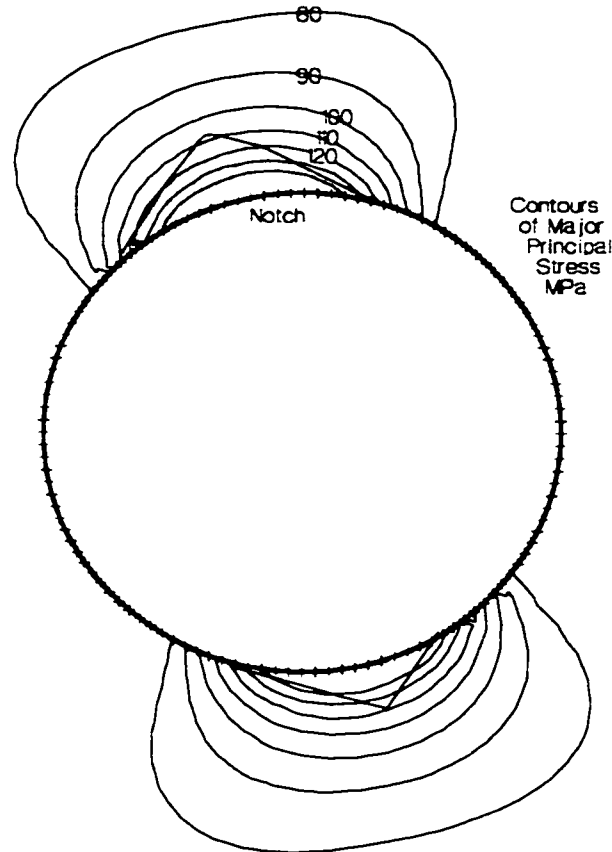


Figure 5.44: Major principal stress contours (3D stress field) and notch geometry.

According to Martin et al. (1998), conventional continuum elasto-plastic analyses or the Hoek-Brown frictional criterion applied to elastic analyses cannot adequately delineate the failure zone. Read et al. (1998) suggest that it is not possible to predict the damage zone around excavations in high deviatoric field stress environments using 2D analyses. Presumably, this is because of the dominant effect of stress rotations in front of and behind the advancing face.

Martin's 2D damage limit corresponds to an outer spatial limit of crack initiation but does not, in itself, guarantee failure. Read et al. (1998) explain that the level of confinement at which the damage threshold is crossed and stress rotations, during excavation, within these damage zones determine the extent of damage propagation and the degree of ultimate failure. The composite effect cannot be explicitly considered in 2D analyses. Martin's deviatoric stress damage threshold, does however, provide a reasonably reliable tool to implicitly delineate damage and failure for cases with relatively simple excavation induced stress paths.

In the area of the eventual notch formation, the elastic stresses calculated for the tunnel using 2D analysis are, however, representative of the final stress state and also coincide with the maximum deviatoric stress levels experienced by the rockmass prior to notch development. It is reasonable to assume then that damaged rock delineated in this way represents the extent of reduced yield strength. The propagating notch is thus halted when it reaches beyond this damaged zone and encounters rock without previous damage and without the associated strength loss.

5.5.2 Victor Mine Shaft

Another case example of an insitu yield threshold is INCO's newly excavated Victor Mine shaft at Blue Lake in the Sudbury area. A preliminary progress report by Dawson (1997) indicates that the shaft was being excavated as a 7.3m circular section down beyond the norite/granite contact at 760m and was, at the time of his report at 1220m in granites of the Skead Pluton.

Stresses in the Canadian Shield have been measured numerous times at different locations and at different depths. A recent paper by Arjang and Herget (1997) gives an up-to-date summary of this data. The stress-depth relationships for the vertical (minor principal) stress and for the two ratios k_{h1} and k_{h2} relating horizontal stress to vertical stress are given by Arjang and Herget (1997) based on both linear trend and on power law regression analysis. However, based on the assumption that all stress ratios must converge to unity at extremely great depth in a Shield environment (as shear resistance reduces with temperature, pressure and plasticity), these relationships have been redefined and simplified by this author, with virtually no loss in fit quality, and are presented in Figure 5.45a. The relationships are replotted as principal stress trends in Figure 5.45b.

Using these revised assumptions for insitu stress, the Victor shaft has been analyzed using the Kirsch solution for maximum tangential stress on the boundary of a circular opening:

$$\sigma_1 = 3\sigma_{1ff} - \sigma_{3ff} \quad [5.19]$$

and the following assumptions for field stress (D = depth in m; stresses in MPa):

$$\sigma_{VERT} = 0.026D \quad [5.20]$$

$$\sigma_{Hmax} = \sigma_{VERT} \left(1 + \frac{25}{\sqrt{D}} \right); \quad \sigma_{Hmin} = \sigma_{VERT} \left(1 + \frac{8}{\sqrt{D}} \right) \quad [5.21]$$

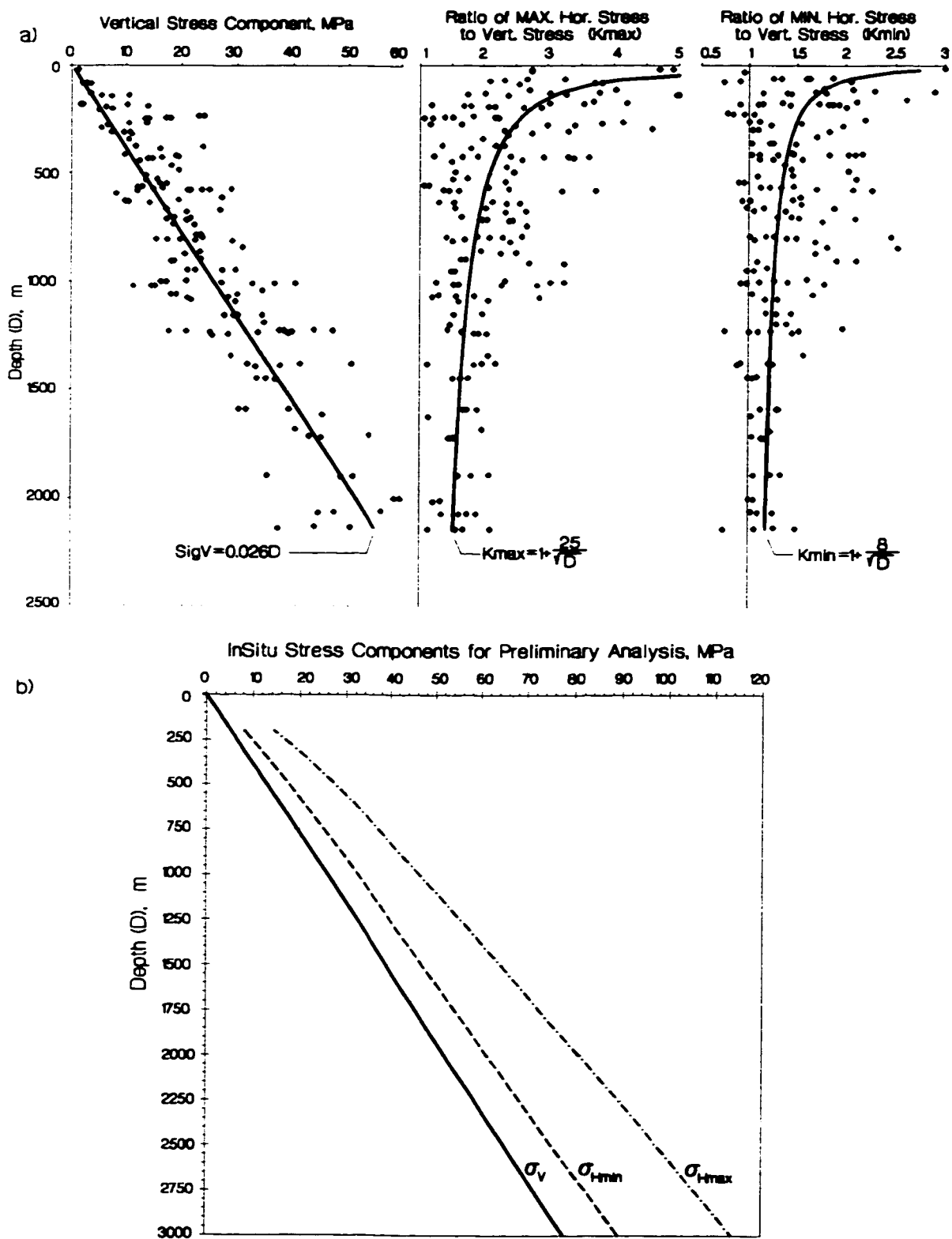


Figure 5.45: Modified insitu stress relationships (based on data from Arjang and Herget 1997).

The uniaxial compressive strength of plutonic granites in the Sudbury area are given by Vasak and Maloney (1995) as approximately 270MPa, while Wiles (1989) suggests a peak laboratory value of 250MPa. A value of 260MPa will be assumed for this analysis.

According to Dawson (1997), at 980m depth, significant stress spalling began to occur as indicated in Figure 5.47, worsening with depth and necessitating the implementation of a systematic destressing program.

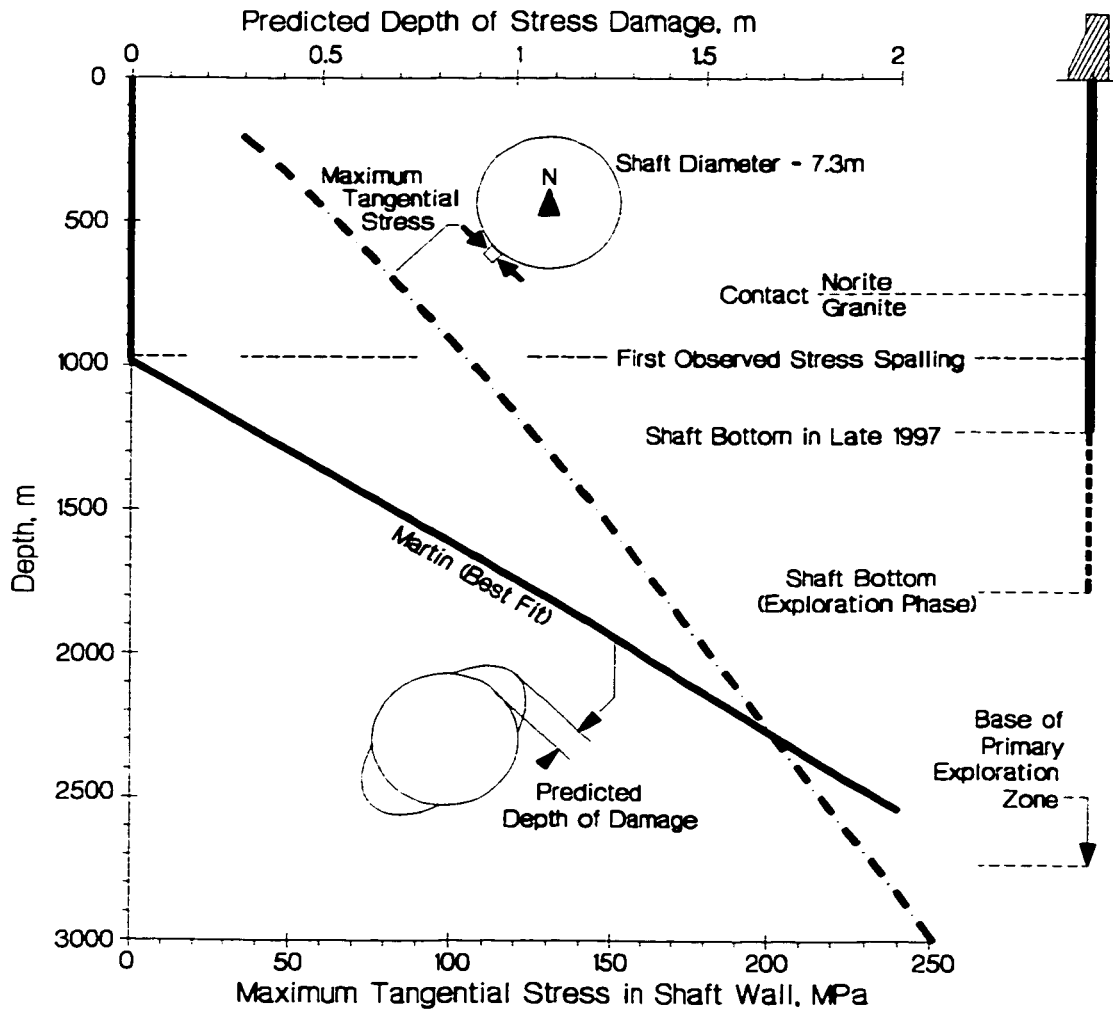


Figure 5.46: Shaft spalling observations and predictions for Victor Shaft.

Destressing is a process where confined charges are detonated in boreholes ahead of the face to prefracture the rock. While this may weaken the rock, it removes some of the brittle character, increasing safety. Screen and eventually shotcrete were subsequently required to contain the blast fractured rock.

Figure 5.46 illustrates that the observations to date correspond with the “best-fit” predictions of Martin et al. (1996) from Figure 5.36 and Equation 5.13. That is, the onset of spalling occurs when the shaft wall stress exceeds 104MPa or 0.4UCS at 980m. This damage was not observed to be related to any structure, although some joints were present. The damage was very similar to that observed in ore passes at Sudbury mines and at the URL tunnel.

The reduction of strength at the shaft boundary could be related to excavation procedures, although great care was taken to practically minimize blast damage with more than 80% of half barrels visible after most rounds. It is more likely that the same processes of damage initiation, stress rotation and strength reduction encountered at the URL are at work here. Similar spalling occurs in bored raises, excavated with minimal disturbance, at comparable depths to the Victor Shaft (Figure 5.47).



Figure 5.47: Typical spall and breakout in vertical bored raise (Hoek and Brown 1980).

It is not possible to confirm the depth of damage predictions for subsequent deepening of the shaft due to the damage caused by the destressing program. The predictions do indicate, however, that before the maximum depth of the planned shaft is reached, the damage zone will exceed the length of the current support system of rebar and bolts. The reinforced rock annulus, however, will likely remain in place and will be sufficient to restrain fallout from the shaft wall, if the bolts are used in combination with a reliable retention system such as shotcrete or a polymer spray-on liner (e.g. Tannant et al. 1999).

5.5.3 Creighton Mine: Deep Levels and SNO Excavation

Creighton Mine is the largest and deepest operating nickel mine in North America. It began as an open pit operation in 1901, progressing underground using a variety of mining methods over the next 90 years. In the deep levels of Creighton Mine (also the site of the Sudbury Neutrino Observatory) illustrated in Figure 5.48, the primary mining method up until the mid 1980's was Mechanical Cut and Fill (MCF). This method involves the creation of a network of stopes across the horizontal extent of the orebody. As each horizon is mined it is filled and the stoping advances vertically typically 4 to 6m. The mining is initiated at 70m level intervals and mined on multiple levels simultaneously.

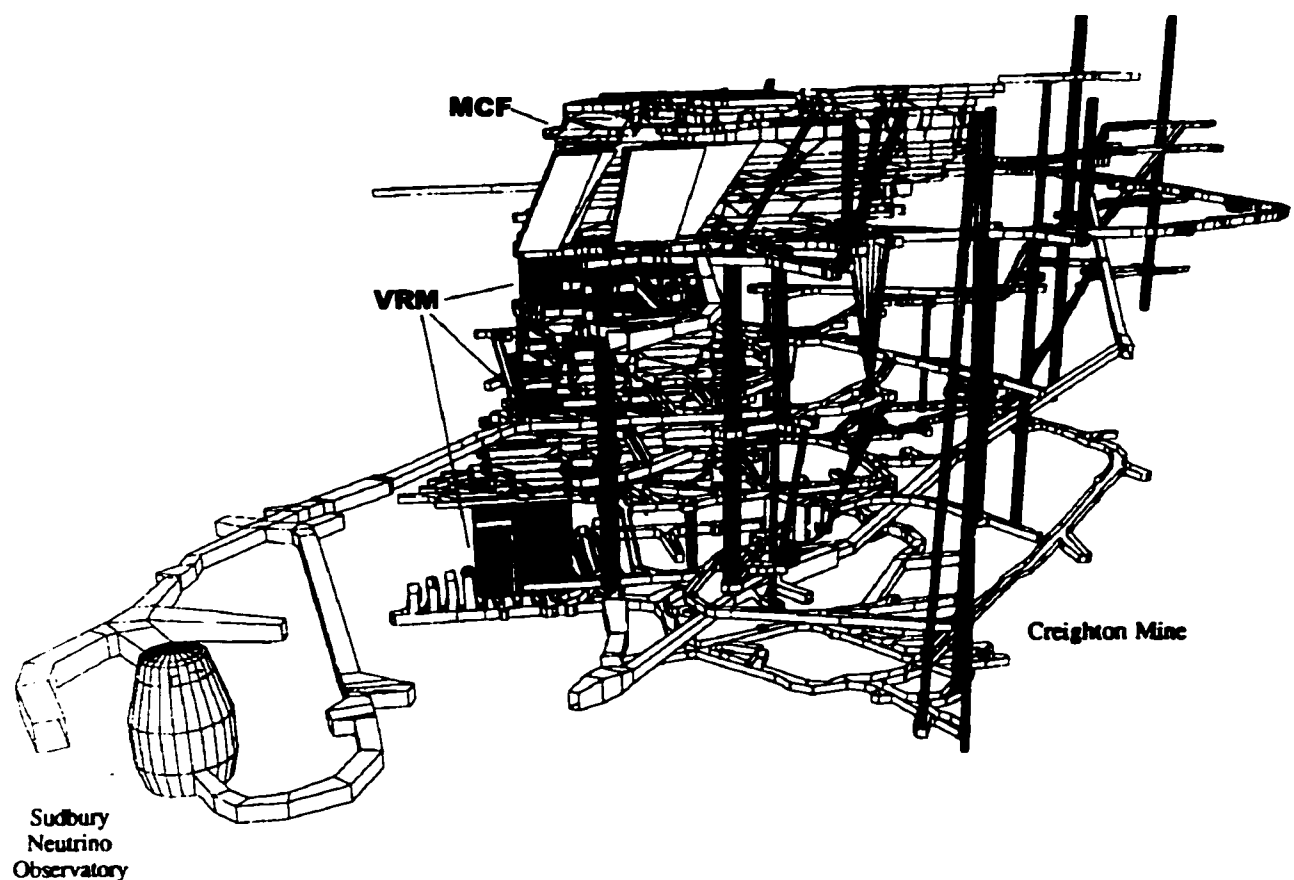


Figure 5.48 Perspective view of Creighton Mine Deep Levels. The upper horizon shown is 6400 level. The Upper most VRM as labeled is the study area. The SNO cavern is in the foreground on 6800 level.

This leads to the creation of highly stressed sill pillars (Figures 5.49 and 5.50) between mining blocks, which in the case of the sills below 1700m at Creighton Mine, failed in a violent fashion (severe rockbursting) when the sills were narrower than 25m (Landriault and Oliver 1992). For the MCF method, miners are continuously exposed to this hazard during the majority of their working shift, putting them at excessive risk of injury or fatality.

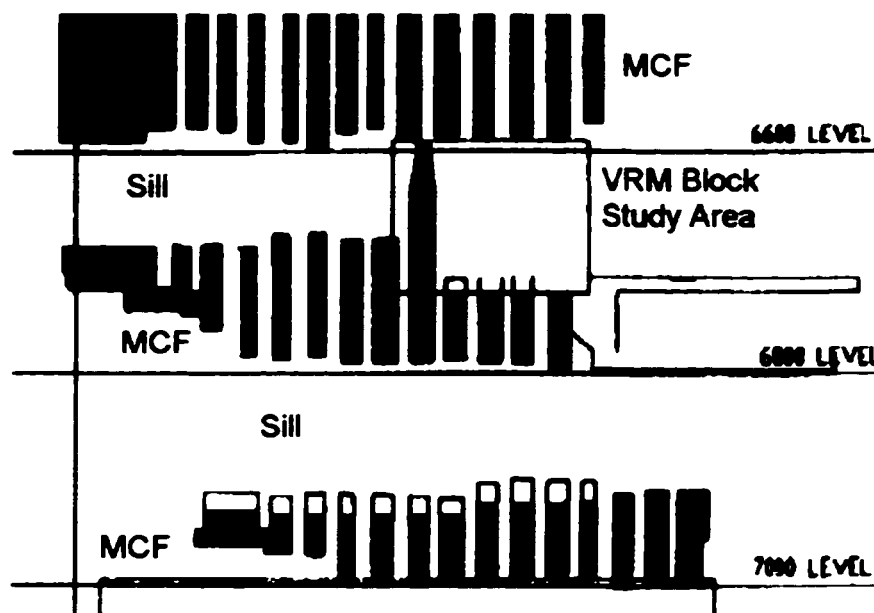


Figure 5.49: Longitudinal section showing the mechanical cut and fill blocks, the sills created by this method and the vertical retreat method test block beneath the 6600 topsill (after Landriault and Oliver 1992).

It was decided in the mid 80's to experiment with the use of the vertical retreat method, VRM, which is now routinely used throughout the Canadian Mining community. This method had the advantage of removing miners from the open stope for most of the mining cycle and did not create horizontal sills. The stopes were to be mined incrementally in 13m square panels. Ultimately these panels would be mined full height (65m).

During the trial documented here, however, the panels would be mined vertically between the topsill and the top of the uppermost MCF horizon as shown in Figures 5.49, 5.51 and 5.52. Figure 5.50 shows the stresses on a north striking plane through the subsequent initial slot area (black zone at left edge of "VRM Block Study Area" in Figure 5.49). Stresses are calculated with a 3Dimensional elastic boundary element model (Map3D) of the full Creighton Deep Zone (Figure 5.51). Upper and lower mining blocks in Figure 5.50 are the 6600 and 6800 MCF blocks respectively.

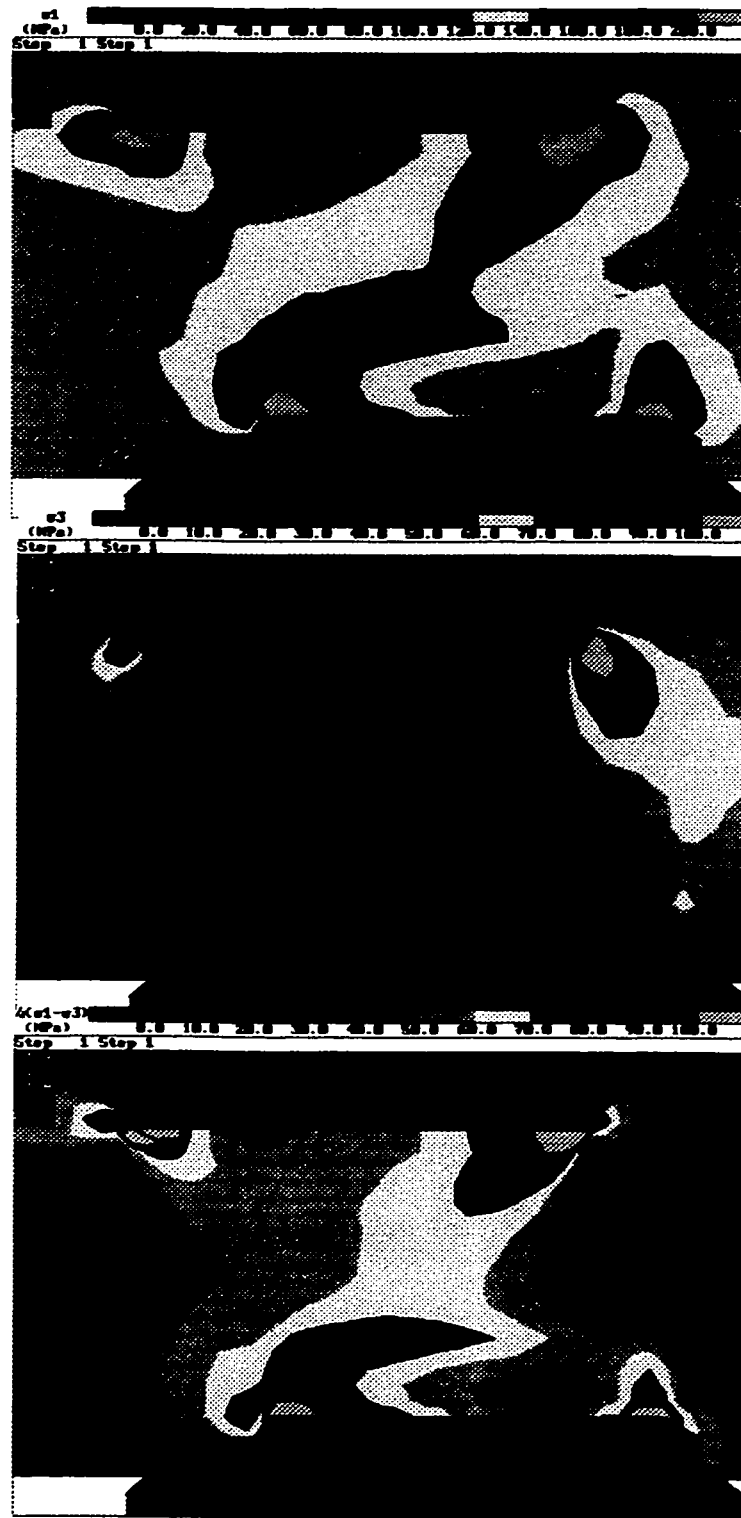


Figure 5.50: Major and Minor (top and middle) principal stresses in the center of the sill beneath 6600 topsill (top of images). The section runs north-south. The lower image is of contours of maximum shear stress (half of deviatoric stress). Stresses analyzed using a 3D boundary element elastic solution (Map3D).

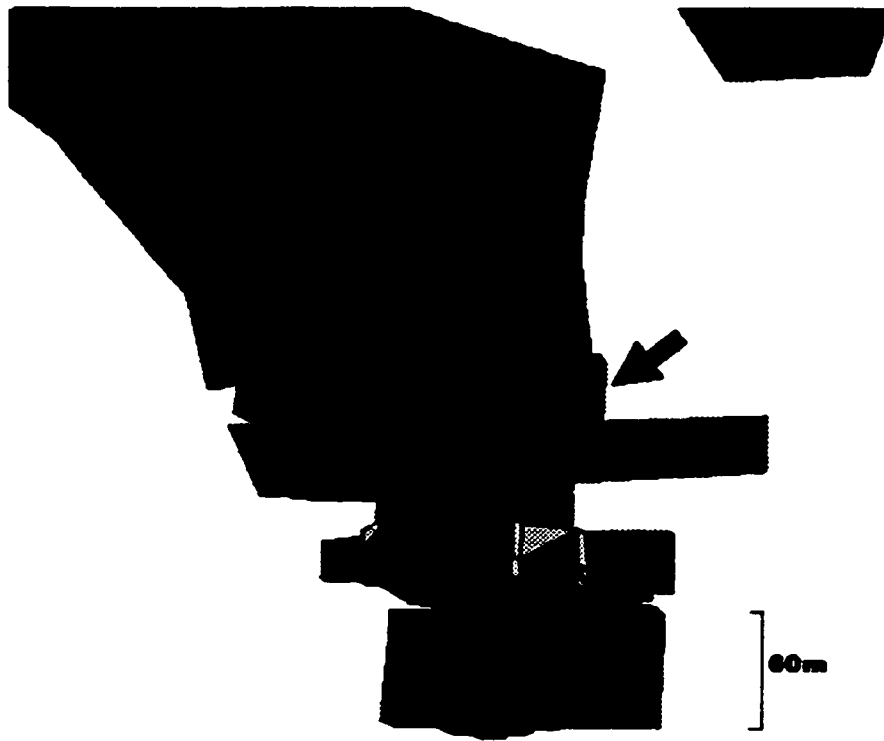
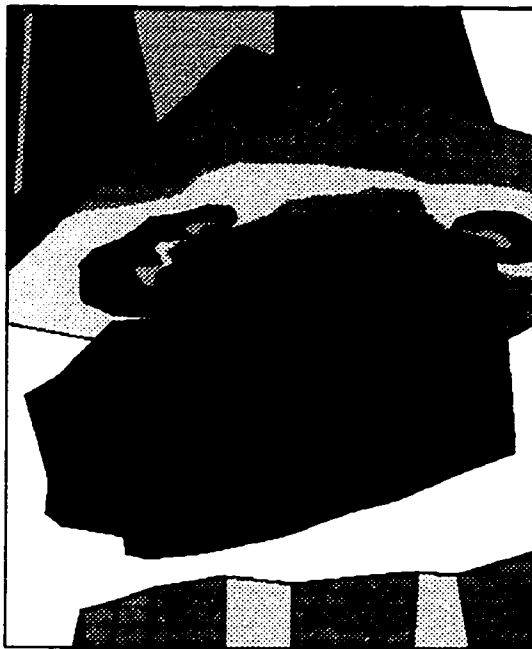


Figure 5.51: Map3D model geometry for completed MCF and VRM stopes for Creighton deep (to 7200 ft level). Arrow shows the 6600-6700 VRM block.



66-6700 VRM

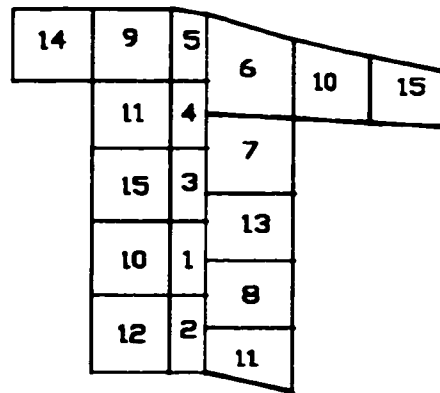


Figure 5.52: Major principal stress around the completed 66-6700 VRM (West). Right Figure shows extraction sequence for study block (plan view).

Stresses used in this current back analysis are based again on the data from Arjang and Herget (1998) as analyzed in the previous Section. A linear gradient (available Map3D stress input option) approximating Equations 5.16 and 5.17 was used in the model for far field stress. The approximation was selected to ensure accurate stress predictions at the 6700 foot level. These stresses are $\sigma_1 = 82\text{MPa}$, $\sigma_2 = 62\text{MPa}$, and $\sigma_3 = 53\text{MPa}$. σ_1 is horizontal and approximately east west, while σ_3 is vertical (in the absence of mining). The stresses and the geometry up to the 5000 foot level were input into the 3D stress model. The upper portion of the mine to surface was simulated in simplified form only since the influence of geometric detail on 6700 level was minimal. A panel extraction sequence shown in plan view (Figure 5.52) was used in the VRM trial and was simulated in stages in this study.

The trial was monitored using a host of extensometers, stress cells and borehole camera devices. The borehole camera information was used in combination with drilling logs (fines, ease of drilling, borehole breakout or visible closure, stuck rods, etc.) from the blastholes in neighbouring panels to delineate the extent of the damaged or yielded zone.

Yielded rock tended to facilitate the drilling of blastholes (6" rotary percussion holes) while rock which had not reached yield resulted in difficult drilling and hole rupture as the stresses were increased around the advancing boreholes. In this case, it became apparent to mine personnel that since damage was inevitable, it was desirable to create damage in areas where it would assist the operations. It was the creation of new stopes into the undamaged rock which resulted in the greatest difficulties and violent failure of stope walls. Zones of observed yielding as recorded by Landriault and Oliver (1992) are shown for six mining stages in Figure 5.53.

In this current study, for each simulation of 3D elastic stresses around the completed mining geometry, a grid of points was overlain in the unmined zone and was sampled, recording the calculated stress state and noting whether the point fell inside or outside the observed yielded zone. The results are shown in Figure 5.54. The filled squares ("yielded") indicate points inside the observed yielded zone while the circles ("intact") represent stress points outside this zone.

The lower bound yield stress for low and moderate confinement (σ_3) follows the relationship:

$$\sigma_1 = (90 \text{ to } 100)\text{MPa} + (1.0 \text{ to } 1.4)\sigma_3 \quad [5.22]$$

where 95MPa is approximately 0.4 to 0.5 times the UCS of the intact Creighton granite and norite respectively (250 MPa and 190 MPa as specified by Wiles 1989).

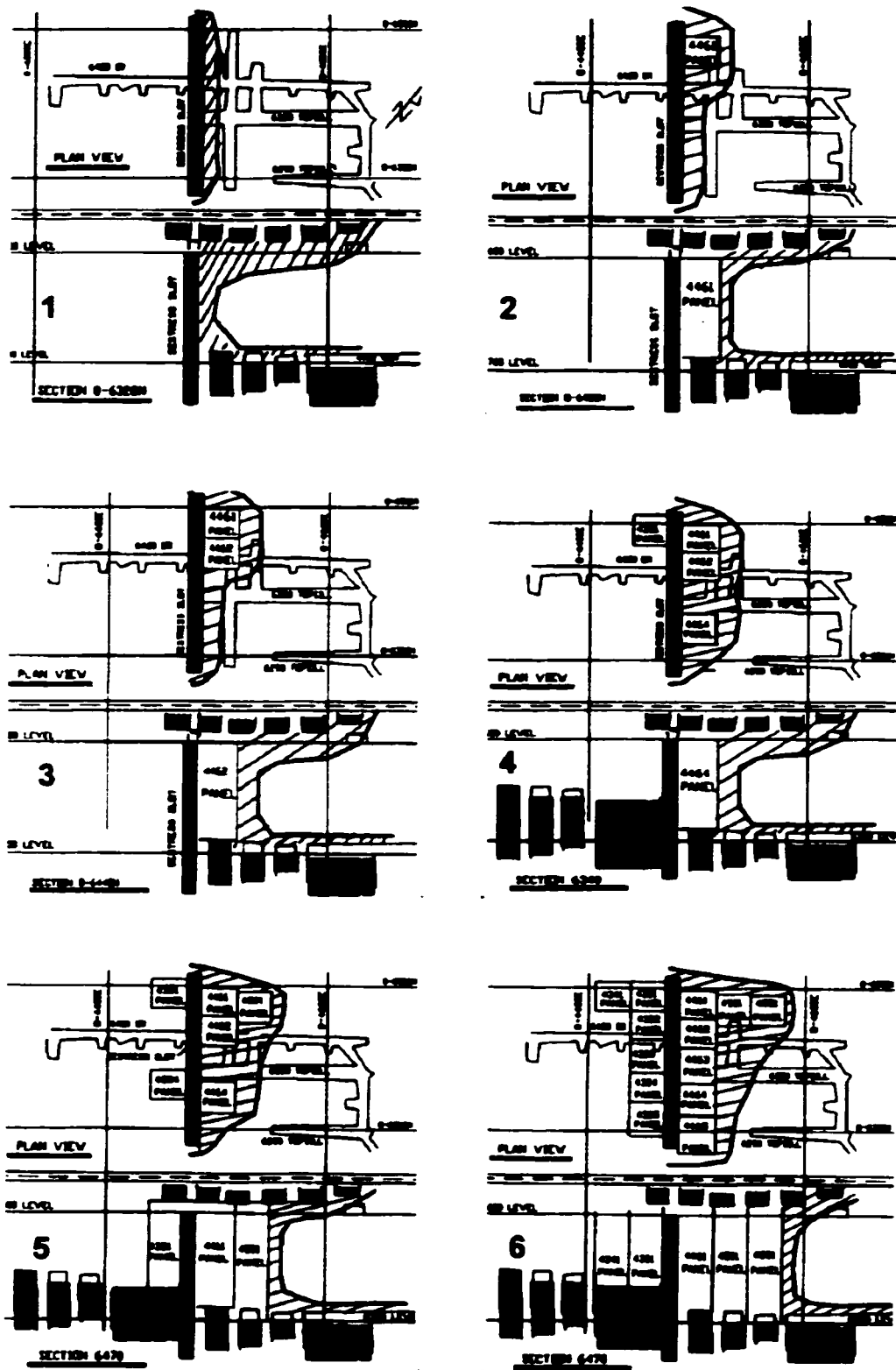


Figure 5.53 Observations of yielding and damage for six excavation stages (modified after Landriault and Oliver 1992).

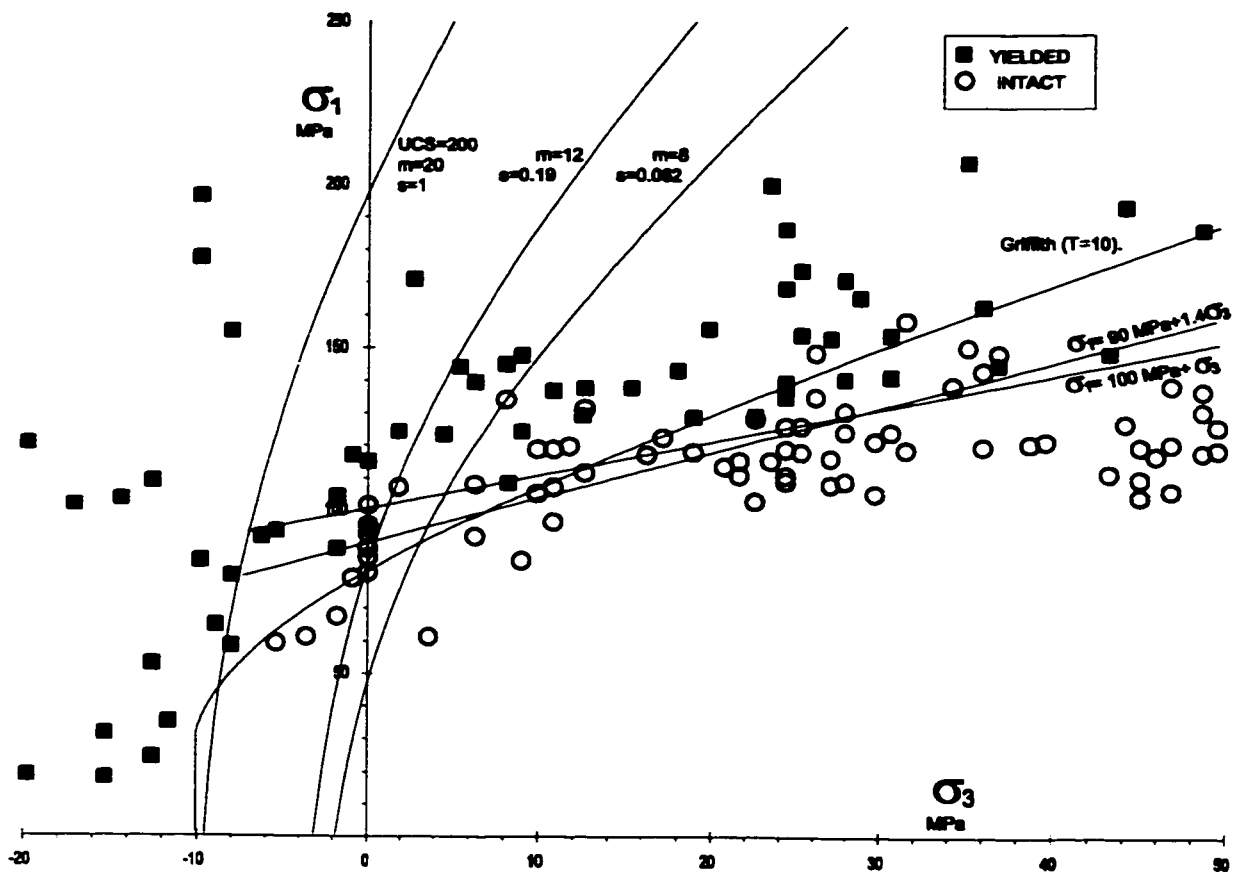


Figure 5.54: Analysis results for grid points through the 6700 level showing damaged and undamaged zones and several likely damage initiation envelopes. The intact envelope and first two (most competent) Hoek and Brown rockmass envelopes (Table 5.1) are shown for comparison.

This apparent yield threshold illustrates that the insitu strength of a moderately jointed rockmass subject to fluctuating stress paths around complex openings follows similar trends to unjointed and undisturbed massive granites such as those found at URL.

5.5.4 Sudbury Neutrino Observatory

A similar result is reported by Castro (1996) based on a detailed instrumentation and modelling study of the Sudbury Neutrino Observatory, situated to the west of the deep levels of Creighton Mine at the 6800 ft (2075m) level as shown in Figure 5.48. In this case observations of insitu yield were made based on the visual detection of open (induced) fractures (> 3mm) using borehole camera data, and using non-linearity of CSIRO stress change cells and extensometer

records (deviation from elastic prediction). Castro assigned a description of elastic or yielded to the locations of his instruments (Figure 5.55) and the dates of each record.

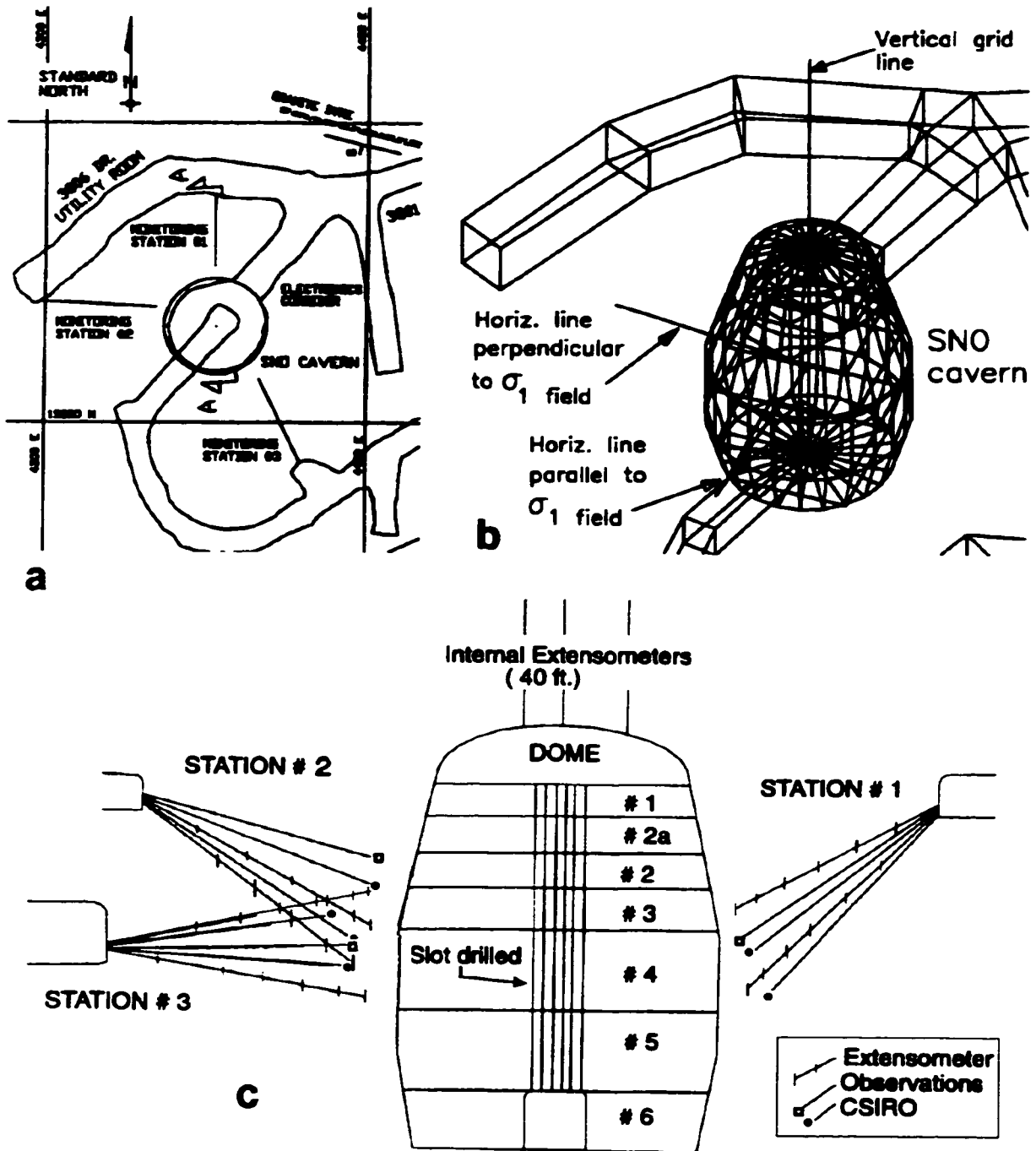


Figure 5.55: Sudbury Neutrino Observatory: a) plan view showing instrument stations; b) numerical model geometry for cavern; c) composite section through instrument stations - numbers indicate excavation stages (modified after Castro 1996).

Based on measured local field stresses (affected by the un-modelled presence of Creighton Mine) in the area of the observatory, calculated the stress state at each of these locations. Castro's data for individual extensometer locations is summarized here in Figure 5.56 as a composite plot for all anchor locations.

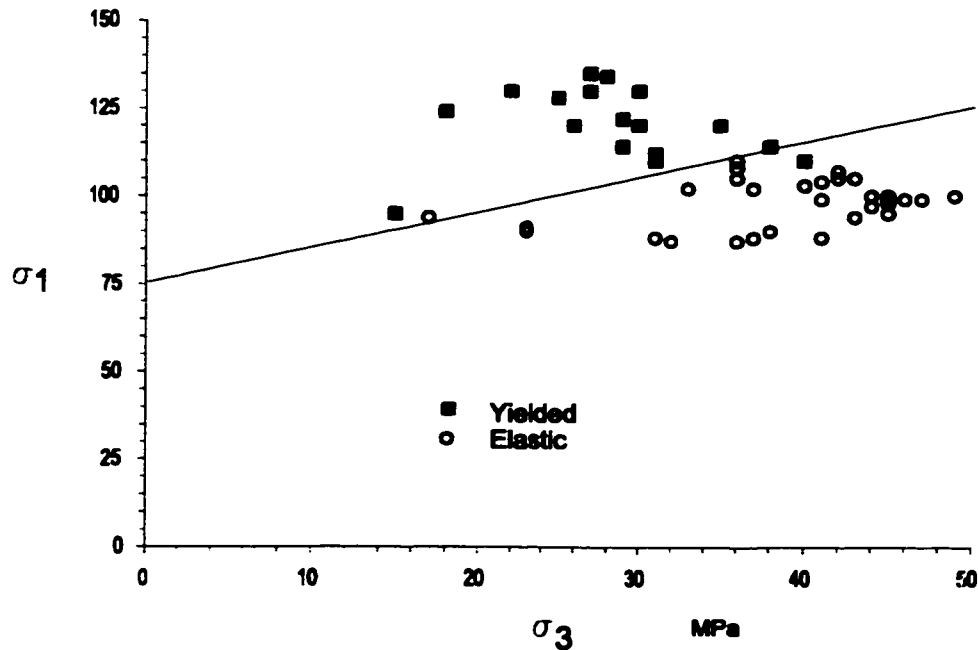


Figure 5.56: Summary of "yield" observations at instrument locations (based on modelling data from Castro 1996).

The constant deviator criterion selected by Castro is shown to be an acceptable separator of the two groups of data (yielded and intact). The intercept, approximately 76MPa, is again in the range of 0.35 to 0.5 times the *UCS* of the norites, depending on the absence (*UCS*=220 MPa) or presence (*UCS*=155 MPa), respectively, of chlorite seams in the samples (Castro 1996).

In the case of Creighton Mine and the SNO cavern, however, it should be noted that a constant σ_1 criterion would also yield an acceptable fit to the data, for non-tensile conditions and for low confining stresses, using a value of $\sigma_1 = 100$ to 110MPa for both cases. All the stress points plotted in either case have a calculated confining stress which is less than the insitu σ_3 (53 MPa), suggesting the possibility of crack dilation upon unloading. This criterion would be indicative of a migrating front of reduced effective confinement (σ_3) due to fracture dilation. Such a front would extend through a larger range of increasing confinement in these rockmasses, as compared to the unjointed URL pluton, due to joint assisted dilation as evidenced by the open joints and fractures in the borehole records of Castro (1996).

5.5.5 Damage Accumulation Levels - Discussion

The range of damage initiation boundary stress and apparent insitu yield threshold (0.3 to 0.5 UCS) is, in part, due to the varying degrees of observational sensitivity in field cases. For example, acoustic emission apparatus used in laboratory experiments is capable of recording the very first crack initiation events. These are likely to be sparsely distributed and infrequent. Damage initiation identified in this way yields the lower bound for the damage threshold. In non-tensile conditions, however, these initial cracks are unlikely to be of consequence. Lateral strain measurements can detect these initial cracks (Chapter 6 and 7) but the impact is minor.

The microseismic system at the URL was a highly sensitive system and was also capable of detecting these initial cracks on a field scale. Damage observed using extensometers and stress change cells (Sudbury Neutrino Observatory) represents an advanced stage of crack accumulation and dilation. Systematic damage accumulation and crack interaction must have occurred for the ground conditioning observed in the Creighton case to have occurred. These increasing levels of damage accumulation (Figure 5.61) are accompanied by increasing levels of strain and dilation.

50% of the UCS represents a reliable upper bound for insitu yield. 30% to 40% of the UCS, used as a constant deviator threshold (or a mildly confinement dependent threshold) for elastic modelling can be used to delineate probable limits for depth of failure in underground excavations. These thresholds appear to be valid in both massive and moderately jointed ground.

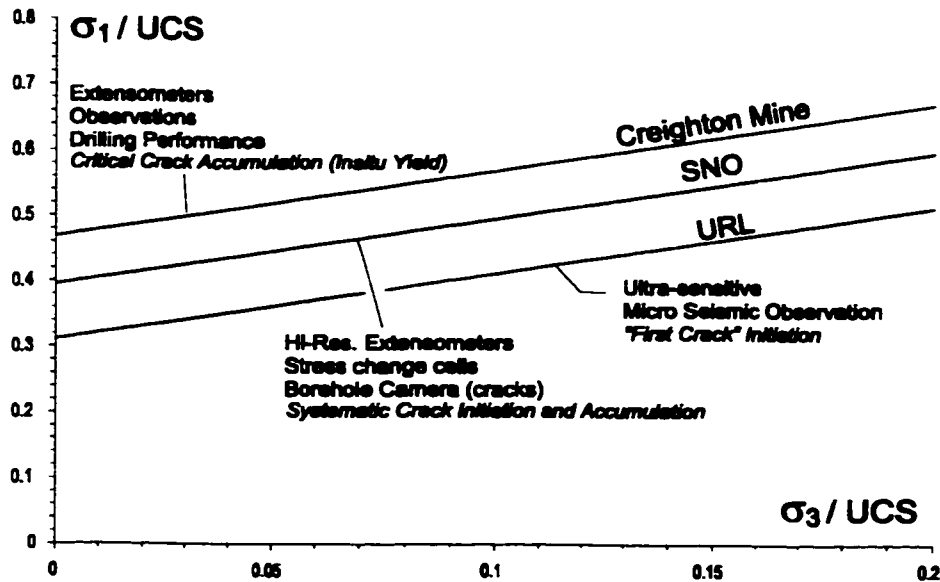


Figure 5.61: Summary of observed damage thresholds (constant deviator shown for example) determined using observational methods of varying sensitivity. (SNO threshold based on norite average; Creighton based on average of granite and norite).

5.6 SUMMARY

The second part of this thesis deals with the important role of inherent or elemental tensile strength and low confining stress on the damage and yield behaviour of hard rocks under induced boundary parallel compressive stress. These two factors combine directly and indirectly to control the insitu strength of these massive or moderately jointed rockmasses. A number of key issues have been introduced or reviewed in this chapter:

- Conventional cohesive-frictional yield criteria and plasticity formulations, including those which incorporate empirical scaling for insitu conditions, perform poorly when applied to highly stressed openings in hard rockmasses.
- Laboratory and field evidence to suggest that in competent rock the near-excavation yield strength is a predictable ratio (approximately 0.4) of the compressive strength of intact laboratory samples and is relatively insensitive to confinement (in near-boundary conditions).
- This insitu yield limit is related to the damage initiation thresholds obtained from laboratory experiments or from microseismic monitoring in the field. Damage initiation is also relatively insensitive to confining stress.
- Yield strength in standard laboratory samples is coincident with long-term strength (under static load), and asymptotic strength for larger samples. This yield threshold also represents the onset of transgranular crack propagation and crack interaction. As such it represents an upper bound for insitu rock strength.
- Crack initiation stress is a consistent material property. A number of factors result in the reduction of insitu yield strength to the crack initiation limit near an excavation boundary.
- Stresses calculated from elastic models (2D or 3D) can be used, in conjunction with a simple near-constant deviatoric stress threshold, to predict depths of failure.

This last point forms a major motivation for this current study. Complex mine geometries, such as the examples shown in Figure 5.62, create significant difficulties, in terms of discretization (meshing) and problem conditioning, for non-linear modelling using domain methods. On the other hand, elastic boundary-element modelling (with surface discretization only) can be done routinely by mine-site personnel. The thresholds discussed in this chapter, as compliments to elastic modelling, offer practical tools for damage delineation, depth of failure prediction and support demand assessment. In order to use these observations with confidence in future design, it is important to gain a further understanding of the mechanisms at work here.

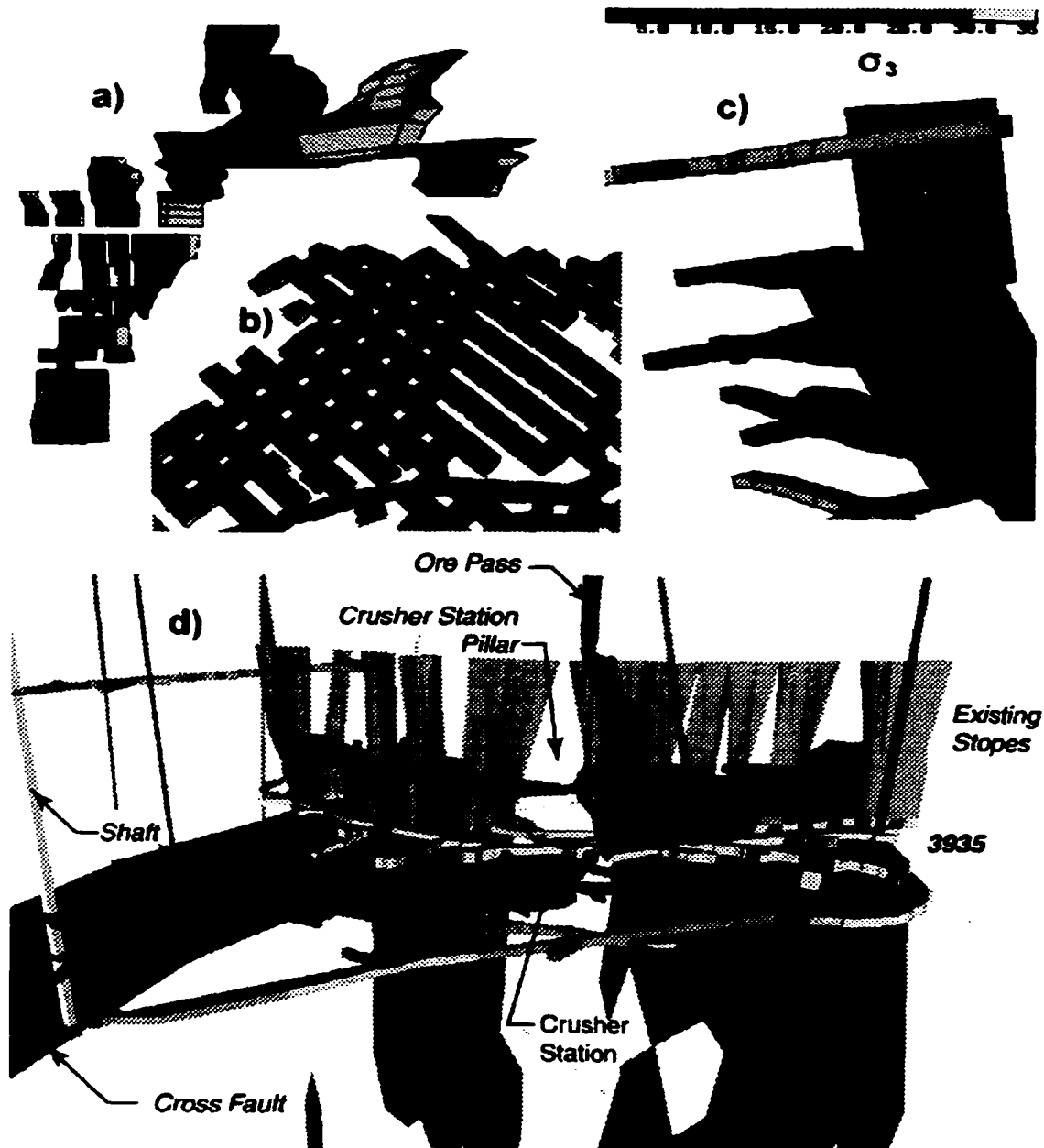


Figure 5.62: Examples of complex mine model geometries: a) Little Stobie Mine, b) McCreedy East Mine; c) Lac Short Mine; d) North Mine. (a, b & d courtesy of GRC; c courtesy V. Falmagne)

To that end, Chapter 6 contains a review and exploration of the basic nature of bonding and extensile crack growth in poly-crystalline solids such as hard rock. Laboratory tests on granite are examined in this context. A linear bonded contact analogue is utilized in Chapter 7 to further explore the nature of damage accumulation and interaction in solids. In Chapter 8 the model as well as real data are used to examine the numerous mechanisms which result in the insitu yield strength reduction and damage thresholds observed in this chapter.

CHAPTER 6

Tensile Strength and Compressive Damage

6.1 INTRODUCTION

An investigation of tensile rupture is of interest in order to ascertain the role of internal tensile stresses and strains in compressive yield and fracture. Chapter 5 presented evidence that in the field, the lower bound for strength of massive rock is controlled by a threshold related to damage initiation. This chapter will investigate the nature of extensile crack initiation, accumulation and interaction and the impact on rupture under various loading conditions.

6.1.1 Extension Cracking and Rock Failure

The propagation of σ_1 -parallel extension cracks is a tensile phenomenon and yet it is observed as a primary damage mechanism at all scales under axial compression at low to moderate confinement (Fig. 6.1). Boundary-parallel spalling (Fairhurst and Cook 1966; Dyskin and Germanovich 1993; Martin et al. 1997) and dilational shear band formation (Dey and Wang 1981; Du and Aydin 1991) are results of parallel extension-crack interaction under these conditions. Shear band formation is, in fact, a secondary process occurring after the interaction and coalescence of extension cracks. These preconditioning microcracks are contained within mineral crystals and along inter-grain boundaries (Moore and Lockner 1995).

While extension cracking is also observed at high confinements, meso- and macroscopic extension cracking (Figure 6.2) is thought, to be a secondary arising from the interaction of in-plane shear faults (Ortlepp 1997). Extension microcracking is still an important primary process for shear propagation at high confinements (Wong 1982) but is limited to a sub-grain scale (Figure 6.3). Extension (Mode I) crack length under high confinement is negligible for distributed

microcracks but becomes significant along with crack concentration at fault asperities (Ortlepp 1997) and shear crack tip process zones (Lockner et al. 1992; Bremaecker and Wei 1994), accounting for the majority of energy consumption during shear rupture (Wong 1982).

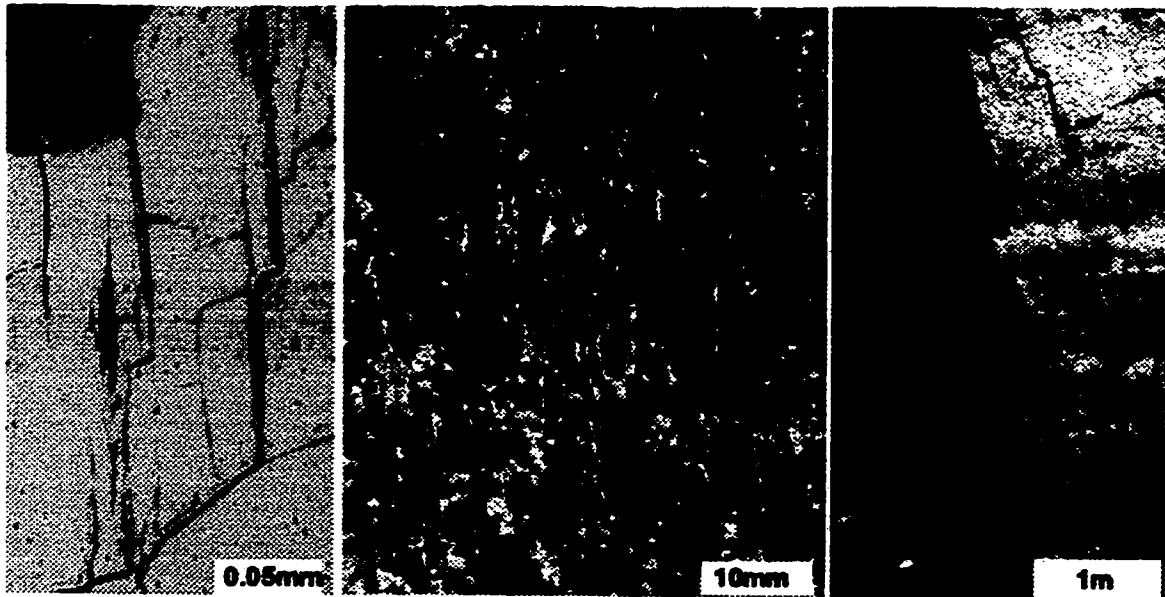


Figure 6.1: a) Axial microcracks in Westerly Granite (modified after Wong 1982); b) cracks (dyed white) in compressive test sample of Lac du Bonnet Granite and c) excavation spall damage (courtesy AECL-URL) In all cases maximum compression is vertical.



Figure 6.2: Macroscopic shear propagation, sloping up to the right, under high confinement with secondary extension and rotational or kink cracks, sloping down to right. Shear extension induced by deep South African gold stopes. (Ortlepp 1997).



Figure 6.3: Microscopic section through shear fault in granite formed at very high confinement with high intensity primary extension cracking around shear surfaces. Maximum compression horizontal (modified after Wong 1982).

In hard rocks such as granite and at normal laboratory loading rates, pure microscopic or mesoscopic shear propagation (Mode II) is normally observed as a primary damage mechanism at very high confinements, greater than 30% of σ_1 (Mogi 1966), or at confining stresses (i.e. σ_3) approaching the magnitude of the unconfined compressive strength of the rock (Jaeger and Cook 1971; Nasser et al. 1997). This results in non-dilatational plastic deformation of materials otherwise considered brittle. Nasser et al. (1997) also report that at such a confining stress level, internal fabric ceases to influence the rock shear strength or the rupture orientation.

Nevertheless, extension cracking is the primary mode of damage at low confining stresses such as those found near excavations. This is significant from a constitutive standpoint since conventional yield and flow models for geo-materials are based on the assumption of shear slip (Chapter 5). In addition, while conventional models used for microseismic studies are based on planar shear source models (Brune 1970; Madariaga 1976; McGarr 1976; Gibowicz and Kijko 1994), seismic events near an active tunnel or mine face (Feignier and Young 1992; Urbancic et al. 1992; Cai et al. 1998) are depleted of shear wave energy and have a dominant "tensile dilation" component.

This observational evidence and the findings detailed in the rest of this thesis support the conclusion that Mode I extension crack growth dominates near excavation damage and yield, mandating the use of updated (tension dominant and confinement dependent) microseismic source models such as that proposed by Cai et al. (1998) and a greater constitutive emphasis on extensile damage and rupture.

Figure 6.4a illustrates three primary theoretical modes of rupture. Most developments in fracture mechanics, related to the rupture of brittle solids at moderate confinements, utilize a tensile or Mode I extension, parallel to σ_1 , of an existing flaw. This flaw responsible for the initiation of extension cracks may itself be a shear or a dilational mechanism (Cook 1965; Ashby and Hallam 1986; Sammis and Ashby 1986), as illustrated in the examples in Figure 6.4b. In turn, macroscopic shear or spalling arises from the coalescence of extended and concentrated axial microcracks (Figures 6.4c, 6.5 and 6.6).

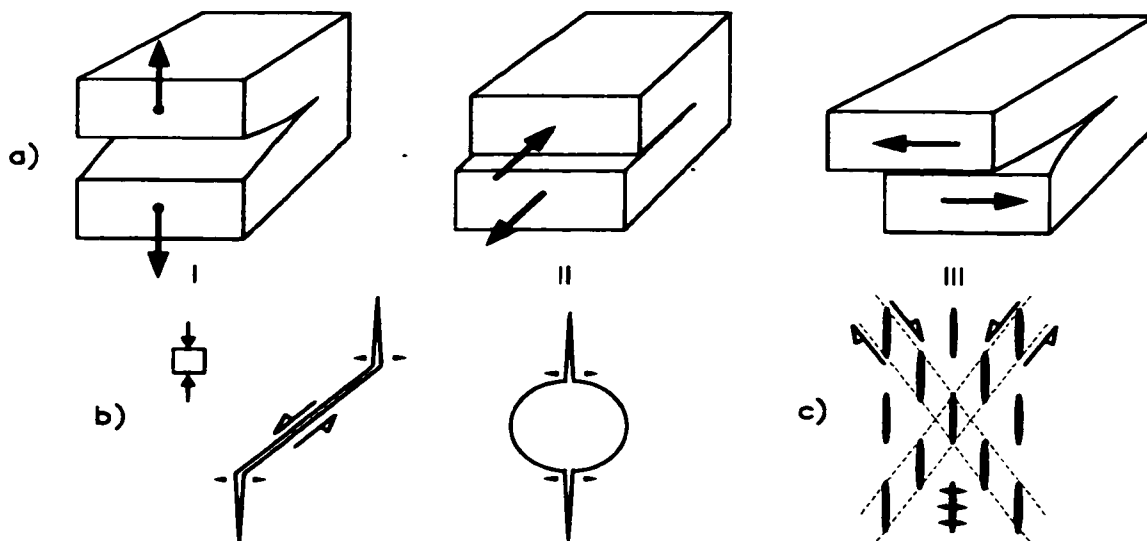


Figure 6.4: a) Modes of solid fracture; b) Mode I crack generation in compression; c) coalescence of axial cracks to form macroscopic rupture.



Figure 6.5: Compression sample of Lac du Bonnet granite (compression horizontal) showing shear surface formed by coalescence of axial (sub-horizontal in picture) extension cracks, forming jagged surface of shear zone (Photo courtesy AECL).

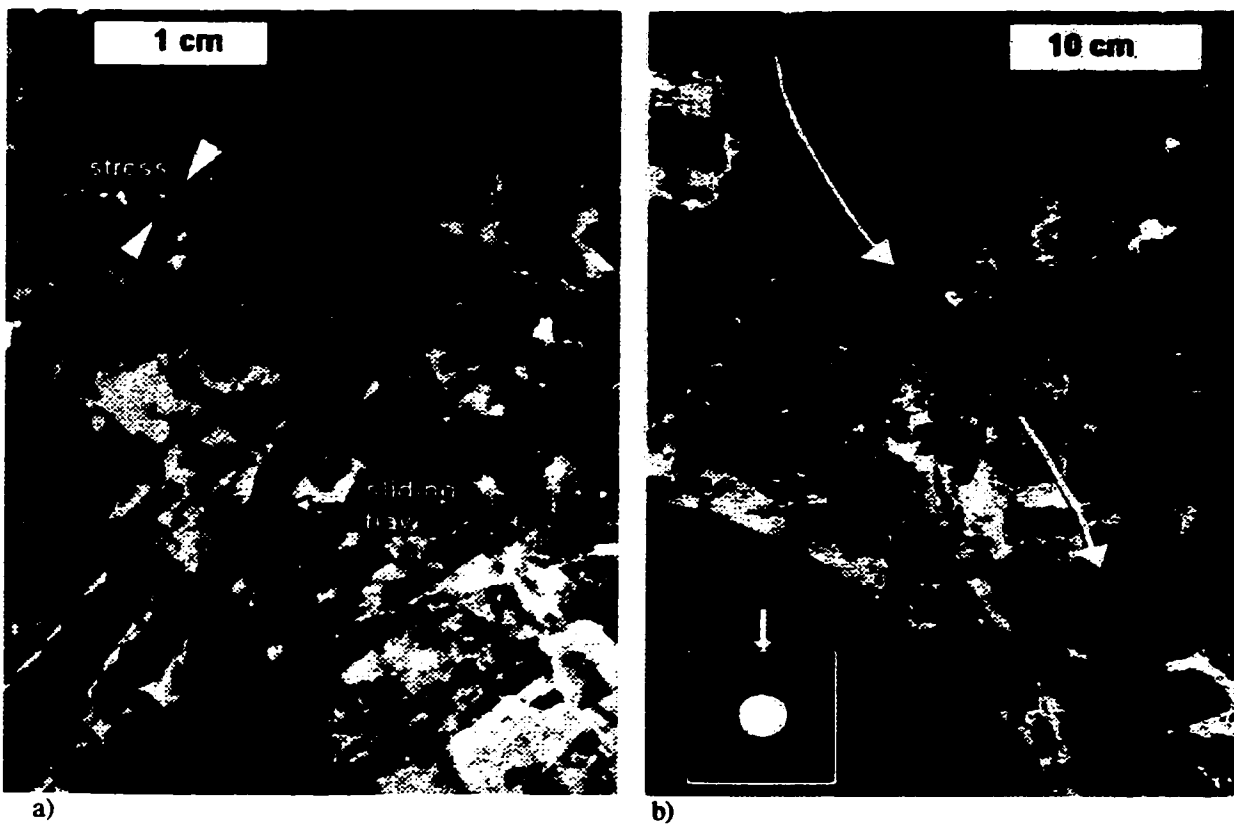


Figure 6.6: a) macroscopic crack forming from interacting microcracks, b) en echelon (shear) array of interacting axial Mode I extension cracks around hole in uniaxial compression. Arrows show stress flow (modified after Lajtai et al. 1994).

In Chapter 5, insitu yield of hard rockmasses, while potentially complex in nature is empirically related to a lower bound stress threshold related to crack initiation. As a corollary, no failure of the rock is possible through cycling, stress corrosion or any other mechanism until the deviatoric, major compressive or tensile stress levels exceed such a threshold. In order to understand the actual degree of in situ strength reduction around excavations, it is important to examine the nature of extension crack initiation and accumulation in bonded solids such as hard rock.

6.1.2 Structure of the Chapter

A review of the physical nature of cohesion bonding and frictional strength in rock materials provides contrast and comparison to other types of strength mechanisms found in metals and soils, materials from which conventional strength criteria were derived before their application in rock mechanics. It will be shown that tensile strength at the atomic level is the dominant property controlling rock damage and ultimate yield at low to moderate confining pressures (and at low to moderate temperatures). The relationships between tensile strength and compressive damage and yield will be examined for typical rock materials, with a particular focus on granite/granodiorite.

The results of a number of standard laboratory tests are presented for Lac du Bonnet granite from Manitoba. These test results are discussed with respect to the demonstrated linkage of damage initiation in tension, mixed loading (tension and compression), and in uniaxial and triaxial compression. The relationship of initial damage to key damage accumulation and interaction thresholds (which in turn determine the yield strength of the sample) is discussed.

Over the last decade, a vast amount of laboratory and insitu testing was carried out on the Lac du Bonnet granite found at the Underground Research Laboratory near Pinawa, Manitoba. The site location has been described in Chapter 5. The test data obtained at the site has been and continues to be a rich resource for research around the world. Just as Westerly Granite (e.g. Tapponier and Brace 1976) was a mainstay of rock mechanics research in the 1970's and 1980's, Lac du Bonnet granite (which contrasts with Westerly granite by a five time increase in average grain size) has become a "standard" rock for the 1990's. This thesis is no exception.

The raw data presented in this chapter has been made available by Atomic Energy of Canada Ltd. and has been reanalyzed by the author for application to this work. The loading tests used here (Figure 6.7) are based on standard rock mechanics practice and include direct tensile tests, Brazilian tests, uniaxial compression and confined compression (axi-symmetric confinement on axially loaded cylindrical samples).

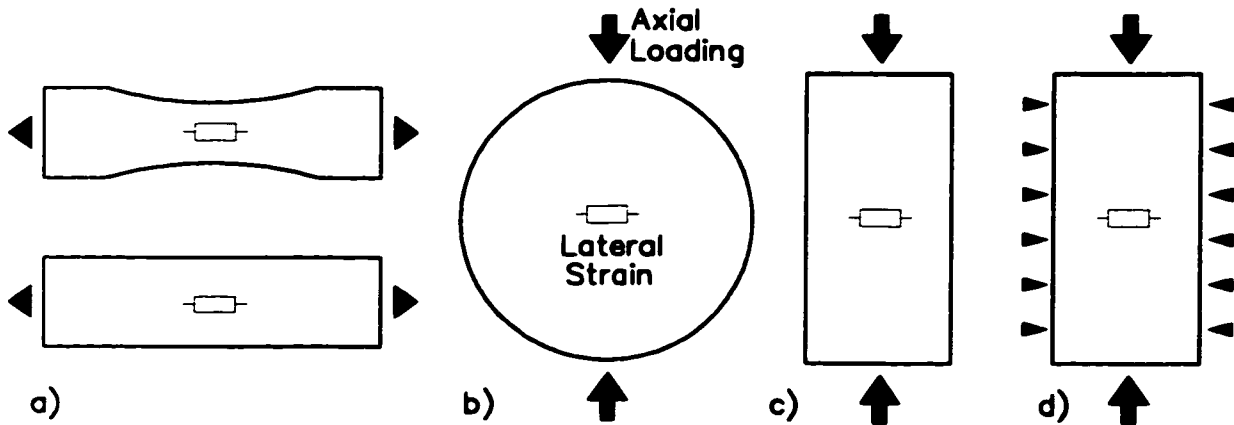


Figure 6.7 Strength testing configurations used in this chapter: a) direct tension; b) Brazilian tension; c) uniaxial compression (*UCS* test) and d) triaxial compression.

Background on these tests and of damage measurement is given in Sections 6.3 and 6.4. Results for Lac du Bonnet granite are then discussed in the remainder of the Chapter. These test configurations are then used as the basis for comparative numerical modelling in Chapter 7.

6.2 ROCK AS A BONDED SOLID

Hard rocks, such as granites, metasediments and others, lie at an upper range of strength and stiffness for composite petrologic materials. Unconsolidated solids such as cohesionless sands or saturated clays occupy the lower range, particularly at low confinements. Intermediate rock types, the so-called soft rocks, include salts (halite, potash) and shales, among others. In engineering practice it is not uncommon to employ similar constitutive laws for inelastic modelling of soil and rock, throughout the entire range of materials described, varying only the absolute and relative magnitude of the model parameters. In near-boundary or low confinement, conditions, however, this approach has met with significant limitations for yield and deformation prediction for excavations in rock (Pelli et al. 1991; Martin, et al. 1998).

Geo-materials occupy three broad groups, in terms of strength characteristics. Uncemented sands, for example, form the class of cohesionless or purely frictional materials (with subgroups related to interlock, dilatancy, collapsibility, etc) as shown in Figure 6.8a. Pure annealed metals also exhibit an initially cohesive (confinement independent shear resistance) response (Illston et al 1979). Saturated clays possess a form of cohesion which, in undrained conditions and using total stresses, completely defines the strength of this material (Figure 6.8b.). In both clays and metals this cohesion can be sustained under significant shear strain. Under drained conditions or if effective stresses are considered, the shear strength of clay is the sum of frictional (confinement dependant) and cohesive strength. Other materials including rock are traditionally assigned combinations of frictional and cohesive strength components, acting simultaneously to define the maximum deviatoric stress at any given confinement (Figure 6.8c). A tensile strength adjustment in the form of a discrete or continuous cutoff is superimposed.

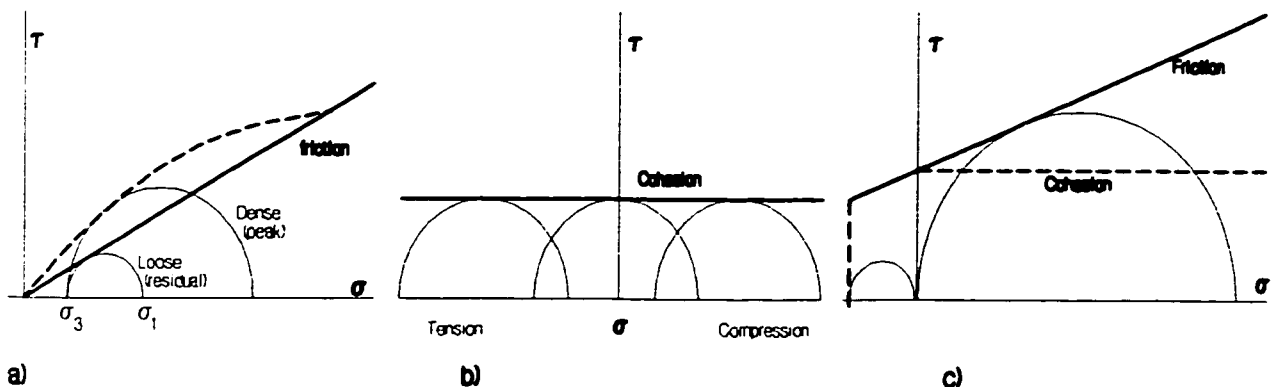


Figure 6.8: Typical yield thresholds for a) purely frictional materials (sand); b) purely cohesive materials (metals) and c) geomechanics models (cohesion + friction).

Some properties of metals are shared by certain rocks, and there is evidence that rock and soil behave in a similar fashion at high relative confining stress (Novello and Johnston 1995). Nevertheless, mechanical differences in the way confinement-dependent and confinement-independent strength components are mobilized result in fundamental behavioral contrasts at lower σ_3 . These differences relate to the molecular bond mechanisms within the materials.

For rock behaviour after the yield threshold is reached, elasto-plastic behaviour (Figure 6.9a) represents the simplest and, to date, most widely used non-linear constitutive model in rock engineering. It is physically realistic, however, only in cases where cohesion and friction act simultaneously to define strength and are strain independent. This is the case (for small amounts of plastic strain) for pure annealed metals and saturated clays, for example. For most dense sands and virtually all rock materials under low to moderate confinements, however, a strain softening model (Figure 6.9b) is utilized. In sands the discrepancy between peak and residual strength results from the additional stress required for dilation as grains must free themselves of mutual interlock before significant plastic shear is possible. In rocks this behaviour is primarily the result of destruction of intermolecular bonding. In the case of shear band formation, dilation within this zone is also a factor. Elastic-plastic or purely ductile behaviour in geomaterials is generally only relevant when σ_3 exceeds 0.3 times σ_1 , according to experiments by Mogi (1966). In the extreme, hard rocks at low confinement can be described by purely brittle post peak behaviour (Fig 6.9c.)

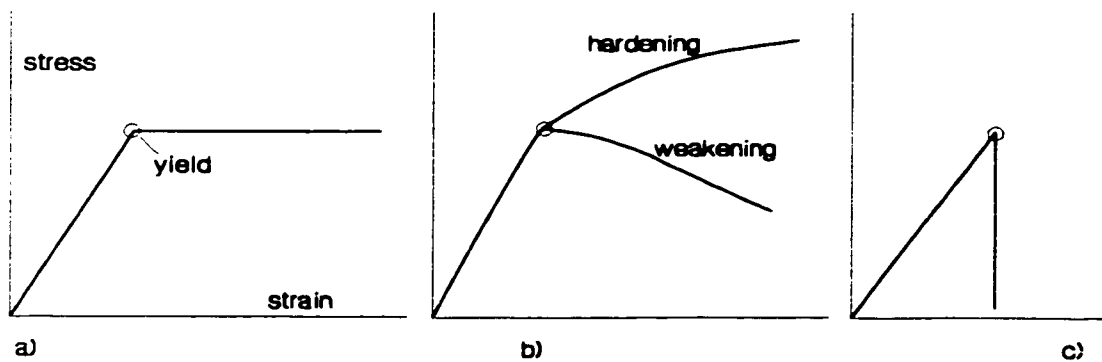


Figure 6.9: Post-yield behaviour: a) elasto-plastic; b) strain hardening/softening; c) perfectly brittle.

Among the bonded solids (excludes purely frictional materials), the differences in yield behaviour can be traced to the nature of the bonds themselves (Fig. 6.10). Pure metals are composed of metallic bonds in which the atomic ions are held tightly within a regular lattice bound by a cloud of “free” electrons. Most minerals found in rock are combinations of ionic and covalent bonds. In the former case the tendency for valence saturation (tendency to “fill” an outer electron layer cations or shed an unsaturated layer altogether) leads to the formation of electrically imbalanced

Legend

BOND TYPE

Damage initiation mechanisms

Strength Components
Tension, Cohesion, Friction

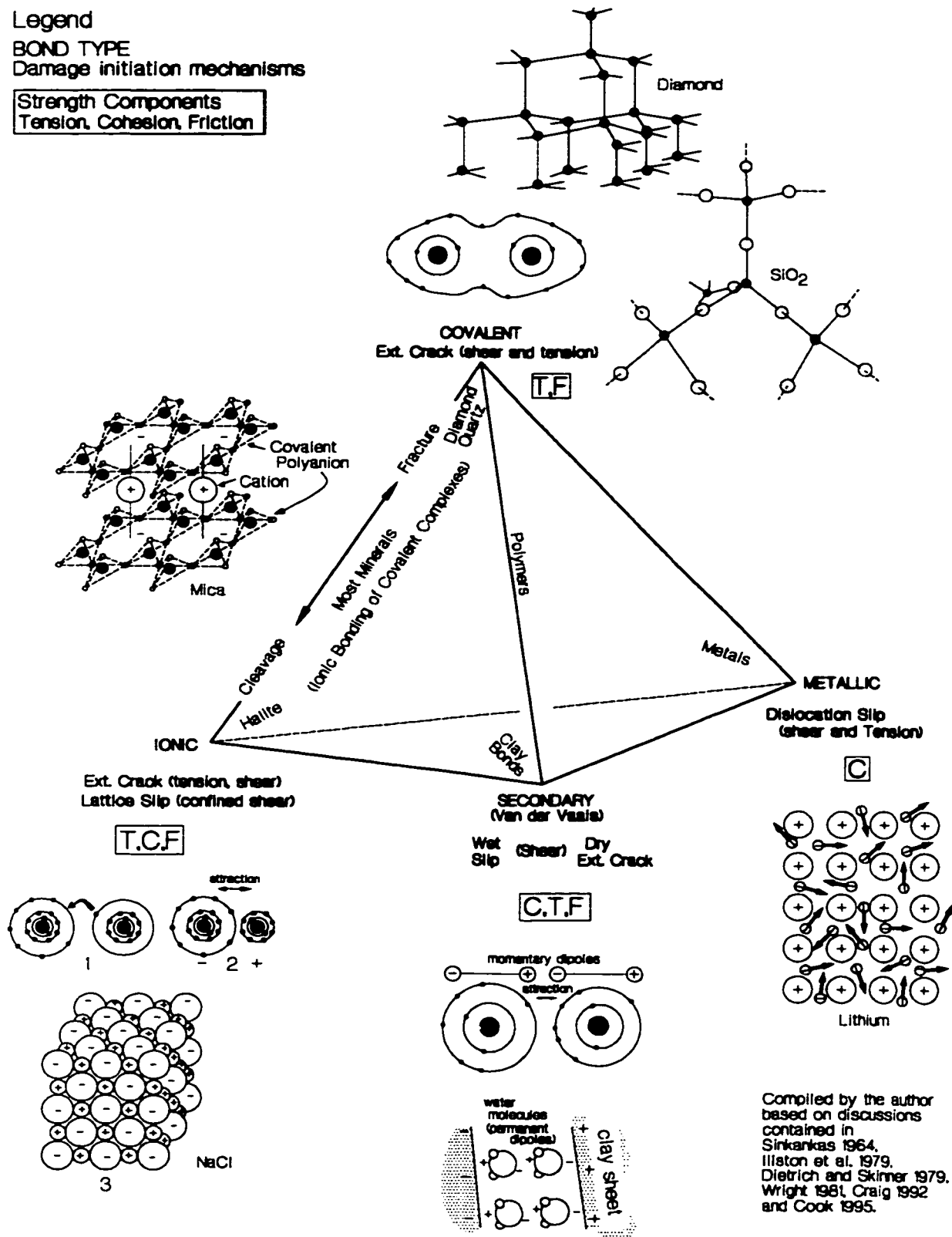


Figure 6.10: Solid bonding types and associated damage mechanisms and dominant macroscopic strength components.

anions (-ve) and cations (+ve) which mutually attract to form ionic bonds. Covalent bonds occur when atoms share electrons in their outer layers to become mutually saturated. Ionically bonded halite (NaCl) and purely covalent diamond (C) represent respective end members of bond types in what is otherwise a continuous series. Most minerals are formed by ionic bonding of covalent complexes (resulting in planes of cleavage in most cases). Cohesive soils such as wet clays are composed of ionic-covalent units which are in turn held together by secondary mechanisms such as Van der Vaal bonding, hydrogen bonding or weak electrostatic attraction.

An idealized atomic bond represents an equilibrium or minimum potential energy state with respect to atomic separation in which the short range repulsive forces between two atomic nuclei are balanced by less severe but longer reaching forces of attraction as shown in Figure 6.11a. Tensile strength of the atomic bond is represented by the maximum net attraction force achieved as two ions are pulled apart (Figure 6.11b). The distributed or discrete nature of the attraction forces distinguishes the different bond types. Typically, a solid containing distributed attractive bond forces is more susceptible to plastic shear deformation as in the case of lattice slip in metals (Figure 6.12). Ionic bonding is normally more discrete although lateral ion (pair) mobility is possible under the appropriate conditions for simple solids such as sodium chloride. Covalent bonds are highly discrete and exist exclusively between individual atomic pairs. Secondary bonding in clays, for example, can be discrete (eg. kaolinite) or distributed (eg. montmorillonite),

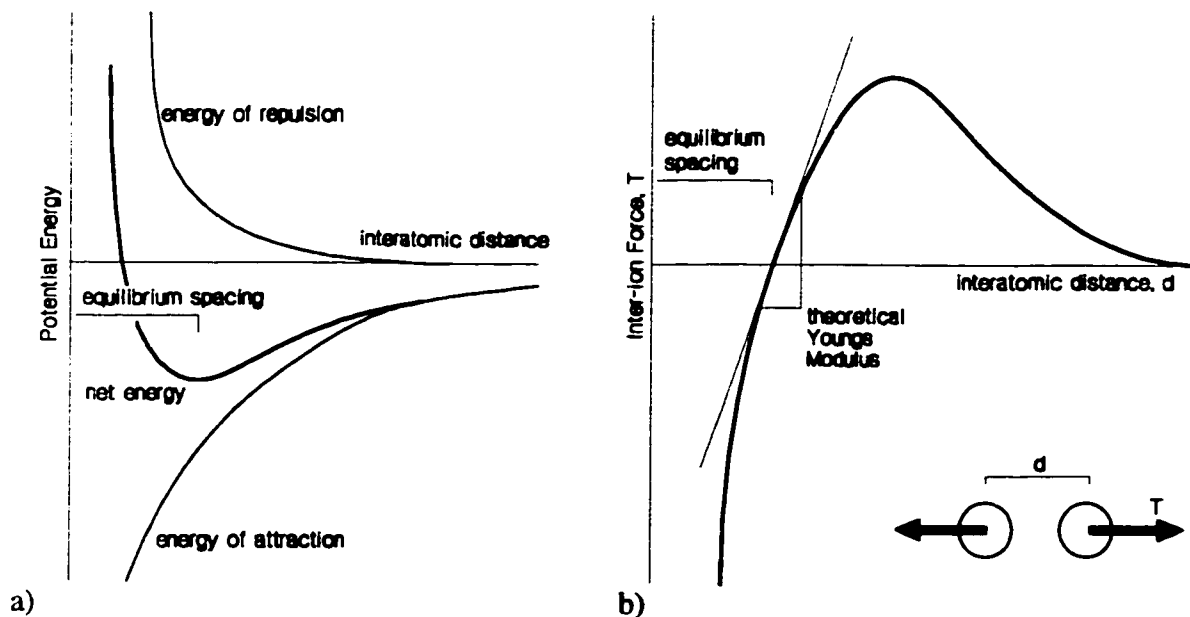


Figure 6.11: a) Potential energies due to atomic repulsion and attraction. b) Bond strength and stiffness.

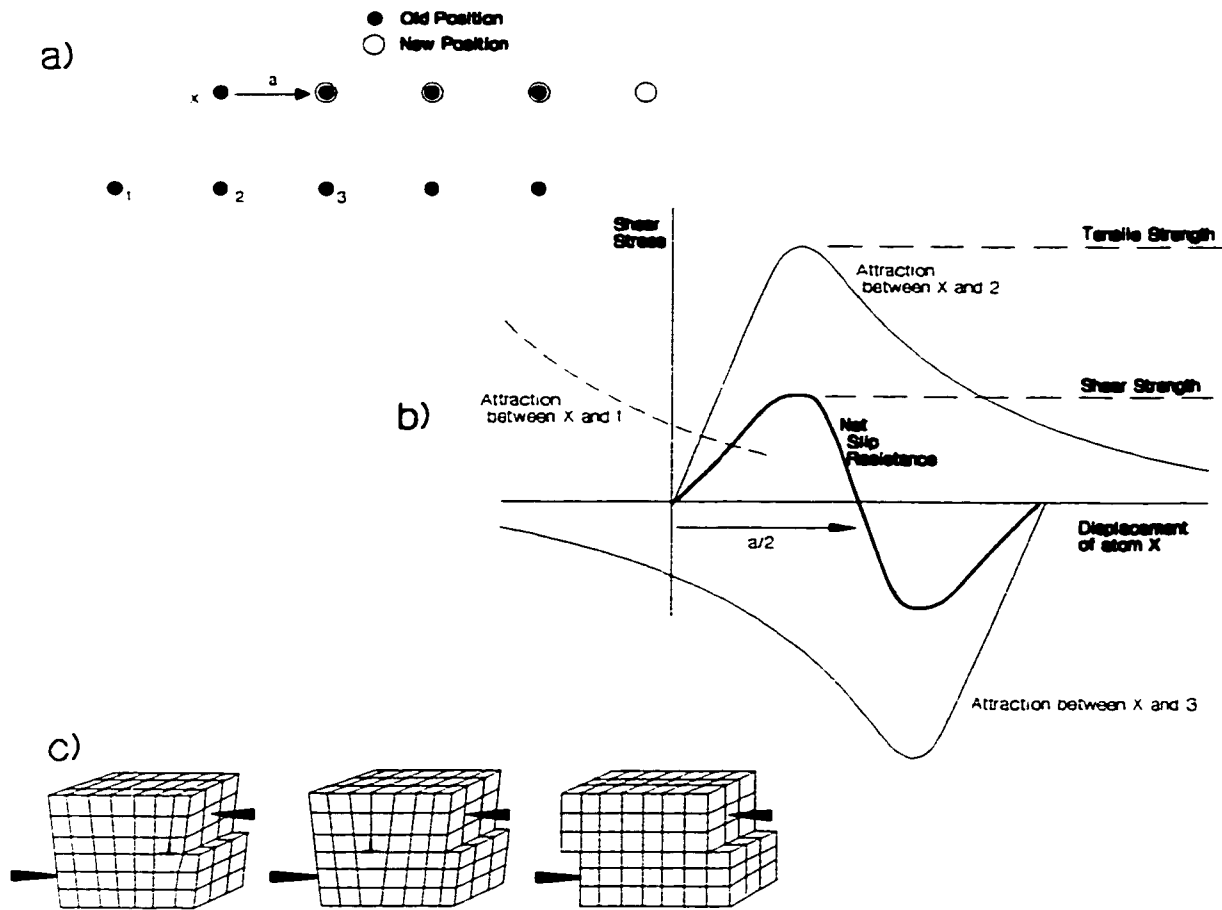


Figure 6.12: Lattice slip: a) continuous slip and b) corresponding stress strain relationship. c) Progressive dislocation slip.

depending on the mineralogy and the water content. Discrete micro-rupture in tension is easier to heal if the bonds are distributed. Discrete bonds can only be broken in tension and are not easily healed (the damage is practically irreversible) at normal temperatures and pressures.

The electron cloud in metals results in a strong but distributed attraction force. In metals the ion lattice has significant tensile strength. Under sustained shear stress, metal ions can shift laterally, with respect to each other, with minimum disturbance in the shared electron cloud. This phenomenon is called lattice slip. In this process ions can readily shift position in response to shearing, taking up a new bonded equilibrium position (Figure 6.12a&b). Relative lateral movement of ions is controlled by lattice mobility (space to move) as much as by the bonds themselves. Line defects, illustrated schematically in Figure 6.12c are called dislocations. These dislocations occur within or at the edge of a crystal and allow lattice slip to occur progressively at

a lower shear strength than would be predicted from the atomic strength of the metal. Since this process results in minimal disturbance of the electron cloud, it occurs far more readily than irreversible tensile separation of atoms (Figure 6.11).

As a result, dislocation slip is the primary mode of plastic yield in metals under compression and in tension (Figure 6.13). At very large strains (> 3% in the case of high grade steel) dislocations converge and interact preventing further lattice slip. At this point the metal will rupture in tension. This so-called dislocation pileup, which inhibits further slip, can also be achieved through work hardening where a strong, stiff (but brittle) metal is required. Annealing is a heating process in which the metal crystal structure is restored allowing for renewed slip and ductile behaviour. The concepts of pure cohesive or confinement independent strength (Fig 6.8b) and of elastic-plastic behaviour (Fig 6.9a) are most applicable to metals, and describe yield and deformation in both tension and compression, forming the basis for the Tresca criterion. The purely cohesive response of metal under compression, as compared to granite, can be seen in Figure 6.14.

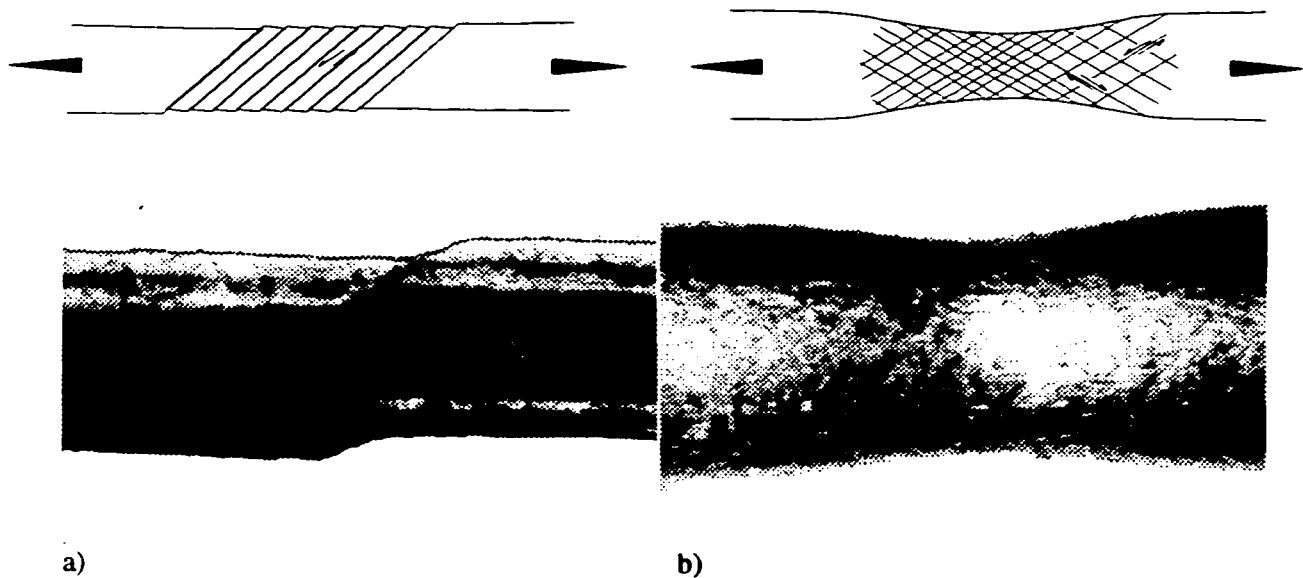


Figure 6.13: Metal bars under direct tension resulting in dislocation slip (plastic shear deformation) a) along a single set of crystal planes; b) opposing slip planes (photos after Illston et al. 1979).

Dislocation slip is a discrete atomic displacement phenomenon which results in macroscopically continuous shear deformation. In saturated clay soils, shear displacement between neighbouring molecular sheets occurs in a microscopically continuous fashion since the interlayer particles

responsible for secondary bonding are increasingly mobile at higher water contents. In addition, in drained conditions, direct physical contact between molecular sheets results in frictional resistance under normal stress. Unlike dislocation slip in metals, the cohesion due to secondary bonding and pressure-dependant contact friction act simultaneously and additively to define the

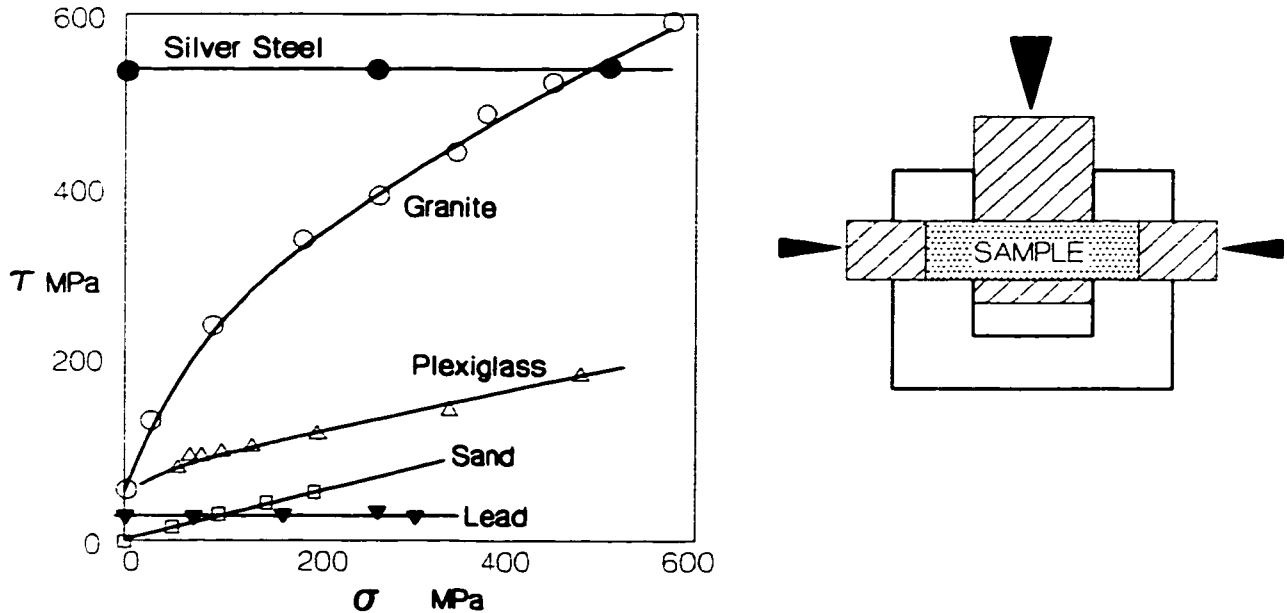


Figure 6.14: Strength vs. Confinement relationships (data from Lundborg 1968). Compare the purely cohesive nature of metals with the confinement dependency of other materials.

macroscopic shear strength of the clay. This is the basis for application, in soil mechanics, of strength models such as Mohr-Coulomb. Another contrast to metals is the relative ease of interlayer separation under direct tensile loading. While shear slip dominates in compression, extensile rupture dominates in direct tension. As clay dries out, the bonding between particles becomes more discrete and tensile cracking dominates behaviour, even in compression (Schmertman and Osterberg 1968).

Lattice or dislocation slip can also occur, although less readily, in simple ionic solids. In the case of halite, large chloride ions are packed together with smaller sodium ions creating an electrically balanced regular solid (See Figure 6.10). The packing in this case is simple enough to facilitate a dislocation style shuffling of the lattice. This does not occur as readily as in metals since the ionic bond is more discrete than the free electron cloud in metals and a dislocation requires the displacement of paired ion units. Under slow loading or under elevated temperatures, shear slip can readily occur in simple ionic solids such as halite and is a primary mechanism of creep in

such solids. This slip is confinement independent (Aubertin and Simon 1997). Under normal loading rates and temperatures in the lab, however, complete and uniform lattice slip is less likely and brittle extensile cracking dominates as in Figure 6.5 (Lajtai et al. 1994).

The competing mechanisms of lattice slip and extension cracking explain the results of Serata (1961). In this work, lateral expansion of salt cylinders was resisted by a steel tube surrounding the sample during axial loading. The confinement provided by the steel tube was calculated from hoop strains. While conventional rubber sleeve biaxial tests showed a confinement dependency for axial strength, the samples tested in the steel tube resulted in a shear strength independent of confinement. It is hypothesized by this author that in the conventional tests, extension cracking was the primary damage mechanism while in the steel tube tests, lattice slip was responsible for the observed yield behaviour. Granites tested by Lundborg (1968), on the other hand, using the same steel tube configuration, resulted in confinement dependent shear strength similar to the conventional tests. The bonding in granite (combination of covalent and ionic) is more complex than in halite and as such, pure lattice shear slip at any appreciable scale is not possible and extension cracking dominates.

For ionically bonded solids, extensile rupture dominates for direct tension, uniaxial compression or increased loading rates. Under these conditions, the behaviour of material such as halite transforms from ductile to brittle since extensile rupture, in contrast to dislocation slip and yield, occurs with an instantaneous strength loss. In this case of lattice slip, once a dislocation cycle is complete, the shear strength of the lattice is restored, resulting in purely plastic behaviour.

Yield of pure covalent solids can only be achieved through extensile rupture following the atomic analogue in Figure 6.11. Composite materials such as the silicate family are composed of complete covalent molecules bound together by varying degrees of complex ionic bonding. Ionic bonding is normally weaker than the covalent structures giving rise to cleavage in these minerals. Unlike halite, however, the complexity of the overall mineral structure does not readily allow for slip dislocation. While plastic shear due to lattice slip within grains of plagioclase, quartz, calcite and other minerals has been observed (Ollson and Peng 1976; Tapponier and Brace 1976; Hobbs et al. 1976) the impact in heterogeneous polycrystalline rock material is limited to the sub-grain scale. This slip can, however, initiate extensile cracking in adjacent grains.

Non-elastic deformation of a typical mineral or rock sample can only be achieved through irreversible extensile rupture (Mode I in Figure 6.4a), either along the cleavage or through the covalent structure, itself. Non-frictional yield strength, therefore, is directly related to the tensile

strength of the crystal structure. While, pure shear cracks (Mode II in Figure 6.4a) have been created in models composed of plaster, shear propagation in rock materials is, in fact, the result of process zone weakening due to tensile microcracks ahead of the shear front or kink rotation of en-echelon tension cracks (Figure 6.15). Mechanisms of extensile cracking under compressive loading are illustrated in Figure 6.16. Extension cracks tend to propagate normal to the direction of minimum principal stress (or parallel to maximum compression). The failure of a laboratory specimen for example involves spalling due to long axial cracks at low confinements (Figure 6.17) or coalescence of small axial microcracks or lattice slip planes at higher confinements, to form a shear band (Hobbs et al. 1976).

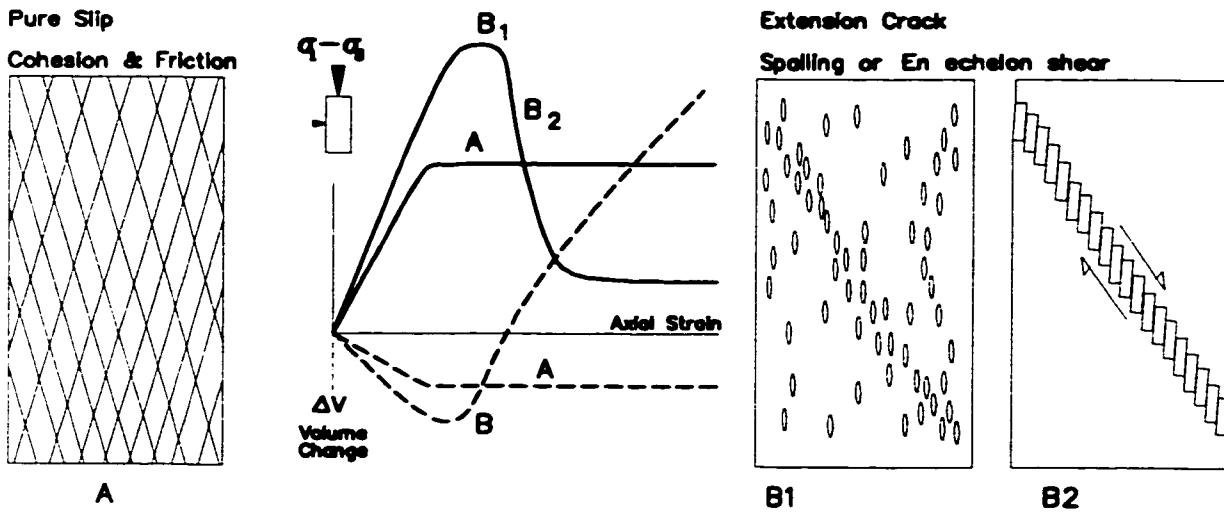


Figure 6.15: Schematic comparison between plastic (continuum) shear (A) and extension crack damage mechanisms (B). B1 illustrates localization and discontinuum transition while B2 indicates full shear development through kink band rotation.

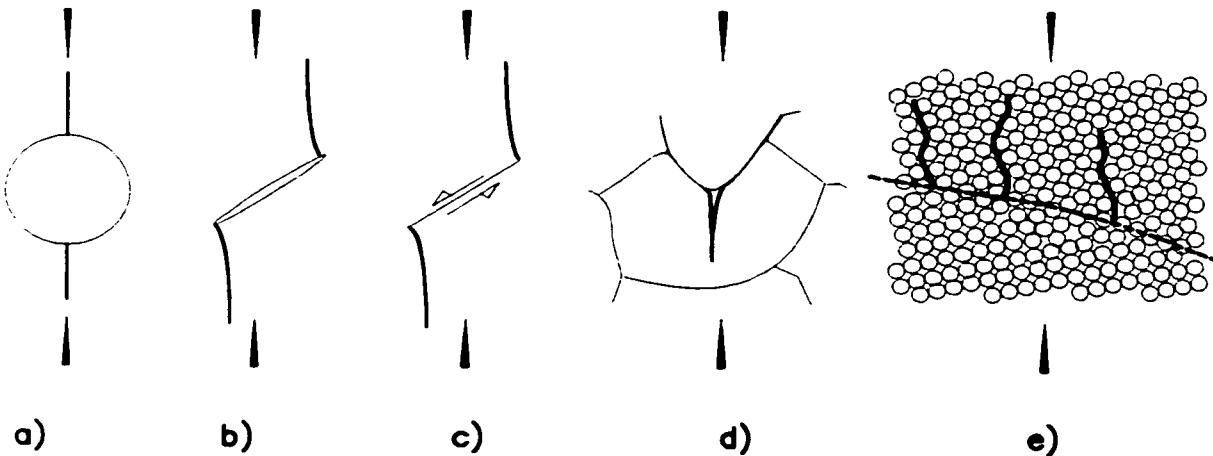


Figure 6.16: Mechanisms of extension crack generation under compressive stress: a) pore; b) Griffith crack; c) sliding crack; d) indentation; e) boundary compliance.

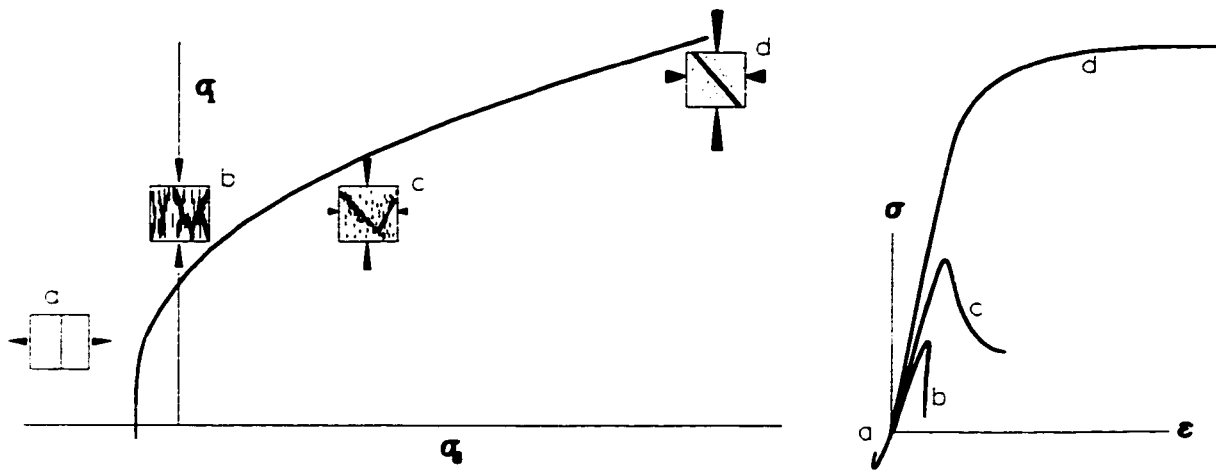


Figure 6.17: Effect of confinement on ultimate rupture mode: a) unstable Mode I crack extension in direct tension; b) quasi-stable Mode I spalling; c) dilational shear by coalescence of axial Mode I microcracks; d) non-dilational shear by coalescence of Mode II lattice slip planes (very high confinement).

In most cases, the surface bonds of extension cracks in ionic or covalent materials readjust to a new equilibrium state and are practically irreversible (without the application of elevated temperature and pressure). This new equilibrium separation distance (between the opposing surfaces) is larger than the original bonded lattice separation in Figure 6.18, resulting in permanent dilation or extension strain within the microcracked body. This is a key difference between this type of damage (dilational) and plastic shear in clays, salts or metals.

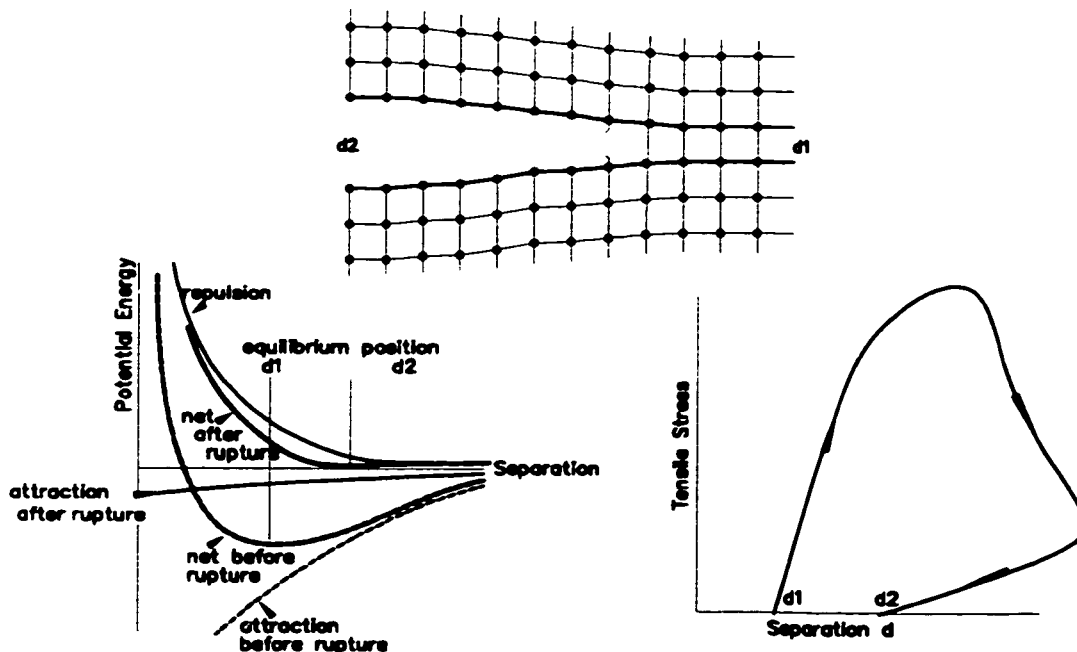


Figure 6.18: Change in minimum potential energy state during bond rupture and resultant irreversible crack dilation (increase in separation d_2-d_1).

Another key consequence of this behaviour is that it does not physically allow for simultaneous mobilization, at the same point, of cohesive (or tensile) strength and friction since tensile-cohesive bonding precludes frictional slip and vice versa. This further enhances the brittle nature of failure at low confinements since cohesion loss is accompanied by the separation of new crack surfaces, depriving the rock of internal frictional resistance until kink rotation (Figure 6.16) results in the re-mating of surfaces. Intact material must be damaged before friction can be active. This lag between critical damage and frictional strength mobilization results in a brittle strength drop at small strains. In the case of pure shear propagation at high confinement (Figure 6.17), frictional resistance immediately replaces cohesion as the localized shear zone propagates. The macroscopic result is a transition from brittle to ductile post-yield behaviour at high confinements as noted by many researchers including Wawersik and Fairhurst (1970).

Although a frictional microscopic shear crack is often employed in fracture mechanics, as a driving mechanism for extension crack initiation (Ashby and Hallam 1986) and therefore as a catalyst for damage and cohesion loss, such cracks are internal and atomically smooth. They possess a minimum friction coefficient less than 25% and as low as 10% of the macroscopic trans-granular shear resistance (Horn and Deere 1962; Lama and Vutukuri 1978). Larger friction values (macroscopic friction) can only be mobilized once sliding rupture surfaces are developed (cohesion loss).

The relationship between sample cohesion loss and friction mobilization has been demonstrated in stiff clays (Schmertman and Osterberg 1968) and recently, in granites by Martin (1994). In the former work, which has been summarized by the author in Figure 6.19, iso-strain thresholds were plotted in stress space as shown. Triaxial compression tests at different confinements were performed on samples of kaolinite and graded sandy clay prepared at different pre-consolidation pressures. Based on the iso-strain contours, effective friction angles and cohesion intercepts could be calculated as functions of axial strain for different pre-consolidation pressures. In the case of the kaolinite, the initial friction, represented by ϕ , is minimal. Cohesive strength dominates at low strain. The friction in both soil materials gradually increases with inelastic strain. Cohesion on the other hand, is practically constant, for kaolinite, over a large range of inelastic strain. This is consistent with the nature of cohesive clay bonding described earlier. For sandy clay, however, the sand particles act as inhibitors to internal slip and create a brittle cohesive component more analogous to that in rock. This component of cohesion drops rapidly as friction is mobilized. The residual (strain-independent) cohesion is due to the clay component alone.

In incremental load cycle tests on granite, Martin (1994) deduced that volumetric strain reversal corresponded to the onset of localized shear nucleation and frictional slip. At a given confinement he could track the cohesion loss and corresponding friction mobilization (Figure 6.20). Clearly, he theorized, frictional strength could not be mobilized until cohesion had been destroyed by crack coalescence along the ultimate slip surface. Remember though, that this friction is distinct from the resistance of microscopic atomically smooth crack surfaces which may be involved in extension wing crack initiation, a necessary precursor to cohesion loss in hard rock materials.

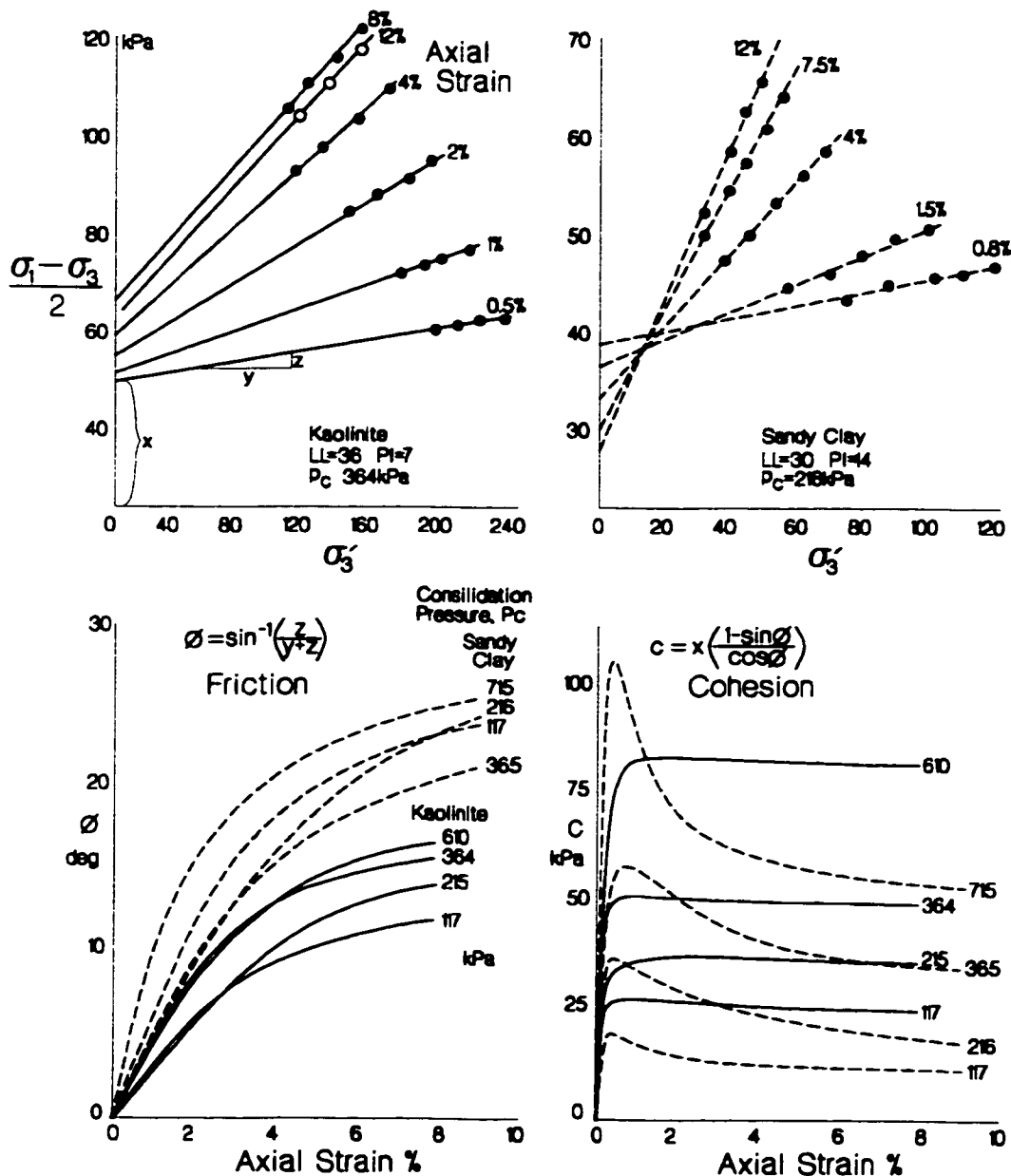


Figure 6.19: Cohesion loss and friction mobilization in two saturated clays (modified after Schmertman and Osterberg 1968).

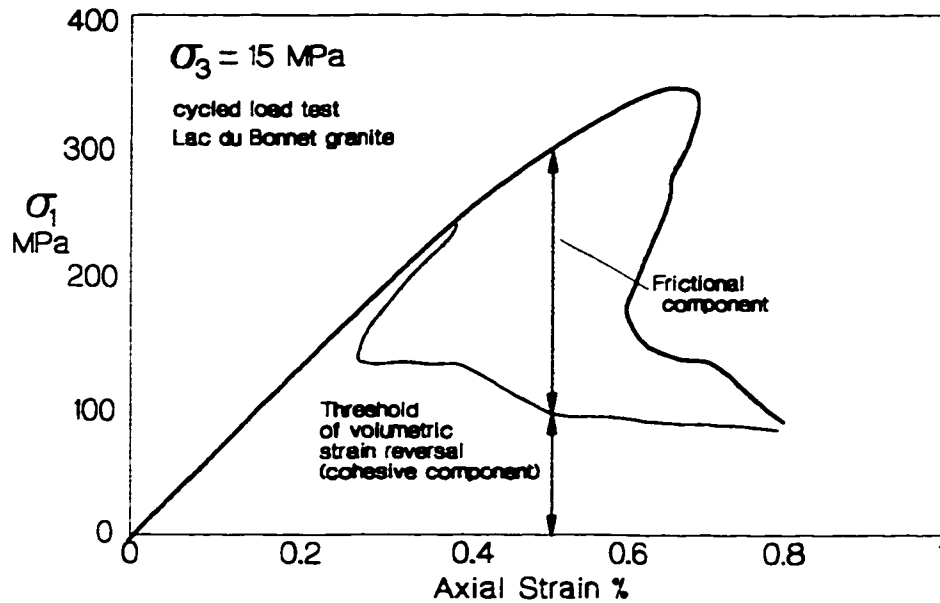


Figure 6.20: Cohesion loss and friction mobilization deduced from cycled loading tests on granite (modified after Martin 1994).

While slip on a crystal dislocation plane is not affected by normal stress, strength loss due to initiation and propagation of extensile microcracks is resisted by such normal pressure. Therefore, in an apparent contradiction, macroscopic “cohesion” in rock must be confinement dependent since extensile cracking or “damage” under deviatoric stress is indeed sensitive to the minor principal stress. It is important, therefore, to differentiate between cohesion at the atomic scale, a term reserved for pure slip within an atomic lattice or involving secondary bonds, and macroscopic cohesion (non-frictional strength or the shear strength at zero confining stress) which is more often controlled, in most rock materials, by microscopic tensile rupture.

It will be demonstrated that a large component of confinement dependency in rock materials, is due to tensile mechanisms unrelated to frictional sliding and yet the term “internal friction” is often employed to explain the confinement dependency of compressive strength. While lower values of friction exist on pure crystalline surfaces and affect the onset of crack damage via the microcrack slip mechanism in Figure 6.16b, the higher values of the friction coefficient often quoted for rock cannot be mobilized until a significant amount of cohesion (atomic and macroscopic) is destroyed.

The stress threshold which marks the accumulation of a critical microcrack density and the onset of crack coalescence defines the true yield point of the rock. This is a confinement dependent but non-frictional threshold (not linked directly to ϕ_{rock}). Confinement dependency of extension crack

growth increases for each stage of crack accumulation and extension. Nevertheless, crack initiation is much less sensitive (although not insensitive as suggested by Martin et al. 1997) to confining stress than is critical crack accumulation and interaction.

Where a shear zone develops by dilation and rotation of axial cracks, there is a lag between cohesion destruction and the development of frictional strength which leads to brittle behaviour. Higher confinements limit the extent of extensile cracking, forcing localization of the eventual shear zone through minimal dilation and minimizing the lag between “cohesion” loss and friction mobilization. The end result is a transition, at high confinement, to a more ductile behaviour.

To summarize, it is possible, from a study of the bonding mechanisms within minerals, to identify several key aspects of damage and yield in brittle rock:

- In most polymineralic rocks, extensile (tensile) microcracking occurs more readily than pure microscopic shear.
- Both spalling and macroscopic plastic shear deformation at small strains are the result of extensile cracking.
- The initiation of extension microcracks are only slightly sensitive to confinement, while crack extension and interaction is very sensitive to low confinement.
- Extensile cracking is dilational in the accumulation phase, becoming even more so during the onset of macroscopic spalling or kink / shear band formation under low confinement.
- Confinement dependence of critical damage (onset of yield) is not directly associated with trans-granular friction, but rather is due to the suppression of dilatancy and crack extension with increasing σ_3 .
- While mineral-mineral friction (sliding flaw) can influence microscopic wing crack extension, (trans-granular) rock frictional strength cannot be mobilized until axial cracks (aligned with σ_1) coalesce locally to create a zone of physical slip well after yield begins.
- The transition from brittle to more ductile behaviour at higher confinements is the result of dilation suppression and the increased relative importance of macroscopic Mode II rupture (through minute but concentrated extension microcracks). Mode II propagation minimizes the lag between cohesion loss and friction mobilization.
- The damage process in hard rock is irreversible (in practical terms).

6.3 DAMAGE INITIATION AND ACCUMULATION

6.3.1 Damage Initiation Criteria

If it is accepted that the initiation and accumulation of extensile crack damage is a necessary precursor to all rupture modes for massive rock, then it is crucial that a suitable criterion be chosen which captures the onset of such damage. A number of phenomenological criterion or so-called damage initiation thresholds have been proposed to predict the onset of rock damage. Most of these criterion have already been introduced in Chapter 5 and several are reviewed again here with respect to damage prediction and the relative role, in each, of tensile and shear mechanisms.

Constant deviator thresholds have been proposed for hard rock (Martin 1994; Castro 1996) based on the Tresca yield criterion:

$$\sigma_1 - A\sigma_3^b \geq \sigma_{ci} \quad [6.1]$$

where A and b are unity, or Von Mises yield criterion;

$$\sqrt{J_2} \geq \sigma_y \quad (J_2 = 2\text{nd invariant of the deviatoric stress tensor}) \quad [6.2]$$

where σ_{ci} and σ_y are constants. These are based on yield via internal frictionless (cohesive) shear. Originally proposed for yield in metals (under compression or tension as in Figure 6.13), these criteria seem to be empirically effective for damage prediction in the field under low confinement conditions (Martin et al. 1996, 1997, 1998; Castro 1996) as discussed in Chapter 5. Pelli et al (1991) had earlier demonstrated the effectiveness, in yield prediction around tunnels, of a similar relationship where A was only slightly greater than unity.

While empirically useful, the confinement-independent cohesion rupture suggested by the Tresca criterion implies a plastic slip mechanism which is inconsistent with the propagation of extension cracks observed in rock (Hallbauer et al. 1973, Tapponier and Brace, 1976 and others) as a primary damage mechanism. The latter, primarily tensile, phenomenon possesses a definite confinement dependency even in the absence of sliding friction.

The original Griffith (1921; 1924) criterion is based on a critical stress concentration around an open but narrow elliptical flaw and attempts to link pure tensile rupture with compressive damage and yield. The Griffith criteria has been unfairly criticized for failing to adequately reflect the ratio of compressive to tensile strengths in rock (Jaeger and Cook 1971), when in fact it is a

damage initiation threshold rather than a peak strength criterion. In direct tension, the damage initiation and peak strength are coincidental while in compression, peak rupture stress is normally at least twice the damage initiation stress (Brace et al. 1966; Scholz 1968; Tapponier and Brace 1976).

Used for initiation, the Griffith concept has validity for low confinement and for globally tensile conditions, and also for highly porous materials with physically open voids. It is somewhat implausible, however, at higher confinements, particularly in low porosity materials dominated by flat planar microcracks, due to crack closure (McClintock and Walsh 1963). The Griffith criterion over-predicts the slope of the damage initiation-confining stress relationship for hard rocks such as granite as discussed in this chapter. Similar models based on tensile cracks emanating from circular pores (Sammis and Ashby 1986), while conceptually sound, also fail to produce realistic results for crack initiation under confined compressive loading.

Models such as the effective-tensile-stress model (Brown and Trollope 1967), the “trellis” model (Trollope 1968; Cundall 1994a) and the similarly posed critical extension strain criteria (Stacey 1981; Stacey and Page 1986) rely on pure and evenly distributed internal tensile strain. In the case of uniaxial compression, these analogues propose that there is an equal internal distribution of lateral compression and tension (resulting in zero net lateral stress). The local and uniformly distributed tension zones are crack nucleation sites. Activation is predicted when the average distributed lateral strain or internal tensile stress reaches a critical limit.

These models are useful in demonstrating conceptually how internal tension arises in a compressive field. The associated criteria, however, result in a relationship in terms of stress which over-predicts the confinement dependency of a crack initiation threshold, resulting in typical axial strength – confining stress slopes (coefficient A in Equation 6.1) of 2 to 6 depending on the magnitude of Poisson ratio or trellis geometry (as discussed in detail in Chapter 7).

In addition, none of these models provide a physically consistent link between tensile and compressive rock response, yielding an over-prediction of direct tensile strength. This and the following chapters will, however, demonstrate that the critical extension strain concept has merit in defining the critical crack interaction and true yield threshold.

Yield criteria such as Hoek-Brown (Hoek and Brown 1980; 1988) and modified Hoek-Brown (Hoek et al. 1992; Hoek and Brown 1998) incorporate the phenomenological assumption of a continuous transition between tensile and shear rupture as confinement increased. These criteria

are oversimplified from a mechanistic point of view although such continuous functions do simplify numerical implementation (Cividini 1993). If appropriately applied, with unconventional selection of key parameters (eg. very low m or slope parameter), the Hoek-Brown criterion can be used effectively to predict insitu damage (Pelli et al. 1991; Martin et al. 1996, 1997). Criteria such as Mohr-Coulomb (Coulomb 1773; Paul 1961; Jaeger and Cook 1971) and Modified Griffith (McClintock and Walsh 1963) are similar in form and all assume varying degrees of dominance of and continuity of transition between tensile rupture and shear failure.

6.3.2 Crack Accumulation and Interaction

Typical failure modes such as spalling and shear failure in hard rock materials can be linked to the exploitation of tensile damage as demonstrated in the particle simulation (PFC^{2D} described in Chapter 7) in Figure 6.21. In this series of experiments, only tensile bond rupture is permitted within the lattice network. No shear rupture of individual bonds is allowed.

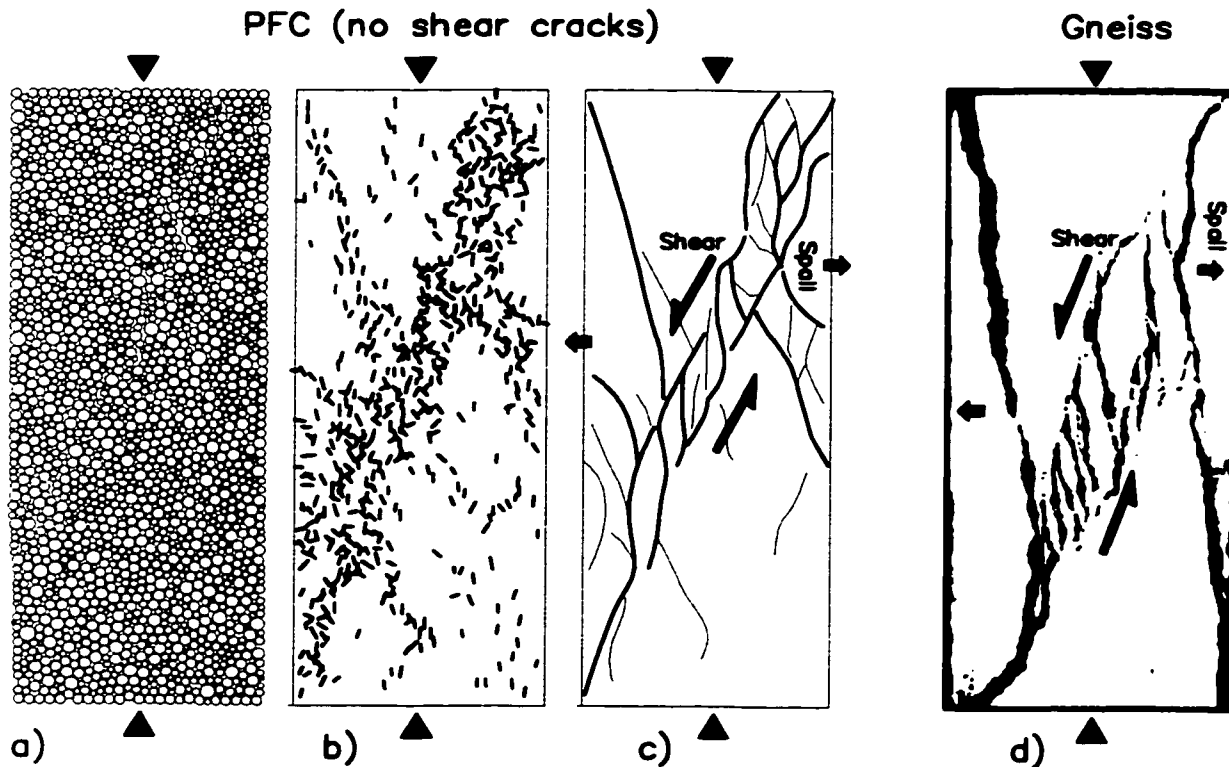


Figure 6.21: Uniaxial compression test simulation performed as part of this work showing final (a) ball, (b) bond rupture and (c) “mesocrack” geometry. No inter-particle shear rupture is allowed – only tensile bond rupture (damage) permitted in these tests. (d) Cross section through actual test (after Li et al. 1998) on Gneiss.

The discs in Figure 6.21a have elastic-brittle tensile bonds at their mutual contacts forming a bond network. The distributed “cracks” in Figure 6.6b indicate sites of bond rupture (note alignment with load axis). Only upon the rupture of a tensile bond is friction allowed to act across the new unbonded contact. In spite of the prevention of shear (cohesive) rupture at the bond level, realistic forms of uniaxial compressive failure and confined shear failure are evident. Compare, for example, the schematic mesocrack geometry from this PFC simulation (Figure 6.21c), and Figure 6.21d from a real test on Gneiss (Li et al. 1998). Three familiar stages of damage are evident. First, primary cracks accumulate and then interact to form mesoscopic structural features (conjugate fractures). Finally, these fractures provide rotational freedom for the generation of a through-going shear zone or extend to form spall fractures.

Clearly, in this model, no material failure can take place, under either tensile or compressive loading conditions, until distributed tensile damage is allowed to initiate and accumulate.

A central hypothesis of this thesis is the notion that compressive rock yield is a function of a critical and predictable crack accumulation density or crack intensity as suggested by Costin (1983). Crack intensity, χ , is normally defined as:

$$\chi = \frac{\lambda \left(\sum c^a \right)}{V} \quad [6.3]$$

where V is the sample volume or area (2D), a is equal to 3 or 2 (equivalent to the dimension of the problem) and c is the half crack length. The geometric constant, λ , describes the volume or area “occupied” by the linear or planar crack (occupied volume assumed to be, for example, square, cubic, spherical or cylindrical). In its simplest form, for 2D cracks of identical length, $2c=2\bar{c}$, each of which is assumed to occupy a square area with side length equal to the crack length ($\lambda=4$), Equation 6.3 reduces to:

$$\chi = \frac{4N\bar{c}^2}{A} \quad [6.4]$$

where N is the number of cracks and A is the sample area. While the geometric factor (4 in this case) is often ignored for simplicity, Equation 6.4 is the relationship used for the simulations in Chapter 7.

Based on near-crack stress studies by Pollard and Segall (1987) and crack connectivity studies by Madden (1984), Lockner et al. (1992) conclude that crack interaction first occurs at an inter-crack separation equal to length, so that the critical distributed crack density is approximated by:

$$\chi_{cr} \approx \frac{1}{(2c)^2} \text{ or } \frac{1}{(2c)^3} \text{ for 2D and 3D respectively} \quad [6.5]$$

where the inter-rack spacing is equal to or less than the mean crack length. Equation 6.5 represents a fully cracked state (unit crack volumes completely fill space).

In a heterogeneous sample, however only two cracks within the critical separation are necessary to commence localized interaction and straining; a requisite for yield. This interaction can occur stochastically at overall crack densities far lower than predicted by Equation 6.5. A homogenous sample must reach a uniform critical crack density before localization can occur, while interaction and localization are the result of stochastic crack accumulation in a heterogeneous sample and can occur much sooner (lower overall density). In such a material, crack interaction and incipient yield can manifest locally prior to significant damage elsewhere in the sample.

In the absence of excessive crack extension ($\Delta c / c_0 \ll 1$) new crack density is a linear function of crack nucleation or number, N , of new cracks. The same is true in the case of the bonded particle simulations in Chapter 7 or in a purely elastic grain-supported material in which new cracks are initially restricted to a finite half-length $c = \bar{c}$ (Fig. 6.22a). If cracks are allowed to extend, say in tension or at a low local confinement, then the local crack density becomes a power function of the local crack length leading more rapidly to critical crack density with fewer nucleations as shown in Figure 6.22b.

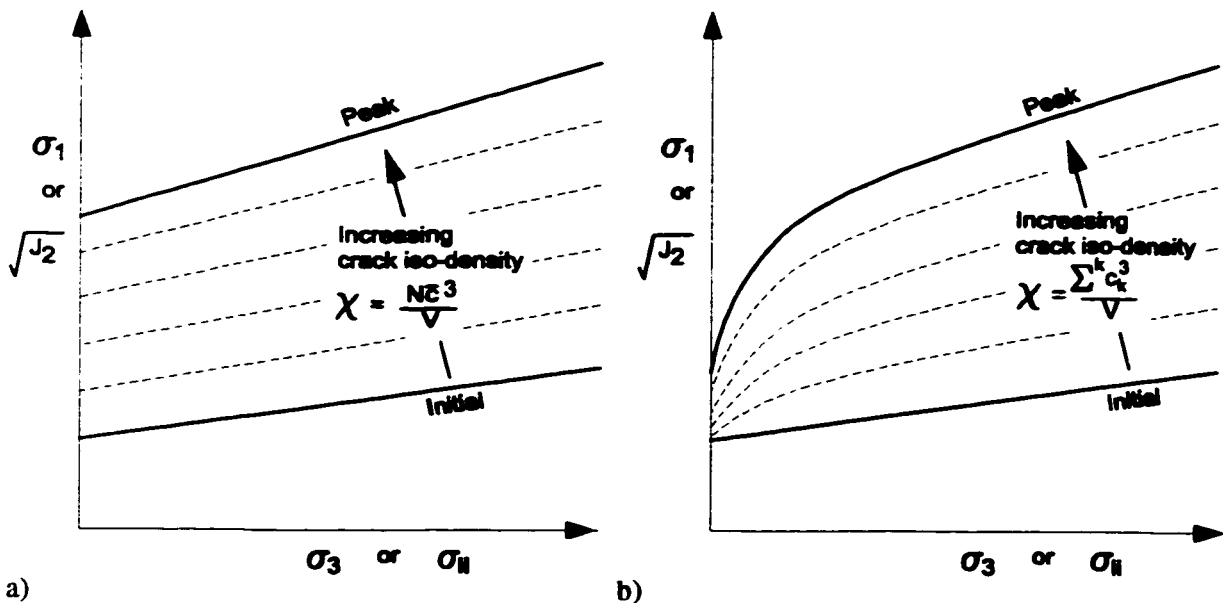


Figure 6.22: Crack iso-density contours for a) non-extending cracks – accumulation only; b) cracks allowed to extend under appropriate (e.g. low confinement) conditions.

Cracks which initiate under predominantly tensile conditions are inherently unstable and propagate instantaneously, while extension cracks generated in compressive conditions require additional load for incremental propagation.

The probability of interaction between cracks, and localization of strain leading to rock failure, is sensitive to inter-crack separation and therefore to crack density (Madden 1984; Lockner et al 1992) which, itself, is a linear function of crack concentration (number per volume) and a quadratic (2D) or cubic (3D) function of crack length. The major compressive stress, σ_{1ext} , required for incremental crack extension (lengthening) varies directly with confining stress, with the slope $\Delta\sigma_{1ext}/\Delta\sigma_3$ increasing as a power function of total crack length (Ashby and Hallam 1986) as suggested by Figure 6.22b. Interaction and localization must therefore be highly sensitive to local confinement near the crack source. It is interesting that this confinement dependency of crack interaction, a precursor to yield, is not directly related to sliding friction as is normally supposed for rock strength.

6.3.3 Rock Testing and Stress Paths

Understanding the inter-relationship between tensile crack propagation and compressive strength is essential for predicting damage accumulation and strength degradation around underground openings. In particular, certain stress paths can result in an increase in the number of microcracks (increasing deviatoric stress at moderate confinements) while others will tend to extend existing cracks (reducing confinement under sustained deviatoric stress). The former stress path is reflected in standard laboratory testing, while the latter trend is responsible for the significant observed reduction in field strength around excavations.

Investigations later in this chapter focus on the relationship between damage under pure tensile loading conditions and the initial damage mechanisms in uniaxial and confined compression. As an intermediate configuration, the Brazilian test provides additional insight into the nature of the damage threshold. The respective loading and geometrical configurations were summarized in Figure 6.7, while the stress paths (in two dimensions or for axisymmetric conditions) are shown in Figure 6.23. Data from the literature as well as test data for Lac du Bonnet granite will be examined for the first four configurations. PFC simulations will be used to investigate key aspects of damage initiation under all five loading conditions.

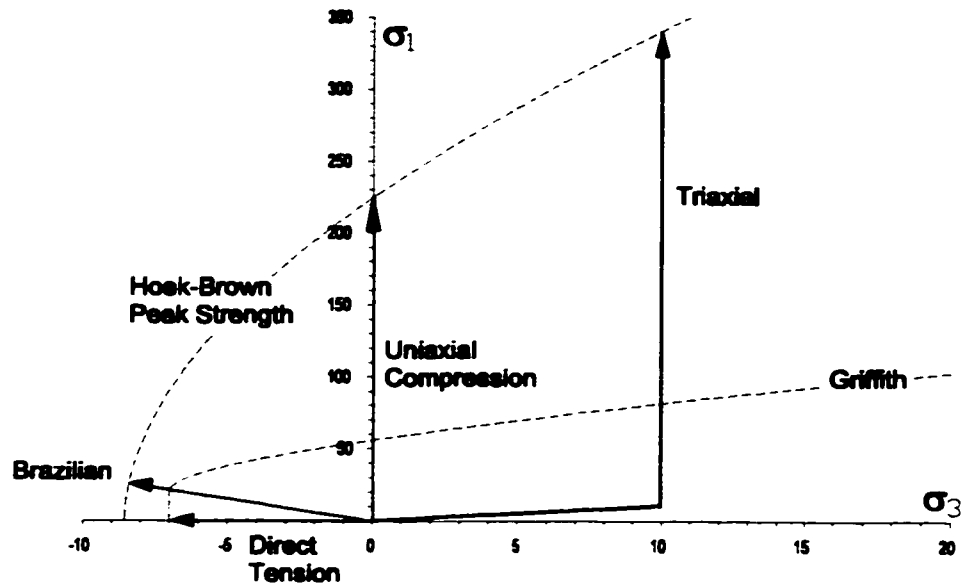


Figure 6.23: Elastic stress paths for different laboratory test configurations.

6.3.4 Damage Measurement

Damage induced by rock loading can be investigated using the electron microscope. Numerous excellent studies on different rock types can be found in the literature (Olsson and Peng 1976; Tapponier and Brace 1976; Wong 1982; Fonseca and Murrell 1985). In addition, acoustic emissions, elastic strain waves emitted when a crack undergoes momentarily unstable propagation to a new equilibrium position, can be monitored and the events can be counted and located within the sample as in the work by Scholtz (1968), Lockner (1993) and Falls (1993), for example. This study will focus on the strain rate changes brought about by damage accumulation, as schematically illustrated in Figure 6.24.

Of particular interest is the relationship between lateral or extension strain and failure. Lateral strain is the most sensitive to the creation and dilation of axial cracks, the primary damage mechanism. Inelastic lateral strain gives the best non-invasive quantification of crack damage accumulation and correlates well with the onset of crack damage as observed using acoustic emission detection (Eberhardt et al. 1998).

Axial stress – axial strain plots are the common form of test data presentation. This relationship, however, offers little insight into the onset and accumulation of damage prior to localized yield. This study will show, however, that crack coalescence and interaction (and the onset of sample yield) is first reflected in the axial stress-strain response.

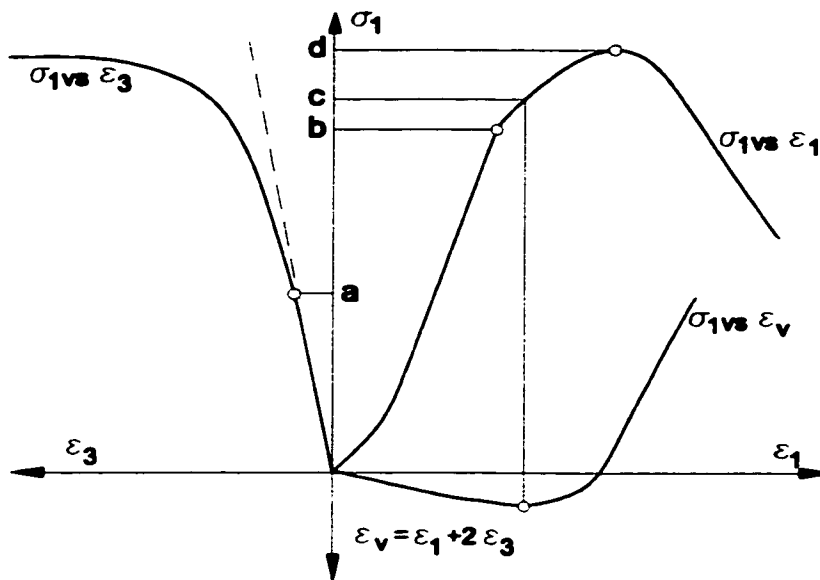


Figure 6.24: Strain thresholds incurred during uniaxial compression loading: a) damage initiation; b) axial non-linearity; c) volumetric strain reversal d) peak strength.

Study of the volumetric strain response had become popular for its heightened sensitivity to damage processes (Brace et al 1966). Volumetric strain reversal is used (Martin 1994) to identify the onset of yield, although Crouch (1970) suggests the use of the lateral strain – axial strain response for the study of damage initiation.

Both the lateral strain – axial strain response and the volumetric strain response suffer from a “lag” at the point of crack interaction and localization. Since this threshold can result in an acceleration of both the axial strain (compression negative) and the lateral strain (expansion positive), the two responses tend to momentarily compensate for one another. In addition, the thresholds are defined by changes in slope of the relationship and as such, detection is hampered by the coincident strain accelerations of both variables.

For these reasons, this work will utilize primarily the lateral strain – applied stress response for damage initiation and also for yield identification in the tensile and Brazilian tests, and the axial stress – axial strain response for yield in compression tests. In a constant strain rate machine with a servo-control, the applied stress experiences a reduction in the rate of increase as yield is approached, while axial and lateral strain accelerate. This superposed response leads to clearer threshold definition. Another advantage over the volumetric strain approach is the transferability to 2D problems such as Brazilian testing and numerical simulations.

Naturally, in the case of tensile testing, the lateral stress (axial with respect to loading but considered lateral for consistency) is used instead of the vertical stress. In this thesis, the term lateral strain is used for convenience but is synonymous with minor principal strain (compression-positive convention), which in all cases investigated, is extensile.

Of particular interest is the relationship between extensile strain, ϵ_3 , and damage initiation. The observed phases of damage initiation may be divided into random initial damage and systematic damage. The latter considers the onset of damage which relates directly to the consistency of orientation (cracks aligned parallel to compressive loading direction) and consistently increasing crack density (χ) accumulation rate:

$$\frac{\partial^2(-\epsilon_3)}{\partial \sigma^2} \propto \frac{\partial^2 \chi}{\partial \sigma^2} = \text{a positive constant} \quad [6.6]$$

It is also of interest, in this study, to identify key thresholds of damage accumulation, namely initiation, coalescence and localization, and to examine the continuity (or discontinuity) of these thresholds through a range of loading conditions from direct tension through to confined compression.

The relativity of these thresholds depends on the rock type, as illustrated for the case of uniaxial compression on in Table 6.1.

Table 6.1: Examples of uniaxial compression thresholds for various rock types.

	Stress threshold in MPa and (multiple of σ_{ci})						
	Dolomite <i>Hatzor & Palchik</i> (1997)	Potash ----- <i>Martin (1994)</i>	Limestone	Granite	Quartzite <i>Bieniawski</i> (1967)	Marble <i>Fonseka et al</i> (1985)	Sandstone <i>Brace et al.</i> (1966)
Crack initiation, σ_{ci}	85	6.5	12	70-80	114	32	121
Non-linear axial stress/strain	na	na	48 (4)	150-180 (2.1)	234 (2)	70 (2.2)	na
Volumetric strain reversal	102 (1.2)	8.5 (1.3)	56 (4.7)	160-190 (2.2)	241(2.1)	na	170 (1.4)
Peak strength (UCS)	117 (1.4)	16 (2.5)	60 (5)	210-240 (3)	283(2.5)	84 (2.6)	234 (1.9)

6.3.5 Comparison of Tensile Strength and UCS

The nature of the rock material also influences the ratio of ultimate compressive and tensile strengths, as summarized in Figure 6.25.

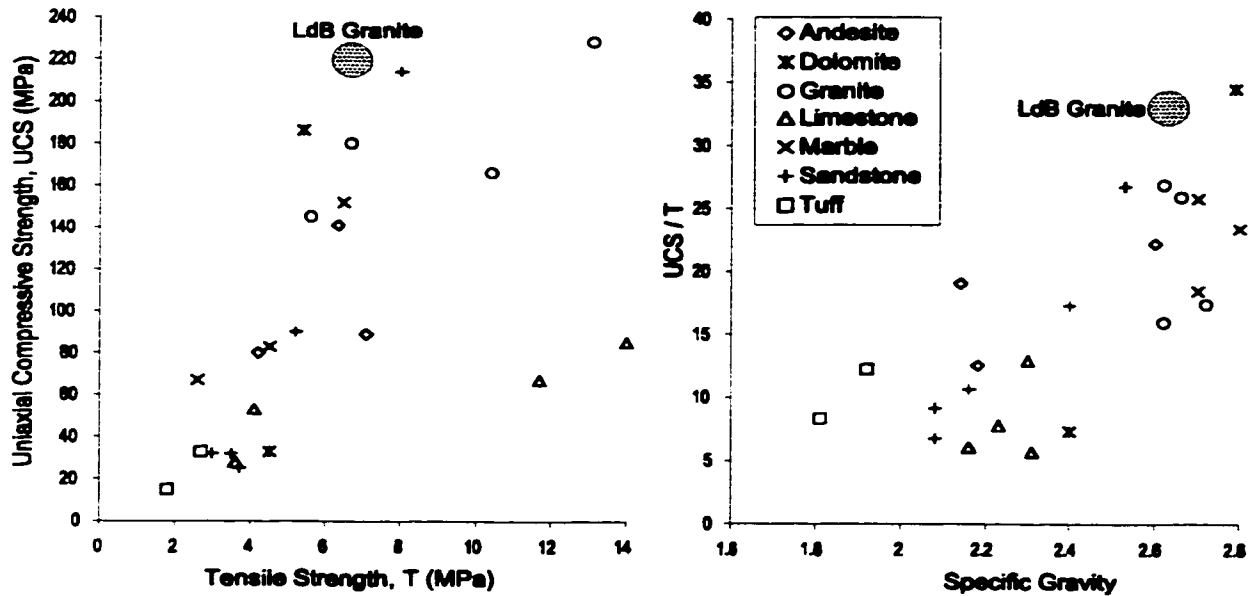


Figure 6.25: Compressive/tensile strength comparison. LdB = Lac du Bonnet Granite data from this study. (Other data from Okubo and Fukui 1996 and from Lama and Vutukuri 1978).

In this summary of experimental data, it can be seen that rocks with greater porosity (lower density) have compressive/tensile strength ratios approaching the theoretical value of 8 predicted by the original Griffith (1924) criterion and a factor of 12 predicted by the extended (3D) Griffith criterion developed for cylindrical geometries (Murrell 1963; Jaeger and Cook 1971). These theoretical values are related to the assumed presence of thin elliptical and ellipsoidal flaws (respectively) which remain open (no shear resistance between the opposing faces) during compression.

6.3.6: Tensile and Compressive Damage: A Case for Distinct Thresholds

The assumptions of Griffith may have increasing validity for higher porosity materials. In low porosity rocks, cracks of infinitesimal aperture can have a profound impact on crack propagation in direct tension while closing and becoming inconsequential under compressive loading. This must be particularly true for rough inter-granular cracks ($\mu > 1$) such as the large iron (-oxide)

lined crack to middle-right in Figure 6.26. Any macroscopic shear rupture must engage friction on these rougher surfaces. Thus the compressive/tensile strength ratio for these rocks is significantly higher than the theoretical prediction.

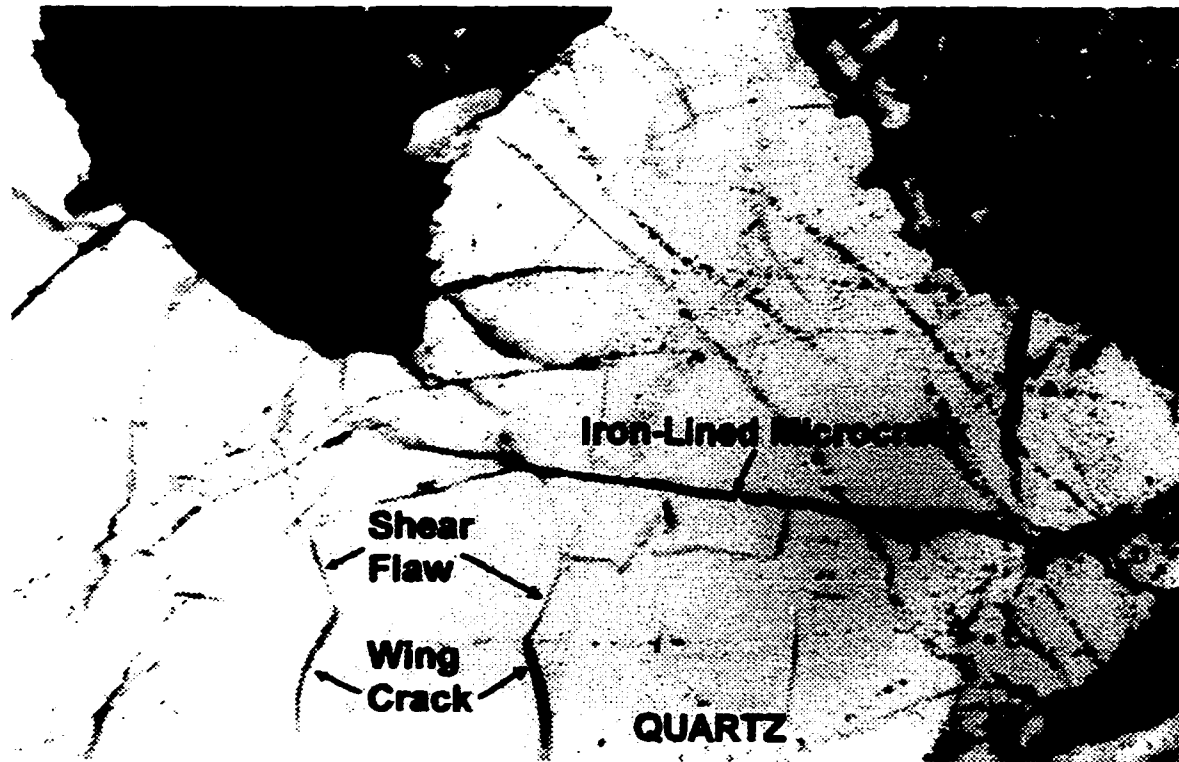


Figure 6.26: Lac du Bonnet Granite (modified/annotated after original micrograph courtesy AECL): large filled, high friction microcrack (middle) in Quartz which could be critical in normal (vertical) applied tension; small, inclined, low friction flaws (lower left) which have generated extension wing cracks under (vertical) compression. Horizontal field width = 2.5mm.

Sliding planes which are perfectly smooth (cleavage, twinning planes, lamellae, intra-granular microcracks), however, can have significantly lower friction ($\mu < 0.3$) according to Horn and Deere (1962) and may become realistic catalysts for wing crack propagation in compression (lower-left in Figure 6.26) as suggested in classic fracture mechanics models (McClintosh and Walsh 1963; Cook 1965; Ashby and Hallam 1986).

Depending on the selected friction coefficient, sliding crack models for wing crack extension will result in a higher ratio (high μ) or a lower ratio (low μ) of compressive to tensile strength than that predicted by Griffith. It is logical to assume that the lower friction values are valid for damage initiation while peak strength and post peak behaviour is influenced in part by the higher trans-granular values of μ . These high values, however, can only be fully mobilized once a

macroscopic rupture surface is formed. At low confinements in brittle rock, therefore, peak strength is more likely to be controlled by the kinematics of crack extension (and interaction) rather than by trans-granular friction.

It is neither contradictory nor tautological to hypothesize that cohesive damage and degradation, through tensile crack extension, can be controlled by mineral friction, while trans-granular or peak frictional strength cannot be mobilized until such cohesion has been destroyed. This latter notion of non-simultaneous cohesion and friction, and the mobilization of peak friction after cohesion loss, is elegantly presented by Schmertman and Osterberg (1968) for stiff soils, and underlies work by Martin (1994) on granites. The concept is utilized successfully by Vasak and Kaiser (1995) in the analysis of near excavation damage.

It is important, however, to distinguish the low values of intra-crystalline friction controlling damage initiation, from the higher macroscopic friction acting on a through-going shear rupture. In addition, it is also important to distinguish between the non-frictional component of rock strength (a confinement dependant cohesive strength) and the true plastic cohesion found in steel and clay. Failure to do so in fracture mechanics and continuum models leads to invalid strength predictions for damage initiation, peak strength and post peak behaviour.

In addition to direct tension and uniaxial compression, this chapter includes examination results from Brazilian tests on Lac du Bonnet granite. This test represents an intermediate loading configuration between direct uniaxial tension and uniaxial compression. Attempts to relate a generalized Mohr envelope to Brazilian test data, as an intermediate loading configuration, have been unsuccessful for rocks with high compressive/tensile strength ratio (Wijk 1983) suggesting a mechanistic separation between the exploitation of damage in shear and in tension. It is interesting that the transition point, in the Griffith criterion (Fig 6.23), between pure σ_3 dominance on tension-normal cracks, and the onset of σ_1 influence (and the criticality of inclined cracks) corresponds to the stress state at the centre of the Brazilian disc ($\sigma_1 = -3 \sigma_3$). Non-vertical cracks are likely to close under appreciable axial compression, nullifying the validity of the Griffith model. Both axial compression and lateral tension are present in this test. The correspondence of the Brazilian results with those obtained in direct tension, therefore, relies on the presence and exploitation of vertical flaws in the centre of the disc.

Triaxial compression tests on granite will also be examined in this chapter to identify key thresholds of damage initiation, accumulation and localization and their relationship to confining stress.

6.4 TEST CONFIGURATIONS

6.4.1 Direct Tensile Testing of Rock Samples

The ISRM Commission on Rock Testing (ISRM 1978) suggests the basic test geometry shown in Figure 6.27a for obtaining tensile strength. The direct tensile results used in this discussion were obtained using a refined specimen geometry (Figure 6.27b), as described by Gorski (1991) and Gorski and Yu (1996). For this geometry, the load is applied via direct pull applied as shown (arrows). This geometry has been refined through the use of numerical model studies to promote rupture across a central plane with uniform stress ($\pm 1\%$) according to axi-symmetric elastic finite element analysis by Gorski and Yu (1991). Hoek and Brown (1980) describe a test to investigate the tensile strength under confined conditions, using the geometry shown in Figure 6.27c, with tension applied through adhesive end contacts and with normal pressure applied through hydraulic means normal to the axially curved portion of the specimen. The PFC simulations in Chapter 7 use variations of these geometries.

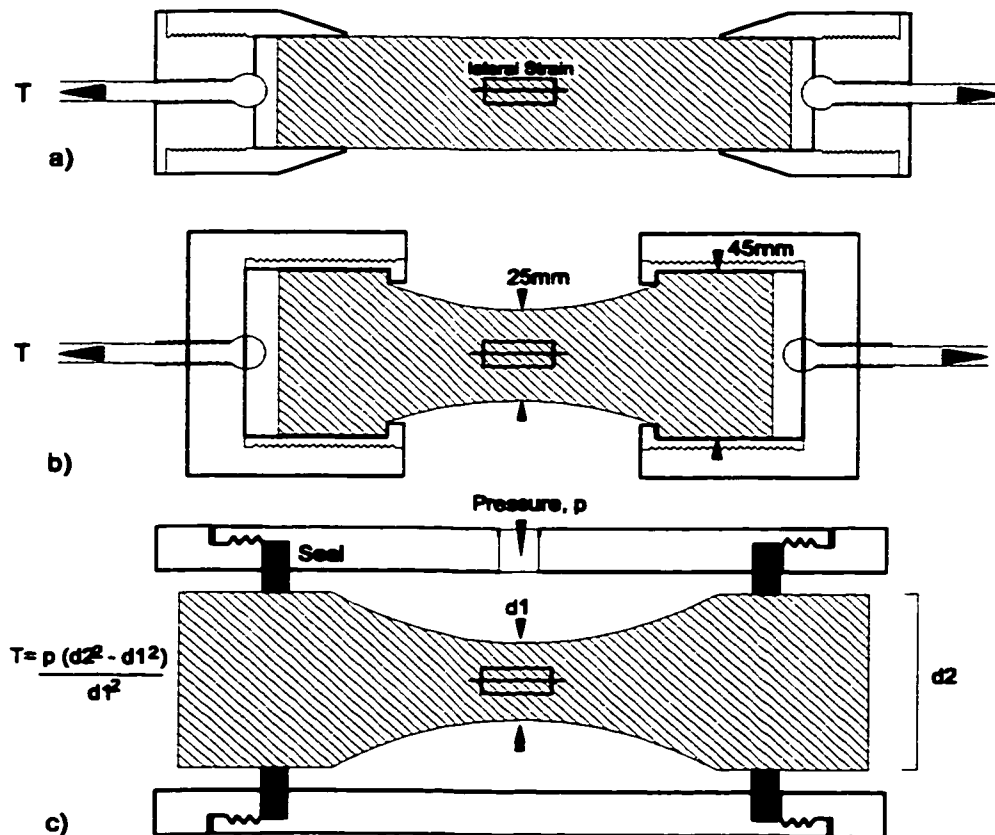


Figure 6.27: a) Direct tensile test configuration; b) Modified test geometry (after Gorski 1991); c) Confined tensile test (after Hoek and Brown 1980).

In comparison to the bounty of published data concerning the compressive strength and deformation of laboratory rock samples, tensile testing data is relatively sparse. Surveying the more than 1000 articles published in the International Journal of Rock Mechanics and Mining Science over the last 20 years, the author could find only 3 which were related to direct tensile testing of rocks (ISRM 1978; Okubo and Fukui 1996; Liao et al. 1997), and only 3 which discussed the mechanics of the Brazilian test (Yanagadini et al. 1978; Wijk 1978; Malan et al. 1994). Perhaps this is due to the commonly held view that that rockmass tensile strength is essentially zero if joints are present and as such the tensile strength of the intact material can have little significance (See PART I of this thesis). It may also be due to the relative difficulty in obtaining reliable tensile strength results in direct testing (Gorski and Yu 1996). By contrast, substantially more articles have dealt with testing to determine Mode I fracture toughness, apparently viewed as a more representative material property and one which can be utilized in generalized yield criteria and constitutive models (e.g. Costin and Holcomb 1983). Nevertheless, in order to compare test results on real rock samples with PFC simulations, tensile strength testing is considered in this chapter.

6.4.2 Fracture Toughness – Mode I and II

Critical stress intensity factors for crack propagation in Mode I and II rupture are defined in Figure 6.28. Derivations of K_{Ic} and K_{IIc} for different loading configurations are given by Paris and Shi (1965). An example configuration for determining Mode I fracture toughness for rock samples is shown in Figure 6.28 based on an equation given by Zietlow and Labuz (1998). Techniques for determining the fracture toughness of pure mineral crystals are discussed in Atkinson and Advis (1980).

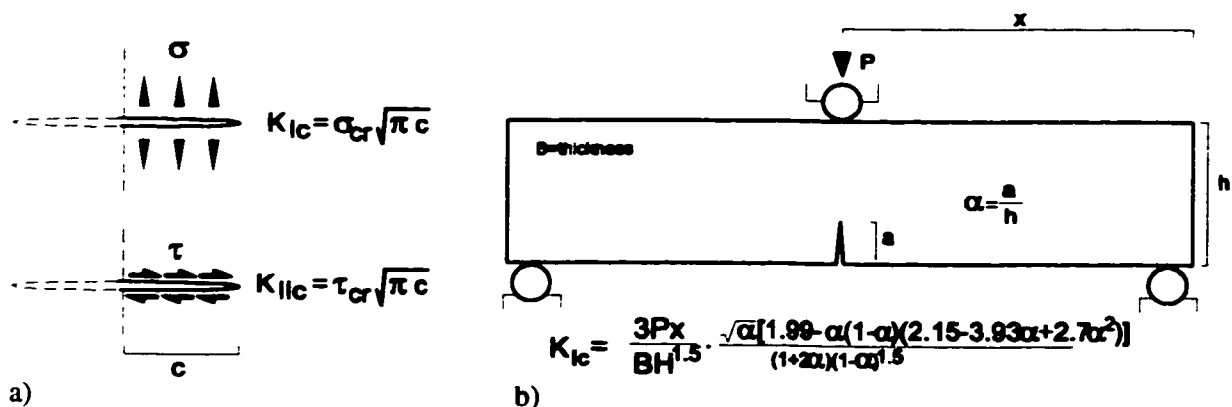


Figure 6.28: a) Mode I and II critical stress intensity factors or fracture toughness; b) Example configuration for K_{Ic} determination (3 Point Bending Test).

There are a wide variety of tests to determine critical fracture stress intensity or fracture toughness, K_I . Mode I is the most common parameter obtained from such tests. These tests include the 3 point bending tests (Figure 6.28), the notched Brazilian test (Krishnan et al. 1998), the double cantilever beam (Laqueche et al. 1986 and Figure 6.29b), the double torsion test (Atkinson 1979), the ring test (Fisher et al 1996), circumferentially cracked round bar (Paris and Shi 1965), and the chevron notched round bar and short-rod tests (Atkinson and Meredith 1987a), to name a few. Mode II fracture toughness is more difficult to determine experimentally. Direct tests include the compact shear test (Laqueche et al. 1986 and Figure 6.29b) while mixed mode (I and II) testing can be performed using the inclined-notch Brazilian test (Krishnan et al. 1998) and the inclined notch semicircular 3 point bending test (Lim et al. 1994).

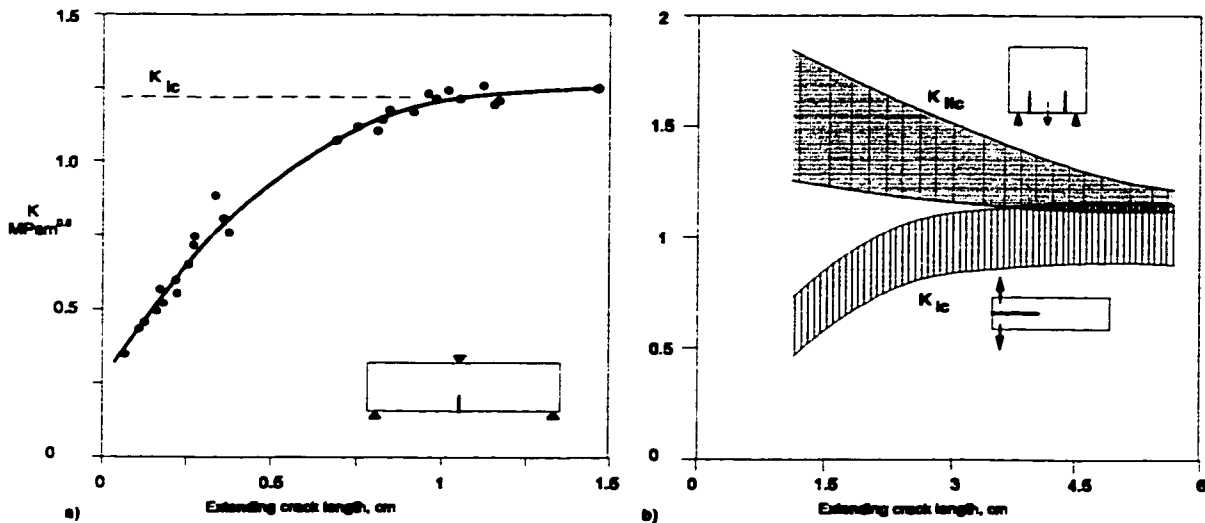


Figure 6.29: Variation of K_I and K_{II} with crack length based on data from a) Okubo and Fukui (1996) and b) Laqueche et al. (1986).

An interesting note, from the point of view of the following discussions, is that the quoted value for K_{Ic} or K_{IIc} is normally an average or an asymptotic value obtained as the crack extends. At very small crack lengths, the critical stress intensity factor is often significantly lower than the nominal value for the composite rock material as shown in Figure 6.29. This is due, in part, to process zone development as the crack extends (Ouchterlony, 1982; Atkinson and Meredith 1987). The energy-dissipating zone causes a hardening in Mode I and a weakening in Mode II. The discrepancy could also be due to the requirement to initiate and connect sub-grain cracks through mineral material at small crack lengths. K_I for atomically sharp cracks within mineral grains is lower than for the host rock. For example, K_I values for feldspar, quartz and biotite are approximately 0.35, 0.39 and 0.15 $\text{MPam}^{0.5}$ respectively (Atkinson and Advis 1980), while quoted values for Lac du Bonnet granite range from 0.96 (Hommand-Etienne et al. 1998) to more than 2 $\text{MPam}^{0.5}$ (Martin 1994). Figure 6.29b suggests the opposite trend for mineral K_{II} values.

6.4.3 Brazilian Test – Indirect Tensile Strength

The Brazilian test was developed as a more practical alternative to the direct testing of concrete (Hondros 1959) and was first used to determine the strength of rock by Berrenbaum and Brodie (1959). The test involves placing a cylindrical disk diametrically between the platens of a compression testing machine. The platens (Figure 6.30a) supply, ideally, a line load or, more practically, a strip load aligned with the diameter of the specimen. For an ideal line load shown in Figure 6.30b, this load configuration produces a lateral tensile stress across the vertical centre-line of the specimen equivalent to:

$$\sigma_x = -\frac{W}{\pi R} \quad [6.7]$$

The vertical compressive stress at the centre of the elastic specimen is given by:

$$\sigma_y = \frac{W(3R^2 + r^2)}{\pi R(R^2 - r^2)} \quad [6.8]$$

For the idealized line load the tension is uniform along the entire central axis, while the compressive stress approaches infinity immediately under the load. In reality the load is distributed across a contact arc. For small contact angles (Figure 6.30c) the lateral stress is tensile and still approximately uniform across a substantial portion of the central axis, becoming compressive near the contacts. The vertical compressive stress, on the other hand is finite under the distributed load. This is an important point to ensure that central tensile rupture occurs before shear failure at the platen contacts.

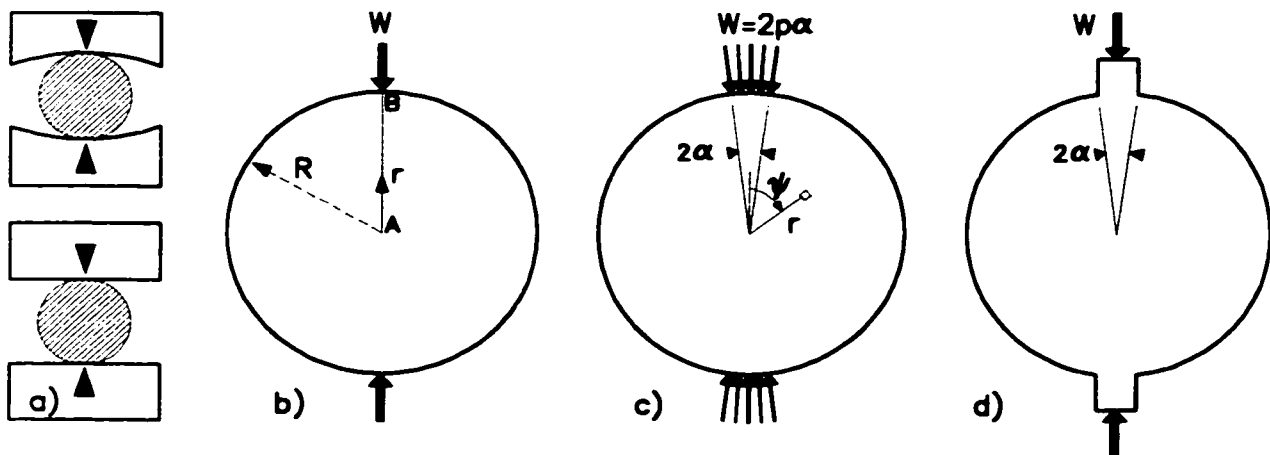


Figure 6.30: Brazilian test geometry a) actual configuration; b) ideal line load; c) analytical arc load; d) elastic boundary element model geometry (Figures 6.31 and 6.32).

Mathematical solutions based on the geometry in Figure 6.30c have been derived by Hondros (1959), and presented by Vardar and Finnie (1975) and Malan et al. (1994). This solution is in the form of a summation:

$$\begin{aligned}\sigma_r &= \frac{2\alpha p}{\pi} + \frac{2p}{\pi} \sum_{m=1}^{\infty} \left(\frac{r}{R}\right)^{2m-2} \left[1 - \left(1 - \frac{1}{m}\right) \left(\frac{r}{R}\right)^2\right] \sin 2m\alpha \cos 2m\theta \\ \sigma_\theta &= \frac{2\alpha p}{\pi} - \frac{2p}{\pi} \sum_{m=1}^{\infty} \left(\frac{r}{R}\right)^{2m-2} \left[1 - \left(1 - \frac{1}{m}\right) \left(\frac{r}{R}\right)^2\right] \sin 2m\alpha \cos 2m\theta \\ \tau_{r\theta} &= \frac{2p}{\pi} \sum_{m=1}^{\infty} \left[\left(\frac{r}{R}\right)^2 - \left(\frac{r}{R}\right)^{2m-2} \right] \sin 2m\alpha \cos 2m\theta\end{aligned}\quad [6.9]$$

A closed form approximation for stresses along the centre-line is given by Jaeger and Cook (1971) and Wijk (1978). The stresses along the vertical axis between the platens are plotted, using the summation in Equations 6.9 ($m=30$), for comparison with the ideal line load solution in Figure 6.30. The data points are from an elastic boundary element model created with the program Examine^{2D} using the geometry in Figure 6.30d. In the model, and in reality, the load distribution at the platens is only symmetrical about the vertical axis and does not exhibit the radial symmetry assumed for the analytical solutions. This explains the deviation between the numerical model and the Hondros solution in the vicinity of the platens. The lateral compression is exaggerated in the analytical solution due to the lateral component of the outer line load distribution. While the solution by Hondros yields the stresses throughout the sample, the Examine^{2D} model is used in Figures 6.31 and 6.32 for this purpose. The results are normalized with respect to the nominal tensile stress from Equation 6.7.

The angular width for the contacts used in the generation of Figures 6.31 and 6.32 is equivalent to that used in the PFC simulations described in Chapter 7. The width used in the testing described in Section 6.7 was not recorded, although 7.5 degrees is a reasonable estimate for hard rock and steel platens (Wijk 1978; 1983). Smaller angles (very stiff rock with extremely stiff platens) could result in compressive (shear) rupture or crushing at the contacts. Wider angles (soft rock and soft inserts or wrap-around platens) can decrease the reliability of the predicted central tension, although contact angles up to 15 degrees provide good correspondence to direct tension results for most hard rock types (Jaeger 1967).

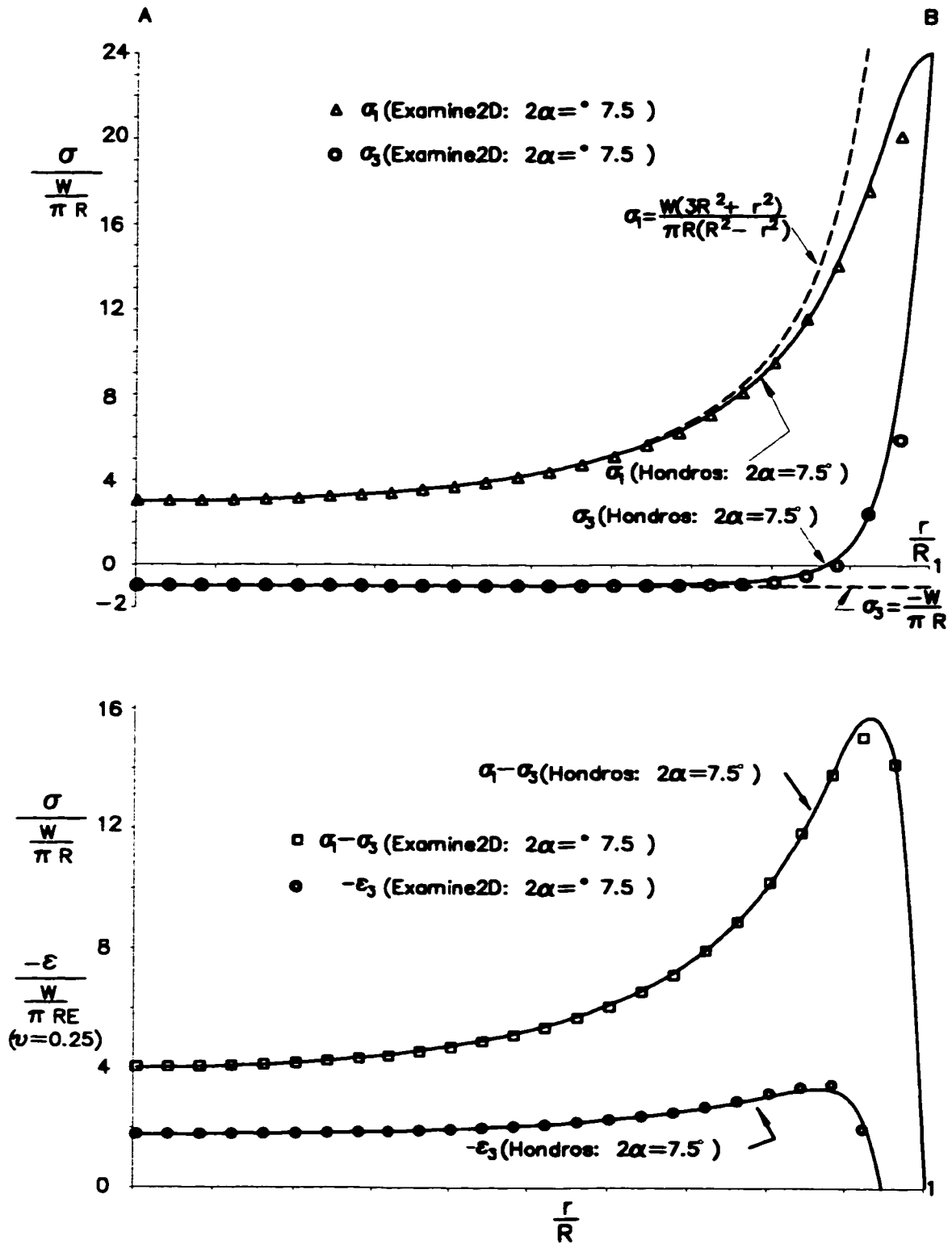


Figure 6.31: Comparison between ideal solution, finite contact width solution (Hondros 1959) and Examine^{2D} results for the specimen centre-line. ϵ_3 is centre-line lateral strain.

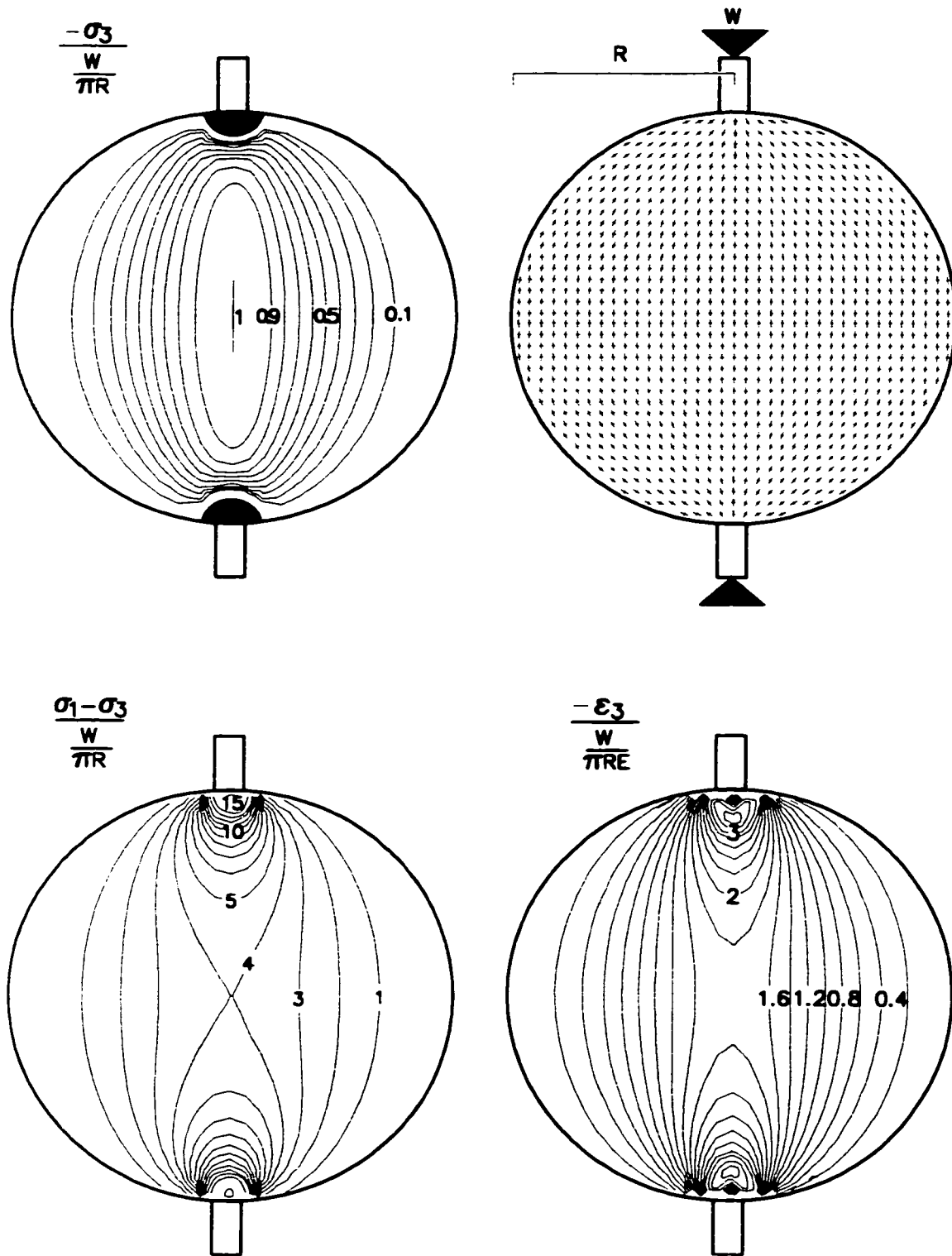


Figure 6.32: Normalized tensile (top-left), deviatoric (bottom left) stresses and minor principal strain (bottom right). Stress trajectories are shown in top right. Note that nominal calculated tensile stress is valid over central 20% of sample. Also note high but spatially constrained deviatoric stress levels near platens.

Correspondence between the results of the direct tensile test and the Brazilian test is governed by the assumption that tensile crack propagation from the centre of the disc will precede shear localization at the loading regions. For the idealized line load case, shear rupture under the load would occur instantaneously due to an infinite deviatoric stress. The deviatoric stress under the platens becomes finite for real contacts with appreciable width as shown in Figure 6.32. The zone of high shear potential is also small compared with the tensile region in the centre of the disc. Tests which fail through shear at the platen region should be rejected.

It is interesting that the stress path for the Brazilian test:

$$\sigma_1 = -3\sigma_3 \quad [6.10]$$

cuts through the Griffith envelope for tensile propagation from open cracks just at the limit of vertical crack dominance as shown in Figure 6.23. The onset of curvature above this point indicates that inclined cracks are more critical than vertical cracks due to the influence of the vertical compressive stress. This is a mechanistic shift from the purely tensile dilation of a vertical crack. A continuous Mohr envelope based, for example, on closed sliding cracks, erroneously predicts a reduced Brazilian strength (Wijk 1983). The Griffith envelope and the Brazilian stress path indicate that the linkage between the Brazilian strength and the direct tensile strength is valid, provided that a wide enough angular range of cracks are “open”. Figure 6.33 illustrates using a simple Mohr construction that all cracks between 0 and 30 degrees from the vertical should be open. A wider range is possible if locked-in internal tension and elliptical crack geometries are considered. Yanagidini et al. (1978) demonstrate that for several rock types, cracking initiates just off centre in the vertical plane and propagates vertically to rupture the specimen. Exceptions to this behaviour would include materials with a low compressive to tensile strength ratio, such as plaster. In this case, shear may dominate (Wijk 1983).

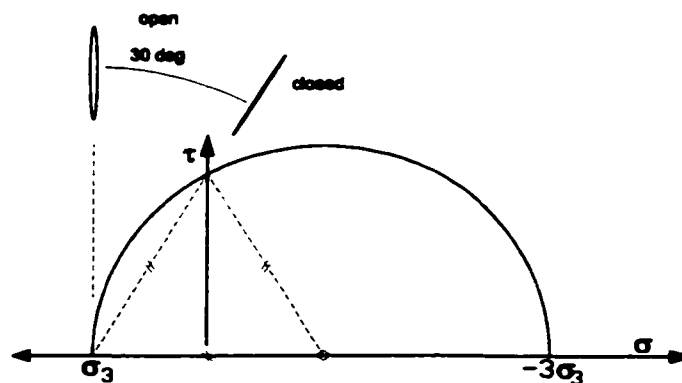


Figure 6.33: Mohr construction of Brazilian test showing range of open (Griffith) flaws available for crack initiation.

6.4.4 Uniaxial and Confined Compression

The most common form of direct strength testing for rock is the uniaxial compressive strength test. In this test a cylindrical sample (typically 50-55mm in diameter unless otherwise stated) with a height to diameter ratio of 2.5 to 3 and with finely machined ends (perpendicular to sample axis, planar and smooth) is placed in a loading frame as shown in Figure 6.34a. The standard loading rate is 0.75MPa per second according to ISRM standards (ISRM 1979).

No lubricating end cap preparation (to reduce end friction effects) beyond machining is recommended since this will induce tensile stresses in the ends of the specimen during loading due to stiffness incompatibilities. Brush platens (described in Brady and Brown 1993) consists of a dense axial array of metal pins that can maintain uniform stress throughout the specimen but are difficult to use. Steel platens apply friction to the ends and limit expansion. This results in a higher level of confinement in the ends of the specimen which increases the peak strength above the point of yield due to the suppression of dilation in the affected areas. Figure 6.35 shows examples of the induced stress distortions induced by restrained end expansion due to “stiff platens”, in the case of a standard test. Also illustrated are the effects of lateral expansion brought about by attempts to use a “lubricating” end cap preparation such as teflon inserts (“soft platens”). In each case the influence of end conditions is felt through 50% of the sample. The magnitude of stiffness contrast is schematic only in this figure, although for a stiff steel platen the contrast is reasonable. A more detailed examination of end effects is given in Peng (1971) for specific cases.

Tests are typically controlled by a feedback servo-control which maintains a constant axial strain rate as the sample yields. Axial strain rate can be varied to maintain desired rates or thresholds of other parameters, such as circumferential (= lateral) strain. This technique was used for so-called “damage controlled” tests performed by Martin (1994). In all tests discussed in this chapter, axial and lateral strain (and therefore volumetric strain; $\epsilon_v = \epsilon_{axial} + 2\epsilon_{lateral}$) are obtained from centre-line strain gauges as shown in Figure 6.34. Loads are provided via an in-line load cell as shown. Cycle tests are performed using threshold increments of load (as in Section 6.8.2) or one of the strain components.

Axi-symmetric triaxial tests (Figure 6.34b) can be performed in the same way using the configuration shown. Confining pressure is maintained as a constant through the pressure control of hydraulic fluid.

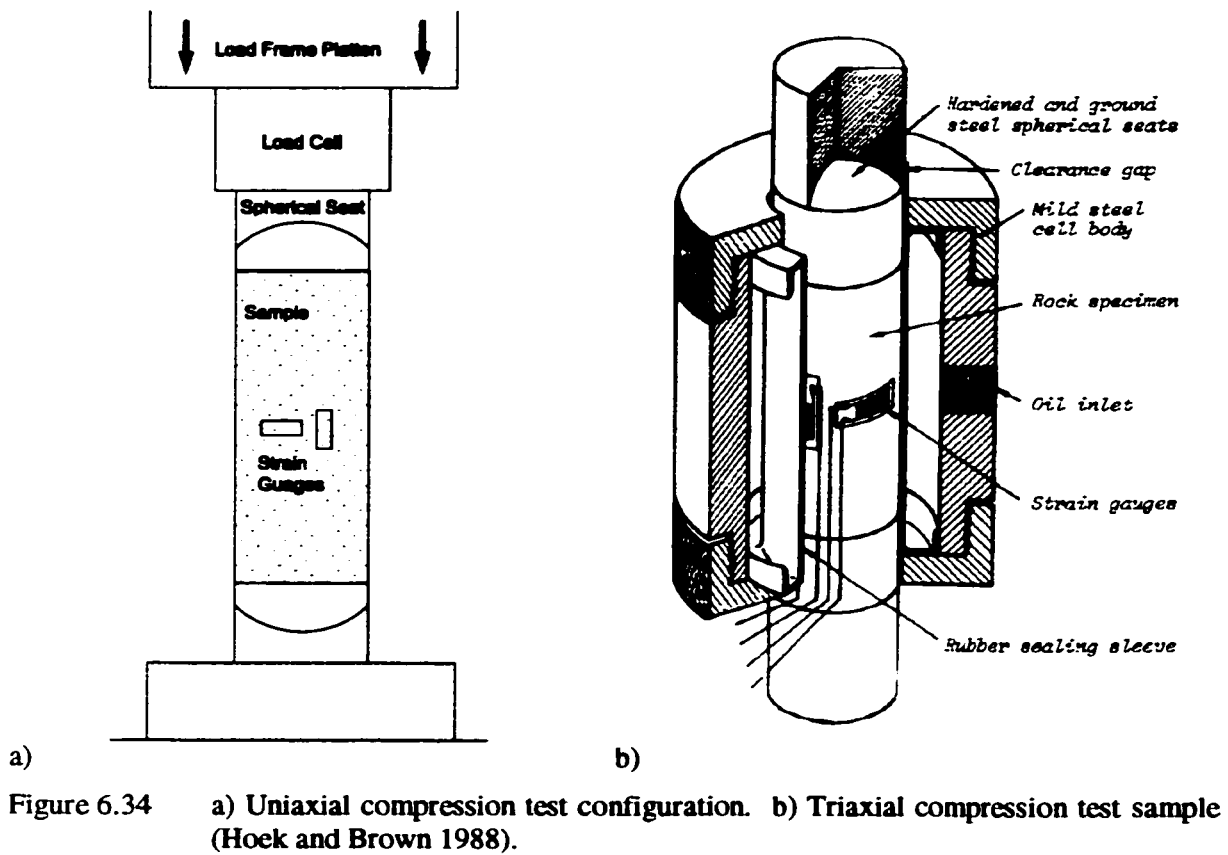


Figure 6.34 a) Uniaxial compression test configuration. b) Triaxial compression test sample (Hoek and Brown 1988).

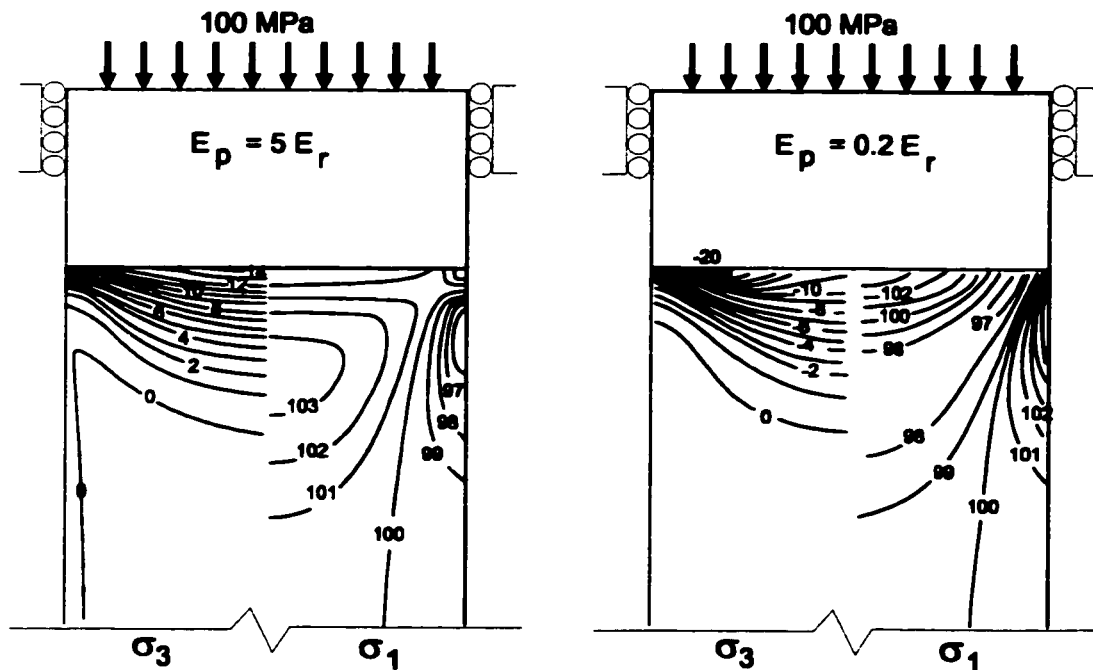


Figure 6.35: Axi-symmetric elastic finite element calculation (Phase²) of stress perturbation due to non-compliant end caps. Left image is for “stiff” end platens. Right image is for “soft” platens. Note confining effect of stiff platens and tensile stresses due to soft platens.

6.5 PROPERTIES OF LAC DU BONNET GRANITE

AECL's Underground Research Laboratory (URL) is a facility excavated in the Lac du Bonnet Batholith near Winnipeg, Manitoba. The batholith is a grey-pink granite, composed predominantly of sub-hedral plagioclase and alkali feldspar, quartz and biotite mica with trace magnetite and other minerals. Original data analysis in this chapter utilizes samples obtained from the Cold Spring Quarry site. Reference is made to and secondary analysis is performed on data from samples obtained at various depths at the URL site. Table 6.2 gives a summary of rock characteristics and mechanical properties determined from this study and by Martin (1994), Martin and Stimpson (1994), Martin and Chandler (1994), Eberhardt et al (1998), Hommand-Etienne et al (1998), Gorski and Yu (1991), Wilkins (1980), Kelly et al. (1993) and Lajtai (1988). The granite is jointed above a major series of fracture zones numbered in Figure 6.36 and is completely massive below the lowermost zone. The Cold Spring Quarry is a surface exposure of the massive granite found at depth at the URL.

Table 6.2: Properties of Lac du Bonnet Granite

Grain size (composition)	
Feldspars (Alkali 42%; Plagioclase 22%)	3.5mm (1 to 7 mm)
Quartz (29%)	2mm (0.3 to 3.5mm)
Biotite (6%)	1mm (0.1 to 2mm)
Elastic Modulus (Tangent Young's Modulus), E	65 to 70 GPa (undamaged) 55 to 60 GPa (at 420 level)
Specific Gravity	2.62
Poisson's Ratio, ν	0.22 to 0.26 (< 0.2 for 420 samples)
Unconfined Compressive Strength, UCS	200 to 230 MPa (undamaged) 150 to 160 MPa (at 420 level)
Hoek-Brown parameter m (peak strength)	31 (undamaged)
Base Friction Coefficient, μ , for composite rock	1
Tensile Strength (Direct and Brazilian)	6.7 to 13.5 MPa (undamaged) (< 2 MPa for 420 level samples)
Fracture Toughness, K_{IC}	0.96 to 1.82 MPam ^{0.5}
Component Mineral Properties, @50% R.H. <i>from Atkinson and Advis (1980), Atkinson and Meredith (1987b) and Horn and Deer (1962)</i>	($K_{IC} - \text{MPam}^{0.5}$), (μ)
Feldspars	(0.31 to 0.39), (0.12)
Quartz	(0.31 to 0.46), (0.16)
Biotite	(0.15), (0.26)

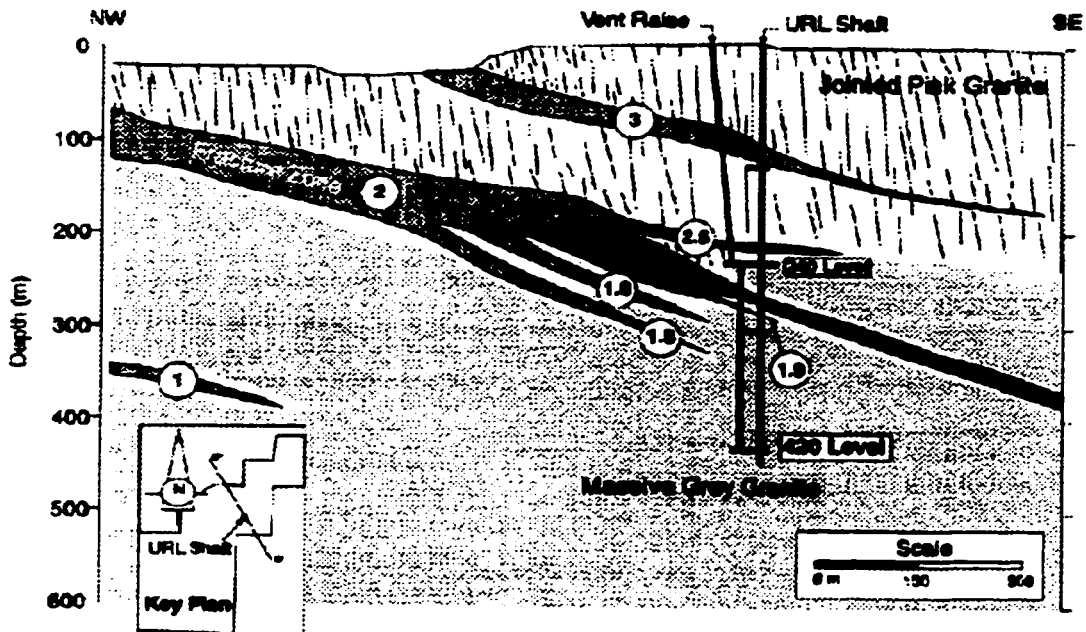
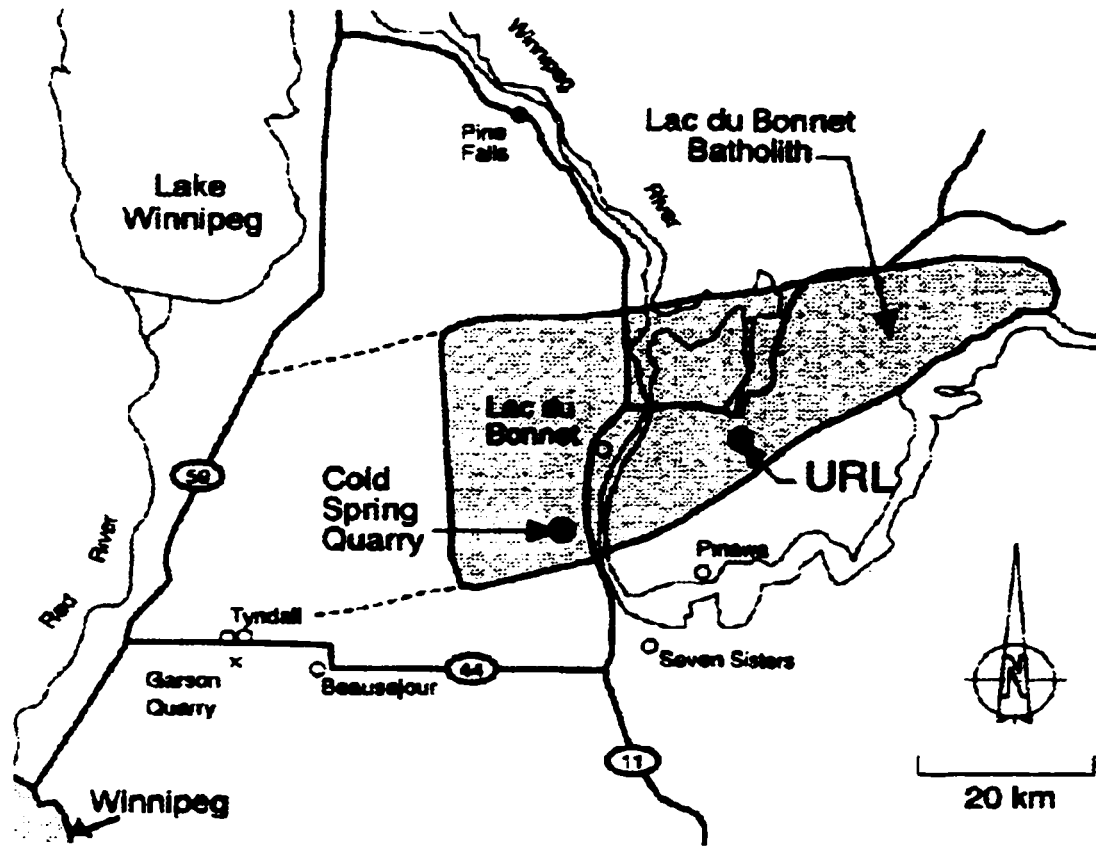


Figure 6.36: Site plan and general section through Lac du Bonnet Batholith (after Martin 1994).

6.6 TENSILE TESTING OF LAC DU BONNET GRANITE

Direct tensile test data was obtained for this study from tests performed for AECL's Pinawa Labs and supplied to the author. The procedures followed in obtaining the data are described in (Gorski 1991). 10 tests were performed on undamaged granite specimens from the URL site in Pinawa.

The tensile tests presented here are performed on samples from Cold Spring Quarry, a surface site nearby the Underground Research Laboratory described in Chapter 5. The test results (Figure 6.37) for direct tension, using the sample configuration illustrated in Figure 6.27b, are summarized in and in Table 6.3.

Table 6.3: Direct tensile test summary data for Lac du Bonnet granite

Sample ID	Microstrain		Elastic Modulus GPa	Stress at Rupture MPa	Microstrain @ Rupture
	@ 2.5MPa	@ 5MPa			
34134	41	90	51.0	8.06	195
34449	41	96	45.5	7.33	165
34763	52	105	47.2	6.81	140
35133	57	131	33.8	6.52	180
35522	48	105	43.9	7.81	175
35860	49	103	46.3	7.57	160
38030	66	156	27.8	5.46	170
38517	51	111	41.7	5.63	120
41043	49	107	43.1	6.72	150
41362	49	112	39.7	6.38	150
Mean			42.0	6.83	161
St. Dev.			6.8	0.88	22

The logged data records from these tests contain a large amount of noise, possibly the result of the load transfer mechanism employed or the data logging itself. Tensile stress is calculated from applied machine loads and central cross-sectional area of the sample. Strains are recorded via surface strain gauges. The data shown in Figure 6.37 has been smoothed via a moving average. Overall, the test results are somewhat non-linear although it is unclear whether this curvature is the result of any permanent softening prior to rupture. Visual observations during the tests suggest that the samples were elastic and undamaged until the moment of rupture.

There is a slight softening apparent between 3.5 MPa and 4.5 MPa. This apparent softening could be the result of the geometrical effects of the dog-bone sample. Such behaviour is observed in PFC simulations (Chapter 7) even in the absence of bond rupture. Alternatively, from a mechanistic viewpoint, non-aligned flaws may have to be "opened" before a sufficient Mode I stress concentration is generated to induce propagation.

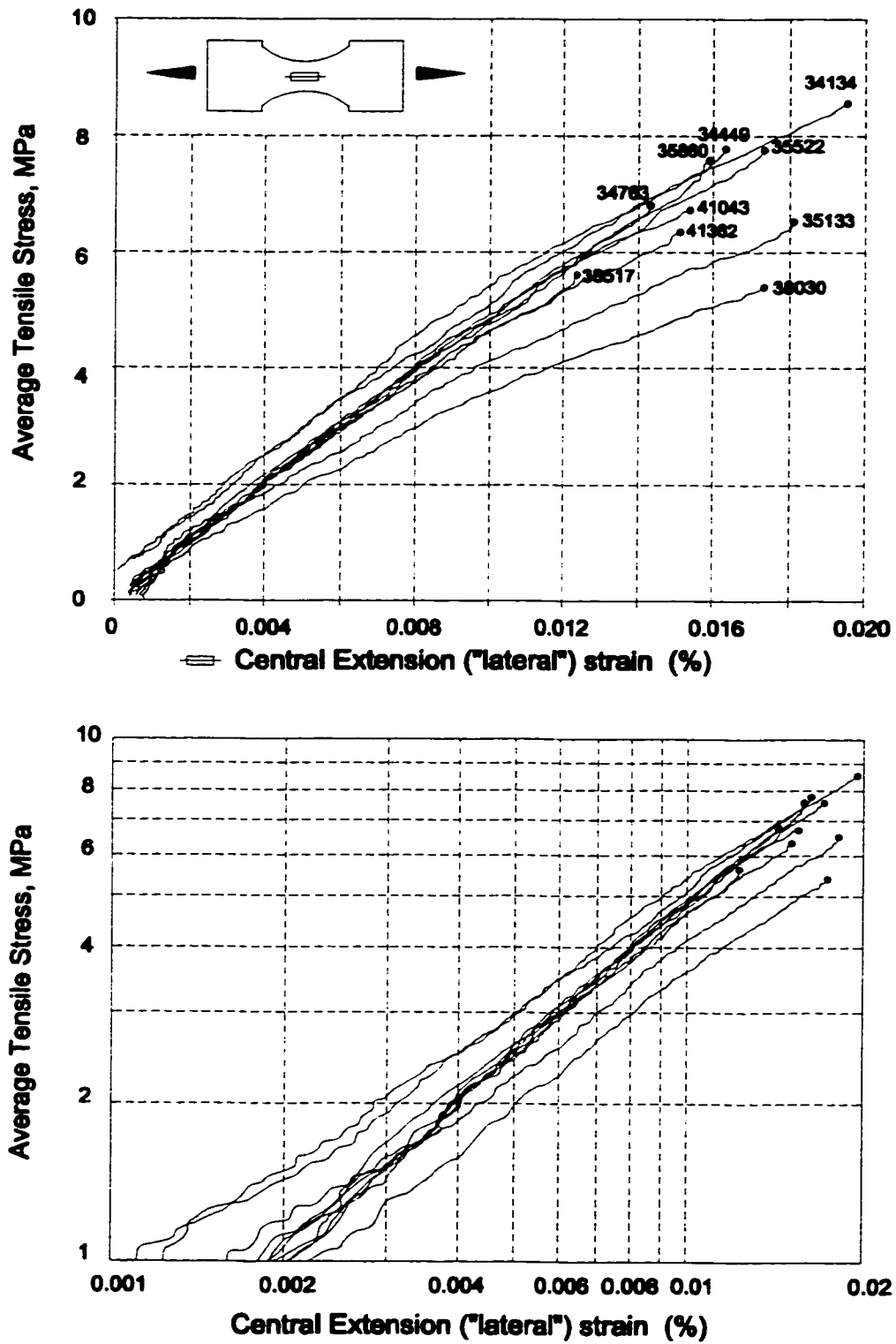


Figure 6.37: Stress / strain results for direct tension samples of Lac du Bonnet Granite. Data acquisition was very noisy and results have been smoothed (moving average). Bottom plot presents the same data in log-log space for comparison to other tests in this section.

Progressive opening of complex flaws would result in the strain dependency of the tangential modulus. The inflection may also be due to the destruction of rock bridges across otherwise continuous cracks or cavities. Microscopic rock bridges have been observed in dolerite (Fonseka et al. 1985) and Barre Granite (Kranz 1979). They are also present in Westerly granites (Sprunt and Brace 1974) and in Lac du Bonnet granites (Figures 6.38 and 6.39 respectively).

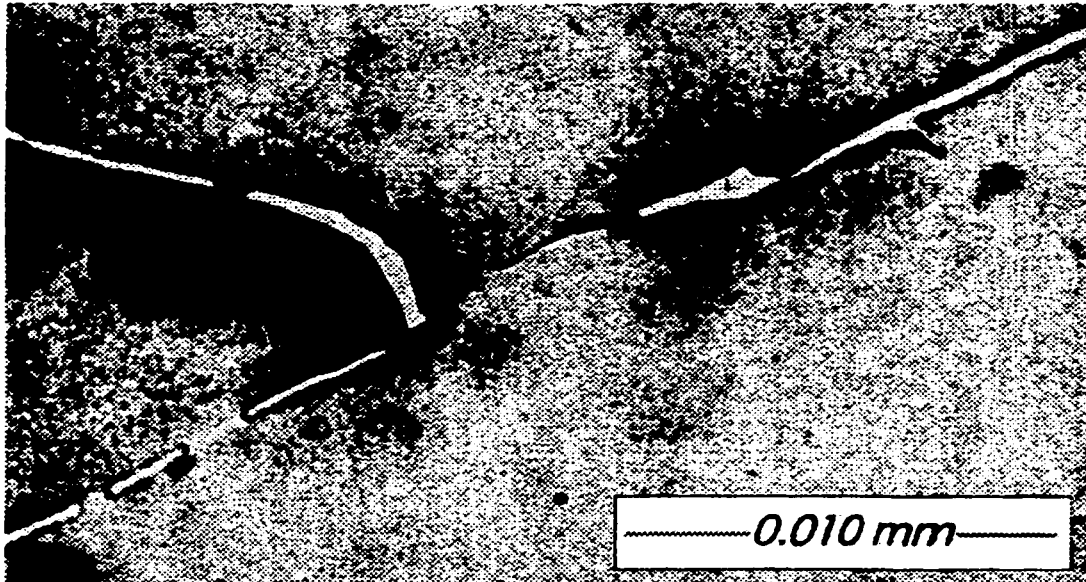


Figure 6.38: Rock bridges disrupting the continuity of microcracks in Westerly Granite (image modified and shade-inverted from Sprunt and Brace 1974).



Figure 6.39: Rock bridges and en echelon microcracks in Lac du Bonnet Granite (modified/annotated after original micrograph courtesy AECL).

Okubo and Fukui (1996) and Krech (1974) have reported post peak quasi-stable crack growth in tuff and in certain sandstones. This may be the result of stable crack growth prior to rupture in tension, due to the clastic nature of the material. On the other hand, fine crystalline rocks such as limestone and basalt, are elastic-brittle in tension. Granites typically show only minimal non-linearity prior to rupture.

It may be concluded, however, that any significant propagation of a single flaw in the central portion of the sample must be accompanied by significant non-linear behaviour, indicated by a change in slope of the log-stress vs log-strain relationship. The log-log presentation is used for other test configurations to isolate significant lateral strain rate deviation and is presented in Figure 6.37. Only two of the samples present any measurable deviation prior to failure. Thus it can be interpreted that the true damage initiation threshold for the tensile test is, within the limits of detection, coincident with sample yield and rupture and that no primary cracking occurs before this point.

The mean tensile strength from these tests is 6.8 (± 0.9) MPa. This is less than the value of 8.8 (± 1.1) MPa obtained by Duevel and Haimson (1997) for Cold Spring Quarry granite but higher than 4.47 (± 1.45) MPa obtained by Gorski (1991). Gorski and Yu (1991) report even lower results (1.5 MPa) at the 420m level et URL due to sample damage and core discing.

The results from Table 6.3 are plotted in Figure 6.40. In these plots the elastic modulus in tension was calculated as the secant from $(\sigma_3)=T=2.5$ to 5 MPa. The rupture strengths are plotted with a best-fit power function. It can be seen that the power exponent (0.547) is reasonably close to that predicted ($1/2$) by the Griffith energy balance criterion (1921; 1924). The strain at failure, on the other hand appears to be independent of modulus. In Figure 6.40, the relationship:

$$T = 33.3\sqrt{E} \quad [6.11]$$

is plotted, as a “best-fit” square-root alternative to the global best-fit line shown, with little increase in residual error. This relationship is of the form predicted by Kemeny and Cook (1987) for penny shaped (3D) cracks in direct tension:

$$T = K_{IC} \sqrt{\frac{\pi}{4c}} = \sqrt{\frac{\pi\gamma}{2c}} \cdot \sqrt{E} \quad [6.12]$$

$$K_{IC} = \sqrt{2\gamma E} \quad [6.13]$$

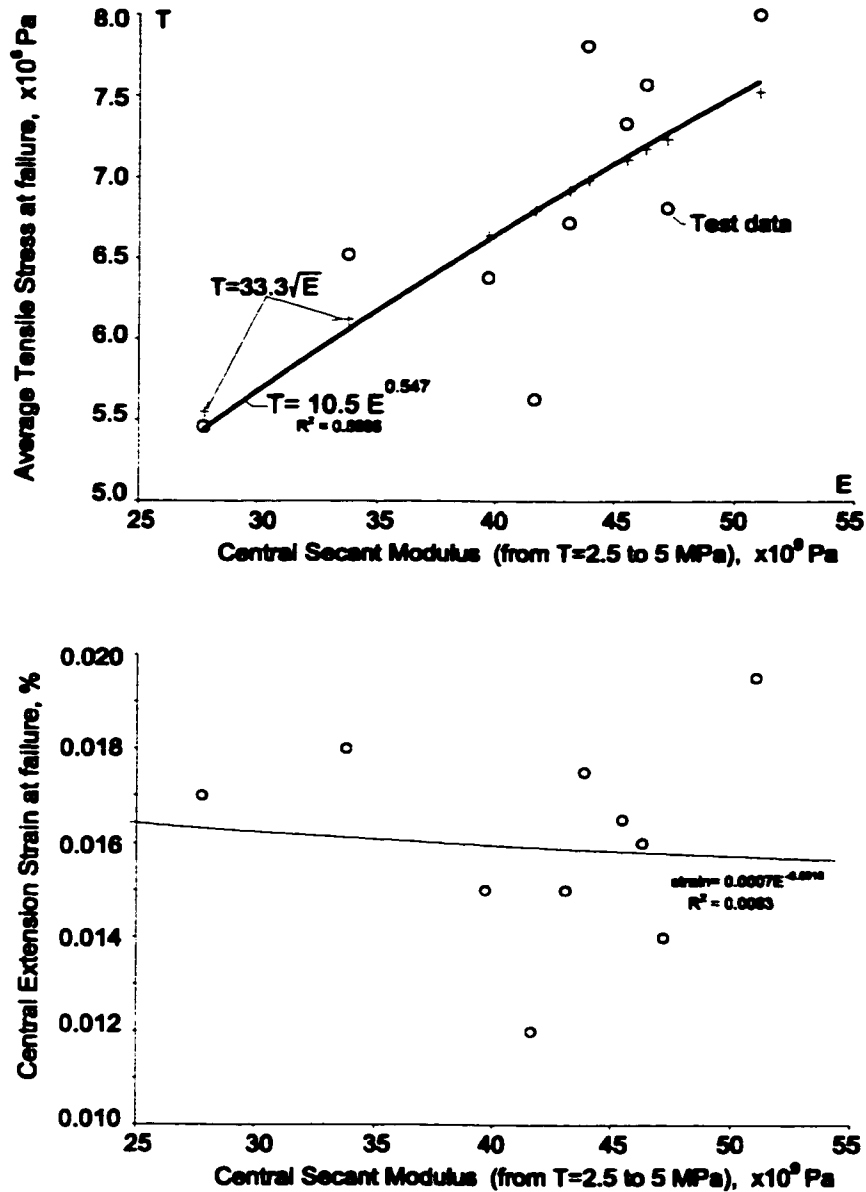


Figure 6.40: Relationship of critical stresses (top) and strains (bottom) to elastic modulus for direct tension tests on Lac du Bonnet Granite.

Combining Equations 6.11 and 6.12 and taking $2c=2\text{mm}$ to 3.5mm , corresponding to a full transgranular crack (Figure 6.41) across the average and maximum grain size (Kelly et al. 1993), of the quartz in Lac du Bonnet granite, yields a surface energy, γ , of 0.7MN/m to 1.4MN/m . These values correspond well to the average and maximum surface energies reported for quartz by Atkinson and Advis (1980) and Brace and Walsh (1962). The maximum crack or grain size (7mm) for the feldspars, however, yields a surface energy of 2.5MN/m , somewhat less than the values reported by the aforementioned authors for feldspars.

Assuming a crack length of $2c=3.5\text{mm}$ (corresponding to the mean feldspar and maximum quartz grain size), taking the average modulus (42GPa) from these tests, and using the corresponding tensile strength, 6.7MPa, a critical Mode I stress intensity factor K_{IC} is backed out of either Equation 6.12 or 6.13 and is equal to $0.32\text{MPam}^{0.5}$. This corresponds closely to the values quoted for feldspars (0.31-0.39) and quartz (0.31-0.46) by Atkinson and Advis (1980), and is at most one third of the values quoted for the composite rock itself (e.g. $K_{IC} = 0.96\text{MPam}^{0.5}$ for LdB granite according to Hommand-Etienne et al 1998). Other authors have found similar mineral/rock or small/large crack ratios of 0.35 for limestone (Ingraffea and Schmidt 1978), 0.4 for schist (Laqueche et al. 1986) and 0.25 for andesite (Okubo and Fukui 1996), for example.



Figure 6.41: Microcracks in LdB granite (modified/annotated after original micrograph courtesy AECL): quartz and feldspar (horizontal field scale =7mm).

By contrast, using the reported K_{Ic} range for Lac du Bonnet granite of 1 to 1.8 $\text{MPam}^{0.5}$ (Hommand-Etienne et al. 1998; Martin 1994) in Equation 6.12, a critical (initial) crack length of between 35 and 110mm is predicted; clearly a nonsensical result for a sample diameter of 25 to 45mm.

It should be stated then that, contrary to current practice, the critical stress intensity factors used to predict for microcrack initiation in direct tension should be 30 to 40% of the values obtained for the composite rock.

6.7 BRAZILIAN TESTING OF LAC du BONNET GRANITE

Brazilian samples were taken from opposing ends of the core segments used in the direct tensile tests. The samples were uniformly 45mm (44.96mm) in diameter and 22.4 (± 0.6)mm in thickness. The samples were tested in two lots, A and B, one for each of the two end cut samples from each specimen, and were monitored throughout the test with axial and lateral strain gauges at the centre of each specimen. Load (W in Equation 6.7) was recorded via a platen load cell. Load was applied using a 2000kN ELE compression press and the test procedure conformed to ISRM standards (ISRM 1978). Test results are summarized in Figure 6.42.

The Brazilian tensile stress in Figure 6.42 and in the rest of this section is calculated as in Equation 6.7. A comparison between the plots of lateral strain vs Brazilian Stress and the results from the direct tension tests in Figure 6.37 reveals a somewhat different near rupture behaviour. In the Brazilian test, lateral strain deviation (from linear behaviour) initiates at a stress significantly lower than the rupture limit (peak). It is difficult from Figure 6.42 to delineate precise thresholds of behavioural change. Viewing the data in log-strain vs log-stress space, however, allows the definition of rate change thresholds which are more diagnostic. Of particular interest is the differentiation of damage initiation, systematic accumulation, damage coalescence and localization and sample rupture. In the direct tensile tests these thresholds are coincidental.

Figure 6.43 illustrates a number of possible threshold indicators for the Brazilian test. For compressive testing, damage initiation can be identified by non-linearity in the axial strain vs lateral strain relationship. Figure 6.43 shows that there is little difference between thresholds identified using axial strain vs lateral strain plots or those obtained from stress vs lateral strain results. Martin (1994) uses volumetric strain reversal in compression to identify crack interaction and localization in compression and also to identify the damage initiation threshold in the Brazilian Test. This threshold, shown for comparison in Figure 6.43c does seem to be coincident in many cases to an observable change in lateral strain rate after crack initiation, identified here as the systematic cracking threshold (b). This systematic crack accumulation or constant rate increase was previously defined in Equation 6.6. A third rate-change appears prior to ultimate rupture (e). This threshold (d) is interpreted as critical localization (development of a primary sample-wide crack) and indicates true rupture stress. In compression, axial stress – strain non-linearity can be used to identify crack coalescence, while in the Brazilian tests, the axial strain vs stress readings (not shown here but presented in Figure 6.42) give little information on internal behaviour prior to rupture.

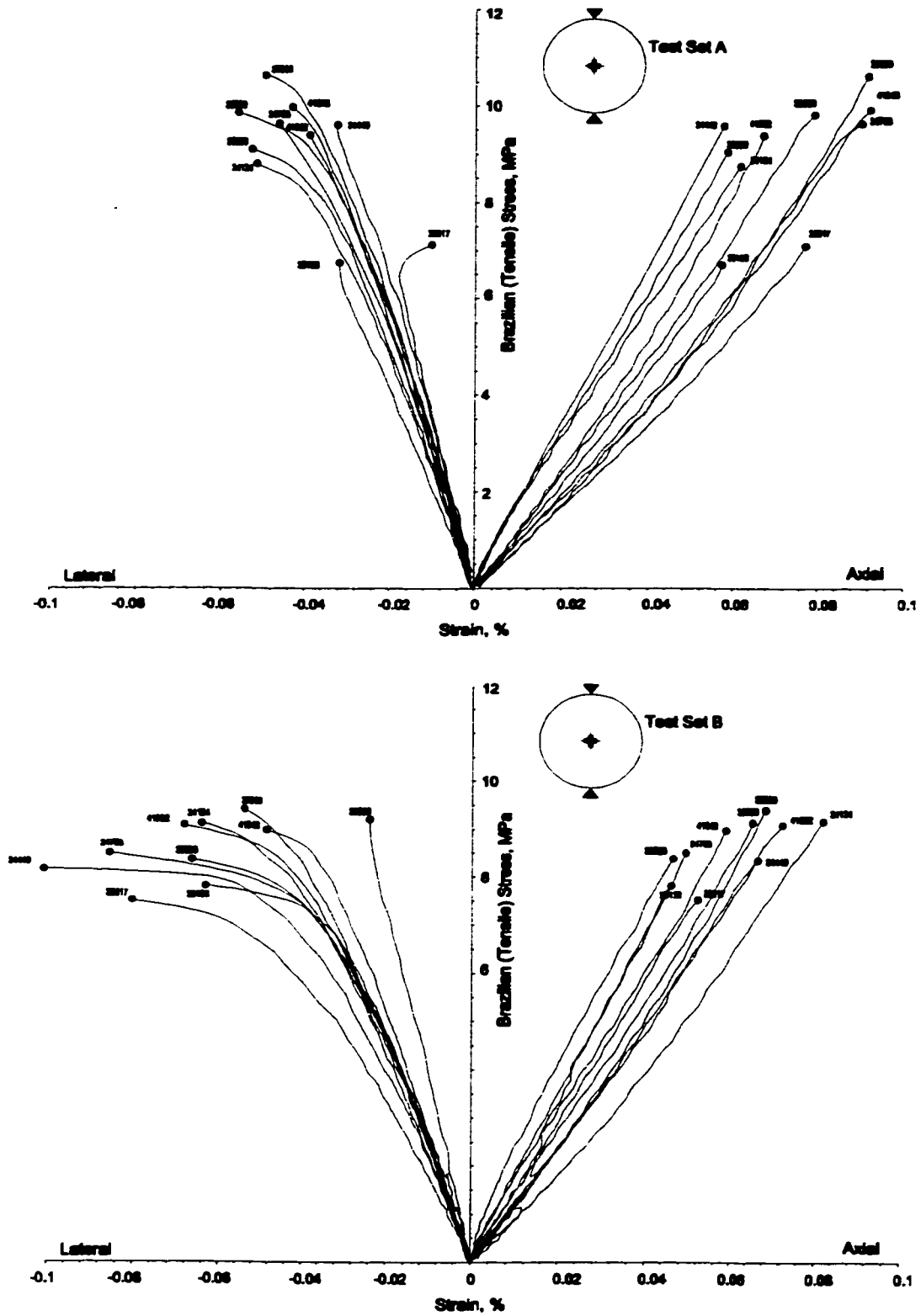


Figure 6.42: Brazilian tensile tests on Lac du Bonnet Granite.

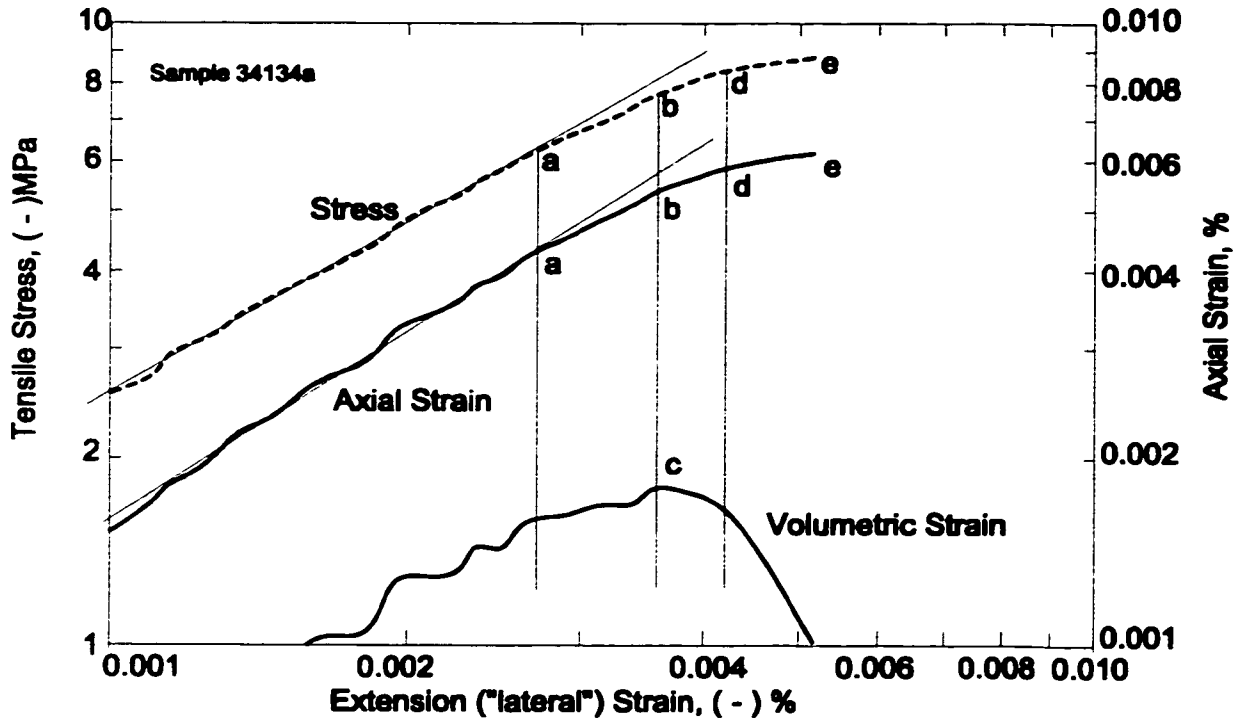


Figure 6.43: Comparison of threshold definition using lateral stress – lateral strain response, axial strain – lateral strain response, and volumetric strain reversal: a) Crack initiation; b) systematic crack accumulation; c) volumetric strain reversal; d) primary crack development and yield; e) rupture.

Two response examples are given in Figure 6.44 along with their direct tension counterparts. Also shown is the volumetric strain given in this case (ignoring out-of-plane strain) by:

$$\epsilon_v = \epsilon_1 + \epsilon_3 = \epsilon_{vertical} + \epsilon_{horizontal} \quad [6.14]$$

From Figure 6.43 it is apparent that rupture in the direct tension test is associated with crack initiation in the Brazilian test. Volumetric strain reversal, proposed by Martin (1994) as a primary diagnostic measurement of critical damage, coincides in these tests with the onset of systematic crack growth, the second of four strain rate changes evident in the test results. True yield is represented by threshold (d) in Figure 6.43. The interpreted thresholds from each test are given in Table 6.4.

It should be noted that the average peak strength obtained here is only two thirds of the average value obtained by Lajtai (1988) and reported by Martin (1994) for 43 tests on samples from the same location. Actual peak strength is dependant on loading rate and platen conditions. A specific reason for the discrepancy in this case is unavailable.

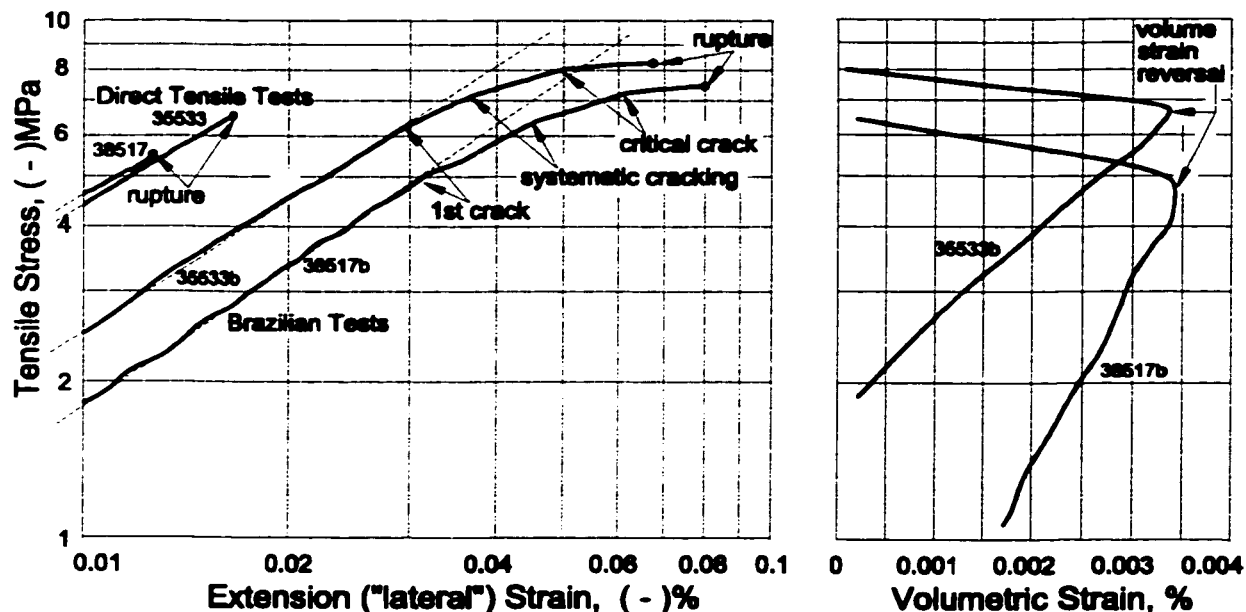


Figure 6.44: Comparison of damage and yield thresholds in the Brazilian Test and in the direct tension test. Identical sample ID numbers indicate samples from the same core stock.

Table 6.4: Summary of crack accumulation thresholds for Brazilian tests (LdB granite).

Sample ID	Crack Initiation		Systematic Cracking		Vol. Strain Reversal		Critical Crack		Peak	
	Stress	Strain	Stress	Strain	Stress	Strain	Stress	Strain	Stress	Strain
34134A	6.3	0.027%	7.6	0.036%	7.6	0.036%	8.4	0.042%	8.8	0.052%
34449A	7.4	0.023%	8.5	0.029%	9.7	0.032%	9.7	0.032%	9.7	0.033%
34763A	5.6	0.021%	7.5	0.031%	8.5	0.037%	8.5	0.037%	9.6	0.046%
35133A	5.9	0.030%	6.7	0.032%	6.7	0.032%	6.7	0.032%	6.7	0.032%
35533A	7.1	0.029%	8.2	0.037%	7.6	0.033%	8.8	0.044%	9.1	0.052%
35860A	7.7	0.027%	8.8	0.033%	10.0	0.040%	9.5	0.036%	10.7	0.050%
38030A	6.3	0.024%	8.4	0.033%	8.9	0.035%	8.9	0.035%	9.9	0.056%
38517A	invalid test									
41043A	8.2	0.031%	9.2	0.036%	9.7	0.039%	9.7	0.039%	10.0	0.043%
41362A	6.9	0.022%	8.6	0.034%	9.0	0.038%	9.1	0.029%	9.4	0.039%
34134B	7.1	0.036%	8.0	0.042%	7.6	0.040%	8.9	0.054%	9.1	0.064%
34449B	6.3	0.035%	7.3	0.046%	6.7	0.040%	7.9	0.055%	8.3	0.065%
34763B	6.2	0.029%	6.8	0.034%	6.2	0.029%	7.4	0.039%	8.5	0.085%
35133B	6.8	0.031%	6.8	0.031%	6.8	0.031%	7.6	0.042%	7.8	0.063%
35533B	6.5	0.030%	7.5	0.040%	6.9	0.035%	8.1	0.051%	8.4	0.066%
35860B	invalid test									
38030B	7.1	0.032%	8.3	0.039%	8.3	0.039%	9.1	0.048%	9.4	0.054%
38517B	4.8	0.030%	6.5	0.047%	4.8	0.030%	7.3	0.062%	7.5	0.080%
41043B	6.7	0.027%	7.8	0.032%	7.8	0.032%	8.7	0.039%	9.0	0.048%
41362B	6.8	0.032%	7.9	0.041%	7.9	0.041%	8.6	0.047%	9.1	0.068%
Mean	6.7	0.029%	7.8	0.036%	7.8	0.036%	8.5	0.042%	8.9	0.055%
St.Dev.	0.8	0.004%	0.8	0.005%	1.4	0.004%	0.9	0.009%	1.0	0.015%

Tests, in which the lateral strain magnitude dropped as failure approached, were not considered for averaging in Table 6.4 since this behaviour indicated that the primary cracking did not occur through the centre of the sample and that failure was likely the result of platen shear or misalignment. As a check on the validity of the tests, Poisson's ratio can be back calculated:

$$\nu = \frac{1}{n} \sum_{k=1}^n \frac{1}{E_k} \left(\frac{E_k \epsilon_{xt} - \sigma_{xt}}{3\sigma_{xt}} \right) \quad [6.15]$$

where the stresses and strains are taken at the point of crack initiation and the vertical stress equal to three times the magnitude of the predicted central tension as per Equation 6.7. Young's modulus is taken from the individual sample values in Table 6.3. A mean Poisson's ratio is so obtained equal to 0.27. While the scatter is high (0.15 standard deviation), this mean compares favorably to the range of 0.22 to 0.26 for Lac du Bonnet Granite found in the literature (Table 6.2).

It is worthwhile to assess the impact of the apparent difference between the elastic moduli in tension and compression. A relationship, reduced from finite element analyses performed by Chen and Stimpson (1993), is plotted in a simplified form in Figure 6.45, illustrating the effect of a lower tensile modulus on the calculated effective tensile stress at the centre of the sample. The average Young's Modulus in Table 6.3 is 42 GPa while the average modulus in compression is 66 GPa for undamaged near-surface Lac du Bonnet Granite (Eberhardt et al. 1998, and this study), a ratio of approximately 64%. Martin and Stimpson (1994) discuss the impact of sample

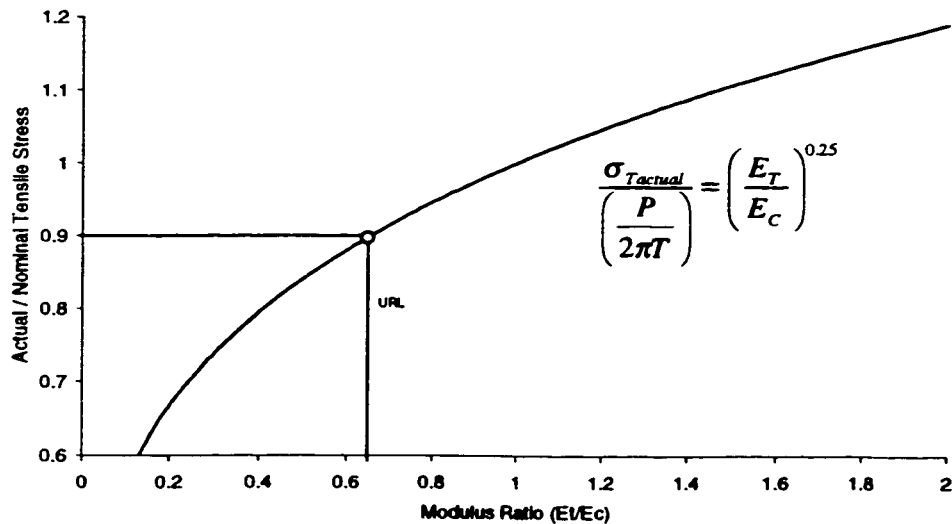


Figure 6.45: Correction of Brazilian test results for non-equal tensile and compression moduli.

damage due to unloading and also due to drilling. It should be anticipated that the value of 42 MPa would be significantly lower than the tensile value parallel to the disc. Most of the significant microcracks generated during sampling propagate normal to the core axis as evidenced by an average 15% reduction in Mode I fracture toughness for loading in this direction (Haimson and Zhao 1991). Nevertheless, using this ratio in Figure 6.45, the true lateral tensile stress is estimated to be 90% of the nominal value, a modest correction.

The average stress and lateral strain (at the centre of the samples) at each threshold is summarized in Figure 6.46 for comparison with the results of the direct tensile test. It is highly noteworthy that the crack initiation threshold for the Brazilian test is equivalent in terms of stress to the rupture threshold in direct tension (as is the systematic crack threshold if the above correction is applied). In terms of strain, however, the Brazilian threshold is almost twice (1.8x) that in the direct tension tests. In addition, crack initiation in the Brazilian test does not immediately lead to unstable rupture as in direct tension. Additional stress and strain is required to overcome toughness hardening and to produce crack coalescence and rupture.

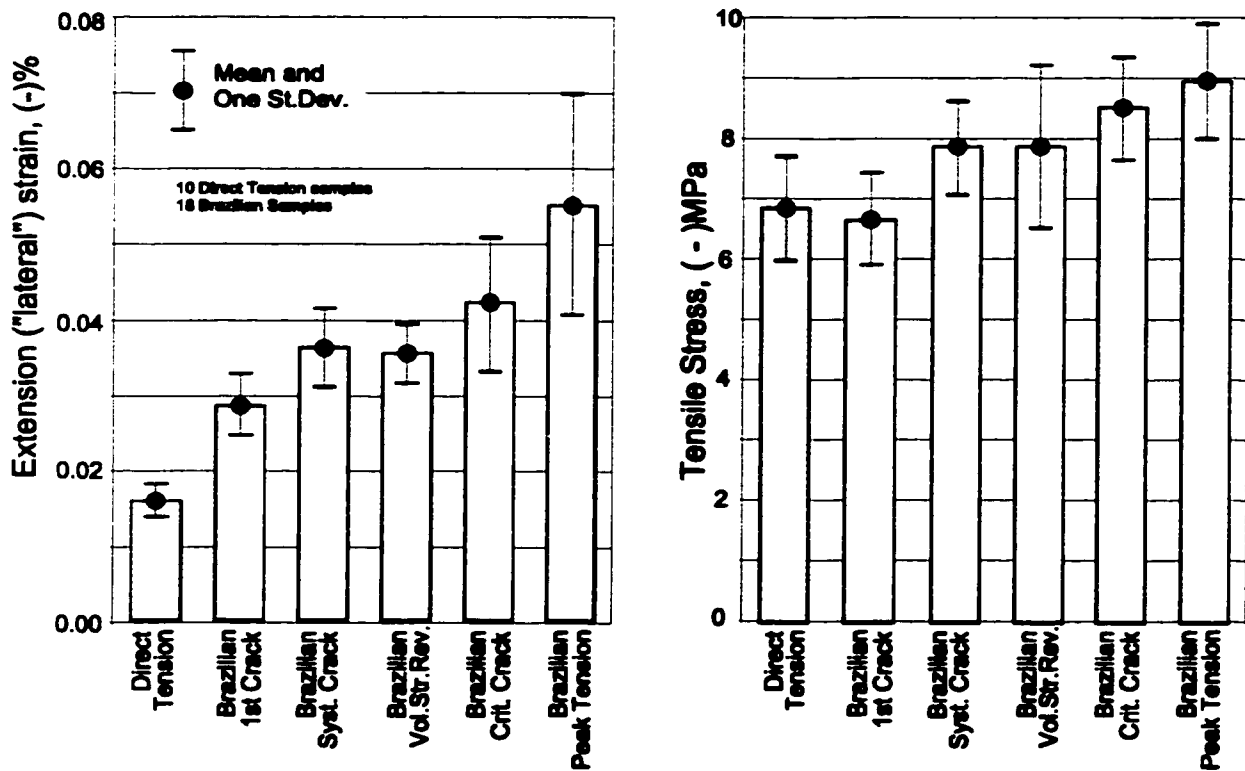


Figure 6.46: Comparison of damage thresholds for the Brazilian test and direct tension.

This quasi-stable crack initiation behaviour is confirmed by acoustic emission studies performed by Falls (1993) using samples of Lac du Bonnet granite. Figure 6.47 shows acoustic emission locations within the sample at various stages of the test. The right hand plots indicate the direction of the extensile direction (seismic source "T axis") where it has been resolved. The peak strength in this test was 7.85 MPa. Cracks occur at the lower abutment early in the test but do not interact with the subsequent tensile cracking in the centre of the disc. This central crack damage progresses in an initially stable fashion prior to full sample rupture.

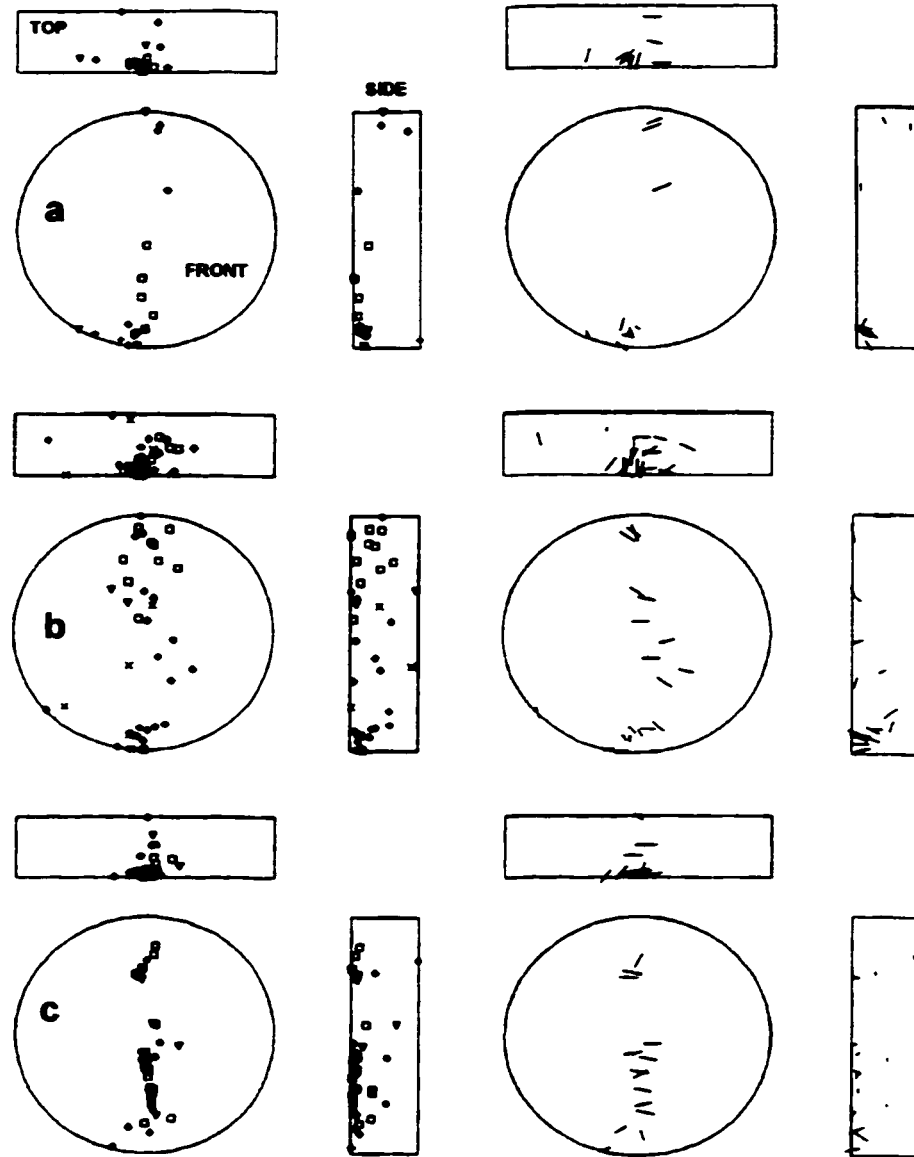


Figure 6.47 Acoustic emissions (left) and tensile axes (right) within Brazilian Test sample at 64-78% (top), 78-93% (middle) and 93-100% (bottom) of failure load (modified after Falls 1993).

6.8 COMPRESSIVE TESTS ON LAC du BONNET GRANITE

6.8.1 Damage Initiation

Numerous compressive tests were performed on the Lac du Bonnet granites as part of the rock mechanics investigations at the Underground Research Laboratory operated by AECL. Some of this test data is summarized by Martin (1994; 1995; 1997). This data was made available to and is reanalyzed here by the author for this study.

6.8.1.1 Confinement Dependency of Crack Initiation

While the inspiration for much of this thesis is the increasing use (Martin et al 1996; 1997; 1998; Read et al 1998; Castro et al. 1995; 1996) of an insitu damage initiation criteria based on:

$$\sigma_1 = \sigma_{ci} + \sigma_3 \quad \text{where } \sigma_{ci} \text{ is a constant} \quad [6.16]$$

no such relationship exists in the body of laboratory data for granite. Rather, Hommand et al (1995) describe a non-linear lateral strain threshold for triaxial tests on Lac du Bonnet granite, corresponding to the stress criterion:

$$\sigma_1 = 72MPa + 1.5\sigma_3 \quad [6.17]$$

This is similar to the relationship:

$$\sigma_1 = 64MPa + 1.4\sigma_3 \quad [6.18]$$

obtained for slow loading of Westerly granite by Brace et al (1966) and coincidental with the slope $(\Delta\sigma_1/\Delta\sigma_3)=1.5$ obtained for sandstone by Pestman and van Munster (1996). Martin (1994) also presents test data for Indiana Limestone which suggests a slope of 1.6 to 2 for this rock type.

Martin (1994) does describe the relationship:

$$\sigma_1 = 49MPa + 0.4\sigma_3 \quad [6.19]$$

for highly damaged (due to stress relief and drilling) samples. This threshold is based on a subjective identification of an inflection in the lateral strain – axial strain relationship. These tests showed a highly non-linear lateral strain response and were difficult to interpret. Martin (pers comm.) agrees that this relationship is weak since accurate interpretation of strain records from damaged samples is very difficult.

The relationship of Hommand et al. (1995), obtained from careful examination of the lateral strain response, will be taken here to represent the nominal damage initiation threshold for undisturbed Lac du Bonnet Granite. It is well established that the onset of lateral strain deviation is coincident with the systematic initiation of microcracks. Eberhardt et al. (1998) recently conducted a series of acoustic emission tests on unconfined samples of Lac du Bonnet granite and demonstrated this relationship as shown in Figure 6.48. This has also been demonstrated by Scholz (1968), Shah and Labuz (1995), and by Falls (1993).

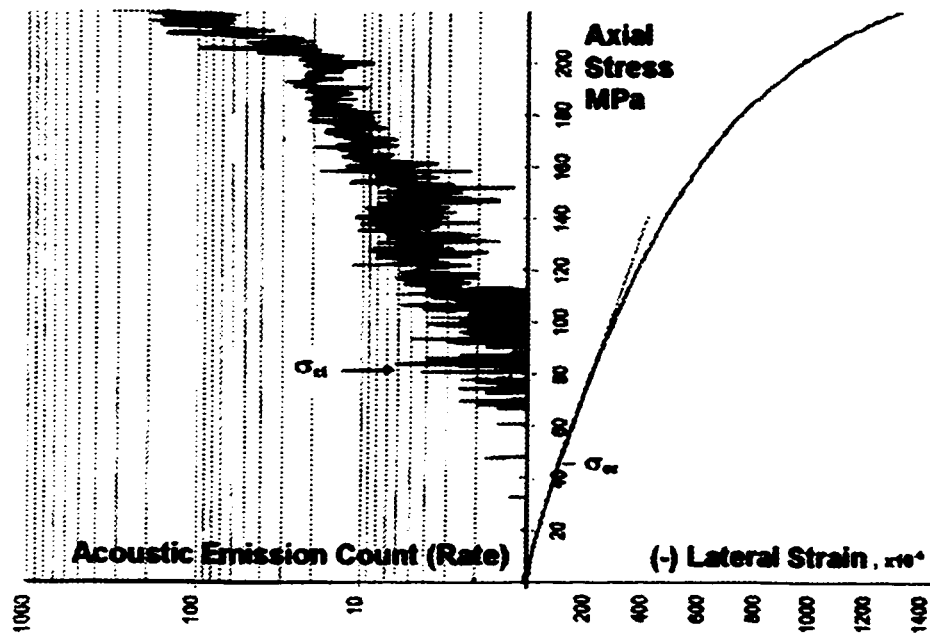


Figure 6.48: Correlation between non-linear lateral strain and microcrack accumulation as indicated by acoustic emissions (modified after Eberhart et al 1998).

Figure 6.49 compares the limit in Equation 6.17 with a number of other damage and failure envelopes. The Griffith envelopes in Figure 6.49 are based on the average tensile stress obtained in Section 6.6. and are obtained as follows for the two dimensional (Griffith 1921; 1924) and the three dimensional axi-symmetrical (Murrell 1963) cases respectively:

$$(\sigma_1 - \sigma_3)^2 = 8T_0(\sigma_1 + \sigma_3) \quad [6.20]$$

$$(\sigma_1 - \sigma_3)^2 = 12T_0(\sigma_1 + 2\sigma_3) \quad [6.21]$$

The Hoek-Brown envelope for peak strength of intact granite (Martin 1994) is shown for comparison, as is the Tresca criterion corresponding to the damage limit in Equation 6.16 using the UCS intercept of 72MPa obtained from Hommand et al. (1995).

LAB DATA FIT (Howland et al. 1986) for Damage Initiation

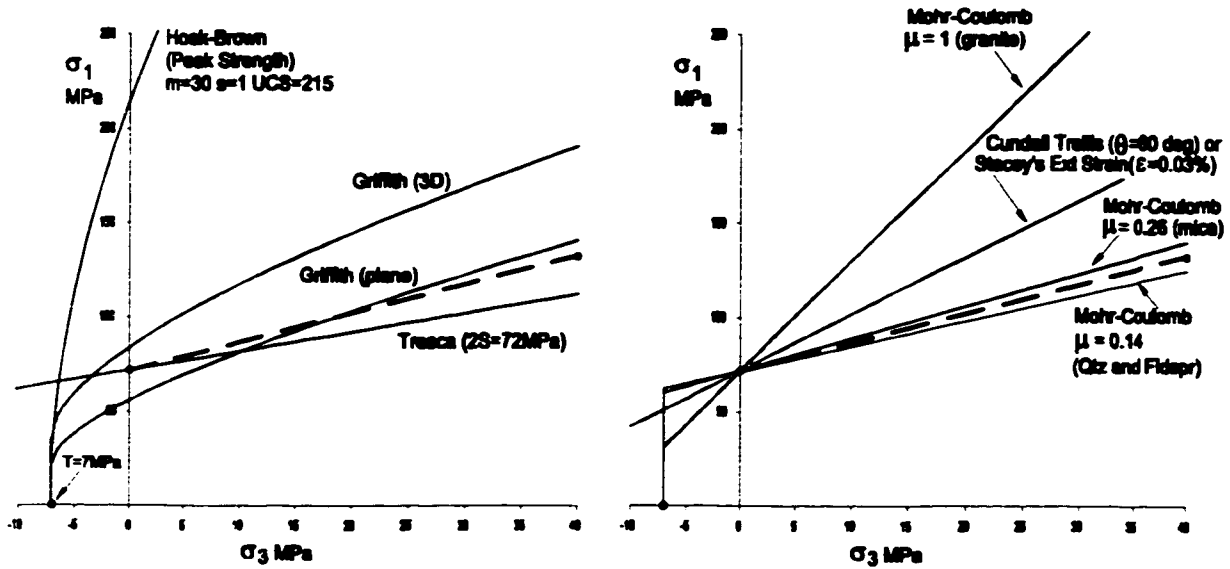


Figure 6.49: Comparison of Lac du Bonnet damage initiation threshold with other criteria.

In Figure 6.49, a number of linear and bilinear envelopes are illustrated. Clearly a Mohr-Coulomb envelope using the friction coefficient, $\mu=1$, for granite (Martin 1994), is unacceptable as a damage initiation threshold. So too is the relationship obtained from Stacey's (1981) extension strain criterion ($\epsilon_{cr}=0.03\%$, $E=60\text{GPa}$, $\nu=0.25$):

$$\sigma_1 = \frac{E}{\nu} \epsilon_{cr} + \frac{1-\nu}{\nu} \sigma_3 = 72 + 3\sigma_3 \quad [6.22]$$

Equation 6.22 is identical to the expression obtained from Cundall's (1994) "Trellis" criterion based on the model of Trollope (1968):

$$\sigma_1 = \sigma_b + \frac{1}{\tan^2 \theta} \sigma_b = 72 + 3\sigma_3 \quad [6.23]$$

using the vertical-datum trellis angle for densely packed discs ($\theta=30$ degrees).

It interesting, however, that the Mohr-Coulomb envelopes passing through the unconfined damage intercept (72 MPa) with slopes given by:

$$\frac{\Delta\sigma_1}{\Delta\sigma_3} = \frac{(\sqrt{1+\mu^2} + \mu)}{(\sqrt{1+\mu^2} - \mu)} \quad [6.24]$$

and using friction coefficients, $\mu=0.14$ to 0.26 , respectively quartz or feldspar and for clean mica (Horn and Deere 1962) the correspondence is quite good. This suggests that a sliding microcrack model may be appropriate for the initial extension of axial microcracks in compression. This was

originally proposed by McClintock and Walsh (1963) although a composite rock friction coefficient was suggested for use, (e.g. $\mu=1$ giving a slope, in Equation 6.24, of 5.8). Hommand-Etienne's slope of 1.5 corresponds to a frictional coefficient of 0.2.

6.8.1.2 Unconfined Crack Initiation

Chapter 5 discussed the apparent correlation between the onset of excavation sidewall damage and the presence of an induced tangential compressive stress greater than one third to one half of the intact rock *UCS*. This is consistent with the ratios obtained for crack initiation in the laboratory. The lower bound ratio (one-third) could relate to initial damage while the upper bound (one half) could relate to the onset of systematic damage (constant accumulation rate increase).

The variation in damage thresholds (with respect to *UCS*) could also be related to the rock type. In a perfect homogenous solid, the onset of crack initiation would be expected to be coincident with failure since crack density would instantaneously reach critical levels once the crack initiation threshold was reached. In heterogeneous materials, additional crack accumulation or incremental crack extension is necessary beyond σ_{ci} to achieve rupture.

As suggested by Tables 6.1 and 6.5, the mechanical nature of the rock also plays a role in the relativity of σ_{ci} and *UCS*. For polycrystalline rock such as granite, quartzite and marble, the ratio of σ_{ci} varies from 2.5 to 3 with respect to *UCS*. It is, however, consistently 2 to 2.2 with respect to critical damage or crack interaction stress as defined by axial stress/strain non-linearity or by volumetric strain reversal. In a clastic material such as sandstone, the σ_{ci} :*UCS* ratio is typically less than 2, although this varies. Limestone, a chemical precipitate, has a very low damage initiation point compared to the ultimate strength. The ratio for Potash is 2.5 with respect to *UCS* but much lower with respect to axial stress/strain deviation. This is due to the fundamentally different nature of bonding and the potential for internal lattice slip or true shear damage in Potash. In addition, crack initiation can occur at between 20% and 75% of peak strength (Lajtai et al. 1994), with the ratio increasing for slower loading rates. Non-linear deformation (due to lattice slip) occurs prior to crack initiation, typically at 40 to 50% of peak stress.

The stress level at which critical damage (defined by volumetric strain reversal) and strain localization occurs is approximately 80% of the ultimate strength in limestone, a ratio somewhat higher but consistent with other rock types. With the exception of the ionic solid Potash, all other rock types in Table 6.5 reach critical damage at a stress level of 70 to 90% of peak strength.

Table 6.5: Examples of uniaxial compression thresholds for various rock types
(See references given for Table 6.1 for different rock types)

	Potash	Dolomite	Limestone	LdB Granite	Quartzite	Marble	Sandstone
Critical Damage / Crack Initiation	1.3	1.2	4.3	2.1	2.1	2.2	1.4
Critical Damage / Peak Strength	52%	87%	87%	72%	82%	77%	74%
Peak Strength / Crack Initiation	2.5	1.4	5	3	2.5	2.6	1.9

Figure 6.25 reflects a similar trend, for the various rock types described above, for the ratio of UCS to tensile strength, suggesting that compressive damage initiation is closely related to rock tensile strength while peak strength is controlled by other factors. Table 6.6 lists the damage initiation threshold for Lac du Bonnet Granite under uniaxial conditions (using lateral strain measurements unless otherwise indicated) by various researchers.

Table 6.6: Damage initiation stress for Lac du Bonnet granite

Surface samples (Cold Spring Quarry to URL 130m Level)

1st Initiation Threshold

- 72 MPa (acoustic emissions) (Hommand et al. 1995)
- 71 MPa (Duevel & Haimson 1997)
- 75 MPa (Read 1994)
- 80 MPa (this study)
- 81 MPa (acoustic emissions) (Eberhardt et al 1998)

2nd Initiation Threshold = Systematic Crack Initiation

- 95 MPa (Duevel & Haimson 1997)
- 100 MPa (Read 1994)
- 93 MPa (this study)
- 104 MPa (acoustic emissions) Eberhardt et al 1999)

240 level samples

1st Initiation Threshold

- 64 MPa (Martin 1994)
- 80 MPa (acoustic emissions) (Eberhardt et al. 1998)

2nd Initiation Threshold

- 103 MPa (acoustic emissions) (Eberhardt et al 1999)

420 level samples (damaged)

1st Initiation Threshold

- 50 MPa range from 40 to 75 MPa due to highly non-linear response (Martin 1994)
- 79 MPa (acoustic emissions) (Eberhardt et al. 1998)

2nd Initiation Threshold

- 102 MPa (acoustic emissions) (Eberhardt et al 1999)

Some of the values above were obtained using acoustic emissions. The first crack initiation threshold corresponds to the first acoustic emission rate increase (eg. Figure 6.48) and acoustic energy rate rise above noise levels. The second crack initiation threshold as quoted above corresponds in the work of Eberhardt et al. (1999), to the first significant acoustic rate increase after primary initiation. The second initiation threshold corresponds to the onset of a sharp increase in and subsequently constant log-rate increase for lateral strain (constant crack accumulation rate increase). Using a similar technique, this author reinterpreted data presented by Duevel and Haimson (1997) to delineate the two thresholds. The same technique is used in the numerical simulations in Chapters 7 and 8.

In summary, the initial damage initiation threshold for undamaged Lac du Bonnet granite ranges from 71 to 81 MPa, while the threshold for systematic damage accumulation (constantly increasing accumulation rate) is 93 to 104 MPa for uniaxial loading in laboratory samples.

6.8.2 Effect of Unloading or Sampling Damage

It is interesting that while the initiation threshold defined by strain readings seems to decrease with depth (and sampling damage), the thresholds defined by acoustic emission rate do not. It is possible that sample damage leads to increased lateral strain (non-linear elastic) but not to a lowering of the threshold for additional damage accumulation. In contrast, the rupture strength in direct tension as discussed in Section 6.6 drops by more than 80% in samples from 420m depth as compared with near-surface samples (Gorski and Yu 1991). It is possible that extension cracks sustained in unloading (sampling damage), may lead to additional elastic lateral dilation (manifested by an increase in Poisson's ratio) but may be too rough, for example, to act as sliding flaws for new extension crack nucleation under compression.

Isotropic damage induced by unloading can reduce the stress required for critical damage or for crack interaction sample yield. Indeed, while Eberhardt et al. (1999) and Lajtai (1988) show a negligible reduction in uniaxial compression damage initiation stress, for URL samples from near surface to 420m depth, they do note a significant reduction in critical damage stress (determined from volumetric strain reversal). Approximate critical damage thresholds range from 155 MPa near surface, to 145 at 240 level and to 110 MPa at 420m. The corresponding peak strengths given by Martin (1994), are 215 MPa, 185 MPa and 155 MPa respectively.

For undamaged samples, the crack initiation threshold in Lac du Bonnet granite, under uniaxial compression is, on average, 35% of the mean peak strength, and 50% of the critical damage

threshold. The systematic cracking threshold, likewise manifests itself at 46% of the peak strength and 63% of the critical damage stress. For Cold Spring quarry samples, the critical damage threshold occurs at 72% of peak strength (*UCS*). At 420m the critical damage or yield threshold is 71% of the corresponding peak strength but only 51% of the undamaged *UCS*

The most notable impact of sample damage is on tensile strength reduction. These unloading cracks are likely to be rough and irregular since they are located primarily at grain boundaries. They can and do have a profound impact on the direct tensile strength (a 80% reduction from surface to 420m level at URL according to Gorski and Yu 1991), but have a negligible impact on crack initiation (Eberhardt et al 1999) in compression. When closed in compression, these unloading cracks do not seem to act as seed flaws for initial wing crack generation. In tests at low confinement, the initial non-linear portion (often called "seating") represents the progressive closure of sub-horizontal and inclined cracks. The remaining open vertical cracks do not easily facilitate additional wing crack growth in the absence of lateral tension.

In unconfined conditions, however, sub-vertical or steeply inclined grain boundary cracks can interact with extending loading-induced wing cracks leading to critical crack interaction and strain localization at a lower stress level than in undamaged samples. This may also be the case with larger flaws and joints insitu. Therefore, while crack initiation stress is insensitive to moderate sample damage, critical crack interaction stress and ultimately peak strength should decline with depth as is the case for URL samples.

Martin and Stimpson (1994) give an excellent discussion of the effects of unloading and sampling damage of Lac du Bonnet granite at depth including the reduction in apparent stiffness at low confinements as shown in Figure 6.50. Secant modulus at low confinements incorporates the effect of crack closure during initial loading. In these tests, the axial stress is equal to the lateral confining stress at the lower terminus of the secant line. The confining stress at which the secant modulus approaches a constant value represents the stress required to completely close cracks caused by unloading. Figure 6.50 indicates an approximate crack closure stress of 15 to 30 MPa.

In the unconfined tests on samples from the 420 level (damaged), Poisson's ratio varied from 0.14 during the early cycles to 0.2 just prior to initial volumetric strain reversal. The lower range is likely due to sub-horizontal crack closure. The initial Young's modulus was approximately 43, rising to 50 MPa prior to yield. Nominal Poisson's ratios taken from tests on surface samples are 0.2 to 0.26 while the undamaged modulus is approximately 70MPa.

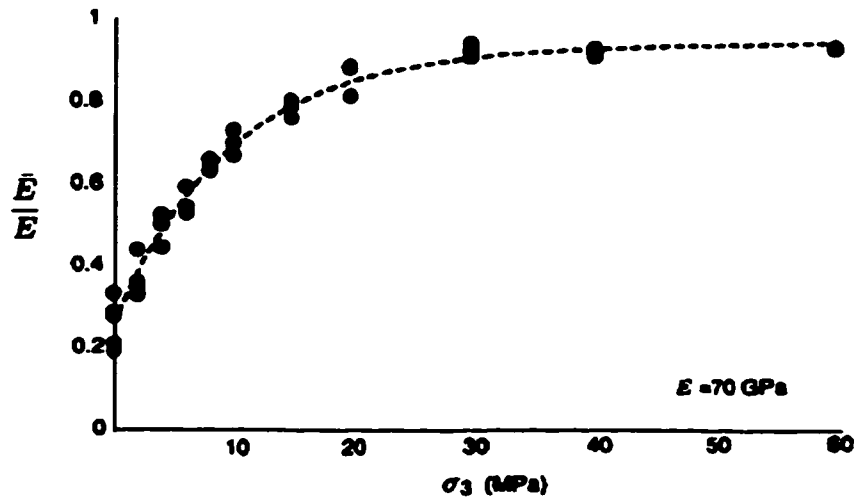


Figure 6.50: Reduction in secant modulus, in damaged granite samples, at low confinements due to open cracks (Martin 1997)

It should be noted that much of the larger scale damage cracks which occur in core obtained from deep locations is due to the drilling process itself and may not be representative of the actual insitu rockmass. In particular, large persistent internal tension cracks are the result of stress concentrations in the core stub as the rotary bit is advanced. This is demonstrated in Figure 6.51 using an elastic and a non-linear finite element simulation (axi-symmetric PHASE² analysis) with a Mohr-Coulomb criteria and a tensile strength cutoff. In this simulation, the axial stress is equivalent to the minor principal stress at the 420m level at URL. the radial stress (normal to symmetry axis) is an approximate average of σ_1 and σ_2 . The left-hand stub represents the newly created core while the adjacent slot represents the advancing diamond bit.

These cracks significantly affect the direct tensile strength (tested parallel to core axis) and the crack closure stress in axial compression. Oblique (oriented away from the axis-normal section) and shorter cracks are more representative of insitu unloading damage.

Unloading damage has only limited impact on compressive damage initiation but significantly affects the compressive yield threshold through an increase in initial crack density and possibly through enhanced potential for axial crack interaction (a reduced critical crack density). The apparent lack of influence of unloading damage on the crack initiation threshold, and the apparent slope of the damage initiation threshold in $\Delta\sigma_1/\Delta\sigma_3$ space, suggest that a closed, smooth sliding intra-granular flaw is responsible for extension crack initiation in compression (as opposed to an open pore mechanism), while any sub- or trans-grain discontinuity can lead to rupture in direct tension, including the irregular grain-boundary cracks created through unloading damage.

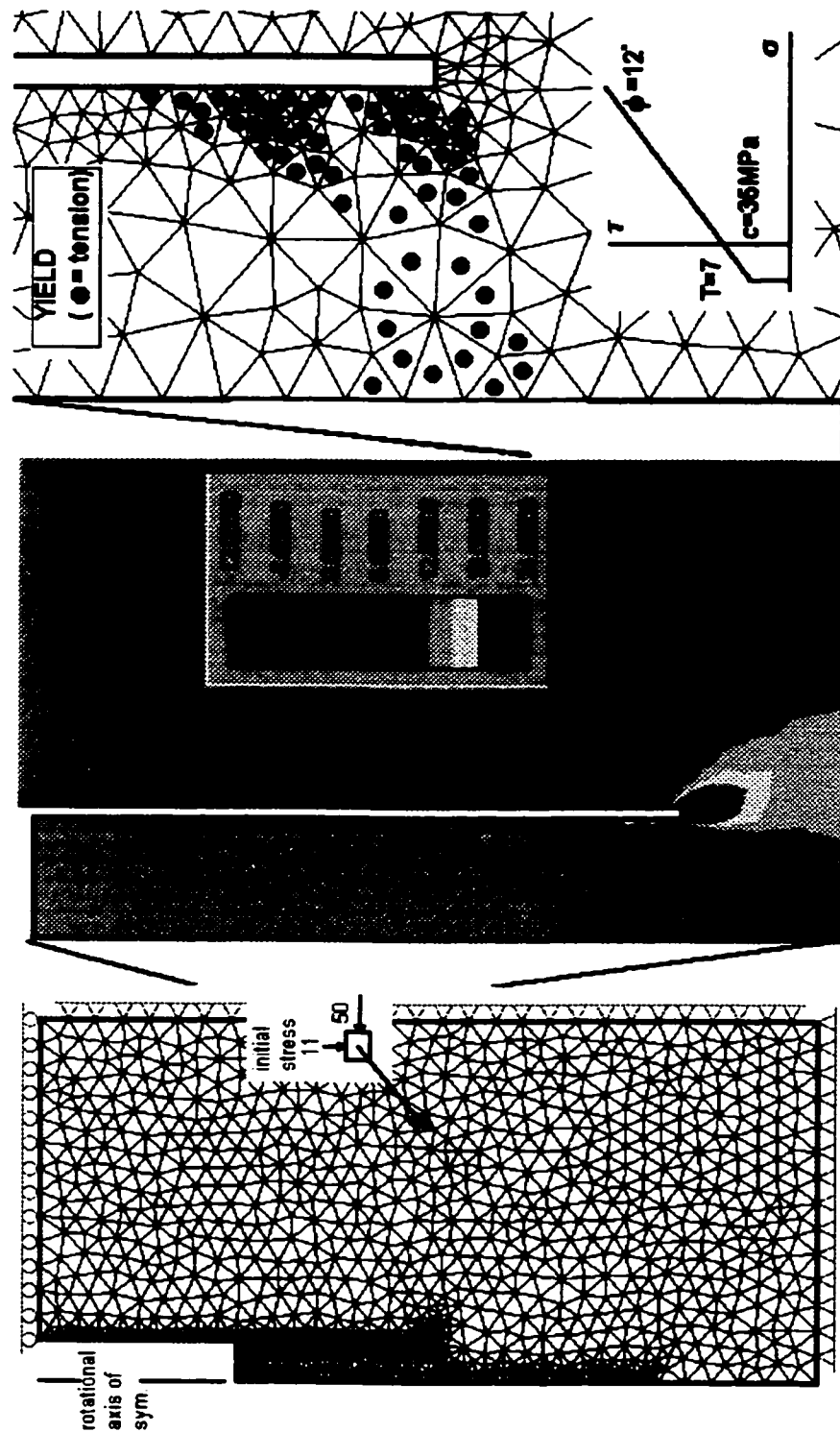


Figure 6.51: Schematic illustration of core axis-normal crack damage due to drilling in high stress environments. PHASE² finite element simulation: axi-symmetrical section about core axis; a) Minor principal elastic stresses and b) yield points showing tensile rupture planes (discing) at core stub.

6.8.3 Sliding Crack Model vs. Griffith Tensile Crack

A likely candidate model for extension crack initiation is the sliding flaw and tensile wing crack model. Other models such as the indentation model and the grain boundary model (Figure 6.16) may also be at work here but are less numerically tractable. While these pre-existing flaws can theoretically be the nucleus of Mode I and Mode II crack initiation and extension, Mode I wing crack extension (from either sliding or open flaw) is favoured for the following reasons.

The nominal Mode II critical stress intensity factor as measured by Laqueche et al. (1986) is approximately equal to the Mode I toughness value for long cracks but increases by more than 50% for smaller mineral-scale cracks (Figure. 6.29). Nominal Mode II toughness can typically be twice the Mode I equivalent for hard rocks (Krishnan et al 1998). Mode I values decrease by as much as two thirds (Ouchterlony 1982; Ingraffea and Schmidt 1978; Okubo and Fukui 1996) for sub-grain crack dimensions.

Combined with the increase in Mode II for small cracks, this suggests that cracks within mineral grains are 4 to 10 times more likely to initiate extensile propagation than shear propagation (if $\sigma_3 = \tau$) in granite or other polycrystalline rocks. It also suggests that the process zone reported around longer propagating cracks (Labuz et al. 1987; Zietlow and Labuz 1998) hardens Mode I rupture (as observed by Krech 1974) while facilitating Mode II propagation, and that extension cracks are a necessary conditioning mechanism for ultimate shear rupture.

Sliding crack expressions abound in the fracture mechanics literature (e.g. Ashby and Hallam 1986). A simple model by Cotterel and Rice (1980) and modified by Pestman and van Munster (1996) is used here. Initiation of nascent (tensile) wing cracks from the ends of an inclined fracture (e.g. Figure 6.4b) as a result of excess shear stress, τ^* , occurs when:

$$\tau^* \geq \frac{\sqrt{3}}{2\sqrt{\pi c}} K_{IC} \quad [6.25]$$

where:

$$\tau^* = \frac{1}{2} \{ (\sigma_1 - \sigma_3) \sin 2\theta - \mu [\sigma_1 + \sigma_3 + (\sigma_1 - \sigma_3) \cos 2\theta] \} \quad [6.26]$$

and:

$$2\theta = \frac{\pi}{2} + \tan^{-1} \mu \quad [6.27]$$

Rearranging Equations 6.25 and 6.26 to obtain an expression for critical σ_1 gives:

$$\sigma_{1cr} = \frac{\sqrt{3}}{(\sin 2\theta - \mu - \mu \cos 2\theta)} \cdot \frac{K_{IC}}{\sqrt{\pi c}} + \frac{(\sin 2\theta + \mu - \mu \cos 2\theta)}{(\sin 2\theta - \mu - \mu \cos 2\theta)} \sigma_3 \quad [6.28]$$

The coefficient for σ_3 above is identical to that in Equation 6.24, giving a slope of 1.5 for a friction coefficient of 0.2. The critical crack half-length for wing crack initiation under uniaxial compression can be obtained:

$$c = \frac{3K_{IC}^2}{\pi\sigma_1^2 (\sin 2\theta - \mu - \mu \cos 2\theta)^2} \quad [6.29]$$

These equations are for wing crack initiation (i.e. beginning at 70.5 degrees from the sliding crack and rapidly curving towards the orientation of σ_1). Pestman and Munster (1996), Ashby and Hallam (1986) provide modified solutions which account for the effect of an extending wing crack (turning and extending parallel to σ_1) on the stability of the composite crack system.

From Equation 6.29, using a friction coefficient of 0.2, an unconfined uniaxial damage threshold of 72MPa and a critical stress intensity factor of 0.96 MPam^{-0.5} as obtained by Hommand-Etienne et al. (1998) from 3-point bending tests, a critical length, $2c = 0.5\text{mm}$ is calculated for the inclined seed crack. This value corresponds to one-half of the average effective diameter of the biotite grains (1mm), one-quarter of the average quartz grains (2mm) and one-seventh of the average feldspar grains (3.5mm) as analyzed by Kelly et al. (1993). The feldspar (alkali and plagioclase) make up 65% of the granite and have a maximum grain size of 7mm.

A maximum natural crack length of one-seventh of the grain size is consistent with electron microscope studies by Sprunt and Brace (1974) on Westerly granite (grain size = 750 μm) which identified a maximum length of 100 μm for low aspect ratio cavities (LARC's or natural microcracks). In this study the longer LARC's were found primarily along grain boundaries and within the plagioclase and mica crystals. Other ratios of maximum microcrack length to grain size (Sprunt and Brace 1974; Howarth 1987) include 1:5 for diabase, 1:11 for gabbro, and 1:10 to 1:5 for granites. The more common microcrack length in Westerley granite was in the range of 10 μm or 1.3% of the grain size.

The minimum critical stress intensity (Mode I) for feldspar according to Atkinson and Meredith (1987) is approximately $0.31 \text{ MPam}^{-0.5}$. Using this value in Equation 6.29, instead of the larger value for the complex Lac du Bonnet granite, gives a critical crack length of 0.05mm. This is equal to 1.5% of the mean plagioclase grain diameter, dimensions compatible with the findings of Sprunt and Brace (1974) for inter-granular LARC's in Westerly granite.

Using a higher value for quartz of $K_{IC} = 0.46 \text{ MPam}^{-0.5}$, quoted by Atkinson and Advis (1980), a critical crack length of 0.12mm is obtained. This is similar to the scale of the shear cracks (with wings) visible in Figure 6.26. and to the smooth portions of the cracks in Figure 6.39.

Since the wing crack is initiated at an angle away from the sharp end of the sliding crack (unlike the direct tension case), the effective K_{IC} for wing crack initiation is likely to be intermediate between the quoted values for the mineral and the rock. In any case, the order of magnitude range, 0.05 to 0.5mm seems reasonable for observed smooth (potentially sliding) cracks in Lac du Bonnet granite.

Remember that the atomically smooth cracks which are active in shear in Figure 6.26 are distinct from the larger and rougher cracks which are likely to be active only in tension.

As previously discussed, the value of $K_{IC}=0.32 \text{ MPam}^{-0.5}$ for Mode I rupture of the dominant feldspar or quartz crystals can be used in the equation (Kemeny and Cook 1987):

$$\sigma_i = T = K_{IC} \sqrt{\frac{\pi}{4c}} \quad [6.30]$$

for a penny-shaped crack in direct normal tension to obtain a critical initial crack diameter of 3.5mm for a tensile strength of 6.8 MPa, a length equivalent to the largest quartz grain diameter and equal to the average feldspar. Candidate cracks for tensile rupture were observed in Figure 6.26 and 6.41.

It is neither necessary nor likely, therefore, that the same cracks are responsible for damage initiation in both tension and compression. Indeed, the larger cracks (Figure 6.26 and 6.41) are highly irregular and interlocked. In shear, this leads to an effective cohesion and high friction which cannot be overcome at lower stresses. In addition the small rock bridges shown in Figure 6.39 add significant cohesion in shear. In tension, on the other hand, such bridges are easily ruptured at low direct and normal tensile stress, leaving the larger cracks to be exploited.

Brace et al. (1972) observed that many of these LARC's were intermittent and in collinear groups, particularly along grain boundaries (Figure 6.52) with intervening bridges typically 10% to 50% of the neighbouring crack length.

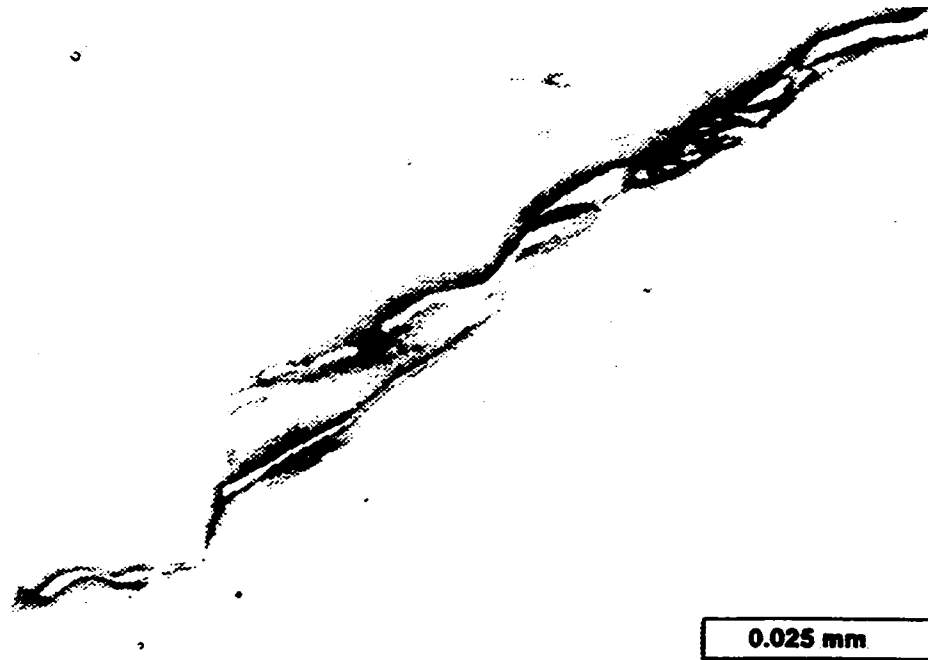


Figure 6.52: Scanning electron micrograph of intermittent cracks along grain boundary between two feldspar grains in Westerly granite. Image inverted. After Hobbs et al (1976) and Brace et al. (1972).

It is reasonable to expect that when these LARC's are "closed" under compressive stress, they could act independently as sliding seed cracks, as assumed in the model in Equation 6.28 to 6.29, with length $2L=50$ to $500\mu\text{m}$. Under purely tensile conditions, and with the grain boundary aligned perpendicular to the tension, these collinear LARC's could coalesce across the intervening bridges at a significantly lower tensile stress (see Chapter 2), T or σ , as predicted by Kemeny and Cook's (1986) expression for rupture of an isolated rock bridge:

$$T = \frac{K_{IC} 2a \sqrt{\pi a}}{\pi w^2} \quad [6.31]$$

where $2w$ is the spacing between bridges (observed intervening LARC length in thin section) and $2a$ is the collinear bridge width. Assuming a bridge width to crack length ratio of 20%, for example, a K_{IC} of $0.32 \text{ MPam}^{-0.5}$ and an initial LARC length of $50\mu\text{m}$, a critical tensile stress of 6.5MPa is obtained for rupture of the bridges, close to the 6.7MPa obtained for a 3.5mm

continuous seed crack in Section 6.6. These same bridges are less susceptible to Mode II rupture when the racks are closed and therefore are unlikely to affect the confined compressive response.

This leads to the anomalously high UCS/T ratio for Lac du Bonnet granite and other low porosity crystalline rocks. In higher porosity rocks with open pores or ubiquitous cleavage cracks, the same flaws are likely to be responsible for damage initiation in both tension and compression, resulting in UCS/T ratios closer to the Griffith predictions.

In addition, rough or intermittent cracks generated during sample extraction and unloading are unlikely to influence the damage initiation stress. The exception would be extension cracks on cleavage planes. These are less likely to develop during unloading since there is no spatial stiffness contrast within a well developed crystal lattice. Such contrasts and associated crack generation would normally occur at grain boundaries as observed by Martin and Stimpson (1994) and are unlikely to generate smooth planar surfaces. As previously mentioned, however, these flaws can significantly alter direct tensile stress and can facilitate premature interaction between extending axial microcracks resulting in a reduced critical damage threshold.

6.8.4 Damage Initiation and Accumulation

Several samples of Lac du Bonnet granite from the Cold Spring Quarry were tested in cycled compression at confinements of 0, 2 and 10 MPa. These tests are presented here to further illustrate key properties of the damage initiation and interaction thresholds. These tests do not represent a statistically significant sample and are used here for illustrative purposes only. The raw data for the 0 and 10MPa confinement tests are summarized in Figure 6.53. The axial stress was cycled with an incremental increase of 5 and 10 MPa, respectively, for these two tests.

Crack closure or seating stress is evident in each case as the onset of temporary stress-strain linearity after an initial period of significant non-linearity (Figure 6.54). Only between this point and crack initiation can the sample be considered truly elastic. The tangential Young's modulus and Poisson's Ratio taken during this portion averages 72 GPa and 0.25 respectively for the three tests. It is interesting that crack initiation (and lateral dilation) occur before 50% of the UCS. The standard practice of estimation of Poisson's ratio is to measure relative strains at 50% of UCS, after inelastic crack accumulation is well established. This leads to erroneously high estimates, for ν , in excess of 0.33 (e.g. Eberhardt et al. 1998) for previously undamaged samples.

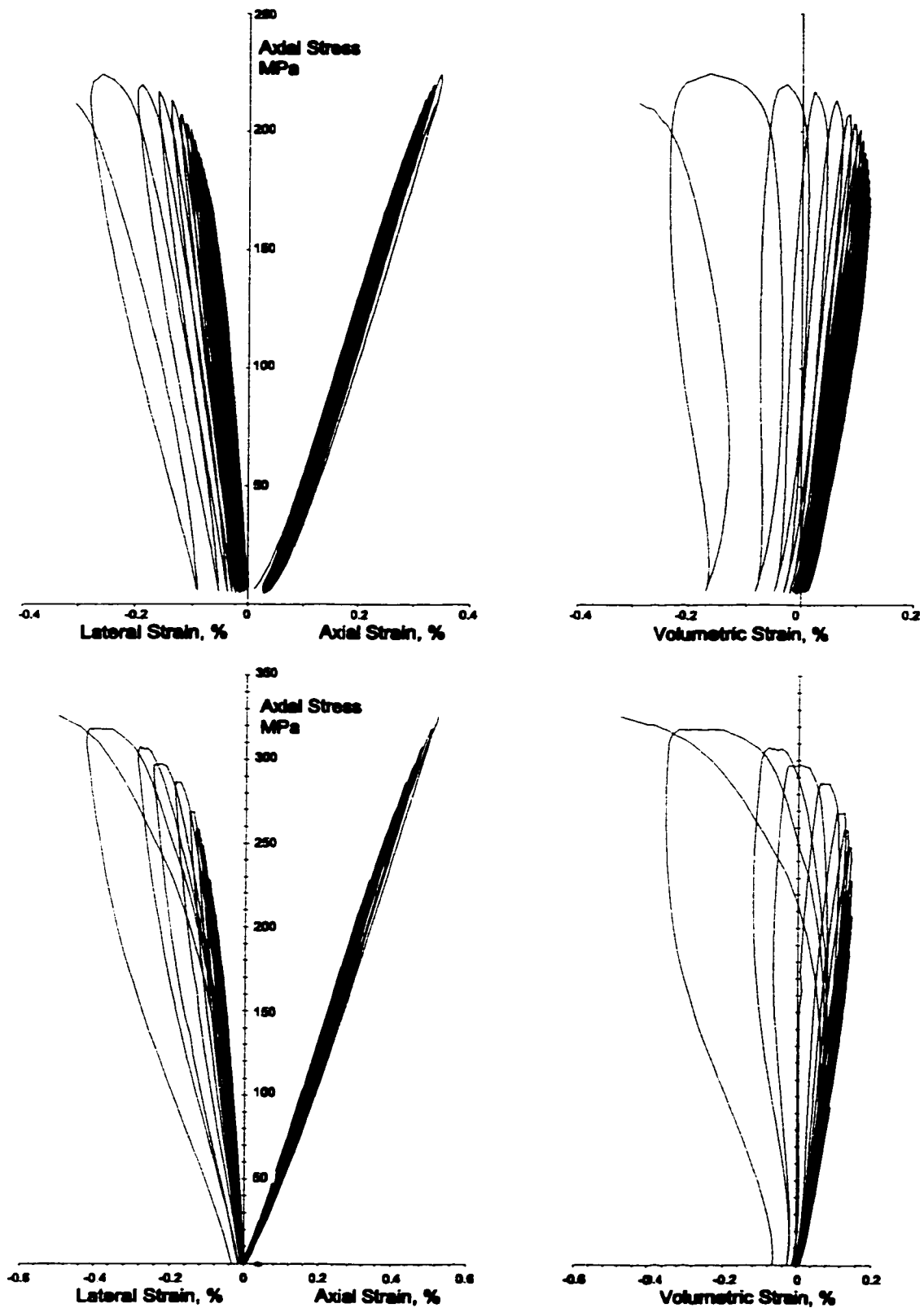


Figure 6.53: Compressive load cycle tests on unconfined (top) and 10MPa confinement (bottom) samples showing axial, lateral and volumetric strain response.

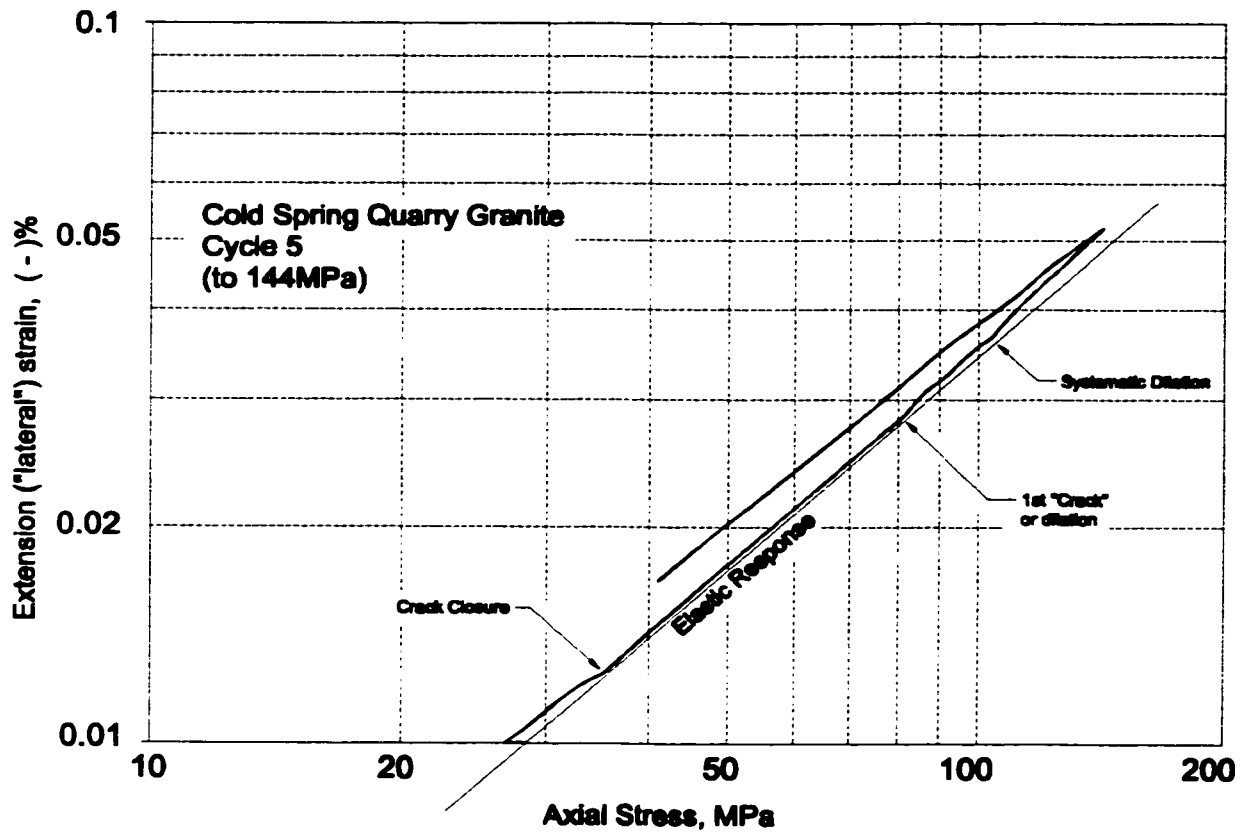


Figure 6.54: Definition of damage thresholds under axial compression. (unconfined sample).

Several damage thresholds are of interest here for undamaged samples. Crack initiation is defined as the first deviation of the lateral strain readings (plotted against axial stress) as shown in Figure 6.54. Systematic dilation or systematic crack accumulation is shown as the onset of constantly increasing lateral strain rate.

It has been proposed in this thesis (See Section 6.3.4) that critical crack damage or critical crack density be interpreted to occur at the first point of non-linearity in the axial stress – axial strain relationship. This should be considered the point of true sample yield. Localization can also be subjectively identified as the point of volumetric strain reversal. In each case the axial stress and lateral strain are recorded. Strain readings are zeroed at the start of axial loading.

For the confined samples, the true (absolute) lateral strain is calculated by adding $E^{-1}(1 - \nu)\sigma_{axial}$ to the negative lateral strain readings in Figure 6.53. The stress and lateral strain at the above damage thresholds, for all three tests, are summarized in Figures 6.55 and in Table 6.7.

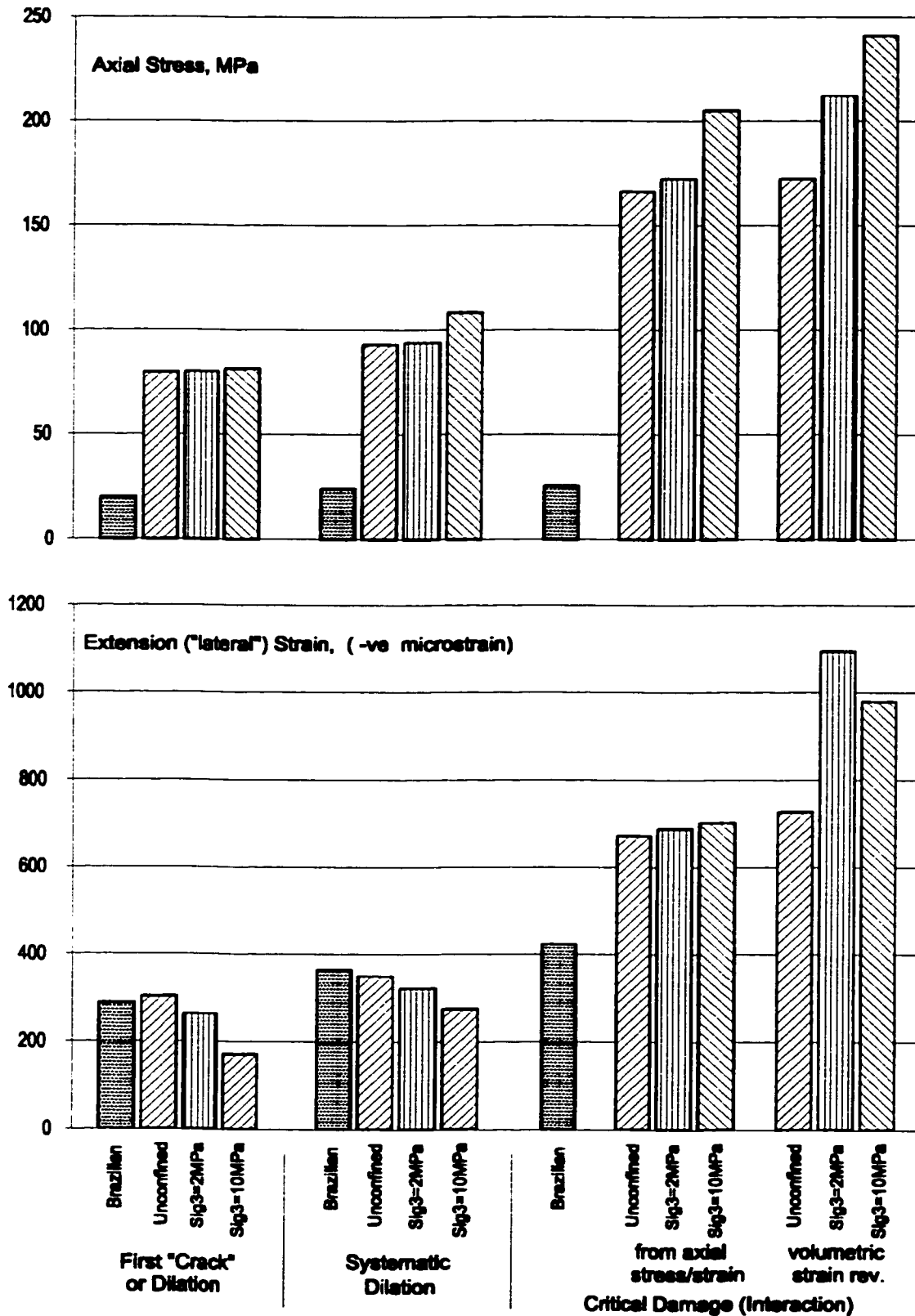


Figure 6.55: Summary of damage thresholds for cycle compression tests and Brazilian tests (top = axial compressive stress; bottom = lateral extension strain).

Table 6.7: Summary of damage thresholds for cycle tests in terms of axial stress and lateral strain (bracketed values are standard deviations where cycles were averaged).

Threshold	Unconfined	$\sigma_1 = 2$ MPa	$\sigma_1 = 10$ MPa
Damage Initiation Stress (MPa)	79.6 (4.4)	80 (4.1)	81.2 (4.2)
Systematic Damage Stress (MPa)	92.9 (7.5)	94.2 (6.3)	108.4 (14.4)
Critical Damage Stress (MPa) <i>Axial Stress/Strain Non-Linearity</i>	166	172	205
Critical Damage Stress (MPa) <i>Volumetric Strain Reversal</i>	172	212	241
Peak Rupture Stress (MPa)	225	252	340
Damage Initiation Strain (- μ strain)	303 (40)	263 (38)	171 (26)
Systematic Damage Strain (- μ strain)	350 (41)	322 (46)	273 (64)
Critical Damage (- μ strain) <i>Axial Stress/Strain Non-Linearity</i>	673	689	703
Critical Damage Strain (- μ strain) <i>Volumetric Strain Reversal</i>	728	1096	982

The results from the Brazilian tests are included in Figure 6.55 for comparison. The transitional nature of the Brazilian tests is illustrated in this figure and in Figure 6.46. Recall that the strains at damage initiation and coincident rupture in the direct tensile test were less than half of the lateral strains recorded at damage initiation in the Brazilian test. Meanwhile, the measured and calculated stresses in each case coincided very well.

In Figure 6.55 we see that the lateral strains are similar at damage initiation and at systematic dilation and damage, for the Brazilian tests and for unconfined direct compression samples. One possibility is that the phenomenon of crack initiation and rupture in the Brazilian test shares mechanisms from both compressive damage and tensile crack propagation. While compression induced cracking occurs near the loading platens, strain observations (and therefore damage threshold identification) are made at the centre of the disc. Observations suggest that crack initiation and propagation here is purely tensile (Yanagadani et al. 1978; Falls 1993).

An alternative explanation is that it is, in fact, the uniaxial compressive sample which is transitional. It is possible and likely that granite, under compressive loading at near zero confinement, involves both exploitation of the smaller sliding flaws (and associated wing crack initiation), and dilation and extension of the larger inter- and intra-granular cracks such as those which are critical to direct tensile failure. This suggests that any compressive initiation or

extension of axial cracks will lead rapidly to spalling and rupture in the presence of lateral tension. It must be this process which leads, in part, to a noted strength reduction for near-excavation rockmasses (Chapter 5), when compared to the results from purely uniaxial or slightly confined (see Figure 6.35) *UCS* tests.

Just as damage initiation in direct tension and in the Brazilian test is a function of critical tensile stress rather than extension strain, Figure 6.55 shows that damage initiation in compression is also a function of stress rather than strain. The lateral extension strain values at damage initiation and at systematic damage (or dilation) are certainly not equal. While the data is limited, the stress levels for damage initiation and for systematic damage suggest a confinement dependency within the range suggested by Equations 6.16 and 6.17. This supports the notion of a stress-based initiation mechanism.

An examination of the lower plot in Figure 6.53 reveals that volumetric strain reversal occurs after significant non-linearity in both lateral and axial strain. In uniaxial conditions the stress and strain threshold for both axial stress-strain non-linearity and volumetric strain reversal are nearly coincident, while under confined conditions there is significant lag between the two, with additional loading required after the former threshold before volumetric strain reversal occurs. It has been suggested here that axial stress-strain deviation is a physically more appropriate criterion for determining the onset of yield in confined samples.

Figure 6.55 offers further support for this position. The lateral extension strains at the onset of axial stress-strain non-linearity are approximately equivalent (given this limited sample) for the three compression samples. It is possible to infer from this that critical damage, or critical crack density is synonymous with a critical extension strain. This would, in turn, suggest that Stacey's (1981) critical strain criterion is applicable to critical damage and crack interaction and not to fracture initiation as originally intended.

Note that the lateral strain at yield in the Brazilian test, taken as either the systematic dilation or "critical damage" limit in Table 6.4, is approximately 50 to 60% of the critical damage strain in confined compression. The lateral strains after the onset of crack interaction are difficult to interpret within this limited data set. This suite of tests is included for illustrative and exploratory purposes only. More work is needed to quantify post yield dilation for constitutive applications. This work is concerned primarily with the thresholds of damage and yield. Section 6.8.4 will examine the confinement dependency, in Lac du Bonnet Granite, of several critical damage thresholds, namely, axial stress-strain non-linearity, volumetric strain reversal and peak strength.

6.8.5 Confinement Dependency of Damage Interaction

A series of cycled loading tests were performed by AECL on granite samples. These tests were performed in a fashion similar to those in the previous section. The loading rate was 0.75 MPa/s, with a data sampling interval of 3 seconds. Load-unload cycles were carried out with 40 MPa increases up to approximately 75% of peak strength. Then the cycles were defined by 0.063mm increments of circumferential strain to prevent rapid sample failure.

The purpose of these tests was to examine the reduction in the volumetric strain reversal threshold with increasing sample damage. This threshold is interpreted by Martin as the cohesion limit or the cohesive component of overall strength. These tests, illustrated in Figure 6.56, will be reexamined here to identify the confinement dependent thresholds for critical damage.

These tests were performed on samples from the 420 level at the URL and so are weaker and softer than the Cold Spring Quarry samples examined earlier. These samples likely contain a higher density of pre-loading microcracks, located predominantly at the grain boundaries. These cracks are created by stiffness contrasts (examined numerically in Chapter 8) at the grain boundaries which result in local tension and microcrack generation upon unloading. These cracks are generally rough and irregular. Martin (1994) and Martin and Stimpson (1994) discuss the impact of these cracks on mechanical and geophysical properties of granite samples extracted from increasing depths at URL.

Martin (1994) was interested in the degradation of the volumetric strain reversal point and the implicit decline in cohesion. This was the motivation behind the series of tests reproduced in Figure 6.56. The relationship of the yield stress and phenomenological cohesion in granite will not be disputed here. However, it is felt that this threshold (b in Figure 6.56) is belated with respect to the true onset of yield.

Axial strain non-linearity (a in Figure 6.56), in hard rocks such as granite, has been forwarded in this thesis as an indicator of the true threshold for crack interaction and yield strength. This threshold occurs significantly prior to volumetric strain reversal at higher confinements. Both thresholds, along with peak strength (c) and the damage initiation threshold from Hommand et al (1995) are summarized in Table 6.8 and plotted in Figure 6.57. The best-fit Hoek Brown envelopes are also plotted for comparison.

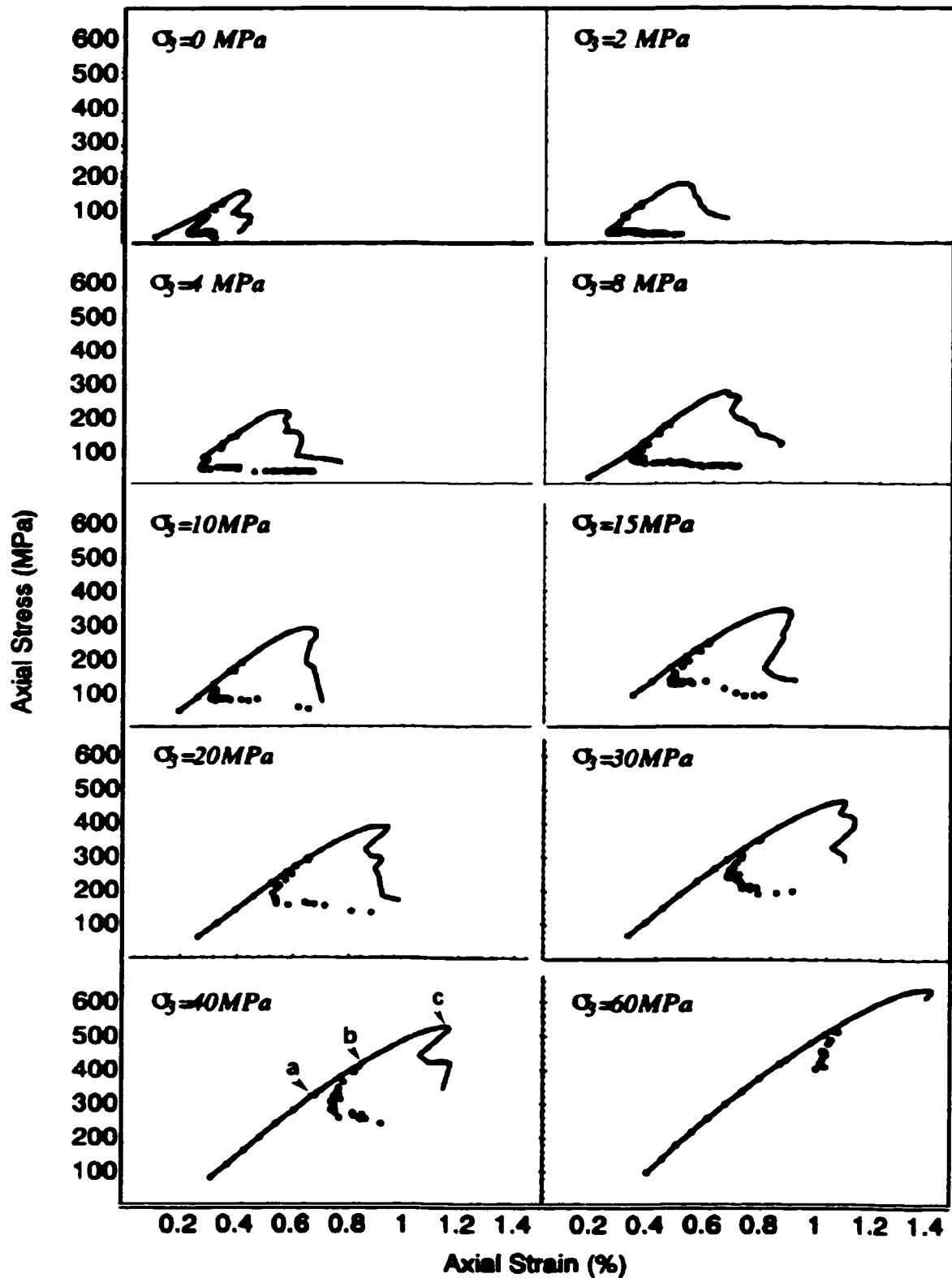


Figure 6.56: Summary of cycled load tests on granite samples at various confinements. The locus formed by the dots indicates the volumetric strain reversal point in each cycle. (based on data from Martin 1994).

Table 6.8: Critical damage thresholds for confined compression tests (URL 420m level)

Confining Stress (lateral pressure, MPa)	Damage and Strength Thresholds (axial stress, MPa)		
	Axial stress-strain non-linearity	Volumetric strain reversal	Peak strength
0	125	125	160
2	125	125	185
4	145	155	220
8	170	185	265
10	185	220	285
15	215	250	340
20	240	290	390
30	270	355	475
40	315	405	530
60	400	520	640

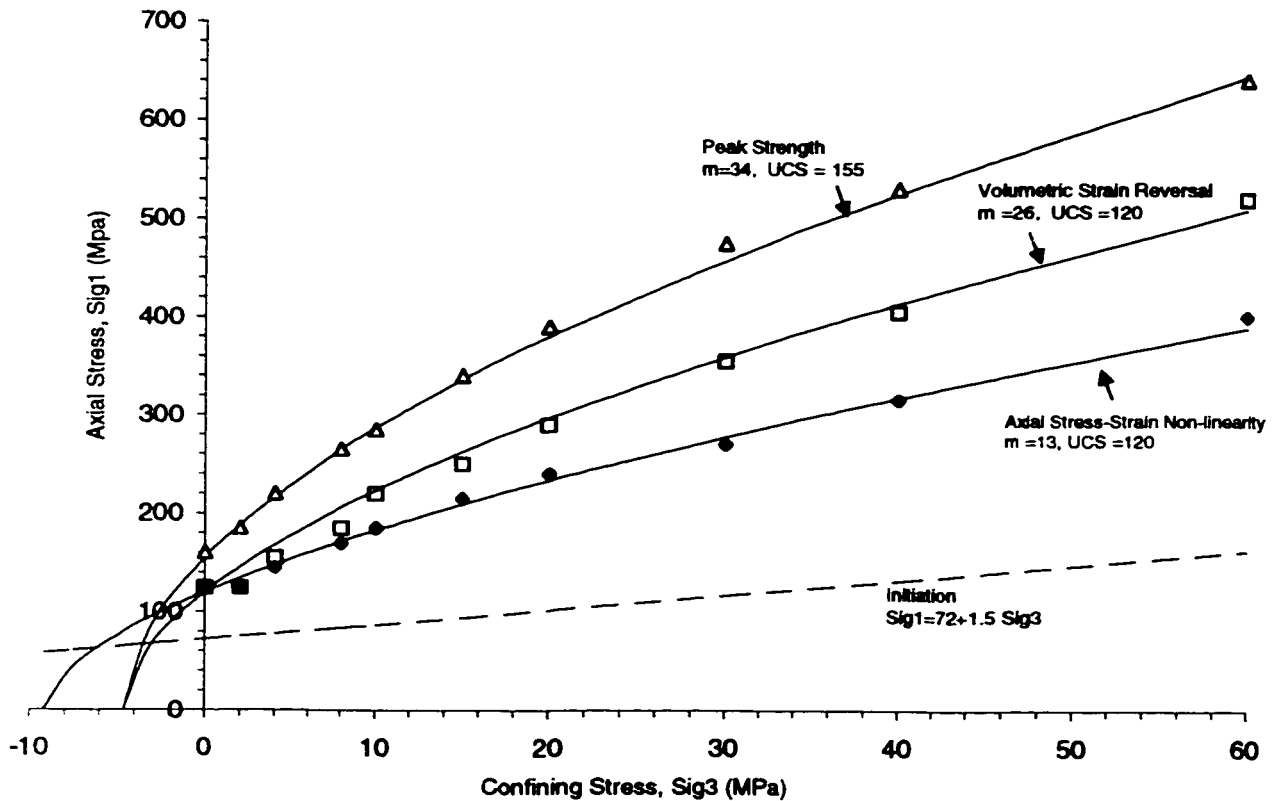


Figure 6.57: Critical damage threshold data from Figure 6.56 and Table 6.8. Best-fit Hoek-Brown envelopes shown for comparison ($s=1$).

In Figure 6.57, it can be seen that axial stress-strain non-linearity occurs simultaneously with volumetric reversal in unconfined compression, indicating that instantaneous crack extension and dilation occurs when axial microcracks first begin to interact. The same coincidence was observed in undamaged samples. In Figures 6.56 and 6.57, however, it is evident that initial crack interaction, while reflected in the axial behaviour, is accompanied by less immediate lateral dilation under confined conditions. Since volumetric strain is the sum of axial and lateral components, this results in a lag between crack interaction and volumetric strain reversal.

In unconfined conditions, crack interaction stress represents a lower bound for long-term strength and therefore must be reflective of insitu-strength. Martin (1994) and others have suggested that volumetric strain reversal is the key indicator of critical damage accumulation and crack interaction. This choice of indicator, although somewhat arbitrary, seems validated by uniaxial or unconfined behaviour. If, however, axial stress-strain non-linearity is an indicator of crack interaction, as proposed in this thesis, then this threshold must represent insitu strength under confined conditions. Figure 6.57 illustrates the significance of this alternative assumption. Figure 6.58 reproduces the data for the axially defined critical damage threshold for closer examination.

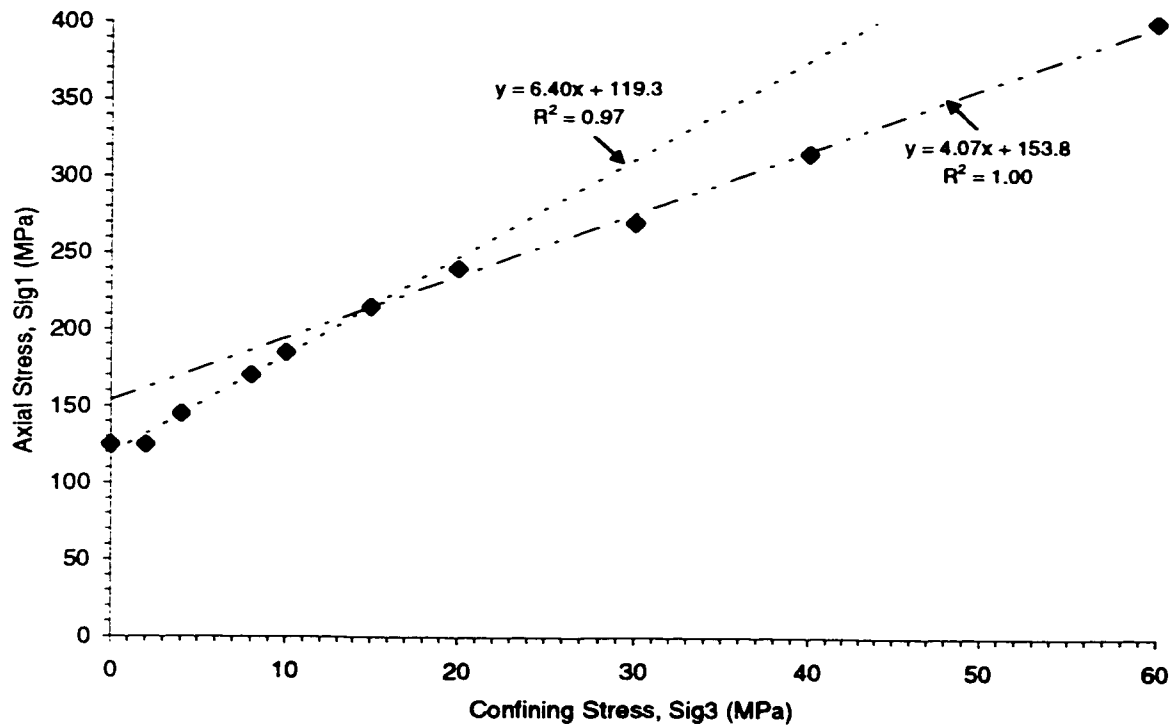


Figure 6.58: Critical damage threshold from axial stress-strain non-linearity. Bilinear envelope generated from best-fit lines through 1st five and 2nd five data points from Table 6.8.

The curved Hoek-Brown envelope masks a distinct bi-linear nature to the critical damage threshold as represented by the data in Figure 6.58. The best-fit lines in this figure are generated from the first and second set (low and higher confinement) of five data points. In spite of the subjectivity of this analysis, it does seem to reasonably represent the trend in the data. At lower confinements a drop in the critical damage threshold begins to occur at a lateral confining stress of 20 to 15 MPa. This is the same range below which the sample stiffness (as defined by the secant modulus) showed a marked decline due to the presence of open cracks (Figure 6.55). Clearly unloading or sampling damage is responsible for a reduction in critical damage interaction threshold at low confinements. The other thresholds, volumetric strain reversal and peak strength also show an increased degradation as well as the confinement is decreased. Volumetric reversal shows a marked drop below 10 MPa (Figure 6.57).

It is also interesting that this confinement limit, of 10 to 15 MPa, for the influence of open cracks also corresponds in magnitude to the inflection point in the lower bound acoustic emission (AE) limit discussed in Figure 5.42 and reproduced in Figure 6.59. Below this confinement the near-face AE initiated at a major principal stress equivalent to the unconfined damage initiation threshold (i.e. slope of 0). Above this limit, the slope of the damage initiation threshold, with respect to minor principal stress, reverted to a value (1.5) corresponding more closely to the laboratory data. The transition in this case occurs at a σ_3 of approximately 10 to 11 MPa, a value which, in turn, corresponds to the minor insitu principal stress (far field).

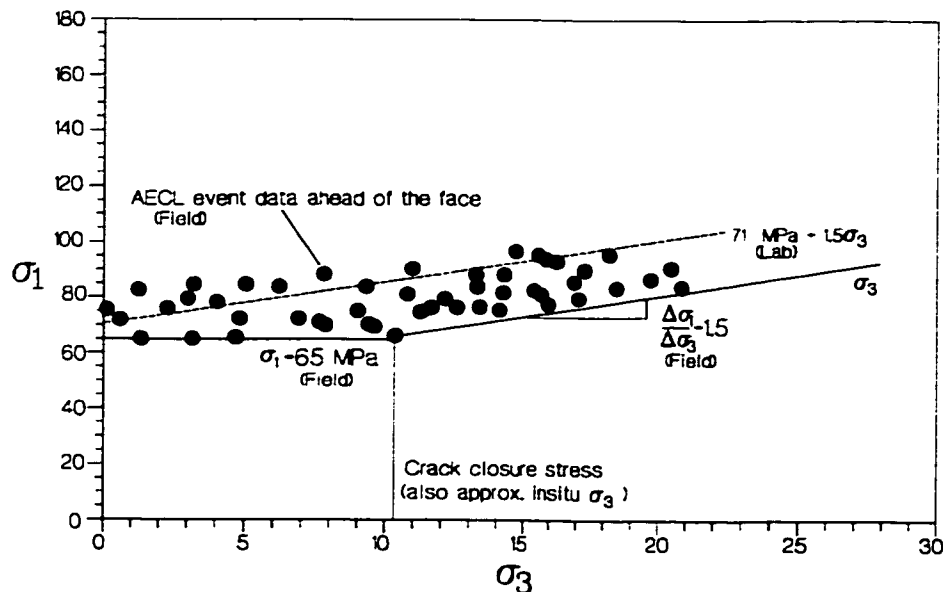


Figure 6.59: Calculated stress state (3D elastic) at locations of recorded AE events in front of mine-by tunnel face at URL. Solid line indicates lower bound insitu threshold; dashed line is lab test mean. Case described in Section 5.5.

Sample damage in the lab does not seem to influence damage initiation according to Eberhardt et al. (1999). In situ, however, the open cracks may be sufficient to create an effective local confinement of zero some distance from the excavation boundary, resulting in a damage initiation criterion which is apparently insensitive to calculated σ_3 . This concept also has an impact on damage propagation predictions and is discussed in detail in Chapter 8.

Returning now to lab data and Figure 6.58, the intercept of the best-fit line at higher confinements is 154 MPa. This is lower than the critical damage thresholds for Cold Spring Quarry granite but very close to the critical damage limit of 156 MPa for 130m level samples from Eberhardt et al. (1999). This would suggest that the rock is unaffected by unloading damage when subjected to compression at high confinements. Indeed, the average peak strength for undamaged Lac du Bonnet granite (from near surface locations the URL site) at 60 MPa is, according to data presented by Martin (1994), approximately 655 MPa. In Table 6.8 the strength of the damage granite is 640 MPa. Compare this 15 MPa or 2.3% reduction with a 50 MPa or 24% reduction in the uniaxial case.

Interestingly enough, the 120 to 125 MPa unconfined compressive strength suggested by Table 6.8 and Figure 6.57 is very close to the tangential boundary stress at which spalling and shear-process zone development is first observed in the advancing URL mine-by tunnel as discussed in Section 5.5.

Finally, consider the slopes of the two best-fit lines in Figure 6.58. Also recall the relationship defining Stacey's extension strain criterion in stress space:

$$\sigma_1 = \frac{E}{\nu} \varepsilon_{cr} + \frac{1-\nu}{\nu} \sigma_3 = \sigma_{cr} + A \sigma_3 \quad [6.32]$$

The slope A for a Poisson's ratio of 0.2 (obtained prior to yield in the 420 samples) is 4. An initial Poisson's ratio of 0.14, as obtained for early cycles in the uniaxial case, yields a slope of 6.14. The correspondence of these values to the confined and unconfined best-fit slopes in Figure 6.58 is appealing evidence for the validity of an extension strain model for critical crack damage or critical crack interaction (the real critical crack density introduced in Figure 6.7). This is the same conclusion drawn from Figure 6.53. While Stacey's (1981) original "fracture initiation" criteria has been demonstrated, in this chapter, to be, in fact, invalid for damage initiation, it seems to have merit for critical damage accumulation and, consequently, for crack interaction and yield strength.

6.9 DISCUSSION

This chapter has demonstrated, through a review of physical bonding processes and observational evidence, that the primary compressive damage mechanism in hard rock materials under low to moderate confinement is tensile microcrack generation. While this concept is not new, it is often overlooked in the interpretation of experimental results and in engineering application.

Under compressive loading, extension cracks can be generated by numerous mechanisms, including pore generated tensile stress, wing crack generation from sliding micro-flaws, cleavage separation and fracture away from non-conformable grain boundaries and others. Macroscopic spalling and shear zone generation at low and moderate confining pressures results from interaction and coalescence (linear or en echelon) of compression-parallel microcracks.

This form of damage leads to lateral expansion (normal to major compression) at the microscopic and macroscopic level, while affecting axial response only after crack interaction and the onset of coalescence and strain localization. The dilational nature of this damage is significant, for example in the selection of source model for the interpretation of microseismic event data obtained near underground excavations. Micro-seismic monitoring and analysis is now routine in Canadian mining and is used to observe and predict the response of the rockmass to excavation disturbance. The discussions in this chapter and in the next provide support for a mechanistically tensile (and confinement dependent) source model such as that presented by Cai et al. (1998) and for the routine application of this model for analysis of near-excavation micro-seismic activity.

In direct and induced global tension, the crack initiation threshold, in terms of stress, is coincident with rupture. Under these boundary conditions, tensile crack propagation is an unstable phenomenon and as such is governed by the weakest elemental link (e.g. the largest crack aligned normal to the tensile stress). Crack accumulation does not play a large role in tensile failure once initiation has taken place. In compression, on the other hand, the tensile (opening) forces at crack tips are dissipated as the extension wing cracks extend away from the initiating flaw. Therefore, the process is initially stable. Damage initiation in compression is also controlled by the weakest element (critical sliding crack, weakest grain), but additional crack accumulation is required to reach a critical crack density at which interaction and macroscopic rupture can commence.

It has been shown that while tensile stress concentrations result in crack extension under compressive conditions or in pure tension, the nature of the critical nucleating or pre-existing flaw in each case is different. Pure tensile loading is capable of exploiting rough, undulating,

interlocking and intermittent microcracks. The cracks, often associated with grain boundaries and trans-granular damage, are normally longer than the smooth cleavage microcracks responsible, according to the discussions in this chapter, for compression damage initiation. Using the same material fracture properties (fracture surface energy, critical stress intensity) there is no reason to expect a continuous transition (i.e. in stress space) between the damage initiation threshold in compression and the damage and rupture threshold in direct tension, such as that predicted by Griffith. A constitutive separation is preferred (rather than a continuous yield and flow rule) between yield in tension and that due to deviatoric compressive stress.

The confinement dependency of the damage initiation threshold relates to the internal mechanism which dominates microcrack generation. In granites the slope of this threshold (in $\sigma_1:\sigma_3$ space) indicates a sliding crack mechanism if mineral friction coefficients are used and atomically smooth cleavage or fracture surfaces are assumed. Photographic and experimental evidence suggests that these are valid assumptions. At low to moderate axial compressive stress, σ_1 , crack initiation under direct lateral tension σ_3 is independent of σ_1 , as evidenced by the Brazilian test. The nature of the transition between direct tensile crack generation and crack initiation in compressive conditions is still poorly understood. The next chapter will investigate this further using a numerical analogue.

While rupture is coincident with crack initiation in conditions of direct tension, extension cracks cannot propagate indefinitely in uniformly confined or uniaxially compressive conditions. Crack interaction is necessary for macroscopic fracture to take place. This interaction can only take place at a critical crack density once a significant number of distributed cracks have been generated or if a finite distribution of cracks can extend (propagate) sufficiently to mutually interact. In the former case, this critical crack density is a linear function of crack number. In the second case, critical crack density is a quadratic or cubic function of crack length. Crack initiation rate (with increasing stress) is a function of elemental strength distribution (weak links). An upper bound for critical crack density and crack interaction stress (deviatoric or σ_1) should therefore be easily predicted from the material composition. At moderate confinements, this threshold (for σ_1) should be a linear stress function (for a given initiation model) of σ_3 .

Crack propagation length, however, is controlled by confining stress normal to the propagating crack. As such, local tension in a heterogeneous solid arises at low global confinement. This tension leads to the premature extension of initiated cracks and a drop in the critical σ_1 required to attain critical crack density. This is the source of the non-linearity of yield and strength envelopes

at low confinement. At very high confinements, a second source of non-linearity becomes important as frictionless lattice slip mechanisms become more influential.

Under moderate confinement or non-tensile uniform stress conditions, critical crack density should be and indeed appears to be directly related to a characteristic lateral extension strain. Such a criterion has been used in the past in attempts to quantify the damage initiation threshold. It is demonstrated here, however, that this concept is applicable, instead, to critical crack damage or critical crack density definition. This threshold defines the point of crack interaction and the true yield point (given various system and time dependent yield processes) of the material.

Critical damage and crack interaction is best defined, under confined conditions, by axial (parallel to σ_1) stress-strain non-linearity, and not by volumetric strain reversal as previously proposed. As discussed, this threshold is related to a constant threshold of extension strain (and uniform crack accumulation) at moderate confinements. At low confinements, particularly in damaged rock, this threshold decreases, as crack extension increases, requiring less crack accumulation to achieve the same geometric crack density.

Sample and insitu rockmass damage due to unloading is typically in the form of rough, undulating grain boundary cracks (where the instigating local stiffness contrasts are the highest). These cracks have a significant impact on direct tensile strength since these cracks (which are longer than the intra-granular microcracks) can be directly exploited in tension at a lower threshold stress than the undamaged rock. These cracks have negligible impact on crack initiation in compressive conditions and moderate confinement. They do, however, interact with new induced axial extension cracks and therefore have a detrimental impact on the required density of new cracks required for initiation. This in turn reduces critical interaction stress and peak strength.

The effect of unloading damage is minimized at high confinements. A small cohesion drop is evident due to the reduction in crack interaction stress. The slope of the critical damage and peak strength threshold is unaffected at high confinements, by previous sample damage.

There is a coincidence between the confining stress limit, above which damage effects are minimized, and the previous insitu minor principal stress (far field or virgin stress). This represents crack closure. While difficult to physically substantiate, a likely explanation is that geo-tectonic unloading occurs at a rate which can be accommodated by the slow internal creep (stress readjustment) rates in granite. Excavation and sampling rates, however, are many orders of

magnitude more rapid and therefore, the rock can only respond to residual internal tension (developed by inter-granular stiffness contrasts) by cracking. The residual crack closure stress in lab samples and in the field, therefore, corresponds approximately to the insitu confinement prior to excavation.

Damage initiation stress, although the source of a great deal of recent investigation, should not be considered as a bona fide strength threshold. It does, however, indicate the lower bound, at low confinements, to which in situ material strength can decline. Criteria based on damage initiation, are therefore empirically successful in delineating the radial (but not always spatial) extent of excavation induced failure in many case examples.

True insitu strength is more likely linked to the minimum stress required to affect crack interaction under various confinement conditions. It has already been demonstrated by numerous researchers, as summarized in Chapter 5, that peak strength in the lab is a function of loading rate and sample configuration. A critical damage accumulation or crack interaction threshold represents a more universal rock strength limit. In this chapter (and in the next), this threshold is shown to correspond to axial stress-strain non-linearity in laboratory samples. Strength beyond the point of crack interaction and localization is controlled by the mobilization of trans-granular friction. Laboratory samples are geometrically constrained allowing this mobilization to take place. Large samples and insitu rockmasses around larger excavations are less constrained. Dilatant crack growth inhibits frictional contact after yield. Large strain is required to reestablish surface contact and frictional strength. cohesion loss, on the other hand is a small strain process. The result is brittle failure and non-frictional strength insitu.

The conditions for crack propagation are linked to crack normal confining stress. Extension cracks propagate parallel to σ_1 and normal to σ_3 . It is not clear, therefore, how the intermediate stress influences these processes. Crack accumulation is affected, statistically, since fewer pre-existing cracks are eligible for slip, and wing crack nucleation, at a given stress level. This requires work beyond the scope of this thesis to resolve. As such, the investigations in this thesis are based on relationships in σ_1 and σ_3 space. This also facilitates comparison between axisymmetric lab testing and two dimensional numerical simulation. Conversion to a three dimensional criterion will be discussed in principal only in this thesis.

CHAPTER 7

A Bonded Contact Analogue for Damage Accumulation

7.1 INTRODUCTION

The previous chapter examined a suite of test data for Lac du Bonnet granite, with the specific aim of identifying key thresholds of damage initiation, systematic accumulation, critical interaction and localization. It was emphasized that the main damage mechanism in granite is extensile crack growth parallel to the direction of maximum sample compression. In addition, it was demonstrated that the classic microscopic shear slip mechanism, cited in numerous fracture mechanics models, is a viable source of the crack opening force required to generate extension cracks in compression. Other mechanisms are undoubtedly active as well.

Sample response after critical crack interaction takes place, may also be dominated by large scale spalling or macroscopic shear. A clear distinction was made between the nature of the initiating slip mechanism (microscopic intragranular and atomically smooth flaw) and the localized macroscopic shearing active during sample rupture. The latter shear mechanism can arise by coalescence or interaction of propagating extension microcracks. Dilation during the formation of a macroscopic shear zone (and associated cohesion loss) may delay the development of maximum sliding friction. Separation of the active strength components in hard rock contrasts with materials such as saturated clays in which cohesion and friction act simultaneously during plastic shear.

In the former case, as conceptual alternatives to slip on an initiating microscopic flaw, any mechanisms capable of generating locally exaggerated shear strain can create sufficient extensile "crack opening force" for damage initiation. Several such mechanisms, including the sliding flaw,

are schematically illustrated in Figure 7.1a. Figure 7.1b illustrates a bonded disc or lattice analogue for these mechanisms. This analogue is examined and utilized in this chapter.

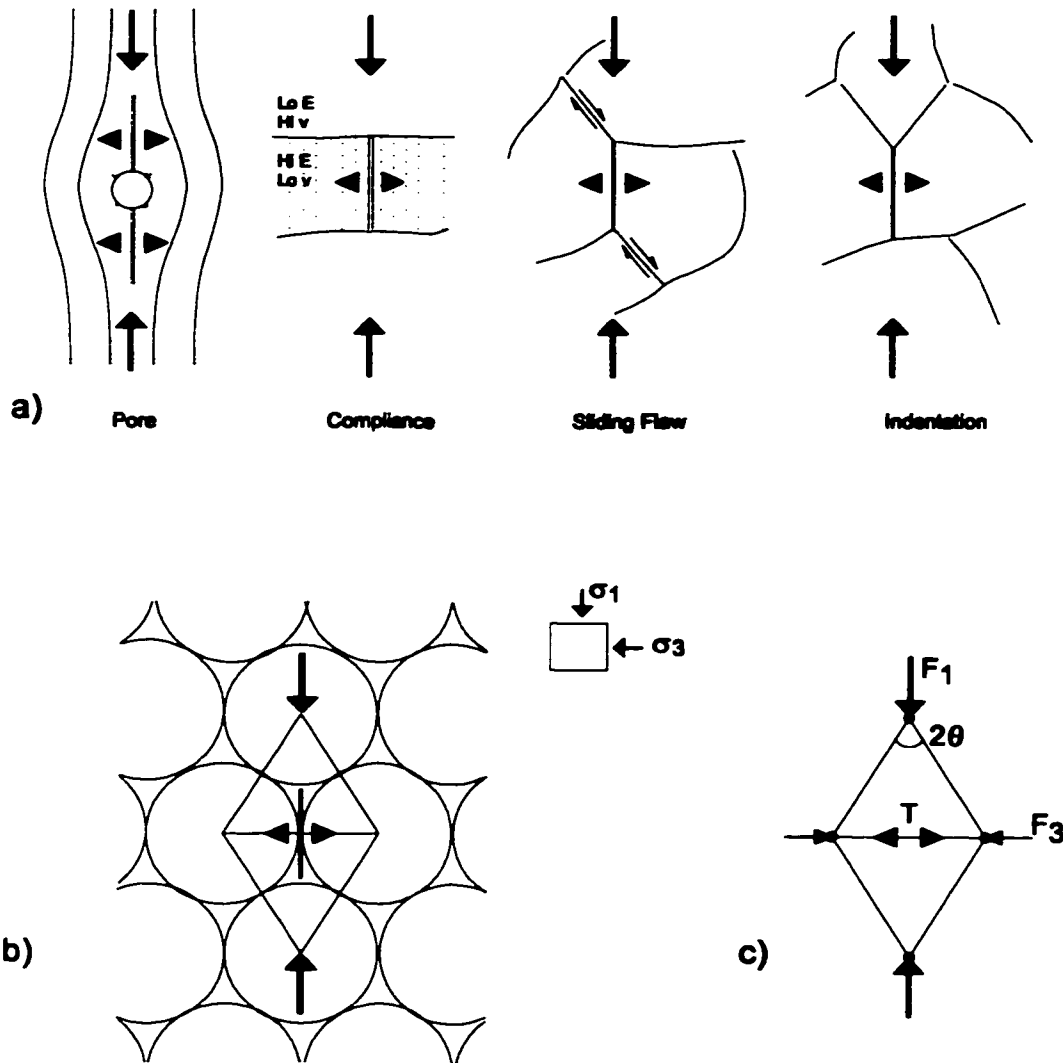


Figure 7.1: a) Schematic illustration of mechanisms which generate a crack extension force under deviatoric loading. b) Trellis, bonded disc or lattice analogue.

It was suggested in Chapter 6 that the onset of microcrack interaction (a precursor to the development of a shear zone or of macroscopic spalling) defined the true yield strength of the rock. Crack accumulation prior to this point is a distributed phenomenon which should be independent of sample shape or scale. The cracks nucleate in a random and distributed fashion in response to local heterogeneous stresses or strains and elemental strengths. The probability that new cracks will occur adjacent to existing cracks, thereby inducing interaction, increases as more cracks fill the volume. This point of initial crack interaction is a probabilistic event which should

be related to a critical crack intensity (density of uniformly distributed cracks). Localization is a consequence of crack interaction. It involves a dimensional reduction (say from a volume to a plane) in subsequent crack and strain distribution.

Beyond this yield threshold and critical crack intensity, the sample performance and peak strength is controlled by geometry, scale and system (boundary) conditions. Long term strength of uniaxially compressed laboratory samples has also been shown (Martin 1994; Laijtai 1988) to correspond to this threshold. It can be concluded, therefore, that the onset of crack interaction and localization within intact laboratory samples should also define an upper bound for strength insitu. True insitu strength, however, can be much lower than this yield threshold.

As discussed in Chapters 6 and 7, the stress threshold for damage initiation, obtained from laboratory testing or acoustic emission studies, corresponds to a lower bound for in situ strength of massive to moderately jointed rockmasses. Joint strength, naturally, dominates behaviour in highly jointed or sheared rockmasses (Hoek and Brown 1998).

In order to further investigate the relationship between extensile damage and macroscopic spalling and shear failure, this chapter will explore the nature of damage initiation, accumulation and interaction using a lattice or bonded disc analogue. This model is not, at this time, intended as a viable tool for large scale excavation modelling, although excavation scale simulations have been performed by others (Potyondi et al. 1996; Potyondi and Cundall 1998). Nor is it intended as a constitutive analogue for post yield behaviour of rock. It does, however, represent an intriguing analogue for exploration of damage accumulation prior to peak strength and key related issues.

In this model, the extension forces resulting in "crack initiation" are the result of compressive stress/force flow tortuosity, resulting in effective local tension within a trellis-like internal geometry (Figure 7.1; b and c). Inter-particle slip can only occur via normal particle separation (bond extension and tensile rupture) and by cohesive bond rupture (and subsequent frictional slip). The relative dominance of tensile and shear bond rupture can be controlled by the specification of bond tensile and cohesive strength. Contact friction is active only after bond rupture. The individual bond or contact normal and shear stiffnesses and the respective tensile strength and cohesion are the only pre-yield constitutive parameters of importance in this model and are the only user-defined contact properties (specified as means and standard deviations for the whole assembly). Large scale sample behaviour is a stochastic result of heterogeneity within the assembly.

The simulations in this work are performed using the discrete element model, PFC (Particle Flow Code). Numerous versions of this simple distinct element approach have been developed by various researchers (Cundall 1978; Rothenburg 1980; Thallak and Gray 1993; Yao and Kim 1996 and others). The model chosen for this work was developed by Itasca (1995a). PFC, essentially a computational engine, incorporates Itasca's FISH language giving the user the ability to develop sophisticated assembly, control, data tracking and output routines for specific research simulations, as was the case for this work.

While the bonded disc or lattice analogue is probably more appropriate for cemented granular solids such as sandstone, it nevertheless provides a window into the complex nature of damage accumulation in polycrystalline rock. As such it provides useful insight for the interpretation of actual test results, and helps to improve understanding of rock damage and yield strength, the main focus of this thesis. Numerical experimentation in this chapter focuses on the role of tensile strength and damage accumulation at low confinement.

7.1.1 Stress Flow and Bond Rupture - A Schematic Model

If a uniform trellis is assumed (Figure 7.1c), and if the shear and moment stiffnesses of the grain boundaries are significantly less than the normal stiffnesses, then the rupture criterion based on the tensile strength, T , of the central contact is given by (Cundall 1994a):

$$F_1 \tan \theta = F_3 + T \quad [7.1a]$$

$$\sigma_1 = \frac{F_1}{2L \sin \theta}; \quad \sigma_3 = \frac{F_3}{2L \cos \theta} \quad [7.1b]$$

$$\sigma_1 \sin^2 \theta = \sigma_3 \cos^2 \theta + \frac{T}{2L} \cos \theta \quad [7.1c]$$

$$T = -2L \sigma_b \cos \theta \quad [7.1d]$$

$$\sigma_1 = \frac{-\sigma_b}{\tan^2 \theta} + \frac{1}{\tan^2 \theta} \sigma_3 = \sigma_{ci} + \frac{1}{\tan^2 \theta} \sigma_3 \quad [7.1e]$$

If an average lattice angle of 45 degrees can be assumed for an undamaged isotropic rock (polycrystalline lattice), then it can be seen that the damage initiation criterion can be expressed in terms of a constant deviatoric or Tresca criterion ($\sigma_1 - \sigma_3 = \sigma_c$). If the angle is not 45 degrees the expression can be reexpressed in a form analogous to the extensional strain criterion proposed by Stacey (1981). For a trellis half-angle of 30 degrees, as in the case of a dense hexagonal packing of discs (Figure 7.1c), this relationship becomes:

$$\sigma_1 = \sigma_{ci} + 3\sigma_3 \quad [7.2]$$

This is the same result obtained from Stacey's extension strain criterion (modified for plane problems) using Poisson's ratio, ν , equal to one third:

$$\sigma_1 = \frac{-E\epsilon_b}{\nu} + \frac{1}{\nu}\sigma_3 = \sigma_{ci} + 3\sigma_3 \quad [7.3]$$

where $\nu = \frac{1-\lambda}{3+\lambda} = \frac{1}{3}$ for $\lambda = \frac{k_s}{k_n} = \frac{\text{bond shear stiffness}}{\text{bond normal stiffness}} = 0$ for an idealized 2-D particle array

with a maximum coordination number (number of contacts per disc) of 6 corresponding to dense hexagonal packing (Bathurst and Rothenburg 1988). The calibrated model in this work uses a bond shear stiffness, k_s , equal to 40% of k_n .

While attempts have been made to base a constitutive model (including damage evolution) entirely around this lattice example (Cundall 1994a; Cundall et al. 1996), and a corresponding flow rule, with limited initial success, the model does give ample justification for exploring brittle rock behaviour though the use of a simplified discrete contact model.

Stress flow through real polycrystalline materials, however, is not likely to be uniformly distorted as implied by the homogenous trellis model in Figure 7.1b and 7.2a. A more realistic analogue is the stochastic lattice model represented by Figure 7.2b.

For the random lattice there is no tractable geometric relationship between the local trellis angle, the average regional stress state and the forces acting on the trellis arms since there is no relationship between the shape of one trellis cell and its nearest neighbour in either direction. In addition, a narrower trellis locally would imply a greater local stiffness parallel to the long direction, which in turn would attract a higher stress concentration. This would offset the effect of Equation 7.1b. It is not reasonable to simply use the average intercontact angle (this would result in a much larger value for less dense assemblies) since more obtuse angles are unlikely to enclose a breakable central contact (as in Figure 7.1c).

For a single critical trellis cell (i.e. the cell responsible for the first "crack" initiation event) within a statistically isotropic assembly (Figure 7.3), it can reasonably be assumed that the external boundary stresses applied to the assembly are related to the trellis forces by a probability constant, ξ , which should be the same for vertical and horizontal stresses, regardless of the shape of the individual cell.

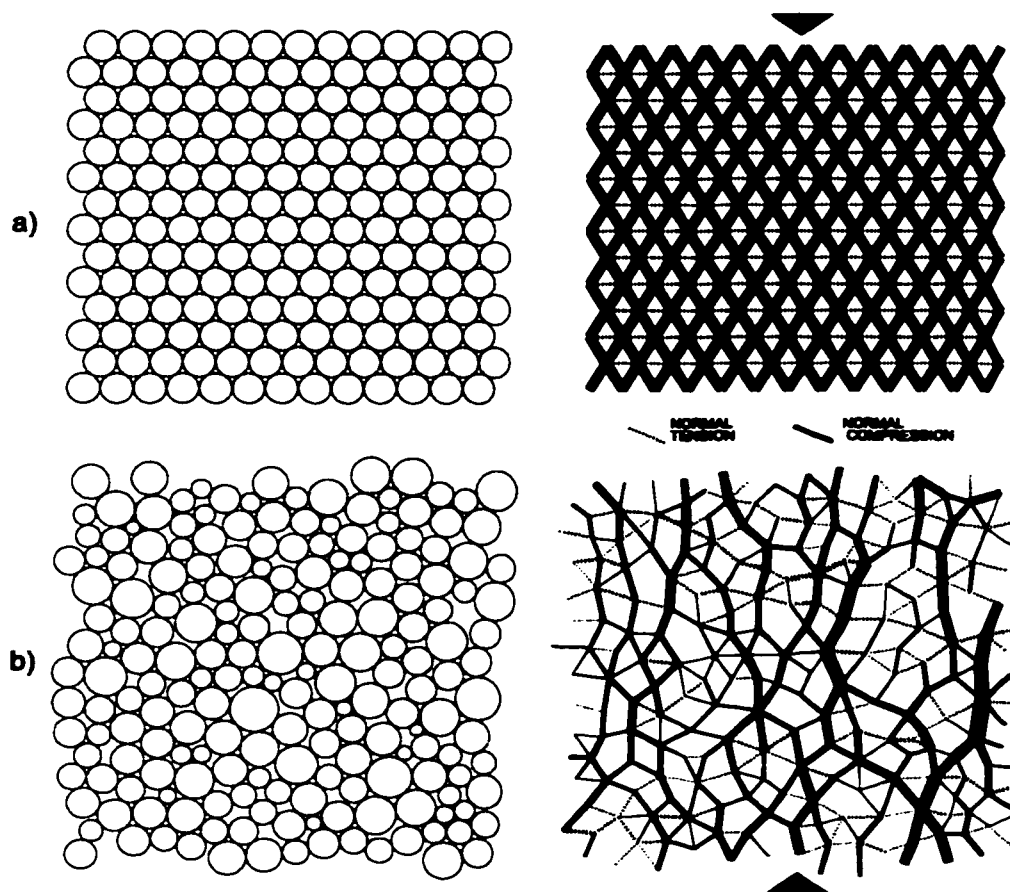


Figure 7.2: An a) homogenous and b) stochastic lattice with resultant contact forces for uniaxial loading.

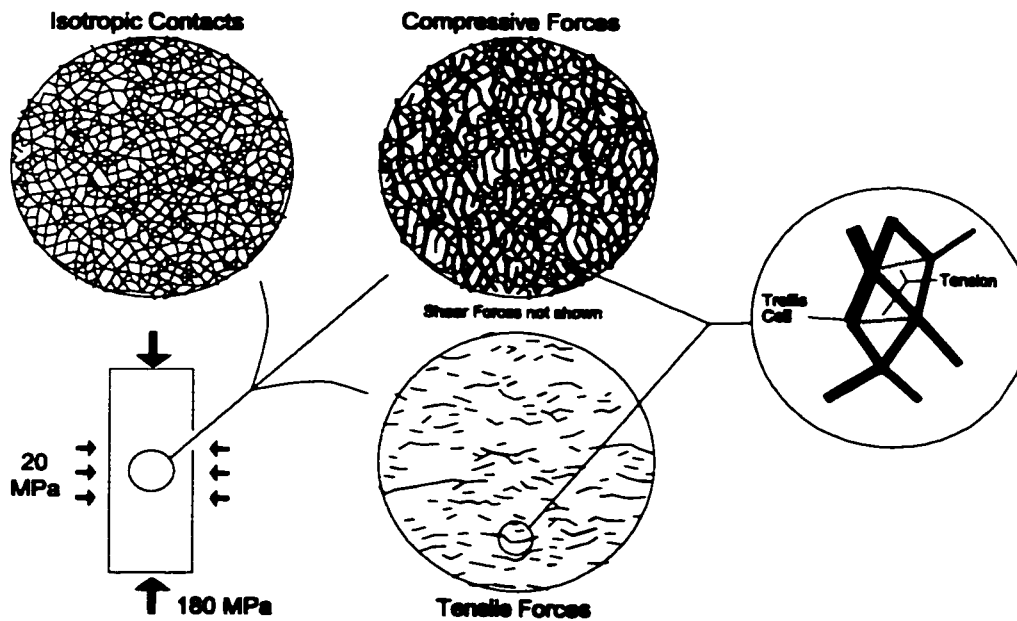


Figure 7.3: Tensile force generation within trellis cells under confined loading (PFC simulation).

This assumption negates Equation 7.1b, resulting in a trellis rupture criterion:

$$F_1 \tan \theta = F_3 + T \quad [7.4a]$$

$$\sigma_1 = \frac{F_1}{\xi}; \quad \sigma_3 = \frac{F_3}{\xi} \quad [7.4b]$$

$$\sigma_1 = \sigma_{ci} + \frac{1}{\tan \theta} \sigma_3 \quad [7.4c]$$

The slope in Equation 7.4c differs from Equation 7.1e by a factor $1/\tan \theta$. For a 30 degree trellis half angle (a dense local disc packing), the criterion for crack initiation (at the most critical cell) in the random trellis assemblies becomes, for a two dimensional analogue:

$$\sigma_1 = \sigma_{ci} + 1.7\sigma_3 \quad [7.5]$$

As discussed in Chapter 6, Equation 7.2 resembles Stacey's (1981) extension strain criteria and may be more representative of average sample conditions and therefore of critical crack accumulation or critical average crack density. Indeed, it was demonstrated in Chapter 6 that crack interaction (and the onset of axial yield) in laboratory compression samples begins at a critical lateral strain and a stress threshold reminiscent of Stacey's criterion. Equation 7.5, on the other hand is closer to the relationships obtained for damage initiation in lab samples (Chapter 6) and from acoustic emissions and back analysis in the field (Chapter 5). One of the hypotheses of this thesis is that Stacey's concept of critical extension strain applies to critical crack intensity and the onset of crack interaction (meso-crack formation) rather than micro-crack initiation as conventionally assumed.

As one interpretation of internal mechanics, it will be shown in this chapter that Equation 7.5 adequately predicts damage initiation in random assemblies of discs. Likewise, Equation 7.1e adequately reflects the onset of damage interaction in these numerical simulations. It is important to note that damage initiation and the confinement dependency described by Equations 7.4 and 7.5 relates to a single critical or weak link trellis cell or element within the numerical sample. Equations 7.1 and 7.2 relate to spatially averaged conditions within a random sample.

Alternatively, if the half angle, θ , of a bonded disc assembly is equal to π/γ where γ is the average coordination number (number of contacts per disc), then the slope in Equation 7.5 becomes 1.1 to 1.3 for an average coordination number of 4.2 to 4.8, the range for the simulations in this thesis. The corresponding slope in Equation 7.1 becomes 1.2 to 1.7. Although these values are not unreasonable, the use of the averaged intercontact angle in this manner is not appropriate, since wider trellis angles are unlikely to enclose intact (and subsequently breakable) lateral bonds.

Of equal importance is the general relationship, at a given confinement, between damage initiation, crack interaction stress and peak strength. PFC allows simulation of bonded assemblies with random internal structure and variable bond stiffness and strength. Simulated cracks form as tensile or shear contact loads exceed the specified contact bond strength resulting in crack accumulation and ultimate sample yield as in Figure 7.4. Such a model undergoes all of the same crack accumulation stages as a real heterogeneous material, as will be shown, and allows for an illustrative examination of these thresholds.

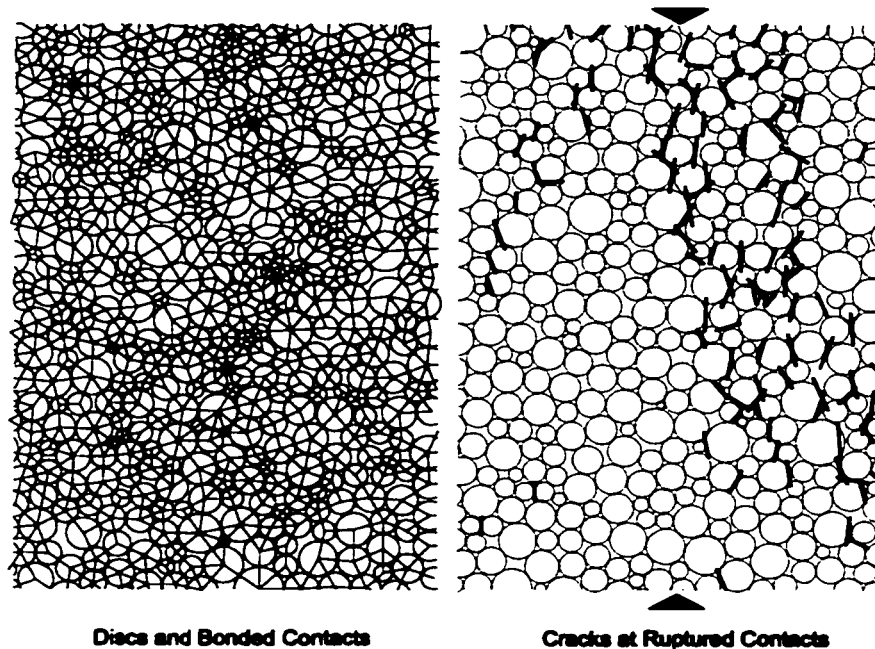


Figure 7.4: Crack accumulation (normal to ruptured contacts) in PFC sample under compressive load.

7.1.2 Numerical Model Selection

The bonded disc or linear contact lattice model, represented by the PFC assembly in Figure 7.4, was selected for its potential to simulate key aspects of the observed micro-behaviour of particulate solids under loading, such as heterogeneity of stress and strain (contact force and particle displacement), internal cracking (contact rupture), internal rotations and localization phenomenon. While a sub-component of this work is to assess the adequacy of the bonded disc model for hard rock simulations, the model is used primarily as a damage accumulation analogue for comparison to rock and rockmass studies. The details of discrete element modelling are not a focus of this work. A brief description of the model follows.

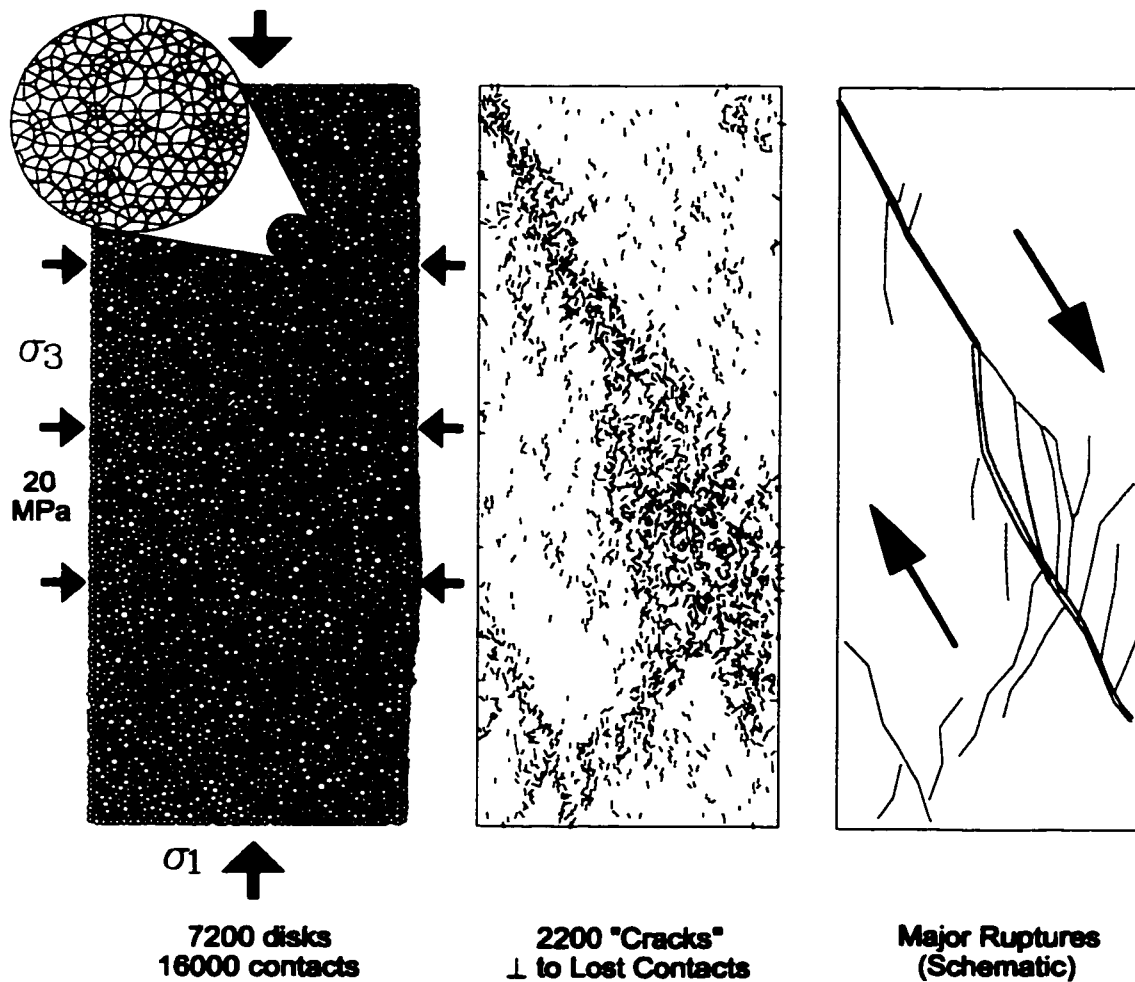


Figure 7.5: PFC simulation of confined loading test illustrating micro-crack accumulation, localization and macroscopic behaviour.

The discrete element model dates back to work by Cundall (1971; 1978) and Cundall and Strack (1979) and can be used to model any assembly of discrete interacting components such as blocks (Cundall and Hart 1993), bonded and unbonded polyhedra (Handley 1995; Grabinsky 1989) or spherical particles (Cundall 1988). Discrete disc models have been used extensively to simulate behaviour of unbonded particulate material (Rothenburg 1980; Cundall et al. 1982; Corkum 1986; Rothenburg and Bathurst 1989; Bathurst and Rothenburg 1988, 1990; Ting et al. 1989). Two and three dimensional particle models (discs, spheres, ellipses and ellipsoids) have been the basis for the development of micromechanical constitutive models for granular materials (Bathurst 1985, Rothenburg 1986; Cundall et al. 1989). Rothenburg (1986) and Heidari (1995) used discrete disk and sphere (3D) approaches to investigate the development of internal contact and force-transfer anisotropy within granular samples. The results were used to develop a critical

state model which was implemented into a finite element code. Three dimensional simulations and constitutive studies have also been performed using ellipsoidal particles (Quadfel 1998).

Bonded particle model work has largely been limited to conceptual work and model development to date. This type of model has been used to simulate generic brittle rock biaxial compression response (Potyondi et al. 1995), tensile response (Yao and Kim 1996), fracture propagation (Gumbsch 1995; Schlangen and Van Mier 1995), concrete-anchor interaction (Van Mier and Vervuurt 1995), explosion damage (Donze et al. 1996), borehole breakout (Thallak and Gray 1993; Potyondi et al. 1996) and large scale fault propagation (Donze et al. 1994, Scott 1996).

A similar approach based on initial work by Potyondi et al. (1995; 1996) will be taken in this thesis for cohesive polycrystalline rock. The lattice model in Figure 7.5 is actually generated as an array of rigid discs with linear-elastic contacts. The contact model represents bonds which are allowed to rupture in direct extension or in pure shear as evident in the results shown in Figure 7.6. While Hertzian contact logic (Mindlin 1949) can also be employed to simulate non-linear compliance (Walsh and Grosenbaugh 1979), this additional complexity is not warranted here.

By default, friction is mobilized at a contact only once the bond is (irreversibly) broken. Bond mechanics will be discussed presently. A two dimensional approach was used in this work, although expansion to three dimensions would be a worthwhile exercise for future investigation.

The program PFC-2D from Itasca (1995) was used in its commercial maiden release format (the algorithm dates back to Cundall (1978)). It is at present a simple mechanical model with simplified contact logic and minimal information tracking facilities. In order to perform any advanced modelling, the user is required to write custom control, constitutive and data recording routines in a proprietary FISH language which is interpreted by the PFC compiler at run time. This allows a great deal of flexibility without the overhead of maintaining a large amount of "house-keeping" code for displacement and contact tracking, etc.

Numerous FISH routines were developed by the author to facilitate model assembly, boundary control, internal parameter tracking and crack fabric analysis. In addition, all of the output presented in this thesis is created using numerical or graphical (dxf vector format) modules written for this purpose by the author. A number of simulation (servo) control and sample assembly routines were provided to the author by D. Potyondi and by P. Cundall (pers. comm 1994) and were also used in modified form.

While other codes exist, (Rothenburg 1980; Corkum 1986), PFC-2D (Itasca 1995a) has been chosen as the computational vehicle for this research due to its commercial availability and its PC-based code. The primary attraction of this particular code is its FISH language capacity. This language, is a FORTRAN style script language which allows the user to access most of the internal functionality of the software in order to customize the model behaviour. Because the basic PFC package is essentially a simple "black box" particle interaction code, the facility for customization is essential for research purposes. While a 3-D version is available from Itasca, it is felt that for bonded solids, plane behaviour is sufficient for the purposes of this study.

Up to 50000 2-D particles can be simulated with the resources available to this author. In order to reduce run times, typical sample sizes range from 2000 to 12000 discs and 10000 to 50000 contacts (2 contacts for each physical link). Corresponding run times (for compression test samples) on a Pentium II 300MHz system ranged from a minimum of 12 hours to several days depending on the loading rate and the peak sample strength.

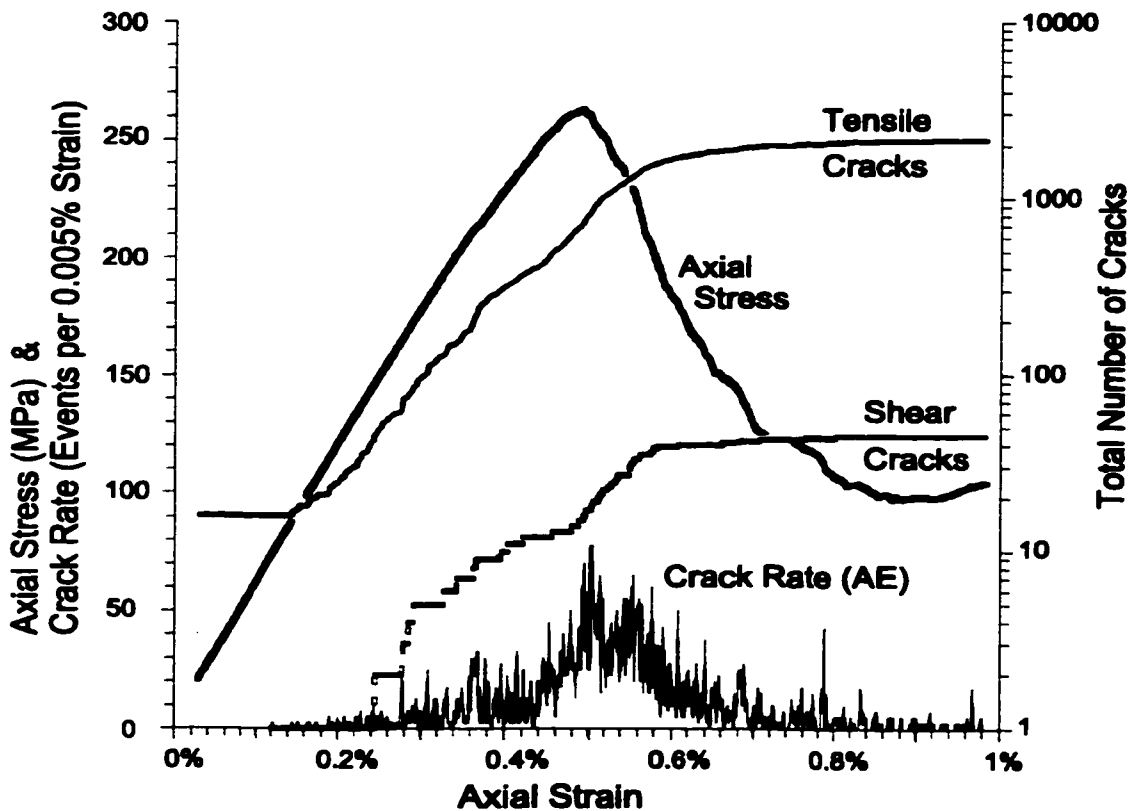


Figure 7.6: Typical results from simulation in Figure 7.5, showing relative accumulation of tensile (extension) cracks and shear (cohesive) cracks. Model parameters are discussed in detail later in this chapter.

7.2 DISCRETE ELEMENT BASICS

7.2.1 Computation cycle and contact stiffness

The basic computational structure of PFC, as illustrated in Figure 7.7, is the same as for any distinct element method (Cundall 1971; Cundall and Strack 1979). PFC is a sub-class of the distinct element method, known as a discrete element code since it allows finite displacements and rotations of discrete bodies including complete detachment. It also recognizes new contacts automatically as the calculation progresses (Cundall and Hart 1992). A simplification of the general method is made in PFC through the use of fixed geometry (disc) and rigid (non-deformable) particles. As mentioned, all stress/strain behaviour is the result of linear contact stiffnesses (force vs overlap distance) and contact bond rupture (crack generation).

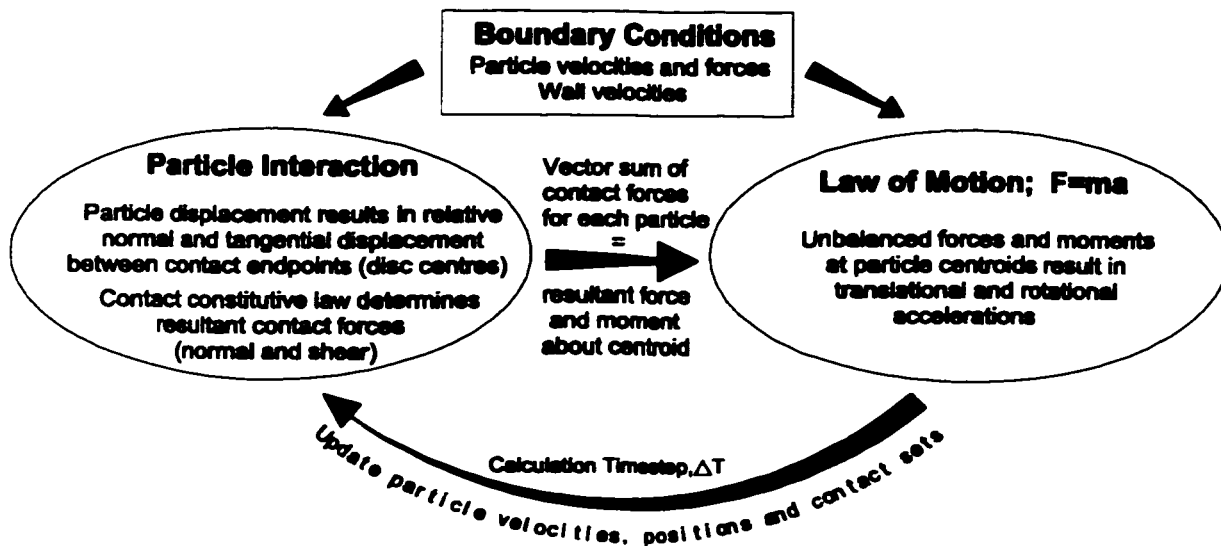


Figure 7.7: Basic calculation cycle in PFC simulations.

The force displacement law is applied at each contact. Interparticle overlap is computed from the position and size of the disks on either side of the contact or for a single particle and a wall structure as shown in Figures 7.8 and 7.9.

The resultant normal force vector, \mathbf{F}_k , of interaction, for the k th contact, is calculated directly from the degree of total normal overlap (U_k^n) according to a linear elastic constant, k_n :

$$\mathbf{F}^n = k_n U^n \mathbf{n} \quad [7.6]$$

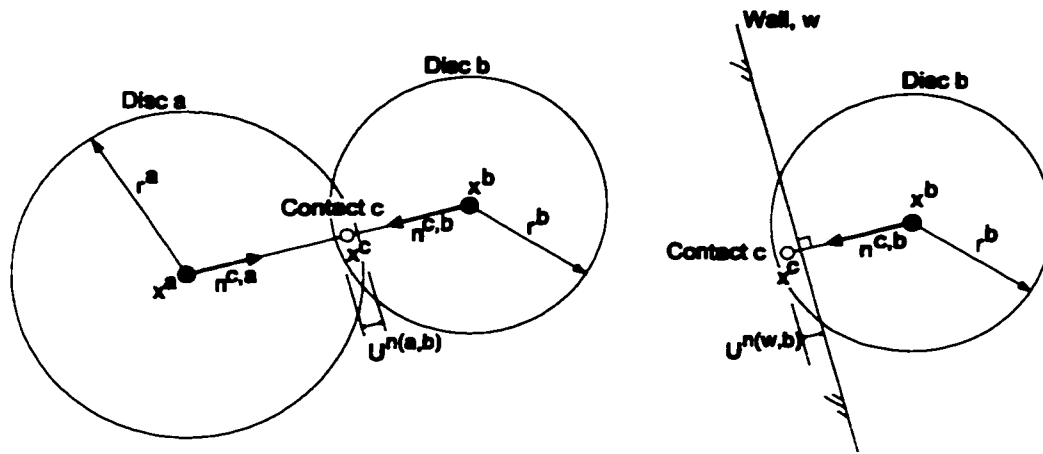


Figure 7.8: a) ball-ball contact, and b) ball-wall contact.

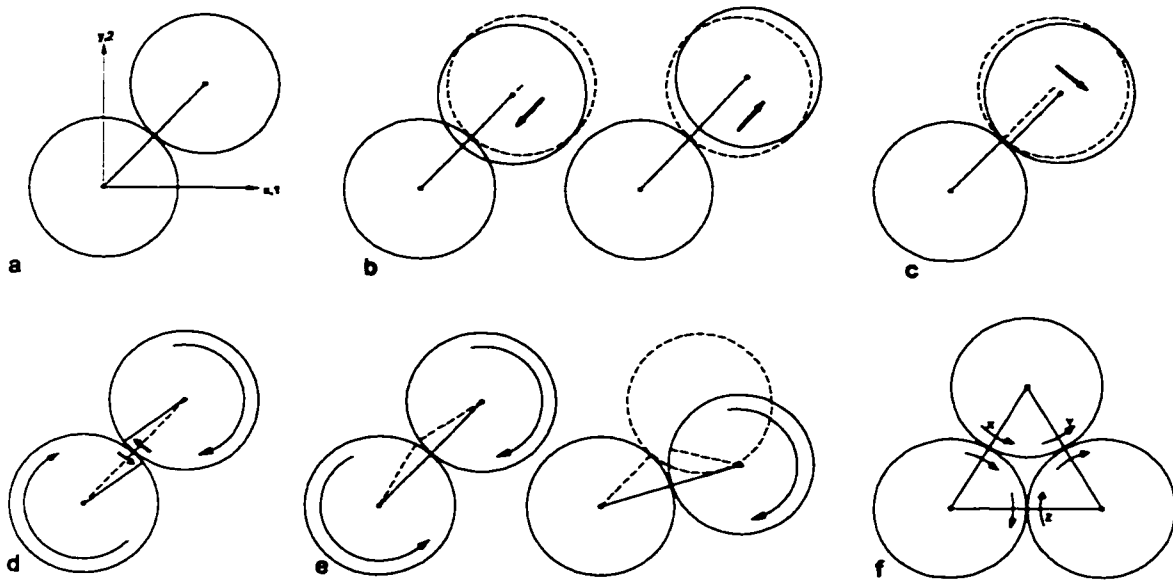


Figure 7.9: a) Initial contact geometry; b) normal contact compression and elongation (tension); c) contact shear without rotation; d) contact shear due to rotation; e) complementary rotation without shear (no resistance); and f) lattice trapping in disc assembly – rotation creates shear resistance in at least one contact (which thereby resists rotation).

Shear force is computed incrementally. The resultant shear force must be calculated by first summing incremental relative shear increments (the relative total shear is initialized at zero on formation of a contact), which are a function of both translational and rotational displacement increments for each particle. The incremental shear force at the contact is then given by:

$$\begin{aligned} \Delta \mathbf{F}^s &= -k_s \Delta U^s \mathbf{t} = -k_s \mathbf{V}^s \Delta t \\ \mathbf{F}_{t+\Delta}^s &= \mathbf{F}_t^s + \Delta \mathbf{F}^s \end{aligned} \tag{7.7}$$

where t is the tangent unit vector for the contact and V is the calculated relative shear velocity at the contact. Δt is the timestep. There is no resistance to rotation except for that generated by relative slip at the contact. A rolling contact is unresisted except by kinematic restrictions within a dense assembly.

These two contact force components are adjusted to satisfy the contact constitutive relationships (e.g. friction) if applicable. The adjusted forces are vectorially summed at the centre of each disc, resulting in net forces and moments (resulting from unbalanced contact shear components) which are translated into translational and rotational accelerations using the equations of motion. For this purpose the particles are given a density. Gravitational forces are not active in these simulations. These net accelerations are integrated using a centred finite difference procedure to obtain translational displacements and rotational velocities. The velocities at the middle of the next timestep are calculated and used over the full timestep to calculate the new position of the particle. New overlaps and incremental shear displacements can then be computed and the computation cycle then repeats itself.

The computational timestep must be calculated in such a way as to be less than a critical timestep related to the minimum eigenperiod of the system. This timestep is automatically optimized within PFC for a multiparticle system. The derivation of this calculation is given by Itasca (1995a) along with a discussion of the local non-viscous damping technique used in the model.

In a time stepping solution such as that used in PFC it is important that loading rates (i.e. platen velocities) are slow enough to allow adequate inertial transfer throughout the sample. Rapid loading results in more distributed damage while slow loading rates yield localized fracture growth. This contrast arises in a heterogeneous model since fewer material elements can yield in a given time increment, for slow loading, resulting in more focussed progression of existing composite macrocracks.

The information handling systems in PFC for tracking particles, contacts and the creation and destruction of contacts will not be discussed here. These are described in detail elsewhere (Itasca 1995a) and are of little interest in this current study. A complete listing of similar "book-keeping" computer code is given in Corkum (1986). An excellent discussion of contact tracking and book-keeping in 3-dimensions is given by Quadfel (1998).

7.2.2 Contact Models

The normal and shear forces at a given contact are defined respectively (for the linear contact model) as a linear function of the normal overlap and of the sum of elastic shear displacement increments. Shear forces and tensile normal forces are adjusted according to the yield criterion of the contact. Non-linear or Hertzian contacts (Mindlin 1949) are permitted but will not be discussed here at this time.

In PFC, the stiffnesses are defined for a given disc and the contact stiffness is the harmonic average of the stiffnesses of the two discs which make up the contact. In this thesis, this calculation will be maintained with one modification. Since the contacts are being used to represent both the interparticle stiffness and the stiffness of the particles themselves, the contribution of the stiffness from each contacting disk will be scaled to the relative diameters of the disks. Non-uniform diameters are being used throughout this analysis, and the total contact stiffness should reflect this, since the absolute displacement across the contact is currently used in the compliance equation, without regard for particle size. In terms of displacement stiffness, therefore, a small particle (more strain for the same absolute displacement) should be stiffer than a large particle.

In the simple slip model, the limiting tangential or shear force permitted across a contact is a linear function of the normal force and a friction coefficient. The total shear force is continually adjusted every calculation cycle as long as the balls are in contact.

Normal and shear bond models are available in which the tensile strength and cohesive shear strength are specified as constants. The normal contact bond is linear elastic in compression and tension (Figure 7.10a). Failure cannot occur in compression. If the normal strength is exceeded in tension (bond extension) then the bond breaks. In the default PFC contact model, the cohesion (shear strength) acts exclusive of friction in response to relative shear displacement at the contact. The cohesive shear bond (non-frictional) must be broken before friction is allowed to act. A FISH constitutive model was also used in this work to investigate the influence of a simultaneous Mohr-Coulomb shear bond (simultaneous cohesion and friction). The action of the slip model and the frictionless shear bond is illustrated in Figure 7.10b. A bond rupture in either tension or compression destroys the whole bond (i.e. tensile rupture destroys cohesion as well and vice-versa). Contact forces are reset to zero, in the case of tensile rupture, or to the limiting value allowed by friction for a compressed contact (Figure 7.10c). Frictional slip becomes and remains

active until contact separation occurs. In other words, bonds (tensile and cohesive) are irreversibly broken while contacts can be gained and lost during assembly deformation.

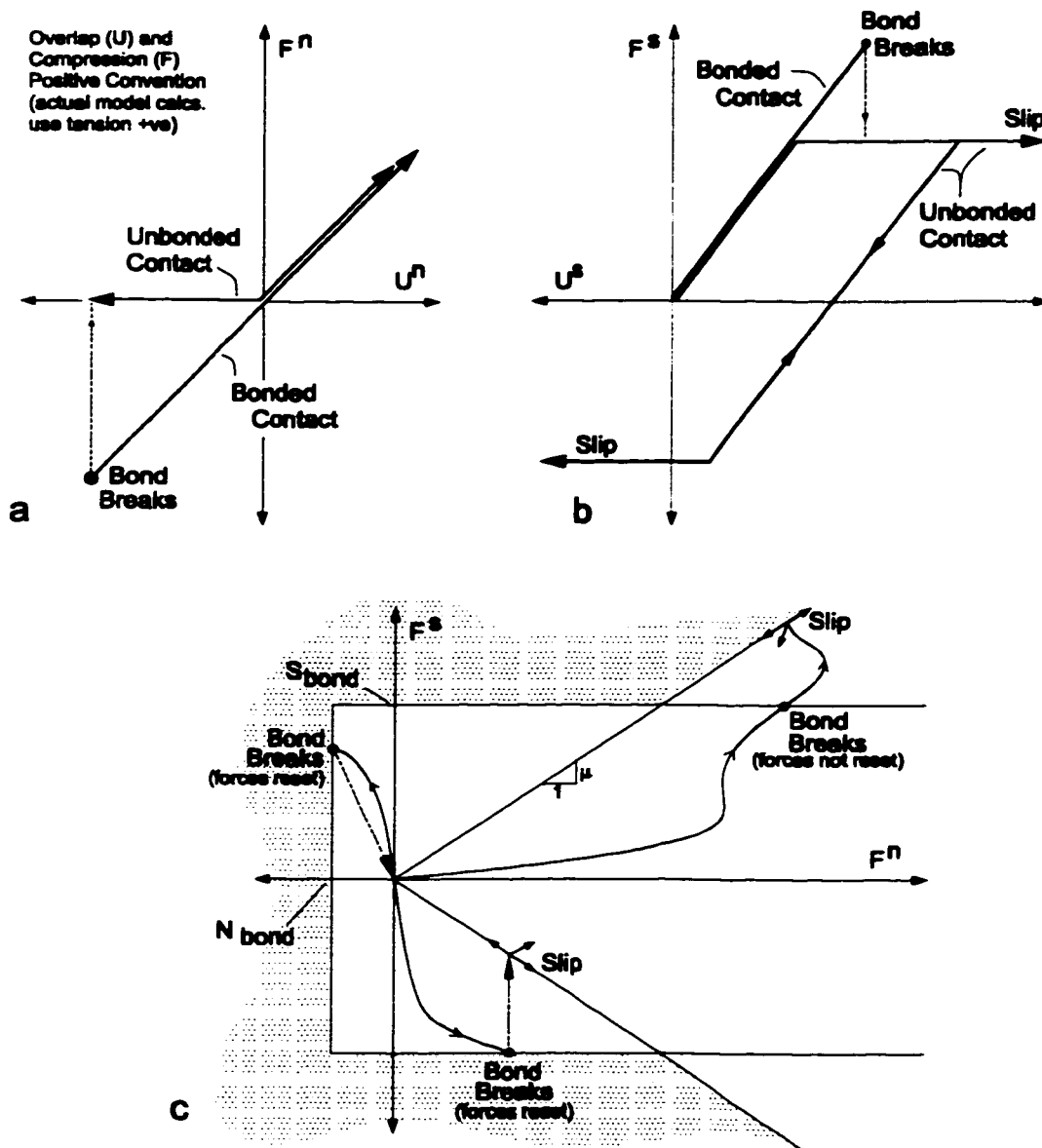


Figure 7.10: a) Behaviour of normal component of contact bond model; b) behaviour of shear component of contact bond model and frictional slip model (bonding and slip are mutually exclusive); c) General bond and frictional slip envelopes for PFC bonds.

The contacts and bonding models described thus far resist only normal displacement between balls (overlap or extensional strain) and relative surface shear displacement. Relative rotation of particles in contact is permitted without resistance (Figure 7.9e). Oda et al. (1982) found rotation

to be of minimal influence in a compact assembly of bonded disks (due to lattice trapping as in Figure 7.9f). The effect of rotation after localized bond rupture and shear zone formation may, however, be significant. Attempts were made in this work to control rotation by first disallowing any particle rotation (permitting translation only) and then by imposing a resisting moment on discs with increased rotational velocity. Neither approach proved successful. PFC provides a so-called parallel bond structure which is capable of providing resisting moments at contacts. This model is significantly more complex than the simple normal/shear bond making calibration more difficult. It was decided to restrict this work to the simpler alternative.

7.2.3 Stresses and Strains

Stresses and strains must be calculated differently here than in a continuum model. Stress is a continuum quantity and therefore does not exist at each particle. Stresses in a biaxial sample can be estimated by integrating the forces at each ball-wall contact in the direction of interest and dividing this quantity by the wall surface area. While this is adequate for the simulation of compressional loading (since this is the "stress" which the simulated testing unit would measure), it is not adequate for the study of true internal constitutive behaviour.

For a generalized plane disc assembly (Bathurst and Rothernburg, 1988), the average stress tensor can be expressed in terms of a summation over all contacts, c , defined in Figure 7.8 and given by:

$$\bar{\sigma}_{ij} = \frac{1}{V} \sum_{c \in V} f_i^c l_j^c \quad [7.8]$$

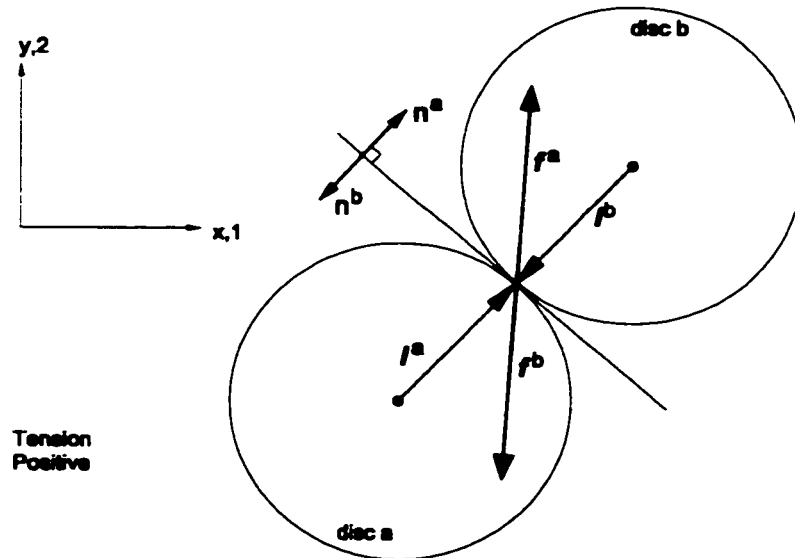


Figure 7.11: Contact normal (n), contact vector (l) and force vector (f) definitions.

where f_j^C and l_j^C refer to scalar components of contact forces and contact vectors respectively (two calculations pairs for each physical contact).

The summation is over a large volume, V (in two-dimensions a unit thickness is assumed). In the simulations for this work, the stresses are calculated within a measurement circle overlain on the assembly. A number of calculations can be made within the circle including coordination number, percentage of sliding contacts, and porosity, n . The average stress tensor within the circle is calculated as follows:

$$\sigma_{ij} = - \left(\frac{1-n}{\sum_{N_P} V^P} \right) \sum_{N_P} \sum_{N_C} |x_i^C - x_i^P| n_i^{(C,P)} f_j^C \quad [7.9]$$

where the summations are taken over the N_p discs with centroids contained within the measurement circle, for each of the N_C contacts attributed to each disc. In addition:

V^P is the volume (area) of the particle assuming a unit thickness

x_i^P and x_i^C are the location components of a particle centroid and a contact point

$n_i^{(C,P)}$ is the normal vector component directed from a particle centroid to a contact

f_j^C is the force component acting at the contact.

Strain and strain rate cannot be calculated directly, as in the case of stress within the particulate model, since the deformations of the void spaces must be included in the conceptual definition of strain (whereas the forces within the void space are zero). A direct approach for the calculation of strain from a plane disc model is given by Kruyt and Rothenburg (1996).

Alternatively, PFC uses a least squares approach to match the predicted and measured velocities of all balls within the measurement circle. The strain rate tensor is related to a velocity gradient tensor α_{ij} , where i and j are directional indices (1,2). This procedure, detailed by Itasca (1995a), is summarized by the solution of the following for N_p discs or particles within a measurement circle:

$$\begin{bmatrix} \sum_{N_P} \tilde{x}_1^{(p)} \tilde{x}_1^{(p)} & \sum_{N_P} \tilde{x}_1^{(p)} \tilde{x}_1^{(p)} \\ \sum_{N_P} \tilde{x}_1^{(p)} \tilde{x}_1^{(p)} & \sum_{N_P} \tilde{x}_1^{(p)} \tilde{x}_1^{(p)} \end{bmatrix} \begin{Bmatrix} \dot{\alpha}_{i1} \\ \dot{\alpha}_{i2} \end{Bmatrix} = \begin{Bmatrix} \sum_{N_P} \tilde{v}_i^{(p)} \tilde{x}_1^{(p)} \\ \sum_{N_P} \tilde{v}_i^{(p)} \tilde{x}_2^{(p)} \end{Bmatrix} \quad i = 1,2 \quad 7.10$$

where (p) indicates a particular particle within a measurement circle, where x and V are centroid location and velocity, respectively and where:

$$\tilde{V}_i^{(p)} = V_i^{(p)} - \bar{V}_i; \quad \bar{V}_i = \frac{\sum V_i^{(p)}}{N_p} \quad [7.11]$$

$$\tilde{x}_i^{(p)} = x_i^{(p)} - \bar{x}_i; \quad \bar{x}_i = \frac{\sum x_i^{(p)}}{N_p} \quad [7.12]$$

Through this solution, the velocity gradient tensor, $\dot{\alpha}_{ij}$, is obtained:

$$\dot{\alpha}_{ij} = \dot{\varepsilon}_{ij} + \dot{\omega}_{ij} \quad [7.13]$$

The symmetric part of this tensor is the rate-of-deformation or strain rate tensor, $\dot{\varepsilon}_{ij}$. The anti-symmetric part is the spin or rotational tensor, $\dot{\omega}_{ij}$. Stepwise integration of the velocity gradient tensor (over a series of timesteps) results in a displacement gradient tensor. The symmetric portion of this tensor is the strain tensor, ε_{ij} .

For the samples in this work, rotation is minimal prior to yield. After the onset of localization, however, internal rotation may take place. For this reason the off-diagonal terms of the displacement gradient tensor (rather than the strain tensor) are used as another indicator of crack interaction and sample yield. For compression tests, with loading aligned with the reference axes, non-zero off-diagonal terms for α_{ij} indicate rotation and discontinuum behaviour associated with localized yield. The diagonal terms of the strain tensor, ε_{ij} , are equal to the corresponding terms of the displacement gradient tensor, α_{ij} .

Strains in compressive samples (test simulations) are recorded via the platen movement (wall displacement divided by sample length) and also by individual strain calculations within measurement circles. Stresses are also calculated using measurement (stress and strain sampling) circles and by calculating the reaction forces on the platens.

7.2.4 Fabric and Damage

The only built-in facility to track the disruption of contacts (formation of cracks) is the tracking of total fraction of slipping contacts within a measurement circle. Any other instantaneous description of internal fabric must be accomplished via FISH routines.

7.2.4.1 Fabric and Crack Tensors

The fabric tensor describes the density of contacts (bonded or frictional) as a function of orientation while the crack tensor describes the density of broken bonds or crack normals. For this work, a contact or a crack are assumed to occupy an area equal to their length squared.

The normalized fabric tensor (not used in this work) is given approximately by:

$$F_{ij}^* = \frac{1}{M} \sum n_i n_j \quad [7.13]$$

where M is the total number of contacts in the sample and \mathbf{n} is the contact unit vector. The standard fabric tensor F_{ij} as defined by Bathurst and Rothenburg (1990) is given by:

$$F_{ij} = m_v F_{ij}^* \quad [7.14]$$

where $m_v = M / V$ is the number of assembly contacts (each physical contact contributes two assembly contacts) per unit volume or area. This fabric descriptor is used extensively for micromechanical studies of cohesionless granular materials but is of less use in the simulation of bonded solids.

Cracks are formed when contact bonds are broken (Figure 7.12a). The crack tensor, used in this work, describes the distribution, with respect to direction of crack normals (Figure 7.12b) and is given by:

$$R_{ij} = \frac{1}{A} \sum_{k=1}^N [(d^2) n_i n_j]_k \quad [7.15]$$

where $d=2r$ is the average diameter of the adjoining discs and \mathbf{n} is the crack normal (equivalent to the pre-existing contact unit vector). The d^2 term contributes crack size (representative area) information to the tensor. N is the total number of cracks.

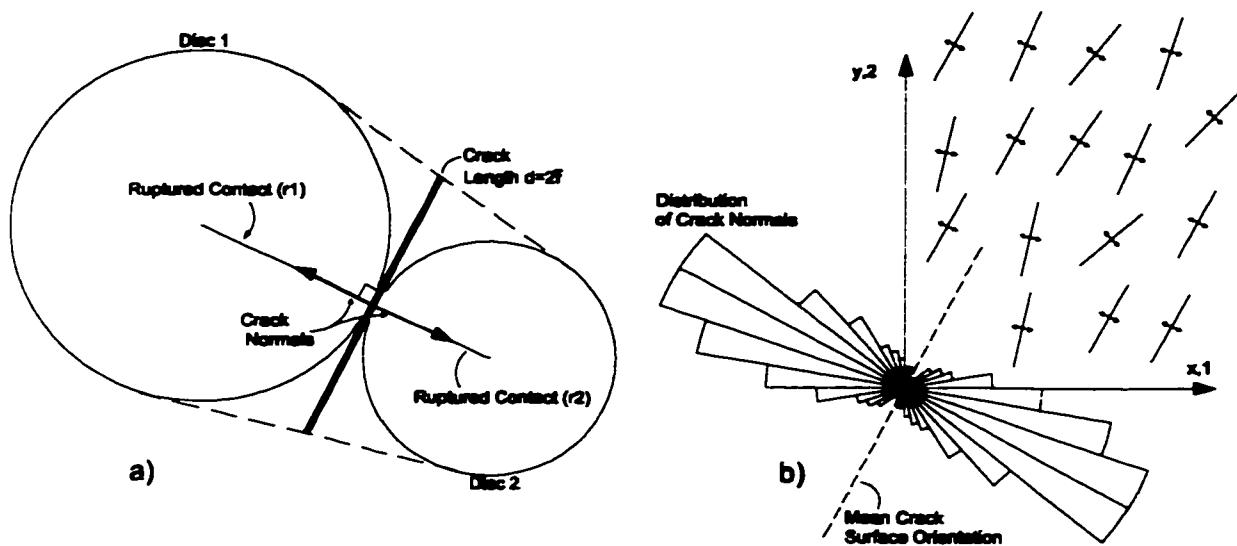


Figure 7.12: a) Crack definition; b) distribution of crack normals with respect to direction.

The fabric description can be made instantaneously at any time in the simulation by looping through the existing contacts. Cracks, the other hand, must be created and stored at the timestep of bond rupture and are stored in a FISH data structure external to the main program. The crack tensor is continuously additive and is updated as required from the crack array. Clearly the changes in the fabric and crack tensors are inversely related in the case of tensile rupture. A new crack represents a lost contact bond. In the case of shear rupture and in the case of subsequent closure of a tensile crack, however, a crack (broken bond) and a contact (frictional) can coexist between the same two discs.

Forms of this tensor are simple but effective tools for quantifying the development of damage in solids. Oda (1982; 1983) describes the properties and mechanical usage of this tensor. It is possible to equate the instantaneous strength and stiffness of the model to this tensor. Cundall (1994) and Cundall et al. (1996) present a simple anisotropic and damage controlled adaptation of the Hoek and Brown (1988) criterion and test it against observed excavation response with some success. In Cundall's work, the cohesive parameter, s , is a function of the damage tensor which in turn, evolves as a function of plastic strain.

The first (isotropic) invariant of the crack tensor represents the overall magnitude of damage while the second (deviatoric) invariant indicates the anisotropy of damage.

7.2.4.2 Crack Intensity

A scalar crack density or crack intensity (assuming a unit thickness out of plane) is obtained from the first invariant of the crack tensor:

$$\chi_d = (R_{11} + R_{22}) = \frac{1}{A} \sum d^2 \quad [7.16]$$

where $d = 2r$ is the crack length. As such this crack intensity is four times the value, χ , which is based on the crack radius and which is used by Kemeny and Cook (1986) and in Chapter 2 of this thesis. This crack intensity term, simplified for two dimensions treats the crack as a square of length d (rather than a circle, cylinder or sphere) as in the conventional forms used in fracture mechanics. It differs from other 2-dimensional crack density terms used in the literature only by a constant geometric multiplier.

It should be noted that the tensor and crack intensity calculation in PFC does not account for crack interaction. Because of this, a disperse array of non-colinear cracks has the same tensor and crack density as a connected link of the same number of cracks. For real rock samples, however, experimentally determined crack tensors for lab samples would consider linear connected arrays of microcracks as single mesocracks, giving a larger crack density. This is because the square of the sum (of interacting crack lengths) is greater than the sum of squares in Equation 7.16.

Broken bonds in PFC simulations are treated independently of one another without regard for interaction. In reality and mathematically, the r-squared term in the tensor and density expression above should account for long interacting arrays of cracks and be able to convey this state difference in the mechanical equations. This will be addressed in Chapter 9.

This crack density term should not be confused with a similar and often used expression which is simply the number of cracks within an area or volume. This latter term is termed the *crack number*, $n_v = N / A$, in this work. N is the total number of cracks (one physical contact or one pair of assembly contacts gives way to a single crack).

7.4.2.3 Crack anisotropy

The crack density is a scalar and isotropic parameter which does not convey information about the anisotropy of crack formation under deviatoric loading. Figure 7.13 illustrates the distribution of normals (with respect to orientation) for an isotropic and anisotropic array of cracks. A two

dimensional tensor such as Equation 7.15, can describe such distributions. The crack anisotropy can be characterized by the second invariant of the tensor:

$$\alpha = \frac{2}{\chi} \sqrt{\frac{1}{4}(R_{11} - R_{22})^2 + R_{12}^2} \quad [7.17]$$

The crack tensor, therefore can be alternatively expressed as:

$$R_{ij}n_i n_j = \frac{\chi}{2} (1 + \alpha \cos 2(\theta - \theta_0)) \quad [7.18]$$

The density of cracks $\Delta\chi(\theta)$ within an angular interval between θ and $\Delta\theta$ can be given by:

$$\begin{aligned} \Delta\chi(\theta) &= \chi S(\theta) \Delta\theta \\ \text{where} & \\ S(\theta) &= \frac{1}{2\pi} (1 + \alpha \cos 2(\theta - \theta_0)) \end{aligned} \quad [7.19]$$

is a second order Fourier approximation of the density distribution and where θ_0 is the orientation of the major principal anisotropy and α is the coefficient of anisotropy.

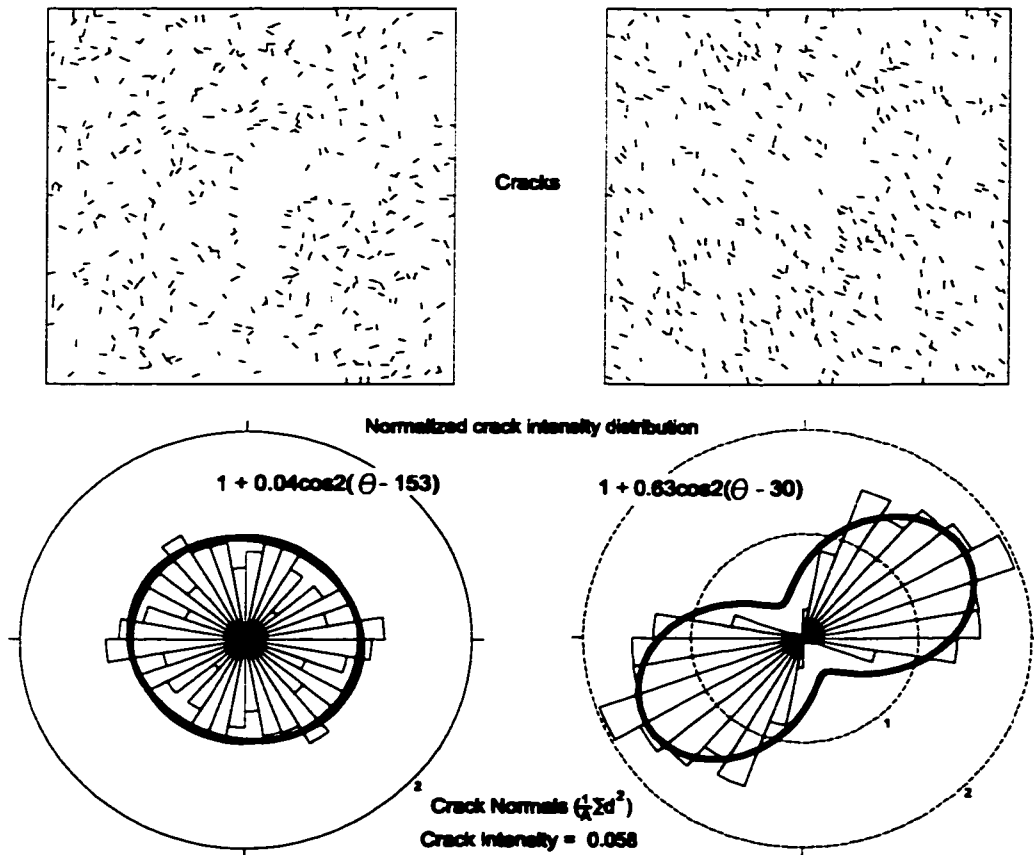


Figure 7.13: Tensor approximations for an isotropic and anisotropic assembly of cracks.

For a completely isotropic array of cracks, $\alpha = 0$. For an array of mutually parallel cracks $\alpha = 1$. For reference, all angles are taken counterclockwise positive from the right horizontal direction. Each crack contributes 2 opposing normals to the rose diagram in Figure 7.13 necessitating the factor 2 in Equation 7.17 and 7.18 in order that the conventional form of $S(\theta)$, typically used for assembly contact fabric description (Rothenburg and Bathurst 1989), can be used here.

7.2.4.4 Crack interaction

The crack number or the crack intensity can be used to identify the onset of crack growth and to track the accumulation of distributed cracks. As discussed in Chapter 6, it is of interest here to determine the point of initial crack interaction. Interaction can be arbitrarily assumed to occur when two cracks are within a specified distance of each other. This first interaction is the result of clustering probability (as more distributed cracks occur the probability that the next crack will occur next to an existing crack increases).

A simple index used in this study is the separation index (S_d). This index is simply the number of pairs of cracks with a mutual separation of less than the average crack diameter (d). This is consistent with the findings of Lockner et al. (1992) and Madden (1984) who demonstrated that crack interaction becomes significant when crack separation approaches one crack length.

This chapter will examine the correlation of observed crack clustering with other indirect indicators such as axial stress-strain non-linearity, volumetric strain reversal, kinetic and frictional energy rate increase, peak anisotropy and crack rate acceleration. Several of these indirect indicators were examined for real granite samples in Chapter 6.

7.2.4.5 Energy Measurements and Damage

PFC permits the tracking of internal energy components within the sample. These components include current total kinetic energy and cumulative frictional energy loss. Kinetic energy is calculated as the sum of $\{(mass)(velocity)^2 / 2\}$ for all of the discs in the assembly. Frictional loss is the cumulative sum of the product of (shear force)(Δ displacement) at all sliding contacts. Either value will tend to increase substantially as localization and meso-scopic shear develop in the sample. Both energy terms, however, are unresponsive to the initiation and accumulation of uniform non-interacting damage. These measurements are used, therefore as yield indicators (critical interaction and strain localization in the following experiments).

7.2.5 Stress and Strain Relationships

7.2.5.1 Elastic Strain - Young's Modulus and Poisson's Ratio

The stiffness of an assembly of contacts is related to the contact density as well as the normal and shear stiffnesses of the contacts. According to Bathurst and Rothenburg (1988) the following relationship applies for a dense two dimensional system with an average physical contact length (distance between disc centres), d_0 :

$$\sigma_{ij} = A_{ijkl} \epsilon_{kl} \quad i, j, k, l = 1, 2$$

$$A_{ijkl} = \frac{\xi k_n \bar{d}_0 m_v^*}{2\pi} \int_0^{2\pi} \left(n_i n_j n_k n_l + \frac{k_s}{k_n} t_i n_j t_k n_l \right) d\theta \quad [7.20]$$

where k_n is equal the normal inter-particle contact stiffness defined in terms of force (per strain) and ξ is a system constant. Shear stiffness, k_s , is similarly defined. In this formulation $n=(\cos\theta, \sin\theta)$ and $t=(-\sin\theta, \cos\theta)$ and m_v^* is the density of physical contacts and is equal to $0.5m_v$.

For PFC simulations a conversion is necessary. PFC calculates the contact stiffness as the harmonic average of the stiffness values k_n^* specified for two adjoining discs. In addition the stiffness for the contact is defined in terms of force per displacement (overlap or extension). The effective k_n in Equation 7.20 is therefore equal to $0.5d(k_n^*)$. Using this definition of contact stiffness (which differs from the force/strain definition in Bathurst and Rothenburg 1988) the bulk moduli of the simulated material can be calculated:

$$K = \frac{\xi m_v^* \bar{d}_0^2 k_n^*}{8} = \frac{\sigma_{11} + \sigma_{22}}{2(\epsilon_{11} + \epsilon_{22})} \quad [7.21]$$

$$G = \frac{\xi m_v^* \bar{d}_0^2 k_n^*}{8} \left(\frac{1 + \lambda}{2} \right) = \frac{\sigma_{11} - \sigma_{22}}{2(\epsilon_{11} - \epsilon_{22})} = \frac{\sigma_{12}}{2\epsilon_{12}} = \left(\frac{1 - \nu}{1 + \nu} \right) K \quad [7.22]$$

where $\lambda = k_s/k_n$. ξ is typically close to but slightly less than unity for dense samples ($\lambda=6$) according to Bathurst and Rothenburg (1988). In these cases Poisson's Ratio can also be calculated (for dense arrays of 2D discs):

$$\nu = \frac{1 - \lambda}{3 + \lambda} \quad [7.23]$$

These relationships have validity for the calculation of elastic constants in PFC models although the required constant ξ tends to be much smaller than unity (≈ 0.75) in contrast to the work of Bathurst and Rothenburg (1988). One reason for the discrepancy is the wider range of particle radii used in this work and the resultant lower coordination number (≈ 4.5). Equation 7.23 is also in error for lower coordination numbers.

Kruyt and Rothenburg (1996) developed a variation of Equations 7.21 and 7.22, based on the assumption of uniform stress, a situation assumed to apply for a coordination of 4. These relationships, modified for to account for the definition of k_n^* and m_v^* are as follows:

$$K^\sigma = \frac{k_n^*}{2m_v^* \left(\bar{d} \tan \frac{\pi}{\gamma} \right)^2} \quad [7.24]$$

$$G^\sigma = \frac{k_n^*}{2m_v^* \left(\bar{d} \tan \frac{\pi}{\gamma} \right)^2} \left(\frac{2\lambda}{1+\lambda} \right) \quad [7.25]$$

In this case, Poisson's ratio can be derived as:

$$\nu^\sigma = \left(\frac{1-\lambda}{1+3\lambda} \right) \quad [7.26]$$

Alternatively, K^ϵ , G^ϵ and ν^ϵ , obtained directly from Equations 7.21, 7.22 and 7.23 with constant $\xi=1$, were found to correspond to the assumption of uniform strain (dictated by disc packing) existing at a coordination number of 6.

Kruyt and Rothenburg (1996) proposed a heuristic relationship for the range $4 \leq \gamma \leq 6$ to determine the stiffness parameters for intermediate value of coordination number, γ .

$$K(\gamma) = \frac{\gamma-4}{2} K^\epsilon + \frac{6-\gamma}{2} K^\sigma \quad [7.27a]$$

$$G(\gamma) = \frac{\gamma-4}{2} G^\epsilon + \frac{6-\gamma}{2} G^\sigma \quad [7.27b]$$

$$\nu(\gamma) = \frac{\gamma-4}{2} \nu^\epsilon + \frac{6-\gamma}{2} \nu^\sigma \quad [7.27c]$$

This set of relationships is shown in this thesis to be reasonable for characterizing the PFC models used in this work. Neither out-of-plane stress nor out-of-plane strain is considered here or

in the numerical simulation. Nevertheless, for in-plane response, Young's modulus can be calculated from:

$$E(\gamma) = 2(1 + \nu(\gamma))G(\gamma) = 2(1 - \nu(\gamma))K(\gamma) \quad [7.28]$$

These relationships are presented for verification purposes only and as a starting point for the calibration exercise in Section 7.5. In this section, it is shown that the predicted values are adequate for intermediate values of λ . For extreme values of λ near 0 or 1, the Shear Modulus and Poisson's ratio deviate significantly from experimental results.

7.2.5.2 Strain Measurement

For actual model tests, elastic parameters are evaluated and tracked by direct measurement for the samples in this work. Stresses and strains are calculated as described in Section 7.2.3, based on contacts contained within so-called measurement circles. A typical configuration would include measurement circles located at the top, middle and bottom of a compressive sample as shown in Figure 7.14.

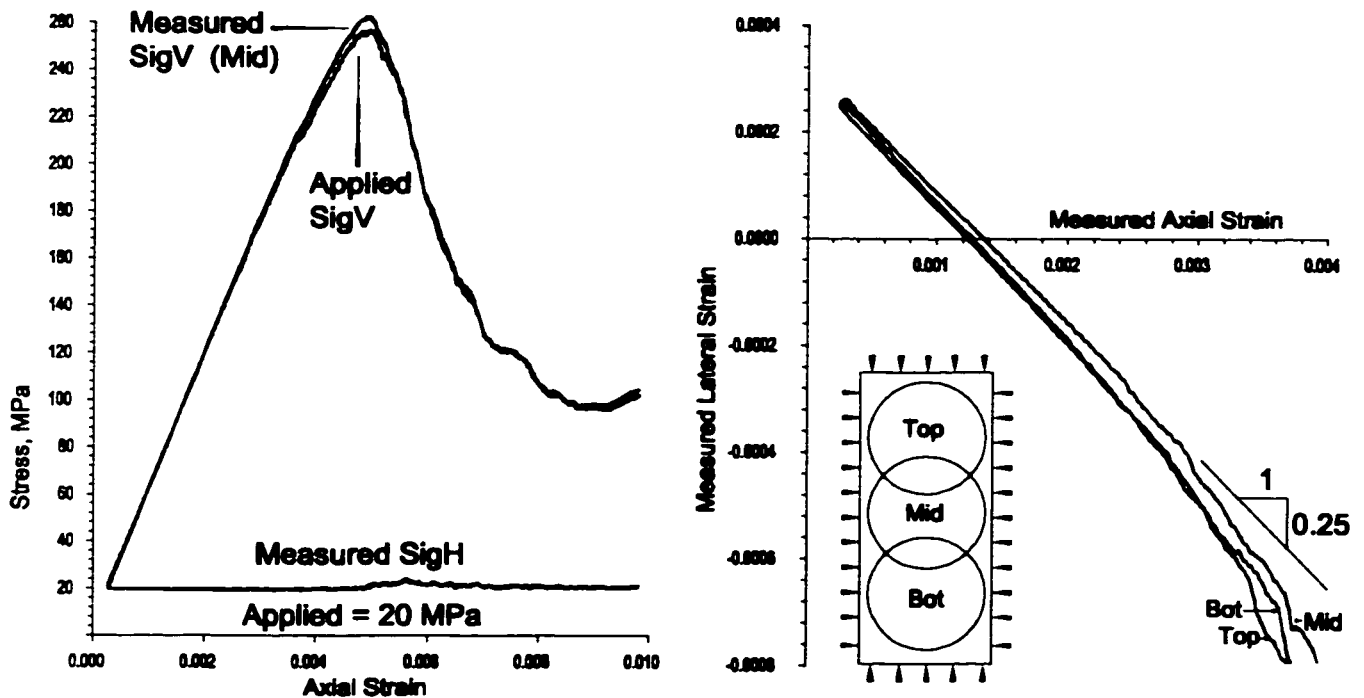


Figure 7.14: Comparison (left) of stresses “measured” within the sample (Mid) and calculated from the boundary platens or sidewall discs (Applied). Measured strains (right) within the top middle and bottom portions of the sample.

Prior to yield, the measured and applied stresses and strains correspond very well. As larger inelastic strains accumulate within local regions, the values deviate. The instantaneous discrepancy between applied and measured values of stress and strain increase for faster loading rates.

7.2.5.3 *Linear and Non-Linear Strain*

Effective secant Young's modulus and secant Poisson's ratio (or secant strain ratio) are continuously calculated based on the current stresses and strains relative to the stresses and strains at the start of the tests. Results are recorded for every 100 time steps in the simulations. Tangent Young's modulus and tangent strain ratio are updated every 100 timesteps via a simple backward difference calculation, taken over the preceding 500 time steps (for smoothing). The calculations are illustrated schematically in Figure 7.15.

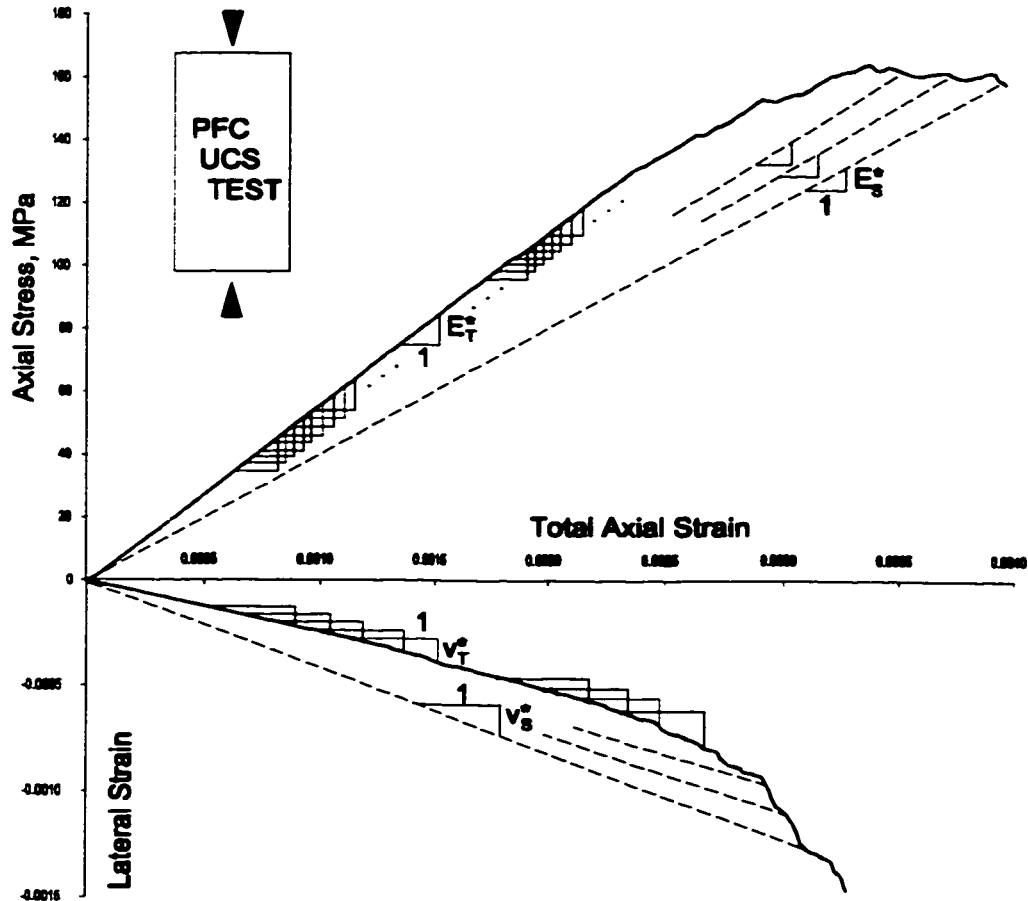


Figure 7.15: Experimental determination of instantaneous modulus and strain ratio.

Typical results from a uniaxial compression test are illustrated in Figure 7.16. The first consistent increase in tangent strain ratio, v_T^* , is highly diagnostic in determining the onset of systematic cracking. Critical crack density and the onset of crack interaction is indicated by a drop in tangent modulus, E_T^* .

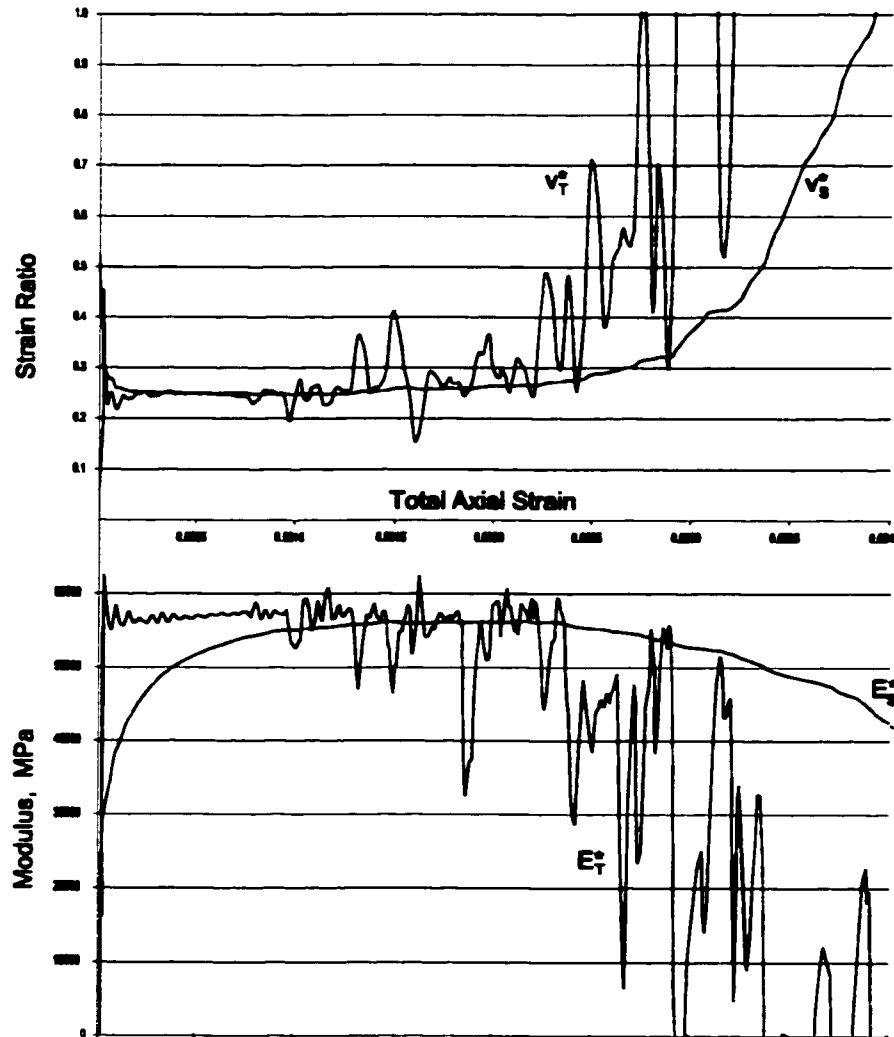


Figure 7.16: Typical variation, during an unconfined compression test simulation, of effective tangent modulus, E_T^* , secant modulus, E_S^* , tangent strain ratio, v_T^* , and secant strain ratio, v_S^* .

7.2.5.4 Inelastic Strain and Dilation

Figures 7.17 and 7.18 illustrate two common yield patterns for compressive samples. Figure 7.17 illustrates the post peak axial strain response as measured within three circular regions. The progressive accumulation of cracks with respect to axial stress is shown for comparison. In this case the localized failure zone is in the upper part of the sample.

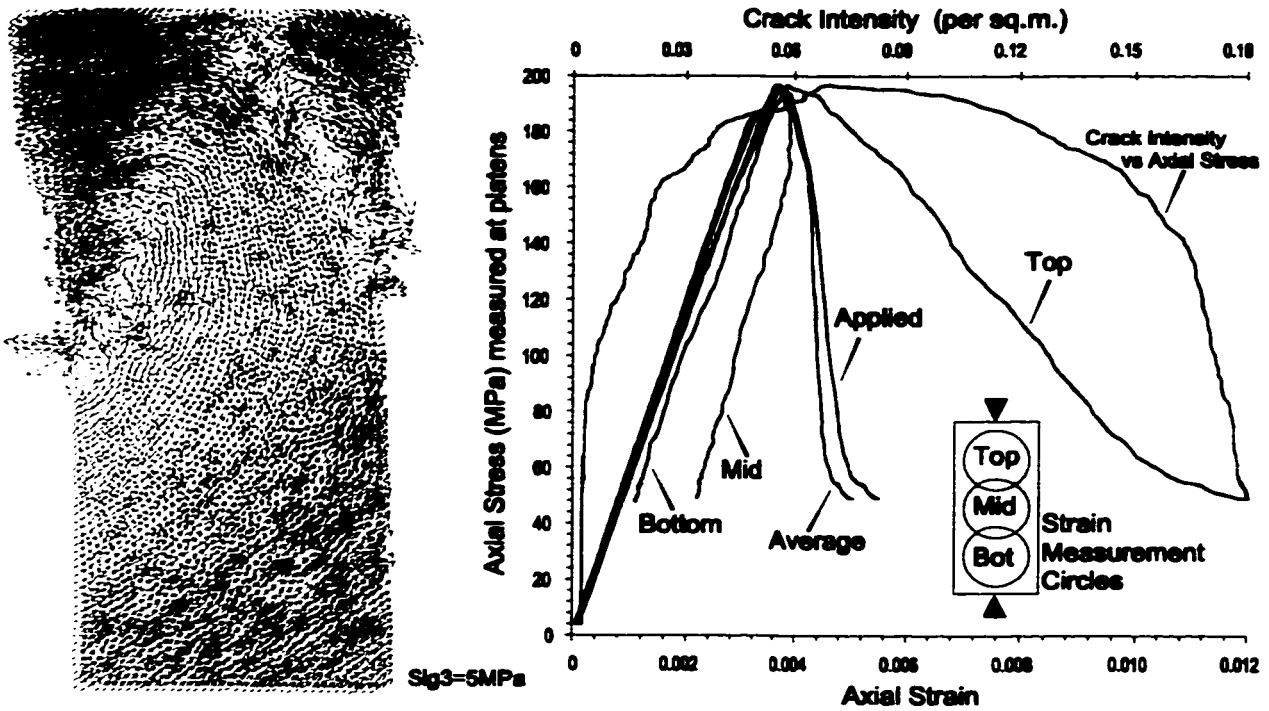


Figure 7.17: Post peak velocities (showing failure surfaces) and axial stress-strain response measured in three sample areas (constant lateral stress = 2.5 MPa). Crack intensity development is also shown.

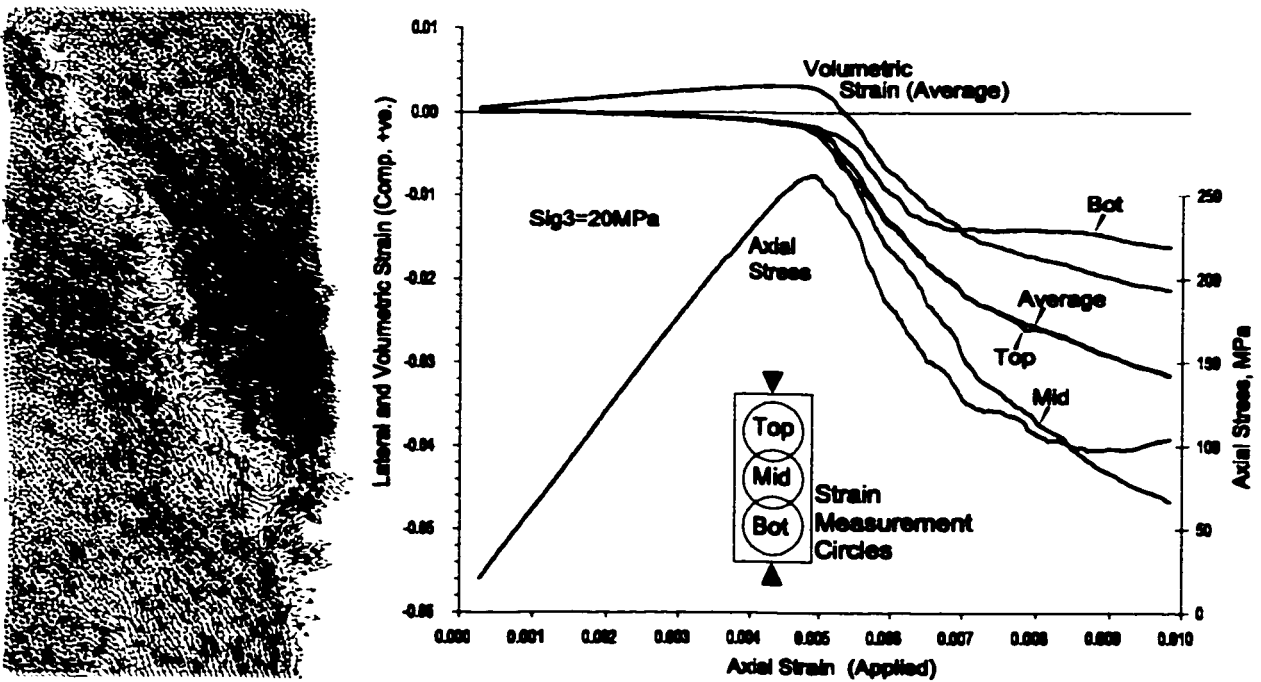


Figure 7.18: Sample tested at 20 MPa of lateral stress. Comparison of lateral strain measurements. Volumetric strain response is calculated as the average from the three areas.

The stress-strain response varies in degree of brittleness depending on the location of the strain measurement. Intact portions of the sample release strain energy into the failure surface giving the impression of a hyper-brittle response. The top circle, which is crossed by the failure surfaces, shows considerably more positive axial strain during the post peak stress drop region. This is an important analogy to consider when interpreting real strain gauge data. The average response (from three circles) corresponds well to the applied platen stress and strain throughout the test.

Figure 7.18 illustrates a similar problem with lateral strain measurement. Apparent post peak behaviour will depend on the location of the strain circle or strain gauge and is not a unique material response. In this work, the average or the applied stress strain relationships are used for interpretation. This thesis is primarily concerned with continuum stress, strain and crack accumulation behaviour prior to peak load - up to and including the continuum/discontinuum behavioural transition. Detailed interpretation of the post peak (discontinuum) response of real or simulated samples is beyond the scope of this work. The reader is referred to Aglawe (1999) for recent advances in understanding this region of post-peak behaviour.

7.2.6 Other Internal Descriptors

7.2.6.1 *Coordination Number, Porosity, Sliding Fraction*

Coordination number and porosity are recorded within a measurement circle (internal PFC functions) in the centre of the sample. Sliding fraction is the ratio (to total contact number) of contacts which are unbonded with a shear stress equal to the frictional shear strength (cannot be greater for unbonded contacts). Intact bonded contacts are not considered to slip regardless of their shear force component.

7.2.6.2 *Cumulative Rotation*

For diagnostic purposes, the cumulative (sum of all discs) rotational velocity is recorded. An increase in magnitude (above zero) in velocity indicates the onset of damage interaction.

7.2.6.3 *Crack number and crack rate*

Cumulative crack number (total number of broken bonds) is recorded as is the number of bonds which broke in either tension or shear. Crack rate is the number of cracks which occur within 1000 or 5000 timesteps. This is directly analogous to acoustic emission rate.

7.3 CREATION AND CALIBRATION OF MODEL

For purposes of experimentation it was desired to create a calibrated PFC material for use in all simulations which mimicked the strength and deformation properties of Lac du Bonnet granite. Initial calibration and therefore most of the simulations were based on granite samples from the 240m and 420m levels at the URL (see Chapter 6). The peak strength and deformation properties, therefore, are based on rock samples which are now assumed to be damaged. The calibration which follows is reasonable for the exploration in this thesis.

7.3.1 Unconfined Compression of Lac du Bonnet Granite

The target properties for the simulations which follow are loosely based on laboratory test parameters for lac du Bonnet Granite, discussed in Chapter 6 and summarized in Table 7.1. The target strengths were based on 240 and 420 level samples.

Table 7.1: Target Parameters for Granite Simulation

Grain Diameter Mean (std. dev.)	3.2 mm (0.8mm) <i>Actual mean generated 3.1mm</i>
Unconfined Compressive Strength, UCS	180 MPa
Damage Initiation Threshold	60 to 100MPa
Young's Modulus	55 to 60 GPa
Poisson's Ratio	0.25
Residual Friction Coefficient	$1 = \tan(45 \text{ degrees})$

The parameters which can be controlled and calibrated in PFC simulations are summarized in Table 7.2 along with the baseline values used in most of the following analyses (unless otherwise indicated). These values were established in the calibration discussed later in this section.

For a number of reasons which will be discussed presently, it is not possible to obtain a universally calibrated sample which will simulate the real behaviour of granite in tensile, confined compressive and post peak yield conditions. Upon examination, however, these shortcomings provide valuable insights into the nature of hard rock strength, as will be discussed later in this and the following chapter.

Table 7.2: Parameters (calibrated for this work) used in “granite” simulations

Model Parameter	Mean	Relative Standard Deviation
Normal Bond Stiffness, k_n	160000 MN/m <i>average contact stiffness one half of nominal bond stiffness = 80000</i>	+/- 10 to 15%
Shear Bond Stiffness, k_s <i>0.4 x k_n</i>	64000 MN/m <i>average contact stiffness one half of nominal bond stiffness = 32000</i>	Primary variation (+/- 10 to 15%) directly dependent on K_n variation. Additional (secondary) 15% variation superimposed.
Contact Moment Stiffness	nil <i>except for that provided by lattice trapping</i>	n/a
Normal Bond Strength	0.3 MN	+/- 20 to 30%
Shear Bond Strength	1.2 MN	+/- 10 to 15%
Friction coefficient	1 <i>active only for ruptured bonds</i>	nil
Grain Size (diameter)	3.2 mm nominal <i>3.1 actual</i>	+/- 25%
Coordination Number, γ	Approx. 4.5 <i>typically 4.2 to 4.8</i>	n/a
Lithification Pressure <i>(see next section)</i>	20 MPa	

7.3.2 Sample Creation

In order to create a densely packed heterogeneous sample for testing, a procedure is used which is illustrated in Figure 7.19. The porosity, n , is specified as are the sample dimensions H , W , and the maximum and minimum disc radii r_{min} and r_{max} representing a range of one standard deviation to either side of the mean (Gaussian normal distribution). The initial "lithification" pressure is also specified.

The first step is to place horizontal and vertical "walls" enclosing a space equivalent to the desired sample dimensions. The walls are extended past the sample to allow for independent movement of each wall. The walls are initially fixed (no degrees of freedom). For purposes of loading the sample, these walls are eventually allowed normal translation only.

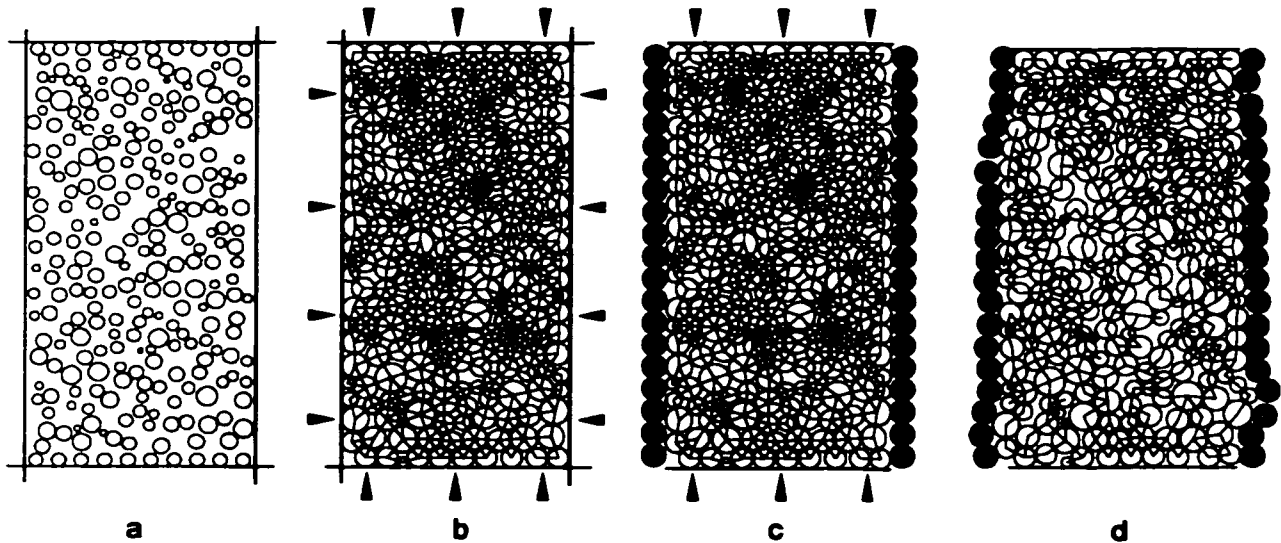


Figure 7.19: Sample assembly: a) generation of platen disc layers (top and bottom) and distributed internal discs with varying (under-sized) radii; b) radius expansion under specified lithification pressure and bond formation; c) sidewall control discs (constant horizontal force) replace lateral walls while top and bottom walls converge to axially load sample; d) final ruptured sample.

In order to achieve a smooth loading surface, a line of sequentially contacting discs with uniform radii (equivalent to the desired sample mean) are generated inside of each platen wall (i.e. top and bottom for compressive testing). These platen discs are then reduced in size to approximately 60% to allow interaction with the sample discs during the following disc expansion process (adapted from Potyondi et al. 1995).

Next, the approximate number of discs, N , required to achieve the desired porosity, n , within a sample area of A is calculated:

$$N = \frac{A(1-n)}{\pi \bar{r}^2} \quad [7.29]$$

These discs, normally distributed about the mean radius, are generated randomly throughout the sample without overlap. The initial range of radii will be 60% of those in Equation 7.29. This is to allow for easier placement and for expansion during the densification process (explosive

repulsion). In the absence of friction or bond strength (normal contact stiffness only) the discs are expanded (within fixed walls) by a factor of 1.7 and the sample is then allowed to cycle until disc rearrangement results in static equilibrium. This generates disc overlap and unbalanced normal forces within the sample. The sample is allowed to equilibrate (by induced disc reorganization). This should result in a sample with near zero internal pressure. With the walls remaining in a fixed state, the radii are iteratively expanded further (no friction or bond strength) to create the desired isotropic "lithification" pressure. Unless otherwise stated this pressure is 20MPa in the samples presented in this chapter.

At this point the average coordination number and the porosity should be at their target values. Locally, however, there may still be individual discs which possess fewer than three contacts and which are trapped within larger bridged meso-voids. These discs are termed floaters and are iteratively shrunk, translated and expanded, by a FISH routine (floater2.drv) supplied to the author by P. Cundall (personal communication 1997), until an acceptable number of contacts are achieved for each offending disc.

Bonds are now formed at each contact. These bonds possess a specified variation of stiffness (normal and shear) as well as variable strength (tensile and cohesive) as specified in Table 7.2 and illustrated in Figure 7.20.

Frictional strength is specified for each contact but is not active until bond rupture occurs. The data array for crack information storage is initialized at this time. Any bonded contact which ruptures from this point forward is recorded as a crack.

The sample can now be unloaded (or loaded) by allowing the walls to move under "servo-control". At each time step the wall (normal) velocity is adjusted, according to the difference between the actual wall stress (due to summed wall-disc contact forces) and the desired stress, in order to compensate for this difference. In most cases in this thesis, the sample is fully unloaded prior to application of subsequent confining or axial stress. Parameter histories are initialized at this time, although in some compressive test cases, the histories were initialized later after application of confining stress.

Due to variable contact stiffnesses, locked in under isotropic compression, the sample contains heterogeneous local contact forces (as shown in the "cutaway" schematic in Figure 7.21a). Depending on the lithification pressure, consequent tensile damage (crack formation) occurs

during unloading (Figure 7.12b). Greater damage is sustained in samples lithified under higher pressures (Figure 7.21c).

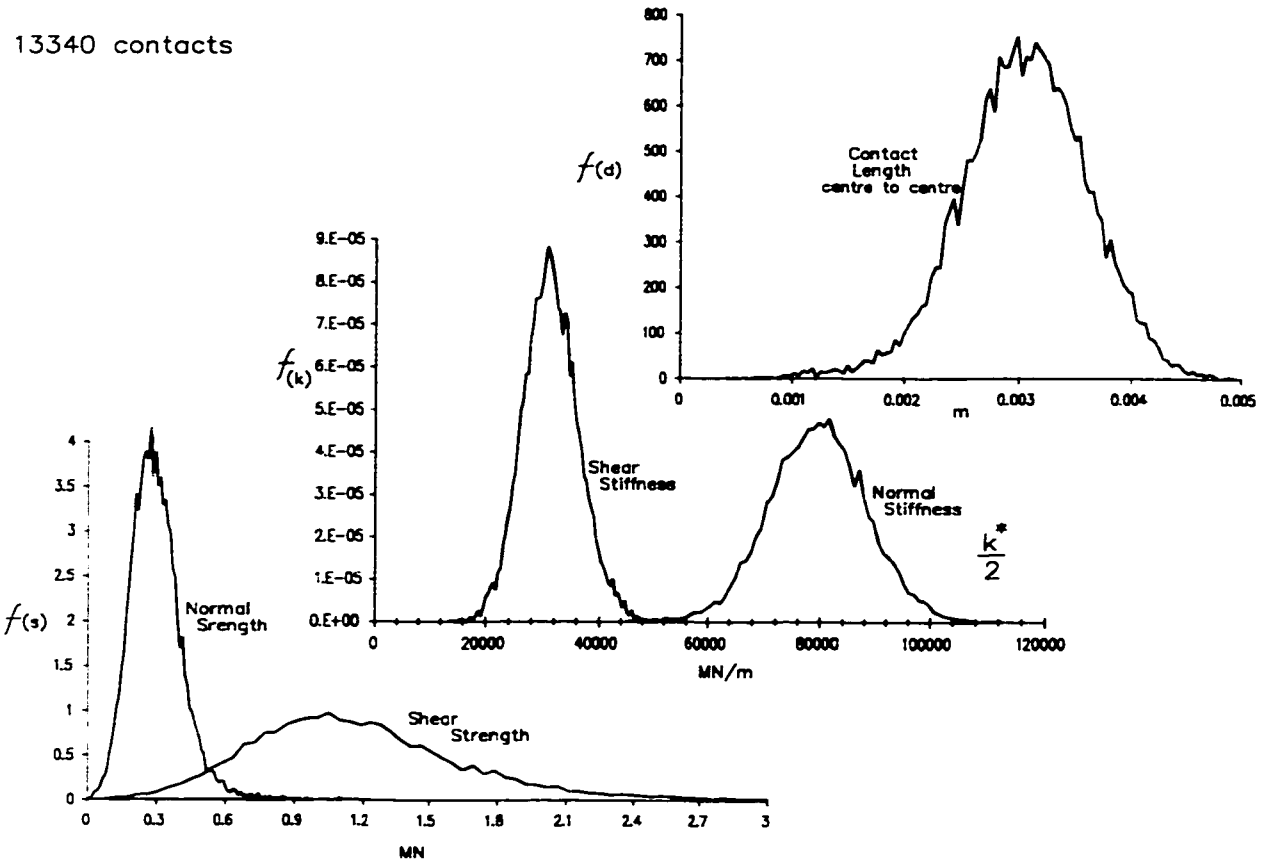


Figure 7.20: Typical Variation, in PFC samples, of contact bond strength, stiffness and length.

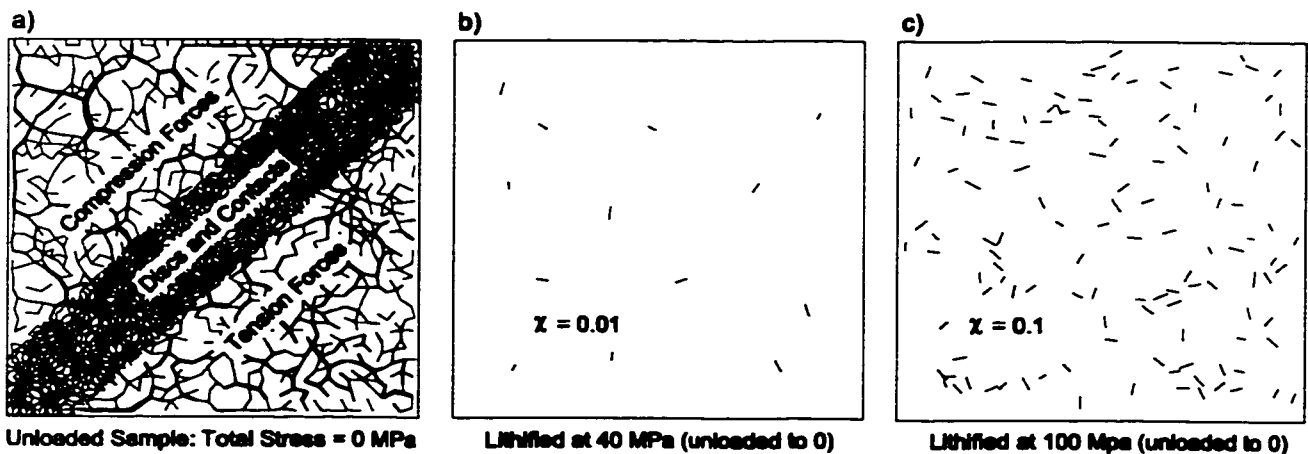


Figure 7.21: a) Internal stresses (cutaway view) in unloaded sample due to contact heterogeneity; b) unloading damage under low lithification pressure and c) under high lithification pressure.

Philosophically, this numerical “lithification” pressure represents present-day insitu conditions rather than original deep-earth pressures. It is possible to argue that geological unloading rates (e.g. due to erosion) are slow enough that stress relief occurs through concentrated extension cracking (joints). Distributed micro-damage such as that simulated here is likely the result of rapid unloading due to excavation.

The ratio between lithification pressure (20MPa) and contact tensile strength employed for most of this work was selected to minimize unloading damage (although several cracks do form in each sample) while achieving optimum densification ($\gamma=4.3$ to 4.5 for this grain size range).

Compression samples are generated and lithified in their final dimensions (aspect ratio between 2 to 1 and 3 to 1). Tensile and Brazilian tests are “cut” from more euhedral samples. Unloading of non-square samples results in minor anisotropy of residual internal forces and of crack damage. Due to the low number of induced unloading cracks, this was not considered to be significant.

After unloading, the sample is then reloaded hydrostatically to the desired confinement. Motion is halted and the sidewalls are replaced by columns of equi-dimensional discs (Figure 7.19c) which apply a constant boundary stress to the sample (next section). The sample can then be loaded by gradually converging the top and bottom wall platens to apply axial load.

7.3.3 Boundary Conditions

After unloading (of the initial lithification pressure) the sample can be stressed, in two directions (for rectangular samples) and in tension or compression in one or more of the following ways.

7.3.3.1 *Lateral Stress/Strain Control and Confining Stress*

Servo-Control (walls): Normal velocity of walls is continually updated to maintain a prescribed average wall stress determined from the sum of ball-wall contact forces (divided by the active length of the wall). This is adequate for controlling the internal confining stresses of an undamaged sample but results in local stress variation after sample yield due to discontinuous sample dilation.

Constant Stress Flexible Boundary: After unloading from lithification pressure and after the appropriate confining stress has been applied through the use of servo-controlled walls (above), each sidewall of the sample is deleted and replaced with a line of discs contacting the side of the

sample. These discs are generated with a constant radius (equal to 98% of the mean sample disc radius) and spaced to accommodate 2% vertical strain. These discs are assigned a constant horizontal unbalanced force (calculated to yield the appropriate lateral sample stress. At each time step, the unbalanced force acting on each membrane disc is adjusted to maintain the prescribed lateral force (and sample stress) component. This technique allows for discontinuous deformation at constant local confining stress.

7.3.3.2 *Deviatoric Stress/Strain Application*

Compressive Test Platens: These platens are simply walls (normally the top and bottom walls of a compression sample) which are assigned a fixed (vertical) velocity. Other than the contact stiffness of the wall (arbitrarily set to twice the ball-ball stiffness in this case) the wall represents a rigid system and cannot store strain energy. The post peak response of the sample can therefore be recovered. The stress, generated as the normalized sum of ball/wall contact forces, is recorded as the platens converge. The platens are gradually accelerated (from zero to the desired platen velocity) to avoid shocking the sample. Otherwise, in the iterative scheme where only the neighbouring discs are affected (in a single timestep) by an instantaneous movement in the platen, sudden velocity increase would lead to very high initial unbalanced forces and unpredictable damage to the near-boundary contacts.

Brazilian Test Platens: The Brazilian Test samples are prepared in the same manner as compressive samples, within a square region bounded by walls and with a uniform layer of discs at the top and bottom platens. After lithification and unloading, the sidewalls are removed and a circular region is overlain in the square, with a diameter slightly larger than the sidelength. Discs outside of this region are removed, leaving a Brazilian sample with a small flat platen region, approximately 7 to 8 degrees degrees wide, at the top and bottom of the sample.

Tensile Test Platens: In this case a band of discs, typically six discs wide, at opposite ends of the sample are given "infinite" bond strength. The discs in the outer half of each band (three discs wide) are assigned a constant (outward) velocity. The inner half of the platen bands are free to adjust their velocities but cannot break. This provides a smooth transition zone between the platens and the rest of the sample, which is necessary to avoid premature rupture due to strain incompatibility between the elastic sample and the effectively rigid platens.

7.3.4 Bond Stiffness Calibration

The PFC model stiffness parameters for the default case were determined through the following calibration procedure. Using the sample preparation procedure in Section 7.5.3 with a lithification pressure of 20MPa and a normal stiffness, k_n^* , of 160000 MN/m (determined from trial and error substitution in Equation 7.27) results in an average coordination number of 4.2 to 4.5. The samples tested in this calibration had an average γ of 4.23 and a mean physical contact density, m_v^* of approximately 260000 m⁻² (e.g. 15600 contacts in 0.06m²). The final mean contact length after disc expansion is approximately 0.0031m. From Table 7.1 the target bulk modulus of granite is 37 to 40 GPa. The calculated bulk modulus of the PFC sample is given, by combining Equations 7.21, 7.24 and 7.27a:

$$K = \frac{4.23 - 4}{2} \frac{260000 \cdot 3.1^2 \cdot 160000}{8} + \frac{6 - 4.23}{2} \frac{160000}{2 \cdot 260000 \cdot \left(0.0031 \cdot \tan \frac{\pi}{4.23}\right)^2} = 39400 \text{ MPa}$$

[7.30]

In order to obtain the target Poisson's ratio of 0.25, a number of tests were carried out, varying $\lambda = k_t/k_n$. Here the ratio of incremental lateral strain and incremental axial strain are used as in Figure 7.15. Values are taken from average tangential increments between 20% and 40% of ultimate strength and are summarized in Figure 7.22. Note that the conventional practice of measuring stiffness parameters at 50% of U.C.S. is flawed, both in this simulation and in reality, since in many cases inelastic damage has already begun, causing an increase in lateral strain rate as shown in Chapter 6 and again in the simulations in this chapter.

Equation 7.27c suggests a desired value of $k_t/k_n = 0.4$ to obtain a Poisson's Ratio of 0.25, a relationship which is confirmed in Figure 7.22. A comparison of model calculations, for Poisson's ratio, with the idealized results for $\gamma=6$ (Equation 7.23) and with experimental results by Bathurst and Rothenburg (1988) are shown in Figure 7.23. Figure 7.24 shows the measured bulk modulus and Young's modulus (2D plane case) for the simulations with varying λ . The invariance of K, with respect to λ , is confirmed. The value of Young's modulus, using $k_n^*=160000\text{MN/m}$ and $\lambda=k_t/k_n=0.4$, is "experimentally" determined to be 58 GPa, as desired.

A comparison of measured shear modulus and the shear modulus calculated from Equation 7.27 is shown in Figure 7.25.

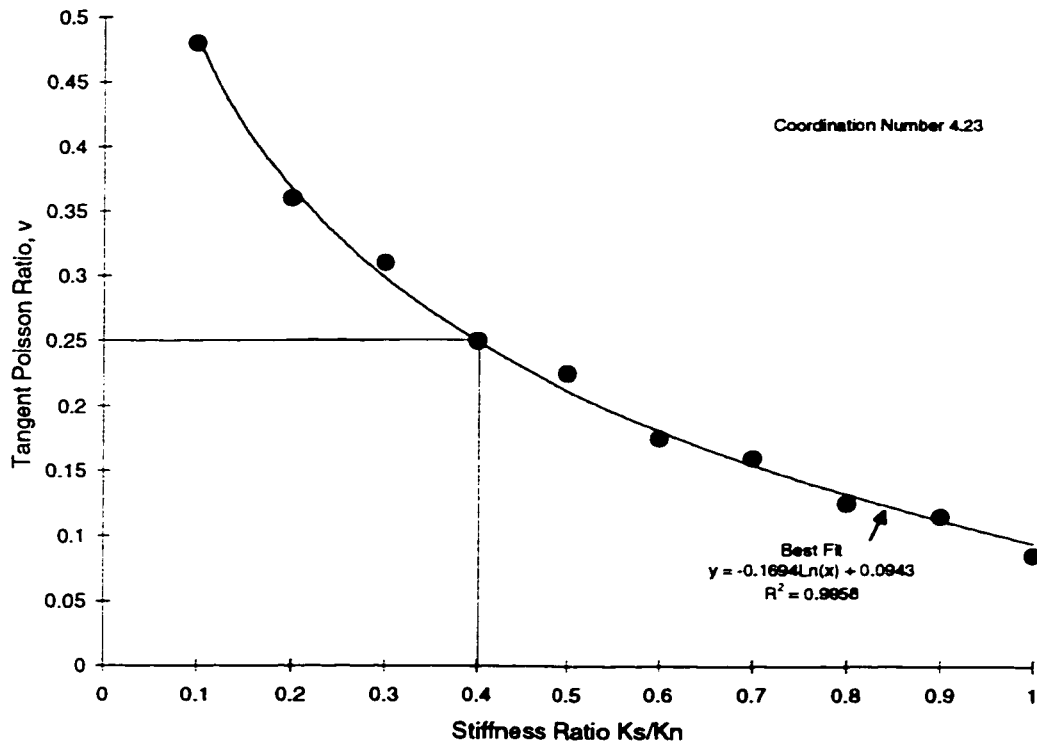


Figure 7.22: Experimentally determined values of Poisson's ratio for PFC simulations.

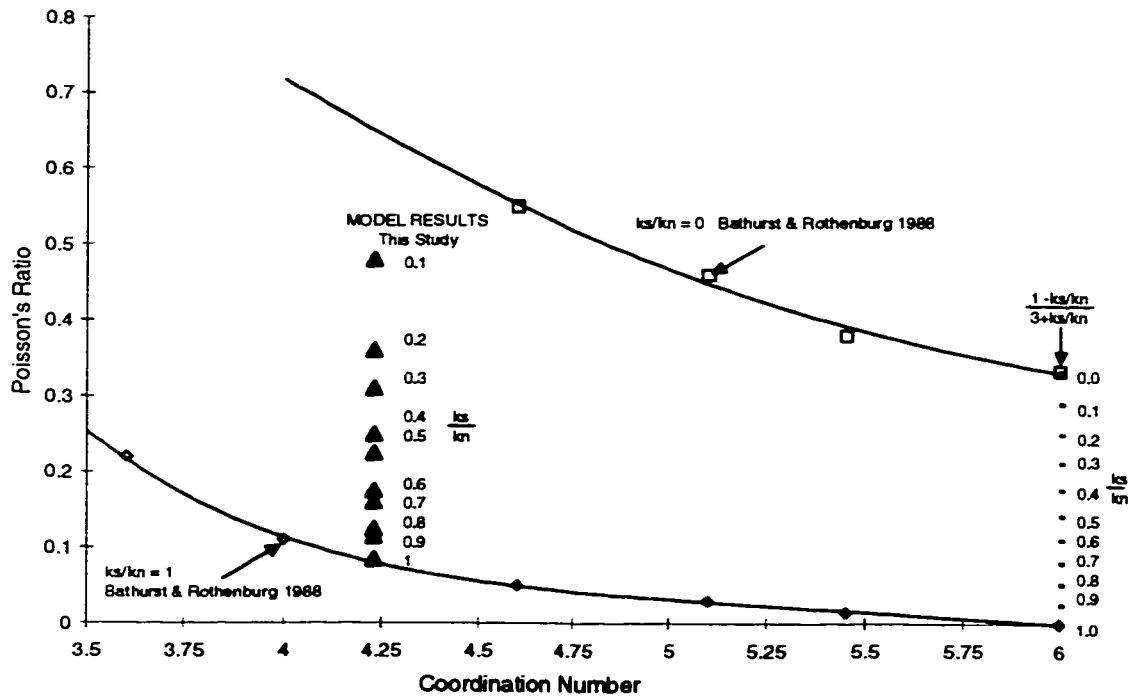


Figure 7.23: Comparison of model results with simulations by Bathurst and Rothenburg (1988) and ideal results for dense assemblies ($\gamma=6$).

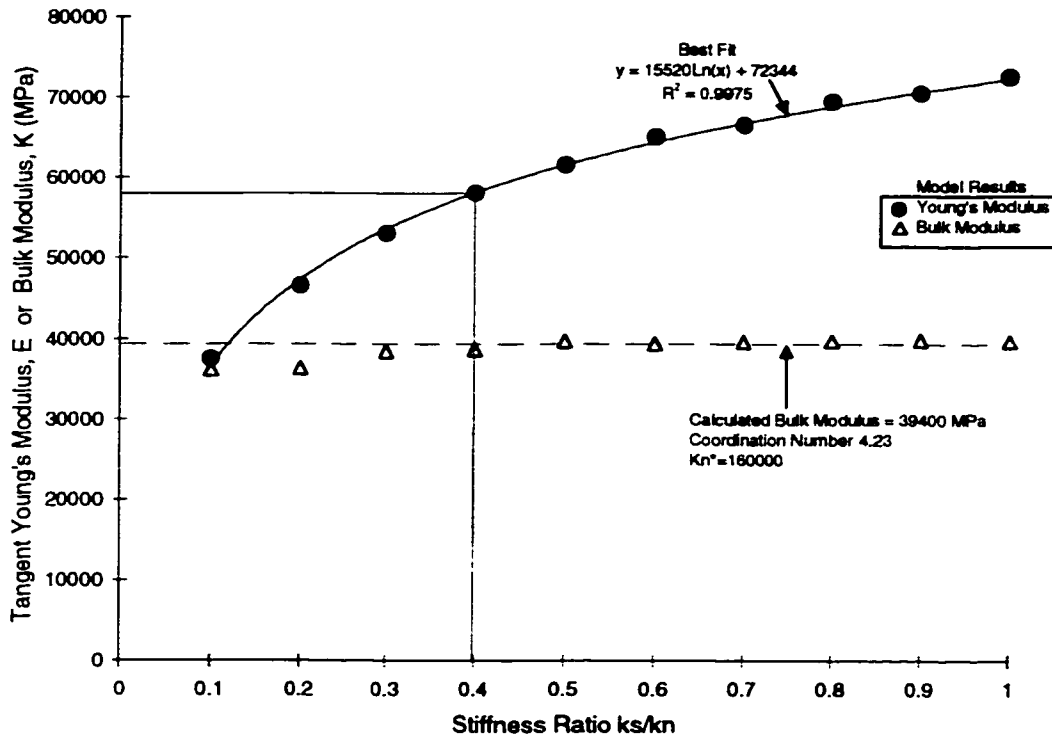


Figure 7.24: Measured variation of Young's modulus and invariance of bulk modulus with respect to $\lambda = k_s/k_n$.

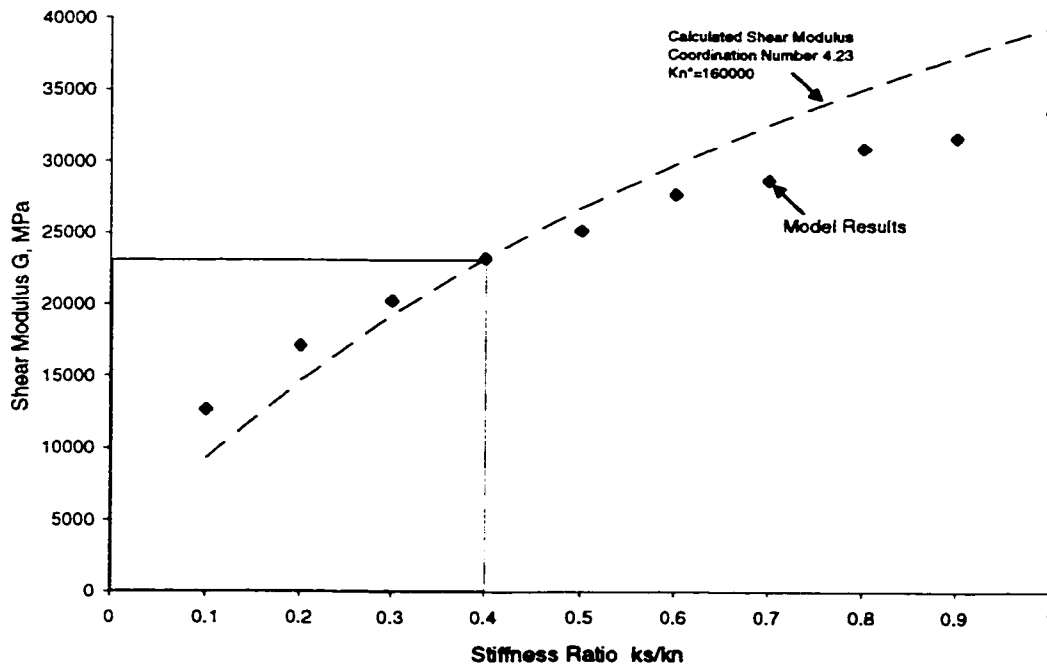


Figure 7.25: Measured shear modulus from PFC simulation compared with predicted relationship (to $\lambda = k_s/k_n$).

The correspondence in Figure 7.25 is good for the stiffness ratio of interest ($\lambda=0.4$) but deviates for extreme values. In addition, the predicted Poisson's ratio for $\gamma=4$ and $\lambda=1$ is nil according to Equation 7.27 while experimental results in this work show a higher result (Figure 7.23). Particle rotation and the effects of an irregular lattice are likely the cause of the discrepancy. Particle rotation increases significantly for coordination numbers below 4.5 (Bathurst and Rothenburg 1988). For pre-peak sample behaviour in bonded models, however, this is of little concern for the range of parameters selected.

The key contact stiffness parameters k_n^* and k_s^* are thus determined to be 160000 MN/m and 64000 MN/m respectively and are not varied again for the remainder of this chapter.

7.3.5 Bond Strength Calibration

Consistent with the previous discussions relating compressive strength to internal tensile resistance, the target compressive strength of approximately 170 to 180 MPa was initially achieved through the adjustment of mean normal (tensile) bond strength while maintaining a high value for shear strength. The variation in normal bond strength was chosen to provide significant heterogeneity while avoiding the occurrence of zero strength elements. A 30% (with respect to mean) relative standard deviation was therefore selected. Negative strength contacts (generated statistically) were assigned zero strength (broken). The effect of heterogeneity is explored in Chapter 8.

The ratio of shear strength to normal (tensile) strength is a more difficult parameter to determine. Clay materials and Plaster of Paris possess a shear strength (cohesion) approximately equal to the tensile strength. The Griffith (1924) criterion predicts a cohesion value two times the tensile strength. Fracture studies by Okubo and Fukui (1996) and Laqueche et al (1986) described in the previous chapters showed that for very small cracks (smaller than the grain size), the shear resistance increased while the tensile strength decreased, resulting in a factor of approximately 4.

Figures 7.26 and 7.27 illustrate the impact of varying shear and normal strengths on sample behaviour in uniaxial compression. Figures 7.28 and 7.29 illustrate the total and relative normal and shear crack densities (which stabilise at residual strength) for uniaxial tests. Figure 7.30 illustrates the impact on confined strength for different assumptions of strength ratio. The confined behaviour is examined in more detail in Section 7.8.

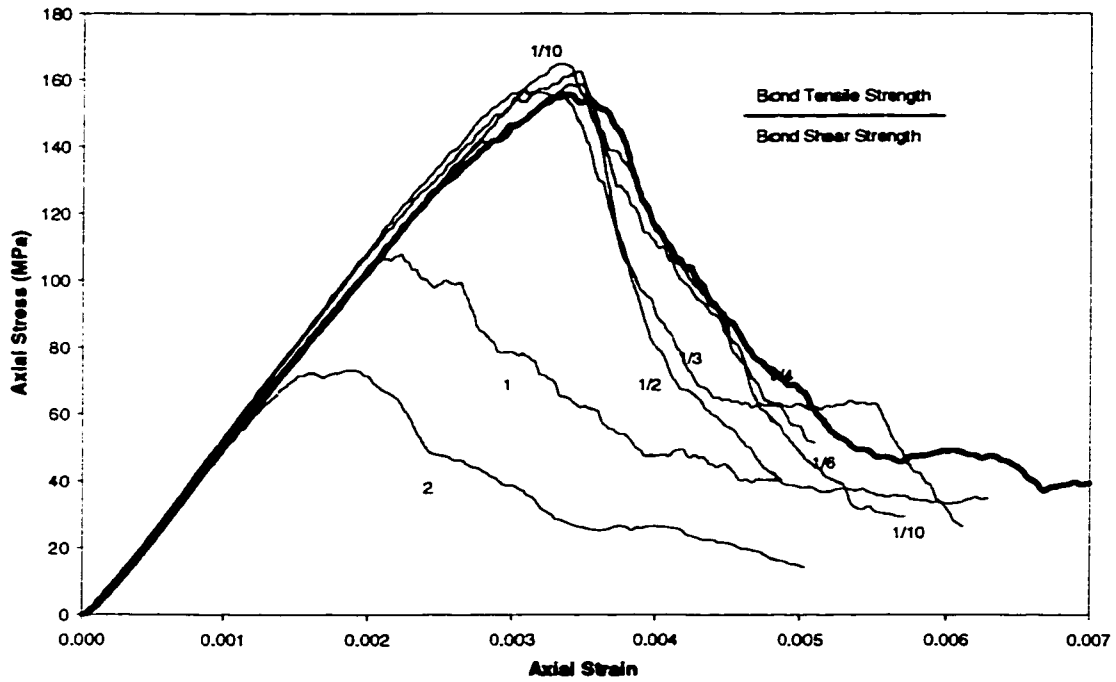


Figure 7.26: Uniaxial compression simulations with normal bond strength held constant ($N=0.3$ MN) as shear bond strength varied as shown (80x200mm samples with 3.1mm mean disc diameter).

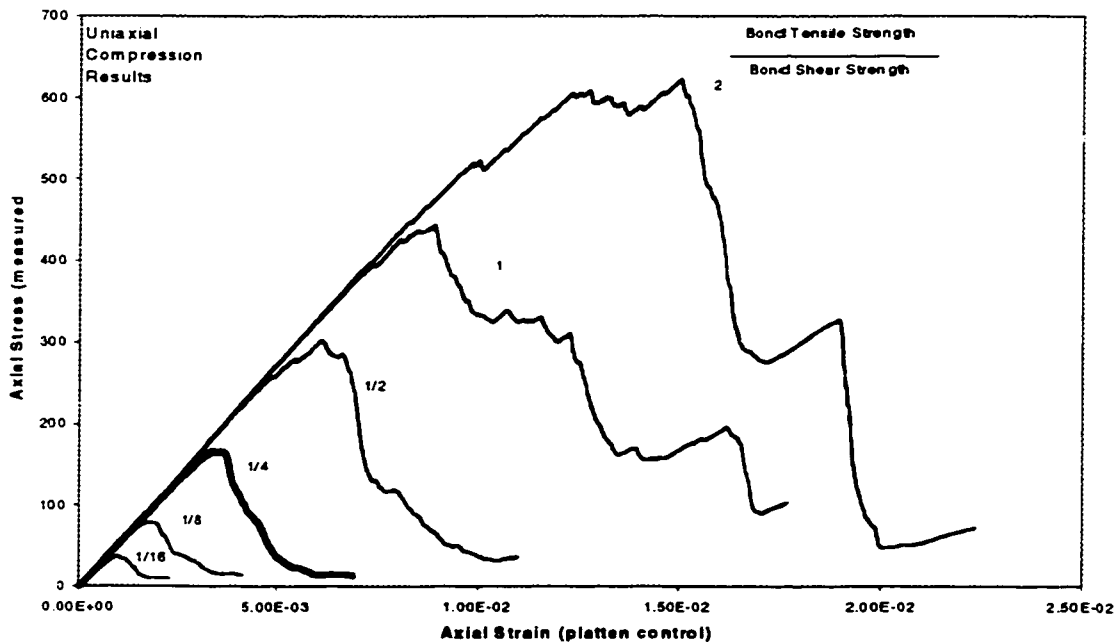


Figure 7.27: Uniaxial compression simulation with bond shear strength held constant ($S=1.2$ MN) as normal bond strength varied.

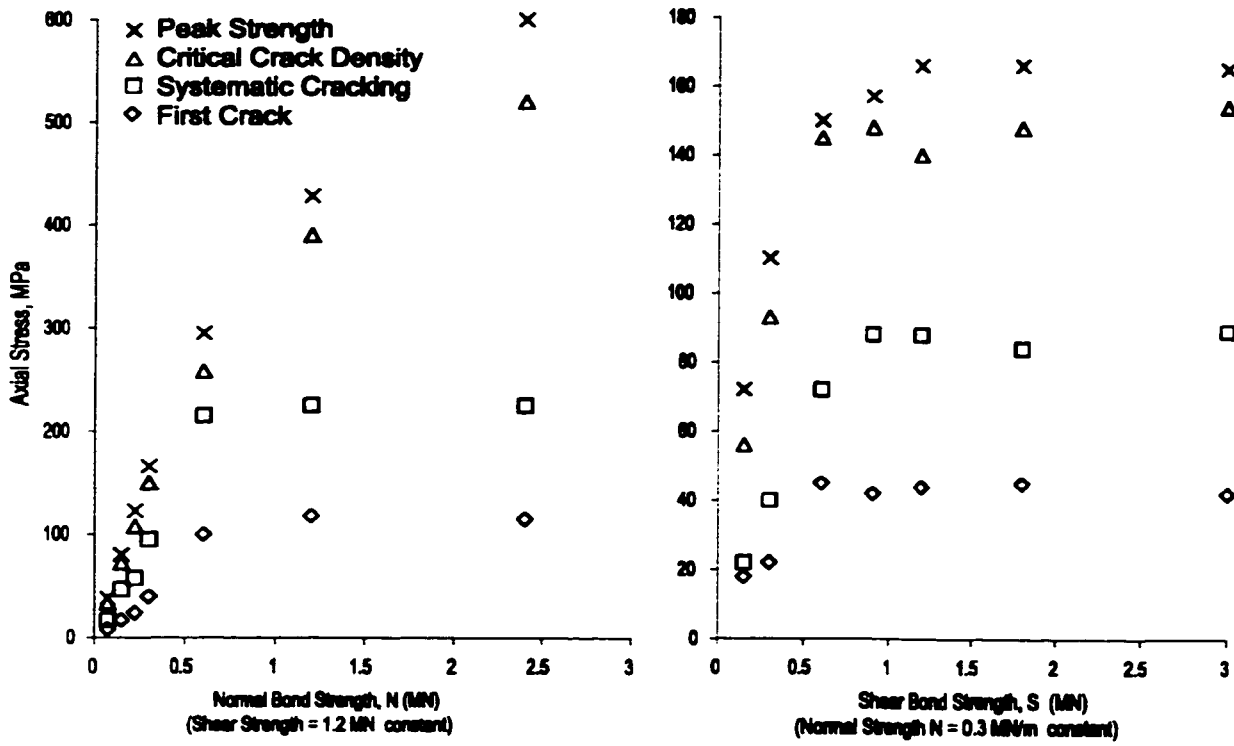


Figure 7.28: Results of simulations as in Figures 7.26 and 7.27. Damage thresholds are determined as described later in this chapter.

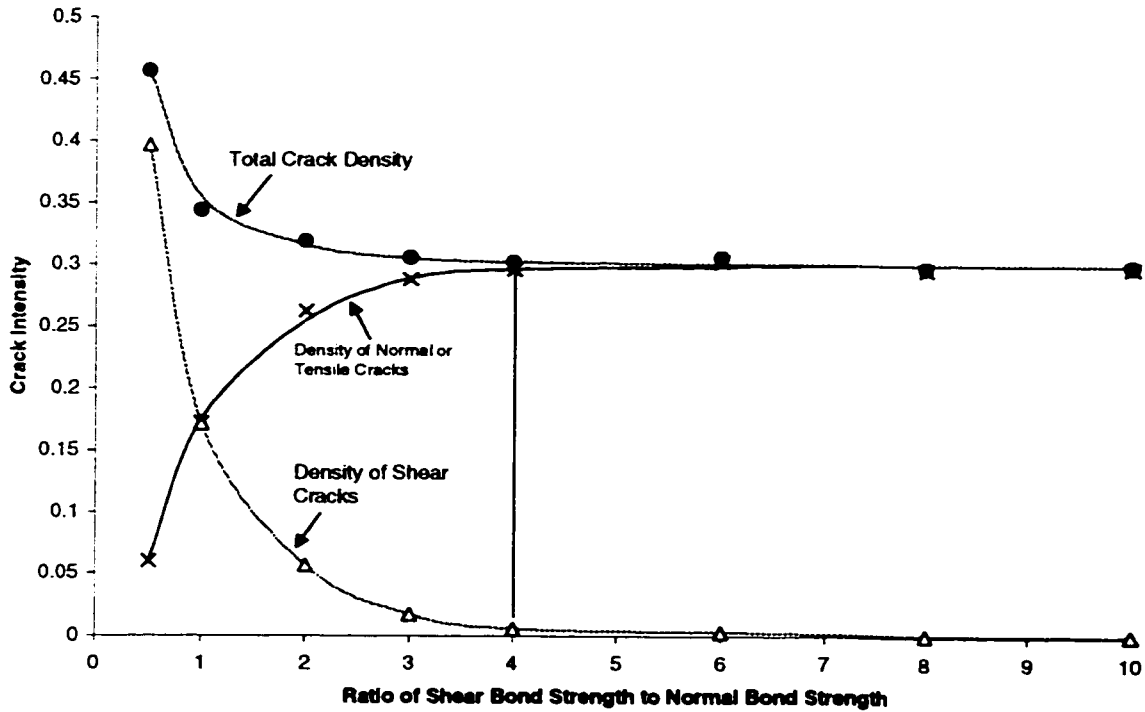


Figure 7.29: Total and component crack densities for strength calibration tests (crack intensities at residual strength).

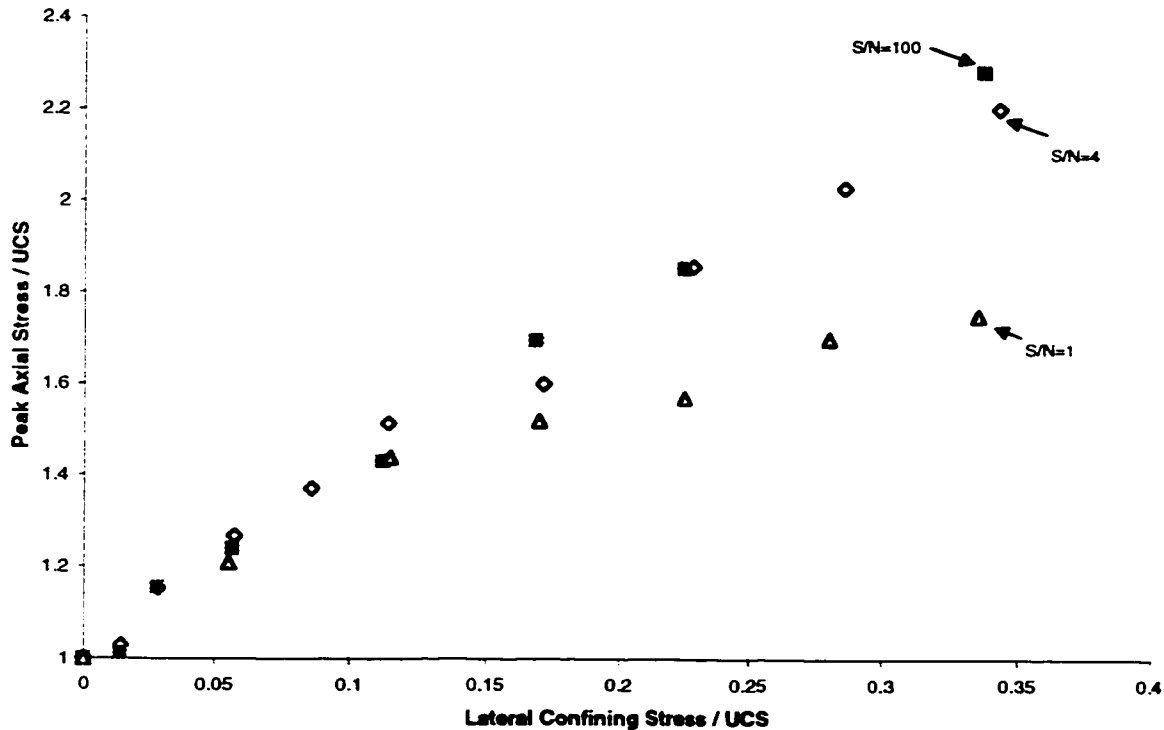


Figure 7.30: Peak strength data for confined tests with different S/N ratios.

For the disc models, a low ratio of shear strength to tensile strength (less than 2) results in unrealistic truncation of strength at moderate confinements, as cohesive failure dominates, as shown in Figure 7.30. The simulations using “infinite” particle shear strength are shown to be realistic. The physical difficulty of generating microscopic shear fractures in complex polycrystalline solids such as granite was discussed in Chapter 6. In low confinement conditions, visible micro-crack development is primarily extensional in nature in this case. Figure 7.29 indicates that this is the case in the model when the ratio of shear strength to normal tensile strength is greater than 4. Nevertheless, it was deemed presumptuous to prevent inter-particle shear rupture altogether. A lower bound shear/tensile strength ratio of 4 was therefore considered reasonable for granite simulations. These samples will be compared to samples in which shear bond failure is prevented (normal tensile rupture only).

The inter-particle contact friction coefficient was set to 1 ($\phi=45^\circ$) for the slip model. This was initially selected to correspond with the residual friction angle obtained from triaxial tests and from sliding friction tests by Martin (1994). Granite peak strength in the particle simulations are relatively unaffected by the selected value of inter-particle friction as shown in Figure 7.31. As demonstrated by Rothenburg (1986), Bathurst and Rothenburg (1990) and Heidari (1995), actual

values of residual sample friction in cohesionless particle model samples are only slightly dependent on the actual value of contact friction. As long as sufficient friction is available to form relatively intact particle clusters within the sample, frictional strength is generated by evolved contact layout and force anisotropies. This is probably true as well within the residual sliding zone in these initially bonded models, although the calculation of the various anisotropies would require selection of contacts within the shear zone. Such a detailed analysis is beyond the scope of this work.

Figure 7.31 illustrates residual strength at large strain for ruptured models in this work. Particle cluster interactions, fabric and force anisotropies enhance internal sample friction for low contact values. Particle rotation, on the other hand, limits the sample friction when higher contact values are used. Very high values of contact friction ($\mu \gg 1$) may reproduce the residual behaviour of granite samples while having little effect on peak strength at low to moderate confining stresses; the focus of this work. Pre-peak thresholds (damage initiation and interaction) are primarily the result of extension rupture (cracking) of contacts and are therefore unaffected by the selected value of contact friction.

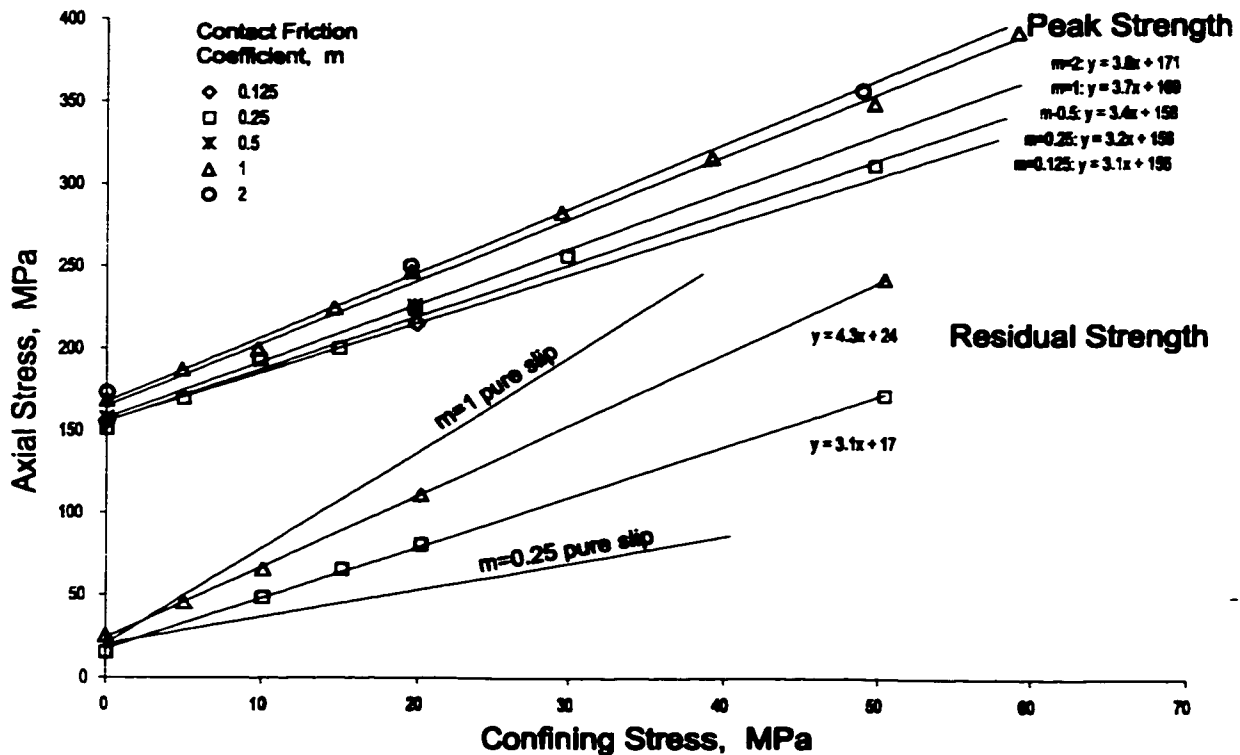


Figure 7.31: Peak and residual sample strength envelopes for different contact friction coefficients.

7.3.6 Loading Rate

For default damping parameters, high loading rates or platen velocities result in numerical oscillations within the sample. It is important that the velocity of converging or diverging platens be such that perturbations can be dissipated throughout the sample faster than new loads and displacements are applied. In general, the effect of loading rate was most pronounced on the post peak response (Figure 7.32). Faster platen velocities resulted in less brittle behaviour.

Slower loading in the PFC simulations resulted in more localized rupture zones. This is expected since, for slower loading rates, fewer contacts rupture at each timestep, allowing for load redistribution and consequent concentration of subsequent damage around previous contact rupture points. For faster loading rates, more distributed cracks can occur (in a heterogeneous material with a given strength distribution) in each timestep resulting in a more distributed rupture network.

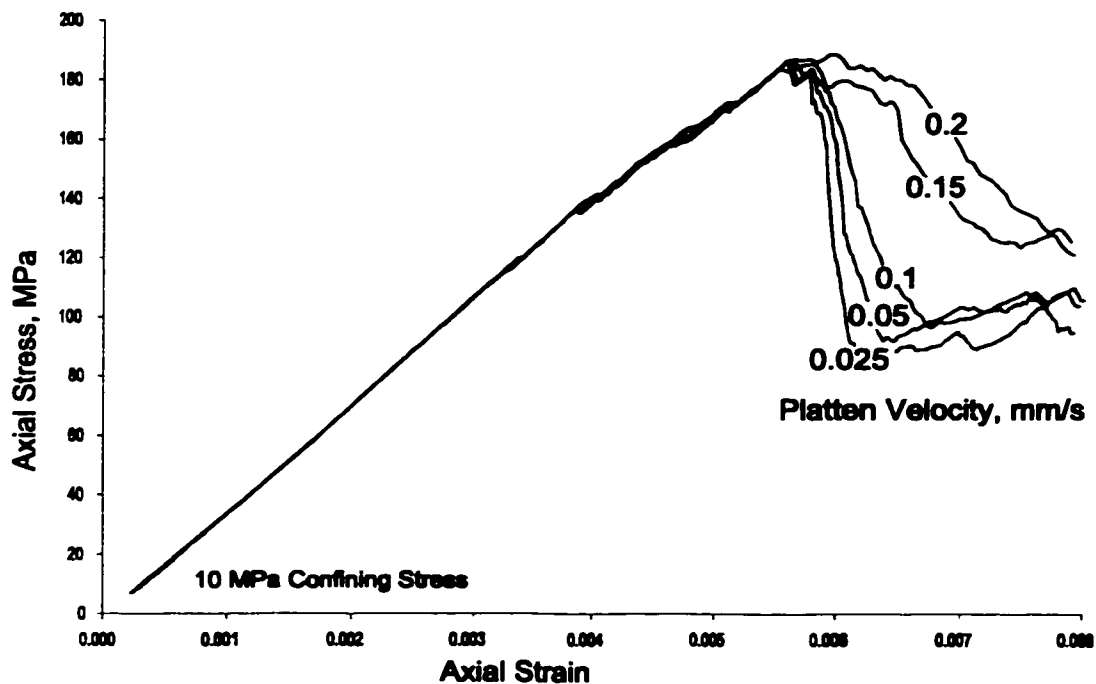


Figure 7.32: Effect of numerical loading rate on post peak behaviour.

A nominal platen velocity of 0.1 mm /s was determined to be acceptable for the reduction of runtime and the minimisation of numerical noise. This translates to approximately 7.5×10^{-6} mm of platen convergence per timestep for a 270x100mm sample (an average sample size for this study). Tensile and Brazilian Test platens act at 20% and 50% of this rate, respectively.

7.3.7 Shape Effects

A series of analyses were performed to investigate the influence of sample shape on model behaviour as shown in Figure 7.33.

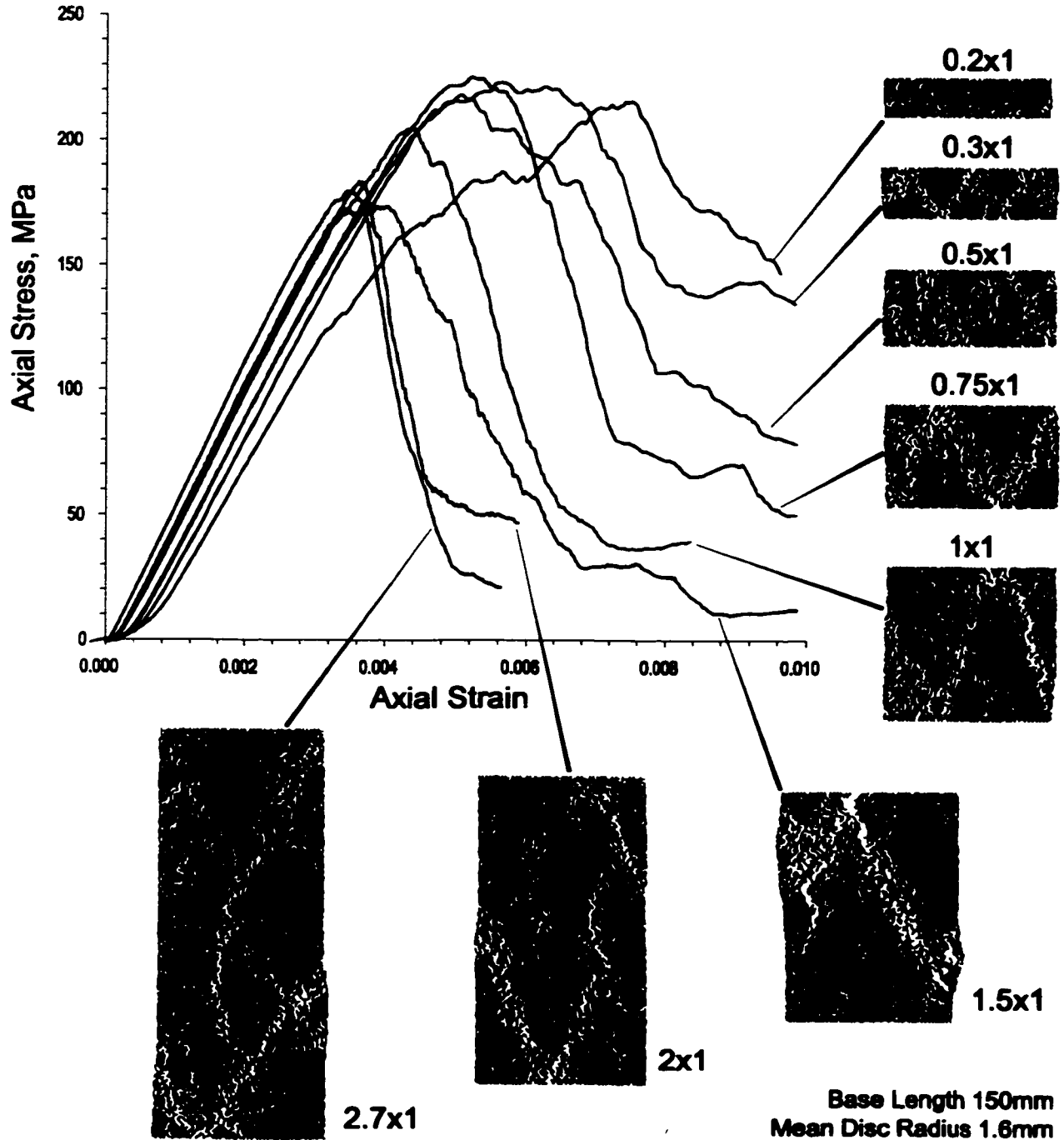


Figure 7.33: Uniaxial compression tests with varying sample aspect ratio.

The sample images are composed of remaining intact contacts. Failure zones are identified by regions of white indicating ruptured bonds and dilation. The axial strains plotted in this figure are calculated from platen displacements and represent average strains in the sample. Stresses are also measured from the platens in this plot.

The initial strain due to “seating” as the platens (solid walls) converge on the sample are exaggerated for smaller samples. The measured modulus does not vary except for very squat samples. Here disc-platen interactions, which represent finite displacements, are averaged over a shorter sample height resulting in larger calculated strains and a lower apparent modulus.

Post peak response is also displacement, rather than strain, controlled as the failure localises to a rupture band. These displacements averaged over a shorter height give the impression of a more gradual post peak strength drop for squatter samples.

Sample peak strength rises for sample with a height less than 1.5 times the width. This is due to the inability of a 30 degree failure surface (inclined from the vertical), which is the natural orientation in these simulations, to traverse the sample from sidewall to sidewall. Additional damage and strain is necessary to fail the sample. In these tests the platens were frictionless. Experiments by Ormonde and Szwedzicki (1993) show a more pronounced increase in strength and in post peak ductility for squat samples, probably due to the effects of platen contact friction.

7.3.8 Locked in Stresses

A lithification pressure of 20 MPa was adopted for standardisation of test samples. With the heterogeneity in strength and stiffness, unloading from this pressure results in a small amount of accumulated damage (broken contacts) and a significant amount of internal tension. With strain continuity maintained within the sample, variations in stiffness result in distributed compressive and tensile contact forces which sum to create a net stress of zero in all directions over a significant sample as shown in Figure 7.34.

If the tensile forces exceed the bond strength, unloading or sampling damage results, as shown in Figure 7.35. The effect of heterogeneity and lithification pressure are explored in detail in Chapter 8. Using standard material properties and 20MPa of initial pressure, this unloading damage results in an average initial crack density, χ_d (Equation 7.16) of approximately 0.002. This level of damage is minimal, while 20MPa of initial pressure allows for a suitably dense sample.

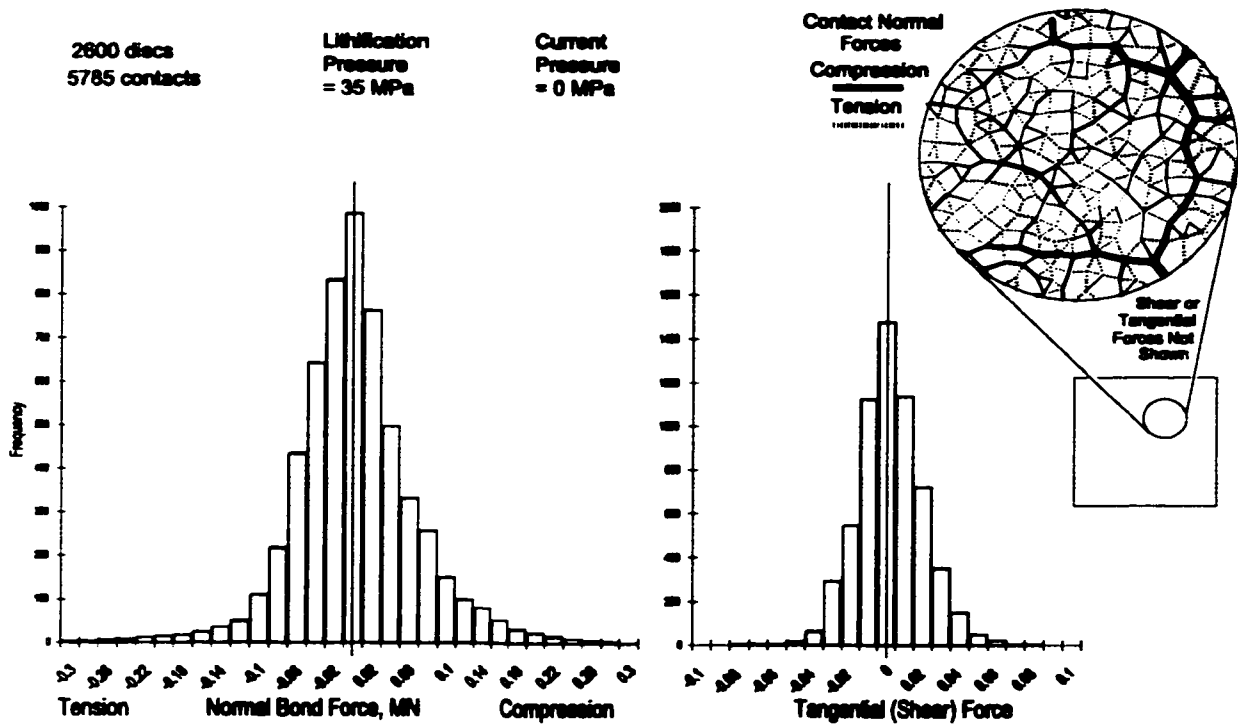


Figure 7.34: Residual forces in contacts after unloading from lithification pressure. Force distribution is isotropic.

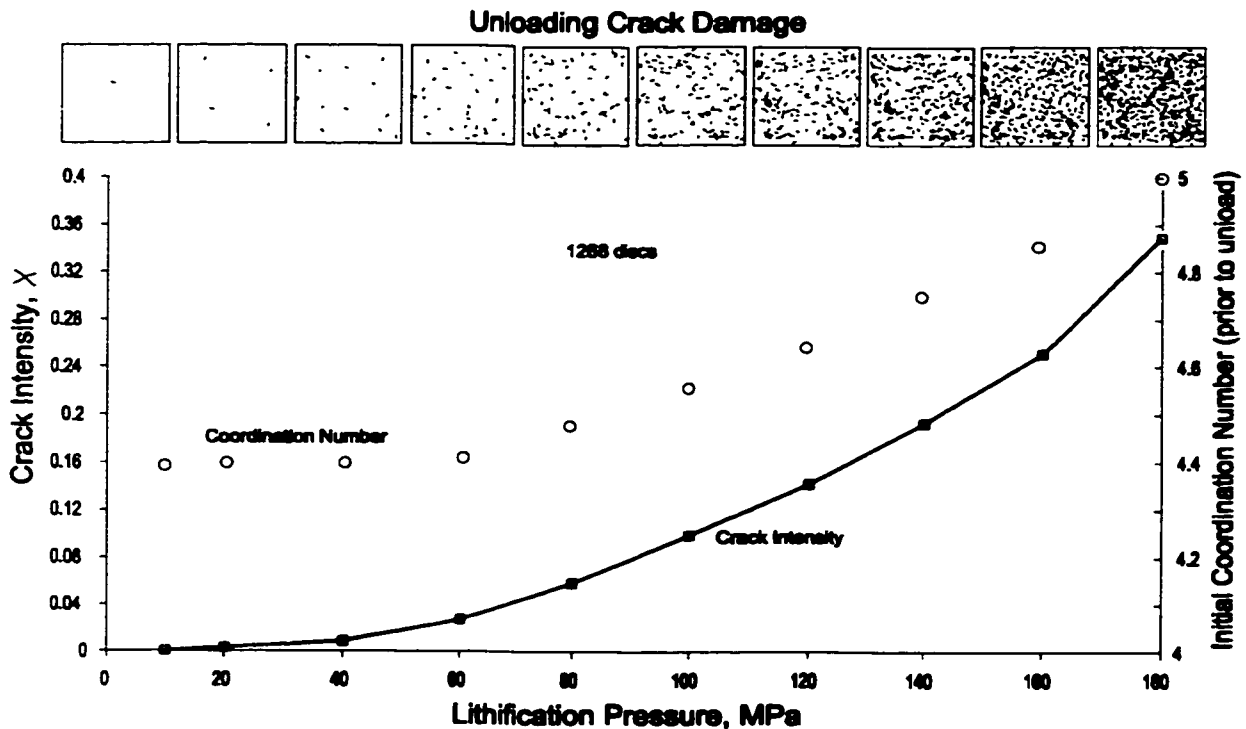


Figure 7.35: Samples lithified at different pressures and unloaded. Coordination numbers are measured prior to unloading. Damage accumulates during the unloading process.

7.4 COMPRESSIVE SAMPLE BEHAVIOUR

The intent of the numerical experimentation in this chapter is to relate results of these simulations to real granite behaviour as described in Chapter 6. Clearly this approach has some difficulties associated with it. The PFC simulations are plane models. They are neither plane stress nor plane strain and they are not axi-symmetric. Particular difficulties arise if post peak behaviour is to be examined in detail. This discontinuum phase of sample failure is likely to be dependent on geometry and dimensional space.

Accumulation of distributed, non-interacting crack damage in a two dimensional space should, however, mimic similar accumulation in a distributed volume. This work is concerned with damage processes leading up to sample failure and as such the analogue should be appropriate.

This section will describe the general behaviour of 2D bonded particle simulations of compressive tests. It will also summarise the suite of damage indicators used to interpret the results. Finally a summary of damage thresholds and associated test measurements is given for comparison to granite testing and also to direct tension, indirect tension and confined compression studies discussed later in the chapter.

7.4.1 Typical Test Results

Approximately 160 compressive samples were "prepared" and tested under various boundary conditions during this study. Three typical compressive samples, tested at 0MPa, 20MPa and 60MPa confining stress (lateral stress) are illustrated in Figure 7.36. These samples were unloaded to an unconfined state from a 20MPa "lithification" pressure after bond strengths and stiffnesses were established. As previously noted, some damage occurs during this process due to internal tensile stresses resulting from local stiffness variation. Using servo-controlled walls with a single degree of (normal translational) freedom, a hydrostatic pressure was applied corresponding to the nominal test confinement. At this point the sidewalls are replaced with a line of discs of fixed radius (same as the average for the sample). These discs are separated by 5% of the radius to allow for vertical strain and are assigned a constant horizontal unbalanced force calibrated to result in the desired pressure over the entire side of the sample. This unbalanced force is maintained through velocity adjustment as the test progresses.

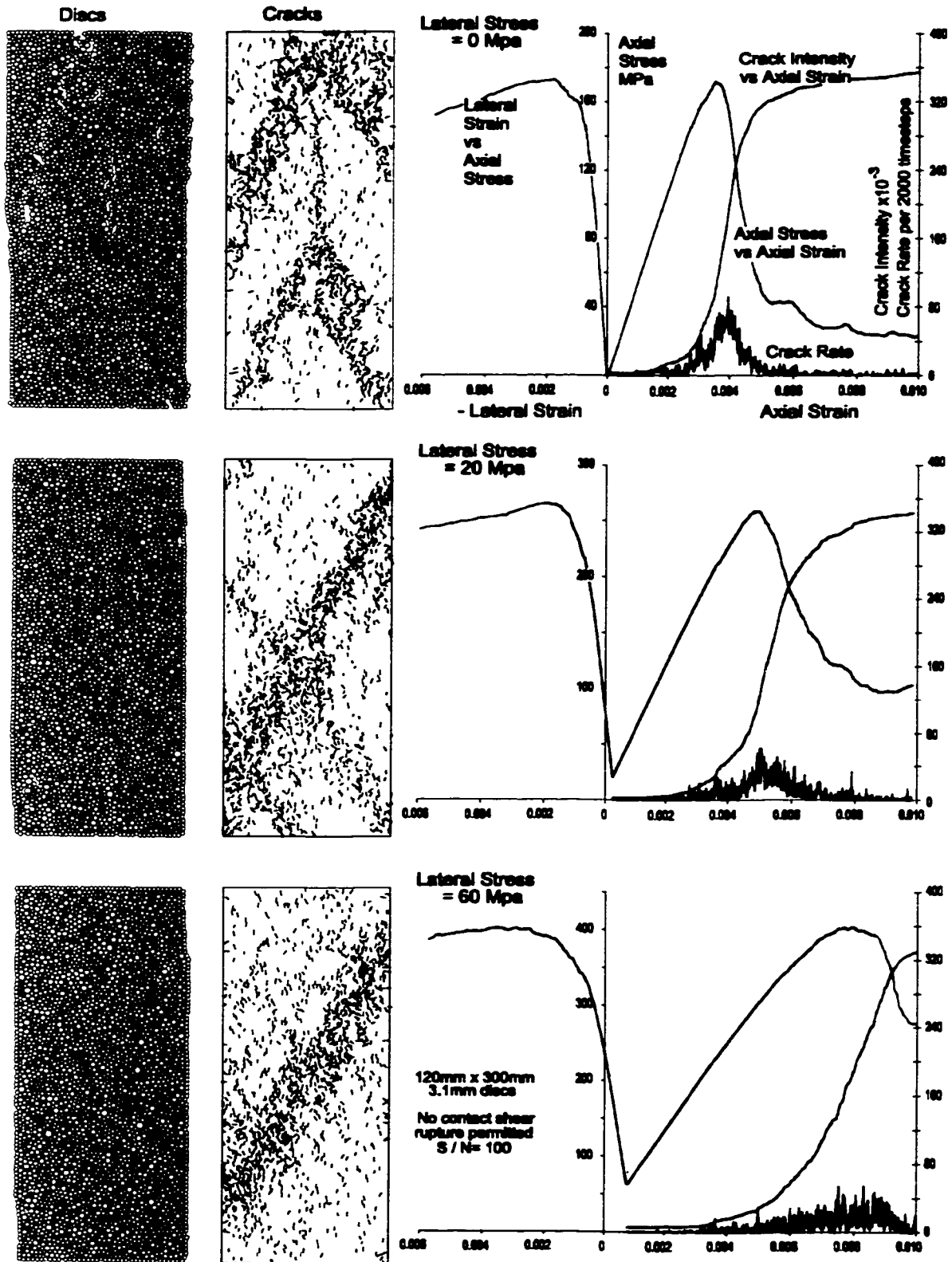


Figure 7.36: Sample performance at 0, 20 and 60 MPa of confining pressure. In these tests, $S/N = 100$. Samples with $S/N = 4$ performed comparably.

7.4.2 Damage Thresholds

One of the primary purposes of this numerical investigation is to illuminate the nature of key damage thresholds for analogous comparison to the granite tests in Chapter 6. Damage accumulation in unconfined and confined tests is illustrated in Figure 7.36 in the stages of simulated acoustic emissions (crack rate), increasing crack intensity and lateral strain.

Key damage classes or thresholds include pre-existing damage due to unloading, initial (new) crack formation, systematic crack growth, primary crack interaction, localization of damage and strain, damage at peak strength and ultimate damage accumulation. These thresholds are identified as schematically summarized in Figure 7.37. Incremental damage accumulation is illustrated in the example in Figure 7.38.

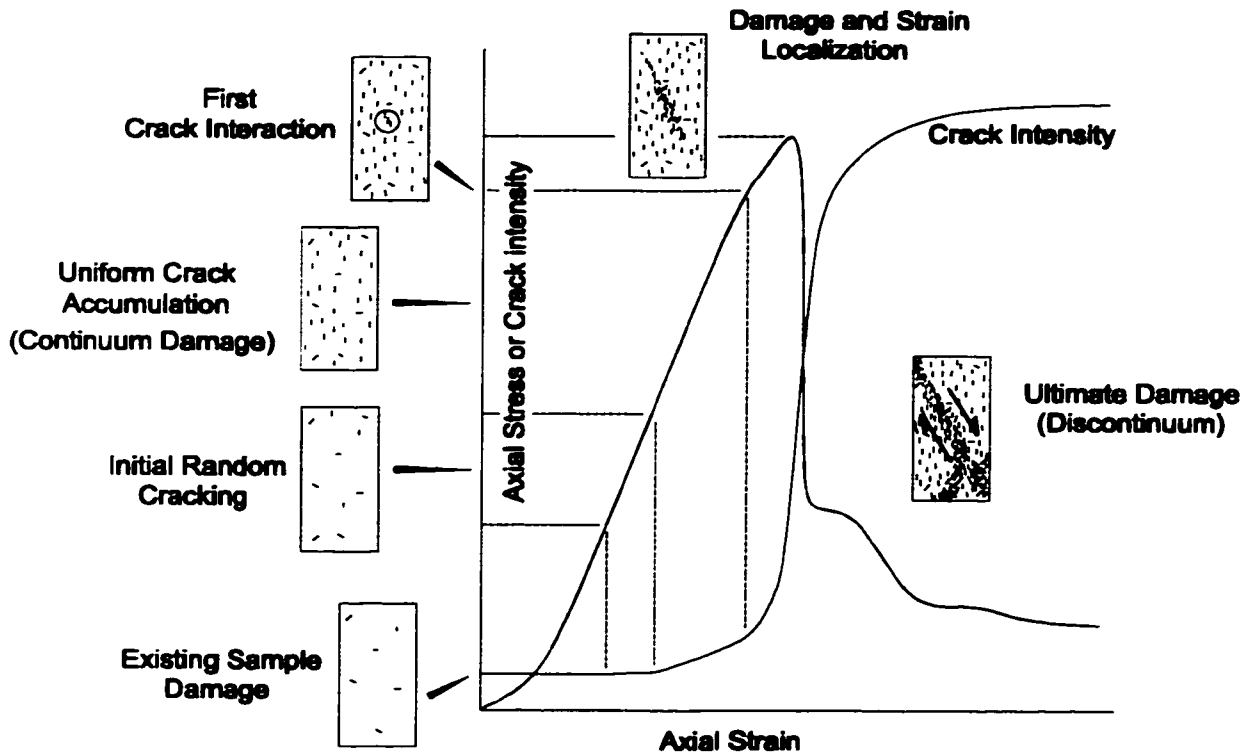


Figure 7.37: Stages of damage accumulation (schematic).

The precise instance (with respect to stress or strain) of these thresholds cannot always be conclusively determined from a single indicator. Such is also the case in real material testing as noted by Eberhardt et al. (1998; 1999). The following sub-sections describe the suite of damage classes and indicators.

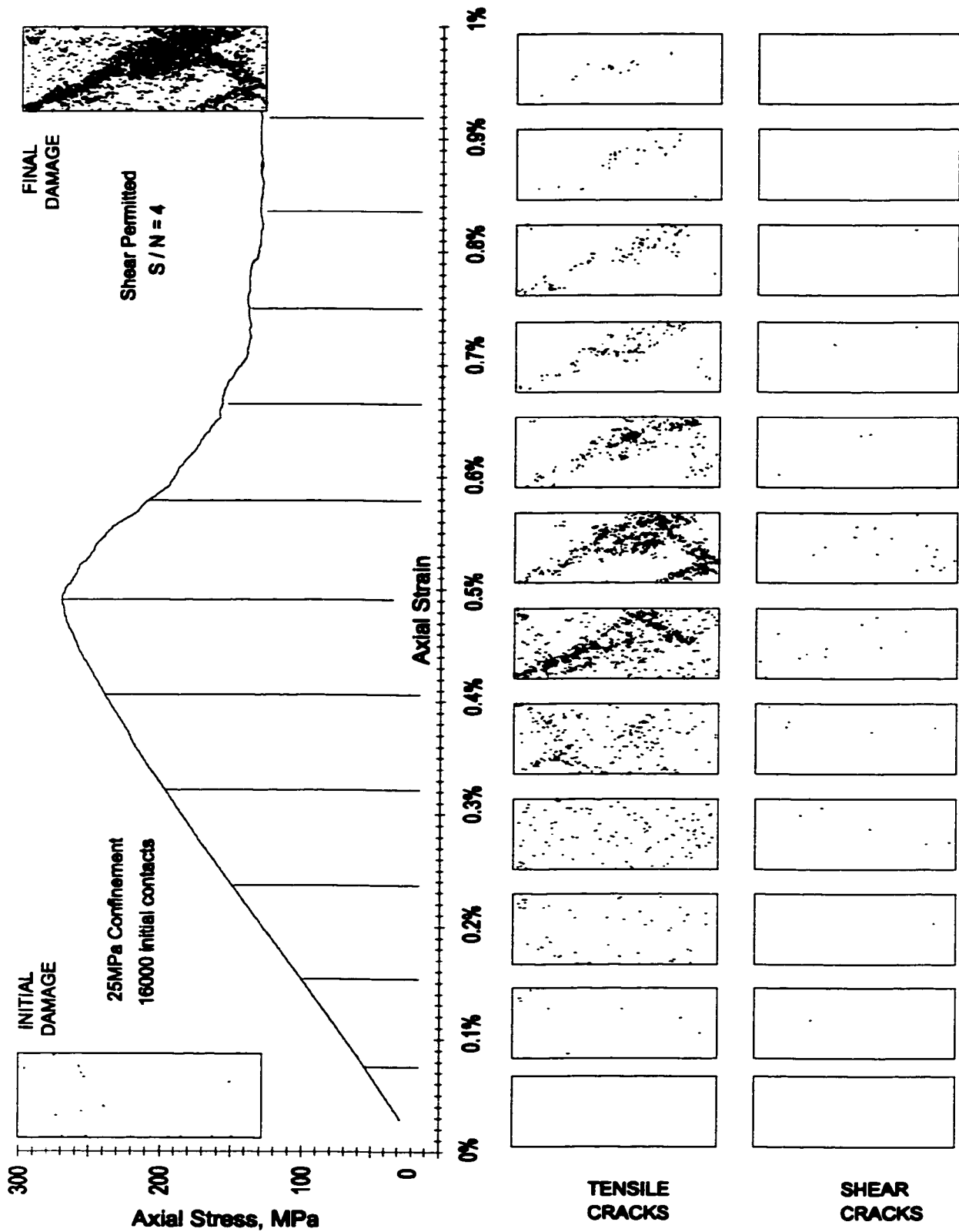


Figure 7.38: Example of damage accumulation in confined compression test.

Using a typical sample (2.5 MPa confining stress), illustrated in Figure 7.39, Figures 7.40 through 7.42 illustrate the effects and identification of induced accumulated damage during compressive testing.

7.4.2.1 *Sampling or Unloading Damage*

As discussed in Section 7.5 a typical sample will sustain damage during unloading from its lithification pressure. A pressure of 20 MPa is used in most of these simulations to minimize this damage. The effect of existing damage is investigated in Chapter 8. Increasing initial damage is also incurred as higher confining stresses are applied (hydrostatically) prior to deviatoric loading.

7.4.2.2 *First Crack (Loading)*

In the context of PFC simulations, this threshold is simply the point of first new crack formation during loading. Crack number and crack intensity are directly reported in the sample records (indirect assessment via strain readings is necessary for real samples). In some cases one or two new cracks appear near the ends of the sample shortly after the application of load. These seating cracks are typically unrelated to the incremental application of load and are typically randomly oriented. Such cracks are not, wherever identified, considered as relevant.

7.4.2.3 *Systematic Crack Growth and Crack Density*

Initial crack formation may be an isolated event related to a model contact with unusually low strength (an outlier to the normal distribution) or may be the result of local platen interference or other boundary interaction. Of greater interest is the onset of systematic crack accumulation. In this phase, crack density increases steadily with increasing load. This can be identified as a log rate increase in crack density with respect to load (Figure 7.40) and an increase in lateral strain rate or in the tangential (Poisson's) strain ratio.

It is also typically accompanied by an increase in the rate of crack anisotropy. Cracking prior to this point may not be directly related to the applied stress field and may not be axially aligned. Systematic extension cracks are normal aligned with the maximum compression and therefore contribute to a higher crack anisotropy for the sample. A measurable non-linearity in volumetric strain (related to lateral strain and effective Poisson's ratio) also signifies systematic crack accumulation.

7202 Bonded Discs 16006 Initial Bonds

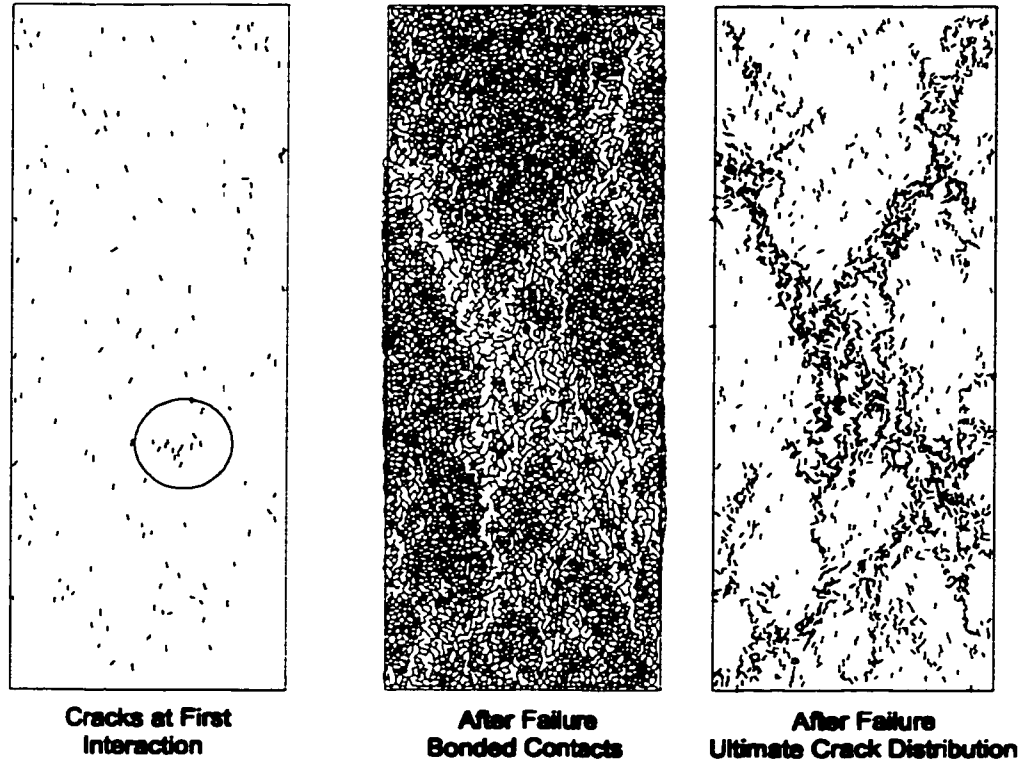


Figure 7.39: Accumulated damage at first interaction (critical crack intensity) and after failure (2.5MPa lateral confinement).

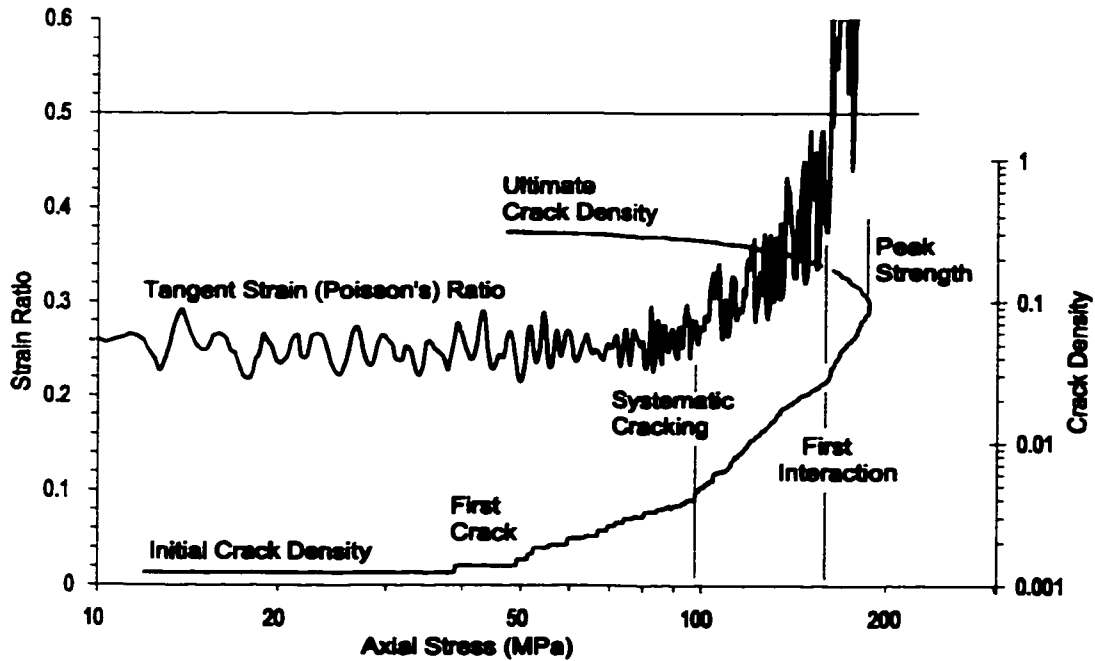


Figure 7.40: Identification of damage thresholds from crack intensity and tangent strain increase.

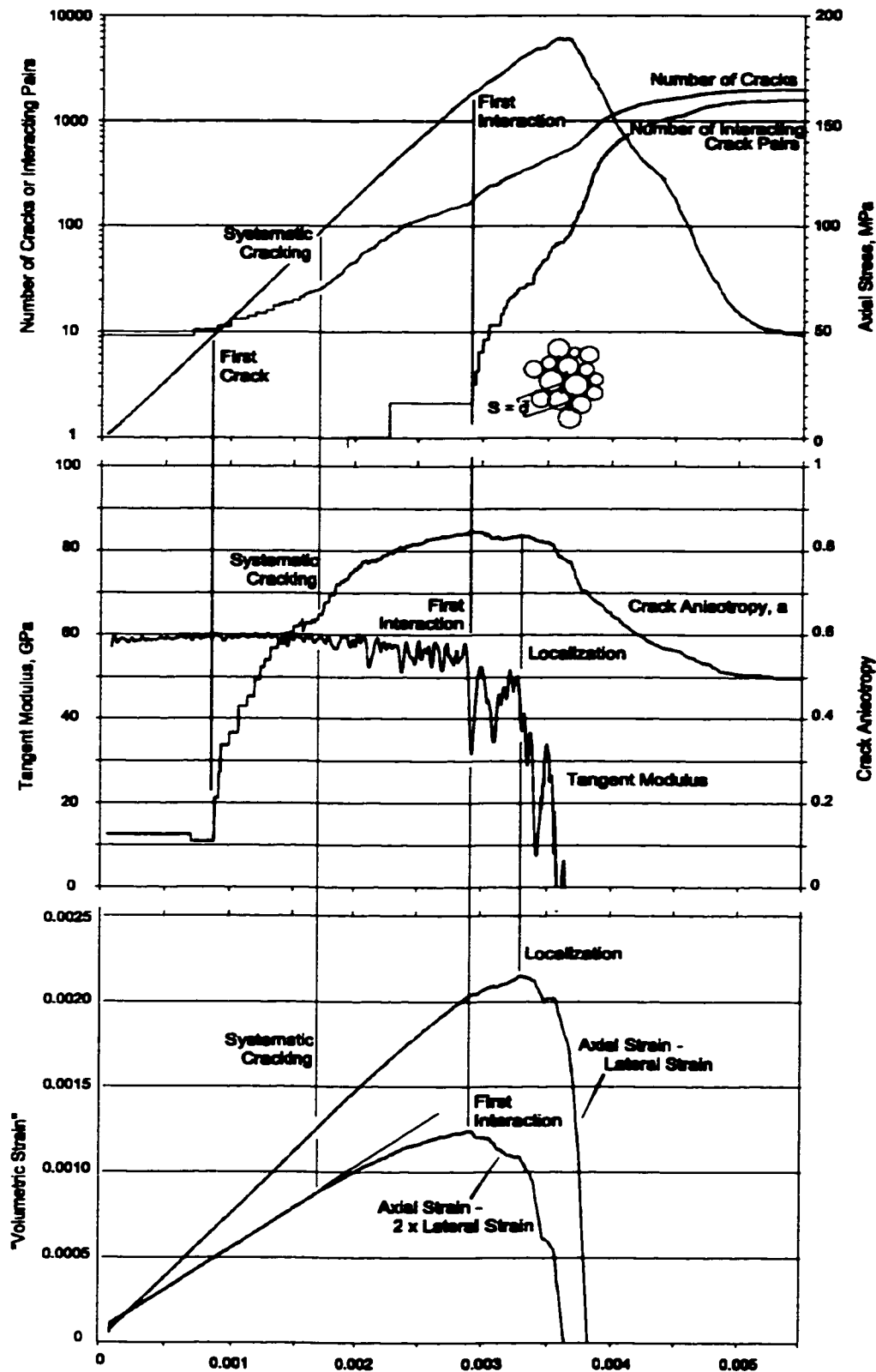


Figure 7.41: Damage threshold identification from record of interacting crack pairs (top), crack anisotropy and tangent modulus (middle) and from volumetric strain (bottom).

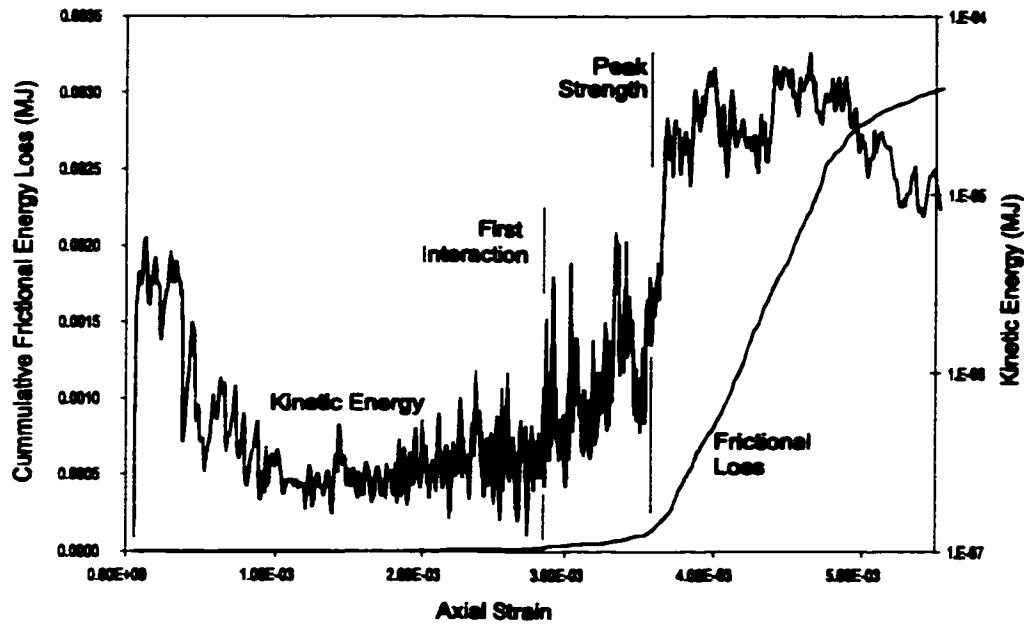


Figure 7.42: Damage threshold identification from kinetic energy and frictional loss.

7.4.2.4 *Primary (First) Interaction*

This threshold is the most important for linking laboratory results to insitu conditions. It is proposed, in this work, to represent true material yield as a threshold which is independent of the boundary conditions. A simple index which tracks the number of crack pairs with a mutual disc separation of less than one average crack diameter can be used conclusively to identify crack interaction and clustering. A more robust statistical clustering indicator for real seismic data has been developed by Falmagne (1999) and has been used with success to indicate rockmass yield, based on monitoring of induced microseismic emissions around rock excavations at depth.

In Chapter 6, first interaction was determined by the onset of non-linear axial stress-strain behaviour. In uniaxial samples, this also corresponded to volumetric strain reversal, an indicator used by Martin (1994) and others. For confined axi-symmetric tests, however, initial crack interaction within a volumetrically distributed crack array precedes the initial genesis of the final slip plane (strain localization). The latter event is coincidental to a reversal of the 2D equivalent "volumetric" strain. Initial interaction, however, coincides to the reversal of a pseudo-3D quantity (Figure 7.41) which is calculated as the vertical strain less twice the lateral strain (this is the same relationship used in 3D). Non-linearity of axial stress-strain is used to detect this threshold, although this non-linearity is easier to deduced from a plot of instantaneous (apparent) tangent

Young's Modulus. Instantaneous Poisson's ratio also show a marked increase. Crack accumulation rate undergoes a sharp increase once cracks begin to interact. For unconfined compression, peak crack anisotropy coincides with initial crack interaction (Figure 7.41). As confinement increases, anisotropy peaks with the onset of localization as a shear zone fully develops and oblique cracks are generated through kink and rotational processes.

Other indicators also react to crack interaction as well. A significant first rise in the internal kinetic energy (Figure 7.42) coincides with crack interaction as does an increase in frictional energy loss and fraction of sliding contacts within the sample.

7.4.2.5 *Damage and Strain Localization*

Localization can be defined as the transition to a state in which the front of the propagating shear or spall zone dominates further crack formation or damage accumulation. For uniaxial samples, the onset of strain localization is often indistinguishable from initial crack interaction. For confined tests, the formation of a localized shear zone requires input of additional energy (stress and strain). This threshold is, in the opinion of the author, not a material property. Strain localization, whether coaxial, in the case of macroscopic spalling or oblique, in the case of a planar shear zone, involves a dimensional reduction in the displacement field. As such, it must be subject to geometric constraints and boundary conditions.

Volumetric reversal (calculated as the sum of vertical strain and lateral strain) is synonymous with a jump in instantaneous strain ratio to above 1 (in plane simulations – 0.5 for 3D), as shown in Figures 7.16, 7.40 and 7.41. A second set of substantial increases in crack accumulation rate, total kinetic energy and frictional energy loss also accompany this threshold (Figure 7.42). As mentioned, peak crack anisotropy is also an indicator of damage and strain localization. Although not shown here, non-zero values for the off-diagonal terms of the velocity gradient tensor indicate the onset of internal disc rotation. Total rotational velocity (ideally zero for initial elastic loading) can be tracked, with a significant increase coincident with this threshold.

7.4.2.6 *Peak and Ultimate Damage*

Peak strength occurs when the stored strain energy outside of the localized shear or spall zone in the rest of the sample and in the loading system, is more than that required to continue the propagation of the localized rupture front.

The crack density at peak strength is recorded for comparison. The bulk of the final damage occurs beyond peak and is centred around the developing shear and spall zones. Beyond peak strength in shear-type failures it is often difficult to determine what proportion of the damage is primary (with respect to the development of the shear or spall zone) and what proportion represents secondary damage such as sub-axial tearing induced by asperity interference. In these simulations and in lab samples the primary rupture and displacement rate discontinuity surface changes location several times during post peak strain softening.

In most cases, the damage accumulation rate drops off considerably once residual strength is achieved and the final failure surface is established and all of the associated asperities have been destroyed. Theoretically dilation should also cease beyond this point (although this is not always the case in these simulations). The final level of damage is called ultimate damage in this work.

This continuum-discontinuum transition represented in Figure 7.36, and which is typical of failure behaviour for bonded solids, casts doubt on the validity of continuum techniques such as plasticity and damage mechanics for describing the post peak domain. A detailed examination of this behavioural domain is beyond the scope of this work, although significant advances in understanding post peak discontinuum behaviour around hard rock excavations have been made recently by Aglawe (1999).

7.4.3 Dilation Phases

For completeness it is of interest to examine the axial - lateral strain relationships (dilation) at different points in the loading and yield process (Figure 7.43). Actual magnitudes of dilation rates are likely to be unique to the model and have little resemblance to post peak response of granite, for example. Relative stages of dilation, however, as identified in Figure 7.43 for a lightly confined compression sample are likely to have basis in reality. Strains in these figures are averaged values for the sample.

An elastic phase is followed by an initial inelastic dilation phase related to systematic distributed crack nucleation. For unconfined samples the dilation is likely to be greater as new cracks extend further and open. Crack interaction is marked by a dilation rate increase, with a more substantial increase through peak strength. Full development of the rupture zone occurs during the strength drop post peak and is accompanied by the maximum dilation rate approaching 80 degrees in this case, driven primarily by kink band rotation. Dilation continues at a lower rate after shear zone

development as asperities are overcome. At very high strains (not tested) and for an infinitely larger sample, the dilation rate should drop to zero as steady state conditions are achieved.

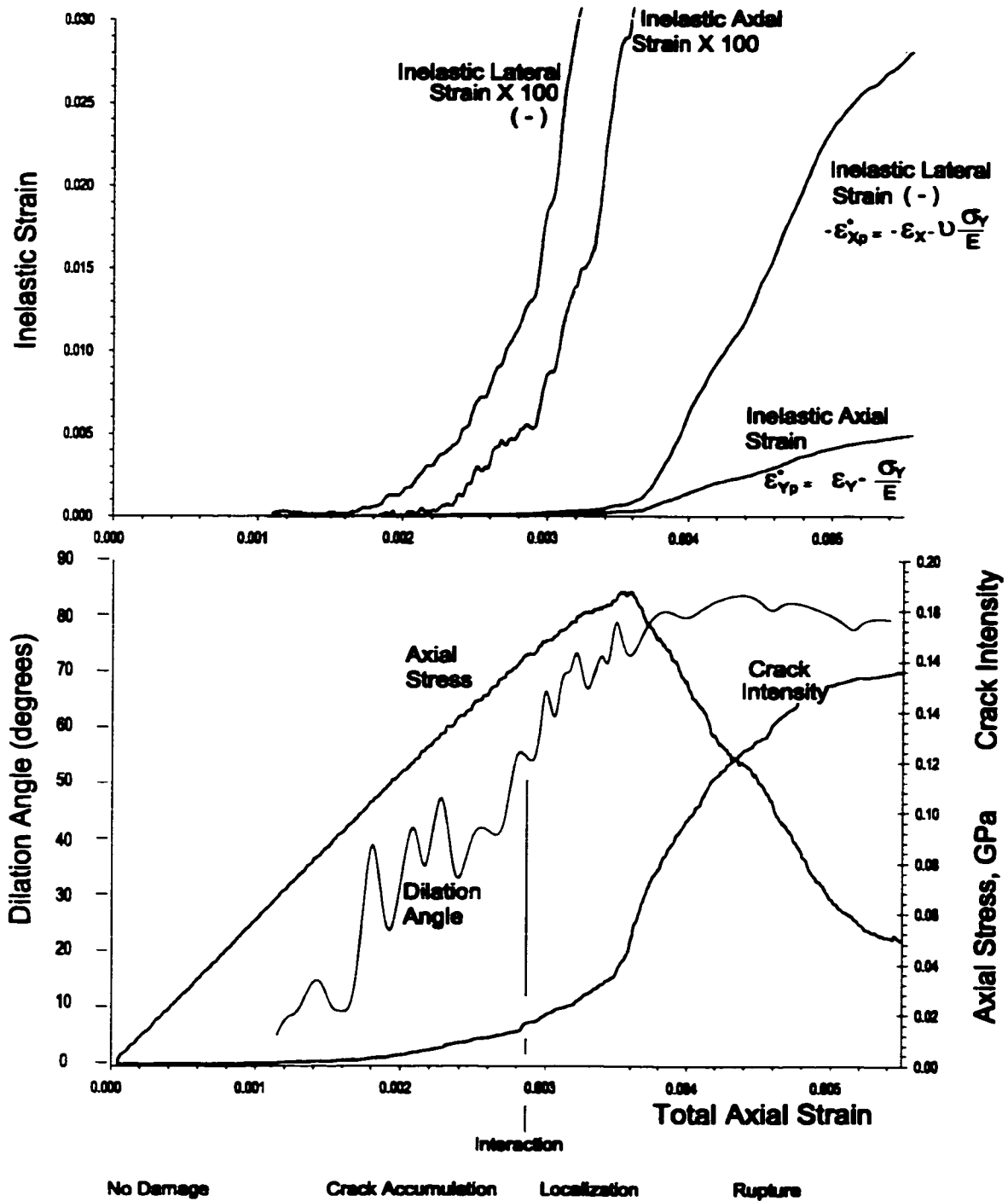


Figure 7.43: Top: Inelastic strain calculated from total strains shown at two different resolutions ("x100 magnification" gives detail at yield). Bottom: Relative lateral strains expressed as dilation angle (wrt. axial strain).

7.4.4 Tensile vs. Shear Bond Strength

The stiffness parameters and their variabilities, once established during the calibration process were not altered again during the course of this work. On the other hand the assumptions regarding bond strength properties evolved as part of this research. The default case for many of the simulations involved a bond shear strength which was 4 times the tensile or normal bond strength. In most uniaxial test cases, this resulted in a very small number of bond shear cracks (less than 2% of the total at residual strength).

The samples in Figure 7.36 were formulated with shear strength 100 times the normal bond strength. This resulted in zero shear ruptures for these confining pressures. The potential for minor shear cracking ($S/N = 4$) had little effect on the nature of damage accumulation and failure surface formation resulting in less than a 5% reduction in strength at 60 MPa and negligible difference at lower confinements.

Of particular interest in these samples is the nature of the meso- and macroscopic rupture surfaces in these simulations. Connecting clusters of unit cracks (ruptured contacts) from the sample in Figure 7.36 have been linked in Figure 7.44 to form mesocracks.

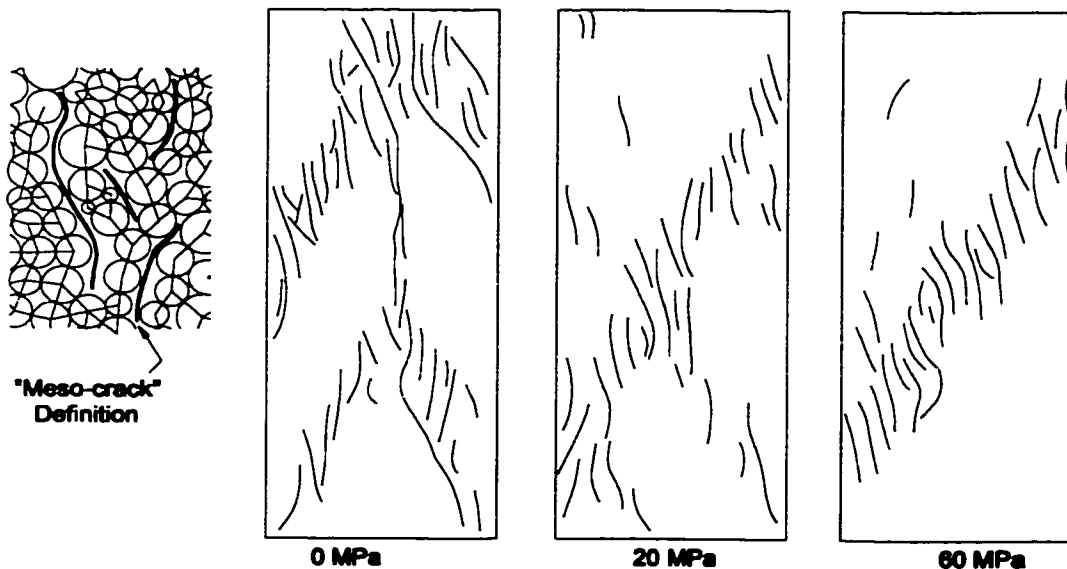


Figure 7.44: Mesocrack geometry for samples in Figure 7.36. Mesocrack definition is based on geometric crack connectivity logic as shown in left-hand inset (relative inset magnification=6x with respect to right hand images).

In turn these define sample-scale zones of spalling and shear deformation. In the unconfined case, failure occurs as a combination of local shear or kink zones and long axial macro-cracks (e.g.

centre of sample). In the confined case (20MPa) a well defined and familiar shear zone has developed with an echelon “tension” gashes reminiscent of the granite compression sample in Figure 7.46. The zone of localized kink band or shear deformation is even more pronounced in the 60 MPa sample.

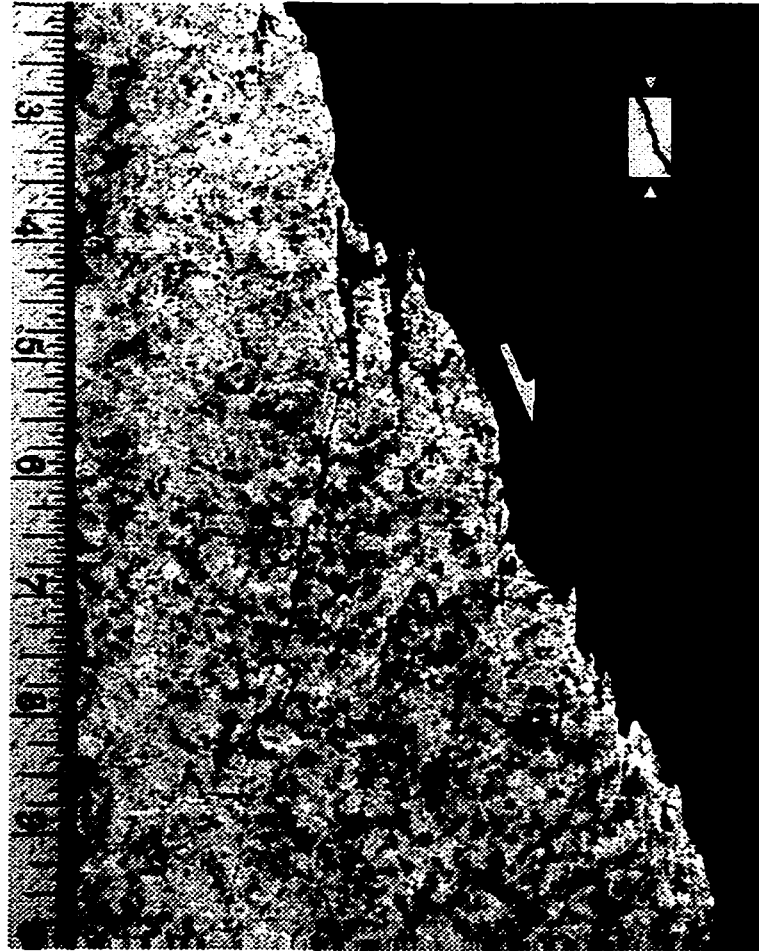


Figure 7.45: Detail of macroscopic shear "surface" from a compression test on granite showing an echelon sub-axial tension gashes (modified after Martin 1994).

It is important to note again that no shear rupture of particle contacts took place in these samples. All of the macroscopic behaviour including dilational shear is the end result of tensile damage (extension cracking). Similar behaviour was noted in the sample with $S/N = 4$ in which shear crack growth did not exceed 0.5% of the total in uniaxial tests and 2.5% in the case with $\sigma_3 = 60\text{MPa}$ (1% at peak strength).

One of the key findings of this thesis is that complex rupture processes, including macroscopic shear zone development, can be the result of elemental rupture which is exclusively tensile in

nature. This seems at odds with the underlying shear slip mechanisms which form the basis of conventional constitutive models for geomaterials. While much has been made, in fracture mechanics, of the importance of Mode I crack growth in the damage process (Chapter 6), the genesis of large scale shear zone development is still interpreted using a slip discontinuity analogues (Braemaeker and Wei 1994). Observed En echelon extension fractures and other secondary features are often described as the result of rather than the cause of shear zone development (Price and Cosgrove 1990).

In addition, conventional seismic source models used in the interpretation of local, mining induced micro-seismicity and acoustic emissions are based on a shear slip analogue (Gibowicz and Kijko 1994; Urbancic et al. 1992). Microseismic events in the vicinity of an advancing excavation, however, are observed to be depleted of shear energy (Feignier and Young 1992) and have strong dilational displacement ("moment tensor") components. This observational evidence as well as the results of this current research validates the mechanics and supports the engineering application of models based on tensile mechanisms, such as that developed by Cai et al. (1999).

Figure 7.36 and Figure 7.44 illustrate a model tested at 60MPa of confinement in which the shear zone is clearly apparent and yet all primary and secondary rupture is the result of extension cracking (normal bond failure). As confinement increases the width of the shear zone reduces (in this case limited by the kinematics of finite non-reducible particle diameters) and becomes less dilatant. If shear microcrack growth (shear bond rupture) is allowed, then such micro-rupture becomes more important (dislocation slip in feldspars for example) in the macro-scale shear zone development process at high confinements.

It is interesting that the shear zone develops as a planar feature, with subsequent coplanar, propagation. Braemaker and Wei (1994) demonstrated, using a non-dilatant slip discontinuity model, that this was the mode which produced the "maximum release of strain energy". This appears to be the case, as well, when the shear propagation is related to frontal extension cracking as in these simulations.

The primary purpose of this work is to study the nature of crack accumulation and most importantly, crack interaction in a variety of confinement conditions. The mechanics of crack interaction determine the ultimate strength as well as the ultimate rupture geometry.

The orientation, β , from the vertical, of the final shear zone ranges from 26 degrees for unconfined samples to 30 degrees at 60 MPa. Using the familiar derivation:

$$\beta = 45^\circ - \frac{\phi}{2} \quad [7.31]$$

the friction angle (for a Mohr-Coulomb material) is back-calculated as 38 to 30 degrees (at 0 and 60 MPa respectively). This range corresponds to the "measured" value estimated from confined tests in Figure 7.31 but not to the nominal friction angle of 45 degrees specified for the slip contacts. There is evidence, however, to suggest that for brittle bonded solids, the orientation of the ultimate shear zone is related to crack interaction potential rather than internal friction.

Du and Aydin (1991) and Dey and Wang (1981) demonstrated that the critical angle, in fracture mechanics models, for interaction between two extending cracks is 28 to 30 degrees. This corresponds to the preferred orientation in PFC simulations where cohesive shear crack accumulation is hindered (by a high contact bond shear strength) or prevented (Figure 7.46a). When shear crack growth is favoured (for example by an S/N ratio less than or equal to unity). The ultimate failure surface in the PFC samples is oriented at close to 45 degrees (equivalent to $\phi=0$) regardless of the contact friction angle active after bond rupture (Figure 7.46b). In these cases the peak strength is also cohesive ($\phi=0$) beyond a threshold confinement (Figure 7.30).

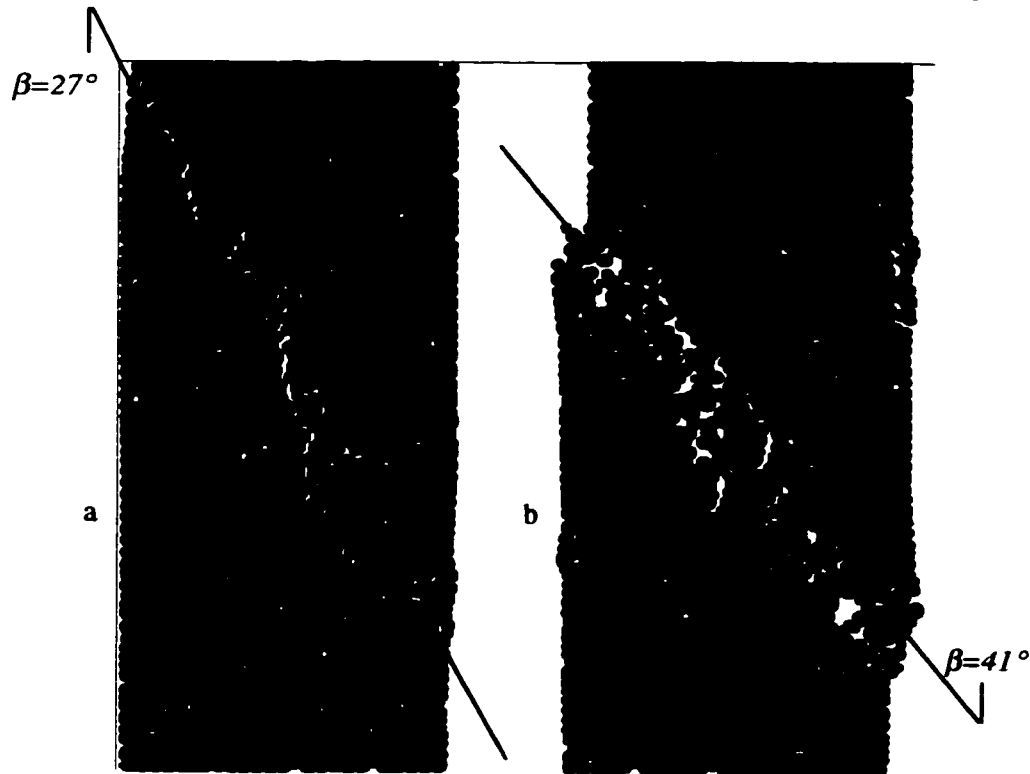


Figure 7.46: Sample failure for shear/normal strength ratios: $S/N=4$ (a) and $S/N=0.5$ (b). Ratio of shear to normal cracks at end of test: 2% (left) and 700% (right). Inter-disc friction angle (after bond rupture) in both cases = 45 degrees.

7.4.5 The Importance of Crack Interaction

The critical separation for interaction, according to Lockner et al. (1992) and Madden (1984), is given by $S/d < 1$ to 1.1, where S is the separation and d is the crack length. Figure 7.41 showed that non-linear axial behaviour, which implicitly signals the oblique interaction of axial cracks, is coincident with a significant increase in crack pairs separated by less than one crack length. This threshold is the most important for understanding rock strength.

Under compressive loading, isolated axial cracks (parallel to maximum compression) do not distort the axial stress field. Interacting cracks on the other hand disturb the flow of stress, creating new and increased local stress concentrations, leading to the attraction and acceleration of local damage accumulation. Subsequent crack accumulation and propagation is no longer a function only of the applied stress and the elemental strength distribution within the assembly but rather, is controlled by these larger scale stress concentrations.

Lajtai (1988) showed that long-term strength of granite lab samples (under sustained load) converged asymptotically to a threshold equivalent to that of volumetric strain reversal (shown in Chapter 6, for uniaxial cylindrical samples, to be equivalent to the threshold of crack interaction or axial strain non-linearity). It will be shown in this chapter that crack interaction, hereby determined to represent true yield strength, occurs at a critical crack density, which is also related to a critical extension strain normal to the direction of major principal compressive loading.

This crack density is sensitive to crack length, which is constant in PFC simulations. In low confinement conditions, however, initiating cracks in materials such as granite extend significantly further for the same deviatoric stress level. Longer cracks interact with fewer initiation events (critical separation is equal to the crack length). In other words, the critical crack density is reached with fewer initiation events (less crack accumulation). Isolated initiation events are stress driven and so crack interaction and sample yield occur at a lower deviatoric stress when crack extension is encouraged (low confinement).

This phenomenon is not present in PFC simulations due to the absence of crack tip concentrations that are present in real cracked solids. Fixed length cracks can coalesce to form macrocracks but cannot spontaneously extend in isolation. This limitation is particularly evident in the direct tensile tests in Section 7.9. The PFC models however afford the unique opportunity to study interaction in the absence of crack extension (crack accumulation only). The findings of this model study can then be extrapolated (Chapter 8) to incorporate the effects of crack extension in low confinement insitu conditions and to discuss the general impact on insitu strength reduction.

7.5 UNIAXIAL COMPRESSION TEST SUMMARY

A number of uniaxial tests were performed during the course of this work, each with a different random seed for disc generation and contact property assignment, resulting in unique "specimens" for each test. In all cases the mean contact length (and disc diameter) was approximately 3.1mm while the sample size ranged from 40x15mm to 450x180mm, maintaining a sample height to width ratio of 2.5-2.7. The stiffness parameters were maintained as listed in Table 7.2. Only the general range of contact parameters can be specified within these samples. Contact constitutive models are highly simplified. Actual sample strength, damage thresholds and complex non-linear "macroscopic" behaviour are stochastic products of each assembly. As such the results presented hereafter should be viewed as numerical experimentation rather than deterministic numerical modelling. Accepting the limitations of the model described thus far, the PFC assemblies will hereafter be discussed as a series of virtual laboratory test samples.

In order to establish a set of baseline properties and threshold values, this section summarises the discussions to date with reference to uniaxial compression samples. Tables 7.3 and Table 7.4 summarise stress, damage and strain parameters which define the various damage and accumulation thresholds discussed in this thesis. The thresholds are determined using the relationships discussed in Section 7.6. 14 uniaxial test samples are represented in the data in the following tables. Only samples within the dimensional range from 210x80mm (2100 discs) to 300x120 (4500 discs) were used to obtain the average values in this table to avoid significant scale effects (Chapter 8). Shear crack growth had negligible effect on uniaxial samples when ($S/N=4$) and so these results are pooled with several of the "no shear" samples ($S/N>10$).

Table 7.3: Primary mechanical properties (14 samples).

Property	Mean	St. Dev. (Relative)
Young's Modulus (between 25% and 50% UCS) (GPa)	58400	740 (1.2%)
Poisson's Ratio	0.254	0.0067 (2.8 %)
Unconfined Compressive Strength, UCS (MPa)	172	6.7 (3.9 %)
Systematic Crack Initiation Stress (MPa)	90	6.0 (6.9%)
Crack Interaction (Initial Yield)		
Stress (MPa)	146	6.4 (4.3%)
Lateral Extension Strain	0.00071	0.000032 (4.5%)
Critical Crack Density, χ_d	0.030	0.0023 (7.7 %)
Crack Anisotropy		
Maximum (at interaction or localization)	0.78	0.04 (6.5%)
Ultimate (at residual strength)	0.5	0.02 (4.4%)

Table 7.4 Detailed Damage Threshold Data

Threshold:	First Crack	Systematic Damage	Crack Interaction	Localization	Peak	Ultimate
Measurement: (prior to threshold)	mean (n=14) standard deviation (relative st. dev. %)					
Axial Stress MPa	49 5 (10)	90 6 (7)	147 6.4 (4)	161 4.3 (3)	176 6.7 (4)	28 8.9 (32)
Axial Strain (x10 ⁻³)	0.73 0.36 (49)	1.74 0.15 (9)	2.7 0.24 (9)	3.25 0.27 (8)	3.5 0.31 (9)	5.8 0.67 (12)
Lateral Strain (x10 ⁻³)	0.23 0.04 (18)	0.45 0.04 (9)	0.71 0.032 (5)	1.04 0.056 (5)	1.55 0.13 (9)	28 11 (39)
Crack Intensity; $\chi_d = A^{-1} \Sigma d^2$ (d=2r) Note: $\chi_d = 4\chi$	0.0026 0.0021 (80)	0.0078 0.002 (26)	0.030 0.0024 (8)	0.050 0.0046 (18)	0.085 0.0053 (13)	0.30 0.027 (18)
Shear/Normal Cracks (when applicable)	0.23 0.18 (76)	0.12 0.96 (80)	0.056 0.027 (49)	0.044 0.021 (47)	0.039 0.01 (27)	0.018 0.0045 (25)
Crack Anisotropy	0.36 0.26 (73)	0.65 0.1 (15)	0.78 0.05 (7)	0.78 0.033 (4)	0.76 0.031 (4)	0.49 0.02 (4)

These thresholds will be compared, in the following sections, to their counterparts in direct tension, indirect (Brazilian) and confined tension, and confined compression. This study will provide insights into the nature of damage accumulation in the absence of unstable crack propagation (resulting from crack tip singularities). The role of crack extension is examined in Chapter 8. Table 7.5 provides a comparison between the damage thresholds in the PFC simulations of uniaxial compression and the corresponding thresholds in Lac du Bonnet granite.

Table 7.5: Uniaxial compressive stress in MPa and lateral strain (x10⁻³) damage thresholds in PFC simulations and Lac du Bonnet granite for 240 level to surface quarry.

	First Crack Initiation	Systematic Crack Initiation	Crack Interaction	Crack Localization	Peak Strength
PFC Model	49 (0.23)	90 (0.45)	146 (0.71)	161 (1.04)	176 (1.55)
LdB Granite	64 (insitu) to 80 (0.30)*	93 to 103 (0.35)*	134 to 173 (0.7)*		180 to 225 (2.4)*

* lateral strains for surface samples only

As a further indication of the general validity of the linear bonded contact model for simulation of crack accumulation and interaction, Figure 7.47 compares the crack intensity thresholds from Table 7.4 with experimental studies on marble by Wong et al. (1996). In this study, the initial crack density on a two-dimensional section through each sample was compared with the subsequent result from a UCS test on the same material. The crack densities calculated for the marble samples have been multiplied by a factor of $4\pi/3$ to account for the difference in crack density definitions between this current work and that of Wong et al. 1996. In Figure 7.47 the crack density at peak strength in Table 7.4 corresponds to the minimum initial damage state plotted by Wong et al. (1996). For crack densities above this level, the peak sample strength drops rapidly.

At damage levels in excess of the ultimate threshold (at residual strength) in Table 7.4, the marble strength becomes asymptotic at a lower bound which is similar to the crack initiation thresholds for the PFC samples. While the similarity of the magnitudes (for marble and for PFC simulations) of this lower bound are probably coincidental, the general concept of strength reduction, with increasing damage, to a threshold defined by the threshold for (new) damage initiation, is central to this thesis, since it provides another validation of the empirical insitu yield criteria summarized and demonstrated in Chapter 5.

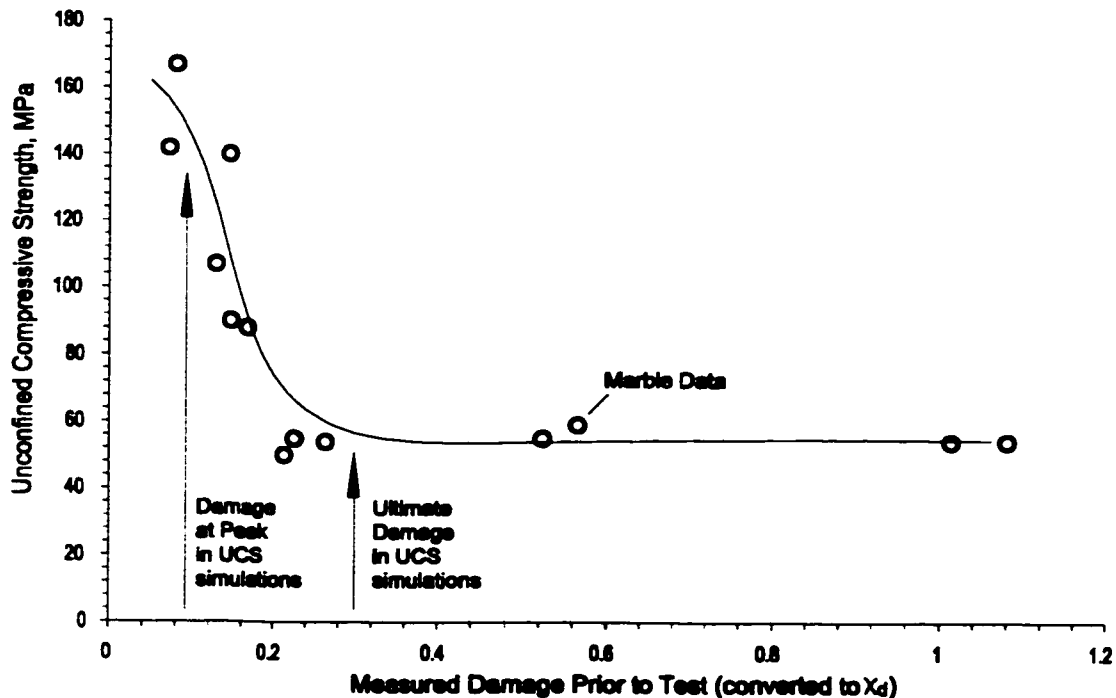


Figure 7.47: Comparison of PFC damage (at peak strength and at residual strength or ultimate damage) with marble test data from Wong et al. (1996).

7.6 COMPRESSION AT LOW TO MODERATE CONFINEMENT

The next series of simulations in this chapter involve confined compression tests. As in the uniaxial compression simulations, the primary focus here is the development of damage and lateral strain and the thresholds of damage initiation, systematic damage nucleation, crack interaction, strain localization and peak strength.

Shear/normal bond strength ratios of 4 and 100 were used in these simulations. No noticeable difference was observed between the two sets of tests. In the lower ratio tests, shear cracks increased as a percentage of the total at every stage but did not appear to be related to crack interaction and had a minor effect on behaviour. At higher confinements shear cracks may become a dominant damage mechanism. This study is restricted to relatively low confining stress (below 60 MPa) and so the data from the two sets of tests are analysed together. Figure 7.48 illustrates stress-strain data for one set of tests ($S/N = 4$).

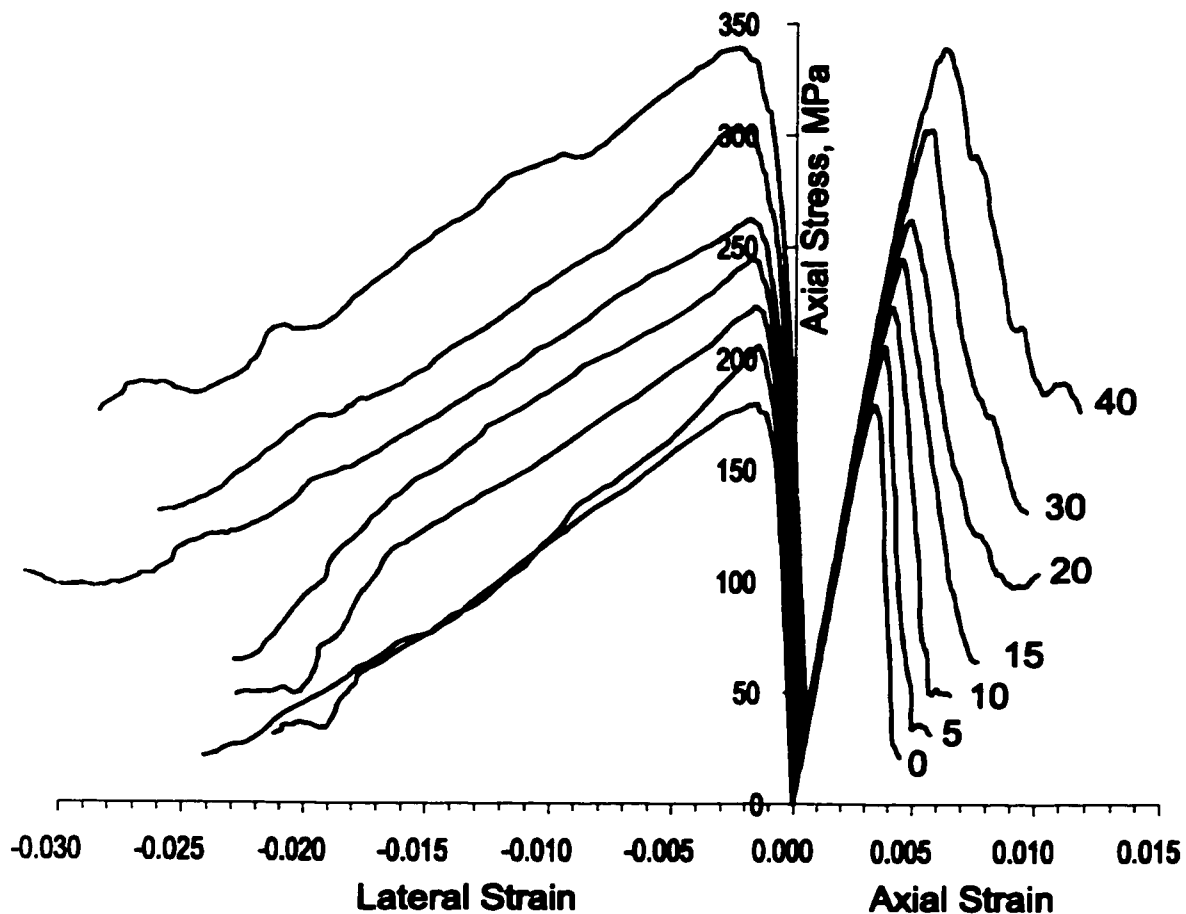


Figure 7.48: Stress – strain response for typical confined compression test simulations ($S/N = 4$; sample size 400x150mm).

7.6.1 Damage Thresholds

Figure 7.49 illustrates damage thresholds determined using the techniques described in Section 7.6. The thresholds, from bottom to top, are first (new) crack initiation, systematic (constant rate increase, tangent strain ratio increase) damage accumulation, crack interaction (clustering, crack rate acceleration, axial strain non-linearity), localization (2D volumetric strain reversal) and peak strength.

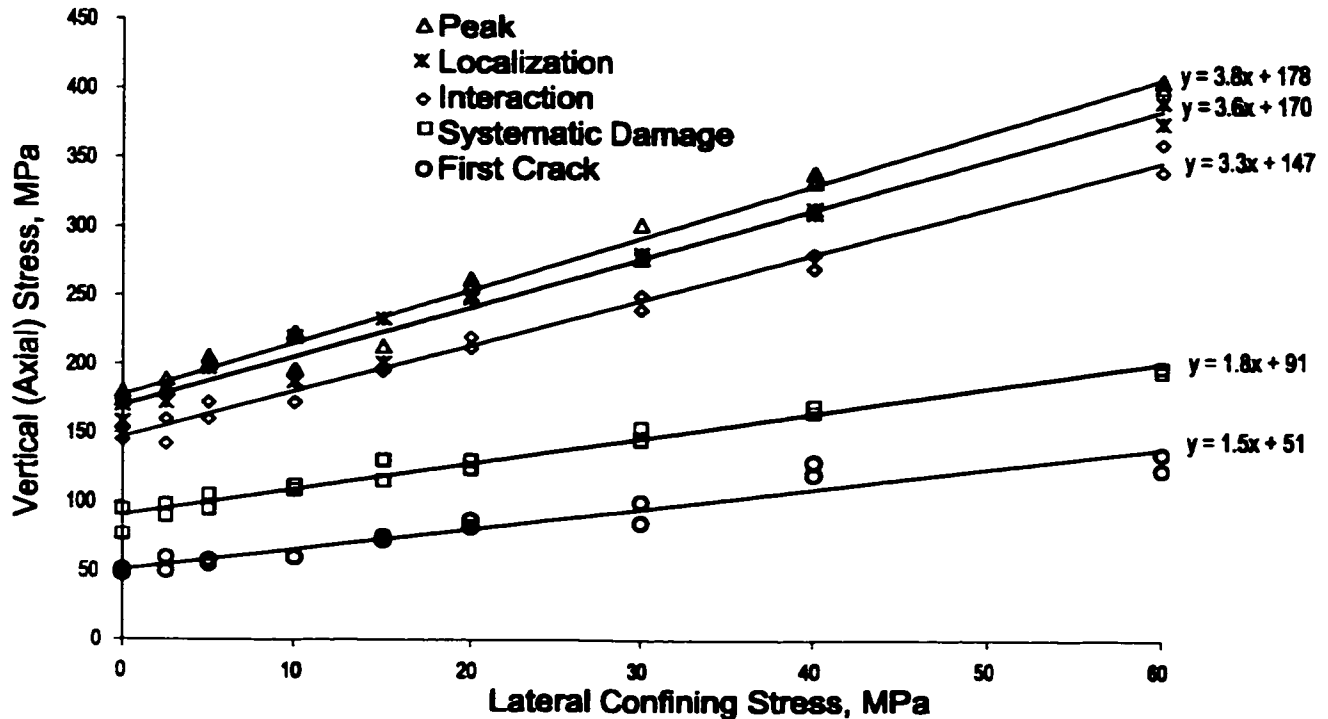


Figure 7.49: Damage thresholds for confined compression test simulations.

The peak strength envelope in Figure 7.49 is approaching the maximum confinement dependency achievable with this model (slope of 3.8 to 4 independent of contact friction as shown in Figures 7.30 and 7.31). Peak strength in this model is insensitive to the frictional slip resistance between broken contacts (friction is not active until after bond rupture) since more than 99% of all cracks prior to peak are extensile. Lower values of bond shear strength (S) can reduce this slope to unity for higher confinements (Figure 7.30) as shear crack growth becomes dominant.

In the opinion of this author, the limiting slope of the peak strength threshold, with respect to confinement, is controlled by the particle geometry. Mesocracks cannot form in a collinear fashion but rather, they must take a tortuous path between the particles. In a granite the cracks can grow through the grains in the later stages of pre-peak loading (as observed by Martin 1994)

resulting in arrays of high aspect ratio rock bridges between parallel cracks. This would yield a higher crack anisotropy than the maximum recorded in these tests (0.8).

Rothenburg and Bathurst (1989) have demonstrated that frictional strength of sands can be directly determined as a function of contact and internal force anisotropy. It is interesting that the slope of 3.9 found to be an upper bound in these bonded particle simulations is very similar to results obtained by Hoek and Brown (1980) for marble (4.0), sandstone (4.4) and limestone (3.8). These rocks are granular in nature with weak grain boundaries. As such the crack pathways are likely to be inter-granular as is the case with PFC simulations.

Rocks which are dense and polycrystalline can sustain trans-granular crack growth and therefore higher crack anisotropy prior to peak strength. It follows from the above logic, then, that these rocks should have higher confinement dependencies in terms of peak strength. Examples from Hoek and Brown (1980) include granite (9.0), gabbro (8.0), chert (8.0) and quartzite (7.0).

Localization marks the onset of internal rotation and strain concentration (from the volume to the failure plane). Given the internal geometry of the disc model, and the freedom of rotation for unbonded discs, it is not surprising that there is little lag between this localization threshold and peak strength. This contrasts with the results obtained for granite in the previous chapter.

Trans-granular crack growth in undamaged granite samples does not occur until after crack interaction has initiated (critical crack damage as defined by Martin 1994). The bonded lattice model should therefore offer a valid analogue for damage accumulation up until this compressive stress threshold. In tension, cracks in granite extend spontaneously upon initial nucleation. This does not occur in the PFC simulations as discussed in the next section. The relative uniaxial compressive stress at crack interaction is approximately 85% of the *UCS* and the slope with respect to confinement is approximately 3.3. These values are close to the relative threshold and slope in granite.

Likewise the slopes of the damage initiation and systematic damage accumulation thresholds in Figure 7.49 reflect the range of 1.4 to 2 quoted in Chapter 6 for hard rocks. In addition, the relative uniaxial intercepts of 30% and 50%, respectively, of the *UCS* also reflects real hard rock behaviour.

7.6.2 Damage and Lateral Strain

Figure 7.50 shows the crack intensity measured at crack interaction, peak strength and at residual strength (ultimate damage). It is evident that crack interaction occurs at a constant crack density in these simulations. In these examples the random seed is varied so that the samples are effectively unique. A slight increase is evident in the 60 MPa sample, likely due to the development of spurious shear cracks.

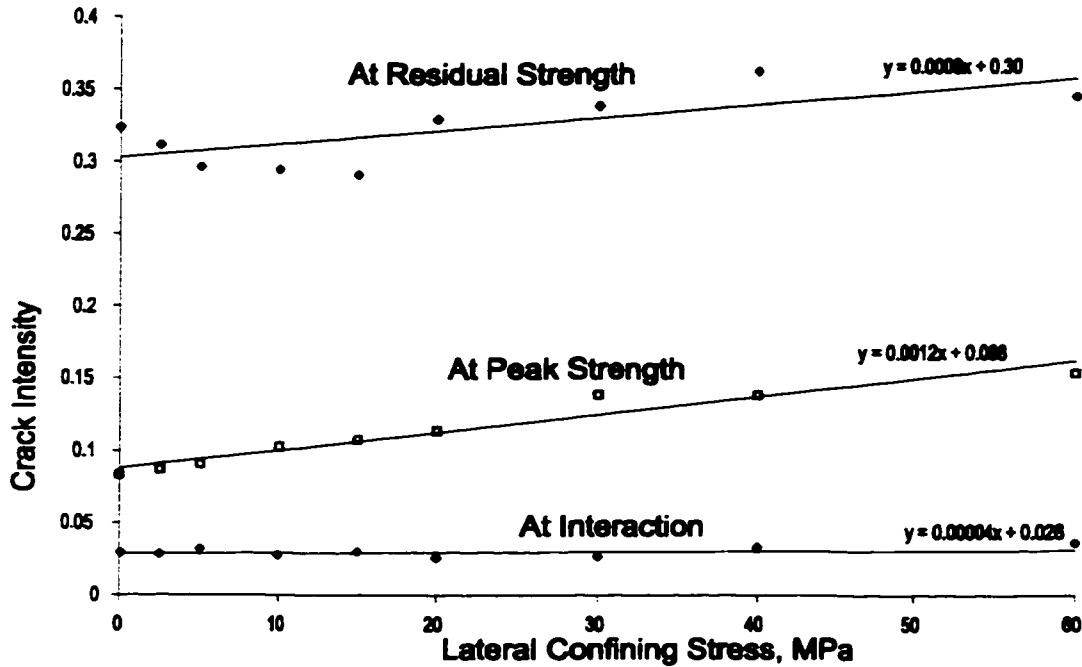


Figure 7.50: Crack intensities measured at interaction peak and residual strength.

This observation is consistent with one of the key hypotheses of this thesis. Initial crack nucleation involves distributed isolated events driven by elemental strength distribution (a function of bond strength heterogeneity and lattice geometry variation). Crack interaction or true yield occurs when enough cracks have accumulated to increase, to near certainty, the probability that the next nucleating crack will fall close enough to another to induce interaction.

The total amount of cracking required to completely fail the sample is reflected in the range of crack intensity 0.3 to 0.35. A slight increase is evident for confined samples although this trend is not well defined. The crack damage present at peak strength, on the other hand varies from 30% of the ultimate total for unconfined samples to 50% of the total at 60 MPa confining stress. This reflects the stable nature of micro and mesocrack growth at higher confinements.

In the set of tests in which $S/N=4$, shear cracks become more prevalent as confinement is increased. In the extreme, it should be expected that non-dilatant shear crack propagation would dominate failure at very high confinements. For the low to moderate confining stresses investigated here, the relative abundance of shear cracks is illustrated in Figure 7.51 for the thresholds of crack interaction, peak strength and residual strength.

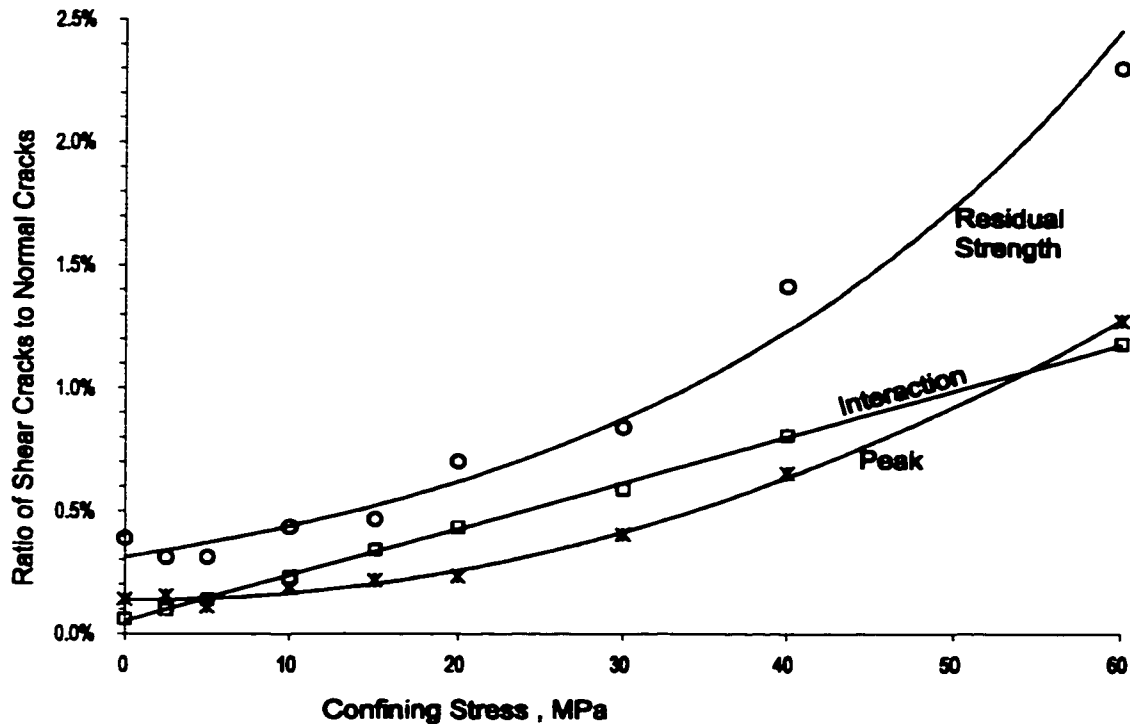


Figure 7.51: Relative proportions of shear cracks with respect to normal cracks for samples with $S/N=4$.

Figure 7.52 illustrates iso-intensity contours for crack damage in principal stress space. This graphic is limited to the stress path shown. This plot is derived by contouring (using cubic polynomial surface regression in the data analysis software SURFER) the stress paths for the various tests using crack intensity as the z variable. There is an increase in crack intensity at interaction for higher confinements but in general the interaction threshold corresponds to an iso-intensity of approximately 0.03. This is only 10% of the cracking required to fail the sample but represents the onset of yield. Only crack intensities up to peak strength are shown in Figure 7.52.

Figure 7.53 illustrates a similarly derived iso-strain plot for total lateral strain including initial compression under the confining stress. Under higher confinements, initial cracking occurs under a state of net compressive strain. At the point of crack interaction, however, the threshold extension strain is relatively independent of confinement.

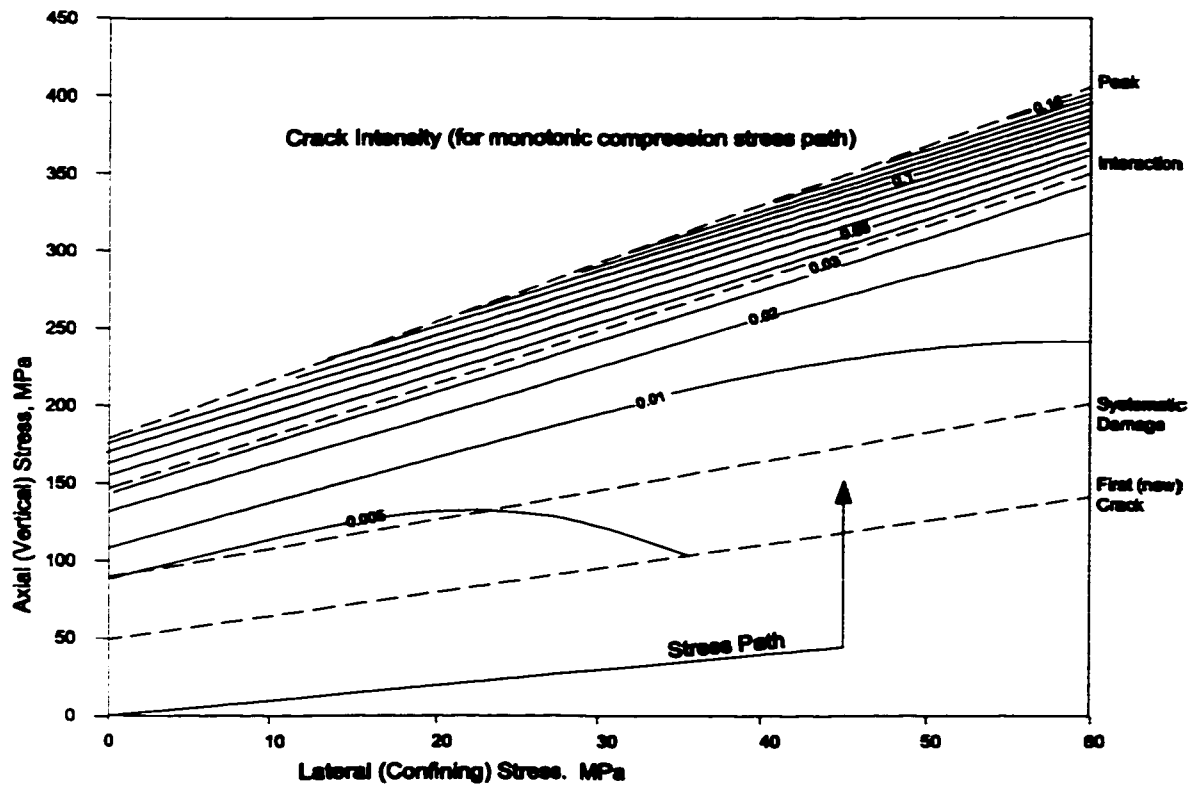


Figure 7.52: Crack density intensity contours for stress path shown.

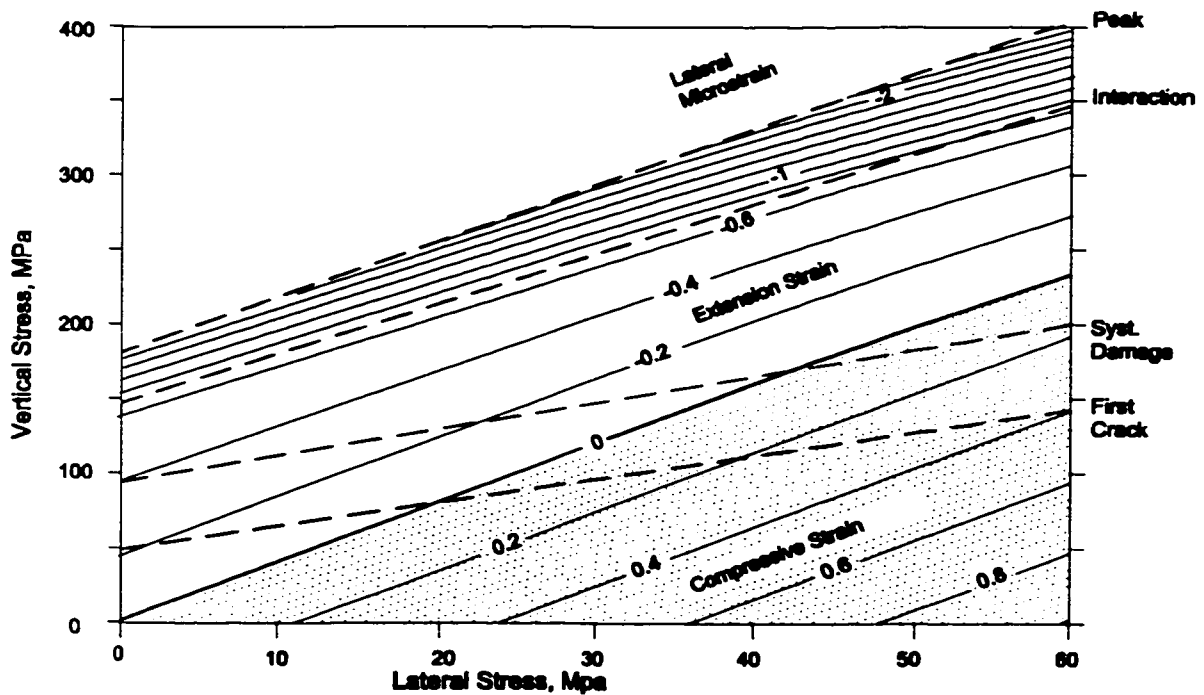


Figure 7.53: Contours of total lateral strain for the same stress path as Figure 7.52.

A summary of the lateral strain measurements (average within three measurement circles) is given in Figure 7.54. The equivalent elastic strain (based on the stresses at interaction) is shown for comparison. The reason for the increase in inelastic dilation, prior to interaction, at higher confinements is unclear.

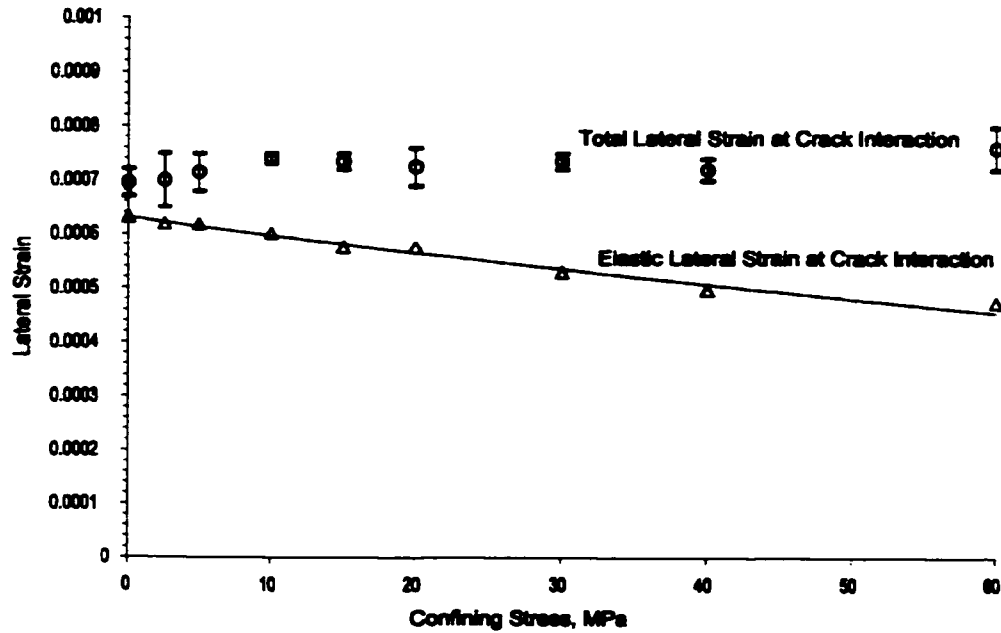


Figure 7.54: Total and elastic lateral strains at crack interaction.

7.6.3 Peak and Post Peak Strain

Figure 7.55 illustrates the effect of damage interaction on axial strain (parallel to maximum compression and primary microcrack orientation). The total axial strains are plotted (bottom axis) as are the inelastic (or plastic = p) strain calculated as:

$$\varepsilon_{axial}^p = \varepsilon_{axial} - \frac{1}{E}(\sigma_{axial} - \nu\sigma_{lateral}) \quad [7.32]$$

where E and ν are tangential values obtained prior to systematic crack damage accumulation. Sample peak strength at higher confinements requires increasing degrees of inelastic strain. This is a reflection of the additional crack accumulation required to propagate a through-going failure surface at higher confinements. In contrast to the confinement related increase in axial and lateral plastic strain prior to yield and peak strength, the post peak dilation reduces for confined samples as shown in Figure 7.56. This plot compares the inelastic portions of deviatoric and volumetric strain. These are obtained in a fashion similar to Equation 7.32 involving the bulk and shear moduli of the assembly (determined in Section 7.5).

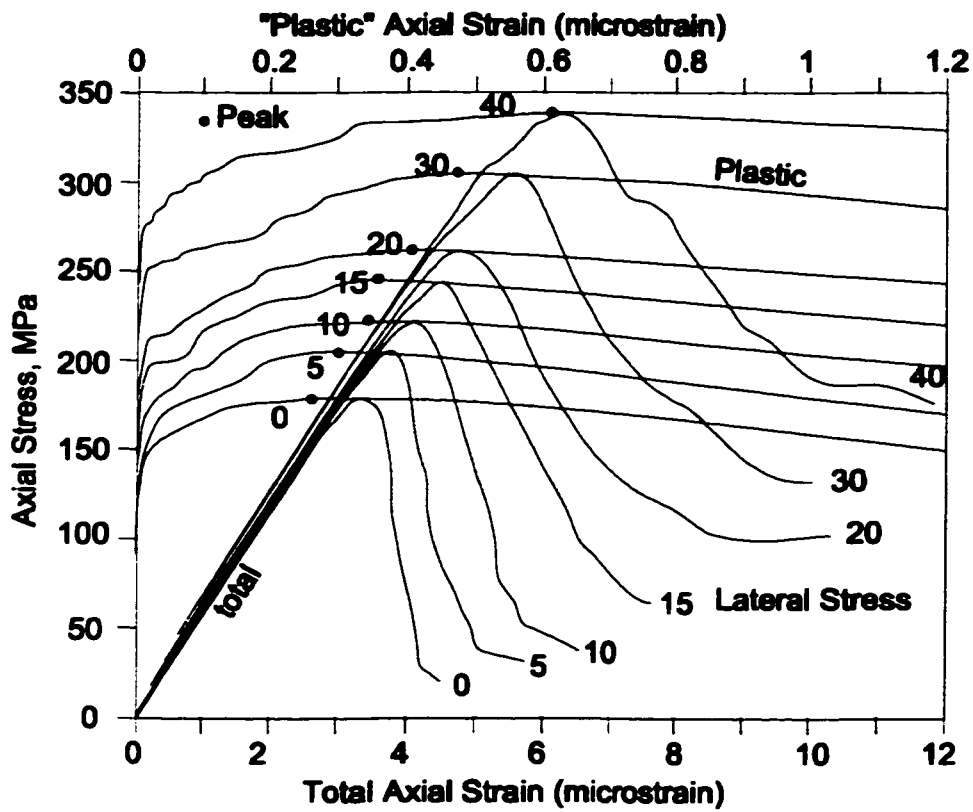


Figure 7.55: Total and inelastic axial strain for confined compression.

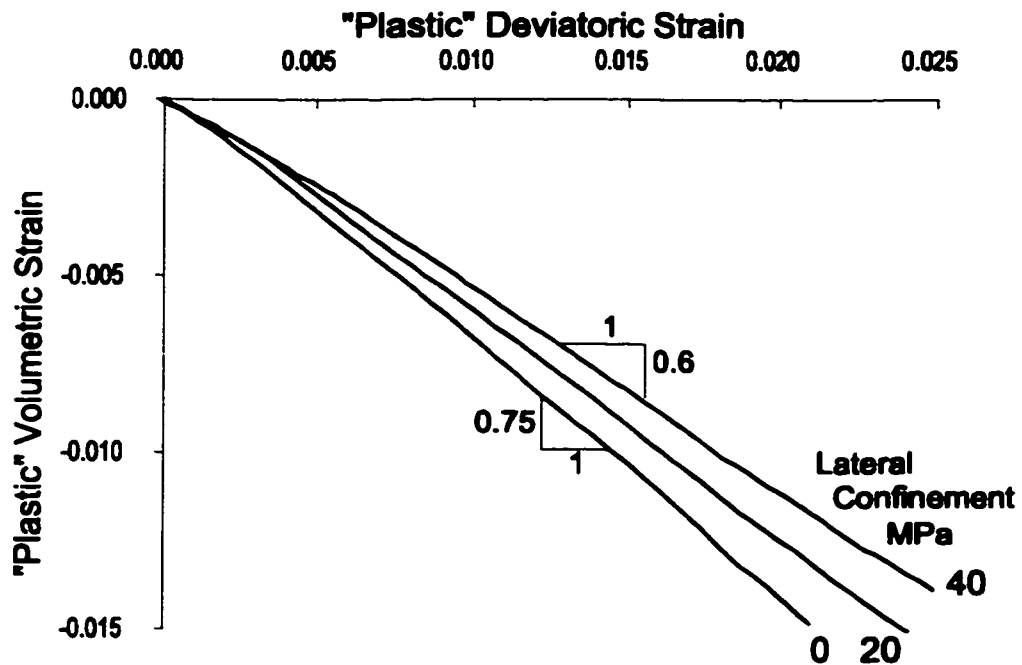


Figure 7.56: Comparison of inelastic deviatoric and volumetric strain.

7.6.4 Compression Test Simulation Summary

The series of numerical simulations in unconfined and confined compression provide a basis for understanding the role of damage accumulation and interaction in real materials. For example, it is evident that crack initiation is not related to average lateral (crack normal) extension strain in these simulations nor, apparently in real rock such as granite (Chapter 6). This is contradictory to the conventional interpretation of Stacey's (1981) extension strain criterion. It is, rather, related to the lower bound strength of isolated elements (trellis cells or sliding cracks, for example). Crack initiation at higher confinements, in fact occurs under conditions of average lateral compressive strain. In such an instance, individual elements or cells experience tensile deformation of lateral contacts, but as a whole the sample experiences compressive strain relative to the initial state.

Crack interaction, on the other hand, is related to a critical crack density (for low to moderate confinements) and also a corresponding critical extension strain. This strain does not necessarily correspond to elastic strains. The accumulated plastic strain (lateral) prior to crack interaction is greater in the case of confined samples. Dilation after yield, on the other hand, reduces as confining stress increases. After crack interaction takes place, full localization and peak strength require larger amounts of damage and corresponding plastic strain at higher confinements.

The confinement dependency of the crack interaction threshold is a function of continuum stress-strain relationships rather than frictional mechanisms. The slope (with respect to confinement) of the peak strength envelope also has little to do with the specified contact friction angle. Apparent friction in granular materials develops as a result of crack anisotropy (Rothenburg and Dusseault 1987; Rothenburg and Bathurst 1989; Heidari 1995; Quadfel 1998). While difficult to analytically describe, the same must be true for cracks (and the intervening material bridges) in a bonded solid. Confinement dependency increases with greater axial alignment and greater average length:spacing ratio of the accumulating cracks. Crack anisotropy is limited (to about $\alpha < 0.8$) in the bonded disc simulations due to the inability to fracture through the discs. In real rock such as granite, longer cracks and higher aspect ratio contact bridges within the developing failure zone result in higher values of apparent friction. Longer cracks at lower confinements lead to higher confinement slopes (and a non-linear strength envelope).

The point of departure, in terms of behavioural similarity, between the bonded contact analogue and the granite samples in Chapter 6, is the point of crack interaction. In order to further understand the relationship between damage initiation, crack interaction and material strength, a series of tensile test simulations are carried out here to track these thresholds in tensile conditions.

7.7 TENSILE TEST SIMULATIONS

Granite sample behaviour under direct tension and compression was compared in Chapter 6. The stress (tensile) at which failure occurred in direct tension was found to be less than one thirtieth ($1/30^{\text{th}}$) of the uniaxial compressive stress. Plane and axi-symmetric formulations of the Griffith criterion predict ratios of $1/8$ and $1/12$ respectively. Interestingly, crack initiation, as measured by lateral strain measurements and by acoustic and microseismic monitoring, occurs at approximately 9 to 11 times the lab tensile strength for field and lab conditions respectively. In addition, the tensile test data examined in Chapter 6 suggests that no detectable damage occurs prior to rupture. This evidence suggests that sample rupture in tensile tests is related to crack initiation, whereas in compression, crack accumulation must occur and individual cracks must interact to create critical macroscopic rupture surfaces. The reasons for this are given by the familiar schematic by Hoek (1968), shown again in modified form in Figure 7.57. Cracks initiated in tension immediately propagate in an unstable fashion because each incremental crack extension leads to an increase in the crack tip stress concentration. This means that once a crack is initiated, it cannot stabilize until the boundary stress is removed.

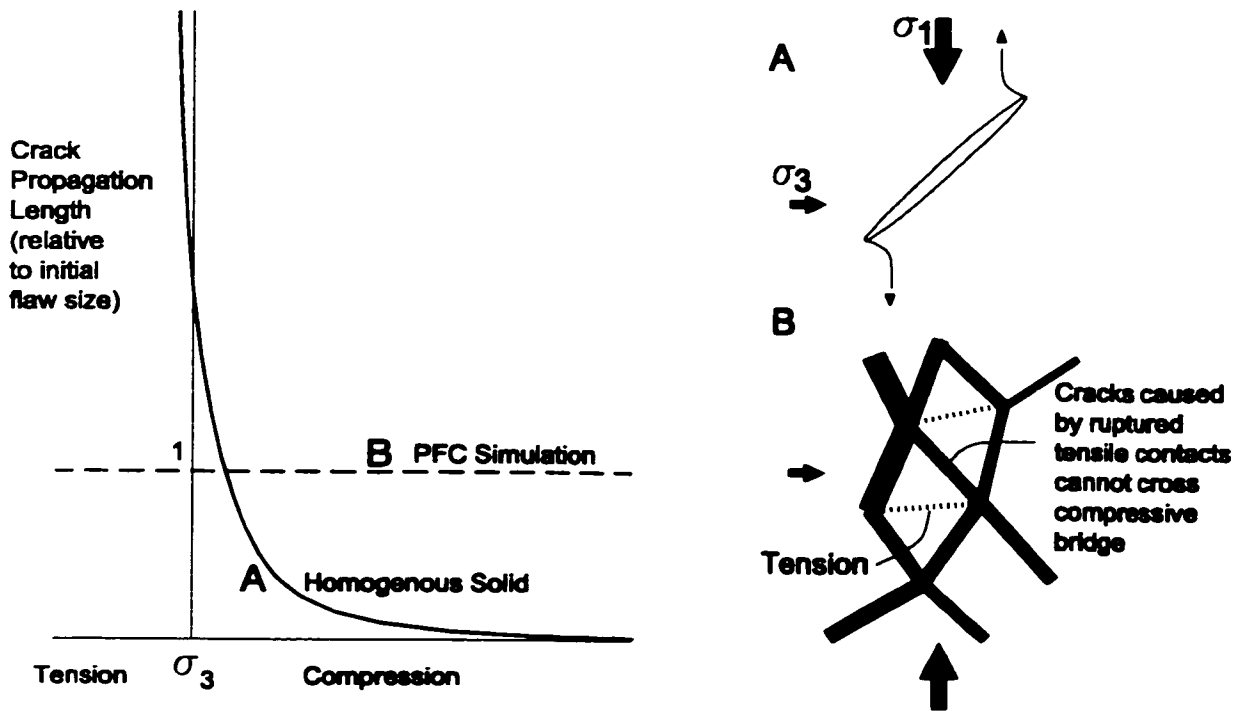


Figure 7.57: Comparison of spontaneous crack propagation (upon initiation) as a function of confinement, for (A) homogenous solids and (B) lattice or bonded contact model.

In contrast, a PFC bond rupture, in isolation, does not create the same singular stress concentration present at the tip of an extending microcrack within a continuum. The loss of a contact may result in a finite increase in load in neighbouring, and similarly oriented intact contacts. This increase is not necessarily enough however, to cause subsequent rupture of these adjacent contacts. Due to stiffness variability, the load previously carried by the ruptured contact may be redistributed away from the neighbouring bonds. This is called lattice trapping.

Since bond rupture in a heterogeneous lattice does not mandate an overload in neighbouring contacts, crack propagation length is therefore the same as the initial trellis cell dimension (analogous to the initial flaw size in fracture mechanics) as shown in Figure 7.57. Accumulation of isolated cracks in PFC simulations is therefore a highly stable process, requiring further load for each additional crack to occur. This is true in tension as well, contrasting sharply with the real behaviour of rocks such as granite in which tensile failure is determined by the weakest link (as discussed in Chapter 8).

While this is a major limitation of linear bond lattice models such as PFC, it also provides an opportunity to examine tensile behaviour in the absence of crack propagation. Once again, the focus of this discussion is the nature of damage accumulation and interaction. Post peak or post rupture behaviour, typically the domain of damage mechanics, is beyond the scope of this work.

7.7.1 Tensile Test Samples

Two types of samples are prepared and tested in this Section (Figure 7.58). These are a rectangular sample, with a horizontal dimension equal or greater than twice the vertical dimension, and a dumbbell sample similar to the granite test samples in Chapter 6. In either case, the sample was lithified as a square and subsequently cut to shape (by eliminating unnecessary discs and contacts) to ensure uniformity of disc and contact placement at the top and bottom edges of the final sample. It was felt that tensile samples could be more susceptible to edge flaws than samples tested in compression. For the confined tensile tests samples in Section 7.8, the sample was lithified in its final form since a smooth upper and lower surface were required for confinement application.

A column of discs at each lateral end of the specimens served as constant velocity platens. Discs at opposite ends had constant and opposing assigned velocities, placing the sample in increasing tension. Unbalanced horizontal forces in the platen discs resulting from the maintained velocities were summed to compute the applied lateral tensile stress (dividing through by sample height).

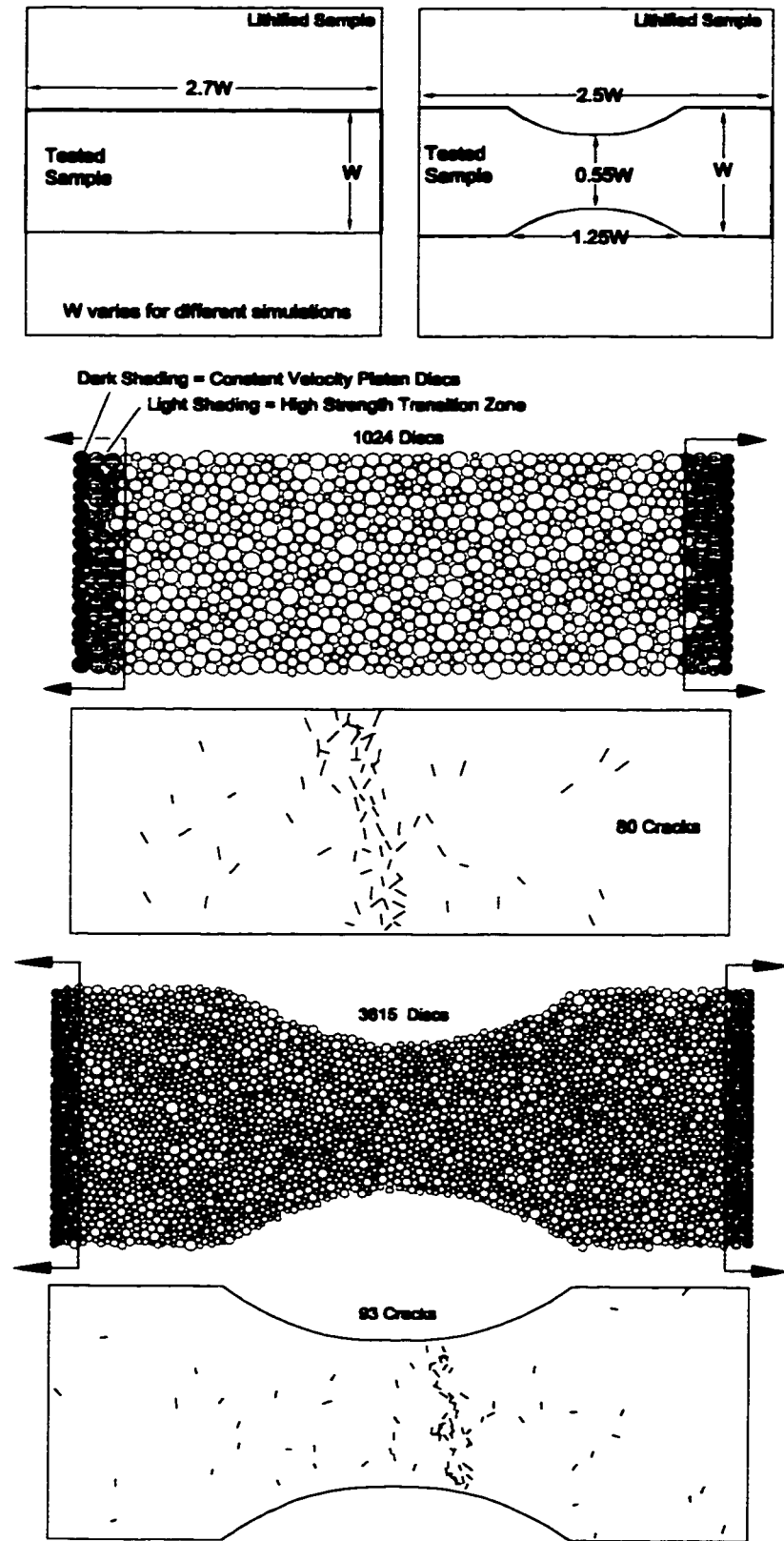


Figure 7.58: Two sample configurations (rectangular and “dumbbell”) for tensile test simulations.

Stresses and strains are measured via the platen displacements and forces and are also computed via a centrally located measurement circle. In the case of the dumbbell sample, stress, the lateral stress at the sample centre (mid), can be also be estimated using the total end force divided by the central dimension ($0.55W$). Strains computed within a circle inscribed in the central neck of the sample are used for these tests. For elastic strain only, the internal (centre) strain is found to be approximately 1.38 times the applied strain (displacement over sample length).

Contacts within a band several average disc diameters thick, at each lateral end of the specimen, were assigned high contact strengths to prevent rupture due to near-boundary displacement compatibility problems. As in the case of compressive testing, the velocities of the platens were gradually increased to avoid shocking the sample.

7.7.2 Typical Results

The results of two typical tests with each of the two geometries are summarized in Figures 7.59 to 7.60. Figure 7.61 illustrates the internal contact forces and crack accumulation within the sample (at stress level A and B indicated in Figure 7.60).

For the standard rectangular configuration, five of the six thresholds of induced damage, first identified in the compressive samples, are evident in direct tension (for PFC samples). The distinction between first cracking and systematic cracking is not always immediately evident, although on average two initiation thresholds are present. While crack accumulation results in occasional fluctuations in the lateral stress-strain curve in Figure 7.59, the first major and sustained non-linearity occurs at the point of the first crack interaction. As in the compressive samples, this threshold is also clearly denoted by a sudden increase in the number of so-called interacting pairs of cracks. These are cracks which form within one average crack length of each other ($S \leq 1d$ where S is the separation between crack centres and d is the average crack length).

Critical crack intensity at the point of interaction is approximately 0.028, close to the average value of 0.03 for uniaxial test samples. It must be remembered that unstable propagation of isolated cracks (single broken contacts) is not possible in PFC. In this environment of pure crack accumulation (nucleation without extension), it should be expected that the critical crack density, at which a new crack is likely to form next to an existing crack (and thereafter interact with that crack), should be the same in tension and in compression. This critical intensity is a probabilistic consequence of the internal contact strength distribution and therefore represents a true material property, along with the stress and strain levels associated with it.

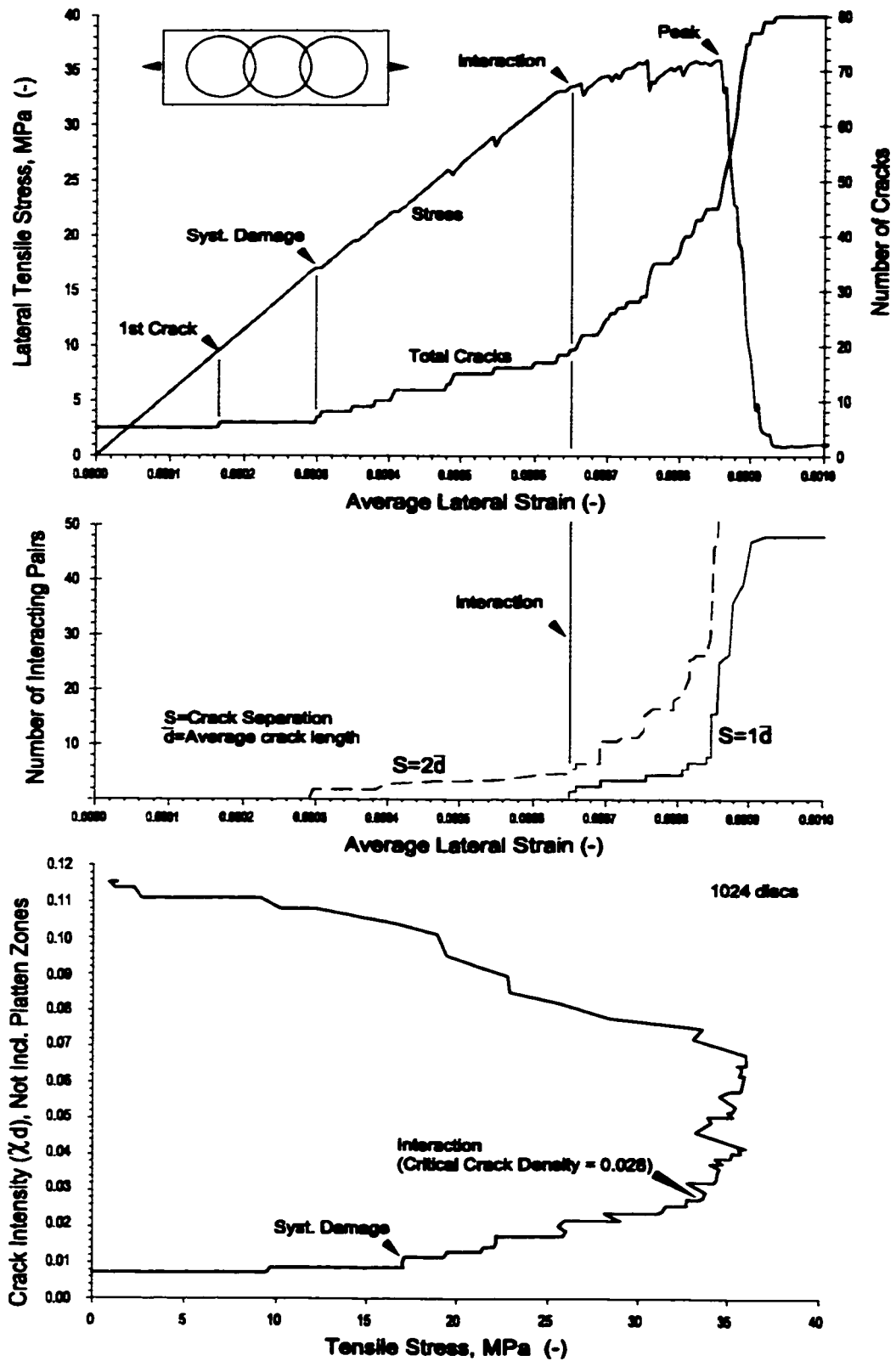


Figure 7.59: Damage threshold detection in tensile test simulations (rectangular samples).

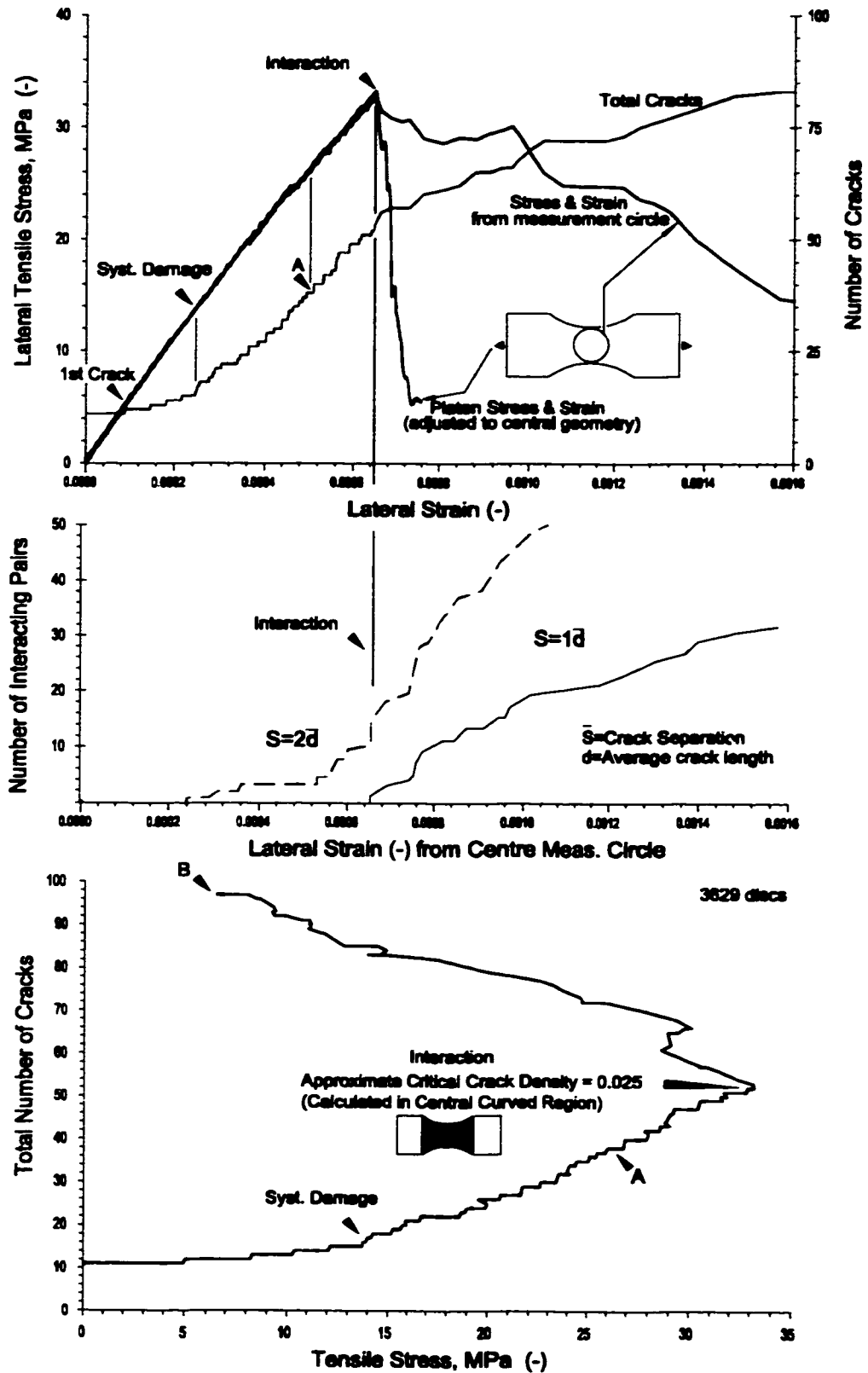


Figure 7.60: Damage threshold detection in tensile test simulations (dumbbell samples).

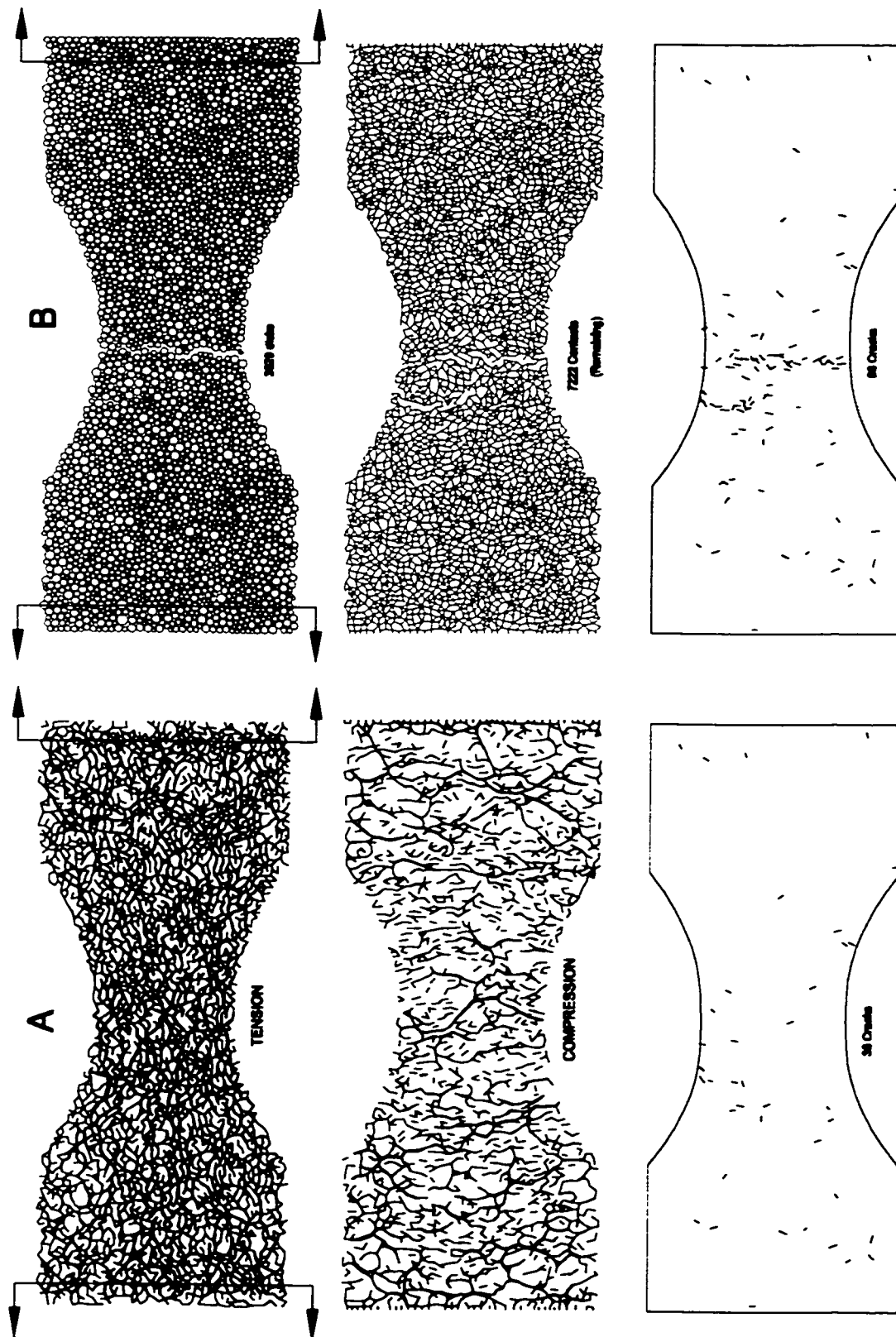


Figure 7.61: Contact force and crack distribution in a tensile sample at approximately 75% of interactions stress (A); Disc, intact bond and crack distribution after failure (B).

In the rectangular test configuration, crack interaction does not immediately lead to localization and failure in the PFC simulations. Additional loading and strain is required to rupture the sample. A typical crack pattern after rupture of a rectangular sample configuration is shown in Figure 7.58.

In the dumbbell samples, crack initiation and systematic damage occur more distinctly, and are identified as before. In these samples, crack interaction, as illustrated in the example in Figure 7.60 immediately precipitates failure of the sample. In this case crack interaction, localization and rupture are indistinguishable. Critical crack intensity is difficult to calculate because of the variable cross-sectional geometry and non-uniform stress. A crude estimate of 0.025 (at interaction) for the example in Figure 7.60 is calculated using only the area within the curved portion of the sample.

The tensile stress at which interaction occurs in both configurations is similar (approximately 33 MPa) as is the critical lateral extension strain (0.00063 to 0.00066). Table 7.6 lists the average threshold data for 5 rectangular and 8 dumbbell samples ranging in size from 1000 to 4000 discs. In nearly all cases, sample rupture (localization and peak strength) occurred at the point of crack interaction. The stresses and strains quoted for “localization and peak” in Table 7.6 are for rectangular samples only.

Table 7.6 Damage threshold data for direct tension

Threshold:	First Crack	Systematic Damage	Crack Interaction	Localization and Peak
Measurement: (prior to threshold)			mean	
			standard deviation	
			(relative st. dev. %)	
Lateral Stress MPa	10.8 2.8(17)	17.7 2.7(16)	33.5 1.8(5)	39.8 1.9(5)
Lateral Strain ($\times 10^{-3}$)	0.18 0.046(26)	0.31 0.045(15)	0.66 0.034(5)	0.83 0.048(6)

Of particular interest is the similarity of the values (lateral strain and crack intensity) for crack interaction with those from the uniaxial compressive testing in Table 7.4. Nevertheless, the relative values (approximately 1/5 with respect to UCS in Tables 7.3 and 7.4) for crack interaction stress and peak tensile strength are disproportionately high, compared to granite and most other rocks (recall that the PFC samples were “calibrated” in unconfined compression tests). This discrepancy is investigated in the next section and in Chapter 8.

7.8 TENSILE STRENGTH AND CONFINEMENT

Hoek-Brown (1988) and linear Mohr-Coulomb criteria use non-linearity and a tensile cutoff, respectively, to capture the low relative values of tensile strength in rocks. PFC simulations, on the other hand, seem to result in significantly higher relative tensile strength, apparently consistent with a comprehensive linear strength envelope as illustrated in Figure 7.62. The damage and strength transition between uniaxial tension and uniaxial compression is examined in this section.

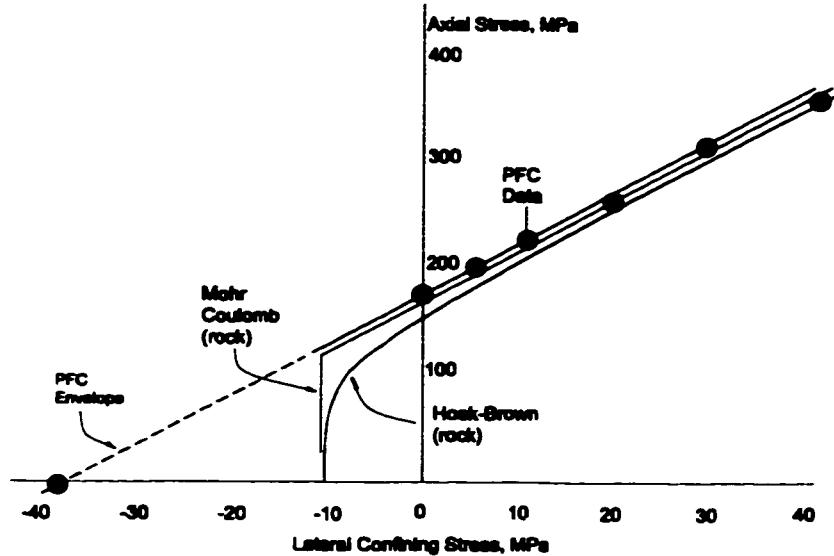


Figure 7.62: Discrepancy between relative rock tensile strength and PFC results (schematic).

7.8.1 Confined Direct Tensile Tests

Numerical experimentation allows the use of testing configurations which would be difficult to implement for real samples. The author was unable to locate tabulated data regarding the transitional strength of rock through the range of loading in which $\sigma_T < \sigma_3 < 0$ and $\sigma_1 > 0$. The Brazilian test provides data for the stress path $\sigma_1 = -3\sigma_3$ and will be examined in Section 7.8.2. In this section, a series of tests are described in which a rectangular sample (Figure 7.63) is loaded vertically in unconfined compression to pre-set stress levels. At each of these compressive increments, the sample is then pulled laterally in increasing tension (under constant vertical compression). This allows incremental testing throughout the entire region $\sigma_T < \sigma_3 < 0$ and $\sigma_1 > 0$.

Using the fixed crack length limitation of PFC to advantage, it is possible to investigate the nature of crack accumulation in these conditions. It will be shown that the near-linear envelope shown in

Figure 7.62 is the result of this limitation and that, conversely, unstable propagation of isolated tension cracks results in the truncation of theoretical strength envelopes for real materials.

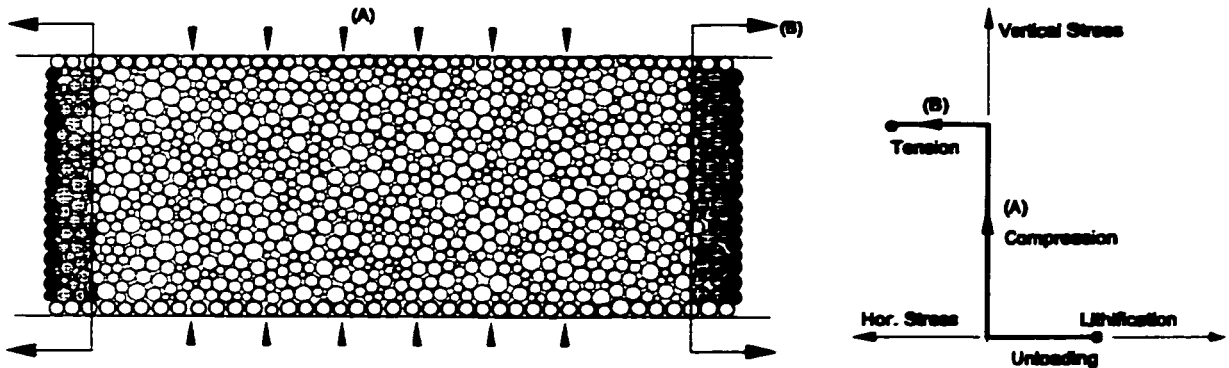


Figure 7.63: Sample preparation and stress path for confined tension tests.

Figure 7.64 illustrates tensile stress, extension strain and crack accumulation responses for three stages of compressive loading. The lateral strain at which the tensile stress rises above zero indicates strain due to the Poisson effect during compressive loading. These plots represent total extension strain.

Of particular interest here is the uniformity of critical lateral strain for crack interaction. The sample responses show marked non-linearity and crack accumulation rate increase at total extension strains of 0.00066 to 0.0070.

The critical crack number values are equally invariant for lower levels of compressive stress. At higher compressive increments, additional cracks are introduced near the edges of the sample by the transition from vertical compression strain to lateral extension. It is possible that the transition is performed too abruptly. These additional cracks are not apparently involved in the ultimate sample failure but do result in an offset in the crack accumulation plot for higher compressive increments as in Figure 7.64.

Figure 7.65 illustrates the measured lateral extension strain (combined Poisson extension and direct lateral straining) at the various damage thresholds for increasing vertical compression increments. While no definite relationship exists for crack initiation or systematic damage, crack interaction occurs within a consistent range of total extension strain. Figure 7.66 shows the corresponding thresholds in stress space for this series of tests. Total sample damage for the two limiting and one intermediate state is also shown.

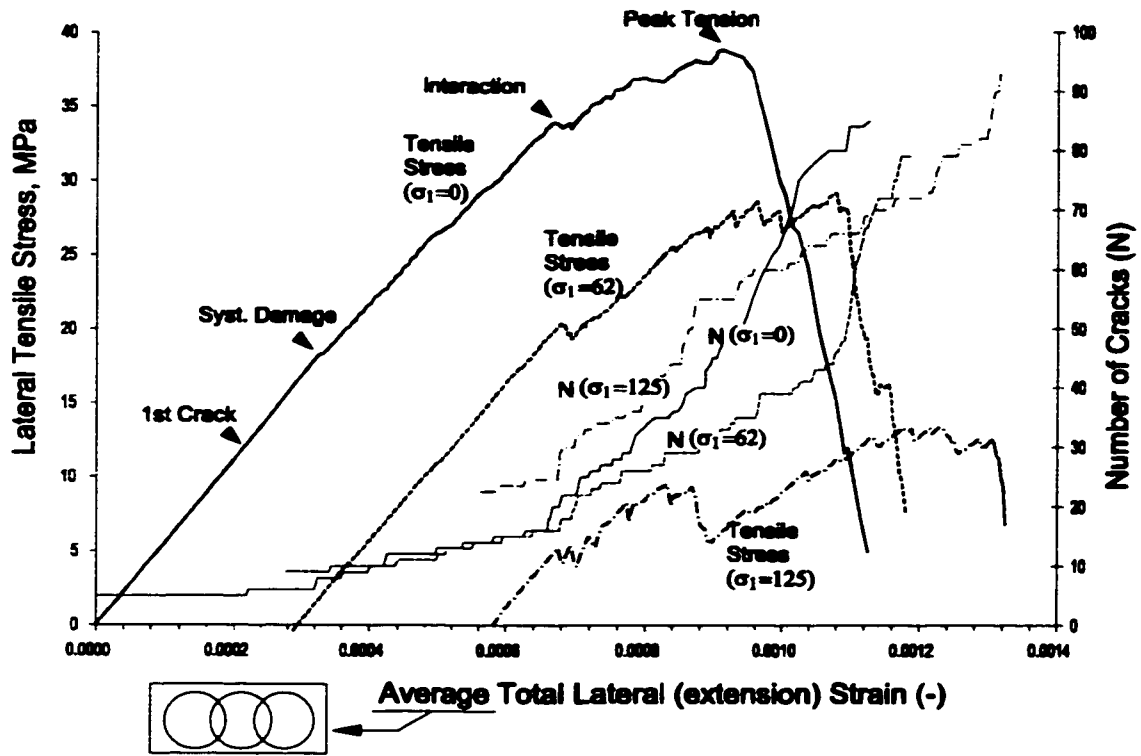


Figure 7.64: Tensile stress – lateral strain and crack accumulation for three examples of confined compression simulations.

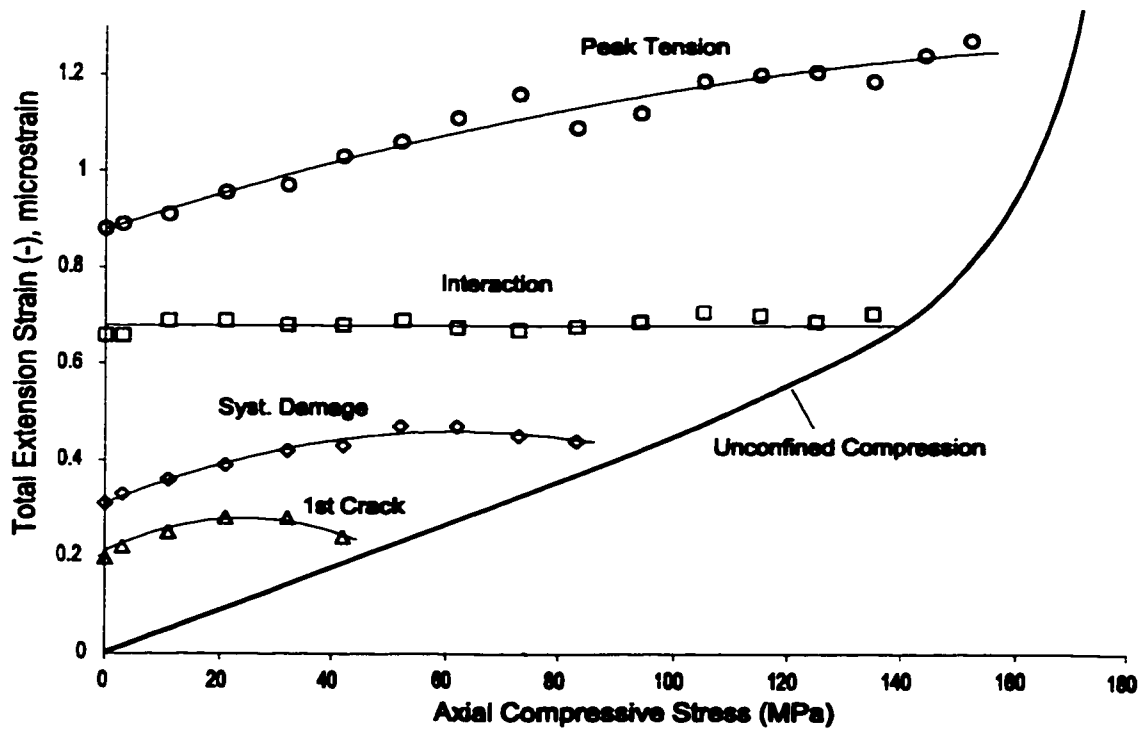


Figure 7.65: Total lateral strain measured for confined tensile tests.

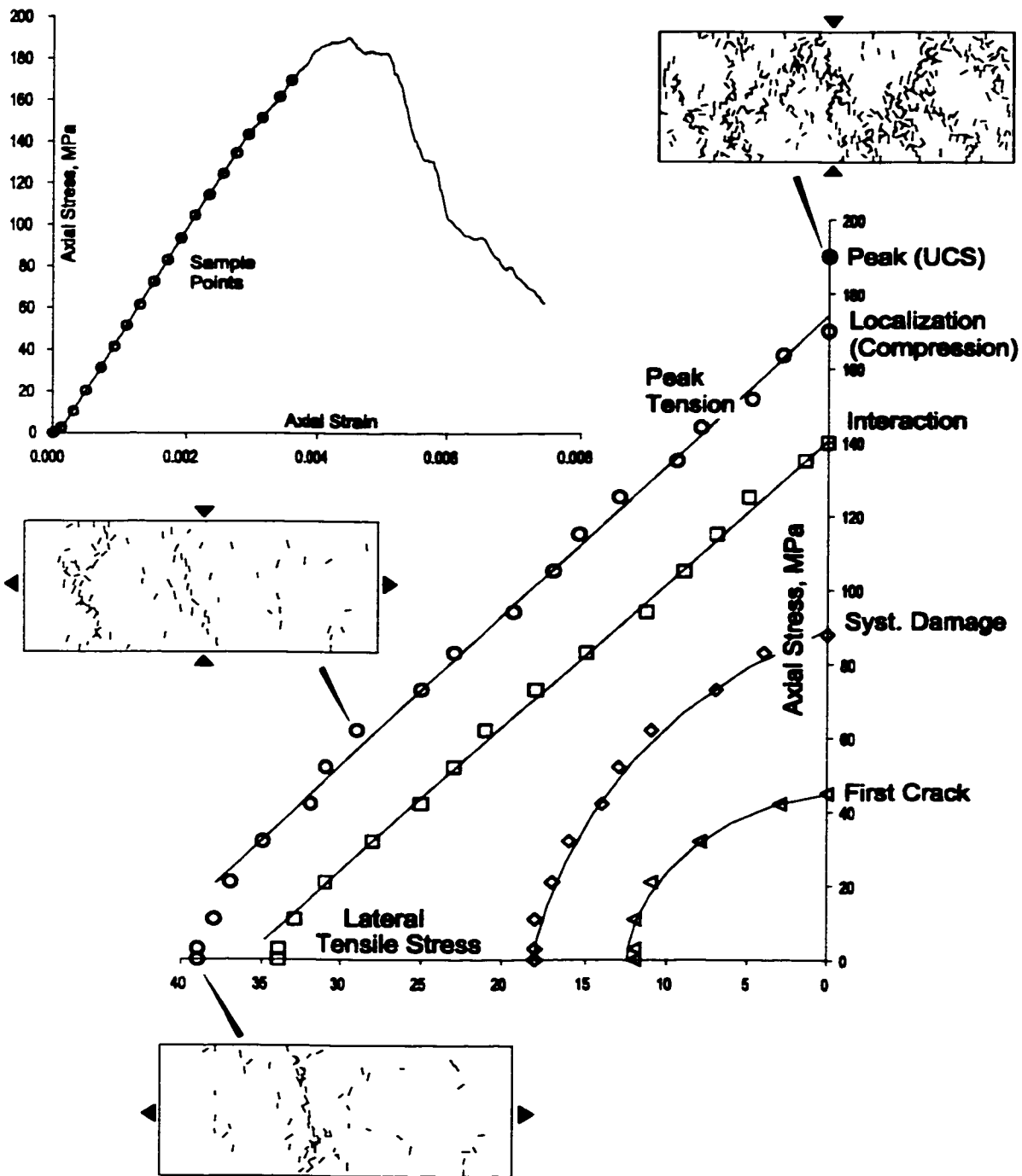


Figure 7.66: Crack damage thresholds determined from confined compression simulations.

It is apparent from this study that, in the absence of isolated crack extension (nucleation only), a continuous transition exists for all of the key thresholds of damage. Peak tensile stress is related to the localization threshold for compression. In the absence of tensile stress, peak (vertical) compressive stress is higher than can be obtained under lateral tension.

The relationship of the yield threshold, defined by crack interaction, to crack intensity and total extension strain has been discussed. Of equal interest is the relationship between crack initiation in tension and compression. Crack initiation and systematic cracking in the PFC tensile test simulations occur in a range of stress more representative of the granite results in Chapter 6. Accepting, once again, that any cracks initiating in direct tension (in real solids) are likely to propagate instantaneously, the PFC results indirectly provide evidence that tensile strength obtained in stress controlled laboratory tests is related to crack initiation in compression and not to peak strength. This explains the high ratios of UCS/T found in polycrystalline rocks such as granite, for example.

7.8.2 Brazilian Test Simulation

For completeness and for comparison to the results in Chapter 6, a series of Brazilian test simulations were also carried out.

Square samples, with a line of uniform discs across the top and bottom walls, were lithified and unloaded. The sidewalls were then removed and a circle was overlain. The radius of the circle was selected such that a row of uniform discs formed a “smooth” contact surface at the top and bottom of the specimen with an angular width of approximately 7.5 degrees (the contact width analysed in Chapter 6). The theoretical tensile stress (for line loading) is calculated as $W/(\pi R)$ where W is the vertical force applied to the contact surfaces and R is the radius of the sample.

Figure 7.67 shows the stress response and crack accumulation at different loading stages. Damage thresholds are identified, in part by the crack accumulation rate as shown. Crack initiation and systematic damage occur at stress levels (tension) consistent with the average thresholds in direct tension (Table 7.6). Crack interaction and peak tension, however, occur at reduced levels of stress. Crack interaction begins below the central region of the sample, and spreads into the central region as localization progresses.

Figure 7.68 illustrates, for a larger test sample, the internal contact forces at an applied stress level below the crack interaction threshold. In order to confirm the validity of the contact model simulation, an array of measurement circles was generated as shown and the local stresses in each circle measured using Equation 7.9. The grid values were exported and contoured as shown using a commercial data mapping package (SURFER). The correspondence with the calculated continuum stresses (Figure 6.32) is sufficient to validate the approach.

Instability of Hard Rockmasses: The Role of Tensile Damage and Relaxation

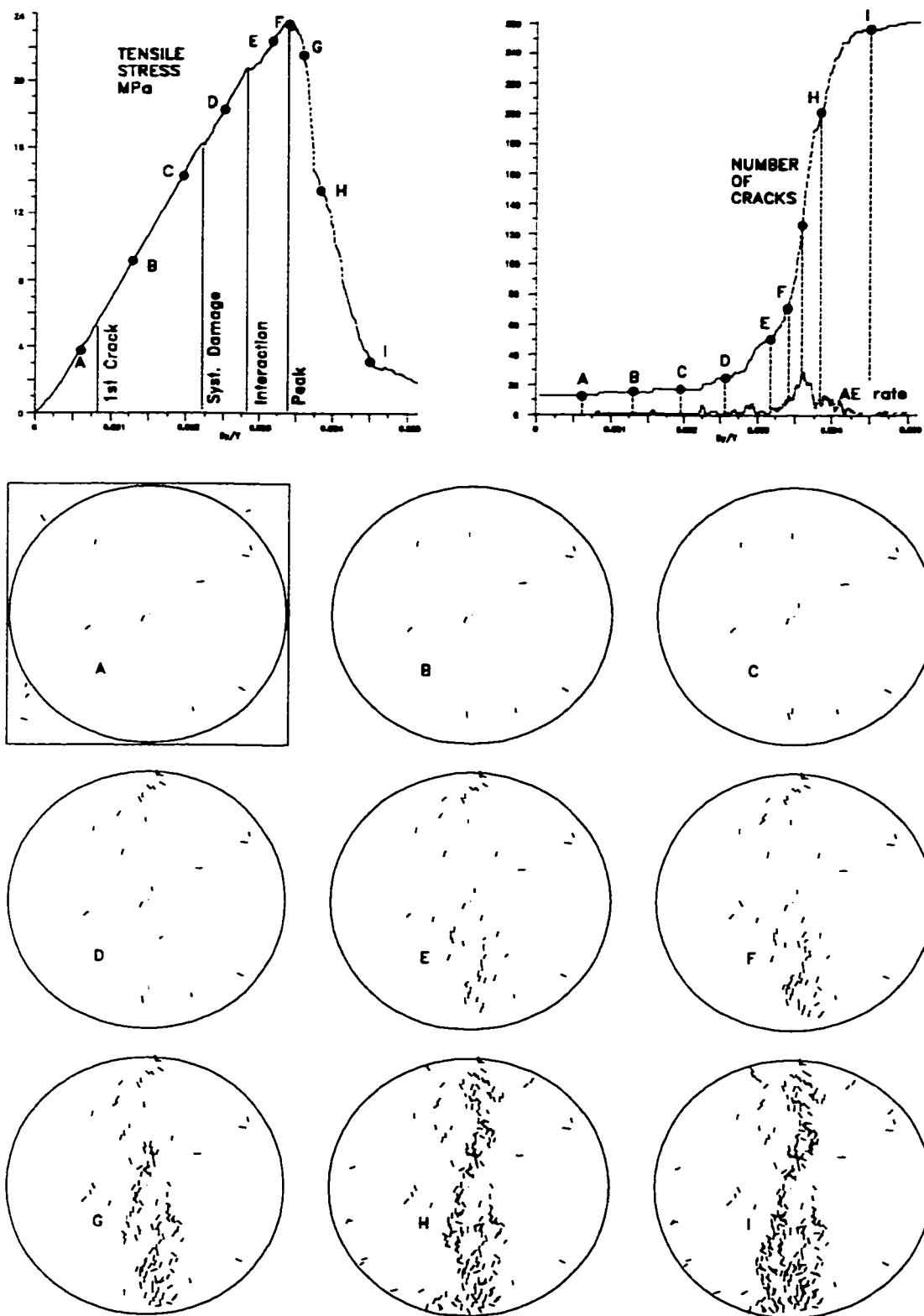


Figure 7.67: Stress strain response and cumulative damage at increasing vertical strain.

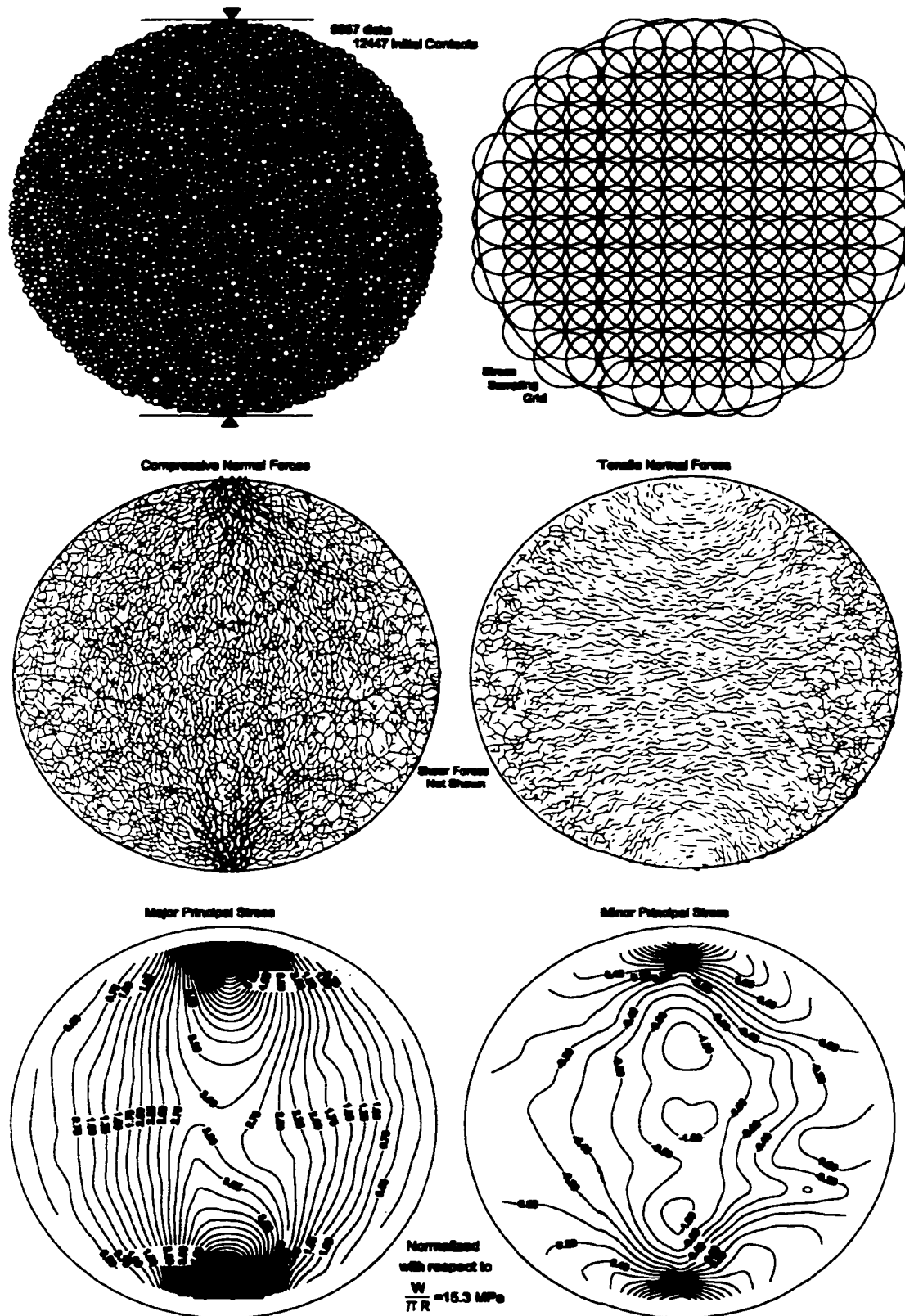


Figure 7.68: Test configuration showing stress sampling grid, contact forces and calculated equivalent stress distribution. Sample at approximately 60% peak load.

The stress state contoured in Figure 7.68 is marked as 'A' in Figure 7.69. This figure illustrates typical strain response averaged from three measurement circles aligned along the central tension zone as shown. The tension plotted on the vertical axis is calculated from platen forces. The vertical strain in this figure is the actual average strain and differs from the normalised platen closure used in subsequent plots. The primary post peak damage state is also shown. Note the correspondence with the contoured tension in Figure 7.68. Additional secondary damage will accumulate beyond this point as the two separating halves of the disc are crushed.

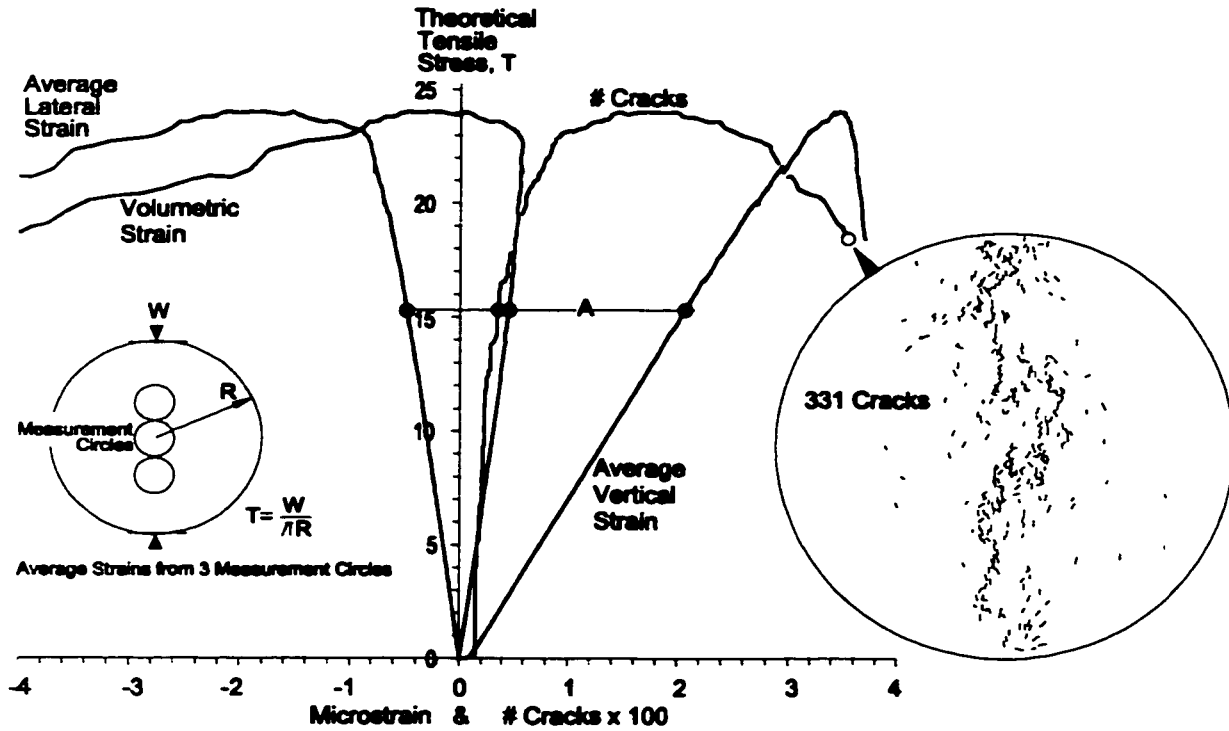


Figure 7.69: Stresses and strains (averaged over circles shown) for typical Brazilian test.

For a different sample, Figure 7.70 compares the measured central stresses (horizontal and vertical) with the theoretical relationships. Prior to sample rupture, the stresses calculated from the discrete contact forces match the continuum response. The lower plot in Figure 7.70 compares the measured stresses for the three measurement circles shown. The tensile horizontal stresses are consistent through the three zones while the compressive vertical stresses increase away from the centre. This explains the off-centre initiation of damage in most of the tests.

Example results are shown in Figure 7.71 of a damage accumulation study, considering vertical strain, lateral extension strain, crack accumulation and crack interaction (neighbouring pairs).

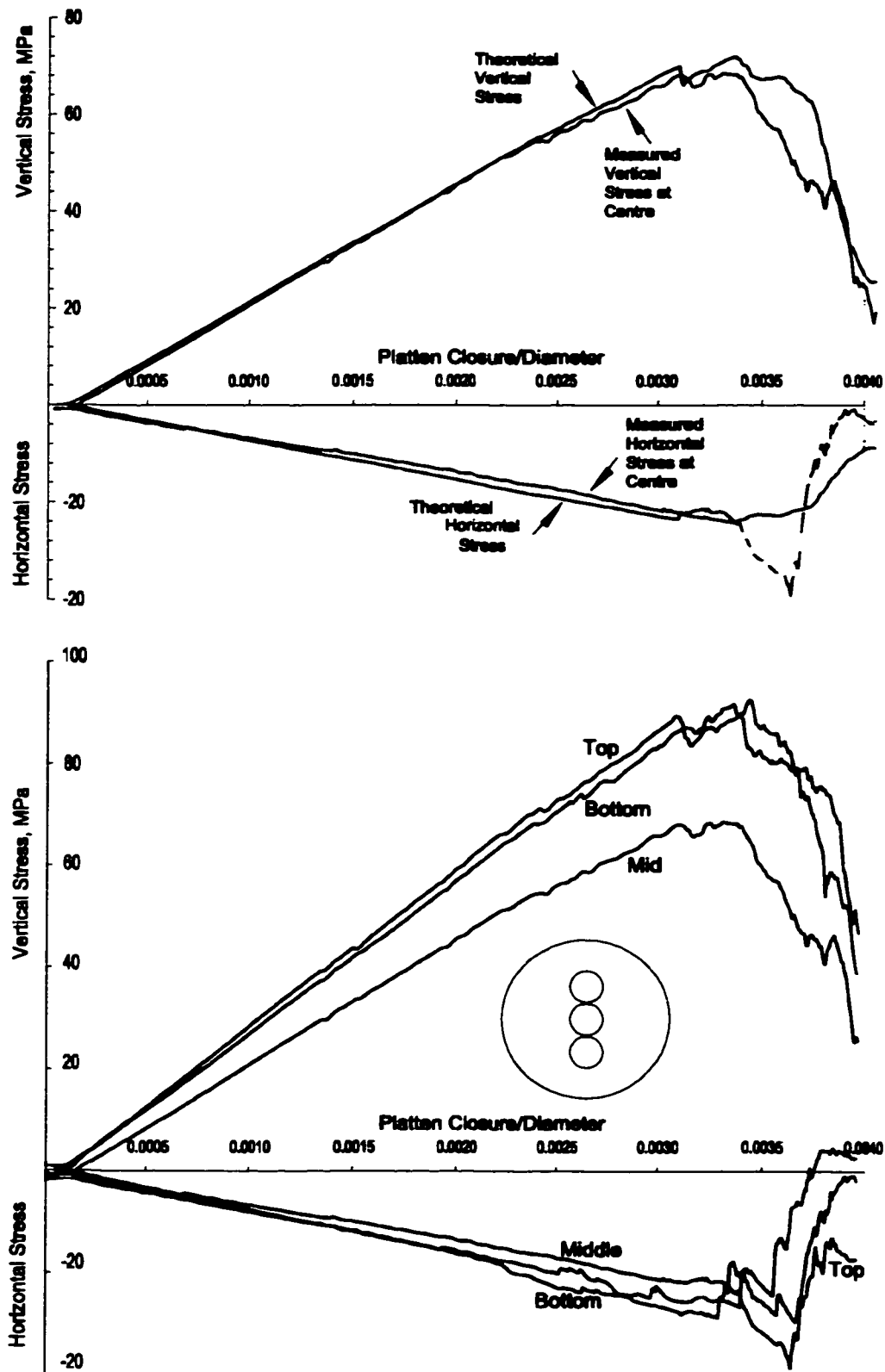


Figure 7.70: Comparison of measured and theoretical stresses at sample centre (top plot) and comparison of measured strains in regions as shown.

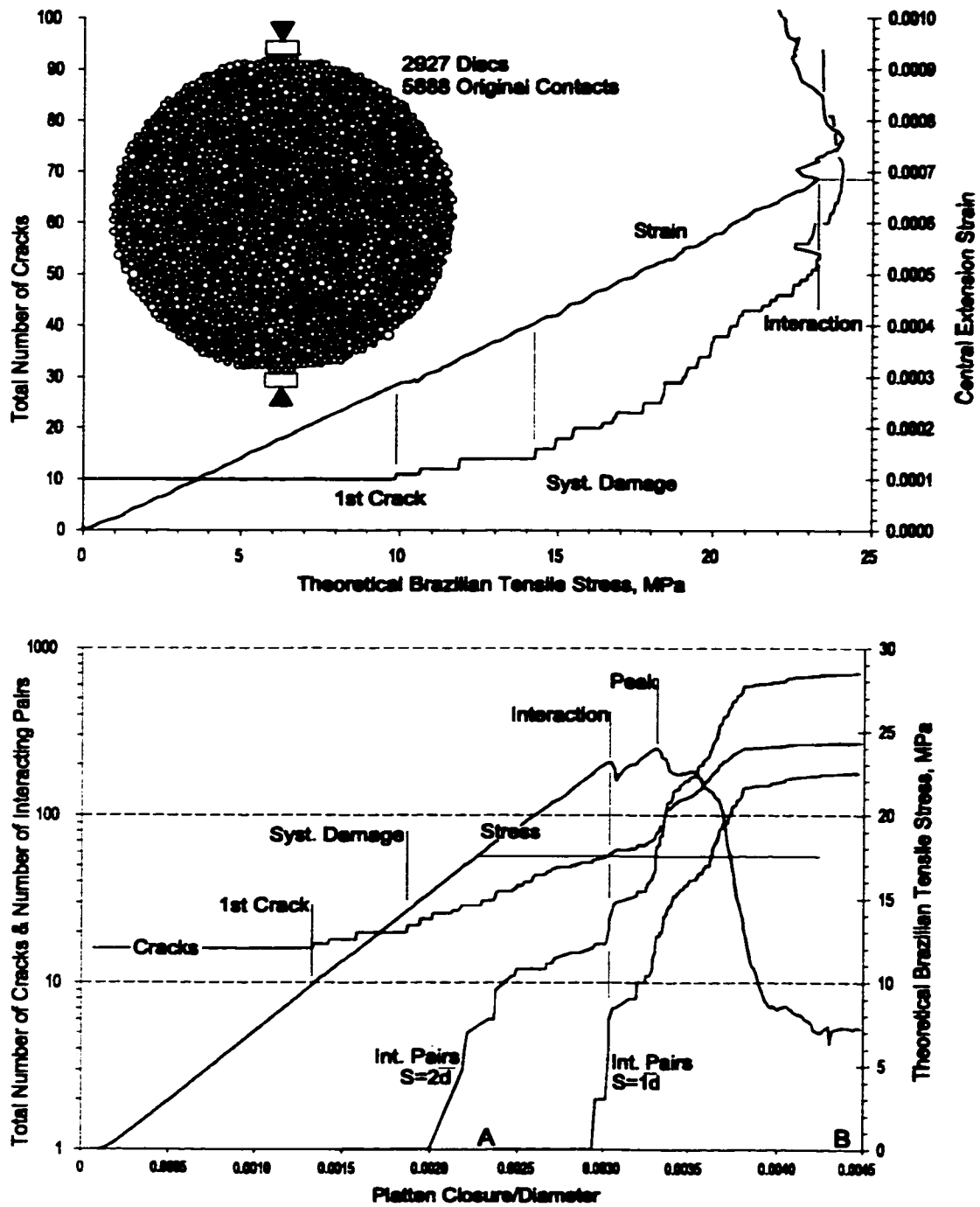


Figure 7.71: Damage thresholds in the Brazilian test.

Contact bonds (remaining), induced cracks and internal forces, for the states 'A' and 'B' in Figure 7.71 are illustrated in Figure 7.72. Note the concentration of vertical compressive loads after rupture accompanied by a lateral force "shadow" around the rupture zone.

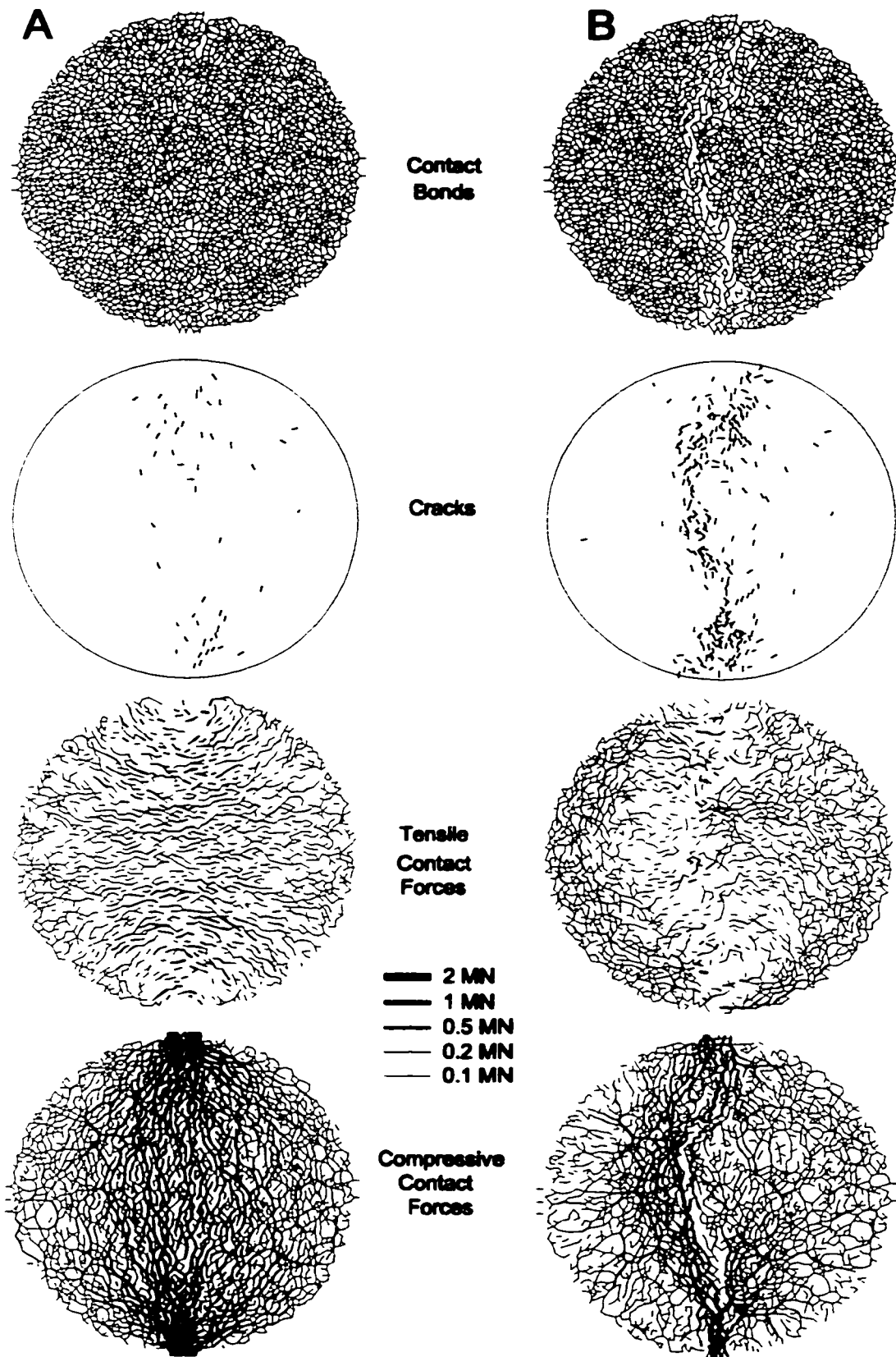


Figure 7.72: Sample damage and internal forces at stages marked in Figure 7.71.

Table 7.7 summarises the damage threshold parameters, averaged for 6 tests ranging in diameter from 145mm to 280mm (particle diameter = 3.2mm). Crack intensity is not an appropriate measure in this case since the stress field is not uniform over the sample area.

Table 7.7 Detailed Damage Threshold Data

Threshold:	First Crack	Systematic Damage	Crack Interaction	Localization and Peak
Measurement: (prior to threshold)	mean (n=6) standard deviation (relative st. dev. %)			
Lateral Stress MPa	8.8 3.1(35)	15.2 1.8(11)	20.6 1.6(8)	23.9 1.7(7)
Lateral Strain (x10 ⁻³)	0.25 0.09(36)	0.52 0.07(13)	0.69 0.03(4)	0.87 0.09(10)

The range of tensile stress for each pre-peak threshold compares well to the stress path in Figure 7.73, indicating that, in the absence of crack extension, the Brazilian test is a valid representation of a transitional stress state between direct uniaxial tension and unconfined compression. The value of total extension strain at crack interaction is, again, consistent with the results of both tensile and compressive testing. In addition, this level of strain (0.00065 to 0.00073 for the six samples averaged above) corresponds to the threshold value measured in the granite compression samples in Chapter 6.

In the granite tests in Chapter 6, the Brazilian tension results (peak) were consistently higher than the strength obtained from direct tension. Failure of granite samples in direct tension must occur as the result of the unstable propagation of a single initiating crack. In fact, the range of crack initiation stress for the PFC tensile samples is close to the granite tensile strengths.

In the Brazilian tests on granite, the stress-strain response indicated additional damage (inelastic strain) after crack initiation and prior to sample rupture. It is possible, in the Brazilian test, that random initial cracks do not propagate due to lattice trapping (tensile cracks surrounded by compressive elements). Granite, as a poly-crystalline solid, may have similarly distorted force pathways resulting in compressive cut-off of initial random cracks similar to lattice trapping in the PFC simulations (Figure 7.57). Failure in the granite Brazilian test occurs rapidly due to crack extension, after systematic crack accumulation begins. In Figure 7.73, this occurs at a higher measured tension than first crack initiation in the direct test. This explains the higher peak values for the Brazilian tests (on granite) as compared to the direct tension results.

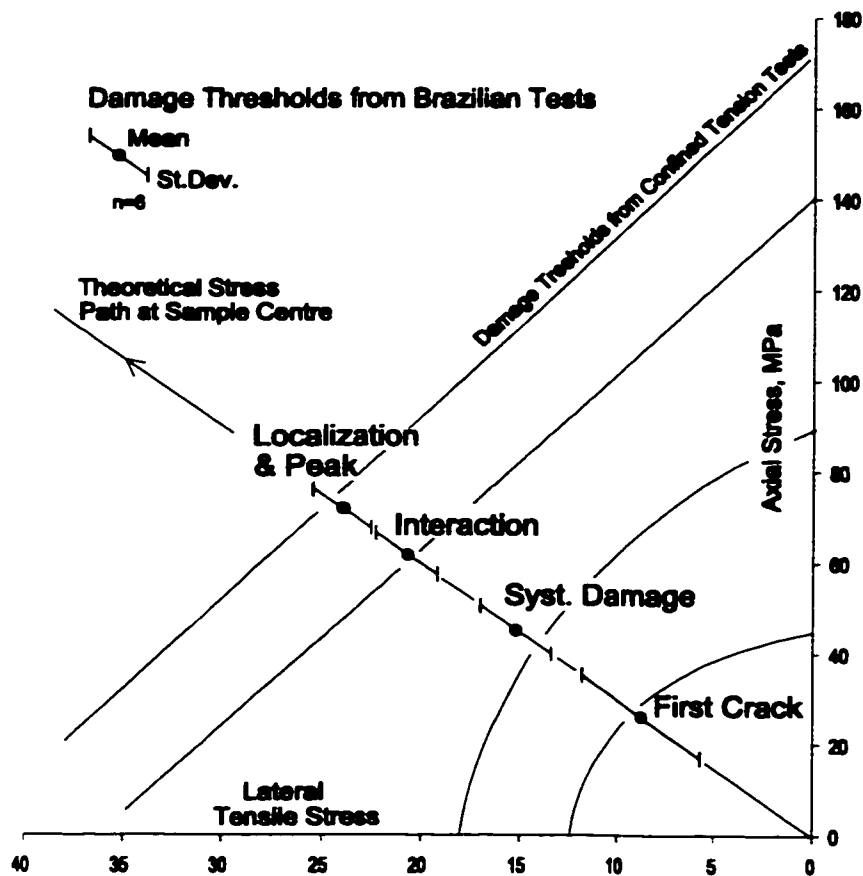


Figure 7.73: Comparison of Brazilian Tests damage thresholds with confined tension simulations.

7.8.3 Critical Crack Intensity in Tension and Compression

There is no validity in recording crack intensity in the Brazilian test. Crack intensity, as a state parameter, is only valid as long as the stress and strain gradients are minimal across the region of interest. This is not the case in the Brazilian test.

The crack intensities estimated at crack interaction in the rectangular and dumbbell tensile tests were approximately 0.028 and 0.025, respectively. These are consistent with the average of 0.03 for the uniaxial tests and for the range 0.028 to 0.034 for the series of confined compression tests in Section 7.6, further validating crack interaction as a comprehensive yield threshold.

Ultimate crack intensity for tensile tests (post peak and sample rupture) ranges from 0.05 to 0.11, or approximately one sixth to one third of the crack intensity required to fail a sample in compression.

7.9 DISCUSSION AND SUMMARY

The purpose of this chapter has been two-fold. It was of interest to assess the appropriateness of the bonded disc analogue for simulation of polycrystalline rock damage and failure. Secondly, the model provided a means of investigating damage accumulation and the relationship to rock yield in a number of laboratory test simulations under various stress conditions. In both cases the emphasis here is on low confinement conditions, since this is the environment of interest when dealing with rock failure around excavations (Chapter 5).

7.9.1 The Bonded Disc Analogue for Rock Failure

One of the most important factors in determining rock strength in low confinement and in tensile conditions is the stability of crack propagation after initiation. At high confinements, cracks can only extend to a fraction of the scale of the initiating flaw or nucleation mechanism. At lower confinements crack extension becomes significant, ultimately becoming fully unstable in tensile conditions such that a crack propagates spontaneously and uncontrollably upon initiation. This behaviour results from the near-singular tensile stress concentration active at the tips of a crack normal to a tensile applied stress. This concentration subsides if the tension gives way to modest compressive confinement. In tension, therefore, isolated crack propagation dominates the damage process (and ultimately peak strength) while in compressive conditions, crack accumulation is required to induce yield and rupture. This is a major factor influencing the low ratios of tensile strength to compressive strength in low-porosity solids such as granite.

In the bonded disc analogue (PFC), cracks occur due to discrete bond ruptures (contacts) and as such do not induce a singular crack tip stress which serves to extend the cracks. The individual cracks are limited to the size of the individual trellis cell. After the rupture of a bonded contact, surrounding contacts may absorb a finite amount of force redistribution in much the same way as a well engineered truss accommodates isolated yield of component members. The lattice will fail if enough contacts rupture, overloading the remaining network. Failure cannot occur, however, as the result of a single crack initiation event.

This contrast in behaviour affects the validity of laboratory simulations as detailed in this chapter but also limits the validity of excavation scale modelling (Potyondi et al. 1996). Unstable crack propagation is a key component of brittle rock failure and is needed to simulate spalling at excavation boundaries and tensile fracture. Stress corrosion can be invoked as a means of

focusing damage and precipitating concentrated bond rupture (Potyondi and Cundall 1998) although this does not change the fundamental limitation of the contact model.

In short, tensile failure in granite is coincident with damage initiation. In compression, crack accumulation, interaction and localization are required to cause failure. In PFC simulations in direct and confined tension, damage accumulation and interaction must also take place, following the same stress-strain relationships active in compression, before sample rupture can occur. This contrast is summarised in Figure 7.74.

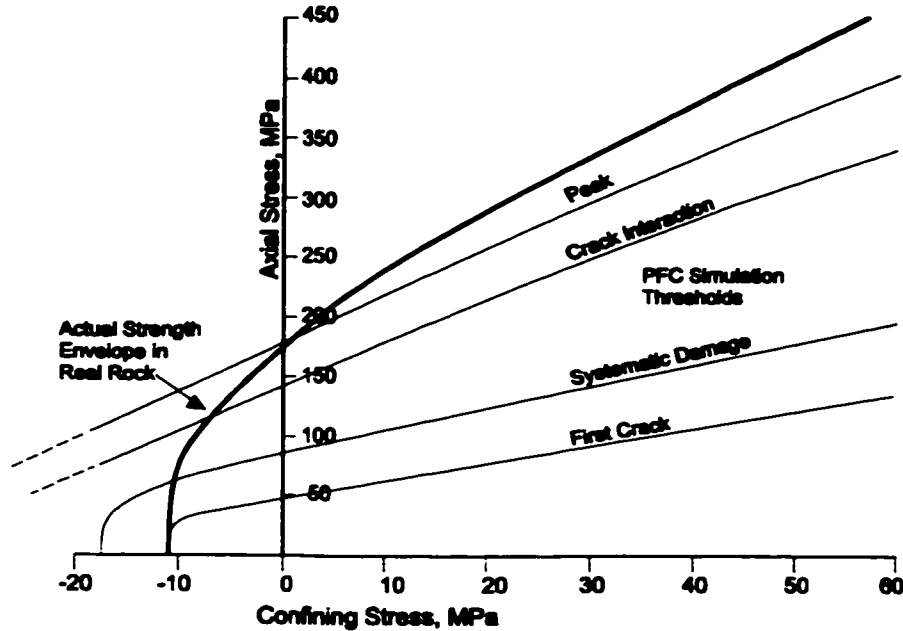


Figure 7.74: Contrast between PFC damage thresholds and granite strength.

Another consequence of this limitation is the reduction in apparent peak friction angle at lower compressive confining stresses (Figure 7.74). Apparent friction prior to full shear band formation and discontinuum slip, is the result of geometric and force flow anisotropy through the zone of incipient shear band formation. Sliding friction in bonded solids does not mobilise until a suitable shearing surface has evolved. Cracks which extend upon initiation lead to high pre-peak crack and rock bridge anisotropy (cracks aligned with maximum compression). Such arrays are highly sensitive to confinement resulting in the high value for empirical frictional resistance typical of granite. The model simulations on the other hand result in similar “kink-band” formation although the component mesocracks are composed of numerous contact cracks aligned at subvertical angles (since the mesocracks must form around and not through the solid discs. This results in reduced pre-peak anisotropy and consequently reduced apparent peak friction.

Nevertheless, in spite of these limitations, the bonded disc analogue affords a unique opportunity to examine damage accumulation in the absence of extension, and to draw conclusions, thereby, regarding the nature of yield in real materials. The role of crack extension in rock damage will be further investigated in Chapter 8.

In fact the model is sound for simulations under compressive confinement, where crack extension is limited in real materials. Simulations in which shear bond rupture was prevented, resulted in highly realistic macroscopic shear band formation in compressive samples, verifying that such shear failure can indeed occur as the result of extension crack accumulation as discussed in Chapter 6.

7.9.2 Lessons Regarding Rock Damage and Yield

Accepting the limitations of the numerical model as discussed above, a number of observations and conclusions can be made, regarding damage and strength in granite, based on the simulations in this chapter combined with the observations of Chapter 6:

- Grain boundary extension crack damage can result during unloading in heterogeneous materials. The amount of initial damage increases with initial lithification pressure. (The effect of initial damage is investigated in Chapter 8).
- Tensile strength of hard rocks such as granite are related to the threshold of crack initiation, in compressive loading conditions, and not to peak strength. Any attempts to correlate unconfined compressive stress and tensile stress should be viewed as empirical only and have no mechanistic basis.
- The relationship between compressive damage initiation and tensile strength is continuous for transitional loading states when the mechanism of damage is the same as in the model. As noted in Chapter 6 for rocks such as granite, the initiating flaw in tension (rough grain boundary crack) may be physically distinct from the nucleating mechanism in compression (atomically smooth intragranular crack). This results in a truncated relationship and a lower relative tensile strength for granite.
- In the absence of crack extension, tensile rupture would have to involve the same phases of initiation, accumulation, interaction and localization necessary for failure in compression. Conversely, any mechanism that promotes crack extension in globally compressive

conditions, should result in a peak strength reduction ultimately to a lower bound defined by crack initiation.

- Crack initiation, both in granite and in the lattice model, is the result of local stress conditions, rather than extension strain as postulated by Stacey (1981) and others since. In fact, crack initiation at higher confinements occurs in fully compressive strain conditions.
- The Brazilian test represents a true transitional scenario between direct tension and uniaxial compression, in an environment of inhibited crack extension. In rocks such as granite, crack extension, beyond initial wing crack growth, is controlled primarily by the tensile stress component. Rupture in the Brazilian test, therefore, is a measure of the direct tensile strength rather than strength along the transitional stress path it represents.
- Crack interaction can be identified by axial stress-strain non-linearity, increased lateral strain and crack accumulation, the appearance of neighbouring crack pairs ($S < ld$), and kinetic energy increase. It represents the onset of non-uniform sample behaviour and is a precursor to full strain localization. Crack interaction marks the threshold of sample yield.
- Crack interaction occurs at a constant critical crack intensity (approximately 0.03) for the low and moderate confinement conditions tested. This threshold is also marked by a consistent limit of total lateral extension strain (0.0007). In the absence of crack extension as in the PFC simulations, the critical crack intensity and lateral strain thresholds are valid from direct uniaxial tension through to confined compression. As such these thresholds represent true material strength properties.
- Yield is related to critical crack intensity. Crack intensity can be increased by crack extension. Any mechanism which enhances crack extension will therefore bring about the critical crack intensity at a lower stress threshold. This is explored further in Chapter 8.
- Cracks tend to interact at oblique angles in compression. These simulations and other fracture mechanics studies show that macrocracks form from microcracks interacting at approximately 30 degrees from the vertical at a separation of $S < ld$. While pre-existing crack damage may not be immediately mobilised under the current stress field and may not influence additional isolated crack growth, cracks inclined to maximum compression may afford easier connectivity between extending axial cracks, thereby encouraging interaction and possibly reducing the yield strength of the material. This is examined in the next chapter.

- The amount of inelastic strain and additional damage, after crack initiation, required to reach peak strength increases for compressive conditions and for higher confining stresses. Post peak dilation reduces at higher confining stress.
- Localized shear zone formation, in the bonded disc models, can be achieved solely through the mechanism of extension crack accumulation, supporting the notion that extension cracking is the primary mode of damage in bonded solids for low to moderate confining pressures.
- Dilational extension crack growth delays the development of contact friction, until kink rotation and renewed crack surface contact is achieved, resulting in brittle failure. The elastic interface between compressive and extensional lateral strain has a slope in stress space:

$$\begin{aligned} \frac{\Delta\sigma_1}{\Delta\sigma_3} = \frac{1}{\nu} = 4 & \quad \text{for plane problems with } \nu = 0.25 \\ \frac{\Delta\sigma_1}{\Delta\sigma_3} = \frac{1-\nu}{\nu} = 3 & \quad \text{for axisymmetric problems with } \nu = 0.25 \end{aligned} \quad [7.33]$$

similar to Mogi's line (1966):

$$\frac{\Delta\sigma_1}{\Delta\sigma_3} = 3.4 \quad [7.34]$$

which empirically divides brittle failure from ductile behaviour in compressive tests of numerous rock types. Crack initiation, on the other hand, occurs below Mogi's line at higher confinements. This suggests that crack accumulation in globally compressive conditions results in ductile failure (non-dilatant cracks allow continuous transition between cohesion loss and friction development) whereas dilatant crack accumulation in conditions of globally extensile strain delay friction mobilisation, leading to brittle behaviour.

- Apparent friction at peak strength is unrelated to interparticle contact friction. It is likely controlled by lateral strain relationships and crack anisotropy. Sliding friction is mobilized post peak as a continuous shear zone or surface is created.

A number of these issues will be explored in the next chapter, with reference to insitu strength reduction as a function of heterogeneity, scale effect, surface geometry and local effective confinement.

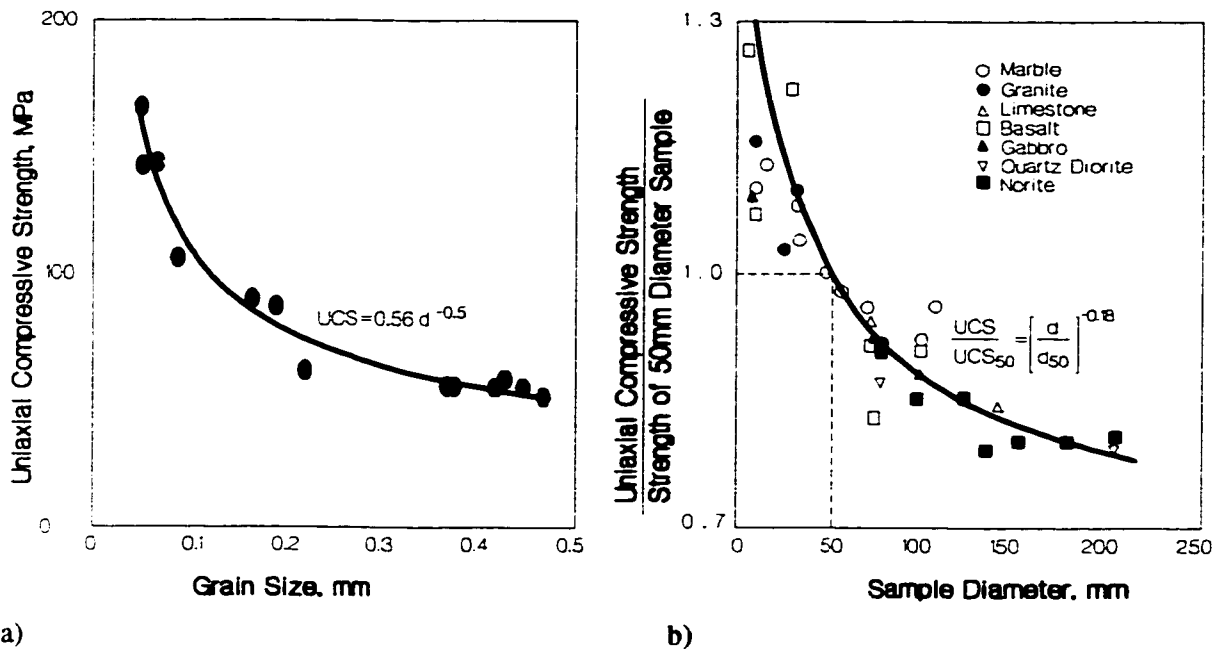
CHAPTER 8

Insitu Strength Reduction: Heterogeneity, Scale, Stress Path and Confinement

8.1 INTRODUCTION

The foregoing chapters illustrate, through a review of the work of other researchers and through the novel use of a particle or lattice model, that extensile or tension crack damage starting at the grain scale is the primary mechanism of rupture for rocks in compression. This scale of cracking is ubiquitous in laboratory as well as insitu samples under compressive and deviatoric stress. While the importance of such damage has been clearly demonstrated, consideration of distributed crack initiation, accumulation and interaction does not on its own provide an explanation for the discrepancy, described in Chapter 5, between laboratory sample strength and insitu strength in massive or jointed rockmasses. The important influence of heterogeneity, scale effect and effective confinement on rock behaviour and strength will be examined in this chapter.

Most rock types exhibit a limited scale dependency, both in terms of grain and sample size, for strength and other behavioral properties (Figure 8.1). As will be shown, there is a direct link between this scale dependency and the internal heterogeneity for undisturbed rock samples up to certain size or limiting scales. Field scale heterogeneity has long been cited (Hoek and Brown 1980; 1988) as the main reason for significantly reduced rockmass strength in the field. In the case of a moderately jointed rockmass, however, the presence of large scale jointing or other heterogeneity may affect only certain components of strength. Other scale effects arise due to dimensional reduction during strain and damage localization.



a) b)
 Figure 8.1: Strength of rock samples versus a) grain size (marble after Wong et al. 1996) and b) sample size (after Hoek and Brown 1980).

Crack initiation, for example appears to be relatively invariant (Martin, 1994; Castro 1996) beyond laboratory sample dimensions. Damage localization and the ultimate failure stress, however, can be reduced in the field to a level as low as crack initiation stress, as discussed in Chapter 6 and as illustrated for field scale samples in Figure 8.2.

In addition to scale effects arising from material variability and fracture mechanics, stress path related damage and confinement variability combine to further reduce field strength.

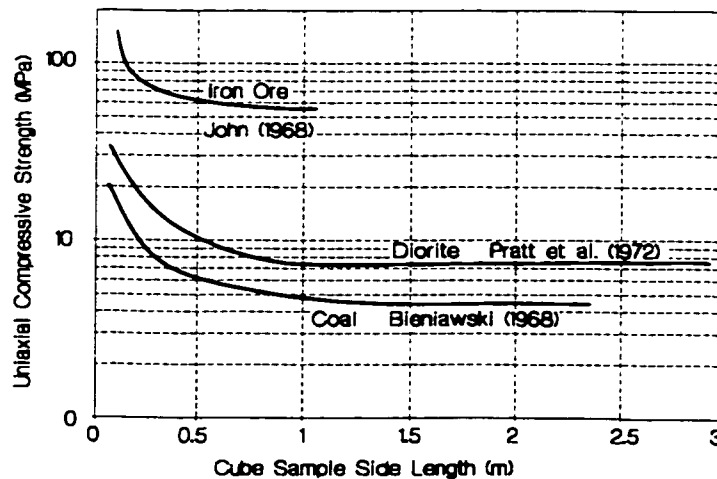


Figure 8.2: Effect of sample size on compressive strength (after Bienawski 1968).

Material and structural heterogeneity and local surface geometry create local regions of confinement reduction. These zones can have a significant impact on crack extension and therefore, on crack interaction and insitu strength.

8.1.1 Strength Reduction Mechanisms

A commonly cited mechanism for strength variation and scale effect is the inherent elemental strength distribution within the material. Grain scale strength variation can occur as a result of varying materials (grains of different minerals). This is analogous to the parametric variability employed in the PFC models described thus far and illustrated in Figure 8.3.

Strength variation can also result from stress concentrations due to the presence of pores and cracks within crystals or at crystal boundaries. This is the essence of linear elastic fracture mechanics. Scale effect in this context, applies to the size of the inherent and critical flaws rather than to the size of the sample, unless the two are related (as in Griffith's (1921) experiments).

Scale effect, in terms of peak sample strength, can arise due to a transition between volumetric crack accumulation and localized planar failure. Strain energy reserve at a given state increases with the sample volume (V) while the energy required to propagate a planar shear surface or zone increases as a function of fracture surface area or as $V^{2/3}$. This results in a scale effect for post yield strength.

Stress rotation during the excavation of an advancing tunnel can lead to insitu strength reduction through the creation of additional damage. Numerical simulations in this section will also demonstrate that pre-existing crack damage (non-persistent cracking) can reduce the critical damage threshold significantly, due to increased opportunity for crack interaction. The threshold for new crack initiation, as a lower bound for strength, is much less sensitive to pre-existing isotropic damage. A monotonic loading path results in a quantity of axially aligned (parallel to maximum compression) microcracks within a material as discussed in Chapters 6 and 7. Pestman and van Munster (1996) showed that the final amount of damage, in an axi-symmetric sample at given uniaxial compressive stress, was the same for the case of a uniaxial loading path from zero stress and for the case of lateral unloading from a confined state to uniaxial compression. If the loading axes are rotated, while stresses are above the damage initiation threshold, however, additional damage should be introduced since different elements (e.g. sliding flaws) are activated.

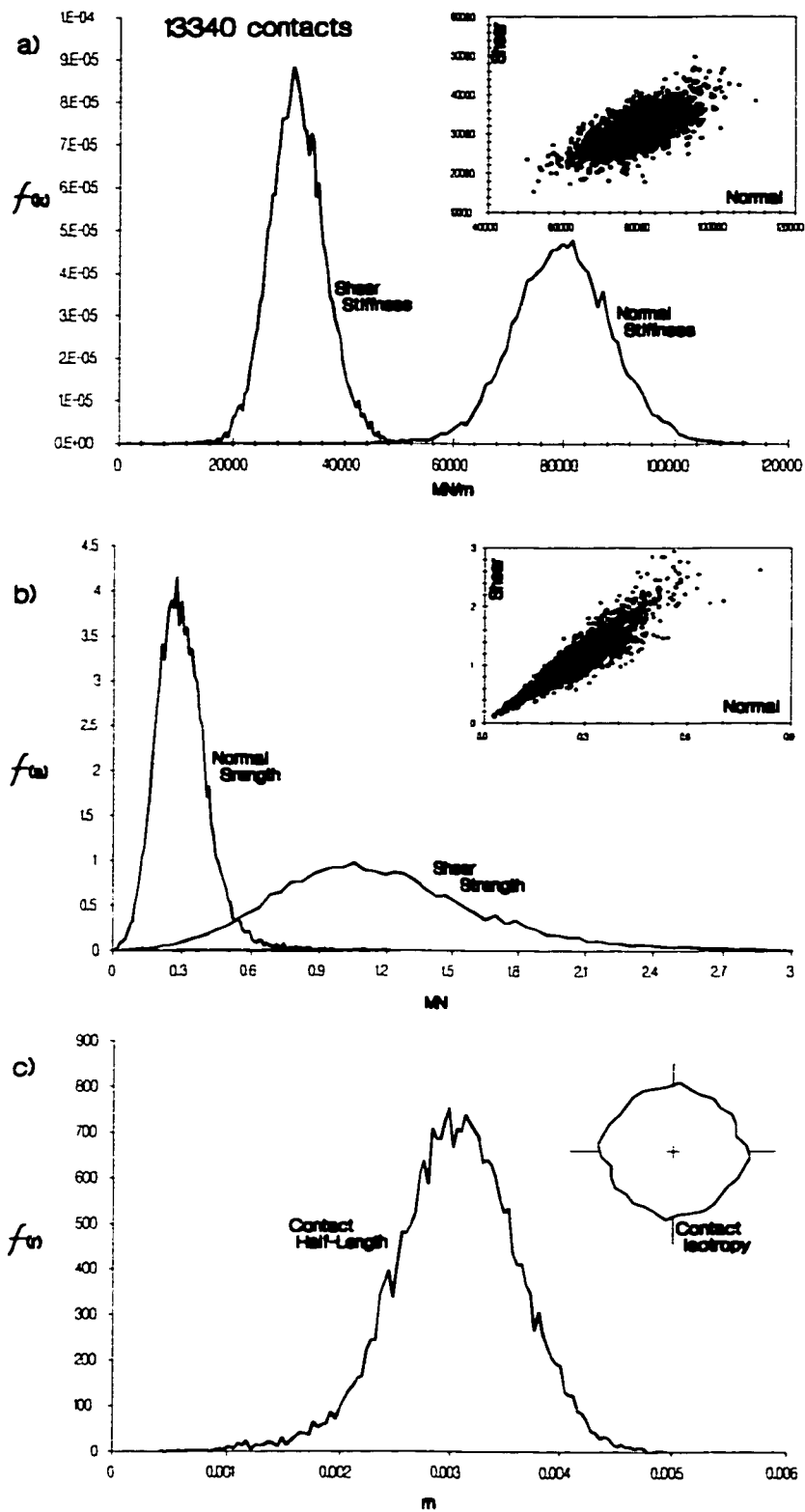


Figure 8.3: Variation in a) strength, b) stiffness, and c) length of contacts within PFC lattice model (standard assumed means and variabilities used throughout this thesis).

Stress divergence, caused by material heterogeneity, can result in low confinement or local tensile stresses in a material which is globally confined (according to isotropic continuum assumptions), as shown in Figure 8.4.

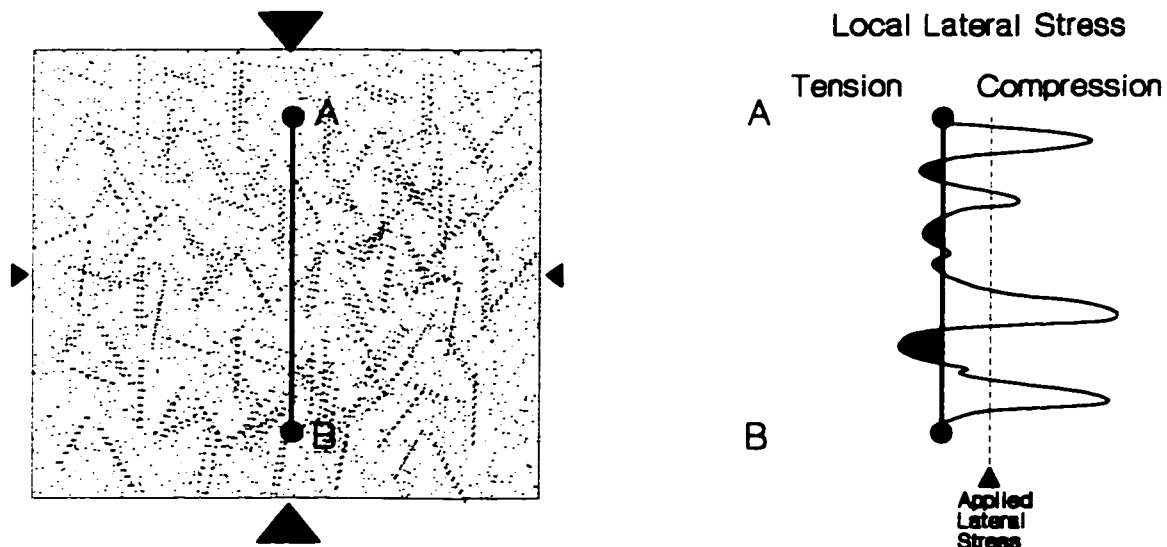


Figure 8.4: Local variation in stress field due to material or structural heterogeneity (based on Cook 1995 and Gramberg 1989).

This stress diversion can occur at different scales:

- Micro-fabric, within individual crystals and within assemblies of crystals, can create a trellis effect, generating tensile loading within the atomic or granular structure under applied compression (as in the bonded contact analogue in Chapter 7). Variations in crystalline structure (grain stiffness, boundary properties and contact orientation) create tortuous stress paths that result in local zones of high compression and extension.
- Non-uniform distribution of minerals within a crystalline solid can result in larger scale tortuosity of stress flow and larger zones of extension inducing crack growth during unloading or sampling at depth.
- Field scale jointing delineates blocks of rock which form zones of equal internal stress, expanding the scale of stress differentiation and localized yield. Furthermore, damage due to cracking can lead to induced heterogeneity and anisotropy of stiffness (as well as ultimate strength). This stiffness variability, in turn, can influence stress flow, particularly in areas of high stress or strain gradient.

Tortuosity of stress flow due to material heterogeneity, rockmass structure, discrete damage zones and excavation surface geometry (corners, irregular or re-entrant surfaces, curvature) has a particular impact on the level of local confinement within near-excavation zones. This in turn can have a significant impact on damage accumulation, crack extension and interaction, and ultimately on the apparent insitu strength of the rockmass.

In particular, any mechanism which reduces confinement in a local region, will increase the potential for crack propagation (after initiation) as illustrated in Figure 8.5. Longer cracks have a higher potential for interaction given the same number of crack nucleations. Apparent crack interaction stress and therefore insitu strength, can be significantly reduced.

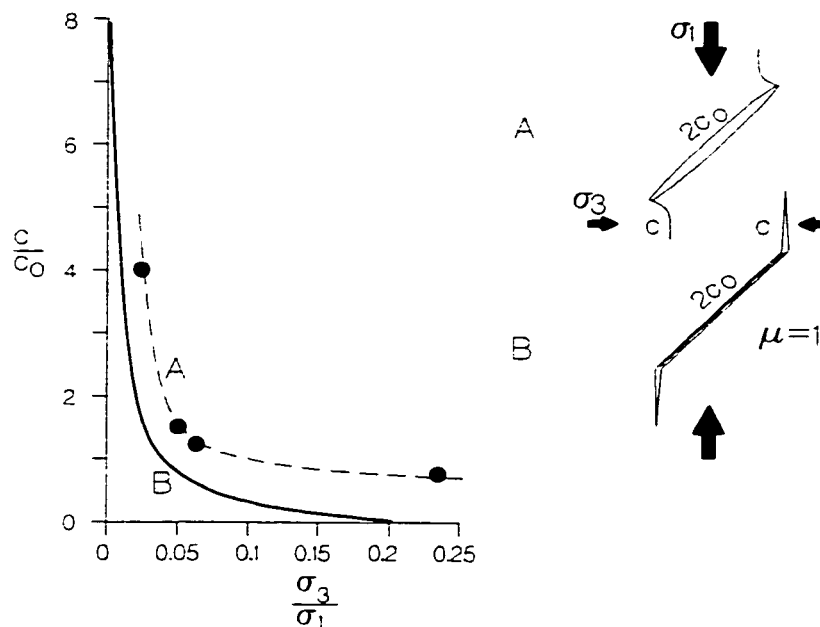


Figure 8.5: Effect of confinement on crack propagation length, c , with respect to initial flaw half length, c_0 , based on experimental data (A) for an open crack (Hoek 1968) and a sliding crack (B) relationship calculated by Martin (1997).

Cracks which initiate at low stress levels tend to dilate, in effect creating reduced confinement in the immediate region around the crack, exacerbating the impact of low confinement on further initiation and propagation (i.e. by reducing the effective σ_3 within a damaged rockmass below that predicted by continuum analysis). This concept is illustrated schematically in Figure 8.6.

A number of these mechanisms of insitu strength reduction will be examined in this chapter.

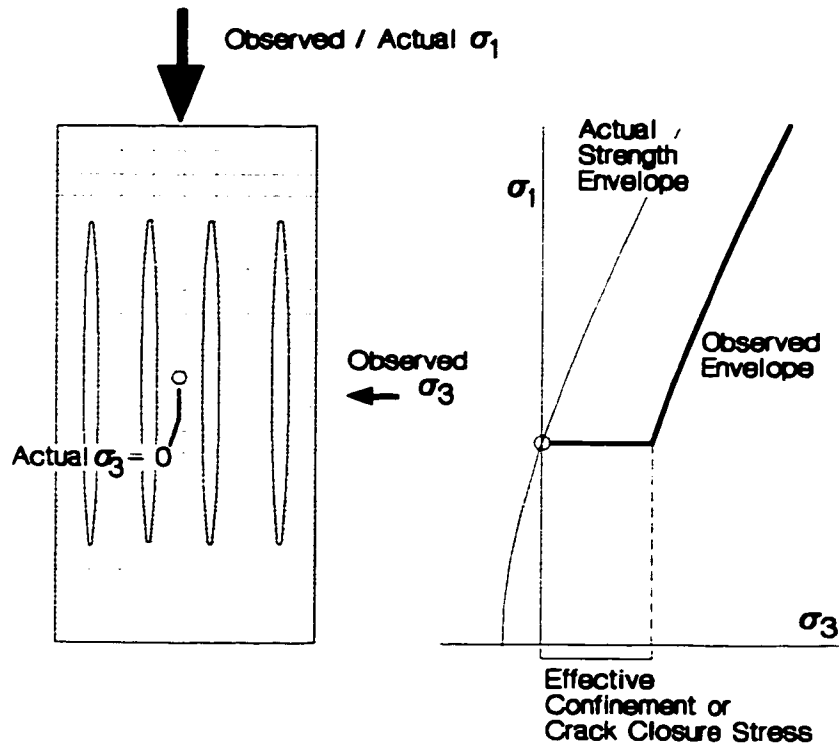


Figure 8.6: Schematic of effective confinement (or effective gap) concept.

The interrelated effects of heterogeneity and scale will be discussed. The weak-link concept, presented in Sections 8.2 and 8.3, is utilized to investigate these effects on tensile strength and crack initiation. The weak-link descriptor can refer to granular strength elements or to micro-flaws within the material. This concept has been invoked in the past to explain material strength distribution and is used here to investigate the link between heterogeneity and scale effect.

The analogue, while valid for crack initiation and therefore tensile strength, is limited, in describing compressive strength of polycrystalline solids. Initial crack accumulation does not immediately result in failure and interaction controls compressive yield in these materials (as discussed in Chapters 6 and 7). Crack interaction and critical crack density are only indirectly related to the weak-link characterisation of the component strength distribution as demonstrated by a statistical analogue for interaction developed in Section 8.4.

Other mechanisms must be invoked to explain the reduction of compressive strength insitu. Stress path and damage accumulation, as well as the effect of confinement variability and geometry effects will be investigated in Sections 8.5, 8.6 and 8.7.

8.2 ELEMENTAL VARIATION and DAMAGE INITIATION

Polymineralic rocks contain grains of different strength and stiffness. In addition, these grains may also vary in stiffness and as a result, loading paths and elemental stress distribution through heterogeneous samples are not uniform at the grain scale. So-called “weak-link” models apply to crack initiation and have been applied in the literature, to peak strength, with only limited validity and success. As the name implies, these “serial” models presume that the stability of a heterogeneous material sample of given size is controlled by, and therefore can be predicted based on, its weakest link. For compressive failure which is a more “parallel” process, it will be shown in this chapter that the weak-link theory has only limited and indirect applicability to predictions of yield and peak strength.

8.2.1 Elemental Strength Variation and Weak-link Theory

One of the most obvious forms of material heterogeneity is elemental strength. According to the most basic assumptions, the limiting element or the so-called “weakest link” controlling rock strength would presumably be the weakest mineral of significant presence (non-trace). In marbles, the weak-link may take the form of critically oriented calcite grains which undergo dislocation slip within the crystal lattice at lower deviatoric stresses. This creates a slip discontinuity at grain boundaries that has been observed (Olsson and Peng 1976) to induce crack initiation and extension in surrounding grains and along grain boundaries (Figure 8.7).

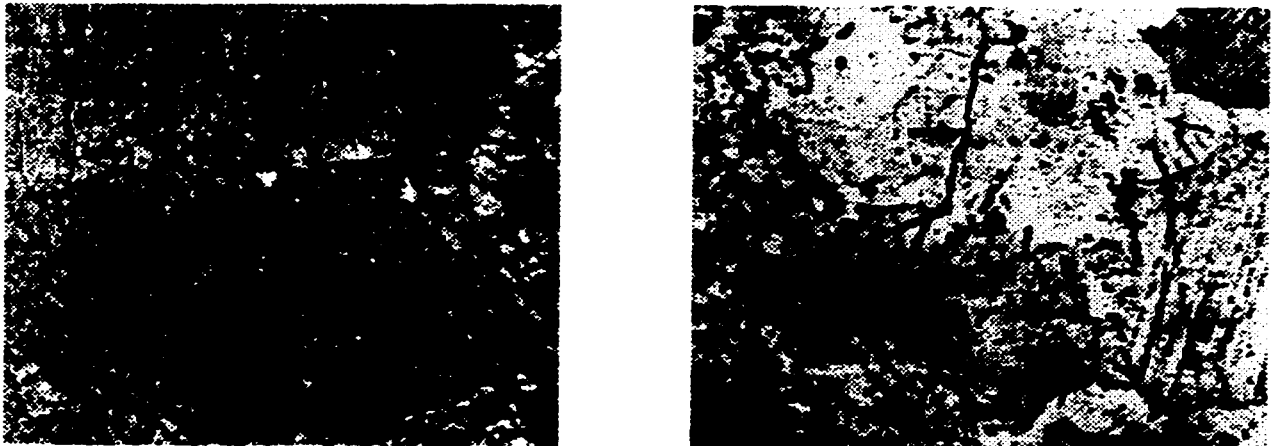


Figure 8.7: Laminae slip in critically oriented calcite grains inducing compression-parallel cracking in surrounding grains (after Olsson and Peng 1976).

Granites typically contain alkali and plagioclase feldspars and quartz in roughly equivalent percentages and also contain lesser amounts of micas such as biotite. Under local shear stress, the biotite grains could form a “weak-link” in compression even though the percentages are low. Separation and ultimately kinking (along [001] cleavage) can create a catalyst for trans-granular crack propagation through a slip flaw or weak inclusion mechanism. Tapponier and Brace (1976) suggest that peak compressive stress in tests on Westerly granite coincides (possibly coincidentally) with kinking (Figure 8.8) in biotite grains which make up only 5 to 10% of Westerly Granite.

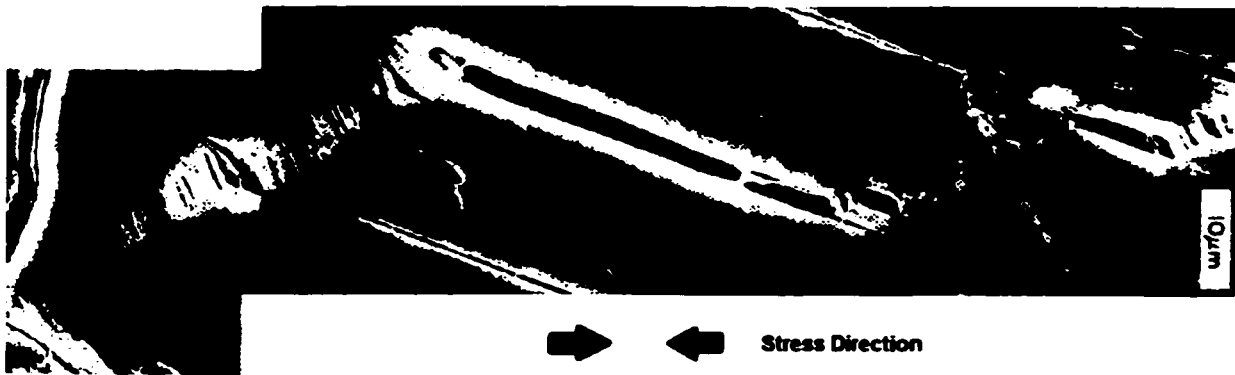


Figure 8.8: Cleavage [001] separation and kinking in biotite grains (Westerly Granite) close to peak stress (after Tapponier and Brace 1976).

It should be noted, however, that while cleavage separation is likely to affect the onset of cracking in other minerals, kinking of biotite may be a consequence rather than a cause of brittle or plastic deformation in surrounding grains. The weak-link notion for crack initiation is, nevertheless, supported by the observation (Tapponier and Brace 1976) that weak magnetite grains, occurring in trace densities, also split and crushed at low stresses, creating small plastic inclusions which served as nucleation sites for larger cracks in other minerals (Figure 8.9).

Lac du Bonnet granite and “granodiorite” (local classifications as discussed by Read (1994)) contain the four dominant mineral types with the percentages and material parameters listed in Table 8.1. The relative content of biotite alone, as a potential weak-link is at odds with the higher strength of the granodiorite (230 MPa - Martin et al. 1997) compared with 210 MPa for the granite. The grain size distribution from URL samples are shown in Figures 8.10 and 8.11.



Figure 8.9: Crushed magnetite grain creating subsequent soft inclusion or focused dilation source, inducing cracks in surrounding grains. Stress direction same as in Figure 8.7 (after Tapponier and Brace 1976).

Table 8.1: Key minerals affecting the strength of Lac du Bonnet Granite.

	Plagioclase	Alkali Feldspar	Quartz	Mica (Biotite)
Percentage ¹				
Granite	22	42	29	6
"Granodiorite"	24	35	29	11
Fracture Surface Energy (Jm ⁻²)	4.1 ²		4.0 ²	0.38 ²
K _{IC} (MPa·m ^{0.5})	0.31 to 0.39 ²		0.31 to 0.46 ^{2,3}	< 0.15 [001] ²
Base Friction μ @ 50% R.H. & (Saturated)	0.12 (0.77) ⁴		0.16 (0.51) ⁴	0.26 (0.13) ⁴

¹ Kelly et al. (1993); ² Atkinson and Meredith (1987), Atkinson and Advis (1980); ³ Ball and Payne (1976); ⁴ Horn and Deere (1962)

Read (1994) summarizes crack initiation data (Figure 8.12) from Lajtai (1988) which shows a bimodal distribution of crack initiation stress for granite-granodiorite samples. Similar bimodal strength distributions, for sound dry granite, have been obtained by Kittl et al. (1990) and by Eberhardt et al (1998; 1999). Compressive strength data for feldspathic sandstone of homogenous mineral composition (Kostak and Bielenstein 1971) shows a monomodal normal distribution (Figure 8.13).

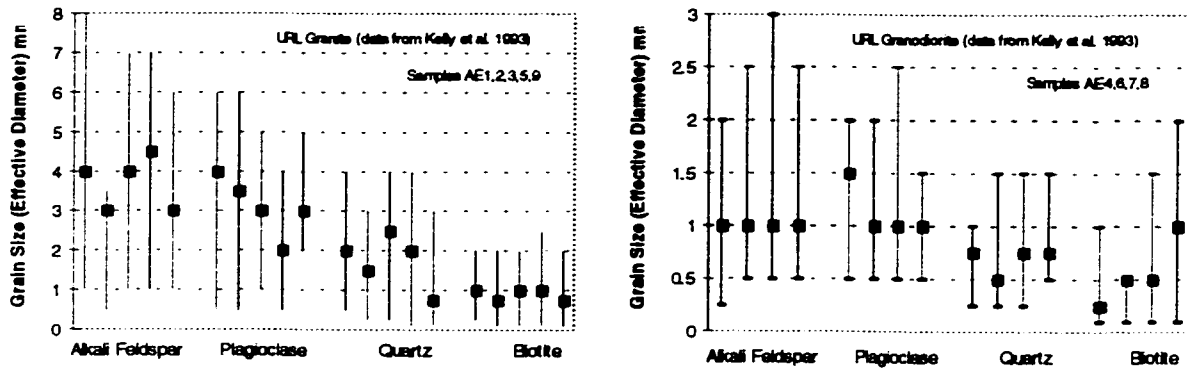


Figure 8.10: Grain size of mineral components for Lac du Bonnet granite and granodiorite.

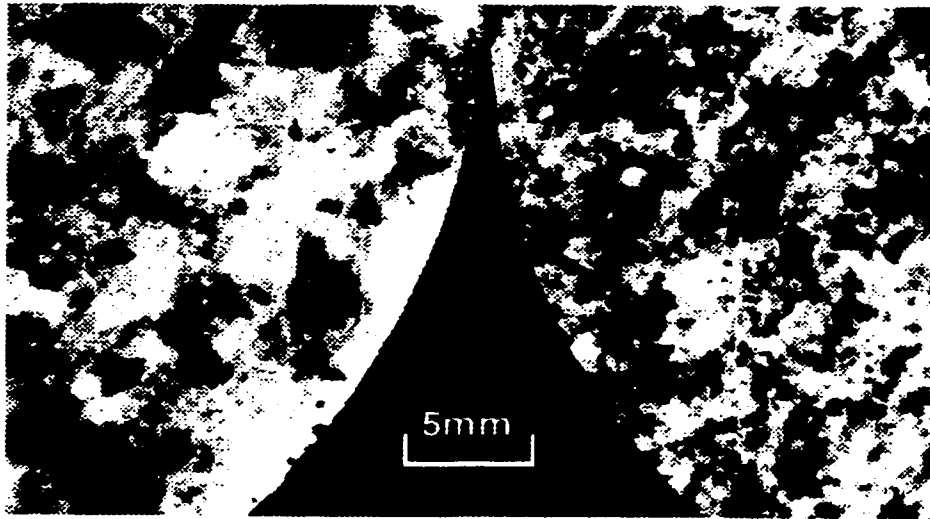


Figure 8.11: Grain size and uniformity contrast between URL granite (left) and granodiorite (right). The granodiorite is also more equi-granular. (Photo courtesy AECL).

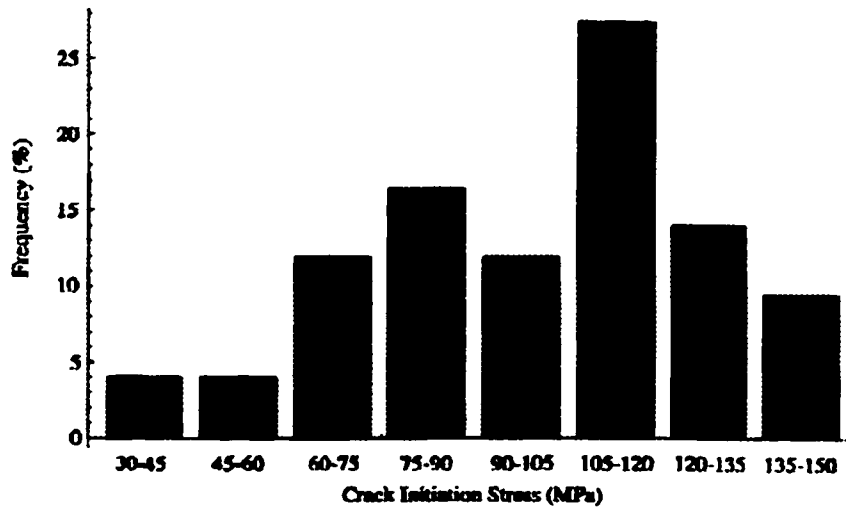


Figure 8.12: Crack initiation stress for Lac du Bonnet granite and granodiorite (Read 1994).

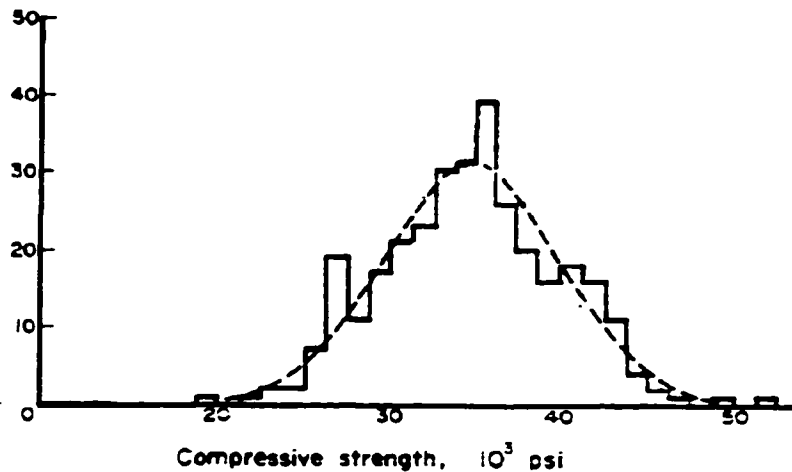


Figure 8.13: Strength data for homogenous sandstone (Kostak and Bielenstein 1971).

It is suggested by Read (1994) that the granite as defined in Table 8.1 comprises the bulk of the lower initiation peak ($\sigma_{ci} = 64\text{-}75$ MPa) as reported by Martin and Chandler (1994) and Martin (1997) due to the presence of larger (and weaker) feldspar crystals. The finer and more uniformly grained granodiorite samples show a higher initiation stress (100 MPa) corresponding perhaps to fracture of quartz grains or cleavage of smaller feldspar grains. The alkali feldspar is the most abundant mineral (42%) in the granite and has the largest grain size (4mm). Such a larger grained and more prevalent mineral would likely form the dominant load-bearing skeleton within the granite mass and would therefore be expected to dominate ultimate behaviour.

In the granodiorite at URL the grain size of all grains is roughly equal (1mm) and somewhat more uniformly distributed. It is likely that the greater homogeneity of mineral composition and grain size in the granodiorite (clearly visible in Figure 8.11) contributes to the higher strength, by providing an enhanced structural role for the stronger quartz grains, and by providing more uniform internal load distribution, counteracting the higher percentage of “weaker” biotite mineral. In addition, the smaller grain size limits the inter- and intra-granular flaw size which in turn increases the theoretical crack extension stress. Finally, the bimodal distribution may simply reflect the subjective observation of either the crack opening threshold or the crack extension threshold discussed in Chapter 6, or the thresholds associated with random initial cracking and the subsequent onset of systematic crack accumulation (Chapter 7).

In short, the effect of heterogeneity on composite rock damage strength is the result of numerous interacting mechanisms and cannot be attributed solely to the mineral strength.

8.2.2 Elemental Stiffness Variation

Elemental stiffness variation can affect damage initiation stress and overall sample compressive strength by concentrating compressive stresses (contact loads in PFC simulations) and enhancing locally induced tensile stresses. Figure 8.14 illustrates the force pathways through a regular lattice with uniform contact stiffness. The trellis geometry and uniform stiffness gives rise to uniform compression and uniform tensile contact loads (for lateral contacts) throughout the sample.

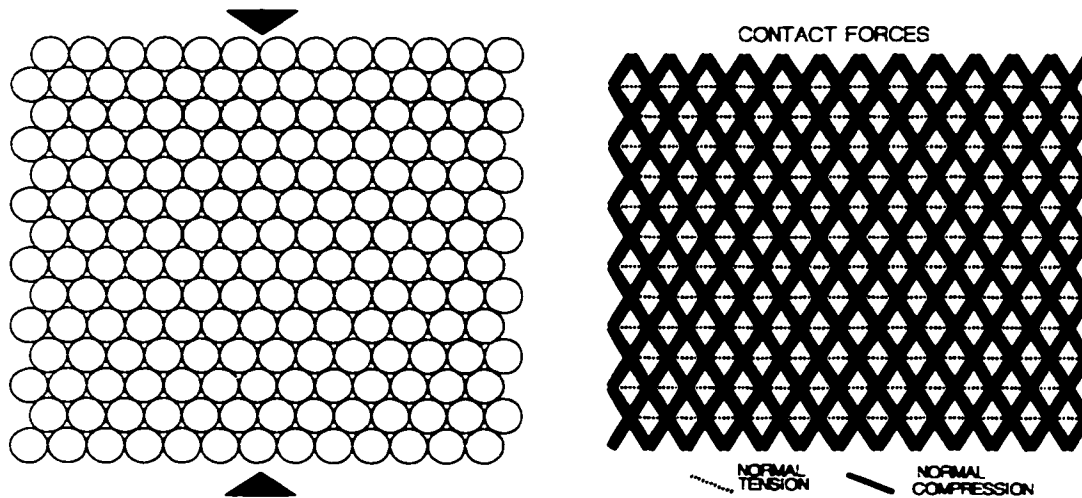


Figure 8.14: Force pathways through a uniform lattice under uniaxial compressive stress.

In contrast, Figure 8.15 illustrates the effect on internal contact forces of a non-uniform lattice with stiffness variation ("standard variation used in Chapter 7"). The resultant local contact force variation results in higher tensile values (critical for rupture) than the uniform lattice in Figure 8.14. This heterogeneity also results in larger regions of calculated stress variation (Figures 8.15c and d). These stresses are calculated, from the contact forces in the PFC model, within measurement circles (shown in Figure 8.15a) using Equation 7.9 and contoured using external software (Surfer). The concentrated tensile forces lead to contact rupture (crack initiation) at a lower applied stress than in the uniform case, even if the elemental strengths are uniform. In addition, the larger regions of low confinement as shown for the heterogeneous sample in Figure 8.15, promote extension of nucleating cracks, thus promoting premature crack interaction and sample yield. This is examined in detail later in this chapter.

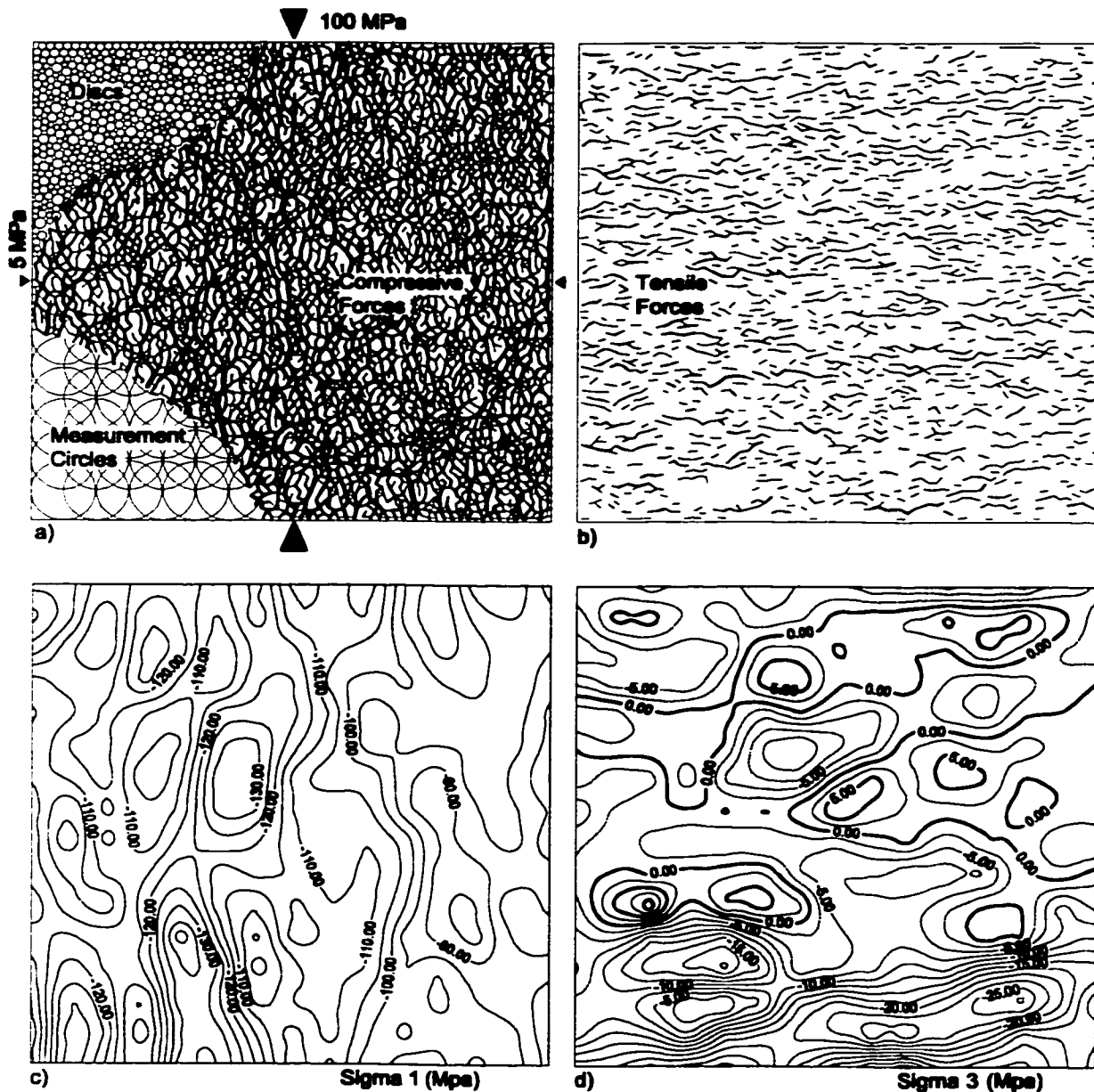


Figure 8.15: Compressive (a) and Tensile (b) contact forces in heterogeneous assembly (disc radius and contact stiffness). Cutaway insets in (a) show disc assembly and stress measurement circles for creation of stress contours (c & d - tension +ve).

The model in Figure 8.15 is analogous to stiffness contrast at a grain scale. A similar effect occurs at the sub-grain scale for polycrystalline assemblies (Figure 8.16) due to compliance contrasts at grain boundaries. This assembly was created by allowing a random “melt” of identically sized particles (Figure 8.16a) to compress and lithify under hydrostatic pressure, resulting in a realistic crystallization effect (Figure 8.16b), with features such as grain boundaries, internal crystal lattices and twinning planes (Figure 8.16c).

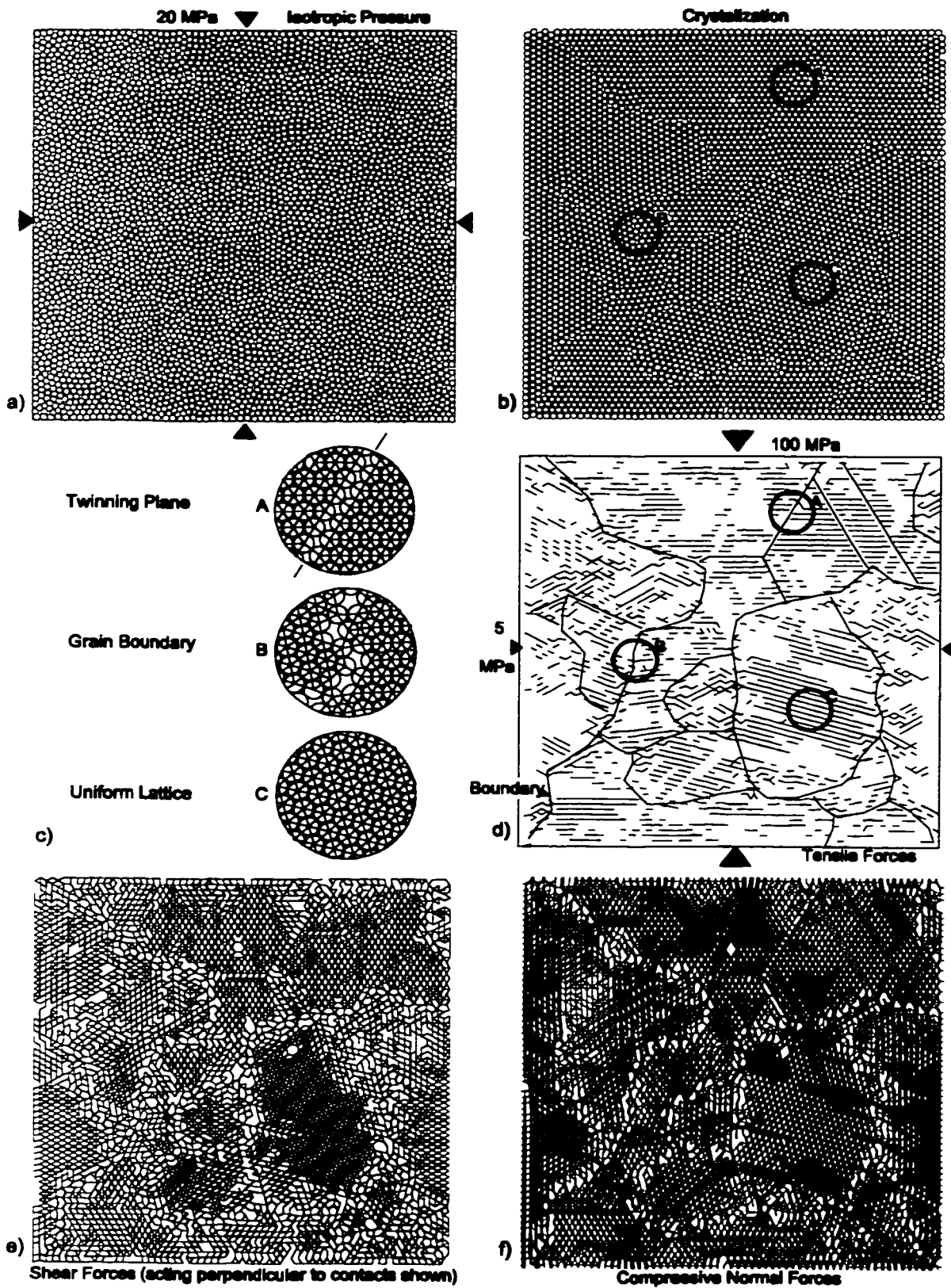


Figure 8.16: Uniform "melt" (a) compressed to form a crystal network (b & c). Internal tensile (d), shear (e) and compressive (f) forces generated by confined compression.

The assembly was then compressed axially after unloading. Irregular atomic mating at grain boundaries (outlined in Figure 8.16d) induces uneven stress or force transfer through the crystal network. The tensile, shear and compressive contact forces are illustrated in Figures 8.16d, e and f, respectively. Within the crystals the force distribution can be relatively uniform. The contoured stresses and the creation of heterogeneous stress "islands" are shown in Figure 8.17.

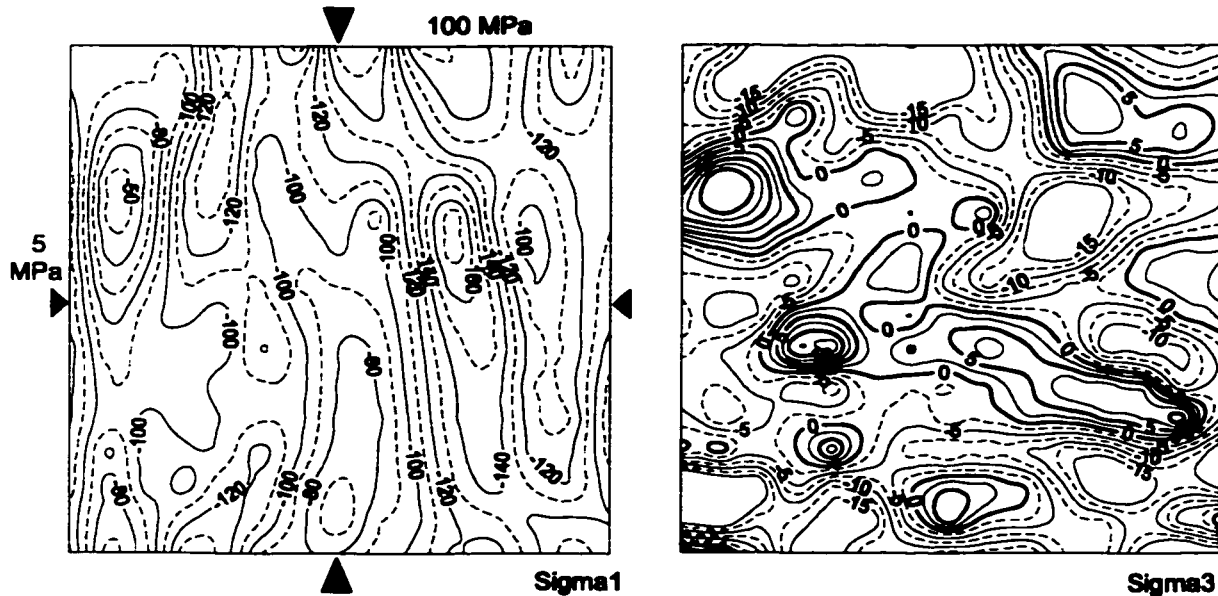


Figure 8.17: Internal stress distribution (tension +ve) within the crystal lattice. Sample dimensions and measurement circle size and distribution are the same as shown in Figure 8.15a.

Geometric interference can create increased compressive forces and Brazilian-type tensile forces as shown in the insert in Figure 8.16c for the uniform lattice (sample C). If an extension crack initiates within this crystal, the uniformity of contact loading will allow it to propagate in an unstable fashion out to the crystal boundary. The abrupt change in lattice force distribution at the crystal interface as well as the interference of the irregular grain boundary itself will temporarily arrest crack growth. Martin (1994) observed that prior to critical damage, stress cracks rarely traverse grain boundaries. This trans-granular jump is responsible for the discrete "packets" of energy release that are observed as acoustic emissions.

This crystal model is intended only as an illustrative case. Clearly, in a model of this scale, the effects of the outer sample boundaries affect the internal force distribution and the process of damage initiation, accumulation and interaction.

8.2.3 Contact Property Variation - Compression Simulations

The relative impact of elemental strength variation on crack initiation, accumulation and localization can be seen in PFC simulations in which the mean strength and stiffness are kept constant while the standard deviations (normal distributions) vary as shown in Table 8.2. Figure 8.18 shows the relative variation of contact strength (with respect to the input mean) for a representative trio of otherwise identical samples. Sample VAR1 possesses some variation even

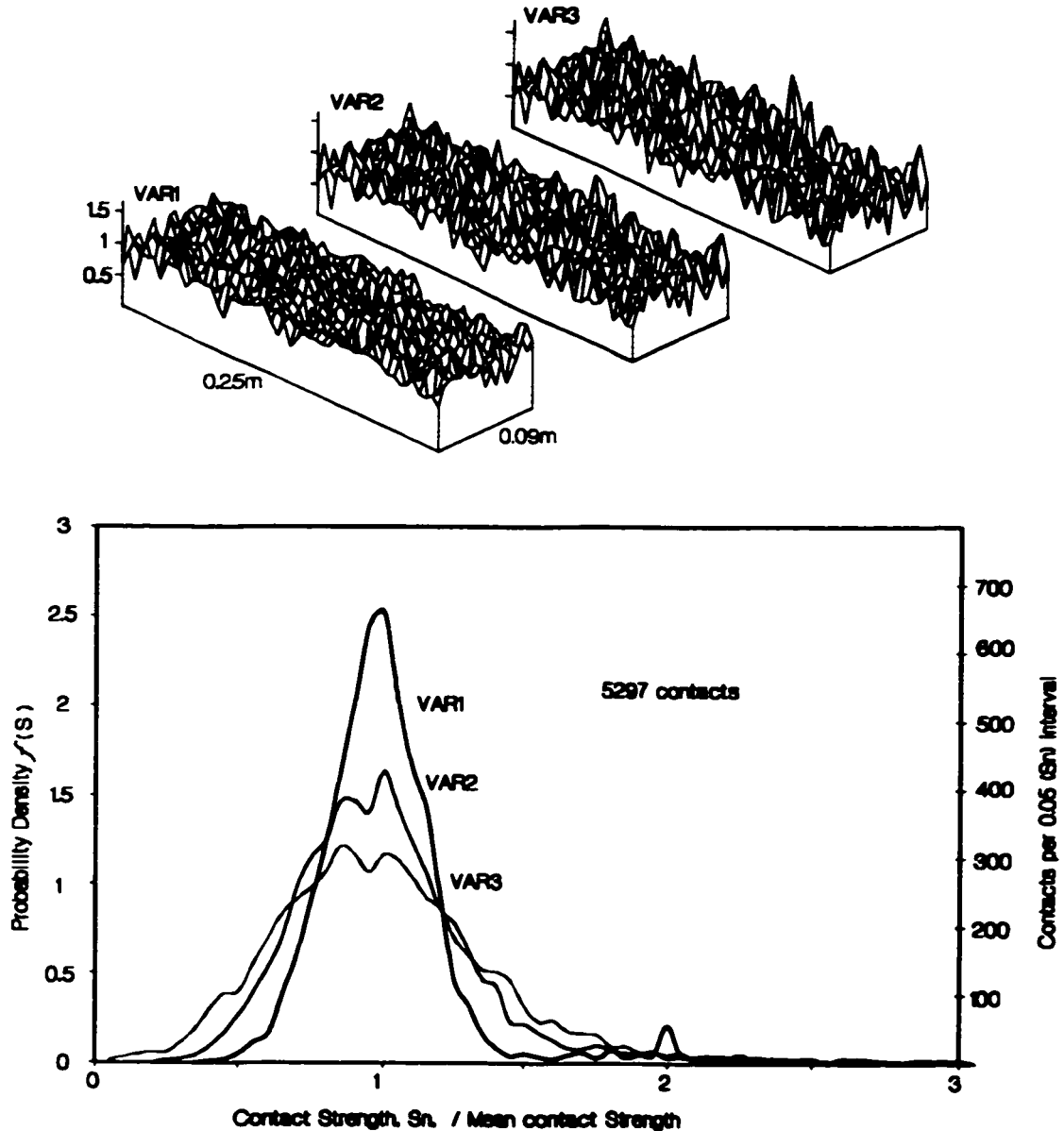


Figure 8.18: Spatial distribution and sample probability density distributions for elemental strength (tensile bond strength - force) for 3 PFC samples in Table 8.2.

though the input parameters in Table 8.2 specified zero variability. This is due to a variation in particle (and therefore contact) width. In these and all other PFC simulations the strength (specified as a force term) is scaled according to the contact radius.

Table 8.2: Parameters used in PFC simulations shown in Figures 8.19 through 8.21.

mean disc radius	0.0016m (std. dev. 0.0004)	
sample dimensions	0.250 x 0.090m	
#discs, contact pairs	2784,5959	
mean K_n, K_s	1.6e5, 0.64e5 MN/m	
Mean N, S	0.3,1.2 MN	
	Stiffness K_n, K_s (std. dev. / mean)	Strength N, S (std. dev. / mean)
VAR1	0	0
VAR2	0.1	0.2
VAR3	0.15	0.3

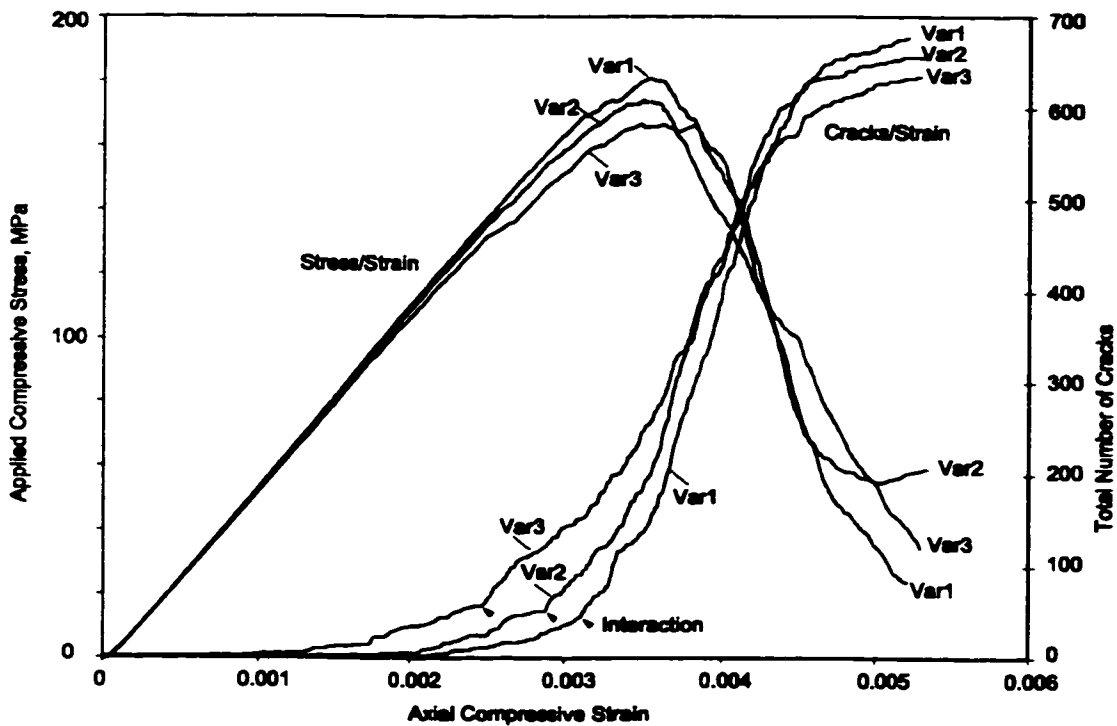


Figure 8.19: Axial response and crack accumulation for heterogeneous samples in Table 8.2.

It is apparent from Figure 8.19 that moderate to high variability in stiffness and strength contributes to crack initiation (first crack) at lower stress. The change in peak strength, however, is

relatively minor (10% for the samples shown). Pre-peak strain hardening is evident in the case of high variability samples while the uniform samples (VAR1) appear more elastic-brittle in their behaviour. In all cases, virtually all of the damage is in the form of tensile bond rupture. As such, even in the uniform samples, systematic crack initiation (Figure 8.20) begins at approximately 55% of peak with a gradual accumulation of damage prior to localization and peak strength. It is interesting to note that the heterogeneous sample (VAR3) contains less total damage (fewer cracks) at residual strength than the more homogenous sample.

Figure 8.20a illustrates a comparison between the cumulative distribution curves, obtained from an integration of the density distributions in Figure 8.18, and the crack accumulation histories in Figure 8.19. It can be seen that, initial crack growth and the trend of crack accumulation (labeled "Crk" in Figure 8.20a and plotted with respect to the top and right axes), correspond very closely to the cumulative distribution curves for elemental strength (labeled "Str" and plotted with respect to the bottom and left axes). Prior to the point labeled "systematic damage" there is a tail of low strength elements and a corresponding period of minor random crack growth, visible in the results of VAR3, which seem to disappear in the more uniform samples. Figure 8.20b is a schematic identifying typical thresholds observed in the PFC simulations. The log-constant period of systematic crack growth is analogous to the AE accumulation phase in laboratory tests.

The stress level - crack accumulation relationship for both this initial cracking stage and the log-constant systematic cracking phase seems to mimic the elemental cumulative strength distribution for the sample. The exception is the uniform sample VAR1 which appears in Figure 8.20a to exhibit greater initial variability in contact rupture load than would be indicated by its elemental strength distribution. This is due to an underlying level of heterogeneity induced by the non-uniform load paths through the random lattice or clastic model.

At a certain critical stress level, just prior to peak in these simulations, the crack accumulation rate increases dramatically, and no longer mimics the elemental strength distributions, as crack interaction takes place and continued cracking becomes driven by localized stress perturbations around crack clusters. From Figure 8.20 it is apparent that crack initiation and early accumulation seem to directly correspond to the weak-link hypothesis while the interaction and localization stress (and consequently peak strength) is controlled by a critical crack which bears only an indirect relationship to elemental strength. The difference in the critical crack intensities at which

interaction occurs, correspond to the respective initial crack accumulation (number and intensity) prior to systematic crack growth. This phase of cracking, associated with weak-link elements seems to be unrelated to the ultimate array of cracks which cause yield and failure of the sample.

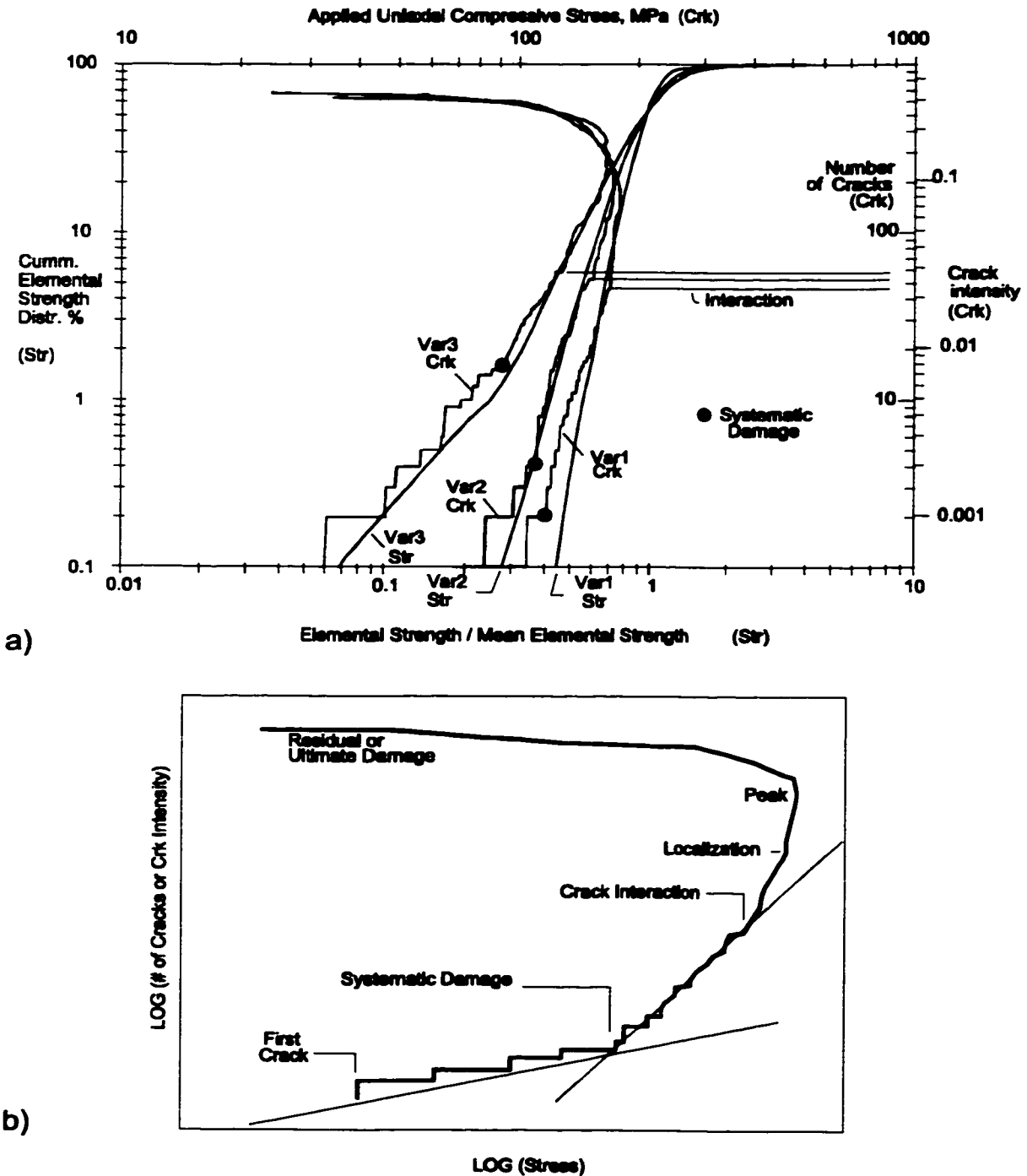


Figure 8.20: a) Crack accumulation and elemental strength distribution in heterogeneous samples; b) crack damage thresholds (schematic).

8.3 SCALE EFFECT

Scale effect is a natural consequence of the weak-link notion of elemental strength. Both the size of the sample and the size of the characteristic flaw are important considerations. In certain situations the two are related. In others, the flaw size is limited by a characteristic dimension such as the grain size. A direct scale effect, with respect to sample size, is apparent for damage initiation only in the former case. Larger samples, however, contain a larger quantity of weaker flaws. Crack initiation stress may drop in larger samples as a consequence.

The weak-link concept applies to sample yield and failure, only if damage initiation is directly related to failure. As discussed before, this is the case in tension but not in compression. Other factors influence the scale effect in compression such as the relationship between strain energy within a (3Dimensional) volume and energy absorbed in the creation of a localized (2 dimensional) fracture surface. Several aspects of scale effect are examined in this section.

8.3.1 Effect of Internal Flaw Size

While there is evidence that the shear or tensile strength of particular minerals or appropriately oriented grains result in a weak-link effect for a heterogeneous sample, it is more generally accepted that the primary source of strength reduction and scale effect is the presence of pores, cracks and discontinuous grain boundaries within the rock which concentrate stresses to induce extension cracking. While some minerals contain more defects than others (e.g. biotite) and themselves form weak-links for crack initiation, defects also occur within amorphous or monomineralic material and are themselves a form of heterogeneity impacting macro-behaviour.

Existing defects within the laboratory sample, and present at varying scales insitu, are normally cited as the cause of reduced material strength. The defects create concentrated stresses at their edges or tips creating an observed reduction in macro-sample strength. This concentration increases for larger cracks resulting in a scale-effect directly reducing initiation strength. This indirectly (compressive loading) or directly (tensile loading) reduces rupture strength. This is the essence of the Griffith approach to rock strength (Griffith 1920; 1921) which offered a viable explanation for the drastic reduction in tensile strength of glass rods (several orders of magnitude from the theoretical molecular strength) as the diameter is increased (Figure 8.21). This finding was also the foundation for much of modern fracture mechanics.

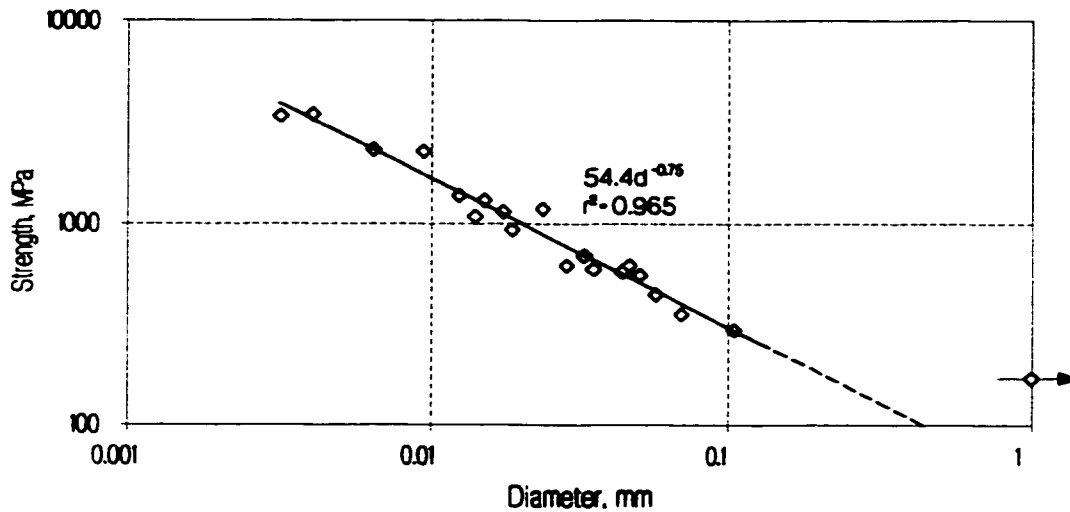


Figure 8.21: Tensile strength reduction with increasing rod diameter from experimental data reported by Griffith (1921). Strength for 1mm corresponds to nominal tensile strength for larger samples.

The scale relationship for glass wires in Figure 8.21 was approximated by Griffith as:

$$154.5 \text{ MPa} + 680 \text{ MPa}(\text{mm}^{-1})/ d \quad [8.1]$$

where d is the rod diameter in millimeters. The best-fit power law relationship for Griffith's data for glass filaments less than 1mm in diameter is actually of the form:

$$\sigma(\text{MPa}) = 54.4[d(\text{mm})]^{-3/4} \quad [8.2]$$

Griffith formulated, based on energy principles as discussed earlier in detail, a relationship between the tensile strength of a material, σ_t , and the size of a critical flaw, in his case an elliptical void of high aspect ratio (Figure 8.22a).

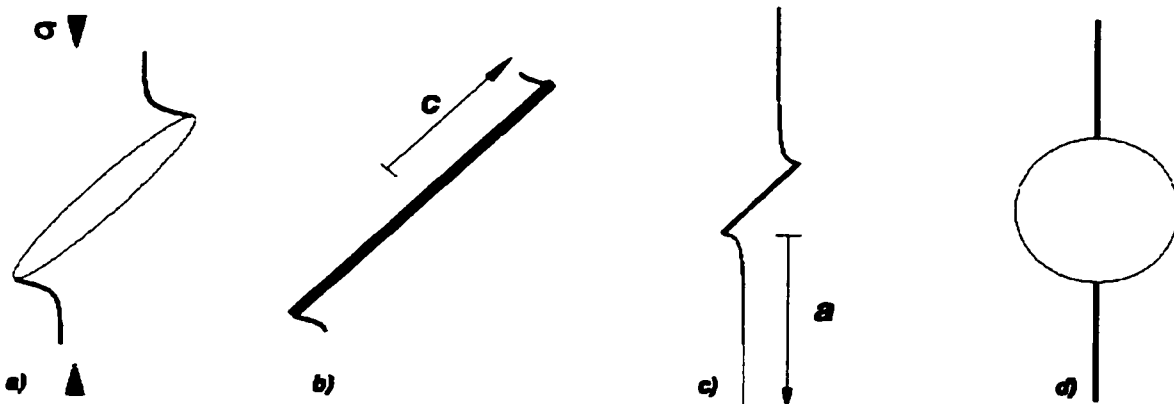


Figure 8.22: Flaws and crack nucleation: a) elliptical crack; b) sliding crack with nascent wing cracks; c) sliding crack with developed wing cracks of length a ; d) circular pore.

The relationship in uniaxial tensile conditions for the critical two dimensional crack (aligned perpendicular to loading) of length $2c$ is:

$$\sigma_T = \sqrt{\frac{2E\gamma}{\pi c}} = \frac{K_{IC}}{\sqrt{\pi c}} \quad [8.3]$$

where E is the Young's modulus, and γ is the surface energy. K_{IC} is the critical stress intensity factor, a measurable index describing the state of stress and strain at the crack tip. For a circular crack in three dimensions (Kemeny and Cook 1986):

$$\sigma_T = \sqrt{\frac{4\pi}{c}} K_{IC} \quad [8.4]$$

Cotterell and Rice (1980) define the conditions (in terms of net shear traction, τ_{cr}) for wing crack initiation (no initial wing cracks) from a two dimensional inclined sliding flaw (Figure 8.22b) of length $2c$ to be:

$$\tau_{cr} = \sqrt{\frac{3}{4\pi c}} K_{IC} \quad [8.5]$$

where τ_{cr} is related to the applied principal field stresses as a function of crack friction angle, ϕ , and crack normal orientation, θ (angle from vertical):

$$\tau_{cr} = \frac{1}{2} [(\sigma_1 - \sigma_3) \sin 2\theta - \tan \phi (\sigma_1 + \sigma_3 + (\sigma_1 - \sigma_3) \cos 2\theta)] \quad [8.6]$$

Once wing cracks initiate and begin to grow (Figure 8.22c), the relationship becomes a more complex function of the variables c , σ and a , where σ is the normal stress perpendicular to the wing cracks of length a (Pestman and van Munster 1996):

$$\tau_{cr} = \frac{(K_{IC} + \sigma_3 \sqrt{\pi a}) \left(\sqrt{\pi (a + L(3\pi^{-2} \cos^2 \theta))} \right)}{2L \cos \theta} \quad [8.7]$$

Pure in-plane initiation of a shear crack has a similar form to Equations 8.3 and 8.4 with K_{IC} replaced by K_{IIC} , the critical intensity factor for Mode II rupture (Kemeny and Cook 1986).

Extension cracking from a perfectly circular or spherical pore (Figure 8.22d) does not, in theory, have a size dependency. If a minute crack is present on the pore surface or once extension is initiated from an ideal pore, however, the propagation stress becomes instantaneously dependent on

both the pore diameter and the length of the propagating crack, making large pores which are stressed beyond the crack initiation threshold much less stable than small pores (Sammis and Ashby, 1986).

8.3.2 Fracture Initiation, Propagation and Yield

Linear elastic fracture mechanics dictates an inverse square root scale effect for all forms of isolated crack initiation and propagation. This is a natural consequence of the assumption that the elastic strain energy reserve, W_e , available is proportional to the square of the stress and to the volume occupied by the crack while the energy dissipated in fracture creation, W_f , is proportional only to the surface area of the crack (assuming infinitely stiff loading system, no energy loss or residual storage):

$$W_e = W_f \quad [8.8a]$$

$$\xi \sigma^2 L^3 = \gamma L^2 \quad [8.8b]$$

$$\sigma = \sqrt{\gamma \xi} \cdot (L)^{-0.5} \quad [8.8c]$$

$$\frac{\sigma_A}{\sigma_B} = \left(\frac{L_A}{L_B} \right)^{-0.5} \quad [8.8d]$$

where γ and ξ are constants. This is clearly the case for the marble samples in Figure 8.1a. In the case of marble, the governing defects are closely related to the grain size (Wong et al 1996; Olsson and Peng 1976).

Linear elastic fracture mechanics (LEFM) suggests an infinite strength of a perfect atomic solid or of extremely small samples. This may be of little consequence if atomically sharp cracks are assumed and if c is much larger than the inter-atomic spacing. Non-linear models account for the presence of a non-linear or inelastic process zone in front of an advancing crack, the effect of which becomes highly significant for small cracks, blunting the stress concentration (Bazant and Kazemi 1990). A more general transitional relationship (loosely based on the principals of non-linear fracture mechanics) proposed by Bazant (1993) for strength, σ , as a function of crack d :

$$\sigma = A(1 + Bd^{2r})^r \quad [8.9]$$

where d is the dimension (length units), and A , B and C are constants and where r is found in the case of concrete strength data (Bazant and Pfeiffer 1987) to be close to 0.5, yielding a capped

inverse square root relationship.

L in Equation 8.8 has come in the literature to represent the sample dimensions (as in, for example, Tsoutrelis and Exadaktylos 1993). This is based on the assumption that the sample instantaneously fails through a single plane (shear or extensile) and does so with full consumption of strain energy (elastic-brittle behaviour). In truth, such a plane cannot form without the interaction of distributed extending microcracks which are more likely to obey Equation 8.8 with respect to grain or initial flaw size than with respect to sample size, unless a relationship exists between the two dimensions.

The exponent in the general LEFM relationship in Equation 8.9, differs from Equation 8.2, indicating that there is not a simple linear relationship between sample size and critical flaw size in tensile rupture of glass fibres. Griffith's fibres are more sensitive to scale than indicated by an inverse square root relationship. In Griffith's experiments the size of the flaw present was likely related to the fabrication process and subsequently exacerbated by internal cooling stresses. The flaw size is likely to increase more than linearly with the fibre diameter. Equation 8.9 is applicable only if the flaws in samples of different size are geometrically similar (Bazant 1993).

Natural materials show less scale dependency at practically significant dimensions than exhibited by the exponent (-0.5) in Equation 8.8. Lundborg (1967) found an exponent of (-0.25) for peak compressive strength of granite samples. Examination of strength data from Martin and Chandler (1994) reveals a strength-scale relationship with an exponent of approximately (-0.16) for samples larger than 50mm in diameter. Figure 8.1.b suggests an exponent of (-0.18) for the normalized scale relationship for a composite suite of rock data, although individual rock types such as marble within this dataset exhibit negative exponent relationships of smaller magnitude. Evans et al. (1961) report a dependency as low as (-0.11) for marble and (-0.09) for concrete. Wijk et al. (1977) performed direct tension tests on granite, over a range of diameters from 5mm to 64mm, which show no apparent scale dependency at all (Figure 8.23).

One reason for the variation in scale effect is the relationship between initial flaw size and sample size. There is no reason to expect that the flaw dimensions continuously scale with the sample volume. In laboratory experiments on intact, undisturbed samples, the limit of the scale effect for crack initiation and local propagation is related to the maximum flaw dimension and therefore, to the grain size as illustrated in Figure 8.24 using data for crack size / grain size data for marble.

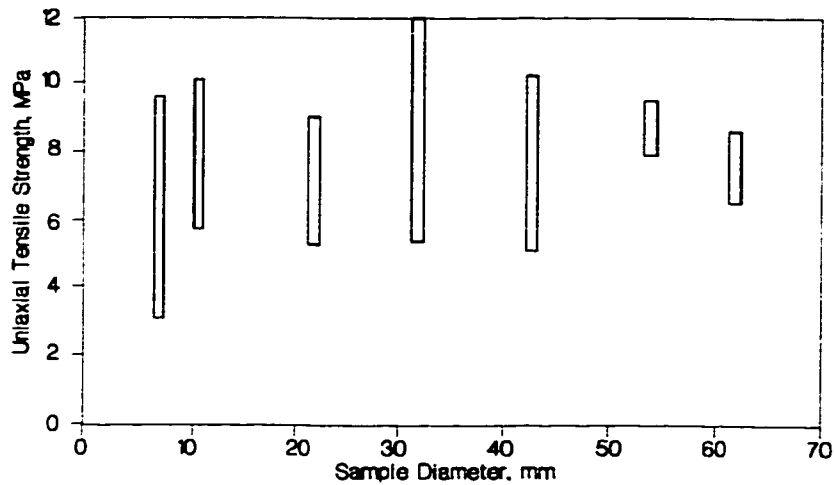


Figure 8.23: Effect of sample scale on direct tensile strength (data from Wijk et al 1977).

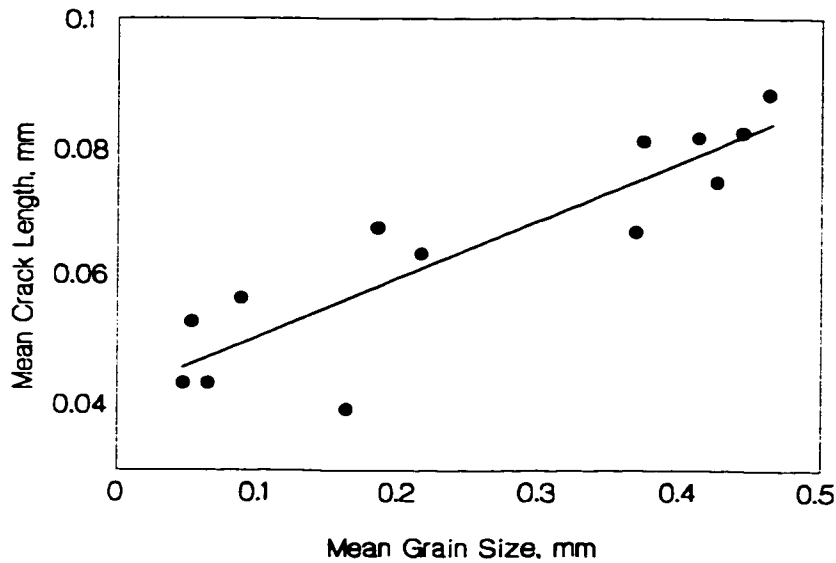


Figure 8.24: Crack length and grain size relationship in marble (after Wong et al 1996).

Even in undisturbed but jointed rock, however, the controlling dimension for initiation is likely to be related to the grain scale and not to the block size. In the case of a sliding crack induced Mode I initiation model for granite, the maximum friction coefficient for smooth intra-granular cracks is 0.3 from Table 8.1. The minimum residual friction coefficient of polished macroscopic granite surfaces, on the other hand, is greater than 1 (Martin 1994). Actual joints in granite are likely to have much higher coefficients under small strain. This means that the joints are unlikely to result in a drop in the initiation threshold. Grain scale asperities (which must be damaged for macro-slip) are likely to control the initial yield strength for macro-scale joints.

8.3.3 Scale Effects in Compressive Test Simulations

To explore the role of scale with respect to crack initiation and accumulation in a material with a characteristic dimension such as a polycrystalline or clastic rock, a number of PFC compression test simulations were performed on samples of varying size (Table 8.3 and Figures 8.25 and 8.26).

Table 8.3: Scale effect simulation samples

Sample	BS00	BS01	BS10*	BS02	BS03	BS04	BS05	BS06
	BA00	BSA1	BA10*	BSA2	BSA3	BSA4	BSA5	BSA6
Width	15	30	45	60	90	120	150	180
Height, mm	37.5	75	112.5	150	225	300	375	450
# of discs	73	276	608	1066	2373	4193	6527	9377
contact pairs	190	676	1436	2329	5782	9184	14309	20603

Internal parameters as in VAR3 in Table 8.2: BS0 and BSA similar series with different random seeds.

*samples did not yield complete results

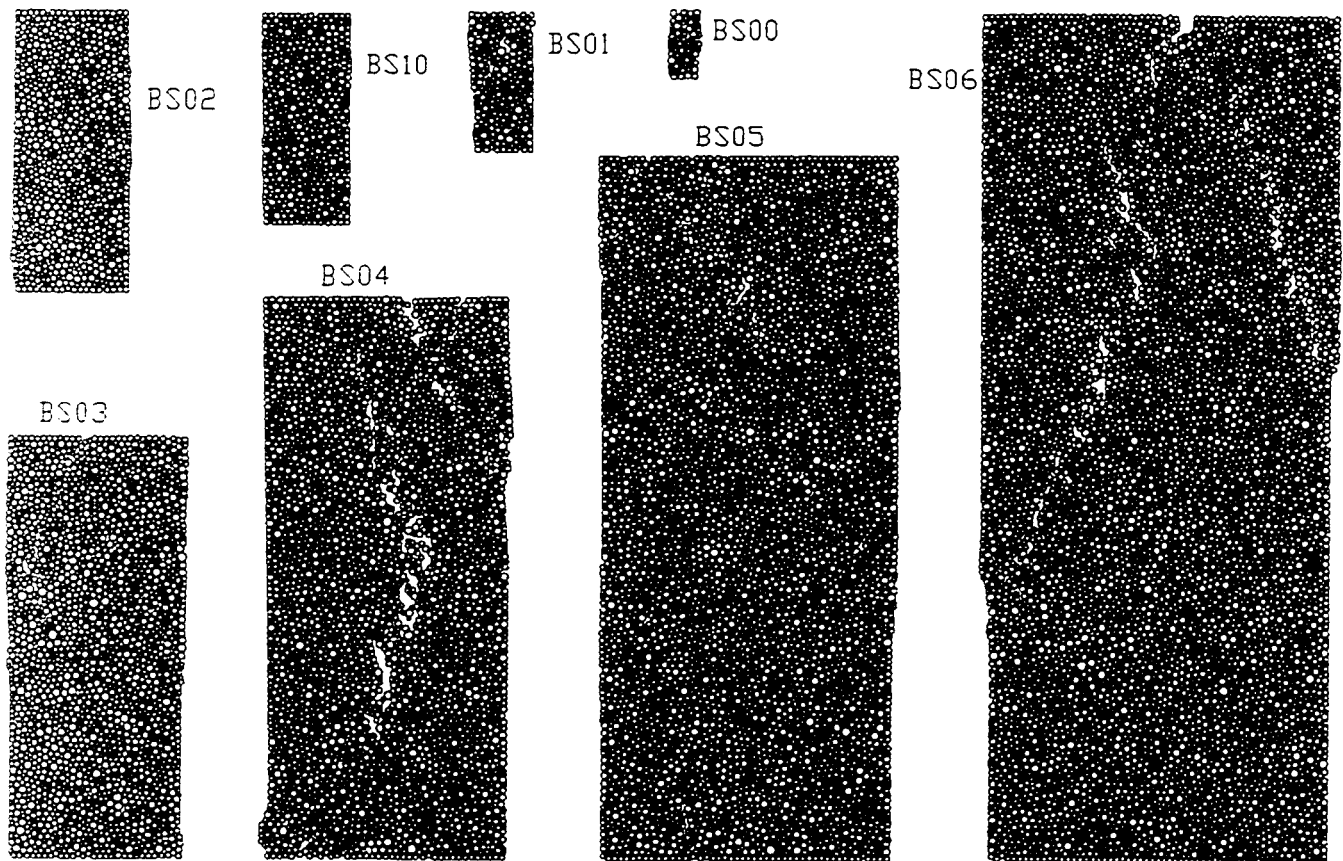


Figure 8.25: Samples (after failure) used in PFC scale effect study. (BSA series had different random seeds and therefore different particle arrangements).

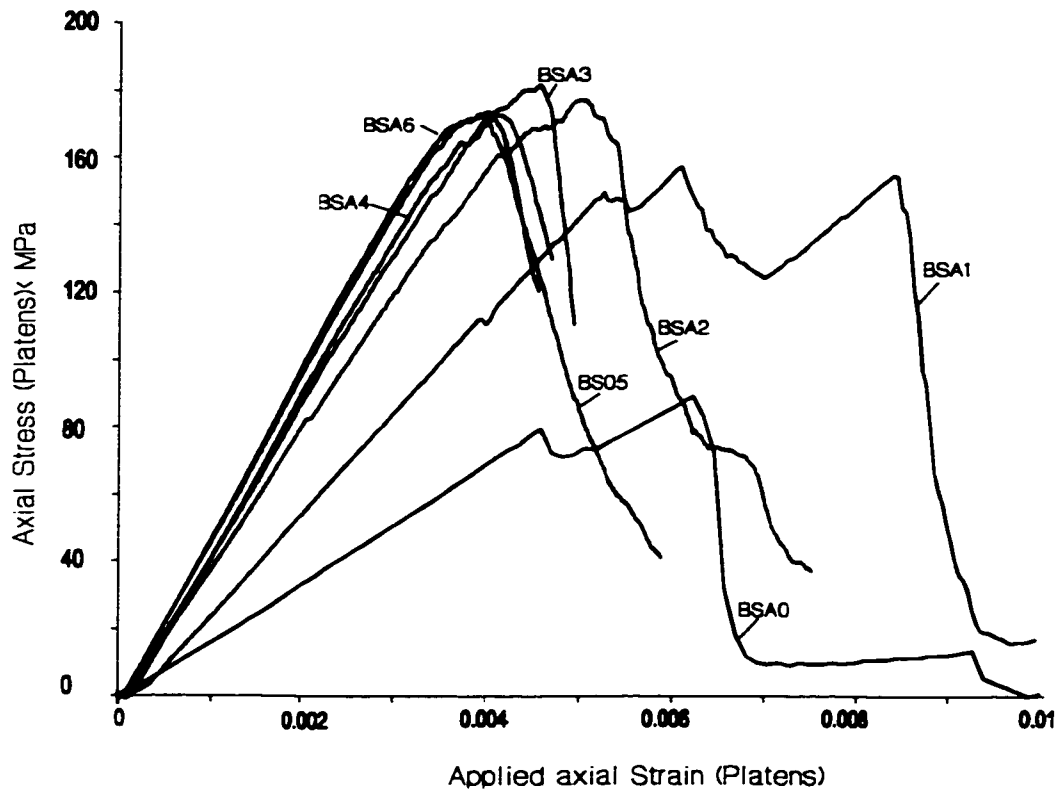


Figure 8.26: Stress-Strain responses (top) and crack accumulation (bottom) for PFC scale effect samples.

The elemental strength distribution (not including the effect of variable stiffness) is shown in Figure 8.27 for each sample. Even though the input variabilities (i.e. as specified for an infinite population of contacts) were identical for the seven samples, the four smallest samples (BS/BA) 00 and 01 show a marked increase in the strength of their weakest elements in accordance with weak-link probability theory. A smaller sample contains fewer members from the "tails" of the strength distribution and therefore contains fewer "weak-links". This is discussed in the next section. This results in an elevated crack initiation stress (for the first crack) in these two samples. This effect quickly subsides with increasing scale as shown in Figure 8.27 as weaker elements accumulate in larger samples. Notice, however, that the threshold for systematic crack damage exhibits less scale effect than first crack initiation.

In addition, the peak strength (Figure 8.26) of the smallest samples, predicted to be the highest are in fact, the lowest. This is due to the increased rotational and translational freedom for individual particles within a small assembly. For the same reason, the smallest samples exhibit a lower modulus. This stiffness effect is likely to be an artifact of PFC modelling, related to platen contact distribution, and likely does not have physical significance for a real solid.

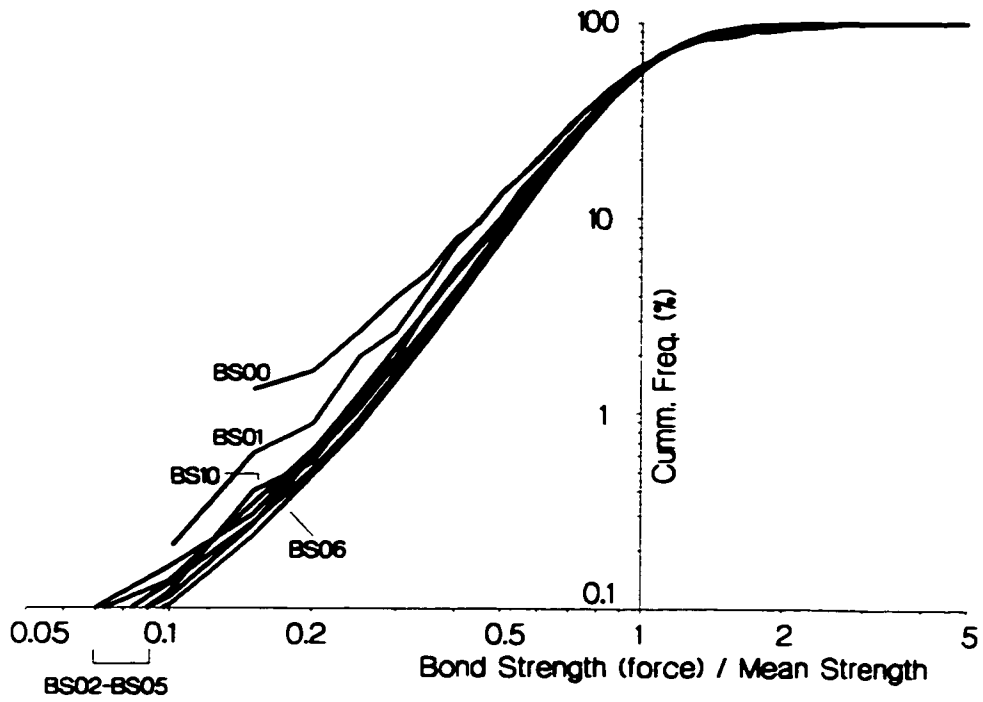


Figure 8.27: Cumulative contact strength distribution for PFC scale effect samples.

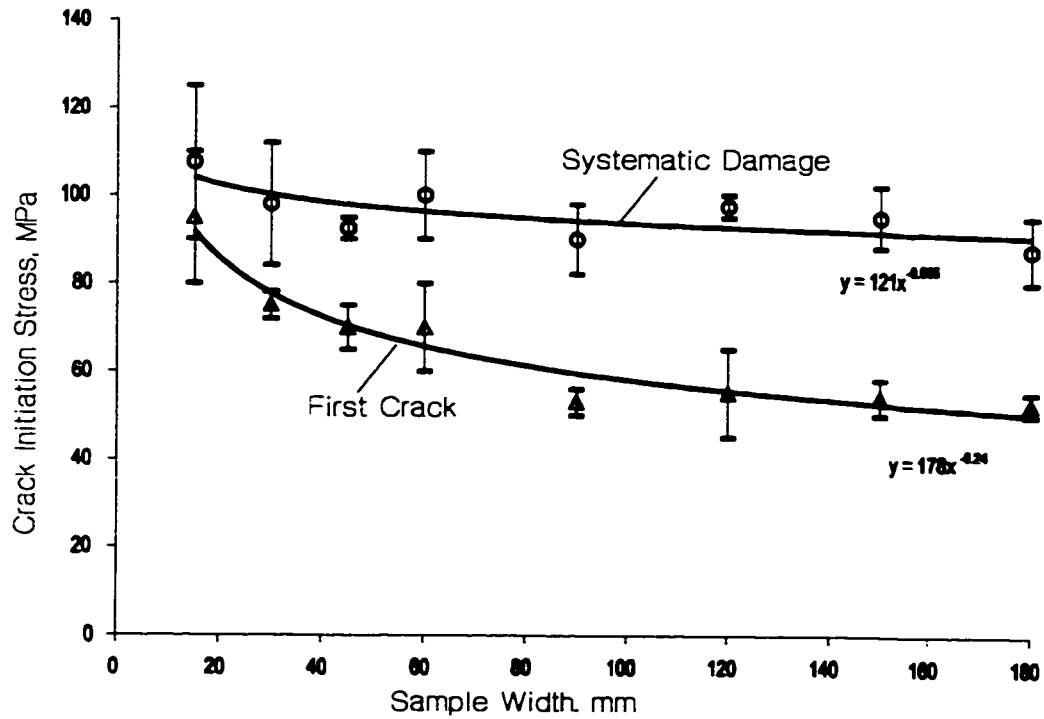


Figure 8.28. Crack initiation thresholds for PFC samples. Best-fit linear and power functions are shown.

Nevertheless, in small samples a single bond rupture is more likely to impact the stability of the entire sample. Martin and Chandler (1994) show that for small samples of granite, the predicted increase in strength is truncated as smaller samples fail prematurely (Figure 8.29). This effect was also found in a number of rock types by Hawkins (1998) as shown in Figure 8.30.

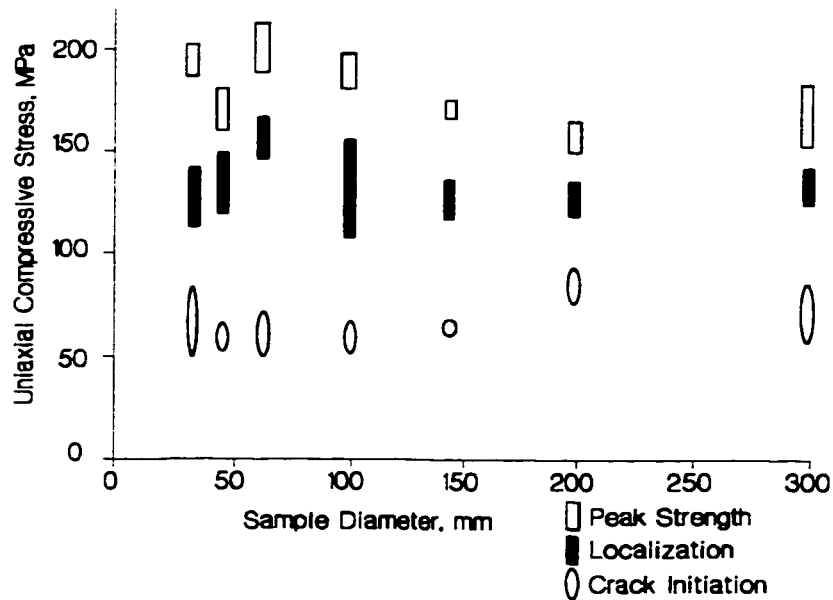


Figure 8.29: Effect of sample diameter on strength thresholds for Lac du Bonnet granite (data from Martin and Chandler (1994)).

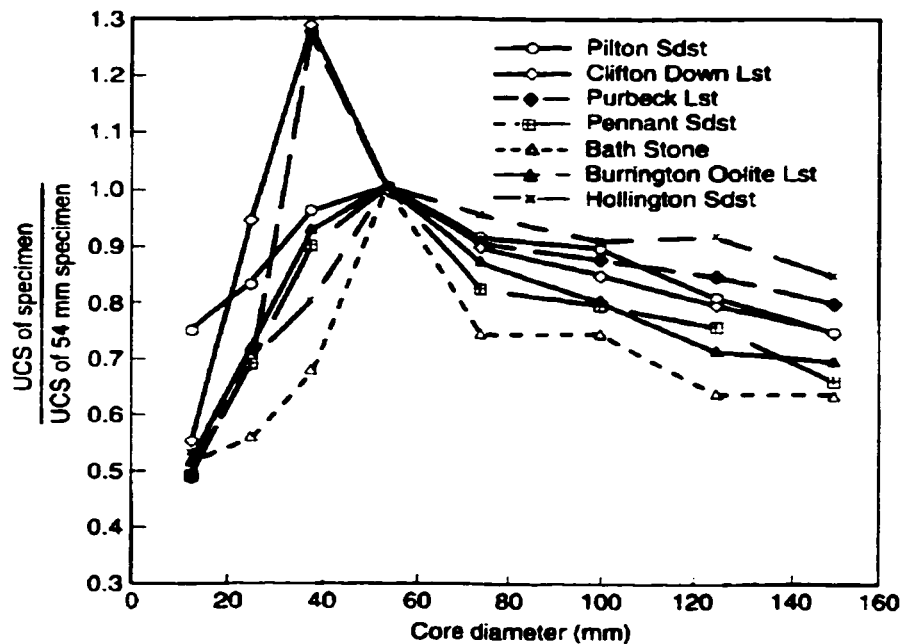


Figure 8.30: Effect of scale on sample strength for various rock types (Hawkins 1998). Note truncation of strength increase for very small samples ($D < 50$ mm).

Martin and Chandler (1994) also show that scale dependency for localization and peak strength in geometrically similar uniformly loaded samples (Figure 8.29) is asymptotic beyond upper bound diameters (approximately 100mm and 150mm respectively in this case).

A fractal approach to the scaling relationship (Tsoutrelis and Exadaktylos 1993; Chelidze and Guegen 1990) has been used to account for the lower negative exponent relationships, assumed to be the result of the tortuous and pseudo-three dimensional nature of induced fracture networks, through a modified form of Equation 8.8:

$$\left(\frac{\sigma}{\sigma_0}\right)^2 = \frac{L^D}{L^3} = L^{-(3-D)} \quad [8.10]$$

$$\left(\frac{\sigma_A}{\sigma_B}\right) = \left(\frac{L_A^{(3-D_A)}}{L_B^{(3-D_B)}}\right)^{-1/2} \quad [8.11]$$

where σ_0 is the strength of a unit volume, A and B represent comparative samples of arbitrary dimension, L , and D is the fractal dimension of the failure surface network (ranging from 2 for a perfect plane to 3 for an instantaneous crushing of the entire specimen). Here it is assumed that the samples and the rupture geometries are similar such that $D_A = D_B$. For an example dimension, D , of 2.5, the scaling exponent would be 0.25, a more reasonable value. If the shear zone undergoes complete fracture over a width which scales with sample dimension, L , such that the ratio of the shear zone volume and the sample volume is constant, then the fractal dimension would approach 3 and there would be no scale dependency. Equation 8.10 reduces to the form of Equation 8.8 if failure occurs via an instantaneous shear rupture along a perfect plane with fractal dimension 2. Crack localization after interaction, therefore, manifests itself as a drop in fractal dimension (within a constant sample volume) of the crack network.

For the purposes of analysis in two dimensions, the fractal dimension, D , is determined according to Chelidze and Guegen (1990) and Pietgen and Saupe (1988) from:

$$L_C = \xi L_S^D$$

$$D = \frac{\log L_{C1} - \log L_{C2}}{\log L_{S1} - \log L_{S2}} \quad [8.12]$$

where ξ is a scaling constant, L_C is the total length of cracks, L_S is the linear sample dimension (side length) and the subscripts 1 and 2 denote two geometrically similar samples of different size.

For a uniformly distributed (non-localized) crack network in 2 dimensions, D is 2 and ξ is related to the global crack density.

Equation 8.12 can be used to assess the fractal dimension of the crack network of PFC models at key stages in uniaxial test simulations including the onset of localization, peak strength and complete fracture. Taking N as the number of cracks in the sample and d as the mean crack length (assumed equal to the mean disc diameter in this case), L_C is simply calculated as Nd and L_S is the equivalent square dimension of the sample.

Crack length accumulation, calculated simply as the sum of all individual crack lengths, was studied in detail for the fourteen samples from the PFC scale effect study. Three accumulation landmarks were recorded, namely interaction, peak and total length (at residual strength). The summed crack length at the instance of interaction was determined using three criterion illustrated in Figure 8.31. These criterion have been described in Chapter 7.

These localization stress thresholds correspond to an instantaneous total crack length (i.e. just prior to localization). These total lengths are plotted with respect to the sample dimension (width) in Figure 8.32. The fractal dimension for crack length accumulation is simply the slope in this log-log plot. The best-fit constants for the power law relationships for localization are essentially similar for the three indicators and the fractal dimensions (exponents or log-log slopes) range from 1.99 to 2.02 indicating, for a two dimensional analysis, that accumulation prior to interaction and localization is a purely volumetric phenomenon and according to Equations 8.10 and 8.11 should be free from energy based scale effects. In other words, interaction leading to subsequent localization begins at a characteristic crack density, independent of sample volume, at least in cases where the range of crack lengths is fairly narrow. This can be seen in Figure 8.33. The deviation or inverse scale effect for very small samples has already been ascribed to increased rotational and translational freedom.

An important aspect of this conclusion is that in PFC the range of crack lengths is fixed and so the crack density is simply a linear function of the crack initiation count or number of cracks. In reality the crack density must be a power function of the crack length which may vary significantly. Critical density and therefore the localization threshold are reached earlier if individual cracks are forced to extend due to other influences besides material strength and axial load.

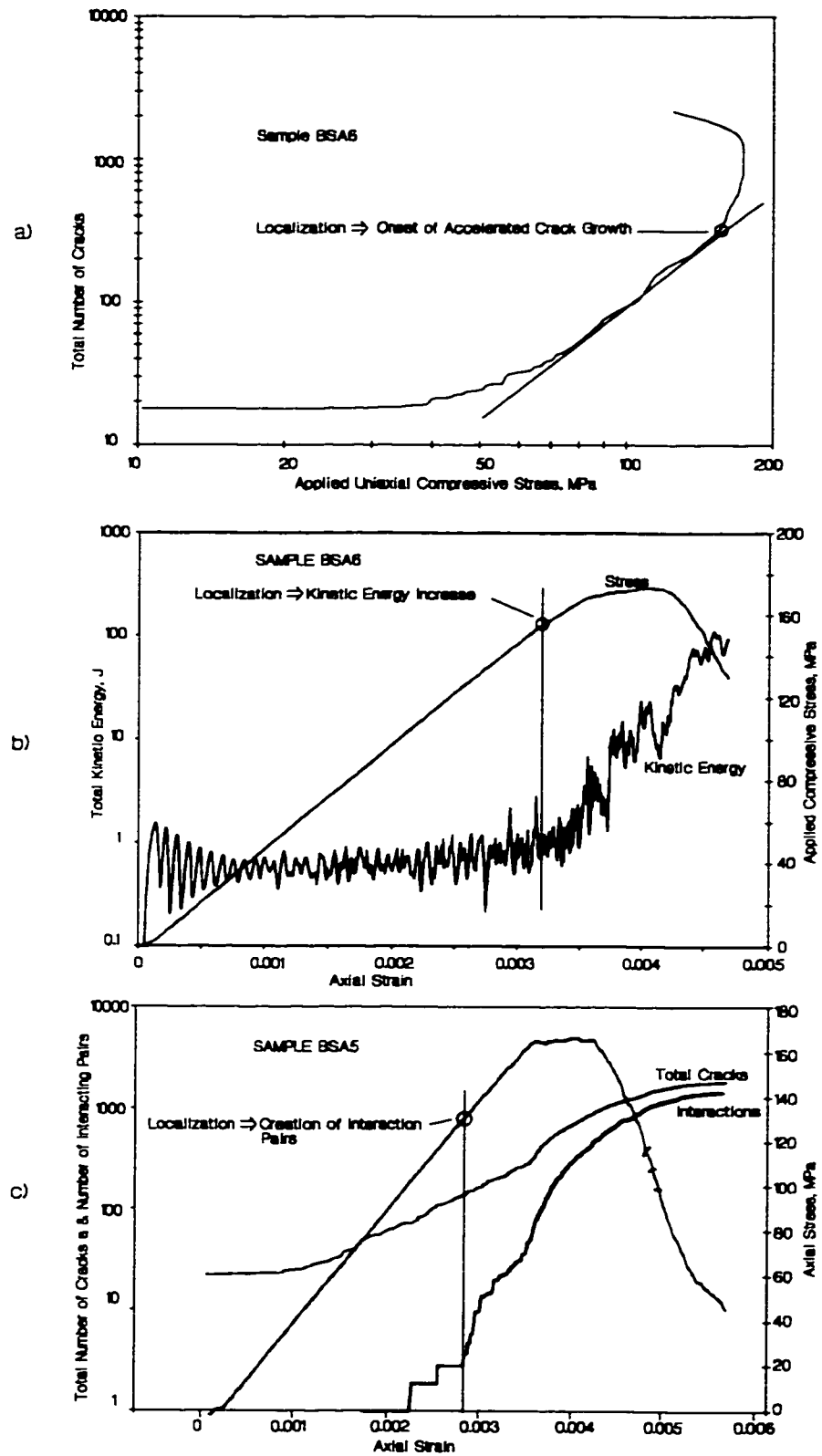


Figure 8.31: Localization indicators for PFC simulations: a) accelerated crack growth; b) kinetic energy increase; c) interacting crack pairs.

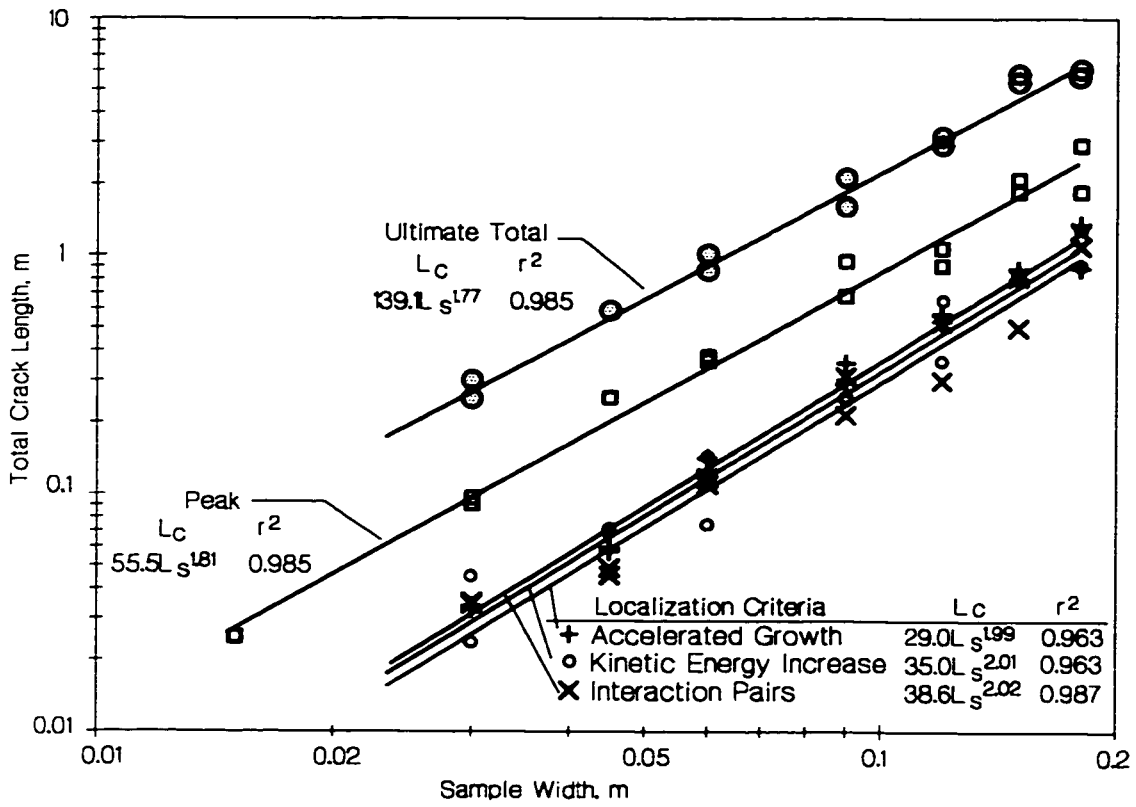


Figure 8.32: Estimation of fractal dimension for crack arrays at key thresholds.

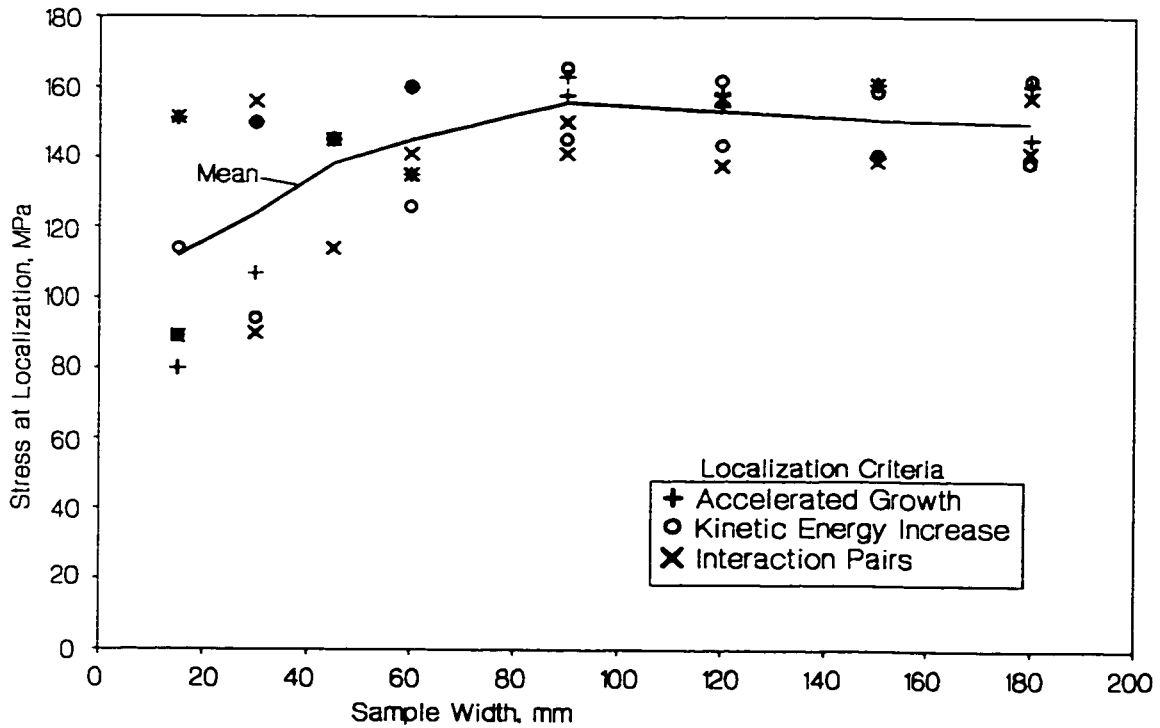


Figure 8.33: Localization stress threshold for samples of varying scale.

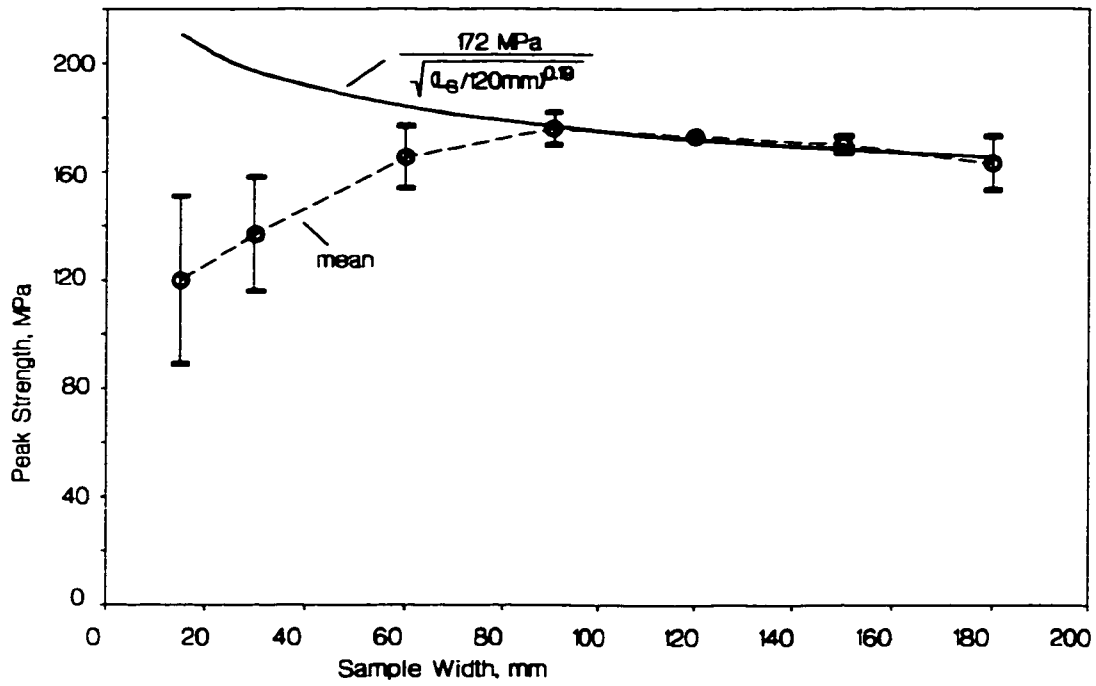


Figure 8.34: Scale effect for peak strength. Best-fit for larger samples normalized with respect to strength at 120mm.

For the PFC simulations, a qualitative examination shows that, while additional distributed damage occurs after crack interaction, the final shear zone after failure is of similar width (a function of the grain size) independent of the dimensions of the sample (Figure 8.35). This is consistent with the rationale behind the fractal dimension calculations for scale effect.

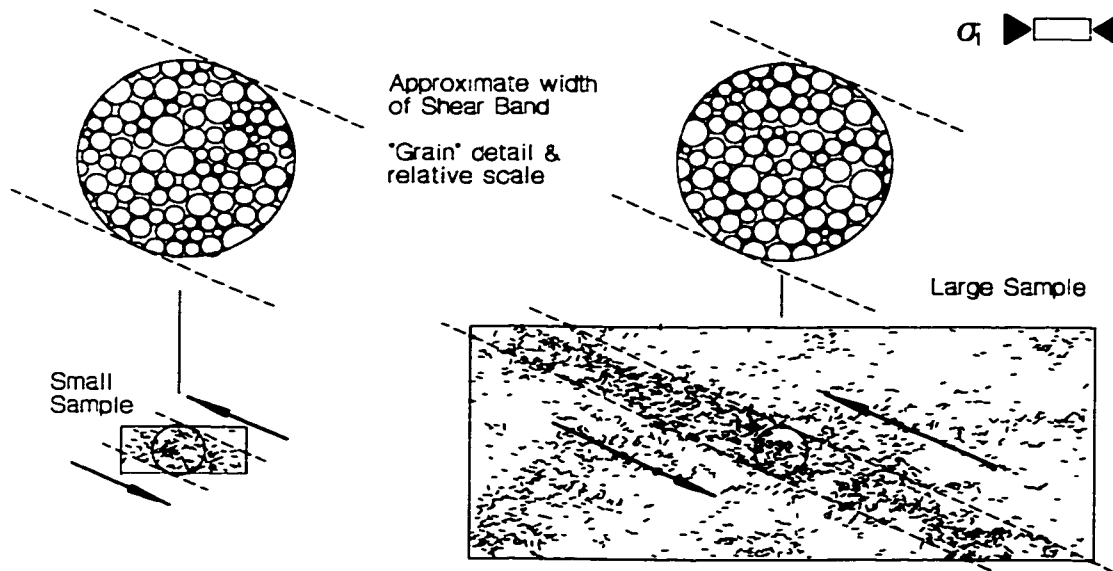


Figure 8.35: Scale independence (with respect to sample size) of shear zone development.

The fractal accumulation dimensions at peak strength and at residual strength are obtained from Figure 8.32. By the time peak strength is achieved, the cracks have significantly localized to a more planar (or linear in these 2D analyses) accumulation geometry as evidenced by the fractal dimension 1.81. At residual strength the ultimate total crack accumulation is even more planar with a dimension of 1.77 (An exclusive and perfectly linear failure surface would have a dimension of 1). The dimension at peak yields a scale effect exponent of $-\frac{1}{2}(2-1.8)$ or -0.1. With the exception of the spurious inverse scaling for small samples, this exponent fits the strength versus scale data in Figure 8.34. It is also more in keeping with the scaling data obtained for marble and concrete (Evans et al. 1961) and slightly less than that of granite (Martin and Chandler, 1994).

From this simple analysis it can be deduced that scale effects in crack accumulation (pre-peak) and crack interaction, are likely related to accumulation potential and internal properties while scale effects for peak strength are controlled by energy balance. As a stochastic consequence of initiation and uniform accumulation (a volumetric process), the onset of crack localization should not possess an energy based scale dependency according to Equations 8.10 and 8.11 and is more likely controlled indirectly by the grain size. Peak strength for conventional shear failure, on the other hand, is a consequence of the formation of a continuous separation plane (slip or extension) which traverses the sample after localization. The energy reserve to form this plane or zone (after initial interaction) depends on the relationship between sample volume and fracture area as illustrated in Equation 8.8. For planar or localized shear zone failure, peak strength should converge to the interaction stress threshold (Smith 1995). Martin (1994) has shown that for large samples, peak strength is coincident with the interaction threshold.

Carrying the energy balance logic through to the post peak region, it should also follow that larger samples become more brittle since a smaller relative portion of the strain energy stored within the volume of the sample is dissipated through the creation of a pseudo-planar failure surface or shear zone (Wawersik and Fairhurst 1970).

While physically schematic in nature, the fractal crack concept is useful in understanding the role of heterogeneity beyond the weak-link model. Materials such as marble may have a strong characteristic dimension, limiting crack propagation to, for example, a single grain or grain boundary segment (Olsson and Peng 1976; Wong et al. 1996). This creates difficulty in planar macrocrack propagation, resulting instead in a more three dimensional fracture network and a reduced scale effect as compared to a more heterogeneous material with a less defined

characteristic dimension such as granite (cracks extend beyond grain boundaries at stresses above 0.7 times the *UCS* (Martin 1994)). In the form of Equation 8.6, marble has an exponent of (-0.11) according to Evans et al. (1961) compared to granite with (-0.25) according to Lundborg (1967).

For field scale sample tests, summarized by Bieniawski (1968), scale effect becomes negligible in samples greater than 0.75 to 1.5m, several orders of magnitude larger than the grain size (cleat size for coal samples) and much larger than the characteristic dimension limiting scale effect for the coarse-grained Lac du Bonnet granite. Note that in these tests (Figure 8.2), however, the lower bound for strength is approximately one quarter to one third of the strength of a conventional laboratory scale specimen. This would suggest, based on the discussions in Chapters 6 and 7, that the lower bound for strength is the close to the crack initiation strength. While this may be somewhat circumstantial or tautological evidence, it is consistent with the tests by Martin (1994) and the tensile experiments by Wijk et al. (1977). It can be concluded with minimal reservation then, that tensile strength and (uniaxial) compressive crack initiation threshold is a constant for large samples or insitu rockmasses, independent of sample or volume scale.

It is not immediately evident, however, how the localization threshold could be a direct function of the sample volume (except through increased accumulation predicted by the statistical weak-link model discussed in the following section). If indeed the asymptotes in Figures 8.1 and 8.2 are coincident with the initiation threshold, it would seem that the rockmasses contain other macroscopic sources of heterogeneity such as joints or cleats. While these larger features may not affect the initiation stress, they cause the localization threshold to collapse such that failure occurs once initiation has commenced.

In summary, scale effect in peak strength beyond the crack interaction threshold is the result of energy conversion from volume-based strain energy to plane-based fracture surface energy. The stress required for localization, however, is linked to crack density (probability of crack interaction increases with crack density and crack length) which is linked to crack initiation strength distribution or elemental strength heterogeneity. A heterogeneous sample will therefore exhibit a greater ratio of peak strength to initiation stress. Crack initiation and therefore crack interaction under uniform stress conditions should be related to grain scale heterogeneity and should not have a scale effect related directly to sample volume (except through the statistical weak-link models discussed in the next section). Conditions which cause cracks, once initiated, to extend more or less readily, will increase the interaction probability.

8.4 STATISTICAL WEAK-LINK THEORY

The Weibull distribution (Weibull 1939; 1951), applied to material strength specifies an inherent variability in elemental strength given by the density function (Jardine 1973):

$$f(\sigma) = \frac{m}{\sigma_0} \left(\frac{\sigma - \sigma_i}{\sigma_0} \right)^{m-1} \exp \left[- \left(\frac{\sigma - \sigma_i}{\sigma_0} \right)^m \right] \quad \text{for } \sigma > \sigma_i \quad [8.14]$$

where σ_i is the lower bound strength threshold (often but not of necessity set to zero as in Tang and Kaiser 1998), n is the number of elements, σ_0 is a scaling constant and m defines the shape (spread and skew) of the curve and can be considered as a heterogeneity index. When $m=1$ the distribution is negative exponential. As m becomes large ($m \gg 1$), the distribution narrows and approaches a normal relationship as shown in Figure 8.36.

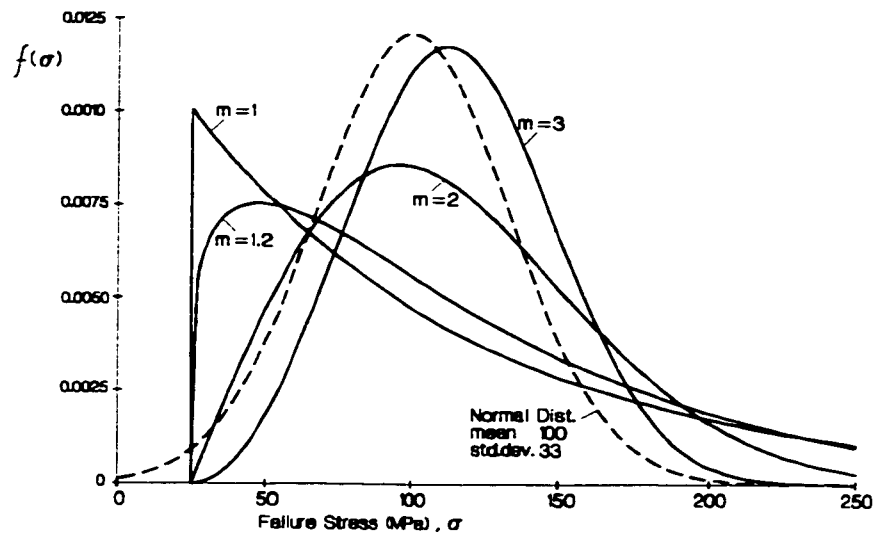


Figure 8.36: Examples of density distributions for different heterogeneity indices (m). Normal function shown for comparison.

8.4.1 A Serial Model for Crack Initiation and Accumulation

A statistical approach linking heterogeneity and scale effect is the Weibull “series-system” (Jardine 1973) or “weak-link” (Illston et al. 1979) model (Figure 8.37). This model has been applied to rock, concrete and general material strength (Weibull 1939; 1951; Kittl et al 1990; Tang and Kaiser 1998; Tano 1993). This model, for crack initiation, is introduced here and then developed further by the author as a tool for understanding damage interaction.

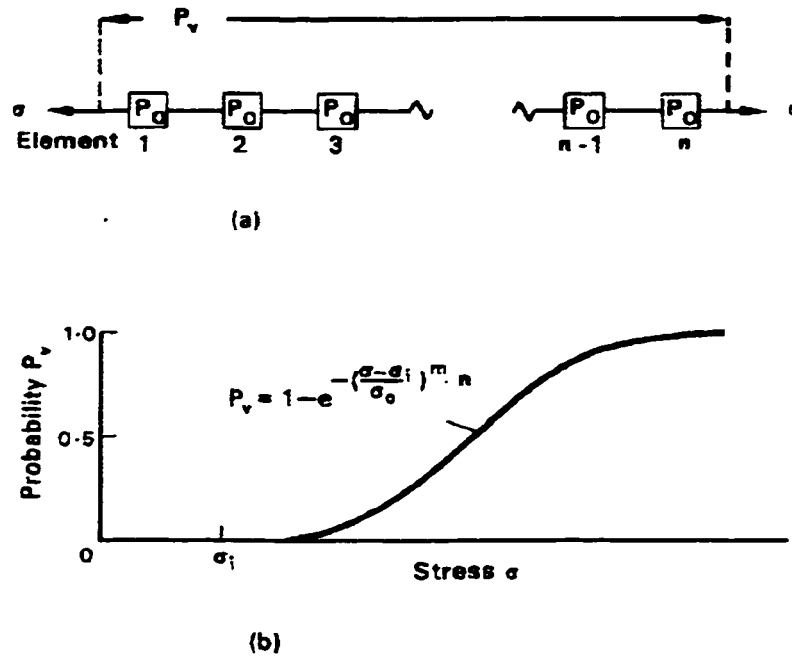


Figure 8.37: Weibull weak-link model: a) schematic representation of global dependency on elemental rupture probabilities; b) Composite failure probability (cumulative distribution). Modified after Illston et al (1979).

As shown by Figure 8.37b, for a series system composed of elements with a cumulative probability of failure given by $P_0(\sigma)$, the “weak-link” elements governs overall stability and the cumulative probability of system failure $P_v(\sigma)$ is given by (Jardine 1973):

$$1 - P_v(\sigma) = (1 - P_1(\sigma)) \times (1 - P_2(\sigma)) \times \dots \times (1 - P_n(\sigma)) = \prod_{i=1}^n (1 - P_i(\sigma)) \quad [8.15]$$

$$P_v(\sigma) = 1 - (1 - P_1(\sigma))^n \quad \text{when } P_1(\sigma) = P_2(\sigma) = \dots = P_n(\sigma) \quad [8.16]$$

According to the Weibull model, the cumulative distribution $P(\sigma)$ for the strength of a continuous sample of sample V , with internal strength variability given by Equation 8.14 and constant uniform stress, σ , is given by (Kittl et al 1990):

$$P(\sigma) = 1 - \exp \left[- \left(\frac{\sigma - \sigma_i}{\sigma_0} \right)^m \cdot \frac{V}{V_0} \right] \text{ for } \sigma > \sigma_i \quad [8.17]$$

where V_0 is the unit volume according to Illston et al. (1979). Theoretically and in order to be compatible with the original discrete model in Figure 8.37, V_0 , should represent the elemental

volume (e.g. the grain size) such that V/V_0 is equal to n . This will be the case for comparisons to the numerical results in this chapter.

It is not possible, however to sample the strength of, for example, a large population of individual grains in a rock. Used for the peak strength comparison of laboratory scale samples, V_0 , could be assigned to the volume of the standard sample ($V/V_0 = 1$ for testing) used to determine the statistical constants in Equation 8.14. This is valid since the selection of σ_0 and m is dependent on the sampling volume and V_0 anyway. Once selected, V_0 should be kept constant for future use of the calculated σ_0 and m .

A larger volume, V , will likely contain more of the lower strength elements contained in the assumed distribution and will therefore have a lower ultimate strength, particularly in tension since the weakest link is the critical link. The Weibull model provides a relationship between relative sample volume, V (or linear dimension, d), and relative strength (assuming equal probability of failure) of two samples, A and B:

$$\frac{\sigma_A - \sigma_i}{\sigma_B - \sigma_i} = \left(\frac{V_A}{V_B} \right)^{-\frac{1}{m}} = \left(\frac{d_A}{d_B} \right)^{-\frac{3}{m}} \quad [8.18]$$

Clearly, from Equation 8.13, for probabilities of failure to be equal for two otherwise identical samples of different volumes such than $V_A > V_B$, the applied stress level in question must be lower for sample 1. In other words, sample A has a lower overall strength than sample B due solely to a larger test volume. In order to obtain the relationship in Figure 8.1b for strength versus diameter, d :

$$\frac{\sigma_c}{\sigma_{c50}} = \left(\frac{50}{d(\text{in mm})} \right)^{0.18} \quad [8.19]$$

From Equation 8.18, an m of 16.7 is required for the heterogeneity index if σ_i is assumed to be zero. For a population of granite samples with a diameter of 50mm and a median uniaxial strength 200 MPa this results in a range (99% confidence) of 150 MPa to 225 MPa, comparable to results reported in the literature (Martin 1994). Herget's (1988) scale relationship for coal samples, similar to Equation 8.16 but with an exponent of 0.6 corresponds to an m of 5, indicating a wider variation in elemental strength than the hard rocks presented in Figure 8.1b. Evans et al. (1961) report significantly lower variation, requiring an $m > 30$ to validate the form of Equation 8.18.

The relationship between heterogeneity index m , lower bound strength threshold, σ_i , sample volume, V , and strength (assuming $P(\sigma)=50\%$ and $d_0=50\text{mm}$) is illustrated in Figure 8.38 as obtained from the expression:

$$\sigma = \sigma_0 \left[-\frac{d_0^3}{d^3} \ln(1 - P(\sigma)) \right]^{\frac{1}{m}} + \sigma_i \quad [8.20]$$

It is assumed that the distributions in Figure 8.38a and b are obtained using tests on 50mm diameter samples with a granite-like compressive strength (200 MPa).

Note the similarity between the curve for $m=17$ and the relationship in Figure 8.1.b. The selection of $m = 6$ yields the inverse square root relationship predicted by linear elastic fracture mechanics for geometrically similar samples of varying dimension or for large intact samples of varying characteristic internal scale (e.g. grain size) as shown in Figure 8.1.a. Also of significance is the concept of a lower bound sample strength with respect to increasing volume, resulting from a limiting minimum elemental strength. In fracture mechanics this would be a characteristic dimension such as a maximum crack length or grain size.

There is, however, no experimentally verified superior value or physical significance to the form of the Weibull density function (Equation 8.14) for rock applications. By admission, “the only merit in the selected function is that it is the simplest expression of the appropriate form” (Weibull 1951). In many cases such as that shown in Figure 8.11, a normal distribution of strength should equally suffice for application as a weak-link model. Frenkel and Kontorova (1943) proposed an alternative expression for the weakest link theory using a more familiar normal distribution.

Considering a sample with randomly distributed flaws yielding a normal distribution of strength:

$$P(\sigma) = \frac{1}{s\sqrt{2\pi}} \exp \left[-\frac{(\sigma - \mu)^2}{2s^2} \right] \quad [8.21]$$

where in this case μ and s are the mean and variance of the strength (limiting stress for extension) of a flaw. If n is the number of flaws in a unit volume and V is the volume of the sample, then the strength of the sample, S , is approximated by:

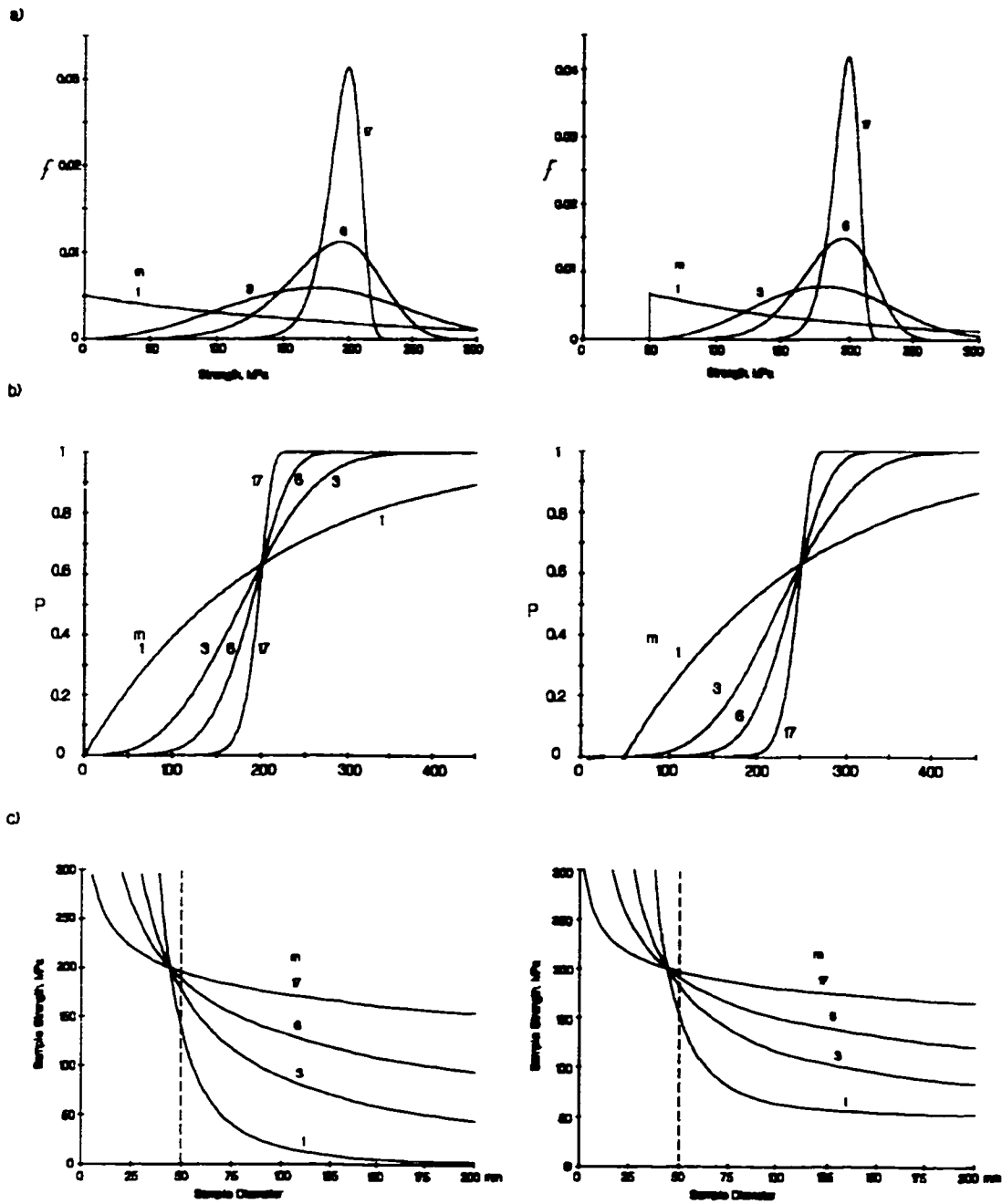


Figure 8.31: Example relationship between Weibull heterogeneity and strength - scale relationship. a) $\sigma_0=200\text{MPa}$, $\sigma_f=0\text{MPa}$, $V_0=50\text{mm}$; b) $\sigma_0=150\text{MPa}$, $\sigma_f=50\text{MPa}$, $V_0=50\text{mm}$.

$$S = \mu - \sqrt{2s \left(\ln \frac{V}{V_0} \right) - \ln(2\sqrt{\pi})} \quad [8.22]$$

where V_0 is the volume of a characteristic strength unit (grain) or flaw.

For the purposes of practical testing, V_0 can again be set to the volume of the standard test specimen with which μ and s were determined. As noted by Brady (1969), there is sufficient freedom in either bi-parametric formulation (Equation 8.22 or 8.15) to fit experimental data as required. For example, Tano (1993) reports m exponents of 4.4, 5.1 and 5.0 for norite, quartzite and sandstone respectively, as obtained from standard laboratory samples.

From Figure 8.36 it is apparent that Weibull distributions with $m > 3$ are indistinguishable, for practical purposes, from a normal distribution. The normal distribution model (used in the bonded contact simulations), contains familiar and independent parameters. Weibull model parameters bear little intuitive physical significance although the formulation allows for simple inclusion of a lower bound strength and negative skew.

The most significant mechanistic problem with the weak-link concept for uniaxial and confined compression is that extension cracks, which form in compression, are generally stable. When secondary mechanisms are disallowed, a single crack is unlikely to be responsible for the failure of the whole sample as may be the case in pure tension. In other words, heterogeneity, in the form of variable fracture toughness or crack length and orientation, resulting in a scale dependent “weak-link” material strength, is unlikely to be the sole contributor to the reduction of insitu strength.

It has been established that most of the initial crack accumulation is in the form of axial crack extension. This form of isolated, highly anisotropic damage does not initially have an appreciable effect on the axial compressive loading path through the sample. In addition, the induced lateral tensile stresses resulting in crack formation are likely to be extremely local. Hence, initial crack growth has little significant effect on the axial transmission of stress and does not significantly disturb the rest of the sample.

Accumulation of “weak-links” in hard rock eventually results in the potential for localized interaction of cracks, resulting in an indirect probabilistic relationship between the weak-link initiation stress and localization. For materials with a similar elemental strength distribution under uniform stress conditions, the ratio of localization stress to initiation stress should be consistent. It has already been discussed, however, that rock insitu, even in the absence of macro-scale discontinuities, does not have the same asymptotic localization strength as laboratory samples. Other direct and indirect mechanisms of heterogeneity must be active in controlling the propagation and interaction of initiated cracks.

8.4.2 A New Statistical Model for Interaction

If the series-system or weak-link model represents one extreme of statistical failure paradigms, the other extreme is the parallel system illustrated in Figure 8.39 in which the probability of system failure is determined by the probability that all components will fail (stability is assured if at least one element remains intact). This could also be called a “strongest-link” model. In rock compression it is unlikely that this model is valid up until the point of failure since it assumes that each component failure (P_o are component failure probabilities) occurs independently without influencing the input (σ in this case) for the other components. This is a valid assumption only for non-interacting crack accumulation prior to localization. The model is, nevertheless, presented here for comparison and for use in a new composite model for interaction.

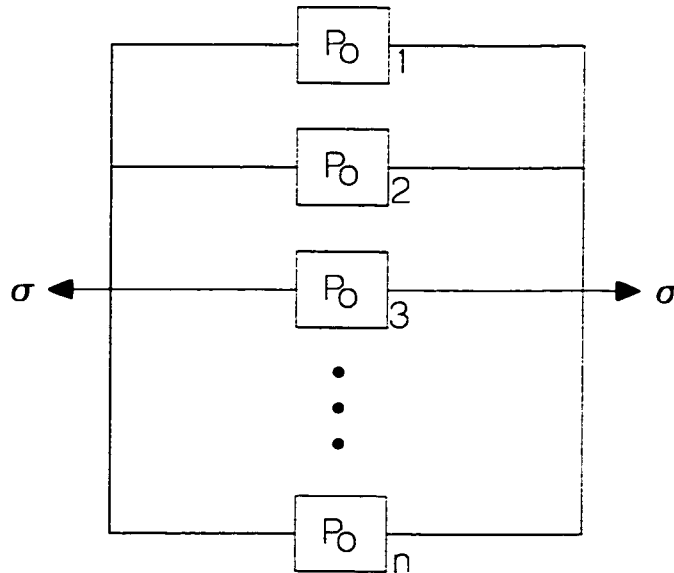


Figure 8.39: “Strongest-Link” parallel system.

Following the logic of the previous section, the probability of parallel system failure is given by:

$$P_V(\sigma) = \prod_{i=1}^n P_i(\sigma) = (P_1(\sigma))^n = (1 - (1 - P_1(\sigma)))^n \text{ when } P_1(\sigma) = \dots = P_n(\sigma) \quad [8.23]$$

which for the Weibull density function becomes:

$$P(\sigma) = \left(1 - \exp \left[- \left(\frac{\sigma - \sigma_i}{\sigma_0} \right)^m \right] \right)^{\frac{v}{v_0}} \text{ for } \sigma > \sigma_i \quad [8.24]$$

Of particular interest, here, is that the influences of heterogeneity and scale are reversed as compared to the weak-link model. Heterogeneous materials are stronger than uniform samples and larger samples are stronger than smaller samples. In either case this reversal is the result of the need for all elements to fail before the sample fails (in the series system, only one element failure was required for sample failure). Rockmass behaviour is unlikely to conform to this "strongest-link" analogue. Compressive strength is not directly governed by the weakest link model, either.

It was demonstrated in Chapter 7 that failure of a sample is inevitable once local crack interaction has occurred. This system is analogous to the series-parallel configuration presented in Figure 8.40. System failure occurs when failure of all elements within a single (parallel) tier has occurred, corresponding to a single localized cell of interaction (of two or more critically oriented cracks) within a rockmass. The more elements within each tier (the more local cracks required for critical interaction) the stronger the sample will be. In addition, the more potential interactions for each crack, the weaker the sample will be.

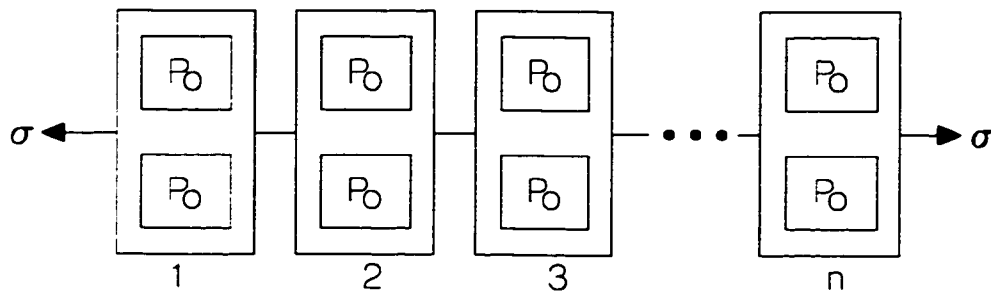


Figure 8.40: Series-parallel system. Both (parallel) elements within a single (serial) tier are required for sample failure.

The probability of sample failure for the series-parallel system, using the Weibull density function is given by:

$$P_V(\sigma) = 1 - \prod_{i=1}^n \left(1 - \prod_{j=1}^k P_j(\sigma) \right) = 1 - \left(1 - (1 - (1 - P_1(\sigma)))^k \right)^n \quad [8.25]$$

where \$k\$ is the number of elements in a tier (\$k=2\$ in Figure 8.40.) and \$n\$ is the number of tiers. Modifying the schematic in Figure 8.40 so that any neighbouring elements can form an interaction and applying the Weibull function:

$$P_V(\sigma) = 1 - \left(1 - \left(1 - \exp \left[- \left(\frac{\sigma - \sigma_i}{\sigma_0} \right)^m \right] \right)^k \right)^{f \left(\frac{V}{V_0}, k, x \right)} \quad \text{for } \sigma > \sigma_i \quad [8.26]$$

where $f()$ is a function describing the nature and interrelationship of each tier and x is the number of potential interactions for each element. $P_V(\sigma)$ is the probability of a critical interaction and consequent sample yield at a stress σ . For the case where $k=2$, and the sample is large (ignoring boundary limitations on interaction):

$$f(\) = \frac{x}{2} \left(\frac{V}{V_0} \right) \quad [8.27]$$

The scale effect for uniaxial sample strength with respect to volume is given by:

$$\sigma = \sigma_0 \left(- \ln \left[1 - \left(1 - (1 - P_V(\sigma)) \left(\frac{x}{2} \frac{V}{V_0} \right)^{-1} \right)^{\frac{1}{2}} \right] \right)^{\frac{1}{m}} + \sigma_i \quad [8.28]$$

As the overall (single) elemental failure density (i.e. the crack density) increases, the probability of interaction increases. The probability of system or sample failure, however, is only indirectly influenced by the likelihood of initial elemental failure rather than directly controlled by it as in the weak-link model. In addition, the model predicts that a more homogenous material will have a smaller ratio of localization stress to initiation stress. This is illustrated schematically in Figure 8.41 for two dimensional samples of different variability with $x=4$. For 50mm samples of significantly heterogeneous samples ($m=3$) crack initiation begins at stresses approximately 25% of localization strength while for a highly homogenous sample ($m=27$) the two thresholds converge. The heterogeneity parameters in this case apply to an elemental volume (grain scale).

Figure 8.42 illustrates a comparison to PFC model results. Arbitrarily selecting 1% probability for the weak-link initiation model (Equation 8.20) as representative of the "first crack", the statistical model is calibrated to the PFC observations in Section 8.3.3 (crack initiation). The same parameters are then used in the series-parallel system for interaction (Equation 8.28) and compared with the thresholds from the PFC simulations. In this example, each element can interact with 4 neighbors ($x=4$ for PFC simulations) and the probability of "failure" refers to the occurrence of a

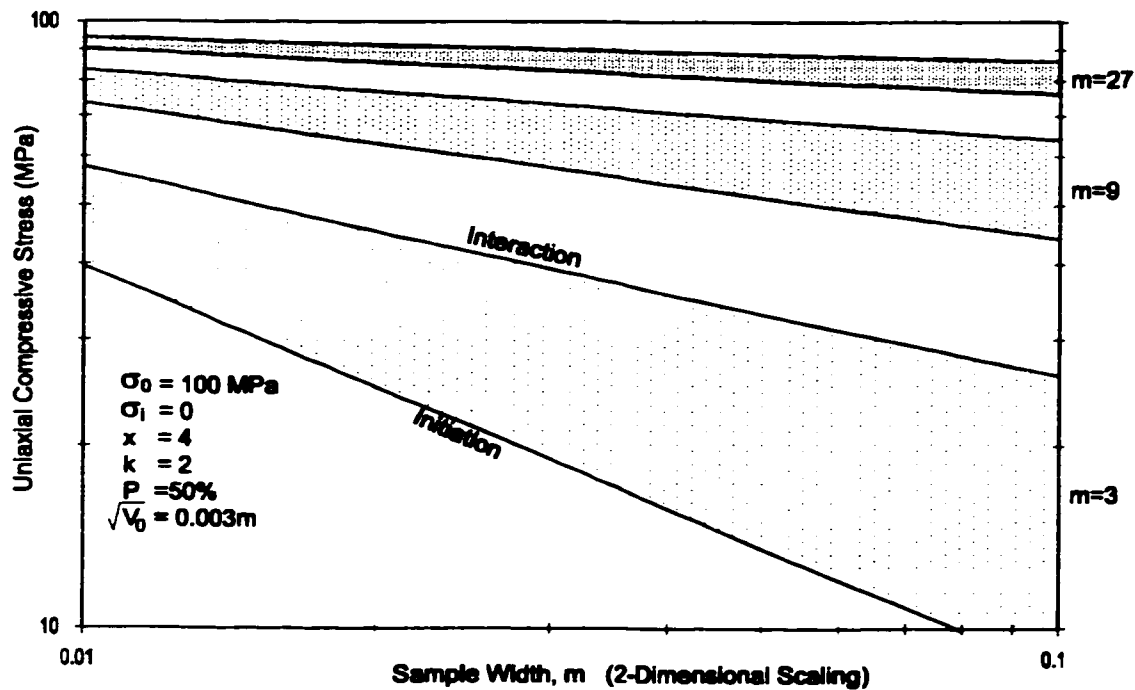


Figure 8.41: Relative crack initiation (from Equation 8.20) and crack interaction (Equation 8.28) thresholds predicted by statistical model.

single "critical" interaction. For larger samples the correspondence is good. For smaller samples, rotation and boundary interaction dominate, reducing the interaction threshold to the initiation stress. This effect is not included in Equation 8.28.

Two alternative calibrations and comparisons are given in Figure 8.43. In one case the crack initiation curve (for 1% probability in Equation 8.20) is calibrated for systematic crack damage as identified in the simulations in Section 8.3.3. A second calibration is presented, this time using 50% probability as representative of "failure" or critical interaction. Both resultant predictions for crack interaction, according to Equation 8.28, show close correspondence to the model data.

While the calibration for damage initiation can involve different assumptions, in all cases the calibrated parameters result in the correct forward approximation of the interaction threshold lending credence to the hypothesis that interaction (yield) is a probabilistic result of damage initiation and accumulation. A key consequence of this hypothesis is that interaction and subsequent yield can occur at much lower crack densities than normally assumed in fracture interaction models (e.g. Ashby and Hallam 1986) based on interaction of a predetermined and uniformly distributed array of extending cracks.

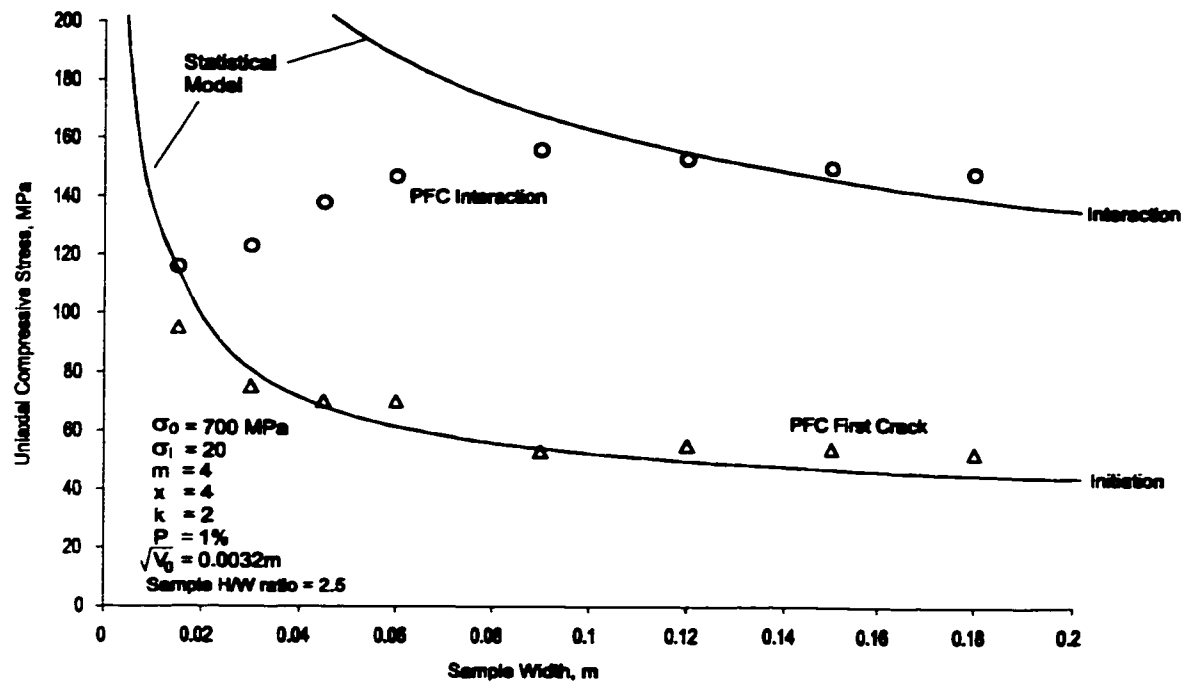


Figure 8.42: Comparison of series-parallel predictions with PFC (calibrated for "first crack").

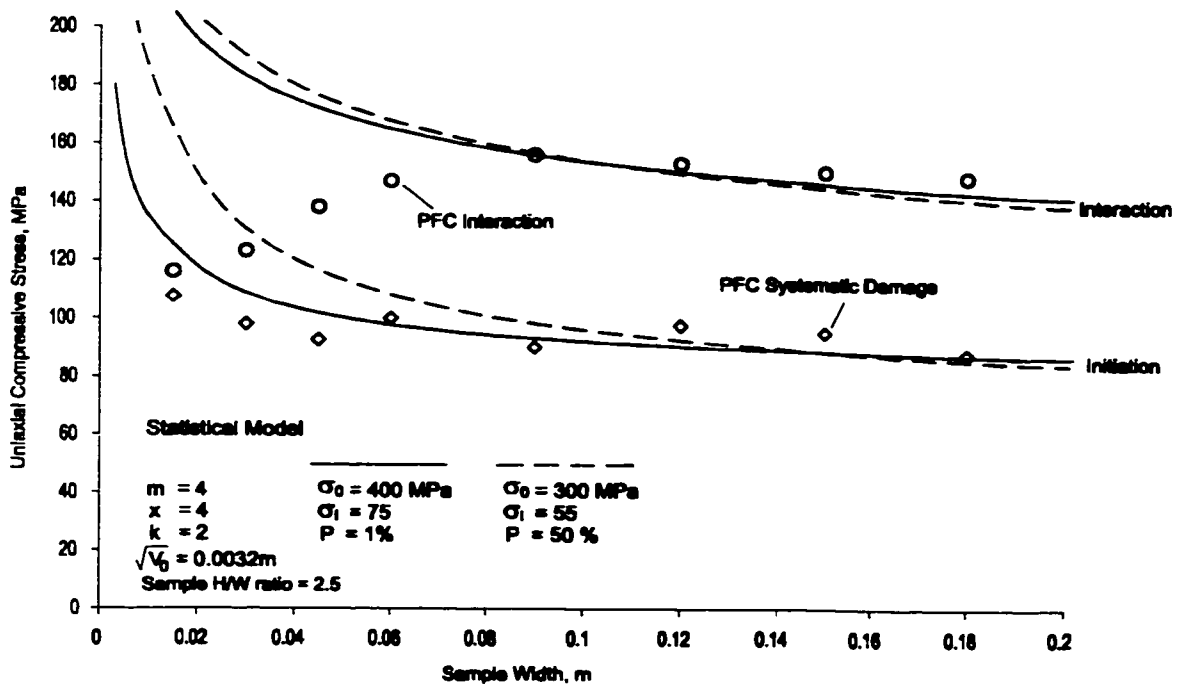


Figure 8.43: Comparison of series-parallel predictions (calibrated for "systematic damage").

This simple interaction model is used in the following sections as a framework for discussions of the influence of pre-existing damage and the effects of crack length and confinement.

8.5 THE EFFECT OF PRE-EXISTING DAMAGE

Most of the previous discussions and numerical experiments have focussed on the nature of damage and the key damage thresholds for monotonic loading (axial compression and deviatoric stress after hydrostatic confinement). In the context of this Section, "pre-existing" damage refers to cracks which are not associated directly with this stress path.

Pestman and van Munster (1996) showed, for sandstone test samples with invariant principal stress directions, that confined stress paths do not result in more damage than that incurred in uniaxial compression, provided that the current damage iso-surface (assumed for monotonic compression) has not been exceeded. This is illustrated in Figure 8.44. In other words, at stresses below yield, the stress path of uniaxial compression incurs the most damage. The steeper half of the bi-linear crack intensity iso-surface in the left image of Figure 8.44 is the result of additional crack extension at lower confinements (rather than a tendency for new crack nucleations).

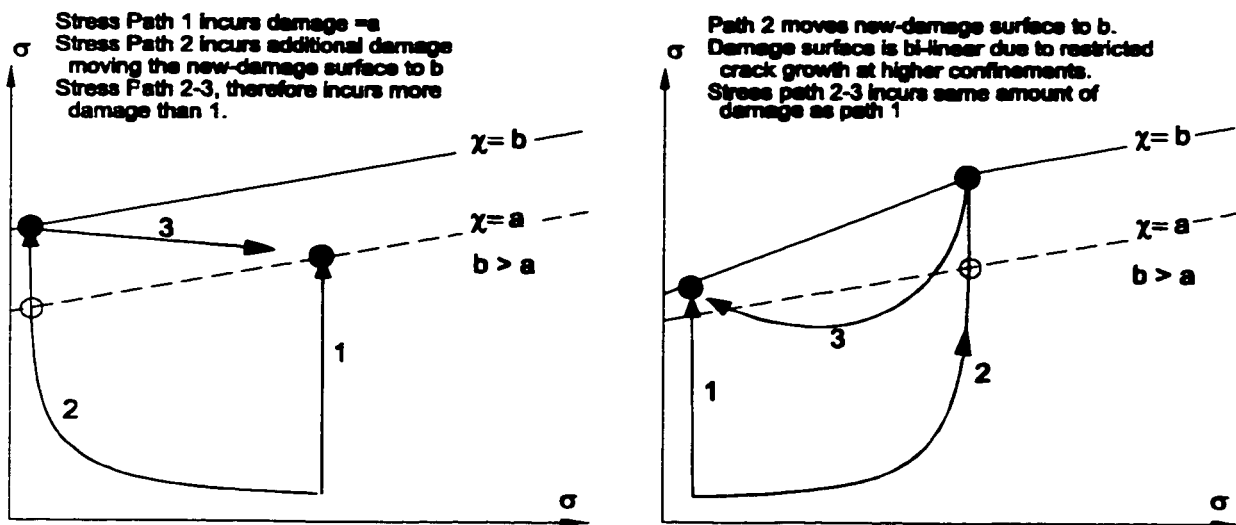


Figure 8.44: A schematic illustration of stress path related damage in the absence of stress rotation (based on the experimental findings of Pestman and van Munster (1996)).

Additional damage may be associated with previous loading, in excess of the current state, with unloading from a hydrostatic or deviatoric initial pressure (as discussed in Chapter 7 and summarized in Figure 8.45). It may also be the result of stress rotations during the advancement of an excavation in three dimensions (as described in Martin 1994 and Kaiser et al.1999). Stress paths involving high deviatoric stress, under low or negative confinement, are of particular

importance for the creation of additional damage initiation and crack extension. This particular stress path is discussed in Section 8.6. This section will deal with pre-existing cracks of uniform length as in the PFC simulations.

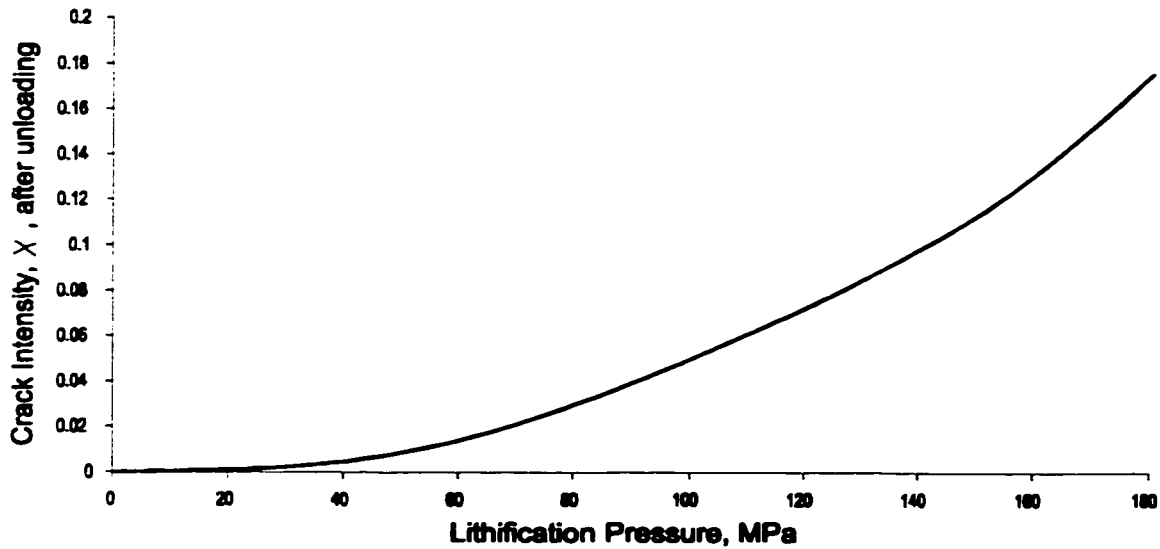


Figure 8.45: Isotropic damage (crack intensity) incurred in heterogeneous PFC samples from Chapter 7, during virgin unload from hydrostatic lithification pressure.

8.5.1 A Statistical Model for Pre-Existing Damage

The statistical interaction model from Section 8.4.2 may be extended to account for the presence of pre-existing damage. As is the case in the PFC simulations, all cracks are assumed to be of the same length. In addition, the number of potential interactions for each crack is 4, corresponding approximately to the coordination number of the assemblies and the "rule" that cracks within a separation equal to one average length may interact. A single pair of neighbouring cracks determines "first interaction". The model is a combination of a series (weak-link) model and a series-parallel model as shown in Figure 8.46.

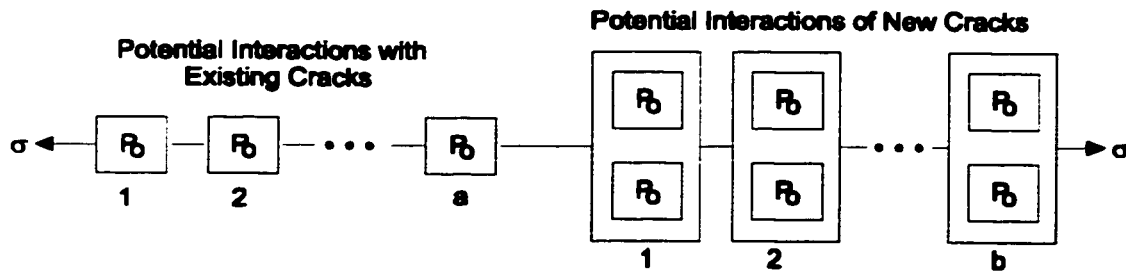


Figure 8.46: Statistical model incorporating pre-existing cracks.

The undamaged sample is assumed to correspond to the series-parallel model in Section 8.4.2. Each isolated pre-existing crack has a two-fold effect on the model. Four potential interaction pairs (tiers with $k=2$) are removed from the right group in Figure 8.46 (b←b-4). These are replaced by four single links on the left side (a←a+4). These single links represent the four potential cracks, which, by their mere formation, form a de-facto interaction with the adjacent pre-existing crack.

Combining Equation 8.25 with Equation 8.15, the following model represents the probability of interaction (either between new crack pairs or between a new and a pre-existing crack) within the sample of volume or area V :

$$1 - P_V(\sigma) = \left\{ \prod_{h=1}^a (1 - P_h(\sigma)) \right\} \times \left\{ \prod_{i=1}^b \left(1 - \prod_{j=1}^k P_j(\sigma) \right)_i \right\} \quad [8.29]$$

or:

$$P_V(\sigma) = 1 - (1 - P_1(\sigma))^a \left(1 - (1 - (1 - P_1(\sigma)))^k \right)^b \quad \text{for } P_1(\sigma) = \dots = P_a(\sigma) = P_b(\sigma) \quad [8.30]$$

From Section 8.4, assuming a Weibull strength distribution:

$$(1 - P_1(\sigma)) = \exp \left[- \left(\frac{\sigma - \sigma_i}{\sigma_0} \right)^m \right] \quad [8.31]$$

For $k=2$, $x=4$ (x = number of possible interactions for each element of volume or area V_0) and a initial crack density χ :

$$a = 4\chi \frac{V}{V_0} \quad [8.32]$$

$$b = \frac{4}{2} \frac{V}{V_0} - 4\chi \frac{V}{V_0} \quad [8.33]$$

resulting in the model:

$$P_V(\sigma) = 1 - \exp\left(-\left(\frac{\sigma - \sigma_i}{\sigma_0}\right)^m \cdot \frac{4\chi V}{V_0}\right) \times \left(1 - \left(1 - \exp\left(-\left(\frac{\sigma - \sigma_i}{\sigma_0}\right)^m\right)\right)^k\right)^{\frac{(2-4\chi)V}{V_0}} \quad [8.34]$$

This model, developed here for 2Dimensional analysis, is valid in three dimensions provided that the number of possible elemental interactions, x , is suitably adjusted. Example crack interaction thresholds, based on the three calibrations in Figures 8.42 and 8.43, are illustrated in Figure 8.47.

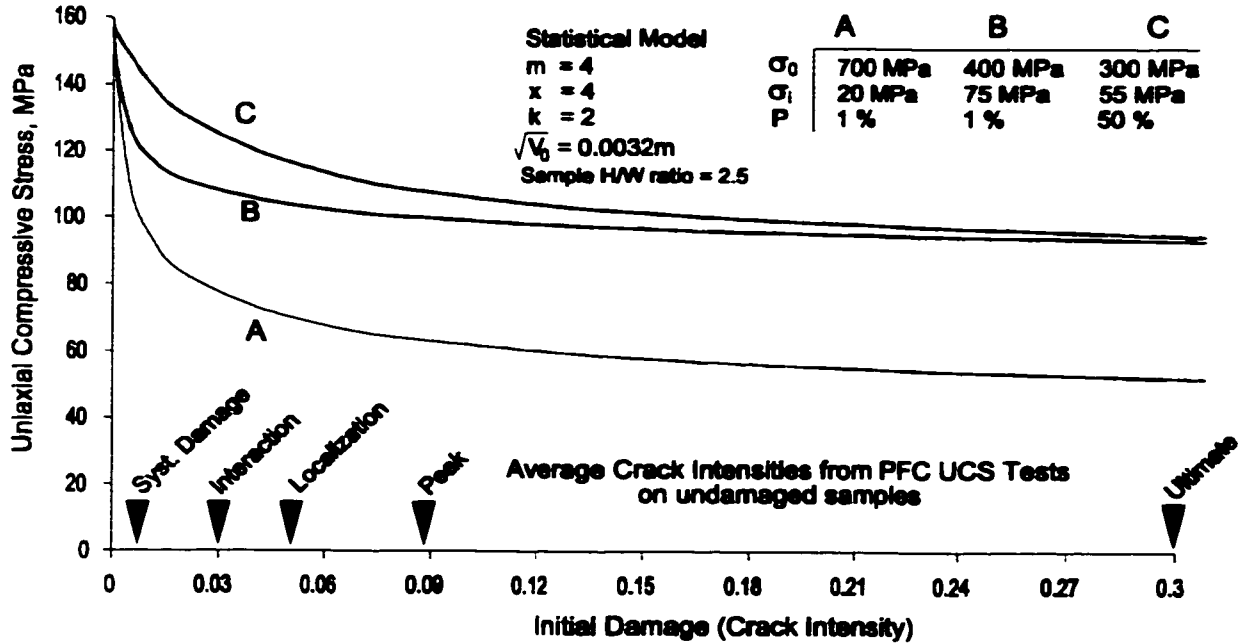


Figure 8.47: Crack interaction threshold as a function of initial damage (statistical model predictions based on parameters from Figures 8.42 and 8.43).

These trends compare conceptually with data from damaged marble tests in Figure 8.48. In this data there is likely a certain amount of inert or inherent damage which is included in the observations, resulting in an offset from the vertical (undamaged) axis. This is analogous to the numerous pores and non-contacting neighbors (discs), in "undamaged" PFC samples, which are not initially bonded and therefore are not counted as cracks.

The data in Figure 8.48 is plotted with respect to total damage and also with respect to sub-vertical damage (between 20 and 30 degrees from the vertical). This latter group was deemed critical by Wong et al (1996).

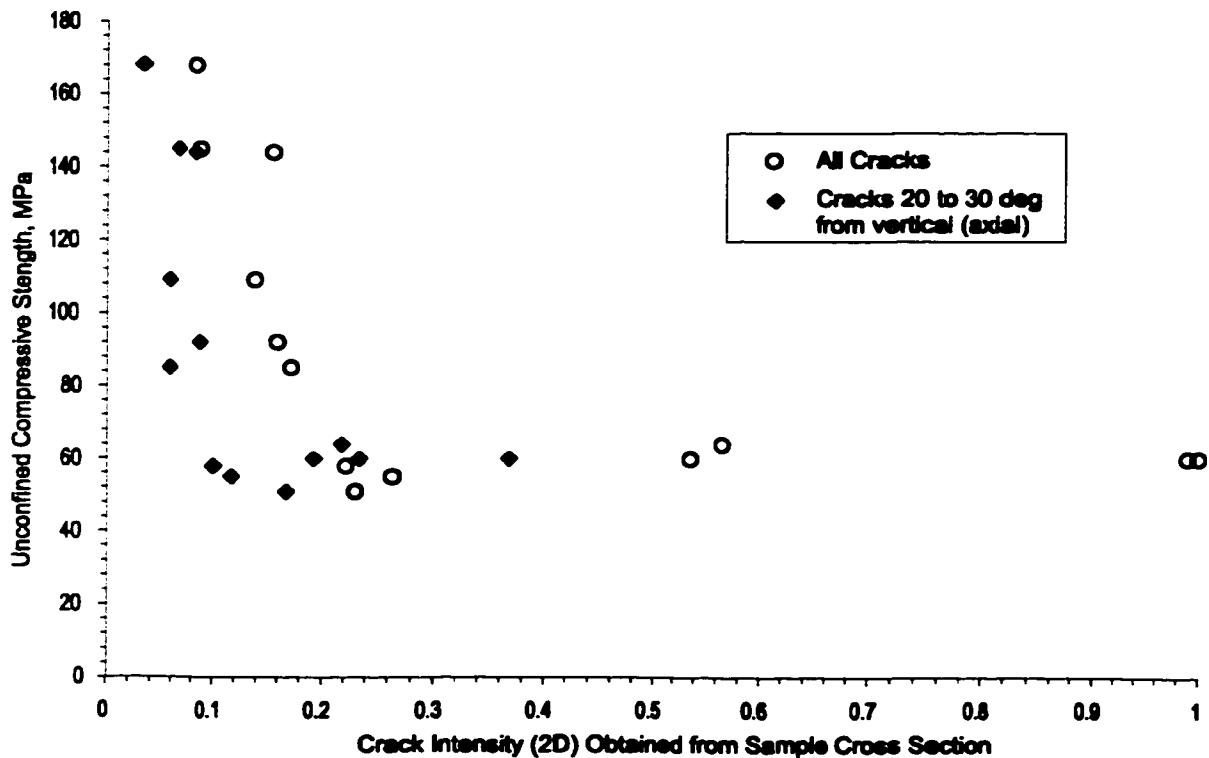


Figure 8.48: Observed crack damage and compressive strengths for samples of marble (based on data from Wong et al. 1996).

Of interest in both the model and in the real data is the asymptotic nature of strength for large amounts of damage. This lower bound for the marble data in Figure 8.48 is approximately one third of the maximum strength, evidence that the lower bound strength for damage rock is controlled by the threshold for crack initiation, and that crack initiation itself, is relatively insensitive to the amount of pre-existing damage.

8.5.2 UCS Simulations with Pre-existing Damage

A number of unconfined compression samples were prepared in a manner similar to the tests in Chapter 7. While isotropic damage could have been created by increasing the lithification pressure, as was done in Section 7.5, a more general and direct approach was used. After unloading from a lithification pressure of 25MPa, a number of cracks (broken contacts) were induced, oriented isotropically or according to a directional preference. In this way, the effect of initial crack density on compressive strength under monotonic loading could be investigated.

The cracks were generated by systematically breaking bonds according to a defined probability function:

$$P(\text{crack}) = \frac{N_{\text{cracks}}}{N_{\text{contacts}}} (1 + \alpha \cos 2(\theta - \theta_0)) \quad [8.35]$$

where N refers to the number of desired cracks and the number of initial contacts, α is the target crack anisotropy and θ_0 is the angle of principal anisotropy (of crack normals). θ is the selected crack normal orientation. For each contact a random number is generated (0 to 1). If this number is less than $P(\text{crack})$, the contact is broken and a crack is generated. Equation 8.35 ensures that cracks with the target orientation are given preference. The contact array is looped through repeatedly until the target number of cracks is achieved.

Since the contacts in the data list are themselves in random order (as compared to their spatial location), a sequential pass through the list ensures random and uniform distribution of cracks throughout the sample. The target α is set to 1 although the maximum anisotropy obtained in the samples is approximately 0.8. For the isotropic sample, α is set to zero.

Typical crack arrays, generated through this process, are illustrated in Figure 8.49. A number of uniaxial compression tests were performed on these and similarly damaged samples. Key crack thresholds were identified using the same multi-parameter criterion described in Chapter 7 for compressive testing. The thresholds for first crack, systematic damage, crack interaction and peak strength are plotted for isotropic damage ($\alpha=0$), in Figure 8.50, with respect to crack intensity. Recall that crack intensity in this work is calculated as $\Sigma d^2/A$ and is 4 times the value used by Kemeny and Cook (1986) and approximately 4.05 times the value used by Wong et al. (1996).

Figure 8.50 illustrates a rapid decline in the interaction threshold and the peak strength beyond an initial crack intensity of 0.05. For comparison, the average crack intensity (for an initially undamaged sample) at crack interaction is approximately 0.03. The crack interaction threshold becomes asymptotic at a level below 100 MPa for large mounts of pre-existing damage. This is similar to the behaviour noted by Wong et al. (1996) as shown in Figure 8.47. It also corresponds to the asymptotic reduction of the critical crack damage threshold (interaction and localization), noted by Martin (1994) and summarized in Figure 8.51.

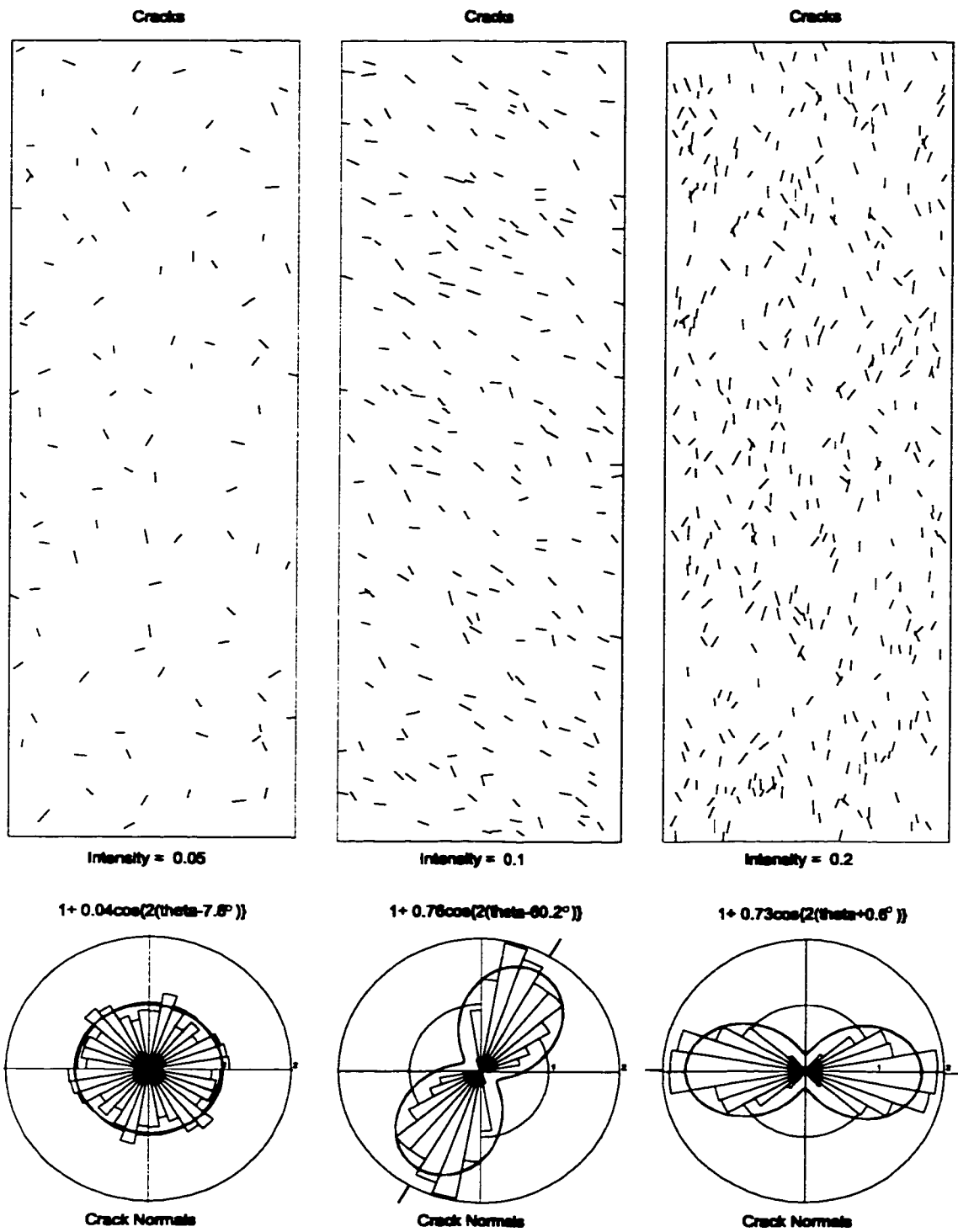


Figure 8.49: Typical crack arrays generated after unloading from lithification pressure (and before compression testing). Crack orientations referred to in subsequent discussions refer to orientation of principal anisotropy for crack normals (0 degrees = horizontal - right).

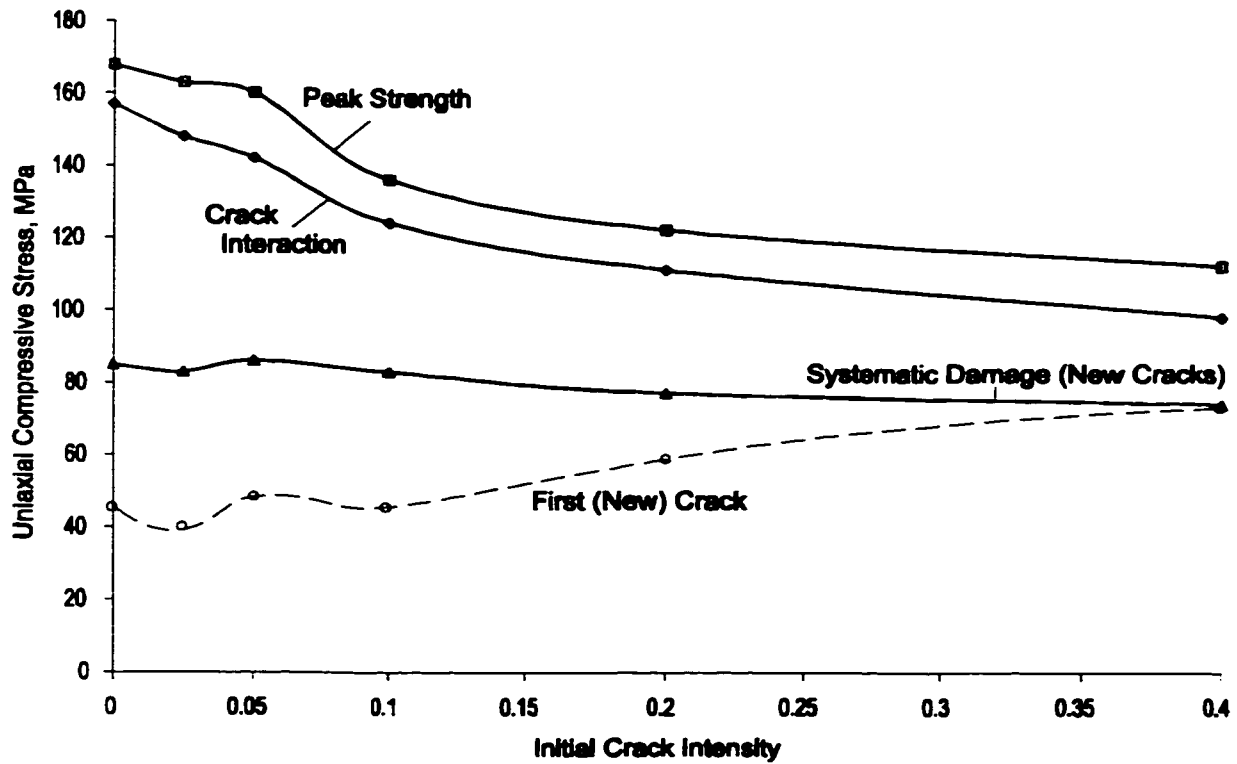


Figure 8.50: Influence of pre-existing isotropic cracks on new damage thresholds.

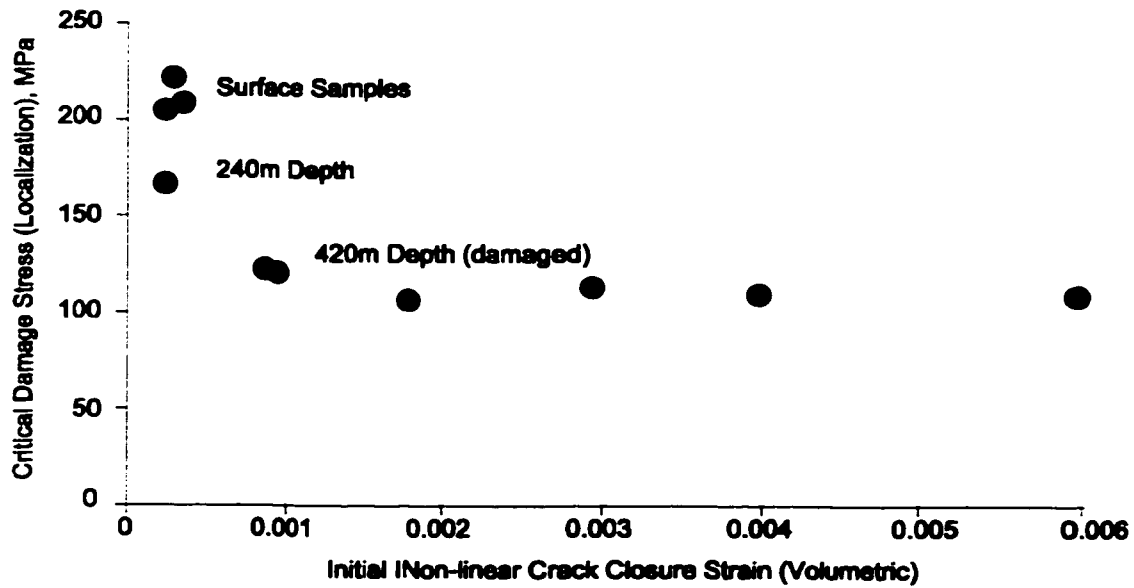


Figure 8.51: Reduction of critical damage threshold with initial damage in Lac du Bonnet granite. Crack closure strain used as an index for crack intensity (Martin 1994).

In Martin's investigation, the initial non-linear component of the volumetric strain response is interpreted as crack closure strain, an index for initial crack intensity. In these samples it can be assumed that the initial pre-existing cracks are the result of unloading and are likely dilated (open) in the absence of stress. Crack closure strain is an imprecise but qualitatively useful measure of internal damage. In the PFC simulations the initial damage is the result of statistical selection and is likely unrelated to unloading. Crack closure strain may therefore be an inconclusive measure.

In the simulations summarized in Figure 8.50, it is also significant to note that the threshold for systematic crack accumulation (new cracks) is relatively invariant for the levels of damage shown. This indicates that this pre-existing damage does not influence the nucleation of new cracks but rather encourages premature interaction and ultimately lower strength.

Compressive test results for crack arrays with predominant orientations are shown in Figures 8.52 and 8.53. For this particular model (with an interparticle friction angle of 45 degrees), the critical orientation for internal cracks should be 22.5 degrees. This appears to be the case, both for crack interaction and peak strength in Figure 8.52. The effect of crack orientation is only highly significant for large crack intensities (greater than 0.2 in this case). Likewise, the threshold stress for systematic crack initiation is only affected by pre-existing damage for crack orientations less than 30 degrees and only for very high crack intensities (0.4 in this case). For comparison, the maximum crack intensity after full sample rupture (undamaged *UCS* samples) is 0.3.

Steep cracks, sub-parallel to the direction of maximum compression, also have the most impact on elastic parameters. Steep cracks increase Poisson's Ratio and reduce the tangent (and secant) modulus. It is not surprising that the effect of pre-existing damage on elastic properties becomes significant at crack intensities beyond the average of 0.09 obtained at peak strength in PFC (*UCS*) simulations. Cracks perpendicular to maximum compression (90 degrees) have almost no impact on strength or stiffness for moderate levels of damage. In reality, as in Martin and Stimpson (1994) this type of damage significantly lowers the secant modulus. These cracks are associated with unloading and are therefore, likely to be open under zero stress. Crack closure, leading to an initially soft response and the reduction of the secant modulus, must occur before the nominal stiffness is achieved. In the PFC simulations, the statistically generated initial damage is not related to unloading and therefore need not be initially "open".

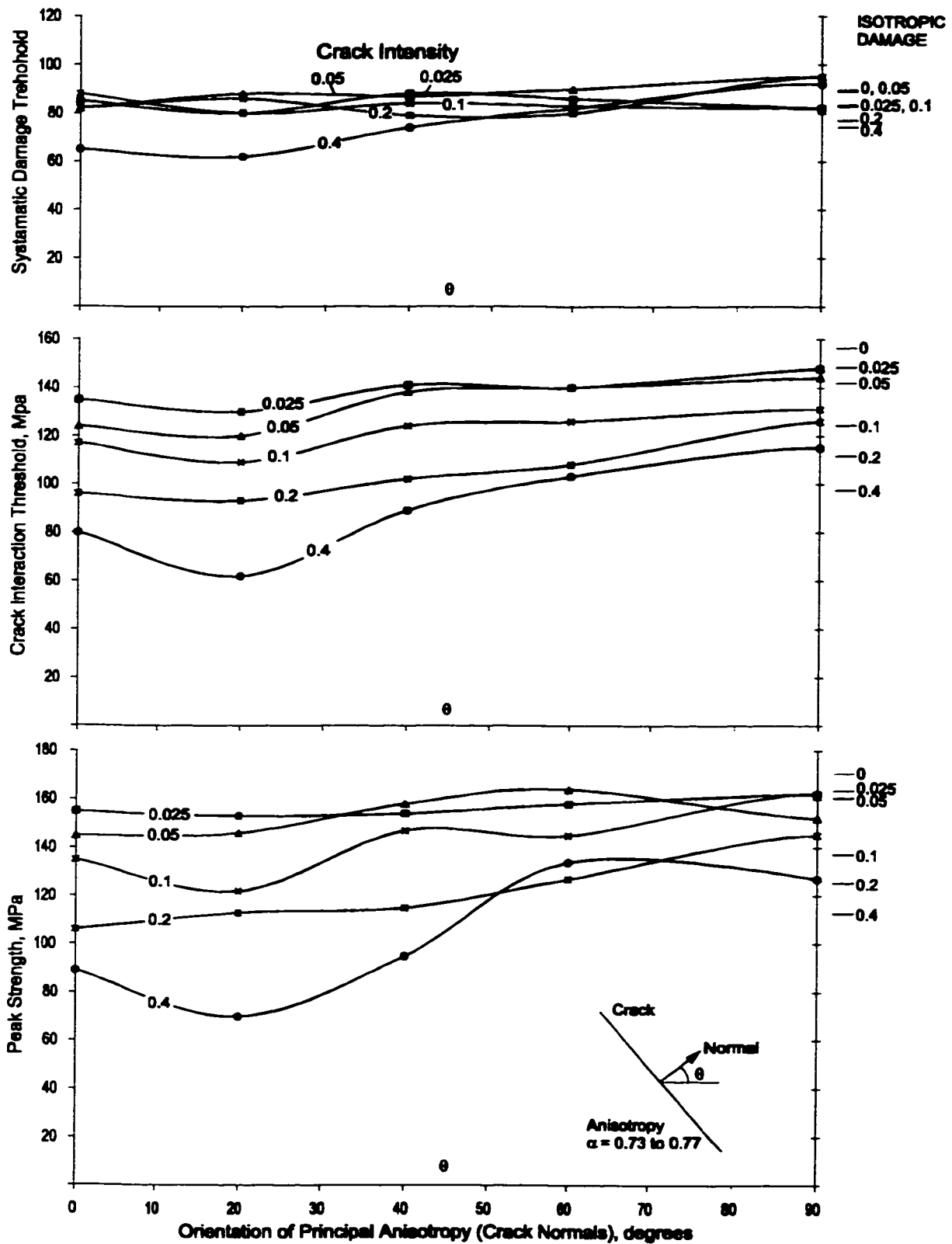


Figure 8.52: Influence of intensity and orientation of pre-existing damage on new damage and strength thresholds.

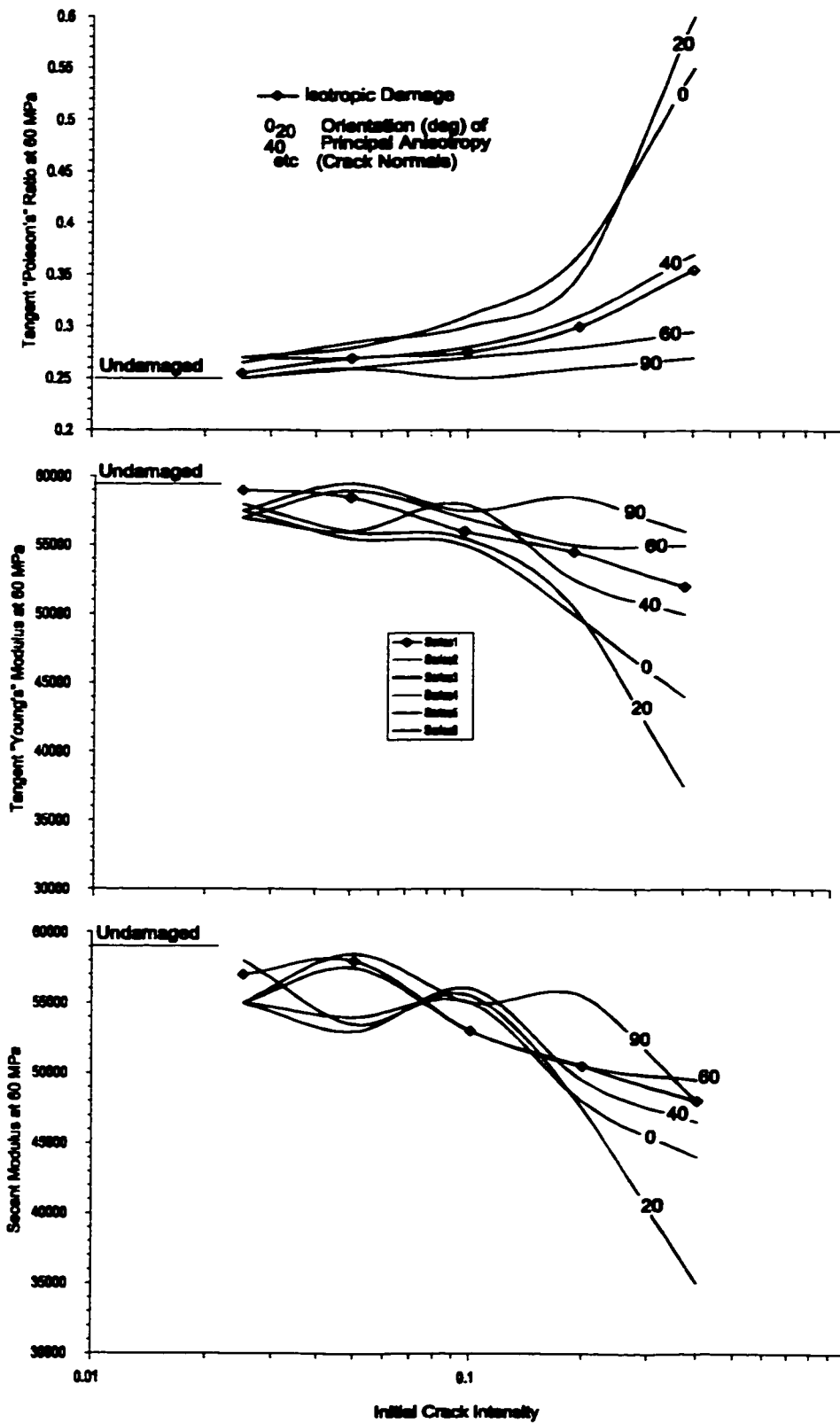


Figure 8.53: Influence of intensity and orientation of pre-existing damage on stiffness parameters (measured prior to systematic damage).

The best-fit exponential functions for the tangent stiffness values in Figure 8.53 (mid) are plotted in Figure 8.54. For isotropic damage, the effect on stiffness is less in compression than in tension due to normal crack closure as would be expected. Fully closed, non-sliding cracks have no effect. Another parameter of interest is the total lateral strain at crack interaction, plotted for the principal orientations of pre-existing damage in Figure 8.55.

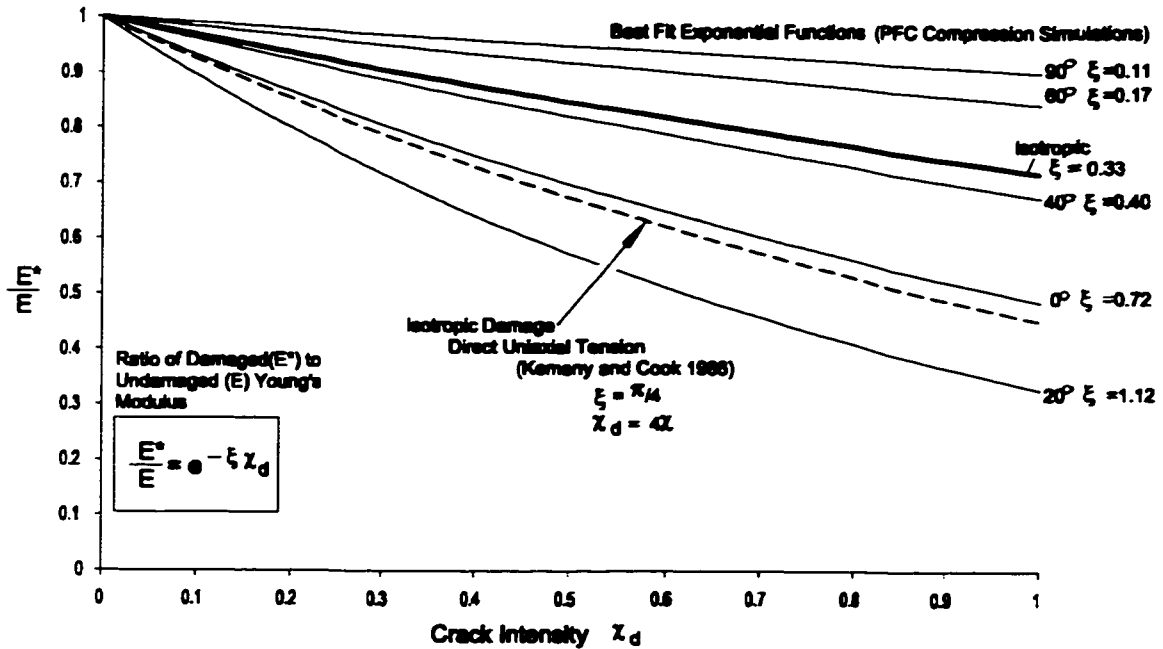


Figure 8.54: Exponential functions to moduli from simulations (Figure 8.53-mid). Theoretical relationship for isotropic damage in direct tension is shown for comparison.

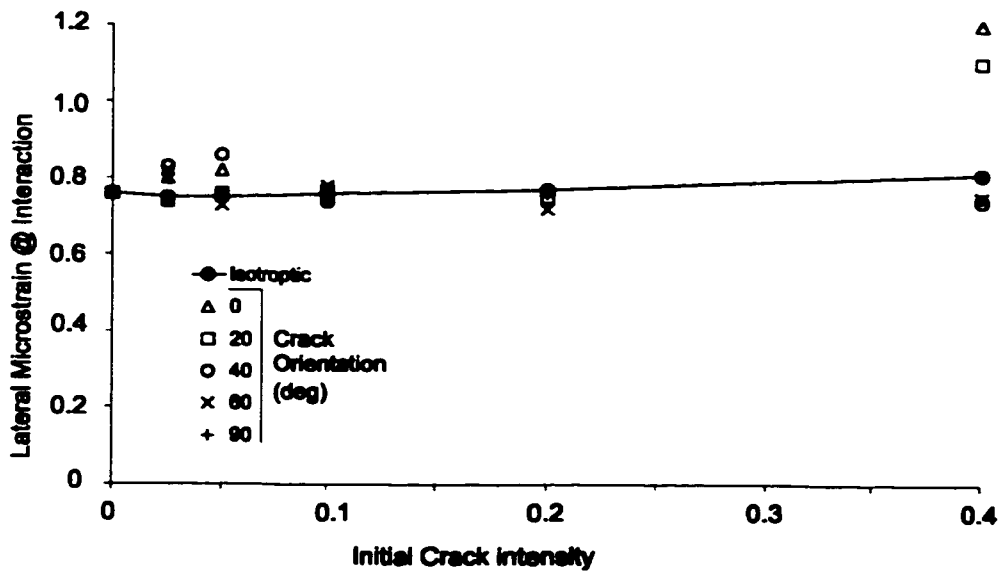


Figure 8.55: Lateral strain at crack interaction for previously damaged samples.

It is interesting that while the critical stress at interaction declines with damage, the critical extension (lateral) strain remains relatively invariant. For compression-parallel and steeply inclined damage, the lateral strain at interaction does increase for damage levels in excess of 0.1 (the normal damage range at peak uniaxial strength for intact samples).

8.5.3 Comparison of UCS Simulations to Statistical Model

One important conclusion from this work is that for moderate damage levels, strength reduction is the result of increased statistical potential for interaction (between new cracks and existing cracks) rather than the result of any direct impact of crack initiation or local weakening. This is further validated by the comparison in Figure 8.56 between the simulation data and the statistical model developed in Section 8.5.1. In this plot, the model parameters corresponding to a 50% probability of systematic damage initiation are used (obtained from Figure 8.43 and curve C in Figure 8.47). An upper and lower bound corresponding to 5% and 95% probabilities are also shown. For comparison, the average crack intensities at key damage thresholds in UCS tests are also indicated in Figure 8.56.

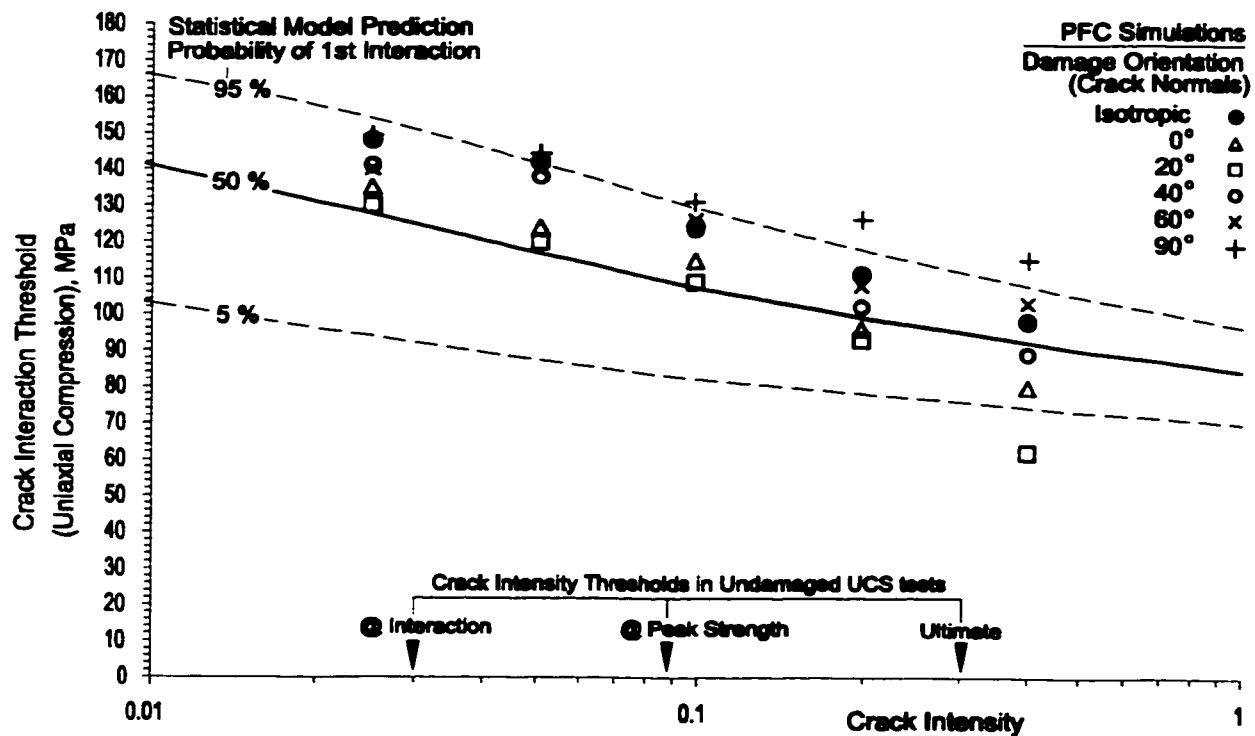


Figure 8.56: Comparison of PFC simulation results to statistical interaction model (with pre-existing damage).

The PFC data for 0 and 20 degree damage (parallel and sub-parallel to maximum compression) best follow the predicted curve (50%) for damage levels below that required for peak strength. This is expected since the compression induced damage for which the curves were calibrated is also predominantly oriented at less than 30 degrees. Oriented cracks which are more perpendicular to maximum compression (40, 60 and 90 degrees) are frictionally stable and are less likely to lead to a significant interaction. 22.5 degree cracks are the least stable (for a friction angle of 45 degrees) and are virtually guaranteed to result in a critical interaction.

For isotropic crack populations, only a portion of the damage is oriented favorably for dilation or sliding leading to significant interaction with new cracks. Therefore, for a given crack intensity, isotropic damage is less severe than critically oriented damage.

The correspondence between PFC data and the statistical interaction model (even for steep cracks) breaks down for large amounts of damage. In particular, at crack intensities greater than that required to totally fail uniaxial compression samples, the lower angle pre-existing cracks, within these populations, can no longer be considered isolated (an assumption in the statistical model). Instead they begin to interact with each other (without the need for new damage), thereby directly affecting the nucleation and accumulation of induced initial crack growth.

8.5.4 Stress Path and Damage Initiation

The importance of stress rotation above the damage initiation threshold is evident in the data from the URL mine-by experiment (Martin 1994). In Figure 8.57, the stress paths at two points (10mm and 0.5m from the tunnel roof) are plotted for a 20m chainage ahead and behind the advancing tunnel face. In this figure, the stresses and geometries are rotated to align with the coordinate axes (major principal compressive stress is horizontal). The ultimate failed notch geometry is not modeled here but is illustrated at the bottom of the figure.

The relative orientations, with respect to the far field directions, are noted. The maximum rotation for a point near the tunnel roof is about 25 degrees (close to the "worst-case" angle from the PFC simulations). After the tunnel has advanced some distance the major compressive stress above the roof rotates back to within several degrees of the original orientation. In the mean-time the stress path near the boundary incurs crack damage which is at a critical angle to adversely affect the ultimate yield strength of the rock above the tunnel. As a result the notch begins to form at about 100 to 110 MPa, far below the 160 to 170 MPa yield strength for undamaged rock.

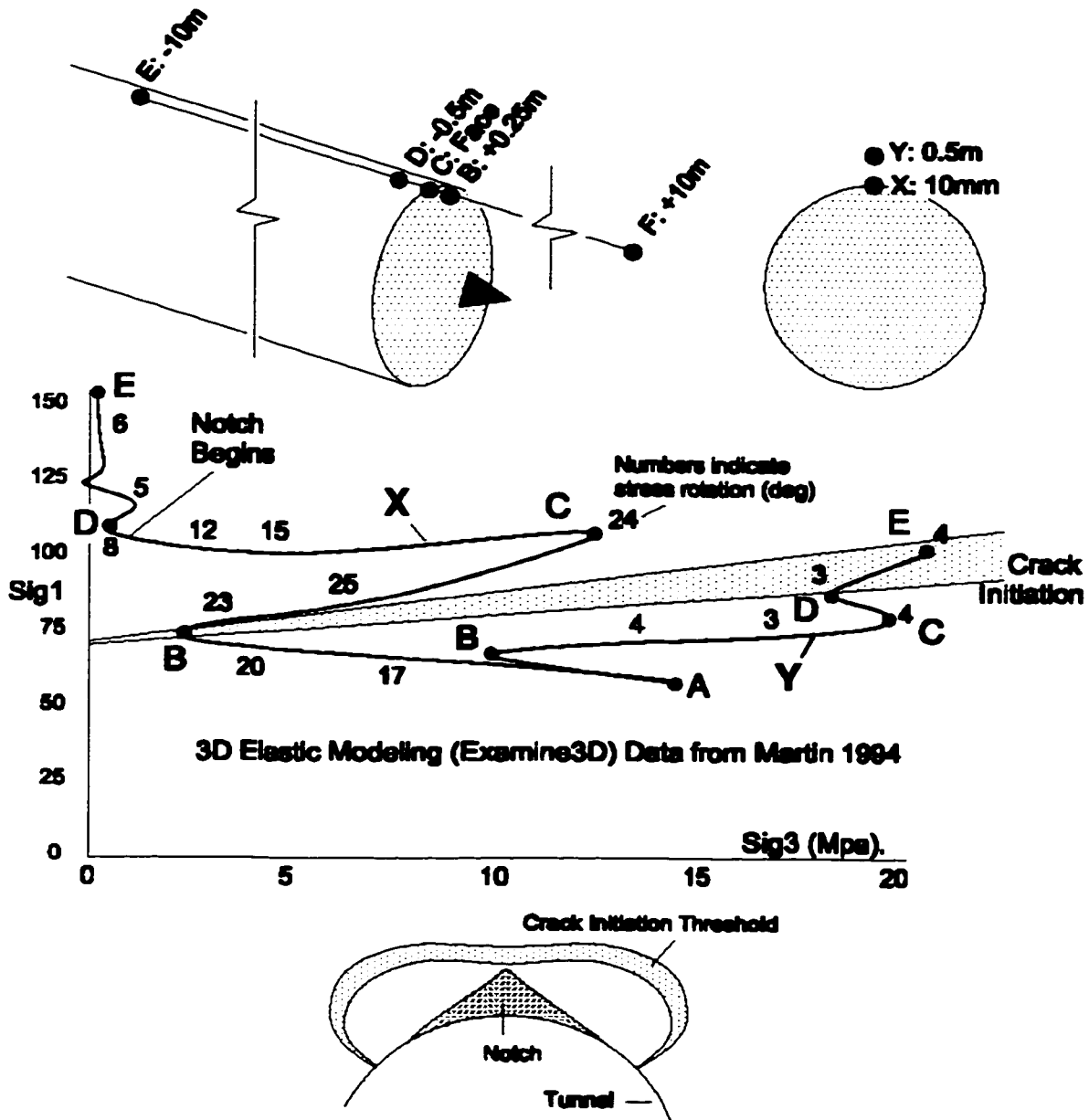


Figure 8.57: Stress paths for two locations in the roof of an advancing tunnel and comparison between failure geometry and damage initiation limits from 2D elastic models.

In contrast, the stress path 0.5m above the roof does not cross the initiation threshold and has much smaller angles of stress rotation. The consequent reduction in strength in this area is likely to be minimal. While increased confinement above a propagating notch contributes to arrest further failure, the notch is stabilized when it reaches rock without significant stress path related damage and strength reduction. This is the major reason why crack initiation contours seem to delineate the extent of failure for practical purposes as discussed in Chapter 5.

8.5.5 Effect of Confinement and Pre-existing Damage (No Crack Extension)

Finally, the influence of initial crack damage under confined compression was investigated. A series of simulations were performed in which isotropic damage corresponding to a crack intensity of 0.2 was introduced into a number of samples. These samples were initially lithified at a pressure of 25 MPa. Results were compared to an otherwise identical series of undamaged samples. Figure 8.58 illustrates the peak strength response. A reduction in uniaxial compressive intercept is apparent but there is no effect on the slope of the envelope. This corresponds to granite test observations by Martin and Stimpson (1994).

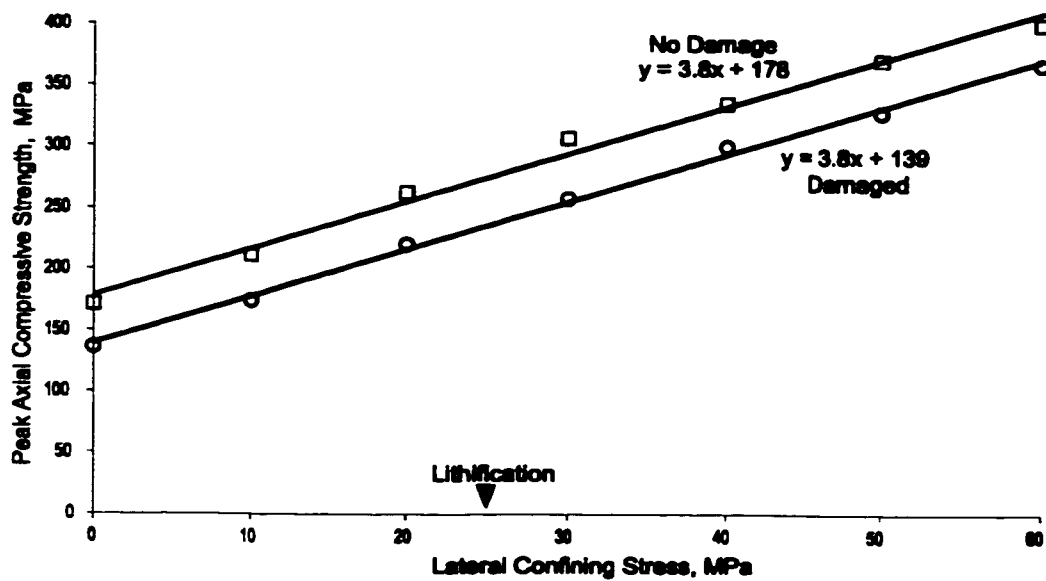


Figure 8.58: Effect of isotropic damage on confined peak strength ($\chi_c=0.2$).

Figure 8.59 illustrates the observed effect of initial damage on the crack interaction threshold and the systematic damage threshold (new cracks). The minimum axial stress for crack interaction drops 30% in uniaxial conditions for this level of damage. The effect becomes much less at higher confinements. In particular the confining stress corresponding to the initial lithification pressure seems to form a transition between high and low influence for initial damage. This transition zone also manifests itself in the systematic damage threshold for damaged samples. The threshold has a near-zero slope before this critical confinement, rising parallel to the undamaged threshold at higher confinements.

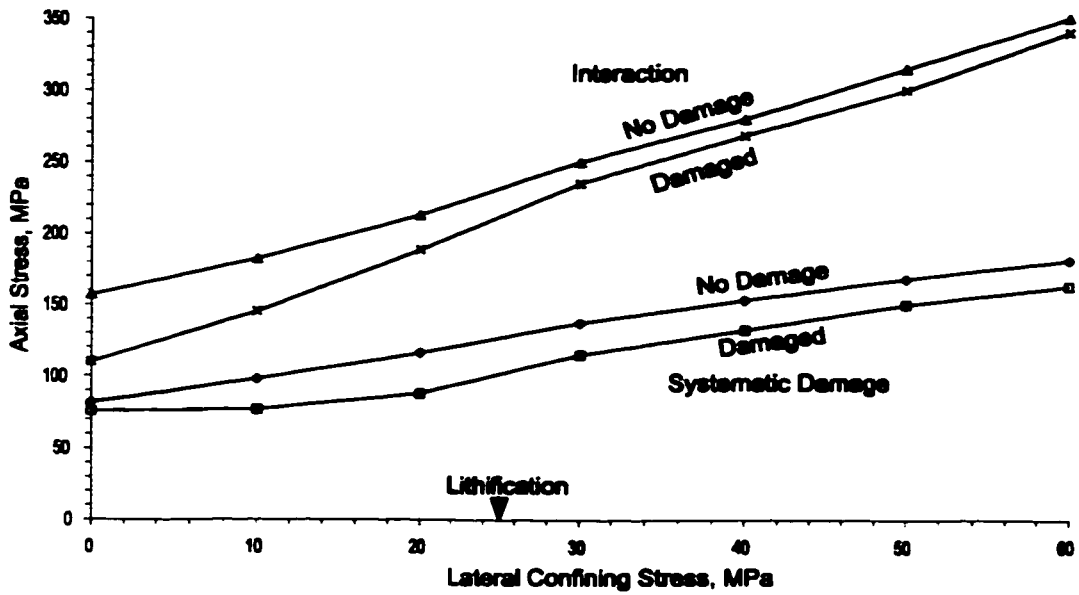


Figure 8.59: Effect of confinement and isotropic damage on new damage thresholds ($\chi_d=0.2$).

Some of the initial damage in these PFC simulations may correspond to open cracks, creating a confinement shadow effect (Figure 8.6) resulting locally in effectively uniaxial conditions. The impact is the same as that observed in the lab and insitu for Lac du Bonnet granite (Figure 8.60) obtained from the 420m level at the URL and therefore assumed to be highly damaged. Both the crack interaction threshold in lab samples and the crack initiation threshold, obtained in the field

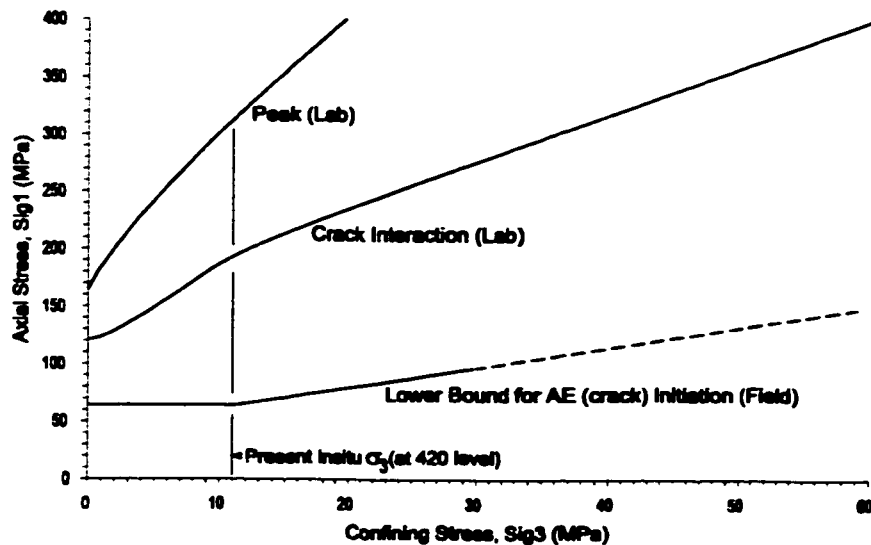


Figure 8.60: Damage thresholds for damaged Lac du Bonnet granite (URL 420 level). Damage initiation and crack interaction thresholds from data in Section 6.7. Peak Strength from Martin and Stimpson (1994).

from microseismic or acoustic emission data (AE), show the same bi-linear nature straddling a confining stress equal to the minimum insitu principal stress.

This effect is simulated for a square opening in Figure 8.61. In this highly schematic example, using elastic boundary elements to simulate a square opening in a stressed infinite medium, a series of frictionless displacement discontinuity elements are added, above the excavation, to simulate the disruption of lateral stress transfer caused by boundary-parallel damage. Crack damage extends the envelope of zero confinement into the rockmass above the back. While the stresses at the seismic data points in Figure 8.60 are calculated using an elastic continuum, the schematic in Figure 8.61 explains why the effect of (calculated) confinement is negated near the boundary. Once cracks are closed at a threshold confining stress (apparently related to the present insitu stress field), the expected confinement dependency is restored. Another interesting effect in the model in Figure 8.61 is the increase in boundary-parallel compressive stress above the excavation in the damaged zone. Aglawe (1999) found a compressive stress reduction due to damage around curved boundaries.

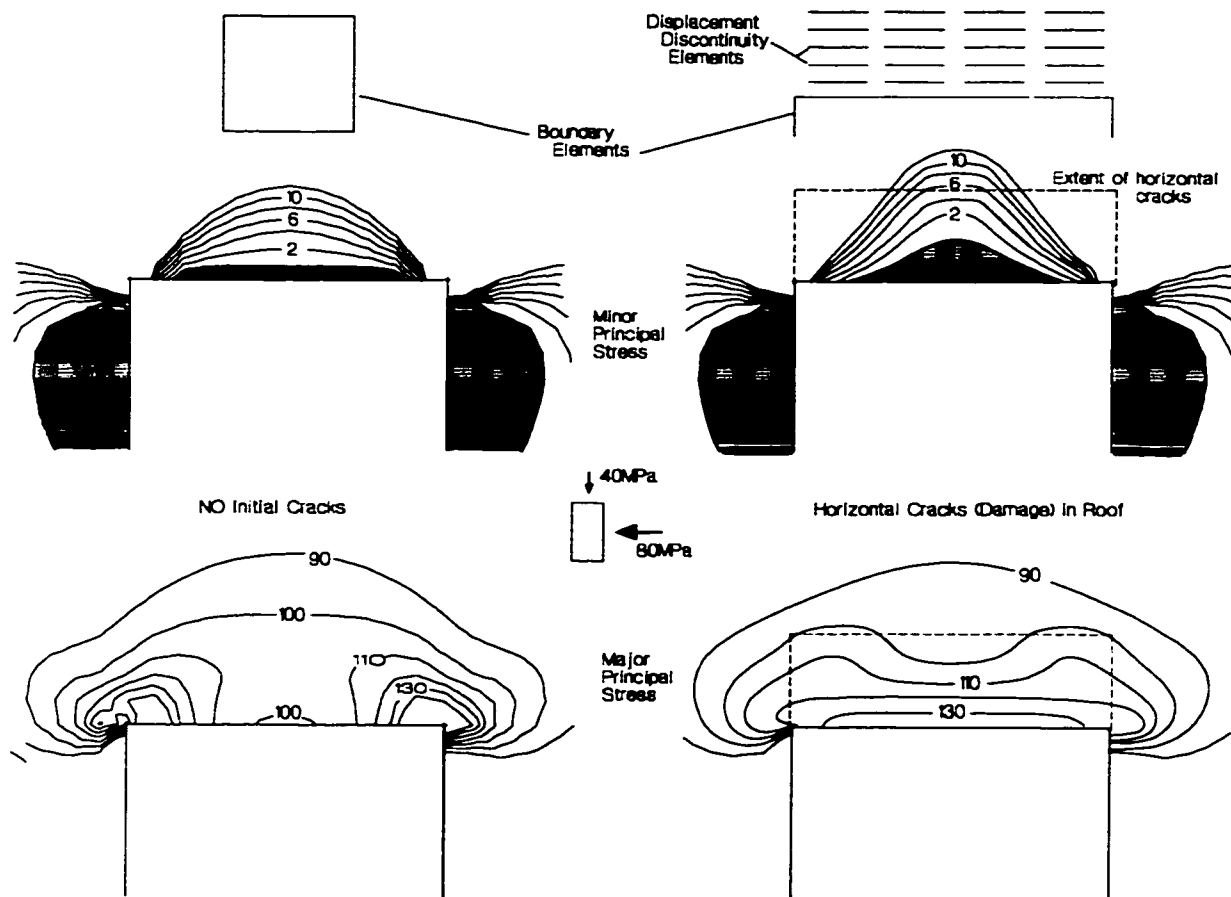


Figure 8.61: Elastic model schematically illustrating the effect of boundary-parallel damage.

8.5.6 Effective Gap

The concept of effective confinement or more appropriately, effective "gap" can be implemented into strength criteria in the same way as effective stress is taken into account for situations where water pressure is significant. Consider Figure 8.62.

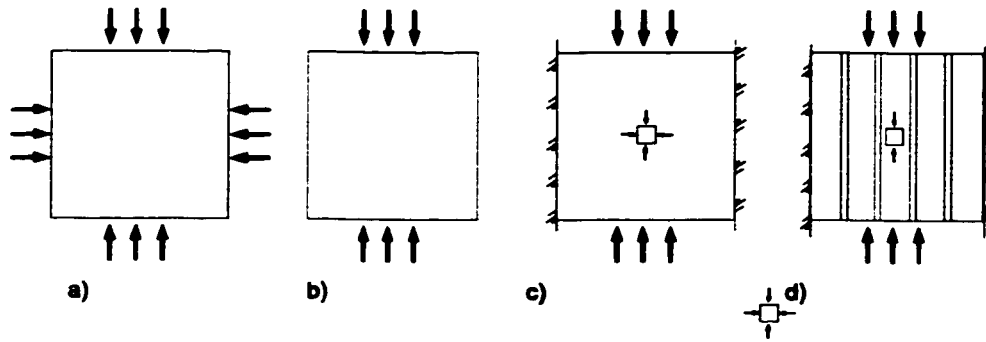


Figure 8.62: Effective gap concept. A stressed medium: a) deviatoric applied compression; b) uniaxial applied compression; c) confined compression (oedometer stress path); d) effective uniaxial state due to "gap".

In a), an elastic continuum is subjected to an applied stress field. This stress field is uniform throughout. In b) the medium is subjected to uniaxial compression. In c) compression is applied to a medium with constrained lateral boundaries, generating a lateral stress calculated by elastic theory. In d), vertical gaps within the medium prevent the immediate buildup of lateral stress due to Poisson's effect. The vertical stress required to close the gaps (represented by a distributed gap "strain" ϵ_{gap}) is given by:

$$\Delta\sigma_1 = \frac{E}{\nu(1+\nu)} \epsilon_{gap} \quad [8.36]$$

Alternatively the applied lateral stress in a) is shadowed in the vicinity of open cracks. The "effective confinement" in these regions is equal to the applied stress less a crack closure pressure. In the vicinity of open crack damage, therefore, it can be assumed that the rock behaviour is dominated by locally uniaxial compression. This results in an apparent strength reduction when elastically calculated stresses are used. This is illustrated, for example, in Figure 8.63. In this scoping analysis, elastic boundary elements (Examine^{2D}) were used to delineate open oval cracks in an infinite medium.

The pressure or confinement required to close these cracks and restore continuity of elastic stress flow can be determined experimentally. In Figure 8.64, cylinders of damaged Lac du Bonnet granite (URL - 420 level) are subjected to increasing hydrostatic pressure while the axial and

circumferential strains are monitored. A transition occurs between a softer bulk modulus and a stiffer modulus, which by bi-linear construction is centered about σ_0 , the crack closure stress. For these samples this stress is coincident with the insitu minor principal stress (11-12 MPa). The higher axial strains are the result of additional damage normal to the sample axis which occurs during coring in a stressed medium (a precursor to discing). This was discussed in Chapter 6.

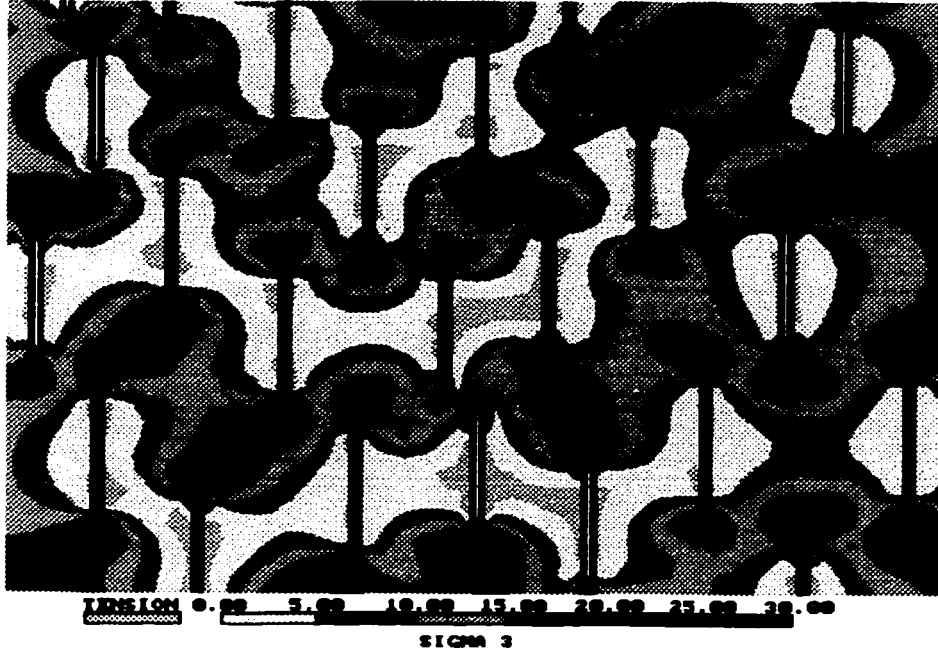


Figure 8.63: Elastic boundary element model with open cracks. Hydrostatic applied stress state ($\sigma=20\text{MPa}$), $\chi_d=0.4$. Note confinement shadows around and between cracks.

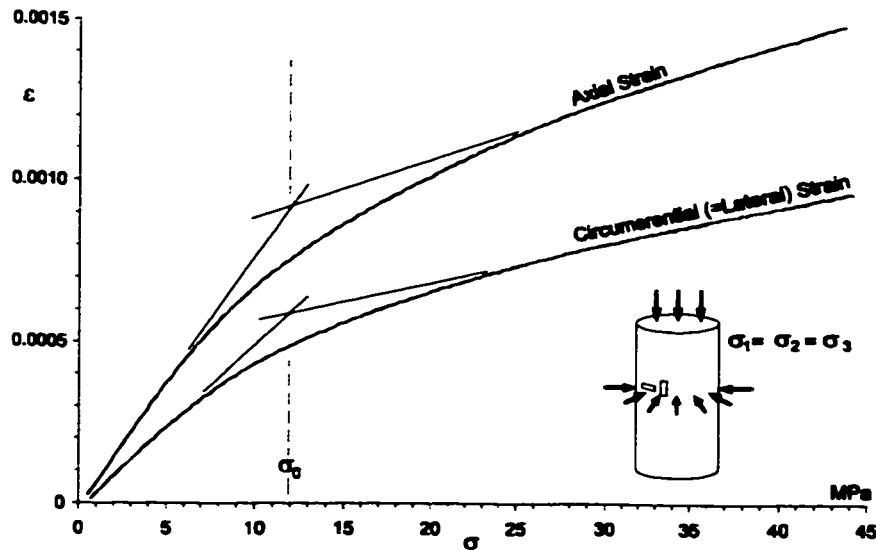


Figure 8.64: Estimation of crack closure stress from hydrostatic loading data (Lac du Bonnet granite (URL - 420 level)).

This effect can be implemented in a conventional strength or damage criterion as shown in Figure 8.65. An adjustment is made to the minor principal stress prior to application of the criterion. A hyperbolic tangent function is used to maintain a uniaxial "effective stress" state for low confinements and to achieve a finite reduction, equal to the crack closure stress, at higher applied confinements. This adjustment yields results for damage initiation which correspond to the trend for "damaged" PFC simulations and for insitu AE (Figure 8.60) at the URL.

The adjustment to the crack interaction threshold in the example in Figure 8.65 is less convincing when compared to Figures 8.59 or 8.60. Reduction of this threshold, for moderate initial damage levels, is dominated by the factors already discussed in this chapter. For higher damage levels, when the yield strength approaches the crack initiation stress, the effective gap concept becomes important in predicting insitu strength. The adjustment can be applied, as well, to tensile stresses, phenomenologically accounting for tensile strength reduction as shown.

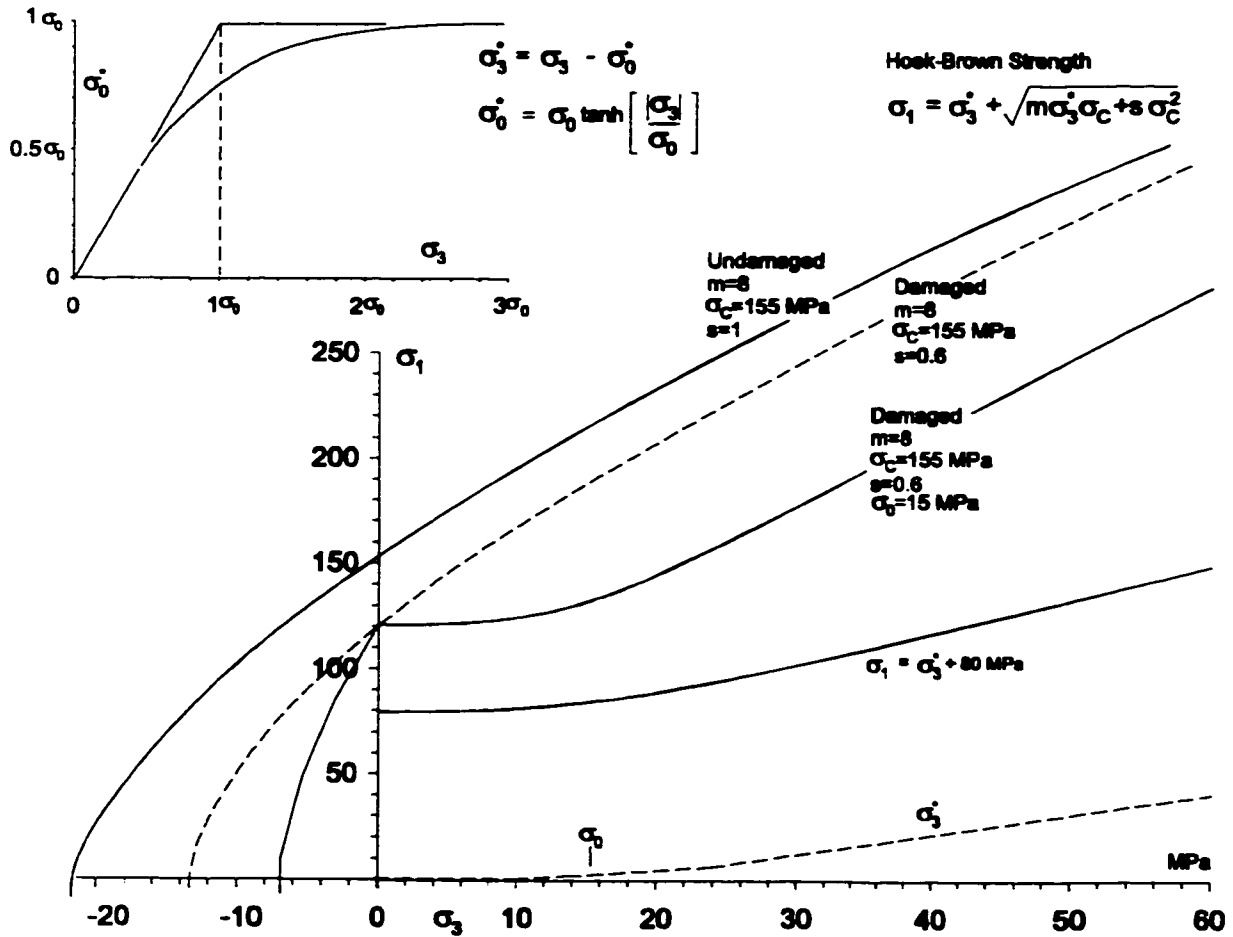


Figure 8.65: Effective confinement adjustment for insitu strength and damage prediction.

8.6 THE EFFECT OF CRACK LENGTH AND CONFINEMENT

As discussed in Chapter 6 and as shown in the simulations in Chapter 7, crack initiation is relatively insensitive to confining stress. For a sliding flaw with wing cracks, for example, the first phase of crack extension after initiation is dominated by the wedging action (crack opening force) of the initiating flaw. Wing cracks initiate, at about 70 degrees with respect to the plane of the initial flaw, and grow in a curved fashion towards the direction of maximum compression. As cracks propagate further, parallel to maximum compression, a second phase of extension is dominated by the confining stress acting normal to the extending wing cracks. Cracks become stable at this point for even modest confining stresses. On the other hand, slightly tensile stress conditions normal to the direction of extension can result in catastrophic propagation.

The previous discussions in this and in the previous chapter have focussed on behaviour due to the accumulation of fixed-length cracks, corresponding loosely to the first stage of crack growth mentioned above. In fact, critical damage associated with crack interaction and yield is profoundly affected by crack length, which in turn is primarily influenced by boundary interaction and effective confining stress. We return, then, to the previously mentioned and fundamental limitation of PFC modelling: the inability to simulate crack tip stress concentration (when the "crack" and disc scales are similar) and the inability to model the consequently unstable propagation of a single microcrack. Other tools, in conjunction with PFC simulation, will be used in this section to indirectly investigate the effect of confinement dependent microcrack extension.

8.6.1 Statistical Consideration of Crack Length

Using the model developed in Section 8.5, the impact of relative crack length (as compared to a single elemental unit), can be incorporated by simply increasing the number of potential interactions for each element. Here a larger crack occupies a larger volume that encloses or is adjacent to a larger "selection" of possible interaction "mates". Equation 8.27, describing the number of potential interaction pairs in the two-dimensional (series-parallel) sample becomes:

$$f() = \frac{x}{2} \left(\frac{V}{V_0} \right) (L^*)^2 \quad [8.37]$$

where L^* is the relative crack length (normalized with respect to the initial elemental dimension

($V_0^{1/2}$). For $x=4$ and $k=2$, the function for interaction stress from Equation 8.28 is then:

$$\sigma = \sigma_0 \left(-\ln \left[1 - \left(1 - (1 - P_V(\sigma)) \left(\frac{v_0}{2v(L^*)^2} \right)^{\frac{1}{2}} \right) \right]^{\frac{1}{m}} \right) + \sigma_i \quad [8.38]$$

This result is plotted in Figure 8.66, using the model parameters from the second calibration from Figure 8.43 (dashed line). The 50% probability curve resulting from these parameters is supplemented by 5% and 95% cumulative probability limits. The calibration (based on the first crack initiation threshold) from Figure 8.42 is also used here to illustrate the effect of assumed crack length on interaction potential. The decline in the interaction threshold with increasing crack length is clearly demonstrated. In this statistical model, interaction with the sample boundaries is

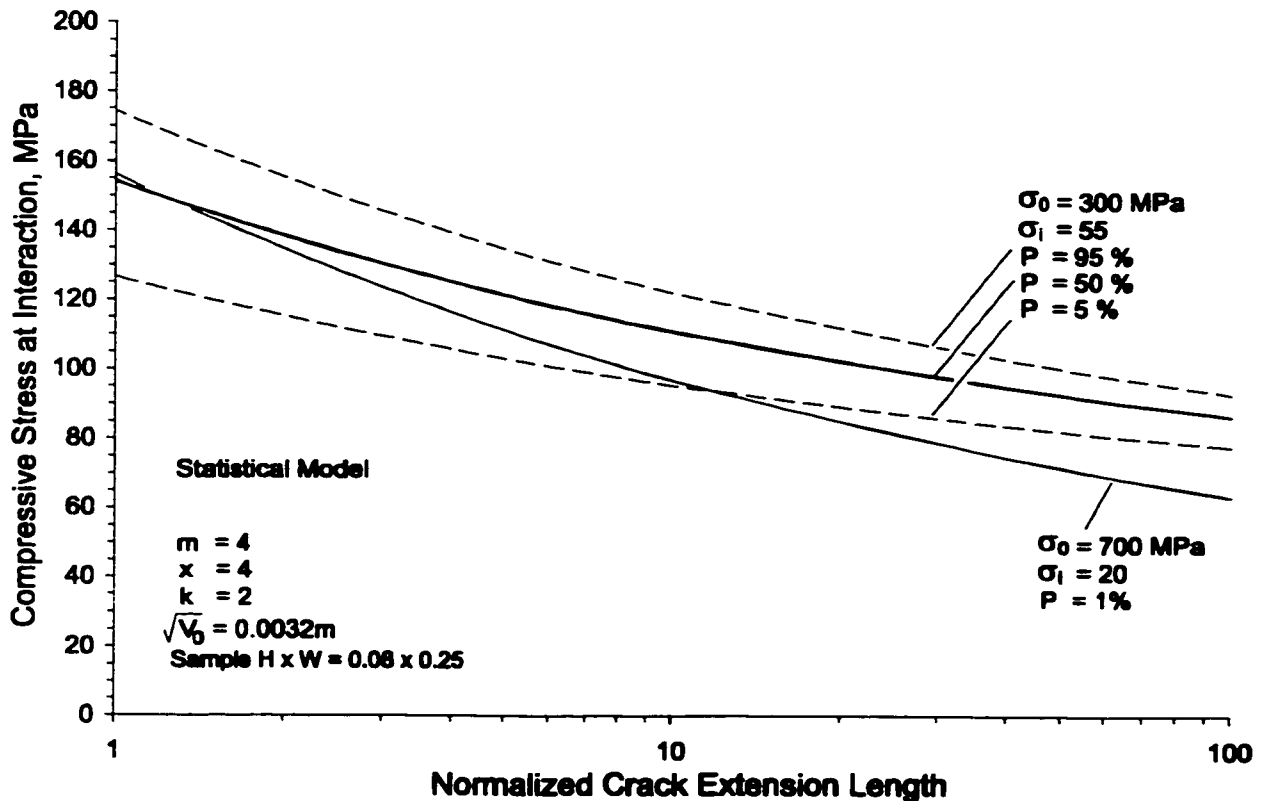


Figure 8.66: Effect of assumed crack extension length on crack interaction stress (statistical model using calibration parameters from Section 8.4).

not considered. If it were, the decline in yield strength would be even more severe as demonstrated using fracture mechanics by Dyskin and Germanovich (1993).

In order to assess the additive impact of crack length on insitu strength, the statistical model can be modified to account for both crack length and pre-existing damage:

$$P_V(\sigma) = 1 - \exp\left(-\left(\frac{\sigma - \sigma_i}{\sigma_0}\right)^m \cdot \frac{4f(L^*)\chi_0 V}{V_0}\right) \times \left(1 - \left(1 - \exp\left(-\left(\frac{\sigma - \sigma_i}{\sigma_0}\right)^m\right)\right)^k\right)^{\frac{V}{V_0}(2(L^*)^2 - 4f(L^*)\chi_0)} \quad [8.39]$$

As before, interaction is assumed when the intercrack separation is less than or equal to one average crack length. The initial crack intensity (χ_0) is calculated for pre-existing cracks of elemental length. The term $4f(L^*)\chi$ determines the number of potential interactions (parallel tiers in the model) affected by the presence of a pre-existing crack.

In this model it is assumed that cracks grow to relative length L^* immediately upon initiation (stable crack propagation length is a function of increasing stress after initiation). It can also be assumed that pre-existing damage does or does not extend upon loading. In the first case pre-existing damage spontaneously extends to length L^* upon loading such that $f(L^*)=(L^*)^2$ in Equation 8.39. In the second extreme, pre-existing cracks do not extend (but can still interact with extending new cracks) and have a constant length equal to the elemental dimension such that $f(L^*)=((1+L^*)/2)^2$ in Equation 8.39.

In Figure 8.67 the composite result is shown for both assumptions regarding the propagation of pre-existing cracks. The model parameters are based on the $P=50\%$ calibration (for systematic damage initiation) from Figure 8.43.

While this model is grossly over-simplified, it is clear that the combined effect of moderate levels of pre-existing damage and crack extension ($\chi_0 < 0.03$, $L^* < 4$) is sufficient to reduce damage initiation and sample yield strength to the level of systematic damage initiation. This model is calibrated for uniaxial compression but the relative reduction of yield strength (interaction threshold should be valid for higher confinements as well. Crack extension length, however, is restricted at higher confinements.

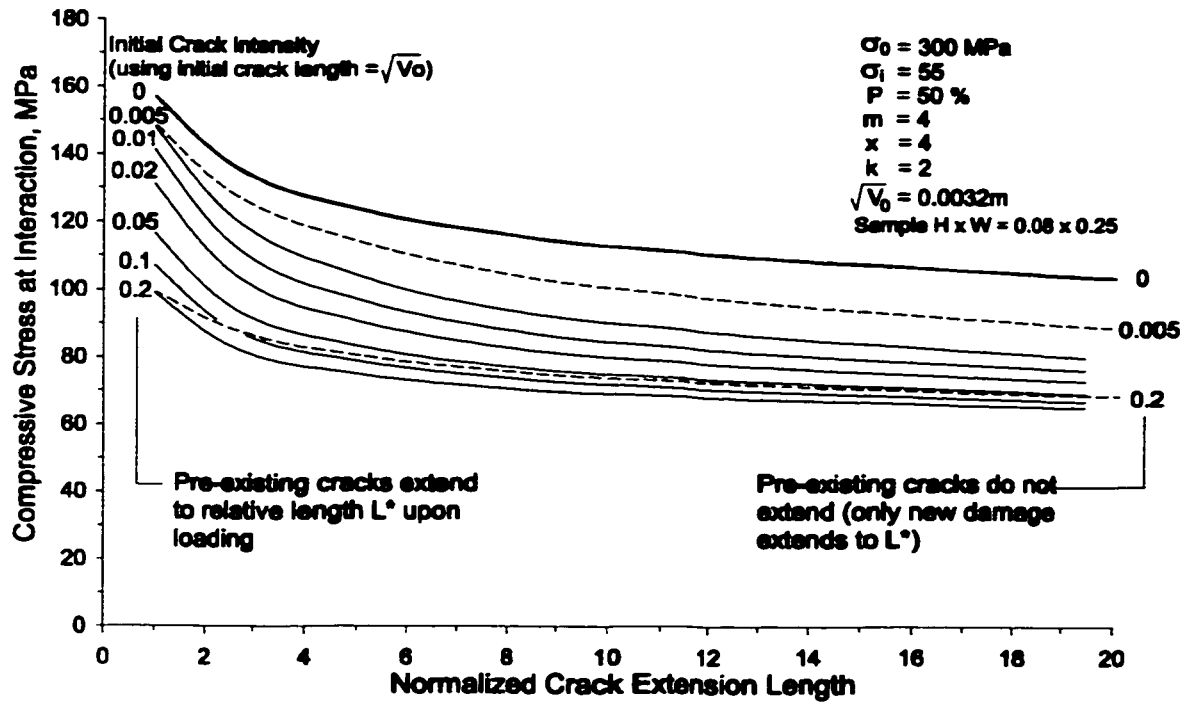


Figure 8.67: Composite effect of crack propagation length and pre-existing damage on yield strength (crack interaction). Two assumptions for extension of pre-existing cracks are used in Equation 8.39 and shown here.

8.6.2 Effect of Confinement on Isolated Crack Propagation

In order to assess the relationship between microcrack propagation and confining stress, consider again the sliding flaw and wing crack analogue. Clearly there is no direct physical connection between the sliding crack model and the PFC bond rupture mechanism. The sliding flaw is used here as a mechanical analogue for generating the required crack opening force for crack initiation. Equation 8.7 gives one deviation for propagating wing cracks under confined compression. Another alternative expression (Mode I stress intensity factor for an isolated sliding crack of length $2c$ and $\mu = \tan\phi$ and with propagating wing cracks each of length a) is given by Ashby and Hallam (1986):

$$K_I = \frac{-\sigma_1 \sqrt{\pi c}}{(1+L)^{\frac{3}{2}}} \{1 - \lambda - \mu(1 + \lambda) - 4.3\lambda L\} \left\{ 0.23L + \frac{1}{\sqrt{3(1+L)}} \right\} \quad [8.40]$$

where $\lambda = \frac{\sigma_3}{\sigma_1}$ and $L = \frac{a}{c}$. The orientation, θ (angle of crack normal with respect to horizontal), of

the critical flaw is incorporated into this derivation and is equal to $\frac{1}{2} \tan^{-1}\left(\frac{1}{\mu}\right)$.

Rearranging Equation 8.40 with respect to σ_3 and replacing K_I with K_{IC} give an expression for the confining stress required to prevent further propagation at a given σ_1 :

$$\sigma_3 = \frac{1}{1 + \mu + 4.3L} \left[\sigma_1(1 - \mu) - K_{IC} \frac{(1+L)^{1.5}}{\sqrt{\pi c}} \left(0.23L + \frac{1}{\sqrt{3(1+L)}} \right)^{-1} \right] \quad [8.41]$$

An example illustrating this relationship is shown in Figure 8.68.

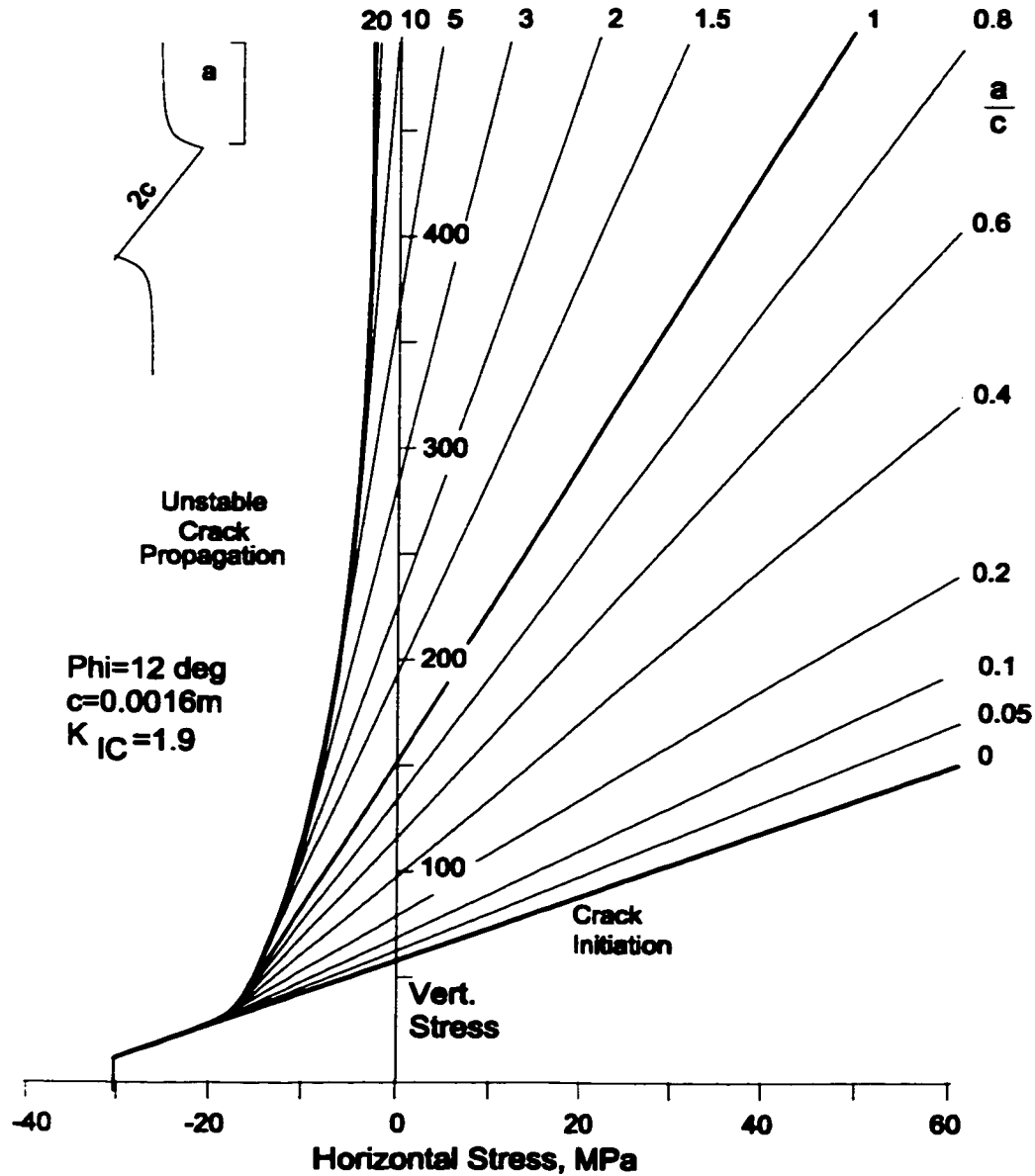


Figure 8.68: Confining stress and crack propagation for sliding crack analogue.

In the case of tensile stresses large enough to separate the surfaces of the initial (sliding) flaw, the critical σ_3 is given by:

$$\sigma_3 = \frac{-K_{IC}}{\sqrt{\pi c(L + \sin \theta)}} \quad [8.42]$$

The actual critical value is given by the most compressive value of σ_3 from either Equation 8.41 or 8.42. Parameters for the plot in Figure 8.68 are chosen such that crack initiation in uniaxial compression is the average of the "first crack" and the "systematic damage thresholds" in previous PFC simulations. The friction angle is chosen to achieve an initiation slope of 1.5. This results in a curve for $a/c=1$, which corresponds approximately to sample yield. An alternative result, "calibrated" for crack initiation using a friction angle of zero is shown in Figure 8.69. In this simplified case, the angle of the critical flaw is 45 degrees.

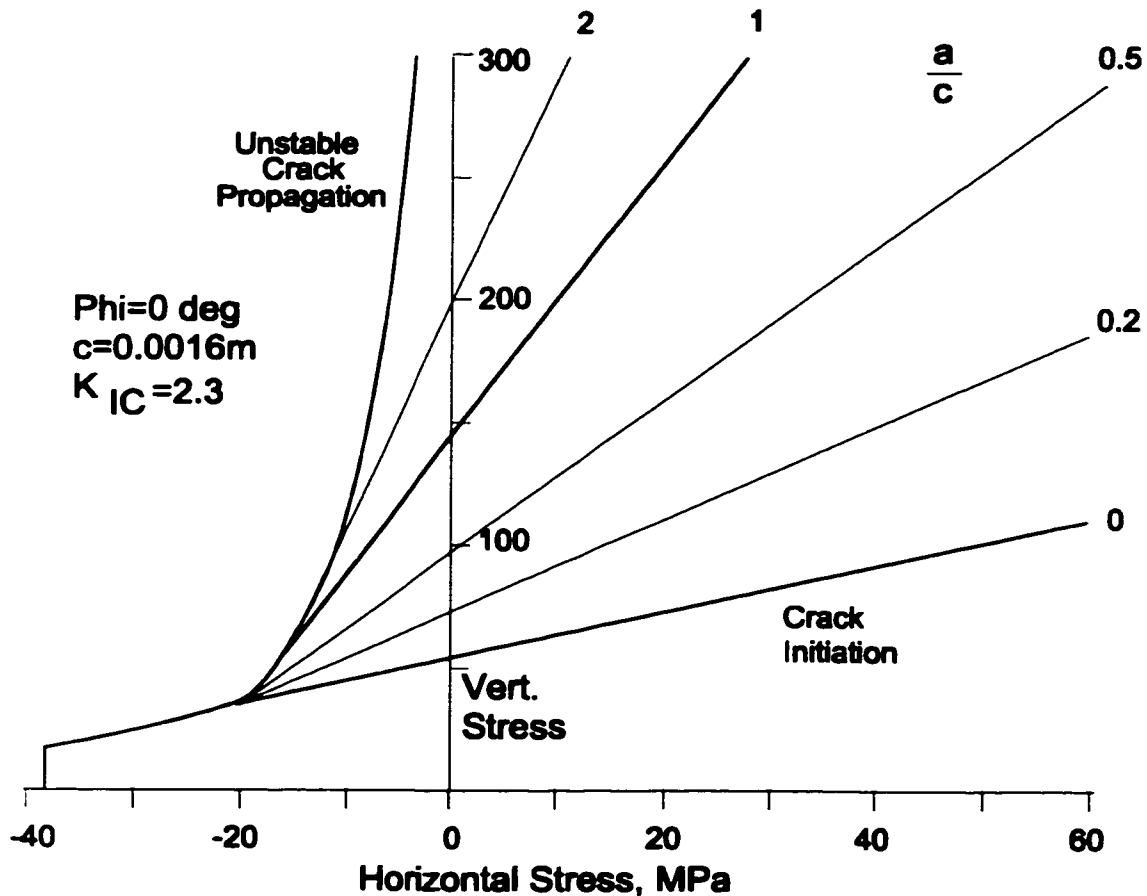


Figure 8.69: Alternative example relationship between confining stress and crack propagation for sliding crack analogue (friction angle = 0).

The curved envelope to the left of the vertical axis is the limit of stable crack propagation at which:

$$\frac{\partial K_I}{\partial L} = 0 \quad [8.43]$$

To the right of this limit an increase in σ_1 or a decrease in σ_3 is required to induce an incremental extension of the wing cracks. To the left of this limit, catastrophic propagation and failure will occur instantaneously upon initiation. The linear thresholds represent stable crack propagation lengths for a given stress state.

The trellis analogue discussed at the beginning of Chapter 7 offered an explanation for the confinement dependency observed (in the absence of pre-rupture friction) for damage accumulation and specifically for the crack interaction threshold in PFC simulations. Equation 8.41 and Figure 8.68 illustrate an additional impact of confinement when crack propagation length is considered. In Figures 8.68 and 8.69, note that the confinement dependency for longer crack propagation is virtually independent of the friction acting on the original flaw.

For isolated cracks, propagation can be arrested with very little confinement and stable propagation is possible (according to the analogue in Equation 8.41) for small amounts of lateral tension. This contrasts with the conventional interpretation of normalized experimental results plotted by Hoek (1968), shown in Figure 8.5, which seem to show that unstable propagation is inevitable in unconfined conditions (tension not required). Only for very large cracks does the unstable propagation limit in Figure 8.68 become coincident with the unconfined compression axis. The calculated relationship in Figure 8.5 uses $c=1m$. Therefore, it is an interpretive error to normalize the results with respect to initial flaw size as in Figure 8.5.

This is significant because unstable propagation does not occur until well after crack initiation in carefully prepared cylindrical *UCS* samples in the lab. This is because the sample geometry and testing conditions (normally stiff platens) restrict local tensile stresses in the sample (Section 6.3.4). As a result, cracks are not observed to extend significantly beyond the grain scale until after crack interaction has begun and volumetric strain reversal has occurred (Martin 1994).

In the field, conditions at excavation boundaries are not as controlled. The effect of heterogeneity and geometry on local confinement and crack intensity is discussed in Section 8.7.

8.6.4 Effect of Propagation on Critical Crack Density

Crack interaction models such as that proposed by Ashby and Hallam (1986) are typically based on a fixed array of cracks which extend until interaction occurs. In contrast, the numerical simulations (PFC) in this and the previous chapter are based on a constant crack length (prior to crack interaction). Crack accumulation (generation of new cracks) occurs with increasing deviatoric stress due to strength and stiffness heterogeneity.

A relationship between the stress state and crack propagation length for a sliding crack analogue was offered in Section 8.6.3. It is possible, for illustration purposes, to combine crack accumulation results from PFC simulations with the fracture model. A revised yield surface can be obtained which incorporates stochastic crack nucleation and mechanistic crack extension.

Figure 8.70 illustrates the two complimentary models. The sliding crack model has been calibrated such that the crack initiation threshold corresponds to the "first crack" threshold in the numerical simulations. As a result, the equilibrium threshold for $a/c=1$ corresponds to the onset of crack interaction in unconfined compression for the PFC samples. The lower portion of Figure 8.70 illustrates the crack intensity contours in stress space for simple monotonic loading.

An assumption must be made regarding the "standard" crack extension which corresponds to the fixed crack length in PFC. One option is to assume that PFC cracks correspond to an a/c ratio of 1 for uniaxial compression (at this point the PFC yield surface and critical crack intensity contour intersect the equilibrium threshold for $a/c=1$). It is assumed that crack interaction is governed by crack separation, S , relative to crack length, $2c$, where $S < 2c$ assures interaction. Therefore, the critical crack intensity (0.03 for PFC simulations) must be constant regardless of crack length (longer average crack length means that fewer cracks are required for interaction). Therefore a new yield surface can be drawn connecting the locus of points (in stress space) at which the following equality holds:

$$\frac{\chi_d}{a_0^2} a^2 = 0.03 \quad [8.44]$$

where χ_d is the crack intensity from PFC simulations (Figure 8.70), a is the normalized wing crack length from the fracture model and $a_0 = 1$ (model crack length a/c at crack interaction in uniaxial compression).

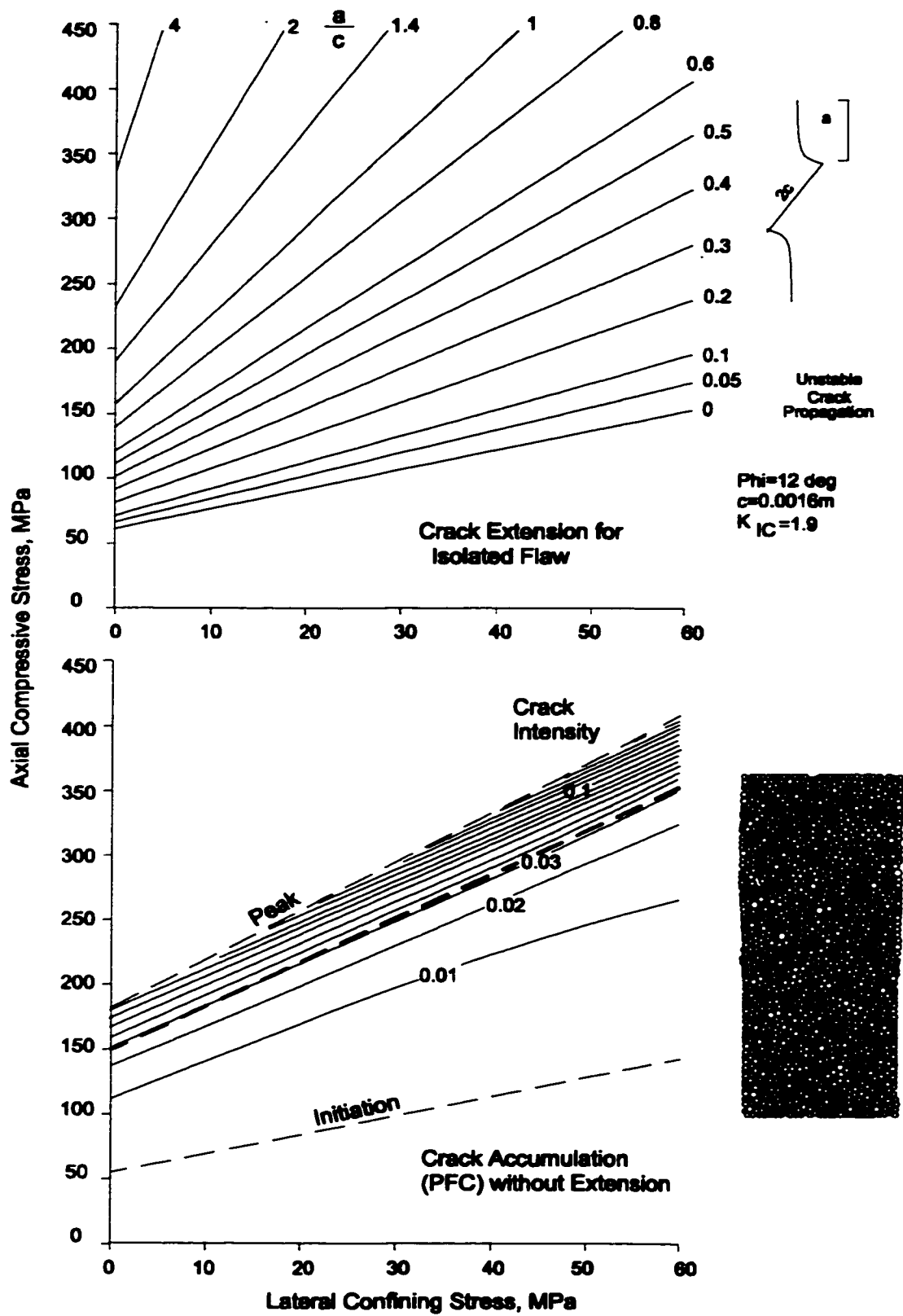


Figure 8.70: Crack extension (top) and crack accumulation (bottom).

In PFC the sliding flaw does not exist. The kinematics of the trellis create the crack opening force analogous to the sliding flaw. To be consistent, therefore, only the wing crack length (and not the composite crack length) is considered in this analysis.

An alternative assumption (Assumption 2 in Figure 8.17) is to use as a standard, the confined case (60 MPa), represented by the intersection of the $\chi_c=0.03$ contour and the threshold $a/c=0.5$. The true composite yield surface then is represented by the locus of points for which Equation 8.44 is true when $a_0=0.5$ is substituted. Both alternative corrections are presented in Figure 8.71.

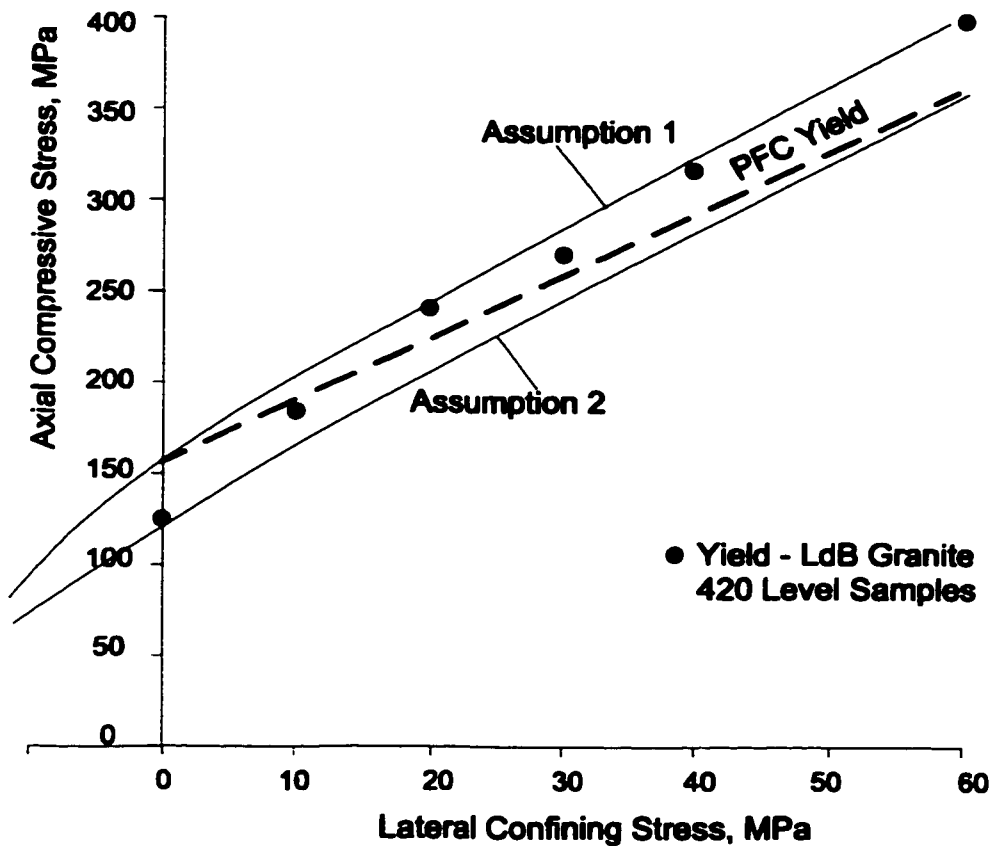


Figure 8.71: Correction of critical crack intensity (interaction) threshold, accounting for crack extension. Granite data shown for comparison.

The result in either case is a steepening of the yield slope in $\sigma_1:\sigma_3$ space. This accounts in part for the discrepancy between the maximum slope achievable in PFC simulations and the response of granite, for example. Sample data for granite (Chapter 6) is included in Figure 8.71. The comparison is favorable for moderately confined samples. The drop in strength at lower confinements has already been accounted for as the result of pre-existing sample damage.

8.6.4 Crack Interaction with a Free Surface

derived a further relationship, using fracture mechanics and beam theory, incorporating the effect of confinement and crack length on crack interaction with a free surface. This derivation is summarized in Appendix D. Near a free boundary, a beam of thickness, t , is formed by the propagating crack. As the beam becomes more narrow (as the crack grows) it bends and allows further freedom of movement on the initial sliding flaw. This additional displacement, in turn, increases the stress intensity factor at the crack tip propagation further propagation.

The incremental stress intensity due to the presence of a free surface is given

$$K_I^{surf} = \frac{1}{2\sqrt{2\pi}} \left(\frac{c}{t}\right)^{\frac{1}{2}} \sigma_1 \sqrt{\pi c} \left[\frac{1 - \frac{4}{\sqrt{(3\sqrt{2})}} \frac{c}{t} \left(L + \frac{1}{\sqrt{2}}\right)^2 \lambda}{1 + \frac{12}{\pi^2} \frac{c^2}{t^2} \left(L + \frac{1}{\sqrt{2}}\right)^2 \frac{\sigma_1}{E}} \right] \quad [8.45]$$

Using superposition, this increment is added to the value, K_I , calculated in Equation 8.40 for an isolated crack in an infinite medium. E is the Young's Modulus of the intact material. For simplicity, a 45 degree crack is used in the derivation of K_I^{surf} . This is consistent with a frictionless initial flaw (Figure 8.67). Ashby and Hallam (1986) suggest that the stress intensity increment in Equation 8.45 can also be added, with minimal error to the base value for a flaw with moderate friction (Figure 8.68).

Combining Equation 8.46 and 8.41, setting $(K_I + K_I^{surf})$ to K_{IC} , and then solving for critical σ_3 :

$$\sigma_3 = \frac{\sigma_1 \left(C_1(1 - \mu) + \frac{C_2}{1 + C_4\sigma_1} \right) - \frac{K_{IC}}{\sqrt{\pi c}}}{C_1(1 + \mu + 4.3L) + \frac{C_2 C_3}{(1 + C_4\sigma_1)}} \quad [8.46]$$

where:

$$C_1 = \left(0.23L + \frac{1}{\sqrt{3(1+L)}} \right) \frac{1}{(1+L)^{3/2}}, \quad C_2 = \frac{1}{2\sqrt{2\pi}} \left(\frac{c}{t}\right)^{\frac{1}{2}},$$

$$C_3 = \frac{4 \left(1 + \frac{1}{\sqrt{2}}\right)^2}{\sqrt{(3\sqrt{2})}} \left(\frac{c}{t}\right) \quad \text{and} \quad C_4 = \frac{12}{\pi^2 E} \left(1 + \frac{1}{\sqrt{2}}\right)^2 \left(\frac{c}{t}\right)^2$$

A tension cut-off (Equation 8.40) can be applied as in Section 8.62. The derivation for the boundary interaction effect in Equation 8.42 is specifically for a sliding crack, and so this cut-off will be ignored in this section. Notice that under confined compression, it is not possible to normalize this function with respect to stress intensity factor or initial crack length. The following results (Figures 8.72 and 8.73) therefore employ non-normalized parametric values based loosely on the crack initiation threshold from the PFC simulations.

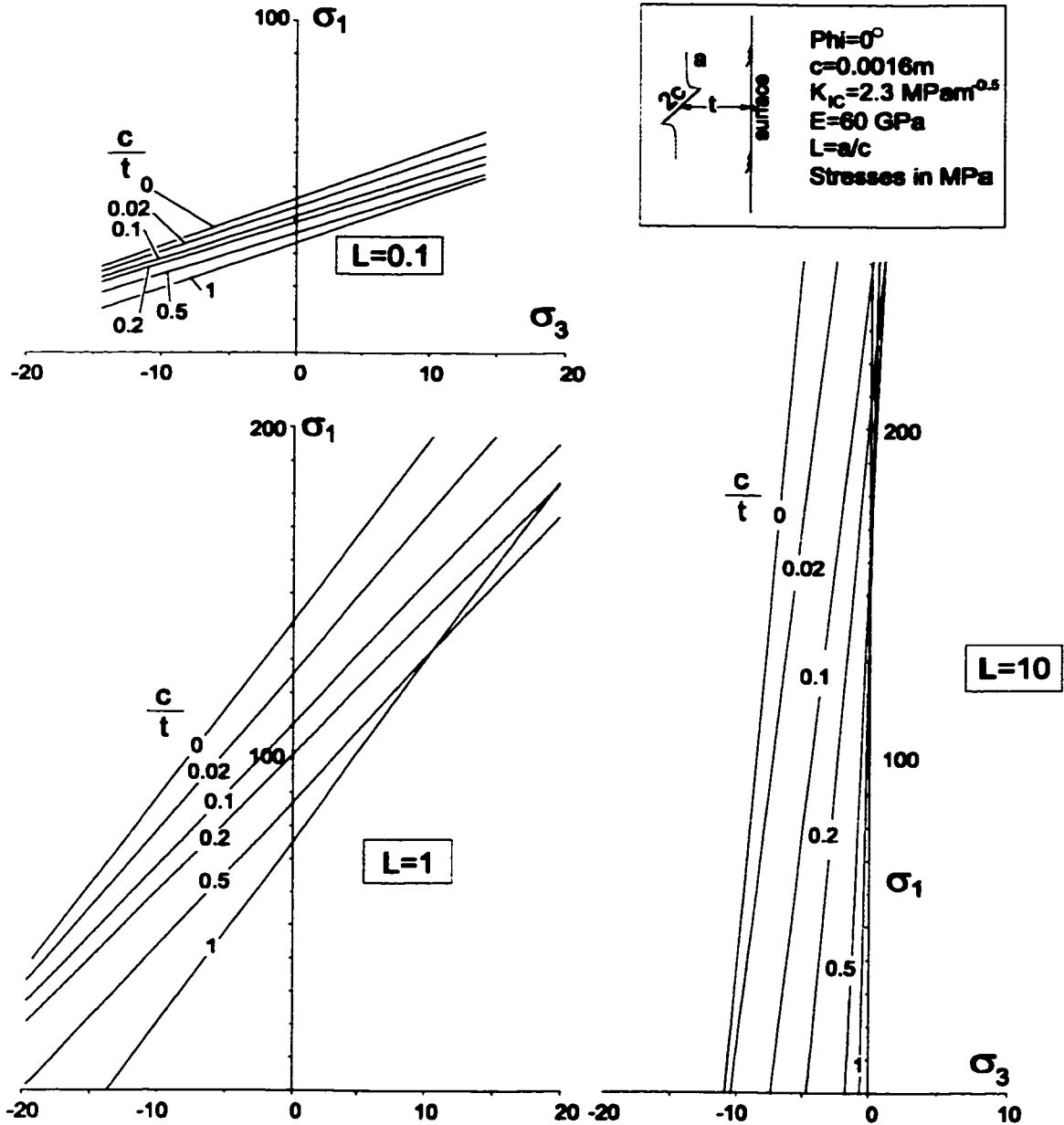


Figure 8.72: Effect of crack-surface separation on equilibrium crack length thresholds (cracks extend for σ_1, σ_3 above and to the left of threshold). Note that a nearby surface ($c/t \rightarrow 1$) has a greater destabilizing effect on longer cracks (e.g. $L=10$).

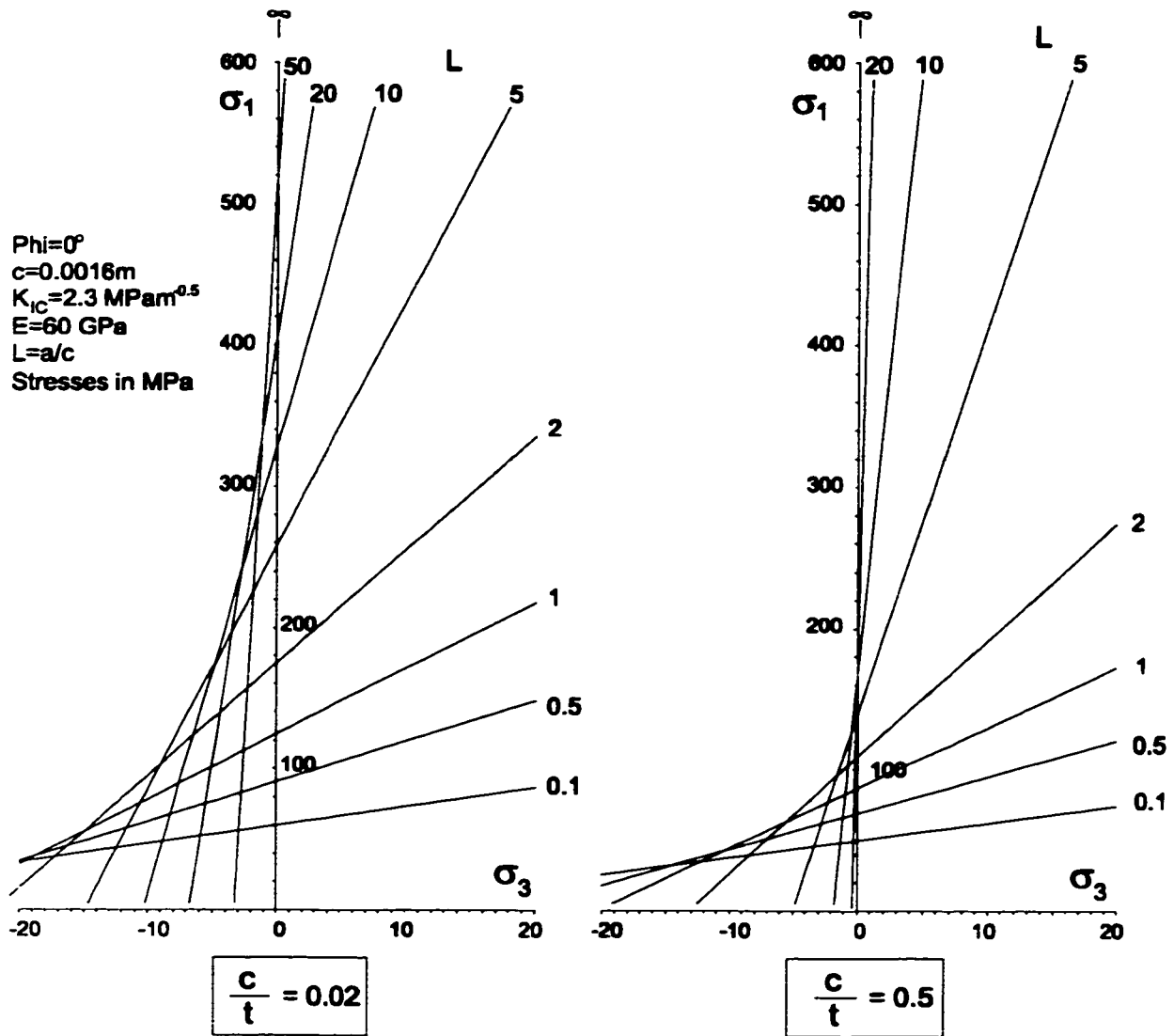


Figure 8.73: Effect of crack length on fracture equilibrium in the presence of a free surface. Upper left region bounded by composite thresholds indicates unstable propagation.

The PFC simulations serve as an experimental datum in which individual crack propagation is prevented. Since the PFC simulations are, in turn, loosely based on granite testing, the results here should at least qualitatively reflect rock behaviour as well. The purpose is to compare directly the impact of near-surface crack propagation on yield strength and rupture. In the field cases discussed in Chapter 5, the first observed failure (representing lower-bound insitu strength) was often in the form of thin surface spall damage, reflecting highly continuous crack propagation from near-surface flaws or nucleation sites. In the author's experience, the thickness of this surface spall is often of similar scale as the grain size of the rockmass.

In Figure 8.72, the equilibrium thresholds for several normalized wing crack lengths are illustrated. The ratio higher values for c/t indicate closer proximity to the free surface while a value of 0 indicates an isolated crack in an infinite medium. The presence of a free surface has measurable but relatively minor impact on crack initiation and short wing crack propagation ($L=0.1$). For longer cracks ($L=1$) the equilibrium stress (e.g. uniaxial compression) drops by nearly 50% for a crack within one elemental unit (initial flaw half-length) of the surface. For long cracks the effect is even greater.

Figure 8.73 shows the same relationship re-plotted for different crack lengths. An example of a distant crack ($c/t=0.02$) and a near-surface crack ($c/t=0.5$) are shown. Clearly for cracks close to the surface, the nominal compressive or deviatoric stress required to effect a given extension length is reduced considerably. Crack propagation also becomes much more sensitive to the presence of spurious tensile stresses (such as those which are present near an irregular boundary or in a highly heterogeneous material (Section 8.7)).

As in Figures 8.68 and 8.69, the upper right boundary formed by the convergence of the iso-extension contours represents the limit of stable propagation. Combining the limits for different crack-surface distances results in Figure 8.74.

While the left portions of these envelopes may be truncated in reality by direct tensile rupture of boundary-parallel cracks (not considered here), the intercepts with the uniaxial compression axis are highly significant. For this set of example parameters (calibrated for first crack initiation in PFC simulations) the threshold for unstable propagation of near-boundary cracks drops, in uniaxial compression, to approximately 95 MPa or slightly more than half of the unconfined compressive strength of the PFC UCS samples and (perhaps coincidentally) equal to the threshold stress for onset of systematic crack accumulation.

This relative reduction in threshold stress for near-boundary damage is consistent with field observations (Chapter 5). An example of spall damage is shown in Figure 8.75 from the Underground Research Laboratory (URL-AECL). These slabs, which have a separation equal to the grain size, were observed to begin forming when the excavation boundary stress (calculated from elastic models) reached 100 to 120 MPa, or approximately one half of the UCS for the intact rock. The layering represents crack response (increased extension) to the progressive migration of the free ($\sigma_3=0$) surface into the rockmass during the damage process.

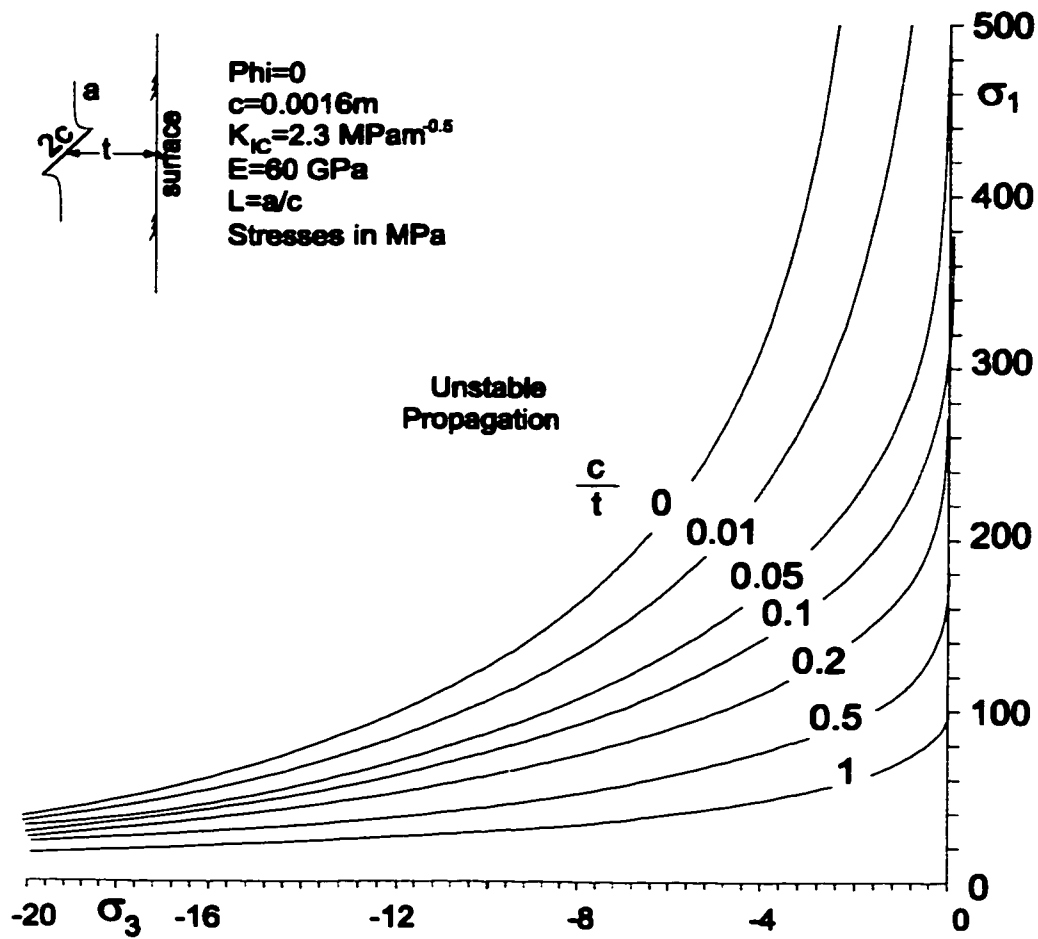


Figure 8.74: Limits of stable propagation for a single crack near a free surface.

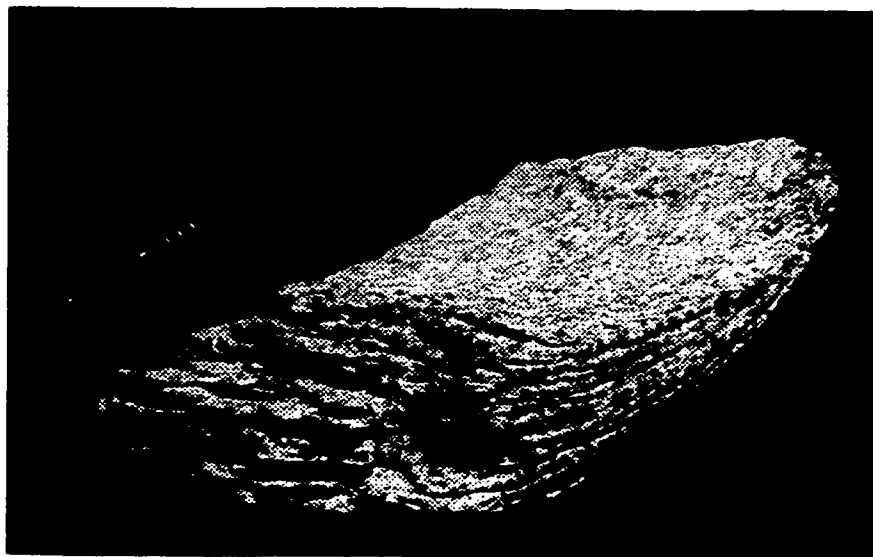


Figure 8.75: Grain scale spall damage from tunnel boundary (courtesy of AECL Ltd.).

The foregoing discussion explains the appearance of spall damage at lower than expected stress levels in underground excavations. It does not, however, explain why this phenomenon is not a factor in laboratory testing. One possible answer to this problem lies in the geometry and boundary stress conditions found in laboratory (cylindrical) samples.

Figure 8.76 shows a schematic comparison between an excavation sidewall and a cylindrical laboratory sample. In the first case, a boundary-parallel crack propagates from an initiating flaw near the free surface. For small strains the flaw displaces and the wing cracks propagate, aided by the enhanced stress intensity component (Equation 8.45) resulting from "beam" deflection. The deflecting surface skin offers little feedback resistance.

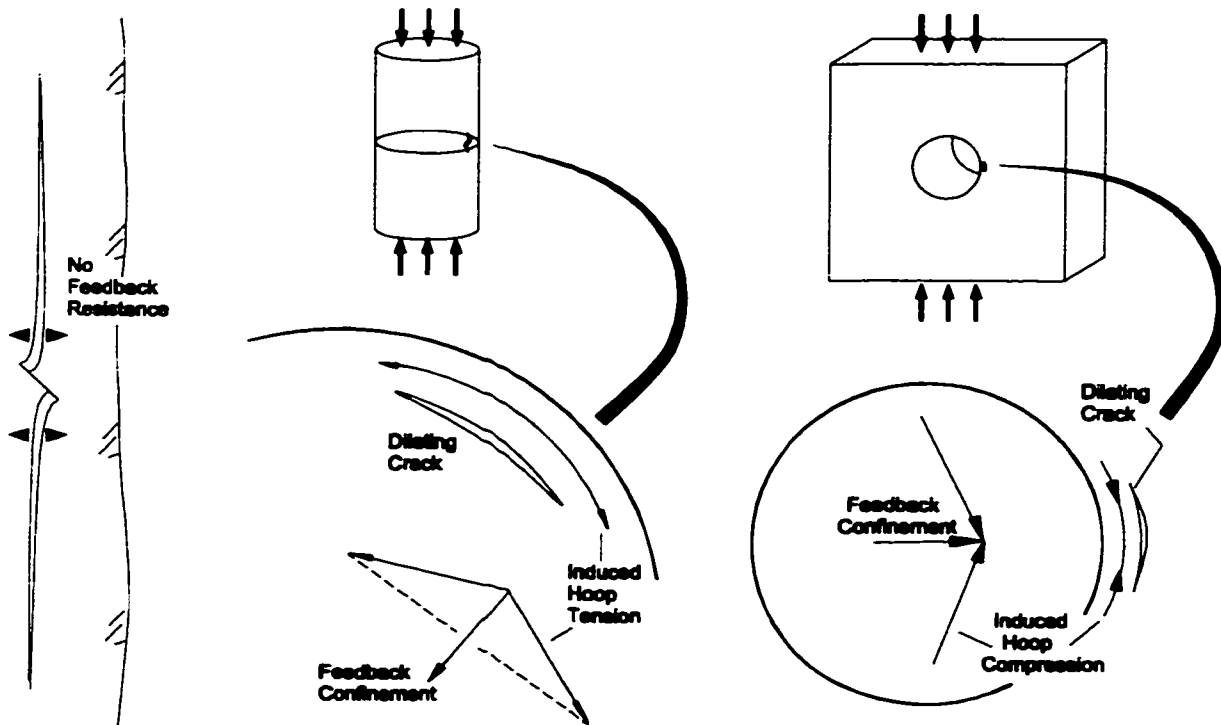


Figure 8.76: Comparison of boundary conditions for dilating cracks insitu and in lab samples.

Consider now the cylindrical sample with a dilating crack parallel to the circumference. Dilational strains from a propagating crack will be partially compensated for by an increase in hoop tension in the outer annulus. This in turn applies an increase in confining stress which suppresses further unstable propagation. It is unlikely that cracks will propagate axially (inhibiting the destabilizing contribution of Equation 8.45) if circumferential propagation is suppressed. Once crack interaction takes place (in three dimensions), the continuity of the outer annulus will be disrupted by radial cracks allowing circumferential cracks to propagate without feedback resistance.

Also illustrated in Figure 8.76 is the generation of feedback confinement through hoop compression near small bored holes or in small borehole compression tests. As the crack dilates it displaces into the borehole, compressing the inner annulus of rock. This compression, which cannot develop for flatter wall curvatures, in turn, resolves to a confining pressure suppressing further growth. Unlike the core example, the inner annulus does not ultimately rupture in tension. It must eventually buckle or shear, and does so at a higher stress. Therefore, the effect of scale and reducing borehole diameter on spall strength is therefore greater than a for comparable change in drill core diameter (as in Figure 8.1b). The effect of scale on borehole tests is shown in Figure 8.77.

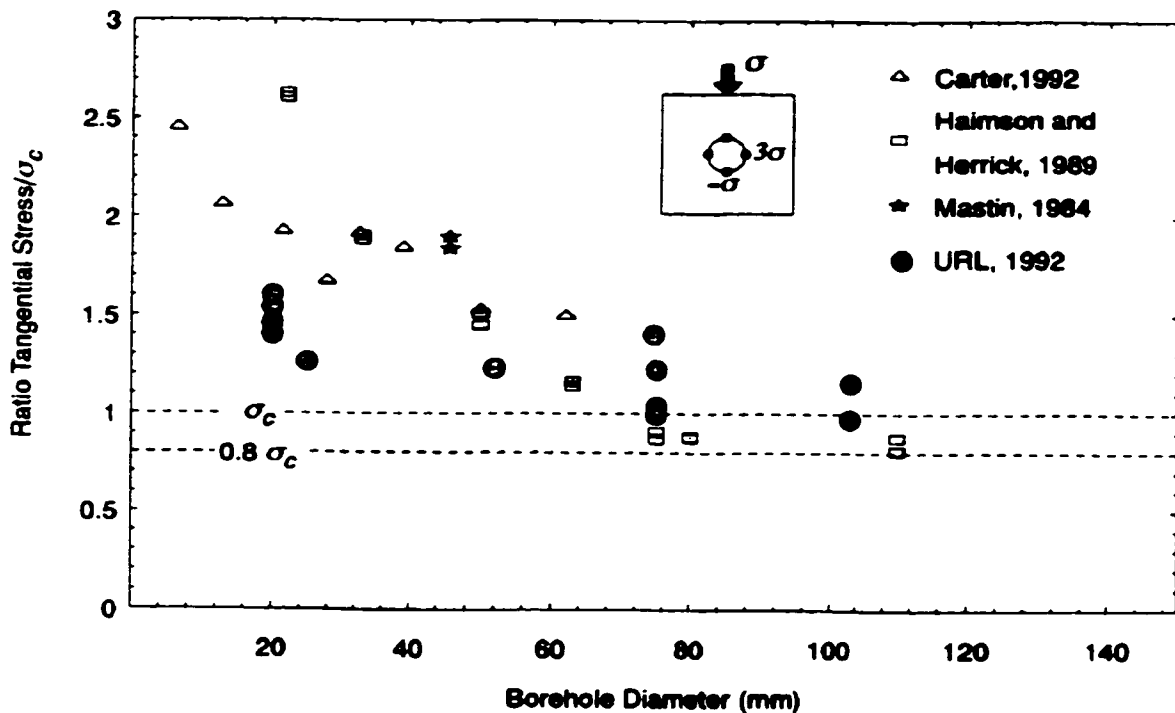


Figure 8.77: Effect of borehole diameter on sidewall failure stress (Martin 1994).

8.6.5 Stress Gradients and Crack Extension

Unstable crack extension is very sensitive to the distance to a free surface. In addition, real underground openings have stress gradients in the radial direction, which limit the extent of crack initiation and propagation. For example, the radial and circumferential stresses around a circular opening in a vertically dominant compressive stress field are given by:

$$\sigma_{\theta\theta} = \frac{p}{2} \left[(1+k) \left(1 + \frac{a^2}{r^2} \right) + (1-k) \left(1 + 3 \frac{a^4}{r^4} \right) \cos 2\theta \right] \quad [8.47]$$

$$\sigma_{rr} = \frac{p}{2} \left[(1+k) \left(1 - \frac{a^2}{r^2} \right) - (1-k) \left(1 - 4 \frac{a^2}{r^2} + 3 \frac{a^4}{r^4} \right) \cos 2\theta \right] \quad [8.48]$$

where p is the vertical stress, k is the horizontal stress ratio, θ is the angle from the horizontal, a is the tunnel radius and r is the radial distance from the tunnel centre. The maximum compressive stress concentration is in the sidewall ($\theta=0$) for $k \leq 1$. The principal stresses so obtained can be substituted into the sum of Equations 8.40 and 8.45 to calculate the induced stress intensity factor for wing cracks initiated by a critical sliding flaw at any distance from the opening. Setting the composite K_I term to K_{IC} , it is possible to iteratively solve for L , the normalized crack extension as shown for three values of stress ratio k in Figure 8.78.

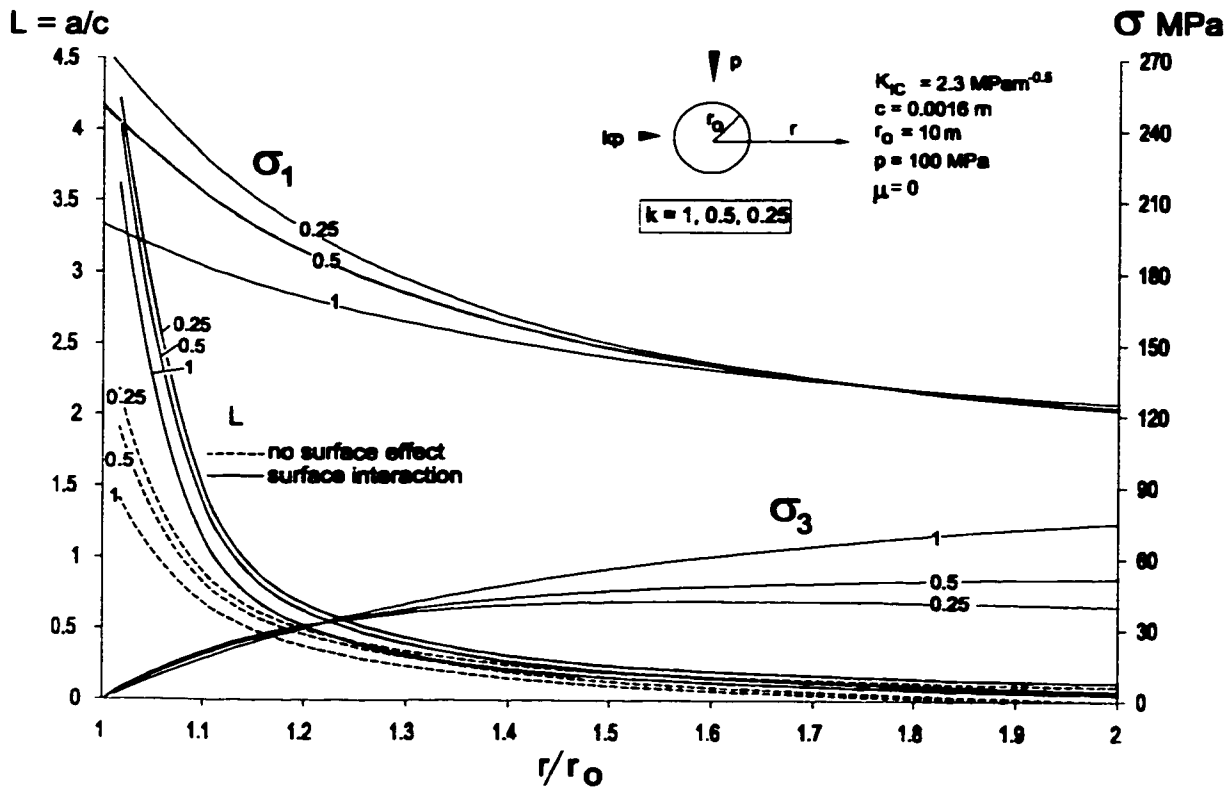


Figure 8.78: Effect of excavation stress gradients on spalling extent (crack propagation).

Whether or not surface interaction effects are taken into account, crack extension ($L > 1$) is effectively suppressed in these examples at a distance equal to 10 to 20% of the radius. While rock damage (crack initiation) can occur well into the rockmass, practically significant spalling or macrocrack formation must be a progressive process requiring surface slab removal or outward displacement (i.e. to form new free surfaces to continue the spalling process).

8.7 VARIABLE CONFINEMENT AND LOCAL TENSION

The results of most fracture mechanics analyses on grain scale cracks and flaws will indicate an abrupt change in stability conditions once tensile stresses are encountered. In previous sections, it was demonstrated that for a sliding flaw, tension of some magnitude is required to generate unstable propagation for initially small cracks. Zero confinement conditions can also be sufficient for the unstable propagation of cracks near a free surface, given the application of sufficient deviatoric or compressive stress. Yet spalling and continuous boundary-parallel fractures, manifestations of unstable crack growth, are observed to occur where calculated continuum stresses suggest confined conditions ($\sigma_3 \geq 0$).

The influence of pre-existing damage has been explored as a strength reduction mechanism and as a means of confinement shadowing (creation of effectively uniaxial conditions where confined compression is predicted by elastic continuum models). The role of material heterogeneity in generating locally tensile conditions under confined compressive loading is examined in this section. The contribution of geometry and non-uniform yield is also discussed briefly.

8.7.1 Heterogeneity and Local Tension

For compressive test simulations (PFC) at low to moderate confining stresses, more than 99% of the bond ruptures (cracks) are tensile in nature. This is the result of the trellis cell mechanism discussed in Chapter 7. This mechanistic analogue is an alternative to the sliding flaw model used in fracture mechanics. The trellis bond rupture is restricted in propagation to one contact length. The loss of the element can lead to overstress in neighbouring cells but the crack itself is not self-propagating. In the fracture model, the wing cracks emanating from the initiating flaw can, with the appropriate boundary conditions, propagate indefinitely. In particular the presence of tensile stress creates unstable crack propagation after initiation.

For the sliding crack model, the stress intensity factor at the ends of the wing cracks reduces as the crack grows, requiring an input of additional external stress for incremental (stable) propagation. At a certain point this intensity factor reaches a minimum with respect to crack length. Beyond this point additional length results in an increase in stress intensity which in turn promotes further extension. This minimum is referred to as the unstable propagation limit as in Figure 8.68.

A series of PFC simulations were performed (using the standard parameter set from Chapter 7) to identify local zones of tension which arise (under mean compressive confinement) due to stiffness heterogeneity. A grid of measurement circles as shown in Figure 8.79 was used to contour and analyze the variation in stress within the uniformly loaded sample.

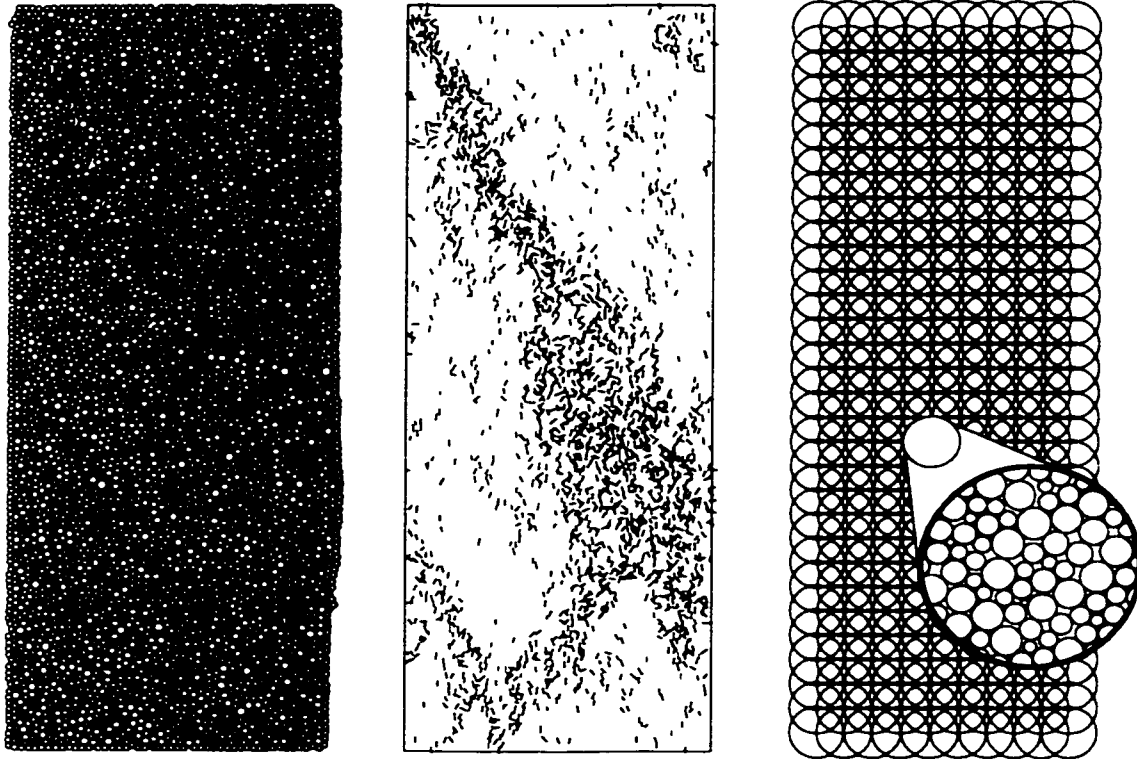


Figure 8.79: PFC test sample (left) for this study (0.15mx0.4m, 7200 discs); crack array after sample failure (middle) and sampling array (right) for local stress contouring. Inset: spatial coverage of stress sampling circle.

From the example calculations in Figure 8.68, it is evident that a crack propagation length of 5 to 10 times the length of the initial flaw is coincident with unstable propagation for the range of compressive stresses involved here. The measurement circles are approximately 8 times the mean particle diameter (and crack length), as shown in Figure 8.79. This ensures a representative sample measurement for the identification of unstable propagation conditions (i.e. tensile stress).

In Figures 8.80 to 8.82, the minimum principal stress distribution is contoured, at different axial compression levels, for samples with increasing mean applied confining stress. As expected, the spatial coverage of tensile zones increases with deviatoric stress and decreases with increasing confinement.

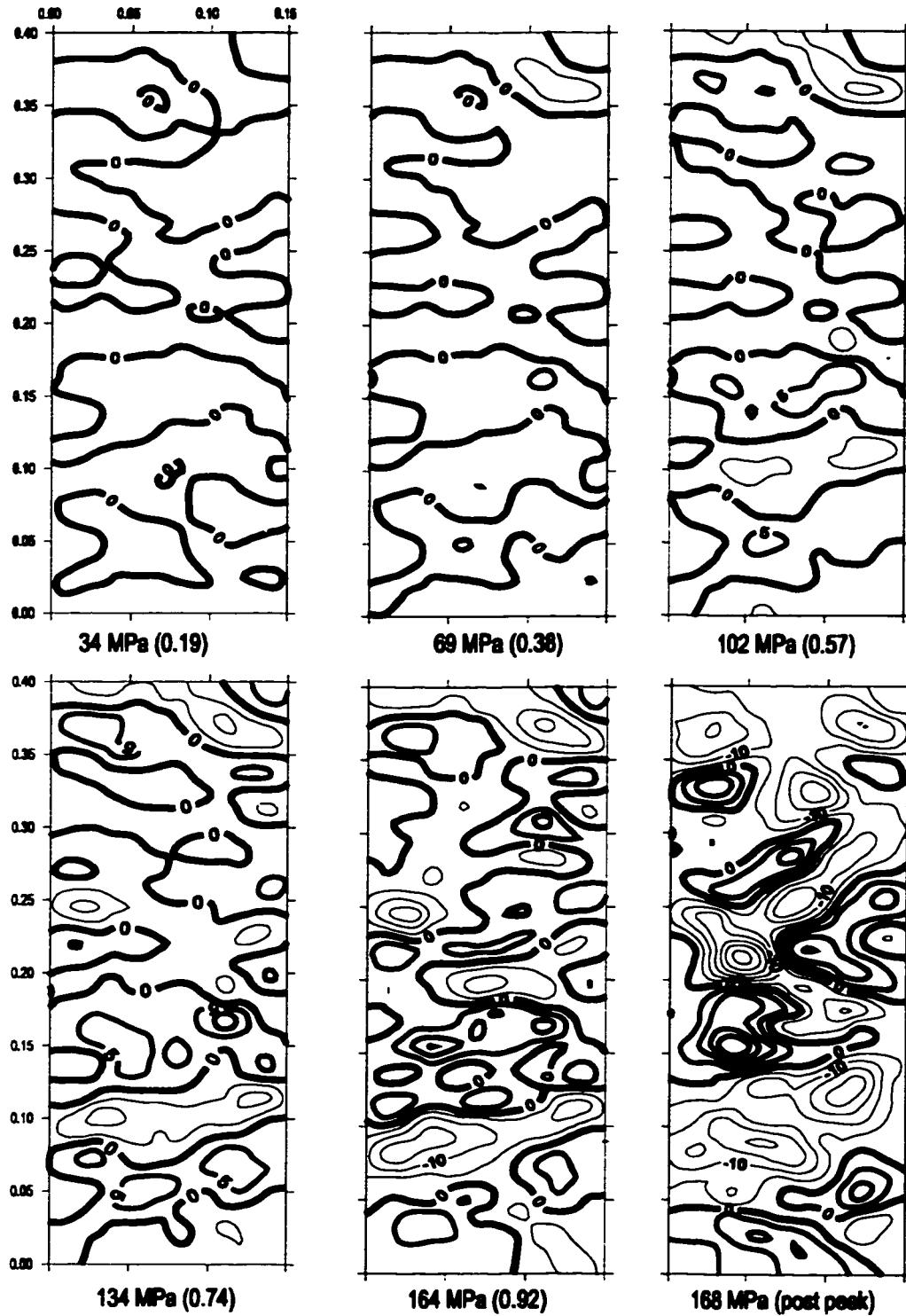


Figure 8.80: Internal distribution of minor principal stress for uniaxial compression sample (Contour interval = 5MPa, thick lines indicate tension, internal contour labels are tension positive convention). Stress levels under each sample are the applied axial stress (bracketed values are ratio of peak strength = 180MPa).

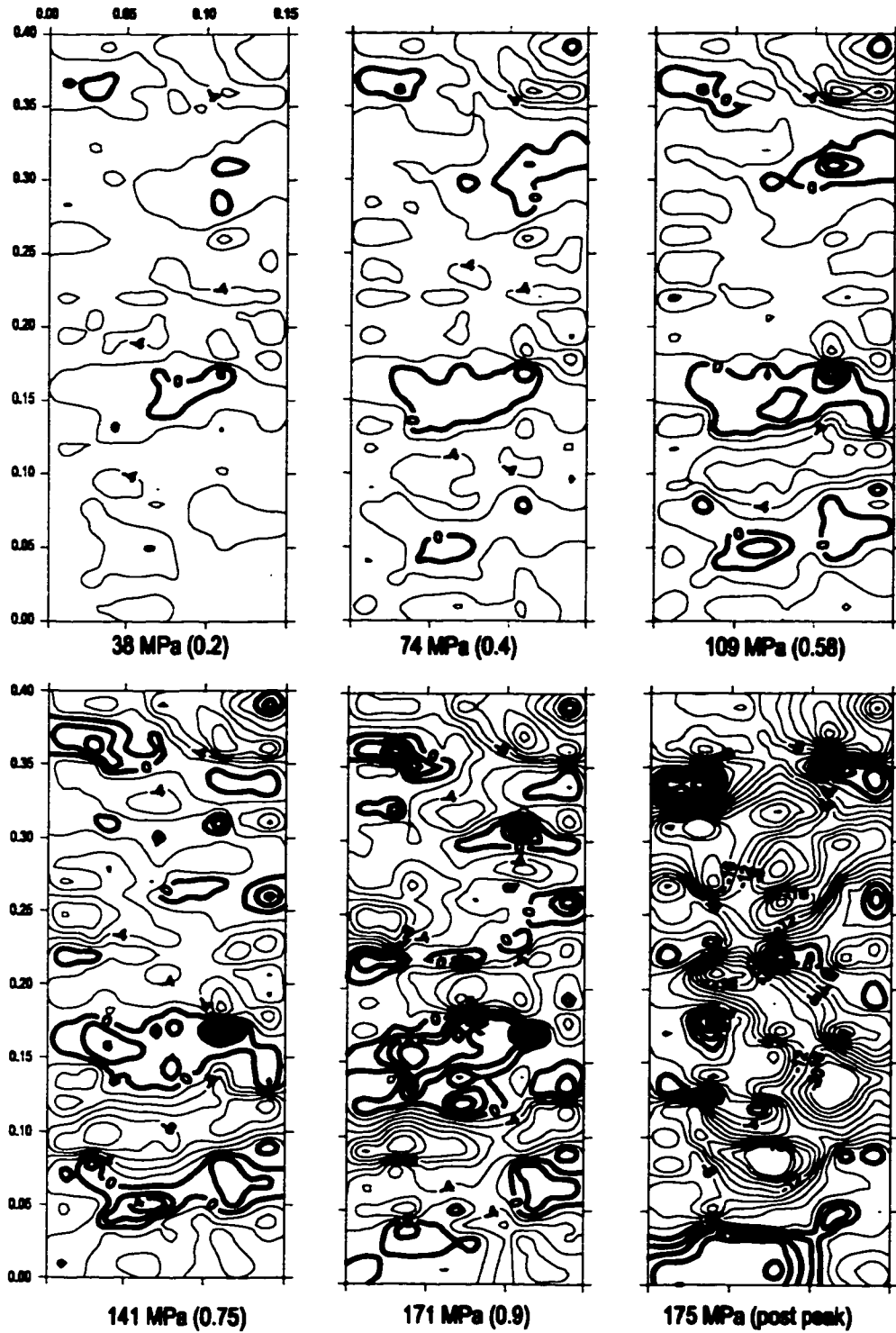


Figure 8.81: Distribution of minor principal stress for compression at 2.5 MPa of applied lateral confinement (Interval = 5MPa, thick lines = tension, internal contour labels are tension positive convention). Stress levels under each sample are the applied axial stress (bracketed values are ratios of peak strength = 189 MPa).

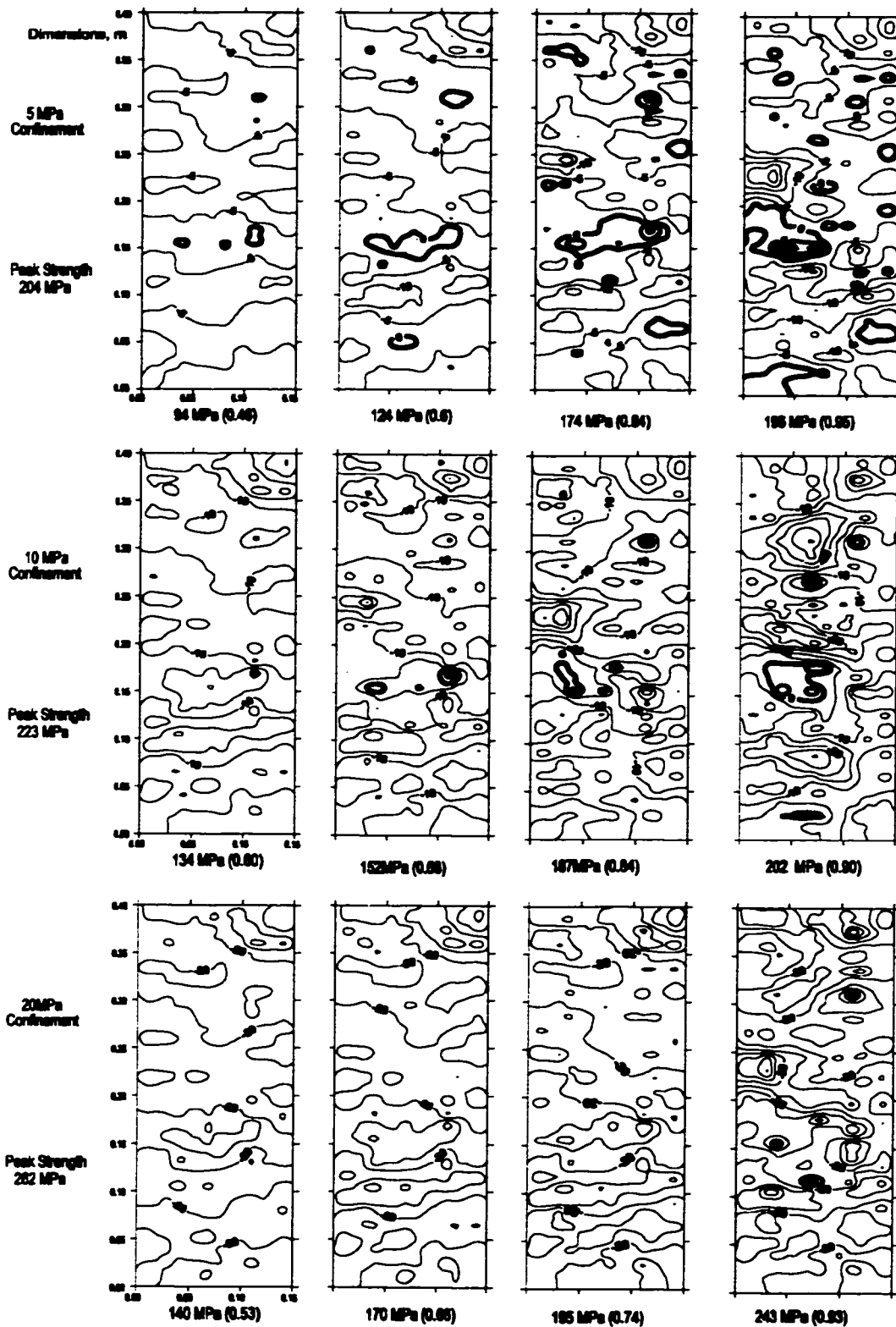


Figure 8.82: Samples tested at increasing confinements using contour properties from Figures 8.80 and 8.81.

Samples with mean confinement greater than 20 MPa showed negligible tensile coverage prior to peak strength. In order to get a more useful quantification of the extent of these zones, each stress state (i.e. each measurement circle result) can be plotted with respect to principal stresses (or horizontal and vertical normal stresses). This has been done for two levels of axial loading and for two levels of confinement in the examples in Figure 8.83. In this Figure each data point represents one measurement circle which itself represents approximately one percent of the sample area with a 200% over-coverage due to overlap (300 sample circles).

The threshold for systematic crack initiation or systematic damage accumulation along with representative Hoek Brown and Mohr-Coulomb envelopes for peak strength are shown for comparison to mean stresses. The ellipses represent one, two and three standard deviations (1σ , 2σ , 3σ), for a bi-variate normal distribution and therefore enclose approximately 68.3%, 95.5% and 99.7% of the global population respectively. The cross hairs represent the principal orientation of the ellipses which are centered on the mean stress state. Of interest in this study is the proportion of the population which lies in the tensile region and within the zone of unstable crack propagation. While cracks do not extend in this way in PFC simulations, this is a test for appropriate conditions in a real bonded solid.

The stress path in these simulations involves hydrostatic confinement followed monotonic axial compression (application of deviatoric stress). The simulations are interrupted at numerous loading stages so that the internal stresses can be sampled. The variability limits (ellipses) can be plotted together for a complete test as shown in Figure 8.84a. The leftmost (most tensile) extent of each of the variability limits (1σ , 2σ , 3σ) are traced through the test as shown. For comparison, the same analysis is performed using only those sampling circles containing current cracks (within an timestep interval centered on the specified stage) as shown in Figure 8.84b. After crack initiation and some accumulation, the variability limits are similar to those for the complete sample. there is no apparent preference, with respect to local stress state, for crack initiation. The connected variability limit traces for the complete sample (Figure 8.84a) are used henceforth for convenience.

By inspection, the percentages of the total population of stress points, falling to the left of the limit traces for 1σ , 2σ and 3σ are approximately (i.e. nominally for the purposes of this study) 0.1%, 1% and 10% respectively. These three limit traces are plotted for different mean confining stresses in Figure 8.85.

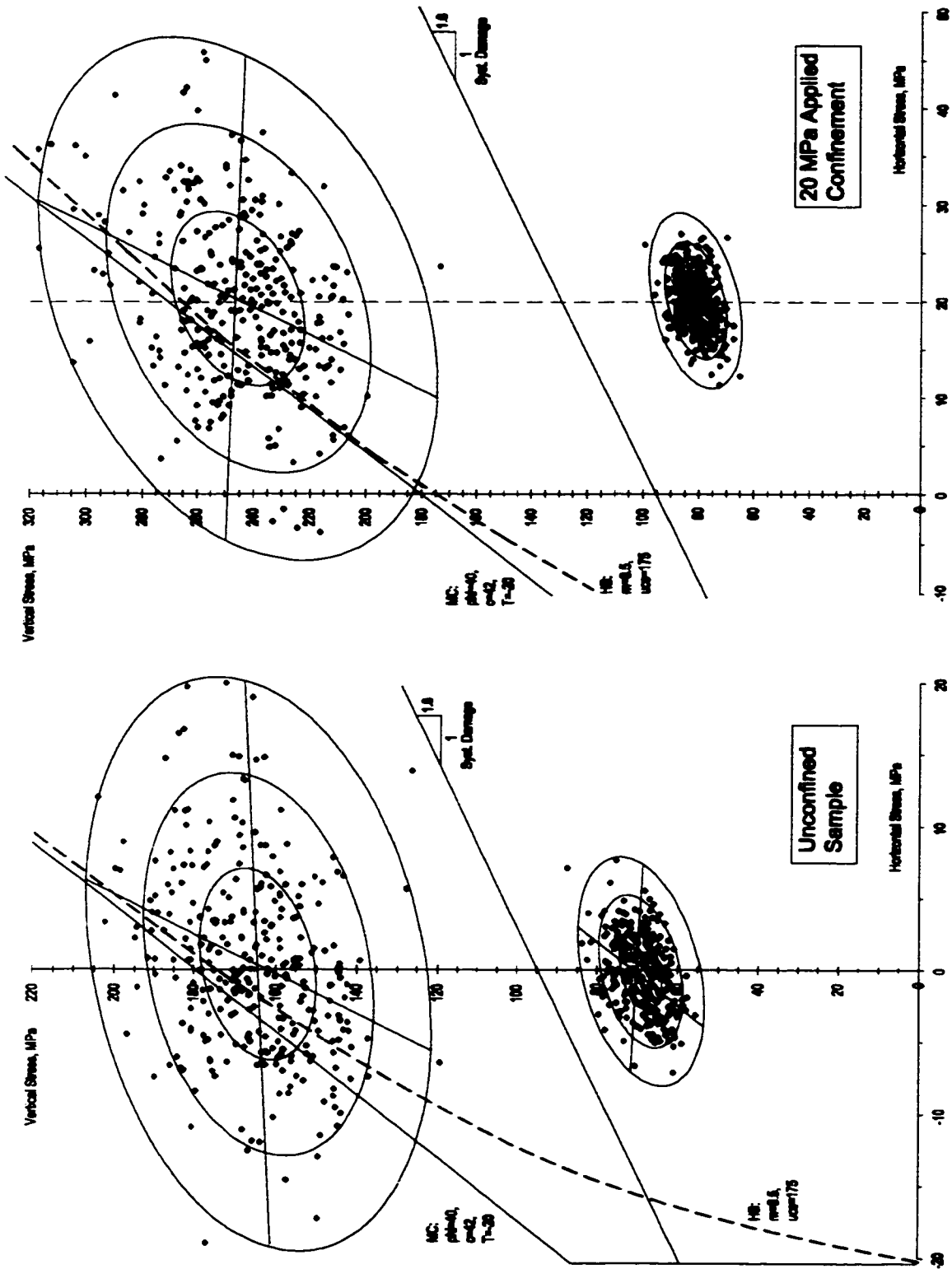


Figure 8.83: Distribution of sampled local stress states in a) uniaxial compression and b) compression at 20MPa confinement. Ellipses represent 1, 2, and 3 standard deviations for a bivariate normal distribution.

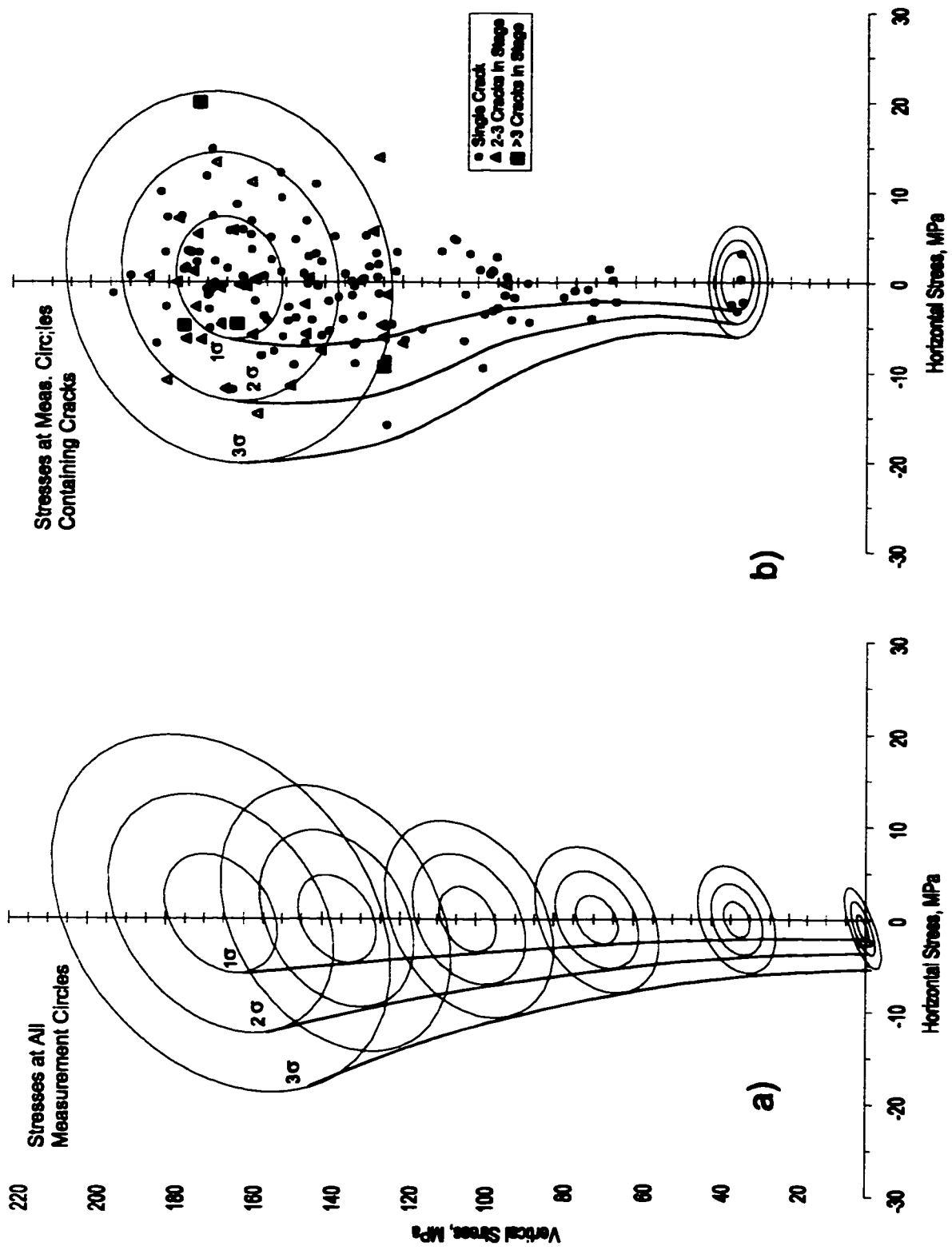


Figure 8.84: a) Connected variability limit traces for low confinement in a uniaxial compression test; b) limits from population of measurement circles containing cracks.

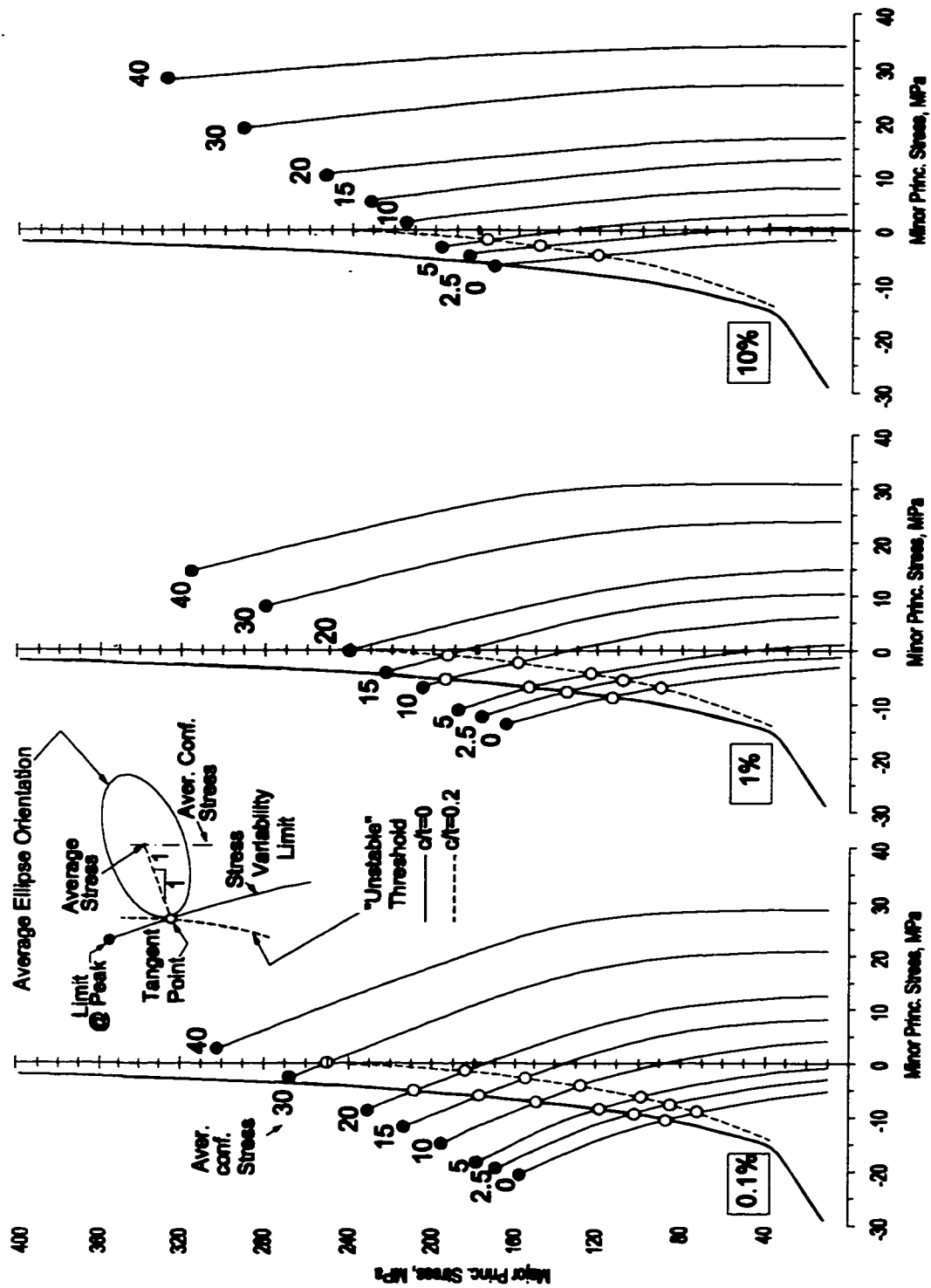


Figure 8.85: Confinement variability limit traces for different applied (average) confining stresses and different limit assumptions. Plots from left to right correspond to nominal limits of spatial distribution of 0.1%, 1% and 10% (relative area covered by limit condition). Solid and dashed thresholds are unstable propagation limits for an isolated crack and a near-surface crack respectively.

Superimposed on the variability limit traces in Figure 8.85 are unstable crack propagation limits for an isolated crack and a near-surface crack ($c/t=0.2$) based on Figures 8.68 and 8.74 respectively. These limits are based on the sliding crack analogue and are used here for illustrative purposes only. They represent the limits of unstable propagation for any initiating crack (such propagation is not directly permitted in PFC simulations). The crack thresholds and the variability limits (0.1%, 1% and 10%) are somewhat arbitrary and are used here for conceptual demonstration purposes.

While the solid circles in Figure 8.85 represent the variability limits at peak strength, the open circles mark intersections between these limits and the crack instability envelopes. As such they represent premature yield due to localized spalling and enhanced crack interaction potential due to crack propagation (as in Section 8.6.1). The resultant reduction in observed strength at lower confinements is illustrated for isolated cracking and near-surface cracking, in Figures 8.86 and 8.87 respectively.

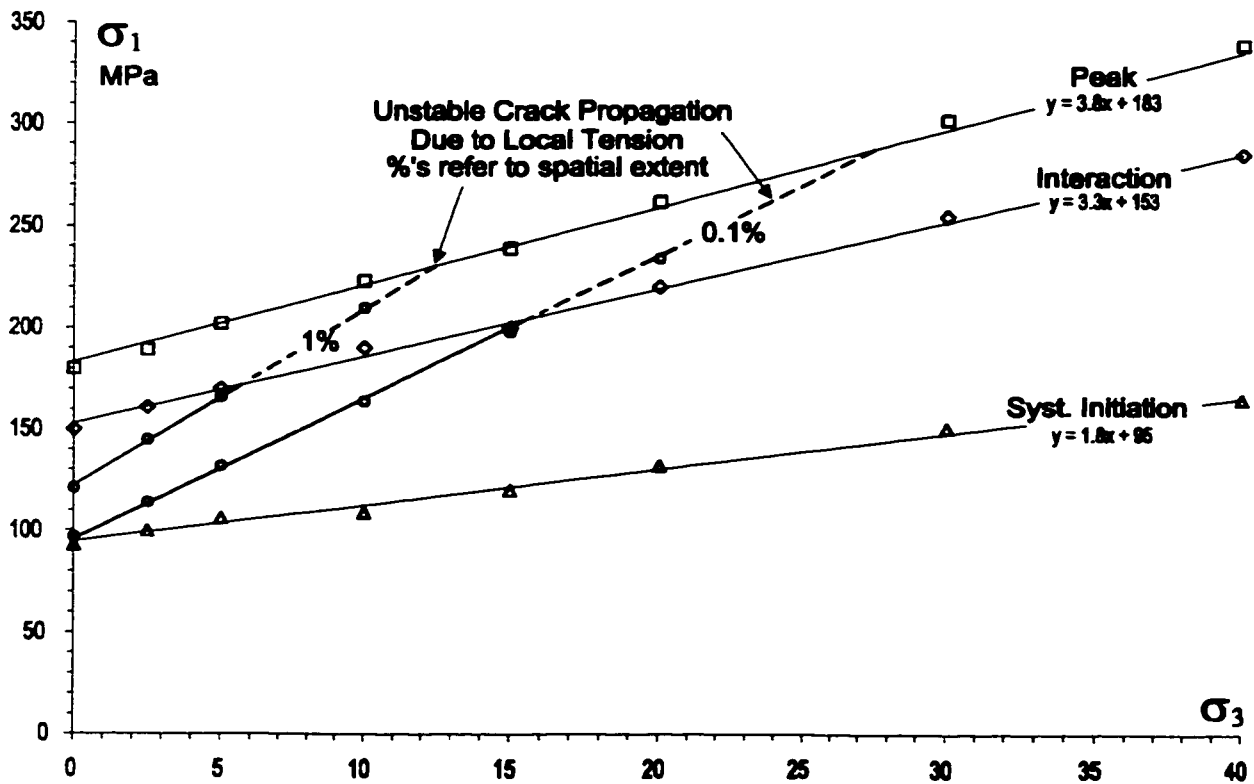


Figure 8.86: Strength reduction due to local tensile zones and isolated crack propagation.

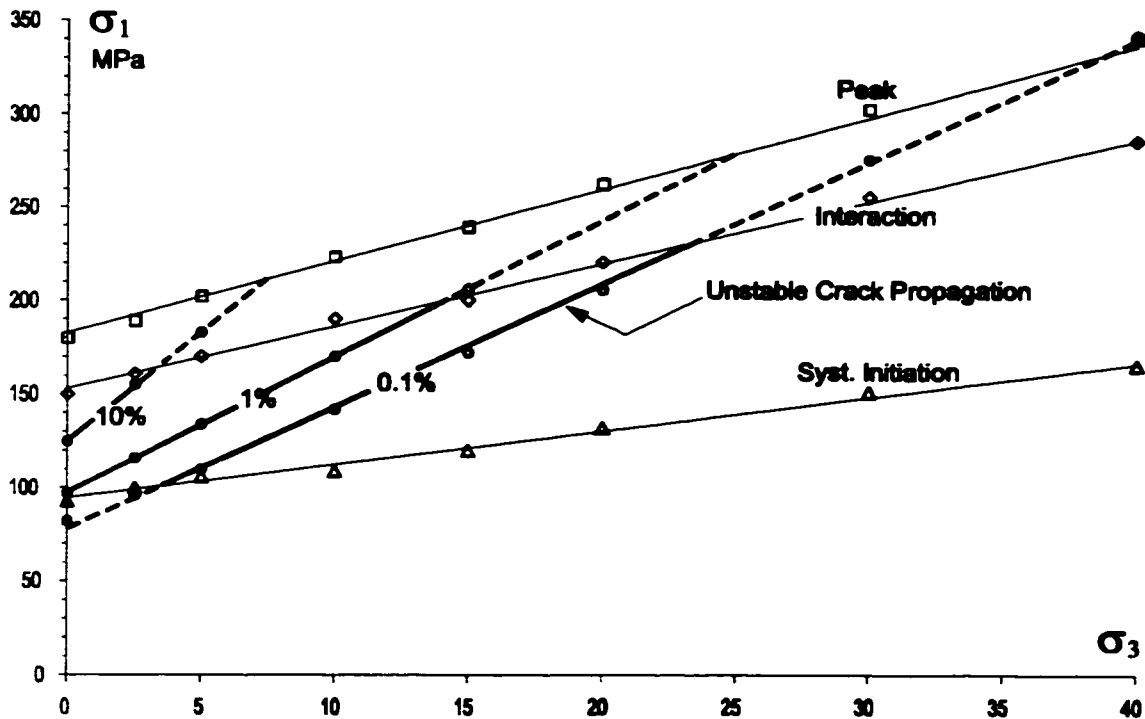


Figure 8.87: Strength reduction due to local tensile zones and near-surface crack propagation.

The 0.1% limit represents a convenient and reasonable lower bound for strength (crack propagation and yield perhaps detectable using acoustic emissions) while the 1% limit could represent reasonable limits of visual detection in the field. Certainly a 10% spatial involvement in unstable crack propagation would represent definitive and significant yield.

It would be reasonable, if the simulation material were real rock, to expect a 20 to 25% reduction, in the detectable yield threshold due to internal crack extension and surface spalling, due only to the effects of internal stiffness heterogeneity and stress flow tortuosity. Combined with the effects of pre-existing damage and inherent scale effects (Section 8.3) it is reasonable to expect the near-surface yield strength, even of massive unjointed rock, could fall to the limit of systematic crack initiation for low confinement conditions. The effects of pre-existing damage and internal stress heterogeneity are subdued by higher confining stresses.

The previous discussion utilized crack instability limits at finite tensile stresses for low applied deviatoric stress. For long term stability, it is necessary to consider the presence of any local tension. If tension is present, then cracks may be open, allowing environmental weakening and stress corrosion to take place (Diederichs 1987). Figure 8.88 illustrates the mean applied stress states required to reduce the spatial coverage of local tensile stress to the limits shown.

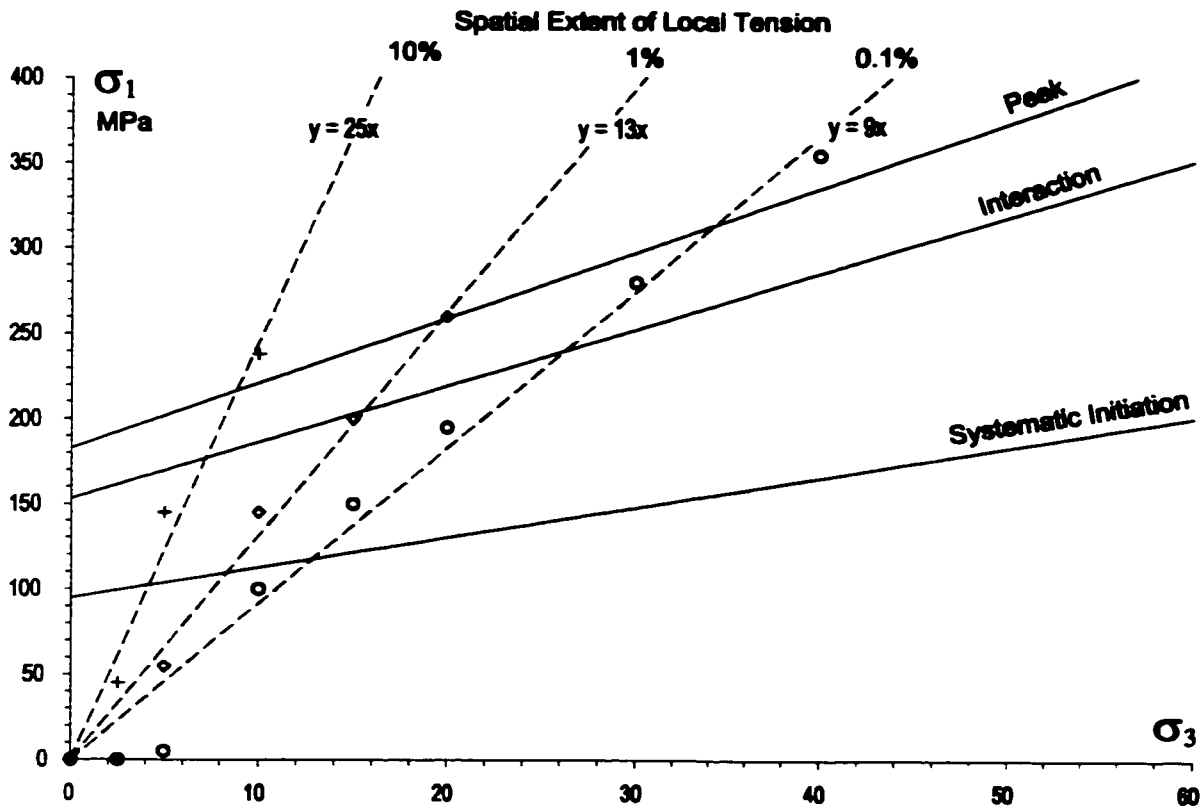


Figure 8.88: Loci of required applied stress to minimize local tension within the sample (i.e. restrict the spatial coverage (2D) to the limits (0.1%, 1% and 10%) shown).

8.7.2 Geometric Sources Of Local Tension

Tensile rupture, or more importantly compression induced spalling, aided by boundary-normal tension can occur due to small fluctuations in excavation geometry. Unless these "as-built" conditions are accurately modeled, their effects will not be predicted. In particular re-entrant geometries are susceptible to the destabilizing effects of tensile or negative confinement.

One example is illustrated using a simple elastic boundary element model (Examine^{2D}) in Figure 8.89. Here, a rectangular opening is constructed in a highly deviatoric insitu stress field. Stress flow around a perfectly orthogonal excavation is represented by the contours around the floor of the tunnel. The roof, however, has a re-entrant nature (an apparent sag). This commonly occurs due to blast hole deviation and is the result of difficulties in setting up for drilling in a corner. Often the corner holes rise up at an angle and create this effect upon excavation.

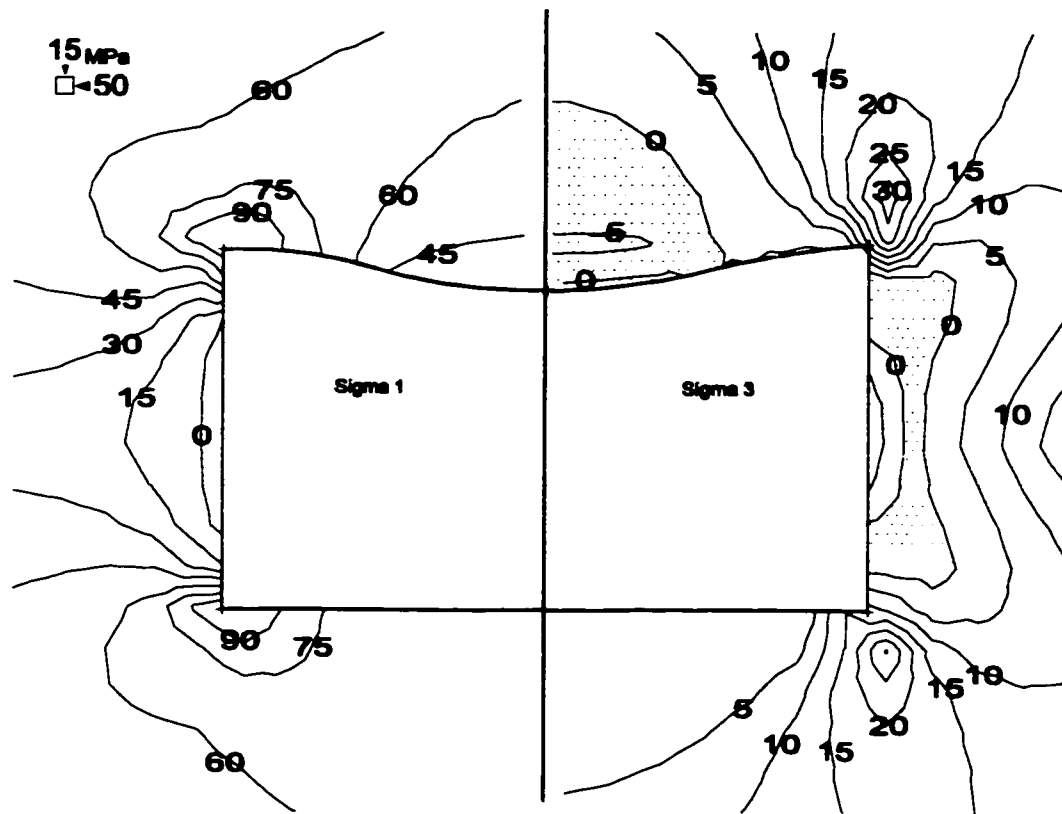


Figure 8.89: Stress flow around an excavation with re-entrant roof geometry.

The effect of this minor as-built geometric anomaly is obvious. A large dome of tension is created above the roof (excavation back). This in itself may be sufficient to generate spalling or slabbing. If the compressive stresses parallel to the back are high enough (near or above the crack initiation threshold) then such damage may be generated well into the back, creating an arch of intact rock and causing a groundfall. Such geometry induced slabbing may occur upon excavation or may be delayed requiring extreme caution and multiple rounds of scaling (manual removal of fractured material using an extended pry bar) prior to primary support installation.

Small areas of curved excavation boundaries or corners of rectangular openings may be subjected to concentrated compressive stress resulting in shearing or local crushing. Alternatively joint bounded wedges may be squeezed out or may simply fall from the sides of stressed boundaries. The removal of this material by gravity or through scaling or support installation activities creates a local change in the boundary geometry and in the associated stress flow. In the illustrative elastic model in Figure 8.90, a small (8 degree) notch is created in a circular boundary (stresses similar to the URL "mine-by" experiment recorded by Martin (1994) and described in Chapter 5). This notch

schematically represents the initial process zone or the start of shear (crushing) failure as stresses are increased by tunnel advance. If this yielded material is allowed to fall out, the effect on stress flow is seen in Figure 8.90. While the undamaged tunnel roof induces a smooth deviatoric and confining stress gradient, the presence of the notch results in increased values for both principal stresses above the notch and, more importantly, the generation of tension to either side of the notch. The geometry flanking the notch is reminiscent of the Brazilian Test configuration with the same result. Under the combined influence of geometry-induced tension and increased compression, these flanking areas will split, creating the secondary spall damage and triangular failure geometry observed by Martin (1994).

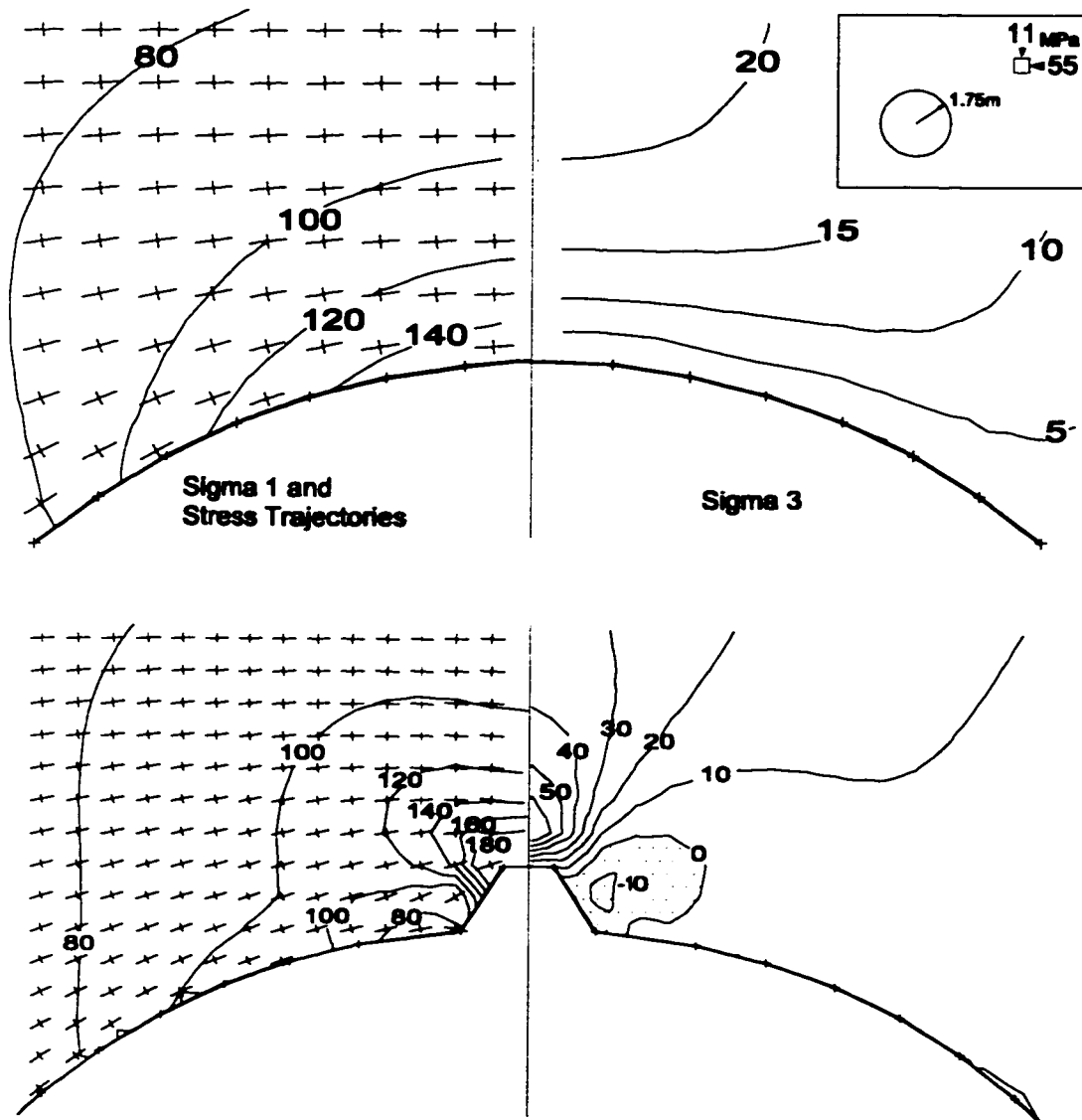


Figure 8.90: Effect of a notch on boundary stresses around a circular opening.

8.8 PRIMARY SHEAR FAILURE AND LOCAL TENSION

It has been demonstrated that the accumulation and ultimate interaction of short "stable" extension cracks results in a composite kink rotation or macroscopic shear zone responsible for typical "shear" or crushing failure of hard rock under compressive loading. The smooth continuous boundary-parallel failure surfaces associated with spall damage are the result of unstable Mode I extension of cracks beyond the grain scale. This extension requires, in most cases, at least a minute amount of normal tensile stress even at moderately high levels of crack parallel compression. In conditions of nominally compressive average confinement, this tension can result from internal stress flow tortuosity or from locally re-entrant boundary geometries as shown in Section 8.7. Of equal or greater significance is the effect of propagating local shearing on the surrounding near-boundary rockmass stresses.

8.8.1 The Effect of Notch Propagation - Circular Tunnel

In this section a non-linear (plasticity) finite-element model (Phase²) is used to demonstrate this effect in a schematic and non-rigorous fashion. For the first simulation, the F.E. mesh and boundary conditions (with initial internal stresses and body forces), as well as the Mohr-Coulomb yield criterion, are shown in Figure 8.91.

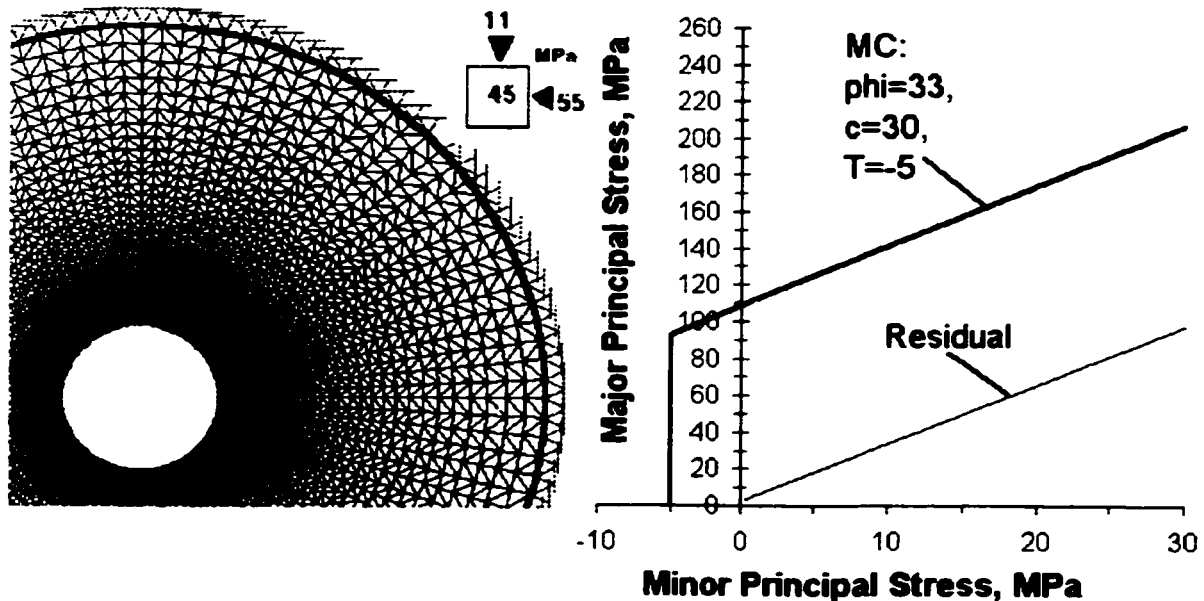


Figure 8.91: Finite element mesh and yield criterion for URL simulation.

The geometry and stress state are based on the URL mine-by experiment summarized in Chapter 6 and detailed by Martin (1994). The yield function is based on the crack interaction threshold for damaged Lac du Bonnet granite (Chapter 7). The slope of this function is less than that determined from peak strength or from volumetric reversal (critical damage in Martin 1994). Here, as discussed in Chapter 7, the "friction angle" represents the confinement dependency of critical interaction rather than the sliding friction of the rock itself. Normally, a higher residual angle should be used for "residual friction" (due to actual slip after rupture). This plasticity formulation does not permit residual friction higher than the peak and so the same value is used (without cohesion) to represent the strength of yielded rock. The tensile strength (T) is based on the test average of undamaged (≈ 7 MPa) and damaged (2 to 4 MPa) samples. Due to core discing effects the damaged lab samples yield unrepresentative low results as discussed in Chapter 6.

The stresses and yielded zones after failure has stabilized are shown in Figure 8.92 for the region of the tunnel roof. In reality a 0.5m high triangular notch developed above the roof spanning 70 degrees of the tunnel perimeter (Martin 1994). In this simulation the yield zone has propagated approximately 0.75m above the tunnel. Shear zone migration is arrested by the build-up of high confining stresses at the notch tip. In reality it may be arrested earlier by a higher yield strength beyond the zone of initial unloading and excavation damage. This is the zone delimited by comparing the elastic stresses to the crack initiation threshold as discussed in Chapter 6. Initial stress levels, prior to notch development, beyond that of crack initiation indicates the potential for damage which can reduce the ultimate yield strength (as shown earlier in this chapter).

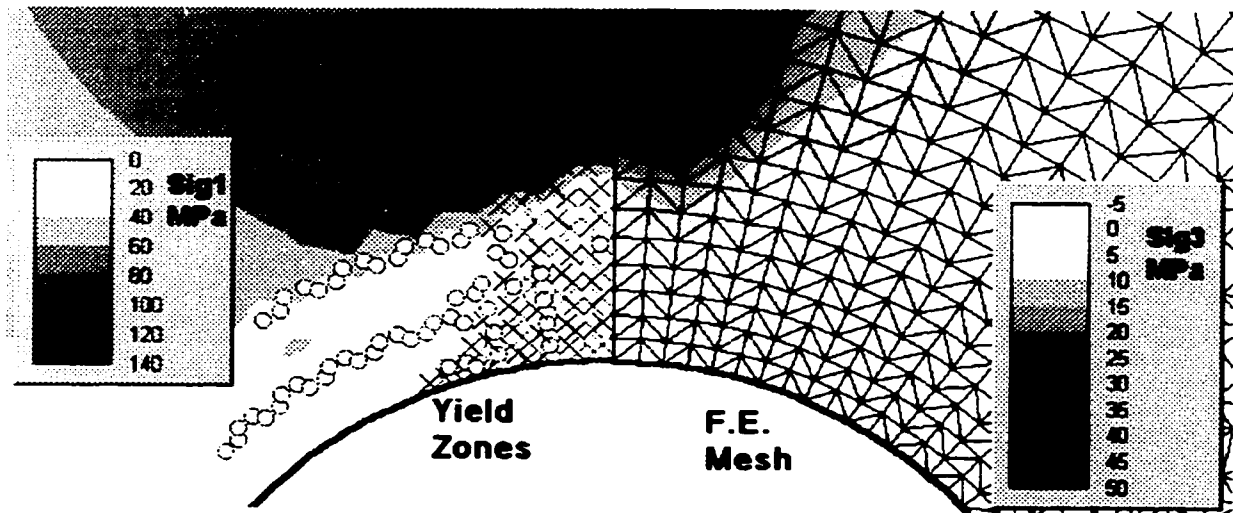


Figure 8.92: Post-failure stresses and yield zones above circular opening.

Also mechanically significant are the boundary-parallel slabs which have developed from secondary tensile rupture. The orientation and extent of this tensile propagation are influenced by the radial F.E. mesh. Nevertheless, it is clear that shear strain discontinuity at the boundary of the yielding (shearing) zone is responsible, through a tearing action, for Mode I propagation of highly continuous extension cracks and secondary spall or slabbing failure. This shear strain transition is represented by the abrupt increase in vertical displacement within the shearing zone in Figure 8.93.

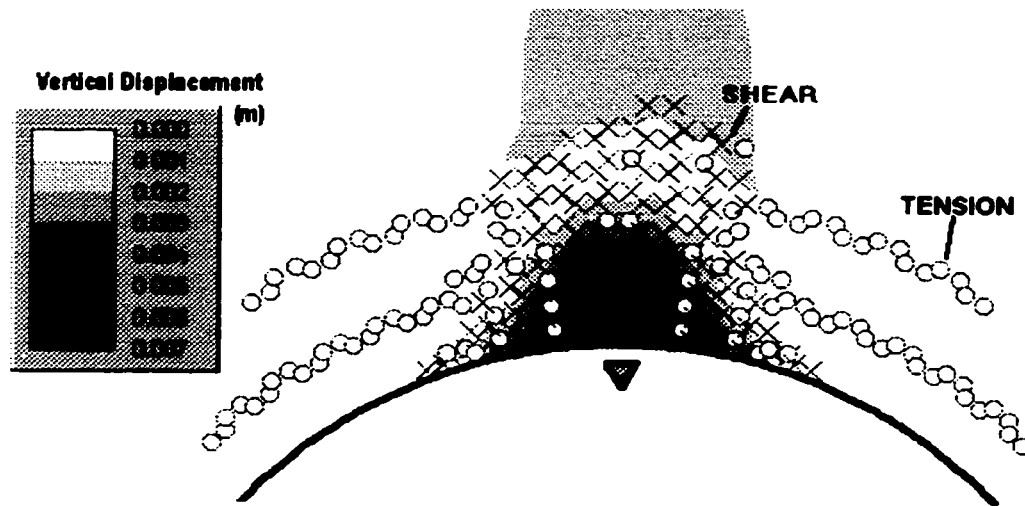


Figure 8.93: Yield zones and vertical displacement distribution above circular opening.

In this particular model, the tensile cut-off is reset to zero upon tensile rupture. The material can still carry full shear stress provided that no tension is present. This allows the slabs to develop as in Figure 8.93. Plasticity formulations, which reset both strength components to residual values upon yield via either mode, such as those based on the Hoek-Brown criterion, cannot simulate this effect.

The simulation in Figure 8.93 used a non-associative and non-dilatant flow rule (no volumetric expansion upon yield such that dilation angle $\psi=0$). In Figure 8.94, a 45 degree dilation angle, ψ , is used to simulate expansion during shear. The result is restricted propagation in the vertical direction but greatly exacerbated tensile boundary-parallel spalling at the flanks of the developing notch.

It is important to recognize this bimodal process when back-analyzing failures and calibrating strength models. These simulations also indicate the important roles that tensile strength and effective near-boundary confinement have on rockmass stability in highly stressed environments.

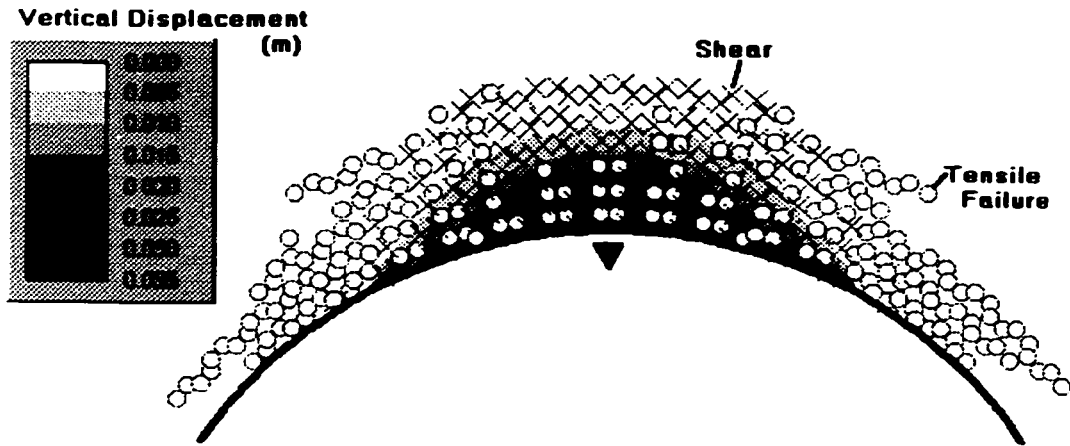


Figure 8.94: Yield zones and vertical displacement for dilatant flow rule.

The previous simulations, while illustrative, are highly influenced by the regular F.E. grid. For a valid comparison to reality, a randomized grid should be used wherever possible for plasticity problems. Such a grid is illustrated in Figure 8.95

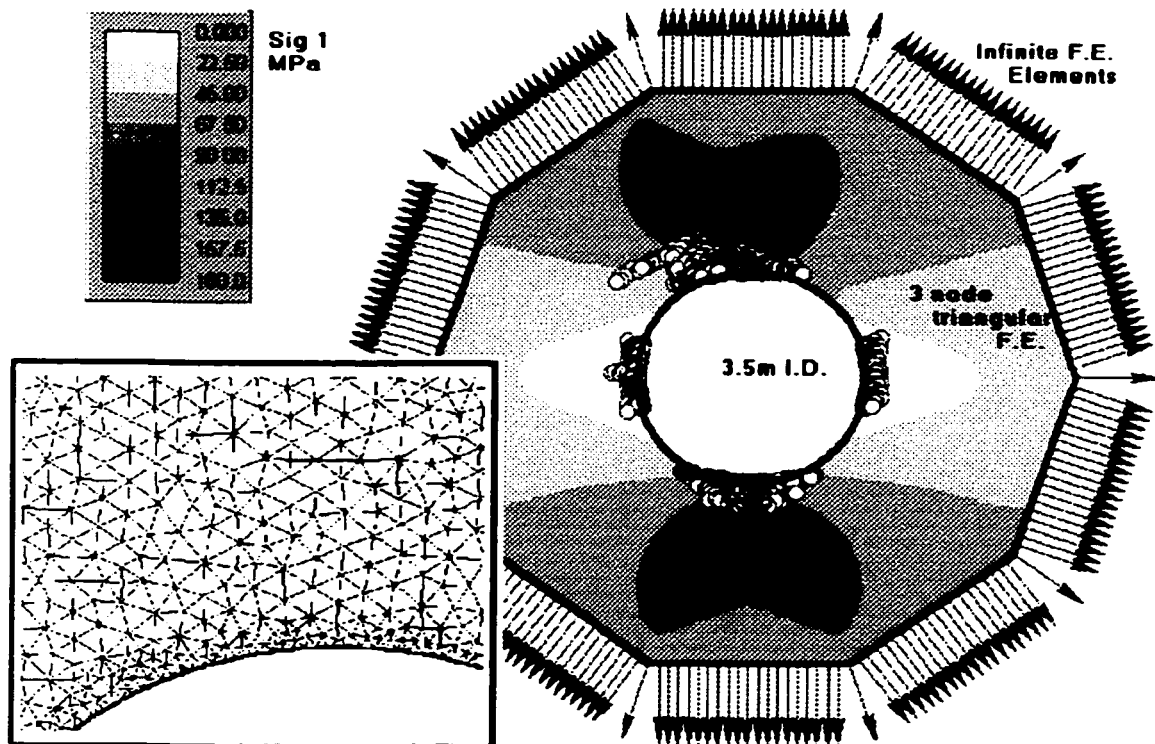


Figure 8.95: Boundary conditions, random mesh and post failure results for URL simulation.

In this simulation (Phase²) the fixed boundary nodes are replaced with infinite finite elements to simulate the far field and allow closer outer discretization boundaries. The mesh is discretized using Delaunay triangulation (Schroeder and Shepard 1988; Grabinsky and Curran 1993). The major principal stresses are plotted after yield has stabilized. In all of these simulations the geometry and the principal stresses are rotated to align with the coordinate axes.

Tensile cracking occurs at the sidewalls in the simulation. This is due to direct tension normal and parallel to the boundary as predicted by elastic stresses. Notches are visible in the roof and in the floor. In this model body forces are present (gravity acting downwards) and so the roof failure is more pronounced than the floor as is expected and observed (Martin et al. 1997).

A close-up of the modeled roof area is illustrated in Figure 8.96a). Notice that only a small portion of the overall yield zone has failed in shear (according to the 3D Mohr-Coulomb criterion). The shear or process zone initiates at a point on the boundary which is tangent to maximum far field compression as expected. As the notch progresses, tensile spalling occurs, which is, at first, symmetrical, and then asymmetrical about the shear notch. In addition to the final wedge-shaped failure zone notch (as outlined) defined by connected and yielded elements, a few continuous tensile cracks propagate off to the right and terminate within the rock.

The asymmetrical nature of failure development is confirmed by field observations in Figure 8.96b). In this case the location of the initial process zone seems to have relocated from the centre-line (with respect to field stresses) to the top of the first spall cusp ("Feb.21"). After that the failure progresses with the shear process zone to the right and the tensile spalling to the left. While the modeled failure zone rotates away from the centreline, the circumferential extent corresponds well to the observations while the radial extent is only slightly greater in the model. This simulation, as in the previous case utilizes the crack interaction threshold for laboratory samples of damaged Lac du Bonnet granite. It is likely that the actual failure zone is limited by the extent of this initial unloading and excavation induced damage and the associated near-boundary reduction in shear (crack interaction) strength.

The idea of a central process zone generating adjacent boundary-parallel slabs was suggested by Martin (1994) to explain the geometry of the notch at the URL (Figure 8.97). If these slabs are not released freely (e.g. by corner constraints) subsequent buckling of these slabs can result in violent ejection events (as discussed in detail by Aglawe 1999).

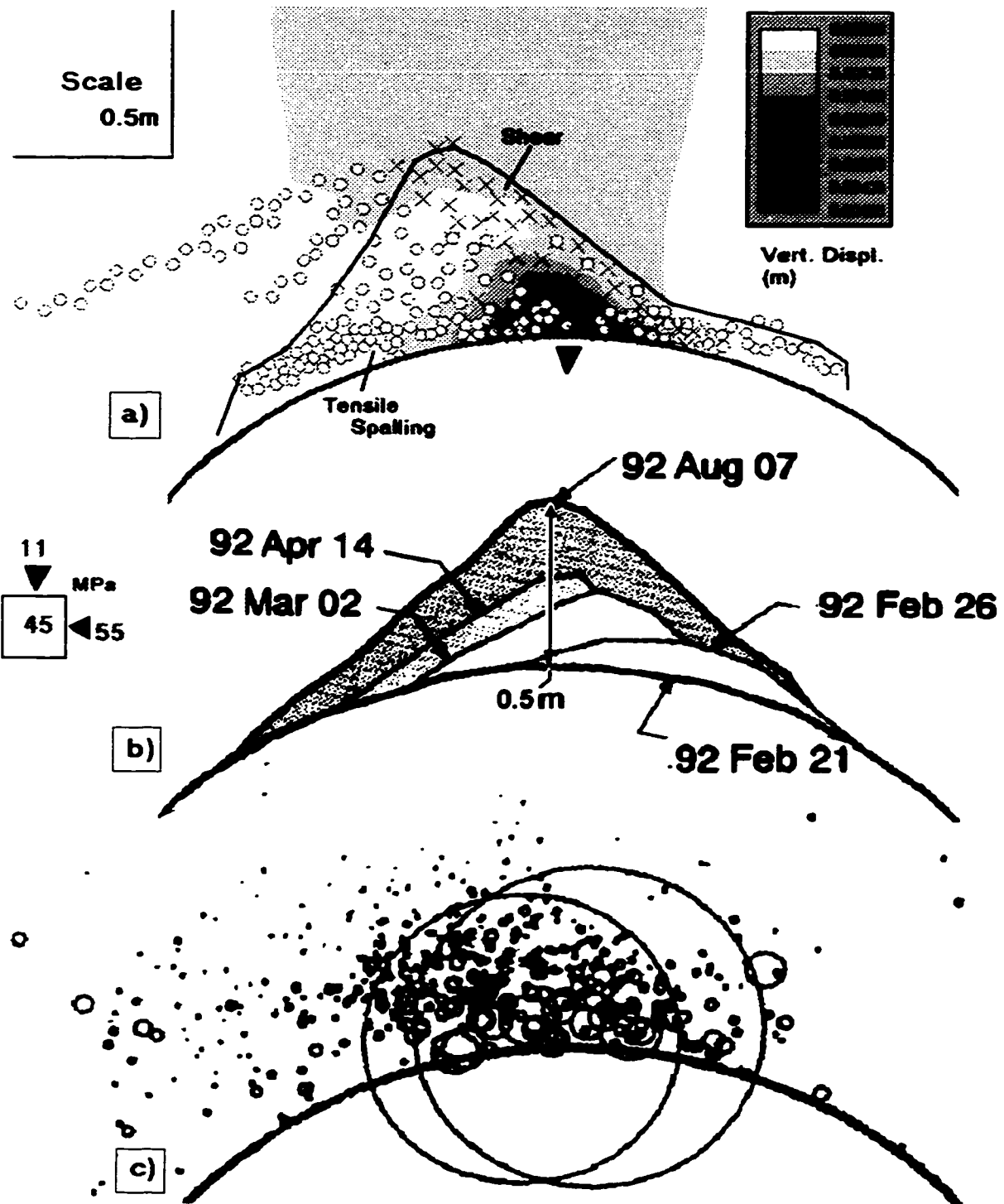


Figure 8.96: a) Yield zones from random mesh model of URL "mine-by" tunnel. Interconnected yield zones bounded by "notch" profile; b) Actual observed notch development (after Martin 1994). Microseismic events recorded during period of notch development (data reanalyzed and presented by Cai et al 1998).

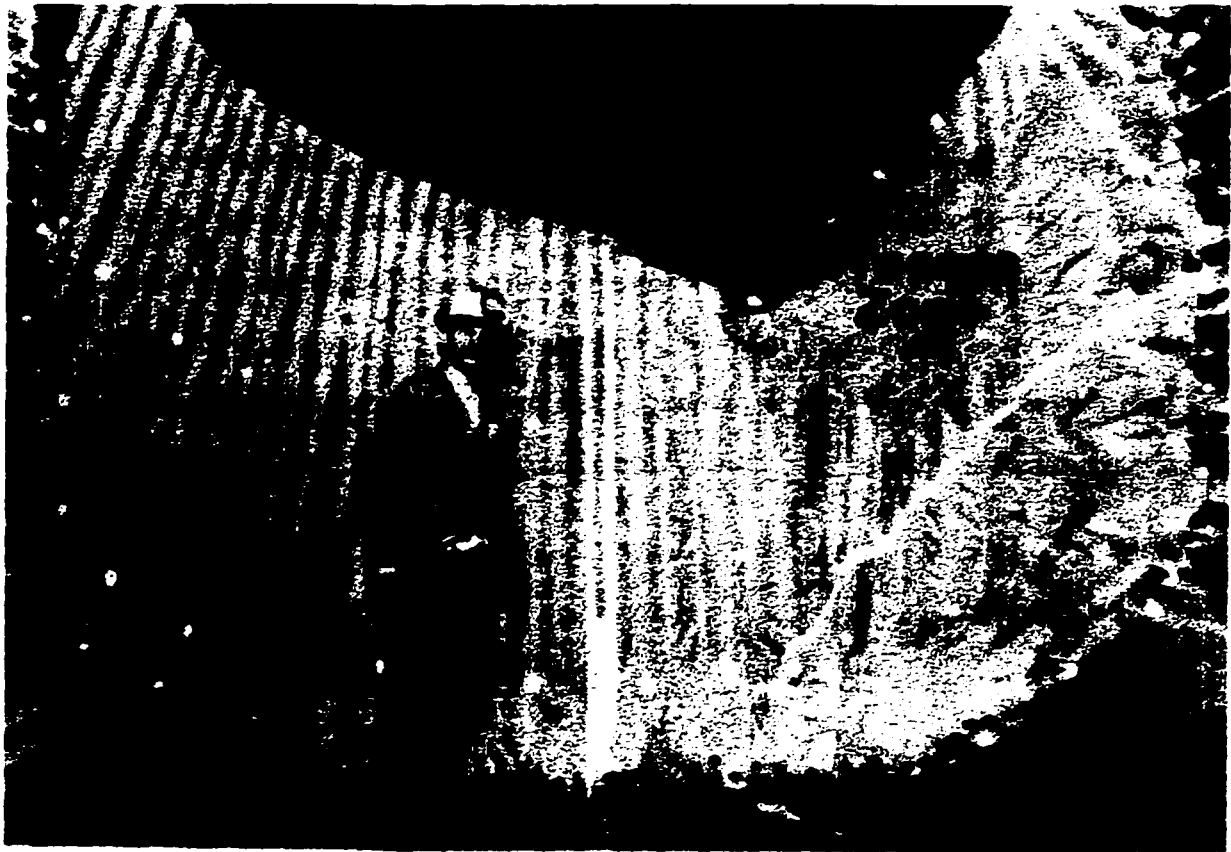


Figure 8.97: Excavated cross-section (Top photo) through the floor notch at the URL "mine-by" tunnel showing the smooth sides generated by tensile slabbing; Bottom photo shows a close-up of the highly fractured notch-tip process zone. (Photos and annotation from Martin 1994).

The microseismic data collected during the period of notch formation (Figure 8.96c) clearly shows intense crack clustering and interaction occurring in the main notch region. It also shows spurious events occurring to the left of the notch in the area of the deeper terminating tension cracks predicted by the model in Figure 8.96a. This microseismic data was reanalyzed using a tensile source model (Cai et al. 1998). The sizes of the circles represent apparent source dimensions based on this model.

These scoping analyses indicate that the crack interaction threshold, represented in a Mohr-Coulomb form with $\phi=30$ to 35 degrees, is valid for non-linear modelling of progressive failure in hard rock. It also shows that tensile failure, associated mechanically and spatially with primary shearing, is a major factor in the final failure geometry. The unconfined intercept for insitu yield strength should correspond to a lower range of crack interaction threshold values for damaged laboratory samples (obtained from the depth of interest). This value is normally 0.4 to 0.5 times the peak *UCS* of undamaged (near-surface) samples of a comparable rock.

8.8.2 Corner Crushing and Wall Tension - Rectangular Tunnel

A mechanism similar to the process zone related spalling in Section 8.8.1 is the development of a "baggage zone" (a term coined by Kaiser et al. 1995, based on underground observations) around rectangular excavations at depth. This is illustrated in Figure 8.98.

In Figure 8.98a, elastic finite element analysis reveals moderate compressive stresses and low compressive confining stresses near the sidewalls of the excavation. High corner stresses indicate the potential for highly localized and confined shear failure. Elastic analysis, however, shows no cause for concern in the sidewall regions.

In Figure 8.98b, plastic yield is allowed to occur. As predicted, shear failure is modeled in the corners. These localized shear zones, however, generate extensive tensile spalling and slab generation (boundary-normal tension cracking) in the sidewall zones. These zones of tensile failure cover more than 5 times the area of primary shear failure. Similar results were obtained using finite difference modelling by Vasak and Kaiser (1995). Body forces (gravity) result in preferential displacement (kick-out) at the base of the walls. This model has vertically dominant field stress. In regions with higher horizontal stresses (e.g. Canadian Shield) this baggage zone forms in the roof, necessitating removal or additional back (roof) support.

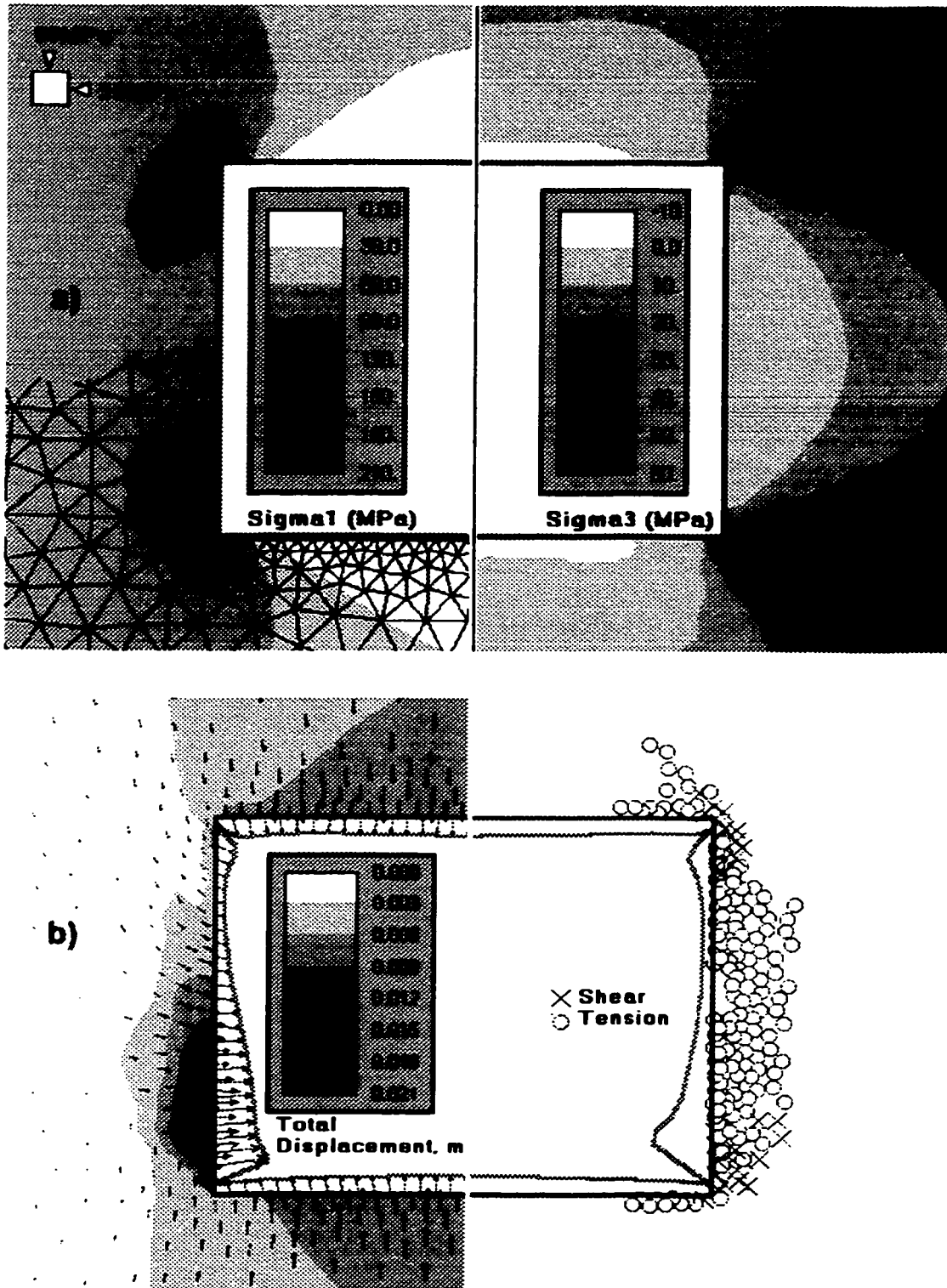


Figure 8.98: a) Elastic finite element results for stresses around a rectangular opening in a deviatoric initial stress field; b) Total displacement and yield zone for plasticity simulation (same material parameters as in Section 8.8.1).

8.8.3 Geometric Correction Around Mine Pillars

The creation of spall zones around non-circular openings can be considered a form of geometric correction. Such a correction normally decreases the radius of curvature (of the intact wall), steepening the radial stress gradient thereby increasing the confining stresses in the rockmass a small finite distance beyond the new boundary. While tangential stress in the same sidewall or roof can also be increased by this process, elevated confinement boosts the yield strength, arresting the propagation of failure. As pointed out by Kaiser et al. (1995), this process should be considered inevitable around rectilinear openings at depth, the result of a crack initiation and damage accumulation within the wall. This is also observed in underground pillars as in Figure 8.99b.

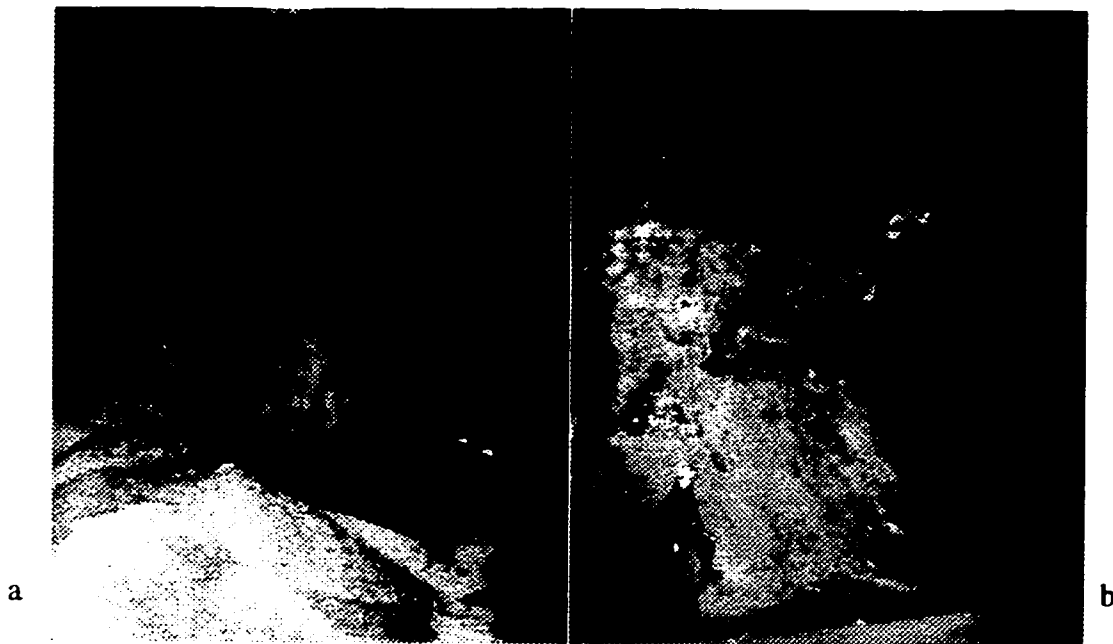


Figure 8.99: a) Undamaged and b) significantly spalled but internally competent (core intact) pillars at the Black Angel Mine, Greenland (photos courtesy E. Hoek).

As demonstrated in this chapter, damage nucleation can be exploited by low confinement (crack extension), surface interaction, local tensile stresses or localized corner shear leading to full span crack propagation and spalling. The stress level at which this occurs in real rockmasses will be close to the damage initiation threshold. While visibly alarming, such damage should not be confused with engineering failure of the excavation (particularly for observational back-analysis).

While rigorous excavation-scale analyses, using PFC, are beyond the scope of this work, a simple pillar simulation (Figure 8.100) was performed to illustrate this process. The pillar geometry in Figure 8.100a is created by cutting into a rectangular lithified assembly under hydrostatic applied

stress (30MPa). Axial stress is then increased by platen convergence, simulating further room extraction away from the pillar. The sidewalls are frictionless acting as symmetry boundaries.

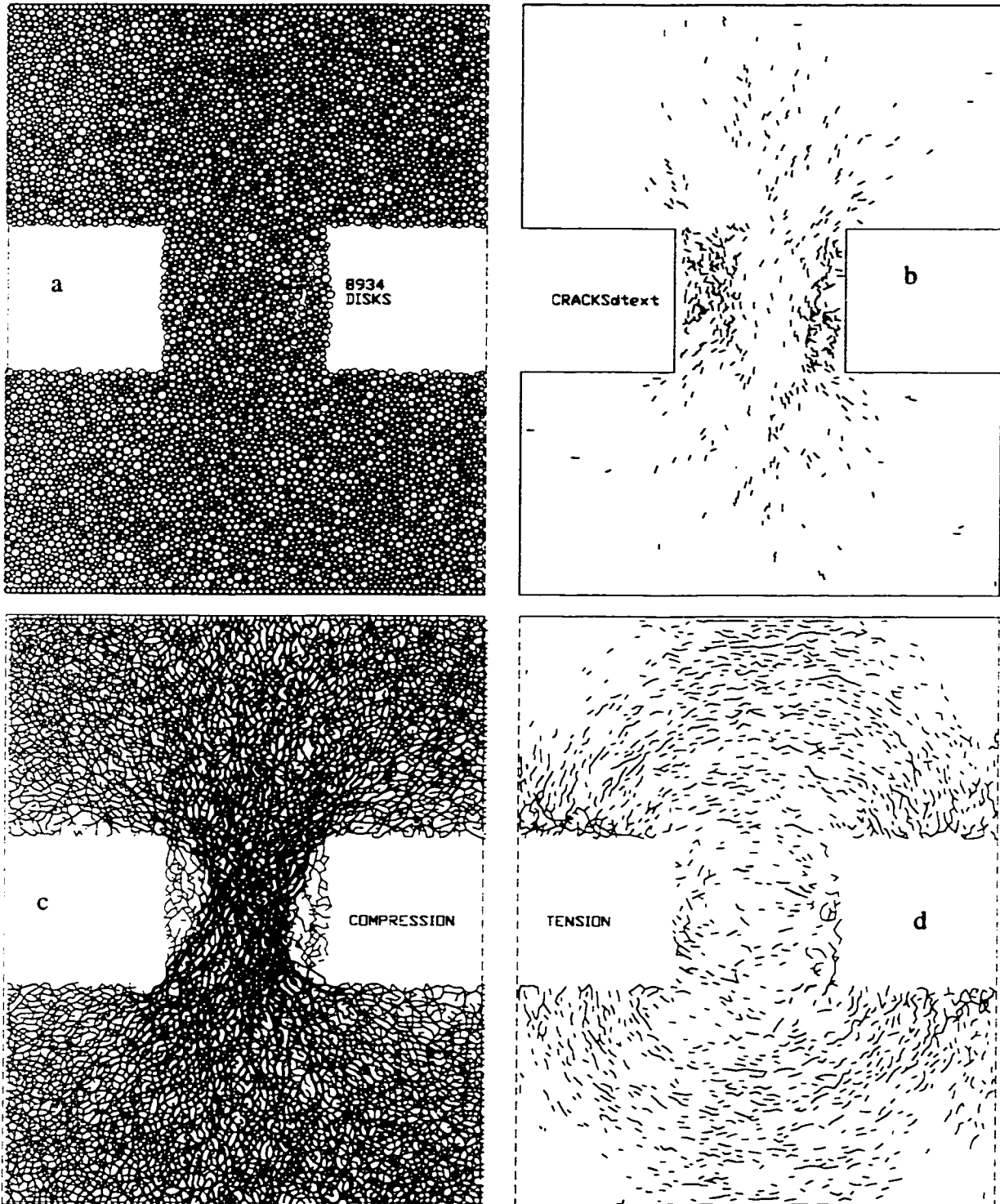


Figure 8.100: Pillar simulation: Discs (a) Cracks (b) and forces (c & d) immediately prior to core yield (Figure 8.101). Note "spall" damage in pillar sidewalls.

The cracks shown in Figure 8.100b are almost entirely tensile in nature and define two baggage zones evident by the absence of compressive forces in the sidewall areas of Figure 8.100c. The contact forces shown in Figure 8.100c and d are for the damage state in Figure 8.100b. The simulation was allowed to run until the core of the pillar yielded at an average axial stress of 450 MPa, far in excess of that predicted by elastic analysis (Figure 8.101).

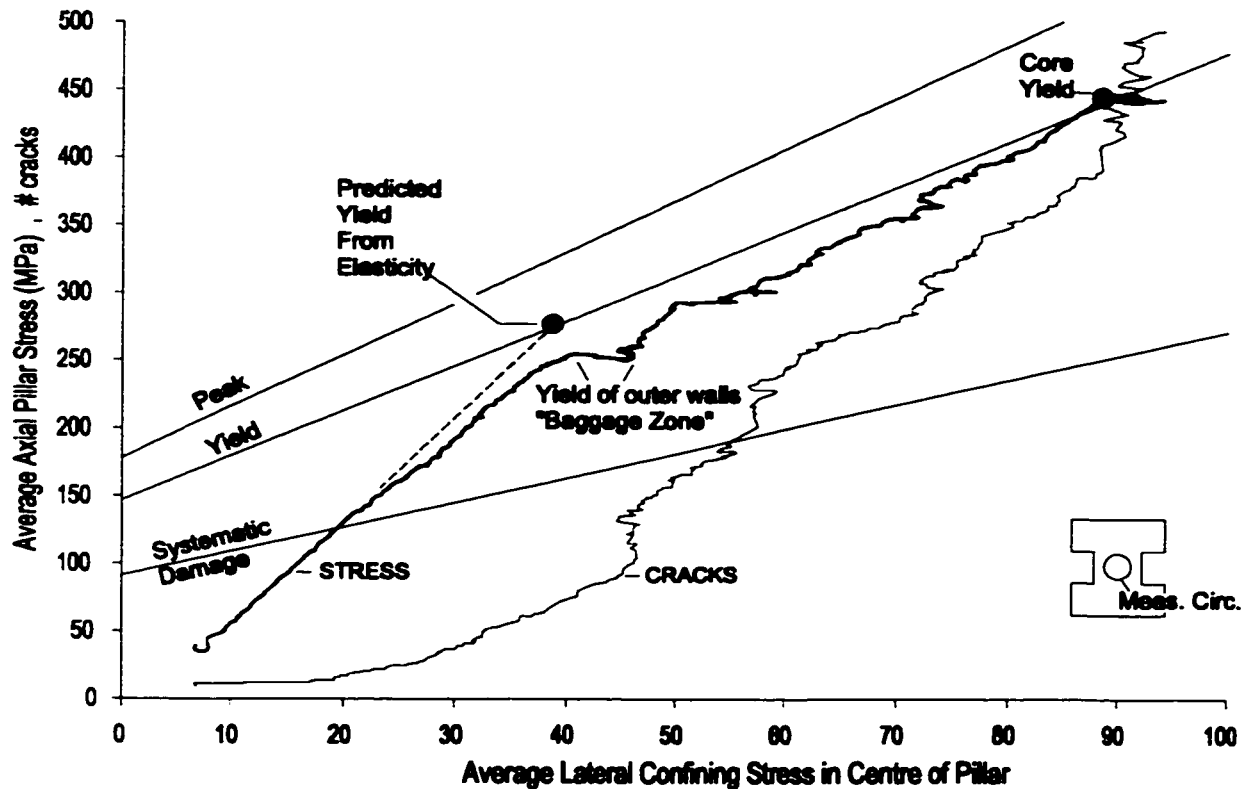


Figure 8.101: Average (core) stress path and crack accumulation for pillar in Figure 8.100.

Once the spalling process initiates, damaged baggage zones create a curved inner wall geometry for the intact pillar core. As a result of this geometry change (and convergence of stress flowlines through the pillar) the relative rate of confinement increase within the central core of the pillar outstrips the increase in axial stress. As such, the peak strength envelope of the material is not reached within the core until a much higher axial stress. Recall that individual cracks cannot extend in this model without interaction. In real rockmasses, the mechanisms outlined in this chapter would lead to crack extension and pillar spall at stress levels close to damage initiation.

For slender pillars, these baggage zones converge resulting in collapse. For very wide pillars, the baggage zones will mimic the single excavation in Figure 8.98. While giving the appearance of failure, such zones would have little impact on the overall stability of the wider pillar.

8.9 DISCUSSION

A number of complimentary mechanisms were presented to explain the reduction, of insitu yield strength, to a predictable lower bound threshold in massive or moderately jointed rockmasses.

While the presence of ubiquitous structure (joints) has been cited in the past to explain this reduction, the relative insitu strength obtained with exacting excavation methods in massive granite, for example, is similar to that observed for a moderately jointed rockmass in a mining environment. It is possible to conclude from this that rough intermittent jointing does not have a significant effect on rockmass yield in high stress conditions.

The size of the ("weak link") internal flaws responsible for crack initiation is a controlling factor for damage thresholds, although this scale effect is limited by a characteristic dimension such as the grain size. Crack initiation beyond the grain scale, is therefore not dependent on sample size.

The effect of scale was shown in this chapter to impact maximum peak strength, while the yield threshold (in compression) was less sensitive (a function of scale-dependent crack interaction probability). In near-excavation conditions, a number of factors contribute to increase the crack interaction potential, thereby decreasing the stress levels at which yield occurs. A lower bound for this decline is the threshold for crack initiation.

These mechanisms include, the effect of unloading damage, the interaction of extending cracks with the excavation surface and a number of mechanisms (heterogeneity, geometry, localized shear) responsible for the generation confinement reduction and of local tensile stresses within the near-excavation rockmass. These mechanisms can work together to affect the crack interaction potential, effectively reducing the yield strength.

The formation of spall "baggage zones" decreases the radius of wall curvature and increases the near-excavation confining stresses beyond the spall zone (e.g. Crescent "baggage" or spall zones result in curved walls around an initially square opening). As a result, rock strength increases beyond the spall front and such failure is often self-arresting.

For reasons described above the spall damage itself, may become fully developed at stress levels only slightly above the crack initiation threshold. The limits of damage (and subsequent failure), can therefore be predicted, based on elastic modelling of initial excavation geometries. After initial spalling, subsequent damage can be similarly predicted using elastic analysis of the new as-built geometry (new model geometry = [excavation + baggage] as shown by Kaiser et al. 1995).

CHAPTER 9

Summary, Conclusions and Recommendations

9.1 SUMMARY

This thesis has been an exploration of the important roles of tensile strength, and of low and negative confining stresses on the mechanics, the sequence and the extent of rockmass yield and failure in underground hard rock excavations. This study was achieved, in part, through the use of two simple mechanical analogues for block and particle contact interaction.

9.1.1 Tensile Strength and Relaxation in Structural Domains

Part I, including Chapters 2, 3 and 4 dealt with the role of residual tensile strength and abutment or boundary-parallel relaxation in the stability and failure of jointed rockmasses.

Structural components within the rockmass control the kinematics of failure and, for simplicity and conservative design predictions, are typically assumed to be fully persistent (no rock bridges connecting a rock wedge to the host medium, for example). In the limit, frictional strength at abutments and on gravity-driven sliding surfaces is normally considered in the assessment of failure potential.

However, the effects of residual tensile strength due to rock bridges or incomplete jointing and the influence of internal rockmass stresses (providing clamping to a gravity driven wedge, for example), can be significant factors controlling both the extent and timing of such failures. Loss of clamping forces due to complex mining geometries is a major catalyst for catastrophic roof collapses.

Flat excavation boundaries, such as drift roofs or stope walls, in laminated and cross-jointed rockmasses do not follow elastic beam theory due to the inability to carry deflection induced tension parallel to the beam. Stability is achieved through the development of a compression arch. This arch, however, is very sensitive to the displacement or confining conditions at the abutments. Outward displacement of the abutments due to stress relaxation, for example, can potentially compromise the stability of the intervening roof or wall. This effect was examined in detail as was the influence of beam-building due to incomplete separation of the laminations (inter-bed residual tensile strength).

Components of this study included the following:

- An examination, in Chapter 2, of failures in isolated drifts in Canadian Mines showed that the limiting height of large, structurally controlled groundfalls is significantly less than that predicted from an assessment of ubiquitous joint structure and limit equilibrium analysis. Non-persistent jointing and clamping forces are identified as key factors in this discrepancy. A study was made of the stabilizing effects, on structurally bounded blocks and wedges, of small amounts of tensile strength, provided by incomplete separation of joint or fracture planes. The “beam building” action of these rock bridges in laminated ground was also addressed. In addition, the important impact of boundary-parallel confinement or relaxation on the stability of both rock wedges and laminated beam structures was discussed.
- In order to provide a tool for further examination of these issues, for laminated rockmasses, a simple voussoir beam analogue was revisited, with additional improvements and an improved solution procedure. This analogue, described in Chapter 3, was verified using case studies and discrete element modelling. Upper-bound span (or lower-bound thickness) criteria have been traditionally associated with this model. For design applications as well as for use in this study a rational “yield” criterion based on critical beam deflection and parametric sensitivity was introduced and used to generate universal engineering design charts for excavations in laminated ground.
- In Chapter 4, the voussoir beam model was applied to the study of residual tensile strength and abutment relaxation and the contributions to the stability or failure of laminated rockmasses above excavations. Empirical stability prediction tools were modified to account for these factors. Key considerations for support design were addressed.

9.1.2 Tensile Strength and Relaxation in Stressed Rockmasses

Part II, including Chapters 5 through 8, dealt with near-boundary yield of massive or moderately jointed rockmasses. Insitu strength reduction of rockmasses, as compared to test strengths of intact core samples, is typically explained by the presence of joints, fractures and imperfections. In massively to moderately (i.e. non-persistently) jointed rock, however, the impact of macroscopic jointing is less obvious. Rather, insitu strength, in the vicinity of underground openings, consistently corresponds to a stress level and confinement dependency that reflects the threshold for systematic crack initiation and accumulation in laboratory samples.

In laboratory tests, long-term and large-scale sample test strengths correspond to a threshold for the interaction of otherwise isolated cracks. In tests on intact core samples, crack interaction occurs at a stress level (for unconfined compression) of approximately twice the systematic crack initiation and accumulation threshold stress. In the field, therefore, crack interaction must occur at stress levels close to crack initiation resulting in a consequent yield and peak strength drop.

The goal of Part II of this thesis was to explore the nature of insitu strength reduction and to provide an understanding of the tensile nature of rock damage (microcracking) and the associated impact of low near-boundary confining stresses of crack accumulation, propagation and interaction. To this end:

- The empirical success of an insitu strength criterion, based on damage initiation, was discussed and verified in Chapter 5, with important questions posed as to the mechanical nature of this criterion.
- The dominance, in polycrystalline (hard) rock, of internal tensile strength on stability under compressive loading was discussed at the atomic level and at the scale of laboratory samples in Chapter 6. Granite was used as the test material. A number of key damage thresholds were established including first crack initiation, systematic damage accumulation, crack interaction, localization and, of course, peak strength. The relationships of these thresholds to each other and to strain and strain rate measurements, were examined for direct tension, indirect tension, unconfined compression and confined compression testing.
- A novel approach to solid modelling, using a clastic analogue with inter-particle bonding, was described in Chapter 7 and then applied to the simulation of laboratory (strength) tests on granite. A number of key observations were made regarding the relationship between damage initiation and interaction, of crack interaction and sample yield, the relationship between

crack interaction and total lateral strain, and of the relationship between tensile strength and compressive strength for the model samples and by extrapolation, for granite.

- Finally, in Chapter 8, a combination of experimental data, numerical simulation, statistical modelling and fracture mechanics was used to explain the mechanisms of strength reduction insitu (as compared to laboratory testing). Hard rock yield around underground excavations was established as a fundamentally tension driven process, limited as a lower bound by the requirements of Mode I crack initiation and as an upper bound by crack interaction. In this context the role of pre-existing extensile damage, surface interaction, and local confinement in the reduction of insitu strength was examined.

9.2 CONCLUSIONS

9.2.1 Wedge Stability in Underground Excavations

Due to the effects of clamping, the failure of full span wedges, defined completely by non-sheared joints which dip in excess of 60 degrees, is uncommon in isolated drifts of euhedral cross section. Such failures can and do occur in areas where clamping stresses are reduced by large span deflections or by the creation of unfavorable and stress-shadowing stope geometries nearby. Even mild clamping stresses, when present and when integrated over the surface of rough joints, can apply very large restraining forces for stability of roof wedges. For confined drift backs, away from mining activity, it can be assumed that failure of steep wedges is not probable.

In moderately jointed rockmasses short-term stability is enhanced by incomplete separation on joint planes and the consequent residual tensile strength. Rock bridges covering less than 1% of the total joint area are sufficient to replace most common mining support systems. This internal support, however, is sensitive to the effects of atmospheric attack and stress corrosion and can therefore only be considered for primary (first-pass) support design (an important consideration for project cycling and development costs). Permanent support in high traffic areas should still be designed using limit equilibrium assumptions for shallow to moderately steep wedges.

9.2.2 The Voussoir Analogue

An improved and corrected iterative approach to a classic analogue is presented for stability assessment of laminated ground. The analogue has been verified using case study data and numerical modelling. It is a valid approach for stability prediction provided that the following limitations are observed:

- The model not recommended for very large spans (>60m for horizontal or >100m for steeply inclined faces) since other mechanisms not covered by the model assumptions may be active.
- No low to mid angle jointing or more than three joint sets are present, and the rockmass itself is of a classification of “fair” to “very good” (RQD>50% for example).
- The effective lamination thickness and the boundary-parallel rockmass modulus can be estimated with some degree of certainty.

Support pressures and interlayer tensile strength can be simulated as a negative overburden pressure. Abutment relaxation can be included in the model as an effective initial abutment gap.

9.2.3 Stability of Laminated or Blocky Rockmasses

Using a combination of the voussoir analogue and ground reaction concepts, it was demonstrated that minimal inter-bed tensile strength is required to maintain stable composite beam thicknesses provided that deflection is permitted. The same conclusion applies to support design. The beam must be allowed to deflect, in order to generate a stabilizing compression arch while being held together in a stiff fashion so that the component laminations deflect as one. Compound cablebolt systems provide such a compromise.

Numerous situations arise in modern underground mining where the backs or walls of drifts or stopes become relaxed in the direction parallel to the face. This can arise from geometry changes, unfavourable insitu stress ratios, reentrant surfaces, undercutting or abutment shear. The effect of these changes can be approximated by considering the effects of an initial gap at the abutments. This gap can be included in the solution for the voussoir beam. This gap requires an initial outward displacement of the compression arch, which is introduced prior to calculating the deflection induced shortening, stress generation and establishment of moment equilibrium.

The modified voussoir model demonstrates that very little displacement is required to significantly reduce, for example, the maximum stable span for a given thickness. For a 1m lamination thickness and a rockmass modulus of 10GPa, a symmetrical relaxation displacement of 25mm reduces the critical span from 23m to 12m, a reduction of close to 50%. This amount of relaxation is not severe for a span of this size, and yet the impact on stability is significant. Demand for residual tensile strength or artificial support is dramatically increased by the presence of abutment relaxation.

Open stopes are often difficult to support, and scale (unsupported span size) is often linked to the economics of operation. Larger unsupported stopes increase production rate and reduce development and backfill costs. Unplanned dilution due to the destabilizing impact of relaxation can be economically devastating in this scenario. Relaxation can be minimized or avoided by optimization of geometries and sequencing and by avoidance of hangingwalls undercut.

For the purposes of stress modelling, abutment relaxation due to geometric factors can be identified by an equivalent tensile stress parallel to the face. This equivalent stress can be used in modified and recalibrated versions of common empirical tools to assess the impact on stability and critical dimensions for drifts and stopes.

9.2.4 Empirical Insitu Strength

In numerous case studies documented by other researchers and in field examples examined in this work, the onset of visible or recordable (using microseismic techniques) yielding, around deep underground excavations in massive or moderately jointed hard rock, initiates at a stress level of one third to one half of the laboratory *UCS* (unconfined compressive strength). The lower ratio corresponds to minor surface damage while a value of one-half of the *UCS* consistently represents an upper bound stress level for practically significant rock yield.

Plotted in $\sigma_1:\sigma_3$ space, the slope (confining stress dependency) of this insitu yield threshold is only slightly greater than unity (1.0 to 2.0), contrasting with the slopes of 6 to 8 associated with internal frictional strength of hard rock test samples.

An empirical strength criterion:

$$\sigma_1 = [0.3 \text{ to } 0.5]U.C.S. + [1 \text{ to } 2]\sigma_3 \quad [9.1]$$

has proven successful in numerous mining and tunnelling analyses, for predicting the radial extent (although not the shape) of damage and groundfall potential. The mechanisms which result in this relationship have been investigated and are summarized in the following sections.

9.2.5 Rock as a Bonded Solid

Damage processes in hard rocks such as granites, norites and others, are fundamentally tensile in nature at low to moderate confining stresses. The composite mineral framework within crystals as

well as the polycrystalline structure itself precludes the ductile slip mechanisms found in metals and in saturated clays and other geo-materials.

Numerous nucleating mechanisms, including sliding on internal flaws, deformation of open flaws, as well as geometric and compliance incompatibilities at crystal boundaries, all operate to generate the necessary crack-opening force for extensile crack growth. These extension microcracks grow parallel to the direction of maximum compression until crack interaction occurs.

As a consequence of the extensile (and therefore dilatant) nature of rock damage, sliding friction ($\mu=1$ for granite) cannot be mobilized until rock yield has progressed significantly and strain localization has taken place. Friction controlling crack initiation, if a sliding flaw analogue is invoked, is represented by a much smaller coefficient ($\mu=0.15$ to 0.2), corresponding to friction on atomically smooth surfaces.

Crack initiation threshold stress is a material property related to the internal elemental strength of the material. Crack accumulation and interaction are indirectly related to this strength distribution. Crack interaction represents true yield strength. Post yield behaviour (peak strength and post peak response) is controlled by test conditions and sample geometry.

In laboratory samples, crack interaction is best detected from a deviation in axial stress-strain response. Volumetric strain reversal, a popular index for yield, is more representative of strain localization, an intermediate stage between yield and failure.

In direct tension, failure is coincident with crack initiation. Crack accumulation and interaction is required in compressive conditions in order for yield to occur. Attempts to relate tensile strength directly to compressive strength have therefore been unsuccessful. In polycrystalline materials, rough and undulating intergranular flaws on the scale of the grain dimension may open in direct tension, creating critical crack tip stress concentrations, and consequent extension and rupture. These flaws are tightly interlocked and inert under compressive stresses. Cracks in compression arise from smaller mobile (atomically smooth) flaws within crystals or from smaller disconnected pores and cracks at grain boundaries. Therefore, crack initiation in compression, while theoretically linked to material tensile strength may not correspond to conventional relationships predicted by fracture mechanics (which invoke an initiating flaw of equal length in both circumstances).

Crack interaction and yield, in compression, is related to a critical extension strain (total strain). This is in contradiction to the critical extension strain concept typically invoked for damage initiation based on elastic continuum conditions. (For highly confined samples, crack initiation can occur under net compressive lateral strain). For Lac du Bonnet granite this critical extension strain is approximately 0.0007. This critical extension strain is directly related to a critical crack intensity. At this damage level, crack interaction is inevitable. Extension cracks dilate in a direction normal to maximum compression and therefore induce an associated extension strain. This extension strain criterion does not apply, in most circumstances, to yield in direct or Brazilian tension because these failure modes are coincident with crack initiation, not interaction.

9.2.6 A Bonded Disc Analogue for Rock

A discrete element model using rigid discs connected by linear elastic - brittle contacts can adequately represent many aspects of polycrystalline rock response to compressive stress including:

- Elastic response (Young's modulus, Poisson's ration and shear modulus)
- Damage initiation
- Damage accumulation and inelastic lateral strain response
- Critical crack accumulation and crack interaction

The model is used successfully in this work as a damage accumulation analogue. The major limitations of the model for general modelling of bonded solids include:

1. Inherent stability of crack (ruptured bond) formation and the inability to extend cracks due to crack tip concentrations.
2. Limited upper bound for crack anisotropy (<0.8) due to pseudo-hexagonal contact state.
3. Particle rolling is permitted and bonded contacts afford no moment resistance other than lattice trapping.

Limitation 1 is critical for the effective simulation of tensile and spalling failure. Only cracks which interact to form a macro-rupture, numerous disc diameters in length, can generate a self-sustaining "crack tip concentration". Individual ruptured contacts or "isolated cracks" cannot extend. Unstable crack propagation under tensile loading, immediately upon crack initiation, is highly characteristic of bonded solids such as granite.

Limitations 2 and 3 limit the apparent confinement dependency of peak strength. In rock materials, the yield strength is represented by crack interaction which has a non-frictional confinement dependency related to Mode I influence of the confining stress on crack tip concentrations. Peak strength on the other hand is related to crack and contact force anisotropy. In granite, an array of compression parallel cracks, prior to sample failure, provides a higher level of anisotropy than the bonded disc model, and therefore displays a higher apparent friction at peak strength. Actual sliding friction is only fully mobilized well after peak strength has been reached.

Particle rolling (3) also reduces the maximum residual friction (below the nominal contact friction coefficient).

In spite of these limitations, the model is highly useful in providing an analogue for crack accumulation without the effects of crack extension. This provides a compliment to fracture mechanics models which deal with crack extension within a fixed array of nucleation sites (extension without accumulation). This is a key aspect of this work.

The model sheds light on key aspects of rock strength including the following:

- Grain stiffness heterogeneity can result in intergranular cracking during unloading from insitu confining stress.
- Crack interaction and macroscopic shear formation can occur as a consequence of purely tensile damage (even if microscopic shear rupture is prevented).
- In the absence of crack extension, yield in tension and compression occur at similar crack intensities and represent end members of a continuous strength relationship. In these conditions the Brazilian test represents an intermediate stage of this relationship. In reality, failure in tension is coincident with crack initiation and is not directly related to yield in compression.
- Crack interaction, which can be represented by the occurrence of two cracks within one crack length of each other, does indeed coincide with axial stress-strain non-linearity, as suggested in the granite study. This threshold is one of probability and occurs at a much lower crack intensity (0.03) than predicted by fracture mechanics models involving uniform arrays.
- Crack interaction in the model is also associated with a total lateral extension strain of 0.0007, coincident with the results of the granite. This is not a trivial result since the model was calibrated using the elastic response and unconfined compressive strength only.

- Both granite test results and the bonded disc simulations suggest that rock yield strength can be represented by the Mohr Coulomb criterion using an effective friction angle of 30 to 35 degrees, reflecting the stress requirements of constant critical total strain (and not actual sliding friction).

9.2.7 In situ strength reduction

A number of mechanisms work together in outwardly competent massive rock to affect a significant reduction in insitu strength.

Crack initiation, demonstrated in this work to represent a robust lower bound for insitu strength, is only mildly affected by:

- Scale effect resulting in higher probability of weak-link inclusion in a larger sample.
- Excessive damage resulting in extension of potential sliding flaws within crystals.
- Confinement shadowing resulting from stiffness contrasts or open crack damage.

The stress level at which crack interaction and rock yield occurs (true long-term and scale independent strength) is, on the other hand dramatically effected by:

- Scale effect resulting in higher probability of weak-link crack accumulation and interaction potential in a larger sample.
- Pre-existing damage which provides statistical opportunity for pre-mature crack interaction (interaction at lower new crack accumulation levels).
- Stress rotation during excavation (in three dimensions) resulting in oblique crack damage (critically oriented at 20 to 30 degrees to the final direction of major principal compression) further enhancing crack interaction potential and a reduction in yield stress.
- Surface interaction and crack extension - providing the potential for unstable spall crack propagation or enhanced interaction probability.
- Increased crack extension and interaction potential due to near-zero and negative effective confinement due to stiffness heterogeneity and surface anomalies.

If all of these mechanisms are active the insitu yield strength around deep excavations in hard rock will reduce to or near to the threshold of systematic crack initiation, as observed in numerous field case studies in this work and in the literature.

With the exception of scale effect, these mechanisms of yield strength reduction are active only at low confining stresses. Therefore, the effect is felt only in the vicinity of an excavation. In addition, near-boundary dilation of pre-existing damage (effective gap) may result in an apparent confinement independence for rock strength. As cracks close farther into the rockmass, confinement dependency of crack initiation and of yield strength returns.

The empirical success of the Tresca-like relationship for insitu rock strength is the result of these near-boundary effects and, while useful for near-excavation damage prediction, should not be viewed as applicable within a confined rockmass.

Finally, it is important to recognize that much of the ultimate spatial extent of observed failure in hard rock environments is caused by rupture which is tensile in nature. The catalyst may be unfavourable geometry or localized crushing such as in the case of initial notch formation or corner crushing. A common example is the ubiquitous curved "baggage zone" of spalled and fractured rock which forms around rectangular excavations, posing a collapse hazard and increasing support demands.

Accurate modelling of this process using conventional plasticity formulations requires a mechanistic separation between tensile rupture and shear flow rules. Since propagating cracks (under crack normal tension) do not immediately affect the flow of crack-parallel compressive stress, a yield function and flow rule which does not distinguish between the two failure modes (such as Hoek-Brown) may not be adequate for this purpose.

9.3 RECOMMENDATIONS

This work has involved an exploration of the mechanics and principals governing the influence of tensile strength and low confining stresses on rock strength and rockmass stability. From an examination of this body of research, it is possible to suggest a number of avenues for further theoretical and applied research and development.

9.3.1 Structural Failure and the Voussoir Model

It is desirable to develop an understanding of the effects of non-symmetrical deflection in inclined beams and a means of inclusion into the model. The former may be achieved through rigorous numerical experimentation.

An approximate or a rigorous solution is needed for estimating the stabilizing effect of 2 and 3Dimensional confining stresses on non-symmetrical underground wedges of arbitrary geometry.

Semi-empirical tools are needed for the consideration of confining stress and rock bridges (incomplete jointing) in design assessments.

9.3.2 The Bonded Disc Analogue

Several desirable model enhancements and experimental topics for further research include:

- The inclusion of moment stiffness at particle contacts.
- A stress-corrosion model which relates strength decay to the presence of neighbouring cracks. This would encourage the development and propagation of continuous macro-cracks.
- A nearest-neighbour algorithm to calculate crack intensity based on arrays of interacting cracks (intensity varies as the sum of the square of crack lengths).
- logic to fracture particles (into smaller particles) upon high diametric loading
- An investigation into crack accumulation and interaction in 3Dimensions.

9.3.3 Rock Strength and Damage Assessment

It would be useful to correlate the Brazilian test results of numerous rock types to crack initiation in compression. At present the initiation threshold is expressed as a ratio of peak strength. This, however, is misleading since it is the expression of a material property as a function of an experimental value dominated by system effects and boundary conditions.

A new seismic data analysis tool is needed (e.g. a clustering index as in Falmagne 1999) to detect the onset of crack interaction from acoustic and micro-seismic monitoring data obtained from the lab and from the field.

Improved instrumentation is required to detect damage extent prior to failure (non-destructive assessment of crack-damaged rock in-place).

REFERENCES

- Abel, J.F. and Lee, F.T. 1973. Stress changes ahead of an advancing tunnel. *Int. J. Rock Mech. Min. Sci. & Geomech. Abstr.*, **10**, 673-697.
- Aglawe, J.P. 1999. *Unstable and Violent Failure Around Underground Openings in Highly Stressed Ground*. Ph.D. Thesis, Dept. of Mining, Queen's University, 320p.
- Andreev, G.E. 1991. A review of the Brazilian test for rock tensile strength determination. Part I: calculation formula. *Mining Science and Technology*, **13**, 445-456.
- Arjang, B. and Herget, G. 1997. In situ ground stresses in the Canadian Hardrock Mines: An Update. *Int. J. Rock Mech. Min. Sci. & Geomech. Abstr.*, **34** (3-4), Paper No. 015.
- Ashby, M.F. and Hallam, S.D. 1986. The failure of brittle solids containing small cracks under compressive stress states. *Acta Metall.*, **34** (3), 497-510.
- Atkinson, B.K. 1979. Fracture toughness of Tennessee Sandstone and Carrara Marble using the double torsion testing method. *Int. J. Rock Mech. and Min. Sci. and Geomech. Abstr.*, **16** (1), 49-54.
- Atkinson, B.K. 1987. Introduction to fracture mechanics and its geophysical applications. in *Fracture Mechanics of Rock*. London: Academic Press, 534p.
- Atkinson, B.K. and Advis, V. 1980. Fracture mechanics parameters of some rock-forming minerals determined using an indentation technique. *Int J. Rock Mech. Min. Sci. and Geomech. Abstr.*, **17**, 383-386.
- Atkinson B.K. and Meredith, P.G. 1987a. Experimental fracture mechanics data for rocks and minerals. in *Fracture Mechanics of Rock*, London: Academic Press, (ed. Atkinson), 534p.
- Atkinson, B.K. and Meredith, P.G. 1987b. The theory of subcritical crack growth with applications to minerals and rocks. *Fracture Mechanics of Rock*, London: Academic Press, 111-167.

- Aubertin, M. and Simon, R. 1997. A damage initiation criterion for low porosity rocks. *Int J. Rock Mech. Min. Sci.*, **34** (3-4), Paper 017.
- Ball, A. and Payne, B.W. 1976. The tensile fracture of quartz. *Journal of Materials Science*, **11**, 731-740.
- Bardet, J.P. and Proubet, J. 1991. A numerical investigation of the structure of persistent shear bands in granular media. *Geotechnique*, **41** (4), 599-613.
- Barton, N. 1983. Application of Q-System and Index tests to estimate shear strength and deformability of rockmasses. *Proc. Int. Symp. on Engineering Geology and Underground Construction, IAEG, Lisbon, 2*, II51-II70
- Barton, N. 1988. Predicting the behaviour of underground openings in rock. Fourth Manuel Rocha Memorial Lecture. *NGI Publication No 172*.
- Barton, N. 1988. Rockmass classification systems and tunnel reinforcement selection using the Q-system. *Rock Classification Systems for Engineering Purposes. A.S.T.M. 984* (ed. Kirkaldie), American Society for Testing and Materials, 59-88.
- Barton, N., Grimstad, E., Aas, G., Opsahl, O.A., Bakken, A. Pedersen, L., and Johansen, E.D. 1992. Norwegian Method of Tunnelling. *World Tunnelling and Subsurface Excavation*. August, 324-331.
- Barton, N.R., Lien, R. and Lunde, J. 1974a. Analysis of rockmass quality and support practice in tunnelling, and a guide for estimating support requirements. *NGI Internal Report*, 19th June.
- Barton, N.R., Lien, R. and Lunde, J. 1974b. Engineering classification of rock masses for the design of tunnel support. *Rock Mech.*, **6** (4), 189-239.
- Barton, N.R., Løset, F., Lien, R. and Lunde, J. 1980. Application of Q-system in design decisions concerning dimensions and appropriate support for underground installations. In *Subsurface Space* (ed. M. Bergmand). New York: Pergamon, **2**, 553-561.
- Bathurst, R.J. 1985. *A Study of Stress and Anisotropy in Idealized Granular Assemblies*. PhD Thesis. Dept. of Civil Engineering, Queen's University.
- Bathurst, R.J. and Rothenburg, L. 1988. Micromechanical aspects of isotropic granular assemblies with linear contact interactions. *Journal of Applied Mechanics*, **55**, 17-23.

References

- Bathurst, R.J. and Rothenburg, L. 1990. Observations on stress-force-fabric relationships in idealized granular materials. *Mechanics of Materials*, **9**, 65-80.
- Bawden W.F. 1993. The use of rock mechanics principles in Canadian hard rock mine design. *Comprehensive Rock Engineering*, Pergamon Press, **5**, 247-290.
- Bazant, Z.P. 1993. Scaling laws in mechanics of failure. *Journal of Engineering Mechanics*. **119** (9), 1828-1844.
- Bazant, Z.P. and Kazemi, M.T. 1990. Size effect in fracture of ceramics and its use to determine fracture energy and effective process zone length. *L. Am. Ceram. Soc.*, **73** (7), 1841-53.
- Bazant, Z.P. and Pfeiffer, P.A. 1987. Determination of fracture energy from size effect and brittleness number. *ACI Mat. Journal*, **84**, 463-480.
- Beer, G. and Meek, J.L. 1982. Design curves for roofs and hangingwalls in bedded rock based on voussoir beam and plate solutions. *Trans. Inst. Min. Metall*, **91**, A18-A22.
- Beer, G., Meek, J.L. and Cowling, R. 1981. Prediction of behaviour of shale hangingwalls in deep underground excavations. *5th I.S.R.M. Symposium, Melbourne*, D45-D51.
- Beichuan, H. 1991. *Damage Mechanics of Jointed Rock Masses and Application to Tunnelling*. Ph.D. Thesis. University of Innsbruck.
- Berrenbaum, R. and Brodie, I. 1959. Measurement of the tensile strength of brittle materials. *British Journal of Applied Physics*, **10**, 281-286.
- Berry, J.P. 1960. Some kinetic considerations of the Griffith criterion for fracture. Part I: Equations of motion at constant force. *J. Mech. Phys. Solids*, **8**, 194-206.
- Berry, J.P. 1960. Some kinetic considerations of the Griffith criterion for fracture. Part II: Equations of motion at constant deformation. *J. Mech. Phys. Solids*, **8**, 207-216.
- Bétournay, M.C. 1987. A Design Philosophy for Surface Crown Pillars in Hard Rock Mines. *CIM Bulletin*, 1987, **80** (90), 45-61.
- Bieniawski, Z.T. 1967. Mechanisms of brittle fracture of rock: Part I: Theory of the fracture process; Part II: Experimental studies; Part III: Fracture under tension and under long term loading. *Int J. of Rock Mech. and Min. Sci.*, **4**, 395-430.
- Bieniawski, Z.T. 1968. The effect of specimen size on the compressive strength of coal. *Int J. Rock Mech. Min. Sci.*, **5**, 325-335.

- Bieniawski, Z.T. 1989. *Engineering Rock Mass Classifications*. New York: Wiley.
- Bieniawski, Z.T. 1993. Classification of rockmasses for engineering: the RMR system and future trends. *Comprehensive Rock Engineering*, (ed. Hudson), Oxford: Pergamon, 3, 553-573.
- Bieniawski, Z.T. and Hawkes, I. 1978. Suggested methods for determining tensile strength of rock materials. *Int. J. Rock Mech. Min. Sci. & Geomech Abstr.*, 15, 99-103.
- Bieniawski, Z.T., Denkhaus, H.G. and Vogler, U.W. 1969. Failure of fractured rock. *Int. J. of Rock Mech. and Min. Sci.*, 6, 323-341.
- Bobet, A. and Einstein. H.H. 1996. Fracture coalescence in rock material under uniaxial and biaxial loading. *Rock Mechanics-NARMS '96*, (eds. Aubertin et al.), Rotterdam: Balkema, 1603-1609.
- Brace, W.F. 1960. An extension of the Griffith theory of fracture to rocks. *Journal of Geophysical Research*, 65 (10), 3477-3480.
- Brace, W.F. and Byerlee, J.D. 1968. Recent experimental studies of brittle fracture of rocks. *Proc. 8th U.S. Symp. on Rock Mechanics*, Minneapolis, (ed. Fairhurst), AIME, 58-81.
- Brace, W.F., Paulding, B.W. and Scholz, C. 1966. Dilatancy in the fracture of crystalline rocks. *Journal of Geophysical Research*, 71 (16), 3939-3953.
- Brace, W.F., Silver, E., Hadley, K. and Goetze, C. 1972. Cracks and pores, a closer look. *Science*, 178, 162-164.
- Brace, W.F., and Walsh, J.B. Some direct measurements of the surface energy of quartz and orthoclase. *Am. Miner.*, 47, 1111-1122.
- Brady, B.H.G. and Brown, E.T. 1993. *Rock Mechanics for Underground Mining*. Chapman and Hall, 1993, 571p.
- Brady, B.T. 1969. A statistical theory of brittle fracture for rock materials. Part I. Brittle failure under homogenous axisymmetric states of stress. *Int. J. Rock Mech. Min. Sci.*, 6, 21-42.
- Bremaecker and Wei. 1994. The propagation of a single shear crack: a displacement discontinuity model. *PAGEOPH*, 142 (3-4), 568-585.
- Brown E.T. and Trollope D.H. 1967. The failure of linear brittle materials under effective tensile stress. *Rock Mech. Engng Geol.*, 5, 229-241.

References

- Brummer, R.K. 1987. *Fracturing and Deformation at the Edges of Tabular Gold Mining Excavations and the Development of a Numerical Model Describing such Phenomena*. Ph.D. Thesis, Ran Afrikaans University.
- Brune, J.N. 1970. Tectonic stress and the spectra of seismic shear waves from earthquakes. *J. Geophys. Res.*, **75**, 4997-5009.
- Budiansky, B. and O'Connell, R.J. 1976. Elastic moduli of a cracked solid. *Int. J. Solids Structures*, **12**, 81-97.
- Butenuth, C. 1997. Comparison of tensile strength values of rocks determined by point load and direct tension tests. *Rock Mechanics and Rock Engineering*, **30** (1), 65-72.
- Byerlee, J.D. 1967. Frictional characteristics of granite under high confining pressure. *J. Geophysical Research*, **72**, 3639-3648.
- Byerlee, J.D. 1968. Brittle-ductile transition on rocks. *J. Geophysical Research*, **73**, 4741-4750.
- Cai, M. Kaiser, P.K. and Martin, C.D. 1998. A tension model for the interpretation of microseismic events near underground openings. *Pure and Applied Geophysics Journal, PAGEOPH*, **153**, 67-92.
- Carter, B.J. 1992. Size and stress gradient effects on fracture around cavities. *Rock Mech Rock Engng.*, **25** (3), 167-186.
- Castro, L. 1996. *Analysis of Stress-Induced Damage Initiation around Deep Openings Excavated in a Moderately Jointed Brittle Rockmass*. Ph.D. Thesis, University of Toronto.
- Castro, L., McCreath, D. and Kaiser, P.K. 1995. Rockmass strength determination from breakouts in tunnels and boreholes. *Proc. 8th ISRM Congress, Tokyo*, **2**, 531-536.
- Castro, L., McCreath, D. and Oliver, P. 1996. Rockmass damage initiation around the Sudbury Neutrino Observatory Cavern. *Rock Mechanics-NARMS '96*, (eds. Aubertin et al.), Rotterdam: Balkema, **2**, 1589-1595.
- Chelidze, T. and Guegen, Y. 1990. Evidence of fractal fracture. *Int J. Rock Mech. Min. Sci. and Geomech. Abstr.*, **27** (2), 223-225.
- Chen, R. and Stimpson, B. 1993. Interpretation of indirect tensile strength when moduli of deformation in compression and in tension are different. *Rock Mechanics and Rock Engineering*, **26** (2), 183-189.

- Cheng, H. 1994. *Continuum Damage Theory for Geomaterials and its Application to Coupling in Transport Processes*. Ph.D. Thesis, University of Waterloo.
- Cividini, A. 1993. Constitutive behaviour and numerical modelling. *Comprehensive Rock Engineering: Principles, Practice and Projects*, Oxford: Pergamon, **1**, 395-426.
- Cook, N.G.W. 1965. The failure of rock. *Int J. Rock Mech. and Min. Sci.*, **2**, 389-403.
- Cook, N.G.W. 1972. The siting of mining tunnels and other factors affecting their layout and design. *Papers and Discussions: Association of Mine Managers of South Africa*, 199-215
- Cook, N.G.W. 1995. Müller Lecture: Why rock mechanics? *Proc. Int. Cong. on Rock Mechanics. Tokyo*, (ed. Fujii), **3**, 975-994.
- Corkum, B.T. 1986. *The Discrete Element Method in Geotechnical Engineering*. M.A.Sc. Thesis, University of Toronto.
- Corlett, A.V. 1956. Rock Bolting in the Voussoir Beam: the Use of Rock Bolts in Ground Support. *CIM Bulletin*, **LIX**, 88-92.
- Costin, L.S. 1983. A microcrack model for the deformation and failure of brittle rock. *Journal of Geophysical Research*, **88** (B11), 9485-9492.
- Costin, L.S. 1985. Damage mechanics in the post-failure regime. *Mechanics of Materials*, **4**, 149-160.
- Costin, L.S. and Holcomb, D.J. 1983. A continuum model of inelastically deformed brittle rock based on the mechanics of microcracks. *Proc. Int. Conf. on Constitutive Laws for Engineering Materials*, Tucson, 185-195.
- Cotterell, B. and Rice, J.R. 1980. Slightly curved or kinked cracks. *Int. J. Fracture*, **16**, 155-169.
- Coulomb, C.A. 1773. Sur une application des règles de Maximis et Minimis a quelques problèmes de statique relatifs à l'Architecture. *Acad. Roy. des Sciences Memoires de math. et de physique par divers savans*, **7**, 343-82.
- Craig, R.F. 1992. *Soil Mechanics*. London: Chapman Hall. 427p
- Crawford, A.M. and Bray, J.W. 1983. Influence of the insitu stress field and joint stiffness on rock wedge stability in underground openings. *Canadian Geotechnical Journal*, **20**, 276-287.

References

- Crouch, S.L. 1970. Experimental determination of volumetric strains in failed rock. *Int. J. Rock Mech. Min. Sci. & Geomech. Abstr.*, **7**, 589-603.
- Cundall, P.A. 1971. A computer model for simulating progressive large scale movements in blocky rock systems. *Proc. of the Symp. of the Int. Soc. of Rock Mech.*, Nancy, France, **1**, Paper II-8.
- Cundall, P.A. 1978. BALL-A program to model granular media using the distinct element method. *Technical Note: Dames and Moore Advanced Technology Group*, London.
- Cundall, P.A. 1988. Computer simulations of dense sphere assemblies. *Micromechanics of Granular Materials*, (eds. Satake and Jenkins), Amsterdam; Elsevier, 113-123.
- Cundall, P.A. 1994a. A preliminary constitutive model for extension fracture based on micromechanics. Report to CSIR Division of Mining Technology, January.
- Cundall, P.A. 1994b. Modelling of the notch formation in the URL Mine-by Tunnel. *Report to Underground Research Laboratory, AECL*, April.
- Cundall, P.A. and Hart, R.D. 1992. Numerical modelling of discontinua. *J. Engr. Comp.*, **9**, 101-103.
- Cundall, P.A. and Hart, R.D. 1993. Numerical modelling of discontinua. *Comprehensive Rock Engineering: Principles, Practice and Projects*, Oxford: Pergamon, **2**, 231-243.
- Cundall, P.A. and Strack, O.D.L. 1979. A discrete numerical model for granular assemblies. *Geotechnique*, **29**, 47-65.
- Cundall, P.A., Drescher, A. and Strack, O.D.L. 1982. Numerical experiments on granular assemblies; measurements and observations. *IUTAM Conference on Deformation and Failure of Granular Materials*, Delft, 355-369.
- Cundall, P.A. Jenkins, J.T. and Ishibashi, I. 1989. Evolution of elastic moduli in a deforming granular assembly. *Powders and Grains*, (eds. Biarez and Gourves), Rotterdam: Balkema, 319-322.
- Cundall, P.A., Potyondi, D.O. and Lee, C.A. 1996. Micromechanics-based models for fracture and breakout around the mine-by tunnel. *Proc. Canadian Nuclear Society Int. Conf. on Deep Geological Disposal of Nuclear Waste*, Winnipeg.
- Dawson, V. 1997. Shaft Sinking at Victor. *Back to Basics: Practical Uses of Technology*, 13th Mine Operators' Conference.

- Deere, D.U. 1968. Geological considerations. *Rock Mechanics in Engineering Practice* (eds. Stagg and Zienkiewicz), London: John Wiley and Sons, 1-20.
- Desai, C.S. and Siriwardane, H.J. 1984. *Constitutive Laws for Engineering Materials, with Emphasis on Geologic Materials*. New Jersey: Prentice-Hall Inc.
- Dey, T.N. and Wang, C.Y. 1981. Some mechanisms of microcrack growth and interaction in compressive rock failure. *Int. J. Rock Mech. Min. Sci. & Geomech. Abstr.*, **18**, 199-209.
- Diederichs, M.S. 1987. *Mechanisms of Water and Humidity Dependent Effects on Rock Strength and Deformation Characteristics*. BAsC thesis, University of Toronto, 94p.
- Diederichs, M.S. and Kaiser, P.K. 1999. Tensile strength and abutment relaxation as failure control mechanisms in underground excavations. *Int. J. Rock Mech. Min. Sci. & Geomech. Abstr.*, **36**, 69-96.
- Diederichs, M.S. and Kaiser P.K. 1999. Stability of large excavations in laminated hard rock masses: the voussoir analogue revisited. *Int. J. Rock Mech. Min. Sci. & Geomech. Abstr.*, **36**, 97-117.
- Diederichs, M.S., Hutchinson, D.J. and Kaiser P.K. 1999. Cablebolt Layouts Using the Modified Stability Graph. *CIM Bulletin*. (in press).
- Dietrich, R.V. and Skinner, B.J. 1979. *Rocks and Rock Minerals*. New York: John Wiley and Sons.
- Donze, F. and Magnier, S.A. 1995. Formulation of a 3D numerical model of brittle behaviour. *Geophys. J. Int.*, **122**, 790-802.
- Donze, F., Magnier, S. and Bouchez, J. 1996. Numerical modelling of a highly explosive source in an elastic-brittle rockmass. *Journal of Geophysical Research*, **101** (B2), 3103-3112.
- Donze, F., Mora, P. and Magnier, S. 1994. Numerical simulation of faults and shear zones. *Geophys. J. Int.*, **116**, 46-52.
- Drucker, D.C. and Prager W. 1952. Soil mechanics and plastic analysis or limit design. *Quart. Appl. Math.*, **10** (2), 157-165.
- Du, Y. and Aydin, A. 1991. Interaction of multiple cracks and formation of echelon crack arrays. *Int. J. for Numerical Methods in Geomechanics*, **15**, 205-218.

References

- Duevel, B. and Haimson, B. 1997. Mechanical characterization of pink Lac du Bonnet Granite: Evidence of nonlinearity and anisotropy. *Int. J. Rock Mech. Min. Sci. & Geomech. Abstr.*, **34** (3-4), Paper No. 117.
- Dunn, D.E. 1966. Molecules crack rocks. *Science News*, **90**, 69.
- Dyskin, A.V. and Germanovich, L.N. 1993. Model of rockburst caused by cracks growing near free surface. *Rockbursts and Seismicity in Mines*. Rotterdam: Balkema, 169-174.
- Eberhardt, E., Stead, D. and Stimpson, B. 1999. Effects of sample disturbance on the stress-induced microfracturing characteristics of brittle rock. *Canadian Geotechnical Journal*, **36** (2), 239-250.
- Eberhardt, E. D. Stead, Stimpson, B. and Read, R.S. 1998. Identifying crack initiation and propagation thresholds in brittle rock. *Canadian Geotechnical Journal*, **35** (2), 222-233.
- Elsworth, D. Wedge stability in the roof of a circular tunnel: plane strain condition. *Int. J. Rock Mech. and Min. Sci. and Geomech. Abstr.*, **23** (2), 177-182.
- Evans, I., Pomeroy, C.D. and Betenbaum, R. 1961. The compressive strength of coal. *Colliery Engng.*, **38**, 123-127 and 172-178.
- Evans, W.H. 1941. The strength of undermined strata. *Trans. Inst. Min. Metall*, **50**, 475-500.
- Ewy, R.T. and Cook, N.G.W. 1990. Deformation and fracture around cylindrical openings in rock. Parts I and II. *Int J. Rock Mech. and Min. Sci. and Geomech Abstr.*, **27**, 387-427.
- Fairhurst, C. 1971. Fundamental considerations relating to the strength of rock. *Colloquium on Rock Fracture*. Dept. of Geophysics; Ruhr University, Bochum, 56p.
- Fairhurst, C. 1990. General report: deformation, yield, rupture and stability of excavations at depth in rock. *Rock at Great Depth*, (eds. Maury and Fourmaintraux), Rotterdam: Balkema, 1103-1114.
- Fairhurst, C. and Cook, N.G.W. 1966. The phenomenon of rock splitting parallel to the direction of maximum compression in the neighbourhood of a surface. *Proc. of the 1st Congress of the International Society of Rock Mechanics*, Lisbon, 687-692.
- Falls, S. 1993. *Ultrasonic Imaging and Acoustic Emission Studies of Microcrack Development in Lac du Bonnet Granite*. PhD. thesis. Queens University.

- Falmagne, V., 1999. *Quantification of Rockmass Degradation based on Microseismic Monitoring Data and Application to Mine Design*. Ph.D. Thesis (in progress), Dept. of Mining Engineering, Queen's University, Kingston, Ontario, Canada.
- Fayol, M. 1885. Sur les mouvements de terrain provoques par l'exploitation des mines. *Bull. Soc. l'Industrie Minerale*, **14**, 818.
- Feignier, B., and Young, Y.P. 1992. Moment tensor inversion of induced microseismic events: Evidence of non-shear failures in the $-4 < M < -2$ moment magnitude range. *Geophysical Research Letters*, **19** (14), 1503-1506.
- Fisher, M.P., Elsworth, D., Alley, R.B. and Engelder, T. 1996. Finite element analysis of the modified ring test for determining Mode I fracture toughness. *Int. J. Rock Mech. and Min. Sci. and Geomech. Abstr.*, **33** (1), 1-18.
- Fonseka, G.M. and Murrell, S.A.F. and Barnes, P. 1985. Scanning electron microscope and acoustic emission studies of crack development in rocks. *Int. J. of Rock Mech. and Min. Sci. and Geomech Abstr.*, **22** (5), 273-289.
- Fowell, R.J. and Xu, C. 1994. The use of the cracked Brazilian disc geometry for rock fracture investigations. *Int. J. Rock Mech. Min. Sci. & Geomech Abstr.*, **31** (6), 571-580.
- Frenkl, J. and Kontorova, T.A.A. 1943. A statistical theory of the brittle strength of real crystals. *J. Phys. U.S.S.R.*, **7**, 108.
- Georgiannopoulos, N.G. 1979. *A Critical State Approach to Rock Mechanics*. Ph.D. Thesis. University of London.
- Georgiannopoulos, N.G. and Brown, E.T. 1978. The critical state concept applied to rock. *Int. J. Rock Mech. and Min. Sci. and Geomech. Abstr.*, **15**, 1-10.
- Germanovich, L.N., Salganik R.L., Dyskin, A.V. and Lee, K.K. 1994. Mechanisms of brittle fracture of rock with pre-existing cracks in compression. *PAGEOPH*, **143** (1/2/3), 117-149.
- Gibowicz, S.J. and Kijko, A. 1994. *An Introduction to Mining Seismology*. Academic Press.
- Gibowicz, S.J., Young, R.P., Talebi, S., and Rawlence, D.J. 1991. Source parameters of seismic events at the Underground Research Laboratory in Manitoba, Canada: Scaling relations for the events with moment magnitude smaller than -2. *Bull. Seism. Soc. Am.*, **81**, 1157-1182.

References

- Gorski, B. 1991. *The tensile strength of cold spring quarry granite determined by using for different test procedures*. CANMET report MRL 91-040(TR).
- Gorski, B. and Yu, Y.S. 1991. *Tensile strength tests on URL rock samples from Borehole 401-009-HF1*. CANMET report MRL 91-080(TR).
- Gorski, B.P. and Yu, Y.S. 1996. A new laboratory test apparatus for determination of rock tensile strength. *Rock Mechanics*, (Aubertin, Hassani and Mitri eds.), Rotterdam: Balkema, 2, 1539-1542.
- Grabinsky, M. 1989. *An Angular Discrete Element Model for Geomechanics*. M.A.Sc. Thesis. Dept. of Civil Engineering, University of Toronto, 80p.
- Grabinsky, M.W.F. and Curran, J.H. 1993. Efficient mesh generation procedures for finite element analysis of underground structures. *Int. J. Rock Mech. and Min. Sci. and Geomech. Abstr.*, 30 (6), 591-600.
- Gramberg, J. 1989. *A non-conventional view on rock mechanics and fracture mechanics*. Rotterdam: Balkema, 250p.
- Greenspan, M. 1944. Effect of a small hole on the stresses in a uniformly loaded plate. *Quarterly Applied Math.*, 2, 60-71.
- Greer, G.J. 1989. Empirical modelling of open stope stability in a vertical crater retreat application at INCO's Thompson Mine. *91st Canadian Institute of Mining AGM*, 12p.
- Griffith, A.A. 1921. The phenomena of rupture and flow in solids. *Phil. Trans. Royal Soc. London*, 221A, 163-198.
- Griffith, A.A. 1924. Theory of rupture. *1st Int. Congr. Applied Mechanics*, Delft, 55-63.
- Gumbsch, P. 1995. An atomistic study of brittle fracture: toward explicit failure criteria from atomistic modelling. *J. Material Research*, 10 (11), 2897-2907.
- Gutberlet, M. 1997. *Rock softening due to microseismically-induced damage*. Diploma Thesis submitted to Geomechanics Research Centre, Laurentian University, Sudbury, Canada, March, 111p.
- Gyenge, M., Gorski, B. and Shimotani, T. 1982. *Strength determination of rocks at Copper Cliff South Mine*. CANMET Report # MRP/MRL 82-8(TR).

- Haimson, B.C. and Herrick, C.G. 1989. Borehole breakouts and insitu stress. In *Proc. 12th Annual Energy-Sources Technology Conf. and Exhibition, Drilling Symposium*. New York: American Society of Mechanical Engineers, 17-22.
- Haimson, B.C. and Zhao Z. 1991. *Laboratory hydraulic fracturing tests in Lac du Bonnet granite from the Underground Research Laboratory*. Contract Report, AECL.
- Hallbauer, D.K., Wagner, H. and Cook, N.G.W. 1973. Some observations concerning the microscopic and mechanical behaviour of quartzite specimens in stiff, triaxial compression tests. *Int. J. Rock Mech. and Min. Sci. and Geomech. Abstr.*, **10**, 713-726.
- Handley, M.F. 1995. *An Investigation into the Constitutive Behaviour of Brittle Granular Media by Numerical Experiment*. Ph.D. Thesis. University of Manitoba.
- Hart, R.D. 1993. An introduction to distinct element modelling for rock engineering. *Comprehensive Rock Engineering*, **2**, 245-261.
- Hatzor, Y.H. and Benary, R. 1998. The stability of a laminated voussoir beam: back analysis of a historic roof collapse using DDA. *Int. J. Rock Mech. and Min. Sci. and Geomech. Abstr.*, **35** (2), 165-182.
- Hatzor, Y.H. and Palchik, V. 1997. the influence of grain size and porosity on crack initiation stress and critical flaw length in dolomites. *Int. J. Rock Mech. and Min. Sci.*, **34** (5), 805-816.
- Hawkins, A.B. 1998. Aspects of rock strength. *Bulletin of Engineering Geology and the Environment*, **57** (1), 17-30.
- Heidari, A.A. 1995. *Numerical Implementation of an Advanced Constitutive Model for Granular Materials*. Ph.D. Thesis. University of Waterloo.
- Herget, G. 1988. *Stresses in Rock*. Rotterdam: Balkema.
- Hiramatsu, Y. and Oka, Y. 1966. Determination of the tensile strength of rock by a compression test of an irregular test piece. *Int. J. of Rock Mech. Min. Sci.*, **3**, 89-99.
- Hobbs, B. E., Means, W.D. Williams, Paul F. 1976. *An Outline of Structural Geology*. New York: John Wiley and Sons. 571p.
- Hobbs, B.E., Muhlhaus, H.B. and Ord, A. 1977. Instability, softening and localization of deformation. *Deformation Mechanisms, Rheology and Tectonics*, (eds. Knipe and Rutter), Geological Society Special Publication No. 54, 143-165.

References

- Hobbs, D.W. 1967. Rock tensile strength and its relationship to a number of alternative measures of rock strength. *Int J. Rock Mech. and Min. Sci.*, **4**, 115-127.
- Hoek, E. 1965. *Rock Fracture under Static Stress Conditions*. PhD Thesis. University of Cape Town.
- Hoek E. 1968. Brittle failure of rock. in *Rock Mechanics in Engineering Practice*, (ed. Stagg and Zienkiewicz), 99-124.
- Hoek, E. and Brown, E.T. 1980. *Underground Excavations in Rock*. London: Inst. of Mining and Metallurgy. 358p.
- Hoek E. and Brown, E.T. 1988. The Hoek-Brown failure criterion-a 1988 update. *Rock Engineering for Underground Excavations*, Proc. 15th Canadian Rock Mech. Symp., (ed. Curran), University of Toronto: Dept. of Civil Engineering, 31-38.
- Hoek, E. and Brown, E.T. 1998. Practical estimates of rock mass strength. *Int J. Rock Mech. and Min. Sci.*, **34** (8), 1165-1186.
- Hoek E., Kaiser, P.K. and Bawden, W.F. 1995. *Support of Underground Excavations in Hard Rock*. Rotterdam: Balkema, 215p.
- Hoek, E., Wood, D. and Shah, S. 1992. A modified Hoek-Brown criterion for jointed rockmasses. *Eurock '92*, (ed. Hudson), London: Brit. Geology Soc., 209-214.
- Holcomb, D.J. 1993. General theory of the Kaiser effect. *Int J. Rock Mech. and Min. Sci. and Geomech Abstr.*, **30** (7), 929-935.
- Holcomb, D.J. and Costin, L.S. 1986. Detecting damage surfaces on brittle materials using acoustic emissions. *Transactions of the ASME*, **53**, 536-544.
- Hommand, F., D. Hoxha, J.F. Shao, M. Sibai, G. Duveau. 1995. *Endommagement de granites et de marnes: Essais mecaniques, identification des parameters d'un modele d'endommagement et simulation*. Final Report B RP O.ENG/O.LML 95.015. ENGS Laboratoire de Géomécanique, Nancy.
- Hommand-Etienne, F. Hoxha, D. and Shao, J.F. 1998. A continuum damage constitutive law for brittle rocks. *Computers and Geotechnics*, **22** (2), 135-151.
- Hondros, G. 1959. The evaluation of Poisson's ratio and the modulus of materials of a low tensile resistance by the Brazilian (indirect tensile) test with particular reference to concrete. *Aust. J. Appl. Sci.*, **10**, 243-264.

- Horn, H.M. and Deere, D.H. 1962. Frictional characteristics of minerals. *Geotechnique*, **12**, 319-335.
- Howarth, D.F. 1987. The effect of pre-existing microcavities on mechanical rock performance in sedimentary and crystalline rocks. *Int. J. Rock Mech. and Min. Sci. and Geomech Abstr.*, **24** (4), 223-234.
- Hudson, J.A. 1969. Tensile strength and the ring test. *Int. J. Rock Mech and Min. Sci.*, **6**, 91-97.
- Hudson, J.A., Liu, E. and Crampin, S. 1996. The mechanical properties of materials with interconnected cracks and pores. *Geophys. J. Int.*, **124**.
- Hutchinson, D.J. 1998. *Intersection Support Demand Assessment Guidelines*. Report to INCO Mines Technical Services.
- Hutchinson, D.J. and Diederichs, M.S. 1996. *Cablebolting in Underground Mines*. Bitech Publishers: Vancouver, 416p.
- Illston, J.M., Dinwoodie, J.M. and Smith, A.A. 1979. *Concrete, Timber and Metals*. New York: Van Nostrand Reinhold, 663p.
- Inco Limited. 1991. *Simulation of bulk mining at depth with backfill on Ontario mines*. Mines Research Department, March.
- Ingraffea, A.R. and Schmidt, R.A. 1978. Experimental verification of a fracture mechanics model for tensile strength prediction of Indiana limestone. in *Proc. 19th U.S. Symposium of Rock Mech*, Reno: Univ. Nevada, 247.
- International Society for Rock Mechanics Commission on Standardization of Laboratory and Field Tests. 1978. Suggested methods for determining the tensile strength of rock materials. *Int. J. Rock Mech. and Min. Sci. and Geomech Abstr.* **15**, 99-103.
- International Society for Rock Mechanics Commission on Standardization of Laboratory and Field Tests. 1979. Suggested methods for determining the uniaxial compressive strength and deformation of rock materials. *Int. J. Rock Mech. and Min. Sci. and Geomech Abstr.* **15**, 319-368.
- Irwin, G.R. 1957. Analysis of stresses and strains near the ends of a crack traversing a plate. *J. Appl. Mech.*, **24**, 361-364.
- Itasca 1996. *UDEC: Universal Distinct Element Code*. Version 3.00
- Itasca, 1995a *PFC-Particle Flow Code. Modelling Software*. Version 1.0. Itasca Ltd.

References

- Itasca, 1995b *FLAC-Fast Lagrangian Analysis of Continua*. Modelling software. Version 3.3. Itasca Ltd.
- Jaeger, J.C. 1967. Failure of rocks under tensile conditions. *Int. J. Rock Mech. and Min. Sci.*, **4**, 219-227.
- Jaeger J.C. and Cook, N.G.W. 1971. *Fundamentals of Rock Mechanics*. London: Chapman and Hall. 514p.
- Jain, S.K. 1980. *Fundamental Aspects of the Normality Rule*. Blacksburg: Engineering Publications, 168p.
- Jardine, A.K.S. 1973. *Maintenance, Replacement and Reliability*. London: Pitman. 200p
- Jiayou, L., Lihui, D., Chengjie, Z. and Zebin, W. 1991. The brittle failure of rock around underground openings. *Proc. Conf. on Rock Mech and Rock Physics at Great Depth. Pau France*. (ed. Maury and Fourmaintraux).Rotterdam: Balkema **2**. 567-574.
- Kachanov, M. 1980. Continuum model of a medium with cracks. *J. Eng. Mech.*, **106**, 1039-1051.
- Kaiser, P.K. 1994. Observational modelling approach for design of underground excavations. *SANGORM '94*, Pretoria: I.S.R.M, 1-7.
- Kaiser, P.K., 1995. Observational modelling approach for design of underground excavations. *Proc. Int. Workshop on Observational Method of Construction of Large Underground Caverns in Difficult Ground Conditions*, Tokyo, 1-17.
- Kaiser, P.K. and Maloney, S., 1992. The role of stress change in underground mining. *Eurock '92*, Balkema, Rotterdam. 396-401.
- Kaiser, P.K. and McCreath, D.R. 1993. Rock mechanics considerations for drilled or bored excavations in hard rock. *Tunnelling and Underground Space Technology*, **9** (4), 425-437.
- Kaiser, P.K. and Tang, C.A. 1998. Numerical simulation of damage accumulation and seismic energy release in unstable failure of brittle rock-Part II: Rib pillar collapse. *Int Journal of Rock Mech., Min Sci. and Geomech Abstr.* **35** (2), 123-134.
- Kaiser, P.K., Diederichs, M. and Yazici, S. 1992. Cablebolt performance during mining induced stress change-three case examples. *Rock Support in Mining and Underground Construction*, (eds. Kaiser and McCreath), Rotterdam: Balkema, 377-384.

- Kaiser, P.K., Falmagne, V., Suorineni, F.T., Diederichs, M. and Tannant, D.D., 1997. Incorporation of rockmass relaxation and degradation into empirical stope design. 99th Canadian Institute of Mining AGM.
- Kaiser, P.K., McCreath, D. and Tannant, D. 1995. *Canadian Rockburst Support Handbook*. Sudbury: Geomechanics Research Centre.
- Kaiser, P.K., McCreath, D. and Tannant, D. 1996. Overview of the Canadian Rockburst Support Handbook. *CIM-AGM 96*, Edmonton.
- Kaiser, P.K., Yazici, S. and Nosé, J. 1992. Effect of stress change on the bond strength of fully grouted cables. *Int J. of Rock Mech. Min. Sci & Geomech. Abstr.*, **29** (3), 293-306.
- Kaiser, P.K., Yazici, S., and Maloney, S. 1999. Mining-induced stress change and consequences of stress path on excavation stability - A Case Study. *Int. J. of Rock Mech. Min. Sci & Geomech. Abstr.*, May.
- Kelly, D., Peck, D.C. and James, R.S. 1993. *Petrography of granitic samples form the 420m Level of the Underground Research Laboratory, Pinawa, Manitoba*. Contractor's report to AECL Research, Laurentian University.
- Kemeny, J.M. and Cook, N.G.W. 1986. Effective moduli, non-linear deformation and strength of a cracked elastic solid. *Int. J. Rock Mech. and Min. Sci. and Geomech. Abstr.*, **23** (2), 107-118.
- Kemeny, J.M. and Cook, N.G.W. 1987. Crack models for the failure of rocks in compression. *Constitutive Laws for Engineering Materials: Theory and Applications*, (eds. Desai et al.), Amsterdam: Elsevier, **2**, 879-887.
- Kirsten, H.A.D. and Klokow J. 1979 Control of fracturing in mine rock passes. *Proc. 4th. Int. Congr. ISRM, Montreux*, **1**, 203-210.
- Kittl, P., Leon, M., Diaz, G. and Lillo, A. 1990. Probabilistic compressive strength of sound dry granite. *Rock Mechanics and Rock Engineering*, **23**, 21-28.
- Koiter, W.T. 1961. An infinite row of parallel cracks in an infinite elastic sheet. *Problems of Continuum Mechanics*, (ed. Radok), Philadelphia, Soc. Indust. and Appl. Mathematics.
- Kostak, B. and Bielenstein, H.U. 1971. Strength distribution in hard rock. *Int. J. Rock Mech. Min. Sci.*, **8**, 501-521.

References

- Krajcinovic, D. and Fonseka, G.U. 1981. The continuous damage theory of brittle materials. Part I: General theory. *Journal of Applied Mechanics*, **48**, 809-815.
- Kranz, R.L. 1979. Crack growth and development during creep of Barre Granite. *Int. J. Rock Mech. and Min. Sci. and Geomech. Abstr.*, **16**, 23-35.
- Krech, W.W. 1974. The energy balance theory and rock fracture energy measurements for uniaxial tension. in *Advances in Rock Mechanics, Proc. 3rd Congress of the Int. Soc. for Rock Mech.*, Denver., **VII**, Part A., 167-173.
- Krishnan G.R., Zhao, X.L. Zaman, M and Roegiers, J.C. 1998. Fracture toughness of soft sandstone. *Int. J. Rock Mech. and Min. Sci.*, **35** (6), 695-710.
- Kruyt, N.P. and Rothenburg, L. 1996. Micro-mechanical definition of the strain tensor for granular materials. (*draft paper*).
- Kuijpers, J.S. and Napier, J.A.L. 1996. Effective growth rules for macro fracture simulation in brittle rock under compression. *Eurock '96.*, Turin, Rotterdam: Balkema.
- Kulatilake, P. Panda, B.B. and Wang, S. 1996. Possible correlations between rockmass properties and fracture tensor parameters. *Rock Mechanics-NARMS '96*, (eds. Aubertin et al.), Rotterdam: Balkema, 1193-1200.
- Kulatilake, P.H.S.W. and Wu, T.H. 1984. Estimation of mean trace length of discontinuities. *Rock Mechanics and Rock Engineering*, **17**, 215-232.
- Labuz, J.F., Shah, S.P. and Dowding, C.H. 1987. The fracture process zone in granite: evidence and effect. *Int. J. Rock Mech. Min. Sci. & Geomech. Abstr.*, **24** (4), 235-246.
- Lade, P.V. 1993. Rock strength criteria: The theories and the evidence. *Comprehensive Rock Engineering: Principles, Practice and Projects*, Oxford: Pergamon, **1**, 255-284.
- Lajtai, E.Z. 1969. Strength of discontinuous rocks in direct shear. *Geotechnique*, **19** (2), 218-233.
- Lajtai, E. Z. 1988. *The deformation, fracture and strength of Lac du Bonnet granite*. Research Report 19. University of Manitoba. Geological Engineering Dept.
- Lajtai, E. Z. and Bielus, L. P. 1986. Stress corrosion cracking of Lac du Bonnet granite in tension and compression. *Rock Mechanics and Rock Engineering*, **19**, 71-87.
- Lajtai, E.Z., Carter, B.J. and Duncan, E.J.S. 1994. En echelon crack-arrays in Potash Salt Rock. *Rock Mechanics and Rock Engineering*, **27** (2), p89-111.

- Lajtai, E.Z. and Dzik, E.J. 1996. Searching for the damage threshold in intact rock. *Rock Mechanics*, (Aubertin, Hassani and Mitri eds.), Rotterdam: Balkema, 701-708.
- Lajtai, E.Z., Schmidtke, R.H. and Bielus, L.P. 1987. The effect of water on the time dependent deformation and fracture of a granite. *Int. J. Rock Mech. Min. Sci. & Geomech. Abstr.*, **24** (4), 247-256.
- Lama, R.D. and Vutukuri, V.S. 1978. *Handbook on Mechanical Properties of Rocks (Volumes I to IV)*. Germany: TransTech.
- Landriault, D. and Oliver, P. 1992. The distress slot concept for bulk mining at depth. *Rock Support in Mining and Underground Construction*, (eds. Kaiser and McCreath), Rotterdam: Balkema, 211-217.
- Lang, T.A. and Bischoff, J.A. 1984. Stability of reinforced rock structure. *Design and Performance of Underground Excavations* (eds. Brown and Hudson). London: British Geotechnical Society, 11-18.
- Laqueche, H. Rousseau, A. and Valentin, G. 1986. Crack propagation under Mode I and II loading in slate schist. *Int. J. Rock Mech. Min. Sci. & Geomech. Abstr.*, **23** (5), 347-354.
- Laubscher, D.H. 1977. Geomechanics classification of jointed rock masses-Mining applications. *Trans. Inst. Min. Metall.*, **86**, A1-A8.
- Lauffer, H. 1958. Gebirgsklassifizierung für den Stollenbau. *Geology, Bauwesen*, **24** (1), 46-51.
- Lee, M.Y. and Haimson, B.C. 1993. Laboratory study of borehole breakouts in Lac du Bonnet Granite: A case of extensile failure mechanism. *Int. J. Rock Mech. Min. Sci. and Geomech. Abstr.*, **30** (7), 1039-1045.
- Li, C. and Nordlund, E. 1993. Experimental verification of the Kaiser effect in rocks. *Rock Mechanics and Rock Engineering*, **26**, 333-351.
- Li, C., Prikryl, R. and Nordlund, E. 1998. The stress-strain behaviour of rock material related to fracture under compression. *Engineering Geology*, **49**, 293-302.
- Liao, J.J., Yang, M.T. and Hsieh, H.Y. 1997. Direct tensile behaviour of transversely isotropic rock. *Int. J. Rock Mech. Min. Sci.*, **34** (5), 837-850.
- Lim, I.L., Johnston, I.W., Choi, S.K. and Boland, J.N. 1994. Fracture testing of a soft rock with semi-circular specimens under three-point bending. Part 2: Mixed mode. *Int. J. Rock Mech. and Min. Sci. and Geomech. Abstr.*, **31** (3), 199-212.

References

- Liu, Z.L., Myer, L.R. and Cook, N.G.W. 1994. Numerical simulation of the effects of heterogeneities on macro-behaviour of granular materials. *Computer Methods and Advances in Geomechanics*, (eds. Siriwardane and Zaman), 611-616.
- Lockner, D. 1993. The role of acoustic emission in the study of rock. *Int. J. Rock Mech. and Min. Sci. and Geomech. Abstr.*, **30** (7), 883-899.
- Lockner, D.A., Moore, D.E. and Reches, Z. 1992. Microcrack intersection leading to fracture. *Rock Mechanics*, (eds. Tillerson and Wawersik), Rotterdam: Balkema, 807-816.
- Lundborg, N. 1967. The strength-size relation of granite. *Int. J. Rock Mech. and Min. Sci.*, **4**, 269-272.
- Lundborg, N. 1968. Strength of rock-like materials. *Int. J. of Rock Mech. Min. Sci.*, **5**, 427-454.
- Madden, T.R. 1984. Microcrack connectivity in rocks: a renormalization group approach to the critical phenomena of conduction and failure in crystalline rocks. *J. Geophys. Res.*, **88**, 585-592.
- Madariaga, R. 1976. Dynamics of an expanding circular fault. *Bull. Seismol. Soc. Am.*, **66**, 639-666.
- Malan, D.F., Napier, J.A.L. and Watson, B.P. 1994. Propagation of fractures from an interface in a Brazilian test specimen. *Int. J. Rock Mech. Min. Sci. & Geomech Abstr.*, **31**(6), 581-596.
- Maloney, S., Fearon, R., Nosé, J. and Kaiser, P.K. 1992. Investigations into the effect of stress change on support capacity, *Rock Support in Mining and Underground Construction*, Balkema, Rotterdam, 367-376.
- Maloney, S.M. and Kaiser, P.K. 1991. Stress change and deformation monitoring for mine design: A case study. *Field Measurements in Geomechanics*, Balkema, Rotterdam, 481-490.
- Maloney, S.M. and Kaiser, P.K. 1993. *Field Investigation of Hanging Wall Support by Cable Bolt Pre-reinforcement at Winston Lake Mine*. Research Report, Geomechanics Research Centre, Laurentian University, Canada, 140p.
- Martin, C.D. 1989. Failure observations and insitu stress domains at the Underground Research Laboratory. *Proc. Conf. on Rock Mech. and Rock Physics at Great Depth*, Pau, France. (eds. Maury and Fourmaintraux), Rotterdam: Balkema, **2**, 719-726.

- Martin, C.D. 1994. *The Strength of Massive Lac du Bonnet Granite around Underground Openings*. Ph.D. Thesis. University of Manitoba.
- Martin, C.D. 1995. Brittle rock strength and failure: Laboratory and in situ. *Proc. ISRM Congress*. Tokyo.
- Martin, C.D. 1997. Seventeenth Canadian Geotechnical Colloquium: The effect of cohesion loss and stress path on brittle rock strength. *Can. Geotech. J.*, **34** (5), 698-725.
- Martin, C.D. and Chandler, N.A. 1994. The progressive fracture of Lac du Bonnet granite. *Int. J. of Rock Mech and Min. Sci and Geomech. Abstr.*, **31** (6), 643-659.
- Martin, C.D. Diederichs, M. and Hajiabdolmajid, V. 1998. Damage mechanisms in brittle rock masses. *Proc. of the Canadian Geotechnical Society*.
- Martin, C.D., Kaiser, P.K. and Alcott, J.A. 1996. Predicting the depth of stress-induced failure around underground openings. *49th Canadian Geotechnical Conference*, St. John's, **1**, 105-114.
- Martin, C.D., Kaiser, P.K. and Maybee, G. 1998. A failure criterion for the stability of drifts and pillars. *CIM AGM*, Montreal, 8p.
- Martin, C.D., Kaiser, P.K. and McCreath, D.R. 1998. Hoek-Brown parameters for predicting the depth of brittle failure around tunnels. *Canadian Geotechnical Journal*. (Accepted)
- Martin, C.D. and Read, R.S. 1996. AECL's mine-by experiment: A test tunnel in brittle rock. *Rock Mechanics-NARMS '96*, (eds. Aubertin et al.), Rotterdam: Balkema, 13-24.
- Martin C.D., Read, R.S. and Martino, J.B. 1997. Observation of brittle failure around a circular test tunnel. *Int. J. of Rock Mech. and Min. Sci.*, **34** (7), 1065-1073.
- Martin, C.D. and Stimpson, B. 1994. The effect of sample disturbance on laboratory properties of Lac du Bonnet granite. *Can. Geot. J.*, **31**, 692-702.
- Martin, C.D., Young, R.P. and Collins, D.S. 1995. Monitoring progressive failure around a tunnel in massive granite. *Proc. ISRM Congress*, Tokyo, 9p.
- Mastin, L.G. 1984. *Development of Borehole Breakouts in Sandstone*. M.S.Thesis. Stanford University, Palo Alto, California, 101p.
- Mathews, K.E., Hoek, E., Wyllie, D.C. and Stewart, S.B.V. 1981. *Prediction of stable excavations for mining at depth below 1000 metres in hard rock*. CANMET Report DSS

References

- Serial No. OSQ80-00081, DSS File No. 17SQ.23440-0-9020, Ottawa: Dept. Energy, Mines and Resources, 39p.
- McClintock, F.A. and Walsh, J.B. 1963. Friction on Griffith cracks in rocks under pressure. *Proc. 4th U.S. National Congress on Applied Mechanics, AIME*, **2**, 1015-1021.
- McCreath, D. and Diederichs, M.S. 1994. Assessment of near-field rock mass fracturing around a potential nuclear fuel waste repository in the Canadian Shield. *Int. J. of Rock Mech and Min. Sci and Geomech. Abstr.*, **31** (5), 457-470.
- McGarr, A. 1976. Seismic moments and volume changes. *J. Geophys. Res.*, **81**, 1487-1494.
- McGarr, A. 1984. Some applications of seismic source mechanism studies to assessing underground hazard. In *Rockburst and Seismicity in Mines* (eds. Gay and Wainwright), South African Inst. Min. Metal., 199-208.
- Mendecki, A.J. 1997. Quantitative seismology and rock mass stability. In *Seismic Monitoring in Mines*, London: Chapman and Hall, (ed. Mendecki), Chapter 10, 178-219.
- Miller, F. and Choquet, P. 1988. Analysis of the failure mechanism of a layered roof in long hole stopes at Mines Gaspé. *90th CIM AGM*, Edmonton, Paper No. 120.
- Milne, D. 1996. *Underground Design and Deformation based on Surface Geometry*. Ph.D. Thesis, Dept. of Mining and Mineral Processing, University of British Columbia.
- Milne, D., Pakalnis, R.C. and Felderer, M. 1996. Surface geometry assessment for open stope design. *Rock Mechanics: Proc. Of the 2nd North American Rock Mechanics Symposium*, Balkema, Rotterdam, **1**, 315-322.
- Milne, D.M., Pakalnis, R.C. and Lunder, P.J. 1995. Approach to the quantification of hanging-wall behaviour. *Trans. Instn. Min. Metall.*, **105**, A69-A74.
- Mindlin, R.D. 1949. Compliance of elastic bodies in contact. *J. Appl. Mech.*, **16**, 259-268.
- Mogi K. 1966. Pressure dependence of rock strength and transition from brittle fracture to ductile flow. *Bull. Earthquake Res. Inst. Japan*, **44**, 215-232.
- Moore, D.E. and Lockner, D.A. 1995. The role of macrocracking in shear-fracture propagation in granite. *Journal of Structural Geology*, **17** (1), 95-114.
- Mottahed, P. and Ran, J. 1995. Design of jointed roof in stratified rock based on the Voussoir beam mechanism. *Canadian Institute of Mining Bulletin*, **88** (994), 56-62.

- Mulhaus, H. 1993. Continuum models for layered and blocky rock. *Comprehensive Rock Engineering: Principles, Practice and Projects*, Oxford: Pergamon, 2, 209-230.
- Murrell, S.A.F. 1963. A criterion for brittle fracture of rocks and concrete under triaxial stress and the effect of pore pressure on the criterion. Proc. Fifth Rock Mech. Symp., Univ. of Minnesota, in *Rock Mechanics* (ed. Fairhurst) Oxford: Pergamon. 563-577.
- Murrell, S.A.F. 1965. The effect of triaxial stress systems on the strength of rocks at atmospheric temperatures. *Geophys. J.*, 10, 231-281.
- Myer, L.R., Kemeny, J.M. Zheng, Z., Suarez, R., Ewy, R.T. and Cook, N.G.W. 1992. Extensile cracking in porous rock under differential compressive stress. Micromechanical modelling of quasi-brittle materials behaviour, (ed. Li), *Applied Mechanics Reviews*, 45 (8), August, 263-280.
- Napier, J.A.L. and Hildyard, M.W. 1992. Simulation of fracture growth around an opening in highly stressed, brittle rock. *J. S. Afr. Inst. Min. Metall.*, 92 (6), 159-168.
- Nasseri, M.H., Rao, K.S. and Ramamurthy, T. 1997. Anisotropic behaviour of schistose rocks and effect of confining pressure on them. *Environmental and Safety Concerns in underground Construction*, (eds. Lee, Yang and Chung) Balkema, Rotterdam, 445-450.
- Nemat-Nasser, S. and Horii, H. 1980. Compression-induced nonplanar crack extension with application to splitting, exfoliation and rockburst. *Journal of Geophysical Research*, 87 (B8), 6805-6821.
- Newman, D.A. and Bennett, D.G. 1990. The effect of specimen size and stress rate for the Brazilian test – A statistical analysis. *Rock Mechanics and Rock Engineering*, 23, 123-134.
- Nickson, S.D. 1992. *Cable Support Guidelines for Underground Hard Rock Mine Operations*. M.A.Sc. Thesis, Dept. of Mining and Mineral Processing, University of British Columbia, 343p.
- Novello, E.A. and Johnston, I.W. 1995. Geotechnical materials and the critical state. *Geotechnique*, 45 (2), 223-235.
- Obert, L. and Duvall, W.I. 1966. *Rock Mechanics and the Design of Structures in Rock*. John Wiley and Sons, Inc., 649p.
- Oda, M. 1982. Fabric tensor for discontinuous geological materials. *Soils and Foundations*, 22 (4), 96-107.

References

- Oda, M. 1983. A method for evaluating the effect of crack geometry on the mechanical behaviour of cracked rock masses. *Mechanics of Materials*, **2**, 163-171.
- Oda, M., Konishi, J. and Nemat-Nasser, S. 1982. Experimental micromechanical evaluation of strength of granular materials: Effects of particle rolling. *Mechanics of Materials*, **1**, 269-283.
- Oda, M. Yamabe, T. and Kamemura, K. 1986. A crack tensor and its relation to wave velocity anisotropy in jointed rock masses. *Int. J. of Rock Mech. and Min. Sci. and Geomech. Abstr.*, **23** (6), 387-397.
- Okubo, S. and Fukui, K. 1996. Complete stress-strain curves for various rock types in uniaxial tension. *Int. J. Rock Mech. Min. Sci. and Geomech. Abstr.*, **33** (6), 549-556.
- Olsson, W.A. and Peng, S.S. 1976. Microcrack nucleation in marble. *Int. J. of Rock Mech. and Min. Sci. and Geomech. Abstr.*, **13**, 53-59.
- Onagi, D.P., Keith S.G. and Kuzyk, G.W. 1992. Non-explosive excavation technique developed for the excavation of AECL's Mine-by experiment test-tunnel at the URL. *Proc. 10th TAC Annual Canadian Tunneling Conference*, Vancouver: BiTech Publishers, 1-11.
- Ormonde, R. and Szwedzicki, T. 1993. Monitoring of post failure pillar behaviour. *Geotechnical Instrumentation in Open Pit and Underground Mining*, (ed. Szwedzicki), Rotterdam: Balkema.
- Ortlepp, W.D. 1997. *Rock Fracture and Rockbursts - An Illustrative Study*. Monograph Series M9. South African Institute of Mining and Metallurgy. Johannesburg.
- Ortlepp, W.D. and Gay, N.C. 1984. Performance of an experimental tunnel subjected to stresses ranging from 50 MPa to 230 MPa. *Proc. ISRM. Symp: Design and Performance of Underground Excavations* (eds. Brown and Hudson), London: British Geotechnical Society, 337-346
- Ortlepp, W.D., O'Ferral, R.C. and Wilson, J.W. 1972. Support methods in tunnels. *Assoc. Mine Managers of South Africa: Papers and Discussions*, 167-195.
- Ortlepp, W.D. and Stacey, T.R. 1994. Rockburst mechanisms in tunnels and shafts. *Tunnelling and Underground Space Technology*, **9** (1), 59-65.
- Ouchterlony, F. 1982. *Fracture toughness testing of rock*. Part 2 of Lectures at the CISM. SveDeFo Rep. DS 1982:5

- Pan, X.D. and Hudson, J.A. 1988. A simplified three dimensional Hoek-Brown yield criterion. *Rock Mechanics and Powerplants*, (ed. Romana), Rotterdam: Balkema, 85-103.
- Paris, P.C. and Shi, G.C. 1965. Stress analysis of cracks. in *Fracture Toughness Testing and its Applications*. ASTM STP 381. p30-83.
- Parker, J. 1970. Temperature and humidity affect strength of rock structures at White Pine. *Transactions of the Society of Mining Engineers of AIME*, **247** (1), 142-144.
- Passas, N, Butenuth, C. de Freitas, M.H. 1998. Strain associated with failure in tension for a porous rock. *Bulletin of Engineering Geology and the Environment*, **57** (1), 31-40.
- Paul, B. 1961. Modification of the Coulomb-Mohr theory of fracture. *J. Appl. Mech.*, **28**, 259-268.
- Pelli, F., Kaiser, P.K. and Morgenstern, N.R. 1991. An interpretation of ground movements recorded during construction of the Donkin-Morien tunnel. *Can. Geotech. Journal*, **28** (2), 239-254.
- Peng, S.D. 1971. Stresses within elastic circular cylinders loaded uniaxially and triaxially. *Int. J. Rock Mech. Min. Sci. & Geomech. Abstr.*, **8**, 399-432.
- Pestman, B.J. and Van Munster, J.G. 1996. An acoustic emission study of damage development and stress-memory effects in sandstone. *Int. J. Rock Mech. Min. Sci.*, **33** (6), 585-593.
- Pietgen, H.O. and Saupe, D. 1988. *The Science of Fractal Images*. New York: Springer Verlag. 312p.
- Pollard, D.D. and Segall, P. 1987. Theoretical displacements and stresses near fractures in rock: with applications to faults, joints, veins, dykes and solution surfaces. *Fracture Mechanics of Rock*, Academic Press, London, 277-351.
- Potvin, Y. 1988. *Empirical Open Stope Design in Canada*. Ph.D. Thesis, Dept. of Mining and Mineral Processing, University of British Columbia, 343p.
- Potvin, Y. and Milne, D. 1992. Empirical cablebolt support design. *Rock Support*, (eds. Kaiser and McCreath), Rotterdam: A.A.Balkema, 269-275.
- Potyondi, D. and Cundall, P.A. 1998. Modelling notch-formation mechanisms in the URL Mine-by test tunnel using bonded assemblies of circular particles. *Int. J. Rock Mech. Min. Sci.*, **35** (4-5), Paper No. 67.

References

- Potyondi, D., Cundall, P.A. and Lee, C. 1995. *Modelling of notch formation in the URL Mine-By Tunnel. Phase I: Micromechanical experiments*. Report to AECL.
- Potyondi, D., Cundall, P.A. and Lee, C. 1996. *Modelling of notch formation in the URL Mine-By Tunnel. Phase II: Tunnel Simulations*. Report to AECL.
- Price, N.J. and Cosgrove, J.W. 1990. *Analysis of Geological Structures*. Cambridge: Cambridge University Press, 502p.
- Priest, S.D. and Hudson, J.A. 1981. Estimation of discontinuity spacing and trace length using scanline surveys. *Int. J. Rock Mech. Min. Sci. & Geomech. Abstr.*, **18**, 183-197.
- Priest, S.D. and Selvakumar, S. 1982. The failure characteristics of selected British rocks. *Report to Department of the Environment and Transport*, London, 65-123.
- Pritchard, C.J. and Hedley, D.G.F. 1993. Progressive pillar failure and rockbursting at Denison Mine. *Proc. of the Symp. of Rockbursts and Seismicity in Mines*, (ed Young), Rotterdam: Balkema, 111-116.
- Pusch, R., and Stanfors, R. 1992. The Zone of Disturbance around Blasted Tunnels at Depth. *Int. J. Rock Mech. Min. Sci. & Geomech. Abstr.*, **29** (5), 447-456.
- Quadfel, H. 1998. *Numerical Simulations of Granular Assemblies with Three-Dimensional Ellipsoid-Shaped Particles*. PhD Thesis, Dept. of Civil Engineering, University of Waterloo, 299p.
- Ran, J.Q., Passaris, E.K.S. and Mottahed, P. 1994. Shear Sliding Failure of the Jointed Roof in Laminated Rock Mass. *Rock Mechanics and Rock Engineering*, **27** (4), 235-251.
- Read, R.S. 1994. *Interpreting Excavation Induced Displacements around a Tunnel in Highly Stressed Granite*. Ph.D. Thesis. University of Manitoba.
- Read, R.S., Chandler, N.A. and Dzik, E.J. 1998. In situ strength criteria for tunnel design in highly stressed rock masses. *Int. J. Rock Mech. and Min. Sci.*, **35** (3), 319-368.
- Read, R.S. and Martin, C.D. 1991. Monitoring the excavation-induced response of granite. *Proc. 33rd U.S. Symposium on Rock Mechanics*, Rotterdam: Balkema, 201-210.
- Reyes, O. 1991. *Experimental Study and Analytical Modelling of Compressive Fracture in Brittle Materials*. Ph.D. Thesis. Massachusetts Institute of Technology.
- Rothenburg, L. 1980. *Micromechanics of Idealized Granular Systems*. Ph.D. Thesis. Carleton University.

- Rothenburg, L. 1986. An advanced constitutive model for granular materials. *Report to Gulf Canada Resources Ltd. WRI 450-09.*
- Rothenburg, L. and Bathurst, R.J. 1989. Analytical study of induced anisotropy in idealized granular materials. *Geotechnique*, **4** (4), 601-614.
- Rothenburg, L. and Dusseault, M.B. 1987. Application of a new constitutive model for granular materials to oil sands. *Progress Report to Alberta Oil Sands Technology and Research Authority*, Dept. of Civil Engineering, University of Waterloo, 144p.
- Rudnicki, J.W. and Rice, J.R. 1975. Conditions for the localization of deformation in pressure-sensitive dilatant materials. *J. Mech. Phys. Solids*, **23**, 371-394.
- Sammis C.G. and Ashby, M.F. 1986. The failure of brittle porous solids under compressive stress states. *Acta Metall.*, **34** (3), 511-526.
- Schmertman, J.H. and Osterberg, J.O. 1968. An experimental study of the development of cohesion and friction with axial strain in saturated cohesive soils. *Proc. ASCE Research Conference on Shear Strength of Cohesive Soils*, 643p.
- Schlangen, E. and Van Mier, J.G.M. 1995. Crack propagation in sandstone: combined experimental and numerical approach. *Rock Mechanics and Rock Engineering*, **28** (2), 93-110.
- Schmidtke, R.H. and Lajtai, E.Z. 1985. The long term strength of Lac du Bonnet granite. *Int. J. Rock Mech and Min. Sci. and Geomech Abstr.*, **22** (6), 461-465.
- Scholtz, C.H. 1968. Experimental study of the fracturing process in brittle rock. *Journal of Geophysical Research*, **73** (4), 1447-1454.
- Scholtz, C.H. 1968. Microfracturing and the inelastic deformation of rock in compression. *J. Geophysical Research*, **73** (4), 1417-1432.
- Schroeder, W.J. and Shepard, M.S. Geometry based fully automatic mesh generation and the Delaunay triangulation. *Int. J. Numer. Meth. Engng.* **26**, 2503-2515
- Scott, D.R. 1996. Seismicity and stress rotation in a granular model of the brittle crust. *Nature*, **381**, 592-595.
- Sellers, E.J. 1994. *An Anisotropic Damage Model for Rock*. Ph.D. Thesis, University of Capetown.

References

- Serafim, J.L. and Pereira, J.P. 1983. Considerations of the geomechanical classification of Bieniawski. *Proc. Int. Symp. Engineering Geology and Underground Construction*. LNEC, Lisbon, 1, II.33-II.42.
- Serata, S. 1961. Transition from elastic to plastic states of rocks under triaxial compression. *Proc. 4th Symposium on Rock Mech. Penn. State. Univ.*, 73p.
- Shah, K.R. and Labuz, J.F. 1995. Damage mechanisms in stressed rock from acoustic emission. *Journal of Geophysical Research*, **100** (B8), 15527-15539.
- Shah, S. 1992. *A Study of the Behaviour of Jointed Rock Masses*. PhD Thesis. Dept. Civil Engineering, University of Toronto.
- Sih, G.C. 1973. *Handbook of Stress Intensity Factors*. Inst. of Fracture and Solid Mechanics, Lehigh University, Bethlehem.
- Simpson, D.R. and Fergus, J.H. 1968. The effect of water on the compressive strength of diabase. *Journal of Geophysical Research*, **73** (20), 6591-6594.
- Sinkankas, J. 1964. *Mineralogy*. New York: Van Nostrand Reinhold, 585p.
- Smith, E. 1995. The size effect expression for an elastic softening material. *Mechanics of Materials*, **19**, 261-270.
- Snyder, V.W. 1983. Analysis of Beam Building using Fully Grouted Roof Bolts. *Proc. Of the Int. Symp. on Rock Bolting*, Balkema, Rotterdam, 187-194.
- Sofianos, A.I. 1986. Stability of rock wedges in tunnel roofs. *Int. J. Rock Mech. and Min. Sci. and Geomech. Abstr.*, **23** (2), 119-130.
- Sofianos, A.I. 1996. Analysis and Design of an Underground Hard Rock Voussoir Beam Roof. *Int. J. Rock Mech. Min. Sci. & Geomech. Abstr.*, **33** (2), 153-166.
- Sofianos, A.I. and Kapenis, A.P. 1998. Numerical evaluation of the response in bending of an underground hard rock voussoir beam roof.. *Int. J. Rock Mech. Min. Sci. & Geomech. Abstr.*, **35** (8), 1071-1086.
- Sprunt, E.S. and Brace, W.F. 1974. Direct observation of microcavities in crystalline rocks. *Int J. Rock Mech. Min Sci. & Geomech. Abstr.*, **11**, 139-150.
- Stacey, T.R. 1981. A simple extension strain criterion for fracture of brittle rock. *Int. J. of Fracture*, **18**, 469-474.

- Stacey, T.R. and De Jongh C.L. 1977. Stress fracturing around a deep level bored tunnel. *J. S. Afr. Inst. Min. Metall*, **78**, 124-133.
- Stacey, T.R. and Page, C.H. 1986. *Practical Handbook for Underground Rock Mechanics*. TransTech, Germany, 145p.
- Sterling, R.L. 1980. The Ultimate Load Behaviour of Laterally Constrained Rock Beams. *The State of the Art in Rock Mechanics: Proc. of the 21st U.S. Symposium on Rock Mechanics*, 533-542.
- Stillborg, B. 1994. *Professional Users Handbook for Rock Bolting*. TransTech, Germany, 164p.
- Stimpson, B. and Ahmed, M. 1992. Failure of a Linear Voussoir Arch: a Laboratory and Numerical Study. *Can. Geotech. J.*, **29**, 188-194.
- Suorineni, F.T. 1998. *Effects of Faults and Stress on Open Stope Design*. Ph.D. Thesis, Dept. of Earth Sciences, University of Waterloo.
- Tang, C.A. and Kaiser, P.K. 1998. Numerical simulation of cumulative damage and seismic energy release during brittle rock failure-Part I: Fundamentals. *Int. J. of Rock Mech. and Min. Sci.*, **35**, 113-122.
- Tannant, D. Barclay, B., Espley, S. and Diederichs, M.S. 1999. Field trials of thin spray on membranes for drift support. *Proc. Congress of the Int. Soc. Rock Mechanics, Paris*.
- Tannant, D.D. and Diederichs, M.S. 1997. *Cablebolt Optimization in #3 Mine*. Report to Falconbridge Ltd., Kidd Mines Division, 65p.
- Tano, H. 1993. Proposal for a probabilistic model on the stress-strain relation of rock and its application to some rocks. *Assessment and prevention of failure phenomena in rock engineering* (ed. Pasamehmetoglu et al.). Rotterdam: Balkema, 245-250.
- Tapponier, P. and Brace, W.F. 1976. Development of stress induced microcracks in Westerly granite. *Int. J. of Rock Mech. and Min. Sci. and Geomech. Abstr.*, **13**, 103-112.
- Terzaghi, K. 1946. Rock defects and loads on tunnel supports. *Rock Tunnelling with Steel Supports* (ed. Proctor and White). Youngstown, OH, Commercial Shearing and Stamping Company. **1** 17-99.
- Thallak, S.G. and Gray, K.E. 1993. Discrete particle modelling for analysis of borehole stability: applications in petroleum geomechanics. *1st Can. Symp. on Numerical Modelling Applications in Mining and Geomechanics*, Montreal.

References

- Ting, J.M., Corkum, B.T. Kauffman, C.R. and Greco, C. 1989. A discrete element numerical model for soil mechanics. *ASCE Journal of Geotechnical Engineering*, **115** (3).
- Trollope, D.H. 1968. The mechanics of discontinua or elastic mechanics in rock problems. *Rock Mechanics and Eng. Practice*, (eds. Stagg and Zienkiewicz), Wiley, 275-320.
- Tsoutrelis, C.E. and Exadaktylos, G.E. 1993. Effect of rock discontinuities on certain rock strength and fracture energy parameters under uniaxial compression. *Geotechnical and Geological Engineering*, **V11**, 81-105.
- Urbancic, T.J., Young, R.P., Bird, S., and Bawden, W. 1992. Microseismic source parameters and their use in characterizing rock mass behaviour: Considerations from Strathcona Mine. *Proc. CIM AGM*, May, 36-47.
- Van Mier, J.G.M and Vervuurt, A. 1995. Lattice model for analyzing steel-concrete interface behaviour. in *Mechanics of Geomaterial Interfaces*, (eds. Selvadurai and Boulton), Amsterdam: Elsevier, 201-225.
- Vardar, O. and Finnie, I. 1975. An analysis of the Brazilian disk test using the Weibull treatment of brittle fracture. *Int. Journal of Fracture*, **11** (3), 495-508.
- Vardoulakis, I and Sulem, J. 1993. Application of bifurcation theory to rock mechanic problems. *Comprehensive Rock Engineering: Principles, Practice and Projects*, Oxford: Pergamon, **1**, 575-609.
- Vasak, P. and Kaiser, P.K. 1995. Tunnel stability assessment during rockbursts. *3rd Canadian Conference in Computer Applications in the Mineral Industry*, Montreal.
- Vasak, P. and Maloney, S. 1995. *Uniaxial compressive strengths of ore and granite from McCreey East Mine*. Report to Inco Limited, Ontario Division, June 13.
- Vermeer, P.A. and de Borst, R. 1984. Non-associated plasticity for soils, concrete and rock. *Heron*, **29** (3).
- Villaescusa, E. 1996. Excavation design for bench stoping at Mount Isa Mine, Queensland, Australia. *Trans. Instn. Min. Metall.*, **106** (A1-A10).
- Villaescusa, E. and Brown, E.T. 1992. Maximum likelihood estimation of joint size from trace length measurements. *Rock Mechanics and Rock Engineering*, **25**, 67-87.
- Walsh, J.B. 1965. The effect of cracks in the compressibility of rocks. *J. Geophys. Research*, **70**, 381-389.

- Walsh, J.B. and Grosenbaugh, M.A. 1979. A new model for analyzing the effect of fractures on compressibility. *Journal of Geophysical Research*, **84** (B7), 3532-3536.
- Wawersik, W.R. and Brace, W.F. 1971. Post-failure behaviour of a granite and diabase. *Rock Mechanics*, **3**, 61-85.
- Wawersik, W.R. and Fairhurst, C. 1970. A study of brittle rock fracture in laboratory compression experiments. *Int. J. Rock Mech. Min. Sci.*, **7**, 561-575.
- Weibull, W. 1939. A statistical theory of the strength of materials. *Proc. Royal Swedish Inst. Eng. Research*, Stockholm, **151**, 115-145.
- Weibull, W. 1951. A statistical distribution function of wide applicability. *Journal of Applied Mechanics*, September, 293-297.
- Weiderhorn, S.M., Freiman, S.W., Fuller, E.R., Simmons, C.J. 1982. Effects of water and other dielectrics on crack growth. *Journal of Materials Science*. **17**. p3460-3478.
- Wickham, G.E., Tiedeman, H.R. and Skinner, E.H. 1972. Support determination based on geologic predictions. *Proc. North American Rapid Excavation and Tunnelling Conference, Chicago*. New York: Soc. Min. Engrs., Am. Inst. Min. Metall. Petr. Engineers (ed. Lane and Garfield), 43-64.
- Wiederhorn, S.M. and Bolz, L.H. 1970. Stress corrosion and static fatigue of glass. *Journal of the American Ceramic Society*, **53** (10), 543-548.
- Wiid, B.L. 1970. The influence of moisture on the pre-rupture fracturing of two rock types. *Proceedings of the 2nd Congress of the I.S.R.M.*, **2** (3-4), 239-245.
- Wijk, G. 1978. Some new theoretical aspects of indirect measurements of the tensile strength of rock. *Int. J. Rock Mech. Min. Sci. & Geomech Abstr.*, **15** (4), 149-160.
- Wijk, G. 1981. *The tensile strength of pre-compressed Bohus granite*. SveDeFo Rep., DS 1981:20.
- Wijk, G. 1983. *The Brazilian test and a Mohr Coulomb failure criterion*. SveDeFo Rep., DS 1983:7.
- Wijk, G., Rehbinder, G. Logdstrom, G. 1977. The relation between the uniaxial tensile strength and the sample size for Bohus granite. *Rock. Mech.*, **10**, 201-219.
- Wiles, T. 1989. *Strength parameters at Creighton Mine 400 orebody*. Internal Inco Report, 11p.

References

- Wiles, T.D. 1996. *MAP-3D Version 36. A mining analysis program in three dimensions*. Mine Modelling Ltd. Copper Cliff, Ontario.
- Wilkins, B.J.S. 1980. Slow crack growth and delayed failure of granite. *Int. J. Rock Mech. Min. Sci. & Geomech. Abstr.*, **17**, 365-369.
- Willard, R.J. and McWilliams, J.R. 1969. Microstructural techniques in the study of physical properties of rock. *Int. J. Rock Mech. Min. Sci. & Geomech. Abstr.*, **6**, 1-12.
- Wiseman, N. 1978. *A study of the factors affecting the design and support of gold mine tunnels*. Chamber of Mines South Africa. COM Research Report No.50/78.
- Wiseman, N. 1979. *Factors affecting the design and condition of mine tunnels*. Chamber of Mines South Africa. COM Research Report No.45/79.
- Wong, R.H.C., Chau, K.T. and Wang, P. 1996. Microcracking and grain size effect in Yuen Long Marbles. *Int. J. of Rock Mech. and Min. Sci. and Geomech. Abstr.*, **33** (5), 479-485.
- Wong, T.F. 1982. Shear fracture of Westerly granite from post failure behaviour. *Journal of Geophysical Research*, **87** (B2), 990-1000.
- Wong, T.F. 1982. Micromechanics of faulting in Westerly granite. *Int. J. Rock Mech. Min. Sci. & Geomech. Abstr.*, **19**, 49-64.
- Wood, D.M. 1990. *Soil Behaviour and Critical State Soil Mechanics*. Cambridge: Cambridge University Press.
- Wright, J.B. 1981. Earth Materials: Minerals and Rocks. in *The Cambridge Encyclopedia of Earth Sciences* (ed. Smith), New York: Crown Publishers/Cambridge University Press, 68-92.
- Yanagidini, T. Sano, O. Terada, M. and Ito, I. 1978. The observation of cracks propagating in diametrically-compressed rock disks. *Int. J. Rock Mech. Min. Sci. & Geomech Abstr.*, **15** (5), 225-236.
- Yao, C. and Kim, K. 1996. Simulation of tensile failure in disk using random lattice network model (sic.). *Rock Mechanics-NARMS '96*, (eds. Aubertin et al.), Rotterdam: Balkema, 663-668.
- Zietlow, W.K. and Labuz, J.F. 1998. Measurement of the intrinsic process zone in rock using acoustic emission. *Int. J. Rock Mech. Min. Sci. & Geomech Abstr.*, **35** (3), 291-301.

Software Summary

The following is a list of commercial engineering and scientific software used for this work:

- DIPS** *Data Interpretation using Projected Stereonets* *
Interpretation and analysis of oriented geological data
RocScience Inc. 31 Balsam Ave. Toronto, Ont. M4E 3B5
* created by M.S. Diederichs
- EXAMINE^{2D}** *Excavation Analysis for MINEs (2D)* **
Two dimensional boundary element modelling of stress flow
around underground openings
RocScience Inc. 31 Balsam Ave. Toronto, Ont. M4E 3B5
** with contributions by M.S. Diederichs
- EXAMINE^{3D}** *Excavation Analysis for MINEs (2D)*
Three dimensional boundary element modelling of stress flow
around underground openings
RocScience Inc. 31 Balsam Ave. Toronto, Ont. M4E 3B5
- MAP3D** Three dimensional boundary element modelling of stress flow
around underground openings
Mine Modelling Ltd.
c/o Geomechanics Research Centre, Laurentian University, Ramsey Lake Road
Sudbury, Ontario. P3E 2C6
- PFC^{2D}** *Particle Flow Code (2D)*
Discrete element simulation (discs)
Itasca Consulting Group, Thresher Sq. E., 708 S. 3rd St., Suite 310
Minneapolis, Minnesota 55415
- PHASE²** *Finite Element Analysis for Excavations*
RocScience Inc. 31 Balsam Ave. Toronto, Ont. M4E 3B5
- SURFER** Contouring, Gridding, and Surface Mapping for Scientists and Engineers
Rockware, 2221 East Street # 1, golden Colorado, 80401
- UDEC** *Universal Distinct Element Code*
Itasca Consulting Group, Thresher Sq. E., 708 S. 3rd St., Suite 310
Minneapolis, Minnesota 55415
- UNWEDGE** *Underground WEDGE analysis*
Ubiquitous wedge analysis for underground openings
RocScience Inc. 31 Balsam Ave. Toronto, Ont. M4E 3B5

APPENDIX A

Effect of Confining Stress on a Symmetric Roof Prism

The following derivation is based in part on the solution presented by (Brady and Brown, 1993). The purpose of this simple (2D) solution for a symmetrical triangular roof prism, is to assess, in a scoping fashion, the impact of a horizontal force on the pullout resistance for roof wedges.

A.1 HORIZONTAL FORCE AND PULLOUT FORCE

The solution of Brady and Brown (1993), presented here is developed in terms of a horizontal force, H , acting on a rigid wedge with deformable joint interfaces as seen in Figure A.1a.

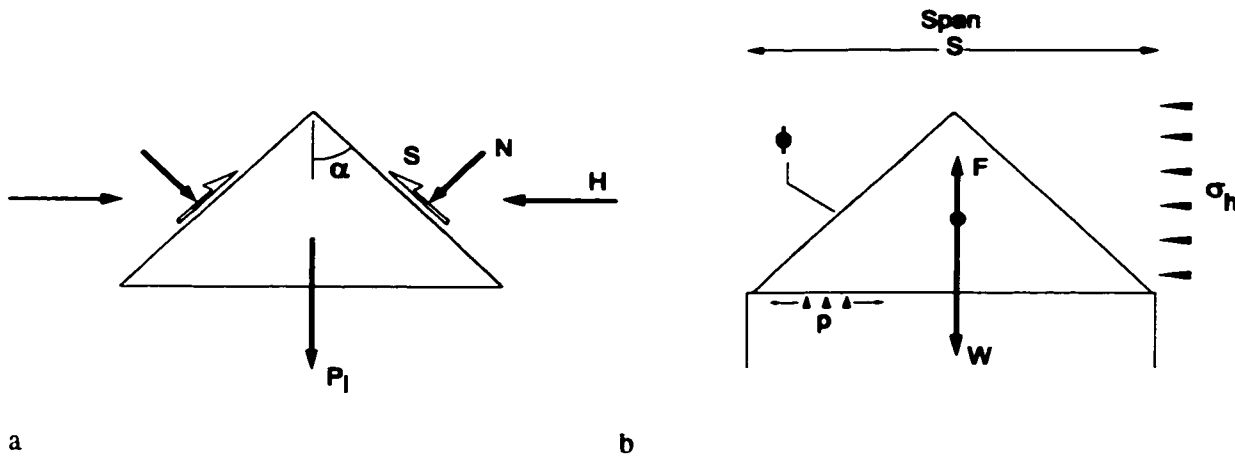


Figure A.1: Confined roof wedge.

To obtain equilibrium in the free body diagram of Figure A.1a, the required pullout force, P_1 , which includes the body force applied by gravity, must be equal and opposite to the resultant of N and S , the normal and shear forces acting on the joint surfaces:

$$P_1 = 2(S \cos \alpha - N \sin \alpha) \quad [\text{A.1}]$$

where for horizontal equilibrium:

$$H = N \cos \alpha + S \sin \alpha \quad [\text{A.2}]$$

and for a purely frictional surface, the limiting value of $S = N \tan \phi$. This leads to:

$$P_l = 2N(\tan \phi \cos \alpha - \sin \alpha) = 2N \sec \phi \sin(\phi - \alpha) \quad [\text{A.3}]$$

For a positive value of N (compression), any such wedge will be “squeezed” out by the field forces (independent of gravity and weight) when $\alpha > \phi$. Stability may be possible for $\alpha < \phi$, warranting a further analysis of this case.

Prior to any displacement of the wedge the initial normal and shear forces N_0 and S_0 are given by:

$$N_0 = H_0 \cos \alpha \quad , \quad S_0 = H_0 \sin \alpha \quad [\text{A.4}]$$

Upon application of a downward force P, a downward displacement u_y occurs which results in relative shear (tangential) and normal displacements of the joint surfaces:

$$u_s = u_y \cos \alpha \quad , \quad u_n = u_y \sin \alpha \quad [\text{A.5}]$$

The final normal and shear forces, N and S , after displacement are related as:

$$N = N_0 - K_n u_n = H_0 \cos \alpha - K_n u_y \sin \alpha \quad [\text{A.6}]$$

$$S = S_0 + K_s u_s = H_0 \sin \alpha + K_s u_y \cos \alpha = (H_0 \cos \alpha - K_n u_y \sin \alpha) \tan \phi \quad [\text{A.7}]$$

Solving for u_y using the last equality in Equation A.7:

$$u_y = \frac{H_0 \sin(\phi - \alpha)}{(K_s \cos \alpha \cos \phi + K_n \sin \alpha \sin \phi)} \quad [\text{A.8}]$$

Substitution of Equation A.8 into Equations A.6 and A.7 gives:

$$\begin{aligned} N &= H_0 \left(\cos \alpha - \frac{K_n \sin \alpha \sin(\phi - \alpha)}{K_s \cos \alpha \cos \phi + K_n \sin \alpha \sin \phi} \right) \\ &= H_0 \cos \alpha \frac{K_s \cos^2 \alpha + K_n \sin^2 \alpha}{K_s \cos \alpha \cos \phi + K_n \sin \alpha \sin \phi} \end{aligned} \quad [\text{A.10}]$$

Similarly:

$$S = H_0 \sin \alpha \frac{K_s \cos^2 \alpha + K_n \sin^2 \alpha}{K_s \cos \alpha \cos \phi + K_n \sin \alpha \sin \phi} \quad [\text{A.11}]$$

The change in horizontal force, assuming a rigid wedge and external medium such that relaxation occurs only on the joint interface is given by:

$$\Delta H = H_0 \left(\cos(\phi - \alpha) \frac{K_s \cos^2 \alpha + K_n \sin^2 \alpha}{K_s \cos \alpha \cos \phi + K_n \sin \alpha \sin \phi} - 1 \right) \quad [\text{A.12}]$$

Substituting Equation A.10 into Equation A.3, the limiting vertical force P_l is obtained (minimum pullout force required to remove wedge for $\alpha < \phi$):

$$P_l = 2H_0 \sin(\phi - \alpha) \frac{K_s \cos^2 \alpha + K_n \sin^2 \alpha}{K_s \cos \alpha \cos \phi + K_n \sin \alpha \sin \phi} \quad [\text{A.13}]$$

A.2 FACTOR OF SAFETY, STRESS, AND SPAN

The factor of safety, $F.S.$, for wedge pullout (fallout) is given by the ratio of required pullout force, P_l , to actual pullout force, P :

$$F.S. = \frac{P_l}{P} = \frac{P_l}{W - F} \quad [\text{A.14}]$$

where W is the weight of the wedge in Figure A.1b, and $F = pS$ is the support force (support pressure, p , integrated over the base of the wedge or prism of span S for a unit section thickness). W , for a unit thickness of wedge (prism) and a unit weight of γ is:

$$W = \frac{1}{2} \gamma S \frac{S}{2 \tan \alpha} = \frac{\gamma S^2}{4 \tan \alpha} \quad [\text{A.15}]$$

the horizontal force, H_0 , can be determined from the average elastic stress, $\bar{\sigma}_h$, acting across the height of the wedge:

$$H_0 = \bar{\sigma}_h \frac{S}{2 \tan \alpha} \quad [\text{A.16}]$$

Substitution of Equation A.16 in Equation A.13 and then further substitution into Equation A.14 along with Equation A.15 gives, for an unsupported wedge ($F=0$):

$$F.S. = \frac{2 \left(\frac{\bar{\sigma}_h S}{2 \tan \alpha} \right) \left(\frac{K_s \cos^2 \alpha + K_n \sin^2 \alpha}{K_s \cos \alpha \cos \phi + K_n \sin \alpha \sin \phi} \right) \sin(\phi - \alpha)}{\left(\gamma \frac{S^2}{4 \tan \alpha} \right)} \quad [\text{A.17}]$$

$$= \frac{4 \bar{\sigma}_h}{\gamma S} \left(\frac{K_s \cos^2 \alpha + K_n \sin^2 \alpha}{K_s \cos \alpha \cos \phi + K_n \sin \alpha \sin \phi} \right) \sin(\phi - \alpha)$$

the result used in Section 2.4.1 of this thesis.

APPENDIX B

NTBEAM: Routines for Parametric Voussoir Solutions

The Voussoir solution outlined in Chapters 3 and 4 was incorporated into a C++ driven computer program in order to produce the plots and solutions presented in this thesis. Figure B.1 illustrates the options available for solution. The program can give a single solution for a set of parameters or it can solve for a critical value (e.g. Figure B.2) given a suite of the remaining parameters.

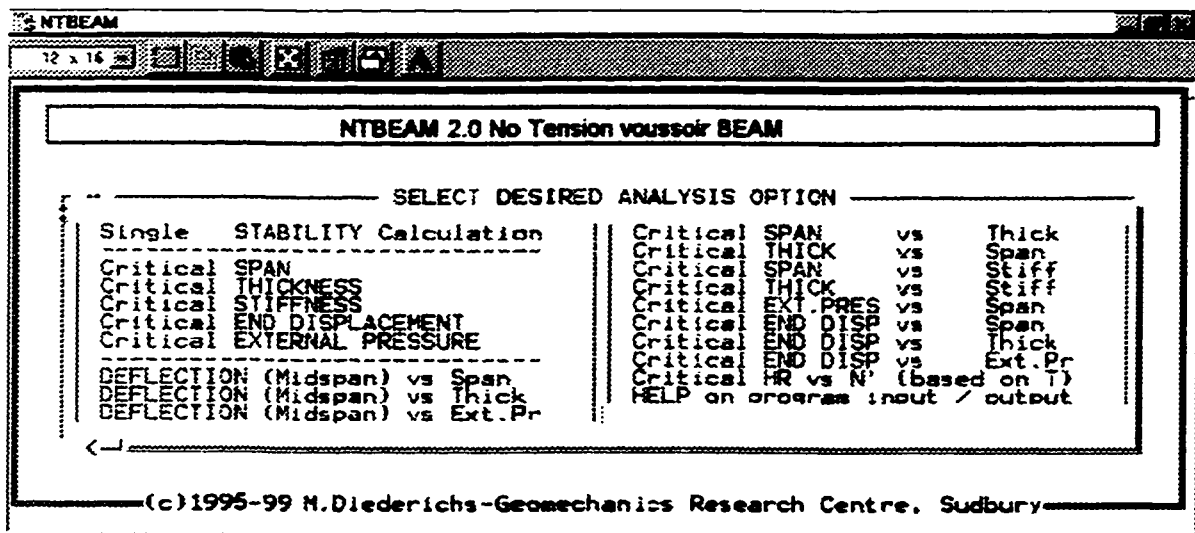


Figure B.1: Solution options for NTBEAM (voussoir)

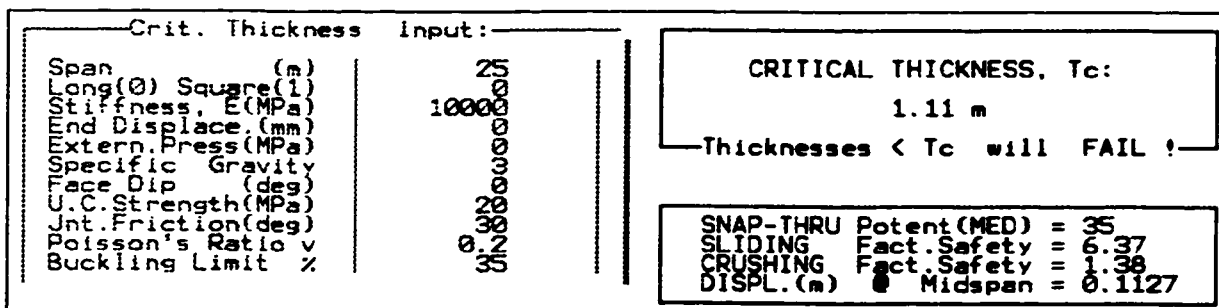


Figure B.2: Example solution for critical thickness

This solution is in the form of a generalized bisection algorithm which iteratively solves for the critical value (separating the domain of "stable" and "failed" solutions). It can also generate bi-

parametric solutions (matrix of critical values based on two varying parameters) for input into a plotting package such as EXCEL^(Microsoft). This latter option was used to produce the numerous output plots in Chapters 3 and 4.

Routine summary for NTBEAM

MAIN()

- Main program routine
- Menu option selection
- Parametric selection
- Performs single root bisection solution for individual critical parameters
- Calls:
 - twosolve (...) Iterative two variable (N and Z) solution
 - critical (...) Loop routine to produce EXCEL data files for parametric plots
 - help() Help routine

TWOSOLVE (...)

- Routine for iterative solution of two parameter problem
- Contains algorithm outlined in Figure 3.8 flow chart.
- Calculates buckling limit, B.L. (Chapter 3), factor of safety for sliding and crushing, and displacement.
- Diagnostic mode permits output of internal functions and variables described in chapter 3 (e.g. f_{max} , $N_{critical}$, $Z_{critical}$)

CRITICAL (...)

- Generation of bi-parametric matrices for input into EXCEL (spreadsheet and plotting)
- Calculates critical value of one parameter for a range of two other parameters
- Calls:
 - twosolve (...)

Numerous supporting subroutines including interactive data input and menu routines written using:

FACT 1.0	Front-end in AsCii Text (c)1995 Mark Diederichs (DOS-based) Interface routines for data entry, file selection and data display:
data_entry	data entry and menu display
data_select	data select (eg for menus and values etc)
editor	string editor
fileselect	select a file, change a drive, change a directory
... and numerous other minor screen manipulation and i/o routines written and compiled with Borland Turbo c++	

APPENDIX C

Catalogue of FISH Control Routines for PFC Simulations

The discrete element package PFC2D from Itasca Ltd. contains basic assembly and control routines. In order to create samples, control boundary conditions, calculate and track sample parameters or to generate and store crack data from broken contacts ("cracks" not part of PFC data structure), the user needs to write problem specific routines in a run-time compiled language called FISH. In addition, all of the graphical output in this thesis was created with FISH routines created by the author.

This FORTRAN-like language contains link-list structures for data tracking, arithmetic functions, and disc and contact data access functions. The following is a catalogue of the functions used and created for the purposes of this research.

C.1 FISH Routines Created by Itasca Ltd.

These routines (D. Potyondi, pers. comm. 1996) were supplied to the author and used in unmodified form:

<code>biax_servo</code>	Adjust wall velocities to maintain applied stress
<code>expand_radii</code>	Expand discs (assembly densification and lithification)
<code>get_badd</code>	Access list address for disc
<code>get_servo_gain</code>	Control routine for <code>biax_servo</code>
<code>get_wadd</code>	Access list address for wall
<code>install_iso_stress</code>	Create sample with specified internal pressure
<code>install_ws</code>	apply desired stress in sample by wall adjustment

iso_stress	Calculate average (hydrostatic) stress within sample
make_walls	Generate bounding walls for a rectilinear assembly
sample_radii	Calculate average radius of assembly discs
floater2.drv	set of routines to ensure a minimum number of contacts per particle (correct internal bridging or eliminate "floating" particles P. Cundall, pers. comm. 1996)

C.2 FISH Routines Modified by the Author

These routines were created by Itasca Ltd. (D. Potyondi, pers. comm. 1996) and significantly modified by M. Diederichs for use in this work:

accel_platens	Apply platen velocity incrementally to avoid shocking sample
assemble_sample	Main routine for random assembly sample creation
eyy_wall	Calculate strains from wall deformation ("update_strains" calculates internal assembly strains)
get_wss	Calculate wall stress (from contact forces)
install_bondstiff	Assign varying (heterogeneous) contact stiffnesses over assembly
install_bondstrengths	Assign varying (heterogeneous) contact strength over assembly
install_meas_circles	Initialize measurement circles for stresses and strains
set_sample_dimensions	Initialize sample dimensions
stress_meas	Update sample stresses (via measurement circles)
update_strains	Update sample strains from strain rates (via measurement circles)

C.3 FISH Routines Created by the Author

These routines were created by Mark Diederichs (1996-1998) specifically for this research

assemble_hexlr_samp	Assemble sample with hexagonal packing •
assemble_hexud_samp	Assemble sample with hexagonal packing •
assemble_homo_samp	Assemble sample with cubic structure •
bilinear_tension	Contact logic - different stiffness in tension and compression (results inconclusive)
braz_sample	Cut Brazilian test sample from square lithified sample

Appendix C: Catalogue of FISH Control Routines for PFC Simulations

bxcontfile	Create x,y array of stress points and send to file
bxcontinit	Initialize sample for output of stress points (create array of measurement circles)
bxcrkfile	Create x,y file of crack distribution
conthisto	Output disc and contact location and properties for histogram or variability surface plotting
crk_form	Create crack (from broken contact)
crk_getdata	Access crack information
crk_init	Initialize crack tracking arrays
crk_intensity	Calculate crack numbers, tensor components
crk_newblk	Initialize crack memory structure (external to PFC data lists)
crk_rate	Calculate instantaneous crack rate
cum_rvel	Calculate absolute cumulative rotational velocity (diagnostic)
DXF Graphical output routines	
dxf_circle	Generic circle output
dxf_end	Generic dxf endfile info
dxf_end_pline	Generic polyline end block
dxf_header	Generic dxf header info
dxf_line	Generic line output
dxf_pline	Generic polyline output
dxf_solid	Generic solid output
dxf_start_pline	Generic polyline start
dxf_text	Generic text output
dxf_vertex	Generic vertex output
dxfball	Output all disc entities
dxfbrazil	Output of Brazilian geometry
dxfcbond	Output all bonded contacts
dxfcforce	Output contact forces (scaled tension, compression and shear)
dxfcont	Output all contact entities
dxfcrack	Output all crack entities (normal to broken contacts)
dxfcrk_rose	Dxf file creation routine for crack orientation rosette and tensor
dxfmaxforce	Determine max force for scaling
dxfout	Main dxf option selection
dxfwall	Output wall entities
exx_wall	Calculate strains from flexible walls
cyy_wall	Calculate strains from flexible walls

getclust	Calculate number of neighbouring crack pairs for interaction tracking
histout	Generate ascii files of parameter histories
make_pillar	Cut square holes in either side of sample and adjust wall properties for pillar simulations
memblock	General memory allocation
mid_x_slice	Create tension sample (rectangular or dumbbell) from square lithification sample
mohr_coulomb_cont	Contact logic - coincident friction and cohesion contact strength (results inconclusive)
poisson	Calculate instantaneous Modulus and Poisson's Ratio (tangential and secant)
purge_balls	Eliminate free discs during simulation
random_crk	Generate a random isotropic or anisotropic array of initial cracks according to specified distribution function
rose	Dxf file creation for contact, force and contact property distribution rosette
rotate_init	Initialize rotation tracking
tens_test_x	Tensile test main control routine
tns_bdry	Create tensile platen strips
tns_boundstr_x	Impose stiffness and strength adjustment to tensile platen discs
tns_init_sample	Initialize sample and tension test parameters
tns_relax_x	Allow sample to relax from compressive loading
tns_sxx	Calculate the applied tensile stress (from velocity controlled platens)
velbc_x	Control lateral tensile test "platens" (vertical bands of control discs)
wall_stop	Halt compressive test platens (multiphase testing)
x_membrane	Create and control flexible (stress control) membrane for confining stress application (vertical)
y_membrane	Create flexible (stress control) membrane for confining stress application (horizontal)

...and numerous other minor supporting FISH functions

APPENDIX D

Stress Intensity Factors For A Sliding Crack

Numerous authors have presented variations of analytical model solutions, based on linear elastic fracture mechanics, for Mode I wing crack initiation and extension from an initial sliding flaw. The following derivations are based on detailed calculations of Ashby and Hallam (1986), abridged, summarized and adapted for consistent nomenclature and stress convention here, by the author. The resulting solutions, based on these derivations are used in Chapter 8. Several typographical errors in the published work have been corrected here.

D.1 WING CRACK INITIATION

Consider the crack in Figure D.1.

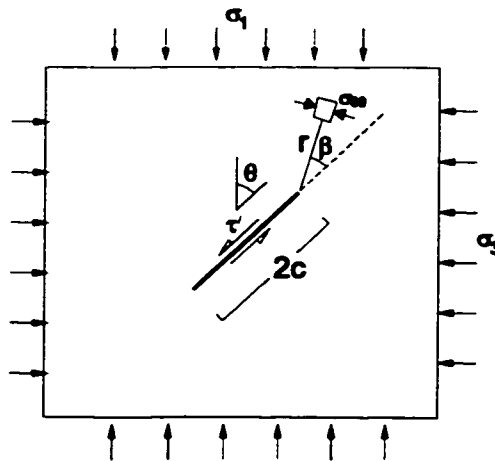


Figure D.1: Geometry for wing crack initiation

The tensile stresses at a distance, r , from the tip at an angle θ , to the crack plane is:

$$\sigma_{\theta\theta} = \tau' \frac{3\sqrt{\pi c}}{2\sqrt{2\pi r}} \sin \beta \cos \frac{\beta}{2} \quad [D.1]$$

where for a friction coefficient of μ the net shear stress, τ' , on the crack surface is:

$$\tau' = \frac{1}{2}(\sigma_1 - \sigma_3) \sin 2\theta - \mu(\sigma_1 + \sigma_3 + (\sigma_1 - \sigma_3) \cos 2\theta) \quad [D.2]$$

The Mode I stress intensity on a very small wing crack of length a at an angle β can be approximated by $\sigma_{\theta\theta} \sqrt{(\pi a)}$ using the value of $\sigma_{\theta\theta}$ at $r=a/2$:

$$K_I = \tau' \frac{3}{2} \sqrt{\pi c} \sin \beta \cos \frac{\beta}{2} \quad [D.3]$$

Maximizing K_I with respect to β gives (for $\beta = 70.5^\circ$):

$$K_I = \tau' \frac{2}{\sqrt{3}} \sqrt{\pi c} \quad [D.4]$$

Expanding the expression for τ' and maximizing again with respect to θ , gives the critical crack orientation of:

$$\theta = \frac{1}{2} \tan^{-1} \frac{1}{\mu} \quad [D.5]$$

D.2: WING CRACK GROWTH FOR AN ISOLATED CRACK

Consider the potential energy, P , of a body containing the idealized crack in Figure D.2, with the simplified wing cracks assumed to be parallel to maximum compression.

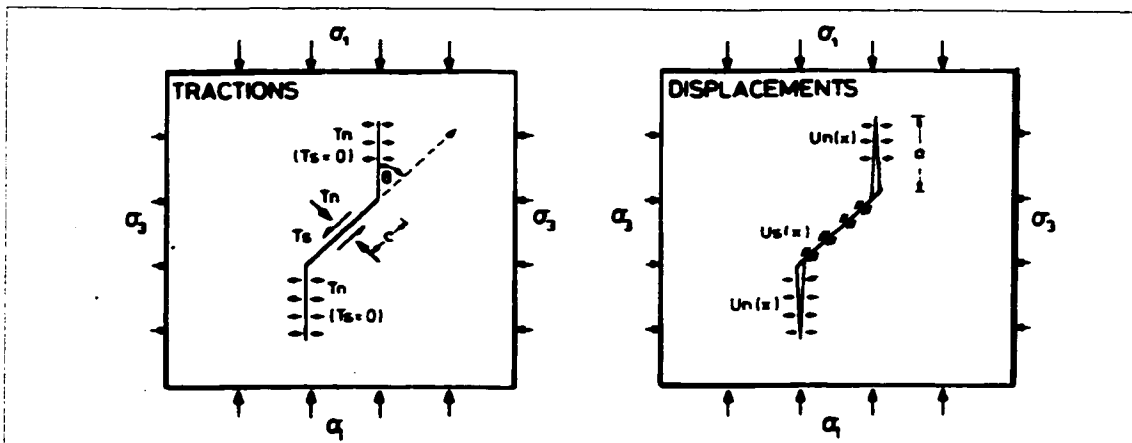


Figure D.2: Nomenclature for a sliding crack with idealized wing cracks

At the initial state the crack is pinned (no displacement) and a steady-state field stress is applied. At this point the stored energy is U_0 . If the crack restraint (pinning) is gradually relaxed, allowing the crack to slide and the wing cracks to separate and open, the tractions on the crack surface do work, W . In addition elastic energy components, U_I and U_{II} are stored in the body, associated with the Mode I (wedging) field and the Mode II (sliding) field, respectively. The total potential energy is given as:

$$P = U_0 + U_I + U_{II} - W \quad [D.6]$$

The total work done, by the sliding crack and by the opening wing cracks, is:

$$W = \frac{1}{2} \sum (\text{Force} \times \text{Displacement}) = \frac{1}{2} \int_{S_1} 2T_1 u_1(x) dS_1 + \frac{1}{2} \int_{S_2} 2T_2 u_2(x) dS_2 \quad [D.7]$$

where S_1 is the main surface, S_2 is the wing crack surface, $T_1 (= \tau')$ and u_1 are the shear traction and shear displacement (constant along sliding portion) while $T_2 (= \sigma_3)$ and u_2 are the wing crack normal traction and displacement (falling linearly to zero at crack tip). Normal tractions on the sliding crack do no work. Considering the kinked composite crack as a straight crack of length $2(a+c)$, the displacements are given by:

$$u_1(x) = \pm \frac{\alpha_1 \delta \left((a+c)^2 - x^2 \right)^{0.5}}{a+c} \quad [D.8]$$

$$u_2(x) = \pm \frac{\alpha_2 \delta (a+c-x)}{a+c} \quad [D.9]$$

where α_1 and α_2 are geometric constants (accounting for the kinked overall shape and the geometric simplification of the wing crack) and 2δ is the maximum relative sliding displacement. For a sample of width, b , the work done is obtained by substituting these displacements in Equation D.7:

$$W = \alpha_1 \tau' cb \delta \left(\left(1 - (1+L)^{-2} \right)^{0.5} + (1+L) \arcsin(1+L)^{-1} \right) - \alpha_2 \sigma_3 a L b \delta \quad [D.10]$$

where $L = a/c$. Expanding terms as a power series:

$$W = 2\alpha_1 \tau' cb \delta \left(1 - \frac{1}{6(1+L)^2} \right) - \alpha_2 \sigma_3 a L b \delta \quad [D.11]$$

The first term in the summation pair above is the work due to shearing and is almost independent of L . Equation D.11 can therefore be approximated by:

$$W = 2ab\delta(\alpha_1\tau' - \alpha_2\sigma_3L/2) \quad [\text{D.12}]$$

2δ is the maximum relative sliding displacement on the central sliding crack segment. this displacement can be resolved into a normal and shear components, δ_n and δ_s , relative to the average plane of the composite crack (sliding crack + wing cracks) so that $\delta^2 = \delta_n^2 + \delta_s^2$ and:

$$\delta_n = \delta \frac{L\sin\theta}{(\sin^2\theta + (\cos\theta + L)^2)^{0.5}} \approx \frac{\delta L}{\sqrt{2(1+L)}} \quad [\text{D.13}]$$

$$\delta_s = \delta \frac{1 + L\cos\theta}{(\sin^2\theta + (\cos\theta + L)^2)^{0.5}} = \frac{\delta}{1+L} \quad [\text{D.14}]$$

These displacements, acting on the composite crack, create stored elastic energy within the surrounding body equivalent to:

$$U_I + U_{II} = \alpha_3 E_0 b (\delta_n^2 + \delta_s^2) = \alpha_3 E_0 b \delta^2 \quad [\text{D.15}]$$

where α_3 is another geometric constant and E_0 is the elastic modulus of the body material. Next, Equation D.6 is minimized to obtain the minimum potential energy with respect to δ (initial energy U_0 is independent of δ for constant crack length):

$$\frac{dP}{d\delta} = \frac{d}{d\delta} (U_I + U_{II} - W) = 0 \quad [\text{D.16}]$$

giving:

$$\delta = \frac{c}{E_0} \left(\frac{\alpha_1\tau' - \frac{\alpha_2}{2\alpha_3}\sigma_3L}{\alpha_3} \right) \quad [\text{D.17}]$$

According to Tada et al. (1973) the two displacement components δ_n and δ_s , applied at the centre of the composite crack, induce Mode I stress intensities at the crack tip equivalent to:

$$K_I^n \approx 0.4 \frac{E_0 \delta_n}{\sqrt{a+c}} \quad [\text{D.18}]$$

$$K_I^s \approx \frac{E_0 \delta_s}{\sqrt{a+c}} \quad [\text{D.19}]$$

Crack initiation (nascent wing crack initiation at an angle of 70 degrees to the sliding crack plane) is controlled by the intensity factor K_I^s given by Equation D.19. After some extension the wing

Appendix D: Stress Intensity Factors For A Sliding Crack

crack turns and becomes normal to σ_3 , and as such eventually becomes dominated by K_I^n in Equation D.18. This transition is accommodated by multiplying K_I^s by $(1+L)^{-0.5}$:

$$K_I = K_I^n + \frac{K_I^s}{\sqrt{1+L}} \quad [\text{D.20}]$$

so that when $a \gg c$ (or $L \gg 1$), K_I^s disappears. For $a=0$, δ_n reduces to zero as, therefore, does K_I^n . Using Equation D.20 together with Equations D.13, D.14, D.17, D.18 and D.19 gives the result:

$$K_I = \frac{\sqrt{\pi c}}{\sqrt{2\pi}(1+L)^{3/2}} \left(\frac{\alpha_1}{\alpha_3} \tau' - \frac{\alpha_2}{2\alpha_3} \sigma_3 L \right) \left(0.4L + \frac{1}{\sqrt{1+L}} \right) \quad [\text{D.21}]$$

A final step involves the solution for the two ratios of geometric constants above. For $L=0$ Equation D.21 must reduce to the initiation condition (Equation D.4) so:

$$\frac{\alpha_1}{\alpha_3} = \frac{2\sqrt{2\pi}}{\sqrt{3}} \quad [\text{D.22}]$$

and for $L \gg 1$ and σ_3 is tensile (negative), Equation D.21 must reduce to $K_I = |\sigma_3 \sqrt{\pi l}|$, the crack initiation criterion for direct tension. This gives:

$$\frac{\alpha_2}{\alpha_3} = \frac{2\sqrt{2\pi}}{0.4} \quad [\text{D.23}]$$

Assembling these results gives the required stress intensity for wing crack propagation:

$$K_I = \frac{\sqrt{\pi c}}{(1+L)^{3/2}} \left(\frac{2}{\sqrt{3}} \tau' - \frac{L}{0.4} \sigma_3 \right) \left(0.4L + \frac{1}{\sqrt{1+L}} \right) \quad [\text{D.24}]$$

Substituting for the net effective shear stress, τ' , given in Equation D.2, using the critical crack orientation given by Equation D.5, and using $\lambda = \sigma_3 / \sigma_I$ gives the equation:

$$K_I = \frac{\sigma_I \sqrt{\pi c}}{(1+L)^{3/2}} (1 - \lambda - \mu(1 + \lambda) - 4.3\lambda L) \left(0.23L + \frac{1}{\sqrt{3(1+L)}} \right) \quad [\text{D.25}]$$

used in Section 8.6 of this thesis.

D.3 INTERACTION WITH A FREE SURFACE

Consider a plate, as shown in Figure D.3, of height h , width w , and depth b , containing a central (sliding) crack of length $2c$ with wing cracks extending to a length a . For a plate much larger than the composite crack the stress intensity is as given in Section D.2.

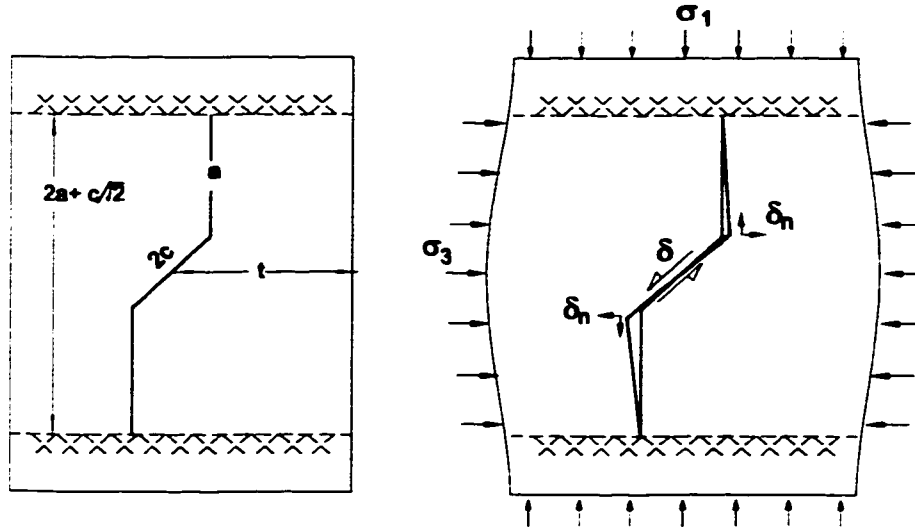


Figure D.3: Effective beam created by crack-surface interaction

If the plate is narrow, the crack splits it into vertical beams or columns of length $2(a+c(\cos\theta))$. To simplify assume $\theta=45^\circ$ so that $\cos\theta=1/\sqrt{2}$. The premise here is that the beam bends outward allowing additional sliding displacement at the central crack further increasing the stress intensity at the wing crack tips.

In Figure D.3, the composite beam on the left side of the central crack is made up of two half beams of length $(a+c/\sqrt{2})$. The half beams have different widths equal to $0.5(w\pm c/\sqrt{2})$. A sliding displacement δ causes outward and downward displacements of the centre of the beam, bending the beam and causing alternate compression and extension in the lower and upper halves respectively, storing elastic energy.

The extent of sliding is calculated by minimizing the elastic energy in the system with respect to δ . Theoretically, minimization should first be done with respect to θ , but experiments by Ashby and Hallam (1986) indicate the simplification $\theta=45^\circ$ is not only numerically desirable (outward and downward displacements, δ_n , are equal) but also preserves the most critical case.

A uniaxially compressive field stress σ_1 is applied with the crack welded shut. The crack is then gradually relaxed and allowed to slide through a displacement of 2δ , bending the beam outward.

The change in elastic energy of one beam is:

$$U = \frac{bt^3\delta_n^2 E}{\left(a + \frac{c}{\sqrt{2}}\right)^3} + \sigma_1 bt \delta_n \left(\frac{\delta_n E}{\sigma_1 \left(a + \frac{c}{\sqrt{2}}\right)} - \frac{c}{t\sqrt{2}} \right) \quad [\text{D.26}]$$

Minimizing with respect to δ_n gives:

$$\delta_n = \frac{\sigma_1 c}{2\sqrt{2}Et} \left(\frac{a + \frac{c}{\sqrt{2}}}{1 + \frac{t^2}{\left(a + \frac{c}{\sqrt{2}}\right)^2}} \right) \quad [\text{D.27}]$$

replacing this result in Equation D.26 and minimizing with respect to a (assuming $t^2/a^2 \ll 1$) gives the crack driving force:

$$G = -\frac{1}{b} \frac{dU}{da} = \frac{1}{4} \frac{\sigma_1^2 c^2}{E 2t} \quad [\text{D.28}]$$

and the associated stress intensity increment due to the presence of the surface under σ_1 (compression positive) is:

$$K_t^{surf(\sigma_1)} = \sqrt{EG} = \frac{1}{2\sqrt{2}\pi} \left(\frac{c}{t}\right)^{0.5} \sigma_1 \sqrt{\pi c} \quad [\text{D.29}]$$

A confining stress, σ_3 , applies a distributed load ($\sigma_3 b$ per unit length) to the outer surfaces of the beam. This generates a moment, m_3 :

$$m_3 = -2\sigma_3 b \left(a + \frac{c}{\sqrt{2}}\right)^2 \left[\left(\frac{x}{2\left(a + \frac{c}{\sqrt{2}}\right)} \right)^2 - \frac{x}{2\left(a + \frac{c}{\sqrt{2}}\right)} + \frac{1}{6} \right] \quad [\text{D.30}]$$

where x is measured from one end of the beam. The energy in the beam (upper and lower halves) due to this moment is:

$$U_3 = \frac{1}{2EI} \int_0^{2(a+c)} m_3^2 dx = \frac{\sigma_3^2 b^2 \left(a + \frac{c}{\sqrt{2}}\right)^5}{54EI} \quad [\text{D.31}]$$

The crack driving force is:

$$G = \frac{1}{b} \frac{dU}{da} = \frac{4}{3} \frac{\sigma_3^2}{Et^3} \left(a + \frac{c}{\sqrt{2}} \right)^4 \quad [\text{D.32}]$$

giving a contribution to K_I of :

$$K_I^{surf(\sigma_1)} = \sqrt{EG} = -\sigma_3 \left(\frac{4}{3\pi} \right)^{1/2} \left(\frac{c}{t\sqrt{2}} \right)^{3/2} \left(L + \frac{1}{\sqrt{2}} \right)^2 \sqrt{\pi c} \quad [\text{D.33}]$$

so that:

$$K_I^{surf} = K_I^{surf(\sigma_1)} + K_I^{surf(\sigma_3)} \quad [\text{D.34}]$$

This result, K_I^{surf} , is subject to a multiplier, f , to account for buckling as the crack grows large and σ_I increases to create an end load in the beam, P , approaching:

$$P_{crit} = \frac{\pi^2 EI}{(1 + c\sqrt{2})^2} \quad [\text{D.35}]$$

A perfectly straight, uniform beam buckles catastrophically while one which is already bent collapses progressively so that the deflections become increasingly large as P approaches P_{crit} . Assuming a linear (first order) progression to this progressive collapse, the multiplying factor becomes:

$$f = \frac{1}{1 - \frac{P}{P_{crit}}} = \frac{1}{1 - \frac{12}{\pi^2} \frac{\left(a + \frac{c}{\sqrt{2}} \right)^2}{t^2} \frac{\sigma_1}{E}} \quad [\text{D.36}]$$

multiplying this factor by the right side of Equation D.34, substituting for the two component intensities and using $\lambda = \sigma_3/\sigma_1$ and $L = a/c$ gives:

$$K_I^{surf} = \frac{1}{2\sqrt{2}\pi} \left(\frac{c}{t} \right)^{1/2} \sigma_1 \sqrt{\pi c} \left(\frac{1 - \frac{4}{\sqrt{3}\sqrt{2}} \frac{c}{t} \left(L + \frac{1}{\sqrt{2}} \right)^2 \lambda}{1 - \frac{12}{\pi^2} \frac{c^2}{t^2} \left(L + \frac{1}{\sqrt{2}} \right)^2 \frac{\sigma_1}{E}} \right) \quad [\text{D.37}]$$

the result used in Section 8.6 of this thesis. The total stress intensity, K_I , is the sum of Equations D.37 and D.25.